materials

Special Issue Reprint

Testing of Materials and Elements in Civil Engineering (2nd Edition) Volume I

Edited by
Krzysztof Schabowicz

www.mdpi.com/journal/materials

MDPI

Testing of Materials and Elements in Civil Engineering (2nd Edition) —Volume I

Testing of Materials and Elements in Civil Engineering (2nd Edition) —Volume I

Editor

Krzysztof Schabowicz

MDPI • Basel • Beijing • Wuhan • Barcelona • Belgrade • Manchester • Tokyo • Cluj • Tianjin

Editor
Krzysztof Schabowicz
Wroclaw University of
Science and Technology
Poland

Editorial Office
MDPI
St. Alban-Anlage 66
4052 Basel, Switzerland

This is a reprint of articles from the Special Issue published online in the open access journal *Materials* (ISSN 1996-1944) (available at: https://www.mdpi.com/journal/materials/special_issues/testing_civil_engineering_2nd).

For citation purposes, cite each article independently as indicated on the article page online and as indicated below:

LastName, A.A.; LastName, B.B.; LastName, C.C. Article Title. *Journal Name* **Year**, *Volume Number*, Page Range.

Volume I
ISBN 978-3-0365-7888-0 (Hbk)
ISBN 978-3-0365-7889-7 (PDF)

Volume I-II
ISBN 978-3-0365-6654-2 (Hbk)
ISBN 978-3-0365-6655-9 (PDF)

Contents

About the Editor

Krzysztof Schabowicz

Krzysztof Schabowicz is author and co-author of 7 books, over 300 publications and 10 patents and has more than 1000 citations in the Web of Science. He serves as an Editor of *Materials* (MDPI) and Editorial Board member of *Civil Engineering and Architecture* (HRPUB) and *Nondestructive Testing and Diagnostics* (SIMP). He has developed more than 300 reviews of journal and conference articles. He is co-author of 10 patents and 1 patent application and is a member of the Polish Association of Civil Engineers and Technicians (PZITB) and of the Polish Association of Building Mycology (PSMB). His research interests include concrete, fiber-cement, ultrasonic tomography, impact-echo, impulse-response, GPR and other non-destructive tests, and artificial intelligence, among others.

Preface to "Testing of Materials and Elements in Civil Engineering (2nd Edition) —Volume I"

Last year, we ran a successful Special Issue on "Testing of Materials and Elements in Civil Engineering", with over 50 papers published. The field of materials testing in civil engineering is very wide and interesting from an engineering and scientific point of view. Therefore, we have decided make a second edition dedicated to this topic.

This new Issue is proposed and organized as a means to present recent developments in the field of materials testing in civil engineering. The articles highlighted in this Issue should relate to different aspects of the testing of different materials in civil engineering, from building materials and elements to building structures. The current trend in the development of materials testing in civil engineering is mainly concerned with the detection of flaws and defects in elements and structures using destructive, semidestructive, and nondestructive testing.

The topics of interest include but are not limited to:

- Testing of materials and elements in civil engineering;
- Testing of structures made of novel materials;
- Condition assessment of civil materials and elements;
- Detecting defects that are invisible on the surface;
- Damage detection and damage imaging;
- Diagnostics of cultural heritage monuments;
- Structural health monitoring systems;
- Modeling and numerical analyses;
- Nondestructive testing methods;
- Advanced signal processing for nondestructive testing.

Krzysztof Schabowicz
Editor

materials

MDPI

Article

Analysis of the Frequency of Acoustic Emission Events in Terms of the Assessment of the Reduction of Mechanical Parameters of Cellulose–Cement Composites

Anna Adamczak-Bugno *, Aleksandra Krampikowska and Grzegorz Świt

Faculty of Civil Engineering and Architecture, Kielce University of Technology, 25-314 Kielce, Poland; akramp@tu.kielce.pl (A.K.); gswit@tu.kielce.pl (G.Ś.)
* Correspondence: aadamczak@tu.kielce.pl

Abstract: The article proposes the application of the acoustic emission method as a technique for the evaluation of mechanical parameters of cellulose–cement composites. The analysis focused on frequency values in a time series analysis of elements subject to three-point flexural stress. In the course of a statistic analysis, it has been demonstrated that a significant reduction of the recorded frequency values is associated with a considerable reduction in strength. This allowed the authors to determine the range of frequencies related to the depreciation in the strength of an element. The tests were carried out on elements cut from a full-size cellulose–cement board. Samples exposed to potential operational factors (environmental and exceptional) were analysed. It was shown that the frequencies recorded before reaching the maximum load during bending of samples exposed to environmental factors (water and low temperature) were significantly different (were much lower) from the sounds emitted by elements subjected to exceptional factors (fire and high temperature). Considering the fact that the analysed frequencies of acoustic emission events occur before the maximum stresses in the material are reached and the elements are destroyed, this provides the basis for the use of the acoustic emission method to assess the condition of cellulose–cement composites in terms of lowering mechanical parameters by observing the frequency of events generated by the material during load action. It was found that generating by material frequencies above 300 kHz during bending does not result in a significant decrease in mechanical parameters. The emission of signals with frequencies ranging from 200 to 300 kHz indicate that there was a decline in strength exceeding 25% but less than 50%. The registration of signals with frequencies below 200 kHz indicates that the reduction in mechanical parameters was greater than 50%.

Keywords: cement–cellulose composites; ventilated façade; acoustic emission method; frequencies of acoustic emission signals

Citation: Adamczak-Bugno, A.; Krampikowska, A.; Świt, G. Analysis of the Frequency of Acoustic Emission Events in Terms of the Assessment of the Reduction of Mechanical Parameters of Cellulose–Cement Composites. *Materials* **2021**, *14*, 5882. https://doi.org/10.3390/ma14195882

Academic Editors: Krzysztof Schabowicz and F. Pacheco Torgal

Received: 14 September 2021
Accepted: 4 October 2021
Published: 8 October 2021

1. Introduction

Building materials produced on the basis of cement reinforced with organic fibres have been used in the building industry for over a century. It is believed that this type of material was invented by Ludwik Hatschek, a Czech engineer who patented the methodology of manufacturing panels known as 'Eternit'. Cement elements with an additive of asbestos fibres exhibited relatively high strength parameters, while also being non-absorbent and non-flammable [1–8]. Those very features made Eternit one of the most popular types of roofing in the 1980s and 1990s. Their popularity decreased when it was revealed that asbestos fibres have carcinogenic properties. From then on, efforts have been undertaken to develop a replacement technology. Over the course of the performed research, cement matrices were strengthened using various types of organic fibres, variable, e.g., by origin or length [9–12].

One of the most common fibrous cement composite products are panels based on a cement matrix reinforced with cellulose fibres. These panels, apart from Portland cement

and organic fibres, can also contain synthetic fibres as well as special additives or admixtures, which improve their strength and performance parameters [13–17].

Most cellulose–cement panels are designed for internal and external use (e.g., as siding elements in ventilated facade systems). Due to working conditions present in the case of their external use, as facade elements, it is necessary to determine the effect of any potential operating factors on the parameters of the boards. Many literature sources cite examples that demonstrate the deterioration of aesthetics as well as of the mechanical parameters of the panels due to the impact of external conditions [18–22]. Due to the fact that cellulose–cement panels are currently also used in buildings classified as tall buildings and high-rise buildings, for safety reasons, it is necessary to develop a method which would facilitate the determination of the actual condition of the panels during their routine inspections. This would help to eliminate any possibility of façade siding elements falling down from the building, resulting in personal and material hazards [23–28].

The operating conditions of cellulose–cement panels primarily include the effects of water and moisture, resulting in the cyclical soaking and drying of the panels, as well as the regular changes between above-zero and sub-zero temperatures. In addition, when analysing the service life of the boards, the possible occurrence of exceptional conditions must be taken into consideration, among which the effects of fire and high temperatures seem the most destructive [29–34].

Considering that cellulose–cement panels must be inspected at the site of their installation, it is necessary to develop a non-destructive methodology that would enable their monitoring, preferably remotely. The acoustic emission method is the one which is becoming increasingly popular when used to this end, as it allows for the observation of load-related active destructive processes in materials. Acoustic emission has been successfully implemented as a research methodology for the diagnosis of engineering structures made of concrete and steel. The results of tests performed on cellulose–cement panels have also been documented in literature. Previous analyses were performed using neural networks as well as the acoustic emission method, with the application of the energy-related and time/frequency-related approach [35–40].

The implementation of the abovementioned models in the context of the acoustic emission method requires the performance of analyses using specialised software, the so-called artificial intelligence, to facilitate the learning of neural networks, the classification of AE signals, as well as the performance of a time and frequency analysis. However, based on the performed research, the authors have observed that the frequency of events is one of the most variable parameters of acoustic emission, sensitive to changes in the mechanical parameters of a material. Therefore, they performed an analysis that allowed them to determine the significance of these changes and to associate them with a specific degree of reduction of the strength of cellulose–cement elements [41–43].

Testing the dynamic parameters of composites is an issue widely described in the literature in relation to composite layered structures [44] and GFRP composites [45]. Due to the use of modern research techniques and computer methods, it is possible to accurately assess the influence of geometric parameters of an element on mechanical indicators both in static and fatigue tests [44,45].

The basic research question posed by the authors concerned checking whether the frequencies of acoustic emission events are related to the mechanical parameters of composites, and if so, whether the relationship between them is statistically significant. The next question was to check how the potential operating conditions affect the mechanical parameters and frequency of acoustic emission events.

The authors decided to observe the frequency of AE events emitted by cellulose-cement composites because in other publications, this parameter allowed for the tracking of changes in mechanical parameters in brittle materials [46,47].

The novelty of the research carried out consists in the observation of one selected energetic parameter of the acoustic emission. In previous publications on cellulose–cement composites, the use of the AE method was associated with the procedure of teaching

neural networks or unsupervised signal classification, which requires specialised software and skills. The AE event frequency analysis can be performed immediately after the measurement and even during the measurement without the need to transfer data, which significantly extends the availability of the acoustic emission method as a tool for assessing changes in mechanical parameters in cellulose–cement composites.

The main benefit of the present research study for researchers and users concerns the ability to refer, when assessing the mechanical parameters by observing the frequency of AE events, to the results obtained for samples of cement–cellulose composites exposed to potential operational factors. The presented results and the criteria proposed in the conclusion were also confirmed during other analyses, which concerned the classification of 14 parameters of AE events, the observation of time–frequency spectra, and the study of the microstructure of the material. According to the authors, the proposed research procedure is the basis for the creation of simplified guidelines enabling the inspection of the condition of cellulose–cement composites without the need to use specialised analysis software.

2. Materials and Methods

The tests were performed on elements cut out of full-size cellulose–cement panels. Cuboidal samples of the dimensions of 300 × 50 × 8 m^3 were cut out of stock panels of the dimensions of 1.25 × 3.10 m^2, 8 mm in thickness. The samples were cut parallel to the length of the panels. A 50 mm marginal zone of the panels was omitted during preparatory work. A view of the test stand is shown in Figure 1.

Following the tests, frequency values in the analysed time series for the tested elements were monitored. In addition, changes of the loading force F in time were also observed.

On the basis of the completed preliminary tests, it was confirmed that cellulose–cement panels demonstrated the mechanical parameters declared by the manufacturer. The chemical formula of the panels and the details of their technological process are patent-protected, and any information referring to the specific components, their quantities and suppliers, as well as any production details are very restricted. According to the manufacturer's declaration, the tested fibre-cement panels were made using basic components such as: Portland cement CEM I 42.5N, cellulose fibres, or PVA synthetic fibres. The elements also contained an additive in the form of lime powder. The manufacturing process of the panels was based on Hatschek's process. The scope of application of the panels was declared by the manufacturer as indoor and outdoor. The average technical parameters declared by the manufacturer of the panels are included in Table 1.

Table 1. The declared average technical parameters of the boards.

Density	Dry state	PN-EN 12467	≥1.58	g/cm^3
Flexural Strength	Perpendicular	PN-EN 12467	25.0	N/mm^2
Flexural Strength	In parallel	PN-EN 12467	18.0	N/mm^2
Modulus of Elasticity		PN-EN 12467	12,000	N/mm^2
Stretching with Humidity	30–95%		1.0	mm/m
Porosity	0–100%		<18	%

The tests were performed on cellulose–cement panels operating in conditions of an environmental and exceptional nature. The following research cases have been identified:

- air-dry condition;
- saturation with water for 1 h;
- saturation with water for 24 h;
- 25 bathing–drying cycles;
- 50 bathing–drying cycles;
- 10 freezing–unfreezing cycles;
- 25 freezing–unfreezing cycles;
- 50 freezing–unfreezing cycles;
- 100 freezing–unfreezing cycles;

- direct contact with a flame for 2.5 min;
- direct contact with a flame for 5 min;
- direct contact with a flame for 7.5 min;
- direct contact with a flame for 10 min; and
- contact with the temperature of 230 °C for 3 h.

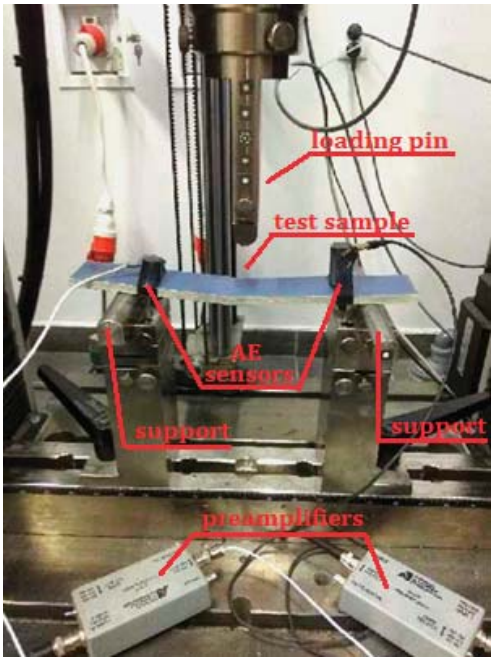

(**a**)

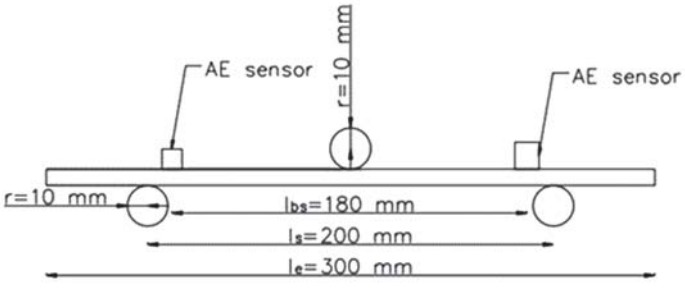

(**b**)

Figure 1. Test stand diagram: (**a**) a photograph of one of the samples and (**b**) the load diagram.

Panels in the first case P_1—the reference case—were stored in the conditions of constant temperature and humidity (+23 °C, 60% humidity). This case was considered as a benchmark.

Samples from series $P_2 \div P_3$ were submerged in water of room temperature (approximately 23 °C) for a period of 1 and 24 h, upon which they were subjected to wet flexure tests.

Bathing and drying cycles (cases $P_4 \div P_5$) were performed by alternately submerging the samples in water of an ambient temperature higher than 5 °C (approximately 23 °C) for 18 h and drying them in a ventilated drier at a temperature of 60 °C (±5 °C) and relative

humidity lower than 20% for 6 h; the number of cycles depended on the research case (P_4—25 cycles; P_5—50 cycles).

Cyclical freezing and unfreezing (cases $P_6 \div P_9$) was performed in a specific air-water environment via alternate cooling (freezing) in a freezer, in a temperature of −20 °C (±2 °C) for 2 h and this temperature was maintained for another hour, followed by subsequent heating (unfreezing) in a water bath at a temperature of 20 °C (±2 °C) for two hours and this temperature was maintained for another hour. During the cooling and heating cycles (freezing and unfreezing), the samples were positioned in a manner that ensured free circulation of the conductive medium (air in the freezer or water in the bath).

The baking of the fibre-cement panels took place in a laboratory oven (Kedndrolab, Warsaw, Poland) at a temperature of 230 °C. The duration of the baking was 3 h, which led to the total destruction of the fibres in the material.

The impact of fire is an exceptional factor that involves exposure to high temperatures which occur in the case of events such as a building fire. The process of the destruction of fibre-cement panels involved the direct application of a flame, resulting in the surface temperature of the panel reaching approximately 400 °C for a time of 2.5 to 10 min, recorded at 2.5-min intervals (cases $P_{10} \div P_{13}$).

Table 2 presents a list of test cases of cellulose–cement composites with the adopted sample designation.

Table 2. Table of research cases of cellulose–cement composites with the adopted sample designation.

Case No.	Test Case	Designation
1.	Air-dry condition	P_1
2.	Saturation with water for 1 h	P_2
3.	Saturation with water for 24 h	P_3
4.	25 bathing–drying cycles	P_4
5.	50 bathing–drying cycles	P_5
6.	10 freezing–unfreezing cycles	P_6
7.	25 freezing–unfreezing cycles	P_7
8.	50 freezing–unfreezing cycles	P_8
9.	100 freezing–unfreezing cycles	P_9
10.	Direct contact with a flame for 2.5 min	P_{10}
11.	Direct contact with a flame for 5 min	P_{11}
12.	Direct contact with a flame for 7.5 min	P_{12}
13.	Direct contact with a flame for 10 min	P_{13}
14.	Contact with the temperature of 230 °C for 3 h	P_{14}

Each research case included 10 samples. The static scheme and the dimensional proportions of the samples were adopted in accordance with [48], product specification and test methods.

Flexural tests of cement-fibre composites were performed using a Zwick Roell strength testing machine with a loading range of 0 to 10 kN. When testing fibre-cement samples, a constant increment in the crossbar movement was set at 0.1 mm/min. The spacing of supports in the machine was 200 mm and the force was applied axially.

The measurements of the acoustic emission used two frequency sensors: VS30-SIC (Vallen Systeme GmbH, Wolfratshausen, Germany) with flat characteristics in a range of 25–80 kHz, and VS150-RIC (Vallen Systeme GmbH, Wolfratshausen, Germany), with a measuring range of 100–450 kHz and a peak frequency of 150 kHz, alongside a 28 V AE signal preamplifier operating in three ranges: 20, 40, and 60 dB. In the preamplifier, the AE signal from the sensor was amplified and transmitted to an AE processor, where preliminary filtration was performed in order to eliminate the acoustic background originating from the surroundings of the monitored element. Subsequently, the signal was transformed into digital form. Further processing of the digital data was carried out using AE signal analysing software: Vallen VisualAE and Vallen VisualClass.

Sensors recording the signals were placed in close proximity to the supports. The indicated locations of the sensors were selected in view of the relatively small dimensions of the sample and to ensure repetitiveness of the provided results. In each measurement case, the surface of the sensors was covered with silicone gel in order to achieve a better coupling between these elements. Pilot tests confirmed the correctness of the registration of the signals with the method of installation of the AE sensor as described above. As a standard benchmark, the Hsu–Nielsen pencil test (fracturing of the lead core of a 2 H pencil) was used to verify the correct operation of the sensors and the apparatus.

The application of the acoustic emission method during the three-point flexural test of fibre-cement panels facilitated the evaluation of changes in the mechanical parameters of these composites by associating the frequency of AE signals with the destructive processes taking place in the material, which gradually proceeded during bending.

3. Results

During the three-point bending tests, various mechanisms of sample destruction were observed. Elements in the air-dry state, soaked in water, subjected to cyclic bath-drying, and cyclically frozen–thawed (research cases P_1–P_9) due to the presence of reinforcing fibres deteriorated due to exceeding tensile stresses (damage was associated with a decrease in loads without breaking the sample). In the case of samples set on fire and fired in the furnace (cases P_{10}–P_{14}), a brittle mechanism of destruction was observed, specifically high energy, sudden fracture, and breakage of the samples into two parts.

Following the completion of the tests, the frequency values of AE signals in the analysed time series were monitored for the tested elements. In addition, the maximum values of loading force F were analysed for each sample.

With regard to samples from research cases P_1–P_9 (Figures 2–10), the occurrence of the highest frequencies with values up to 5×10^4–10×10^4 kHz was recorded at the time of the sample-breaking. Before reaching the maximum stress, the frequencies in the range of 10–870 kHz were recorded.

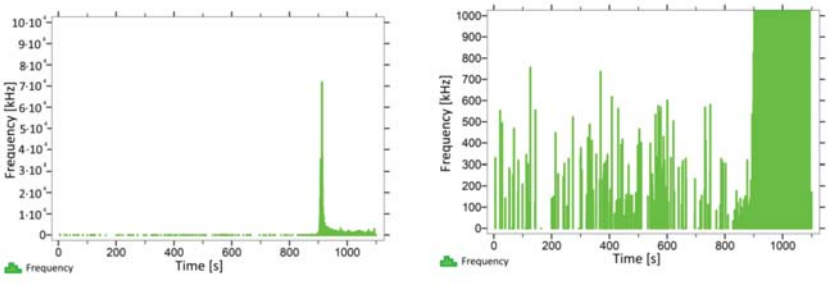

Figure 2. Graph of frequency distribution during the test for a representative sample from series P_1: (**a**) considering the entire occurring frequency range and (**b**) with details about the frequency range before the moment of breakage.

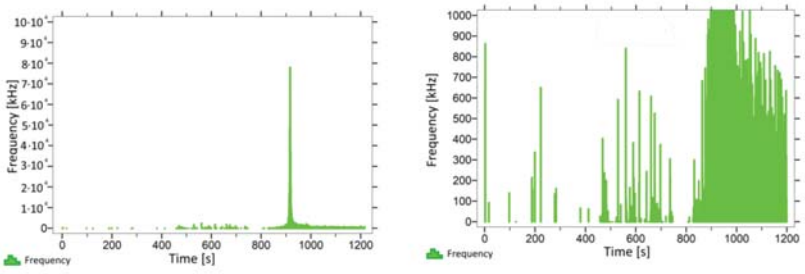

Figure 3. Graph of frequency distribution during the test for a representative sample from series P_2: (**a**) considering the entire occurring frequency range and (**b**) with details about the frequency range before the moment of breakage.

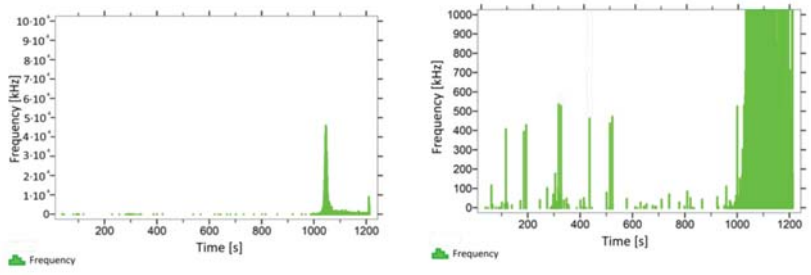

Figure 4. Graph of frequency distribution during the test for a representative sample from series P_3: (**a**) considering the entire occurring frequency range and (**b**) with details about the frequency range before the moment of breakage.

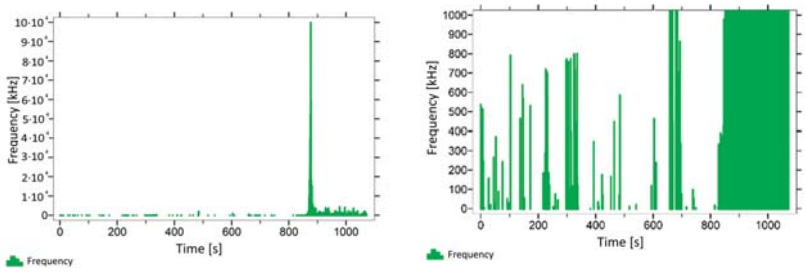

Figure 5. Graph of frequency distribution during the test for a representative sample from series P_4: (**a**) considering the entire occurring frequency range and (**b**) with details about the frequency range before the moment of breakage.

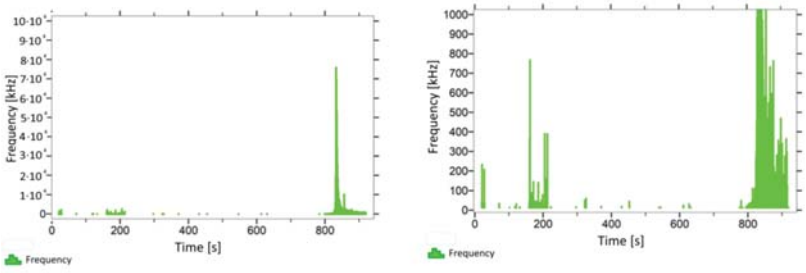

Figure 6. Graph of frequency distribution during the test for a representative sample from series P_5: (**a**) considering the entire occurring frequency range and (**b**) with details about the frequency range before the moment of breakage.

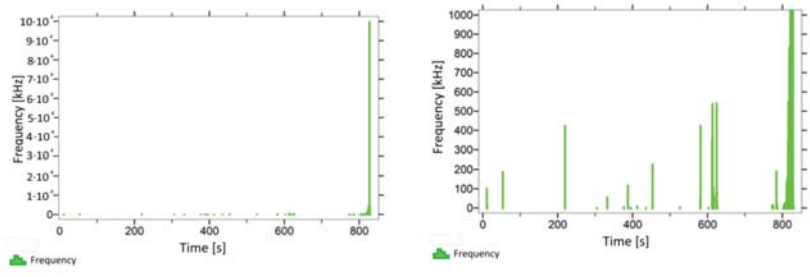

Figure 7. Graph of frequency distribution during the test for a representative sample from series P_6: (**a**) considering the entire occurring frequency range and (**b**) with details about the frequency range before the moment of breakage.

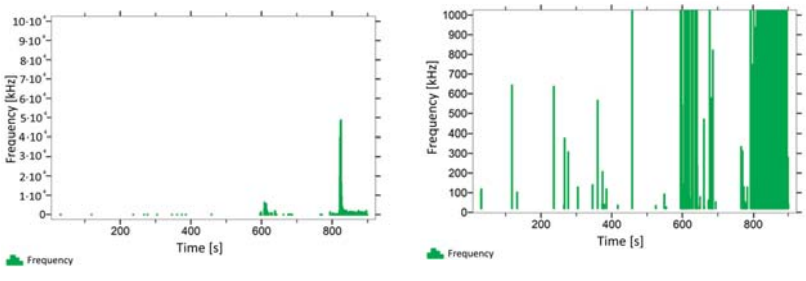

Figure 8. Graph of frequency distribution during the test for a representative sample from series P_7: (**a**) considering the entire occurring frequency range and (**b**) with details about the frequency range before the moment of breakage.

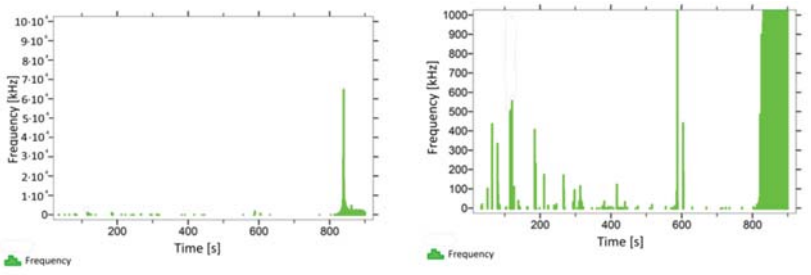

Figure 9. Graph of frequency distribution during the test for a representative sample from series P_8: (**a**) considering the entire occurring frequency range and (**b**) with details about the frequency range before the moment of breakage.

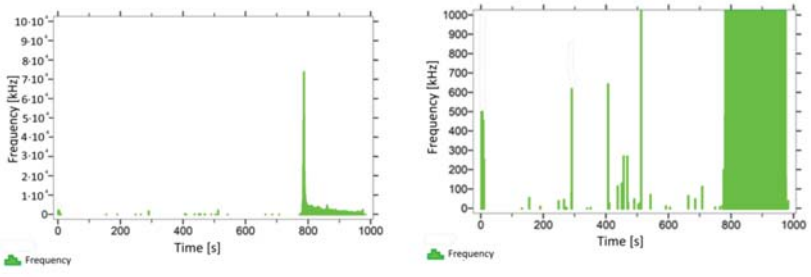

Figure 10. Graph of frequency distribution during the test for a representative sample from series P_9: (**a**) considering the entire occurring frequency range and (**b**) with details about the frequency range before the moment of breakage.

With regard to the exemplary sample from the research case P_{10} (Figure 11), the occurrence of the highest frequencies with values up to 3×10^4 kHz was recorded at the moment of the sample-breaking. Prior to reaching the maximum stress, frequencies mainly in the 5–400 kHz range were recorded.

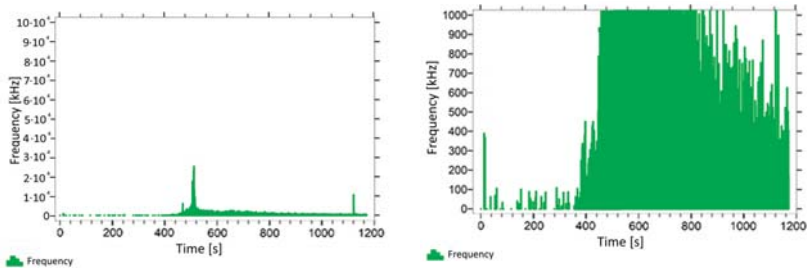

Figure 11. Graph of frequency distribution during the test for a representative sample from series P_{10}: (**a**) considering the entire occurring frequency range and (**b**) with details about the frequency range before the moment of breakage.

With regard to the samples from test cases A_{11}–P_{14} (Figures 12–15), the frequencies did not exceed the value of 1×10^4 kHz in the entire analysed waveform. Prior to reaching the maximum stresses, the frequencies mainly in the 5–190 kHz range were recorded.

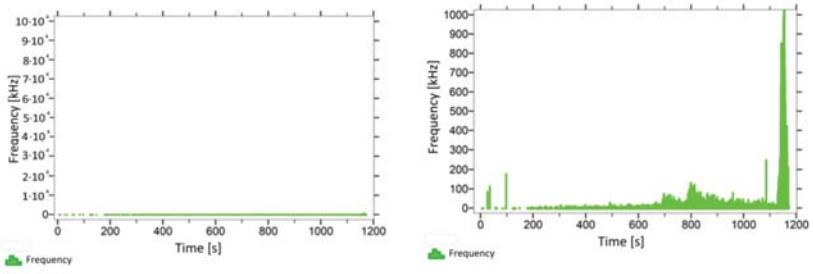

Figure 12. Graph of frequency distribution during the test for a representative sample from series P_{11}: (**a**) considering the entire occurring frequency range and (**b**) with details about the frequency range before the moment of breakage.

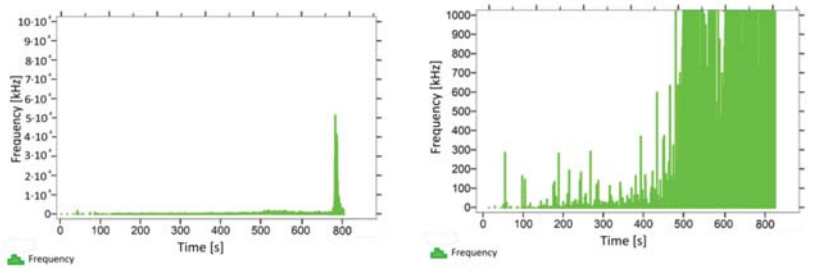

Figure 13. Graph of frequency distribution during the test for a representative sample from series P_{12}: (**a**) considering the entire occurring frequency range and (**b**) with details about the frequency range before the moment of breakage.

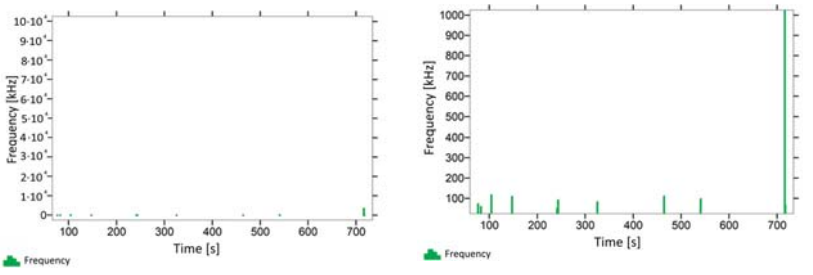

Figure 14. Graph of frequency distribution during the test for a representative sample from series P_{13}: (**a**) considering the entire occurring frequency range and (**b**) with details about the frequency range before the moment of breakage.

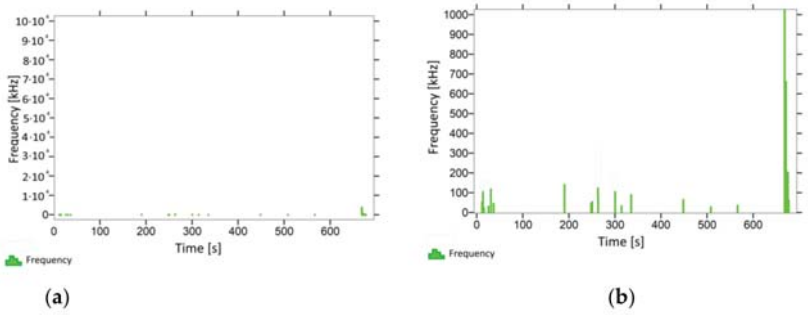

Figure 15. Graph of frequency distribution during the test for a representative sample from series P_{14}: (**a**) considering the entire occurring frequency range and (**b**) with details about the frequency range before the moment of breakage.

3.1. Frequencies Analysis Results

3.2. Statistical Analysis of the Obtained Results

A statistical analysis of the obtained test results was performed in order to verify the usefulness of the analysis of the frequency of acoustic emission events for the purposes of the assessment of the deterioration of the mechanical parameters of cellulose–cement composites. During its first stage, this analysis involved a comparison of the results obtained for samples from the individual test cases with respect to specific quantitative variables. In the next step, the relationships between the indicated changes were examined (the significance of correlations was checked), followed by the use of classification trees utilising the CHAID algorithm to divide the results obtained for an analysed parameter within a given group and to determine any significant changes of these parameters. In order to confirm the possibility of using the frequencies accompanying changes in the mechanical parameters of cellulose–cement composites in the analysis, group-classifying data was used, with a subsequent performance of a test which compared the frequency distribution in the resulting groups in relation to the mechanical parameters of the samples.

The analysis utilised the IBM SPSS Statistics 26 software. The value of 0.05 was adopted as the significance level. The Shapiro–Wilk test was chosen for the analysis of the normality of distributions, while Levene's test was used to examine the homogeneity of variances. Due to the absence of normal distribution for certain data and considering the lack of homogeneity of variances in most cases, a group of non-parametric tests for independent variables was used to mutually compare the average distributions, particularly the Kruskal–Wallis test for multiple groups.

At first, appropriate tests were performed for all data in order to select suitable groups of tests for the analysis of the data. The analysed groups were approximately equinumerous. Therefore, normal distributions of data in the individual groups were analysed using the Shapiro–Wilk test. In the case of most data, no reasons were found to reject the hypothesis of the normal distribution; however, there were cases in which the data did not have a normal distribution.

The absence of homogeneous variances was observed in most of the groups. Therefore, in order to analyse the distributions, a decision was made to use the non-parametric Kruskal–Wallis test for independent variables.

3.2.1. Kruskal–Wallis Test Results for Independent Samples: Average Frequency of AE Events before Reaching F_{max}

When analysing the graphic presentation of the Kruskal–Wallis test results for independent samples, expressed by the average frequency of AE events before reaching F_{max} (Figure 16), we could observe that the maximum average frequency of signals was recorded for elements of research case P_1 (samples in an air-dry condition). Additionally, this case had the widest dispersion of results. Research cases P_{11} (samples ignited for 5 min) and P_{13}

(samples ignited for 10 min) contained singular data which can be considered as statistical outliers. The lowest values of the average frequency of AE events before reaching Fmax were recorded for case P_{14} (the baked samples).

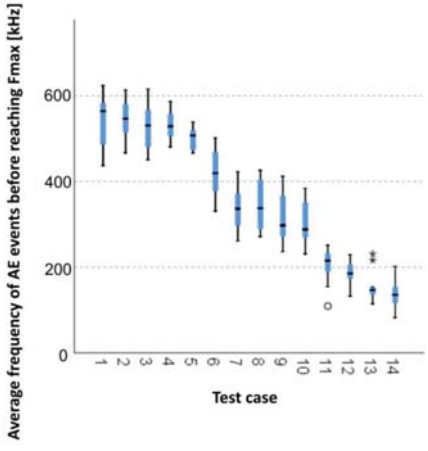

Figure 16. Graphic presentation of the Kruskal–Wallis test results for independent samples: average frequency of AE events before reaching F_{max}.

3.2.2. Kruskal–Wallis Test Results for Independent Samples of the Breaking Force F_{max}

When analysing the graphic presentation of the Kruskal–Wallis test results for the independent testing of the breaking force F_{max} (Figure 17), we could observe that the maximum breaking force was recorded for elements from research case P_5 (samples subjected to bathing and drying in 50 cycles). Additionally, this case had the widest dispersion of results. Research cases P_{11} (samples ignited for 5 min) and P_{12} (samples ignited for 7.5 min) contained singular data which can be considered as statistical outliers. The lowest values of breaking force F_{max} were recorded for case P_{13} (samples ignited for 10 min).

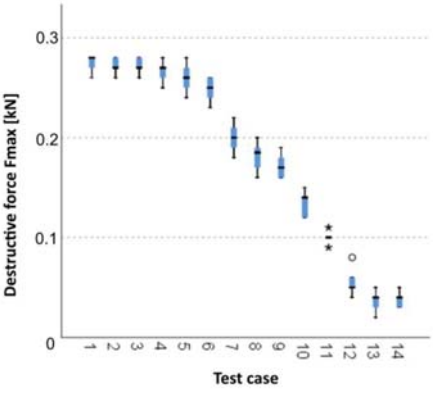

Figure 17. Graphic presentation of the Kruskal–Wallis test results for independent samples of the breaking force F_{max}.

3.2.3. Classification Trees

Classification trees utilising the CHAID algorithm were used in order to check the significance of the changes occurring in the parameters (frequency and breaking force).

1. Average frequency of AE events before reaching F_{max}:

Five groups were identified (Figure 18). With each consecutive group, there was a significant reduction of the average frequency of AE events:

- Group 1, 2, 3, and 4;
- Group 5 and 6;
- Group 7, 8, and 9;
- Group 10 and 11; and
- Group 12, 13, and 14.

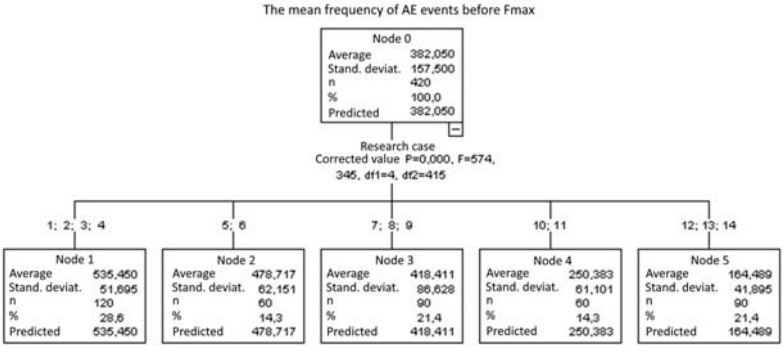

Figure 18. Classification tree for the average frequency of AE events before reaching F_{max}.

2. Breaking force F_{max}:

Five groups were identified (Figure 19). With each consecutive group, there was a significant reduction of the F_{max} breaking force:

- Group 1, 2, and 3;
- Group 4 and 6;
- Group 5, 7, 8, and 9;
- Group 10 and 11; and
- Group 12, 13, and 14.

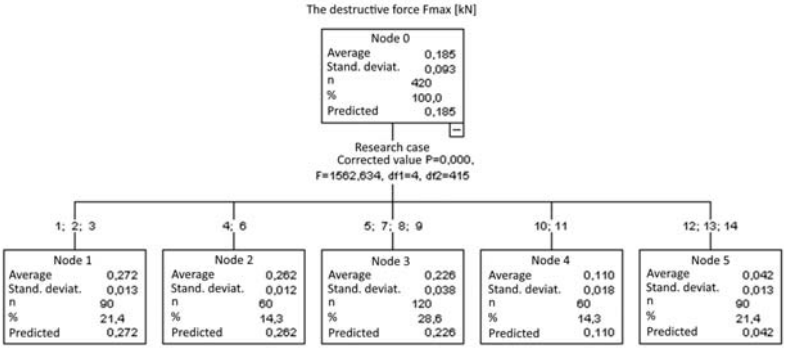

Figure 19. Classification tree for the breaking force F_{max}.

3.2.4. Kruskal–Wallis Test for Independent Samples: Average Frequency of AE Events before Reaching F_{max} and the Breaking Force F_{max}

Data used for the formation of groups in terms of changes in mechanical parameters obtained by means of classification trees was used to check the correlation of frequency changes with changes in mechanical parameters. An appropriate test that compared frequency distributions in these groups was selected: on each occasion, due to the absence of a normal distribution of frequencies in the individual groups, the non-parametric Kruskal–Wallis test was chosen. Mean values for each group were compared and, subsequently,

confidence intervals were also assessed for the mean values (whether they overlapped each other). The Bonferroni test was used as a post-hoc test.

Five groups were identified (Figure 20). With each consecutive group, there was a significant reduction of the F_{max} breaking force:

- Group 1: 1, 2, and 3;
- Group 2: 4 and 6;
- Group 3: 5, 7, 8, and 9;
- Group 4: 10 and 11; and
- Group 5: 12, 13, and 14.

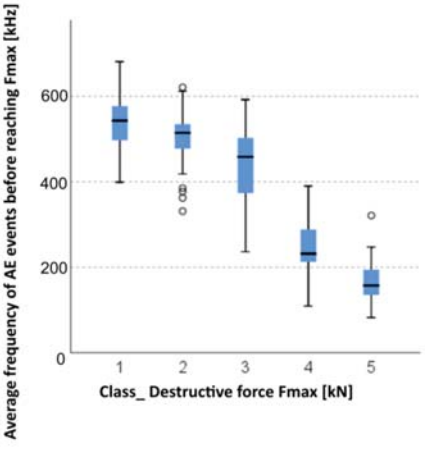

Figure 20. Graphic presentation of the Kruskal–Wallis test for independent samples: average frequency of AE events before reaching F_{max} and the breaking force F_{max}.

The absence of a normal distribution was observed for the data. Therefore, the non-parametric Kruskal–Wallis test was chosen. At first, descriptive statistics were found for the groups. The Kruskal–Wallis test statistics $T = 327.370$, $p = 0.000$, and thus the frequencies in groups differed from each other in a statistically significant manner. The post-hoc Bonferroni test was performed in the second phase. In each case, between any two groups, the results differed from each other in a statistically significant manner. In each subsequent group, the frequencies were significantly lower (Figure 20). Moreover, we could observe that, although the frequency intervals overlappws each other (min/max), confidence intervals for the mean value did not overlap each other.

4. Discussion

When analysing the graphs shown in Figures 2–15, we can observe that subjecting the tested elements to two groups of operating conditions (environmental and exceptional) resulted in significant differences in the emitted frequency ranges. Changes in the mechanical parameters of samples operating in an air-dry condition, saturated with water, subjected to cyclical baths and drying, as well as cyclically frozen and unfrozen during external loading are associated with the emission of low-frequency signals of up to 200 kHz and high-frequency signals of even up to 800 kHz. Most of the recorded frequencies exceeded the 200 kHz threshold and certain events generated sounds at a level of 500–800 kHz. An opposite situation occurred in the case of samples ignited for a time longer than 2.5 min or baked. The flexure of elements subjected to the impact of temperature caused events with considerably lower frequencies, only some of which exceeded a value of 100 kHz.

Based on the completed statistical analysis, it was demonstrated that some of the operating conditions, namely cyclical freezing–unfreezing, igniting with a flame, and baking at a temperature of 230 °C, which were applied to the cellulose–cement elements,

have a significant effect on the change of the mechanical parameters. Conversely, the reduction in the strength of the panels was strictly related to a change in the acoustic characteristics registered during bending, in this case, identified with the average frequency of events before reaching F_{max}. The performed statistical analysis allowed the authors to confirm the usefulness of the acoustic emission method in the assessment of changes in mechanical parameters of fibre-cement composites.

5. Conclusions

Considering the results of the tests and the performed statistical analysis, as well as the resultant preliminary conclusions indicating the usefulness of the acoustic emission method for the assessment of changes in the mechanical parameters of cellulose–cement composites, it was concluded that:

- an analysis of the frequency of AE events can be the basis for assessing the condition of cement–cellulose boards;
- an analysis of the obtained measurement results using the acoustic emission method enables the determination and assessment of the degree of changes in the mechanical parameters under the influence of the operational factors of the tested cement–cellulose boards;
- the intensity of changes taking place in the material and their impact on the strength parameters can be illustrated by using three terms referring to the condition of cement–cellulose elements, namely insignificant change, significant change, and critical change;
- a non-significant change in the mechanical parameters is associated with the emission of events before reaching the maximum load, with an average frequency above 300 kHz, while a significant change in mechanical parameters is identified with the average frequency of AE signals in the range of 200–300 kHz, and critical change in mechanical parameters has an average AE signal frequency of less than 200 kHz; and
- insignificant change in mechanical parameters is associated with a reduction of the bending strength by no more than 25% in relation to the reference panels, while a significant change is a reduction in strength by more than 25% but less than 50%, and the deterioration of strength properties by more than 50% is classified as a critical change in mechanical parameters.

The limits of the proposed method relate primarily to the limitations of the acoustic emission method itself. The main limitation is the ability to register only active processes in the material that lead to the release of elastic energy. Another disadvantage is the fact that the measurement enabling the frequency analysis to assess the condition of the cellulose–cement composite is longer compared to other diagnostic methods, e.g., the ultrasound method.

Further research, according to the authors, should concern the analysis of the frequency of events emitted by cellulose–cement composites with different fibre contents, as well as of the impact of UV radiation and an aggressive environment (related to the phenomenon of acid rain) on the mechanical parameters and sounds generated by the material.

Author Contributions: Conceptualisation, A.A.-B. and A.K.; methodology, G.Ś.; software, G.Ś.; validation, G.Ś., A.A.-B. and A.K.; formal analysis, A.A.-B.; investigation, A.A.-B.; resources, G.Ś.; data curation, A.A.-B.; writing—original draft preparation, A.A.-B.; writing—review and editing, A.K.; visualisation, G.Ś.; supervision, G.Ś. All authors have read and agreed to the published version of the manuscript.

Funding: This research study received no external funding.

Institutional Review Board Statement: Not applicable.

Informed Consent Statement: Not applicable.

Data Availability Statement: Not applicable.

Conflicts of Interest: The authors declare no conflict of interest.

References

1. Ardanuy, M.; Claramunt, J.; Toledo Filho, R.D. Cellulosic Fibre Reinforced Cement-Based Composites: A Review of Recent Research. *Constr. Build. Mater.* **2015**, *79*, 115–128. [CrossRef]
2. Schabowicz, K.; Gorzelańczyk, T. Fabrication of fibre cement boards. In *The Fabrication, Testing and Application of Fibre Cement Boards*, 1st ed.; Ranachowski, Z., Schabowicz, K., Eds.; Cambridge Scholars Publishing: Newcastle Upon Tyne, UK, 2018; pp. 7–39, ISBN 978-1-5276-6.
3. Faruk, O.; Bledzki, A.K.; Fink, H.P.; Sain, M. Biocomposites reinforced with natural fibers. *Prog. Polym. Sci.* **2012**, *37*, 1552–1596. [CrossRef]
4. Tonoli, G.H.D.; Santos, S.F.; Savastano, H.; Delvasto, S.; de Gutiérrez, R.M.; de Murphy, M.D.M.L. Effects of natural weathering on microstructure and mineral composition of cementitious roofing tiles reinforced with fique fibre. *Cem. Concr. Compos.* **2011**, *33*, 225–232. [CrossRef]
5. Morton, J.H.; Cooke, T.; Akers, S.S. Performance of slash pine fibers in fiber cement products. *Constr. Build. Mater.* **2010**, *24*, 165–170. [CrossRef]
6. Savastano, H.; Warden, P.G.; Coutts, R.S.P. Microstructure and mechanical properties of waste fibre–cement composites. *Cem. Concr. Compos.* **2005**, *27*, 583–592. [CrossRef]
7. Khorami, M.; Ganjian, E. The effect of limestone powder, silica fume and fibre content on flexural behaviour of cement composite reinforced by waste Kraft pulp. *Constr. Build. Mater.* **2013**, *46*, 142–149. [CrossRef]
8. Claramunt, J.; Ardanuy, M.; Parés, F.; Ventura, H. Mechanical performance of cement mortar composites reinforced with cellulose fibres. In *Proceedings of the 9th International Conference on Composite Science and Technology, Sorrento, Italy, 24–26 April 2013*; DESTech Publications: Lancaster, PA, USA, 2013; pp. 477–484.
9. Claramunt, J.; Ventura, H.; Parés, F.; Ardanuy, M. Natural fibre nonwovens as reinforcement for cement mortar composites. In Proceedings of the 1st International Conference on Natural Fibers—Sustainable Materials for Advanced Applications, Universidade do Minho, Guimarães, Portugal, 9–11 June 2013; pp. 191–192.
10. Coutts, R.S.P. A Review of Australian Research into Natural Fibre Cement Composites. *Cem. Concr. Compos.* **2005**, *27*, 518–526. [CrossRef]
11. Claramunt, J.; Ardanuy, M.; García-Hortal, J.A.; Filho, R.D.T. The hornification of vegetable fibers to improve the durability of cement mortar composites. *Cem. Concr. Compos.* **2011**, *33*, 586–595. [CrossRef]
12. Ferreira, S.R. *Influence of Hornification on Fiber-Matrix Adhesion and Mechanical Behavior of Cementitious Composites Reinforced with Short Sisal Fibers*; Universidade Federal de Feira de Santana: Feira de Santana, Brazil, 2012.
13. Melo Filho, J.D.A.; Silva, F.D.A.; Toledo Filho, R.D. Degradation kinetics and aging mechanisms on sisal fiber cement composite systems. *Cem. Concr. Compos.* **2013**, *40*, 30–39. [CrossRef]
14. Mohr, B.J.; Biernacki, J.J.; Kurtis, K.E. Microstructural and chemical effects of wet/dry cycling on pulp fiber–cement composites. *Cem. Concr. Res.* **2006**, *36*, 1240–1251. [CrossRef]
15. Claramunt, J.; Ardanuy, M.; García-Hortal, J.A. Effect of drying and rewetting cycles on the structure and physicochemical characteristics of softwood fibres for reinforcement of cementitious composites. *Carbohydr. Polym.* **2010**, *79*, 200–205. [CrossRef]
16. Mohr, B.J.; Nanko, H.; Kurtis, K.E. Durability of kraft pulp fibre-cement composites to wet/dry cycling. *Cem. Concr. Compos.* **2005**, *27*, 435–448. [CrossRef]
17. Adamczak-Bugno, A.; Świt, G.; Krampikowska, A. Application of the Acoustic Emission Method in the Assessment of the Technical Condition of Steel Structures. *IOP Conf. Ser. Mater. Sci. Eng.* **2019**, *471*, 032041. [CrossRef]
18. Pizzol, V.D.; Mendes, L.M.; Savastano, H.; Frías, M.; Davila, F.J.; Cincotto, M.A.; John, V.M.; Tonoli, G.H.D. Mineralogical and microstructural changes promoted by accelerated carbonation and ageing cycles of hybrid fibre–cement composites. *Constr. Build. Mater.* **2014**, *68*, 750–756. [CrossRef]
19. Adamczak-Bugno, A.; Świt, G.; Krampikowska, A. Assessment of Destruction Processes in Fibre-Cement Composites Using the Acoustic Emission Method and Wavelet Analysis. *IOP Conf. Ser. Mater. Sci. Eng.* **2019**, *471*, 032042. [CrossRef]
20. Tonoli, G.H.D.; Santos, S.F.; Joaquim, P.; Savastano, H. Effect of accelerated carbonation on cementitious roofing tiles reinforced with lignocellulosic fibre. *Constr. Build. Mater.* **2010**, *24*, 193–201. [CrossRef]
21. Bentchikou, M.; Guidoum, A.; Scrivener, K.; Silhadi, K.; Hanini, S. Effect of recycled cellulose fibres on the properties of lightweight cement composite matrix. *Constr. Build. Mater.* **2012**, *34*, 451–456. [CrossRef]
22. Schabowicz, K. Aging of ventilated facades made of fiber-cement panels. *Insulations* **2020**, *25*, 72–74. (In Polish)
23. Schabowicz, K.; Sulik, P.; Zawiślak, Ł. Reduction of load capacity of fiber cement board facade cladding under the influence of fire. *Materials* **2021**, *14*, 1769. [CrossRef] [PubMed]
24. Świt, G.; Adamczak, A.; Krampikowska, A. Wavelet Analysis of Acoustic Emissions during Tensile Test of Carbon Fibre Reinforced Polymer Composites. *IOP Conf. Ser. Mater. Sci. Eng.* **2017**, *245*, 22–31. [CrossRef]
25. Li, Z.; Zhou, X.; Bin, S. Fibre-Cement extrudates with perlite subjected to high temperatures. *J. Mater. Civ. Eng.* **2004**, *3*, 221–229. [CrossRef]
26. Zieliński, A.; Kaszyńska, M. Calibration of Steel Rings for the Measurement of Strain and Shrinkage Stress for Cement-BasedComposites. *Materials* **2020**, *13*, 2963. [CrossRef] [PubMed]

27. Schabowicz, K. Modern acoustic techniques for testing concrete structures accessible from one side only. *Arch. Civ. Mech. Eng.* **2015**, *15*, 1149–1159. [CrossRef]
28. Kaczmarek, M.; Piwakowski, B.; Drelich, R. Noncontact Ultrasonic Nondestructive Techniques: State of the Art and Their Use in Civil Engineering. *J. Infrastruct. Syst.* **2017**, *23*, 45–56. [CrossRef]
29. Chinh, L.M.; Adamczak, A.; Krampikowska, A.; Swit, G. Dragon bridge-The world largest dragon-shaped (ARCH) steel bridge as element of smart city. *E3S Web Conf.* **2016**, *10*, 00106. [CrossRef]
30. Schabowicz, K.; Józwiak-Niedzwiedzka, D.; Ranachowski, Z.; Kudela, S.; Dvorak, T. Microstructural characterization of cellulose fibres in reinforced cement boards. *Arch. Civ. Mech. Eng.* **2018**, *4*, 1068–1078. [CrossRef]
31. Wutke, M.; Lejzerowicz, A.; Garbacz, A. The Use of Wavelet Analysis to Improve the Accuracy of Pavement Layer Thickness Estimation Based on Amplitudes of Electromagnetic Waves. *Materials* **2020**, *13*, 3214. [CrossRef]
32. Stark, W. Non-destructive evaluation (NDE) of composites: Using ultrasound to monitor the curing of composites. In *Non-Destructive Evaluation (NDE) of Polymer Matrix Composites. Techniques and Applications*, 1st ed.; Karbhari, V.M., Ed.; Woodhead Publishing Limited: Cambridge, UK, 2013; pp. 136–181.
33. Debowski, T.; Lewandowski, M.; Mackiewicz, S.; Ranachowski, Z.; Schabowicz, K. Ultrasonic tests of fibre-cement boards. *Weld. Rev.* **2016**, *10*, 69–71. (In Polish)
34. Drelich, R.; Gorzelanczyk, T.; Pakuła, M.; Schabowicz, K. Automated control of cellulose fibre cement boards with a non-contact ultrasound scanner. *Autom. Constr.* **2015**, *57*, 55–63. [CrossRef]
35. Ranachowski, Z.; Schabowicz, K. The contribution of fibre reinforcement system to the overall toughness of cellulose fibre concrete panels. *Constr. Build. Mater.* **2017**, *156*, 1028–1034. [CrossRef]
36. Schabowicz, K.; Gorzelanczyk, T.; Szymków, M. Identification of the degree of degradation of fibre-cement boards exposed to fire by means of the acoustic emission method and artificial neural networks. *Materials* **2019**, *12*, 656. [CrossRef]
37. Goszczyńska, B.; Świt, G.; Trąmpczyński, W.; Krampikowska, A. Application of the acoustic emission method of identification and location of destructive processes to the monitoring concrete bridges. In Proceedings of the 7th International Conference of Bridge Maintenance, Safety and Management, IABMAS 2014, Shanghai, China, 7–11 July 2014; pp. 688–694.
38. Lim, M.K.; Cao, H. Combining multiple NDT methods to improve testing effectiveness. *Constr. Build. Mater.* **2013**, *38*, 1310–1615. [CrossRef]
39. Szewczak, E.; Winkler-Skalna, A.; Czarnecki, L. Sustainable Test Methods for Construction Materials and Elements. *Materials* **2020**, *13*, 606. [CrossRef]
40. Łazarska, M.; Wozniak, T.; Ranachowski, Z.; Trafarski, A.; Domek, G. Analysis of acoustic emission signals at austempering of steels using neural networks. *Met. Mater. Int.* **2017**, *23*, 426–433. [CrossRef]
41. Wozniak, T.Z.; Ranachowski, Z.; Ranachowski, P.; Ozgowicz, W.; Trafarski, A. The application of neural networks for studying phase transformation by the method of acoustic emission in bearing steel. *Arch. Civ. Mech. Eng.* **2014**, *59*, 1705–1712.
42. Adamczak-Bugno, A.; Krampikowska, A. The Acoustic Emission Method Implementation Proposition to Confirm the Presence and Assessment of Reinforcement Quality and Strength of Fiber–Cement Composites. *Materials* **2020**, *13*, 2966. [CrossRef] [PubMed]
43. Adamczak-Bugno, A.; Świt, G.; Krampikowska, A. Fibre-Cement Panel Ventilated Façade Smart Control System. *Materials* **2021**, *14*, 5076. [CrossRef]
44. Zangana, S.; Epaarachchi, J.; Ferdous, W.; Leng, J.; Schubel, P. Behaviour of continuous fibre composite sandwich core under low-velocity impact. *Thin-Walled Struct.* **2021**, *158*, 107157. [CrossRef]
45. Ferdous, W.; Manalo, A.; Peauril, J.; Salih, C.; Raghava Reddy, K.; Yu, P.; Schubel, P.; Heyer, T. Testing and modelling the fatigue behaviour of GFRP composites—Effect of stress level, stress concentration and frequency. *Eng. Sci. Technol. Int. J.* **2020**, *23*, 1223–1232. [CrossRef]
46. Marzec, A.; Lewicki, P.P.; Ranachowski, Z.; Dębowski, T. Cereal Food texture evaluation with application of mechanical and acoustical method. In *Nondestructive Testing of Materials and Structures*; Centre of Excellence for Advanced Materials and Structure: Warsaw, Poland, 2003; pp. 111–133.
47. Lewicki, P.P.; Marzec, A.; Ranachowski, Z. Acoustic properties of crunchy products. In Proceedings of the 3rd International Workshop on Water in Food, Lausanne, Switzerland, 29–30 March 2004.
48. *EN 12467:2012 Fiber-Cement Flat Sheets—Product Specification and Test Methods*; European Committee for Standardization: Brussels, Belgium, 2012.

materials

MDPI

Article

Data-Driven Techniques for Evaluating the Mechanical Strength and Raw Material Effects of Steel Fiber-Reinforced Concrete

Mohammed Najeeb Al-Hashem [1], Muhammad Nasir Amin [1,*], Waqas Ahmad [2], Kaffayatullah Khan [1], Ayaz Ahmad [3], Saqib Ehsan [4], Qasem M. S. Al-Ahmad [1] and Muhammad Ghulam Qadir [5]

[1] Department of Civil and Environmental Engineering, College of Engineering, King Faisal University, Al-Ahsa 31982, Saudi Arabia
[2] Department of Civil Engineering, COMSATS University Islamabad, Abbottabad 22060, Pakistan
[3] MaREI Centre, Ryan Institute and School of Engineering, College of Science and Engineering, National University of Ireland Galway, H91 TK33 Galway, Ireland
[4] Department of Civil Engineering, NFC Institute of Engineering and Fertilizer Research, Faisalabad 38090, Pakistan
[5] Department of Environmental Sciences, Abbottabad Campus, COMSATS University Islamabad, Abbottabad 22060, Pakistan
* Correspondence: mgadir@kfu.edu.sa; Tel.: +966-13-589-5431; Fax: +966-13-581-7068

Abstract: Estimating concrete properties using soft computing techniques has been shown to be a time and cost-efficient method in the construction industry. Thus, for the prediction of steel fiber-reinforced concrete (SFRC) strength under compressive and flexural loads, the current research employed advanced and effective soft computing techniques. In the current study, a single machine learning method known as multiple-layer perceptron neural network (MLPNN) and ensembled machine learning models known as MLPNN-adaptive boosting and MLPNN-bagging are used for this purpose. Water; cement; fine aggregate (FA); coarse aggregate (CA); super-plasticizer (SP); silica fume; and steel fiber volume percent (Vf SF), length (mm), and diameter were the factors considered (mm). This study also employed statistical analysis such as determination coefficient (R^2), root mean square error (RMSE), and mean absolute error (MAE) to assess the performance of the algorithms. It was determined that the MLPNN-AdaBoost method is suitable for forecasting SFRC compressive and flexural strengths. The MLPNN technique's higher R^2, i.e., 0.94 and 0.95 for flexural and compressive strength, respectively, and lower error values result in more precision than other methods with lower R^2 values. SHAP analysis demonstrated that the volume of cement and steel fibers have the greatest feature values for SFRC's compressive and flexural strengths, respectively.

Keywords: concrete; steel fibers; steel fiber-reinforced concrete; compressive strength; flexural strength

Citation: Al-Hashem, M.N.; Amin, M.N.; Ahmad, W.; Khan, K.; Ahmad, A.; Ehsan, S.; Al-Ahmad, Q.M.S.; Qadir, M.G. Data-Driven Techniques for Evaluating the Mechanical Strength and Raw Material Effects of Steel Fiber-Reinforced Concrete. *Materials* **2022**, *15*, 6928. https://doi.org/10.3390/ma15196928

Academic Editor: Krzysztof Schabowicz

Received: 14 September 2022
Accepted: 1 October 2022
Published: 6 October 2022

Publisher's Note: MDPI stays neutral with regard to jurisdictional claims in published maps and institutional affiliations.

1. Introduction

The simple production method for concrete and the abundant availability of its ingredients and several applications make it the most widely used construction material around the globe. The nature of concrete is conventionally brittle, having low strain capacity, toughness, and energy absorption capability. Accordingly, researchers are searching for ways to minimize the brittleness of typical concrete by enhancing its tensile strength. The dispersed incorporation of short-discrete fibers in conventional cementitious concrete is emerging as an effective method of enhancing concretes' capacity for energy absorption [1–4]. Multiple researchers have explored the addition of steel/synthetic/natural fibers to concrete as reinforcement for improving characteristics like fatigue resistance, toughness, ductility, and resist propagation of cracks in concrete [5–16]. Steel fibers are incorporated into concrete to enhance its post-cracking phenomenon and toughness [17–20]. SFRC have multiple applications in different sections of the construction industry like building, pavements,

rehabilitation, and repair. The enhanced mechanical properties of SFRC, as reported by some of the researchers, for different applications are summarized in Table 1.

Table 1. Reported applications and properties of SFRC.

Study Findings	Conducted Studies				
	Purkiss [21]	**Patil and Sangle [22]**	**Noaman, et al. [23]**	**Boulekbache, et al. [24]**	**Gholamhoseini, et al. [25]**
Studied Properties of SFRC	Residual Flexural Strength Residual Compressive Strength	Compressive Strength Flexural Strength	Compressive Strength Flexural Strength	Compressive Strength Flexural Strength	Compressive Strength Flexural Strength
Reported Outcomes	78–91% loss@800 °C 57–74% loss@800 °C	45.7 MPa 5.3 MPa	47 MPa 3.0–3.9 MPa	27–28.5 MPa 3.5–5.5 MPa	33.8–36.2 MPa 3.9–4.3 MPa
Considered Applications	Refractory Material	Beams	-	Structural Beams	Slabs

Currently, the practice adopted for evaluating the mechanical properties of SFRC is the performance of the entire experimental program. A considerable amount of time and cost is involved in determining an accurate connection between properties of material and mix design through experimentation [26]. The variable SFRC parameters are the aggregates, cement, water, admixture/super-plasticizer, additive material and fiber (i.e., steel fibers) contents, and the admixture type. Despite the considerable experimental research in the literature, it is hard to forecast the characteristics of SFRC with different mixtures with the help of computational approaches. Hence, the current work is focused on estimating SFRC mechanical characteristics by employing a soft computational approach.

The employment of soft computational techniques may assist in resolving multiple complex problems in various fields of engineering [27–29]. ML techniques may be applied to forecast the ultimate outcome after incorporating a database as input parameters. Two ML approaches, a single model-based standalone method and ensemble Bagging and AdaBoost models, are employed in this research for the estimation of SFRC properties. Per the reported studies, ensemble modelling techniques are more effective than an individual model as shown in Table 2. Chaabene et al. [30] reported a detailed assessment of applying ML techniques for predicting the mechanical properties of concrete. Furthermore, multiple types of research have been conducted to estimate the mechanical properties of different concrete types like self-healing concrete [31], high-performance concrete (HPC) [32–36], phase change materials-integrated concrete [37], and recycled aggregate concrete (RAC) [38–41]. Han et al. [33] employed machine learning techniques for estimation of HPC compressive strength. The input parameters included age, water, cement, coarse aggregates, sand, fly-ash, and GGBFS, and five variable combinations were considered. The accurate compressive strength of HPC was obtained by the developed model. In this study, the SFRC compressive strength is predicted by applying soft computational approaches. The current research will provide a base for conserving cost and time of future researchers.

Table 2. ML techniques used in the previous studies.

Ref.	Material Type	Properties Predicted	ML Techniques Employed	No. of Input Parameters	Data Points	Best ML Technique Recommended
[42]	Concrete-Filled Steel Tubes	Ultimate axial capacity	Gene expression programming	6	227	-
[43]	Recycled aggregate concrete	Split-tensile strength	Gene expression programming, artificial neural network, and bagging regressor	9	166	Bagging regressor
[44]	Rice husk ash concrete	Compressive strength	Gene expression programming and random forest	6	192	Gene expression programming
[45]	Geopolymer concrete	Compressive strength	Decision tree, bagging regressor, and AdaBoost	9	154	Bagging regressor
[46]	Fly ash-based concrete	Compressive strength	Gene expression programming, artificial neural network, decision tree, and bagging regressor	7	98	Bagging regressor
[47]	Fly ash-based concrete	Compressive strength	Gene expression programming, decision tree, and bagging regressor	8	270	Bagging regressor

ML techniques have demonstrated possible prediction results with least difference in trials for various concrete types. For said purpose, experimental methods, including casting and testing procedures, consume considerable cost, effort, and time. Therefore, the current need is to develop data modeling-based algorithms in line with closely linked in-dependent parameter identification and the instant decrement in input matrix dimensions. The application of soft computational approaches is gaining more importance for predicting concrete materials' behavior in civil engineering. ML is an alternative technique for predicting SFRC's compressive and flexural strengths to conserve experimental cost and time. The current study involves applying an individual ML model and multiple ensembled ML techniques to predict SFRC compressive and flexural strengths. In addition, the influence of raw materials on mechanical properties remains largely unexplored in contemporary study and is still very limited. The integration of SHapley Additive exPlanations (SHAP) with ML algorithms is also performed in this paper, addressing a current research need. SHAP analysis is intended to provide in-depth knowledge of SFRC mix design in terms of its mechanical strength factors via complicated nonlinear behavior and the description of input factors' contributions by assigning a weighting factor to each input component. MLPNN is taken as an individual ML model, while MLPNN-AdaBoost and MLPNN-Bagging are taken as ensembled machine learning algorithms. In addition, statistical analysis is performed for the evaluation of all the considered models, and all said ML algorithms are compared as well. Afterwards, based on numerous statistical factors' performance, a superior model is proposed for predicting SFRC properties. As a whole, a correlation for valuable structure properties is established in this research by applying interpretable machine learning techniques through feature importance.

2. Soft Computing Techniques

2.1. Multilayer Perceptron Neural Network (MLPNN)

The ANN model is among the most effective ML models. Its potential to resolve nonlinear issues has made it widely applied in hydrological and environmental engineering areas. Among multiple ANN models, the multilayer perceptron ANN (MLPNN) is the one that is used most frequently. The MLPNN model's architecture comprises three layers: an input one followed by one or more hidden ones, and the output one. The three conventional functions of activation are; logsig, tansig, and purelin. Activations, weights, and bias functions are among the most important parts in both the output and hidden layers. The training of the model governs the parameters or weights of the model. The hidden layers employ the function of tansig activation; however, purelin is used for the output layer. The best structure is extracted by fivefold cross-validation. The top ANN model came out with three layers that are hidden (i.e., 9, 3, and 2) having optimal numbers of neurons against every hidden layer [48]. A typical/conventional neural network is shown in Figure 1. The composition of these networks is at three stages in a way that the input is transmitted by forward-pass, weight is multiplied by it, and the prediction of model output is made. The predicted results are then compared with the considered inputs. The input factors are considered for the model prediction outcomes. Based upon the objectives and performance, various loss functions are employed. The partial derivatives for cost function, linked with individual factors back in operation, are generated by backward propagation. Gradient descent is used for back loss propagation and model weight updating during this method.

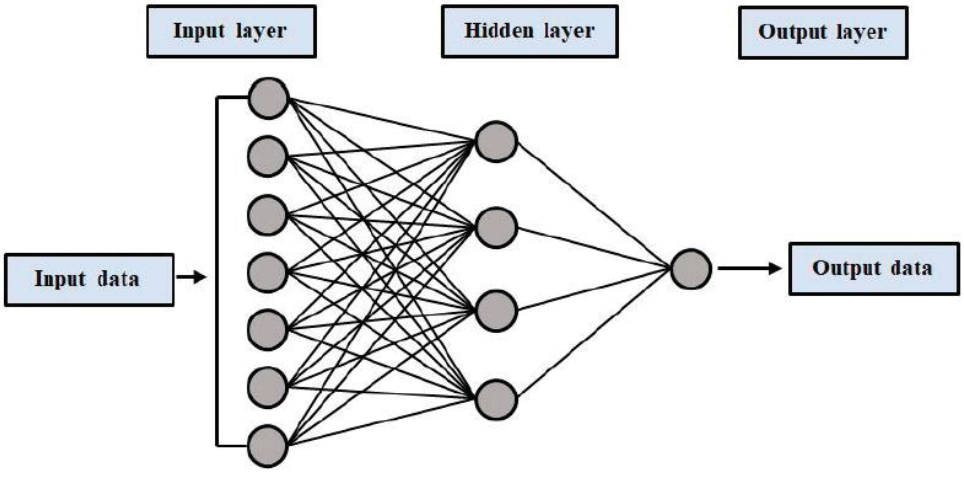

Figure 1. Architecture of a typical neural network [49].

2.2. MLPNN Bagging and MLPNN AdaBoost Techniques

The accuracy of prediction and recognition of ML can be improved by using ensemble approaches. These approaches usually help resolve problems by aggregating and integrating various algorithms having weaker predictions. A smart learner can be made by intelligently developing different sub-models (i.e., A, B, ... N) along with the alteration of data for training and the merging of average and votes of combination measures, to obtain the correct result of projecting sub-models, for making an ideal model. The most frequently adopted ensembled modelling approach is Bagging, which implies the resampling bootstrap technique for calculating benefits and gathering the data. During this method, the first set of training with fractional algorithms is substituted for the actual algorithm. Some samples of data may seem in different algorithms, whereas few of them do not even appear in any model product. The average from all component models' output is taken to calculate the final outcome model.

The Bagging approach, like boosting, creates a cumulative model that constructs multiple more precise components compared with non-ensemble models. Furthermore, the weighted averages are used in the Boosting process based on sub-models to determine their inclusion in the final model. Based upon MLPNN-like individual learners, the current work predicts the flexural and compressive strengths of SFRC using Bagging and Adaptive Boosting (AdaBoost) approaches.

3. Dataset

The literature-based dataset that was used comprises 150 mix ratios with 9 contribution parameters [50–66]. All the samples were water cured at 28 days. Figures 2 and 3 exhibit the dataset that was employed to estimate SFRC strengths. These include water (kg/m^3), cement (kg/m^3), coarse aggregate (CA) (kg/m^3), fine aggregate (FA) (kg/m^3), superplasticizer (SP) (%), silica fume (%), volume fraction of steel fiber (Vf SF) (%), SF Length (mm), and SF diameter (mm). The prediction variables for output parameters (i.e., compressive and flexural strength) relied on the above-mentioned input parameters. Python scripting in Spyder Anaconda software was used to predict compressive and flexural strength.

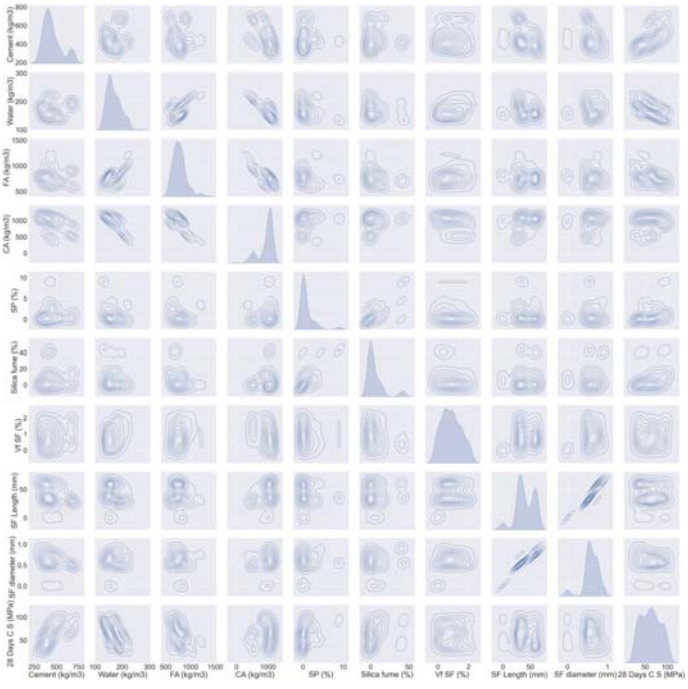

Figure 2. Data description of compressive parameters.

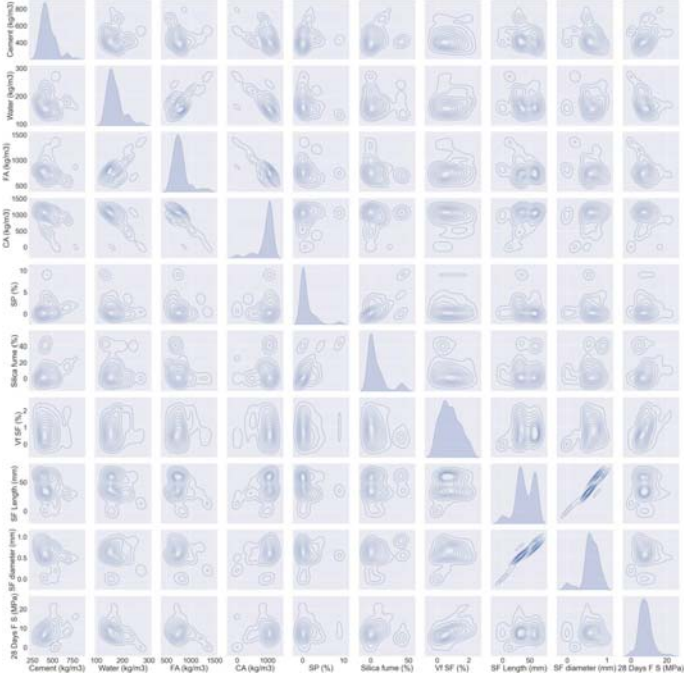

Figure 3. Data description of flexural parameters.

4. Results and Discussion

4.1. Multiple-Layer Perceptron Neural Network (MLPNN)

The comparison of the MLPNN algorithm projected and experimental values for SFRC compressive strength are shown in Figure 4. MLPNN shows a reasonably estimated outcome with minimal variation in SFRC compressive strength. The appropriateness of the MLPNN model is represented by an acceptable R^2 of 0.79. The error distribution of MLPNN predicted and experimental values for SFRC compressive strength are illustrated in Figure 5. The average error values for SFRC compressive strength are 8.69 MPa: 46% of the error values are below 5 MPa, 29% of these values range between 5 and 10 MPa, and 25% are more than 10 MPa.

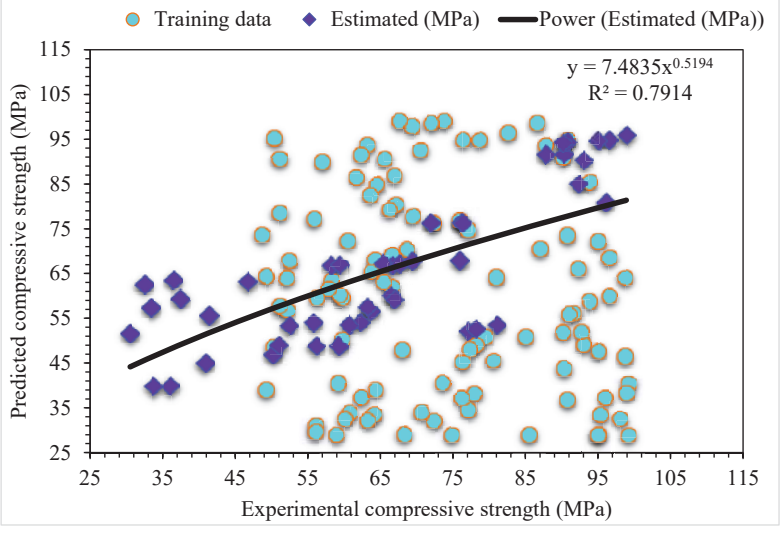

Figure 4. Experimental and MLPNN predicted results for compressive strength.

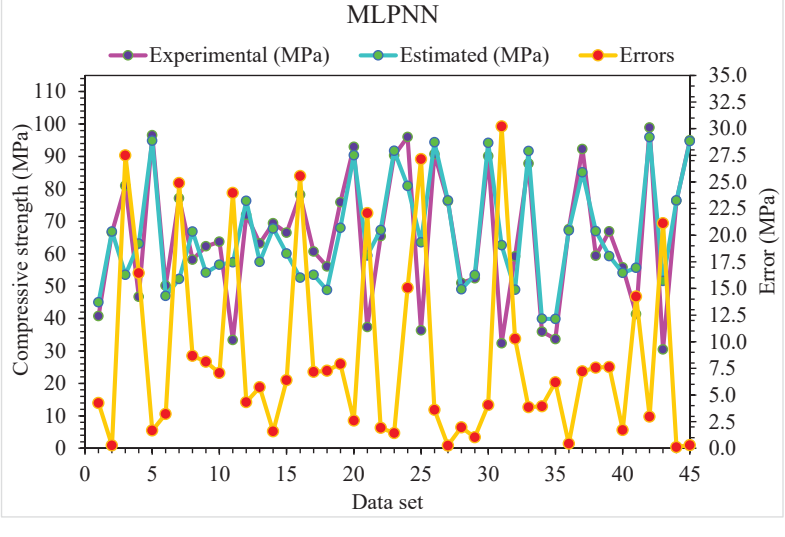

Figure 5. Experimental and MLPNN predicted values with errors for compressive strength.

The MLPNN projected and investigational results for SFRC flexural strength are presented in Figure 6. The R^2 of 0.81 reveals the less appropriate outcome. Similarly, the projected results for the flexural strength of SFRC with the help of MLPNN lie in suitable array. The distribution of error for MLPNN projected, and investigational flexural strength of SFRC is shown in Figure 7. Nearly one third of values, 29%, are below 1 MPa, 66% are in the range of 1 to 5 MPa, and the remaining 5% are above 5 MPa.

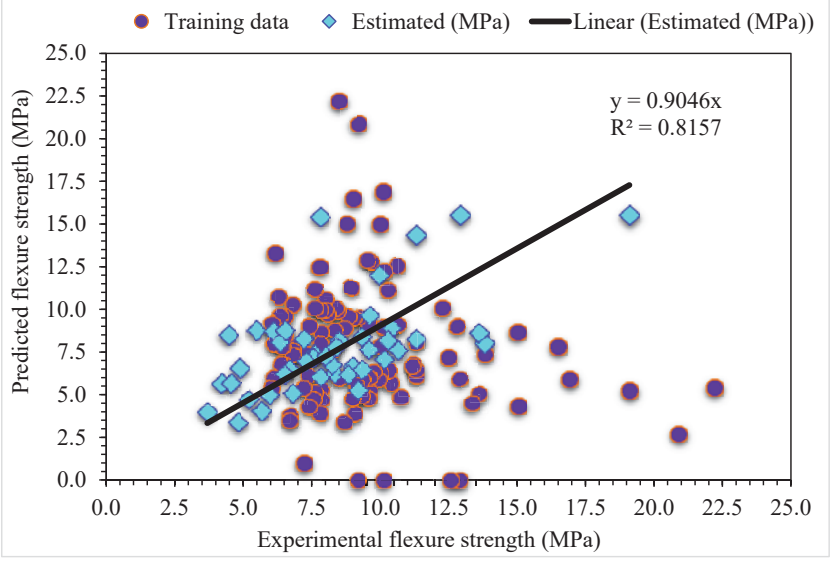

Figure 6. Experimental and MLPNN predicted results for flexural strength.

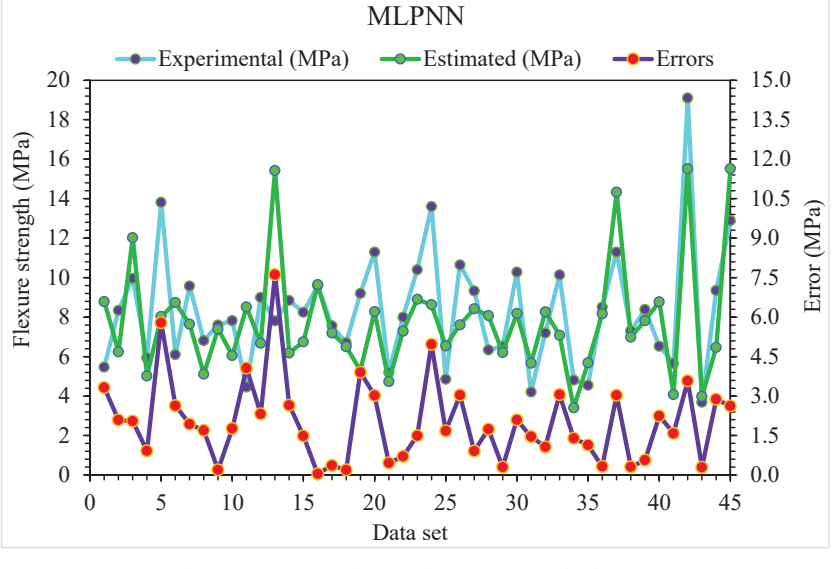

Figure 7. Experimental and MLPNN predicted values with errors for flexural strength.

4.2. MLPNN-AdaBoost

Figure 8 shows the predicted MLPNN-AdaBoost algorithm and investigational results for compressive strength of SFRC. The R^2 of 0.95 for MLPNN-AdaBoost depicts a higher accuracy of outcomes than that of the MLPNN algorithm. Figure 9 represents the distribution of error for MLPNN-AdaBoost estimated and investigational results for the compressive strength of SFRC. It may be seen that 62% of values are below 5 MPa, 29% of these values range from 5 and 10 MPa, and 9% of values are above 10 MPa. The higher R^2 and lower error values show more precision of the MLPNN-AdaBoost model than MLPNN.

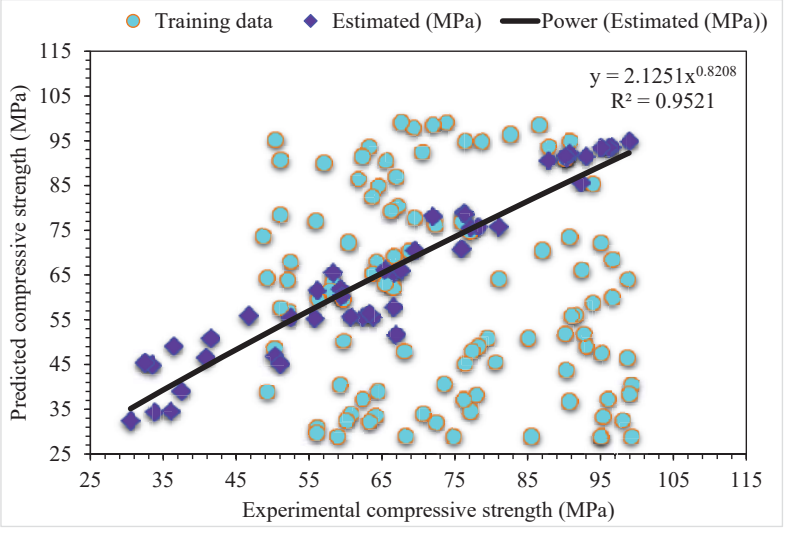

Figure 8. Experimental and MLPNN-AdaBoost predicted results for compressive strength.

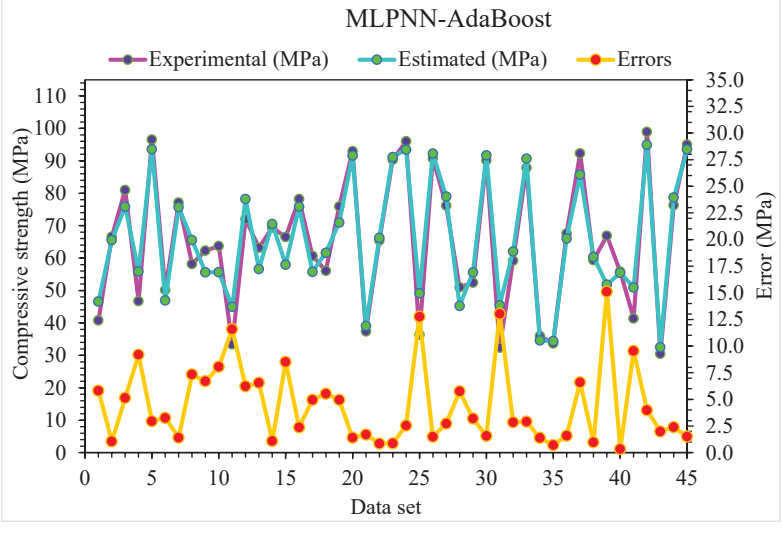

Figure 9. Experimental and MLPNN-AdaBoost predicted values with errors for compressive strength.

The MLPNN-AdaBoost model's estimated and investigational results were compared for SFRC flexural strength (Figure 10). MLPNN-AdaBoost depicts reduced variation in error for SFRC flexural strength and highly precise predicted results. The adequacy of the MLPNN-AdaBoost model is represented by an acceptable R^2 of 0.94. The error distribution of MLPNN-AdaBoost predicted and experimental SFRC flexural strength is illustrated in Figure 11. The average error value for SFRC flexural strength is 1.57 MPa: 47% of total error values are below 1 MPa, 53% of these values are between 1 and 5 MPa, and no value is more than 5 MPa.

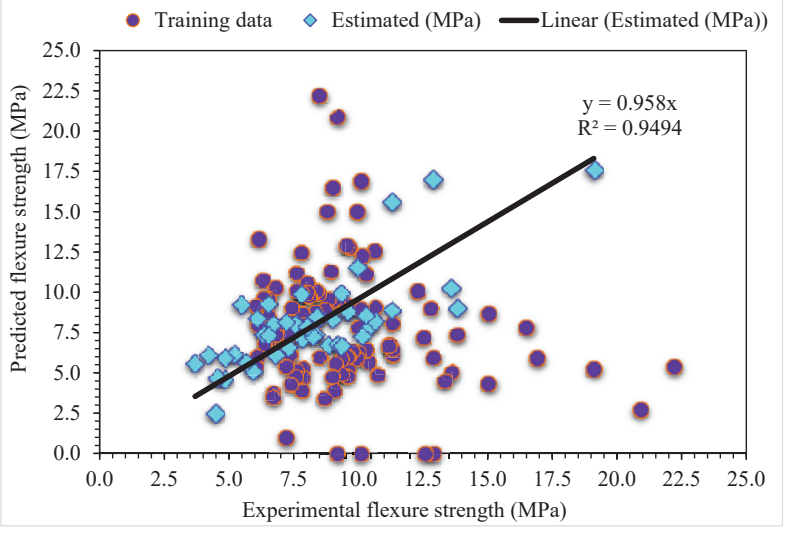

Figure 10. Experimental and MLPNN-AdaBoost predicted results for flexural strength.

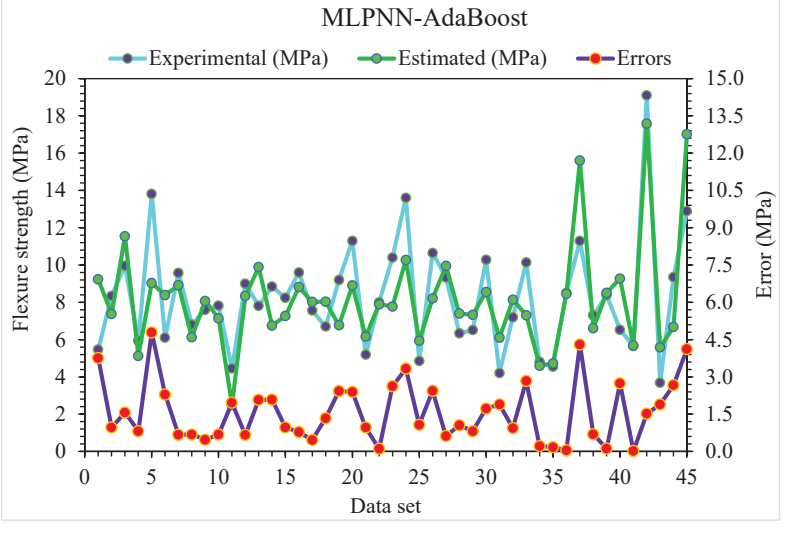

Figure 11. Experimental and MLPNN-AdaBoost predicted values with errors for flexural strength.

4.3. MLPNN-Bagging

Figure 12 shows the projected and investigational outputs in case of MLPNN-Bagging for SFRC compressive strength. The R^2 of 0.89 for this model depicts comparatively less appropriate results than the above-mentioned ensembled MLPNN-AdaBoost model. The estimated SFRC compressive strength outcomes for MLPNN-Bagging are superior to the individual MLPNN model. Figure 13 depicts the distribution of error for MLPNN-Bagging projected and investigational results for SFRC compressive strength: 49% of values are below 5 MPa, 28% are from 5 to 10 MPa, and the remaining 22% of these values are higher than 10 MPa. The R^2 and error values for SFRC compressive strength in the case of MLPNN are more precise than the MLPNN-Bagging model. At the same time, the MLPNN ensembled machine learning algorithms error and R^2 values are satisfactory. Therefore, this result shows the higher accuracy of estimation outcomes of MLPNN compared to other considered models.

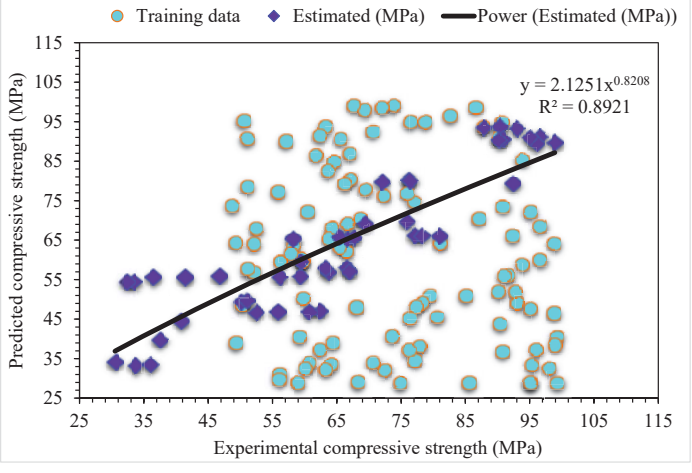

Figure 12. Experimental and MLPNN-Bagging predicted results for compressive strength.

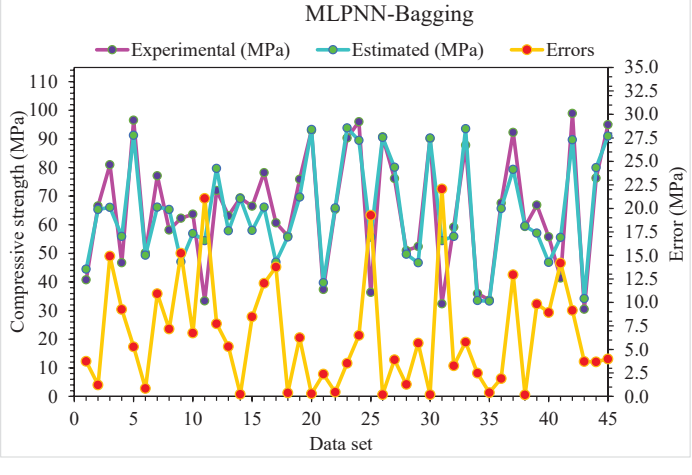

Figure 13. Distribution of experimental and MLPNN-Bagging predicted values with errors for compressive strength.

The estimated MLPNN-AdaBoost and investigational results for SFRC flexural strength are presented in Figure 14. The R^2 of 0.92 for MLPNN-AdaBoost displays less accurate outcomes compared with MLPNN-AdaBoost. The distribution of error for the MLPNN-AdaBoost estimated and investigational results for SFRC flexural strength are presented in Figure 15. It is assessed that 33% of values are below 1 MPa, 62% lie in the 1 to 5 MPa range, and 4% are above 5 MPa. The higher R^2 and lower error values demonstrate the higher accuracy of MLPNN-AdaBoost compared with MLPNN. In contrast, the attained R^2 and error values for MLPNN-Bagging ensembled machine learning algorithms are suitable: this result showed the most accuracy for estimation outputs of MLPNN-AdaBoost compared with the other considered algorithms.

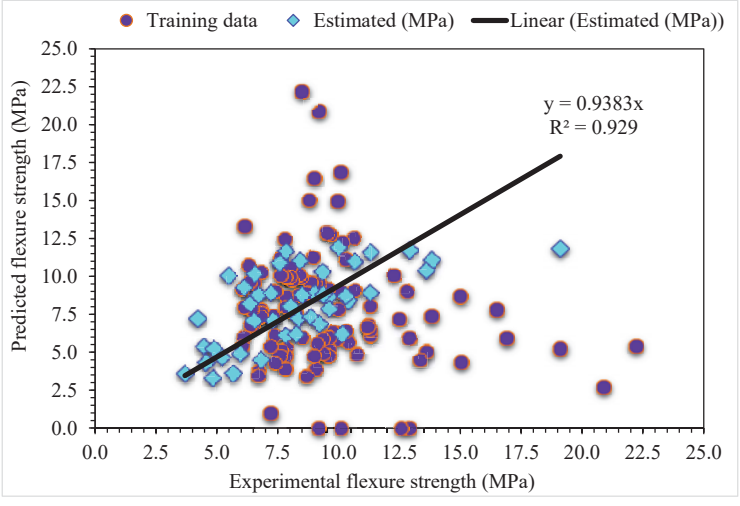

Figure 14. Experimental and MLPNN-Bagging predicted results for flexural strength.

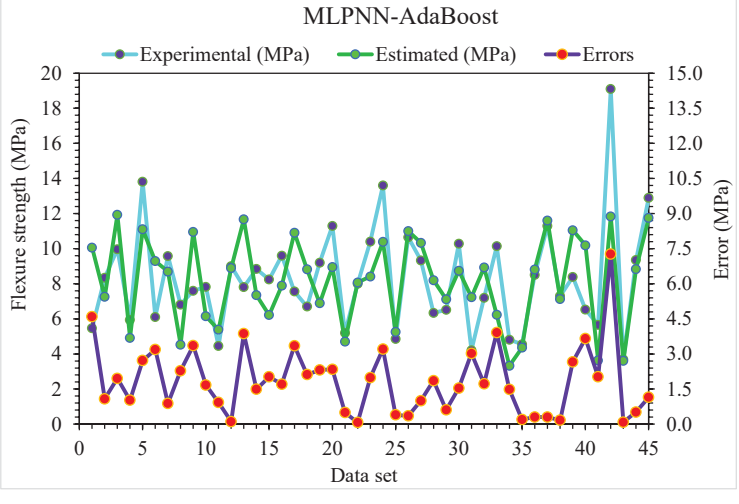

Figure 15. Distribution of experimental and MLPNN-Bagging predicted values with errors for flexural strength.

4.4. Comparison of All Models

The k-fold technique was adopted for cross-validation in order to assess the performance of model while implementation. The performance of a model is determined by employment of statistical checks [67–70]. Normally, in the said k-fold process, there is splitting data in 10 clusters for random spreading by repeating this process 10 times for attaining suitable results. Table 3 provides the employed statistical checks. The compressive strength R^2 values for MLPNN, MLPNN-Bagging, and MLPNN-AdaBoost models were 0.79, 0.89, and 0.95, respectively, as presented in Figure 16a–c. In the case of flexural strength, the R^2 values for MLPNN, MLPNN-Bagging, and MLPNN-AdaBoost model were 0.81, 0.92, and 0.94, respectively, as presented in Figure 17a–c. It is observed that the R^2 for MLPNN-AdaBoost is higher than those of the other considered algorithms, having lower error values for the SFRC compressive and flexural strengths.

Table 3. Statistical checks of comparison of this study with the literature.

Material Type	Parameters	Techniques	MAE (MPa)	RMSE (MPa)	R^2	References
SFRC	Compressive strength	MLPNN	8.7	12.3	0.79	This study
SFRC		MLPNN-AdaBoost	4.5	5.8	0.95	This study
SFRC		MLPNN-Bagging	6.6	8.8	0.89	This study
SFRC	Flexural strength	MLPNN	2.0	2.6	0.81	This study
SFRC		MLPNN-AdaBoost	1.6	2.0	0.94	This study
SFRC		MLPNN-Bagging	1.8	2.3	0.92	This study
Recycled coarse aggregate concrete (RCAC)	Compressive strength	SVM-AdaBoost	7.7	9.5	0.94	Amin, et al. [71]
Geopolymer concrete	Compressive strength	MLPNN	5.8	7.4	0.81	Amin, et al. [72]
Geopolymer concrete	Compressive strength	Support vector machine	6.7	8.1	0.78	Amin, et al. [72]
Waste marble powder Concrete (WMC)	Compressive strength	DT-AdaBoost	3.9	7.9	0.91	Khan, et al. [73]
Fly ash concrete	Compressive strength	Decision Tree	-	-	0.88	Khan, et al. [74]
Fly ash concrete	Compressive strength	MLP	-	-	0.90	Khan, et al. [74]
Fly ash concrete	Compressive strength	Bagging	-	-	0.93	Khan, et al. [74]
Geopolymer concrete	Compressive strength	Decision Tree	4.1	6.2	0.88	Zou, et al. [75]
Recycled coarse aggregate concrete (RCAC)	Compressive strength	DT-XGBoost	7.7	10.5	0.94	Amin, et al. [71]

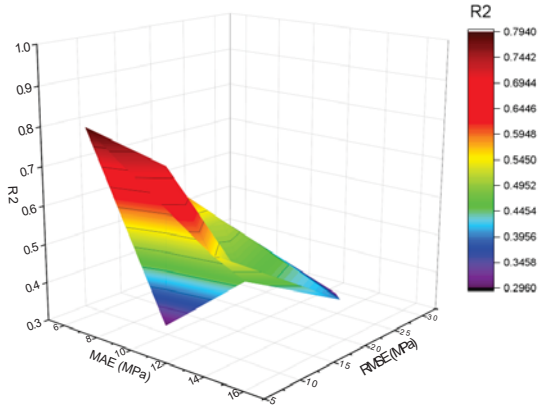

(**a**)

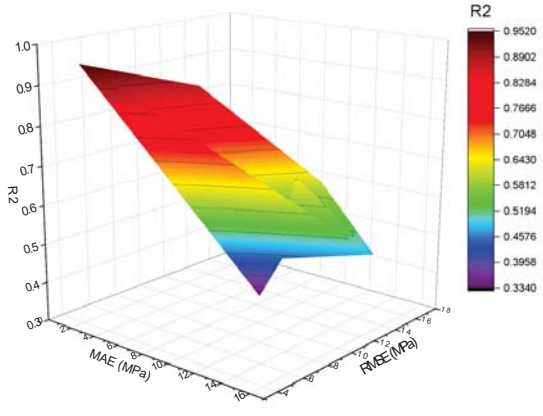

(**b**)

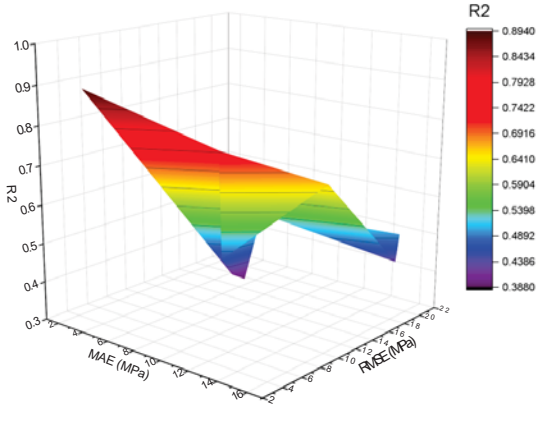

(**c**)

Figure 16. Compressive strength statistical representation: (**a**) MLPNN; (**b**) MLPNN-AdaBoost; (**c**) MLPNN-Bagging.

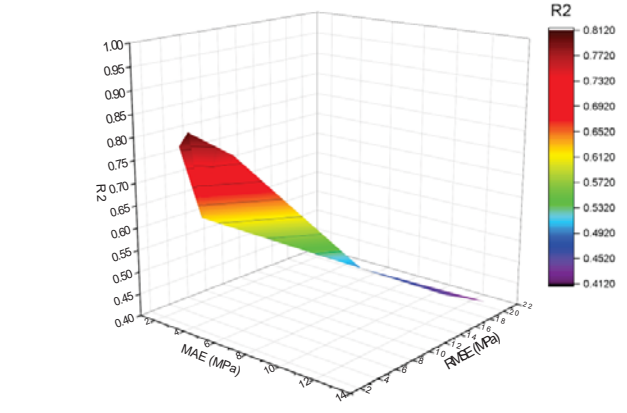

(**a**)

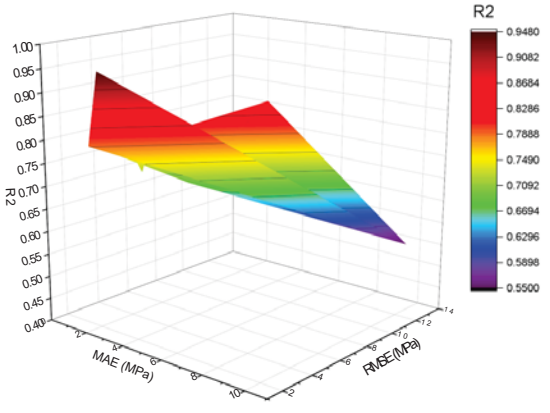

(**b**)

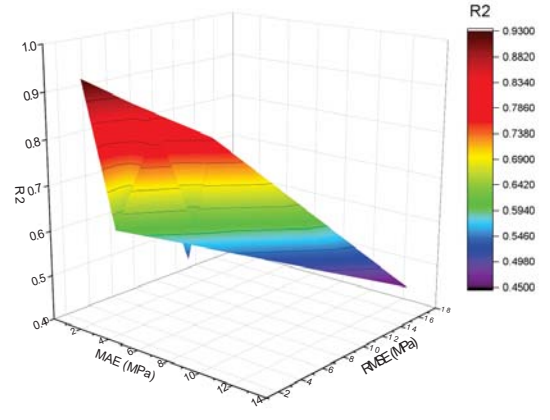

(**c**)

Figure 17. Flexural strength statistical representation: (**a**) MLPNN; (**b**) MLPNN-AdaBoost; (**c**) MLPNN-Bagging.

The comparison of current models with the models in the literature is shown in Table 3. SFRC compressive strength is estimated by applying ensembled ML techniques in the current study, which intends to offer reliable and efficient results as compared to the other studies in the literature. The R^2 of 0.95 for MLPNN-AdaBoost outcomes provides a more precise estimation of SFRC compressive strength. The ensembled MLPNN-AdaBoost ML models perform better in predicting compressive strength by utilizing an optimized model extracted from 20 sub-models, as presented in Figure 18a,b. It can be observed that ensembled MLPNN-AdaBoost models depict more accuracy and lower error than other models as well as the models reported in the literature. Despite this, SFRC flexural strength is estimated by applying ensembled ML techniques in the current study, which intends to offer reliable and efficient outcomes. The R^2 of 0.94 in the case of MLPNN-AdaBoost results provides a more precise estimation for the compressive strength of SFRC. Out of 20 sub-models, an optimized model is used to estimate SFRC flexural strength in the case of ensembled MLPNN-AdaBoost ML models that perform better (Figure 19a,b). In comparison with other models, the ensembled MLPNN-AdaBoost models show higher accuracy and lower error.

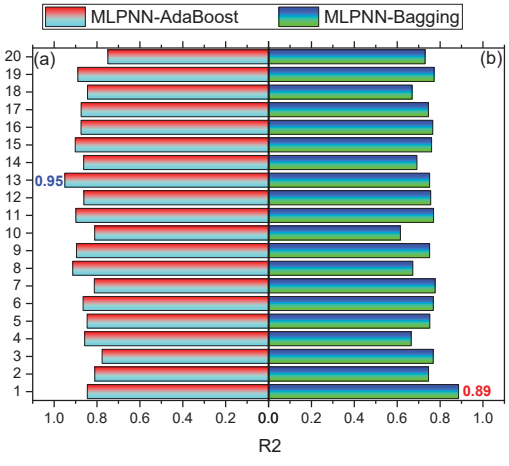

Figure 18. Compressive strength sub-models results: (**a**) MLPNN-AdaBoost; (**b**) MLPNN-Bagging.

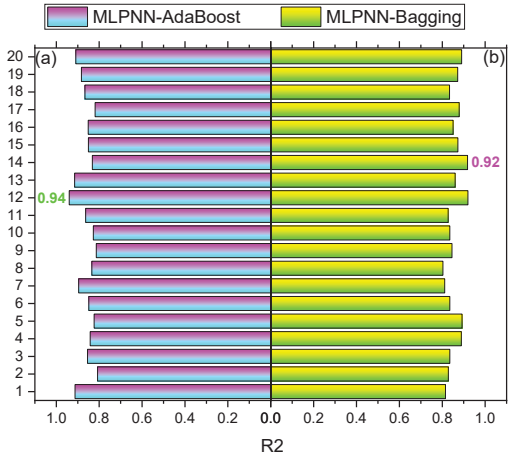

Figure 19. Flexural strength sub-models results: (**a**) MLPNN-AdaBoost; (**b**) MLPNN-Bagging.

5. Feature Importance of ML Models for Compressive and Flexural Strength

A thorough explanation is also given in the current research of the ML algorithm and interactions of considered input features. Different feature importance correlation for compressive strength of SFRC is shown in Figure 20. It can be observed that the feature value of cement feature is highest, i.e., 0.46, for SFRC compressive strength estimation. The cement feature has a positive influence, which means that by enhancing the cement content, the SFRC compressive strength increases. The SHAP plot (Figure 21) also shows that cement has the highest impact on SFRC compressive strength. The water feature has the second highest feature value of 0.26 for SFRC compressive strength; however, it influences negatively. Increasing the amount of water will reduce the compressive strength (Figure 21). Thirdly, the main factor for SFRC is silica fume, and this feature has approximately 0.1 feature value (Figures 20 and 21). Further, the content of silica fume as a feature is positively influencing the SFRC compressive strength. It means that enhancement in its content turns into more compressive strength of SFRC. Coarse aggregate is next in line with a feature value of almost 0.8, but, in this case, the increase in coarse aggregate content up to optimum content only results in enhanced compressive strength. Beyond this optimum content of coarse aggregates, the SFRC compressive strength decreases. This behavior shows coarse aggregates' positive and negative influence on SFRC compressive strength. Similarly, the feature value for sand, super-plasticizer is next, followed by steel fiber length, volume and diameter. All these considered features have more or less the same feature values near zero, showing their minimal impact on compressive strength of SFRC.

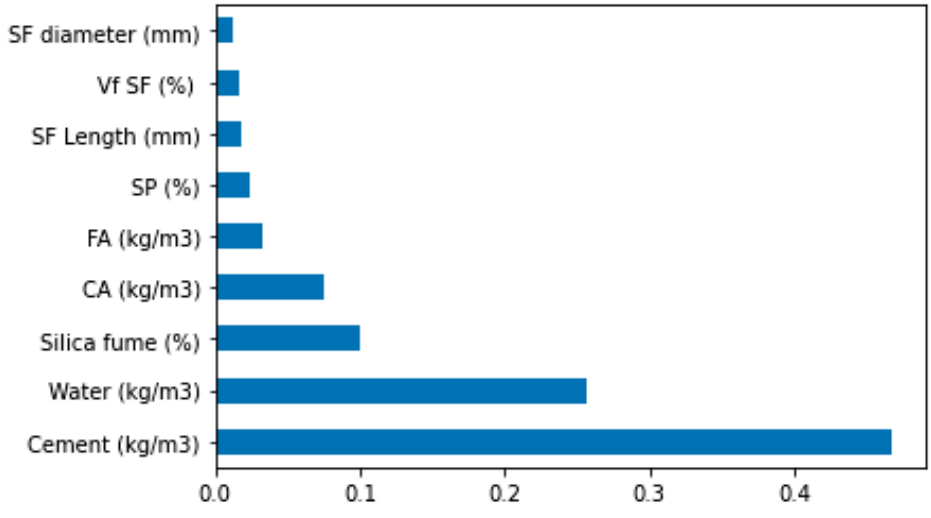

Figure 20. Compressive strength feature importance.

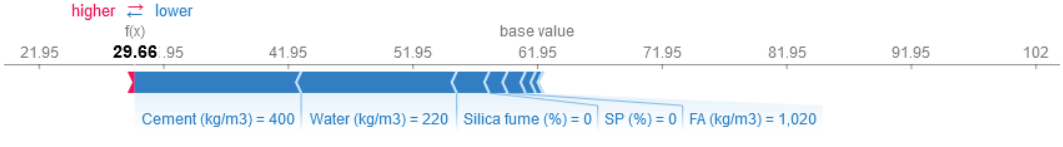

Figure 21. Compressive strength SHAP plot.

Similarly, Figures 22 and 23 present the features' importance correlations and features and SHAP plot for SFRC flexural strength. In this scenario, it is indicated in Figure 22 that the volume content of steel fiber has the highest feature value of 0.24 for flexural strength

prediction of SFRC. It may also be observed from Figure 23 that the enhancing content of steel fiber volumes is increasing the SFRC flexural strength and vice versa. The second highest feature value of 0.22 is for coarse aggregates feature in the case of SFRC flexural strength. At the third level, the water has a feature value of 0.18, but with a negative influence, which means the enhancement in water content causes a reduction in flexural strength (Figure 23). Figure 22 depicts that the cement feature has a feature value up to 0.14 and positively influences the flexural strength of SFRC. The higher the cement content, the more the SFRC flexural strength (Figure 23). Afterwards, the silica fume, an important feature of SFRC, has a feature value of 0.11 for SFRC flexural strength, which is almost the same as for compressive strength of SFRC. The enhancing silica fume results in more SFRC flexural strength (Figure 23). Subsequently, the fine aggregates feature has a feature value of almost 0.07, followed by the feature values of super-plasticizer, steel fiber diameter, and length. The same feature values for all these features are nearly zero, depicting their lesser influence on SFRC flexural strength. The database used in the current study is the base of this prediction, and highly accurate results can be achieved with added data points.

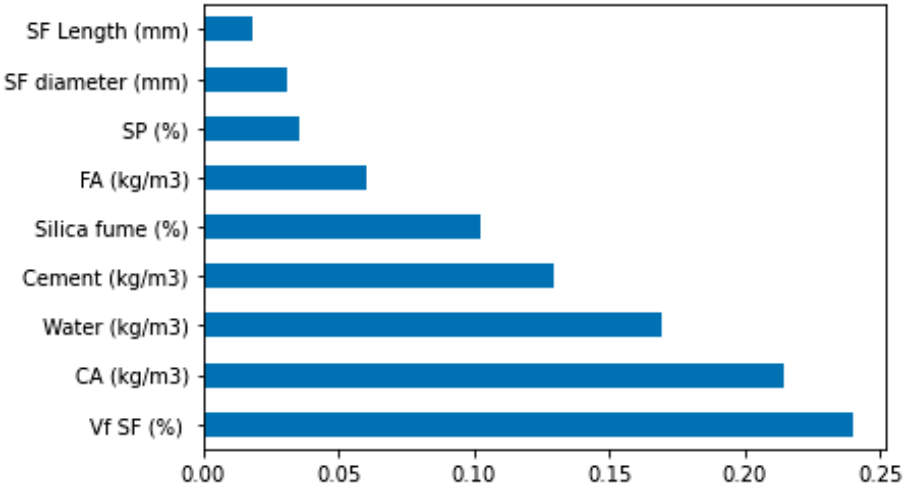

Figure 22. Flexural strength feature importance.

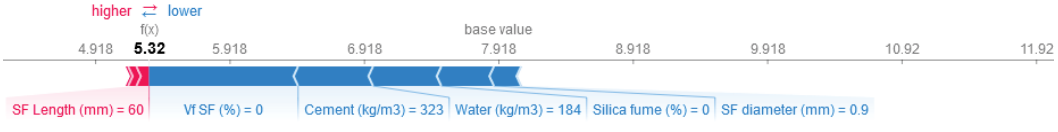

Figure 23. Flexural strength SHAP plot.

This study assessed the compressive and flexural strength of 150 mixture proportions using 9 input factors with satisfactory performance. A substantially more accurate model might be generated by increasing the number of datasheets, importing a significantly larger number of mixes, and taking into account a greater number of input parameters. In order to increase the quantity of data points and outcomes in future research, it is recommended that experimental work, field testing, and numerical analysis utilizing a variety of techniques be employed (e.g., Monte Carlo simulation, among others). To improve the models' performance, environmental conditions (such as high temperatures and humidity) might be incorporated in the input parameters along with a full explanation of the raw materials. The detailed limitations of machine learning models to estimate the strength properties of concrete is already reported in the literature [76].

6. Conclusions

The main aim of the current study is to determine the precision level of soft computational techniques to estimate SFRC compressive and flexural strengths. The considered input parameters for said prediction are cement, water, fine aggregate (FA), coarse aggregate (CA), super-plasticizer (SP), silica fume, the volume fraction of steel fiber (Vf SF), SF length (mm), and SF diameter (mm). The conclusions are as follows:

- As demonstrated by the R^2 of 0.95, the MLPNN-AdaBoost technique may be applied for precise estimation of SFRC compressive strength from its actual dataset. In contrast, individual ML MLPNN and ensembled MLPNN-Bagging ML models have R^2 values of 0.79 and 0.89, respectively, providing satisfactory results for SFRC compressive strength.
- The predicted compressive strength of SFRC is optimized by employing 20 sub-models from 10 to 200 estimators. SFRC compressive strength is more effectively predicted by an ensembled model MLPNN than other models. K-fold validation outcomes show that MLPNN models have lower MAE and RMSE with higher R^2 for SFRC compressive strength than other considered models. The model for having the best prediction for SFRC compressive strength is MLPNN.
- Statistical checks like RMSE and MAE are used to evaluate the model's performance. However, the superiority of MLPNN is demonstrated by its having a higher determination coefficient and fewer error values for SFRC compressive strength. The MLPNN is the most effective soft computational technique for predicting SFRC compressive strength.
- The cement content has the highest influence on compressive strength prediction of SFRC, followed by the contents of water, silica fume, and coarse aggregates, as revealed from SHAP analysis. The diameter of steel fibers has the least influence on SFRC compressive strength. The SHAP plot shows that the cement and silica fume content positively influence the compressive strength of SFRC.
- SFRC flexural strength is accurately predicted from its actual data by the MLPNN-AdaBoost technique as evident from the R^2 of 0.94. However, the R^2 of 0.81 and 0.92 in the case of individual MLPNN and ensembled MLPNN-Bagging ML models, respectively, estimated suitable results for SFRC flexural strength.
- The predicted flexural strength of SFRC is augmented by employing 20 sub models from 10 to 200 estimators. The more precise estimation of SFRC flexural strength is come out in case of an ensembled MLPNN model compared to other models. After applying the k-fold checks, the MLPNN algorithms are come out with higher R^2 values and lower RMSE and MAE values for SFRC flexural strength than other models.
- MLPNN is come out with the best prediction for SFRC flexural strength. RMSE and MAE statistical checks are applied to evaluate the performance of the model. Similarly, the higher determination coefficient with lower values of error show the superiority of MLPNN for the prediction of SFRC flexural strength. Among soft computational techniques, MLPNN emerged as the most effective technique for the estimation of SFRC flexural strength.
- It is revealed from SHAP analysis that the volume of steel fiber significantly influenced the predicted SFRC flexural strength, followed by contents of coarse aggregates, water, cement, and silica fume. However, the SFRC flexural strength is least influenced by steel fiber length. The SHAP plot shows that the steel fiber volume positively influences the flexural strength of SFRC.

Author Contributions: M.N.A.-H.: Funding Acquisition, Resources, Visualization, Writing—reviewing and editing. M.N.A.: Conceptualization, Funding acquisition, Resources, Project administration, Supervision, Writing-Reviewing and Editing. W.A.: Conceptualization, Data curation, Software, Methodology, Investigation, Validation, Writing—original draft. K.K.: Methodology, Investigation, Writing—Reviewing and Editing. A.A.: Resources, Visualization, Writing-Reviewing and Editing. S.E.: Visualization, Validation. Q.M.S.A.-A.: Visualization, Resources. M.G.Q.: Funding acquisition, Writing—Reviewing and Editing. All authors have read and agreed to the published version of the manuscript.

Funding: This work was supported by the Deanship of Scientific Research, Vice Presidency for Graduate Studies and Scientific Research, King Faisal University, Saudi Arabia (Project No. GRANT1406), through its KFU Research Summer Initiative. The APC was also funded by Project No. GRANT1406.

Institutional Review Board Statement: Not applicable.

Informed Consent Statement: Not applicable.

Data Availability Statement: The data used in this research have been properly cited and reported in the main text.

Acknowledgments: The authors acknowledge the Deanship of Scientific Research, Vice Presidency for Graduate Studies and Scientific Research, King Faisal University, Saudi Arabia (Project No. GRANT1406), through its KFU Research Summer Initiative. The authors extend their appreciation for the financial support that made this study possible.

Conflicts of Interest: The authors declare no conflict of interest.

References

1. Naaman, A.E. High Performance Fiber Reinforced Cement Composites. In *High-Performance Construction Materials: Science and Applications*; Shi, C., Mo, Y.L., Eds.; World Scientific Publishing: Singapore, 2008; pp. 91–153.
2. Imam, M.; Vandewalle, L.; Mortelmans, F.; Van Gemert, D. Shear domain of fibre-reinforced high-strength concrete beams. *Eng. Struct.* **1997**, *19*, 738–747. [CrossRef]
3. Furlan, S., Jr.; de Hanai, J.B. Shear behaviour of fiber reinforced concrete beams. *Cem. Concr. Compos.* **1997**, *19*, 359–366. [CrossRef]
4. Kene, K.S.; Vairagade, V.S.; Sathawane, S. Experimental study on behavior of steel and glass fiber reinforced concrete composites. *Bonfring Int. J. Ind. Eng. Manag. Sci.* **2012**, *2*, 125–130. [CrossRef]
5. Cao, M.; Mao, Y.; Khan, M.; Si, W.; Shen, S. Different testing methods for assessing the synthetic fiber distribution in cement-based composites. *Constr. Build. Mater.* **2018**, *184*, 128–142. [CrossRef]
6. Khan, M.; Cao, M.; Hussain, A.; Chu, S. Effect of silica-fume content on performance of $CaCO_3$ whisker and basalt fiber at matrix interface in cement-based composites. *Constr. Build. Mater.* **2021**, *300*, 124046. [CrossRef]
7. Arshad, S.; Sharif, M.B.; Irfan-ul-Hassan, M.; Khan, M.; Zhang, J.-L. Efficiency of supplementary cementitious materials and natural fiber on mechanical performance of concrete. *Arab. J. Sci. Eng.* **2020**, *45*, 8577–8589. [CrossRef]
8. Xie, C.; Cao, M.; Guan, J.; Liu, Z.; Khan, M. Improvement of boundary effect model in multi-scale hybrid fibers reinforced cementitious composite and prediction of its structural failure behavior. *Compos. Part B Eng.* **2021**, *224*, 109219. [CrossRef]
9. Cao, M.; Khan, M. Effectiveness of multiscale hybrid fiber reinforced cementitious composites under single degree of freedom hydraulic shaking table. *Struct. Concr.* **2021**, *22*, 535–549. [CrossRef]
10. Khan, U.A.; Jahanzaib, H.M.; Khan, M.; Ali, M. Improving the tensile energy absorption of high strength natural fiber reinforced concrete with fly-ash for bridge girders. *Key Eng. Mater.* **2018**, *765*, 335–342. [CrossRef]
11. Khan, M.; Cao, M.; Ai, H.; Hussain, A. Basalt Fibers in Modified Whisker Reinforced Cementitious Composites. *Period. Polytech. Civ. Eng.* **2022**, *66*, 344–354. [CrossRef]
12. Zhang, N.; Yan, C.; Li, L.; Khan, M. Assessment of fiber factor for the fracture toughness of polyethylene fiber reinforced geopolymer. *Constr. Build. Mater.* **2022**, *319*, 126130. [CrossRef]
13. Khan, M.; Ali, M. Improvement in concrete behavior with fly ash, silica-fume and coconut fibres. *Constr. Build. Mater.* **2019**, *203*, 174–187. [CrossRef]
14. Ramakrishnan, V.; Wu, G.Y.; Hosalli, G. Flexural fatigue strength, endurance limit and impact strength of fiber reinforced concretes. *Transp. Res. Rec.* **1989**, *1226*, 17–24.
15. Gupta, S.; Rao, V.K.; Sengupta, J. Evaluation of polyester fiber reinforced concrete for use in cement concrete pavement works. *Road Mater. Pavement Des.* **2008**, *9*, 441–461. [CrossRef]
16. Sinha, D.; Mishra, C.; Solanki, R. Comparison of normal concrete pavement with steel fiber reinforced concrete pavement. *Indian J. Appl. Res.* **2014**, *4*, 233–235. [CrossRef]
17. Khan, M.; Cao, M.; Chu, S.; Ali, M. Properties of hybrid steel-basalt fiber reinforced concrete exposed to different surrounding conditions. *Constr. Build. Mater.* **2022**, *322*, 126340. [CrossRef]
18. Li, L.; Khan, M.; Bai, C.; Shi, K. Uniaxial tensile behavior, flexural properties, empirical calculation and microstructure of multi-scale fiber reinforced cement-based material at elevated temperature. *Materials* **2021**, *14*, 1827. [CrossRef]
19. Khan, M.; Cao, M.; Xie, C.; Ali, M. Hybrid fiber concrete with different basalt fiber length and content. *Struct. Concr.* **2022**, *23*, 346–364. [CrossRef]
20. Khan, M.; Cao, M.; Xie, C.; Ali, M. Effectiveness of hybrid steel-basalt fiber reinforced concrete under compression. *Case Stud. Constr. Mater.* **2022**, *16*, e00941. [CrossRef]
21. Purkiss, J. Steel fibre reinforced concrete at elevated temperatures. *Int. J. Cem. Compos. Lightweight Concr.* **1984**, *6*, 179–184. [CrossRef]

22. Patil, S.P.; Sangle, K.K. Tests of steel fibre reinforced concrete beams under predominant torsion. *J. Build. Eng.* **2016**, *6*, 157–162. [CrossRef]
23. Noaman, A.T.; Bakar, B.A.; Akil, H.M.; Alani, A. Fracture characteristics of plain and steel fibre reinforced rubberized concrete. *Constr. Build. Mater.* **2017**, *152*, 414–423. [CrossRef]
24. Boulekbache, B.; Hamrat, M.; Chemrouk, M.; Amziane, S. Flexural behaviour of steel fibre-reinforced concrete under cyclic loading. *Constr. Build. Mater.* **2016**, *126*, 253–262. [CrossRef]
25. Gholamhoseini, A.; Khanlou, A.; MacRae, G.; Scott, A.; Hicks, S.; Leon, R. An experimental study on strength and serviceability of reinforced and steel fibre reinforced concrete (SFRC) continuous composite slabs. *Eng. Struct.* **2016**, *114*, 171–180. [CrossRef]
26. Xu, M.; Bao, Y.; Wu, K.; Xia, T.; Clack, H.L.; Shi, H.; Li, V.C. Influence of TiO_2 incorporation methods on NO_x abatement in Engineered Cementitious Composites. *Constr. Build. Mater.* **2019**, *221*, 375–383. [CrossRef]
27. Shang, M.; Li, H.; Ahmad, A.; Ahmad, W.; Ostrowski, K.A.; Aslam, F.; Joyklad, P.; Majka, T.M. Predicting the Mechanical Properties of RCA-Based Concrete Using Supervised Machine Learning Algorithms. *Materials* **2022**, *15*, 647. [CrossRef]
28. Ahmad, A.; Ahmad, W.; Chaiyasarn, K.; Ostrowski, K.A.; Aslam, F.; Zajdel, P.; Joyklad, P. Prediction of Geopolymer Concrete Compressive Strength Using Novel Machine Learning Algorithms. *Polymers* **2021**, *13*, 3389. [CrossRef]
29. Zheng, D.; Wu, R.; Sufian, M.; Kahla, N.B.; Atig, M.; Deifalla, A.F.; Accouche, O.; Azab, M. Flexural Strength Prediction of Steel Fiber-Reinforced Concrete Using Artificial Intelligence. *Materials* **2022**, *15*, 5194. [CrossRef]
30. Chaabene, W.B.; Flah, M.; Nehdi, M.L. Machine learning prediction of mechanical properties of concrete: Critical review. *Constr. Build. Mater.* **2020**, *260*, 119889. [CrossRef]
31. Ramadan Suleiman, A.; Nehdi, M.L. Modeling self-healing of concrete using hybrid genetic algorithm–artificial neural network. *Materials* **2017**, *10*, 135. [CrossRef]
32. Xu, Y.; Ahmad, W.; Ahmad, A.; Ostrowski, K.A.; Dudek, M.; Aslam, F.; Joyklad, P. Computation of High-Performance Concrete Compressive Strength Using Standalone and Ensembled Machine Learning Techniques. *Materials* **2021**, *14*, 7034. [CrossRef]
33. Han, Q.; Gui, C.; Xu, J.; Lacidogna, G. A generalized method to predict the compressive strength of high-performance concrete by improved random forest algorithm. *Constr. Build. Mater.* **2019**, *226*, 734–742. [CrossRef]
34. Al-Shamiri, A.K.; Yuan, T.-F.; Kim, J.H. Non-tuned machine learning approach for predicting the compressive strength of high-performance concrete. *Materials* **2020**, *13*, 1023. [CrossRef] [PubMed]
35. Dingqiang, F.; Rui, Y.; Zhonghe, S.; Chunfeng, W.; Jinnan, W.; Qiqi, S. A novel approach for developing a green Ultra-High Performance Concrete (UHPC) with advanced particles packing meso-structure. *Constr. Build. Mater.* **2020**, *265*, 120339. [CrossRef]
36. Fan, D.; Yu, R.; Shui, Z.; Wu, C.; Song, Q.; Liu, Z.; Sun, Y.; Gao, X.; He, Y. A new design approach of steel fibre reinforced ultra-high performance concrete composites: Experiments and modeling. *Cem. Concr. Compos.* **2020**, *110*, 103597. [CrossRef]
37. Marani, A.; Nehdi, M.L. Machine learning prediction of compressive strength for phase change materials integrated cementitious composites. *Constr. Build. Mater.* **2020**, *265*, 120286. [CrossRef]
38. Deng, F.; He, Y.; Zhou, S.; Yu, Y.; Cheng, H.; Wu, X. Compressive strength prediction of recycled concrete based on deep learning. *Constr. Build. Mater.* **2018**, *175*, 562–569. [CrossRef]
39. Zhang, J.; Huang, Y.; Aslani, F.; Ma, G.; Nener, B. A hybrid intelligent system for designing optimal proportions of recycled aggregate concrete. *J. Clean. Prod.* **2020**, *273*, 122922. [CrossRef]
40. Han, T.; Siddique, A.; Khayat, K.; Huang, J.; Kumar, A. An ensemble machine learning approach for prediction and optimization of modulus of elasticity of recycled aggregate concrete. *Constr. Build. Mater.* **2020**, *244*, 118271. [CrossRef]
41. Behnood, A.; Golafshani, E.M. Machine learning study of the mechanical properties of concretes containing waste foundry sand. *Constr. Build. Mater.* **2020**, *243*, 118152. [CrossRef]
42. Javed, M.F.; Farooq, F.; Memon, S.A.; Akbar, A.; Khan, M.A.; Aslam, F.; Alyousef, R.; Alabduljabbar, H.; Rehman, S.K. New Prediction Model for the Ultimate Axial Capacity of Concrete-Filled Steel Tubes: An Evolutionary Approach. *Crystals* **2020**, *10*, 741. [CrossRef]
43. Zhu, Y.; Ahmad, A.; Ahmad, W.; Vatin, N.I.; Mohamed, A.M.; Fathi, D. Predicting the Splitting Tensile Strength of Recycled Aggregate Concrete Using Individual and Ensemble Machine Learning Approaches. *Crystals* **2022**, *12*, 569. [CrossRef]
44. Iftikhar, B.; Alih, S.C.; Vafaei, M.; Elkotb, M.A.; Shutaywi, M.; Javed, M.F.; Deebani, W.; Khan, M.I.; Aslam, F. Predictive modeling of compressive strength of sustainable rice husk ash concrete: Ensemble learner optimization and comparison. *J. Clean. Prod.* **2022**, *348*, 131285. [CrossRef]
45. Ahmad, A.; Ahmad, W.; Aslam, F.; Joyklad, P. Compressive strength prediction of fly ash-based geopolymer concrete via advanced machine learning techniques. *Case Stud. Constr. Mater.* **2022**, *16*, e00840. [CrossRef]
46. Song, H.; Ahmad, A.; Farooq, F.; Ostrowski, K.A.; Maślak, M.; Czarnecki, S.; Aslam, F. Predicting the compressive strength of concrete with fly ash admixture using machine learning algorithms. *Constr. Build. Mater.* **2021**, *308*, 125021. [CrossRef]
47. Ahmad, A.; Farooq, F.; Niewiadomski, P.; Ostrowski, K.; Akbar, A.; Aslam, F.; Alyousef, R. Prediction of compressive strength of fly ash based concrete using individual and ensemble algorithm. *Materials* **2021**, *14*, 794. [CrossRef] [PubMed]
48. Hadzima-Nyarko, M.; Nyarko, E.K.; Lu, H.; Zhu, S. Machine learning approaches for estimation of compressive strength of concrete. *Eur. Phys. J. Plus* **2020**, *135*, 682. [CrossRef]
49. Nafees, A.; Khan, S.; Javed, M.F.; Alrowais, R.; Mohamed, A.M.; Mohamed, A.; Vatin, N.I. Forecasting the Mechanical Properties of Plastic Concrete Employing Experimental Data Using Machine Learning Algorithms: DT, MLPNN, SVM, and RF. *Polymers* **2022**, *14*, 1583. [CrossRef]

50. Soulioti, D.; Barkoula, N.; Paipetis, A.; Matikas, T. Effects of fibre geometry and volume fraction on the flexural behaviour of steel-fibre reinforced concrete. *Strain* **2011**, *47*, e535–e541. [CrossRef]
51. Yoo, D.-Y.; Yoon, Y.-S.; Banthia, N. Flexural response of steel-fiber-reinforced concrete beams: Effects of strength, fiber content, and strain-rate. *Cem. Concr. Compos.* **2015**, *64*, 84–92. [CrossRef]
52. Lee, J.-H.; Cho, B.; Choi, E. Flexural capacity of fiber reinforced concrete with a consideration of concrete strength and fiber content. *Constr. Build. Mater.* **2017**, *138*, 222–231. [CrossRef]
53. Köksal, F.; Altun, F.; Yiğit, İ.; Şahin, Y. Combined effect of silica fume and steel fiber on the mechanical properties of high strength concretes. *Constr. Build. Mater.* **2008**, *22*, 1874–1880. [CrossRef]
54. Yoon, E.-S.; Park, S.-B. An experimental study on the mechanical properties and long-term deformations of high-strength steel fiber reinforced concrete. *KSCE J. Civ. Environ. Eng. Res.* **2006**, *26*, 401–409.
55. Abbass, W.; Khan, M.I.; Mourad, S. Evaluation of mechanical properties of steel fiber reinforced concrete with different strengths of concrete. *Constr. Build. Mater.* **2018**, *168*, 556–569. [CrossRef]
56. Yoo, D.-Y.; Yoon, Y.-S.; Banthia, N. Predicting the post-cracking behavior of normal-and high-strength steel-fiber-reinforced concrete beams. *Constr. Build. Mater.* **2015**, *93*, 477–485. [CrossRef]
57. Lee, H.-H.; Lee, H.-J. Characteristic strength and deformation of SFRC considering steel fiber factor and volume fraction. *J. Korea Concr. Inst.* **2004**, *16*, 759–766. [CrossRef]
58. Oh, Y.-H. Evaluation of flexural strength for normal and high strength concrete with hooked steel fibers. *J. Korea Concr. Inst.* **2008**, *20*, 531–539.
59. Song, P.; Hwang, S. Mechanical properties of high-strength steel fiber-reinforced concrete. *Constr. Build. Mater.* **2004**, *18*, 669–673. [CrossRef]
60. Jang, S.-J.; Yun, H.-D. Combined effects of steel fiber and coarse aggregate size on the compressive and flexural toughness of high-strength concrete. *Compos. Struct.* **2018**, *185*, 203–211. [CrossRef]
61. Aldossari, K.; Elsaigh, W.; Shannag, M. Effect of steel fibers on flexural behavior of normal and high strength concrete. *Int. J. Civ. Environ. Eng.* **2014**, *8*, 22–26.
62. Dinh, N.H.; Park, S.-H.; Choi, K.-K. Effect of dispersed micro-fibers on tensile behavior of uncoated carbon textile-reinforced cementitious mortar after high-temperature exposure. *Cem. Concr. Compos.* **2021**, *118*, 103949. [CrossRef]
63. Thomas, J.; Ramaswamy, A. Mechanical properties of steel fiber-reinforced concrete. *J. Mater. Civ. Eng.* **2007**, *19*, 385–392. [CrossRef]
64. Sivakumar, A.; Santhanam, M. Mechanical properties of high strength concrete reinforced with metallic and non-metallic fibres. *Cem. Concr. Compos.* **2007**, *29*, 603–608. [CrossRef]
65. Afroughsabet, V.; Ozbakkaloglu, T. Mechanical and durability properties of high-strength concrete containing steel and polypropylene fibers. *Constr. Build. Mater.* **2015**, *94*, 73–82. [CrossRef]
66. Atiş, C.D.; Karahan, O. Properties of steel fiber reinforced fly ash concrete. *Constr. Build. Mater.* **2009**, *23*, 392–399. [CrossRef]
67. Farooq, F.; Ahmed, W.; Akbar, A.; Aslam, F.; Alyousef, R. Predictive modeling for sustainable high-performance concrete from industrial wastes: A comparison and optimization of models using ensemble learners. *J. Clean. Prod.* **2021**, *292*, 126032. [CrossRef]
68. Aslam, F.; Farooq, F.; Amin, M.N.; Khan, K.; Waheed, A.; Akbar, A.; Javed, M.F.; Alyousef, R.; Alabdulijabbar, H. Applications of gene expression programming for estimating compressive strength of high-strength concrete. *Adv. Civ. Eng.* **2020**, *2020*, 8850535.
69. Ahmad, W.; Ahmad, A.; Ostrowski, K.A.; Aslam, F.; Joyklad, P.; Zajdel, P. Application of Advanced Machine Learning Approaches to Predict the Compressive Strength of Concrete Containing Supplementary Cementitious Materials. *Materials* **2021**, *14*, 5762. [CrossRef]
70. Khan, M.; Cao, M.; Ali, M. Cracking behaviour and constitutive modelling of hybrid fibre reinforced concrete. *J. Build. Eng.* **2020**, *30*, 101272. [CrossRef]
71. Amin, M.N.; Ahmad, W.; Khan, K.; Ahmad, A.; Nazar, S.; Alabdullah, A.A. Use of Artificial Intelligence for Predicting Parameters of Sustainable Concrete and Raw Ingredient Effects and Interactions. *Materials* **2022**, *15*, 5207. [CrossRef]
72. Amin, M.N.; Khan, K.; Ahmad, W.; Javed, M.F.; Qureshi, H.J.; Saleem, M.U.; Qadir, M.G.; Faraz, M.I. Compressive Strength Estimation of Geopolymer Composites through Novel Computational Approaches. *Polymers* **2022**, *14*, 2128. [CrossRef]
73. Khan, K.; Ahmad, W.; Amin, M.N.; Ahmad, A.; Nazar, S.; Alabdullah, A.A.; Arab, A.M.A. Exploring the Use of Waste Marble Powder in Concrete and Predicting Its Strength with Different Advanced Algorithms. *Materials* **2022**, *15*, 4108. [CrossRef] [PubMed]
74. Khan, K.; Ahmad, A.; Amin, M.N.; Ahmad, W.; Nazar, S.; Arab, A.M.A. Comparative Study of Experimental and Modeling of Fly Ash-Based Concrete. *Materials* **2022**, *15*, 3762. [CrossRef] [PubMed]
75. Zou, Y.; Zheng, C.; Alzahrani, A.M.; Ahmad, W.; Ahmad, A.; Mohamed, A.M.; Khallaf, R.; Elattar, S. Evaluation of Artificial Intelligence Methods to Estimate the Compressive Strength of Geopolymers. *Gels* **2022**, *8*, 271. [CrossRef] [PubMed]
76. Khan, M.; Lao, J.; Dai, J.-G. Comparative study of advanced computational techniques for estimating the compressive strength of UHPC. *J. Asian Concr. Fed.* **2022**, *8*, 51–68. [CrossRef]

materials

MDPI

Article

Predicting the Rheological Properties of Super-Plasticized Concrete Using Modeling Techniques

Muhammad Nasir Amin [1,*], Ayaz Ahmad [2], Kaffayatullah Khan [1], Waqas Ahmad [3], Saqib Ehsan [4] and Anas Abdulalim Alabdullah [1]

[1] Department of Civil and Environmental Engineering, College of Engineering, King Faisal University, Al-Ahsa 31982, Saudi Arabia; kkhan@kfu.edu.sa (K.K.); 218038024@student.kfu.edu.sa (A.A.A.)
[2] MaREI Centre, Ryan Institute and School of Engineering, College of Science and Engineering, National University of Ireland Galway, H91 TK33 Galway, Ireland; a.ahmad8@nuigalway.ie
[3] Department of Civil Engineering, COMSATS University Islamabad, Abbottabad 22060, Pakistan; waqasahmad@cuiatd.edu.pk
[4] Department of Civil Engineering, NFC Institute of Engineering and Fertilizer Research, Faisalabad 38090, Pakistan; saqib.ehsan@iefr.edu.pk
* Correspondence: mgadir@kfu.edu.sa; Tel.: +966-13-589-5431; Fax: +966-13-581-7068

Abstract: Interface yield stress (YS) and plastic viscosity (PV) have a significant impact on the pumpability of concrete mixes. This study is based on the application of predictive machine learning (PML) techniques to forecast the rheological properties of fresh concrete. The artificial neural network (NN) and random forest (R-F) PML approaches were introduced to anticipate the PV and YS of concrete. In comparison, the R-F model outperforms the NN model by giving the coefficient of determination (R^2) values equal to 0.92 and 0.96 for PV and YS, respectively. In contrast, the model's legitimacy was also verified by applying statistical checks and a k-fold cross validation approach. The mean absolute error, mean square error, and root mean square error values for R-F models by investigating the YS were noted as 30.36 Pa, 1141.76 Pa, and 33.79 Pa, respectively. Similarly, for the PV, these values were noted as 3.52 Pa·s, 16.48 Pa·s, and 4.06 Pa·s, respectively. However, by comparing these values with the NN's model, they were found to be higher, which also gives confirmation of R-F's high precision in terms of predicting the outcomes. A validation approach known as k-fold cross validation was also introduced to authenticate the precision of employed models. Moreover, the influence of the input parameters was also investigated with regard to predictions of PV and YS. The proposed study will be beneficial for the researchers and construction industries in terms of saving time, effort, and cost of a project.

Keywords: concrete; plastic viscosity; yield stress; modeling; machine learning

Citation: Amin, M.N.; Ahmad, A.; Khan, K.; Ahmad, W.; Ehsan, S.; Alabdullah, A.A. Predicting the Rheological Properties of Super-Plasticized Concrete Using Modeling Techniques. *Materials* **2022**, *15*, 5208. https://doi.org/10.3390/ma15155208

Academic Editor: Krzysztof Schabowicz

Received: 2 June 2022
Accepted: 12 July 2022
Published: 27 July 2022

Publisher's Note: MDPI stays neutral with regard to jurisdictional claims in published maps and institutional affiliations.

1. Introduction

Conventional concrete is one of the most widely used building materials in the world [1–3]. It is considered a complex substance, which is a mixture of fine and coarse aggregates coupled with a cementitious matrix that is suspended in the air [4–6]. However, fresh concrete without enough flowability makes casting, pumping, spreading, and molding around steel reinforcement extremely difficult [7–9]. The product's low strength and poor durability result from inadequate compaction [10–14]. Inadequate cohesion and surface finishing difficulties might also contribute to problems. Fresh concrete must be able to be carried, placed, poured into molds and around reinforcement, compacted, and finished without separating [12,15–19]. To make fresh concrete more fluid, just adding more water is ineffective since the water forms pores that weaken the hardened product [20,21]. Therefore, water-reducing admixtures are desirable and frequently utilized because they can maintain flow at a lower water content, resulting in a substantial boost in concrete's strength and durability [22–24]. For high-rise construction, considerable

attention is paid to making concrete pumpable without segregation and bleeding [25,26]. To avoid cold joints, segregation, honeycombing during pumping, transportation, and placement, and compactions around the reinforcement, freshly mixed concrete must have acceptable flowability [27].

Plastic viscosity (PV) refers to the resistance a fluid presents to free flow [28]. This resistance is caused by friction between the deforming liquid and the particles and liquids in the drilling mud [29]. PV is a Bingham plastic model parameter that represents the slope of the shear stress/shear rate line above the yield point [30]. PV is a crucial rheological property that influences the parameters of drilling fluid [31]. However, experimentally and computationally, the yield stress is associated with common field-friendly measuring methods, such as the slump and slump flow test, for evaluating flowability [32].

Rheology is the study of the deformation and flowability of concrete [33–35]. It entails measuring yield stress and plastic viscosity at various shear rates and times [36–38]. Controlling fresh characteristics enables the production of concrete with the requisite green strength and viscosity [39]. Therefore, the evaluation of fresh characteristics in terms of rheology provides an effective tool for monitoring the requisite flowability in concrete 3-D printing [40–43]. Even though there have been papers written about constitutive equations that describe how fresh concrete behaves rheologically, only the Bingham model and the Herschel and Bulkley (H–B) model have been accepted [44]. For normal slump concrete, Bingham's material model has been demonstrated to suit experimental data fairly well and is defined as follows.

$$\tau = \tau_0 + \mu_p \gamma. \quad (1)$$

where τ, μ_p, and γ. indicates the stress (shear), PV, and shear rate, respectively. Modeling and describing the flow of fresh concrete is based on the assumption that it follows the Bingham model. The rheological properties of concrete have been measured using the same assumption, but the data points are different depending on the testing device [45]. Until a consistent test method for assessing the rheological characteristics of concrete is created, the characterization of concrete's fresh qualities will remain in a state of uncertainty.

The application of predictive modelling techniques to anticipate the various properties of the objects based on the input parameters is gaining popularity [46–52], especially supervised predictive machine learning (PML) algorithms, which can predict the required outcome more precisely. Asri et al. [53] also employed various PML techniques to predict the YS and PV of self-compacting concrete (SCC). They used the number of PML approaches on the data set and predicted the aforementioned result. The Ghanbari et al. [54] study was based on the anticipation of PV of self-compacting fiber reinforced concrete. The study reported better precision for the required outcome. AICHA et al. [55] incorporated the NN model and multi-variable regression to anticipate the rheological parameters of the SCC. A total of 59 data points were retrieved from the literature for running the selected models. Yousef et al. [56] employed the ANN model from PML algorithms to predict the YS and PV of the SCC. The experimental data set was developed for running the model for the predictive result. Mohammed et al. [57] study was based on the application of nonlinear regression (NLR) model and ANN model to investigate the predictive outcome for both the rheological properties and strength of cement paste. They reported that the NLR precision level was better as compared to the ANN model toward the prediction

The purpose of the present study is to introduce the soft computing techniques which can successfully predict the complex, time-consuming, and experimental effort-related properties of concrete in a limited time. These novel approaches can help to execute the project work fluently without waiting for the testing results from the laboratory. This research describes the predictive modeling applications of the rheological properties of super-plasticized concrete. In order to avoid bias and increase the robustness of the study, the artificial neural network (NN) machine learning (ML) approach has been selected from the individual ML approaches, while the random forest (R-F) technique has been selected from the ensemble ML approaches for predicting the outcomes. Ensemble ML algorithms normally use weak learners and split the model into 20-sub models for high accuracy.

The plastic viscosity (PV) and yield stress (YS) have been investigated with NN and R-F approaches from predictive machine learning (PML). Statistical checks and validation approaches were also adopted to confirm the employed model's legitimacy. This research is novel in that it describes the effect of both ensemble (R-F) and individual (ANN) PML methods to anticipate the rheological properties of fresh concrete. This research will be beneficial for construction industries by saving time, experimental effort, and money.

2. Materials and Data Description

The application of Python coding played a vital role in the required models. The Spyder (4.1.4) of anaconda navigator software was used to introduce the relevant coding of Python for running the employed model [58]. The software adopted the six input parameters, including the sand, cement, water, small gravel, medium gravel, and superplasticizers, while each model ran two times for two different outcomes (PV and YS). The set of data, consisting of 139 data points, used for modelling was retrieved from the literature. Moreover, the coding was set in the software which automatically split the data set into training (80%), and testing (20%) purposes. The relation between the experimental result for both outputs and the predictive result from the modelling were compared. The statistical checks in the form of evaluating the various errors using same software were also applied along with the k-fold cross validation approach to satisfy the accuracy level of the models. In contrast, an additional analysis was carried out (sensitivity analysis) to figure out how much each input parameter affects the prediction of the rheological properties of fresh concrete. The descriptive statistical information of the input variables is listed in tabulated form as shown in Table 1. The histogram in Figure 1 gives the information on the relative frequency distribution of each variable used for running the models. However, the detailed adopted research methodology in the form of the flow chart is presented in Figure 2.

Table 1. Statistical description of the concrete's parameters data set.

Input Variables	Maximum	Minimum	Mean	Standard Deviation
Cement (kg)	604.00	410.00	457.79	28.33
Water (kg)	275.00	147.00	186.32	26.97
Fine aggregate (kg)	1064.00	553.00	796.11	105.09
Coarse gravel (5 × 10 mm)	1010.00	0.00	123.59	258.77
Medium coarse gravel (10 × 20 mm)	1080.00	0.00	840.87	264.80
Superplasticizer (L/100 kg cement)	4.60	0.00	1.80	1.67

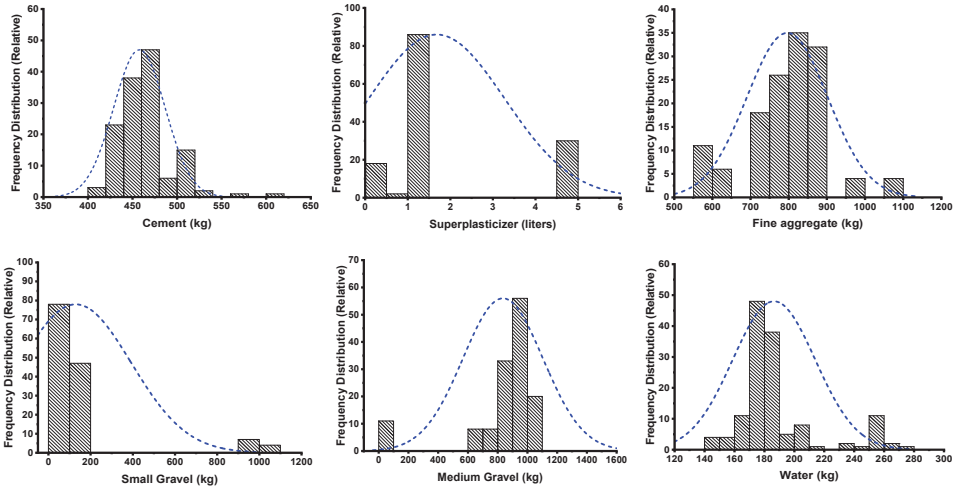

Figure 1. Graphical representation of relative frequency distribution for input parameters.

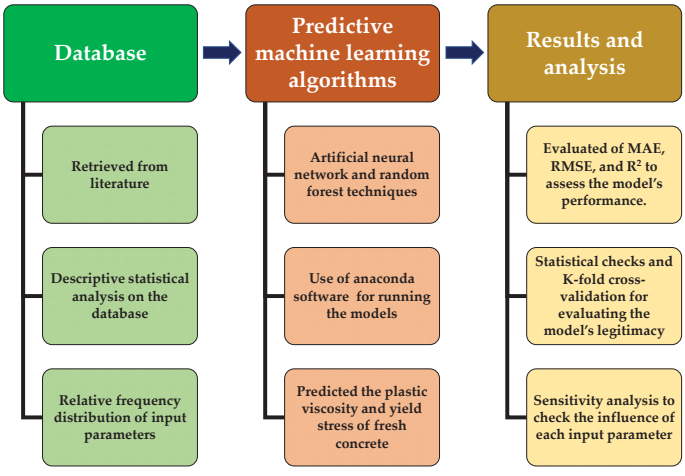

Figure 2. Schematic representation of research's adopted methodology.

2.1. Predictive Modelling Approaches

2.1.1. Artificial Neural Network (NN)

Neural networks (NN) are generally simple and small in size; yet, they feature strong knowledge-and-information-processing capabilities because of their similarities to the human brain [59]. In civil engineering, NNs have been used to find internal damage, identify structural systems, model the behavior of materials, optimize and control structures, monitor underground water, predict how much a shallow foundation will sink, and figure out how much of each ingredient to put in a concrete mix. Input neurons provide the raw content. Weights and biases create connections among input and hidden neurons. Output neurons provide the indication through connections among the hidden and output neurons. Neural networks are used a lot in engineering because they can recognize patterns, learn on their own, organize themselves, and work in real-time. In contrast to many other soft computing techniques, NNs instantly learn from the specified training patterns and builds the relationship between input and output parameters. In addition, NNs impose no constraints on the input parameters for distributions without defined relationships.

2.1.2. Random Forest (R-F)

Leo Breiman proposed R-Fs12 in 2001 as an intelligent combination of classification algorithms based on statistical learning theory [60]. In R-F, the original data are resampled to obtain additional samples mostly via the bootstrap method. After constructing classification trees for each bootstrap sample, the final results are determined by voting on the combined predictions of the classification trees (Figure 1). R-F can be used for both classification and regression applications. It is employed as a regression tool in the current investigation. When utilizing R-F to solve regression problems, the output variables are fitted with values of the input parameters. For each input factor, the data set is divided into many points, and the Sum of Square Error (SSE) is computed at each point for the actual and projected values. The minimum SSE value for this node is then determined. It can also be investigated how important a variable is by switching around all the values of the input variables and measuring how much their accuracy rate changes in the out-of-bag samples (a number of observations that are not used in training and are referred to as the "out-of-bag" data set: OOB data set) [61].

3. K-Fold Cross Validation (C-V)

The estimation of prediction accuracy is crucial if our objective is to predict. The training error is a straightforward approximation of the prediction error; however, it

is biased downwards. C-V, on the other hand, has an upward bias. The upward bias may be minor in leave-one-out cross validation, but it cannot always be ignored in the computationally preferred 5-fold or 10-fold cross validation. Since the training error has a downward bias and C-V has an upward bias, a family that connects the two estimates will contain an appropriate estimate. Generally, the performance of classification algorithms is tested using C-V. First, a data set is randomly partitioned into k distinct folds with roughly the same number of instances. Then, each fold assumes responsibility for evaluating the model suggested by the other k-1 folds. Throughout this procedure, the training data set is partitioned into multiple 'k' smaller pieces. Consequently, the term 'k'-fold was coined. On the basis of a random data set, k-fold is utilized for testing and k-1 for training. The prediction model's efficacy is evaluated using a stratified 10-fold cross-validation method. This approach divides the data set into ten folds at random. Consequently, each fold is utilized just once as a validation set. Finally, the error or accuracy measure for each fold can be compared; if they are comparable, the model is likely to generalize well.

4. Results and Discussion

4.1. Yield Stress Output from NN's Model

The relation between the experimental result and the result obtained from the ANN model for YS showed better accuracy, as indicated by the R^2 value of 0.89, which can be seen in Figure 3. The distribution of the variation between the actual result and ANN's model output can be seen in Figure 4. This difference gave the maximum and minimum values as 59.85 Pa and 1.35 Pa, respectively. However, it was noted that 25.95% of the variation's data lied between the minimum value and 30 Pa, and 27.77% of the data were reported between 30 Pa and 50 Pa. However, 42.59% of these data were reported above 50 Pa.

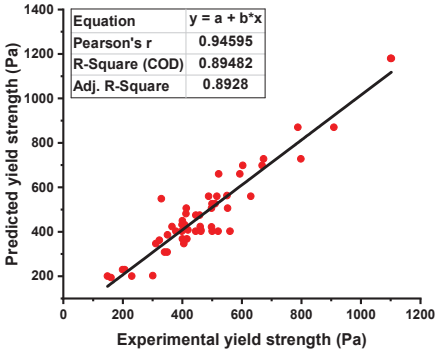

Figure 3. Yield stress relationship for the actual and predicted result of ANN model.

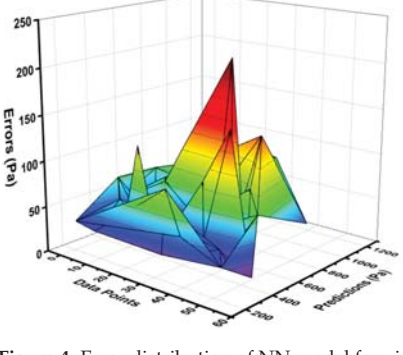

Figure 4. Error distribution of NN model for yield stress.

4.2. Yield Stress Output from R-F Model

R-F model showed strong relation when a comparison was made for the result of YS with the experimental result. R-F gives the R^2 value equal to 0.96, indicating a much high precision level in terms of predicting the YS of the fresh concrete as opposed to the NN model, as shown in Figure 5. The result of the data representing the difference between the real and forecasted values can be seen in Figure 6. This data showed the maximum, minimum, and average values to be 59.85 Pa, 1.35 Pa, and 30.36 Pa, respectively. It was also noted that 50% of these data were lying between a minimum value of 30 Pa, and 40.74% of the data were reported between 30 Pa to 50 Pa. However, only 9.25% of the aforementioned data were noted above 50 Pa.

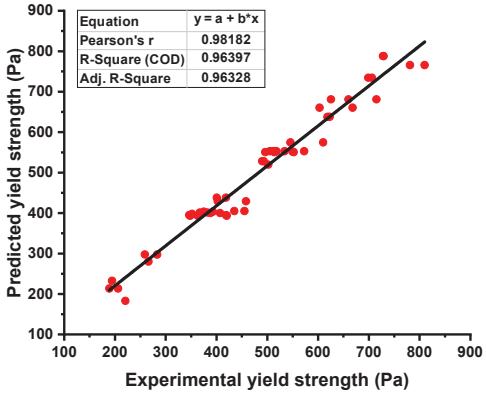

Figure 5. Yield stress relationship for the actual and predicted result of R-F model.

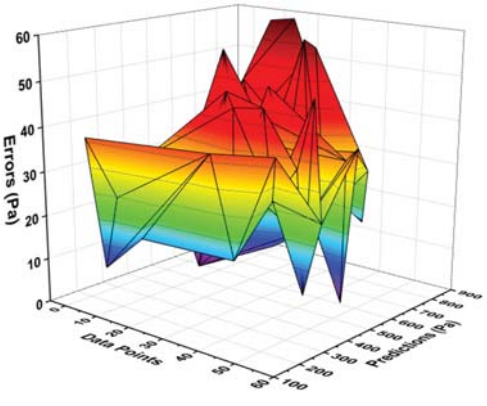

Figure 6. Error distribution of R-F model for yield stress.

4.3. Plastic Viscosity Outcome from NN's Model

When comparing the ANN's model output for the PV of fresh concrete with the experimental result, the precision level in predicting the required result was better. This is indicated by the R^2 value equal to 0.87, as shown in Figure 7. However, the distribution of the difference values between the experimental and predicted ANN models is depicted in Figure 8. This distribution gives the highest, minimum, and average values as 7.72 Pa·s, 0.11 Pa·s, and 3.52 Pa·s. Moreover, it was noted that 33.33% of these data lie between its minimum value and 2 Pa·s, 35.08% of the data lie between 2 Pa·s and 5 Pa·s, and 31.5% of the difference data were reported above 5 Pa·s.

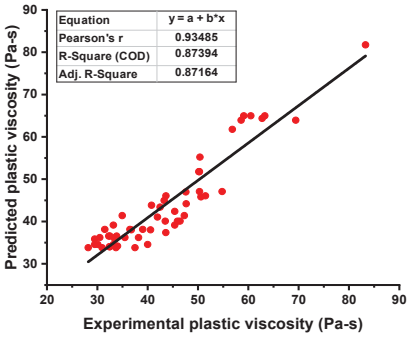

Figure 7. Plastic viscosity relationship for the actual and predicted result of the NN model.

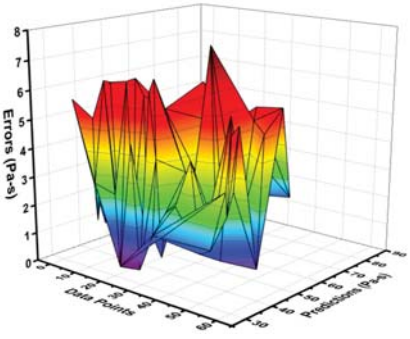

Figure 8. Error distribution of NN model for plastic viscosity.

4.4. Plastic Viscosity Outcome from R-F Model

The relationship for the PV of fresh concrete between the actual and forecasted results of the R-F model showed high accuracy as opposed to the ANN model. This confirmation was made by examining the coefficient of determination (R^2) value equal to 0.96 for the R-F model, the reflection of which can be seen in Figure 9. However, the error distribution for the result of PV of fresh concrete between the experimental and predicted outcome is shown in Figure 10. The distribution gives the highest, minimum, and average values equal to 12.18 Pa·s, 0.589 Pa·s, and 3.59 Pa·s, respectively. In addition, 22.80% of these data were reported between the minimum value (0.589 Pa·s) and 2 Pa·s, 52.63% of the data were between 2 Pa·s and 5 Pa·s, while 24.56% of these data were noted above the 5 Pa·s.

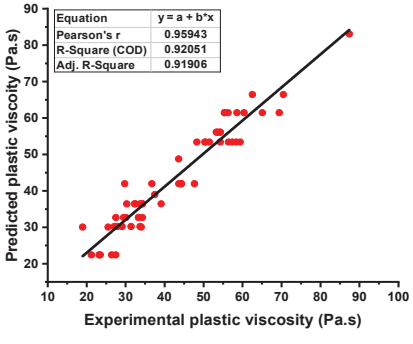

Figure 9. Plastic viscosity relationship for the actual and predicted result of R-F model.

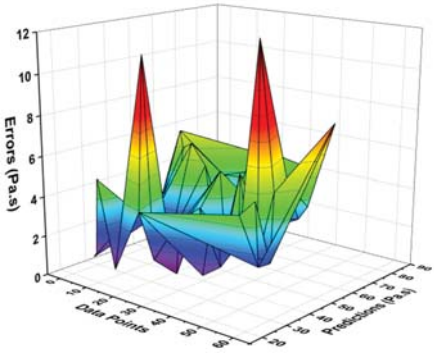

Figure 10. Error distribution of R-F model for plastic viscosity.

5. Result of K-Fold Cross Validation (C-V)

C-V is a statistical method for judging or speculating how well machine learning models really work. Because it is important to know how well the chosen models work, users need a validation method to figure out how accurate the model's data are. For the k-fold validation test, the data set needs to be mixed up randomly and separated into k classes. In this study, experimental sample data were split into 10 subsets. It utilized nine of the ten subgroups, but only one of them was used to test the model. The same part of this process was then performed 10 times to get an average of how accurate these 10 times were. It was clear that the 10-fold cross-validation method gave a good picture of the model's performance and accuracy.

C-V could be used to confirm bias and decrease deviation for the data set. Figures 11–14 show how a correlation coefficient (R^2), a mean absolute error (MAE), and a root mean square error (RMSE) were used for both plastic viscosity (PV) and yield stress (YS) to quantify the impact of cross validation. The ANN model's K-fold C-V for PV gave the highest values for MAE, RMSE, and R^2 as 255.75 Pa·s, 288.47 Pa·s, and 0.95, respectively, as depicted in Figure 11. A steady increase in MAE in the graph was reported until the k-fold value of 4, while an abrupt decrease was reported at values 5 and 7. Similarly, in the case of R^2, after a second k-fold value, the minimum result was reported, which seemed to normally increase until the 10th k-fold value. The maximum values of the same parameters for the R-F model to analyze plastic viscosity are 188.48 Pa·s, 147.38 Pa·s, and 0.97, respectively, as shown in Figure 12. In this case, MAE showed a fluctuation in the result until the end point of the graph, while a decrease in the R^2 result was noted with some variations. Similarly, the maximum values of the ANN's model for MAE, RMSE, and R^2 of YS were noted as 28.36 Pa, 32.42 Pa, and 0.98, respectively, as shown in Figure 13. An abrupt increase in MAE was reported at the initial phase, but it showed a sharp decrease at the stage of the 3rd k-fold. Moreover, R^2 showed a steady decrease until the 6th k-fold and a dramatic increase was reported to reach the maximum value. However, the maximum values for YS of the R-F's model for the same parameters give 25.1 Pa, 29.39 Pa, and 0.96, respectively, as shown in Figure 14. A steady decrease in MAE was noted in this case until the 4th k-fold value and then fluctuated in the MAE result until the last k-fold. However, the R^2 result also showed a declining curve until the 4th k-fold value, and then random changes were noted. In contrast, the statistical checks for the YS and PV of concrete for both the models are listed in Tables 2 and 3, respectively.

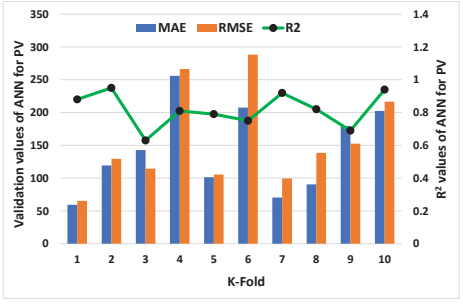

Figure 11. K-fold result of plastic viscosity from ANN model.

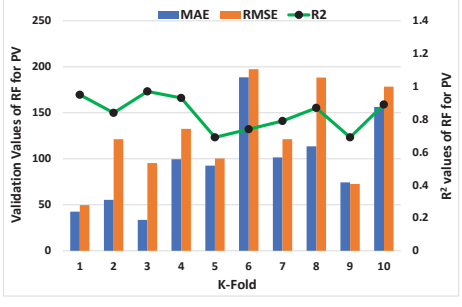

Figure 12. K-fold result of plastic viscosity from R-F model.

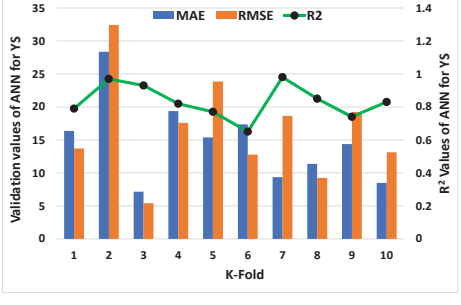

Figure 13. K-fold result of yield stress from NN model.

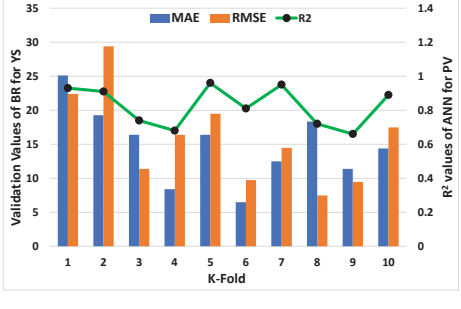

Figure 14. K-fold result of yield stress from R-F model.

Table 2. Statistical outcomes of yield stress for employed models.

PML Approaches	MAE (Pa)	MSE (Pa)	RMSE (Pa)
NN Algorithm	54.34	4491.6804	67.02
R-F algorithm	30.36	1141.7641	33.79

Table 3. Statistical outcomes of plastic viscosity for employed models.

PML Approaches	MAE (Pa·s)	MSE (Pa·s)	RMSE (Pa·s)
NN Algorithm	3.59	17.9776	4.24
R-F algorithm	3.52	16.4836	4.06

6. Sensitivity Analysis (S-A) Outcome

The S-A was introduced to examine the influence and the impact of each input parameter used to determine the predictive outcome for both plastic viscosity (PV) and yield stress (YS). This analysis revealed that the stronger influence on the prediction of rheological parameters was cement, which showed a 32.74% contribution, and superplasticizers with 24.61%. However, other variables contributed less towards the anticipation of rheological parameters of fresh concrete. Contributions made by other variables in descending order were small gravel (14.37%), medium gravel (11.07%), fine aggregate (9.73), and water (7.48%), as shown in Figure 15.

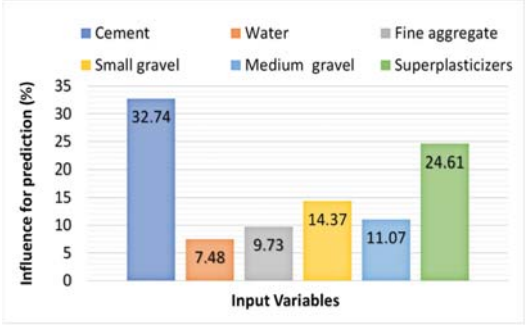

Figure 15. Influence of input parameters on the targeted outcome.

7. Discussion

This study examines the use of machine learning techniques to predict the rheological characteristics of fresh concrete. The selection of ANN and R-F models was based on their classification from different types of ML techniques. ANN belongs to the individual ML approach category, while R-F refers to the ensemble ML algorithm. ANN model uses the connection system of neurons and executes the process accordingly for the required output. However, in addition to its basic execution process, twenty R-F sub-models were trained on data and optimized to get the highest R^2 value. Moreover, the data were also validated by means of K-fold C-V using R^2, MAE, and RMSE. The input parameters played a vital role in the accuracy level of the employed model. The variation in the result may occur from both increasing or decreasing the total number of input parameters. However, the confirmation, such as statistical checks, sensitivity analysis, and validation for the models, was validated to achieve the precision level.

8. Conclusions

This paper proposed a comparison of predictive machine learning (PML) models for the rheological parameters of fresh concrete. The plastic viscosity (PV) and yield stress (YS) properties of the concrete at the initial stage were predicted using artificial neural network

(ANN) and random forest (R-F) models. The following conclusions can be drawn from the study:

- The ML algorithms can be successfully employed to anticipate the rheological properties of fresh concrete.
- R-F approach was efficient in predicting both PV and YS of the fresh concrete.
- The proposed model achieved high predictive precision as indicated by the higher coefficient of determination (R^2) value, equal to 0.92 for PV and 0.96 for the YS of the fresh concrete.
- High predictive accuracy for the R-F model was also confirmed from the statistical checks. The lower values of MAE and RMSE and the high value of R^2 provided the aforementioned confirmation.
- The input parameter with the highest influence was noted as cement, which contributed 32.74% towards the prediction of rheological parameters of concrete.

The data set can be enhanced with the experimental approach to check the performance level of the models with a large data set. The input parameters can be increased with the addition of the chemicals in concrete, the effect of temperature, the water to cement ratio, and the cement to aggregate ratio. Other ML approaches, such as SVM, Adaboost, XGboost, and deep learning methods, can also be introduced to investigate these properties.

Author Contributions: M.N.A.: Conceptualization, Funding acquisition, Resources, Project administration, Supervision, Writing-Reviewing and Editing. A.A.: Conceptualization, Data curation, Software, Methodology, Investigation, Validation, Writing-original draft. K.K.: Methodology, Investigation, Writing—Reviewing and Editing. W.A.: Resources, Visualization, Writing-Reviewing and Editing. S.E.: Visulization, Writing—Reviewing and Editing. A.A.A.: Visualization, Funding acquisition. All authors have read and agreed to the published version of the manuscript.

Funding: This work was supported by the Deanship of Scientific Research, Vice Presidency for Graduate Studies and Scientific Research, King Faisal University, Saudi Arabia [Project No. GRANT347]. The APC was funded by the same "Project No. GRANT347".

Institutional Review Board Statement: Not applicable.

Informed Consent Statement: Not applicable.

Data Availability Statement: The data used in this research have been properly cited and reported in the main text.

Acknowledgments: The authors acknowledge the Deanship of Scientific Research, Vice Presidency for Graduate Studies and Scientific Research, King Faisal University, Saudi Arabia [Project No. GRANT347]. The authors extend their appreciation for the financial support that has made this study possible.

Conflicts of Interest: The authors declare no conflict of interest.

References

1. Alberti, M.G.; Enfedaque, A.; Gálvez, J.C. Comparison between polyolefin fibre reinforced vibrated conventional concrete and self-compacting concrete. *Constr. Build. Mater.* **2015**, *85*, 182–194. [CrossRef]
2. Yang, H.; Liu, L.; Yang, W.; Liu, H.; Ahmad, W.; Ahmad, A.; Aslam, F.; Joyklad, P. A comprehensive overview of geopolymer composites: A bibliometric analysis and literature review. *Case Stud. Constr. Mater.* **2022**, *16*, e00830. [CrossRef]
3. Cao, M.; Khan, M. Effectiveness of multiscale hybrid fiber reinforced cementitious composites under single degree of freedom hydraulic shaking table. *Struct. Concr.* **2021**, *22*, 535–549. [CrossRef]
4. Khalaf, F.M.; DeVenny, A.S. Recycling of demolished masonry rubble as coarse aggregate in concrete. *J. Mater. Civ. Eng.* **2004**, *16*, 331–340. [CrossRef]
5. Yang, D.; Zhao, J.; Ahmad, W.; Amin, M.N.; Aslam, F.; Khan, K.; Ahmad, A. Potential use of waste eggshells in cement-based materials: A bibliographic analysis and review of the material properties. *Constr. Build. Mater.* **2022**, *344*, 128143. [CrossRef]
6. Khan, K.; Ahmad, W.; Amin, M.N.; Nazar, S. Nano-silica-modified concrete: A bibliographic analysis and comprehensive review of material properties. *Nanomaterials* **2022**, *12*, 1989. [CrossRef]
7. Kwon, S.H.; Jang, K.P.; Kim, J.H.; Shah, S.P. Materials, State of the art on prediction of concrete pumping. *Int. J. Concr. Struct.* **2016**, *10*, 75–85. [CrossRef]

8. Kim, J.S.; Kwon, S.H.; Jang, K.P.; Choi, M.S. Concrete pumping prediction considering different measurement of the rheological properties. *Constr. Build. Mater.* **2018**, *171*, 493–503. [CrossRef]
9. Khan, U.A.; Jahanzaib, H.M.; Khan, M.; Ali, M. *Improving the Tensile Energy Absorption of High Strength Natural Fiber Reinforced Concrete with Fly-Ash for Bridge Girders*; Trans Tech Publications: Zurich, Switzerland, 2018.
10. Pekmezci, B.Y.; Voigt, T.; Wang, K.; Shah, S. Low compaction energy concrete for improved slipform casting of concrete pavements. *ACI Mater. J.* **2007**, *104*, 251.
11. Khan, M.; Cao, M.; Ai, H.; Hussain, A. Basalt fibers in modified whisker reinforced cementitious composites. *Period. Polytech. Civ. Eng.* **2022**, *66*, 344–354. [CrossRef]
12. Zhang, N.; Yan, C.; Li, L.; Khan, M. Assessment of fiber factor for the fracture toughness of polyethylene fiber reinforced geopolymer. *Constr. Build. Mater.* **2022**, *319*, 126130. [CrossRef]
13. Ashfaq, M.; Lal, M.H.; Moghal, A.A.B. *Utilization of Coal Gangue for Earthworks: Sustainability Perspective, Advances in Sustainable Construction and Resource Management*; Springer: Berlin/Heidelberg, Germany, 2021; pp. 203–218.
14. Moghal, A.A.B.; Ashfaq, M.; Al-Obaid, A.A.K.H.; Abbas, M.F.; Al-Mahbashi, A.M.; Shaker, A.A. Compaction delay and its effect on the geotechnical properties of lime treated semi-arid soils. *Road Mater. Pavement Des.* **2021**, *22*, 2626–2640. [CrossRef]
15. Bartos, P. *Fresh Concrete: Properties and Tests*; Elsevier: Amsterdam, The Netherlands, 2013.
16. Elinwa, A.U.; Ejeh, S.P.; Mamuda, A.M. Assessing of the fresh concrete properties of self-compacting concrete containing sawdust ash. *Constr. Build. Mater.* **2008**, *22*, 1178–1182. [CrossRef]
17. Tattersall, G.; Baker, P. The effect of vibration on the rheological properties of fresh concrete. *Mag. Concr. Res.* **1988**, *40*, 79–89. [CrossRef]
18. Arshad, S.; Sharif, M.B.; Irfan-ul-Hassan, M.; Khan, M.; Zhang, J.-L. Efficiency of supplementary cementitious materials and natural fiber on mechanical performance of concrete. *Arab. J. Sci. Eng.* **2020**, *45*, 8577–8589. [CrossRef]
19. Xie, C.; Cao, M.; Guan, J.; Liu, Z.; Khan, M. Improvement of boundary effect model in multi-scale hybrid fibers reinforced cementitious composite and prediction of its structural failure behavior. *Compos. Part B Eng.* **2021**, *224*, 109219. [CrossRef]
20. Rehman, A.U.; Kim, J.-H. 3D concrete printing: A systematic review of rheology, mix designs, mechanical, microstructural, and durability characteristics. *Materials* **2021**, *14*, 3800. [CrossRef]
21. Negahban, E.; Bagheri, A.; Sanjayan, J. Composites, Pore gradation effect on Portland cement and geopolymer concretes. *Cement* **2021**, *122*, 104141.
22. Schmidt, W.; Brouwers, H.; Kuehne, H.-C.; Meng, B. Effects of the characteristics of high range water reducing agents and the water to powder ratio on rheological and setting behavior of self-consolidating concrete. *Adv. Civ. Eng. Mater.* **2014**, *3*, 127–141. [CrossRef]
23. Khayat, K.H.; Assaad, J.J. Effect of w/cm and high-range water-reducing admixture on formwork pressure and thixotropy of self-consolidating concrete. *ACI Mater. J.* **2006**, *103*, 186.
24. Sun, Y.; Gao, P.; Geng, F.; Li, H.; Zhang, L.; Liu, H. Thermal conductivity and mechanical properties of porous concrete materials. *Mater. Lett.* **2017**, *209*, 349–352. [CrossRef]
25. Li, H.; Sun, D.; Wang, Z.; Huang, F.; Yi, Z.; Yang, Z.; Zhang, Y. A review on the pumping behavior of modern concrete. *J. Adv. Concr. Technol.* **2020**, *18*, 352–363. [CrossRef]
26. Jang, K.P.; Kwon, S.H.; Choi, M.S.; Kim, Y.J.; Park, C.K.; Shah, S.P. Experimental observation on variation of rheological properties during concrete pumping. *Int. J. Concr. Struct. Mater.* **2018**, *12*, 79. [CrossRef]
27. Kashani, A.; Ngo, T. *Production and Placement of Self-Compacting Concrete, Self-Compacting Concrete: Materials, Properties and Application*; Elsevier: Amsterdam, The Netherlands, 2020; pp. 65–81.
28. Chidiac, S.; Mahmoodzadeh, F. Plastic viscosity of fresh concrete–A critical review of predictions methods. *Cem. Concr. Compos.* **2009**, *31*, 535–544. [CrossRef]
29. Ahmadpour, A.; Sadeghy, K.; Maddah-Sadatieh, S.-R. The effect of a variable plastic viscosity on the restart problem of pipelines filled with gelled waxy crude oils. *J. Non-Newton. Fluid Mech.* **2014**, *205*, 16–27. [CrossRef]
30. Rogovyi, A.; Korohodskyi, V.; Medvediev, Y. Influence of Bingham fluid viscosity on energy performances of a vortex chamber pump. *Energy* **2021**, *218*, 119432. [CrossRef]
31. Ren, Q.; Tao, Y.; Jiao, D.; Jiang, Z.; Ye, G.; de Schutter, G. Plastic viscosity of cement mortar with manufactured sand as influenced by geometric features and particle size. *Cem. Concr. Compos.* **2021**, *122*, 104163. [CrossRef]
32. Ghafari, E.; Costa, H.; Júlio, E.; Portugal, A.; Durães, L. The effect of nanosilica addition on flowability, strength and transport properties of ultra high performance concrete. *Mater. Des.* **2014**, *59*, 1–9. [CrossRef]
33. Kim, B.Y.; Park, J. *Rheology and Texture Properties, Surimi Surimi Seafood*; Marcel Dekker Inc.: New York, NY, USA, 2000; pp. 267–324.
34. Cao, M.; Mao, Y.; Khan, M.; Si, W.; Shen, S. Different testing methods for assessing the synthetic fiber distribution in cement-based composites. *Constr. Build. Mater.* **2018**, *184*, 128–142. [CrossRef]
35. Khan, M.; Cao, M.; Hussain, A.; Chu, S. Effect of silica-fume content on performance of $CaCO_3$ whisker and basalt fiber at matrix interface in cement-based composites. *Constr. Build. Mater.* **2021**, *300*, 124046. [CrossRef]
36. Sarwar, W.; Ghafor, K.; Mohammed, A. Modeling the rheological properties with shear stress limit and compressive strength of ordinary Portland cement modified with polymers. *J. Build. Pathol. Rehabil.* **2019**, *4*, 25. [CrossRef]
37. Aiad, I.; El-Aleem, S.A.; El-Didamony, H. Effect of delaying addition of some concrete admixtures on the rheological properties of cement pastes. *Cem. Concr. Res.* **2002**, *32*, 1839–1843. [CrossRef]
38. Mohammed, A.; Mahmood, W.; Ghafor, K. TGA, rheological properties with maximum shear stress and compressive strength of cement-based grout modified with polycarboxylate polymers. *Constr. Build. Mater.* **2020**, *235*, 117534. [CrossRef]

39. Abidin, N.E.Z.; Ibrahim, M.H.W.; Jamaluddin, N.; Kamaruddin, K.; Hamzah, A.F. The effect of bottom ash on fresh characteristic, compressive strength and water absorption of self-compacting concrete. In *Applied Mechanics and Materials*; Trans Tech Publications: Bäch, Switzerland, 2014.
40. Buswell, R.A.; de Silva, W.L.; Jones, S.Z.; Dirrenberger, J. 3D printing using concrete extrusion: A roadmap for research. *Cem. Concr. Res.* **2018**, *112*, 37–49. [CrossRef]
41. de Schutter, G.; Lesage, K.; Mechtcherine, V.; Nerella, V.N.; Habert, G.; Agusti-Juan, I. Vision of 3D printing with concrete—Technical, economic and environmental potentials. *Cem. Concr. Res.* **2018**, *112*, 25–36. [CrossRef]
42. Zareiyan, B.; Khoshnevis, B. Effects of interlocking on interlayer adhesion and strength of structures in 3D printing of concrete. *Autom. Constr.* **2017**, *83*, 212–221. [CrossRef]
43. Duballet, R.; Baverel, O.; Dirrenberger, J. Classification of building systems for concrete 3D printing. *Autom. Constr.* **2017**, *83*, 247–258. [CrossRef]
44. Güneyisi, E.; Gesoglu, M.; Naji, N.; İpek, S. Evaluation of the rheological behavior of fresh self-compacting rubberized concrete by using the Herschel-Bulkley and modified Bingham models. *Arch. Civ. Mech. Eng.* **2016**, *16*, 9–19. [CrossRef]
45. Brower, L.E.; Ferraris, C.F. Comparison of concrete rheometers. *Concr. Int.* **2003**, *25*, 41–47.
46. Khan, K.; Ahmad, W.; Amin, M.N.; Aslam, F.; Ahmad, A.; Al-Faiad, M.A. Comparison of Prediction Models Based on Machine Learning for the Compressive Strength Estimation of Recycled Aggregate Concrete. *Materials* **2022**, *15*, 3430. [CrossRef]
47. Zhu, Y.; Ahmad, A.; Ahmad, W.; Vatin, N.I.; Mohamed, A.M.; Fathi, D. Predicting the splitting tensile strength of recycled aggregate concrete using individual and ensemble machine learning approaches. *Crystals* **2022**, *12*, 569. [CrossRef]
48. Wang, Q.; Ahmad, W.; Ahmad, A.; Aslam, F.; Mohamed, A.; Vatin, N.I. Application of soft computing techniques to predict the strength of geopolymer composites. *Polymers* **2022**, *14*, 1074. [CrossRef] [PubMed]
49. Khan, M.; Lao, J.; Dai, J.-G. Comparative study of advanced computational techniques for estimating the compressive strength of UHPC. *J. Asian Concr. Fed.* **2022**, *8*, 51–68. [CrossRef]
50. Song, Y.; Zhao, J.; Ostrowski, K.A.; Javed, M.F.; Ahmad, A.; Khan, M.I.; Aslam, F.; Kinasz, R. Prediction of compressive strength of fly-ash-based concrete using ensemble and non-ensemble supervised machine-learning approaches. *Appl. Sci.* **2022**, *12*, 361. [CrossRef]
51. Zou, Y.; Zheng, C.; Alzahrani, A.M.; Ahmad, W.; Ahmad, A.; Mohamed, A.M.; Khallaf, R.; Elattar, S. Evaluation of artificial intelligence methods to estimate the compressive strength of geopolymers. *Gels* **2022**, *8*, 271. [CrossRef]
52. Amin, M.N.; Ahmad, A.; Khan, K.; Ahmad, W.; Nazar, S.; Faraz, M.I.; Alabdullah, A.A. Split tensile strength prediction of recycled aggregate-based sustainable concrete using artificial intelligence methods. *Materials* **2022**, *15*, 4296. [CrossRef]
53. El Asri, Y.; Benaicha, M.; Zaher, M.; Alaoui, A.H. Prediction of plastic viscosity and yield stress of self-compacting concrete using machine learning technics. *Mater. Today Proc.* **2022**, *59*, A7–A13. [CrossRef]
54. Ghanbari, A.; Karihaloo, B.L. Prediction of the plastic viscosity of self-compacting steel fibre reinforced concrete. *Cem. Concr. Res.* **2009**, *39*, 1209–1216. [CrossRef]
55. Aicha, M.B.; al Asri, Y.; Zaher, M.; Alaoui, A.H.; Burtschell, Y. Prediction of rheological behavior of self-compacting concrete by multi-variable regression and artificial neural networks. *Powder Technol.* **2022**, *401*, 117345. [CrossRef]
56. el Asri, Y.; Aicha, M.B.; Zaher, M.; Alaoui, A.H. Modelization of the rheological behavior of self-compacting concrete using artificial neural networks. *Mater. Today Proc.* **2022**, *58*, 1114–1121. [CrossRef]
57. Mohammed, A.; Rafiq, S.; Mahmood, W.; Al-Darkazalir, H.; Noaman, R.; Qadir, W.; Ghafor, K. Artificial Neural Network and NLR techniques to predict the rheological properties and compression strength of cement past modified with nanoclay. *Ain Shams Eng. J.* **2021**, *12*, 1313–1328. [CrossRef]
58. Rolon-Mérette, D.; Ross, M.; Rolon-Mérette, T.; Church, K. Introduction to Anaconda and Python: Installation and setup. *Python Res. Psychol.* **2016**, *16*, S5–S11. [CrossRef]
59. Yegnanarayana, B. *Artificial Neural Networks*; PHI Learning Pvt. Ltd.: Delhi, India, 2009.
60. Dai, B.; Gu, C.; Zhao, E.; Qin, X. Statistical model optimized random forest regression model for concrete dam deformation monitoring. *Struct. Control Health Monit.* **2018**, *25*, e2170. [CrossRef]
61. Janitza, S.; Tutz, G.; Boulesteix, A.-L. Random forest for ordinal responses: Prediction and variable selection. *Comput. Stat. Data Anal.* **2016**, *96*, 57–73. [CrossRef]

materials

MDPI

Article

Application of Soft-Computing Methods to Evaluate the Compressive Strength of Self-Compacting Concrete

Muhammad Nasir Amin [1,*], Mohammed Najeeb Al-Hashem [1], Ayaz Ahmad [2], Kaffayatullah Khan [1], Waqas Ahmad [3], Muhammad Ghulam Qadir [4], Muhammad Imran [5] and Qasem M. S. Al-Ahmad [1]

[1] Department of Civil and Environmental Engineering, College of Engineering, King Faisal University, Al-Ahsa 31982, Saudi Arabia
[2] MaREI Centre, Ryan Institute and School of Engineering, College of Science and Engineering, National University of Ireland Galway, H91 TK33 Galway, Ireland
[3] Department of Civil Engineering, COMSATS University Islamabad, Abbottabad 22060, Pakistan
[4] Department of Environmental Sciences, Abbottabad Campus, COMSATS University Islamabad, Abbottabad 22060, Pakistan
[5] School of Civil and Environmental Engineering (SCEE), National University of Sciences & Technology (NUST), Islamabad 44000, Pakistan
* Correspondence: mgadir@kfu.edu.sa; Tel.: +966-13-589-5431; Fax: +966-13-581-7068

Abstract: This research examined machine learning (ML) techniques for predicting the compressive strength (CS) of self-compacting concrete (SCC). Multilayer perceptron (MLP), bagging regressor (BR), and support vector machine (SVM) were utilized for analysis. A total of 169 data points were retrieved from the various published articles. The data set was based on 11 input parameters, such as cement, limestone, fly ash, ground granulated blast-furnace slag, silica fume, rice husk ash, coarse aggregate, fine aggregate, superplasticizers, water, viscosity modifying admixtures, and one output with compressive strength of SCC. In terms of properly predicting the CS of SCC, the BR technique outperformed both the SVM and MLP models, as determined by the research results. In contrast to SVM and MLP, the coefficient of determination (R^2) for the BR model was 0.95, whereas for SVM and MLP, the R^2 was 0.90 and 0.86, respectively. In addition, a k-fold cross-validation approach was adopted to check the accuracy of the employed models. The statistical measures mean absolute percent error, mean absolute error, and root mean square error ensure the validity of the model. Using sensitivity analysis, the influence of input factors on the intended CS of SCC was also explored. This analysis reveals that the highest contributing parameter towards the CS of SCC was cement with 16.2%, while rice husk ash contributed the least with 4.25% among all the input variables.

Keywords: concrete; self-compacting concrete; compressive strength; prediction models; machine learning

Citation: Amin, M.N.; Al-Hashem, M.N.; Ahmad, A.; Khan, K.; Ahmad, W.; Qadir, M.G.; Imran, M.; Al-Ahmad, Q.M.S. Application of Soft-Computing Methods to Evaluate the Compressive Strength of Self-Compacting Concrete. *Materials* **2022**, *15*, 7800. https://doi.org/10.3390/ma15217800

Academic Editor: Krzysztof Schabowicz

Received: 1 September 2022
Accepted: 28 September 2022
Published: 4 November 2022

1. Introduction

Self-compacting concrete (SCC), a type of high-performance concrete (HPC) with a superior ability to deform and resistance to segregation, was developed for the first time in Japan in 1986 [1]. SCC has been utilized in Japan for major office buildings as well as innovative types of extruded tunnels combined with steel fibers [2]. The utilization of SCC reduced the construction site noise level and its impact on the environment. SCC is better than regular concrete for many reasons, including (1) eliminating the need for vibration; (2) lowering construction duration and costs of labor; minimizing noise pollution; (4) enhancing the filling volume of highly crowded structural elements; (5) improving the transition zone among the cement paste and reinforcement or aggregate; (6) limiting concrete's permeability and increasing its durability [3,4]. The introduction of SCC allows for the exploitation of replacement materials, industrial waste, and other secondary resources, such as mineral chemicals, and generates interest in carrying out this process [5–7].

In general, the quality of SCC is determined by its compressive strength (CS), which provides a basic indication of concrete because it is linked to the structure of the hardened mixture [8,9]. Typically, the compressive strength of SCC is determined by costly and time-consuming physical trials, therefore the work productivity will be extremely low [10]. On account of its complicated composition, SCC requires a suitable mixed design procedure in order to achieve its desired qualities [11]. For the selected design procedure, the materials used must be balanced with at least one mineral and one or more chemical additives [12]. The difficulty in improving grain size dispersal and packing particles in stronger cohesion for SCC is met by looking for the optimal balance equivalency among the coarse and fine components and the admixtures [13–15]. For this reason, technological advancements make it possible to solve engineering challenges at a lesser cost by employing empirical regression, simulation techniques, and machine learning algorithms [16–18]. These approaches enable the forecasting of the CS of SCC based on the proportions of different components in the mixture that has been created such as aggregate, cement, superplasticizers, and water [19–21].

In recent decades, machine learning (ML) approaches have emerged as an appealing modelling tool appropriate to a broad array of scientific fields, including materials engineering [22–27]. These data sets can be used to build an appropriate surrogate model for predetermined model parameters, hence eliminating the need for costly and time-consuming trials [28]. Considering this, a trend has gained a surge in recent years by using ML techniques to anticipate the CS of concrete material [29–35]. These methods can be utilized for a number of applications, including regression, classification, correlation, and clustering [36–40]. With the advancement of ML approaches, it is consequently uncomplicated to investigate the CS of SCC along with the concrete's other properties [41,42]. Thus, to investigate the strength properties of SCC. Asteris et al. [43] employed the artificial neural network algorithm from ML techniques. The study was based on the prediction of 28 days CS of SCC in a limited time period. Awoyera et al. [44] investigate the predictive accuracy of ANN and GEP approaches for the strength properties of SCC. It was reported that both ANN and GEP successfully anticipated the required properties of SCC.

The purpose of this research is to investigate and evaluate the prediction capabilities of three distinct machine learning techniques for the CS of superplasticized self-compacting concrete (SCC). This research is groundbreaking in that it makes a prediction about the CS of SCC on the data set that was chosen by employing both ensemble machine learning methods (boosting regressor) and individual machine learning approaches (SVM, MLP). This research involves the descriptive analysis of the variables, the application of Python codes for running the employed models, statistical checks for the model's legitimacy, a validation approach for validating the models, and sensitivity analysis to check the impact that the variables have on the predictive outcome. This study has the potential to make a significant contribution to the construction industry's utilization of novel tools and approaches for investigating the various properties of construction materials in a manner that is economical, takes a limited amount of time, and does not require any physical effort in the laboratory.

2. Research Significance

This study presents the implementation of individual machine learning algorithms in addition to ensemble machine learning approaches in order to estimate the compressive strength of self-compacting concrete (SCC). In order to execute the necessary models for the purpose of prediction, the anaconda navigator software was programmed with the Python programming language. Twenty bagging sub-models were trained on the data, and then those models were tuned so that they had the maximum R^2 value. In addition to this, the test data were confirmed by employing k-fold cross-validation in conjunction with R^2, MAPE, MAE, and RMSE. Moreover, the statistical model performance index was utilized in order to contrast individual models with ensemble models (e.g., MAPE, MAE, and RMSE). Furthermore, a comparative study of the obtained results and with the results of similar

published articles has also been carried out in order to have a better understanding of an accurate model for the forecasting of the concrete's strength. This was carried out in order to have a better understanding of the accurate model towards the forecasting of the concrete's strength. In addition, the sensitivity analysis was included in the research in order to analyze the contribution level of each input parameter toward the strength prediction of SCC. This was carried out in order to ensure that the study was as accurate as possible.

3. Materials and Methods

Python coding (attached in Supplementary Data) in the Anaconda navigator software plays a vital role and was used for running all the employed models. The data set of self-compacting concrete (SCC) used for running the models to anticipate the compressive strength (CS) was retrieved from the literature [45–62]. A total of 169 data points (attached in the Supplementary Data) was used for running the selected models. The software automatically splits 70% of the data for training the model and 30% for testing the model. While the k-fold cross validation approach was adopted to validate the required model. To reduce the complexity of the data, the data preprocessing method was adopted. Data preprocessing for data mining addresses one of the most crucial challenges inside the renowned knowledge discovery from data procedure. Data preparation covers data reduction strategies that try to reduce the data's complexity by recognizing and deleting irrelevant and noisy data items. The model's analysis was conducted by using the regression and error distribution processes. Eleven input variables, including cement, limestone powder, coarse aggregate, fly ash, water, fine aggregate, GGBS, silica fume, RHA, superplasticizers, and VMA, were introduced for a single outcome such as compressive strength. The selection of these parameters was based on the importance of their effect in the concrete material. The selected input parameters show a significant effect when evaluating their effect using sensitivity analysis. The influence of all the input parameters was also accessed for predicting the CS of SCC through sensitivity analysis. The descriptive statistical analysis was also incorporated for these parameters as listed in Table 1. The validation method has also been adopted to evaluate the precision level of the employed models. Moreover, the histograms give the relative frequency dispersion of all the variables, as shown in Figure 1. A frequency distribution of all the input variables describes how often different values occur in a complete data set. Relative frequency distributions are valuable because they show how common a value is in a data set in comparison to all other values. In addition, violin plot distribution for all the variables is shown in the Figure 2.

Table 1. Descriptive statistics of variables.

Parameters	Cement (kg/m^3)	Powder (kg/m^3)	Fly Ash (kg/m^3)	GGBS (kg/m^3)	Silica Fume (kg/m^3)	RHA (kg/m^3)	Coarse Aggregate (kg/m^3)	Fine Aggregate (kg/m^3)	Water (kg/m^3)	SP (kg/m^3)	VMA (kg/m^3)
Input's mean	346.04	30.01	106.07	18.75	16.66	5.27	744.66	862.46	178.40	6.90	0.16
Standard Error	7.29	5.04	7.28	4.19	2.78	1.82	8.66	9.30	2.13	0.32	0.03
Input's median	331.33	0.00	108.75	0.00	0.00	0.00	760.50	860.50	180.03	6.09	0.00
Input's mode	500.00	0.00	0.00	0.00	0.00	0.00	837.00	900.00	198.00	6.75	0.00
Standard Deviation	94.46	65.35	94.40	54.35	36.08	23.54	112.28	120.54	27.60	4.12	0.33
Range	420.00	272.00	350.00	330.00	250.00	200.00	427.00	657.00	155.50	22.50	1.23
Minimum	150.00	0.00	0.00	0.00	0.00	0.00	500.00	478.00	94.50	0.00	0.00
Maximum	570.00	272.00	350.00	330.00	250.00	200.00	927.00	1135.00	250.00	22.50	1.23
Sum	58,134.24	5041.60	17,818.98	3150.20	2799.00	885.00	125,103.25	144,893.49	29,970.52	1158.45	27.06

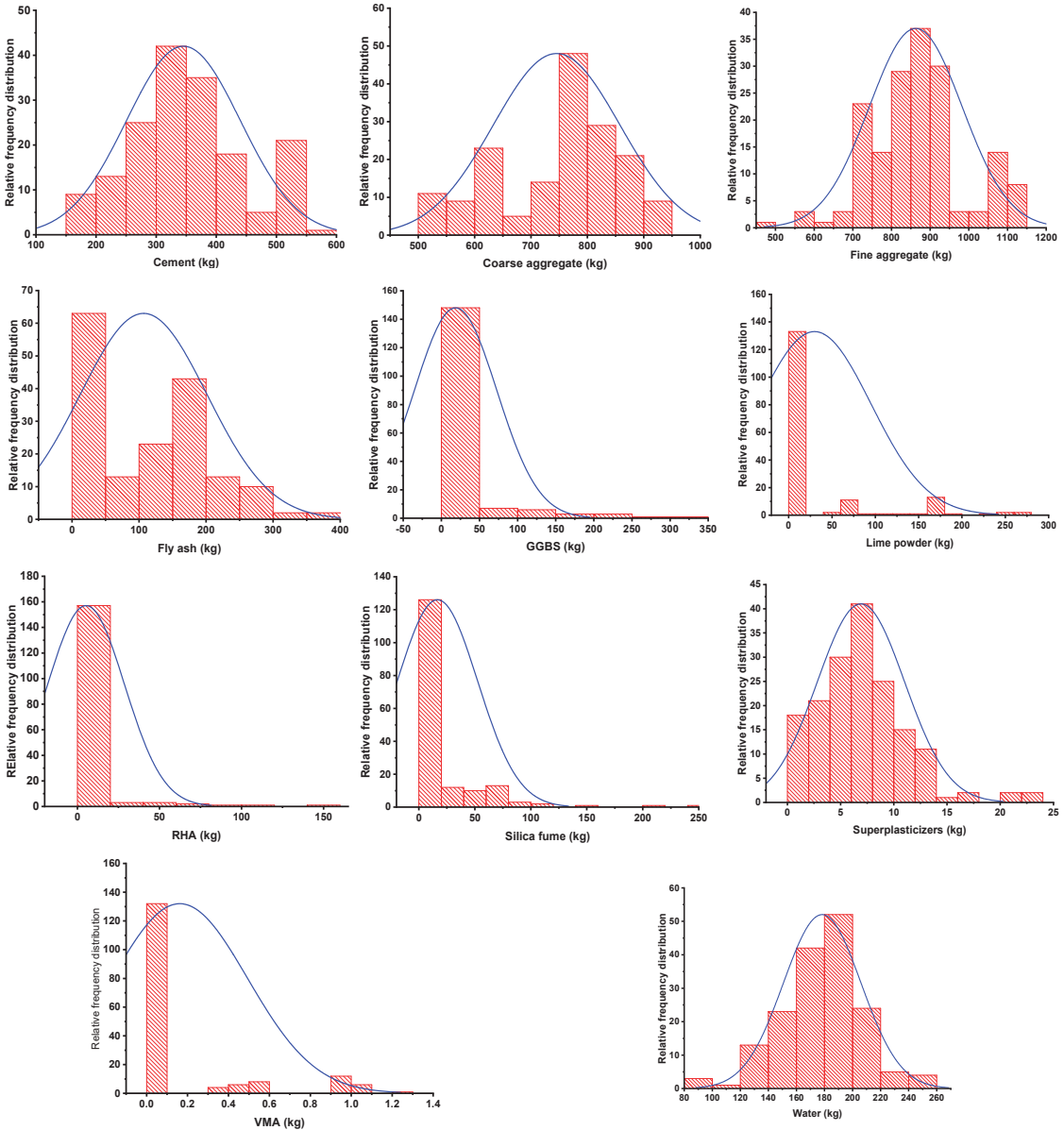

Figure 1. Input parameters' relative frequency distribution.

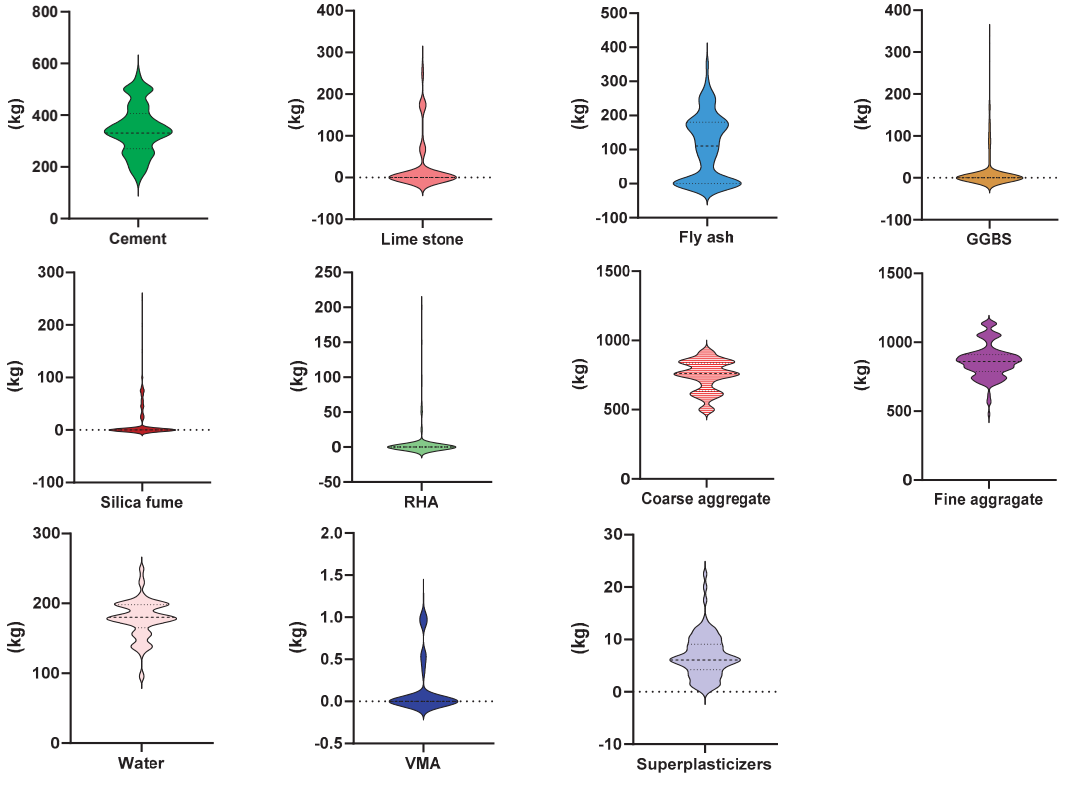

Figure 2. Violin plots distribution of the input parameters.

4. Employed Machine Learning Algorithms

4.1. Multilayer Perceptron (MLP)

An MLP is a type of feedforward ANN that turns a set of inputs into outputs. Between the output and input layers, a targeted graph connects many layers of input nodes. In MLP, the network is trained with backpropagation. It can also connect many loops in a directed graph, with signals moving in only one direction across the nodes. Every entity, with the exception of the input nodes, possesses its very own unique nonlinear activation function. MLPs, which are a form of supervised learning, make use of backpropagation in their learning processes. MLP is often called a deep learning approach because it uses so many layers of neurons. MLP is often used in studies of supervised learning, imputation, parallel distributed processing, and pure science. Machine translation, image recognition, and speech recognition are all examples of applications. To begin, the algorithm selects the predictors that it will be utilized throughout the regression phase in order to locate the variance inflation component (VIF). The VIF then figures out how much an estimated regression coefficient has changed because of collinearity. Figure 3 is a flowchart that shows the whole process of predicting the results of the MLP model.

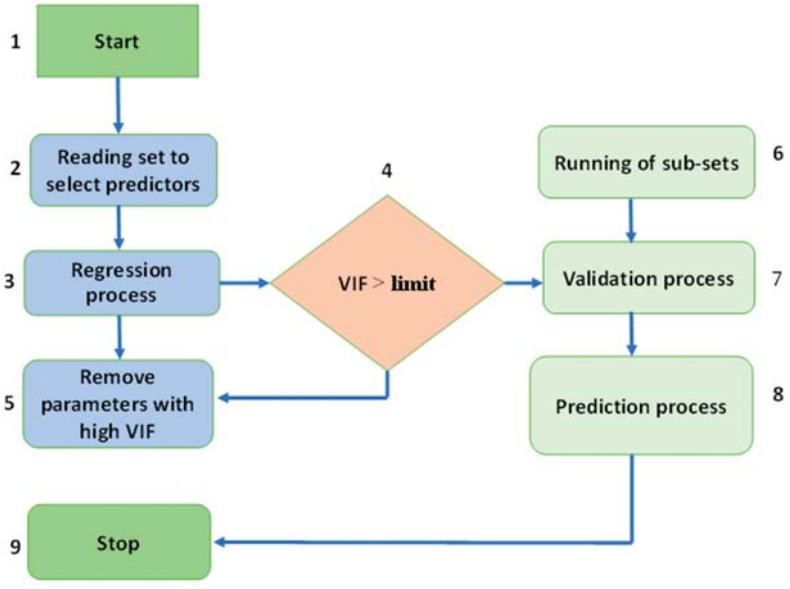

Figure 3. Multilayer perceptron model execution process [63].

4.2. Support Vector Machine (SVM)

SVM refers to a type of algorithm which connected learning algorithms used for evaluating data for both regression and classification. A SVM technique is a description of the samples as points in space that have been drawn in such a way that the patterns of the different classifications are separated by a discrete vector (line/plane) with the largest possible gap. Figure 4 depicts the classification of additional cases based on the side of the vector on which they lie. Figure 5 displays the implementation approach for the SVM model. This model is used to assess the material's strength, taking into account the influence of multiple factors. The optimization strategy is used to determine the SVM model's parameters.

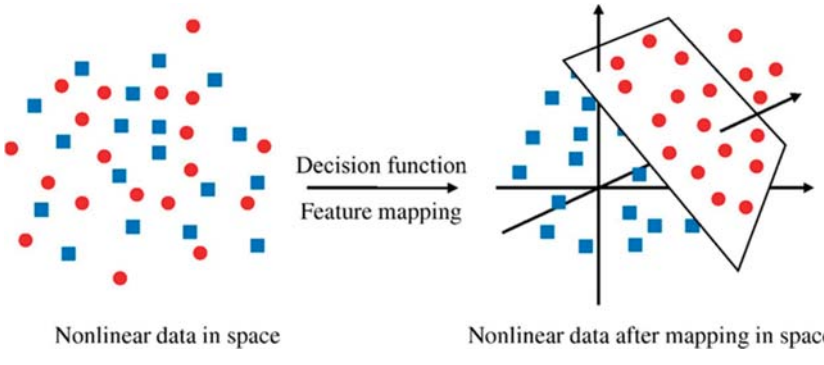

Figure 4. Model mapping of the support vector machine algorithm [64].

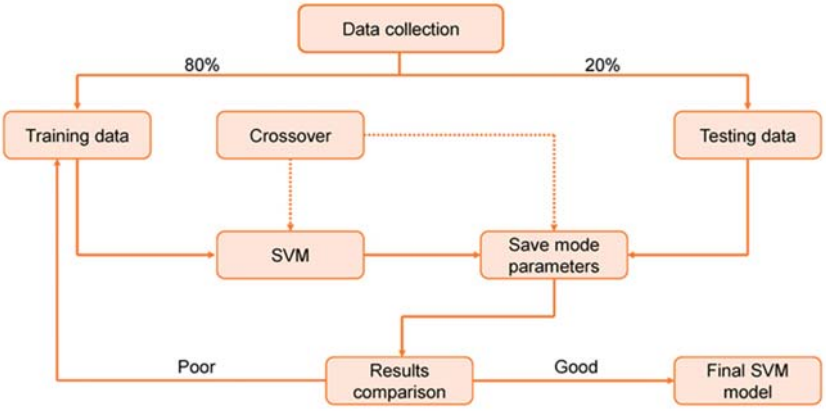

Figure 5. Execution process of the SVM model [65].

4.3. Bagging Regressor (BR)

BR, also referred to as bootstrap aggregation, is a method for combining multiple versions of an anticipated model. Each model is independently trained, then the results are averaged. BR's primary objective is to attain a lesser divergence than any one model. The process of producing bootstrap samples from a selected data point is known as bootstrapping. The samples are formed by selecting and exchanging data points at random. The characteristics of the resampled data are distinct from those of the original data in its totality. It shows how the data are spread out and tends to keep bootstrapped samples from becoming too similar. This means that the data distribution must stay the same while keeping bootstrapped samples from becoming too similar. This aids in the development of robust models. In addition, bootstrapping helps prevent the overfitting issue. When constructing a model, the utilization of a large number of training data sets results in a decreased likelihood of errors and improved performance when applied to test data. This reduces variation by giving the test set a strong base. Multiple permutations of the model ensure that it is not biased towards an inaccurate outcome. The BR model's flowchart can be seen in the Figure 6.

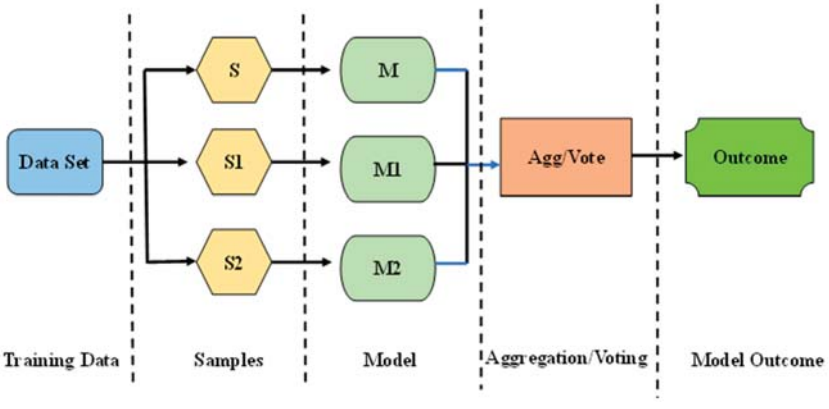

Figure 6. Bagging model execution process for required output.

5. Results and Discussion

5.1. MLP Model Outcome

Figure 7 shows a depiction of the relationship between the actual and anticipated values for the self-compacting concrete's (SCC) compressive strength. This relationship gives the coefficient of determination (R^2) value of 0.86. Figure 8 illustrates the disparity between the actual and expected results. The tabulated information in the figure shows that 'x' is the variable that is being explained, and y is the variable that is being investigated. The slope of the line is denoted by the letter b, and 'a' is the intercept (the value of y when x is equal to 0). The difference depicts the higher and lower values equal to 21.50 MPa, and 0.18 MPa, respectively. Moreover, it has been noted that the 41.18% of the difference data were found between the minimum value (0.18 MPa) and 5 MPa, and 45.10% of the data were noted among 5 MPa, and 10 MPa. However, only 13.73% of the difference data were located above 10 MPa.

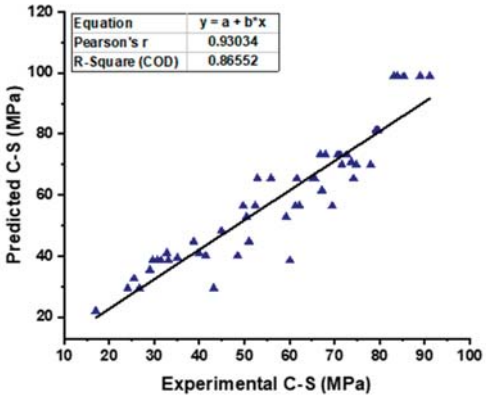

Figure 7. Experimental and predicted outcomes relationship of CS from MLP model.

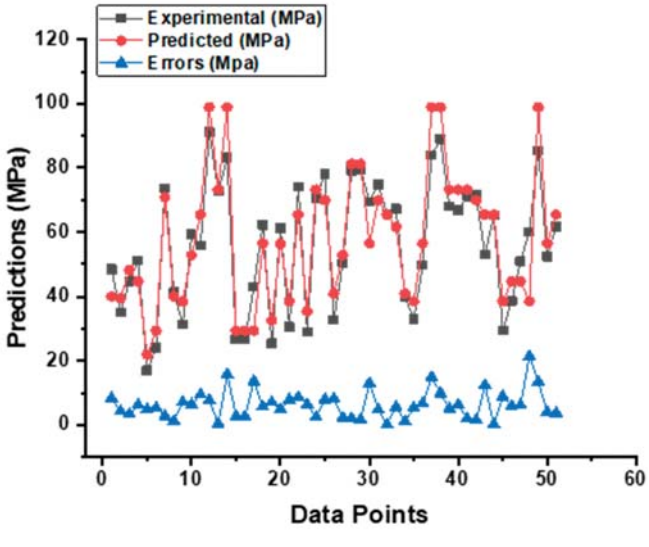

Figure 8. Indication of the error's difference between the actual and forecasted CS result of SCC from ML model.

The box plot as shown in the Figure 9 gives more statistical information such as the minimum, maximum, median, mean, and first and third quartile values for both the experimental and forecasted outcomes from the test set. The values on the graph clearly indicate the difference of predicted and actual results while comparing.

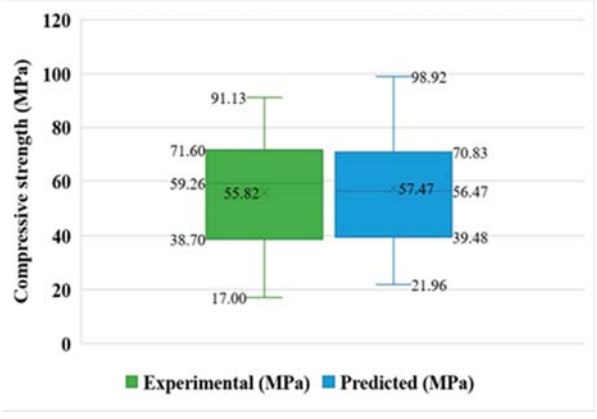

Figure 9. Box plot for predicted and experimental outcomes from MLP model.

5.2. SVM Model Output

As shown in Figure 10, the SVM model provides a superior link between the experimental CS of SCC and the projected outcome when compared to the MLP model, which results in an R^2 value of 0.90 having been determined. Figure 11 is an illustration of the distribution of the data, which shows the disparity between the actual and the targeted values. The greatest value, the minimum value, and the average value, all based on this distribution, are 14.81 MPa, 0.21 MPa, and 5.72 MPa, respectively. In addition, 50.98% of these measurements was obtained between 0.21 MPa and 5 MPa, 33.333% of these measurements was obtained between 5 MPa and 10 MPa, and only 15.61% of these measurements was obtained at or above 10 MPa.

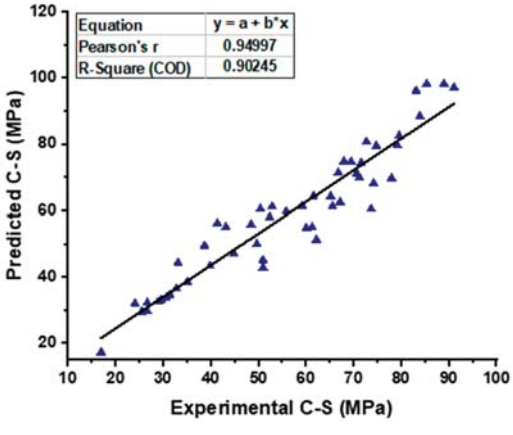

Figure 10. Experimental and predicted outcomes relationship of CS from SVM model.

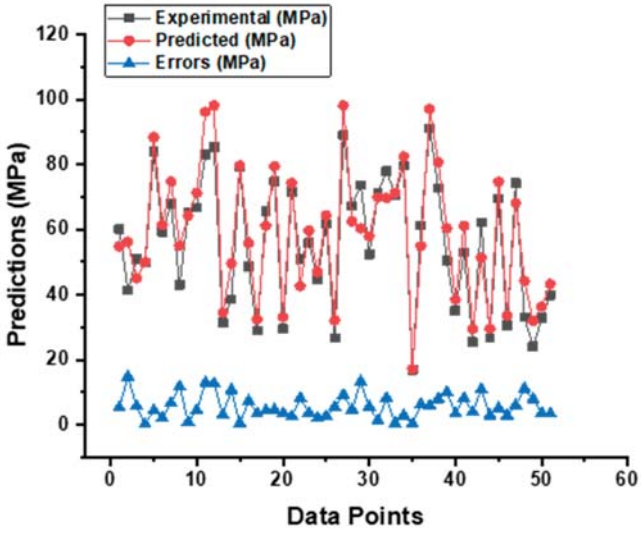

Figure 11. Indication of the error's difference between the actual and forecasted CS result of SCC from SVM model.

In addition, Figure 12 provides additional statistical information, including the minimum, maximum, median, mean, first quartile, and third quartile values for both the experimental and projected outcomes from the test set. The data on the graph make it abundantly evident that there is a disparity between the results that were projected and those that were actually achieved.

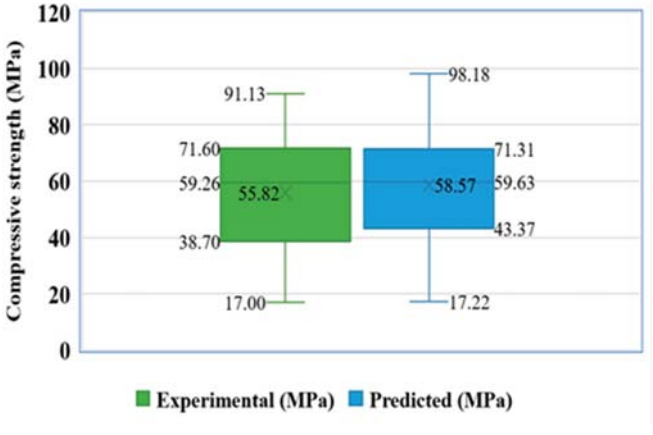

Figure 12. Box plot for predicted and experimental outcomes from SVM model.

5.3. BR Model Outcome

As can be seen in Figure 13, the output of the bagging model demonstrates a strong and better relationship with the experimental CS result of the self-compacting concrete than the predictions of the MLP and SVM models, and it gives an R^2 value of 0.95. This is in contrast to the predictions of the MLP and SVM models. Figure 14 also provides a visual representation of the error's distribution, which is an additional point of interest. The variation produces data with a maximum of 13.05 MPa, a minimum of 0.16 MPa, and

an average of 3.87 MPa, respectively. Additionally, it was seen that 72.55% of this data fell between 0.16 MPa and 5 MPa, while 19.61% of the data were reported to fall between 5 MPa and 10 MPa. However, only 5.88% of these values were found to be higher than the 10 MPa criterion.

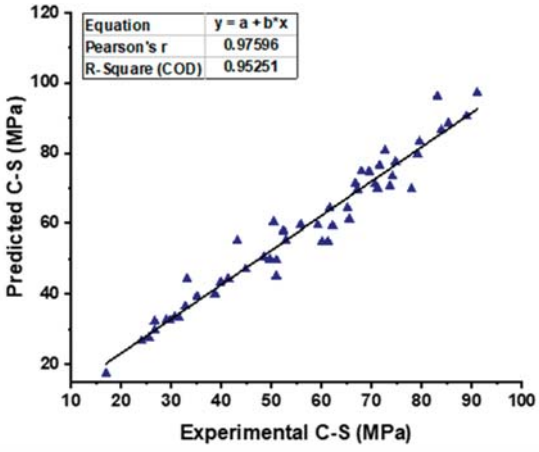

Figure 13. Experimental and predicted outcomes relationship of CS from BR model.

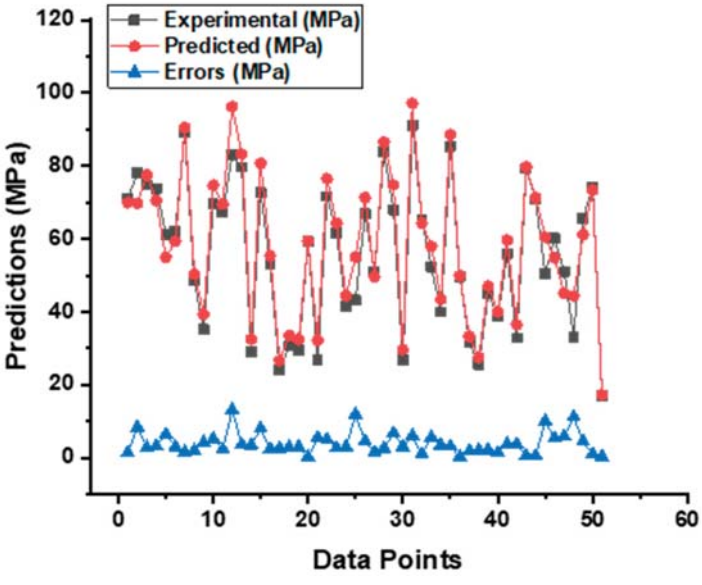

Figure 14. Indication of the error's difference between the actual and forecasted CS result of SCC from BR model.

Moreover, further statistical information is provided in Figure 15, including the minimum, maximum, median, mean, and first and third quartile values for both the experimental and predicted test set results. The discrepancy between the expected and actual outcomes is graphically represented by the graph's values. The result of the Bagging model seems closer with one another (actual and predicted) as opposed to both SVM and ML models.

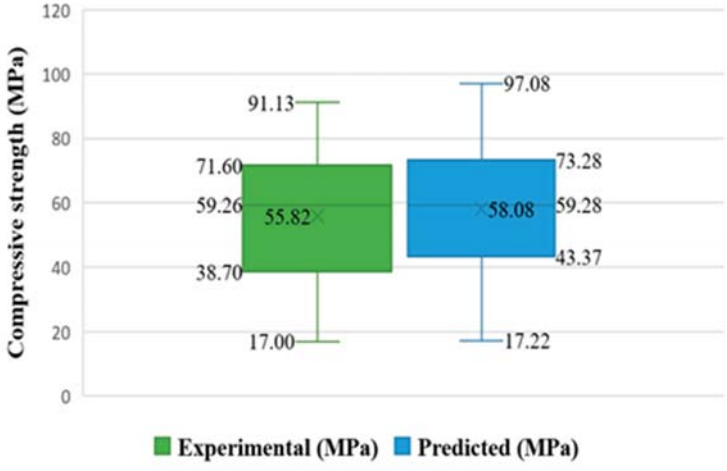

Figure 15. Box plot for predicted and experimental outcomes from BR model.

5.4. K-Fold Cross Validation Outcomes and Statistical Metrics

K-fold and statistical tests were applied to validate the ML algorithms in use. Typically, the k-fold method is utilized to test the viability of a strategy by arbitrarily distributing and dividing relevant data into 10 groups. As shown in Figure 17, nine groups are used to train machine learning models, while one is used to validate them. The ML approach is more accurate when the errors (MAPE, MAE, and RMSE) are minor and R^2 is superior. In addition, the technique must be performed 10 times for a desirable outcome. This huge amount of work is a big reason why the model is so accurate. Moreover, the statistical metrics obtained from the models are listed in the Table 2. In the meantime, Figure 16 gives the statistical information about the accuracy level of the employed models for the CS of SCC. This Tylor diagram also indicates the better performance of the bagging model towards the required outcome as compared to SVM and MLP models. The error percent for BR model is less than 8 MPa, while both MLP and SVM models give the same result equal to 12.96 MPa and 11.44 MPa, respectively.

Table 2. Statistics derived from the employed models.

Algorithms	MAPE (%)	MAE (MPa)	RMSE (MPa)	R^2
MLP	12.96	6.33	7.71	0.86
SVM	11.44	5.71	6.81	0.90
BR	7.81	3.86	4.86	0.95

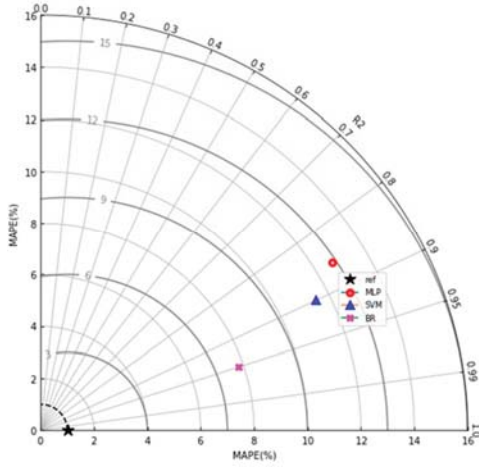

Figure 16. Statistical indication of the model's performance by Taylor diagram.

Using Equations (1)–(3) derived from previous research [66], the statistical prediction performance of the techniques was evaluated.

$$\mathrm{MAE} = \frac{1}{n}\sum_{i=1}^{n}|P_i - Ti| \tag{1}$$

$$\mathrm{RMSE} = \sqrt{\sum \frac{(P_i - T_i)^2}{n}} \tag{2}$$

$$\mathrm{MAPE} = \frac{1}{n}\sum_{t=1}^{n}(A - F/A) \tag{3}$$

where n = number of data points, P_i = anticipated values, and T_i = experimental values, A is the actual values and F is the forecasted values from the data set.

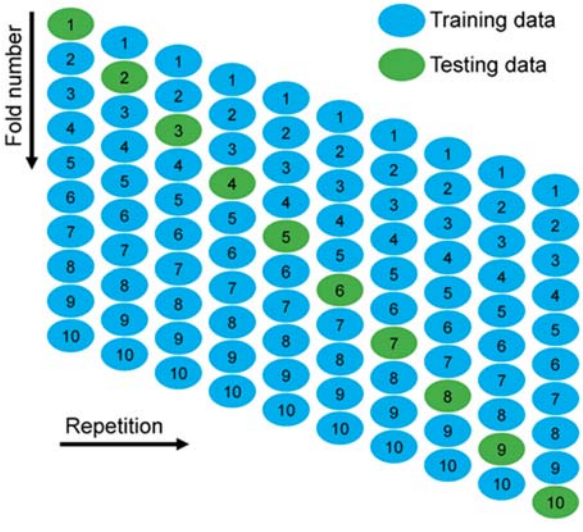

Figure 17. Statistical evaluations of the models used for this investigation [67].

Statistical and k-Fold Analysis

In order to determine whether or not the model being used is legitimate, a k-fold cross validation check was implemented as a standard. To investigate the results, the statistical metrics were taken into consideration: R^2, MAE, RMSE. According to the k-fold study, MLP models had higher values of R^2, MAE, and RMSE, as shown in Figure 18: 0.86, 18.53, and 24.46 MPa, respectively. Similarly, the highest values for the same metrics for SVM models were reported as 0.90, 19.20 MPa, and 20.98 MPa, as shown in Figure 19. However, the higher, lower, and average values of R^2, MAE, and RMSE for the bagging model were noted as 0.95, 19.74 MPa, and 18.94 MPa, respectively, and can be seen in Figure 20.

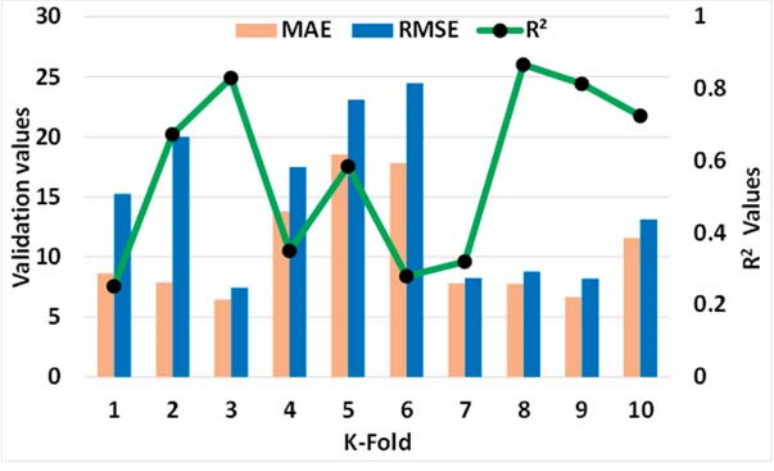

Figure 18. Statistical analysis of MLP model.

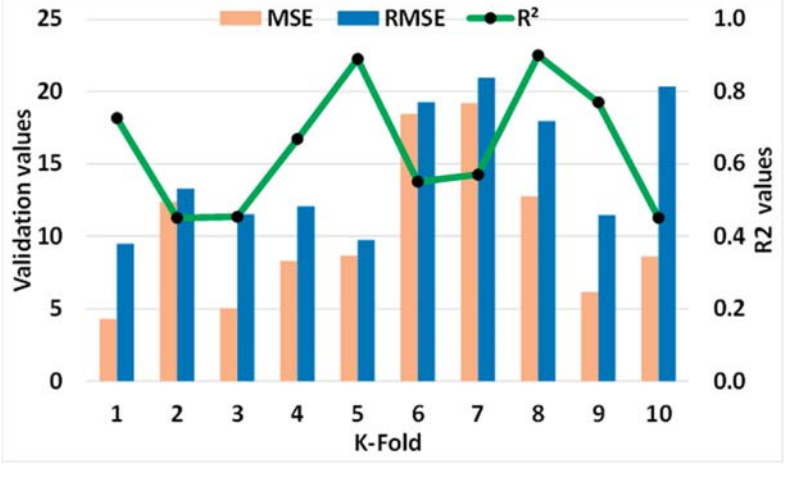

Figure 19. Statistical analysis of SVM model.

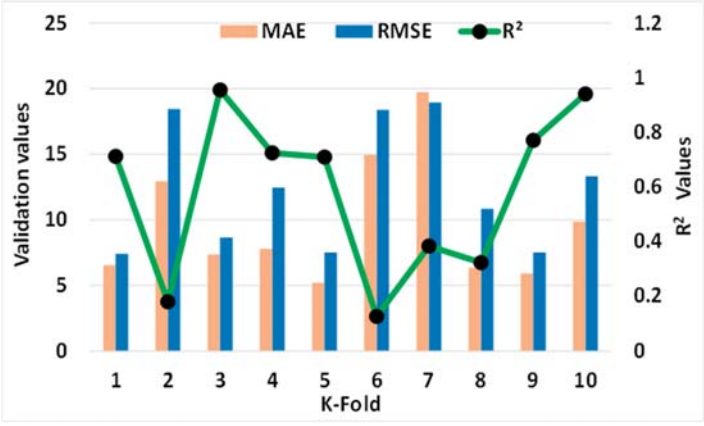

Figure 20. Statistical analysis of BR model.

5.5. Discussion on the Main Findings

This study describes the predictive performance of three different types of ML algorithms for the CS of SCC. The multilayer perceptron (MLP), SVM, and bagging regressor (BR) have been investigated for the analysis. Even though MLP and SVM are individual ML techniques, the precision of their predictive results was noted to be within acceptable limits. The BR belongs to the ensemble ML approach, which normally goes through the process of splitting the model into 20-sub models for optimization to have a strong outcome. The result of the bagging sub-models can be seen in the Figure 21. It has been noted that the input parameters and number of data points have a significant effect on the required outcomes. Therefore, the descriptive statistics of the input variables, relative frequency distribution of the input data, and sensitivity analysis for evaluation of their influence on the outcome were incorporated into the study. It was determined that the correlation between the experimental CS result and the prediction CS result from all employed models was satisfactory. The k-fold cross validation approach was also introduced to check the legitimacy of the models. The comparison of the present study with the other relevant studies has also been taken into consideration and found to have a reasonable and better relationship.

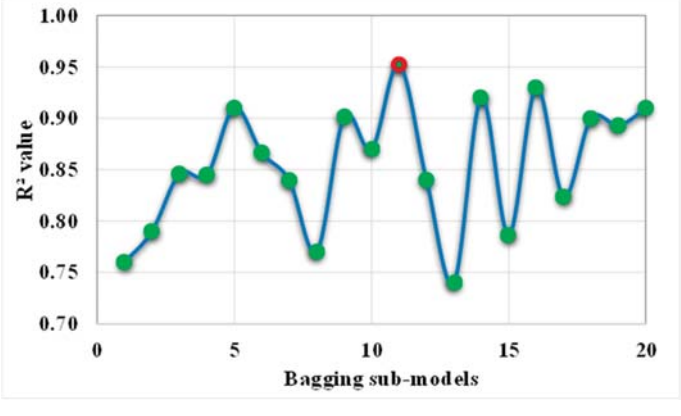

Figure 21. Result of the bagging sub-models.

5.6. Comparison with Other Studies

The result comparison for the application of ML approaches for predicting the same type of outcomes reported in the published articles are listed in the Table 3.

Table 3. Result comparison with published studies.

Employed Algorithms	R^2	MAE (MPa)	RMSE (MPa)	References
DT	0.77	6.38	8.952	[18]
GB	0.85	4.95	7.046	
BR	0.91	4.25	5.693	
ANN	0.85	3.42	4.48	
DT	0.86	2.59	3.77	[68]
SVM	0.84	2.93	4.03	
LR	0.85	2.90	4.02	
DT	0.43		3.90	[69]
RF	0.90		1.14	
ANN	0.95		0.91	
DT	0.90	2.62	3.38	[70]
AdaBoost	0.93	2.16	2.62	
BR	0.96	3.75	1.94	
DT	0.82	7.016	10.43	[67]
AdaBoost	0.90	5.19	7.46	
RF	0.90	5.32	7.60	

6. Sensitivity Analysis

This approach was introduced to investigate the impact of each input variable on the predicted CS of SCC. This analysis reveals that the highest contribution was made by the binding material (cement) by giving 16.25% towards the anticipation of CS of SCC. However, rice husk ash contributed the least (4.25%) to predicting the required outcome. Moreover, the other variables' impact from the analysis in the descending order were reported for superplasticizers (13.44%), silica fume (11%), fly ash (9.94%), coarse aggregate (9.50%), limestone powder (8.90%), fine aggregate (8.80%), VMA (6.65%), and water (6.40) as depicted in the Figure 22. However, the Equations (4) and (5) were used to calculate the percent contribution of each parameter towards the required outcome.

$$N_i = f_{max}(x_i) - f_{min}(x_i) \tag{4}$$

$$S_i = \frac{N_i}{\sum_{j-i}^{n} N_j} \tag{5}$$

where, $f_{max}(x_i)$ and $f_{min}(x_i)$ are the highest and lowest of the anticipated output over the i^{th} output.

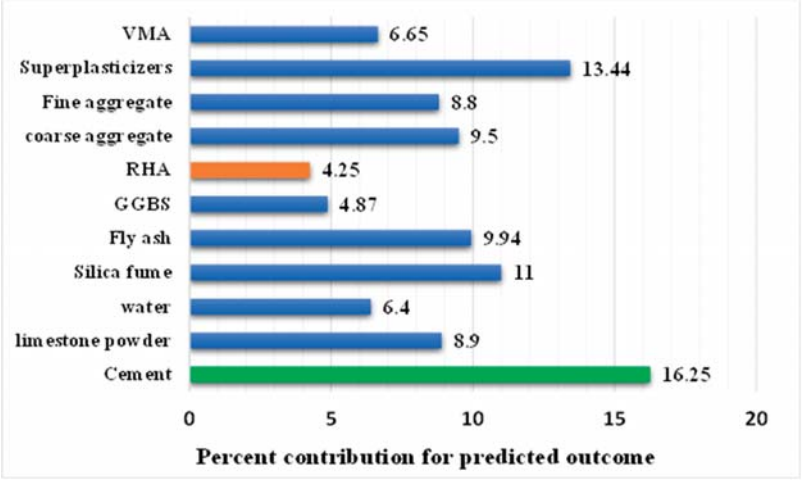

Figure 22. Influence of the input parameters towards the predicted output.

7. Limitations and Future Perspective

The following are the limitations regarding the application of machine learning approaches along with recommendations for future studies.

- The fact that it is difficult to describe how these algorithms arrive at their findings is a key shortcoming of machine learning.
- A machine learning algorithm is analogous to a black box in that it receives inputs and generates outputs without providing an explanation of how the results were generated.
- In addition to the fact that these algorithms operate in a mysterious manner, machine learning is also susceptible to the fallacy of "garbage in, garbage out".
- According to this dictum, the output quality is directly proportional to the quality of the data sets used in the analysis.
- The outputs of the algorithm will reflect any mistakes caused by inaccurate labeling of the images/data that are used as inputs.
- Studies based on ML approaches for the prediction of required outcomes can also be enriched with the application of proper hyperparameters for the employed models. Convergence curves based on the RMSE for the selected models and new evaluation indexes such as PI and A-10index can also be included for checking the accuracy level of the employed models. Moreover, the employed models can also be split into training and testing sets to evaluate their performance separately.

8. Conclusions

This investigation was predicated on the utilization of supervised ML techniques for the purpose of estimating the CS of SCC. For the purpose of predicting the CS of SCC, the MLP, SVM, and the BR were all investigated. Nevertheless, the following inference can be made based on the findings of the study:

- ML algorithms successfully predict the CS of SCC using python coding.
- In contrast to the SVM and MLP models, the BR model demonstrates outstanding predictive performance with a high degree of precision.
- The high coefficient of determination (R^2) value (0.95) for the BR model demonstrates its great accuracy in predicting the CS of SCC.
- The K-fold cross validation and statistical metrics also confirm the legitimacy of the employed models.

- The sensitivity analysis provides the impact of each input parameter towards the anticipation of CS of SCC, and it was found that cement contributed the most towards the required outcome.
- This study can also provide civil engineering researchers with a better understanding of how to select the suitable machine learning (ML) algorithms for researching the strength qualities of any form of concrete. The study further provides insight into the significance of input characteristics for the anticipated outcome. Moreover, the experimental approach should also be included for data points (results) to have a better accuracy level of the employed models. Consequently, it is essential to use the required measures and methods for selecting the input variables. Overall, the application of soft computing techniques and tools provides a simple and cost-effective method for analyzing the properties of complicated materials such as concrete.

Supplementary Materials: The following supporting information can be downloaded at: https://www.mdpi.com/article/10.3390/ma15217800/s1.

Author Contributions: M.N.A.: conceptualization, funding acquisition, resources, project administration, supervision, writing—reviewing and editing. M.N.A.-H.: funding acquisition, resources, visualization, writing—reviewing and editing. A.A.: conceptualization, data curation, software, methodology, investigation, validation, writing—original draft. K.K.: methodology, investigation, writing—reviewing and editing. W.A.: resources, visualization, writing—reviewing and editing. M.G.Q.: funding acquisition, writing—reviewing and editing. M.I.: visualization, resources. Q.M.S.A.-A.: visualization, resources. All authors have read and agreed to the published version of the manuscript.

Funding: This work was supported by the Deanship of Scientific Research, Vice Presidency for Graduate Studies and Scientific Research, King Faisal University, Saudi Arabia [Project No. GRANT752]. The APC was funded by the same "Project No. GRANT752".

Institutional Review Board Statement: Not applicable.

Informed Consent Statement: Not applicable.

Data Availability Statement: The data used in this research have been properly cited and reported in the main text.

Acknowledgments: The authors acknowledge the Deanship of Scientific Research, Vice Presidency for Graduate Studies and Scientific Research, King Faisal University, Saudi Arabia (Project No. GRANT752). The authors extend their appreciation for the financial support that has made this study possible.

Conflicts of Interest: The authors declare no conflict of interest.

References

1. Okamura, H.; Ouchi, M. Self-compacting concrete. *J. Adv. Concr. Technol.* **2003**, *1*, 5–15. [CrossRef]
2. Ouchi, M.; Nakamura, S.-a.; Osterberg, T.; Hallberg, S.; Lwin, M. Applications of self-compacting concrete in Japan, Europe and the United States. In Proceedings of the 5th International Symposium on High Performance Computing (ISHPC), Tokyo, Japan, 20–22 October 2003; Kochi University of Technology: Kochi, Japan, 2003.
3. Shi, C.; Yang, X.; Yu, Z.; Khayat, H. Design and application of self-compacting lightweight concretes. In Proceedings of the SCC'2005-China: 1st International Symposium on Design, Performance and Use of Self-Consolidating Concrete, Changsha, China, 26–28 May 2005; pp. 55–64.
4. Ozawa, K. High-performance concrete based on the durability design of concrete structures. In Proceedings of the Second East Asia-Pacific Conference on Structural Engineering and Construction, Chlang Mai, Thailand, 11–13 January 1989.
5. Long, G.; Gao, Y.; Xie, Y.; Materials, B. Designing more sustainable and greener self-compacting concrete. *Constr. Build. Mater.* **2015**, *84*, 301–306. [CrossRef]
6. Najim, K.B.; Al-Jumaily, I.; Atea, A.M. Characterization of sustainable high performance/self-compacting concrete produced using CKD as a cement replacement material. *Constr. Build. Mater.* **2016**, *103*, 123–129. [CrossRef]
7. Kumar, K.R.; Shyamala, G.; Awoyera, P.; Vedhasakthi, K.; Olalusi, O. Cleaner production of self-compacting concrete with selected industrial rejects-an overview. *Silicon* **2021**, *13*, 2809–2820. [CrossRef]
8. Domone, P. A review of the hardened mechanical properties of self-compacting concrete. *Cem. Concr. Compos.* **2007**, *29*, 1–12. [CrossRef]

9. Viacava, I.R.; de Cea, A.A.; De Sensale, G.R. Self-compacting concrete of medium characteristic strength. *Constr. Build. Mater.* **2012**, *30*, 776–782. [CrossRef]
10. Bradu, A.; Cazacu, N.; Florea, N.; Mihai, P. Compressive strength of self compacting concrete. *Bul. Inst. Politeh. Din Lasi. Sect. Constr. Arhit.* **2016**, *62*, 59.
11. Malhotra, H. The effect of temperature on the compressive strength of concrete. *Mag. Concr. Res.* **1956**, *8*, 85–94. [CrossRef]
12. Yeh, I.-C. Analysis of strength of concrete using design of experiments and neural networks. *J. Mater. Civ. Eng.* **2006**, *18*, 597–604. [CrossRef]
13. Tangadagi, R.B.; Manjunatha, M.; Seth, D.; Preethi, S. Role of mineral admixtures on strength and durability of high strength self compacting concrete: An experimental study. *Materialia* **2021**, *18*, 101144. [CrossRef]
14. Uysal, M.; Sumer, M. Performance of self-compacting concrete containing different mineral admixtures. *Constr. Build. Mater.* **2011**, *25*, 4112–4120. [CrossRef]
15. Uysal, M.; Yilmaz, K.; Composites, C. Effect of mineral admixtures on properties of self-compacting concrete. *Cem. Concr. Compos.* **2011**, *33*, 771–776. [CrossRef]
16. Xu, Y.; Ahmad, W.; Ahmad, A.; Ostrowski, K.A.; Dudek, M.; Aslam, F.; Joyklad, P. Computation of High-Performance Concrete Compressive Strength Using Standalone and Ensembled Machine Learning Techniques. *Materials* **2021**, *14*, 7034. [CrossRef] [PubMed]
17. Song, Y.; Zhao, J.; Ostrowski, K.A.; Javed, M.F.; Ahmad, A.; Khan, M.I.; Aslam, F.; Kinasz, R. Prediction of Compressive Strength of Fly-Ash-Based Concrete Using Ensemble and Non-Ensemble Supervised Machine-Learning Approaches. *Appl. Sci.* **2022**, *12*, 361. [CrossRef]
18. Khan, K.; Ahmad, W.; Amin, M.N.; Aslam, F.; Ahmad, A.; Al-Faiad, M.A. Comparison of Prediction Models Based on Machine Learning for the Compressive Strength Estimation of Recycled Aggregate Concrete. *Materials* **2022**, *15*, 3430. [CrossRef] [PubMed]
19. Ahmad, A.; Farooq, F.; Ostrowski, K.A.; Śliwa-Wieczorek, K.; Czarnecki, S. Application of Novel Machine Learning Techniques for Predicting the Surface Chloride Concentration in Concrete Containing Waste Material. *Materials* **2021**, *14*, 2297. [CrossRef]
20. Ahmad, A.; Ostrowski, K.A.; Maślak, M.; Farooq, F.; Mehmood, I.; Nafees, A. Comparative Study of Supervised Machine Learning Algorithms for Predicting the Compressive Strength of Concrete at High Temperature. *Materials* **2021**, *14*, 4222. [CrossRef]
21. Ahmad, A.; Chaiyasarn, K.; Farooq, F.; Ahmad, W.; Suparp, S.; Aslam, F. Compressive Strength Prediction via Gene Expression Programming (GEP) and Artificial Neural Network (ANN) for Concrete Containing RCA. *Buildings* **2021**, *11*, 324. [CrossRef]
22. Shang, M.; Li, H.; Ahmad, A.; Ahmad, W.; Ostrowski, K.A.; Aslam, F.; Joyklad, P.; Majka, T.M. Predicting the Mechanical Properties of RCA-Based Concrete Using Supervised Machine Learning Algorithms. *Materials* **2022**, *15*, 647. [CrossRef]
23. Ahmad, A.; Ahmad, W.; Chaiyasarn, K.; Ostrowski, K.A.; Aslam, F.; Zajdel, P.; Joyklad, P. Prediction of Geopolymer Concrete Compressive Strength Using Novel Machine Learning Algorithms. *Polymers* **2021**, *13*, 3389. [CrossRef]
24. Cui, L.; Yang, S.; Chen, F.; Ming, Z.; Lu, N.; Qin, J. A survey on application of machine learning for Internet of Things. *Int. J. Mach. Learn. Cybern.* **2018**, *9*, 1399–1417. [CrossRef]
25. Pandey, P.K.; Aggarwal, P.; Aggarwal, Y.; Aggarwal, S. Prediction of Compressive Strength of Self-Compacting Concrete Containing Silica's Using Soft Computing Techniques. In *Applications of Computational Intelligence in Concrete Technology*; CRC Press: Boca Raton, FL, USA, 2022; pp. 163–181.
26. Onyelowe, K.C.; Ebid, A.M.; Riofrio, A.; Baykara, H.; Soleymani, A.; Mahdi, H.A.; Jahangir, H.; Ibe, K. Multi-Objective Prediction of the Mechanical Properties and Environmental Impact Appraisals of Self-Healing Concrete for Sustainable Structures. *Sustainability* **2022**, *14*, 9573. [CrossRef]
27. Andalib, A.; Aminnejad, B.; Lork, A. Grey Wolf Optimizer-Based ANNs to Predict the Compressive Strength of Self-Compacting Concrete. *Appl. Comput. Intell. Soft Comput.* **2022**, *2022*, 9887803. [CrossRef]
28. Wang, H.; Ma, C.; Zhou, L. A brief review of machine learning and its application. In Proceedings of the 2009 International Conference on Information Engineering and Computer Science, Wuhan, China, 19–20 December 2009; pp. 1–4.
29. Sonebi, M.; Cevik, A.; Grünewald, S.; Walraven, J. Modelling the fresh properties of self-compacting concrete using support vector machine approach. *Constr. Build. Mater.* **2016**, *106*, 55–64. [CrossRef]
30. Aiyer, B.G.; Kim, D.; Karingattikkal, N.; Samui, P.; Rao, P.R. Prediction of compressive strength of self-compacting concrete using least square support vector machine and relevance vector machine. *KSCE J. Civ. Eng.* **2014**, *18*, 1753–1758. [CrossRef]
31. Asteris, P.; Kolovos, K.; Douvika, M.; Roinos, K. Prediction of self-compacting concrete strength using artificial neural networks. *Eur. J. Environ. Civ. Eng.* **2016**, *20*, s102–s122. [CrossRef]
32. Dutta, S.; Murthy, A.R.; Kim, D.; Samui, P. Prediction of compressive strength of self-compacting concrete using intelligent computational modeling. *Comput. Mater. Contin* **2017**, *53*, 167–185.
33. Yuan, X.; Tian, Y.; Ahmad, W.; Ahmad, A.; Usanova, K.I.; Mohamed, A.M.; Khallaf, R. Machine Learning Prediction Models to Evaluate the Strength of Recycled Aggregate Concrete. *Materials* **2022**, *15*, 2823. [CrossRef]
34. Sarkhani Benemaran, R.; Esmaeili-Falak, M.; Javadi, A. Predicting resilient modulus of flexible pavement foundation using extreme gradient boosting based optimised models. *Int. J. Pavement Eng.* **2022**, 1–20. [CrossRef]
35. Wang, J.; Wu, F. New hybrid support vector regression methods for predicting fresh and hardened properties of self-compacting concrete. *J. Intell. Fuzzy Syst.* **2022**, 1–15. [CrossRef]
36. Kumar, B.N.; Kumar, P.P. Prediction on Flexural strength of High Strength Hybrid Fiber Self Compacting Concrete by using Artificial Intelligence. *J. Artif. Intell.* **2022**, *4*, 1–16. [CrossRef]

37. Nehdi, M.; El Chabib, H.; El Naggar, M.H. Predicting performance of self-compacting concrete mixtures using artificial neural networks. *Mater. J.* **2001**, *98*, 394–401.
38. Nguyen, T.T.; Pham Duy, H.; Pham Thanh, T.; Vu, H.H. Compressive Strength Evaluation of Fiber-Reinforced High-Strength Self-Compacting Concrete with Artificial Intelligence. *Adv. Civ. Eng.* **2020**, *2020*, 3012139. [CrossRef]
39. Asri, Y.E.; Aicha, M.B.; Zaher, M.; Alaoui, A.H. Prediction of compressive strength of self-compacting concrete using four machine learning technics. *Mater. Today Proc.* **2022**, *57*, 859–866. [CrossRef]
40. de-Prado-Gil, J.; Palencia, C.; Silva-Monteiro, N.; Martínez-García, R. To predict the compressive strength of self compacting concrete with recycled aggregates utilizing ensemble machine learning models. *Case Stud. Constr. Mater.* **2022**, *16*, e01046. [CrossRef]
41. Balf, F.R.; Kordkheili, H.M.; Kordkheili, A.M. A New method for predicting the ingredients of self-compacting concrete (SCC) including fly ash (FA) using data envelopment analysis (DEA). *Arab. J. Sci. Eng.* **2021**, *46*, 4439–4460. [CrossRef]
42. Kovačević, M.; Lozančić, S.; Nyarko, E.K.; Hadzima-Nyarko, M. Modeling of compressive strength of self-compacting rubberized concrete using machine learning. *Materials* **2021**, *14*, 4346. [CrossRef]
43. Asteris, P.G.; Kolovos, K.G. Self-compacting concrete strength prediction using surrogate models. *Neural Comput. Appl.* **2019**, *31*, 409–424. [CrossRef]
44. Awoyera, P.O.; Kirgiz, M.S.; Viloria, A.; Ovallos-Gazabon, D. Estimating strength properties of geopolymer self-compacting concrete using machine learning techniques. *J. Mater. Res. Technol.* **2020**, *9*, 9016–9028. [CrossRef]
45. Baskar, I.; Ramanathan, P.; Venkatasubramani, R. Influence of silica fume on properties of self-compacting concrete. *Int. J. Emerg. Trends Eng. Dev.* **2012**, *4*, 757–767.
46. Brouwers, H.; Radix, H. Self-compacting concrete: Theoretical and experimental study. *Cem. Concr. Res.* **2005**, *35*, 2116–2136. [CrossRef]
47. Fathi, A.; Shafiq, N.; Nuruddin, M.; Elheber, A. Study the effectiveness of the different pozzolanic material on self-compacting concrete. *ARPN J. Eng. Appl. Sci.* **2013**, *8*, 299–305.
48. Felekoğlu, B.; Türkel, S.; Baradan, B. Effect of water/cement ratio on the fresh and hardened properties of self-compacting concrete. *Build. Environ.* **2007**, *42*, 1795–1802. [CrossRef]
49. Gandage, A.; Ram, V.; Sivakumar, M.; Vasan, A.; Venu, M.; Yaswanth, A. Optimization of class C flyash dosage in self-compacting concrete for pavement applications. In Proceedings of the International Conference on Innovations in Concrete for Meeting Infrastructure Challenge, Hyderabad, India, 23–26 October 2013; pp. 213–226.
50. Gesoğlu, M.; Güneyisi, E.; Özbay, E. Properties of self-compacting concretes made with binary, ternary, and quaternary cementitious blends of fly ash, blast furnace slag, and silica fume. *Constr. Build. Mater.* **2009**, *23*, 1847–1854. [CrossRef]
51. Gesoğlu, M.; Özbay, E. Structures. Effects of mineral admixtures on fresh and hardened properties of self-compacting concretes: Binary, ternary and quaternary systems. *Mater. Struct.* **2007**, *40*, 923–937. [CrossRef]
52. Grdić, Z.; Despotović, I.; Topličić-Ćurčić, G. Properties of self-compacting concrete with different types of additives. *Facta Univ.-Ser. Archit. Civ. Eng.* **2008**, *6*, 173–177. [CrossRef]
53. Memon, S.A.; Shaikh, M.A.; Akbar, H. Utilization of Rice Husk Ash as viscosity modifying agent in Self Compacting Concrete. *Constr. Build. Mater.* **2011**, *25*, 1044–1048. [CrossRef]
54. Phani, S.; Sekhar, S.; Rao, S.; Sravana, P. High strength self-compacting concrete using mineral admixtures. *Indian Concr J* **2013**, *87*, 42–47.
55. Rahman, M.E.; Muntohar, A.S.; Pakrashi, V.; Nagaratnam, B.; Sujan, D. Self compacting concrete from uncontrolled burning of rice husk and blended fine aggregate. *Mater. Des.* **2014**, *55*, 410–415. [CrossRef]
56. Rao, N.; Rao, P.; Sravana, P.; Sekhar, T. Studies on relationship of water-powder ratio and compressive strength of self-compacted concrete. In Proceedings of the 34th Conference on Our World in Concrete and Structures, Singapore, 16–18 August 2009; pp. 1–8.
57. Şahmaran, M.; Yaman, İ.Ö.; Tokyay, M. Transport and mechanical properties of self consolidating concrete with high volume fly ash. *Cem. Concr. Compos.* **2009**, *31*, 99–106. [CrossRef]
58. Sfikas, I.P.; Trezos, K.G. Effect of composition variations on bond properties of self-compacting concrete specimens. *Constr. Build. Mater.* **2013**, *41*, 252–262. [CrossRef]
59. Siddique, R. Properties of self-compacting concrete containing class F fly ash. *Mater. Des.* **2011**, *32*, 1501–1507. [CrossRef]
60. Sonebi, M. Medium strength self-compacting concrete containing fly ash: Modelling using factorial experimental plans. *Cem. Concr. Res.* **2004**, *34*, 1199–1208. [CrossRef]
61. Sukumar, B.; Nagamani, K.; Raghavan, R.S.; Materials, B. Evaluation of strength at early ages of self-compacting concrete with high volume fly ash. *Constr. Build. Mater.* **2008**, *22*, 1394–1401. [CrossRef]
62. Valcuende, M.; Marco, E.; Parra, C.; Serna, P. Influence of limestone filler and viscosity-modifying admixture on the shrinkage of self-compacting concrete. *Cem. Concr. Res.* **2012**, *42*, 583–592. [CrossRef]
63. Khan, K.; Ahmad, A.; Amin, M.N.; Ahmad, W.; Nazar, S.; Arab, A.M.A. Comparative Study of Experimental and Modeling of Fly Ash-Based Concrete. *Materials* **2022**, *15*, 3762. [CrossRef] [PubMed]
64. Ling, H.; Qian, C.; Kang, W.; Liang, C.; Chen, H. Combination of Support Vector Machine and K-Fold cross validation to predict compressive strength of concrete in marine environment. *Constr. Build. Mater.* **2019**, *206*, 355–363. [CrossRef]
65. Amin, M.N.; Khan, K.; Ahmad, W.; Javed, M.F.; Qureshi, H.J.; Saleem, M.U.; Qadir, M.G.; Faraz, M.I. Compressive Strength Estimation of Geopolymer Composites through Novel Computational Approaches. *Polymers* **2022**, *14*, 2128. [CrossRef]

66. Nazar, S.; Yang, J.; Ahmad, A.; Shah, S.F.A. Comparative study of evolutionary artificial intelligence approaches to predict the rheological properties of fresh concrete. *Mater. Today Commun.* **2022**, *32*, 103964. [CrossRef]
67. Wang, Q.; Ahmad, W.; Ahmad, A.; Aslam, F.; Mohamed, A.; Vatin, N.I. Application of Soft Computing Techniques to Predict the Strength of Geopolymer Composites. *Polymers* **2022**, *14*, 1074. [CrossRef]
68. Güçlüer, K.; Özbeyaz, A.; Göymen, S.; Günaydın, O. A comparative investigation using machine learning methods for concrete compressive strength estimation. *Mater. Today Commun.* **2021**, *27*, 102278. [CrossRef]
69. Chopra, P.; Sharma, R.K.; Kumar, M.; Chopra, T. Comparison of machine learning techniques for the prediction of compressive strength of concrete. *Adv. Civ. Eng.* **2018**, *2018*, 5481705. [CrossRef]
70. Ahmad, A.; Ahmad, W.; Aslam, F.; Joyklad, P. Compressive strength prediction of fly ash-based geopolymer concrete via advanced machine learning techniques. *Case Stud. Constr. Mater.* **2022**, *16*, e00840. [CrossRef]

materials

MDPI

Article

New SHapley Additive exPlanations (SHAP) Approach to Evaluate the Raw Materials Interactions of Steel-Fiber-Reinforced Concrete

Madiha Anjum [1], Kaffayatullah Khan [2,*], Waqas Ahmad [3], Ayaz Ahmad [4], Muhammad Nasir Amin [2] and Afnan Nafees [3]

[1] Department of Computer Engineering, College of Computer Science and Information, Technology, King Faisal University, Al-Ahsa 31982, Saudi Arabia
[2] Department of Civil and Environmental Engineering, College of Engineering, King Faisal University, Al-Ahsa 31982, Saudi Arabia
[3] Department of Civil Engineering, COMSATS University Islamabad, Abbottabad 22060, Pakistan
[4] MaREI Centre, Ryan Institute and School of Engineering, College of Science and Engineering, National University of Ireland Galway, H91 TK33 Galway, Ireland
* Correspondence: kkhan@kfu.edu.sa

Abstract: Recently, artificial intelligence (AI) approaches have gained the attention of researchers in the civil engineering field for estimating the mechanical characteristics of concrete to save the effort, time, and cost of researchers. Consequently, the current research focuses on assessing steel-fiber-reinforced concrete (SFRC) in terms of flexural strength (FS) prediction by employing delicate AI techniques as well as to predict the raw material interaction that is still a research gap. In this study, the FS of SFRC is estimated by deploying supervised machine learning (ML) techniques, such as DT-Gradient Boosting, DT-XG Boost, DT-AdaBoost, and DT-Bagging. In addition to that, the performance model is also evaluated by using R^2, root mean square error (RMSE), and mean absolute error (MAE). Furthermore, the k-fold cross-validation method is also applied to validate the model's performance. It is observed that DT-Bagging with an R^2 value of 0.95 is superior to DT-XG Boost, DT-Gradient Boosting, and DT-AdaBoost. Lesser error MAE and RMSE and higher R^2 values for the DT-Bagging model show the enhanced performance of the model compared to the other ensembled approaches. Considerable conservation of time, effort, and cost can be made by applying ML techniques to predict concrete properties. The evaluation of the outcome depicts that the estimated results of DT-Bagging are closer to the experimental results, indicating the accurate estimation of SFRC flexural strength. It is further revealed from the SHapley Additive exPlanations (SHAP) study that the volumetric content of steel fiber highly and positively influences the FS of SFRC.

Keywords: steel fiber; building material; flexural strength; fibers; concrete; mortar; hybrid

Citation: Anjum, M.; Khan, K.; Ahmad, W.; Ahmad, A.; Amin, M.N.; Nafees, A. New SHapley Additive ExPlanations (SHAP) Approach to Evaluate the Raw Materials Interactions of Steel-Fiber-Reinforced Concrete. *Materials* **2022**, *15*, 6261. https://doi.org/10.3390/ma15186261

Academic Editor: Krzysztof Schabowicz

Received: 8 August 2022
Accepted: 1 September 2022
Published: 9 September 2022

1. Introduction

Modern artificial intelligence (AI) approaches are effective for evaluating the difficult problems of the engineering domain. By using these techniques, the output end products can be predicted with a set of input factors. Single-model-based standalone and ensemble, i.e., AdaBoost and bagging, methods are the two primary methods of machine learning (ML) that are used for predicting the properties of concrete. As per the available literature, the prediction performance of ensemble methods is better than the individual machine learning algorithm. Chaabene et al. [1] predicted the mechanical characteristics of concrete by employing ML approaches. Likewise, abundant literature is available on the utilization of ML for predicting different concrete types, such as recycled aggregates [2–5], self-healing [6], materials-integrated [7], and high-performance [8–12] concretes. In a study conducted by Han et al. [9] for predicting high-performance concrete strength via ML approaches, the considered input parameters were i. cement, ii. fine and coarse aggregates, iii. water,

iv. fly ash, v. ground-granulated blast furnace slag, and vi. The ageing period. The study concluded with the highly precise prediction of high-performance concrete strength using the developed ML model. The toughness, ductility, resistance to cracks, mechanical properties, and fatigue resistance of concrete can be enhanced by adding fibers [13–25]. Incorporating steel fibers in cementitious composites can enhance their post-cracking behavior and toughness [26–29]. Different fiber types, such as steel, and artificial and natural fibers, have been explored in various studies for their potential application as construction materials [25,30–35]. In SFRC, additional estimation factors regarding regular concrete are considered, such as the aspect ratio of steel fibers, their type, and the volumetric percentage content. However, the development of appropriate estimation models for SFRC is relatively new. Accordingly, conventional regression models (linear and nonlinear) are employed to determine SFRC flexural strength (FS).

The properties of different concrete types can now be precisely predicted by applying ML approaches. Significant effort, time, and cost are needed during experimental investigations. Hence, to save time it is necessary to develop data-modelling-based algorithms to identify closely linked independent parameters. The necessity is to employ AI techniques to estimate the properties of novel concrete types. ML techniques to predict SFRC FS are an effective alternative to save the cost, time, and effort required for the experimental setup. Accordingly, in the current work, the FS of steel-fiber-reinforced concrete (SFRC) is predicted by using artificial intelligence-based machine learning methods. Subsequently, in this work, the employment of ensemble ML models, such as gradient boosting, AdaBoost, XG Boosting, and bagging ensembled ML approaches, is done to achieve the study objectives. Moreover, the application of statistical checks is also done for the testing of models in addition to the comparison of all the applied models [36–39]. A model with the best performance is proposed based on performance due to applied statistical checks for the prediction of SFRC properties. Afterwards, a game theory approach [40], named SHapley Additive exPlanations (SHAP), is also employed to obtain an enhanced description of applied ML models by global features influences classification and interactions/dependencies. A novel knowledge era is identified by this method in terms of SFRC ingredients' influences on FS. It would assist the researcher's ability to identify adequate SFRC mix combinations and quickly estimate its FS without even performing experimental procedures for trials. It would also aid the upcoming research for the strategical development of SFRC with innovative mechanical properties based on various limitations such as resource availability in the form of cost, material, time, and FS requirements for multiple construction projects.

This study is conducted to extract the effective ML approach to estimate the FS of SFRC precisely. The precise prediction of concrete characteristics would help one to obtain the durable structures' economical, effective, and efficient design, ultimately reducing the time for selecting adequate materials and the resources, cost, and time. Furthermore, the SHAP analysis is conducted for depicting raw ingredients' influence on SFRC FS, which has not been performed yet by the previous scholars and is the novelty of this work. The suggested prediction approaches would also assist scholars in the civil engineering field in developing new materials.

2. SHapley Additive ExPlanations (SHAP)

Moreover, in this work, the identification of global feature impacts and the relations of all the input features with FS of steel-fiber-reinforced concrete, based on game theory model (i.e., SHAP analysis) [41], is made for broadening the explainability of the suggested algorithm. In the procedure of SHAP analysis, each instance prediction is explicated by quantifying the features contribution by using SHapley values, attained by the employment of coalition of game theory. The average of all possible combinations for every feature value is taken to calculate the SHapley value. The SHapley values depict a direct relation with the feature influence. The global feature influence values are quantified by averaging all of the SHapley values of every database feature. Later, the descending order sorting, in terms of importance, for all values is done to draw a plot. A solitary point on the plot

represents the SHapley value for each individual feature and instance. The X-axis shows the SHapley values and the y-axis portray feature importance. The position on the y-axis is directly related to feature influence on steel-fiber-reinforced concrete, where a color scale is used to indicate the feature importance. The plots of SHAP-feature dependence represents the interaction with/impact on steel-fiber-reinforced concrete, having colored the depiction for interactions. More elaborated information can be attained by using this method than partial dependence typical plots [40]. The feature importance (j) for model f outcome; $\phi^j(f)$ is the assigned weight against feature contribution summation for output of model $f(x_i)$ for overall likely feature mixtures [42]. $\phi^j(f)$ is represented via Equation (1), as presented below:

$$\phi^j(f) = \sum_{S \subseteq \{x^1,\ldots\ldots,x^p\}/\{x^j\}} \frac{|S|!(p-|S|-1)!}{p!} \left(f\left(S \sqcup \left\{x^j\right\}\right) - f(S)\right) \quad (1)$$

S = subset of features; $x_j = j$ feature; and p = the number of features in model.

The SHAP technique determines the feature importance by quantifying the errors for prediction while distressing a specific feature value. The estimated error sensitivity is used for assigning weights to feature importance while perturbing its value. The trained ML model performance is explained by using SHAP. SHAP employs a method, i.e., input linear factors addition model demonstration, that is interpretable and is considered by the output of the model. For example, a model having input factors x_i, where the range of i is from 1 to k, k shows the number of input factor, and h (x_s) shows model explanation havng x_s as an input, where Equation (2) is applied for the depiction of an original model $f(x)$:

$$f(x) = h(x_s) = \varnothing_0 + \sum_{i=1}^{p} \varnothing_i x_s^i \quad (2)$$

where

p = number of input feature;

$\varnothing_0$= constant with no input.

The mapping function, i.e., $x = m_x(x_s)$, has a relationship with input x and x_s parameters. In the literature [43], Equation (2) is presented, where the prediction value, i.e., (h ()), was enhanced in terms of $\varnothing_0$, $\varnothing_1$, and $\varnothing_3$, with an observed decrement of h () in terms of $\varnothing_4$, as presented in Figure 1. Three desired characteristics are included in Equation (2), in terms of consistency, local accuracy, and missingness. The reduction minus the attribution is ensured by consistency, that is, allocated to a relevant feature as a feature change of significant influence. In missingness, it is ensured to have no value for importance assigned to the features that are missing, such as $\varnothing_i = 0$ is employed in terms of $x_s^i = 0$. As far as local accuracy is concerned, it is ensured that the summation of features attribution will be taken as a function for the outcome, which requires a model to tie the outcome as a simplified input x_s for f. $x = m_x x_s$ denotes the local precision achievement.

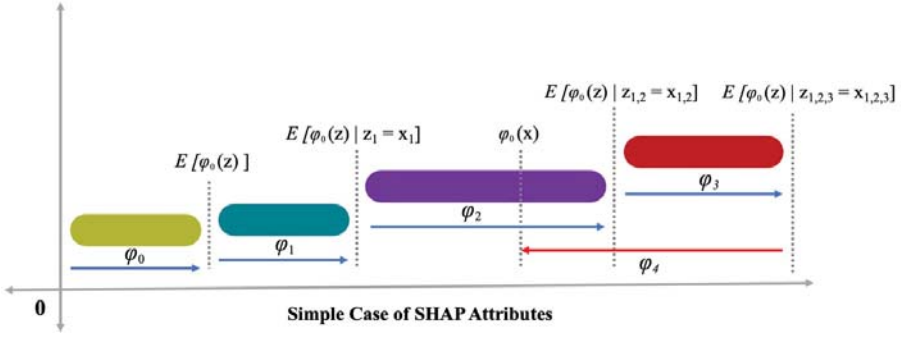

Figure 1. Attributes of SHAP analysis [44].

3. Dataset

The adopted dataset for estimating the FS of SFRC is depicted in Figure 2. The said dataset includes 151 mix designs with nine input parameters and is attained from the literature [34,45–60]. The factors cement (kg/m^3), water (kg/m^3), sand (kg/m^3), coarse aggregate (kg/m^3), superplasticizer (%), silica fume (%), Vf (%), fiber length (mm), and fiber diameter (mm). The variables for estimation in case of FS, which is considered as an output parameter in the current study, are based on input parameters. These variables are illustrated in Figure 2. Anaconda software's Python and Spyder scripting are deployed for the estimation [61]. The histogram for FS being utilized in this work is presented in Figure 3.

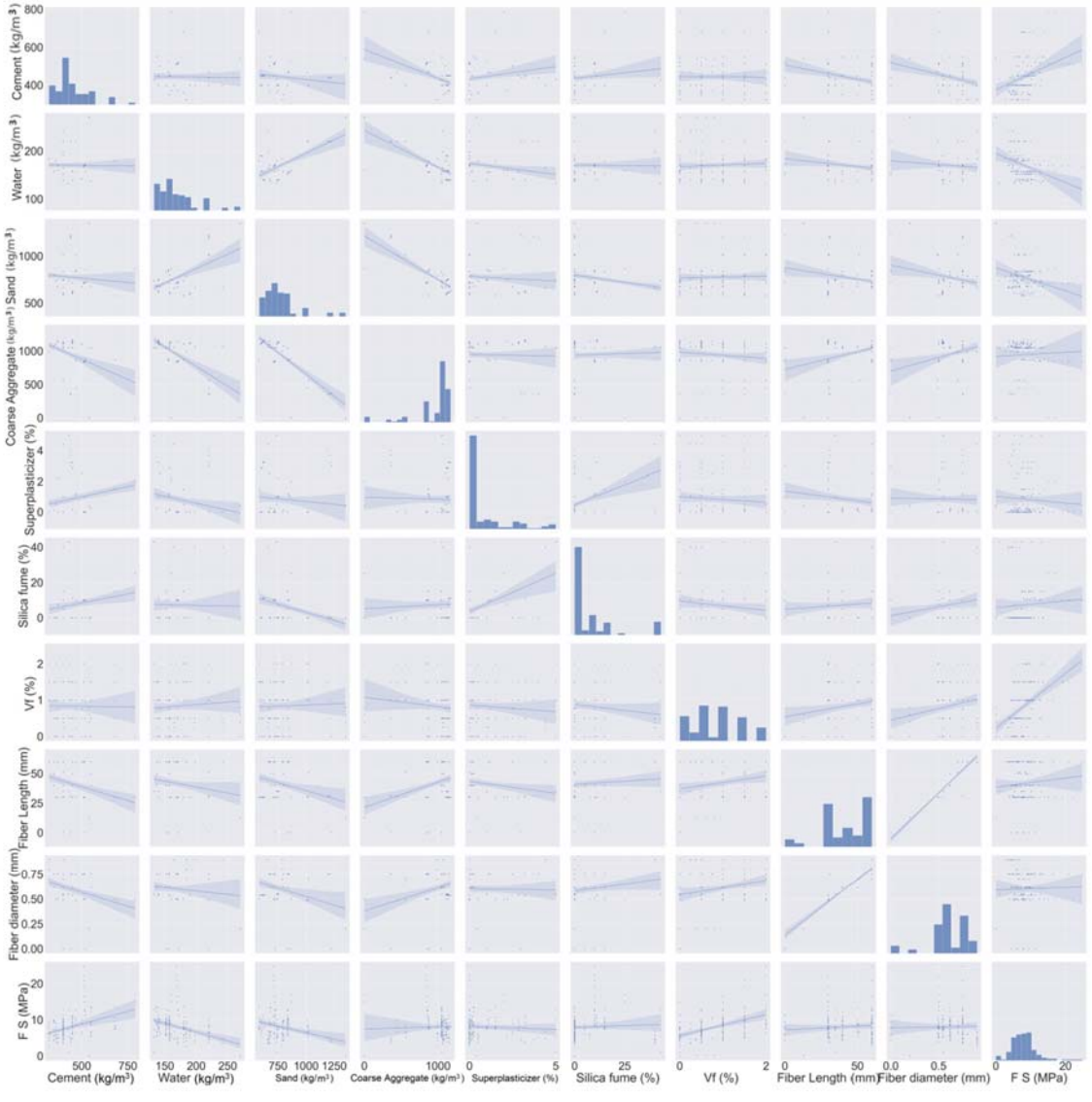

Figure 2. Input and output parameters.

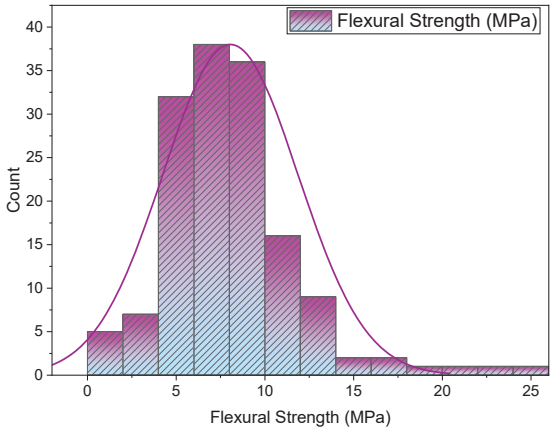

Figure 3. FS distribution.

4. Results and Analysis

4.1. Decision Tree Adaptive Boosting

The experimental and AdaBoost algorithm estimated values comparison for FS of SFRC is shown in Figure 4. Outcomes in the case of AdaBoost are reasonable, having less variation for SFRC FS. The 0.90 R^2 value depicts the AdaBoost model's suitability. Figure 5 shows the experimental and AdaBoost estimated error values distribution for SFRC FS. Figure 5 is plotted with an error difference between the experimental and predicted values on the Z-axis, while the X-axis shows the experimental values and Y-axis presents the predicted values. The error of experimental and estimated AdaBoost algorithm values for FS is 3.41 MPa, and 43% of values are less than 1 MPa, 39% of values are among 1 to 2 MPa, and 18% of values are more than 2 MPa.

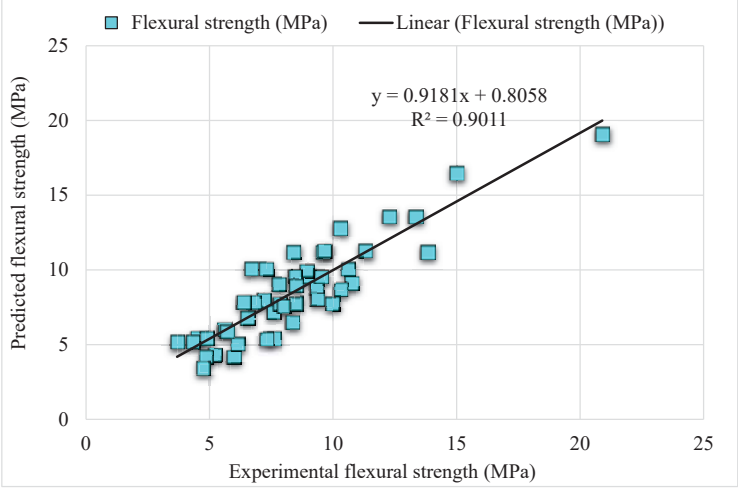

Figure 4. Experimental and AdaBoost predicted results.

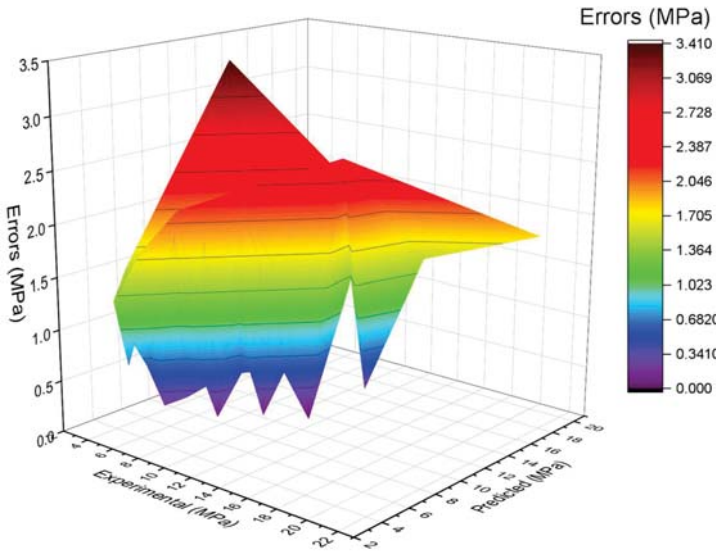

Figure 5. Estimated AdaBoost and experimental values, with errors.

4.2. Decision Tree Bagging

Figure 6 depicts the comparison of the bagging model experimental and predicted error values in the case of SFRC FS. The bagging R^2 of 0.91 indicates highly precise outcomes than the AdaBoost model. Figure 7 illustrates the distribution of error in the case of experimental and bagging estimated values against SFRC FS. It may be noted that the error between experimental and estimated bagging algorithm values is 43% below 1 MPa; 43% is in the range from 1–2 MPa, followed by 13% values that are higher than 2 MPa. Higher R^2 with a lesser error value for the bagging algorithm exhibits higher precision than AdaBoost.

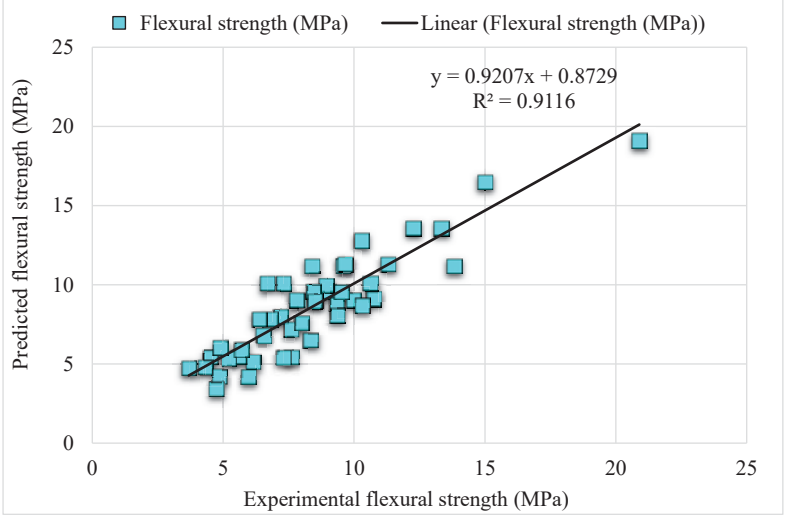

Figure 6. Experimental and bagging predicted results.

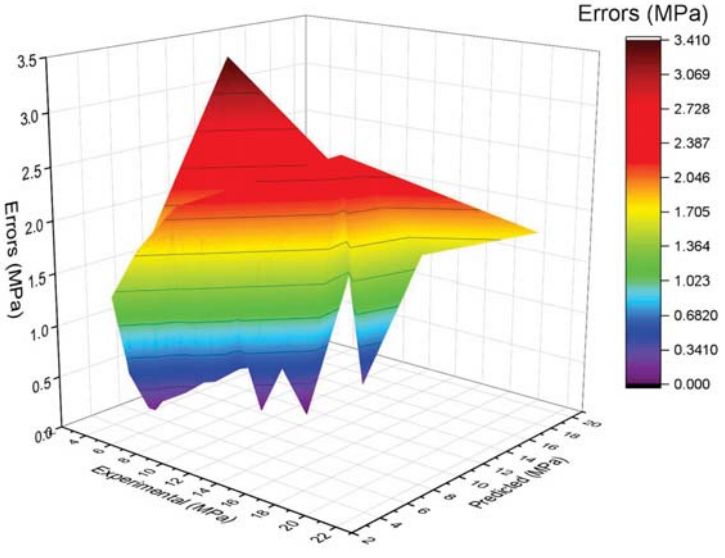

Figure 7. Estimated bagging and experimental values, with errors.

4.3. Gradient Boosting

Figure 8 represents gradient boosting predicted and experimental values for the output parameter of SFRC. The R^2 of 0.92 indicates highly accurate gradient boosting outcomes as compared to the bagging model. Furthermore, it is a highly accurate model among all the other considered models. Figure 9 illustrates the experimental and bagging predicted errors distribution. It is noted that less than 1 MPa, there are 48% values; 50% from 1 to 2 MPa; and above 2 MPa, there are 2% values. In comparison with AdaBoost, the gradient boosting is more precise.

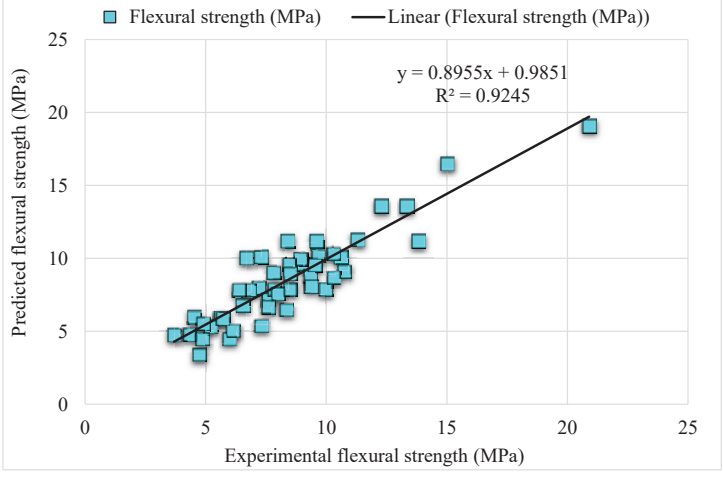

Figure 8. Experimental and gradient boosting predicted results.

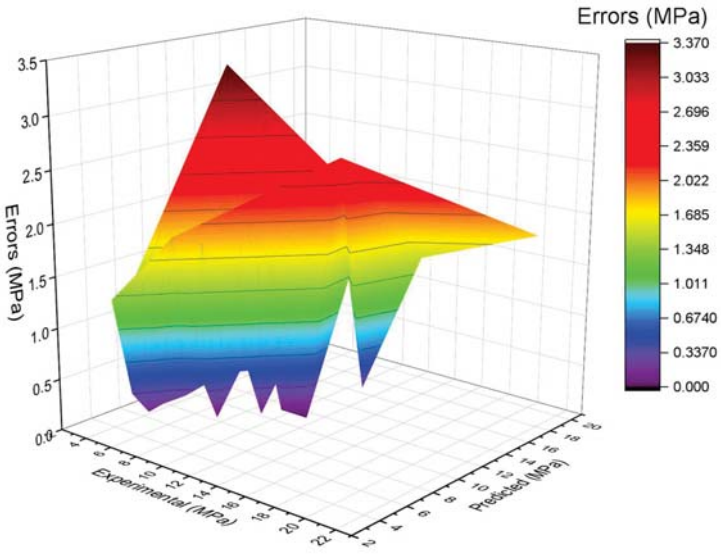

Figure 9. Estimated gradient boosting and experimental values, with errors.

4.4. Extreme Gradient Boosting

Figure 10 illustrates the experimental and estimated extreme gradient boosting values for SFRC considered output parameter. The R^2 of 0.87 for extreme gradient boosting depicts lesser accuracy of outcomes than all other considered algorithms. The experimental and extreme gradient boosting predicted values error distribution for FS of SFRC is presented in Figure 11. Here, 50% of the values are below 1 MPa, 43% are 1 to 2 MPa, and the remaining 7% are above 2 MPa. Lower R^2 and more error values portray unacceptable outcomes of the extreme gradient boosting algorithm than bagging, AdaBoost, and gradient boosting. However, the bagging model's low error and higher R^2 values are adequate and depict accurate prediction. Therefore, as per these findings, it can be said in the case of bagging that it may predict outcomes more accurately than all the considered models.

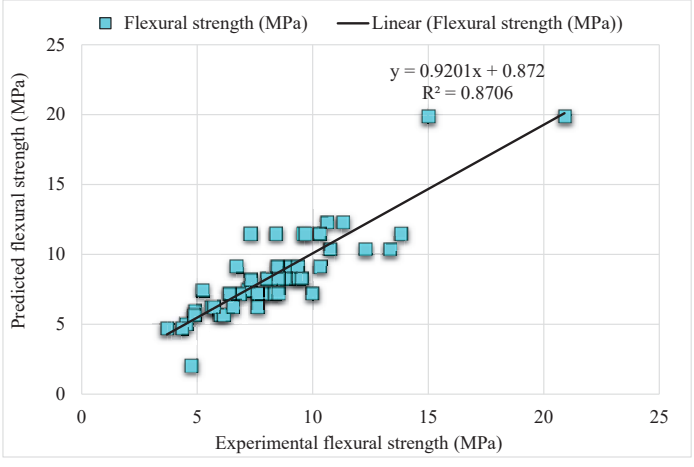

Figure 10. Experimental and estimated extreme gradient boosting outcomes.

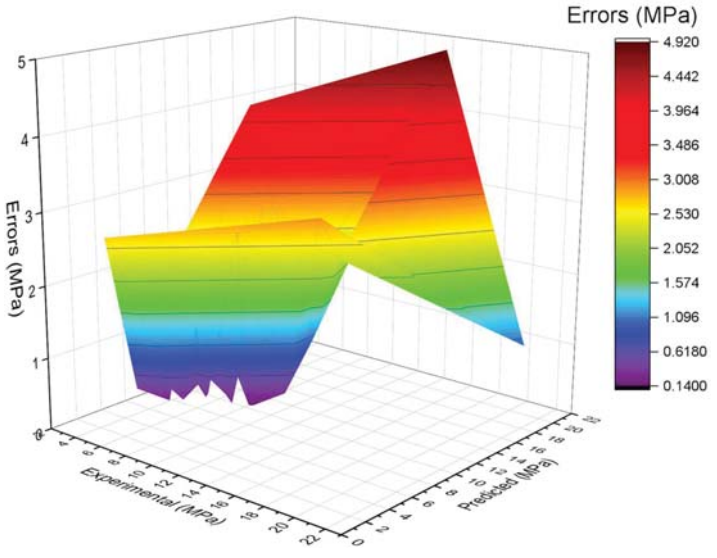

Figure 11. Estimated extreme gradient boosting and experimental values, with errors.

4.5. Comparison of All Models

The model's validity is evaluated during the execution by applying the k-fold cross-validation technique. The performance of models is assessed with the help of statistical checks [36–39]. Generally, the splitting of data in a grouping of 10 for attaining the arbitrary scattering in k-fold cross-validation, and the ten-time repetition of this process, is done to obtain satisfactory outcomes. Table 1 illustrates the statistical checks for all the models. The R^2 of 0.92, 0.87, 0.90, and 0.91 in the case of gradient, extreme gradient, adaptive boosting, and bagging models, as represented in Figure 12a–d. The MAE and RMSE are calculated by employing Equations (3) and (4), from the previous studies [36–39]. It is observed that the gradient boosting has a lower error and higher R^2 values compared to all other considered models for SFRC flexural strength.

$$\mathrm{MAE} = \frac{1}{n}\sum_{i=1}^{n}|x_i - x| \tag{3}$$

$$\mathrm{RMSE} = \sqrt{\sum \frac{\left(y_{pred} - y_{ref}\right)^2}{n}} \tag{4}$$

where n = the total number of data, x, y_{ref} = reference values of the data, and x_i, y_{pred} = predicted model values.

Table 1. Extreme gradient boosting, bagging, and AdaBoost model statistical checks.

Statistical Checks	Approaches			
	Extreme Gradient Boosting	**Decision Tree AdaBoost**	**Decision Tree Bagging**	**Gradient Boosting**
R^2	0.87	0.90	0.91	0.92
RMSE (MPa)	1.65	1.46	1.43	1.34
MAE (MPa)	1.26	1.21	1.18	1.07

SFRC FS is estimated by applying ensembled ML techniques in the current study, which is focused on providing reliable and efficient outcomes. The 0.92 R^2 value for a gradient boosting result with the lowest MAE and RMSE have offered more precise estimations for the FS of SFRC. Out of 20 sub-models, an optimized model for SFRC FS prediction, as presented in Figure 13a–d, the ensembled ML gradient-boosting model has superior performance in terms of MAE (1.07) and RMSE (1.34). Therefore, it is depicted that, among all other models, the ensembled ML gradient-boosting model has provided the highest accuracy and lowest error.

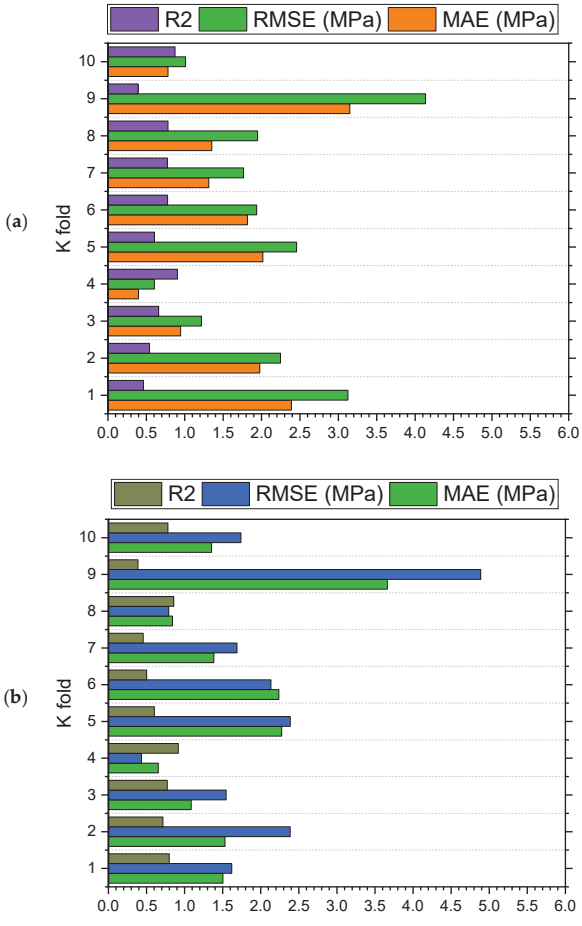

Figure 12. *Cont.*

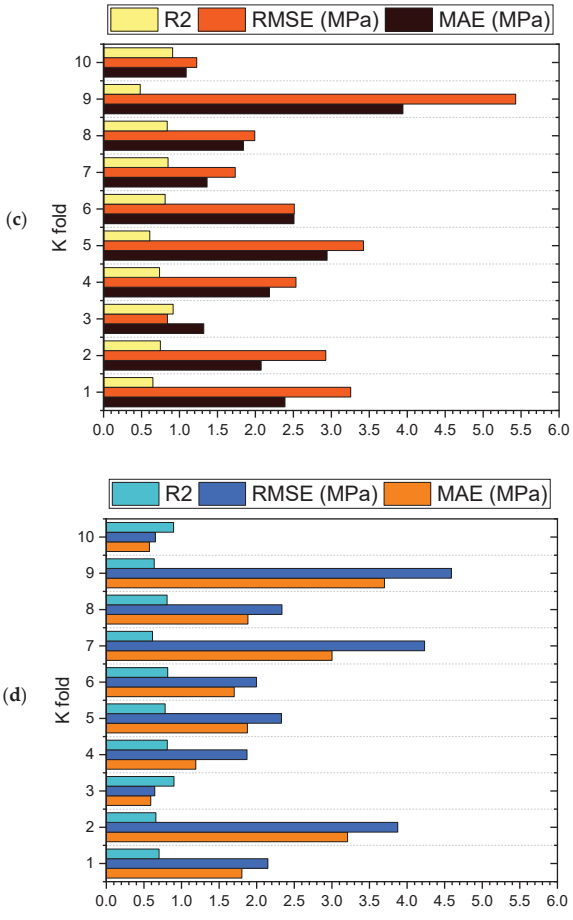

Figure 12. (**a**) AdaBoost; (**b**) bagging; (**c**) gradient boosting; and (**d**) extreme gradient boosting statistical representation.

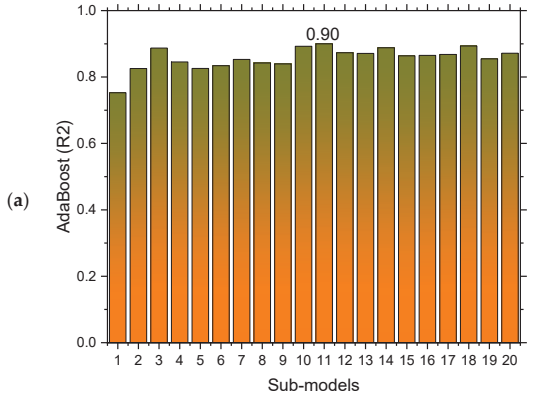

Figure 13. *Cont.*

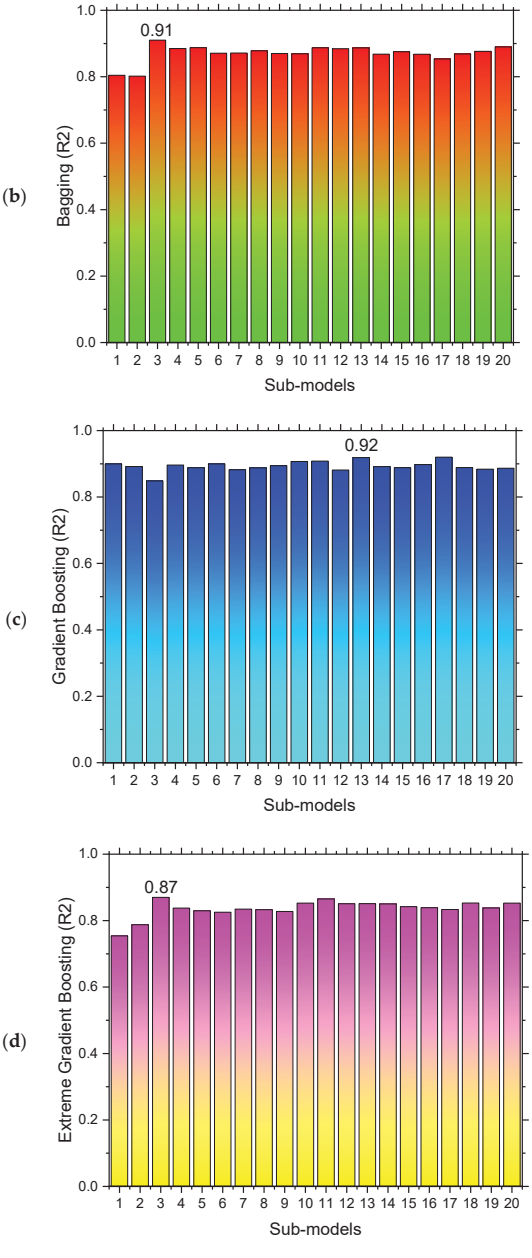

Figure 13. (**a**) AdaBoost; (**b**) bagging; (**c**) gradient boosting; and (**d**) extreme gradient boosting sub models' outcomes.

4.6. Enhanced Explainability for Machine Leaning Algorithms

A detailed explanation of machine learning algorithms and features' relations are presented in this work. At the start, by applying the SHAP tree explainer to the entire dataset, an enhanced illustration for influences of global features by incorporating SHAP explanations is also discussed. The SHAP method is applied [62]. The determination of

the tree-based models' internal structure is carried out with this method, summing up calculations set that is inter-connected with a leaf node of the tree model, resulting in low-order complexity [62]. The model interpretation is conducted for SFRC FS by using SHAP. The relation of different features with SFRC flexural strength is represented by SHAP values (Figure 14).

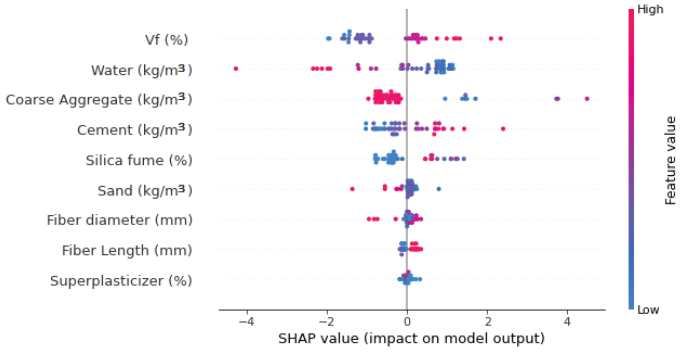

Figure 14. SHAP plot.

It is observed that the volumetric content of steel fiber has a maximum SHAP value for SFRC FS estimation as metallic fibers provide the effect of sewing, ultimately enhancing mechanical characteristics. Therefore, enhancing the steel fibers content would develop more SFRC FS, proving its positive influence. Figure 14 illustrates that the 2nd highest SHAP value is for water content. However, it has a negative influence, which means that increasing the amount of water causes decreased flexural properties of SFRC. In SFRC, the particle packing density theory is the basis of strength; hence, the requirement is to opt for limited water content in this case. Similarly, in the third, the coarse aggregates content also negatively influences SFRC FS. Then, the cement positively impacts the SFRC FS, which means that enhancement in cement content would increase the strength and vice versa. Further, the SFRC properties are significantly influenced by silica fume. Sand, however, shows both positive and negative influences, depending upon the content. Other features such as steel fibers diameter and length and super-plasticizer also have some minor but unique influences on SFRC FS.

The different features' interaction with SFRC FS is depicted in Figure 15. The cement feature interaction is shown in Figure 15a. The amount of cement has major direct impact on SFRC FS. Figure 15b illustrates the negative impact of water for SFRC. Increasing the water content leads to decreasing SFRC FS, leading to a decreasing trend. The sand feature interaction is provided in Figure 15c. The sand content also represents a negative impact on SFRC. However, up to 800 kg/m^3, it is not very effective on the FS of SFRC. Beyond this content of 1300 kg/m^3, it causes a reduction in strength. This might be because more cement paste would be required to coat a larger surface area of sand particles in case of more sand content, ultimately leaving less cement to be accounted for in terms of strength development. Then, in a row, the super-plasticizer content feature depicts both negative and positive interactions, depending upon optimum content (Figure 15d). Up to 3% of the content contributes towards strength enhancement; however, beyond this content, it causes a reduction in strength. The steel fiber volumetric content feature positively influences up to 2% content (Figure 15e), showing its direct relationship with SFRC FS. Similarly, steel fiber length also positively influences and directly relates to SFRC FS, as is evident from Figure 15f. The greater length of steel fibers would enhance the SFRC flexural properties by providing a more effective bridging mechanism.

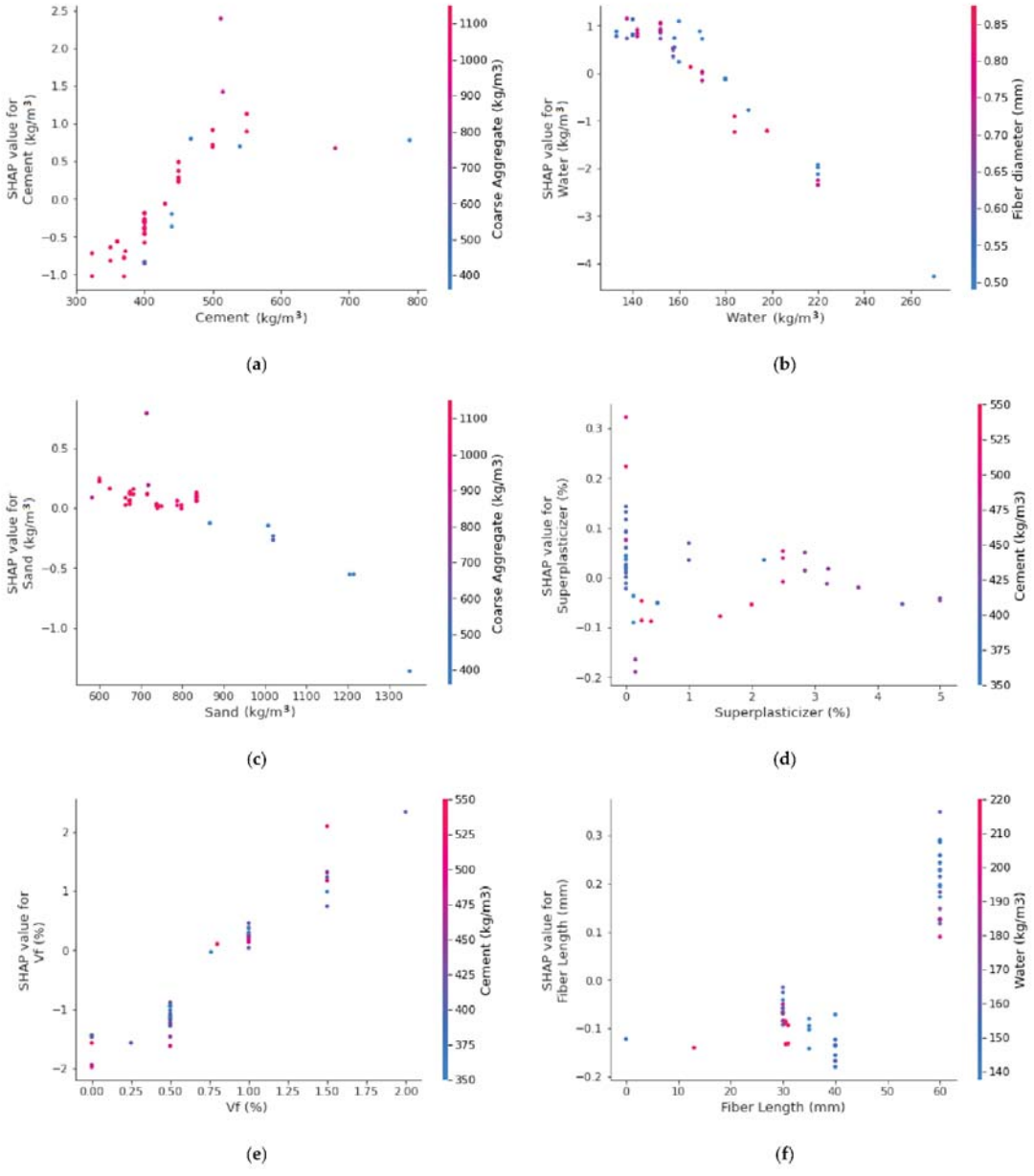

Figure 15. Interaction plot: (**a**) cement; (**b**) water; (**c**) sand; (**d**) superplasticizer; (**e**) Vf; and (**f**) fiber length.

This prediction is based on the database utilized in the current study and focuses on strength prediction. However, the interaction between fiber length and diameter is found based on a limited data set in this study, and more accurate findings can be obtained by including more data points in the future. By expanding the number of data points, importing a slightly higher number of mixes, and taking into consideration a larger number of input factors (fiber length and diameter), a far more accurate model may be constructed

for interaction. To improve the number of data points and outcomes in future studies, it is suggested that experimental work, field testing, and numerical analysis employing a range of approaches be implemented. The limitations of machine learning methods for estimating the strength properties of concrete have already been documented in a previous study [63].

5. Conclusions

Nowadays, the construction industry is focused on utilizing artificial intelligence (AI) approaches to estimate the mechanical properties of concrete. The main focus of this research is to evaluate the accuracy of AI approaches for predicting SFRC FS, in addition to exploring the raw components effect on SFRC flexural strength, which have not been studied yet and constitute a research gap. Nine estimation input parameters are considered, and their interaction is analyzed. Based on the conducted study, the following conclusions are drawn:

The gradient-boosting model's higher R^2 value of 0.92 depicts a highly precise estimation of flexural strength of SFRC out of the actual data, where the extreme gradient boosting, bagging, and AdaBoost have 0.87, 0.90, and 0.91 R^2 values, respectively, in SFRC flexural strength prediction within an acceptable range. Twenty sub-models that range between 10–200 estimators are used to optimize the prediction of SFRC flexural strength. The most effective and accurate forecast for SFRC flexural strength emerged for gradient boosting rather than for the other considered algorithms.

The higher R^2 and lower MAE and RMSE values for SFRC FS prediction from gradient boosting are evident from k-fold cross validation findings. Therefore, it can be claimed as the prediction model with the highest precision for flexural strength of SFRC.

Statistical checks such as MAE and RMSE are also applied to evaluate the models' performance. Here again, the higher coefficient of determination and lower error values in gradient boosting for SFRC flexural strength prediction show their superiority.

Hence, it can be concluded that gradient boosting is the best technique for predicting SFRC flexural strength.

The volumetric content of steel fiber has the highest influence on SFRC flexural strength, followed by the contents of cement, water, and coarse aggregates, as revealed through SHAP observations. Contrary to this, super-plasticizer content has a minimal impact on SFRC flexural strength.

The feature interaction plot portrays that cement content is a major and positive influencing feature on SFRC flexural strength.

Author Contributions: K.K.: conceptualization, funding acquisition, project administration, writing, reviewing, and editing. W.A.: conceptualization, data curation, software, methodology, investigation, validation, supervision, and writing—original draft. M.A.: methodology, investigation, supervision, writing, reviewing, and editing. A.A.: visualization, methodology, software, writing, reviewing, and editing. M.N.A.: resources, validation, writing, reviewing, and editing. A.N.: data curation, software, writing, reviewing, and editing. All authors have read and agreed to the published version of the manuscript.

Funding: This work was supported by the Deanship of Scientific Research, Vice Presidency for Graduate Studies and Scientific Research, King Faisal University, Saudi Arabia (Grant No. 1,321), through its KFU Research Summer Initiative.

Institutional Review Board Statement: Not applicable.

Informed Consent Statement: Not applicable.

Data Availability Statement: All data is available in the paper.

Acknowledgments: The authors acknowledge the Deanship of Scientific Research, Vice Presidency for Graduate Studies and Scientific Research, King Faisal University, Saudi Arabia (Grant No. 1,321), through its KFU Research Summer Initiative.

Conflicts of Interest: The authors declare no conflict of interest.

References

1. Chaabene, W.B.; Flah, M.; Nehdi, M.L. Machine learning prediction of mechanical properties of concrete: Critical review. *Constr. Build. Mater.* **2020**, *260*, 119889. [CrossRef]
2. Deng, F.; He, Y.; Zhou, S.; Yu, Y.; Cheng, H.; Wu, X. Compressive strength prediction of recycled concrete based on deep learning. *Constr. Build. Mater.* **2018**, *175*, 562–569. [CrossRef]
3. Zhang, J.; Huang, Y.; Aslani, F.; Ma, G.; Nener, B. A hybrid intelligent system for designing optimal proportions of recycled aggregate concrete. *J. Clean. Prod.* **2020**, *273*, 122922. [CrossRef]
4. Han, T.; Siddique, A.; Khayat, K.; Huang, J.; Kumar, A. An ensemble machine learning approach for prediction and optimization of modulus of elasticity of recycled aggregate concrete. *Constr. Build. Mater.* **2020**, *244*, 118271. [CrossRef]
5. Behnood, A.; Golafshani, E.M. Machine learning study of the mechanical properties of concretes containing waste foundry sand. *Constr. Build. Mater.* **2020**, *243*, 118152. [CrossRef]
6. Ramadan Suleiman, A.; Nehdi, M.L. Modeling self-healing of concrete using hybrid genetic algorithm–artificial neural network. *Materials* **2017**, *10*, 135. [CrossRef] [PubMed]
7. Marani, A.; Nehdi, M.L. Machine learning prediction of compressive strength for phase change materials integrated cementitious composites. *Constr. Build. Mater.* **2020**, *265*, 120286. [CrossRef]
8. Castelli, M.; Vanneschi, L.; Silva, S. Prediction of high performance concrete strength using genetic programming with geometric semantic genetic operators. *Expert Syst. Appl.* **2013**, *40*, 6856–6862. [CrossRef]
9. Han, Q.; Gui, C.; Xu, J.; Lacidogna, G. A generalized method to predict the compressive strength of high-performance concrete by improved random forest algorithm. *Constr. Build. Mater.* **2019**, *226*, 734–742. [CrossRef]
10. Al-Shamiri, A.K.; Yuan, T.-F.; Kim, J.H. Non-tuned machine learning approach for predicting the compressive strength of high-performance concrete. *Materials* **2020**, *13*, 1023. [CrossRef] [PubMed]
11. Dingqiang, F.; Rui, Y.; Zhonghe, S.; Chunfeng, W.; Jinnan, W.; Qiqi, S. A novel approach for developing a green Ultra-High Performance Concrete (UHPC) with advanced particles packing meso-structure. *Constr. Build. Mater.* **2020**, *265*, 120339. [CrossRef]
12. Fan, D.; Yu, R.; Shui, Z.; Wu, C.; Song, Q.; Liu, Z.; Sun, Y.; Gao, X.; He, Y. A new design approach of steel fibre reinforced ultra-high performance concrete composites: Experiments and modeling. *Cem. Concr. Compos.* **2020**, *110*, 103597. [CrossRef]
13. Cao, M.; Mao, Y.; Khan, M.; Si, W.; Shen, S. Different testing methods for assessing the synthetic fiber distribution in cement-based composites. *Constr. Build. Mater.* **2018**, *184*, 128–142. [CrossRef]
14. Khan, M.; Cao, M.; Hussain, A.; Chu, S. Effect of silica-fume content on performance of CaCO3 whisker and basalt fiber at matrix interface in cement-based composites. *Constr. Build. Mater.* **2021**, *300*, 124046. [CrossRef]
15. Arshad, S.; Sharif, M.B.; Irfan-ul-Hassan, M.; Khan, M.; Zhang, J.-L. Efficiency of supplementary cementitious materials and natural fiber on mechanical performance of concrete. *Arab. J. Sci. Eng.* **2020**, *45*, 8577–8589. [CrossRef]
16. Xie, C.; Cao, M.; Guan, J.; Liu, Z.; Khan, M. Improvement of boundary effect model in multi-scale hybrid fibers reinforced cementitious composite and prediction of its structural failure behavior. *Compos. Part B Eng.* **2021**, *224*, 109219. [CrossRef]
17. Cao, M.; Khan, M. Effectiveness of multiscale hybrid fiber reinforced cementitious composites under single degree of freedom hydraulic shaking table. *Struct. Concr.* **2021**, *22*, 535–549. [CrossRef]
18. Khan, U.A.; Jahanzaib, H.M.; Khan, M.; Ali, M. In Improving the tensile energy absorption of high strength natural fiber reinforced concrete with fly-ash for bridge girders. In *Key Engineering Materials*; Trans Tech Publications Ltd.: Bäch, Switzerland, 2018; pp. 335–342.
19. Khan, M.; Cao, M.; Ai, H.; Hussain, A. Basalt Fibers in Modified Whisker Reinforced Cementitious Composites. *Period. Polytech. Civ. Eng.* **2022**, *66*, 344–354. [CrossRef]
20. Zhang, N.; Yan, C.; Li, L.; Khan, M. Assessment of fiber factor for the fracture toughness of polyethylene fiber reinforced geopolymer. *Constr. Build. Mater.* **2022**, *319*, 126130. [CrossRef]
21. Khan, M.; Ali, M. Improvement in concrete behavior with fly ash, silica-fume and coconut fibres. *Constr. Build. Mater.* **2019**, *203*, 174–187. [CrossRef]
22. Farooqi, M.U.; Ali, M. Contribution of plant fibers in improving the behavior and capacity of reinforced concrete for structural applications. *Constr. Build. Mater.* **2018**, *182*, 94–107. [CrossRef]
23. Farooqi, M.U.; Ali, M. In Effect of Fibre Content on Compressive Strength of Wheat Straw Reinforced Concrete for Pavement Applications. In *IOP Conference Series: Materials Science and Engineering*; IOP Publishing: Bristol, UK, 2018; p. 012014.
24. Farooqi, M.U.; Ali, M. In Effect of Fibre Content on Splitting-Tensile Strength of Wheat Straw Reinforced Concrete for Pavement Applications. In *Key Engineering Materials*; Trans Tech Publications Ltd.: Bäch, Switzerland, 2018; pp. 349–354.
25. Farooqi, M.U.; Ali, M. Effect of pre-treatment and content of wheat straw on energy absorption capability of concrete. *Constr. Build. Mater.* **2019**, *224*, 572–583. [CrossRef]
26. Khan, M.; Cao, M.; Chu, S.; Ali, M. Properties of hybrid steel-basalt fiber reinforced concrete exposed to different surrounding conditions. *Constr. Build. Mater.* **2022**, *322*, 126340. [CrossRef]
27. Li, L.; Khan, M.; Bai, C.; Shi, K. Uniaxial tensile behavior, flexural properties, empirical calculation and microstructure of multi-scale fiber reinforced cement-based material at elevated temperature. *Materials* **2021**, *14*, 1827. [CrossRef] [PubMed]
28. Khan, M.; Cao, M.; Xie, C.; Ali, M. Hybrid fiber concrete with different basalt fiber length and content. *Struct. Concr.* **2022**, *23*, 346–364. [CrossRef]

29. Khan, M.; Cao, M.; Xie, C.; Ali, M. Effectiveness of hybrid steel-basalt fiber reinforced concrete under compression. *Case Stud. Constr. Mater.* **2022**, *16*, e00941. [CrossRef]
30. Achilleos, C.; Hadjimitsis, D.; Neocleous, K.; Pilakoutas, K.; Neophytou, P.O.; Kallis, S. Proportioning of steel fibre reinforced concrete mixes for pavement construction and their impact on environment and cost. *Sustainability* **2011**, *3*, 965–983. [CrossRef]
31. Ahmed, T.; Farooqi, M.; Ali, M. In Compressive Behavior of Rice Straw-Reinforced Concrete for Rigid Pavements. In *IOP Conference Series: Materials Science and Engineering*; IOP Publishing: Bristol, UK, 2020; p. 012004.
32. Ali, B.; Qureshi, L.A.; Kurda, R. Environmental and economic benefits of steel, glass, and polypropylene fiber reinforced cement composite application in jointed plain concrete pavement. *Compos. Commun.* **2020**, *22*, 100437. [CrossRef]
33. Alsaif, A.; Garcia, R.; Figueiredo, F.P.; Neocleous, K.; Christofe, A.; Guadagnini, M.; Pilakoutas, K. Fatigue performance of flexible steel fibre reinforced rubberised concrete pavements. *Eng. Struct.* **2019**, *193*, 170–183. [CrossRef]
34. Aldossari, K.; Elsaigh, W.; Shannag, M. Effect of steel fibers on flexural behavior of normal and high strength concrete. *Int. J. Civ. Environ. Eng.* **2014**, *8*, 22–26.
35. Gupta, S.; Rao, V.K.; Sengupta, J. Evaluation of polyester fiber reinforced concrete for use in cement concrete pavement works. *Road Mater. Pavement Des.* **2008**, *9*, 441–461. [CrossRef]
36. Farooq, F.; Ahmed, W.; Akbar, A.; Aslam, F.; Alyousef, R. Predictive modeling for sustainable high-performance concrete from industrial wastes: A comparison and optimization of models using ensemble learners. *J. Clean. Prod.* **2021**, *292*, 126032. [CrossRef]
37. Aslam, F.; Farooq, F.; Amin, M.N.; Khan, K.; Waheed, A.; Akbar, A.; Javed, M.F.; Alyousef, R.; Alabdulijabbar, H. Applications of gene expression programming for estimating compressive strength of high-strength concrete. *Adv. Civ. Eng.* **2020**, *2020*, 8850535. [CrossRef]
38. Ahmad, W.; Ahmad, A.; Ostrowski, K.A.; Aslam, F.; Joyklad, P.; Zajdel, P. Application of advanced machine learning approaches to predict the compressive strength of concrete containing supplementary cementitious materials. *Materials* **2021**, *14*, 5762. [CrossRef] [PubMed]
39. Ahmad, A.; Ahmad, W.; Aslam, F.; Joyklad, P. Compressive strength prediction of fly ash-based geopolymer concrete via advanced machine learning techniques. *Case Stud. Constr. Mater.* **2021**, *16*, e00840. [CrossRef]
40. Lundberg, S.M.; Erion, G.; Chen, H.; DeGrave, A.; Prutkin, J.M.; Nair, B.; Katz, R.; Himmelfarb, J.; Bansal, N.; Lee, S.-I. From local explanations to global understanding with explainable AI for trees. *Nat. Mach. Intell.* **2020**, *2*, 56–67. [CrossRef]
41. Lundberg, S. *A Game Theoretic Approach to Explain the Output of Any Machine Learning Model*; Github: San Francisco, CA, USA, 2021.
42. Molnar, C. *Interpretable Machine Learning*; Leanpub: Victoria, BC, Canada, 2020.
43. Lundberg, S.M.; Lee, S.-I. A unified approach to interpreting model predictions. In Proceedings of the Advances in Neural Information Processing Systems 30: Annual Conference on Neural Information Processing Systems 2017, Long Beach, CA, USA, 4–9 December 2017; Volume 30.
44. Shen, Z.; Deifalla, A.F.; Kamiński, P.; Dyczko, A. Compressive Strength Evaluation of Ultra-High-Strength Concrete by Machine Learning. *Materials* **2022**, *15*, 3523. [CrossRef] [PubMed]
45. Soulioti, D.; Barkoula, N.; Paipetis, A.; Matikas, T. Effects of fibre geometry and volume fraction on the flexural behaviour of steel-fibre reinforced concrete. *Strain* **2011**, *47*, e535–e541. [CrossRef]
46. Yoo, D.-Y.; Yoon, Y.-S.; Banthia, N. Flexural response of steel-fiber-reinforced concrete beams: Effects of strength, fiber content, and strain-rate. *Cem. Concr. Compos.* **2015**, *64*, 84–92. [CrossRef]
47. Lee, J.-H.; Cho, B.; Choi, E. Flexural capacity of fiber reinforced concrete with a consideration of concrete strength and fiber content. *Constr. Build. Mater.* **2017**, *138*, 222–231. [CrossRef]
48. Köksal, F.; Altun, F.; Yiğit, İ.; Şahin, Y. Combined effect of silica fume and steel fiber on the mechanical properties of high strength concretes. *Constr. Build. Mater.* **2008**, *22*, 1874–1880. [CrossRef]
49. Yoon, E.-S.; Park, S.-B. An experimental study on the mechanical properties and long-term deformations of high-strength steel fiber reinforced concrete. *KSCE J. Civ. Environ. Eng. Res.* **2006**, *26*, 401–409.
50. Abbass, W.; Khan, M.I.; Mourad, S. Evaluation of mechanical properties of steel fiber reinforced concrete with different strengths of concrete. *Constr. Build. Mater.* **2018**, *168*, 556–569. [CrossRef]
51. Yoo, D.-Y.; Yoon, Y.-S.; Banthia, N. Predicting the post-cracking behavior of normal-and high-strength steel-fiber-reinforced concrete beams. *Constr. Build. Mater.* **2015**, *93*, 477–485. [CrossRef]
52. Lee, H.-H.; Lee, H.-J. Characteristic strength and deformation of SFRC considering steel fiber factor and volume fraction. *J. Korea Concr. Inst.* **2004**, *16*, 759–766. [CrossRef]
53. Oh, Y.-H. Evaluation of flexural strength for normal and high strength concrete with hooked steel fibers. *J. Korea Concr. Inst.* **2008**, *20*, 531–539.
54. Song, P.; Hwang, S. Mechanical properties of high-strength steel fiber-reinforced concrete. *Constr. Build. Mater.* **2004**, *18*, 669–673. [CrossRef]
55. Jang, S.-J.; Yun, H.-D. Combined effects of steel fiber and coarse aggregate size on the compressive and flexural toughness of high-strength concrete. *Compos. Struct.* **2018**, *185*, 203–211. [CrossRef]
56. Dinh, N.H.; Park, S.-H.; Choi, K.-K. Effect of dispersed micro-fibers on tensile behavior of uncoated carbon textile-reinforced cementitious mortar after high-temperature exposure. *Cem. Concr. Compos.* **2021**, *118*, 103949. [CrossRef]
57. Thomas, J.; Ramaswamy, A. Mechanical properties of steel fiber-reinforced concrete. *J. Mater. Civ. Eng.* **2007**, *19*, 385–392. [CrossRef]

58. Sivakumar, A.; Santhanam, M. Mechanical properties of high strength concrete reinforced with metallic and non-metallic fibres. *Cem. Concr. Compos.* **2007**, *29*, 603–608. [CrossRef]
59. Afroughsabet, V.; Ozbakkaloglu, T. Mechanical and durability properties of high-strength concrete containing steel and polypropylene fibers. *Constr. Build. Mater.* **2015**, *94*, 73–82. [CrossRef]
60. Atiş, C.D.; Karahan, O. Properties of steel fiber reinforced fly ash concrete. *Constr. Build. Mater.* **2009**, *23*, 392–399. [CrossRef]
61. Pedregosa, F.; Varoquaux, G.; Gramfort, A.; Michel, V.; Thirion, B.; Grisel, O.; Blondel, M.; Prettenhofer, P.; Weiss, R.; Dubourg, V. Scikit-learn: Machine learning in Python. *J. Mach. Learn. Res.* **2011**, *12*, 2825–2830.
62. Lundberg, S.M.; Erion, G.; Chen, H.; DeGrave, A.; Prutkin, J.M.; Nair, B.; Katz, R.; Himmelfarb, J.; Bansal, N.; Lee, S.-I. Explainable AI for trees: From local explanations to global understanding. *arXiv* **2019**, arXiv:1905.04610. [CrossRef] [PubMed]
63. Khan, M.; Lao, J.; Dai, J.-G. Comparative study of advanced computational techniques for estimating the compressive strength of UHPC. *J. Asian Concr. Fed.* **2022**, *8*, 51–68. [CrossRef]

materials

MDPI

Article

Predicting the Durability of Solid Fired Bricks Using NDT Electroacoustic Methods

Vojtěch Bartoň [1,*], Richard Dvořák [2], Petr Cikrle [1] and Jaroslav Šnédar [1]

[1] Institute of Building Testing, Faculty of Civil Engineering, Brno University of Technology, Veveří 331/95, 602 00 Brno, Czech Republic
[2] Institute of Physics, Faculty of Civil Engineering, Brno University of Technology, Veveří 331/95, 602 00 Brno, Czech Republic
* Correspondence: 176012@vutbr.cz

Abstract: Historical buildings and monuments are largely made of brickwork. These buildings form the historical and artistic character of cities, and how we look after them is a reflection of our society. When assessing ceramic products, great emphasis is placed on their mechanical properties, whilst their durability is often neglected. However, the durability or resistance to weathering of masonry elements is just as important as their mechanical properties. Therefore, this work deals with predicting the durability of solid-fired bricks before they are used when reconstructing monuments and historical buildings. Durability prediction is assessed by identifying defects in the material's internal structure. These faults may not be visible on the element's surface and are difficult to detect. For this purpose, non-destructive electroacoustic methods, such as the resonant pulse method or the ultrasonic pulse method, were used. Based on an analysis of the initial and residual mechanical properties after freezing cycles, four durability classes of solid-fired bricks were determined. This work aimed to find a way to predict the durability (lifetime) of an anonymous solid-fired brick, expressed in terms of the number of freeze cycles the brick would last, based on non-destructive measurements.

Keywords: solid fired brick; defects in the internal structure; non-destructive testing; resonant pulse method; material durability; machine learning

Citation: Bartoň, V.; Dvořák, R.; Cikrle, P.; Šnédar, J. Predicting the Durability of Solid Fired Bricks Using NDT Electroacoustic Methods. *Materials* **2022**, *15*, 5882. https://doi.org/10.3390/ma15175882

Academic Editor: Krzysztof Schabowicz

Received: 15 July 2022
Accepted: 22 August 2022
Published: 25 August 2022

Publisher's Note: MDPI stays neutral with regard to jurisdictional claims in published maps and institutional affiliations.

1. Introduction

Historical buildings and monuments are our real wealth. These buildings represent the foundation of our cultural heritage and are the most tangible legacy of our past. The management of monuments is a reflection of society's cultural advancement. An integral part of this reflection is not only the care of historical objects themselves but also the effort to find the most appropriate way to preserve them [1].

Building materials are often assessed primarily in terms of mechanical properties, such as compressive strength or flexural tensile strength [2,3]. In terms of the durability of masonry elements, the frost resistance test, or the ability of the material to withstand repeated freezing and thawing, may be specified [4]. However, these tests are usually destructive or semi-destructive, which is not desirable, especially in the case of monuments. The question of the brickwork's durability is still relegated to the background. However, the durability or the ability of the material to resist external influences (weathering, chemical corrosion, or salt crystallisation) is an equally important factor for a material such as solid-fired bricks. Especially when the brickwork is not protected from the weather by plaster or any other surface treatment. Such masonry forms the visual part of the buildings and is the most susceptible to weather damage. Despite the initial neglect of this issue, the durability of building materials has already been addressed by a number of authors. However, the attention of authors is often directed to the durability of concrete structures [5]. In the case of the authors' focus on the durability of masonry buildings, it is more of an attempt to extend the durability of structures by understanding the defects already

present in masonry buildings and the procedures for reconstruction (restoration) [6–8] or [9] but not the prevention of such defects. Other authors deal with the durability of solid-fired bricks (hereinafter SFB) and the effects that reduce durability; however, this is often a destructive way and the element cannot be subsequently used in historical construction [10,11]. Particularly beneficial to this research were the works of authors dealing with the issue of frost damage to porous materials, which gave a better picture of the effect of the internal structure on the durability of masonry elements [7,12–14].

The effort to understand the influences that reduce the durability of solid brick and the effort to find the most effective ways to renovate existing structures without major interventions is undoubtedly very beneficial. However, there is often a situation where such buildings cannot be reconstructed without replacing (substituting) individual wall elements. In this case, the question arises whether to reconstruct the elements with historical bricks or to use masonry elements made with modern technologies. Both approaches have their advantages and disadvantages.

The main advantage of using modern wall elements lies in the assumption of less variability in their mechanical properties (especially compressive strength or flexural strength), a uniform appearance as well as durability. It is possible to ensure a stable technological process during the commissioning of modern wall elements and adjust it if necessary. However, the emphasis in monuments is often on preserving the authenticity of the brickwork, which is often problematic when modern masonry elements are used (Figure 1a). The main advantage of reusing historic masonry elements (so-called "upcycling") is that the authenticity of the brickwork is preserved (Figure 1b).

(**a**) (**b**)

Figure 1. (**a**) Reconstruction of the Gothic castle in Malbork (Poland) with modern masonry elements, (**b**) Reconstruction of a baroque brick bridge near Mikulov (Czech Republic) with historical masonry elements.

In recent years, the issue of sustainable development has also increasingly come to the fore, and the use of historic wall elements takes on this approach. This is a more environmentally friendly method, as there is no need to produce new masonry elements and the waste from demolished brick buildings is minimised [15].

However, in the case of using historic solid bricks for reconstructing masonry buildings, it is necessary to take into account the great variability of individual elements. Even in the case of taking historic bricks from a single demolished building, the uniformity of the solid bricks is not guaranteed. This is particularly evident during the construction of larger buildings, i.e., masonry elements were supplied from several brickworks at once. It must also be assumed that these buildings have been reconstructed in the past and therefore contain masonry elements from different time periods; this issue has been addressed in the past by authors, e.g., [16]. For these reasons, it is quite difficult to obtain a sufficient quantity of bricks of similar appearance and properties, and it is particularly difficult to demonstrate the requisite quality. When upcycling historic bricks for heritage buildings, it is necessary to consider a number of factors that may affect their quality.

One of the basic factors is the material that was used to produce the historic wall elements. In particular, the type of clay used (ferruginous or loamy). However, it cannot be said that masonry elements made of the same material in the same brickworks will have identical properties or appearances. The quality of the bricks varied even within the same kiln, mainly depending on the bricks' location in the kiln (different firing temperatures). The firing temperature can significantly affect the mechanical properties, colour, dimensions or, for example, the absorption of the elements.

If the firing temperature is too high, the element usually has a darker firing colour (sometimes up to purple), higher compressive strength and significantly lower absorption. However, if the firing temperature is too high, shrinkage of the elements and deformation of edge flatness often occurs (Figure 2a). Conversely, at low firing temperatures, the element typically has a light brown (orange) firing colour, lower compressive strengths, and significantly higher absorption (Figure 2b). The marking of the elements "A5" and "12" is only to simplify the research.

(**a**) (**b**)

Figure 2. (**a**) historical solid brick—high firing temperature, (**b**) historical full brick—low firing temperature.

In terms of the durability of masonry elements, increased water absorption is the most challenging, as it is closely related to resistance to the effects of repeated freezing and thawing [17].

Another factor that significantly affects the durability of masonry elements is their defects. The defects in the elements may have already occurred during the production of the wall elements. Delamination of the individual layers can be mentioned as a defect already occurring during production. When using screw presses, this is a defect in the elements caused by the rotational movement of the mixture used or, in the case of handmade bricks, delamination caused by poor mixing of the clay mass. It mostly manifests only as a result of freezing cycles, when it takes the form of concentric spiral cracks along which the brick gradually crumbles. This type of defect is not only typical of historic bricks but also occurs in abundance in newly manufactured solid-fired bricks.

Other defects in the wall elements may arise due to their history. In particular, when repeated freezing and thawing has caused cracks, chips or microstructural damage to the elements. The main indicator may be the location of the bricks in the past. If the element has been exposed to climatic influences for many years, it can be expected that these defects will occur more frequently. In addition to damage caused by climatic influences acting on the elements, mechanical damage (breaking off of a corner, etc.) may also occur.

When assessing the extent of defects in individual elements, it is important to note that a large proportion of defects are not visible on the surface of the elements. These defects in the internal structure of the elements significantly reduce their durability. These defects are usually caused by increased humidity, when water freezes in winter and increases its volume, causing stresses in the elements. The development of defects in the internal structure need not be linked to the development of defects visible on the surface. The authors of the paper have dealt with this issue in the past. In the framework of [18] 3 types of defect development have been defined:

1. Both surface defects and defects in the internal structure of the element develop;

2. only surface defects develop; the development of defects in the internal structure is negligible;
3. the development of surface defects is indistinct; only defects in the internal structure develop.

The most problematic of the above types of pattern damage is the third case. This is because, in this case, only the internal structure is damaged without damaging the surface of the test sample (Figure 3). Visually, the element may appear free of defects even after a number of freeze cycles, but defects in the internal structure significantly reduce both the mechanical properties of the elements and their durability.

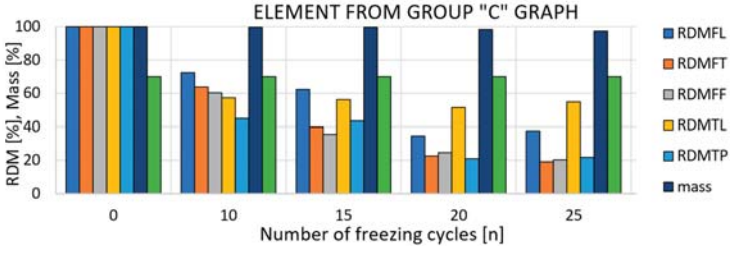

Figure 3. Example of a solid-fired brick of type 3 damage [18].

The reconstruction of monuments with historic solid bricks can therefore be a challenging discipline, particularly because of the great variability and difficulty in monitoring the quality of the elements. Due to the great variety of historical masonry elements, their quality cannot be guaranteed based on standard tests (on 5 or 10 bricks). For this reason, non-destructive methods are proposed that allow many more bricks to be tested, and these can subsequently be incorporated into the structure.

For these reasons, completely non-destructive electroacoustic methods, namely the resonance method and the ultrasonic method, were chosen to predict the masonry elements' durability or resistance to weather conditions (mainly repeated freezing and thawing). Based on the identification of defects in the internal structure of the elements, a total of 4 durability classes were determined with the recommended use of the wall elements. The individual methods and procedures were chosen so they can be applied in practice while ensuring the highest possible reliability. The problem of detecting defects in materials by electroacoustic methods has been addressed in the past by a number of authors, e.g., [5], but here the problem of detecting defects in the material caused by loading (mechanical failure) is addressed.

This work presents an innovative way of using non-destructive resonance and ultrasound methods. Non-destructive methods are commonly used in civil engineering today. However, these methods are mainly focused on mechanical properties. These electroacoustic methods are also used for a kind of identification of defects in the internal structure. However, they are generally applied to concrete structures and there are no clearly defined parameters for detecting defects in the internal structure. This paper deals not only with the actual use of these methods but also with the definition of the parameters that can be used to detect these defects (obtained from the spectrum of natural frequencies) and to predict the durability of the material based on them. Prediction of durability was determined by statistical analysis of a series of experimental measurements. Currently, the method used in-situ is testing fired solid bricks by impacting them with a steel hammer. The evaluation of the quality (durability) of the elements depends only on the individual judgement of the worker based on the acoustic response. Thus, the proposed method is a significant improvement, where a human factor is reduced, and a classification model and algorithm of machine learning are being used.

2. Materials and Methods

This work aims to determine the durability criteria of historic, solid-fired bricks before they are used when reconstructing monuments and historic buildings. The elements must

not be damaged in any way after their durability has been assessed so that they can be incorporated into the structure. For this reason, completely non-destructive electroacoustic methods, such as the resonance method and the ultrasonic pulse method, were used. A balance had to be struck between the complexity of the criteria to be assessed and the greatest possible accuracy of the results. The durability of the masonry elements is assessed by identifying defects in their internal structure. To identify these defects, spectra of the first natural frequencies determined by the resonance method were analysed.

Every rigid material is subject to vibration due to an external impulse. The phenomenon, when the frequency of this introduced impulse is identical to the natural frequency of the element, is called resonance. This phenomenon is exploited by the resonant pulse method. The undeniable advantage of this method is that, in addition to the first natural frequencies, it was possible to record the entire spectrum of frequencies in the chosen range. This fact has been used in this work, where the defects in the internal structure of the elements are identified by analysing the spectrum of the first natural frequencies and then the durability of the masonry elements is predicted. There are countless types of vibrations that can be induced in rigid bodies. As a rule, however, three types of these oscillations are used, namely:

- first natural frequency of longitudinal oscillation—f_L,
- first natural frequency of the torsional oscillation—f_T,
- first natural frequency of transverse oscillation—f_F [19].

In this study, only the first two types of oscillations (longitudinal and torsional) were used. The defects in the internal structure of the elements that appear during transverse vibrations are also largely reflected in the frequency spectrum of the torsional vibrations. An example of determining the first natural frequencies is shown in Figure 4a. A figure of the location of the exciter (hammer strike) and a sensor for each type of oscillation are shown in Figure 4b. Handyscope HS3 (oscilloscope) with a piezoceramic sensor was used to determine the natural frequencies of the test elements.

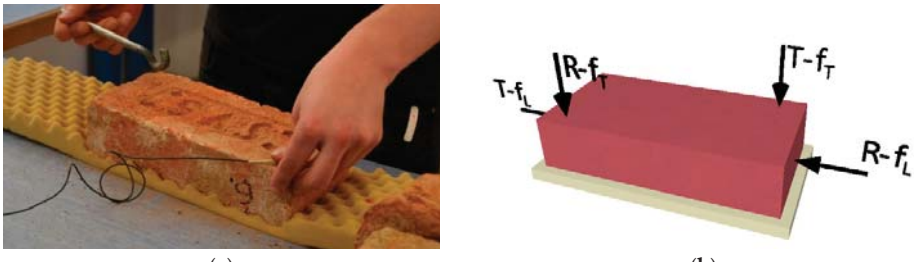

(**a**) (**b**)

Figure 4. (**a**) Example of measuring the first natural frequencies of torsional vibration (f_T), (**b**) Arrangement of sensors ("R") and exciters ("T") for longitudinal (f_L) and torsional (f_T) oscillations.

Another method for detecting defects in the internal structure of the elements was the ultrasonic pulse method, specifically the pundit PL-200 from Screening Eagle (formerly Proceq). The principle of the ultrasonic pulse method is based on the mechanical wave of particles through the environment. In practice, the ultrasonic pulse method is used mainly for determining the uniformity of concrete structures and determining the deformation properties of the material, and, to a lesser extent, for determining the compressive strength of concrete structures. This method can also be used to detect defects in the internal structure [20]. For the purpose of this study, the passage times of the direct sounding in the transverse (T_T) and longitudinal (T_L) directions of the element were measured in three lines (Figure 5a). An example of ultrasonic wave transit times is shown in Figure 5b.

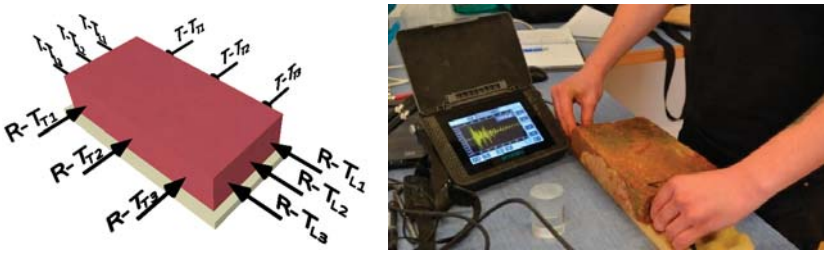

(**a**) (**b**)

Figure 5. (**a**) Positioning of the transducer ("R") and exciter ("T") to determine the transit times in the longitudinal (TL) and transverse (TT) directions (always in 3 lines), (**b**) Example of a longitudinal travel time (TL) measurement.

Prior to conducting laboratory tests to determine the durability criteria for historic solid brick, the applicability of the above methods was verified directly during the reconstruction of a historic brick building. The authors aimed to set the durability criteria for solid bricks so that the durability could be evaluated on-site, if necessary. The authors had a unique opportunity to test the methods on a baroque brick bridge near the village of Mikulov (close to the Czech-Austrian border). This brick bridge is unique for several reasons. Most of the preserved bridges from this period are made of stone masonry. In the case of this bridge, stone masonry was used only at the foot of the piers; the rest of the bridge is made of brickwork. Another unique feature of this bridge is its length; this fifteen-arch bridge is 100 m long. The bridge had been in disrepair for many years, was overgrown with grass and covered with mud deposits. The hope of saving the bridge was raised in 2016 when the project for its restoration began. The reconstruction of the bridge started in 2018 and took 2 years. For its reconstruction, it was decided to "upcycle" the historic wall elements [21,22]. The opening ceremony of the bridge took place in October 2020 and the reconstruction was awarded "Monument of the Year" of the Czech Republic in 2021.

During the reconstruction of the bridge, a series of measurements on the historic in-situ fired bricks were made using the resonance method and the ultrasonic pulse method. Based on these measurements and basic assumptions, wall elements of low quality and wall elements with assumptions for very good quality and durability were selected.

The selected elements were then subjected to a freeze resistance test in the laboratory and then the mechanical properties of the elements were determined. Laboratory tests (determination of frost resistance, flexural tensile strength and compressive strength) confirmed the initial estimates of durability and the quality of the masonry elements made by in-situ non-destructive methods. These results have been published in [23].

The ultrasonic pulse method used during the reconstruction of the bridge did not yield significant results, whereas the resonant pulse method proved to be very promising.

Once the applicability of the in-situ methods had been verified during the reconstruction of the heritage building, the main work to establish the durability criteria for historic solid bricks could begin. The experiment itself is inherently simple. The principle of determining the durability criteria is based on an analysis of the spectrum of the first natural frequencies and their change in the saturated state compared to the dried state. However, a relatively large number of test samples was required. Thus, a total of 41 historic bricks were selected. The test specimens were taken from various demolished buildings over a period of about three years, varying in age (from the Gothic, Baroque and Renaissance periods), size, appearance and expected quality, so that the whole range of test bodies was covered. The test elements were first thoroughly cleaned, and their dimensions were determined. They were subsequently dried to a steady state weight, i.e., a condition where their weight did not change by more than 0.2% during 24 h of drying at 105 °C. For all samples, their dry weights were determined, and any surface defects of the elements were carefully recorded.

The first natural frequencies of the longitudinal $f_{L,V0}$ and torsional $f_{T,V0}$ oscillations were determined using the resonant pulse method. Subsequently, the elements were completely saturated with water. The elements were immersed in distilled water so that they did not touch. The water was then brought to a boil, which was maintained for a further 5 h. The elements were left in the water for a further 16 h; this post corresponds to [24]. In the fully saturated state, the mass and first natural frequencies of the elements were again determined using the resonance method $f_{L,NV0}$ in the longitudinal direction and $f_{T,NV0}$ in the transverse direction.

The masonry elements were divided into a total of 4 durability classes depending on the number of freezing cycles the bricks could withstand. One F-T cycle consists of 16 h of freezing (at −20 °C) and 2 h of thawing in water (at 15 ÷ 30 °C) in an automatic freezer [4]. At the same time, the possible use of elements from each group was defined:

- 1st class—bricks usable in exposed outdoor environments (uncovered ledges, places above ground with rising damp, etc.
- 2nd class—bricks usable in outdoor environments, less exposed areas (e.g., vertical surface masonry except for plinths, masonry infill) or in indoor exposed areas (e.g., wine cellars)
- 3rd class—bricks usable only indoors, in a dry environment
- 4th class—bricks not suitable for reuse.

Input measurements taken prior to the freezing cycles were used to develop the shelf-life prediction model. For the evaluation of the frequency spectra from the resonance method, a feature extraction method was used to obtain the key characteristic parameters of the spectra under consideration. This method is commonly used during the dimensionality reduction of large datasets [25] and is widely used in the prediction of the lifetime of structures in both civil and mechanical engineering. Thus, in addition to the dominant resonant frequency, other parameters such as amplitude, peak width at mid-peak prominence, and peak prominence were extracted from all spectra. From each spectrum, the following parameters of the first three dominant peaks were selected in descending order of prominence. An example of these characteristics is shown in Figure 6 shows the recorded signal.

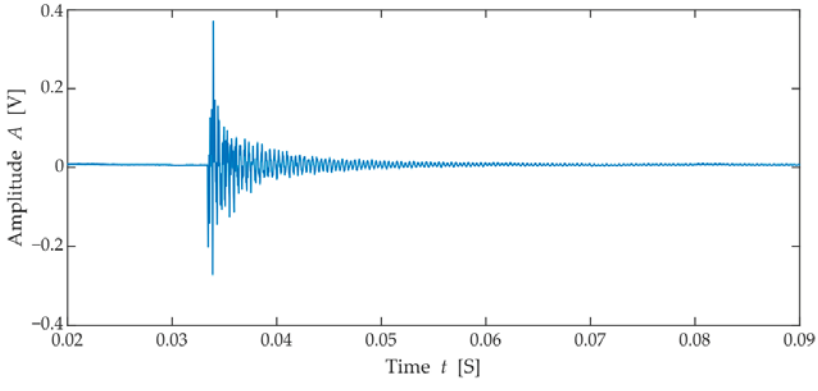

Figure 6. Illustration of acoustic resonance signal: Signal in the time domain.

Figure 7 shows the frequency spectrum with the peaks and their characteristics highlighted.

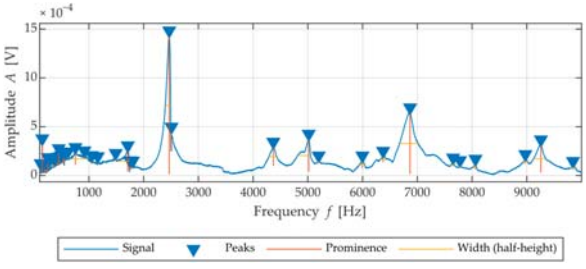

Figure 7. Illustration of acoustic resonance signal: Extracted frequency spectrum with highlighted peaks with various parameters such as frequency, amplitude, width and prominence.

A similar approach in the evaluation of the resonance method can be found in the foreign literature, e.g., [26,27]. The character of the spectrum and the shape of each peak are clearly defined by the metric mentioned above; however, in practice, it is often the case that the technicians performing an inspection using resonance methods use their subjective experience to select a particular peak. In this case, the shape of the peak is assessed by the technician's feelings. Thus, an experienced diagnostician can assess whether the chosen peak matches their experience and notion of a dominant peak. This experience is particularly important when considering highly degraded test bodies where the dominant frequency may not be the one with the highest amplitude. In this case, it is an impetus to identify another metric that would be able to simulate this human factor experience and, in this area, it is advantageous to use a combination of a multi-criteria evaluation algorithm combined with a machine learning model.

The multi-criteria scoring algorithm can assign a score value to a given observation based on the selected weights. The algorithm itself was first published by Saaty [28]. The method was first published in 2021 [29] in the form of using this tool to evaluate frequency peaks. If the evaluated parameters are close to the desired value, the value of the score will be higher. To use this method successfully, the weights of the monitored parameters need to be set. In this case, the weights and setpoints are based on the experience of the technicians and are shown in Table 1.

Table 1. Weights set for scoring frequency peaks (A-amplitude, F-frequency, P-prominence, W-width).

Param.	A	F	W	P	Demand
A	1.0	5.0	1.0	0.2	Max
F	0.2	1.0	0.2	0.1	Max
W	3.0	5.0	1.0	0.3	Min
P	5.0	10.0	3.0	1.0	Max

From these scales, it can be seen that, for example, the value of prominence should reach a maximum value and is more important than amplitude, frequency or width. Conversely, the width of the peak should be as low as possible and is more important than the height of the amplitude or frequency. The frequency value is not very important in this evaluation because different test bodies may have different resonant frequencies depending on their shape, material and internal structure. For the purpose of processing, the natural frequency of the observed peaks was expressed by the relation:

$$f_{RL,RT} = \left| \frac{f_i}{f_{mT,mL}} - 1 \right| \quad (1)$$

where:

- $f_{RL,RT}$ is the frequency ratio [%],
- f_i is the frequency of the dominant peak [Hz],

- $f_{mT,mL}$ is the average frequency in a given test direction (f_{mt} = 2000 Hz, f_{ml} = 4300 Hz).

The average frequencies in a given test direction (f_{mT} and f_{mL}) were determined according to masonry elements without defects in the internal structure—durability class 1 (Figure 8).

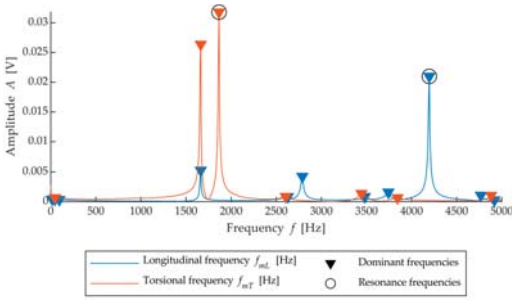

Figure 8. The frequency spectrum of a masonry element without defects in the internal structure.

The variable used for classifying the bricks is, therefore, the relative deviation of the frequency from the specified average SFB frequency in a given testing direction. The resulting value for $f_{RL,RT}$, thus expresses how much a given brick differs in frequency from the average of all observed bricks.

In addition to the aforementioned metrics of the first three peaks, score values were added. The findpeaks function was used to select peaks with parameters of a minimum prominence value of 0.03% of the maximum amplitude of the spectrum and a minimum distance between adjacent peaks of 20 Hz. In this way, 100 peaks from each spectrum were separated. Statistical parameters such as mean, standard deviation, peak-to-peak and skewness were then calculated from these peaks. In this way, a total of 20 parameters were obtained from each measured spectrum in the longitudinal and transverse directions in the fully saturated and fully dried state. The frequency parameters were further supplemented by the A-absorption, which was measured at the beginning of the freezing cycles.

To predict the assigned class, the classification toolbox within Matlab software was used. So, specifically, in this case, it is supervised machine learning where there is a set of observations, x, and their classes are known, y. This set is then divided into a learning set and a test set. For large datasets, this split can be performed by random permutation in the ratio of 75:25. Furthermore, a cross-validation algorithm with transfer can be used for this partitioning. The input dataset is divided into subsets. One subset serves as a test set; the remaining subsets serve as training sets. The classifier trains the model on the training set and uses the test set to test the accuracy and performance of the model. This process is repeated several times, each time with a different subset forming the training and test set. In this paper, cross-validation with a transfer of 5 was used. According to the chosen procedure of extracting the features and creating a classification model, it was possible to determine the reliability of the whole methodology in predicting the probable durability (lifetime) of the test set of measured bricks.

To verify the correct identification of defects in the internal structure of the elements and their durability (resistance to repeated freezing and thawing) by non-destructive methods, a destructive frost resistance test was performed. Test elements in the saturated state were cyclically frozen and thawed. One freezing cycle consisted of 16 h of freezing at −20 °C followed by thawing in water for a minimum of 2 h at +20 °C [4]. The resulting number of freeze cycles for each test sample was then recorded.

During the main experiment, sub-factors that affect the durability of the wall elements were also investigated to understand this issue more comprehensively. For example, the effect of humidity on the first natural frequencies and transit times of ultrasonic waves was investigated. The finding of this sub-work was to determine the parabolic dependence

of the quantities determined by non-destructive methods on the moisture content of the elements. In many papers, a linear dependence is assumed, but in this case, significant errors can be made. Results from this sub-experiment were published in [30]. Another sub-research was to monitor the changes in first natural frequencies and transit times as a function of the number of freeze cycles. In the framework of this work, three possible types of sample defects were determined [18].

3. Results

From initial measurements made on site, it was found that the transit time of ultrasonic waves could not be used as a satisfactory metric for assessing likely durability (resistance to freezing cycles). Figure 9 shows the relationship between the resonant frequency and the velocity of longitudinal ultrasonic waves (p-wave) measured per length of brick in the dried state. The colour shows the number of cycles that each brick lasted before destruction. A dominant diagonal can be observed in the data, which confirms that these observed parameters are correlated; however, in terms of the distribution of bricks that have lasted 25 cycles or more, there is significant mixing with bricks that have already disintegrated after 5–10 cycles. At the same time, a non-negligible number of dependencies can be observed that lie outside the main diagonal, which could be called anomalies. Looking at a similar dependence of water absorption on ultrasound velocity in Figure 10, it can be seen that the average ultrasound velocity lies in the range of 1600–3000 m^{-s-1} and the bricks are mixed throughout the observed range of freezing cycles.

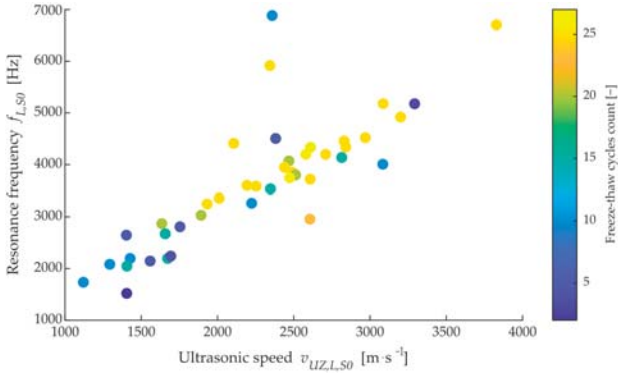

Figure 9. Dependency between longitudinal resonance frequency on ultrasonic velocity (p-wave) in longitudinal axis also in a dried state.

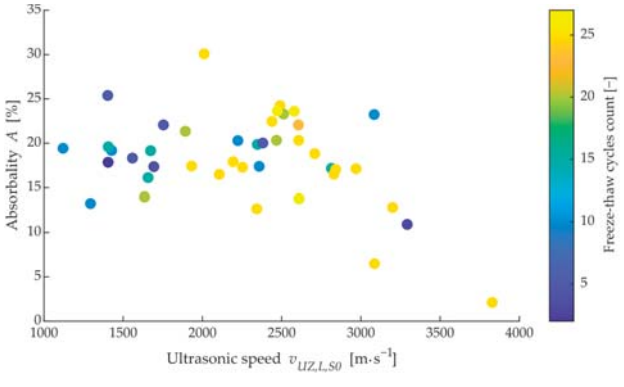

Figure 10. Dependency between water absorbance on ultrasonic velocity (p-wave) in longitudinal axis also in a dried state.

On the other hand, the majority of the measured bricks had a value of absorption A ranging from 12–24%, with an insignificant correlation with ultrasonic velocity, as shown in Figure 11. For the same value of water absorption, there is a brick with both the highest and the lowest durability (lifetime) expressed in the number of freeze cycles. Thus, it can be concluded that the probable lifetime of the brick under consideration cannot be reliably predicted from common parameters such as dominant frequency, ultrasonic velocity, or absorption rate.

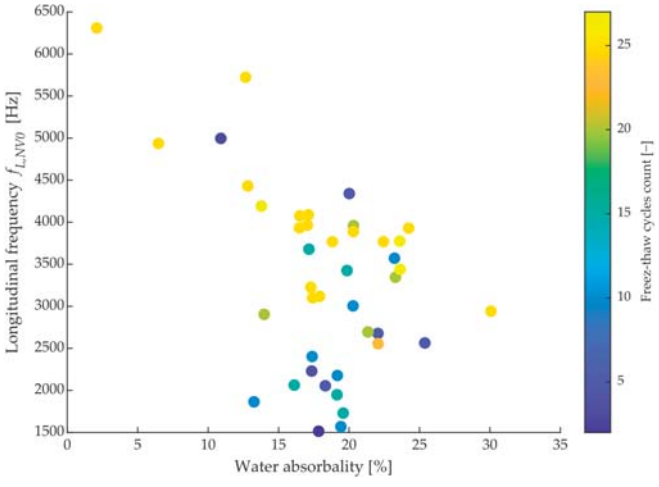

Figure 11. Dependency of longitudinal frequency in the saturated state on measured water absorbability with highlighted freeze-thaw cycles, which each brick endured up to destruction.

Bricks were divided into different classes based on their durability interpreted by a count of F-T cycles, which the bricks withstand in the automatic freezer at set conditions described in Section 2 Materials and Methods. Each class is shown in Figure 12.

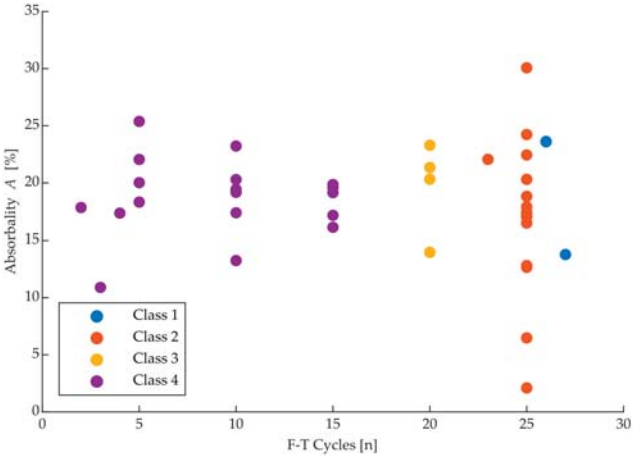

Figure 12. Comparison of a number of F-T cycles and absorbability of bricks with their set classes.

Moving on to the results of the feature extraction algorithm, the application of the multicriteria method to the frequency spectrum peaks will be first up. Statistical comparison in terms of probability of the observed parameters' frequency, peak width amplitude, peak prominence and the corresponding score is shown in Figure 13. This is a total of

4136 observed peaks, which were selected by the findpeaks function from 167 frequency spectra of all 41 measured bricks.

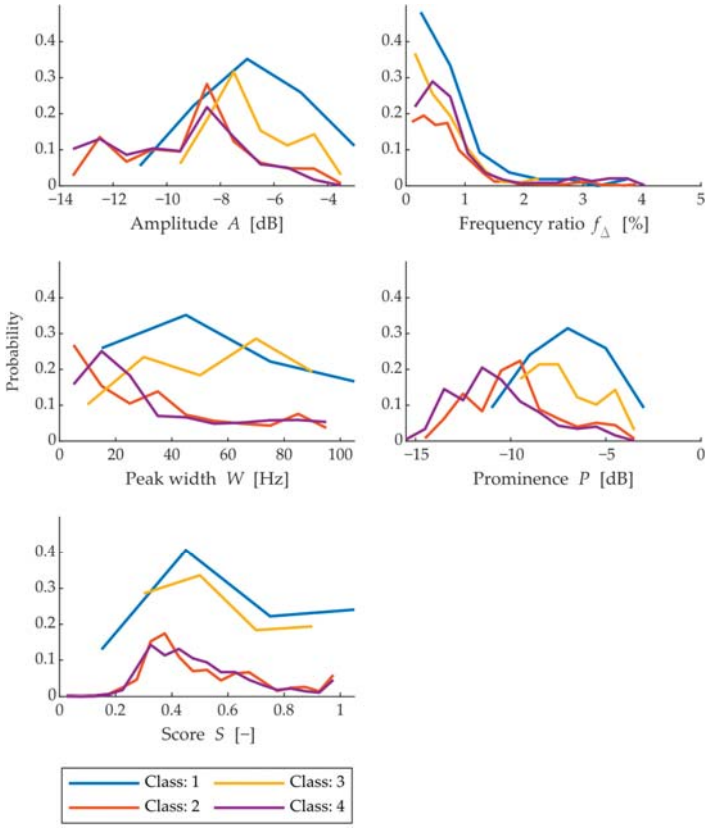

Figure 13. Histogram of peak parameters across all measured frequency spectrums (for peaks with width < 100 Hz).

The amplitude is spaced between −9 and −6 dB. Classes with a higher freeze cycle life generally have higher amplitude, and conversely, classes with lower life have lower amplitude values. However, it is in the middle of the histogram that these parameters overlap. The same is true for the frequency ratio f_R. Perhaps the biggest difference occurs in the case of peak prominence, where each class's peak probability represents a different part of the prominence variance from −4 to −15 dB. Although the classes were designed according to the increasing number of cycles, the order exhibited by the prominence value shows that class 1 is very similar to class 3 and class 4 is very similar to class 2. From this perspective, it can be said that this is the effect of a smaller statistical sample of bricks that would otherwise show a lower prominence value with a higher class.

For a spatial, graphic representation of these quantities, see Figure 14. There are three main point clouds A, B and the largest one C. Clouds A and B are clearly separated by a gap due to the score value, and if only these points were used, there would be relatively high confidence in classifying the bricks. Clouds A and B consist exclusively of classes 2 and 4, which, moreover, supports the previous finding that classes 2 and 4 are very similar. However, these clouds reach a maximum peak width of 13 Hz, which is especially true for extremely narrow and small peaks. In contrast, the peaks located in cloud C are interpenetrating and composed of all the remaining measured peaks, and all classes

are equally represented. Thus, this observation invites the possibility of a multi-stage assessment for the presence of peaks from Cloud A and Cloud B, and then, if peaks from these clouds were not found, a more detailed method would need to be applied.

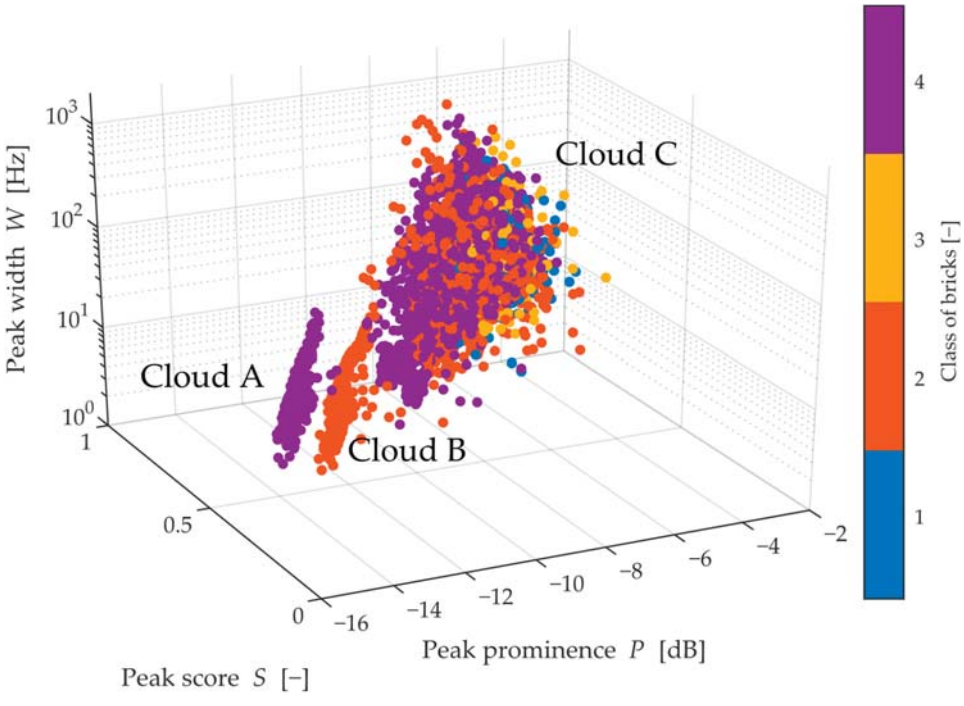

Figure 14. Distribution of peak metrics with a comparison with classes and score of individual peaks.

A more detailed assessment is focused on obtaining the selected 20 parameters and building a classification model based on the principle of an ensemble of classifiers [31]. The statistical comparison of selected parameters is shown in Figure 15.

In the total number of selected parameters, variants such as Freq1, Freq2, etc., are present; in this case, these are the parameters of the dominant peaks in descending order of prominence. The parameters Freq1 or Width1 describe the same peak but in different ways. The statistical parameters are:

- The Kurt and Skew parameters describe the tailedness and skewness of the score distribution of selected peaks from each assessed spectrum,
- MeanScore expresses the average score of the peaks,
- ModeWidth describes the modus of the peak width,
- StdScore expresses the standard deviation of the selected peaks,
- TotalScore expresses the total sum of the scores of the selected peaks.

Figure 15 shows dependencies that are difficult for humans to understand, and even using correlation diagrams they are not a good tool for interpreting this type of data. Since this is multidimensional data, which has a total of 18 dimensions, it is appropriate to assess the individual dependencies using the success of the classification model and the resulting decision diagram. To understand more about the dependence between the parameters, this must be done, in part, by expressing the dependence between the chosen parameters Freq1 and the absorbance and standard deviation of the peak scores. For an example of such a representation, see Figure 16.

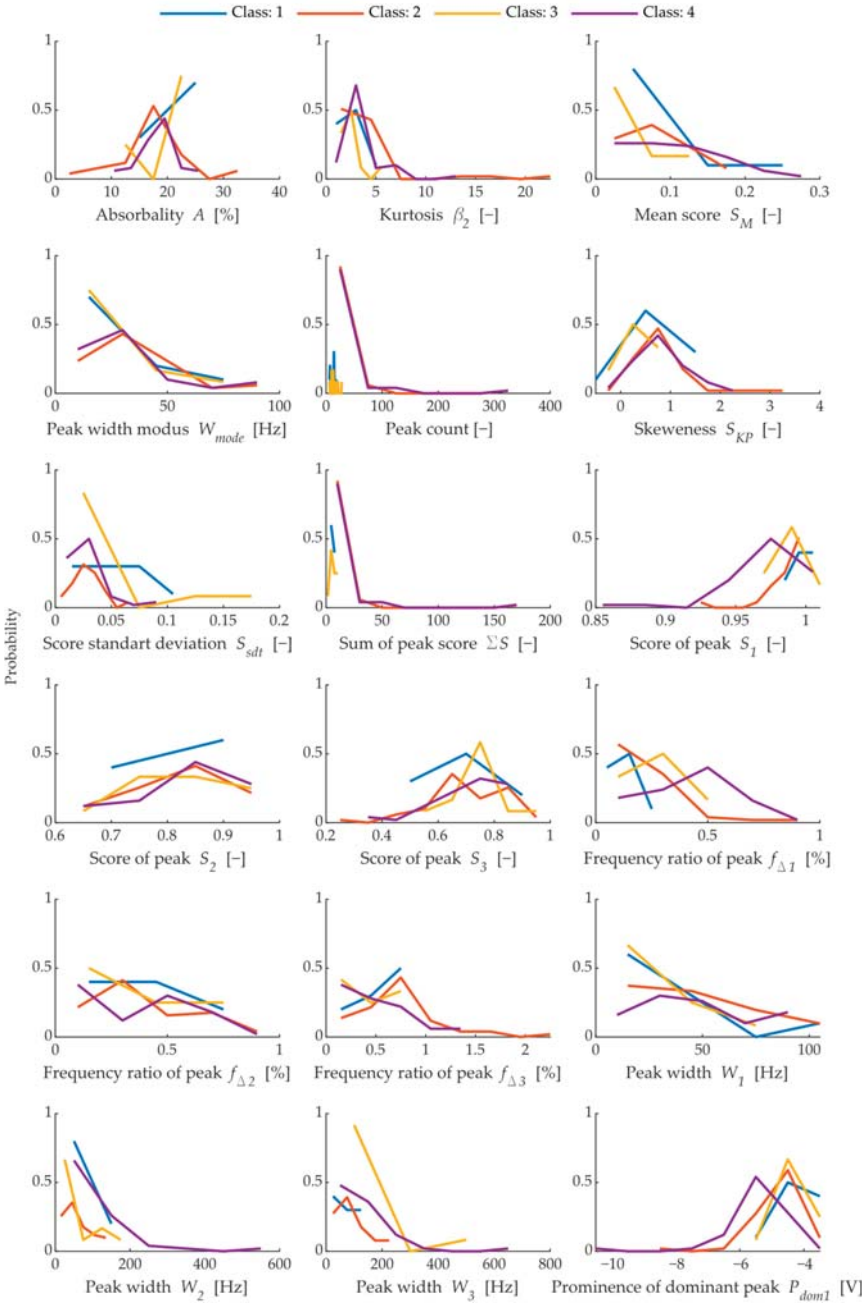

Figure 15. Comparison of all extracted features from the frequency spectrums and properties of fired bricks (absorbability).

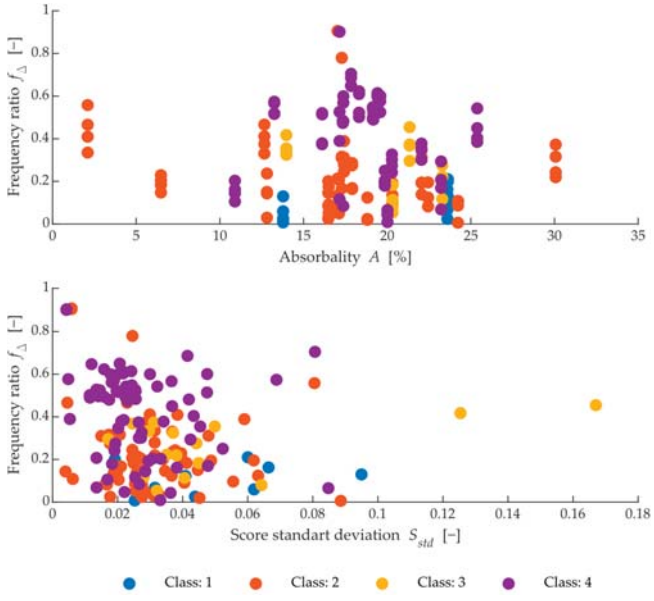

Figure 16. Comparison of absorbability, mean score value (**upper**), prominence of dominant peak and skewness (**bottom**).

These plots in Figure 15 illustrate the probability of each observed variable within the total range of the variable, where classes $1 \div 4$ are represented by different colours. In some parameters, the probability is very similar among all classes, such as the Frequency ratio of the second highest peak $f_{\Delta 2}$. Parameters such as Sum of peak score ΣS and peak count shows a significant difference in probability between class 1, 3 and 2, 4. From all of these parameters, the most variance occurs in the first highest peak $f_{\Delta 1}$, the score of peak S_1 and the prominence of dominant peak $P_{dom}1$. The parameters with the highest variance are the most suitable for classification model generation.

It is evident that approximately 60% of the bricks, which have the highest class and, therefore, can withstand the least number of cycles, cluster around one centre in both cases. The rest of the observations of this class are spread evenly among the other points of classes 1, 2 and 3.

It is similar in the case of the ratio between the frequency ratio and the standard deviation of the frequency peaks. Here it can be seen that class 1 achieves the lowest frequency ratio value, which means that its dominant frequency is closest to the average SFB frequency (f_{mt} = 2000 Hz, f_{ml} = 4300 Hz). At the same time, Class 2 and Class 3 observations and some Class 4 observations are also located in this area.

Thus, from this perspective, it can be shown that it is not possible to successfully classify SFB by classical methods and evaluation because it involves the complex behaviour of several different parameters. Thus, if this classification task is carried out by the algorithm mentioned in [31], it gives a decision as to how and in which situation the proposed classification model is to be used.

Using only a classification model with the ability to distinguish between class 2 and class 4, a fairly satisfactory reliability of 88% for class 2 and 72% for class 4 is obtained. Parameters include the resonant frequency in the fully saturated and dried state, the number of peaks, the difference between the frequency in the fully saturated and dried state, the number of peaks, the width and Poisson's ratio, and the absorbance were used for this model. Model 1 is illustrated using the confusion matrix in Figure 17.

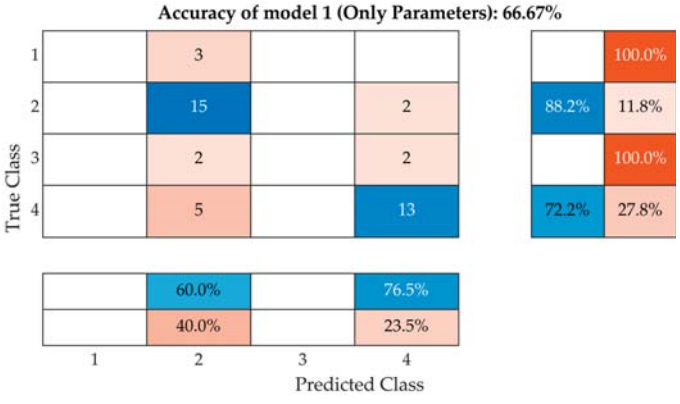

Figure 17. A model with parameters extracted from f_L without statistical parameters and score values.

The resulting model success rate corresponds to the results in Figure 14 and indicates that the two classes are close but can be successfully recognised. From a practical point of view, however, this procedure requires knowledge of absorption rate A, which requires the selected brick to be fully saturated with water and then dried to a stable weight. This procedure is time-consuming and cannot be carried out on bricks that are already in place.

If the parameters described in Figure 15 are used without including the absorption, it results in 25% for class 1, 56% for class 2 and 69% for class 4. The success of Model 2 is shown in Figure 18. In this case, it turns out that both classes 2 and 4 are very close to each other. However, in this case, there is a misclassification of Class 2 bricks into Class 1, 3 and 4 and a misclassification of Class 4 bricks into Class 1, 2 and 3. From this point of view, the model can be used on embedded bricks but has very little reliability.

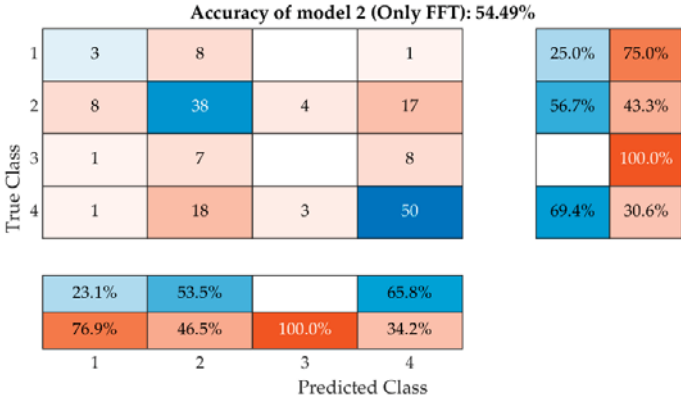

Figure 18. A model with only FFT parameters is known without absorbability.

The last and the most successful model (Figure 19), number 3, uses the parameters used for model 2, enriched with the knowledge of absorbance A, with an overall success rate of 85%. From this perspective, it is the most accurate model so far, achieving 83% accuracy for Class 1, 88% for Class 2, 75% for Class 3 and 86% for Class 4. The model was used from observations of the frequency spectra of both the saturated state and the dried state in both longitudinal and torsional directions. From this point of view, it does not matter whether it is used on a dried or saturated sample.

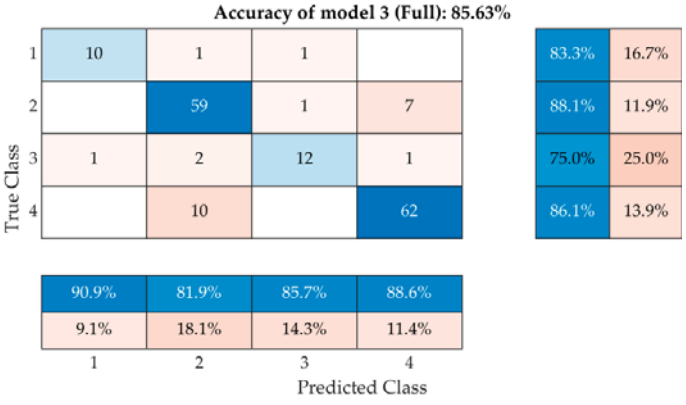

Figure 19. Confusion matrix of the most effective model with all known parameters.

The resulting decision tree for classification is shown in Figure 20. The decision tree is a graph that uses structure of nodes, branches and leaves. Each node is made by binary condition which leads to either a node or a leaf. In this setup a leaf is predicted class. Each node is formed by assessed features. The presented decision tree in Figure 20 was generated by machine learning algorithm, and so are the values of binary condition for each node. This tree clearly shows the importance of absorbance for classification; it is by far the most common parameter used by the model here. The second most common is the parameter Freq1 or the frequency ratio of the first peak. There are also statistical parameters such as kurtosis, skewness, number of peaks or average score of frequency peaks.

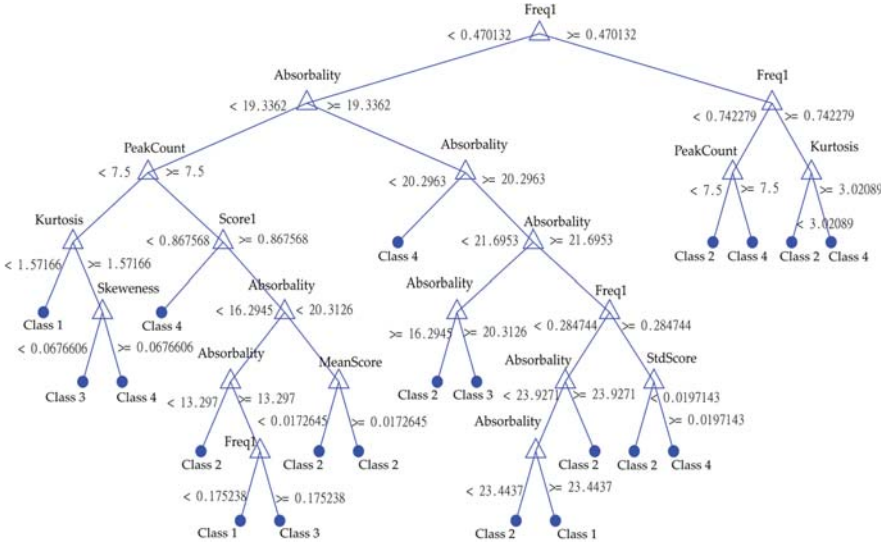

Figure 20. Example of the designed model's classification tree with parameters, conditions and resulting classes.

The analysis makes it possible to determine which state and type of resonance measurement are the most suitable for obtaining the highest classification accuracy for both model 2 and model 3. This comparison is shown in Table 2.

Table 2. Accuracy of model 3 in all combinations of dried or saturated specimens and testing by longitudinal or transverse waves.

Type of IE Testing	Model 2 Accuracy in Different Groups [%]		Model 3 Accuracy in Different Groups [%]	
	S0—Dried	NV0—Saturated	S0—Dried	NV0—Saturated
f_L—longitudinal	69.05	42.86	85.71	90.48
f_t—transverse	56.10	52.38	78.05	88.10

Comparing the success rate of the model, it can be seen that the saturated state in the longitudinal testing direction achieves a success rate of 90.48%. The lowest success rate is 78.05% for the dried state in the transverse testing direction. In the case of model 2, the longitudinal direction in the dry state achieves the highest success rate—69.05%—and the longitudinal direction in the saturated state has the lowest success rate—42.86%.

4. Discussion

For the possibility of "upcycling" historic bricks, for both new buildings and the renovation of historic buildings, it is crucial to choose a durable material that fulfils both a functional and an aesthetic role. The requirements for historic bricks reintegrated into the structure should be the same as for newly manufactured bricks. The results of this work have shown that by using a non-destructive resonance method and the known absorption of solid fired bricks, it is possible to predict their durability (service life) with relatively good accuracy, without failure. The classification tree (Figure 20) demonstrates that absorbability is a significant factor in evaluating the durability of solid-fired bricks. It is a non-linear characteristic that cannot be described by a simple correlation. In the case of the results obtained from the resonance method, a success rate of 85% (Figure 19) was achieved. The disadvantage of this model is the need to know the absorption of the masonry elements. Therefore, this model is difficult to implement in situ and is more suitable for laboratory testing. The ultrasonic pulse method used did not yield significant results already during the initial on-site testing of the methods. This assumption has also been confirmed by laboratory tests and thus, the method is not suitable for the purpose of this paper. The measurement of ultrasound wave propagating through the element provides fewer parameters than the resonance method, where a whole spectrum is a result, and we can observe many different metrics and features. The whole procedure was verified on a selected sample of 41 bricks, which, by their time, age and quality, cover a wide historical and material spectrum. Therefore, it can be stated with some confidence that, within the framework of this study, it is possible to propose a classification model that can predict the probable durability (service life) of a historic brick based on NDT measurements. To bring the method into practice, a similar algorithm will be converted into Python using the SciPy and NumPy libraries, which are commonly used for this type of task. At the same time, the learning dataset will be enlarged to cover more sources of brick measurements. In fact, there was an uneven qualitative representation of bricks in the tested set. Specifically, Class 2 and 4 were represented in greater numbers than Class 1 and 3. Therefore, more class 1 and 3 bricks need to be included so that the entire dataset becomes balanced. Thanks to the current level of microphones currently used in consumer electronic devices, which can be used for the recording of resonance signals of elements tested by the resonance method, we can assume that the proposed classification procedure and algorithm could be used by mobile devices, such as smart phones, or tablets.

Supplementary Materials: The following supporting information can be downloaded at: The following supporting information can be downloaded at: https://www.mdpi.com/article/10.3390/ma15175882/s1, Measured Data S1: data from the resonance method.

Author Contributions: Data curation, R.D.; Supervision, Writing—review & editing P.C.; Writing—original draft, V.B.; Writing—review & editing, J.Š. All authors have read and agreed to the published version of the manuscript.

Funding: This research was funded by Brno University of Technology, Faculty of Civil Engineering—Institute of Building Testing and Specific Research FAST-J-22-8036.

Data Availability Statement: Data supporting the reported results are included in the Supplementary Materials of this article. These are resonance measurement data in csv format.

Conflicts of Interest: The authors declare no conflict of interest.

References

1. *The Study of Historic Buildings*; NPÚ: Prague, Czech Republic, 2011; ISBN 978-80-86516-41-7.
2. *ČSN EN 772-1+A1 (722635)*; Methods of Test for Masonry Units—Part 1: Determination of Compressive Strength. ÚNMZ: Prague, Czech Republic, 2016.
3. *ČSN EN 1052-2*; Methods of Test for Masonry: Part 2: Determination of Flexural Strength. ÚNMZ: Prague, Czech Republic, 2017.
4. *ČSN 72 2609*; Method of tests for masonry units: Specific properties of clay masonry units. ÚTN: Prague, Czech Republic, 2017.
5. Drabkin, S.; Kim, D.S. *Failure Monitoring of Concrete Specimen Using Frequency Characteristics of Ultrasonic Waves*; Special Publication: London, UK, 1994; Volume 143, pp. 257–274.
6. Balksten, K.; Strandberg-de Bruijn, P. Understanding Deterioration due to Salt and Ice Crystallization in Scandinavian Massive Brick Masonry. *Heritage* **2021**, *4*, 349–370. [CrossRef]
7. Stryszewska, T.; Kańka, S. Forms of damage of bricks subjected to cyclic freezing and thawing in actual conditions. *Materials* **2019**, *12*, 1165. [CrossRef] [PubMed]
8. Frumuselu, D. Application of IR thermography to NDT of art monuments. *Non-Destr. Test. Cond. Monit.* **1999**, *41*, 582–584.
9. Witzany, J. Defects and reconstruction of brick buildings. In *Technical Library of an Authorized Engineer and Technician*; ŠEL: Prague, Czech Republic, 1999; ISBN 80-902-6975-3.
10. Zheldakov, D.; Mustafin, R.; Kozlov, V.; Gaysin, A.; Sinitsin, D.; Bulatov, B. Durability control of brickwork's material including operation parameters of the building enclosure. *Math. Model. Eng. Probl.* **2021**, *8*, 871–880. [CrossRef]
11. Ahmadi, S.F.; Reisi, M. Comparison of mechanical and durability properties of concrete and fired facing bricks. In *Proceedings of the Institution of Civil Engineers: Structures and Buildings*; ICE Virtual Library: London, UK, 2020; Volume 173, pp. 512–522. [CrossRef]
12. Fagerlund, G. Critical Degrees of Saturation at Freezing of Porous and Brittle Materials. Ph.D. Thesis, Lund University, Lund, Sweden, 1973.
13. Koniorczyk, M.; Gawin, D.; Schrefler, B.A. Modeling evolution of frost damage in fully saturated porous materials exposed to variable hygro-thermal conditions. *Comput. Methods Appl. Mech. Eng.* **2015**, *297*, 39–61. [CrossRef]
14. Carter, C.B.; Norton, M.G. *Ceramic Materials: Science and Engineering*, 2nd ed.; Springer: Berlin/Heidelberg, Germany, 2013; ISBN 978-1-4614-3523-5.
15. Murmu, A.L.; Patel, A. Towards sustainable bricks production: An overview. *Constr. Build. Mater.* **2018**, *165*, 112–125. [CrossRef]
16. Králíková, M.; Cikrle, P.; Anton, O.; Heřmánková, V. Brick masonry ele-ments in brno in the late 19th century. In *Forum Urbes Medii Aevi*; Archaia: Brno, Czech Republic, 2018; pp. 295–302.
17. Marshall, D.; Worthing, D.; Heath, R. *Understanding Housing Defects*, 4th ed.; Taylor & Francis: New York, NY, USA, 2013; ISBN 9781136153730.
18. Bartoň, V.; Šnédar, J.; Cikrle, P. The expansion of defects of solid fired bricks due to their freezing. In Proceedings of the Conference on Rehabilitation and Reconstruction of Building, Prague, Czech Republic, 11–12 November 2021.
19. *ČSN 73 1372*; Non-Destructive Testing of Concrete—Testing of Concrete by Resonance Method. ÚTN: Prague, Czech Republic, 2012.
20. 2*ČSN 73 1371*; Non-Destructive Testing of Concrete—Method of Ultrasonic Pulse Testing of Concrete. ÚTN: Prague, Czech Republic, 2011.
21. Tomáš, S. Zámeček Portz. Available online: https://www.npu.cz/cs/generalni-reditelstvi-npu/inspirujte-se/6008-zamecek-portz (accessed on 1 December 2019).
22. Projekt Portz Insel. Available online: http://www.mikulov.cz/turistika/pamatky-a-prohlidkove-objekty/portz-insel/projekt-portz-insel/ (accessed on 25 November 2021).
23. Bartoň, V.; Šnédar, J.; Cikrle, P. Non-destructive methods for determining the durability of solid fired bricks during reconstruction of historical buildings. In *Juniorstav 2022—24 Odborná Konference Doktorského Studia—Sborník Příspěvků*; ECON publishing: Brno, Czech Republic, 2022; pp. 332–337. ISBN 978-80-86433-76-9.
24. *ČSN EN 772-7 (722635)*; Methods of Test for Masonry Units—Part 7: Determination of Water Absorption of Clay Masonry Damp Proof Course Units by Boiling in Water. ÚNMZ: Prague, Czech Republic, 1999.
25. Abouzid, H.; Chakkor, O. Dimension Reduction Techniques for Signal Separation Algorithms. Communications in Computer and Information Science. In *Big Data, Cloud and Applications*; Springer: Berlin/Heidelberg, Germany, 2018; pp. 326–340. ISBN 978-3-319-96291-7. [CrossRef]
26. Dorafshan, S.; Azari, H. Deep learning models for bridge deck evaluation using impact echo. *Constr. Build. Mater.* **2020**, *263*, 120109. [CrossRef]

27. Zhang, J.-K.; Yan, W.; Cui, D.-M. Concrete Condition Assessment Using Impact-Echo Method and Extreme Learning Machines. *Sensors* **2016**, *16*, 447. [CrossRef] [PubMed]
28. Saaty, R.W. The analytic hierarchy process—What it is and how it is used. *Math. Model.* **1987**, *9*, 161–176. [CrossRef]
29. Dvořák, R.; Topolář, L. Effect of Hammer Type on Generated Mechanical Signals in Impact-Echo Testing. *Materials* **2021**, *14*, 606. [CrossRef] [PubMed]
30. Bartoň, V.; Šnédar, J.; Cikrle, P. Impact of dampness to changes in the mechanical properties of solid fired bricks. *IOP Sci.* **2021**, *1209*, 012036. [CrossRef]
31. Breiman, L. Random forests. In *Machine Learning*; Springer: Berlin/Heidelberg, Germany, 2001; Volume 45, pp. 5–32.

materials

MDPI

Article

Design Solutions for Slender Bars with Variable Cross-Sections to Increase the Critical Buckling Force

Marius Florin Botis [1] and Camelia Cerbu [2,*]

[1] Department of Civil Engineering, Faculty of Civil Engineering, Transilvania University of Brasov, B-dul Eroilor, No. 29, 500036 Brasov, Romania
[2] Department of Mechanical Engineering, Faculty of Mechanical Engineering, Transilvania University of Brasov, No. 29, B-dul Eroilor, 500036 Brasov, Romania
* Correspondence: cerbu@unitbv.ro

Abstract: In large metal civil constructions (stadium roofs, bridges), slender bars can lose their stability under compression loading. There is a lack in the literature regarding design solutions and methods for increasing the critical buckling force of bars with variable cross-sections. The aim of this research is to present a numerical model with finite elements used for a comparative analysis of increasing the critical force of stability loss in cases of (i) bars with stepwise variation in the cross-sections and (ii) bars with continuous variation in the moment of inertia along the bar axis (parabolic, sinusoidal, triangular, and trapezoidal variation). Considering the large-scale applications in civil engineering, bars that were pin-connected at one end and simple-supported at the other end were analyzed. Firstly, the analytical model was described to compute the critical buckling force for bars with stepwise variation in the cross-sections. Then, a finite element model for a slender bar and the assumptions considered were presented. The results were computed using the MATLAB program based on the numerical model proposed and were validated with the analytical model for stepwise variable cross-sections of the bars. The numerical model was adapted for bars with continuous variation in the moment of inertia along the bar axis. It was shown that, by trapezoidal variation in the second moment of inertia along the axis of a bar, i.e., as buckling occurred in the elastic field, the critical buckling force could be increased by 3.556 times compared to a bar with a constant section. It was shown that there was certain bar with stepwise variation in the cross-section for which the critical buckling force was approximately equal to the one obtained for the bar with sinusoidal variation in the moment of inertia (increased by 3.427 times compared to a bar with a constant section).

Keywords: buckling; stability; civil engineering; slender bars; columns; numerical analysis; variable cross-section

Citation: Botis, M.F.; Cerbu, C. Design Solutions for Slender Bars with Variable Cross-Sections to Increase the Critical Buckling Force. *Materials* **2022**, *15*, 6094. https://doi.org/10.3390/ma15176094

Academic Editor: Krzysztof Schabowicz

Received: 15 July 2022
Accepted: 30 August 2022
Published: 2 September 2022

Publisher's Note: MDPI stays neutral with regard to jurisdictional claims in published maps and institutional affiliations.

1. Introduction

The loss in stability of elements designed for engineering structures remains of great importance and topicality for various applications in civil engineering (stadium roofs, bridges), shipbuilding, and aerospace construction (aircraft). These items are usually made of steel or alloys with high strength characteristics. Depending on the type of the element (slender column, beam, plate, or shell) and on the type of loading, there are different analytical models and numerical models used for the analysis of their stability.

The first problems regarding elastic instability were approached and solved by L. Euler [1,2] in the middle of the 18th century, over 200 years ago. Nowadays, the main problems regarding the theory of elastic stability for different types of elements (columns, beams, frames, rings, curved bars, arches, thin plates, and thin shells), were synthesized by S. P. Timoshenko and J. M. Gere in a reference book in the scientific literature [2]. The loss in stability of structural elements takes place under the action of compressive loads [3,4] or bending (lateral buckling of beams) [2,5,6]. The optimized designs of such elements involve

modifying geometry in order to increase the critical buckling force and ensure a low weight. In the case of steel structures, just decreasing the volume can lead to weight reduction. In the context of the research approached in this article, the control of the variation in the cross-section along the axis of a slender bar subjected to compression is of great importance for increasing the critical buckling force and, last but not the least, for reducing the weight. The problem of designing the shapes of bars concerning the cross-section variation also becomes stringent for bars subjected to compression in tensegrity structures [7] used for roofs in modern civil buildings.

The questions are as follows: which geometric parameter (dimensions, area, or the second moment of inertia) of a cross-section should be considered, and which mathematical function models the continuous variation in the section along the axis of a bar to significantly increase the critical buckling force while keeping the length of the bar and boundary conditions unchanged? What is the best design solution for the shape of a bar: stepwise or continuous variation in the cross-section along the bar axis? Another issue raised is how much the ratio between the critical buckling force and volume of a bar is affected considering the variation in the cross-section along the axis of the bar.

In the last years, many researchers around the world have investigated the stability loss in columns having different boundary conditions and non-uniform cross-sections under the action of axially distributed force [3,4,8]. S. P. Timoshenko and J. M. Gere were among the first researchers who presented a theoretical approach of buckling for bars with changes in the cross-sections without considering an axial distribution of compressive force in the second edition of their book [2] (the first edition of this book was published in 1961).

Eisenberger M. [3] found an exact solution for the buckling loads of columns with polynomial variation in the bending stiffness of the cross-sections under an axial load with a polynomial distribution along the bar axis by considering the determinant of the stiffness matrix to be equal to zero at the stability loss. Considering the Euler–Bernoulli beam theory to model a column with a variable moment of inertia $I(x)$ (linear or parabolic variation) in the rectangular cross-section along its axis, which is subjected to distributed axial force, Darbandi et al. [8] computed buckling loads, taking into account the Wentzel–Kramers–Brillouin method of singular perturbation. Just the buckling loads and corresponding mode shapes for the rectangular variable cross-sections of columns were reported in that research, and those results were compared with the results given by Eisenberger [3].

Coskun and Atay [9] used a variational integration method to compute the normalized critical buckling load for Euler's columns with variable cross-sections with different boundary conditions, considering that the flexural stiffness varied by exponential function or by power function (linear, quadratic, and cubic variation). Their results matched very well with the exact solutions, but the paper did not customize the solutions for different shapes of cross-sections (for example, rectangular, circular, and annular cross-sections). Regarding computation methods, Ma et al. [10] computed critical buckling force considering various higher-order shear deformation beam theories based on Engesser's hypothesis and Haringx's hypothesis in comparison with Euler's theory in order to show the effects of warping shape. That research showed that buckling loads were not influenced by the theory used in the case of very slender columns or in the case of those having high shear rigidity.

Taking into account the achievements of the research mentioned above, we focus on finding an analysis method that allows the accurate calculation of the critical buckling force both for a bar with a stepwise variable cross-section and for a bar with a continuous variable cross-section. The analysis model must be flexible in terms of easy adaptation for any function used for variation in the second moment of inertia of the cross-section along the axis. This is the reason why the research focuses on the use of a finite element method for the numerical analysis of a slender bar subjected to compression in order to compute the critical buckling force. However, only a program made with specific software for calculation (such as MATLAB) can ensure the necessary flexibility, not a commercial one used for finite element analysis. Another problem arises concerning the validation method. In this

context, it is necessary to present the state-of-the-art methods in the literature regarding the numerical methods used to analyze the stability of columns subjected to compression.

Using a finite difference method, Soltani and Sistani [11] also investigated a stability analysis for columns having variable flexural stiffnesses subjected to variable axial force. In that research, a finite difference method was applied in the case of column having a rectangular cross-section or an I-shaped cross-section whose dimensions were variable along the axis of the column in order to compute the critical buckling load. On the other hand, in nanomechanics, there are specific methods to analyze the buckling of nanobeams resting on elastic substrate media [12].

Saraçaoğlu and Uzun [13] showed critical buckling loads obtained with Ansys 19.0 software for certain columns having square or circular cross-sections that were variable along the axis of the column (linear variation combined with a portion having a constant cross-section). Szmidla et al. [14] investigated and showed results concerning a stability analysis for steel columns consisting of portions having inhomogeneous cross-sections (composed cross-sections). Regarding columns with inhomogeneous cross-sections, Li et al. [15] made a parametric optimization of composite columns against buckling.

For columns consisting of certain portions having constant cross-sections, Maalawi [16] approached the optimization of buckling calculation in order to obtain design variables (area of the cross-section, length of each portion, radius of gyration) for the maximization of the critical buckling load and for certain input data (number of portions, boundary conditions, cross-section type).

A localized differential quadrature method was used by Yilmaz et al. [17] in order to compute non-dimensional critical buckling loads for non-uniform columns with continuous elastic restraint and different boundary conditions.

Using a discretized Hencky bar-chain model and a parallel genetic algorithm, Ruocco et al. [4] provided in 2017 an optimization method against buckling for columns with non-uniform variation in the cross-section subjected to both distributed and concentrated compressive forces. In this case, the geometrical variation in the cross-section was not given as input data. The paper [4] reported the optimal variation in the circular cross-section in non-dimensional coordinates and its corresponding non-dimensional normalized buckling load by keeping the same length and volume of the column with a uniform cross-section.

In the literature [18], optimization methods were also presented for columns having thin-walled, open cross-sections in order to obtain the maximum critical buckling by considering the constraint that the volume of the column remained constant.

As mentioned before, a retrospective analysis of the literature highlights the fact that there is a lack of research on design methods and solutions to increase the critical buckling force of slender bars with annular cross-sections subjected to compression by continuous variation in the dimensions of the cross-sections along the axis of the bars. Furthermore, no comparative studies have been reported regarding the critical buckling force for slender bars with continuous annular cross-sections compared to bars with stepwise variable cross-sections.

The present research aims to make some contributions to the scientific literature regarding design solutions for slender bars with variable cross-sections along the bar axis. The research provides a numerical model with finite elements validated by an analytical model, which is used to compute the critical buckling forces both for bars with stepwise variation in the cross-section and for bars with continuous variation in the cross-section along the bar axis. The MATLAB program used in this research based on the finite element model presented allows easy adaptation for any variation function considered for the moment of inertia. Considering variable annular cross-sections, the MATLAB program calculates additionally the inner and outer diameters that define the geometry of the bar. Moreover, a comparison is shown of the critical buckling forces for different particular cases considered for variation in the cross-section. In this way, the comparative analysis leads to finding some functions for variation in the second moment of inertia of the cross-sections, which ensure a major increase in the critical buckling force.

In this context, the main purpose of the research is to present a numerical model with finite elements used for a comparative analysis of increasing the critical buckling force for two types of slender bars subjected to compression: (i) bars with stepwise variation in the cross-section and (ii) bars having annular cross-sections with continuous variation in the moment of inertia along the bar axis. The results are also compared with the values of the critical buckling forces corresponding to bars having constant cross-sections along the bar axis. The case of bars that are pin-connected at one end and simple-supported at the other end is taken into account, considering the wide range of applications of these kinds of bars in engineering construction (stadium roofs, bridges, aircraft, and so on).

The main objectives of the research are: (i) the generalization of an analytical model for the calculation of the critical buckling force for a slender bar with stepwise variation in the cross-section, as well as a bar consisting of three portions; (ii) a numerical analysis using the MATLAB program, which uses modeling with finite elements for a slender bar with a stepwise variable cross-section along the axis of the bar in order to obtain the critical buckling force; (iii) the validation of the finite element model (FEM), with the results obtained with an analytical model for a bar with stepwise variation in the cross-section; (iv) an adaptation of the MATLAB program for a numerical analysis of a bar with a continuous variable cross-section; and (v) a comparison of the results regarding the critical buckling force for slender bars with stepwise variation and with continuous variation in the cross-sections. It is considered that the dimensions of a cross-section vary along the bar axis as the second moment of inertia $I(x)$ varies from I to $4I$. For a slender bar with continuous variation in the cross-section, the following types of variation are considered for the second moment of inertia $I(x)$ along the bar axis: parabolic, sinusoidal, triangular, and trapezoidal. The numerical simulation with FEM is made using a computer program made with MATLAB R2014a software.

All the results are interpreted in terms of the normalized critical buckling force with respect to the critical force for stability loss corresponding to the bars having constant cross-sections along the axes of the bars. It is assumed that all the bars involved in this study lose their stability in the elastic field.

Finally, this research reports accurate results on increasing the normalized critical buckling force for slender bars with stepwise or continuous variations in the cross-sections involved in this study. In this way, this research shows design solutions regarding the mathematical functions for variation in the second moment of inertia of a cross-section along the bar axis in order to increase the critical buckling force for slender bars subjected to compressive loads.

2. Work Methods

2.1. Analytical Model for Buckling of a Column with Pin Connections at Ends with Stepwise Variable Section

In Figure 1, a geometrical model is shown of a bar having a stepwise variable circular cross-section whose bottom end is pin-connected, while the upper end is simply supported. The undeformed and deformed shapes of the bar under compression are shown in Figure 1a. The bar consists in three portions. The first and the third portions have the same values for length l and for the second moment of inertia I of the cross-section. The second bar portion has a cross-section whose moment of inertia I_1 is equal to $k_1 I$, with $k_1 > 1$, and its length is equal to $2k_2 l$. In other words, the parameters k_1 and k_2 represent the ratios of the lengths and of the second moment of inertia, respectively, corresponding to the second and first portions of the bar (Figure 1a). The total length of the column is denoted with l_c (Figure 1a). All portions of the bar are made of the same isotropic material having a modulus of elasticity E. The column is symmetric with respect to its midpoint (Figure 1a), and consequently, the analysis model may be reduced to half of the bar, considering the symmetry conditions (Figure 1b). The shape of the bending-moment diagram for half of the bar is shown in Figure 1c.

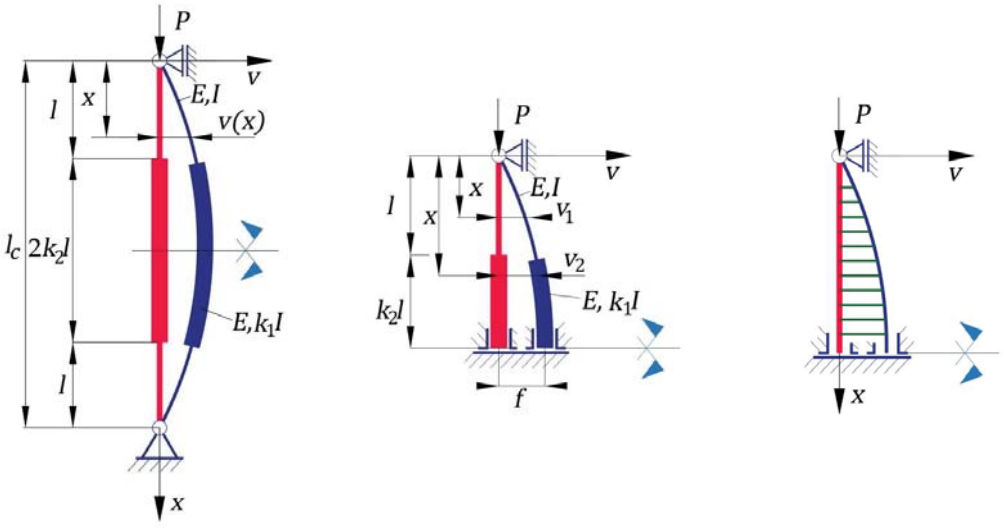

Figure 1. Bar analyzed having a stepwise variable cross-section whose bottom end is pin-connected, while the upper end is simply supported: (**a**) geometrical model of the entire bar and deformed shape at stability loss; (**b**) geometrical model considering the symmetry condition; (**c**) bending-moment diagram.

The main purpose of this subsection is to compare the critical buckling force corresponding to a column having a stepwise variable circular cross-section with the critical buckling force corresponding to a column having the same length and a constant cross-section whose moment of inertia is equal to I. For this purpose, the main objectives are to compute the critical buckling force corresponding to the column having a stepwise variable cross-section and to compare it with the one corresponding to the column with a constant cross-section, as well as an analysis of the rational shapes for buckling in the case of columns having stepwise variable circular cross-sections.

Due to symmetry, the buckling analysis was made by considering a model of half of a column (Figure 1b) with boundary conditions corresponding to the midpoint of the column located on the horizontal symmetry axis.

It was assumed that the column buckled in the elastic domain. This meant that Bernoulli's hypothesis and Euler's relation were valid at buckling.

The bending moment $M_{b1}(x)$ developed at buckling and caused by the compressive force P at the level of the arbitrary cross-section located on the first portion of the column was computed using Equation (1):

$$M_{b1}(x) = -Pv_1(x), \tag{1}$$

where $v_1(x)$ represents the deflection function of the arbitrary cross-section of the first column portion located at distance x with respect to the end of the column (Figure 1b).

In the same manner, the bending moment $M_{b2}(x)$ developed at buckling at the level of the arbitrary cross-section located on the second portion of the column was computed using Equation (2):

$$M_{b2}(x) = -Pv_2(x), \tag{2}$$

where $v_2(x)$ represents the deflection function of the arbitrary cross-section of the second column portion located at distance x with respect to the end of the column (Figure 1b).

To compute the critical buckling force, we used an analytical method. The differential equation of the approximate deformed median fiber corresponding to the first portion of the bar is given in Equation (3):

$$\frac{d^2v_1(x)}{dx^2} = -\frac{M_{b1}(x)}{EI}. \tag{3}$$

Replacing Equation (1), Equation (3) became the following [2]:

$$\frac{d^2v_1(x)}{dx^2} + \frac{Pv_1(x)}{EI} = 0. \tag{4}$$

In the same manner, the differential equation of the approximate deformed median fiber corresponding to the second portion of the bar is given in Equation (5) [2]:

$$\frac{d^2v_2(x)}{dx^2} + \frac{Pv_2(x)}{k_1EI} = 0. \tag{5}$$

The notation α was introduced for the ratio given in Equation (6) [2]:

$$\alpha = \sqrt{\frac{P}{k_1EI}} \quad \text{or} \quad \alpha^2 = \frac{P}{k_1EI}. \tag{6}$$

By using Equation (6), differential Equations (4) and (5) of the approximate deformed median fibers for the bar portions became:

1. Equation (7) for the first portion of the column [2]:

$$\frac{d^2v_1(x)}{dx^2} + \left(\alpha\sqrt{k_1}\right)^2 \cdot v_1(x) = 0, \tag{7}$$

2. Equation (8) for the second portion of the column [2]:

$$\frac{d^2v_2(x)}{dx^2} + \alpha^2 \cdot v_2(x) = 0. \tag{8}$$

Solutions of inhomogeneous second-order differential Equations (7) and (8) were given by Equations (9) and (10) for the first portion and for the second portion of the column, respectively:

$$v_1(x) = C_1 \sin\left(\alpha\sqrt{k_1}x\right) + C_2 \cos\left(\alpha\sqrt{k_1}x\right), \tag{9}$$

$$v_2(x) = C_3 \sin(\alpha x) + C_4 \cos(\alpha x). \tag{10}$$

Integration constants C_i $\left(i = \overline{1,\ 4}\right)$ were computed using the boundary conditions given in Equation (11):

$$\begin{cases} \text{for } x = 0, & v_1(0) = 0; \\ \text{for } x = l + k_2 l, & v_2(l + k_2 l) = f; \\ \text{for } x = l + k_2 l, & \frac{\mathrm{d}v_2}{\mathrm{d}x}(l + k_2 l) = 0, \end{cases} \tag{11}$$

where f represents the deflection of the midpoint of the bar at buckling. The continuity conditions for the deformed shape of the median fiber of the column are given in Equation (12) at the level of the bar cross-section located at distance l with respect to the upper simply supported end of the column:

$$\begin{cases} \text{for } x = l, & v_1(l) = v_2(l); \\ \text{for } x = l, & \frac{\mathrm{d}v_1}{\mathrm{d}x}(l) = \frac{\mathrm{d}v_2}{\mathrm{d}x}(l). \end{cases} \tag{12}$$

The first derivatives of the functions $v_1(x)$ and $v_2(x)$ of the deflections of the arbitrary cross-section corresponding to each column portion were computed using Equations (9) and (10), respectively. In fact, these derivatives represented the functions of the rotations of the arbitrary cross-section and were expressed by Equations (13) and (14):

$$\frac{\mathrm{d}v_1(x)}{\mathrm{d}x} = \alpha\sqrt{k_1}C_1\left[\cos\left(\alpha\sqrt{k_1}x\right) - C_2\sin\left(\alpha\sqrt{k_1}x\right)\right], \tag{13}$$

$$\frac{\mathrm{d}v_2(x)}{\mathrm{d}x} = \alpha[C_3\cos(kx) - C_4\sin(\alpha x)]. \tag{14}$$

By replacing Equations (9), (10), (13), and (14) in the boundary conditions given by Equation (11) and in the continuity conditions given in Equation (12), the system of Equation (15) was obtained:

$$\begin{cases} C_2 = 0; \\ C_3\sin[\alpha l(1+k_2)] + C_4\cos[\alpha l(1+k_2)] = f; \\ \alpha\{C_3\cos[\alpha l(1+k_2)] - C_4\sin[\alpha l(1+k_2)]\} = 0; \\ C_1\sin\left(\alpha l\sqrt{k_1}\right) + C_2\cos\left(\alpha l\sqrt{k_1}\right) = C_3\sin(\alpha l) + C_4\cos(\alpha l); \\ \alpha\sqrt{k_1}\left[C_1\cos\left(\alpha l\sqrt{k_1}\right) - C_2\sin\left(\alpha l\sqrt{k_1}\right)\right] = \alpha[C_3\cos(\alpha l) - C_4\sin(\alpha l)], \end{cases} \tag{15}$$

whose unknown quantities are the integration constants C_i $\left(i = \overline{1,\ 4}\right)$ and the deflection f of the midpoint of the column.

Equation system (15) was reduced practically to the following system of four equations:

$$\begin{cases} C_3\sin[\alpha l(1+k_2)] + C_4\cos[\alpha l(1+k_2)] - f = 0; \\ C_3\cos[\alpha l(1+k_2)] - C_4\sin[\alpha l(1+k_2)] = 0; \\ C_1\sin\left(\alpha l\sqrt{k_1}\right) - C_3\sin(\alpha l) - C_4\cos(\alpha l) = 0; \\ C_1\sqrt{k_1}\cos\left(\alpha l\sqrt{k_1}\right) - C_3\cos(\alpha l) + C_4\sin(\alpha l) = 0. \end{cases} \tag{16}$$

The homogeneous system of Equation (16) had nonzero solutions for C_i $\left(i = \overline{1,\ 4}\right)$ and f if the determinant of the coefficients was zero. This condition led to Equation (17):

$$\mathrm{Det}\begin{bmatrix} 0 & \sin[\alpha l(1+k_2)] & \cos[\alpha l(1+k_2)] & -1 \\ 0 & \cos[\alpha l(1+k_2)] & -\sin[\alpha l(1+k_2)] & 0 \\ \sin\left(\alpha l\sqrt{k_1}\right) & -\sin(\alpha l) & -\cos(\alpha l) & 0 \\ \sqrt{k_1}\cos\left(\alpha l\sqrt{k_1}\right) & -\cos(\alpha l) & \sin(\alpha l) & 0 \end{bmatrix} = 0. \tag{17}$$

The notation ξ was introduced and computed with Equation (18):

$$\xi = \alpha l, \tag{18}$$

and Equation (17) became:

$$\mathrm{Det}\begin{bmatrix} 0 & \sin[\xi(1+k_2)] & \cos[\xi(1+k_2)] & -1 \\ 0 & \cos[\xi(1+k_2)] & -\sin[\xi(1+k_2)] & 0 \\ \sin\left(\xi\sqrt{k_1}\right) & -\sin\xi & -\cos\xi & 0 \\ \sqrt{k_1}\cos\left(\xi\sqrt{k_1}\right) & -\cos\xi & \sin\xi & 0 \end{bmatrix} = 0, \tag{19}$$

whose unknown is ξ. To compute the critical buckling force, the minimum value of the absolute values of the solutions ξ must be used because, for other solutions ξ, the value of the critical force would be greater.

ξ_{min} denoted the minimum value of the absolute values of the solutions ξ of Equation (19).

From Equation (18), the minimum value of α could be computed using Equation (20):

$$\alpha_{min} = \xi_{\min}/l. \tag{20}$$

Equation (20) was replaced in relation (6) in order to compute the critical buckling force for a column having a stepwise variable cross-section:

$$P_{cr} = k_1 \alpha_{\min}^2 EI = k_1 \xi_{\min}^2 \frac{EI}{l^2}. \tag{21}$$

The length l of the first portion was expressed in the function of the total length l_c of the column using Equation (22) according to Figure 1a:

$$l = l_c / [2(1 + k_2)]. \tag{22}$$

Equation (22) was replaced in Equation (21) in order to compute the critical buckling force P_{cr} for a column having a stepwise variable cross-section:

$$P_{cr} = 4k_1(1 + k_2)^2 \xi_{\min}^2 \frac{EI}{l_c^2} = \left(\frac{2\sqrt{k_1}(1 + k_2)\xi_{\min}}{\pi} \right)^2 \frac{\pi^2 EI}{l_c^2}. \tag{23}$$

On the other hand, the critical buckling force P_{cr0} for a column with a constant cross-section whose moment of inertia of the section was I having the same total length l_c with pin connections at its ends was computed as follows:

$$P_{cr0} = \pi^2 EI / l_c^2. \tag{24}$$

Using Equations (23) and (24), the normalized buckling force (denoted with c) was computed as being equal with the ratio between the critical buckling force P_{cr} for a column having a stepwise variable cross-section and the critical buckling force P_{cr0} for a column having a constant cross-section whose moment of inertia of the section was I:

$$c = \frac{P_{cr}}{P_{cr0}} = \left(\frac{2\sqrt{k_1}(1 + k_2)\xi_{\min}}{\pi} \right)^2. \tag{25}$$

It is said that a column is rationally designed if the critical buckling force is increased while the mass of the material of the column is optimal. In structure design, both the mass of the material, which influences the material costs, and the weight of the structure are also important. The manufacturing costs increase due to the additional manufacturing operations required for a column having a stepwise variable cross-section.

In this research, it was said that a column having a stepwise variable cross-section was rationally designed if its ratio between the critical buckling force P_{cr} and the total volume V of the column was greater than the similar ratio computed for a column with a constant cross-section whose moment of inertia of the section was I with the same total length l_c.

The ratio between the critical buckling force P_{cr} and the total volume V of the column was computed as follows, taking into account the geometry of the column shown in Figure 1a:

$$\frac{P_{cr}}{V} = \frac{P_{cr}}{2l(A + A_1 k_2)}, \tag{26}$$

where A represents the cross-sectional areas for the first and the third portions of the column having the length l, while A_1 represents the area of the cross-section for the second column portion whose length is equal to $2k_2 l$.

It was assumed that each portion of the column had a circular cross-section. It may be remarked in Equation (27), which gives the ratio between the moment of inertia I and the second power of the area of the cross-section A for the first portion, whose diameter is denoted with d:

$$\frac{I}{A^2} = \frac{\pi d^4/64}{(\pi d^2/4)^2} = \frac{1}{4\pi} \tag{27}$$

or

$$I = A^2/4\pi. \tag{28}$$

In the same manner, Equation (29) was written for the second portion of the column:

$$I_1 = A_1^2/4\pi. \tag{29}$$

On the other hand, the relation between the moments of inertia I_1 and I corresponding to the first two portions of the column, respectively, is given in Equation (30):

$$I_1 = k_1 I. \tag{30}$$

Equations (28) and (29) were replaced in Equation (30), and it obtained Equation (31):

$$A_1 = A\sqrt{k_1}. \tag{31}$$

Then, relations (22) and (31) were replaced in relation (26), which became:

$$\frac{P_{cr}}{V} = \frac{(1+k_2)P_{cr}}{l_c A\left(1+k_2\sqrt{k_1}\right)}. \tag{32}$$

From Equation (25), the critical buckling force P_{cr} for a column having a stepwise variable cross-section could be computed in the function of the critical buckling force P_{cr0} of a column with a constant cross-section:

$$P_{cr} = cP_{cr0}. \tag{33}$$

The volume of the column with a constant cross-section was:

$$V_0 = l_c A. \tag{34}$$

Replacing Equations (33) and (34) in Equation (32) obtained Equation (35):

$$\frac{P_{cr}}{V} = \frac{(1+k_2)c}{1+k_2\sqrt{k_1}}\frac{P_{cr0}}{V_0}, \tag{35}$$

which led to Equation (36), which computed the rationality factor k_{rat}:

$$k_{rat} = \frac{P_{cr}/V}{P_{cr0}/V_0} = \frac{(1+k_2)c}{1+k_2\sqrt{k_1}}. \tag{36}$$

Replacing the ratio c given by Equation (25) in Equation (36) led to Equation (37):

$$k_{rat} = \frac{P_{cr}/V}{P_{cr0}/V_0} = \frac{(1+k_2)}{1+k_2\sqrt{k_1}}\left(\frac{2\sqrt{k_1}(1+k_2)\xi_{\min}}{\pi}\right)^2 = \frac{4\xi_{\min}^2 k_1(1+k_2)^3}{\pi^2\left(1+k_2\sqrt{k_1}\right)}, \tag{37}$$

which was used to compute the ratio between the rationality factor P_{cr}/V corresponding to a column having a stepwise variable cross-section and the rationality factor P_{cr0}/V_0 corresponding to a column with a constant cross-section.

2.2. Numerical Modeling and Simulation for Loss in Stability of a Column with Pin Connections at Ends with Stepwise Variable Cross-Section

If the compressive stress, which acts on the slenderness of a column, is variable, then the relation between force and displacement may be written with Equation (38):

$$\{dP\} = [K_T]\{\Delta U\}, \tag{38}$$

where infinitesimal variation in the force is denoted with dP. A similar relation may be written with Equation (39):

$$\{\Delta P\} = [K_s]\{\Delta U\}, \tag{39}$$

where finite variation in the force is denoted with ΔP. In Equations (38) and (39), $[K_T] = [K_T\{U\}]$ and $[K_T] = [K_T\{U\}]$ represent the tangent stiffness matrix and the secant stiffness matrix, respectively. The finite variation in the displacements was computed with Equation (40):

$$\{\Delta U\} = [K_T(U)]^{-1}\{\Delta P\} = \frac{[K_T(U)]^*}{\det[K_T(U)]}\{\Delta P\}, \tag{40}$$

where $[K_T(U)]^*$ is the adjunct matrix of the stiffness matrix.

The phenomenon of loss in stability (transition from one equilibrium shape to another equilibrium shape) takes place when the displacements tend toward infinity for a variation ΔP in the compressive force. From a mathematical point of view, this condition is fulfilled if the determinant of the tangent stiffness matrix $[K_T]$ is equal to zero, which was expressed by Equation (41):

$$\det[K_T(U)] = 0. \tag{41}$$

Equation (41) could be written with Equation (42):

$$\det\left[[K] - \lambda\left[K_g\right]\right] = 0, \tag{42}$$

where $[K]$ represents the elastic stiffness matrix of the structure (e.g., the column) obtained by assembling of the stiffness matrices $[K_e]$ corresponding to the finite elements that form the structure; $\left[K_g\right]$ is the geometric stiffness matrix of the structure obtained by assembling of the geometric stiffness matrices $\left[K_{ge}\right]$ corresponding to the finite elements that form the structure; and λ is the common multiplier of the axial forces N acting in the slender bar.

For the finite element of the double-embedded bar type (Figure 2), the elastic stiffness matrix $[K_e]$ and the geometric stiffness matrix $\left[K_{ge}\right]$ were expressed with Equations (43) and (44), respectively:

$$\left[K_{ge}\right] = \begin{bmatrix} \frac{EA'}{l'} & 0 & 0 & -\frac{EA'}{l'} & 0 & 0 \\ 0 & \frac{12EI'}{l'^3} & \frac{6EI'}{l'^2} & 0 & -\frac{12EI'}{l'^3} & \frac{6EI'}{l'^2} \\ 0 & \frac{6EI'}{l'^2} & \frac{4EI'}{l'} & 0 & -\frac{6EI'}{l'^2} & \frac{2EI'}{l'} \\ -\frac{EA'}{l'} & 0 & 0 & \frac{EA'}{l'} & 0 & 0 \\ 0 & -\frac{12EI'}{l'^3} & -\frac{6EI'}{l'^2} & 0 & \frac{12EI'}{l'^3} & -\frac{6EI'}{l'^2} \\ 0 & \frac{6EI'}{l'^2} & \frac{2EI'}{l'} & 0 & -\frac{6EI'}{l'^2} & \frac{4EI'}{l'} \end{bmatrix} \tag{43}$$

$$\left[K_{ge}\right] = \frac{N}{l}\begin{bmatrix} 0 & 0 & 0 & 0 & 0 & 0 \\ 0 & \frac{6}{5} & \frac{l'}{10} & 0 & -\frac{6}{5} & \frac{l'}{10} \\ 0 & \frac{l'}{10} & \frac{2l'^2}{15} & 0 & -\frac{l'}{10} & -\frac{l'^2}{30} \\ 0 & 0 & 0 & 0 & 0 & 0 \\ 0 & -\frac{6}{5} & -\frac{l'}{10} & 0 & \frac{6}{5} & -\frac{ll'}{10} \\ 0 & \frac{ll'}{10} & -\frac{l'^2}{30} & 0 & -\frac{ll'}{10} & \frac{2l'^2}{15} \end{bmatrix} \tag{44}$$

where l', A', and I' are the length, area of the cross-section, and the second moment of inertia of the cross-section, respectively, corresponding to the finite elements double-embedded at both ends.

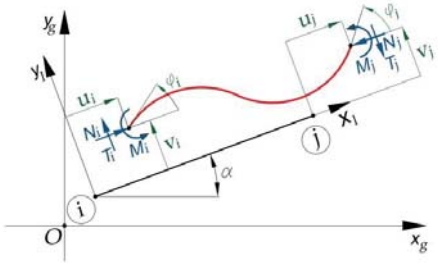

Figure 2. Characteristics of the finite elements of the bar double-embedded at both ends in terms of both the internal forces and flections (displacement and rotation) developed at the nodes.

In this context, the solving of the stability equation involved solving a problem of eigenvectors and eigenvalues. The solutions of the stability equation were the eigenvalues $\lambda_k \ (k = \overline{1,\ n})$ corresponding to the multiplier of the axial forces. For the eigenvalues $\lambda_k \ (k = \overline{1,\ n})$, the corresponding eigenvectors $\{U_k\} \ (k = \overline{1,\ n})$ were determined, which represented the geometric shapes (equilibrium shapes) of the loss in stability. From a practical point of view, only the lowest eigenvalue $\lambda_{\min}$ was of interest, the other values being of interest just from a theoretical point of view.

The numerical model for the calculation of the critical buckling force was validated for a bar having a pin connection at one end and a simple support at the other end. Considering the numerical model previously described, a computer calculation program was written with MATLAB R2014a software for the calculation of the eigenvalues and eigenvectors for the loss in stability of a slender bar subjected to compression. Because just the first value of the critical buckling force and the corresponding deformed shape were of interest, the calculation program reported just the first three values of the critical buckling force and plotted the corresponding eigenvectors.

The assumptions considered in the numerical analysis of the finite elements were the following: (i) the material of the bar was isotropic, homogeneous, and linearly elastic; (ii) the hypothesis of small strains was valid; and (iii) the normal stress σ_p at the proportionality limit was approximately equal to the normal stress at yielding, denoted with f_y, for the material of the bar.

In order to obtain the numerical solution with the finite element method, the main steps covered by the MATLAB program were the following: (i) meshing of the bar in a certain number of finite elements; (ii) computing both the elastic stiffness matrix $[K_e]$ and the geometric stiffness matrix $[K_{ge}]$ corresponding to each finite element according to Equations (43) and (44), respectively; (iii) assembling all the stiffness matrices $[K_e]$ and geometric stiffness matrices $[K_{ge}]$ in order to obtain the elastic stiffness matrix $[K]$ and geometric stiffness matrix $[K_g]$ of the column analyzed; (iv) computing the eigenvalues $\lambda_k \ (k = \overline{1,\ n})$ by solving Equation (42); (v) computing the eigenvectors $\{U_k\} (k = \overline{1,\ n})$ using Equation (40); and (vi) by using the eigenvalues λ_k, computing the critical buckling forces P_{cr}. The smallest critical buckling force corresponded to the minimum eigenvalue $\lambda_{\min}$.

In order to validate the numerical model, the loss in stability was analyzed using the numerical model with 18 finite elements for a bar having a pin connection at one end and a simple support at the other end, for which the geometrical characteristics and the material properties are given in Table 1. Considering the geometrical characteristics of the bar given in Table 1, the following quantities were computed: the area A of the cross-section of 2826 mm^2; the second moment of inertia I of the cross-section, whose value was 2,896,650 mm^4; and the radius i of inertia, having a value of 32.01562 mm.

Table 1. Geometrical characteristics and material properties for the bar analyzed by numerical modeling.

A. Geometrical Characteristics of the Bar			
Characteristic	**Symbol**	**Measure Unit**	**Value**
Bar length	l_c	(mm)	8000
Outer diameter of the circular cross-section	l_c	(mm)	100
Inner diameter of the circular cross-section	d	(mm)	80
B. Properties for S355 Steel [19]			
Young's modulus	E	(MPa)	$2.1 \cdot 10^5$
Normal stress at yielding	f_y	(MPa)	355

For the bar involved, the slenderness ratio λ was computed with Equation (45):

$$\lambda = l/i = 8000/32.01562 = 249.878. \quad (45)$$

For steel of type S355, whose properties are shown in Table 1, the slenderness ratio λ_0 that limited buckling in the elastic field was computed with Equation (46):

$$\lambda_0 = \pi\sqrt{E/\sigma_p} = \pi\sqrt{E/f_y} = 76.37041, \quad (46)$$

where it is assumed that the normal stress σ_p at the proportionality limit is approximately equal to the normal stress at yielding, denoted with f_y, for the material of the bar (Table 1).

The first three eigenshapes and the corresponding eigenvalues for the bar analyzed are shown in Figure 3.

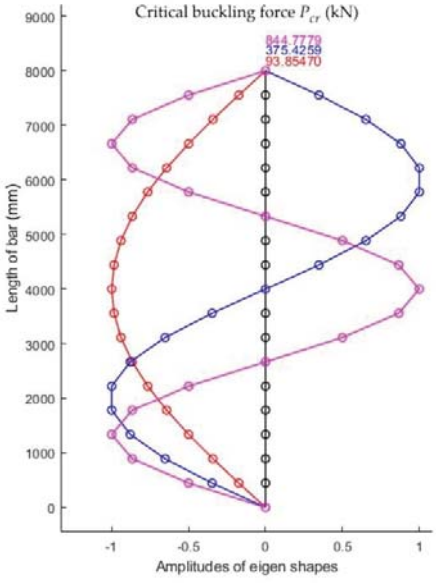

Figure 3. The first three shapes of stability loss and corresponding critical buckling forces for the bar, whose geometrical and material characteristics are given in Table 1.

In Figure 4, the convergence of the critical buckling load P_{cr} obtained with the algorithm of the numerical model is shown related to the number of the finite elements of the

numerical model, and it is analyzed with respect to the critical buckling load of 93.807 kN computed with Equation (24) using the analytical model. By analyzing Figure 4, it can be remarked that the solutions obtained through numerical modeling with the FEM tended asymptotically to the value of 93.86 kN for the numerical model, which had at least six elements. It can be concluded that the numerical model consisting of 18 finite elements provided results that were sufficiently accurate concerning the critical buckling load.

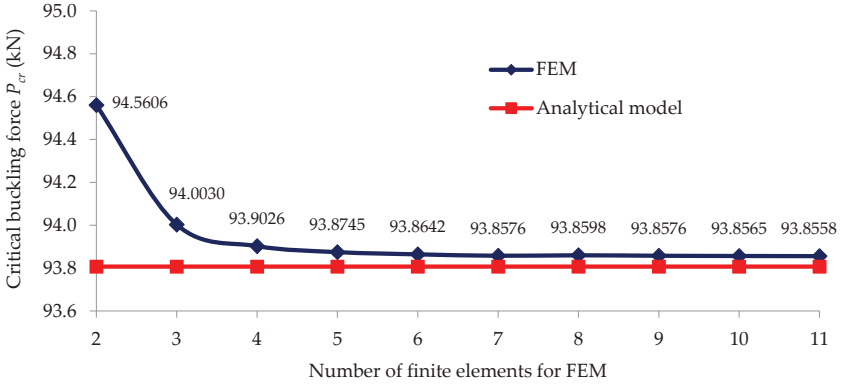

Figure 4. Analysis concerning the convergence of the solution obtained for the critical buckling load by the FEM compared with respect to the value computed with the analytical model.

Six cases of bars with pin connections at one end and simple supports at the other end, shown in Table 2, were analyzed using the numerical model with finite elements in order to show the effects of a stepwise variable cross-section on the critical force of stability loss.

Table 2. Values of the ratios k_1 and k_2 considered for the analyzed cases with the FEM for bars with pin connections at one end and simple supports at the other end.

No.	Code of Case Analyzed	Type of Column	Ratio k_1 * between the Second Moment of Inertia of Portions	Ratio k_2 * between the Lengths of Bar Portions
1	CONST_1I	Column with constant cross-section whose moment of inertia was I	1	0.0
2	STEPWISE405	Column with stepwise variable cross-section	4	0.5
3	STEPWISE410		4	1.0
4	STEPWISE420		4	2.0
5	STEPWISE430		4	3.0
6	CONST_4I	Column with constant cross-section whose moment of inertia was 4*I*	4	0.0

* Ratios k_1 and k_2 are shown in Figure 1a.

In Table 2, two extreme cases were considered for bars whose the second moments of inertia were constant along the bar length *l*: (i) a bar having a second moment of inertia equal to *I* (code CONST_1I); and (ii) a bar having a second moment of inertia equal to 4*I* (code CONST_1I). For both cases, the length *l* of the bar was that given in Table 1, and it was assumed that the bar had an annular cross-section. The value *I* for the second moment of inertia corresponded to an annular cross-section having an inner diameter *d* and an outer diameter *D*, which are also given in Table 1. For the second bar, for which the second moment of inertia was equal to 4*I*, the inner diameter *d* and outer diameter *D* were

computed by considering the area A of the annular cross-section in order for the normal stress in compression to be equal to the normal stress σ_p at the proportionality limit (which was approximately equal to the normal stress at yielding f_y).

The results obtained using the numerical model with 32 finite elements were comparatively analyzed for all the types of columns shown in Table 2.

2.3. Numerical Modeling and Simulation for Loss in Stability of a Column with Pin Connections at Ends with Continuous Variable Cross-Section

2.3.1. Cases Approached and Assumptions concerning the Variation in the Second Moment of Inertia

Four cases of variation in the second moment of inertia $I(x)$ were investigated: (i) parabolic variation; (ii) sinusoidal variation; (iii) triangular variation; (iv) trapezoidal variation; and (v) constant variation.

It was assumed that the arbitrary cross-section of a bar whose area was $A(x)$ was an annular cross-section having an inner diameter $d(x)$ and an outer diameter $D(x)$. The length of the bar was denoted with l. Assuming that the bar must lose its stability in the elastic field (for which Euler's relation is valid), the normal stress σ developed at the arbitrary point of the cross-section must be smaller or equal to the normal stress at the proportionality limit denoted with σ_p, which was considered to be equal to the normal stress at yielding f_y (given in Table 1 for S355 steel). In this context, the area $A(x)$ of the cross-section was computed with Equation (47), considering that the normal stress σ developed at that cross-section was equal to the normal stress σ_p at the proportionality limit for the material of the bar at stability loss:

$$A(x) = P_{cr}/\sigma_p, \tag{47}$$

where P_{cr} is the critical buckling force (or the critical force of stability loss).

For the arbitrary cross-section of the bar, knowing the area $A(x)$ computed with Equation (47) and the variation in the second moment of inertia $I(x)$, the inner and outer diameters of the cross-section were computed with Equations (48) and (49), respectively [20]:

$$d(x) = \sqrt{\frac{8I(x)}{A(x)} - \frac{2A(x)}{\pi}}, \tag{48}$$

$$D(x) = \sqrt{\frac{8I(x)}{A(x)} + \frac{2A(x)}{\pi}}. \tag{49}$$

Equations (48) and (49) show that the wall thickness of the bar cross-section changed along the axis of the bar as long as the ratio between $d(x)$ and $D(x)$ was not constant.

To analyze the critical buckling force P_{cr} for a column with pin connections at both ends whose second moment of inertia I had continuous variation along the axis of the bar, numerical models were used that were similar to the one corresponding with the bar with stepwise variation in the cross-section. In order to analyze the solution convergence for the critical buckling force P_{cr}, the numerical analysis was repeated for FEMs consisting of 20, 80, 100, 200, 400, and 800 elements, respectively. The convergence analysis made for FEMs corresponding to bars with continuous variation in the second moment of inertia along the bar axis led to the conclusion that the solutions for the critical buckling force converged for FEMs consisting of a minimum of 100 elements.

2.3.2. Parabolic Variation in the Second Moment of Inertia of the Cross-Section along the Bar

The consideration of the second moment of inertia $I(x)$ of an arbitrary cross-section with parabolic variation along the bar axis is given by Equation (50):

$$I(x) = Ax^2 + Bx + C, \tag{50}$$

where x represents the position of the arbitrary cross-section with respect to the pin-connected end of the bar.

The constants A, B, C were computed considering that the second moment of inertia was equal with I for the cross-sections of the bar ends, and it was equal to $4I$ for the middle of the bar. These conditions are given by Equation (51):

$$\begin{cases} \text{for } x = 0, & \mathrm{I}(0) = \mathrm{C} = \mathrm{I}; \\ \text{for } x = l/2, & I(l/2) = A(l/2)^2 + Bl/2 + C = 4I; \\ \text{for } x = l, & I(l) = Al^2 + Bl + C = I, \end{cases} \tag{51}$$

and led to the constants given by Equation (52):

$$A = -12I/l^2; \quad B = 12I/l; \quad C = I. \tag{52}$$

By replacing the above constants A, B, and C in Equation (50), the parabolic variation in the second moment $I(x)$ along the axis of the bar is given by Equation (53):

$$I(x) = -\left(12I/l^2\right)x^2 + (12I/l)x + I, \tag{53}$$

which is plotted in Figure 5 for a bar whose length l is given in Table 1 and whose second moment of inertia I of the cross-sections located at the bar ends was computed for an annular cross-section having an inner diameter d and an outer diameter D, which are also given in Table 1.

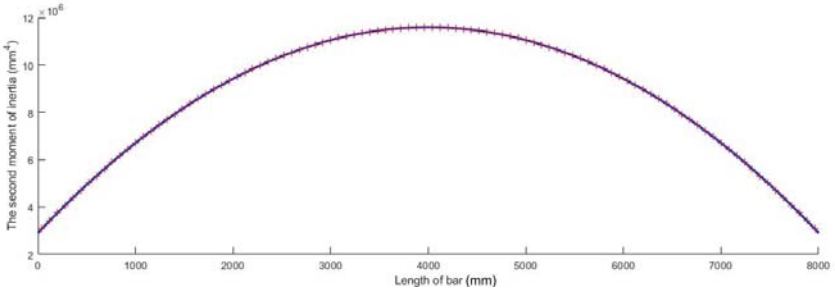

Figure 5. Parabolic variation in the second moment of inertia I along the bar axis.

In Figure 6, a geometrical model is shown of a bar whose parabolic variation in the second moment of inertia $I(x)$ is given by Equation (53).

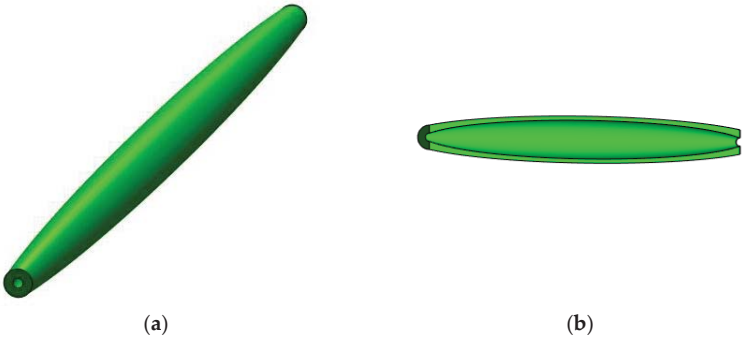

(**a**) (**b**)

Figure 6. Geometrical model for a bar with parabolic variation in the second moment of inertia along the bar axis: (**a**) isometric view and (**b**) longitudinal section.

2.3.3. Sinusoidal Variation in the Second Moment of Inertia of the Cross-Section along the Bar

The variation in the second moment of inertia $I(x)$ of an arbitrary cross-section along the bar axis as a sinusoidal function is given by Equation (54):

$$I(x) = 3I\sin(\pi x/l) + I. \tag{54}$$

Considering the conditions given by Equation (55), it could be checked that the second moment of inertia was equal to I for the cross-sections located at the bar ends, and it was $4I$ for the cross-section located at the middle of the bar:

$$\begin{cases} \text{for } x = 0; & I(0) = 3I\sin(\pi\cdot 0/l) + I = I; \\ \text{for } x = l/2; & I(l/2) = 3I\sin(\pi(l/2)/l) + I = 3I\sin(\pi/2) + I = 4I; \\ \text{for } x = l; & I(l) = 3I\sin(\pi l/l) + I = 3I\sin\pi + I = I. \end{cases} \tag{55}$$

The sinusoidal variation in the second moment $I(x)$ along the axis of the bar given by Equation (54) is plotted in Figure 7 for a bar whose length l is given in Table 1 and whose second moment of inertia I of the cross-sections located at bar ends was computed for an annular cross-section having an inner diameter d and an outer diameter D, which are also given in Table 1.

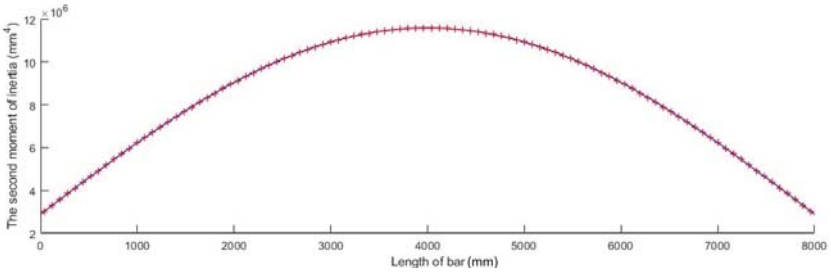

Figure 7. Sinusoidal variation in the second moment of inertia along the bar axis.

In Figure 8, a geometrical model is shown of a bar whose sinusoidal variation in the second moment of inertia $I(x)$ is given by Equation (54).

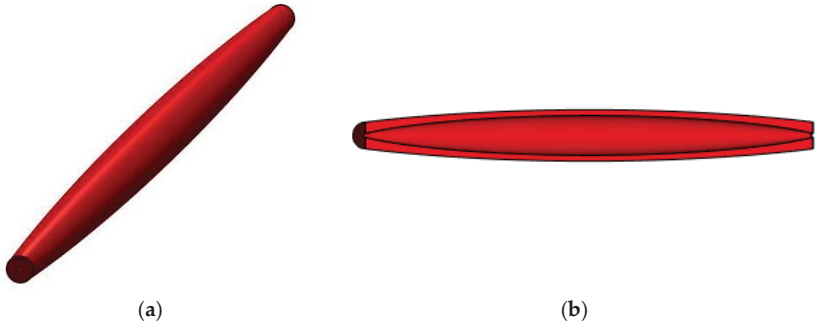

(**a**) (**b**)

Figure 8. Geometrical model for s bar with sinusoidal variation in the second moment of inertia along the bar axis: (**a**) isometric view and (**b**) longitudinal section.

2.3.4. Triangular Variation in the Second Moment of Inertia of the Cross-Section along the Bar

It was considered that the second moment of inertia linearly increased from the value I to the value $4I$ from the pin-connected end of the bar to the middle of the bar, which meant position x of the cross-section was in the range of $[0, l/2]$. Then, the second moment

of inertia linearly decreased from the value $4I$ to the value I from the middle of the bar to the other end of the bar, which meant a variation of x in the range of $[l/2,\ l]$.

A linear function for the second moment of inertia for the first half of the bar, which meant $x \in (0,\ l/2)$, and it was given by Equation (56):

$$I_1(x) = Ax + B, \tag{56}$$

whose constants A and B are computed using the conditions given by Equation (57) regarding the values of the second moments of inertia for the cross-sections located at the pin-end connection and at the middle of the bar:

$$\begin{cases} \text{for } x = 0; & I_1(0) = A{\cdot}0 + B = I; \\ \text{for } x = l/2; & I_1(l/2) = Al/2 + B = 4I. \end{cases} \tag{57}$$

Using the conditions given by Equation (57), the constants A and B were computed, and the results are given in Equation (58):

$$A = 6I/l; \quad B = I. \tag{58}$$

By replacing the constants A and B in Equation (56), a linear function was obtained for the second moment of inertia for the first half of the bar, which is given in Equation (59):

$$I_1(x) = 6Ix/l + I, \quad \text{for } x \in (0,\ 0.5l). \tag{59}$$

A linear function was assumed for the second moment of inertia for the second half of the bar, which meant $x \in (0.5, l)$, and it was given by Equation (60):

$$I_2(x) = Cx + D, \tag{60}$$

whose constants C and D are computed by using the conditions given by Equation (61) regarding the values of the second moments of inertia for the cross-sections located at the middle of the bar and at bar end, which is simple-supported:

$$\begin{cases} \text{for } x = l/2; & I_2(l/2) = Cl/2 + D = 4I; \\ \text{for } x = l; & I_2(l) = Cl + D = I. \end{cases} \tag{61}$$

Using the conditions given by Equation (61), the constants C and D were computed, and the results are given in Equation (62):

$$C = -6I/l; \quad D = 7I. \tag{62}$$

By replacing the constants C and D in Equation (60), a linear function was obtained for the second moment of inertia for the first half of the bar, which is given in Equation (63):

$$I_2(x) = -6Ix/l + 7I, \quad \text{for } x \in (0.5l,\ l). \tag{63}$$

The triangular variation in the second moment $I(x)$ along the axis of the bar given by Equations (59) and (63) is plotted in Figure 9 for a bar whose length l is given in Table 1 and whose second moment of inertia I of the cross-sections located at the bar ends was computed for an annular cross-section having an inner diameter d and an outer diameter D, which are also given in Table 1.

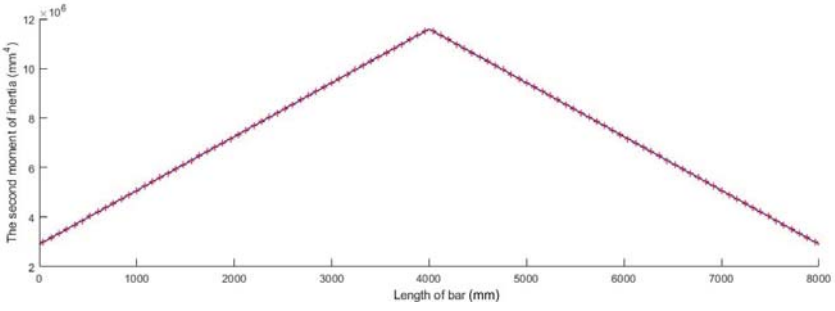

Figure 9. Triangular variation in the second moment of inertia along the bar axis.

In Figure 10, a geometrical model is shown of a bar whose triangular variation in the second moment of inertia $I(x)$ is given by Equations (59) and (63).

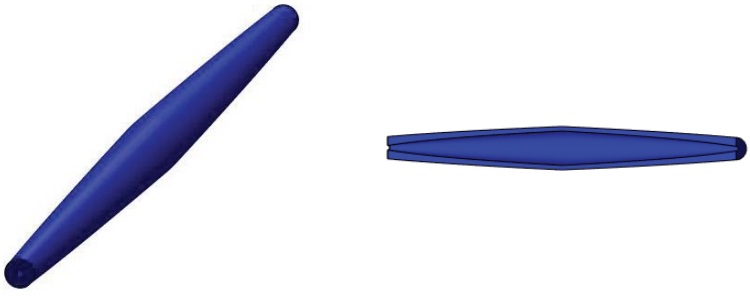

(**a**) (**b**)

Figure 10. Geometrical model for a bar with triangular variation in the second moment of inertia along the bar axis: (**a**) isometric view and (**b**) longitudinal section.

2.3.5. Trapezoidal Variation in the Second Moment of Inertia of the Cross-Section along the Bar

For trapezoidal variation in the second moment of inertia $I(x)$ along the axis of a bar, three portions of the bar length l were considered in order to obtain the functions for such a variation: (i) for the first third of the bar, which meant $x\epsilon(0, l/3)$, the second moment of inertia linearly increased from the value I to the value $4I$; (ii) for the second third of the bar, which meant $x\epsilon(l/3,\ 2l/3)$, the cross-section remained constant, and the second moment of inertia was equal with $4I$; and (iii) for the last portion, which meant $x\epsilon(2l/3,\ l)$, the second moment of inertia linearly decreased from the value $4I$ to the value I.

The linear function corresponding to the first portion is given in Equation (64):

$$I_1(x) = Ax + B, \tag{64}$$

for which the constants A and B are computed using the conditions written in Equation (65):

$$\begin{cases} \text{for } x = 0; & I_1(0) = A{\cdot}0 + B = I; \\ \text{for } x = l/3; & I_1(l/3) = Al/3 + B = 4I. \end{cases} \tag{65}$$

Solving the above system of two equations led to the following values for the constants A and B:

$$A = 9I/l; \quad B = I. \tag{66}$$

By replacing the constants A and B in Equation (64), a linear function was obtained of the second moment of inertia corresponding to the first portion of the bar, as shown in Equation (67):

$$I_1(x) = 9Ix/l + I, \quad \text{for } x \in [0, l/3]. \tag{67}$$

The function for the second moment of inertia corresponding to the second portion of the bar is given by Equation (68):

$$I_2(x) = 4I, \quad \text{for } x \in [l/3,\ 2l/3]. \tag{68}$$

For the third portion of the bar, the function of the second moment of inertia was assumed, as given by Equation (69):

$$I_3(x) = Cx + D, \tag{69}$$

for which constants C and D are computed using the following conditions:

$$\begin{cases} \text{for } x = 2l/3; & I_3(l/3) = 2Cl/3 + D = 4I; \\ \text{for } x = l; & I_3(l) = Cl + D = I. \end{cases} \tag{70}$$

By solving the system of two equations given by Equation (70) and replacing constants C and D in Equation (69), the following function of the second moment of inertia was obtained:

$$I_3(x) = -9Ix/l + 10I, \quad \text{for } x \in [2l/3, l]. \tag{71}$$

Considering the functions given by Equations (67), (68), and (71), trapezoidal variation in the second moment of inertia along the bar axis is graphically shown in Figure 11 for a bar whose length l is given in Table 1 and whose second moment of inertia I of the cross-sections located at the bar ends was computed for an annular cross-section having an inner diameter d and an outer diameter D, which are also given in Table 1. The geometrical model of such a bar is shown in Figure 12.

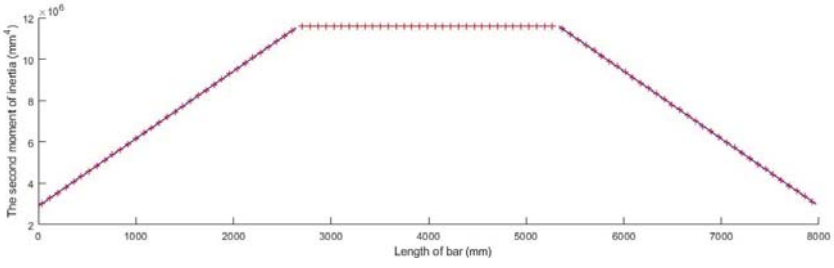

Figure 11. Trapezoidal variation in the second moment of inertia along the bar axis.

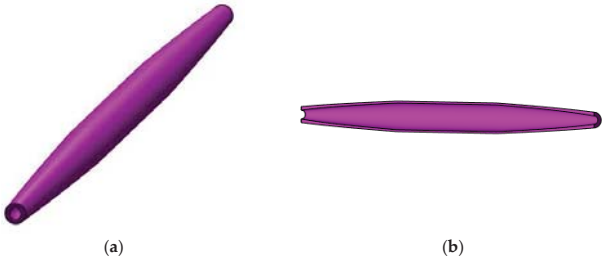

(**a**) (**b**)

Figure 12. Geometrical model for a bar with trapezoidal variation in the second moment of inertia along the bar axis: (**a**) isometric view and (**b**) longitudinal section.

3. Results

3.1. Results Obtained by Analytical Model

Figure 13 shows the variation in the ratio P_{cr}/P_{cr0}. computed with Equation (25) for the case of $k_1 = 4$. related to the value $k_2 \in [0;3]$. It may be observed that, for this design of a column with a variable cross-section, the maximum value of the ratio P_{cr}/P_{cr0}. was equal to 3.69 in the case when k_2. was equal to 3.

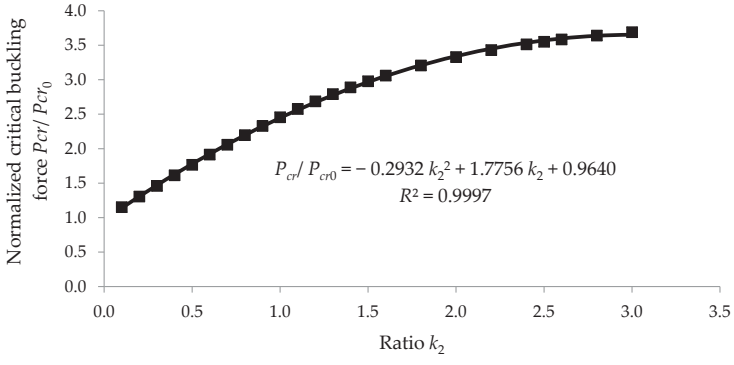

Figure 13. Variation in the normalized critical buckling force P_{cr}/P_{cr0}. computed with Equation (25) considering $k_1 = 4$ related to the ratio k_2.

Figure 14 shows the variation in the rationality factor k_{rat} computed with Equation (37) for the case of $k_1 = 4$. related to the value $k_2 \in [0;3]$. It was observed that the column with a stepwise variable cross-section was more rationally designed because the rationality factor k_{rat}. was always greater than 1, and the greatest value was 2.1086 in the case when k_2. was equal to 3. In fact, for the ratio k_2. in the range of $[2,\ 3]$, the rationality factor k_{rat}. varied between 1.9973 and 2.1086.

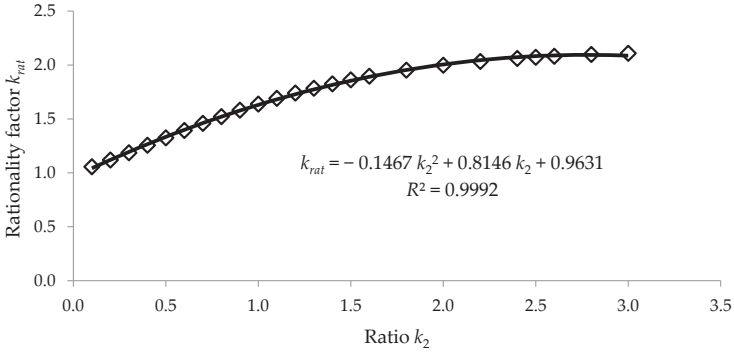

Figure 14. Variation in the rationality factor k_{rat}. computed with Equation (37) considering $k_1 = 4$. related to the ratio k_2.

The least squares method was used for the approximation of the data in both Figures 13 and 14 considering the second-degree polynomial functions. The approximation functions both for the normalized critical buckling load P_{cr}/P_{cr0} and for the rationality factor k_{rat}. are given in Figures 13 and 14, where the value R^2 close to 1 shows that the data were accurately approximated.

3.2. Results by Numerical Modeling for Loss in Stability of a Bar with Pin Connections at Ends with Stepwise Variable Cross-Section

Considering the column with pin connections at its ends and a stepwise variable cross-section shown in Figure 1, the results obtained using the MATLAB calculation program for the numerical model with 32 finite elements are plotted in Figure 15 for all six cases given in Table 2.

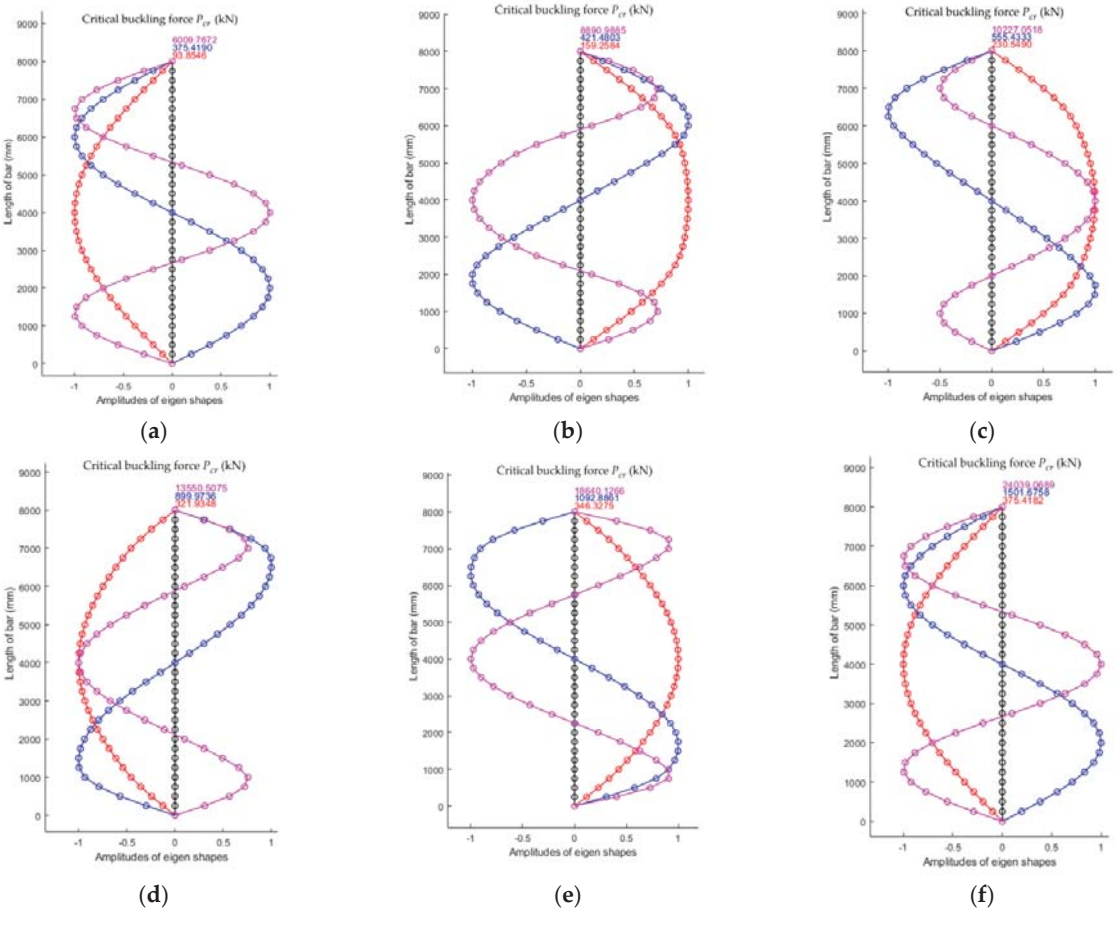

Figure 15. The first three shapes of stability loss and corresponding critical forces P_{cr}. obtained by the FEM for the six cases of bars analyzed: (**a**) CONST_1I; (**b**) STEPWISE405; (**c**) STEPWISE410; (**d**) STEPWISE420; (**e**) STEPWISE430; and (**f**) CONST_4I (details about each case are given in Table 2).

3.3. Validation of the Numerical Model by Theoretical Results for a Column with Stepwise Variable Cross-Section

Table 3 shows the results obtained for the critical buckling force P_{cr}. using both the FEM and the analytical model in the cases of columns with stepwise variable cross-sections and with constant cross-sections involved in this research. It was observed that the numerical model was validated by the results obtained with the analytical model because the maximum error was equal to 3.84%, as shown in Table 3.

Table 3. Comparison between the critical buckling force P_{cr} obtained by the FEM with the one obtained with the analytical model for different cases of bars involved in this research.

Code of Case Analyzed *	Critical Force P_{cr} of Stability Loss (kN)		Error (%)
	FEM	Analytical Model	
CONST_1I	93.8546	93.807	0.05
STEPWISE405	159.2584	165.620	3.84
STEPWISE410	230.5490	230.430	0.05
STEPWISE420	321.9348	312.270	3.10
STEPWISE430	346.3275	346.150	0.05
CONST_4I	375.4182	375.228	0.05

* Details about bars of each case are given in Table 2.

The values of the normalized critical buckling forces obtained by the FEM and by the analytical model are comparatively plotted in Figures 16 and 17, respectively, for the columns with stepwise variable cross-sections and with constant cross-sections. These graphs also show a good correlation between the numerical model and the analytical model.

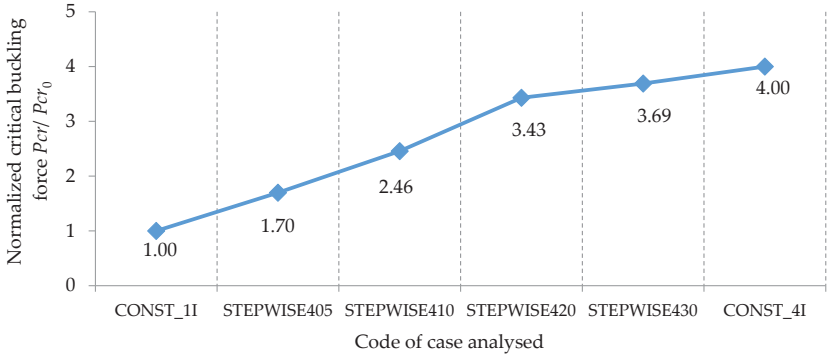

Figure 16. Comparison of the normalized critical buckling forces P_{cr}/P_{cr0}. computed with the finite element models for the bars involved (details about each case are given in Table 2).

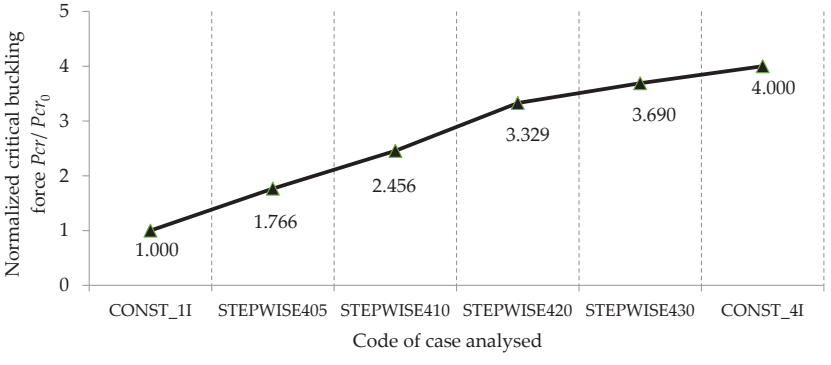

Figure 17. Comparison of the normalized critical buckling forces P_{cr}/P_{cr0} computed with the analytical model for the bars involved in this research (details about each case are given in Table 2).

3.4. Results of Numerical Modeling for Loss in Stability of a Column with Pin Connections at Ends with Continue Variable Cross-Section

3.4.1. Critical Buckling Forces for the Parabolic Variation in the Second Moment of Inertia of the Cross-Section along the Bar

Using the numerical model with 100 finite elements for the bar with parabolic variation in the second moment of inertia, the first three eigenshapes of stability loss were obtained that corresponded to the first three values for the critical buckling force shown in Figure 18. It was observed that the smallest value of the critical force for stability loss F_{cr}. was equal to 329.7439 kN.

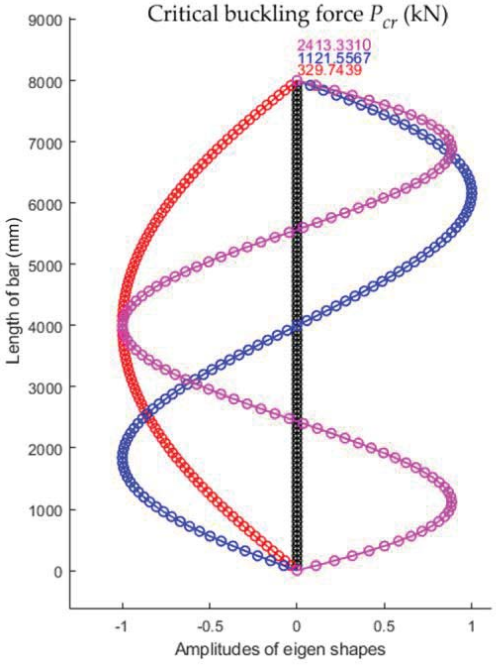

Figure 18. The first three shapes of stability loss and corresponding critical buckling forces for the bar with parabolic variation in the second moment of inertia along the bar axis.

3.4.2. Critical Buckling Forces for the Sinusoidal Variation in the Second Moment of Inertia of the Cross-Section along the Bar

Using the numerical model with 100 finite elements, for the bar with sinusoidal variation in the second moment of inertia, the first three eigenshapes of stability loss were obtained that corresponded to the first three values for the critical buckling force shown in Figure 19. It was observed that the smallest value of the critical force for stability loss F_{cr} was equal to 321.6489 kN.

3.4.3. Critical Buckling Forces for the Triangular Variation in the Second Moment of Inertia of the Cross-Section along the Bar

Using the numerical model with 100 finite elements for the bar with triangular variation in the second moment of inertia, the first three eigenshapes of stability loss were obtained that corresponded to the first three values for the critical buckling force shown in Figure 20. It was observed that the smallest value of the critical force for stability loss F_{cr}. was equal to 275.4322 kN.

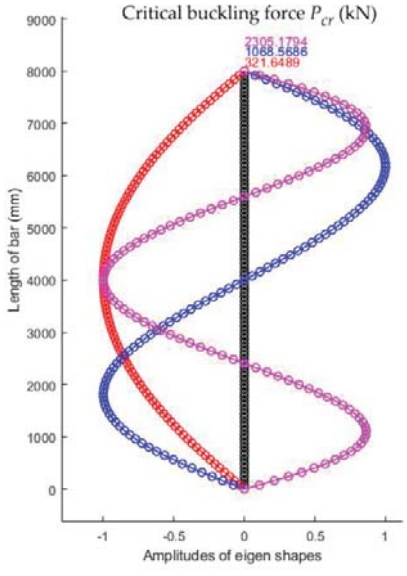

Figure 19. The first three shapes of stability loss and corresponding critical buckling forces for the bar with sinusoidal variation in the second moment of inertia along the bar axis.

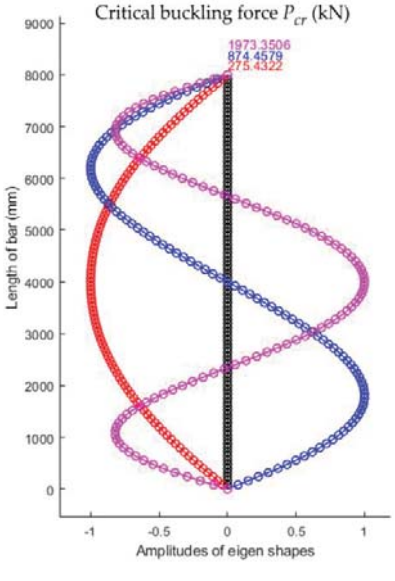

Figure 20. The first three eigenshapes of stability loss and corresponding values for the critical buckling forces for the bar with triangular variation in the second moment of inertia along the bar axis.

3.4.4. Critical Buckling Forces for the Trapezoidal Variation in the Second Moment of Inertia of the Cross-Section along the Bar

Using the numerical model with 100 finite elements for the bar with trapezoidal variation in the second moment of inertia, the first three shapes of stability loss corresponding to the first three values of the critical buckling force were obtained and are shown in Figure 21. These were obtained using the numerical model with finite elements of the bar

with trapezoidal variation in the second moment of inertia along the bar axis. The smallest value of the critical force for stability loss F_{cr}. was equal to 333.7152 kN.

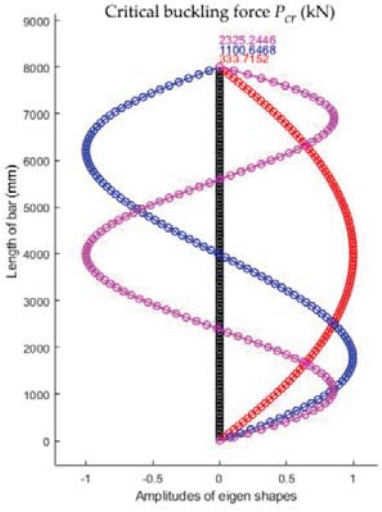

Figure 21. The first three shapes of stability loss and corresponding values for the critical buckling force for the bar with trapezoidal variation in the second moment of inertia along the bar axis.

4. Discussion

In Figure 22, the values of the normalized critical buckling forces P_{cr}/P_{cr0} are comparatively analyzed for all the bars involved in this theoretical research in order to establish the best shapes of both bars with stepwise variable cross-sections and with continuous variable cross-sections, which can lead to a significant increase in the critical buckling force.

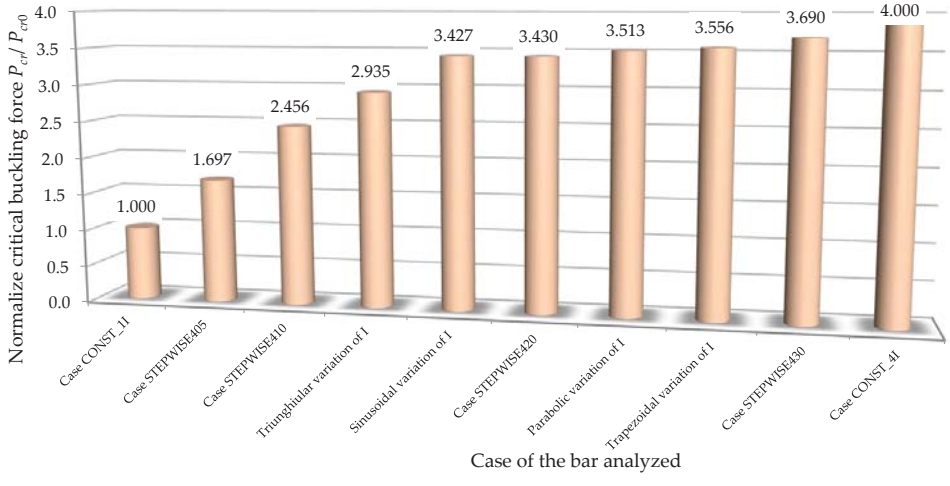

Figure 22. Comparison of the critical buckling force obtained by the FEM for all the cases of bars involved in this research.

By analyzing the results shown in Figure 22, it can be observed that the normalized critical buckling force of 3.43 obtained for the bar with stepwise variation in the cross-section corresponding to case STEPWISE420 was approximately equal to the normalized

critical buckling force of 3.427 obtained for the bar with sinusoidal variation in the second moment of inertia along the bar axis from I to the maximum value of $4I$. This remark is very important as long as the bar with the stepwise variable cross-section is more easily obtained from a technological point of view.

Considering Figure 22, it may be also remarked that the normalized critical buckling force of 3.556 recorded for the bar with trapezoidal variation in the second moment of inertia along the bar axis was close to the normalized critical buckling force of 3.513 obtained for the bar with parabolic variation in the second moment of inertia along the bar axis.

For the bars with variable cross-sections involved in this research, the highest value of 3.69 for the normalized critical buckling force was recorded for the bar with stepwise variation in the cross-section corresponding to case STEPWISE430 (Figure 22).

5. Conclusions

The research presented in this paper is very important for the design of shapes of slender bars that can lose their stability under compression loads. Increasing the critical buckling force for columns with annular cross-sections by stepwise or continuous variation in the cross-sections along the bar axes was proposed. Moreover, the shapes of the slender bars were designed so that these bars lost their stability in the elastic field.

A particular case was considered for which the second moment of inertia varied between the values I and $4I$ along the bar axis. For bars with variation in the cross-sections in three steps, the normalized critical buckling force continuously increased by a second-degree polynomial function reported in the paper related to the ratio k_2 between the lengths of the bar portions. It was shown that the geometry proposed for the bar with stepwise variation in the cross-section was more rational with respect to the bar with a constant cross-section, taking into account the ratio between the critical buckling force and the volume of the bar.

Among the bars involved in this research with continuous variations in the annular cross-sections, it was concluded that the parabolic or trapezoidal variations in the cross-sections were the best solutions. These design solutions led to increases in the critical buckling force by 3.513 times and 3.556 times, respectively, compared with the bar with a constant cross-section along the axis. In fact, the normalized critical buckling forces obtained for both parabolic and trapezoidal variations were close to the one corresponding to case STEPWISE420 with stepwise variation in the cross-section, which was more technologically affordable.

The numerical analysis approach in this research was one of an appropriate design solution to optimize the variation in the cross-section along the axis of a bar by comparing the results in order to maximize the critical buckling force. The numerical model was validated by an analytical model for the bar with stepwise variation in the cross-section, and then the numerical approach was applied for bars with different methods of variation in the second moment of inertia along the bar axis. In fact, the continuous variation in the cross-section was approximated with stepwise variation in the cross-section considering that the bar consisted of a number of portions equal to the number of finite elements considered in the numerical analysis. The main advantage was that the MATLAB program used in this research was not a commercial one, and as a result, the algorithm could be further adapted for other types of variation in the cross-section along the bar axis.

At a time when the rapid printing of construction elements has taken off around the world in the field of construction, the results presented in this paper are of great interest in many applications, taking into account that these results could lead to increasing the critical buckling force for compressed slender bars. However, there is still a need for 3D-printing equipment for construction to be perfected, developed, and made more affordable in terms of cost so that the manufacture of bars with variable cross-sections is easy for construction elements whose shapes have been optimized.

Considering the design solutions for continuous variation in the cross-section presented in this article, it is possible to manufacture sleeves to be welded on compressed bars

of various structures (stadium roofs, steel bridge structures, trusses) to increase the critical buckling force. The sleeves may be welded without removing the bars from the structures. Because the research in this article was limited to slender bars with pin connections at both ends, the study may be continued for other boundary conditions in further research.

Author Contributions: Conceptualization, M.F.B.; formal analysis, M.F.B. and C.C.; investigation, M.F.B. and C.C.; methodology, M.F.B.; supervision, M.F.B.; validation, M.F.B. and C.C.; visualization, M.F.B. and C.C.; writing—original draft, M.F.B. and C.C.; writing—review and editing, C.C. All authors have read and agreed to the published version of the manuscript.

Funding: The authors acknowledge the support of Project No. 11002100 from the Transylvania University of Brasov and a construction company. The authors also acknowledge the support of the Transilvania University of Brasov for providing the software involved and for financial support regarding the publication fees of this article.

Institutional Review Board Statement: Not applicable.

Informed Consent Statement: Not applicable.

Data Availability Statement: Not applicable.

Acknowledgments: The authors acknowledge the support of Project No. 11002100 from the Transylvania University of Brasov and a construction company. The authors also acknowledge the support of the Transilvania University of Brasov for providing the software involved and for financial support regarding the publication fees of this article.

Conflicts of Interest: The authors declare no conflict of interest.

References

1. Boyer, C.B. Leonhard Euler SWISS Mathematician. Available online: https://www.britannica.com/biography/Leonhard-Euler (accessed on 10 July 2022).
2. Timoshenko, S.P.; Gere, J.M. *Theory of elastic stability*, 2nd ed.; Dover Publications, Inc.: Mineola, NY, USA, 2009.
3. Eisenberger, M. Buckling loads for variable cross-section members with variable axial force. *Int. J. Solids Struct.* **1991**, *27*, 135–143. [CrossRef]
4. Ruocco, E.; Wang, C.M.; Zhang, H.; Challamel, N. An approximate model for optimizing Bernoulli columns against buckling. *Eng. Struct.* **2017**, *141*, 316–327. [CrossRef]
5. Dybel, K.; Kampczyk, A. Sensitivity of Geometric Parameters in the Sustainability Development of Continuous Welded Rail. *Acta Tech. Jaurinensis* **2022**. [CrossRef]
6. Vo, D.-Q.; Ton-That, H.L. Free vibration of simply supported steel I-girders with trapezoidal web corrugations. *Rep. Mech. Eng.* **2020**, *1*, 141–150. [CrossRef]
7. Botis, M.F.; Imre, L.; Cerbu, C. Computer-aided design of a tensegrity structure. *Structures* **2022**, *38*, 340–360. [CrossRef]
8. Darbandi, S.M.; Firouz-Abadi, R.D.; Haddadpour, H. Buckling of Variable Section Columns under Axial Loading. *J. Eng. Mech.* **2010**, *136*, 472–476. [CrossRef]
9. Coskun, S.B.; Atay, M.T. Determination of critical buckling load for elastic columns of constant and variable cross-sections using variational iteration method. *Comput. Math. Appl.* **2009**, *58*, 2260–2266. [CrossRef]
10. Ma, W.L.; Jiang, Z.C.; Li, X.F. Effect of warping shape on buckling of circular and rectangular columns under axial compression. *Appl. Math. Model.* **2021**, *89*, 1475–1490. [CrossRef]
11. Soltani, M.; Sistani, A. Elastic stability of columns with variable flexural rigidity under arbitrary axial load using the finite difference method. *Numer. Methods Civ. Eng.* **2017**, *1*, 23–31. [CrossRef]
12. Limkatanyu, S.; Sae-Long, W.; Rungamornrat, J.; Buachart, C.; Sukontasukkul, P.; Keawsawasvong, S.; Chindaprasirt, P. Bending, buckling and free vibration analyses of nanobeam-substrate medium systems. *Facta Univ. Ser. Mech. Eng.* **2022**. [CrossRef]
13. Saraçaoğlu, M.H.; Uzun, S. Stability analysis of columns with variable cross-sections. *J. Struct. Eng. Appl. Mech.* **2020**, *3*, 169–179. [CrossRef]
14. Szmidla, J.; Cieslinska-Gasior, I.; Wiktorowicz, J. The Stability of Geometrically Nonlinear Euler's Column at Stepped Variable of Flexural Rigidity. In Proceedings of the International Conference on Numerical Analysis and Applied Mathematics (ICNAAM), Rhodes, Greece, 22–28 September 2014.
15. Li, X.F.; Xi, L.Y.; Huang, Y. Stability analysis of composite columns and parameter optimization against buckling. *Compos. Part B-Eng.* **2011**, *42*, 1337–1345. [CrossRef]
16. Maalawi, K.Y. Buckling optimization of flexible columns. *Int. J. Solids Struct.* **2002**, *39*, 5865–5876. [CrossRef]
17. Yilmaz, Y.; Girgin, Z.; Evran, S. Buckling Analyses of Axially Functionally Graded Nonuniform Columns with Elastic Restraint Using a Localized Differential Quadrature Method. *Math. Probl. Eng.* **2013**, *2013*, 12. [CrossRef]

18. Alam, M.I.; Kanagarajan, B.; Jana, P. Optimal design of thin-walled open cross-section column for maximum buckling load. *Thin-Walled Struct.* **2019**, *141*, 423–434. [CrossRef]
19. *EN 1993-1-1*; Eurocode 3: Design of Steel Structures–Part 1-1: General Rules and Rules for Building. European Committe for Standardization: Brussels, Belgium, 2005.
20. Botiș, M.F.; Doșa, A. Comparative study statically determined trusses with trapezoidal and parabolic shape with large span. *IOP Conf. Ser. Mater. Sci. Eng.* **2020**, *789*, 12006. [CrossRef]

materials

MDPI

Article

Mechanism and Performance of Bituminous Mixture Using 100% Content RAP with Bio-Rejuvenated Additive (BRA)

Anqi Chen [1,2], Yazhen Qiu [1], Xiangyu Wang [1], Yuanyuan Li [1,*], Shaopeng Wu [3], Quantao Liu [3], Fan Wu [1], Jianlin Feng [1] and Zhuowei Lin [4]

[1] Wuhan Institute of Technology, School of Civil Engineering and Architecture, Wuhan 430205, China; anqi.chen@nottingham.ac.uk (A.C.); qiuyazhen111412@163.com (Y.Q.); wxy20010407@163.com (X.W.); 22004010123@stu.wit.edu.cn (F.W.); 22004010110@stu.wit.edu.cn (J.F.)

[2] Nottingham Transportation Engineering Centre, School of Civil Engineering, University of Nottingham, University Park, Nottingham NG7 2RD, UK

[3] State Key Laboratory of Silicate Materials for Architectures, Wuhan University of Technology, Wuhan 430070, China; wusp@whut.edu.cn (S.W.); liuqt@whut.edu.cn (Q.L.)

[4] School of Literatures, Languages and Cultures, The University of Edinburgh, Edinburgh EH8 9LH, UK; S2249510@ed.ac.uk

* Correspondence: liyy@wit.edu.cn

Abstract: The low RAP content, hot mixing conditions, and the addition of a high ratio of new bitumen and aggregates result in low economic and environmental benefits for current regeneration technologies. A bio-rejuvenated additive (BRA) that can fully (100%) regenerate the RAP without heating is proposed in this paper. To reveal the mechanisms of BRA-rejuvenated RAP, the effects of BRA on the chemical structure and molecular weight of the RAP were investigated using Fourier-transform infrared spectroscopy and gel permeation chromatography. The mechanical performance and water damage resistance of BRA-rejuvenated RAP were studied. Low contents of new bitumen or epoxy resin were suggested to increase the mechanical performance of 100% RAP. The results show that the 1.5% BRA-rejuvenated RAP had the best mechanical performance. The blending of BRA with recycled RAP is a completely physical process, without any chemical reactions. The molecular weight of BRA is lower than that of bitumen; it can substantially increase the content of light components in aged bitumen, and play the role of adjusting and restoring the balance of the components of aged bitumen. The mechanical performance of BRA-rejuvenated RAP is enhanced significantly by adding low dosages of new bitumen or epoxy resin.

Keywords: bio-rejuvenated additive; 100% rejuvenation; reclaimed asphalt pavement; regeneration mechanism; pavement performance

Citation: Chen, A.; Qiu, Y.; Wang, X.; Li, Y.; Wu, S.; Liu, Q.; Wu, F.; Feng, J.; Lin, Z. Mechanism and Performance of Bituminous Mixture Using 100% Content RAP with Bio-Rejuvenated Additive (BRA). *Materials* **2022**, *15*, 723. https://doi.org/10.3390/ma15030723

Academic Editor: Giovanni Polacco

Received: 1 December 2021
Accepted: 5 January 2022
Published: 18 January 2022

1. Introduction

Due to the good viscoelastic properties of bitumen, asphalt pavements are used as the main form of pavement structure worldwide [1]. Bituminous mixtures consist of aggregates, fillers, and organic bituminous binder. The bulk bituminous mixture can build strength after being paved and compacted on the road [2]. During service, the organic bituminous binder is aged by various effects, including environmental factors and vehicle loadings [3], leading to a gradual degradation of pavement performance and the occurrence of stresses in roads, such as cracks, spalling, ravelling, and potholes [4]. Typically, when the pavement condition index (PCI) of a bituminous pavement is lower than 75, the pavement must be repaired (or partially repaired) or reconstructed, resulting in a significant waste of bituminous mixtures [5]. Almost 35% of asphalt pavements in China needed to be repaired from 2016 to 2020, which produced more than 3.4 billion tons of reclaimed bituminous mixture (RAP), causing significant environmental harm and resource waste without being effectively regenerated. The construction of bituminous pavement requires large amounts

of petroleum bitumen and aggregate. In 2020, China's petroleum bitumen production was 62,796,000 tons, with approximately 85% applied to roads and airport runways, and the bitumen and aggregate consumption was estimated to be 53,377,000 tons and 1.07 billion tons, respectively [6,7]. Therefore, the recycling of RAP is of great significance, as it can not only reduce the consumption of petroleum resources, but also reduce the cost of bituminous concrete.

In recent years, the research on RAP has gained more and more attention. Yu [8,9] investigated the fracture properties of the mixtures containing up to 40% RAP with polymer-modified bituminous (PMA) binder, and the results indicated that RAP mixtures with PMA exhibited lower damage accumulation rates than common RAP mixtures. The study of Juliana [8,9] to determine the variability of RAP properties obtained from different projects or sources indicated that there is significant variability in the performance of the RAP. Han [10] studied the impact of RAP on the pavement performance of bituminous mixtures. The findings indicated that the low-temperature performance and fatigue resistance decrease with the increase in RAP content; meanwhile, the water damage resistance of bituminous mixture first increases (with 0–40% RAP), and then decreases (>40% RAP). Wu [11] indicated that the bituminous mixture containing 40% RAP had the greatest shear strength. The RAP increases the potential for low-temperature cracking in bituminous mixtures [12]. Therefore, the RAP and its dosage have a significant influence on the pavement performance [10,13–15] and workability [16,17] of bituminous mixtures. To ensure that the bituminous mixtures containing RAP have good pavement performance [18], the "Technical Specifications for Highway Asphalt Pavement Recycling" in China indicate that the optimal RAP content should be between 15% and 30%, and most uses in actual engineering also do not exceed 30% [19,20]. Currently, both hot and cold recycled RAP technologies require the addition of new materials, such as new bitumen and aggregates [21,22], and the hot mixing process requires heating of both the new materials and the RAP (old and new aggregates are heated separately, with the new aggregates being heated to a higher temperature and acting as a secondary heat source to heat the RAP). These requirements result in high energy consumption [23,24] and low-content RAP recycling [25]. To increase the used content of RAP in bituminous mixtures, it is essential to stimulate and restore the technical properties of the aged bitumen covering the surface of the RAP [26]. The cold mixing technology can reduce the energy consumption and the elimination of lightweight components during heating, which can prevent acceleration of the aging of bitumen, and also reduce the volatility of volatile organic compounds (VOCs).

A bio-rejuvenated additive (BRA) for regenerating 100% RAP with cold mixing technology is proposed in this research. After mixing the BRA with RAP, the BRA can stimulate the aged bitumen, which is coated in a thin layer on the surface of the RAP aggregate, and restores its components and technical properties. To enhance the strength and toughness of BRA-rejuvenated RAP [27], low doses of new bitumen or epoxy resin were added to the 100% cold mixing of RAP with BRA to create a spatial three-dimensional network. Fourier-transform infrared spectrometer (FTIR) and gel permeation chromatography (GPC) were used to determine the chemical structure and molecular weight distribution of BRA-rejuvenated bitumen; the results can reveal the regeneration mechanism of BRA-rejuvenated RAP. In addition, the high-temperature performance, low-temperature performance, water damage resistance, and fatigue resistance of BRA-rejuvenated RAP were investigated extensively to evaluate the pavement performance of BRA-rejuvenated RAP.

2. Materials and Experimental Methods

2.1. BRA

The BRA was produced from the waste residues during the production of cooking oil, and is a sustainable regenerative agent for aged bitumen; it was supplied by the Wuhan Daosheng Transportation Technology Co., LTD, Wuhan, China. The technical parameters of the BRA are shown in Table 1.

Table 1. Technical parameters of BRA.

Technical Parameters	Units	Results	Experimental Methods
25 °C viscosity	cP	15	ASTM D4402
60 °C viscosity	cP	6	ASTM D4402
Specific gravity at 25 °C	-	0.90	ASTM D1475
Flash point	°C	>220	ASTM D92

2.2. Mix Design of BRA-Rejuvenated RAP

The RAP was crushed and divided into four grades of 10–15 mm, 5–10 mm, 3–5 mm, and 0–3 mm; the size distribution of each grade of RAP is shown in Table 2. The bitumen contents of different sizes of RAP aggregates are shown in Table 3. The actual bitumen content of the RAP mix was 4.5%.

Table 2. Particle size distribution of each RAP class.

Sieve Size (mm)	Passing Ratio (%) of Each RAP Aggregate			
	10–15 mm	5–10 mm	3–5 mm	0–3 mm
16	100	100	100	100
13.2	86.9	100	100	100
9.5	46.1	100	100	100
4.75	22.7	33.4	100	100
2.36	12.2	13.6	26.6	99.0
1.18	9.2	10.8	15.8	76.0
0.6	7.4	9.1	13.6	54.5
0.3	6.3	7.8	12.0	42.9
0.15	5.5	6.9	10.7	30.4
0.075	3.1	3.5	6.9	13.9

Table 3. Bitumen contents of different sizes of RAP aggregates.

RAP Aggregate	10–15 mm	5–10 mm	3–5 mm	0–3 mm
Bitumen Content (%)	3.1	3.5	3.6	7.5

The low dosages of new bitumen and epoxy resin were applied as the enhancement additives, in an effort to improve the mechanical properties and road performance of the BRA-rejuvenated RAP. The dosages of new bitumen and epoxy resin are shown in Table 4. The ratio of additives was measured by the weight of the RAP.

Table 4. The dosages of new bitumen and epoxy resin.

Enhancement Additives	Dosages of Additives (%)				
New bitumen (%)	0	0.4	0.7	-	-
Epoxy resins (%)	0	0.5	0.7	1.0	1.5

2.3. Chemical Structure Analysis Tests

The Fourier-transform infrared spectrometer (*FTIR*, NICOLET 6700 FLEX, Thermo Fisher, Waltham, MA, USA) was used to determine the chemical structure of unaged bitumen, aged asphalt, BRA, and BRA-rejuvenated RAP. The testing specimens were prepared at a ratio of 1:20 with carbon disulphide (CS_2) solution according to the film method in GB/T 6040-2019, pressed into shape, and then subjected to FTIR spectroscopy. The scanning spectral wavenumber range of the test instrument was from 4000 cm^{-1} to 400 cm^{-1}.

2.4. Molecular Weight Distribution Tests

Gel permeation chromatography (GPC, Agilent PL-GPC50, Varian, PaloAlto, Santa Clara, CA, USA) was used to measure the molecular weight distribution of the BRA. Firstly, 0.4 mg of BRA and 2 mL of tetrahydrofuran solution were placed in the bottle; then, the sample solution was filtered into the test glass container using a filter with a 0.45 μm pore size microporous filter membrane, and then 50 μL of the sample was injected into the injector. The flow rate of the solution through the gel column was 1 mL/min.

2.5. Mixing and Indoor Regeneration of BRA-Rejuvenated RAP

The different grades of RAP were mixed according to the mix design of the BRA-rejuvenated RAP, and then the BRA was added to the mixing machine and mixed for 120 s. The mixing temperature was atmospheric temperature. Then, the mixture was stored at atmospheric temperature for 24 h to allow the aged bitumen to be fully activated by the BRA. After 24 h, the epoxy resin was added to the BRA-rejuvenated RAP for a second mixing, with a mixing time of 90 s. The mixture was then used to manufacture the test specimens. The Marshall specimens of BRA-rejuvenated RAP were mixed in the same way as commonly used dense-grade HMA, and the specimens were compacted 75 times for each side. The specimens were cured at 40 °C for 2 days. For the BRA-rejuvenated RAP with enhancement additives (new bitumen or epoxy resin), firstly, the new bitumen was heated to 130 °C, and then the BRA was added to the melted bitumen; we then used a high-speed shearing machine to stir the mixture for 15 min. The BRA-modified bitumen was manufactured to regenerate the RAP. The low viscosity of the BRA-modified bitumen ensured that it could mix freely with the RAP at room temperature.

2.6. Asphalt Mixture Tests

2.6.1. Water Damage Resistance Test

The Marshall test and splitting test were used to study the water damage resistance of the mixture; the loading rate was 50 mm/min. For the Marshall test, the unconditioned and the conditional Marshall specimens were held in a 25 °C water bath for 0 and 24 h, respectively; for the splitting test, the unconditioned specimens were held in a 15 °C water bath for 2 h, while the conditional specimens were first held in a 25 °C water bath for 22 h, and then in a 15 °C water bath for 2 h.

2.6.2. Low-Temperature Cracking Resistance Test

The −10 °C semi-circular bending test was used to study the low-temperature cracking resistance of the mixture, using a universal testing machine (UTM-100, IPC Global, Alpharetta, GA, USA). This test was conducted according to the criterion of ASSHTO TP 105-13. The Marshall specimen (φ101.6 mm × 63.5 mm) was cut into two semicircles, and then a 5 mm deep and 3 mm wide groove was cut at the midpoint of the specimen. The specimen was conditioned at −10 °C for 2 h, at a loading rate of 0.5 mm/min.

2.6.3. Fatigue Resistance Test

The fatigue resistance test of the mixture was carried out using a semi-circular bending test; the test was conducted using a universal testing machine ((UTM-100, IPC Global, Alpharetta, GA, USA)). The specimens of the fatigue test were manufactured according to ASSHTO TP 105-13. The stress ratios were 0.3, 0.4, 0.5, 0.6, 0.7, and 0.8. The specimens were conditioned at 25 °C for 6 h; the loading rate was 0.5 mm/min.

2.6.4. Rutting Resistance Test

The rutting resistance of BRA-rejuvenated RAP was investigated with the wheel tracking test. The size of the rutting resistance test was 300 mm × 300 mm × 50 mm. Before the test, the specimens were conditioned at 60 °C for 6 h. The contact pressure of the loading wheel and the specimen surface was 0.7 MPa, and the rolling speed was 42 times/min. The dynamic stability was calculated by taking the test data from 45 min to 60 min.

2.7. Technical Map

The Technical map of this research is shown in Figure 1.

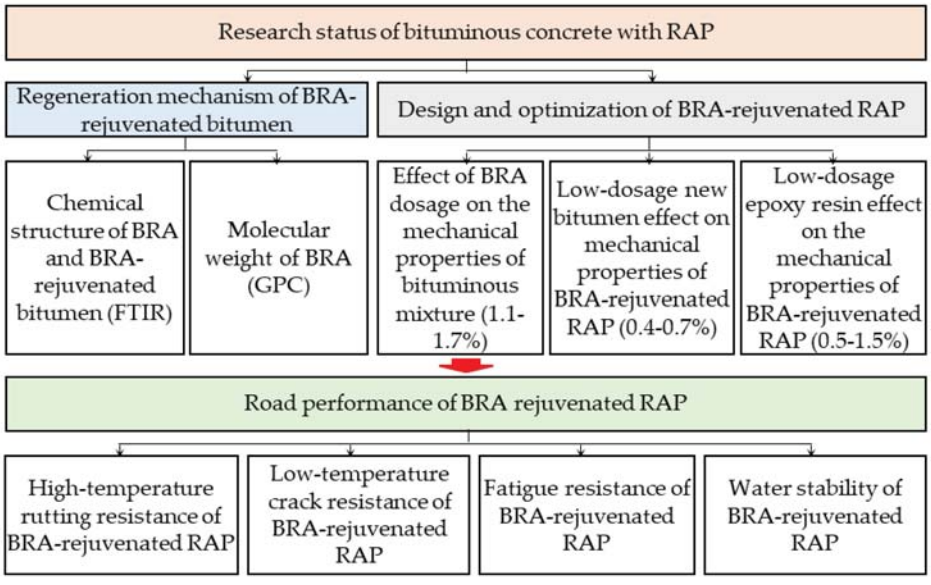

Figure 1. Technical map. (Where, BRA: Bio-rejuvenated additive; RAP: Reclaimed bituminous mixture; GPC: gel permeation chromatography; FTIR: Fourier transform infrared spectrometer).

3. Results and Discussions

3.1. Regeneration Mechanism of BRA-Rejuvenated RAP

3.1.1. Molecular Weight of BRA

The microscopic molecular structure of a substance can significantly affects its macroscopic technical properties. The bitumen's molecular weight also affects its macroscopic technical properties. Normally, the higher the average molecular weight, the worse the low-temperature performance. A previous study has shown that the chromatogram of 70# bitumen can be divided into three parts: RT < 16.7 min, 16.7 < RT < 18.8 min, and RT > 18.8 min. These three parts correspond to the large molecular size (LMS), medium molecular size (MMS), and small molecular size (SMS), respectively. Their number-average molecular weight and weight-average molecular weight are each ~434 Da. The chromatogram of BRA is shown in Figure 2. The molecular weight of BRA is much lower than that of the 70# bitumen, with a number-average molecular weight of 500 Da, and a weight-average molecular weight of 512 Da.

The chemical composition of bitumen can be changed under the action of heating, oxygen, and ultraviolet light [28,29]. After aging, the molecules of bitumen tend to increase, and the light components of bitumen (saturates and aromatics) convert to heavy components (resins and asphaltenes) [30]. The changes in the chemical components in bitumen during aging damage the component balance of bitumen, resulting in an attenuation of the macroscopic physical and rheological properties of the bitumen. For instance, with respect to physical properties, the softening point and viscosity of bitumen increase, while the penetration and ductility decrease; in terms of the rheological properties, the complex modulus of bitumen increases, while the phase angle decreases. The molecular weight of BRA is similar to that of the light components of bitumen; it can increase the contents of the light components (saturates and aromatics) of bitumen and reduce the relative contents of resins and asphaltenes. Therefore, the BRA can rebalance the chemical components of the aged bitumen by decreasing the relative content of large molecules and heavy components.

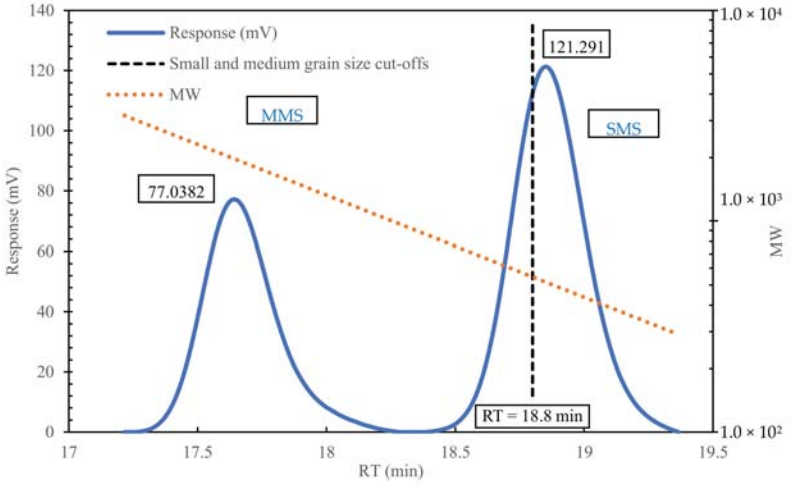

Figure 2. Gel permeation chromatography (GPC) analysis diagram of BRA.

3.1.2. Chemical Structure of BRA-Rejuvenated RAP

FTIR spectroscopy was used to investigate the chemical structure of the bitumen, as shown in Figure 3, where the absorption bands at around 1169 cm^{-1} and 1740 cm^{-1} belong to the characteristic absorption bands of BRA, which can only be found in the FTIR spectra of BRA and BRA-rejuvenated RAP; they cannot be found in the FTIR spectra of unaged bitumen or aged bitumen without BRA, showing that in the BRA-rejuvenated RAP, the BRA was successfully mixed with the aged bitumen. In addition, the FTIR spectrum of the BRA-rejuvenated RAP does not show any absorption band at a new wavenumber, but only a simple superposition of the bitumen and BRA absorption bands, indicating that no chemical reaction between the aged bitumen in the RAP and BRA occurred during the blending process of BRA and RAP. The mixing process of RAP and BRA is a physical process; it takes place mainly due to the penetration and diffusion of BRA into the aged bitumen, after which the BRA can gradually rebalance the chemical components and restore the performance of the aged bitumen covering the surface of the RAP.

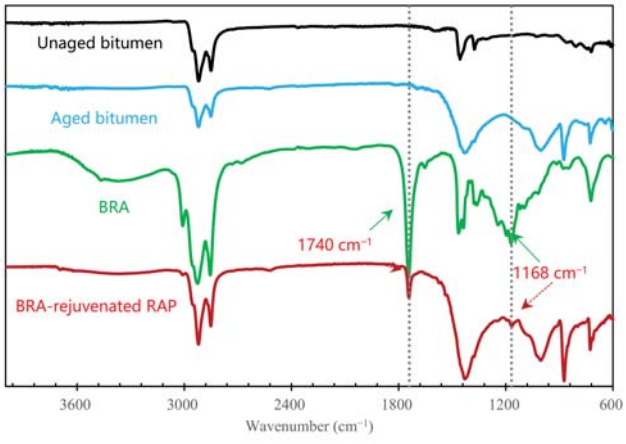

Figure 3. FTIR spectra of BRA and bituminous binders.

3.2. Design and Optimisation of BRA-Rejuvenated RAP

3.2.1. Effect of BRA Dosage on the Mechanical Properties of Bituminous Mixture

The early-stage mechanical properties of BRA-rejuvenated RAP were evaluated by the Marshall strength; the results are shown in Figure 4. As shown in Figure 4, when the BRA dosage was lower than 1.5%, the Marshall stability of the BRA-rejuvenated RAP increased with the increase in the BRA dosage; when the BRA content was higher than 1.5%, the Marshall stability of the BRA-rejuvenated RAP decreased with increasing BRA content. The mixture with 1.5% BRA had the highest Marshall stability, indicating that the BRA-rejuvenated RAP with 1.5% BRA had the best mechanical properties. This is because, on the one hand, BRA can activate the aged bitumen and rebalance its components, while on the other hand, the BRA can soften the aged bitumen, and offer the workability of RAP; the softening effect of BRA on the aged bitumen is also good for the compaction of BRA-rejuvenated RAP. When the BRA dosage is higher than 1.5%, the softening and viscosity reduction effects of BRA on the aged bitumen are dominant, being more obvious than the benefits in terms of workability, and decreasing the strength of the BRA-rejuvenated RAP. Thus, 1.5% BRA was suggested to be the optimal dosage for the rejuvenation of RAP.

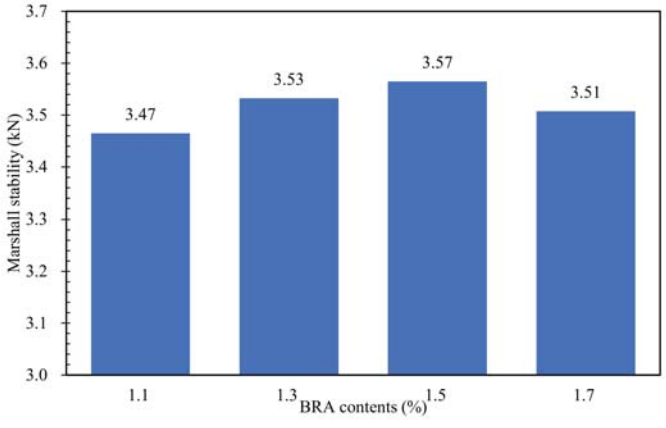

Figure 4. Effects of BRA dosages on the mechanical properties of BRA-rejuvenated RAP.

3.2.2. Effects of Low Dosages of New Bitumen on the Mechanical Properties of BRA-Rejuvenated RAP

The results of the Marshall stability and splitting strength of BRA-rejuvenated RAP with low dosages of new bitumen are shown in Figure 5. As shown in Figure 5, the Marshall stability of BRA-rejuvenated RAP can satisfy the requirement of cold-recycled RAP (>3 kN) in the "Technical Specifications for Highway Asphalt Pavement Recycling" (JTG/T 5521—2019). After adding 0.7% new bitumen, the unconditional and conditional Marshall stability of BRA-rejuvenated RAP increased by 50.2% and 52.5%, respectively. Meanwhile, the unconditional and conditional splitting strength each increased by 195.5%. The results indicate that the conditioned and unconditioned Marshall stability and splitting strength of the BRA-rejuvenated RAP can be significantly increased by the addition of low dosages of new bitumen, and the improvement in mechanical properties was more significant with higher content of new bitumen.

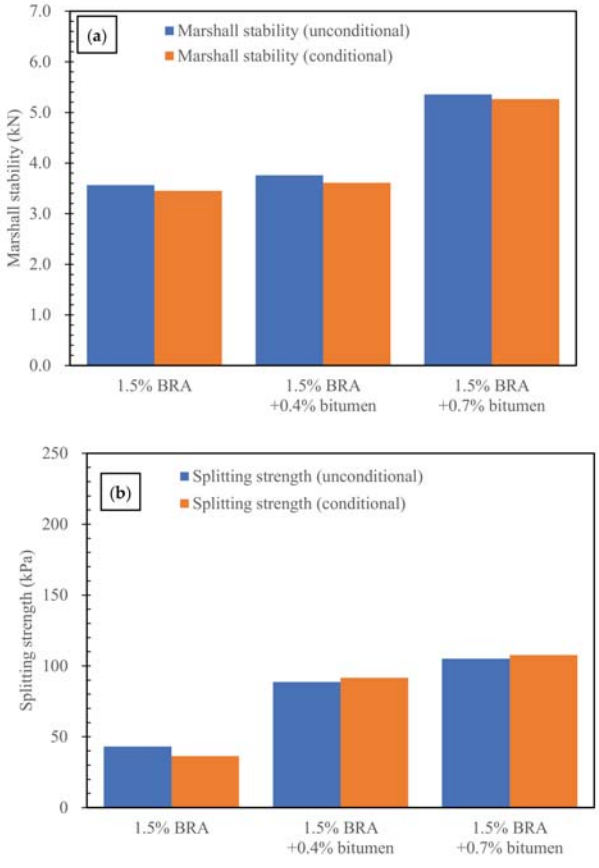

Figure 5. Effects of new bitumen on the mechanical properties of BRA-rejuvenated RAP: (**a**) Marshall stability; (**b**) splitting strength.

3.2.3. Effects of Low Dosages of Epoxy Resin on the Mechanical Properties of BRA-Rejuvenated RAP

Figure 6 shows the results of the mechanical properties of the BRA-rejuvenated RAP with different dosages of epoxy resin. As shown in Figure 6, the epoxy resin can significantly improve the mechanical properties of BRA-rejuvenated RAP, and the improvement increases gradually with the increase in the epoxy resin dosage. The 0.5%, 0.7%, 1.0%, and 1.5% epoxy resin increased the unconditional Marshall stability by 54.0%, 66.0%, 87.8%, and 110.7%, respectively, and increased the unconditional splitting strength by 315.5%, 321.8%, 389.8%, and 394.4%, respectively. Compared with the same content of new bitumen, the beneficial effects of the epoxy resin on the mechanical properties of the BRA-rejuvenated RAP are more obvious. The reason for this is that, after curing, the epoxy resin has a high-strength and high-elasticity effect, and acts as a skeleton stiffener in the BRA-rejuvenated asphalt concrete, resulting in improvement of the early-stage mechanical properties of the recycled RAP.

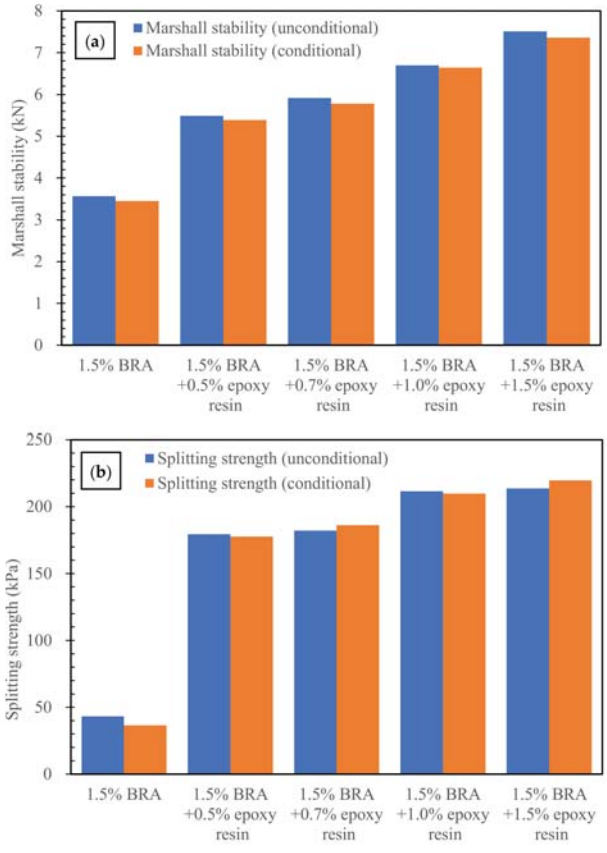

Figure 6. Effects of low dosages of epoxy resin on the mechanical properties of BRA-rejuvenated RAP: (**a**) Marshall stability; (**b**) splitting strength.

Taking the above results of the mechanical properties of the RAP into consideration, the epoxy resin and BRA play different roles in the mixture. Due to the low molecular weight of BRA, the function of BRA is to soften the aged bitumen and decrease its viscosity. Another main function of BRA is to rebalance the chemical components of aged bitumen covering the surface of RAP, and to restore the technical performance of aged bitumen. Therefore, the RAP can be compacted at room temperature. The results show that all of the RAP samples could be compacted without heating. However, due to the low viscosity of bitumen, after curing, the mechanical strength of the RAP mixtures was not high. In order to enhance the mechanical strength of BRA-rejuvenated RAP, the epoxy resin was added to the mixture as a kind of reinforcing agent. After being mixed evenly in the mixture, the epoxy resin acted as a skeleton reinforcement, significantly improving the strength of BRA-rejuvenated RAP.

3.3. Road Performance of BRA-Rejuvenated RAP

3.3.1. Water Damage Resistance of BRA-Rejuvenated RAP

The water damage resistance of BRA-rejuvenated RAP was investigated by using the water-immersed Marshall test and the freeze–thaw indirect tensile strength test [31]. The water-immersed residual strength (IRS) and freeze–thaw indirect tensile strength ratio (TSR) can be used to evaluate the water damage resistance of BRA-rejuvenated RAP [32];

the results are shown in Tables 5 and 6. According to the "Technical Specifications for Construction of Highway Asphalt Pavement" (JTG F40-2004) and "Technical Specifications for Highway Asphalt Pavement Recycling" (JTG/T 5521—2019) in China, in order to satisfy the water damage resistance requirement, the IRS and TSR values of hot-mixed bituminous concrete should be no less than 80% and 75%, respectively. As shown in Tables 5 and 6, the IRS and TSR values of BRA-rejuvenated RAP were 96.8% and 84.4%, respectively. These values are even higher than the water damage resistance requirements of hot-mixed bituminous concrete; therefore, the BRA-rejuvenated RAP has a good water damage resistance. In addition, the IRS values of BRA-rejuvenated RAP with low dosages of new bitumen or epoxy resin generally increase, and eventually approach 100%. With the addition of low dosages of new bitumen or epoxy resin, the TSR values of BRA-rejuvenated RAP increase significantly—0.7% new bitumen and 1.5% epoxy resin improve the TSR values of BRA-rejuvenated RAP by 18.0% and 12.8%, respectively. The results indicate that low dosages of new bitumen or epoxy resin can further improve the water damage resistance of BRA-rejuvenated RAP.

Table 5. Effects of new bitumen on the water damage resistance of BRA-rejuvenated RAP.

Dosage of New Bitumen (%)	0	0.4	0.7
IRS (%)	96.8	96.0	98.3
TSR (%)	84.4	103.4	102.4

Table 6. Effects of epoxy resin on the water damage resistance of BRA-rejuvenated RAP.

Dosage of Epoxy Resin (%)	0	0.5	0.7	1.0	1.5
IRS (%)	96.8	98.2	97.7	99.2	98.0
TSR (%)	84.4	99.0	97.9	99.2	97.2

3.3.2. Low-Temperature Cracking Resistance of BRA-Rejuvenated RAP

The −10 °C SCB test was conducted to investigate the low-temperature cracking resistance of BRA-rejuvenated RAP, and the results are shown in Figure 7 and Table 7. From Figure 7 and Table 7, we can see that the maximum loadings of the BRA-rejuvenated RAP with 0.4% new bitumen, 0.7% epoxy resin, and 1.5% epoxy resin were 511.9 N, 758.6 N, and 1234.2 N, respectively, indicating that the 1.5%-epoxy-resin-reinforced BRA-rejuvenated RAP has the maximum bending and tensile strength. The differences in the the fracture work and fracture energy of BRA-rejuvenated RAP with 0.4% new bitumen and 0.7% epoxy resin was not significant; compared with them, the 1.5%-epoxy-resin-reinforced BRA-rejuvenated RAP showed an increase of 78.3% and 84.5%, respectively, indicating that the low-temperature performance of the 0.4%-new-bitumen- and 0.7%-epoxy-resin-reinforced RAP was essentially the same, while the 1.5%-epoxy-resin-reinforced RAP showed a significant increase.

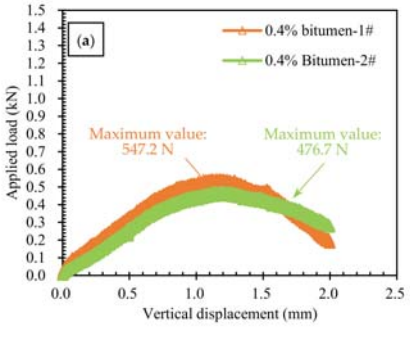

Figure 7. *Cont.*

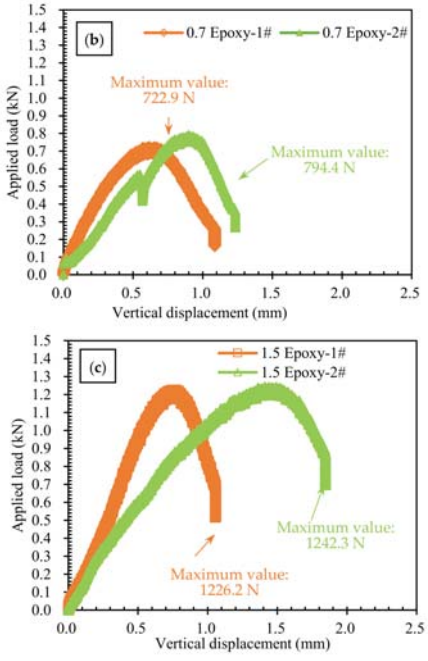

Figure 7. Displacement–load curve of −10 °C SCB test: (**a**) 0.4% bitumen; (**b**) 0.7% epoxy resin; (**c**) 1.5% epoxy resin.

Table 7. Average fracture energy of −10 °C SCB test.

Additives	Dosages (%)	Maximum Loading (N)	Fracture Work (J)	Fracture Energy (J/m^2)
New bitumen	0.4	511.9	6.0	2101.2
Epoxy resin	0.7	758.6	5.8	2045.5
Epoxy resin	1.5	1234.2	10.7	3739.9

3.3.3. Fatigue Resistance of BRA-Rejuvenated RAP

Figure 8 shows the fatigue life results of BRA-rejuvenated RAP under different stress ratio conditions. As shown in Figure 8, compared with the 0.4%-new-bitumen-reinforced BRA-rejuvenated RAP, the fatigue resistance of the BRA-rejuvenated RAP was significantly improved by the addition of 0.7% and 1.5% epoxy resin. At a stress ratio of 0.4, the fatigue life of the 0.7%- and 1.5%-epoxy-resin-reinforced BRA-rejuvenated RAP was 1.6 times and 38.7 times that of BRA-rejuvenated RAP with 0.4% new bitumen, respectively. This indicates that the 0.7% and 1.5% epoxy resin are much more effective in improving the fatigue resistance of the BRA-rejuvenated RAP than the 0.4% new bitumen. The fatigue life of 0.7%-epoxy-resin-reinforced BRA-rejuvenated RAP is the least sensitive to load, which is beneficial to the fatigue performance of the road under large load adjustment. In addition, the fatigue curves can observe a change in the behaviour of epoxy-resin-reinforced BRA-rejuvenated RAP relative to the other two curves. The 1.5%-epoxy-resin-reinforced BRA-rejuvenated RAP has the highest sensitivity to stress ratio. The reason for this is that the mechanical strength of BRA-rejuvenated RAP is significantly enhanced by the 1.5% epoxy resin, and it is stiffer than the other two mixtures with 0% and 0.7% epoxy resin. The stiffness effect of 1.5% epoxy resin exerts a more obvious effect on the fatigue behaviour of

BRA-rejuvenated BRA, but at the 0.7 stress ratio, it is still greater than 0.7%-epoxy-resin-reinforced BRA-rejuvenated RAP.

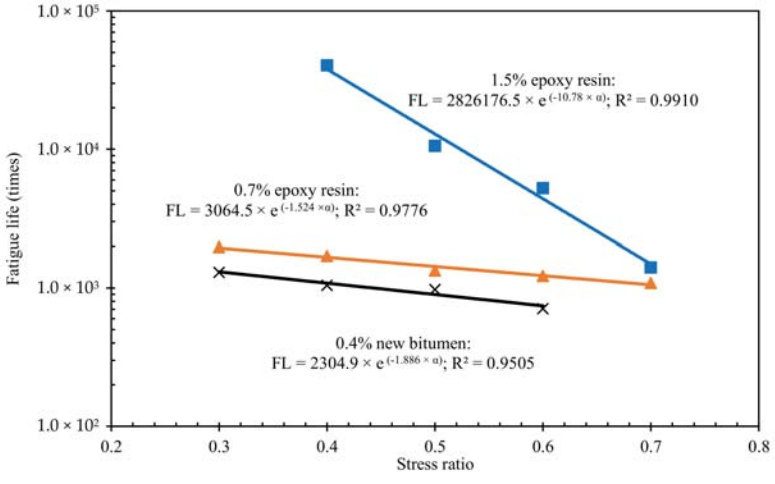

Figure 8. Fatigue life of the BRA-rejuvenated RAP.

3.3.4. High-Temperature Rutting Resistance of BRA-Rejuvenated RAP

The lack of high-temperature rutting resistance is a typical problem for conventional cold-recycled and cold-mixed asphalt mixtures [33]. The high-temperature rutting resistance of BRA-rejuvenated RAP was investigated using the wheel tracking test, and the results are shown in Figure 9. The dynamic stability of the 1.5% BRA-rejuvenated RAP was only 451 cycles/mm, while after the addition of 1.5% epoxy resin and the combined addition of 0.4% new bitumen + 1.0% epoxy resin, the dynamic stability increased to 9545 cycles/mm and 30,000 cycles/mm, respectively. It can be seen that the rutting resistance of the BRA-rejuvenated RAP improved significantly with the addition of low doses of new bitumen and epoxy resin. The reason for this is that, after mixing and rejuvenation of the RAP with 1.5% BRA, there is still a very small amount of aggregate surface that is not covered with bitumen, and after compaction, this type of aggregate becomes the weak point in the BRA-rejuvenated bituminous concrete, resulting in insufficient rutting resistance. The addition of low doses of new bitumen enables the new asphalt to further coat the exposed aggregates and reduce the number of weak points in the bituminous concrete. Based on this, with the composite addition of epoxy resin, the epoxy resin acts as a skeleton reinforcement; therefore, the high-temperature rutting resistance of BRA-rejuvenated RAP can be improved significantly.

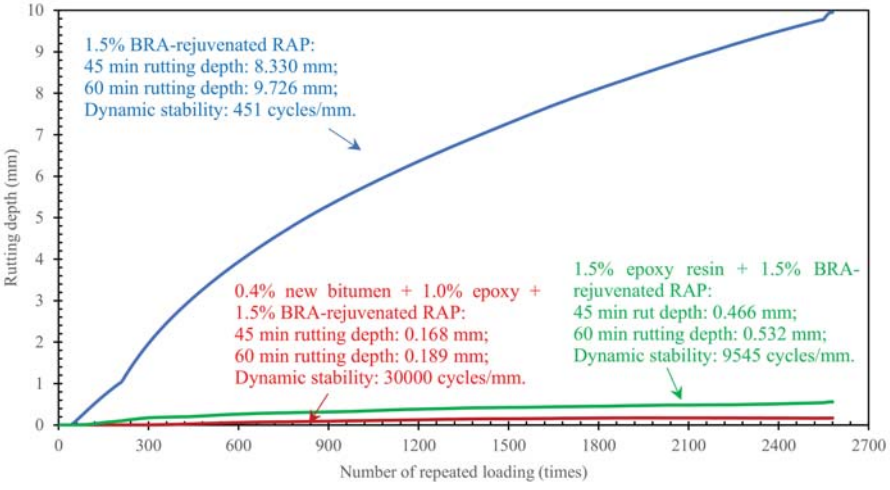

Figure 9. Rutting depth of BRA-rejuvenated RAP.

4. Conclusions

The chemical structure and molecular weight distribution of BRA and bitumen were investigated by FTIR and GPC to reveal the regeneration mechanism of BRA-rejuvenated RAP. In addition, the mechanical and road properties of BRA-rejuvenated RAP were investigated, and technologies were proposed to improve the road properties of BRA-rejuvenated RAP. The main conclusions are as follows:

(1) The molecular weight of BRA is similar to that of the light components of bitumen; it can increase the contents of light components and reduce the contents of heavy components of aged bitumen. The mixing process of RAP and BRA is a physical process; it mainly takes place due to the penetration and diffusion of BRA into the aged bitumen, after which the BRA can gradually rebalance the chemical components and restore the performance of the aged bitumen covering the surface of the RAP;

(2) The mixture with 1.5% BRA has the highest Marshall stability, indicating that the bituminous mixture has the best cohesive and mechanical properties. The early-stage mechanical properties (Marshall stability and splitting strength) of BRA-rejuvenated RAP can be significantly improved by the addition of low dosages of new bitumen (0.4%) and epoxy resin (0.5–1.5%);

(3) The IRS and TSR values of BRA-rejuvenated RAP are even higher than the water damage resistance requirements of HMA (no less than 80% and 75%, respectively), indicating that the BRA-rejuvenated RAP has good water damage resistance. The 0.4%-new-bitumen- and 0.7%-epoxy-resin-reinforced BRA-rejuvenated RAP had essentially the same low-temperature cracking resistance, while 1.5% epoxy resin reinforcement was significantly better. In comparison, the 0.7% and 1.5% epoxy resin reinforcements were much more effective in improving the fatigue resistance of the BRA-rejuvenated RAP than the 0.4% new bitumen. The rutting resistance of the BRA-rejuvenated RAP can be significantly improved by the addition of low dosages of new bitumen and epoxy resin;

(4) The epoxy resin and BRA play different roles in the BRA-rejuvenated RAP. Due to the low molecular weight of BRA, the function of BRA is to soften the aged bitumen and decrease its viscosity. Another main function of BRA is to rebalance the chemical components of aged bitumen covering the surface of RAP, and to restore the technical performance of aged bitumen. Therefore, the RAP can be compacted without heating; however, due to the low viscosity of bitumen, after curing, the mechanical strength of the RAP mixture is not high. The epoxy resin added to the mixture acts as a kind of

reinforcing agent, and forms a skeleton that can significantly improve the strength of the BRA-rejuvenated RAP;

(5) It is feasible to use BRA as a regenerating agent to achieve 100% regeneration of RAP. In addition, the addition of low dosages of new bitumen or epoxy resin can further improve the road performance of BRA-rejuvenated RAP.

Author Contributions: A.C.: conceptualisation, methodology, data curation, writing—original draft preparation, language editing; Y.Q.: methodology, data curation, writing—original draft preparation; X.W.: methodology, data curation, writing—original draft preparation; Y.L.: methodology, investigation, data curation, software, validation, writing—review and editing, funding acquisition, supervision; S.W.: methodology, writing—review and editing; Q.L.: data curation, software, validation, writing—review and editing. F.W.: data curation, writing—original draft preparation; J.F.: data curation, writing—original draft preparation; Z.L.: Visualization, Writing—Reviewing and Editing. All authors have read and agreed to the published version of the manuscript.

Funding: The authors acknowledge the financial support provided by the National Natural Science Foundation of China (No. 52108415), the National Key Research and Development Program of China (No. 2018YFB1600200), the Natural Science Foundation of China (No. 51778515), the Key Technical Innovation Projects of Hubei Province (No. 2019AEE023), the Plan of Outstanding Young and Middle-Aged Scientific and Technological Innovation Team in Universities of Hubei Province (No. T2020010), the Scientific Research Fund of Hunan Provincial Education Department (No. 18A117), and the Key R&D Program of Hubei Province (No. 2020BCB064); the project was also supported by the Science and Technology Projects Fund of Changsha City (No. kq2004065), and with help conducting the tests from Shiyanjia Lab (Available online: https://www.shiyanjia.com/all.html (accessed on 18 December 2021)).

Institutional Review Board Statement: Not applicable.

Informed Consent Statement: Not applicable.

Data Availability Statement: All the data is available within the manuscript.

Conflicts of Interest: The authors declare no conflict of interest.

References

1. Lei, L.; Li, D.; Chen, Y.; Tian, Y.; Pei, J. Dynamic chemistry based self-healing of asphalt modified by diselenide-crosslinked polyurethane elastomer. *Constr. Build. Mater.* **2021**, *293*, 123480.
2. Li, Y.; Feng, J.; Yang, F.; Wu, S.; Liu, Q.; Bai, T.; Liu, Z.; Li, C.; Gu, D.; Chen, A.; et al. Gradient aging behaviors of asphalt aged by ultraviolet lights with various intensities. *Constr. Build. Mater.* **2021**, *295*, 123618. [CrossRef]
3. Hu, J.; Wu, S.; Liu, Q.; Maria, G.H.; Zeng, W.; Shuai, N.; Wan, J.; Dong, Z.; Li, Y.J.M. The Effect of Ultraviolet Radiation on Bitumen Aging Depth. *Materials* **2018**, *11*, 747. [CrossRef] [PubMed]
4. Li, Y.; Wu, S.; Liu, Q.; Dai, Y.; Li, C.; Li, H.; Nie, S.; Song, W.J.C.; Materials, B. Aging degradation of asphalt binder by narrow-band UV radiations with a range of dominant wavelengths. *Constr. Build. Mater.* **2019**, *220*, 637–650. [CrossRef]
5. China, M.o.H.a.U.-R.D.o.t.P.s.R.o. Technical Code of Maintenance for Urban Road; 2016; CJJ 36-2016. Available online: http://www.zzszgl.com/Download/CJJ36-2016.pdf (accessed on 7 May 2021).
6. Gao, J.; Guo, H.; Wang, X.; Wang, P.; Wei, Y.; Wang, Z.; Huang, Y.; Yang, B. Microwave deicing for asphalt mixture containing steel wool fibers. *J. Clean. Prod.* **2019**, *206*, 1110–1122. [CrossRef]
7. Zhou, X.; Ma, B.; Wang, X.; Chen, S. Study of the Interlocking Filling–Graded Composition Design Method of an Asphalt Mixture Mixed with Shape-Memory Epoxy Resin Fibers. *J. Mater. Civ. Eng.* **2020**, *32*, 04020186. [CrossRef]
8. Yan, Y.; Roque, R.; Hernando, D.; Chun, S.J.R.M.; Design, P. Cracking performance characterisation of asphalt mixtures containing reclaimed asphalt pavement with hybrid binder. *Road Mater. Pavement Des.* **2019**, *20*, 347–366. [CrossRef]
9. Montañez, J.; Caro, S.; Carrizosa, D.; Calvo, A.; Sánchez, X. Variability of the mechanical properties of Reclaimed Asphalt Pavement (RAP) obtained from different sources. *Constr. Build. Mater.* **2020**, *230*, 116968. [CrossRef]
10. Han, S.; Cheng, X.; Liu, Y.; Zhang, Y. Laboratory Performance of Hot Mix Asphalt with High Reclaimed Asphalt Pavement (RAP) and Fine Reclaimed Asphalt Pavement (FRAP) Content. *Materials* **2019**, *12*, 2536. [CrossRef]
11. Wu, Z.; Zhang, C.; Xiao, P.; Li, B.; Kang, A. Performance Characterization of Hot Mix Asphalt with High RAP Content and Basalt Fiber. *Materials* **2020**, *13*, 3145. [CrossRef]
12. Ozer, H.; Al-Qadi, I.L.; Carpenter, S.H.; Aurangzeb, Q.; Roberts, G.; Trepanier, J. Evaluation of RAP impact on hot-mix asphalt design and performance. *Asph. Paving Technol. Proc.* **2009**, *78*, 317–348.
13. Ghabchi, R.; Singh, D.; Zaman, M.; Hossain, Z. Laboratory characterisation of asphalt mixes containing RAP and RAS. *Int. J. Pavement Eng.* **2016**, *17*, 829–846. [CrossRef]

14. Asib, A.; Romero, P.; Safazadeh, F.J.C.; Materials, B. An equivalence between methods of aging for determining the low-temperature performance of hot-mix asphalt concrete mixtures containing reclaimed asphalt pavement. *Constr. Build. Mater.* **2019**, *223*, 198–209. [CrossRef]
15. Dissertations, M.E.J.; Gradworks, T. *Performance of Plant Produced HMA Mixtures with High RAP Content in Terms of Low Temperature Cracking, Fatigue Cracking, and Moisture Induced Damage*; University of New Hampshire: Durham, NH, USA, 2012.
16. Abdalfattah, I.A.; Mogawer, W.S.; Stuart, K. Quantification of the Degree of Blending in Hot-Mix Asphalt (HMA) with Reclaimed Asphalt Pavement (RAP) Using Energy Dispersive X-Ray Spectroscopy (EDX) Analysis. *J. Clean. Prod.* **2021**, *294*, 126261. [CrossRef]
17. Pan, Y.; Zhao, Y.; Guo, P. Effects of Reclaimed Asphalt Pavement Contents on Construction Characteristics of Asphalt Mixtures. In Proceedings of the 19th COTA International Conference of Transportation Professionals, Nanjing, China, 6–8 July 2019.
18. Zhou, Z.; Gu, X.; Jiang, J.; Ni, F.; Jiang, Y.J.C.; Materials, B. Fatigue cracking performance evaluation of laboratory-produced polymer modified asphalt mixture containing reclaimed asphalt pavement material. *Constr. Build. Mater.* **2019**, *216*, 379–389. [CrossRef]
19. Xie, Z.; Taylor, A.J.; Tran, N.; Kim, S. Evaluation of Different VMA Estimation Methods for Asphalt Mixtures Containing RAP. *J. Mater. Civ. Eng.* **2020**, *32*, 04020162. [CrossRef]
20. Hansen, K.R.; Copeland, A.; Ross, T.C. *Asphalt Pavement Industry Survey on Recycled Materials and Warm-Mix Asphalt Usage 2016 (Information Series 138) 7th Annual Survey*; National Asphalt Pavement Association: Lanham, MD, USA, 2017. Available online: https://www.asphaltpavement.org/uploads/documents/IS138/IS138-2016_RAP-RAS-WMA_Survey_Final.pdf (accessed on 7 May 2021).
21. Ahmed, A.; Nick, T.; Davide, L.P.J.M. Design considerations of high RAP-content asphalt produced at reduced temperatures. *Mater. Struct.* **2018**, *51*, 91.
22. Dong, F.; Xin, Y.; Bo, X.; Wang, T.J.C.; Materials, B. Comparison of high temperature performance and microstructure for foamed WMA and HMA with RAP binder. *Constr. Build. Mater.* **2017**, *134*, 594–601. [CrossRef]
23. Yang, E.; Xu, J.; Luo, H.; Huang, B.; Li, J.Q.; Qiu, Y. Performance comparison of warm mix asphalt for plateau area Performance comparison of warm mix asphalt for plateau area. *Road Mater. Pavement Des.* **2020**, *23*, 211–221. [CrossRef]
24. Vaitkus, A.; Čygas, D.; Laurinavičius, A.; Perveneckas, Z. Analysis and evaluation of possibilities for the use of warm mix asphalt in Lithuania. *Balt. J. Road Bridge Eng.* **2009**, *4*, 80–86. [CrossRef]
25. Pan, Y.; Li, J.; Yang, T.; Liu, G.; Zhou, J.; Guo, P.; Zhao, Y. Optimization of gradation design of recycled asphalt mixtures based on fractal and Mohr-Coulomb theories. *Constr. Build. Mater.* **2020**, *248*, 118649. [CrossRef]
26. Zaumanis, M.; Mallick, R.B.; Frank, R. Evaluation of different recycling agents for restoring aged asphalt binder and performance of 100 % recycled asphalt. *Mater. Struct.* **2015**, *48*, 2475–2488. [CrossRef]
27. Peiliang, C.; Jianying, Y.; Shuanfa, C. Effects of epoxy resin contents on the rheological properties of epoxy-asphalt blends. *J. Appl. Polym. Sci.* **2010**, *118*, 3678–3684. [CrossRef]
28. Li, Y.; Wu, S.; Liu, Q.; Nie, S.; Li, H.; Dai, Y.; Pang, L.; Li, C.; Zhang, A.J.C.; Materials, B. Field evaluation of LDHs effect on the aging resistance of asphalt concrete after four years of road service. *Constr. Build. Mater.* **2019**, *208*, 192–203. [CrossRef]
29. Li, Y.; Wu, S.; Dai, Y.; Pang, L.; Liu, Q.; Nie, S.; Li, H.; Wang, Z.; Materials, B. Laboratory and field evaluation of sodium stearate organically modified LDHs effect on the anti aging performance of asphalt mixtures. *Constr. Build. Mater.* **2018**, *189*, 366–374. [CrossRef]
30. Li, Y.; Wu, S.; Pang, L.; Liu, Q.; Wang, Z.; Zhang, A.; Materials, B. Investigation of the effect of Mg-Al-LDH on pavement performance and aging resistance of styrene-butadiene-styrene modified asphalt. *Constr. Build. Mater.* **2018**, *172*, 584–596. [CrossRef]
31. Li, C.; Zou, J.; Ke, W.; Wang, G.; Li, C. Laboratory evaluation of asphalt binder modified by waste carbon particles (WCP) reclaimed from printers. *Int. J. Pavement Res. Technol.* **2021**, *14*, 204–212. [CrossRef]
32. Zhang, J.; Li, P.; Sun, C.; Liang, M.; Li, Y.; Yao, Z.; Zhang, X. Effects of Composite Warm Mix Additive (CAR) on the Physical and Rheological Performance of Bitumen and the Pavement Performance of Its Concrete. *Materials* **2019**, *12*, 3916. [CrossRef]
33. Chen, T.; Ma, T.; Huang, X.; Ma, S.; Wu, S. Microstructure of synthetic composite interfaces and verification of mixing order in cold-recycled asphalt emulsion mixture. *J. Clean. Prod.* **2020**, *263*, 121467. [CrossRef]

materials

MDPI

Article

Study of the Interfacial Bond Behavior between CFRP Grid–PCM Reinforcing Layer and Concrete via a Simplified Mechanical Model

Huijuan Dai [1], Bo Wang [2,*], Jiawei Zhang [2], Junlei Zhang [3] and Kimitaka Uji [3]

[1] School of Civil Engineering, Xi'an University of Science and Technology, Xi'an 710054, China; daihuijuan1985@163.com
[2] School of Civil Engineering, Chang'an University, Xi'an 710061, China; zaq197125zaq@163.com
[3] Department of Civil and Environmental Engineering, Tokyo Metropolitan University, Tokyo 192-0397, Japan; zhangjunlei2009@yahoo.co.jp (J.Z.); k.uji@tmu.ac.jp (K.U.)
* Correspondence: chnwangbo@chd.edu.cn; Tel.: +86-137-2045-3378

Abstract: This paper presents the results of pull-out tests conducted to investigate the interfacial bond behavior between a carbon-fiber-reinforced polymer (CFRP) grid–polymer cement mortar (PCM) reinforcing layer and existing concrete, and proposes a simplified mechanical model to further study the interface bond mechanism. Four specimens composed of a CFRP grid, PCM, and concrete were tested. The influence of the type of CFRP grid and the grid interval on the interface bond behavior was discussed. The failure patterns, maximum tensile loads, and CFRP grid strains were obtained. The change process of interface bond stress was investigated based on the grid strain analysis. In addition, the simplified mechanical model and finite element model (FEM) were emphatically established, and the adaptability of the simplified mechanical model was validated through the comparative analysis between the FEM results and the test results. The research results indicate that a CFRP grid with a larger cross-sectional area and smaller grid interval could effectively improve the interface bond behavior. The tensile stress was gradually transferred from the loaded edge to the free edge in the CFRP grid. The interface bond behavior was mainly dependent on the anchorage action of the CFRP grid in the PCM, and the bond action between the PCM and the concrete. The FEM results were consistent with the test results, and the simplified mechanical model with nonlinear springs could well describe the interface bond mechanism between the CFRP grid–PCM reinforcing layer and concrete.

Keywords: CFRP grid; PCM; interface; mechanical model; pull-out test; finite element analysis

Citation: Dai, H.; Wang, B.; Zhang, J.; Zhang, J.; Uji, K. Study of the Interfacial Bond Behavior between CFRP Grid–PCM Reinforcing Layer and Concrete via a Simplified Mechanical Model. *Materials* **2021**, *14*, 7053. https://doi.org/10.3390/ma14227053

Academic Editor: Krzysztof Schabowicz

Received: 11 October 2021
Accepted: 17 November 2021
Published: 20 November 2021

1. Introduction

Carbon-fiber-reinforced polymer (CFRP) has been widely used in the repair and strengthening of concrete structures, because of its favorable and prominent properties (e.g., high strength-to-weight ratio, excellent corrosion resistance, and durability) [1–3]. Recently, a new strengthening technique for concrete structures using CFRP grids and sprayed PCM has caught the attention and interest of the civil engineering realm [4–7]. CFRP grid is made from continuous impregnated high-strength carbon fiber roving alternating in both longitudinal and transverse directions to form a cross-laminated grid structure with a certain rigidity, as shown in Figure 1; it has unique mechanical characteristics compared to other CFRP composites (e.g., CFRP sheets, CFRP plates and strips); that is, the horizontal grids and vertical grids jointly resist the external loads applied on the CFRP grid. Some investigations have found that CFRP grid has a satisfactory strengthening effect in improving the mechanical performance of existing concrete structures, including beams, slabs, and columns in concrete member, as well as large-span structures such as bridges and tunnels [8–11]. In addition, CFRP grid can be applied to strengthen underwater

structures, because of its good bond performance with existing concrete in low-temperature and moist environments [8,12]. Currently, FRP sheets and plates are mainly used as the strengthening materials in the FRP-strengthening technique. However, there are a few drawbacks for the FRP sheets/plates jacketing method, such as the insufficient bond strength between FRP sheets/plates and existing concrete in wet environments. For this new strengthening method, the drawbacks can be effectively avoided by riveting the CFRP grid to the concrete surface. Moreover, as a protective (thermal insulation) system for CFRP grid, PCM significantly improves the peeling resistance, fire resistance, and durability [5,6,13]. PCM, a new type of modified mortar, is formed by adding a certain content of organic polymer to the conventional cement mortar; it has some advantages over the conventional cement mortar, such as high tensile strength, low elastic modulus, favorable impermeability, and frost resistance, as well as excellent bond behavior with the existing concrete [5,6,14,15]. In this new strengthening method with CFRP grid and sprayed PCM, the CFRP grid is installed on the surface of existing concrete via a rivet anchor, and PCM is sprayed on the outside surface of the CFRP grid and concrete. By means of this construction technique, the CFRP grid–PCM reinforcing layer and the existing concrete structure would be given the integrity to resist external force [16–21], which could improve the bearing capacity, stiffness, and durability of existing concrete structures, as shown in Figure 2. Compared with the conventional strengthening method using steel or FRP plates for jacketing, this new strengthening method with CFRP grid and a PCM reinforcing layer has some technical advantages, including lesser thickness of the reinforcing layer (10–20 mm), more convenient construction, lower costs and environmental dependence, etc. [5,6].

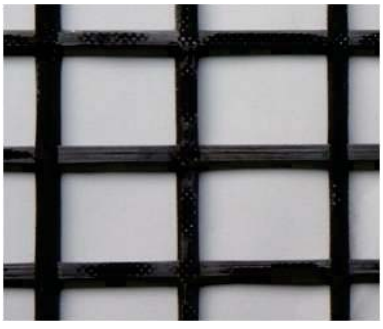

Figure 1. CFRP grid.

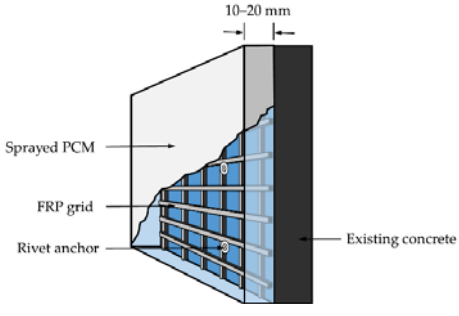

Figure 2. Schematic diagram of strengthened concrete structures using CFRP grid and PCM.

In the past few years, some investigators have studied the effectiveness of CFRP grid in strengthening concrete structures, indicating that this strengthening method could significantly improve the mechanical behavior of concrete structures. Nevertheless, the

tensile strength of CFRP grid has not been fully utilized, due to premature interface debonding of the reinforcing layer [5,6,13,22,23]. Therefore, it is clear that the reliable bond behavior between the CFRP grid, PCM, and concrete is the key to giving full play to the high tensile strength of CFRP grid, and improving the strengthening efficiency. Guo et al. [5,6] investigated the influence of parameters such as the number of grid points, grid interval, and type of PCM on the interface bond behavior, indicating that the interface peeling failure occurs when the tensile stress exceeds the ultimate bond strength between PCM and concrete. Ding et al. [17] conducted a pull-out experiment focusing on the effects of the embedded length of CFRP grid and horizontal grid on the bond behavior of the CFRP grid–concrete interface, and found the critical embedded length required to make full use of the tensile strength of the CFRP grid. Sugiyama et al. [24] tested the interfacial bond strength between the CFRP grid–PCM reinforcing layer and concrete, showing that the type of PCM has no effect on the bond strength. However, considering that the interface between the CFRP grid–PCM reinforcing layer and concrete consists of three materials, and the PCM–concrete interface is divided into a checkerboard pattern by CFRP grid, resulting in a complicated stress state of the interface, experiments alone are not enough to reveal the bond mechanisms between CFRP grid, PCM, and concrete in detail, and further investigations based on mechanical analysis and numerical simulation are needed—similar to the research of N.K. Banjara et al. [25]. Dung [26] studied the shear bond behavior of the interface between concrete substrate and repaired mortar by combining test and finite element analysis; however, the analysis did not consider the role of grid points, and the analysis content was not comprehensive enough.

In this study, pull-out tests of four plate-type specimens with CFRP grid–PCM reinforcing layer and concrete were conducted to ascertain the maximum tensile loads and failure modes corresponding to different CFRP grid types and grid intervals. Based on the experimental results, the preliminary investigation of the bond mechanism between concrete and the CFRP grid–PCM reinforcing layer was carried out via strain analysis of the CFRP grid. Compared with the existing research, interfacial bond strength between the CFRP grid–PCM reinforcing layer and concrete was quantified via strain analysis. In addition, a simplified analysis model was proposed based on mechanical analysis. Compared with the existing models, the proposed model is more convenient to apply. Finally, in order to verify the accuracy of this proposed model, a two-dimensional finite element (FEM) analysis was conducted, putting forward a new method for the follow-up study of concrete strengthened by CFRP grid–PCM.

2. Experimental Program

2.1. Details of Specimens

Four plate-type specimens composed of concrete, CFRP grid, and PCM were fabricated. The investigation variables included the type of CFRP grid (CR6 and CR8) and the grid interval (50 mm and 100 mm). Table 1 summarizes the details of all specimens. Figure 3 shows the specimens' geometry and the arrangement of the strain gauges. The production process of the specimens can be summarized as three stages: When the curing time of concrete in a moist environment reached 21 days, the concrete surface was treated via vacuum blast. After 28 days, the CFRP grid was installed on the concrete surface by coating with epoxy primer and spraying PCM with a thickness of 40 mm. Finally, pull-out tests were carried out after the age of concrete reached 46 days. Tables 2 and 3 show the mix proportions of the concrete and PCM, respectively. The material properties of the concrete and PCM are summarized in Table 4. The material properties of the CFRP grid are shown in Table 5.

Table 1. Types of the specimens.

Specimen	CFRP Grid Type	Grid Interval (mm)	Dimension of Concrete (mm)	Dimension of PCM (mm)
C6D50	CR6	50	300 × 270 × 90	250 × 250 × 40
C6D100	CR6	100		
C8D50	CR8	50	300 × 270 × 90	250 × 250 × 40
C8D100	CR8	100		

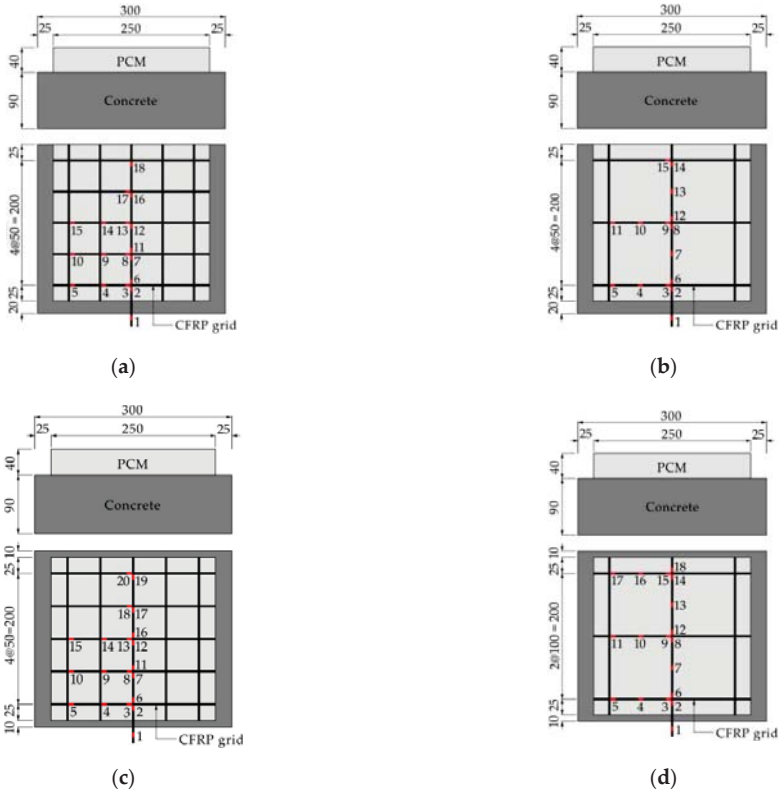

Figure 3. Dimensions of the specimens and arrangement of strain gauges on the CFRP grid. (**a**) C6D50; (**b**) C6D100; (**c**) C8D50; (**d**) C8D100 (units: mm).

Table 2. Mixture proportions of concrete.

Specimen	G_{max} * (mm)	SL * (mm)	W/C (%)	Air Content (%)	Unit Content (kg/m^3)			
					W *	C *	S *	G *
C6D50 C6D100	20	80	58	4.5	174	300	823	985
C8D50 C8D100	20	120	55.6	4.5	158	284	792	1099

* G_{max}: maximum size of coarse aggregate; * SL: slump of concrete; * W: water; * C: cement; * S: fine aggregate; * G: coarse aggregate.

Table 3. Mixture *Proportions* of PCM.

Ready-Mixed Mortar (kg/m^3)	Polymer (kg/m^3)	Water (kg/m^3)
1450	70	239

Table 4. Mechanical properties of concrete and PCM.

Material	Specimen	Compressive Strength (N/mm^2)	Tensile Strength (N/mm^2)	Elastic Modulus (kN/mm^2)
Concrete	C6D50 C6D100	33.2	3.0	25.3
	C8D50 C8D100	36.7	2.87	30.1
PCM	C6D50 C6D100 C8D50 C8D100	47.1	3.21	16.8

Table 5. Mechanical properties of CFRP grid.

Grid Type	Cross-Sectional Area (mm^2)	Tensile Strength (N/mm^2)	Elastic Modulus (kN/mm^2)
CR8	26.4	1400	100
CR6	17.5	1400	100

2.2. Load Program

Pull-out tests were conducted based on JSCE-E 539-2007 [27] and ACI 440.1R-06 [28]. The monotonic tensile load with a loading rate of 200 $N/mm^2/s$ was subjected to a vertical CFRP grid extended from the bond interface. To prevent eccentricity loads during the loading process, four iron blocks and steel plates were used to fix the position of the specimens. The strain gauges were installed on the surface of the CFRP grid to measure the strain values of the CFRP grid. The test schematic is shown in Figure 4.

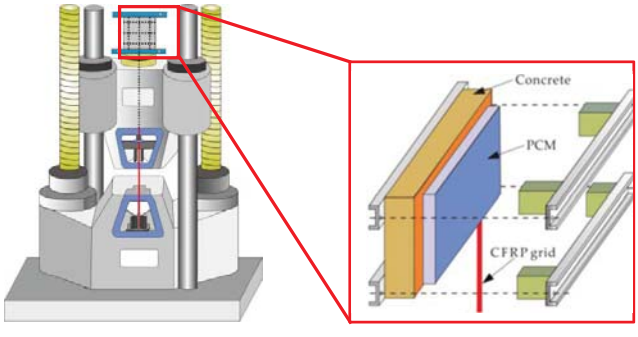

Figure 4. Diagram of specimen loading.

3. Experimental Results and Discussion

3.1. Failure Patterns and Maximum Loads

Figure 5 shows the failure patterns of all specimens. The loading position is at the bottom of the sketch. It can be observed that the vertical tensile grids in all specimens

were pulled out, and PCM developed surface cracks to varying degrees, while the interface between the PCM and the concrete remained intact throughout the whole loading process. This could attributable to the fact that epoxy primer was used on the surface between the CFRP grid–PCM reinforcing layer and the concrete, resulting in the improvement of interface bond action. For the specimens C6D50 and C6D100, no cracks appeared on the surface of the PCM, and the specimens failed due to the vertical tensile grids being pulled out. For the specimens C8D50 and C8D100, the vertical tensile grids were pulled out, and cracks appeared on the PCM. It can be seen that the degree of damage to the CFRP grids for specimens C6D50 and C6D100 was more severe than that for specimens C8D50 and C8D100. This might be attributable to the fact that the ultimate tensile action (24.5 kN) of the CR6-type CFRP grid used in specimens C6D50 and C6D100 was lower than that (36.96 kN) of the CR8-type CFRP grid used in specimens C8D50 and C8D100. Table 6 shows the maximum loads and failure patterns of all specimens. The tensile strength utilization ratio of CFRP was defined as the ratio of the maximum tensile load of the specimens to the test ultimate tensile action of the CFRP grids [29]. The tested ultimate tensile loads of the CR8 and CR6 CFRP grids were 45.07 kN and 28.6 kN, respectively. It can be seen that the tensile strength utilization ratio of the CFRP grid in specimen C6D50 was 84% higher than that in specimen C6D100, and the tensile strength utilization ratio of the CFRP grid in specimen C8D50 was 23% higher than that in specimen C8D100, indicating that the tensile strength utilization ratios of the CFRP grid with small grid intervals were higher than those with large grid intervals. This might be attributable to the fact that the smaller grid interval has more grid points to resist the tensile load, resulting in the higher tensile strength utilization ratio of the CFRP grid for specimens with smaller grid intervals compared to the specimens with larger grid intervals. In addition, it can be seen that the maximum load of specimen C8D50 with the CR8@50-type CFRP grid was 133% higher than that of specimen C6D50 with the CR6@50-type CFRP grid, and the maximum load of specimen C8D100 with the CR8@100-type CFRP grid was 247% higher than that of specimen C6D100 with the CR6@100-type CFRP grid, indicating that the specimen with the larger cross-sectional area of the CFRP grid could obtain a higher tensile capacity under the precondition of reliable interface bonding. Meanwhile, comparing specimens C6D100 and C8D50 showed that the simultaneous use of a CFRP grid with a larger cross-sectional area and smaller grid interval can significantly improve the interfacial bearing capacity between the CFRP grid–PCM reinforcing layer and the concrete.

Table 6. Summary of test results.

Specimen	Maximum Load (kN)	Test Ultimate Tensile Load of CFRP Grid (kN)	Tensile Strength Utilization Ratio of CFRP Grid (%)	Failure Pattern of CFRP Grid	Failure Pattern of PCM	Interface Failure Pattern between Concrete and PCM
C6D50	14.92	28.6	52.2	The vertical grid was pulled out	No significant cracks were observed	Kept intact
C6D100	8.11		28.4			
C8D50	34.72	45.07	77.04		Cracks occurred on the surface	
C8D100	28.12		62.39			

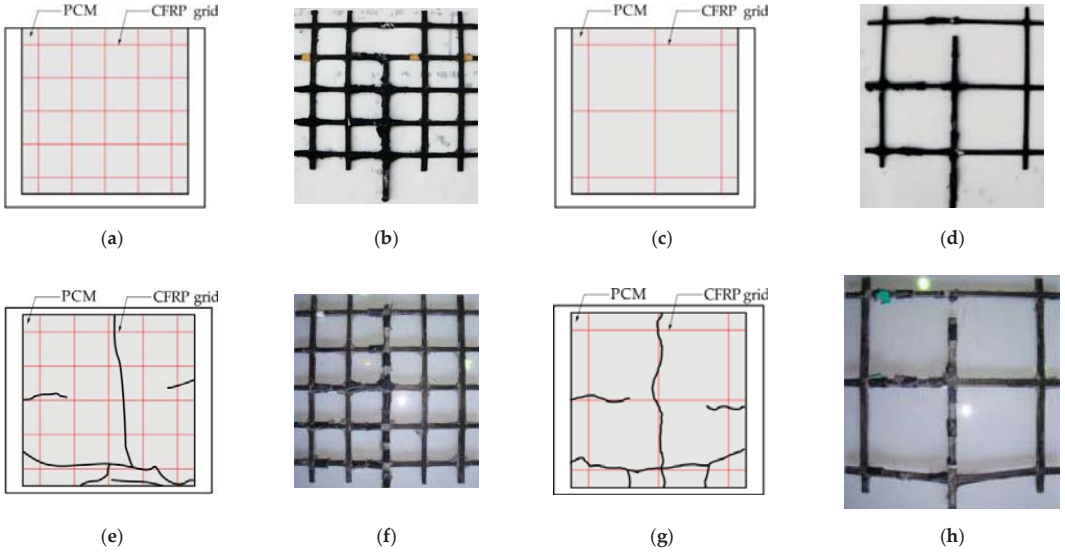

Figure 5. Failure patterns of the specimens: (**a**) failure pattern of PCM for specimen C6D50; (**b**) failure pattern of CFRP grid for specimen C6D50; (**c**) failure pattern of PCM for specimen C6D100; (**d**) failure pattern of CFRP grid for specimen C6D100; (**e**) failure pattern of PCM for specimen C8D50; (**f**) failure pattern of CFRP grid for specimen C8D50; (**g**) failure pattern of PCM for specimen C8D100; (**h**) failure pattern of CFRP grid for specimen C8D100.

3.2. Strain Distribution of CFRP Grids

According to the analysis above, the stress transfer mechanism between the CFRP grid–PCM reinforcing layer and the concrete is rather complicated. So as to preliminarily investigate the mode of tensile stress transfer between the three materials, the specimens C8D50 and C8D100 were taken as examples to analyze the strain distribution of the vertical tensile CFRP grid, as shown in Figure 6. It can be observed that the strain on the vertical tensile grid gradually decreased from the loaded edge to the free edge at the lower load level. However, the strain distribution patterns changed at the higher load level. For the specimen C8D50, as shown in Figure 6a, the strain of grid point GP3 sharply increased and exceeded the strain of grid point GP2 after the tensile load reached approximately 10 kN. This might be attributable to the fact that the restraining action for grid point GP3 from PCM gradually decreased with the increase in the tensile load due to the fracture of PCM (see Figure 5e), resulting in a change in the tensile stress transfer mode of the CFRP grid. For the specimen C8D100, as shown in Figure 6b, when the tensile load exceeded approximately 15 kN, the strain of grid point GP2 increased sharply, while the strain of grid point GP1 increased slightly, indicating that under the higher load, the PCM near the loaded edge fractured severely, and lost its restraining action on the grid points; after this, the tensile load was transferred to other grid points, where the PCM was relatively intact or only slightly fractured. In addition, comparing the strain distributions of two specimens, it can be found that the strain difference between the vertical grid near the loaded edge and the vertical grid far away from the loaded edge for specimen C8D50 was smaller than that for specimen C8D100, indicating that the strain distribution of the vertical grid in specimen C8D50 was more uniform than that in specimen C8D100. This might be explained by the fact that the grid interval of the CFRP grid in specimen C8D50 was smaller than that in specimen C8D100, resulting in more grid points in specimen C8D50 to share the tensile load compared to specimen C8D100.

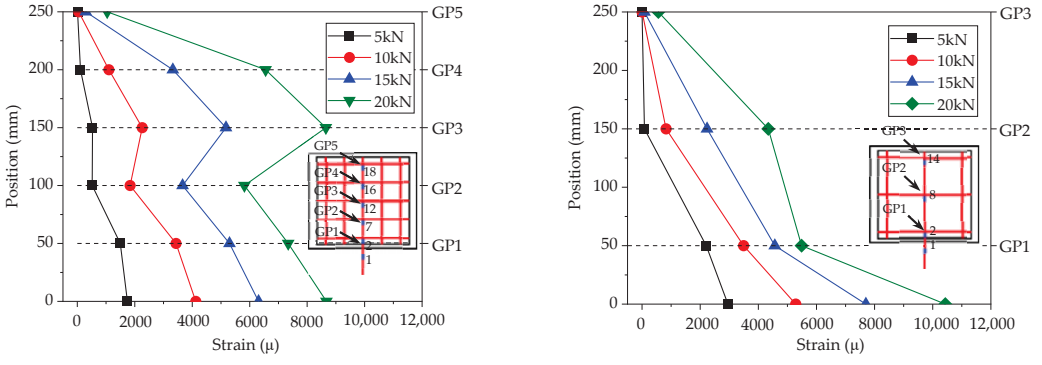

Figure 6. Strain distribution patterns of the vertical grid. (**a**) C8D50; (**b**) C8D100.

4. Interface Bond Mechanism

4.1. General

The tensile stress transfer process between the CFRP grid–PCM reinforcing layer and the concrete can be divided into two stages, as shown in Figure 7. In the first stage, the tensile load applied to the vertical CFRP grid was transferred to the PCM via the anchorage action of the CFRP grid in the PCM, as shown in Figure 7b. In the second stage, the tensile stress borne by the PCM was transferred to the concrete via the interface bond between the CFRP grid–PCM reinforcing layer and the concrete, as shown in Figure 7a. Based on the experimental results mentioned above, it can be seen that the epoxy primer as an interfacial binder could effectively improve the bond behavior between the CFRP grid–PCM reinforcing layer and the concrete. Similarly, the failure modes of the specimens mainly depended on the CFRP grid and the PCM. So as to make full use of the high tensile strength of the CFRP grid, a credible anchorage of the CFRP grid in the PCM must be ensured. Previous investigators have noted that the anchorage action of the CFRP grid in PCM is mainly provided by two parts: the resistant action of the horizontal grid, and the bond action of the vertical grid [30]. In addition, it is clear that the tensile stress transfer mode between the CFRP grid and the PCM changes with the generation of cracks on the surface of the PCM. Consequently, the specimen C8D100 was taken as an example to reveal the stress behavior of the CFRP grid in PCM in further detail, based on the strain analysis of the CFRP grid.

4.2. Load–Strain Difference Curves

As discussed previously, the interface bond between CFRP grid–PCM reinforcing layer and concrete can be significantly improved by using the epoxy primer, and the tensile bearing capacity of the specimen is determined by the anchorage action of the CFRP grid in the PCM. So as to further clarify the anchorage action of the CFRP grid in the PCM, the resistant action of the horizontal grid and bond action of the vertical grid were characterized based on the strain difference on both sides of the grid points for the vertical grid, and the strain difference between the bottom and top ends within the grid interval, as shown in Figure 8. The strain values can be measured by strain gauges arranged on the CFRP grid. It was found that, under the lower load, with the increase in the tensile load, the strain difference of grid points near the loaded edge sharply increased, while the strain difference of the grid points far away from the loaded edge increased slightly. This indicates that the tensile stress was transferred from the loaded edge to the free edge by the resistant action of the horizontal grid at the grid points. However, under the higher load, the tensile stress transfer mode changed. As shown in Figure 8a, the strain difference

ε (2CH)–ε (6CH) of grid point GP1 gradually decreased after the tensile load exceeded 8.45 kN, while the strain differences of the remaining grid points continued to increase with the increase in the tensile load. Past a load of 13.18 kN, the strain difference of grid point GP1 was lower than the strain difference ε (8CH)–ε (12CH) of grid point GP2. This phenomenon might be attributable to the fact that the PCM at grid point GP1 fractured, which reduced the resistant action of grid point GP1, resulting in the transfer of tensile stress from grid point GP1 to grid points GP2 and GP3. Accordingly, the resistant action of grid points GP2 and GP3 gradually increased. In addition, it can be found that the strain difference of grid point GP1 began to increase after the tensile load reached 21.47 kN. This might be caused by the pulling out of the vertical grid (2CH) near the loaded edge. As shown in Figure 8b, under the lower load, with the increase in the tensile load, the increase in strain difference within the grid interval near the loaded edge was more significant than that far away from the loaded edge—especially the strain difference ε (12CH)–ε (14CH) far away from the loaded edge, which began to increase until the tensile load reached ~4.83 kN. This indicates that the tensile stress was transferred from the loaded edge to the free edge by the bond action between the vertical grid and the PCM. However, under the higher load (i.e., 13.59 kN), with the increase in the tensile load, the strain difference ε (6CH)–ε (8CH) near the loaded edge gradually decreased, while the strain difference ε (12CH)–ε (14CH) far away from the loaded edge continued to increase. When the tensile load exceeded 17.95 kN, the strain difference ε (12CH)–ε (14CH) was larger than the strain difference ε (6CH)–ε (8CH). This might be attributable to the fact that the fracture of the PCM near the loaded edge reduced the bond action of the vertical grid, resulting in the transfer of tensile stress via the bond action of the vertical grid far away from the loaded edge.

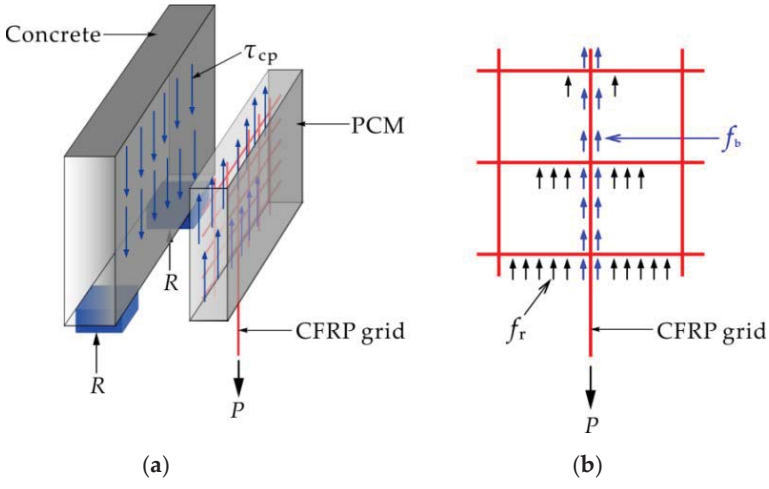

Figure 7. Schematic diagram of the stress transfer process for the specimen: (**a**) interface bond stress between the CFRP grid–PCM reinforcing layer and the concrete; (**b**) anchorage action of the CFRP grid in the PCM. τ_{cp}: bond stress between the reinforcing layer and the concrete; f_b: bond action between the vertical grid and the PCM; f_r: resistant action of the horizontal grid.

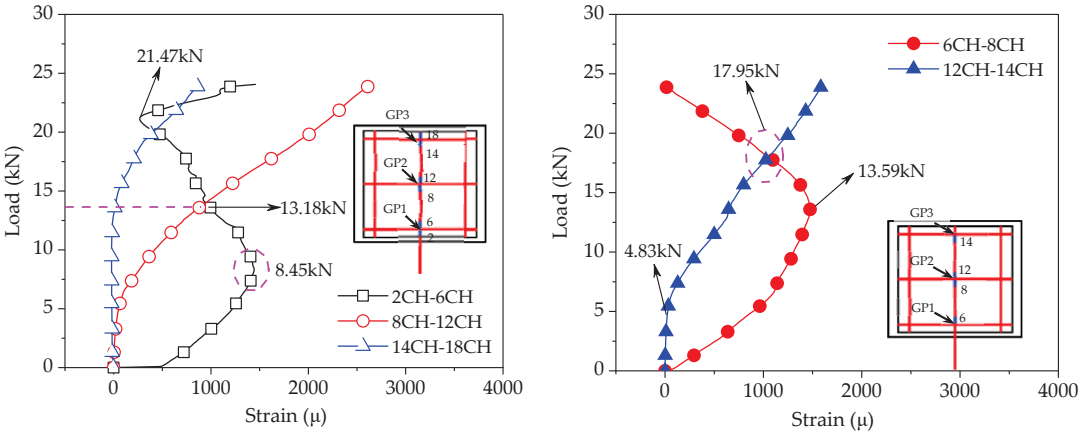

Figure 8. Load–strain difference curves of the grid points: (**a**) strain difference of the grid points; (**b**) strain difference in grid intervals.

5. Simplified Interface Model

5.1. Simplified Mechanical Model

According to the analysis of the interface bond mechanism between the CFRP grid–PCM reinforcing layer and concrete, the tensile stress is balanced by the anchorage action of the CFRP grid in the PCM and the interface bond action between the CFRP grid–PCM reinforcing layer and the concrete. Therefore, a simplified model based on a nonlinear spring system was proposed from the perspective of mechanical analysis, as shown in Figure 9. It is clear that the resistant action of the horizontal grid plays a dominant role in the anchorage action of the CFRP grid in the PCM, so the tensile springs and shear-resistant springs are used to simulate the resistant action of the CFRP grid in the PCM and the interface bond action between the reinforcing layer and the concrete, respectively. In order to reduce the complexity of the model, the two categories of springs are equivalent to the same category of spring in terms of stiffness.

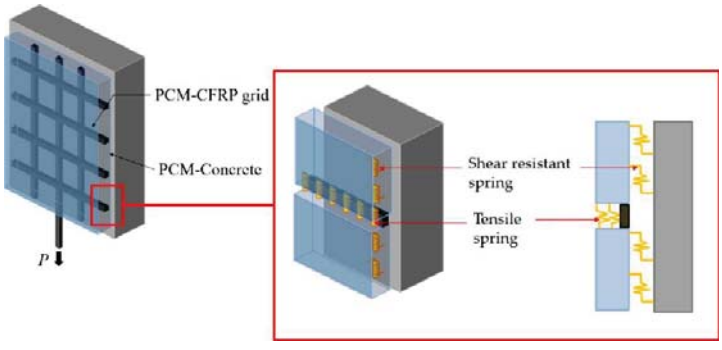

Figure 9. Schematic diagram of the specimen interface.

In view of the brittle failure characteristics of specimens, a nonlinear spring was used for the equivalent simulation. Figure 10 shows the load–deflection curve of the nonlinear spring. The load–deflection curve can be divided into two stages: In the first stage, the

resistant action of the spring increased linearly with the increase in deflection until the spring deflection reached the critical deflection d_t. When the spring deflection was equal to the critical deflection d_t, the resistant action of the spring reached the maximum value R_{max}. In the second stage, the spring deflection increased rapidly and resistant action gradually decreased after the spring deflection exceeded the critical deflection d_t. When the spring deflection reached the maximum value d_{max}, the resistant action of the spring was equal to zero. At this point, the spring failed, and the stress was transferred to the adjacent springs until all springs failed, and the spring system lost its bearing capacity.

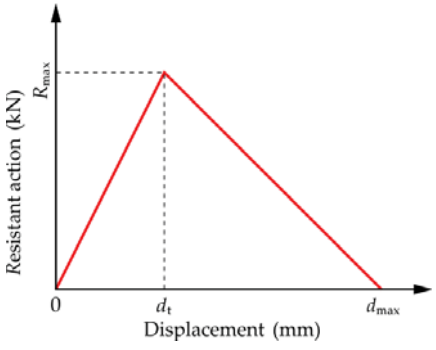

Figure 10. Stiffness curve of the nonlinear spring.

The critical deflection d_t and maximum deflection d_{max} of the nonlinear spring were determined by the concrete material test, and the maximum resistant action R_{max} was determined by the interface shear strength between the PCM and concrete, along with the tensile strength of the PCM. Each spring represents the local interface shear area and tensile area of the PCM. The bearing capacity of the nonlinear spring can be calculated by Equation (1):

$$\begin{aligned} R_{max} &= (R_s + R_t) \times \beta \\ R_s &= h \times s \times \sigma_s \\ R_t &= t \times s \times \sigma_t \end{aligned} \quad (1)$$

where β is the adjustment coefficient; s is the spring spacing; t is the PCM thickness; h is the horizontal grid interval; σ_s is the interface shear strength between the PCM and the concrete; and σ_t is the tensile strength of the PCM.

5.2. Finite Element Analysis

In order to conduct a further investigation of the interface bond mechanism and tensile stress transfer mode between the CFRP grid–PCM reinforcing layer and the concrete, the FEM analysis was carried out on the basis of pull-out tests. At first, the effectiveness of the simplified model was verified via the numerical simulation method. Then, the stress variation of the CFRP grid was explored based on the results of the FEM analysis.

5.2.1. Establishment of the Model

Based on the simplified mechanical model, the two-dimensional FEM model was established using the FEM software ABAQUS. According to the stress behavior of the CFRP grid in the PCM, when the vertical CFRP grid was elongated along the axial direction under the tensile load, the horizontal CFRP grid would generate resistant action and cause apparent lateral deformation. Therefore, beam elements and truss elements were used to simulate the horizontal grid and vertical grid, respectively. Considering that the grid points of the CFRP grid have a certain rigidity, the crossing points of the horizontal and vertical grids were simulated by rigid joints. The nonlinear springs were arranged along the axis of the horizontal grids, and a nonlinear spring was arranged on the two sides of

the grid points to constrain the CFRP grid. Taking the specimen C8D100, for example, the FEM model is shown in Figure 11. The spring stiffness was calculated by Equation (1), where the interface shear strength was obtained via the direct shear tests between the PCM and the concrete [26], and the tensile strength of the PCM was obtained from the material property tests (see Table 4). The critical deformation d_t and maximum deformation d_{max} of the nonlinear spring were 0.1 mm and 0.3 mm, respectively. The tensile strength σ_t of the PCM and interface shear strength σ_s between the PCM and the concrete were 3.21 N/mm^2 and 4.69 N/mm^2, respectively. Spring spacing was 2.5 mm. It was assumed that the stress distribution in the area around each spring gradually decreased, and that only half of the area around each spring plays a role in bearing stress. Thus, the adjustment coefficient was set as 0.5. The bearing capacity of springs at different locations can be obtained by substituting these parameters into Equation (1), as shown in Table 7. It can be seen that the maximum resistant actions R_{max} of the bottom springs were lower than those of the non-bottom springs, because the support area of the CFRP grid near the bottom loaded edge was smaller than that of the CFRP grid far away from the bottom loaded edge.

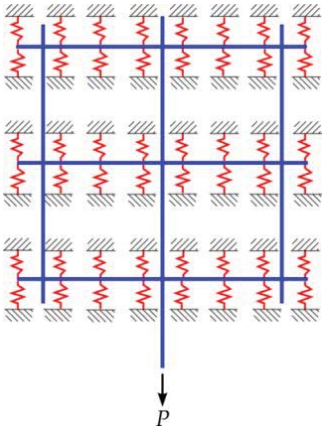

Figure 11. FEM analysis model.

Table 7. The maximum force of the spring.

Specimens	Grid Interval (mm)	Location of Spring	R_{max} (N)
C6D50	50	Non-bottom	453
C8D50		Bottom	307
C6D100	100	Non-bottom	747
C8D100		Bottom	307

5.2.2. Model Verification

Figure 12 shows the deformation of the CFRP grid for the FEM model based on the specimen C8D100. It can be seen that the deformation of the CFRP grid near the loaded edge was larger than that of the CFRP grid far away from the loaded edge, while the tensile stress was gradually transferred from the loaded edge to the free edge. Figure 13 shows the comparison of the maximum tensile loads obtained via the pull-out tests and FEM calculations. It can be seen that the ratios of the test values to the simulation values were close to 1, indicating that the simplified interface model with a nonlinear spring system could effectively reflect the mechanical behavior of the concrete specimens with a CFRP grid–PCM reinforcing layer. There was a certain error between the ultimate load of the FEM results and the test values. The main reason for these differences was that the simplified model considered the interface interaction between the CFRP grid–PCM and the

concrete, as well as the interaction between the CFRP grid and the PCM from the overall point of view, which is an equivalent simplification of the interaction of the various parts. In addition, the nodes of the CFRP grids were regarded as rigid connections, which caused the inaccurate expression of the working performance of the actual nodes under loading.

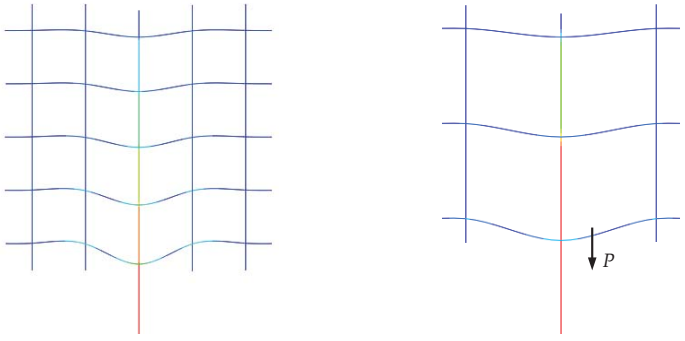

Figure 12. Diagram of specimen deformation. (**a**) diagram of specimens C6D50 and C8D50 deformation; (**b**) diagram of specimens C6D50 and C8D50 deformation.

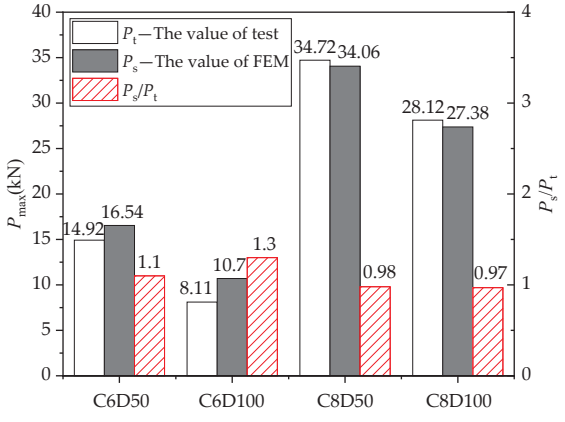

Figure 13. Comparison between the FEM and corresponding experimental results.

The FEM analysis results were compared with the test results, as shown in Figure 14. It can be observed that the pull-out test results and the FEM analysis results were almost identical in the strain distribution patterns of the tensile vertical grids; that is, the tensile strains gradually deceased from the loaded edge to the free edge. Therefore, it is reasonable to reflect the stress transfer change by the equivalent springs in the simplified mechanical model. In addition, the FEM strain values at some grid points were inconsistent with the test strain values. As shown in Figure 14a,c, the FEM strain value of specimens C6D50 and C8D50 at nodes GP1 and GP2 were essentially consistent with the test strain value; however, a discrepancy occurred at GP3. The test strain value increased suddenly at GP3, indicating that the specimen bore a large load and the force transfer form changed, which was probably related to the cracking of the mortar in the test process that was unable to be completed in the simplified simulation. In conclusion, since the simplified model considering the equivalent simplification based on reasonable analysis was the inaccurate simulation of the stress of the original specimens, the stress state of the vertical or transverse reinforcement was different from that in the test, and a certain error occurred between

the FEM value of the node strain and the test value. Further investigations using a fine mechanical model considering grid point failure should be conducted in the follow-up study.

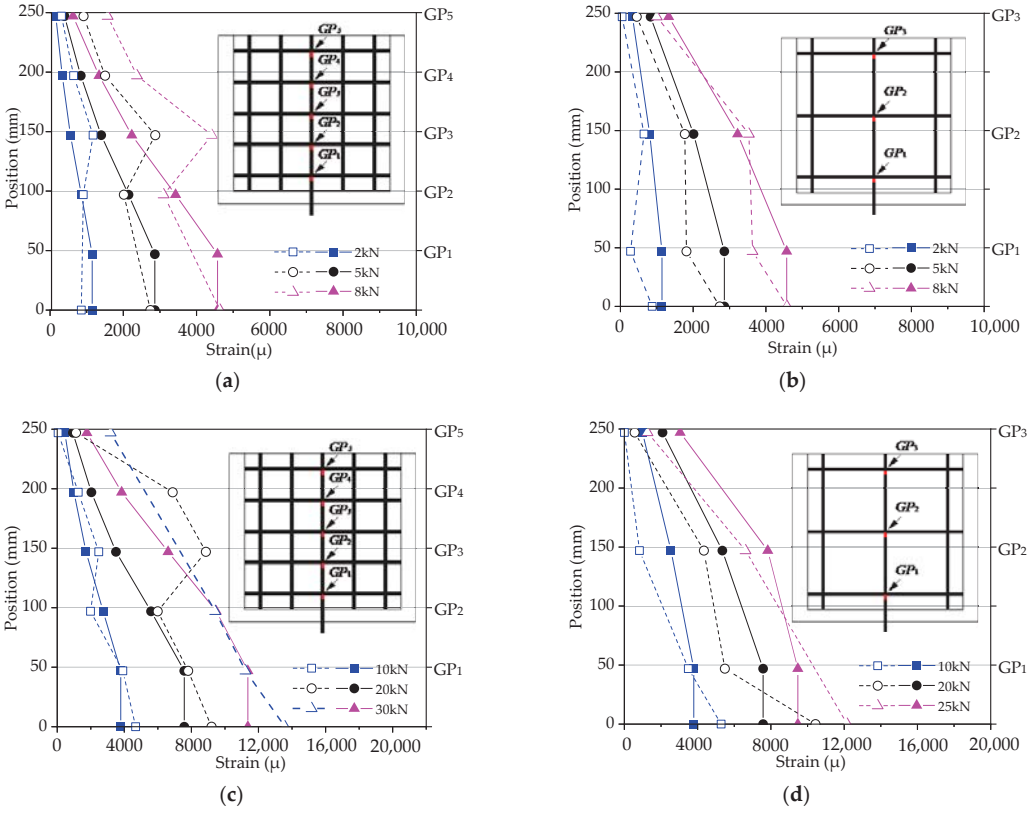

Figure 14. Comparison of strain distribution for vertical grids. (**a**) comparison of strain distribution for vertical grids in specimen C6D50; (**b**) comparison of strain distribution for vertical grids in specimen C6D100; (**c**) comparison of strain distribution for vertical grids in specimen C8D50; (**d**) comparison of strain distribution for vertical grids in specimen C8D100.

5.2.3. Strain Analysis of CFRP Grids

Figure 15 shows the strain distribution in the FEM results to explain the stress transmission change. The results show that the trend of strain distribution on vertical grid points was almost identical for all pull-out specimens during the loading process. There were three stages in the variation of strain distribution with load: In the initial stage, the strain of the vertical grids was concentrated at the loaded edge, indicating that the load was mainly undertaken by GP1 and GP2, and the strain at GP1 was larger than at GP2, owing to the transmission mode of the vertical grid load. With the load increasing, the strain growth tendency from GP1 to GP5 (GP3) decreased, indicating that the load was gradually transferred from the loaded edge to the free edge. In the final stage, the load of specimens was close to its maximum, the spring failure expanded, and the strain at the grid points increased. With all springs failed, the specimens completely lost their carrying capacity. In addition, as shown in Figure 15a,b, comparing the strain distribution at the grid points at a certain load for C6D50 and C6D100 (i.e., 2 kN and 6 kN), it can be seen that with the upward transfer of stress, GP3 in C6D50 is less than GP2 (at the same height) in

C6D100, indicating that more grid points can share the stress with small grid spacing at the identical cross-sectional area. As shown in Figure 15a,c, for specimen C6D50, at a load of 2.0 kN, the grid strain of GP4 and GP5 is close to 0. When the load reaches 10.0 kN, the strain of GP1 to GP5 decreases; due to the large cross-sectional area, the grid point strain of C6D50 is greater than that of specimen C8D50, which is consistent with the results of carrying capacity, indicating that the upper grid point of the vertical grid can effectively bear the load and improves the carrying capacity of the specimens.

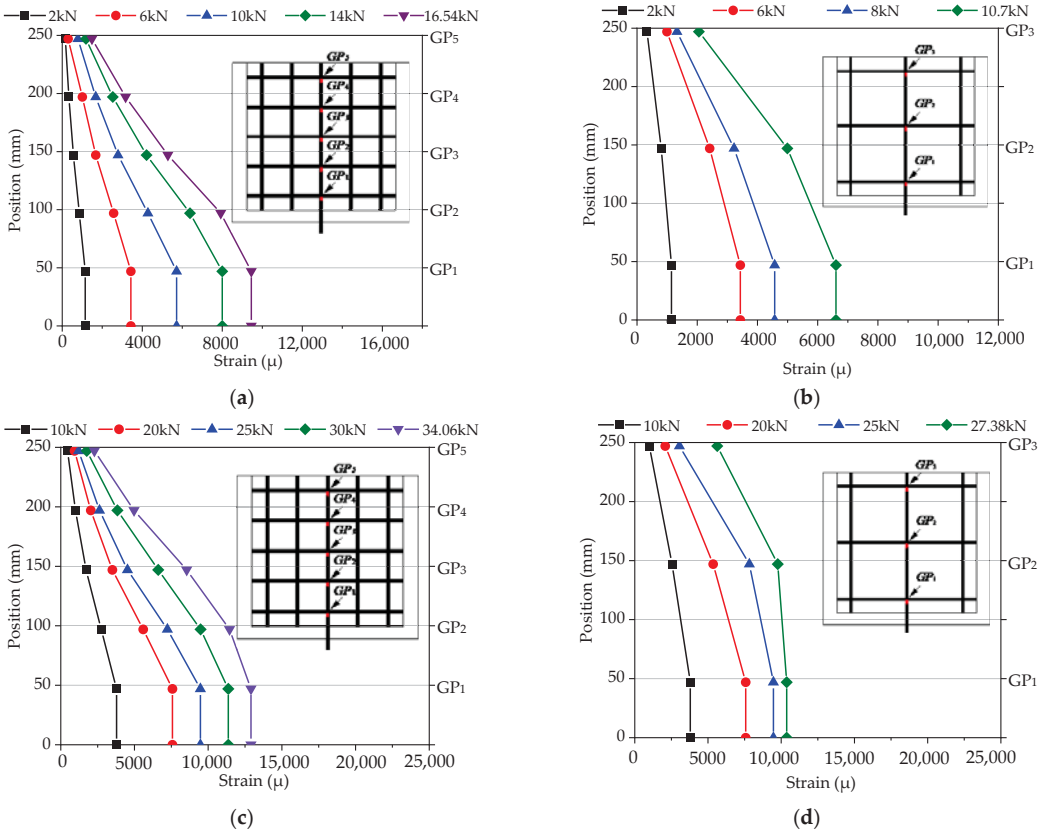

Figure 15. Strain distribution for CFRP grids. (**a**) strain distribution for CFRP grids in specimen C6D50; (**b**) strain distribution for CFRP grids in specimen C6D100; (**c**) strain distribution for CFRP grids in specimen C8D50; (**d**) strain distribution for CFRP grids in specimen C8D100.

5.2.4. Strain Difference Analysis

The variation in strain difference on both sides of vertical grids in different specimens is shown in Figure 16, wherein the load–strain difference curve shows an upward tendency with the increase in pull-out load for all specimens, and the linear relationship mostly occurs in the initial stage. The farther away from the loaded edge, the smaller the strain difference, indicating that the resistance of the transverse reinforcement is smaller. As can be seen from Figure 16a,c, the strain difference at GP1 is close to that of GP2, which shows that the force is mainly undertaken by these two grid points. As the load reached a certain value (specimen C6D50 in 11.8 kN and specimen C8D50 in 17.9 kN), the strain difference of GP1 changed with the gradual failure of some springs at the grid point after the softening stage, and the load was borne by the spring at the next adjacent position. Then, with the

load increasing, the force was continuously transmitted upward, and the resistance of the transverse grids further reduced until the ultimate load. As can be seen from Figure 16b,d, the overall strain difference variations of specimens C6D100 and C8D100 were effectively consistent with the others. However, the strain difference of GP1 was smaller than that of GP2 throughout the whole loaded process, due to the concentrated load at GP1 for the larger grid interval of CFRP grids, resulting in the premature failure of some springs, after which the load was transmitted to GP2, which bore the main load, even if the elastic spring near GP1 did not completely quit working.

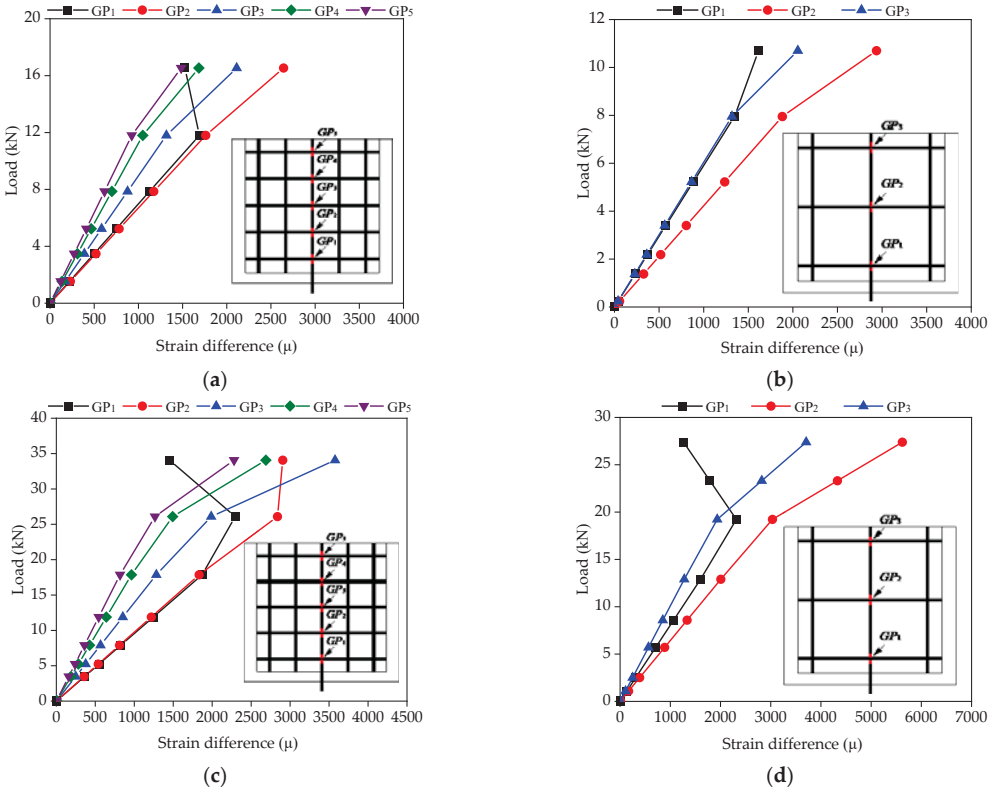

Figure 16. Strain difference distribution for CFRP grids. **(a)** C6D50; (**b**) C6D100; (**c**) C8D50; (**d**) C8D100.

6. Conclusions

In this paper, the interface bond mechanism between the CFRP grid–PCM reinforcing layer and concrete was investigated via pull-out tests, and a numerical simulation method based on the simplified mechanical model was proposed. The main conclusions can be drawn as follows:

(1) The tensile strength utilization ratio of the CFRP grid in specimen C6D50 was 81% higher than in specimen C6D100, and the tensile strength utilization ratio of the CFRP grid in specimen C8D50 was 23% higher than in specimen C8D100. Meanwhile, the maximum load of specimen C8D50 with the CR8@50-type CFRP grid was nearly 2.5 times higher than that of specimen C6D50 with the CR6@50-type CFRP grid, and the maximum load of specimen C8D100 with the CR8@100-type CFRP grid was 3.5 times higher than that of specimen C6D100 with the CR6@100-type CFRP grid. The use of a CFRP grid with a larger cross-sectional area and smaller grid interval

can significantly improve the interfacial bearing capacity between the CFRP grid–PCM reinforcing layer and the concrete. Moreover, the interfacial bond behavior between the reinforcing layer and the concrete can be effectively enhanced by using an interfacial binding agent;

(2) The tensile stress in the CFRP grid deceased gradually from the loaded edge to the free edge. The tensile stress borne by the CFRP grid was transferred to the PCM by the resistant action of the horizontal grid and the bond action of the vertical grid, and then to the concrete by the interface bond between the PCM and the concrete. The interfacial bearing capacity between the CFRP grid–PCM reinforcing layer and the concrete depended on the tensile strength of the CFRP grid, the anchorage action of the CFRP grid in the PCM, and the bond behavior between the PCM and the concrete;

(3) The simplified interface model with a nonlinear spring system could effectively reflect the mechanical behavior of the concrete specimens with the CFRP grid–PCM reinforcing layer, indicating that it can be used to simulate the stress transfer modes and interface bond mechanisms between the CFRP grid, PCM, and concrete;

(4) The stress was gradually transferred from the loaded edge to the free edge through the grid action in the process of drawing the load. There was an obvious turning point in the load–strain difference curve in the CFRP grid, indicating the change in the tendency of the resistance of transverse reinforcement—that is, the stress transfer mode changes with the failure of the springs.

Author Contributions: H.D. modeled the structure and wrote the paper; B.W. designed the study; J.Z. (Jiawei Zhang) contributed to the revision; J.Z. (Junlei Zhang) contributed to the fabrication of specimens and acquisition of data; K.U. designed the experimental program. All authors have read and agreed to the published version of the manuscript.

Funding: The authors gratefully acknowledge the Shaanxi Province Youth Science and Technology Rising Star Foundation (Grant No. 2021KJXX-17), the China Postdoctoral Science Foundation (Grant No. 2017M610616), and the Fundamental Research Funds for the Central Universities (Grant No. 300102280202) for supporting this research.

Institutional Review Board Statement: Not applicable.

Informed Consent Statement: Not applicable.

Data Availability Statement: Data available on request due to restrictions eg privacy or ethical. The data presented in this study are available on request from the corresponding author. The data are not publicly available due to the restriction of follow-up research.

Conflicts of Interest: The authors declare no conflict of interest.

References

1. Gonzalez-Libreros, J.H.; Sneed, L.; D'Antino, T.; Pellegrino, C. Behavior of RC beams strengthened in shear with FRP and FRCM composites. *Eng. Struct.* **2017**, *150*, 830–842. [CrossRef]
2. Tetta, Z.C.; Bournas, D.A. TRM vs. FRP jacketing in shear strengthening of concrete members subjected to high temperatures. *Compos. Part B Eng.* **2016**, *106*, 190–205. [CrossRef]
3. Ye, L.P.; Feng, P. Application and development of fiber-reinforced polymer in engineering structures. *China Civ. Eng. J.* **2006**, *39*, 25–37.
4. Engel, R.S.; Bakis, C.E.; Nanni, A.; Croyle, M.G. FRP Grids for reinforced concrete: An investigation of fiber architecture. In *Proceedings International Composites Expo' 97*; Soc. Plastics Industry: New York, NY, USA, 1997; pp. 6E1–6E6.
5. Guo, R.; Pan, Y.; Cai, L.; Hino, S. Bonding behavior of CFRP grid-concrete with PCM shotcrete. *Eng. Struct.* **2018**, *168*, 333–345. [CrossRef]
6. Guo, R.; Pan, Y.; Cai, L.; Hino, S. Study on design formula of shear capacity of RC beams reinforced by CFRP grid with PCM shotcrete method. *Eng. Struct.* **2018**, *166*, 427–440. [CrossRef]
7. Liang, J.; Uji, K.; Matsumura, S.; Sato, K. Shear strengthening of RC beam with CFRP grid and sprayed mortar. *Proc. Jpn. Concr. Inst.* **2008**, *30*, 607–612.
8. Brunton, J.J.; Bank, L.C.; Oliva, M.G. Punching shear failure in double-layer pultruded FRP grid reinforced concrete bridge decks. *Adv. Struct. Eng.* **2012**, *15*, 601–613. [CrossRef]

9. Jeong, S.K.; Lee, S.S.; Kim, C.H.; Ok, D.M.; Yoon, S.J. Flexural behavior of GFRP reinforced concrete members with CFRP grid shear reinforcements. *Key Eng. Mater. Trans. Technol. Publ.* **2006**, *306*, 1361–1366. [CrossRef]
10. Wei, Y.; Ji, J.; Zhang, M. Experimental investigation on tensile performance of FRP grids and its application as strengthening materials for underwater concrete. *Fiber. Reinf. Plast. Compos.* **2014**, *47*, 10–15.
11. Yost, J.R.; Goodspeed, C.H.; Schmeckpeper, E.R. Flexural performance of concrete beams reinforced with FRP grids. *J. Compos. Constr.* **2001**, *5*, 18–25. [CrossRef]
12. Wan, B.L.; Petrou, M.F.; Harries, K.A. The effect of the presence of water on the durability of bond between CFRP and concrete. *J. Reinf. Plast. Compos.* **2006**, *25*, 875–890. [CrossRef]
13. Chen, W.Y.; Chen, X.B.; Ding, Y. The shear behavior of beams strengthened with FRP grid. In *Advances in FRP Composites in Civil Engineering*; Springer: Berlin/Heidelberg, Germany, 2011; pp. 772–775.
14. Cai, S.H.; Tang, L.F. Study on polymer cement mortar in concrete patching. *J. Yangtze River Sci. Res. Inst.* **2007**, *24*, 44–47.
15. Zhang, D.; Ueda, T.; Furuuchi, H. Intermediate crack debonding of polymer cement mortar overlay-strengthened RC beam. *J. Mater. Civil. Eng.* **2011**, *23*, 857–865. [CrossRef]
16. Ding, L.; Rizkalla, S.; Wu, G.; Wu, Z.S. Bond mechanism of carbon fiber reinforced polymer grid to concrete. In *Advances in FRP Composites in Civil Engineering*; Springer: Berlin/Heidelberg, Germany, 2010; pp. 589–592.
17. Thamboo, J.A.; Dhanasekar, M. Characterisation of thin layer polymer cement mortared concrete masonry bond. *Constr. Build. Mater.* **2015**, *82*, 71–80. [CrossRef]
18. Zhang, D.W.; Ueda, T.; Furuuchi, H. Concrete cover separation failure of overlay-strengthened reinforced concrete beams. *Constr. Build. Mater.* **2012**, *25*, 735–774. [CrossRef]
19. Patnaik, G.; Kaushik, A.; Rajput, A.; Prakash, G. Numerical Study on Perforation Characteristics of Carbon-Fiber Reinforced Composite Laminates Subjected to Impact Loading. In *International Conference on Structural Engineering and Construction Management*; Springer: Cham, Switzerland, 2021; pp. 249–263.
20. Salem, B.; Mkaddem, A.; Rubaiee, S.; Bin Mahfouz, A.S.; Al-Zahrani, A.; Jarraya, A. Combined Approach for Modeling Progressive Damage in Unidirectional CFRP Composites. In *International Conference on Advances in Materials, Mechanics and Manufacturing*; Springer: Singapore, 2021; pp. 308–316.
21. Róyo, P.; Dbski, H.; Teter, A. Buckling and limit states of thin-walled composite columns under eccentric load. *Thin Walled Struct.* **2020**, *149*, 106627.
22. Guo, R.; Hu, W.H.; Li, M.Q.; Wang, B. Study on the flexural strengthening effect of RC beams reinforced by CFRP grid with PCM shotcrete. *Compos. Struct.* **2020**, *239*, 112000. [CrossRef]
23. Zinno, A.; Lignola, G.P.; Prota, A.; Manfredi, G.; Cosenza, E. Influence of free edge stress concentration on effectiveness of FRP confinement. *Compos. Part B Eng.* **2010**, *41*, 523–532. [CrossRef]
24. Sugiyama, K.; Yamaguchi, K.; Nakamura, S.; Hino, S. Stress transfer mechanism of the reinforced interface and seismic retrofit existing RC pier by polymer cement mortar for shotcrete with CFRP grid. *J. Struct. Eng.* **2011**, *57*, 1042–1051.
25. Banjara, N.K.; Ramanjaneyulu, K. Experimental and numerical investigations on the performance evaluation of shear deficient and GFRP strengthened reinforced concrete beams. *Constr. Build. Mater.* **2017**, *137*, 520–534. [CrossRef]
26. Dung, T.V. Numerical Analysis of the Shear Behavior of Reinforced Concrete Beam Strengthened with CFRP and Sprayed Mortar. Ph.D. Thesis, Tokyo Metropolitan University, Tokyo, Japan, 2016.
27. ACI Committee Report. *Guide for the Design and Construction of Structural Concrete Reinforced with FRP Bars*; ACI 440.1R-06; American Concrete Institute: Farmington Hills, MI, USA, 2001.
28. Japan Society of Civil Engineerings. *JSCE/E539-2007 Standard Specification for Concrete Structures*; JSCE: Tokyo, Japan, 2007.
29. Wang, B.; Uji, K.; Wu, T.; Dai, H.; Yan, D.; Guo, R. Experimental investigation of stress transfer and failure mechanism between existing concrete and CFRP grid-sprayed PCM. *Constr. Build. Mater.* **2019**, *215*, 43–58. [CrossRef]
30. Wang, B.; Wang, Z.; Uji, K. Experimental verification of a novel anchorage method of CFRP grid in mortar. *Structures* **2020**, *28*, 1646–1660. [CrossRef]

materials

MDPI

Article

Effect of the Looseness of the Beam End Connection Used for the Pallet Racking Storage Systems, on the Mechanical Behavior of the Bearing Beams

Florin Dumbrava [1,2] and Camelia Cerbu [1,*]

[1] Department of Mechanical Engineering, Faculty of Mechanical Engineering, Transilvania University of Brasov, B-dul Eroilor, No. 29, 500036 Brasov, Romania; florin.dumbrava@unitbv.ro
[2] Product Development Department, S.C. Dexion Storage Solutions SRL, Str. Campului Nr. 1A, 505400 Rasnov, Romania
* Correspondence: cerbu@unitbv.ro; Tel.: +40-722-491-398

Abstract: The worldwide use of pallet racking storage systems leads to the necessity for research regarding the effects of the clearance between the metallic tabs of the connector and upright slots (looseness effect) on the performance of load-bearing beams. Firstly, the looseness angle and the rotational stiffness were experimentally obtained for three types of beam-to-upright connections. A theoretical approach is used to investigate the magnitude of the looseness effects that occurred on the performances of the bearing beam of the pallet storage systems in terms of the bending moment developed at the midpoint of the beam and maximum deflection. Calculation corrections were evaluated for the connections involved in the experimental part, for the case which considers the looseness effects with respect to the case which does not consider the looseness effect. In order to evaluate the effects of the parameters of the connections on calculus corrections, the theoretical model was used for other types of beam-to-upright connections. It is shown that the maximum corrections are 2.99% and 5.16% for the bending moment developed at the midpoint of the beam and for the maximum deflection, respectively. It is proved that the connector type affects the size of the correction.

Keywords: storage systems; looseness; stiffness; beam-end connection; bending; gap; clearance

Citation: Dumbrava, F.; Cerbu, C. Effect of the Looseness of the Beam End Connection Used for the Pallet Racking Storage Systems, on the Mechanical Behavior of the Bearing Beams. *Materials* **2022**, *15*, 4728. https://doi.org/10.3390/ma15144728

Academic Editor: Krzysztof Schabowicz

Received: 10 May 2022
Accepted: 4 July 2022
Published: 6 July 2022

Publisher's Note: MDPI stays neutral with regard to jurisdictional claims in published maps and institutional affiliations.

1. Introduction

Design assisted by testing is a well-known procedure that is often used for design calculus of the pallet storage racking systems. The analysis of the mechanical behavior of semi-rigid connections used on pallet racking systems is generally based on experimental tests according to the European standard EN 15512 [1]. The old version of standard EN 15512 from 2009 [1] was replaced with the updated version, published at the end of 2020 [2]. The procedure for correcting bending moment developed in the bearing beam and deflections caused by the looseness of the beam-end connections was included in the updated version of standard EN 15512-2020 [2]. Looseness effect is not often investigated in steel structure connections. However, this effect has a significant impact on the behavior of the entire structure.

Typical connections used to assembly the uprights with beams, for the racking storage systems, are bolted connections [3,4] and connections with metal tabs [5–9]. Most research on such connections focuses on the analysis of rotational stiffness at ambient temperature [5,6,9] and high temperatures [10]. Bolted connections are a less expensive alternative to tab connectors, used for assembling of the pallet storage systems by taking into account the manufacturing technology of the tab connectors and the upright slots [3]. On the other hand, tab connectors have major advantages in terms of time and flexibility in on-site

installation, but also the disadvantage of the initial looseness that should be considered in the design calculus of the racking storage systems having such connectors.

The investigation method regarding the measuring of looseness for beam-upright connections and the looseness effect on the beam deflection and bending moments are shown in the last version of the EN 15512 standard [2]. The experimental investigation of the looseness for beam-to-upright connections could significantly improve the literature in terms of testing the connection elements used in civil engineering, like the ones addressed in a recently published editorial [11].

A looseness effect can also be noticed in the bolted connection. The main difference between connections with metallic tabs and bolted connection is the slippage occurs, in the first case, at the beginning of the moment-rotation curve.

Considering the clearance between the bolt and hole (Figure 1), the slip effect has a significant effect on bolted connections in cold formed steel sections [12–14]. In the case of the bolted connection, there is a clearance between bolt and hole (Figure 1a), which leads to a sliding effect in the joint after loading. The bolt is subjected to bearing stresses once the slip effect has been overcome. In this phase, the bolt is in contact with the hole, as is shown in Figure 1b.

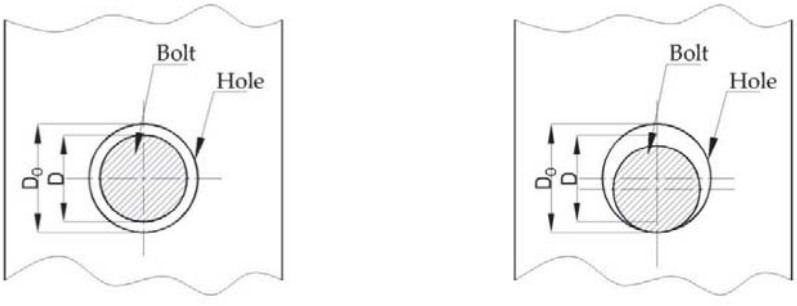

(**a**) (**b**)

Figure 1. Clearance in bolted connections: (**a**) clearance between bolt and hole; (**b**) bolt in contact with the hole.

In literature, there are a lot of scientific works which investigated the behavior of the bolted connections under static or impulsive loads, considering the clearance between bolt and hole [14,15]. By considering the finite element analysis of the models of beam-column connections with bolts, subjected to cyclic loading, Gharebaghi and Hosseini [14] showed that the increasing of the bolt-hole clearance and the decreasing of the pretention force in bolt lead to the reduction of the flexural strength of the bolt connection while the rotation angle increases.

The slip effect depends on the clearance between the bold diameter and the hole. In case of the bolted connections, the slip effect happens after a certain load is reached, as shown in Figure 2 for moment-rotation curve recorded for joint with pre-tensioned bolts [13,15,16].

Gilbert and Rasmussen [3] showed that the looseness in bolted connections subjected to bending moment can be neglected in design at ultimate stress state for drive-in and drive-through storage rack systems. Their results are based on the finite element non-linear analysis of the bolted connections between upright and the portal beam for pallets, subjected to cyclic bending moment.

Galeotti et al. [17] showed the positive effects of adding bolts to tab connections for steel storage systems in order to diminish the effect of pinching phenomenon, which appears especially for dynamical loads (earthquake, cyclic loading). The pinching phenomenon affects the looseness angle of the connection.

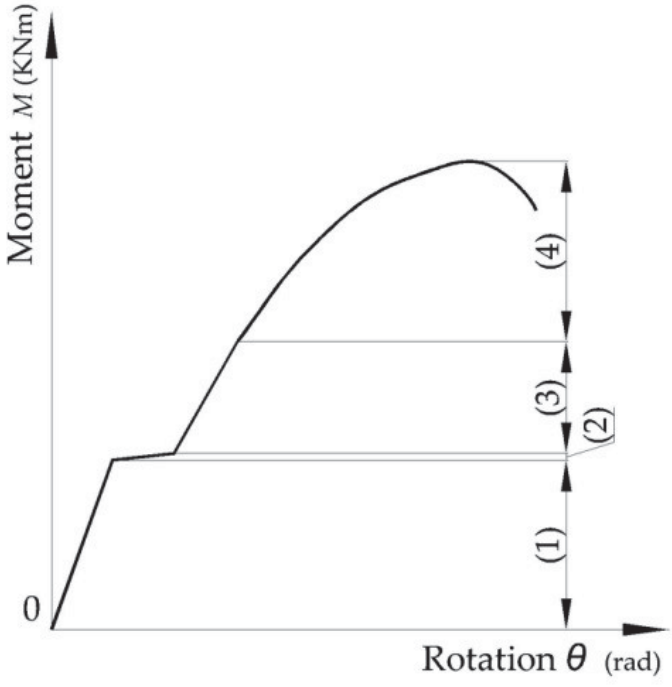

Figure 2. Typical behavior of bolted connections in cold formed steel structures: (**1**) linear behavior before slipping; (**2**) slipping effect caused by clearance between bold and hole; (**3**) linear behavior after cancelling of clearance; (**4**) nonlinear behavior.

Godley and Beale [18] showed that the analysis of the scaffold structures must consider non-linear joint models since the moment-rotation curve is usually not the same for positive and negative rotation and the looseness appears. The looseness influences the overall deflection of the scaffold structure but its effects on the load-bearing capacity for the braced frames may be neglected [18,19]. Prabhakaran et al. [19] showed a method for the non-linear analysis of the scaffold structures, taking into account the looseness effects in the joints.

Contrary to the bolted connections, the European standard EN 15512 [2] and scientific work [3] require considering the looseness of the tab connectors used between the upright and beam in stability analysis of the storage racking systems in the down-aisle direction. The down-aisle represents the direction parallel to a run.

On the other hand, the slip effect (looseness angle, as is mentioned in EN15512) happened at a lower load in case of the tab connections compared with the bolted connections [2]. This can be very simply explained because the bolts are generally pre-tensioned. In the case of the tab connections which are designed for the pallet racking systems, it is difficult to establish a general rule to take in consideration the looseness effect because of different shapes of both the metallic tabs and upright's slots. For these reasons, the agreed procedure is based on experimental tests. The difference between the metal tab width and the upright slot dimensions has a direct impact on the looseness δ (Figure 3). Until the metallic tab will not be in contact with the upright's slot (Figure 3a), the connection will behave like a pinned connection. Once the tab gets in contact with the upright slot (Figure 3b), the connection behaves like a semi-rigid connection.

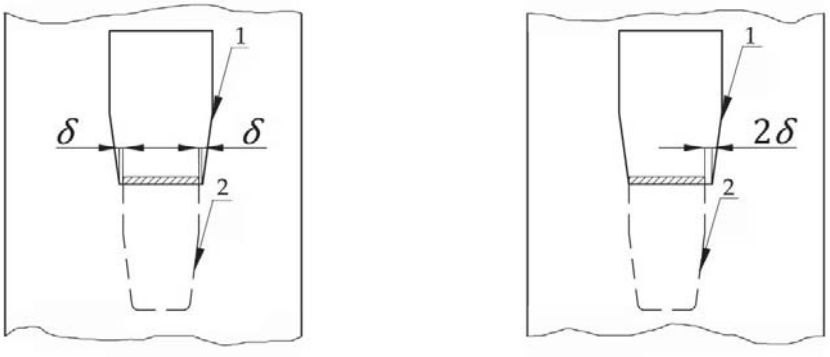

Figure 3. Looseness effect of beam end connector: (**a**) clearance between tab of the beam-end connector and upright slot; (**b**) tab of the connector will is in contact with one side of the upright slot. Note: (**1**) slot of the upright; (**2**) tab of the beam-end connector; δ is clearance.

There are some published papers [5,6,9] which approach the experimental testing of the beam-to-upright end connections for steel storage system, with tab connectors, under bending loading, without considering the looseness effects. Investigations conducted on the rotation stiffness of the tab connections showed that the increasing of the height of the connector or the increasing of the number of the tabs of the connector, respectively, lead to the increasing of the connection rigidity [6,20], while the effect of the gap between the beam and the face of the tab connector could be neglected [20].

Moreover, Escanio [9] validated the numerical models of such a beam-to-upright end connection subjected to bending, by correlation with the experimental results obtained for different combination between three types of uprights and four kinds of beams whose cross sections were different. However, the looseness between the metallic tabs and upright slots was not approached in the experimental program.

In literature, there are also analytical methods used to estimate the rotational stiffness and bending capacity for a rack connection with metallic tabs. The component method represents a good alternative to the experimental tests. Considering the component method, Gusella et al. [8] showed how the connections for racking storage systems are affected by the uncertainty in steel mechanical properties and geometrical features. In another research [21], the values for the initial rotational stiffness of beam-to-upright connections were also evaluated based on component method and compared with the experimental results. In that research, Zhao et al. [21] concluded that the maximum ratio between the theoretical and the experimental results was equal to 1.44 for the beam-to-upright connections involved in their research.

In this context, the accuracy predicting of the mechanical behavior of the tabs connection subjected to bending loading, including the looseness effect, represents an important aspect for the structural behavior of the beam-connector-upright assembly, especially for pallet racking systems. The experimental findings on the rotational stiffness and on looseness of the beam-to-upright connections used for storage racking systems can be used in numerical analysis for prediction of the mechanical behavior of the entire storage structure [22].

The main purpose of this research is to investigate the looseness that occurs in the tab connector in beam-upright connections and to evaluate the influence of looseness effect for the portal beam loaded with pallets, having different types of tab connectors at the beam-ends. For this purpose, the main objectives of this research are: (i) experimental determination of the looseness for three types of beam-connector-upright assemblies involving three types of uprights (different thickness of the section wall); (ii) considering the looseness effect occurring for the tab connections, in an analytical model used for

computing of the bending moment developed at the middle of the beam and maximum deflection of the beam; (iii) comparison regarding to the looseness effect on the bending moment and maximum deflection, for the portal beam loaded with pallets, having different configurations for the beam-end connections.

2. Materials and Methods

2.1. Assemblies Subjected to Looseness Tests

The purpose of the experimental program is to determine the looseness angle for three different beam-to-upright connections, which are presented in Table 1. The corresponding identification codes, which are referred to further in this research, are also shown in Table 1.

Table 1. Upright-connector-beam assemblies tested.

Assembly Code	Upright W * × t *	Beam H ** × W_1 ** × t_1 **	Connector Type	Number of Looseness Tests for Assembly	Number of Bending Tests for Assembly
0-I-5T	90 × 1.50	BOX 150 × 50 × 1.75	5T	4	6
0-II-5T	90 × 1.75			4	6
0-III-5T	90 × 2.00			4	6

* Dimensions of the uprights are shown in Figure 4a. ** Dimensions of the beam are shown in Figure 4b.

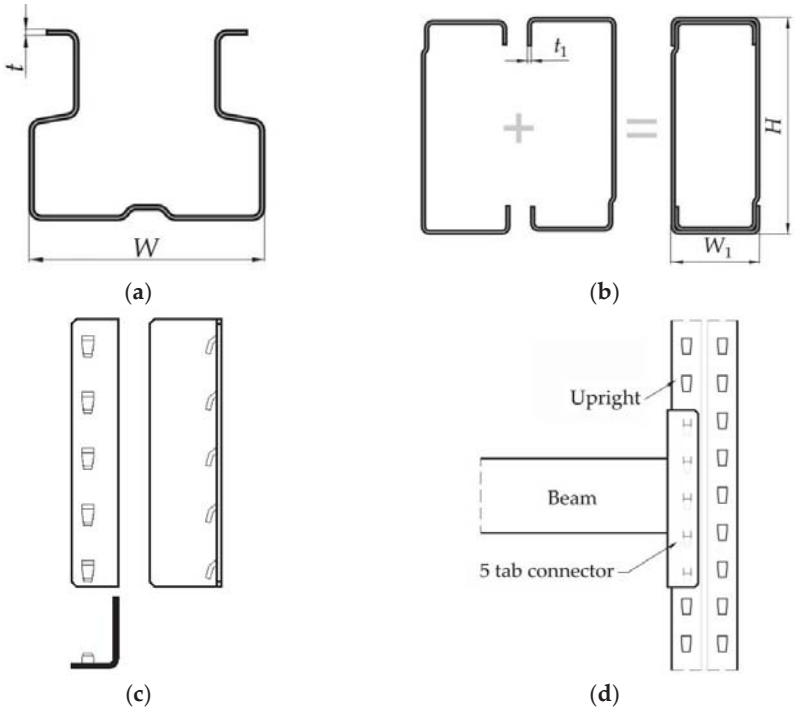

Figure 4. Elements of the upright-connector-beam assemblies tested: (**a**) upright sections; (**b**) beam section; (**c**) connector with 5 tabs; (**d**) sketch of the tested assembly.

The elements of the upright-connector-beam assemblies tested are shown in Figure 4. Three different upright sections (Figure 4a) are used, which have the same shape for cross section, but three different wall thicknesses (1.50 mm, 1.75 mm, and 2.00 mm), as shown in Table 1. The same boxed beam, which is obtained from two C-profiles brought together

(Figure 4b), is connected with the upright with a five tab connector (Figure 4c) that is welded at the end of the beam. For every tested assembly (Figure 4d and Table 1), the same type of five tabs connector was used, denoted as 5T in Table 1. It was used a beam having a large second moment of area with respect to the major axis in order to reduce, as much as possible, the bending effect of the beam in the mechanical tests made for obtaining of the looseness angle.

Test assembly is presented in Figure 4d. A set of four assemblies was prepared for every looseness test setup (penultimate column of Table 1), resulting in total 12 individual tests. A set of six beam-connector-upright assemblies (last column of Table 1) was prepared for each bending test to determine the rotational stiffness.

2.2. Work Method for Bending and Looseness Tests on Beam End Connectors

Three different beam-connector-upright assemblies were investigated in the bending test and then for the looseness angle, as shown in Table 1, in accordance with EN 15512 standard [2].

The experimental test setup is presented in Figure 5 and it is the same for the both bending test and looseness test for the beam end connectors, according to European standard EN 15512 [2]. The scheme of loading is shown in Figure 5a, while a photo of the test stand is given in Figure 5b. Firstly, the bending test of each type of beam-connector-upright assembly was made in order to determine the design moment denoted with M_{Rd} and the rotational stiffness k_m. The bending test for the beam end connectors, and the method for obtaining both the design moment M_{Rd} and the rotational stiffness k_m, are described in detail by the authors of this research in their previously published research [6], according to European standard EN 15512 [2]. For the looseness test, it is mentioned that the loading jack must be capable of applying both downward force and upward force (Figure 5a) in order to apply bending moment in reverse direction.

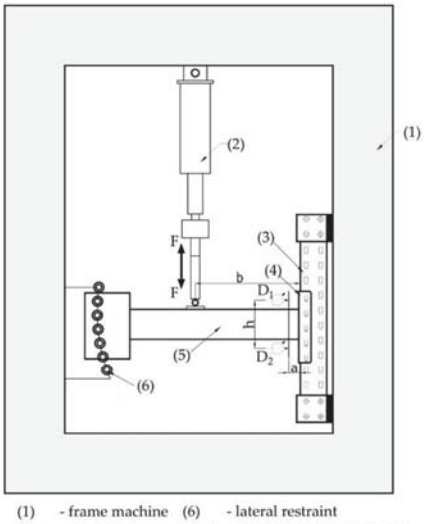

(1) - frame machine
(2) - load jack
(3) - upright
(4) - connector
(5) - beam
(6) - lateral restraint
D_1, D_2 - displacement transducers
h = 200 mm
a = 50 mm
b = 400 mm

(**a**)

(**b**)

Figure 5. Experimental test setup for bending test and looseness test according to European standard EN 15512: (**a**) scheme of the test stand; (**b**) photo of the test stand.

A rigid plate is fixed on the beam, on which the displacement transducers are bearing, to measure the rotation angle of the beam in connection by using the test stand (Figure 5b). In order to avoid the influence of the connector distortion on the rotation angle measured, the distance of 50 mm (dimension a in Figure 5) is set between the connection and the plate fixed on the beam, on which the displacement transducers are bearing, used to measure the rotation angle. This clearance between the connection and the plate fixed on the beam was established according to European standard EN 15512 [2] and the test method was described in other research [23–25]. Prabha et al. [26] used an inclinometer fixed on beam, close to the connection, in order to measure the rotation angle of the beam for evaluation of the stiffness of the connection. It also avoids the effects of the local deformations of the beam which occurred near the connector during the cantilever test. On the other hand, the distance between connector and plate fixed on the beam is required because there is the weld between beam and connector.

For both the bending test and looseness test, the moment-rotation $(M-\theta)$ curve is required to be plotted. Considering the notations shown in Figure 5a, the bending moment M developed at beam end connector and the rotation angle θ of the connector, expressed in radians, are computed by using Equation (1) and Equation (2), respectively [2].

$$M = bF, \tag{1}$$

$$\theta = (D_1 - D_2)/h. \tag{2}$$

In the looseness test, the force F (Figure 5a) was slowly increased until the moment the connector reached a value of 10% of the design moment denoted with M_{Rd}. Further, the load was gradually reduced and then reversed in the opposite direction, until the moment reached 10% of the design moment M_{Rd}, in that direction.

Twice the looseness angle denoted with $2\Phi_l$ was measured for each looseness test by extrapolating the linear parts of the moment-rotation curve towards the origin to find their intersection points with the rotation axis, as shown in Figure 6. The difference between the abscissas corresponding to the two points of intersection obtained in this manner is equal to twice the looseness angle Φ_l of the beam end connector.

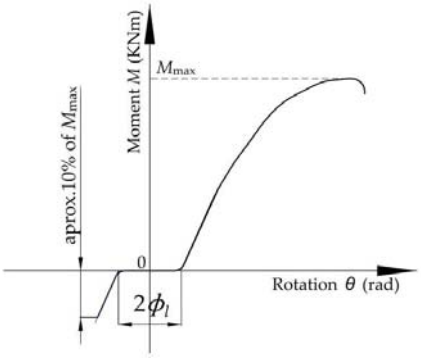

Figure 6. Typical moment rotational curve as test output to determine the looseness angle Φ_l.

All moment rotation $(M-\theta)$ curves obtained for the beam-connector-upright assemblies involved in this research are reported as results. The paper also reports the following data obtained by processing of the experimental data: looseness angle Φ_l, design moment M_{Rd}, and rotational stiffness k_m.

2.3. Theoretical Approach

In fact, the looseness effect is caused by the gap between the width of the metallic tabs of the connector and the width of the slots located on the upright front side. In Figure 7, it is shown how the effect of looseness affects the real deflection of the beams in operation

on storage systems. The beam shape before deformation is drawn with a continuous line. After loading of the beams with pallets, the deformed shape of the beam is drawn with a dashed line without considering the looseness effect, and it is also drawn with a dotted line by taking into account the looseness effect (Figure 7).

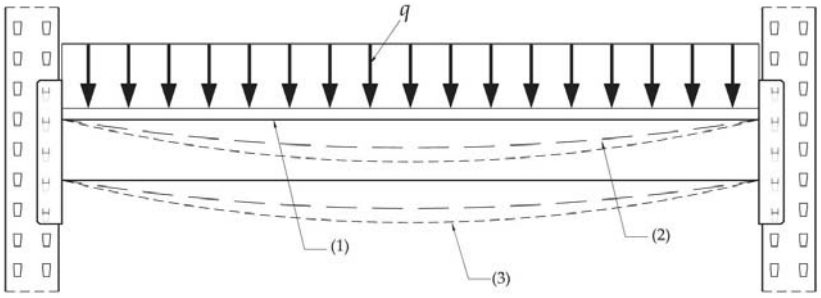

Figure 7. Looseness effect on the deflection of typical beam of the storage racking systems.

It has to be mentioned that the simplified static scheme shown in Figure 7 is considered for the portal beam, in accordance with the Annex C of the European standard EN 15512: 2020 [2], in order to make correction of bending moment and deflection due to looseness. In the design of the pallet racking storage systems, it is usually considered that the distributed force q, acting on the beam shown in Figure 7, is caused by the weight of the pallets supported by the beams of a shelf.

According to Annex C of the European standard EN 15512: 2020 [2], in operation of the tab connections, the rotational stiffness of the connection k_m, which is determined by experimental tests, works once the looseness angle Φ_l is reached. Until this value rotation angle, the connection behaves like a pin-connection. Therefore, theoretical approach to include the looseness effect in the structural design is divided in two steps in Figure 8: the first step is presented in Figure 8a, for which the tab connection behaves like a pin-connection; the second step is presented in Figure 8b, when the tab connection behaves like a semi-rigid connection whose rotational stiffness k_m is experimentally determined.

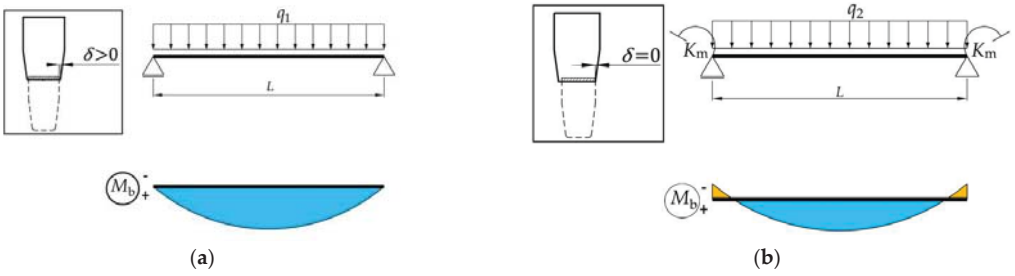

Figure 8. Beam design by considering the looseness effect of beam end connector: (**a**) the first step (pinned connections); (**b**) the second step (semi-rigid connections).

In this manner, the European standard EN 15512: 2020 [2] neglects that the rotational stiffness k_m and the looseness angle Φ_l are experimentally determined in bending test of the beam-connector-upright assembly, when the beam was subjected to the concentrated force applied to its free end, for which the work method is described in Section 2.2 of this research.

It is well-known from literature that the rotation φ of the beam end of the simply supported beam subjected to the uniformly distributed force q is computed by using Equation (3) [27].

$$\varphi = qL^3/(24EI), \tag{3}$$

where E is the modulus of elasticity of the material of the beam; I is the second moment of inertia of the beam cross section with respect to the neutral axis; EI represents stiffness modulus in bending that is constant along the axis of the beam, having the length L.

From Equation (3), it may compute the distributed force q_1 (Figure 8a) that is needed to cover the looseness angle Φ_l by Equation (4).

$$q_1 = 24EI\Phi_l/L^3. \tag{4}$$

The distributed force q_1, acting on simply supported beam (Figure 8a), causes the bending moment $M_{mid,\ \Phi_l}$ developed at the middle of the beam and the maximum deflection $v_{max,\ \Phi_l}$ of the middle of the beam, which are computed by Equation (5) and Equation (6), respectively [27].

$$M_{mid,\Phi_l} = q_1L^2/8. \tag{5}$$

$$\mathrm{v}_{max,\Phi_l} = 5q_1L^4/(384EI). \tag{6}$$

Once the looseness angle Φ_l has been reached, the connection behaves like a semi-rigid connection. From this point further, assuming that the weight of the pallets is placed on the same shelf and is uniformly distributed, the corresponding distributed force q is computed by Equation (7) according to European standard 15512 [2].

$$q = \frac{n_pF_p\gamma_F}{2L}, \tag{7}$$

where n_p is the number of pallets; F_p is the weight of one pallet; γ_F is the load factor that is equal to 1.40 [2].

The uniformly distributed force q_2, which is applied on the beam length L in the second case of loading after the looseness angle Φ_l is covered (Figure 8b), is computed by subtracting the load q_1 from the load q by Equation (8).

$$q_2 = q - q_1 = n_pF_p\gamma_F/(2L) - 24EI\Phi_l/L^3. \tag{8}$$

For the beam shown in Figure 8b, the rotational stiffness of the both end connections is denoted with k_m and it is experimentally investigated according to European standard 15512 [2].

The bending moment $M_{end,\ q_2}$ developed at the both beam end connections and the bending moment $M_{mid,\ q_2}$ developed at the middle of the beam, shown in Figure 8b, are computed by Equation (9) and Equation (10), respectively, according to the recently published paper [6] by the authors of the present research.

$$M_{end,\ q2} = \frac{q_2L^3}{24EI\left(\frac{1}{k_m} + \frac{L}{2EI}\right)}. \tag{9}$$

$$M_{mid,q2} = q_2L^2/8 - M_{end,q2}. \tag{10}$$

The maximum deflection $v_{max,\ q_2}$ of the middle of the beam shown in Figure 8b is computed by using Equation (11), given by the authors in the recently published paper [6].

$$\mathrm{v}_{max,\ q_2} = \frac{q_2L^4(10EI + Lk_m)}{384EI(2EI + Lk_m)}. \tag{11}$$

Using the method superposition of effects, the total bending moment $M_{mid,\,t}$ developed at the middle of the beam and the maximum deflection $v_{max,\,t}$ of the middle of the beam are computed with Equation (12) and Equation (13), respectively.

$$M_{mid,t} = M_{mid,\Phi_l} + M_{mid,q2}. \tag{12}$$

$$v_{max,\,t} = \mathrm{v}_{max,\Phi_l} + \mathrm{v}_{max,\,q_2}. \tag{13}$$

It is noted that both Equations (12) and (13) take into account the looseness effects of the beam-upright connectors located at both beam ends.

If the looseness effects of the beam-upright connectors are neglected, replacing the distributed force q_2 with q in Equations (10) and (11) leads to the mathematical expressions of the bending moment M_{mid} developed at the middle of the beam and of the maximum deflection v_{max}, given by Equation (14) and Equation (15), respectively.

$$M_{mid} = qL^2/8 - \frac{qL^3}{24EI\left(\frac{1}{k_m} + \frac{L}{2EI}\right)}. \tag{14}$$

$$v_{max} = \frac{qL^4(10EI + Lk_m)}{384EI(2EI + Lk_m)}. \tag{15}$$

Finally, the calculation corrections (denoted with *CORR*) concerning the bending moment and maximum deflection considering the looseness effect are computed by Equations (16) and (17), with respect to the case of the beam for which the looseness effects of the beam-upright connectors are neglected.

$$CORR_{M_{mid}} = \frac{|M_{mid,\,t} - M_{mid}|}{M_{mid}} \cdot 100\ (\%). \tag{16}$$

$$CORR_{v_{max}} = \frac{|v_{max,\,t} - v_{max}|}{v_{max}} \cdot 100\ (\%). \tag{17}$$

In order to comparatively analyze the looseness effects on the beam deflection for different combinations of beams, uprights, and connectors, the experimental results shown in Table 2 are additionally considered, reported by the authors in the previously published research article [6] regarding the rotational stiffness k_m and design moment M_{Rd} obtained for other beam-connector-upright assemblies, which are similar to the ones involved in this research. The bending moment developed at the middle of the beam and maximum deflection of the beam are computed by using the Equation (12) and Equation (13), respectively, considering the looseness effects occurred at the connectors with tabs located at both beam ends. The results are compared with the ones obtained by using Equations (14) and (15), which are valid when the looseness effects that occurred at tab connections are neglected.

Table 2. Characteristics of the upright-connector-beam assemblies involved in analysis of the looseness effect on beam's deflection and bending moment developed, adapted from ref. [6].

Assembly Identification Code	Upright W * × t *	Beam (H ** × W_1 ** × t_1 **)	Connector Type	Rotational Stiffness k_m (kN·m/rad)	Design Moment M_{Rd} (kN·m)
A-I-4T	90 × 1.50	A (BOX 90 × 40 × 1.25)	4T	39	1.54
A-I-5T			5T	48	2.30
A-II-4T	90 × 1.75		4T	42	2.43
A-II-5T			5T	76	2.21
A-III-4T	90 × 2.00		4T	45	2.16
A-III-5T			5T	77	2.09

Table 2. *Cont.*

Assembly Identification Code	Upright W * × t *	Beam (H ** × W_1 ** × t_1 **)	Connector Type	Rotational Stiffness k_m (kN·m/rad)	Design Moment M_{Rd} (kN·m)
B-I-4T	90 × 1.50	B (BOX 100 × 40 × 1.25)	4T	35.9	1.38
B-I-5T			5T	57.8	2.24
B-II-4T	90 × 1.75		4T	56	2.03
B-II-5T			5T	86.1	2.36
B-III-4T	90 × 2.00		4T	51.2	2.43
B-III-5T			5T	102	2.18
C-I-4T	90 × 1.50	C (BOX 110 × 40 × 1.25)	4T	43.7	1.70
C-I-5T			5T	77.4	2.15
C-II-4T	90 × 1.75		4T	52.4	2.74
C-II-5T			5T	83.7	2.95
C-III-4T	90 × 2.00		4T	63	2.89
C-III-5T			5T	115	2.61

* Dimensions of the uprights are shown in Figure 4a. ** Dimensions of the beam are shown in Figure 4b.

3. Results and Discussion

3.1. Experimental Results

In Figure 9, the moment-rotation ($M - \theta$) curves recorded in looseness tests are shown for the following beam-connector-upright assemblies: 0-I-5L; 0-II-5L; 0-III-5L.

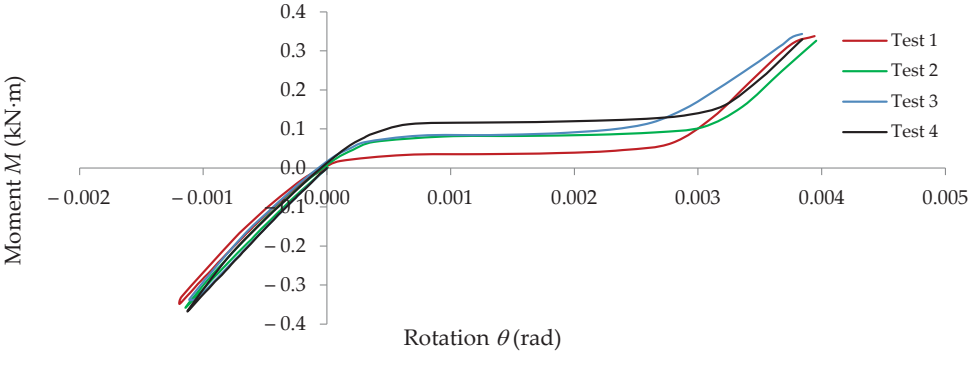

(**a**)

Figure 9. *Cont.*

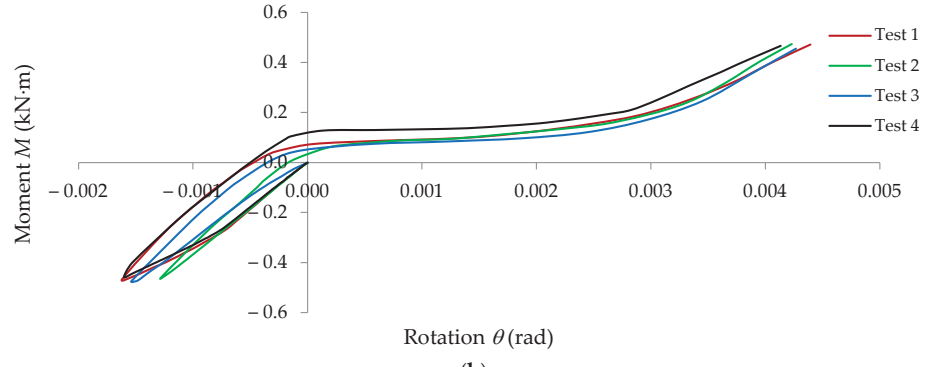

(**b**)

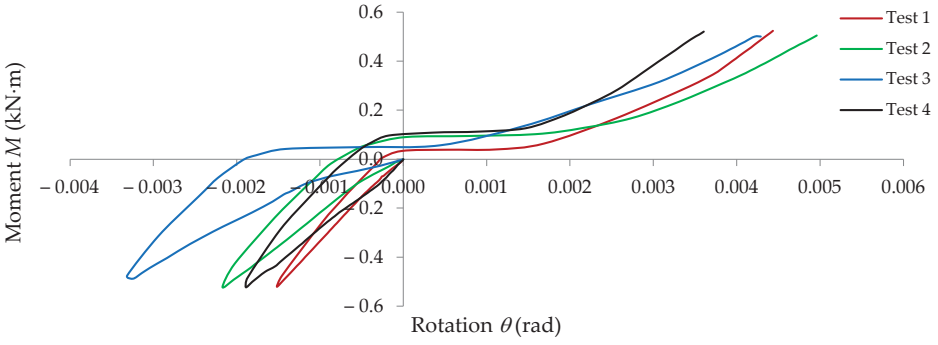

(**c**)

Figure 9. Moment-rotation ($M - \theta$) curves recorded in looseness tests for the beam-connector-upright assemblies: (**a**) 0-I-5L; (**b**) 0-II-5L; (**c**) 0-III-5L.

The moment-rotations ($M - \theta$) curves recorded in bending tests of the three beam-connector-upright assemblies investigated (0-I-5L, 0-II-5L, 0-III-5L) are shown in Figure 10, Figure 11 and Figure 12, respectively.

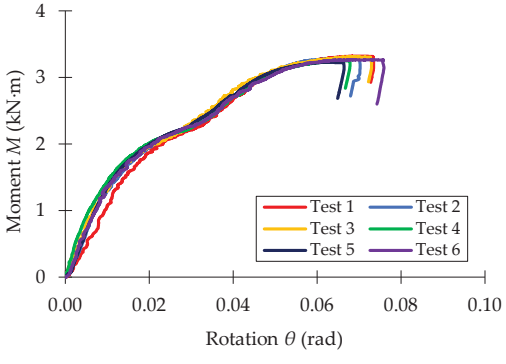

Figure 10. Moment-rotation curve ($M - \theta$) recorded in bending tests for the beam-connector-upright assembly of type 0-I-5T.

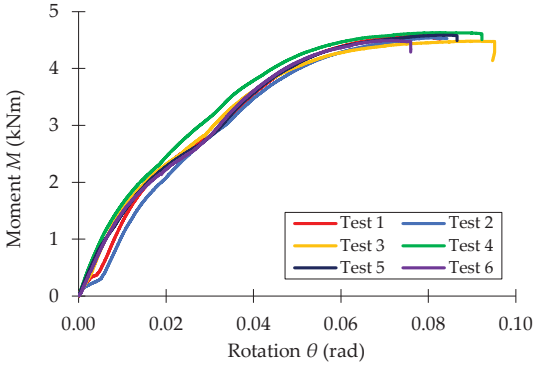

Figure 11. Moment-rotation curve $(M - \theta)$ recorded in bending tests for the beam-connector-upright assembly of type 0-II-5T.

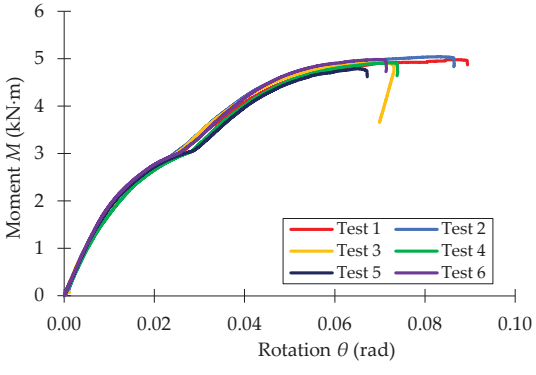

Figure 12. Moment-rotation curve $(M - \theta)$ recorded in bending tests for the beam-connector-upright assembly of type 0-III-5T.

The experimental results regarding the looseness angle Φ_l, design moment M_{Rd}, and rotational stiffness k_m corresponding to the beam-connector-upright assemblies involved in this research are summarized in Table 3.

Table 3. Results obtained in looseness tests and bending tests for all assemblies involved in the experimental program.

Assembly Code	Looseness Angle			Design Moment		Rotational Stiffness	
	$\Phi_{l\,i}$ (rad)	Φ_l (rad)	Stdev (rad)	M_{Rd} (kN·m)	Stdev (kN·m)	k_m (kN·m/rad)	Stdev (kN·m/rad)
0-I-5T	0.00139	0.00133	0.000124	2.91	0.035	72	10.029
	0.00140						
	0.00114						
	0.00137						
0-II-5T	0.00115	0.00116	0.000171	4.02	0.058	96	4.118
	0.00126						
	0.0013						
	0.00092						

Table 3. *Cont.*

Assembly Code	Looseness Angle			Design Moment		Rotational Stiffness	
	$\Phi_{l\,i}$ (rad)	Φ_l (rad)	Stdev (rad)	M_{Rd} (kN·m)	Stdev (kN·m)	k_m (kN·m/rad)	Stdev (kN·m/rad)
0-III-5T	0.00075	0.00080	0.000104	4.32	0.086	114	4.425
	0.00093						
	0.00083						
	0.00069						

3.2. Effects of Looseness of the Semi-Rigid Connections on Mechanical Behavior of the Beam

In order to evaluate the effects of the looseness which takes place at beam-to-upright connections with tabs, it is necessary to investigate the maximum deflection and bending moment developed for the bearing beam being in operation on the storage pallet racking systems. It is considered that the shelf of the storage system consists of two beams having the length of 2.7 m, which must support the maximum weight of 15,000 N corresponding for loading with three pallets. Assuming that the load of 7500 N corresponding to one beam of the shelf is uniformly distributed on the beam length of 2.7 m, the scheme of loading of the bearing beam shows like that shown in Figure 7, subjected to the uniformly distributed force q of 2.78 N/mm (7500 N distributed over 2.7 m).

The looseness effects are investigated for all types of beam-to-upright connections, whose values for the rotational stiffness k_m are given in Tables 2 and 3. Because the looseness angle Φ_l depends mainly on the combination between upright and tabs connectors, it is assumed that the looseness angle Φ_l remains the same for all beam-connector-upright assemblies that combine the same type of upright (type I, II, or III) and connector with 4 tabs (denoted with 4T) or 5 tabs (denoted with 5T). The critical case of the beam-to-upright connections with 5 metallic tabs, denoted with 5T, was involved in looseness tests in this research (Table 1). Taking into account this assumption, the results given in Table 3 for the looseness angle Φ_l were extended for the beam-connector-upright assemblies shown in Table 2. The values of the looseness angle Φ_l, considered in calculus for each connection type, are given in the second column of Table 4.

Table 4. The looseness effects on the bending moment and maximum deflection at the middle of the beam for the upright-connector-beam assemblies involved.

Assembly Code	Looseness Angle Φ_l (rad)	With Looseness Effects		Without Looseness Effects		$CORR_{M_{mid}}$ (%)	$CORR_{v_{max}}$ (%)
		Bending Moment at Mid. $M_{mid,\,t}$ (kN·m)	Max. Deflection at Mid. $v_{max,\,t}$ (mm)	Bending Moment at Mid. M_{mid} (kN·m)	Max. Deflection at Mid. v_{max} (mm)		
0-I-5T	0.00133	3.245	2.83	3.163	2.709	2.59	4.47
0-II-5T	0.00116	3.168	2.753	3.076	2.618	2.99	5.16
0-III-5T	0.00080	3.089	2.662	3.016	2.555	2.42	4.19
A-I-4T	0.00133	2.794	12.383	2.758	12.104	1.31	2.31
A-I-5T		2.692	11.831	2.651	11.511	1.55	2.78
A-II-4T	0.00116	2.753	12.153	2.72	11.897	1.21	2.15
A-II-5T		2.441	10.45	2.394	10.085	1.96	3.62

Table 4. *Cont.*

Assembly Code	Looseness Angle Φ_l (rad)	With Looseness Effects		Without Looseness Effects		$CORR_{M_{mid}}$ (%)	$CORR_{v_{max}}$ (%)
		Bending Moment at Mid. $M_{mid,\,t}$ (kN·m)	Max. Deflection at Mid. $v_{max,\,t}$ (mm)	Bending Moment at Mid. M_{mid} (kN·m)	Max. Deflection at Mid. v_{max} (mm)		
A-III-4T	0.00080	2.709	11.884	2.685	11.7	0.89	1.57
A-III-5T		2.419	10.297	2.387	10.043	1.34	2.53
B-I-4T	0.00133	2.947	10.325	2.911	10.106	1.24	2.17
B-I-5T		2.735	9.429	2.684	9.122	1.90	3.37
B-II-4T	0.00116	2.744	9.455	2.7	9.193	1.63	2.85
B-II-5T		2.522	8.515	2.465	8.174	2.31	4.17
B-III-4T	0.00080	2.774	9.561	2.746	9.39	1.02	1.82
B-III-5T		2.41	8.01	2.368	7.752	1.77	3.33
C-I-4T	0.00133	2.968	8.321	2.923	8.106	1.54	2.65
C-I-5T		2.715	7.478	2.649	7.158	2.49	4.47
C-II-4T	0.00116	2.887	8.043	2.843	7.83	1.55	2.72
C-II-5T		2.668	7.306	2.607	7.012	2.34	4.19
C-III-4T	0.00080	2.79	7.693	2.755	7.524	1.27	2.25
C-III-5T		2.479	6.64	2.426	6.396	2.18	3.81

For the study case considered above, consisting of a beam whose length L is 2.7 m, subjected to the uniformly distributed force q of 2.78 N/mm, having the same beam-to-upright connection at its both ends, the bending moment developed at the middle of the beam and the maximum deflection were computed with Equation (12) and Equation (13), respectively, considering the looseness effects occurred at both beam-end connectors. The results obtained for all beam-connector-upright assemblies are summarized in Table 4. Additionally, the same quantities (bending moment at midpoint of the beam and maximum deflection) were computed for all beam-connector-upright assemblies involved without considering the looseness effect, and the results are also given in Table 4.

To highlight the looseness effects, the calculation corrections concerning both the bending moment M_{mid} developed at the middle of the beam and the maximum deflection v_{max} of the beam are computed with Equation (16) and Equation (17), respectively, with respect to the case of the beam for which the looseness effects of the beam-upright connectors are neglected. The results regarding the calculation corrections are summarized in the last two columns of Table 4. It is remarked that the maximum corrections for both the bending moment developed at the midpoint of the beam and the maximum deflection are recorded for the beam-connector-upright assembly, having the code 0-II-5T.

4. Discussion

In order to interpret the effect of the looseness that occurred at beam-to-upright connections, on the size of the corrections concerning the calculus of both the bending moment M_{mid} developed at midpoint of the beam and the maximum deflection v_{max} of the beam, with respect to the type of the upright and with respect to the rotational stiffness k_m, it is used for the plots shown in Figures 13 and 14.

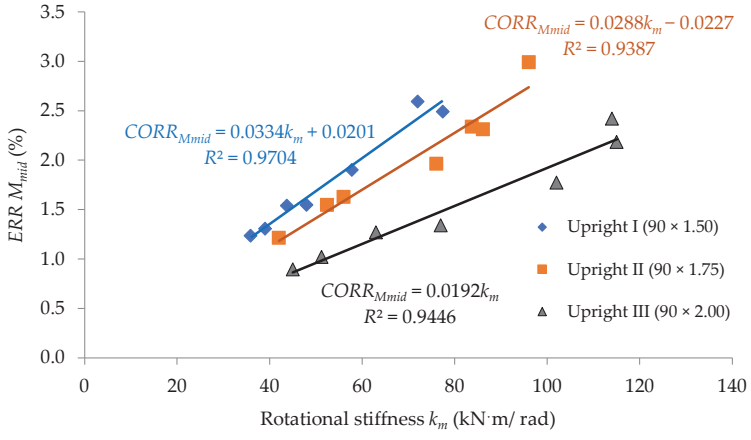

Figure 13. Variation of the calculation correction concerning the bending moment developed at midpoint of the beam related to the rotational stiffness k_m of the connection for each type of the upright involved.

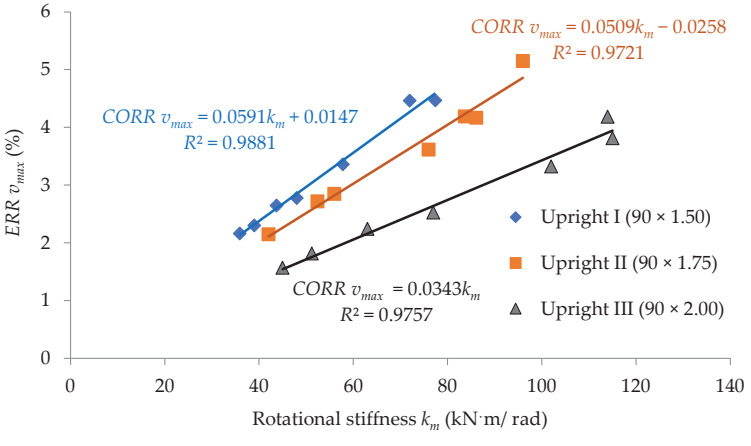

Figure 14. Variation of the calculation correction concerning the maximum deflection of the beam related to the rotational stiffness k_m of the connection for each type of the upright involved.

In Figures 13 and 14, the results regarding the corrections are approximated by using linear functions with respect to the rotational stiffness, k_m, for each type of upright involved in this study. The least squares method was used for approximation of data in both Figures 13 and 14, where the value R^2 close to 1 shows that the data are accuracy approximated. It is observed that for close values of the rotational stiffness k_m, the correction is even greater the thinner the wall thickness of the upright. Those functions shown in Figure 14 could be used in further research to evaluate the size of the corrections, which should be considered in calculation of the maximum deflection v_{max} by considering the looseness effect for a certain type of beam-to-upright connection with tabs. Of course, the approximation functions shown in Figures 13 and 14 only cover the beam-to-upright connections involved in this study.

In Figure 15, the ratio between the bending moment developed at the midpoint of the beam computed by considering the looseness effect of the connection and the same quantity computed without considering that effect is plotted with respect to the rotational stiffness k_m, with two different colors to highlight the effect of the type of the connector. It

may be observed that this ratio is greater for the connector 5T, having five tabs compared to the connector 4T with four tabs.

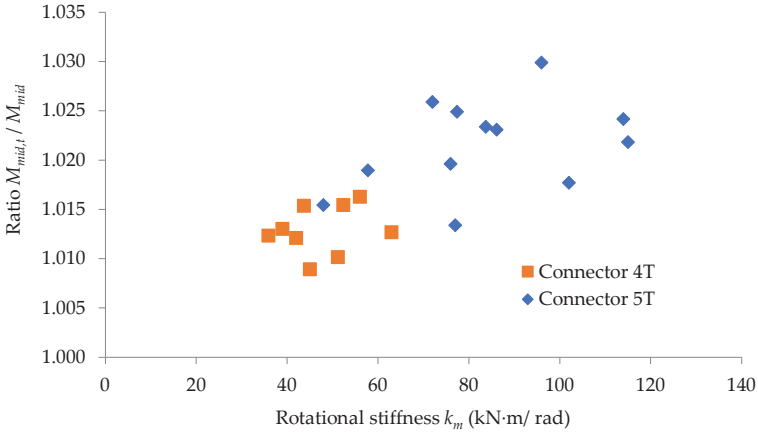

Figure 15. Variation of the ratio $M_{mid,\ t}/M_{mid}$ related to the rotational stiffness k_m of the connection for each type of tabs connector involved.

In a similar way, in the plot shown in Figure 16, it is remarked that the ratio between the maximum deflections computed by considering and without considering the looseness effect is in the range 1.016–1.029 for the connector 4T (with four tabs), while this ratio is in the range 1.025–1.052 for the connector 5T (with five tabs).

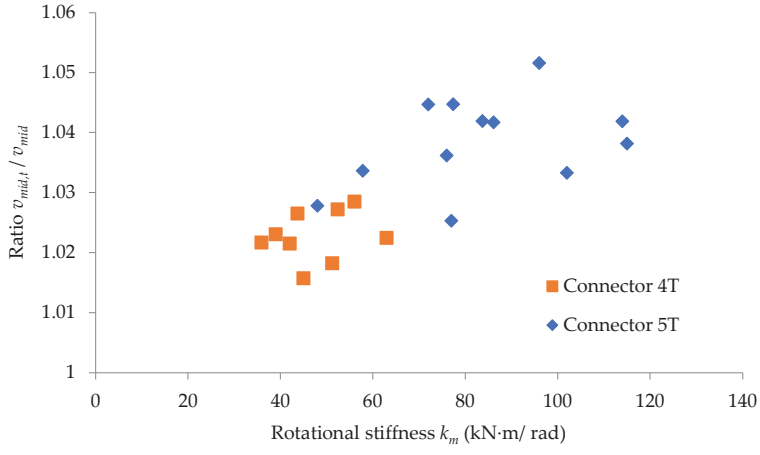

Figure 16. Variation of the ratio $v_{max,\ t}/v_{max}$ related to the rotational stiffness k_m of the connection for each type of tabs connector involved.

The reliability in results concerning the looseness effects could be affected by the magnitude of the vertical load applied to the beam in operation of the storage racking system. Plastic deformation of the tabs of the connector, caused by dynamical loads (earthquake, cyclic loading) applied in the past, could also influence the looseness angle of the tabs connection. Jovanovic et al. [28] have already shown that cyclic loading applied to the beam-to-upright connection of the steel racking systems lead to the increasing of the looseness angle. As a result, the looseness effects on both the deflection of the beam and strength capacity of the beam are much more pronounced in the case of dynamic loading.

5. Conclusions

This paper presents the results experimentally obtained for the looseness angle Φ_l according to the methodology of the European standard 15512 [2], recently updated, for different beam-connector-upright assemblies. Moreover, the effects of the looseness that takes place in connection are evaluated and interpreted concerning the values of the maximum deflection of the bearing beam of the racking pallets system and considering the bending moment developed at the midpoint of that beam.

It may be concluded that there are maximum calculation corrections of 2.99% and 5.16% for the bending moment developed at the midpoint of the beam and for the maximum deflection, respectively, computed by considering the looseness effect with respect to the same quantities computed without considering the looseness effect.

The graphic interpretation of the results proves that the corrections regarding both the bending moment developed at the midpoint of the beam and the maximum deflection are all the more significant the thinner the upright wall. It is also remarked that the ratio between the maximum deflections, computed by considering and without considering the looseness effect, is greater for the connector 5T than for the connector 4T.

In practice, the design engineers should take into account the looseness effects on the maximum deflection of the bearing beam of the racking pallets systems and also on the bending moment developed at the midpoint of the beam, especially for values greater than 80 kN·m/rad of the rotational stiffness of the connection.

Author Contributions: Conceptualization, F.D. and C.C.; methodology, F.D.; validation, F.D. and C.C.; formal analysis, C.C.; investigation, F.D. and C.C.; supervision, C.C.; visualization, F.D. and C.C.; writing of the original draft, C.C. and F.D.; writing—review and editing, C.C. All authors have read and agreed to the published version of the manuscript.

Funding: This research received no external funding.

Institutional Review Board Statement: Not applicable.

Informed Consent Statement: Not applicable.

Data Availability Statement: Not applicable.

Acknowledgments: The authors would like to thank and are grateful to SC Dexion Storage Solutions SRL (Dexion) for good collaboration, for providing of the materials tested and for the technical support. This paper is published with the kind permission of the General Manager, Brian Howson.

Conflicts of Interest: The authors declare no conflict of interest.

References

1. *BS EN 15512*; Steel Static Storage Systems—Adjustable Pallet Racking Systems—Principles for Structural Design. BSI: London, UK, 2009.
2. *EN 15512*; Steel Static Storage Systems—Adjustable Pallet Racking Systems—Principles for Structural Design. BSI: London, UK, 2020.
3. Gilbert, B.P.; Rasmussen, K.J.R. Bolted moment connections in drive-in and drive-through steel storage racks. *J. Constr. Steel Res.* **2010**, *66*, 755–766. [CrossRef]
4. Coelho, A.M.G.; Bijlaard, F.S.K.; da Silva, L.S. Experimental assessment of the ductility of extended end plate connections. *Eng. Struct.* **2004**, *26*, 1185–1206. [CrossRef]
5. Mohan, V.; Prabha, P.; Rajasankar, J.; Iyer, N.R.; Raviswaran, N.; Nagendiran, V.; Kamalakannan, S.S. Cold-formed steel pallet rack connection: An experimental study. *Int. J. Adv. Struct. Eng.* **2015**, *7*, 55–68. [CrossRef]
6. Dumbrava, F.; Cerbu, C. Experimental Study on the Stiffness of Steel Beam-to-Upright Connections for Storage Racking Systems. *Materials* **2020**, *13*, 27. [CrossRef] [PubMed]
7. Dumbrava, F. Research Report: Experimental Research on Stress States and Deformations of Elements (Columns, Beams, etc.). In *The Construction of Thin-Walled Metal Structures*; Transilvania University of Brasov: Brașov, Romania, 2020.
8. Gusella, F.; Arwade, S.R.; Orlando, M.; Peterman, K.D. Influence of mechanical and geometric uncertainty on rack connection structural response. *J. Constr. Steel Res.* **2019**, *153*, 343–355. [CrossRef]
9. Escanio, L.A.; Elias, G.C.; Neiva, L.H.D.; Alves, V.N.; Sarmanho, A.M.C. Analysis of Beam-o-Upright End Connections Steel Storage Systems. *Adv. Steel Constr.* **2020**, *16*, 279–286. [CrossRef]

10. Shah, S.N.R.; Sulong, N.H.R.; Shariati, M.; Khan, R.; Jumaat, M.Z. Behavior of steel pallet rack beam-to-column connections at elevated temperatures. *Thin-Walled Struct.* **2016**, *106*, 471–483. [CrossRef]
11. Schabowicz, K. Testing of Materials and Elements in Civil Engineering. *Materials* **2021**, *14*, 20. [CrossRef] [PubMed]
12. Zadanfarrokh, F.; Bryan, E.R. Testing and Design of Bolted Connections in Cold Formed Steel Sections. In Proceedings of the 11th International Specialty Conference on Cold-Formed Steel Structures, St. Louis, MO, USA, 20–21 October 1992; Missouri University of Science and Technology: St. Louis, MO, USA, 1992.
13. Grondin, G.Y.; Jin, M.; Josi, G. *Slip Critical Bolted Connections—A Reliability Analysis for Design at the Ultimate Limit State*; University of Alberta: Edmonton, AB, Canada, 2007.
14. Gharebaghi, R.; Hosseini, A. Local behavior of column-tree connections with considering bolt-hole clearance and bolt pretension effects. *Int. J. Steel Struct.* **2017**, *17*, 379–388. [CrossRef]
15. Sanborn, M.; Stewart, L.K. Behavior of slip-critical bolted connections subjected to impulsive loads. *Int. J. Impact Eng.* **2020**, *143*, 12. [CrossRef]
16. Kulak, G.L.; Fisher, J.W.; Struik, J.H.A. *Guide to Design Criteria for Bolted and Riveted Joints*, 2nd ed.; John Wiley & Sons: New York, NY, USA, 1987.
17. Galeotti, C.; Gusella, F.; Orlando, M.; Spinelli, P. On the seismic response of steel storage pallet racks with selective addition of bolted joints. *Structures* **2021**, *34*, 3806–3817. [CrossRef]
18. Godley, M.H.R.; Beale, R.G. Analysis of large proprietary access scaffold structures. *Proc. Inst. Civ. Eng. -Struct. Build.* **2001**, *146*, 31–39. [CrossRef]
19. Prabhakaran, U.; Beale, R.G.; Godley, M.H.R. Analysis of scaffolds with connections containing looseness. *Comput. Struct.* **2011**, *89*, 1944–1955. [CrossRef]
20. Asl, M.H.; Farivar, B.; Momenzadeh, S. Investigation of the rigidity of welded shear tab connections. *Eng. Struct.* **2019**, *179*, 353–366. [CrossRef]
21. Zhao, X.Z.; Dai, L.S.; Wang, T.; Sivakumaran, K.S.; Chen, Y.Y. A theoretical model for the rotational stiffness of storage rack beam-to-upright connections. *J. Constr. Steel Res.* **2017**, *133*, 269–281. [CrossRef]
22. Mourya, U.; Jayachandran, S.A. Finite Element Model-Based Dynamic Characteristic Predictions for Cold-Formed Steel Storage Racks. In Proceedings of the Annual Stability Conference Structural Stability Research Council, Denver, CO, USA, 22–25 March 2022; pp. 1–9.
23. Shariati, M.; Tahir, M.M.; Wee, T.C.; Shah, S.N.R.; Jalali, A.; Abdullahi, M.M.; Khorami, M. Experimental investigations on monotonic and cyclic behavior of steel pallet rack connections. *Eng. Fail. Anal.* **2018**, *85*, 149–166. [CrossRef]
24. Yin, L.F.; Tang, G.; Zhang, M.; Wang, B.J.; Feng, B. Monotonic and cyclic response of speed-lock connections with bolts in storage racks. *Eng. Struct.* **2016**, *116*, 40–55. [CrossRef]
25. Ślęczka, L.; Kozłowski, A. Design of beam-to-column joints in steel storage pallet racks by testing and by component method. *Arch. Civ. Eng.* **2008**, *54*, 263–291.
26. Prabha, P.; Marimuthu, V.; Saravanan, M.; Jayachandran, S.A. Evaluation of connection flexibility in cold formed steel racks. *J. Constr. Steel Res.* **2010**, *66*, 863–872. [CrossRef]
27. Cerbu, C. *Strength of Materials. Theory and Applications*; Transilvania University of Brasov: Brașov, Romania, 2014; p. 398.
28. Jovanovic, D.; Zarkovic, D.; Vukobratovic, V.; Brujic, Z. Hysteresis model for beam-to-column connections of steel storage racks. *Thin-Walled Struct.* **2019**, *142*, 189–204. [CrossRef]

materials

MDPI

Article

On Characteristics of Ferritic Steel Determined during the Uniaxial Tensile Test

Ihor Dzioba [1,*], Sebastian Lipiec [1], Robert Pala [1] and Piotr Furmanczyk [2]

[1] Department of Machine Design, Kielce University of Technology, Al. 1000-lecia PP 7, 25-314 Kielce, Poland; slipiec@tu.kielce.pl (S.L.); rpala@tu.kielce.pl (R.P.)
[2] Department of Metal Science and Manufacturing Processes, Kielce University of Technology, Al. 1000-lecia PP 7, 25-314 Kielce, Poland; pfurmanczyk@tu.kielce.pl
* Correspondence: pkmid@tu.kielce.pl; Tel.: +48-41-3424-303

Abstract: Tensile uniaxial test is typically used to determine the strength and plasticity of a material. Nominal (engineering) stress-strain relationship is suitable for determining properties when elastic strain dominates (e.g., yield strength, Young's modulus). For loading conditions where plastic deformation is significant (in front of a crack tip or in a neck), the use of true stress and strain values and the relationship between them are required. Under these conditions, the dependence between the true values of stresses and strains should be treated as a characteristic—a constitutive relationship of the material. This article presents several methodologies to develop a constitutive relationship for S355 steel from tensile test data. The constitutive relationship developed was incorporated into a finite element analysis of the tension test and verified with the measured tensile test data. The method of the constitutive relationship defining takes into account the impact of high plastic strain, the triaxiality stress factor, Lode coefficient, and material weakness due to the formation of microvoids, which leads to obtained correctly results by FEM (finite elements method) calculation. The different variants of constitutive relationships were applied to the FEM loading simulation of the three-point bending SENB (single edge notched bend) specimen to evaluate their applicability to the calculation of mechanical fields in the presence of a crack.

Keywords: S355 steel; uniaxial tensile test; strength properties; true stress-strain relationships

Citation: Dzioba, I.; Lipiec, S.; Pala, R.; Furmanczyk, P. On Characteristics of Ferritic Steel Determined during the Uniaxial Tensile Test. *Materials* **2021**, *14*, 3117. https://doi.org/10.3390/ma14113117

Academic Editor: Krzysztof Schabowicz

Received: 12 May 2021
Accepted: 2 June 2021
Published: 6 June 2021

1. Introduction

The most fundamental test performed to define strength characteristics and plasticity of the material is a uniaxial tensile test. On the basis of this test, the basic material characteristics used in engineering methods of structural strength analysis are determined: yield strength σ_{YS}, longitudinal elasticity modulus E (Young's), ultimate tensile strength σ_{UTS}, and plasticity characteristics-relative elongation A and relative necking Z [1,2]. The most important and most often used are Young's modulus E and yield strength σ_{YS}. The currently applied methods of strength analysis are developed based on the assumption that in the material there is a linear-elastic relationship between stress and stress ($\sigma = E\varepsilon$), and the yield strength is a quantity that limits the scope of applicability of this linear relationship ($\sigma \leq \sigma_{YS}$). It should be noticed that ultimate tensile strength σ_{UTS}, plasticity characteristics: relative elongation A and necking Z play rather an auxiliary role; they enable one to qualitatively assess which material is stronger or more plastic.

However, in the case of strength assessment of components containing crack-like defects, high-stress concentration is observed near the crack tip, the intensity of which reaches several times the values of the yield strength. Moreover, the size of the plastic zone significantly exceeds the one permissible as specified in the requirements of linear fracture mechanics. In this situation, while performing strength analysis, it is essential to apply the model of the non-linear material and defined the relationship between true stress and strain values.

Defining the relationship between true stress-strain, also called the constitutive equation, requires establishing the critical stress and strain of the material. Different methods used to define such relationships were analyzed in the articles [3–6]. However, in summary, the authors of the paper [4] came to the conclusion that, up to date, no uniform and unequivocal method for determining the true stress-strain relation of the material was suggested.

To create a true stress-strain relationship of the material, the data from the uniaxial tensile test are needed. Until the specimen reaches the maximum strength (until necking starts), there is a uniform elongation of the testing coupon of the specimen, and true stress and strain are calculated building upon nominal values based on the Equation (1):

$$\varepsilon_t = \ln(1 + \varepsilon_n); \sigma_t = \sigma_n(1 + \varepsilon_n) \quad (1)$$

During neck formation, the material is deformed unevenly, and different levels of stress and strain occur in various cross-sections of the specimen; the maximum values are in the minimum cross-section of the neck. To determine stress and strain in the minimum cross-section of the neck and, based on their basis, define a relationship of true stress-strain, different methods were developed and proposed.

The approach based on the correlation of stress level in the neck bottom with the use of Bridgman's equation [7] does not enable the assessment of the plastic strain and does not involve material hardening. The extrapolation of the stress-strain relationship obtained as a result of fitting the true stress and strain values by power function over the section of uniform elongation the specimen is frequently applied. The above-mentioned approach is also not suitable since the true stress-strain relationship during necking is described rather by a linear function, not by a power function. More information on this topic is provided in the further part of this paper. Methods for establishing the true stress-strain relationships based on the iterative adjustment are also in use. In this approach is believed that the relationship is true when the numerically calculated load curve of the specimen is compatible with the diagram obtained during the uniaxial tensile test [8–12].

In the method of defining the constitutive relationship of a material developed by Bai and Wierzbicki [13–15], it was proposed to take into account the influence of characteristic values of the stress field-the stress triaxiality coefficient, Lode coefficient, and the plastic strain of a material. In the articles of Neimitz et al. [16–18], some modifications of the Bai and Wierzbicki method were introduced. They allowed for taking into account the emerging inhomogeneity of the material in the areas of high levels of plastic deformation.

The knowledge of constitutive relation is necessary at determining the mechanical fields in elements containing the crack-type defects or sharp notches, where are high level of concentration stress and strain. The obtained values of strain and stress distributions will depend on the correct determination of the material constitutive relationship, which has an impact on the assessment of strength and safety using of the elements [19–22].

The problem of the influence of material inhomogeneity on the process of its destruction is also analyzed in the model known as GNT (Gurson-Needleman-Tvergaard) [23–28]. In the GTN model, the process of void nucleation—growth—coalescence is directly taken into account using certain postulated functions, but the functions must be properly calibrated by experimental and numerical testing.

This article presents experimental and numerical research, the main goal of which was to determine the constitutive relationship between the true strain and stress of the material. The paper addresses test results obtained by the authors on S355 steel of ferrite-pearlite microstructure, although similar results were obtained for other types of ferritic microstructure [29,30]. The results concern the application of different test methods to provide the true stress-strain relationship, including evaluation of the specimen cross-section reduction using the voltage potential change method and video recording; microstructural and fractographic tests carried out with a scanning microscope. Numerical modeling and calculation of stress and strain fields at loading specimen containing crack (SENB) were performed for verification of the constitutive relations correctness.

2. Materials and Research Methods

The material used in tests is S355 steel (former symbol—18G2A steel). It is a structural steel similar to ASTM A765. The chemical composition of S355 steel is presented in Table 1 [31]. It is a low carbon structural steel with a medium level of strength characteristics and suitable weldability. The steels of this grade are widely applied to construct different types of building structures, tanks, and pipelines [32,33]. A laboratory heat-treatment was conducted on specimen sections to reduce the influence of the thermomechanical treatment used during the production of elements in steel plants. The specimens were normalized by annealing it for 20 min at the temperature of 950 °C, and next cooled in the air. Due to such processing were obtained of ferrite-pearlite microstructure (FP), with grain size of 7–20 μm (Figure 1), in the specimens.

Table 1. Chemical composition of S355 steel (weight %).

C	Si	Mn	Cr	Ni	S	P
0.18	0.2–0.5	1.5	max. 0.003	max. 0.003	max. 0.004	max. 0.004

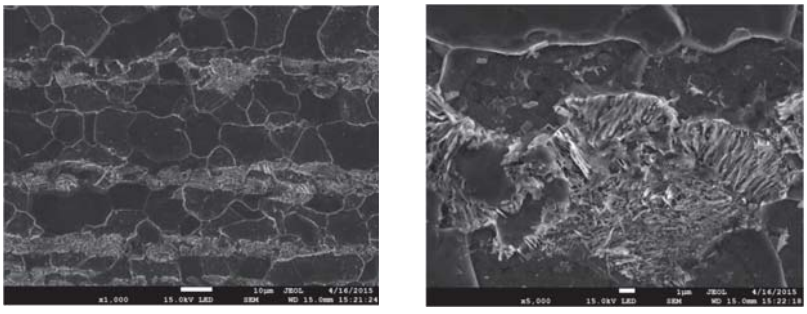

(**a**) (**b**)

Figure 1. Steel S355 of ferrite-perlite (*FP*) microstructure: (**a**) ×1000; (**b**) ×5000.

The uniaxial tensile test in laboratory conditions (at 20–22 °C) was conducted on standard five-fold cylindrical specimens with an initial diameter d_0 of 5.0 or 10.0 mm. Tests were performed with the use of a Zwick-100 testing machine (ZwickRoell, Ulm, Germany) with an electrodynamic drive, equipped in the automated system of loading control and data recording in real-time. The signals of the load force and elongation of the measuring distance were recorded in all tested specimens. In addition, in order to determine the minimum diameter of the specimen, video recording of the neck zone was performed during its elongation, as well as the potential of voltage change [34,35]. The details of this research would be presented in the next chapters of this article. In addition, to define the changes in the microstructure by different strain levels, some tested specimens were subjected to metallographic and fractographic testing on a scanning electron microscope (SEM, JEOL, Zaventem, Belgium) JSM-7100F. Tensile specimens and specimens containing cracks loaded by three-point scheme bending (SENB were also modeled and analyzed using the program for numerical testing ABAQUS (ver. 6.12-2, 3DASSAULT SYSTEMES, Vélizy-Villacoublay, FR-78, France).

3. Experimental Research

Nominal stress-strain curves with Luder's yielding strain plateau were obtained for tested S355 steel (Figure 2). Based on nominal values, true stress and strain values were calculated in the range of uniform elongation (Equation (1)), and they were fitting by the power function, Equation (2):

$$\sigma_t = \alpha \cdot (\varepsilon_t)^n \quad (2)$$

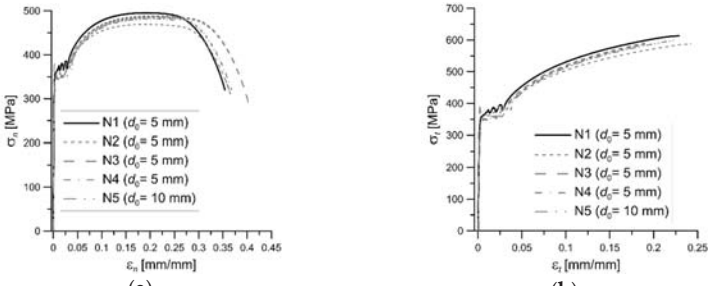

(**a**) (**b**)

Figure 2. The stress-strain plots for specimens of S355 steel: (**a**) nominal values; (**b**) true values.

The appropriate values of strength characteristics and plasticity obtained based on nominal and true data are present in Table 2.

Table 2. The strength and plasticity properties of S355 steel.

S355 Steel	σ_{YS_L}, (MPa)		σ_{YS_H}, (MPa)		σ_{UTS}, (MPa)		E, (GPa)		n		A_5, (%)
	Nom.	True	Nom.	True	Nom.	True	Nom.	True	Nom.	True	Nom.
Average	366.7	368.3	377.5	380.0	489.6	596.9	200	201	7.89	4.78	37.23
Maximum	375.7	379.5	381.9	392.0	495.6	613.3	203	204	8.93	5.08	40.45
Minimum	353.3	356.7	357.6	362.7	479.6	587.9	198	198	6.96	4.28	35.12

3.1. Assessment of Material Strain

Metallographic examinations were conducted on specimen sections made in an axis plane, which was polished and etched with a solution of 3%HNO_3. The aim of this research was to determine the changes in the strain-induced material microstructure. The microstructure was observed along the specimen axis at a different distance from the fracture plane. The exemplary images taken at different distances from the fracture surface are shown in Figure 3. The images provided clearly saw the differences in the material microstructure. With the approaching proximity to the specimen fracture plane, the grains become more stretched out in the direction of specimen tensile force.

It is easy to notice that the grains elongation near the fracture plane is several times bigger as compared to the material undeformed in the gripping section of the specimen. Grains measurement was performed on the microstructure images obtained at the appropriate distances from the fracture in order to determine the quantitative values of deformed material. The measurements were conducted in accordance with the norm requirements [36]. The statistical analysis of data was performed next. The exemplary histograms of the grain length of the microstructure of S355 steel in different distances from the fracture plane and the statistical normal distribution of grain size are shown in Figure 4.

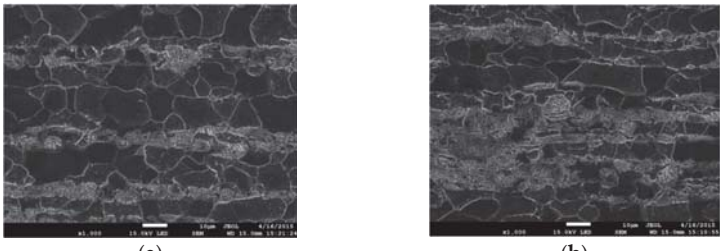

(**a**) (**b**)

Figure 3. *Cont.*

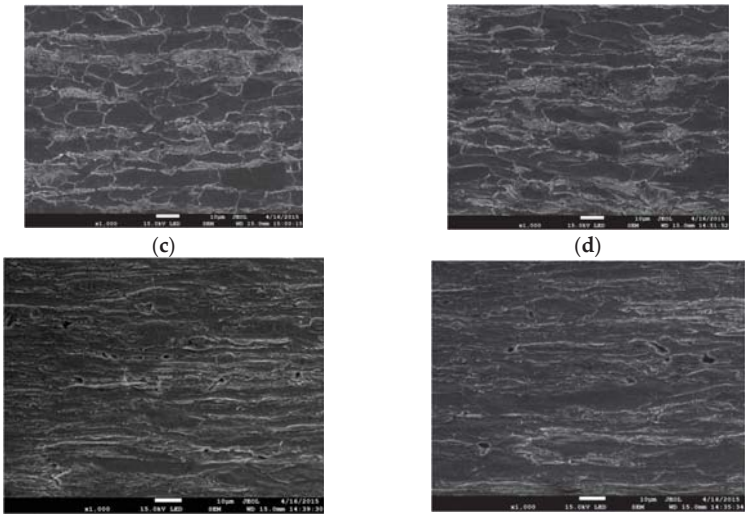

Figure 3. Deformed microstructure of S355 steel at different distance from the fracture plane: (**a**) 17 mm (undeformed material); (**b**) 7 mm; (**c**) 4 mm; (**d**) 2 mm; and (**e**,**f**) 0.1–0.2 mm.

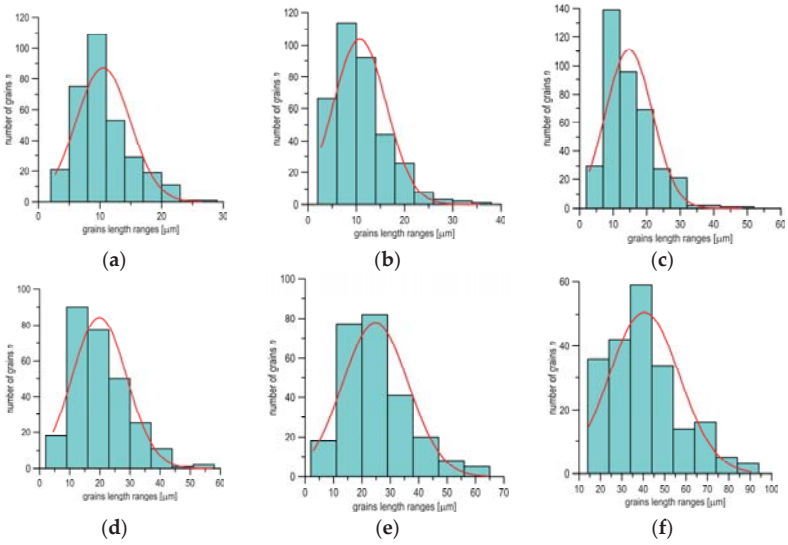

Figure 4. Histograms and graphs for normal distributions of grain length at different distances from the fracture plane of the specimen: (**a**) 17 mm; (**b**) 10 mm; (**c**) 5 mm; (**d**) 3 mm; (**e**) 2 mm; and (**f**) 0.1 mm.

The average grain size in the appropriate distance from the fracture plane was determined based on the statistical normal distribution (Figure 5a). The knowledge of the average grains size enabled to define the grain deformation at appropriate distances from specimen fracture plane. Strain in the appropriate point was calculated as: $\varepsilon_{i\_11} = (l_{i\_11} - l_{0\_11})/l_{0\_11}$, where l_{0_11} and l_{i_11}—are average grains size in the undeformed and deformed state. The strain distribution depending on the distance from the fracture plane, which was obtained based on grain measurements, is shown in Figure 5b. Strain

achieves the maximum value directly near the fracture plane, so that is why the strain level in this region was assumed to be critical. Based on the conducted measurements—ε_{c1_11} = 2.80–3.10 = 280–310%. In a similar way, strains in the perpendicular direction (radial) ε_{i_22} and critical value were determined as ε_{c_22}.

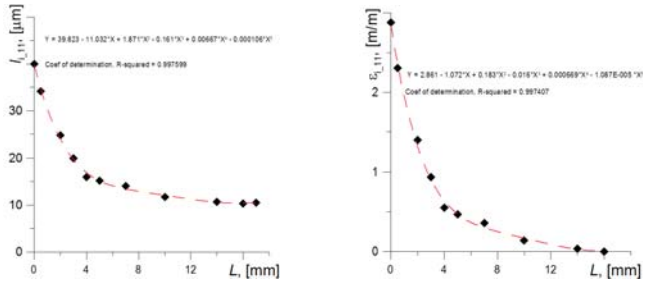

(**a**) (**b**)

Figure 5. Graphs of changes in ferrite grain length (**a**) and strain level (**b**) in a uniaxially tensile specimen made of S355 steel.

The strain level also can be determined with the assumption that the strain is the ratio of the increase in $\Delta\Delta L_i$ to the length of the measuring section ΔL_{i0}, in the case when the length of the segment ΔL_{i0} tends to an infinitely small value d:

$$\varepsilon = \lim_{\Delta L_{i0} \to d} \left(\frac{\Delta\Delta L_i}{\Delta L_{i0}} \right) \tag{3}$$

where: $\Delta\Delta L_i = \Delta L_i - \Delta L_{i0}$; ΔL_{i0}—length of the testing segment before tensile test, ΔL_i—length of the testing segment after tensile test; d—this value can be equated with the microstructure size, namely the size of the grain.

In this approach, the critical level of strain, ε_{c2_11}, was determined by extrapolating the fit function to the size of the deformed ferrite grain. In this approach, the measuring segment of the tested specimen was divided into equal sections by plotting marks, every 2.5 mm, as is illustrated in Figure 6. When the test was performed, the elongation of each section was measured, and the ratio of elongation to the initial length of sections of various lengths $\Delta\Delta L_i/\Delta L_{i0}$ was determined and presented the dependence of these ratios to the length of the initial sections (Figure 6). For example, the photo shows two sections with initial lengths ΔL_{i0} = 5 mm and 15 mm. The next extrapolation of the fit function to the ferrite grain size level (40–42 μm) allows us to estimate the critical deformation value: $\varepsilon_{c2\_11} \approx 2.88$.

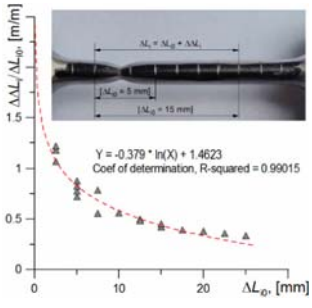

Figure 6. The scheme presents the measurement of strain in a uniaxial tensile test of the specimen (in the photo) and the obtained strain values together with the fitting function.

So, the two approaches presented above are lead to obtaining similar critical strain values from the range of: ε_{c_11} = 2.80–3.10.

3.2. Assessment of the Actual Minimum Diameter of Specimen

During the uniaxial tensile test, the minimum cross-sectional area in the neck permanently changes. To calculate the actual stress in the specimen at uniaxial tensile, it is necessary to know the area of the minimum cross-section of the neck. Two methods were used for this purpose. In the first, video recording of the tensile process was used to record the size of the minimum diameter in time (Figure 7). That allowed to calculate the value of the actual stresses σ_a as the ratio of the actual value of the force to the actual value of the minimum cross-section area S. The stress value at the moment of specimen fracture, determined by this method, is $\sigma_{c1} \approx$ 1275–1300 MPa.

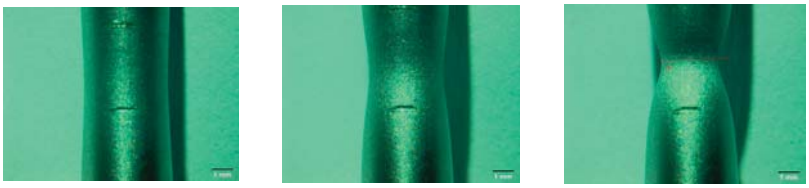

(**a**) (**b**) (**c**)

Figure 7. Examples of forming neck during specimen tensile (recorded by video-camera Olympus): (**a**) ~250 s, start of necking; (**b**) ~350 s; and (**c**) ~450 s, before specimen fracture.

Using video recording also allowed us to establish the elongation of the measured sections in time. On the basis of these measurements, the actual strain values occurring in the specimen tensile process were estimated. This allowed us to present the stress-strain diagram for true values, assuming that $\sigma_a = \sigma_t$ (Figure 8). Based on these results, the stress-strain relationship for actual values on the neck forming section can be described by a linear function.

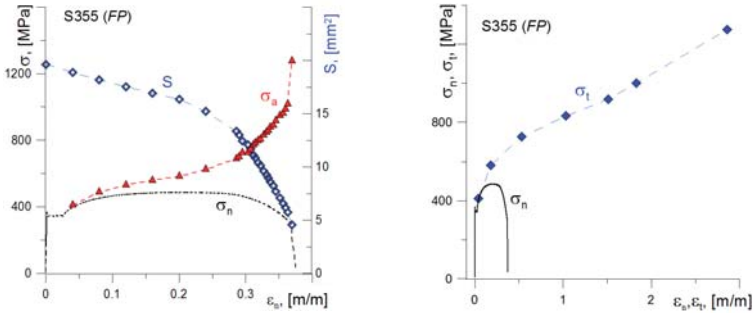

(**a**) (**b**)

Figure 8. (**a**) Reduction in the specimen cross-sectional area S and increase in stresses σ_a during loading; (**b**) the stress-strain plots for nominal and true values.

The second method used to estimate the minimum cross-sectional area was the method of recording the change of the electric voltage potential measured on the tested sample section. This method is often used for determining length or increment of cracks growth in quasi-static or fatigue tests [34,35]. The relationships between the change in nominal stresses (σ_n-t) and the potential value (ΔV-t) over time are shown in Figure 9a. When the specimen is tensile, the values ΔV significantly increase and is inversely proportional to the specimen minimum cross-sectional area S.

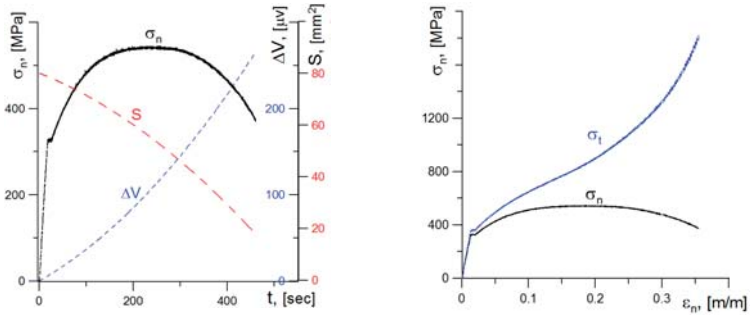

Figure 9. (**a**) The graphs of nominal stresses, potential increase, and minimum specimen cross-section during the tensile test; (**b**) the graphs of nominal and true stresses as a function of nominal strain.

The stress diagram σ_a obtained as the ratio of the actual force values to the minimum cross-sectional area is shown in the Figure 9b. The true stresses increase during specimen tensile and reach a critical value at the moment of specimen breaking at the level of $\sigma_{c2} \approx$ 1870–2000 MPa. These values are higher as compared to those obtained via the method for determining cross-sectional area with video recording—$\sigma_{c1} \approx$ 1275–1300 MPa. The reason for this difference will be analyzed in the further part of this article.

3.3. Numerical Analysis of Stress-Strain State

The results obtained in the experimental tests followed the creation of stress-strain relationships of the tested material. The use of various research methods has led to the presentation of several different variants of the stress-strain relationship of a material. The constitutive stress-strain relationships were defined on the basis of the obtained characteristic values ε_c and σ_c. The correctness of the material relationship was verified by entering it into the numerical model of the specimen that was subjected to the uniaxial tensile test. The result, in the form of the force-elongation relationship of the specimen, obtained by calculating with the use of the finite element method (FEM), was compared with the relationship recorded during the test. The suitable compatibility of graphs obtained by calculation and experimental test should indicate a correctly defined material constitutive relationship.

3.3.1. Numerical Modeling

The numerical modeling of specimens was performed in the ABAQUS program. Due to the fact that in the uniaxial tensile specimen, an axisymmetric state occurs, the model of $\frac{1}{4}$ specimen, which is shown in Figure 10a, was used for the calculations. The load was applied by displacement of the plane of the specimen grip according to those recorded during the experimental tests (Figure 10a). The four-node finite elements were used in the mesh. The mesh was condensed along with the approaching to the blocked radial edge. The selection of the size of finite elements and the change in mesh condensation was preceded by initial calculations in order to obtain the convergence of the results. An enlarged fragment of the concentrated undeformed mesh near the blocked plane is shown in Figure 10b, and the same deformed fragment, in Figure 10c.

Numerical calculations were performed to determine the stress and strain distributions in front of the crack tip. The FEM calculations have been realized on the numerical model of the SENB (single edge notched bend) specimen by using the Abaqus program. The dimensions of the SENB specimen were as follows: W = 24 mm, S = 96 mm, B = 12 mm, a_0/W = 0.55. The 1/4 of the numerical specimen was modeled due to the occurrence of symmetry. The SENB specimen was divided into 21 layers in thickness direction. The eight-node three-dimensional elements were used in the calculation. The possibility of transference was blocked according to the scheme shown in Figure 11 (enabling the

movement of the cracked part of the XOZ specimen, blocking the possibility of movement of the uncracked part of the XOZ specimen along the y-axis, blocking the possibility of moving the central plane of the XOY specimen along the z-axis, blockage of the lower roller). The density of the elements net increases in the direction to crack tip. The crack tip was modeled as an arc of 0.012 mm in the radius. The selection of the finite element size and the partition of the specimen into layers was preceded by preliminary analyses in order to achieve convergent analysis results with the appropriate quality of the finite element mesh.

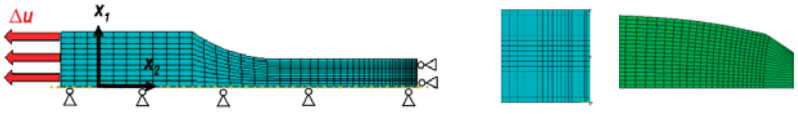

(**a**) (**b**) (**c**)

Figure 10. Numerical model of the tensile specimen (**a**); undeformed mesh fragment near blocked plane (**b**); deformed mesh fragment near blocked plane (**c**).

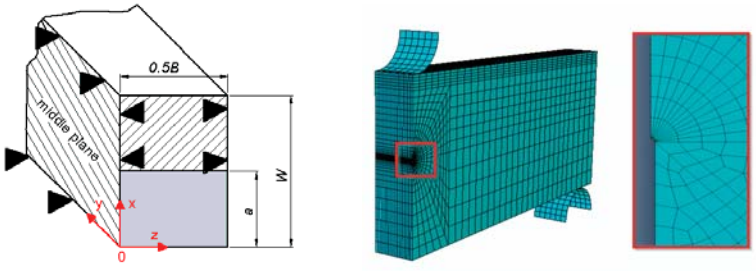

(**a**) (**b**)

Figure 11. Numerical model of SENB specimen: (**a**) scheme of the boundary conditions; (**b**) scheme of the mesh.

3.3.2. The Stress and Strain Distributions in the Neck of the Tensile Specimen

Three variants of the material stress-strain relationships were investigated in a numerical simulation. The constitutive relationship used as the first variant (var. 1) is presented by a stress-strain diagram with critical values: ε_c = 3.2 and σ_c = 1300 MPa (Figure 12a). For the second variant (var. 2), a constitutive relationship was assumed for the critical value of stress at σ_c = 2000 MPa and strain of ε_c = 3.2 (Figure 12b). The calibration method of the constitutive dependence of material suggested by Bai and Wierzbicki [13–15] with the modification of Neimitz et al. [16,17] was also verified (var. 3; Figure 12c). In the Bai and Wierzbicki method, the influence of the stress triaxiality factor in the specimen is taken into account during calibrating of the material constitutive relationship. In turn, the modification proposed by Neimitz takes into account the weakening of the material at the expense of the formation of voids during the neck formation. These suggestions will be further talked over in the Discussion chapter.

The comparison of the curves obtained experimentally and the calculated by FEM for the tensile-loaded specimens are shown in Figure 12d–f. The curve FEM calculated is lower than the experimental one in an interval corresponding to the necking zone for var. 1, Figure 12d. The difference between these curves increases with the necking intensification. Thus, the obtained result indicates that the constitutive relation (var. 1) is not properly.

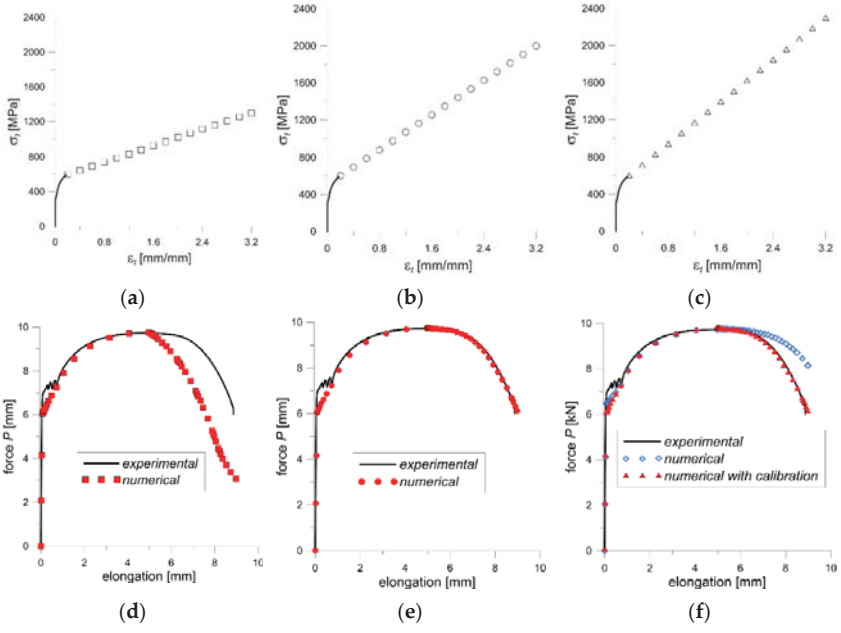

Figure 12. The stress-strain graphs for: (**a**) var. 1, (**b**) var. 2, (**c**) var. 3, and suitable numerical and experimental force-elongation curves for: (**d**) var. 1, (**e**) var. 2, and (**f**) var. 3.

For var. 2 and var. 3, the experimental and computational curves are very close to each other, and they almost overlap (Figure 12e,f). This means that the constitutive relations with the proposed parameters are correct.

An important aspect, which should be taken into consideration, is the character of fracture surface in a specimen subjected to the uniaxial tensile test. The specimen break surface shows two areas, which differ in fracture mechanism (Figure 13). In the central part of the fracture surface is observed zone with radius r_2 called the "cup bottom", which is perpendicular to the specimen axis. That zone consists of many small areas where the fracture process developed mainly according to the void growth and shear mechanisms. While, near the side surfaces of the specimen, the crack development follows along quasi-conical surface mainly according to the shear mechanism. The outside radius (r_1) measured in the neck includes these two areas.

The critical stress level calculated as the force value at fracture to the surface of the inner region leads to the results in the range of 2100–2300 MPa, which is higher than the critical stress value obtained by the method for changing the voltage potential (1870–2030 MPa). Direct application of such a relationship in numerical calculations leads to obtaining values higher than the experimental ones (blue symbols in Figure 12c). However, carrying out calibration taking into account the state of stresses and strains as well as the material weakening (var. 3) leads to the obtaining of computational results consistent with the experimental ones (red symbols in Figure 12c).

3.3.3. Stress and Strain Analysis in Crack Front of the SENB Specimen

Calculations of mechanical fields for the model of the SENB specimen also were performed in order to check the correctness of the results obtained by using different constitutive relations (var. 1, var. 2, and var. 3). For the select point of the specimen deflection (Δu = 1.2 mm), the distributions of the stress and plastic strain in front of the crack tip are presented for the symmetry plane of the SENB specimen, where the highest values occurred (where: σ_{11}—in the direction of crack growth, σ_{22}—in the direction of perpendicular to the

crack plane, σ_{33}—in the direction of the specimen thickness). The stress component σ_{22} and plastic strain ε_{pl} have a dominant role in fracture process initiation [37–41].

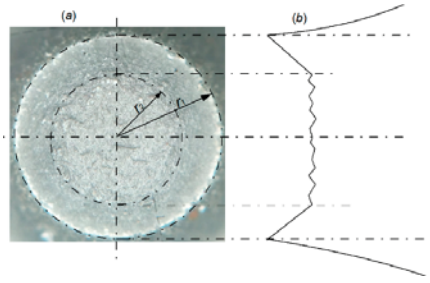

Figure 13. View of break surface of the tensile specimen (**a**) and a scheme of the break plane profile (**b**).

In plastic strain distributions ε_{pl}, the differences are insignificant, while in stress distribution, they are visible (Figure 14). It is clearly noticeable that stress components obtained using a constitutive relationship of var. 1 demonstrate a significant deviation from the results computed of var. 2 and var. 3, especially in of σ_{22} and σ_{33} distributions (Figure 14c,d). In the vicinity of the crack tip, where the highest strain levels are observed, the differences are 100–150 MPa. While receding from the crack tip and along with the decrease in the strain level, the difference between stress distributions determined by assuming various constitutive relations is on the decrease. Thus, the using the constitutive relation of var. 1 in calculations leads to obtaining incorrect stress values, especially in high-strains zone near the crack tip.

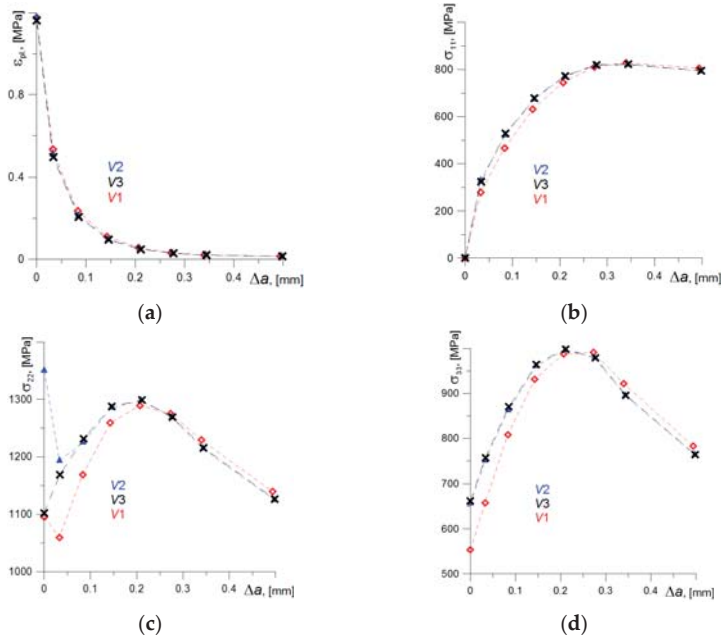

Figure 14. The distributions of plastic strains (**a**) and of stress components (**b**–**d**) in front of the crack calculated by means of FEM.

The stress distributions σ_{22} and σ_{33} were calculated according to constitutive relationships of var. 2 and var. 3 overlap everywhere except the area near the crack tip. The differences in stress distribution curves are observed for σ_{22} stress (Figure 14c). They are due to different assumptions in defining constitutive relations in var. 2 and var. 3. This problem will be discussed in detail in the Discussion chapter below.

4. Discussion

The comparison of the results obtained according to FEM with the experimental results shows that for the correct numerical mapping of the specimen load, the proper definition of the stress-strain relationship of the material is of key importance. However, only the verification carried out using FEM calculations allows indicating the proper of constitutive relation.

The results received according to the methods for determining the constitutive relationship for var. 2 and var. 3 are similar to each other, although they are based on different approaches. In the var. 3 method, developed by Bai and Wierzbicki [13,14], the constitutive relationship is defined based on the characteristics of the stress field, Equation (4):

$$\sigma_{yld} = \overline{\sigma}(\bar{\varepsilon}_p)\left[1 - c_\eta(\eta - \eta_0)\right]\left[c_\theta^s + (c_\theta^{ax} - c_\theta^s)\left(\gamma - \frac{\gamma^{m+1}}{m+1}\right)\right] \tag{4}$$

where:

- $\overline{\sigma}(\bar{\varepsilon}_p)$—the function that describes the true stress-strain relationship, which is obtained experimentally during the tensile test;
- η—triaciality stress factor: $\eta = \frac{\sigma_m}{\sigma_e}$; $\sigma_m = \frac{1}{3}(\sigma_{xx} + \sigma_{zz} + \sigma_{yy})$; σ_e—effective stress; η_0—the reference factor of the triaxial stress factor in the calibrated specimen (for uniaxial tensile specimen—0.33);

Quantities c_η, c_θ^s, c_θ^{ax}, m are usually determined experimentally. Quantities c_θ^s, c_θ^{ax} are related to the Lode angle value: θ ($c_\theta^{ax} = c_\theta^t$ for $\theta \geq 0$, $c_\theta^{ax} = c_\theta^c$ for $\theta < 0$);

The function γ is calculated from the Equation (5):

$$\gamma = 6.46[sec(\theta - \pi/6) - 1] \tag{5}$$

Lode angle is calculated from the Equation (6):

$$\overline{\theta} = 1 - \frac{6\theta}{\pi} = 1 - \frac{2}{\pi} arccos\xi \tag{6}$$

where:

$$\xi = L\frac{9 - L^2}{\sqrt{(L^2+3)^3}} \tag{7}$$

where L is the Lode parameter, calculated from the formula:

$$L = -\frac{2\sigma_{II} - \sigma_I - \sigma_{III}}{\sigma_I - \sigma_{III}} \tag{8}$$

where: σ_I is the biggest and σ_{III} the smallest component of principal stress.

In articles Neimitz et al. [16–18], modification of the factor c_η was suggested, which considered the increasing effect of material weakness along with the increased level of in high plastic strain, Equation (9):

$$c_\eta{}' = c_\eta\left[1 + H\left(\varepsilon_{pl\_0}\right)\left(\varepsilon_{pl\_i} - \varepsilon_{pl\_0}\right)\right]^\alpha \tag{9}$$

where:

ε_{pl_0}—plastic strain level, by which the onset of void coalescence takes place;

α—the exponent takes values in the range from 5.0 to 6.0;

$H(\varepsilon_{pl\_0})$—is a Heaviside function.

The process of nucleation, growth, and coalescence of voids in the material was confirmed by SEM tests of microsection of specimen axial plane after uniaxial tensile (Figure 15). The increase in the number and the size of voids was observed while approaching the plane of specimen fracture plane, where the plastic strain increases, which qualitatively confirms the correctness of modification introduced by Neimitz et al. [16]. A detailed description of determining the quantities used while defining the constitutive relation according to var. 3 on specimens made from S355 steel with different geometrical shapes was described in papers [17,18].

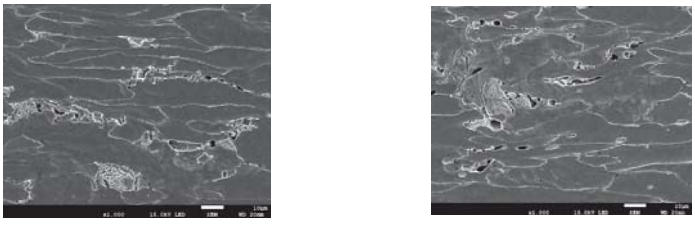

(**a**) (**b**)

Figure 15. Development of voids in a uniaxially tensile specimen: (**a**) ~1.0 mm since the fracture plane; (**b**) directly at the fracture plane.

FEM results similar to var. 3 were obtained using the stress-strain relationship defined on the basis of determining the minimum cross-section of the specimen using the change in voltage potential (var. 2). On the other hand, the results obtained by applying the stress-strain relationship for var. 1, which was defined based on the data of the specimen outside diameter, differ significantly from data for var. 2, var. 3, and of the experiment. Such a result indicates that the true stress determined based on the measurement of the outside minimum diameter in the neck of the specimen is incorrect.

The stress triaxiality factor, *Lode* coefficient, and effect of material weakness in high-strain zones were taken into consideration when determining the constitutive stress-strain relationship for var. 3. However, when defining a constitutive dependency for var. 2 indirectly, only the material weakening effect has been taken into account, while changes in the stress triaxiality factor and *Lode* coefficient are not taken into account. The impact of the stress triaxiality factor and *Lode* coefficient is revealed at high-strain levels when the plastic fracture mechanism occurs through the growth and coalescence of voids; thus, the differences in stresses are recorded for true plastic strains $\varepsilon_{pl} \geq 0.4$.

The calculation of stress distributions by means of FEM indicates that the use of the constitutive stress-strain relationship according to var. 3 leads to obtaining the correct results in the entire diapason of strain values the material. In the case of using the constitutive relationship according to var. 2, the results convergent with var. 3 were received for range $\varepsilon_{pl} < 0.4$, which corresponds to strain up to the beginning of the neck formation for the specimen uniaxial tensile.

The presented approach to defining the constitutive relationship of the true stress-strain of the material allows for the analysis of mechanical fields in areas with very high levels of plastic strains. In tests carried out by the authors, the material weakness effect due to the voids growth was noticed in different types of ferritic steels in tensile and bending tests (Figures 15 and 16) [17,30,42]. The presented method, as well as the GNT method [23–28], allow for the accurate analysis of mechanical fields in areas with very high levels of plastic strain, where the material is no longer actually homogeneous. The problem related to carrying out numerical calculations and determining the distribution of mechanical fields before the tip of crack-type defects is a very important aspect on which the local approach to the analysis of the strength of structural elements is based [43–47].

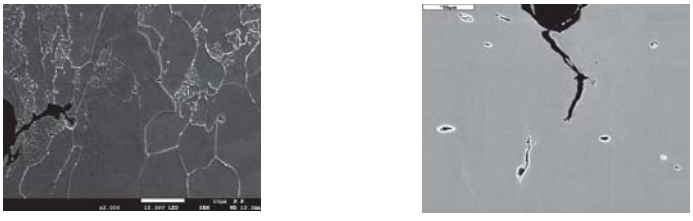

(**a**) (**b**)

Figure 16. Deformed and damaged material in front of crack tip in SENB specimen: (**a**) S355 steel; (**b**) 14MoV6 steel.

5. Summary

This article presents the procedure of defining the true stress-strain relationship. For this purpose, it is necessary to take into account the coefficient of stress triaxiality, *Lode* coefficient, and the phenomenon of material weakening as a result of the development of microvoids. In addition, there is necessary to determine a key material characteristic—critical values of strain and stress. To determine the constitutive relationships of steel S355 during tensile loading, the following characteristics should be received.

Material critical strain value—ε_c. This quantity can be obtained based on the methods described in the article.

- According to the metallographic method based on strain measurement of the material microstructural component—grains;
- According to the method basing on the extension measurement of the decreasing segment of the specimen with the further extrapolation of the fit function to the level corresponding to the grain size of the material. Applying video recording during the uniaxial tensile test enables us to estimate true strain values for each moment of neck formation and not only for the critical when fracture occurs.

Both of these methods can be simultaneously applied during uniaxial tensile on the same specimen. The critical strain level evaluated by using the above-mentioned methods is obtained as an estimated value, thus adopting various approaches allows us to compare the result and its supplement and increase the probability of correctness.

Material critical stress value—σ_c. The article presented a few methods of determining this quantity and carried out verification of its correctness.

- Seemingly the simplest—the force divided by the full cross-section in fracture moment of the specimen does not lead to obtaining the correct material constitutive relationship, which has been confirmed by verification performed by FEM calculations;
- The critical stress values obtained based on the change electric voltage method allow us to obtain the material constitutive relationship, which leads to convergence of the experimental and calculated force-displacement relations.

The use of the constitutive relationship defined by method, which takes into account the impact of high plastic strain, the stress triaxiality factor, Lode coefficient, and material weakness due to the growth of microvoids, allowed proper results in numerical modeled uniaxial tension test and in the test of bending of the specimen with crack (SENB).

Author Contributions: Conceptualization, I.D.; methodology, I.D.; software, S.L.; validation, S.L., R.P.; formal analysis, I.D.; investigation, R.P. and P.F.; data curation, R.P. and P.F.; writing—original draft preparation, I.D.; writing—review and editing, I.D. and S.L.; visualization, S.L. and R.P. and P.F; supervision, I.D. All authors have read and agreed to the published version of the manuscript.

Funding: The research was financed by the National Science Centre, Poland (No. 2017/25/N/ST8/00179).

Institutional Review Board Statement: Not applicable.

Informed Consent Statement: Not applicable.

Data Availability Statement: Data available on the request to the correspondence author.

Conflicts of Interest: The authors declared that they have no conflict of interest to this work.

References

1. ASTM E8/E8M-16ae1. *Standard Test Methods for Tension Testing of Metallic Materials*; ASTM International: West Conshohocken, PA, USA, 2016.
2. PN-EN ISO 6892-1:2020-05. *Metallic Materials—Tensile Testing—Part 1: Method of Test at Room Temperature*; International Organization for Standardization: Geneva, Switzerland, 2019.
3. Baltic, S.; Magnien, J.; Gänser, H.P.; Antretter, T.; Hammer, R. Coupled Damage Variable Based on Fracture Locus: Modelling and Calibration. *Int. J. Plast.* **2019**, *126*, 102623. [CrossRef]
4. Tu, S.; Ren, X.; He, J.; Zhang, Z. Stress–Strain Curves of Metallic Materials and Post-necking Strain Hardening Characterization: A Review. *Fatigue Fract. Eng. Mater. Struct.* **2020**, *43*, 3–19. [CrossRef]
5. Tu, S.; Ren, X.; He, J.; Zhang, Z. Experimenta Measurement of Temperature-Dependent Equivalent Stress-Strain Curves of a 420 MPa Structural Steel with Axisymmetric Notched Tensile Specimens. *Eng. Fail. Anal.* **2019**, *100*, 312–321. [CrossRef]
6. Gromada, M.; Miszuris, G.; Öchsner, A. *Correction Formulae for the Stress Distribution in Round Tensile Specimens at Neck Presence*; Springer Science & Business Media: Berlin/Heidelberg, Germany, 2011.
7. Bridgman, P.W. *Studies in Large Plastic Flow and Fracture with Special Emphasis on the Effects of Hydrostatic Pressure*; Harvard University Press: Cambridge, MA, USA, 1964.
8. Wang, L.; Tong, W. Identification of Post-necking Strain Hardening Behavior of Thin Sheet Metals from Image-based Surface Strain Data in Uniaxial Tension Tests. *Int. J. Solids Struct.* **2015**, *75*, 12–31. [CrossRef]
9. Dunand, M.; Mohr, D. On the Predictive Capabilities of the Shear Modified Gurson and the Modified Mohr–Coulomb Fracture Models over a Wide Range of Stress Triaxialities and Lode Angles. *J. Mech. Phys. Solids* **2011**, *59*, 1374–1394. [CrossRef]
10. Coppieters, S.; Kuwabara, T. Identification of Post-necking Hardening Phenomena in Ductile Sheet Metal. *Exp. Mech.* **2014**, *54*, 1355–1371. [CrossRef]
11. Depreński, Ł.; Seweryn, A.; Bartoszewicz, J. Ductile Fracture of Notched Aluminum Alloy Specimens under Elevated Temperature Part 1—Experimental Research. *Theor. Appl. Fract. Mech.* **2019**, *102*, 70–82.
12. Depreński, Ł.; Seweryn, A. Ductile Fracture of Notched Aluminum Alloy Specimens under Elevated Temperature Part 2—Numerical Modelling and Fracture Criterion. *Theor. Appl. Fract. Mech.* **2019**, *102*, 83–97.
13. Wierzbicki, T.; Bao, Y.; Lee, Y.-W.; Bai, Y. Calibration of Seven Fracture Models. *Int. J. Mech. Sci.* **2005**, *47*, 719–743. [CrossRef]
14. Bai, Y.; Wierzbicki, T. A New Model of Metal Plasticity and Fracture with Pressure and Lode Dependence. *Int. J. Plast.* **2008**, *24*, 1071–1096. [CrossRef]
15. Bai, Y.; Wierzbicki, T. Application of Extended Mohr–Coulomb Criterion to Ductile Fracture. *Int. J. Fract.* **2010**, *161*, 1–20. [CrossRef]
16. Neimitz, A.; Gałkiewicz, J.; Dzioba, I. Calibration of Constitutive Equations under Conditions of Large Strains and Stress Triaxiality. *Arch. Civ. Eng. Mater.* **2018**, *18*, 1123–1135. [CrossRef]
17. Neimitz, A.; Gałkiewicz, J.; Lipiec, S.; Dzioba, I. Estimation of the Onset of Crack Growth in Ductile Materials. *Materials* **2018**, *11*, 2026. [CrossRef] [PubMed]
18. Neimitz, A.; Dzioba, I.; Lipiec, S. Calibration of Constitutive Equations for the Stress Level Estimation in Domain with the Large Strains. *Procedia Struct. Integr.* **2018**, *13*, 862–867. [CrossRef]
19. Koçak, M.; Webster, S.; Janosch, J.J.; Ainsworth, R.A.; Koerc, R. *FITNET: Fitness-for-Service. Fracture-Fatique-Creep-Corrosion*; GKSS Research Centre Geesthacht GmbH: Stuttgart, Germany, 2008.
20. Neimitz, A.; Dzioba, I. Application of the Standard Options of the FITNET Procedure to the Structural Integrity Assessment of Welded Specimens Containing Cracks. *Int. J. Press. Vessel. Pip.* **2007**, *84*, 475–486.
21. Ritchie, R.O.; Knott, J.F.; Rice, J.R. On the relationship between critical tensile stress and fracture toughness in mild steel. *J. Mech. Phys. Solids* **1973**, *21*, 395–410. [CrossRef]
22. Yusof, F. Three-Dimensional Assessments of Crack Tip Constraint. *Theor. Appl. Fract. Mech.* **2019**, *101*, 1–16. [CrossRef]
23. Gurson, A.L. Continuum Theory of Ductile Rupture by Void Nucleation and Growth: Part 1—Yield Criteria and Flow Rules for Porous Ductile Media. *J. Eng. Mater. Technol.* **1977**, *99*, 2–15. [CrossRef]
24. Chu, C.C.; Needleman, A. Void Nucleation Effects in Biaxially Stretched Sheets. *J. Eng. Mater. Technol.* **1980**, *102*, 249–256. [CrossRef]
25. Tvergaard, V. On Localization in Ductile Materials Containing Spherical Voids. *Int. J. Fract.* **1982**, *18*, 237–252.
26. Tvergaard, V.; Needleman, A. Analysis of Cup-Cone Fracture in a Round Tensile Bar. *Acta Metall.* **1984**, *32*, 157–169. [CrossRef]
27. Besson, J.; Steglich, D.; Brocks, W. Modeling of Crack Growth in Round Bar and Plane Strain Specimens. *Int. J. Solids Struct.* **2001**, *38*, 8259–8284. [CrossRef]
28. Tanguy, B.; Luu, T.T.; Perrin, G.; Pineau, A.; Besson, J. Plastic and Damage Behaviour of a High Strength X100 Pipeline Steel: Experiments and Modelling. *Int. J. Press. Vessel. Pip.* **2008**, *85*, 322–335. [CrossRef]

29. Dzioba, I.; Lipiec, S.; Furmańczyk, P.; Pała, R. Investigation of Fracture Process of S355JR Steel in Transition Region Using Metallographic and Fractographic Tests and Numerical Analysis. *Acta Mech. Autom.* **2018**, *12*, 145–150. [CrossRef]
30. Dzioba, I.; Lipiec, S. Fracture Mechanisms of S355 Steel—Experimental Research, FEM Simulation and SEM Observation. *Materials* **2019**, *12*, 3959. [CrossRef] [PubMed]
31. PN-EN 10025-3:2019-11. *Hot Rolled Products of Structural Steels—Part 2: Technical Delivery Conditions for Non-Alloy Structured Steels*; Polish Standardization Resource: Warsaw, Poland, 2019.
32. Boumerzoug, Z.; Derfouf, C.; Baudin, T. Effect of Welding on Microstructure and Mechanical Properties of an Industrial Low Carbon Stee. *Sci. Res. Eng.* **2010**, *2*, 502–506.
33. Dzioba, I. Properties of 13KHMF Steel after Operation and Degradation under the Laboratory Conditions. *Mater. Sci.* **2010**, *46*, 357–364. [CrossRef]
34. ASTM E647-15e1. *Standard Test Method for Measurement of Fatigue Crack Growth Rates*; ASTM International: West Conshohocken, PA, USA, 2015.
35. ASTM E1737-96. *Test Method for J-Integral Characterization of Fracture Toughness*; ASTM International: West Conshohocken, PA, USA, 1996.
36. ASTM E112-13. *Standard Test Methods for Determining Average Grain Size*; ASTM International: West Conshohocken, PA, USA, 2013.
37. Knott, J.F. Micromechanisms of Fracture and the Fracture Toughness of Engineering Alloy. *Fracture* **1977**, *1*, 61–91.
38. Rice, J.R.; Tracey, D.M. On the Ductile Enlargement of Voids in Triaxial Stress Fields. *J. Mech. Phys. Solids* **1968**, *17*, 201–217. [CrossRef]
39. Mohr, D.; Marcadet, S.J. Micromechanically–Motivated Phenomenological Hasford–Coulomb Model for Predicting Ductile Fracture Initiation at Low Stress Triaxialities. *Int. J. Solids Struct.* **2015**, *67*, 40–45. [CrossRef]
40. Faleskog, J.; Barsoum, I. Tension-Torsion Fracture Experiments-Part I; Experiments and a Procedure to Evaluate the Equivalent Plastic Strain. *Int. J. Solids Struct.* **2013**, *50*, 4241–4257. [CrossRef]
41. Xue, L. Damage Accumulation and Fracture Initiation in Uncracked Ductile Solids Subject to Triaxial Loading. *Int. J. Solids Struct.* **2007**, *44*, 5163–5181. [CrossRef]
42. Dzioba, I.; Gajewski, M.; Neimitz, A. Studies of Fracture Processes in Cr-Mo-V Ferritic Steel with Various Types of Microstructures. *Int. J. Press. Vessel. Pip.* **2010**, *87*, 575–586. [CrossRef]
43. Kim, Y.; Chao, Y.J.; Zhu, X.K. Effect of Specimen Size and Crack Depth on 3D Crack-Front Constraint for SENB Specimens. *Int. J. Solids Struct.* **2003**, *40*, 6267–6284. [CrossRef]
44. Tkach, Y.; Burdekin, F.M. A Three-Dimensional Analysis of Fracture Mechanics Test Pieces of Different Geometries. Part 1 Stress-State Ahead of the Crack Tip. *Int. J. Press. Vessel. Pip.* **2012**, *93–94*, 42–50. [CrossRef]
45. Tkach, Y.; Burdekin, F.M. A Three-Dimensional Analysis of Fracture Mechanics Test Pieces of Different Geometries. Part 2 Constraint and Material Variations. *Int. J. Press. Vessel. Pip.* **2012**, *93–94*, 51–56. [CrossRef]
46. He, G.; Bao, C.; Cai, L. Study on Uniform Parameters Characterizing the Crack-Tip Constraint Effect of Fracture Toughness. *Eng. Fract. Mech.* **2019**, *222*, 1–10. [CrossRef]
47. Pineau, A. Development of the local approach to fracture over the past 25 years: Theory and application. *Int. J. Fract.* **2006**, *138*, 139–166. [CrossRef]

materials

MDPI

Article

Creation of a Nanomodified Backfill Based on the Waste from Enrichment of Water-Soluble Ores

Elena A. Ermolovich [1], Alexander L. Ivannikov [2,*], Marat M. Khayrutdinov [3], Cheynesh B. Kongar-Syuryun [2,4] and Yulia S. Tyulyaeva [2]

[1] Department of Applied Geology and Mining, Belgorod National Research University, Pobedy Street 85, 308015 Belgorod, Russia; ermolovich@bsu.edu.ru
[2] Department of Automated Control Systems, National University of Science and Technology "MISIS", Leninsky Avenue 4, 119991 Moscow, Russia; cheinesh.kongar-siuriun@stud.thga.de (C.B.K.-S.); tyulyaeva@edu.misis.ru (Y.S.T.)
[3] Itasca Consultants GmbH, Leithestrasse 111a, 45886 Gelsenkirchen, Germany; profmarat@gmail.com
[4] Department of Mineral Resources and Process Engineering, Technische Hochschule Georg Agricola (THGA), Herner Street 45, 44787 Bochum, Germany
* Correspondence: ivannikov.al@misis.ru

Abstract: The paper analyzes losses during the development of low-value water-soluble ore deposits. The importance of development systems with backfill is shown. The use of industrial wastes of water-soluble ores to replace specially produced inert components in the preparation of backfill seems to be a good way to utilize them. The aim of the work was to create a fill mass with improved strength properties based on industrial wastes of water-soluble ores activated with a nanomodifying material. The characteristics (chemical and granulometric compositions) of an aggregate of the backfill based on the waste from enrichment of water-soluble ores are given. The validation of the hardening mixture compositions for various mining systems was carried out considering: the specified strength, the time of the artificial mass erection, the time to achieve the required strength properties of the material, which determine the possible intensity of the mining operations; method of transporting the backfill. The expediency of using a multilayer fulleroid nanomodifier astralene as a nanomodifying additive has been proved. The effect of the backfill activation with a nanomodifying additive, astralene, on the structural changes of halite wastes from the halurgic enrichment of water-soluble ores (potash) was investigated. To study the strength properties of the fill mass, the comparative analytical method was used. The strength properties of the backfill were measured in standard test periods, taking into account the intensity of hardening of the backfill material (after 7, 14, 28, 60, 90 days). To obtain reliable results, 10 backfill samples were tested at each of the scheduled dates. The shape and chemical composition of crystalline new forms were studied. Studies were performed using X-ray phase analysis and scanning electron microscopy. As a result of uniaxial compression of hardening backfill samples, the dependence of the ultimate strength on the astralene content and the hardening time were established. It has been experimentally proved that the use of a nanomodifying additive, astralene, in the backfill allows an increase in the strength properties of the created artificial mass by 1.76–2.36 times while reducing binder consumption.

Keywords: waste from enrichment of water-soluble ores; artificially supported mining method; backfill; activation; nanomodifier astralene; ultimate compressive strength

Citation: Ermolovich, E.A.; Ivannikov, A.L.; Khayrutdinov, M.M.; Kongar-Syuryun, C.B.; Tyulyaeva, Y.S. Creation of a Nanomodified Backfill Based on the Waste from Enrichment of Water-Soluble Ores. *Materials* **2022**, *15*, 3689. https://doi.org/10.3390/ma15103689

Academic Editors: Krzysztof Schabowicz and Saeed Chehreh Chelgani

Received: 20 March 2022
Accepted: 17 May 2022
Published: 21 May 2022

1. Introduction

The growth of the world's population more than twofold, from 3 billion people in 1960 to 7.7 billion people at present, has entailed a forced increase in agricultural production [1,2]. This has led to increased consumption of mineral fertilizers [3–5]. The growing demand for mineral fertilizers has required an increase in the production capacity of enterprises producing potash fertilizers [6]. Increasing the production of this type of fertilizer requires

an increase in the extraction of potash salts at mining enterprises, which involves a larger amount of reserves in the development.

The increased consumption of potash fertilizers implies the intensification and growth of potash salt extraction, which in turn predetermines the high rates of geotechnology development in general. All of this is accompanied by industrial and environmental risks and induced disasters.

One of the world's largest deposits of potassium–magnesium salts is located in the Russian Federation, in the Perm Territory (59°35′36″ N 56°48′36″ E) (Figure 1).

Figure 1. Location of the Verkhnekamsk deposit.

The Verkhnekamsk potassium–magnesium salt deposit is the main component of the Solikamsk potassium-bearing basin, located in the left-bank part of the Kama river valley. In the north, this deposit is limited by Lake Nyukhti, located in the Krasnovishersk region; in the south, it extends to the Yayva river basin. The length of the explored part of the deposit from north to south is 140 km, and from west to east, about 60 km. The thickness of the ore-bearing strata is about 80 m, and its depth is 400 m. Potash horizons are represented by alternating red layered sylvinites with rock salt interlayers. The thickness of individual potash strata ranges from 0.75 to 5 m.

The salt stratum with a total thickness of up to 550 m is subdivided (from bottom to top) into underlying rock salt (URS-P1br2), potash deposits (P1br3) consisting of sylvinite (SZ) and carnallite (CZ) zones and mantle rock salt (MRS-P1br4) (Figure 2).

All of the main reserves of the Verkhnekamsk potassium–magnesium salt deposit are located on the left bank of the Kama River. There is a small area on the right bank. The total area of the basin is more than 6.5 thousand square kilometers.

The Verkhnekamsk deposit was discovered in 1925, and development has been carried out by the underground method since 1934. Development centers are concentrated in the area of Solikamsk and Berezniki cities (Figure 3). At present, stope and pillar mining is used for the Verkhnekamsk deposit development.

On the basis of the above, creation of nanomodified backfill based on the tailings from enrichment of water-soluble ores, that allows replacing the traditional technology of water-soluble ore mining with a safer one and obtaining an environmental and economic effect, seems to be a very urgent task.

Stope and pillar mining are characterized by high mineral losses. This technology is most often used in the development of water-soluble ores with low value. Extraction of water-soluble ores is characterized not only by high losses (up to 65%) [7] of minerals left in pillars, but also by the formation of a large amount of waste generated during the

extraction and processing of water-soluble ores. The volume of the generated waste is 60–70% of the total volume of the extracted ore mass [7].

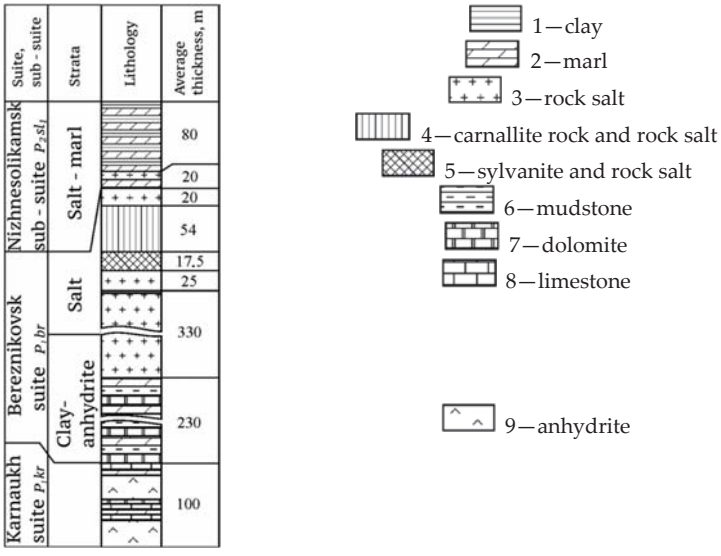

Figure 2. Stratigraphic section of the halogen formation of the Solikamsk depression.

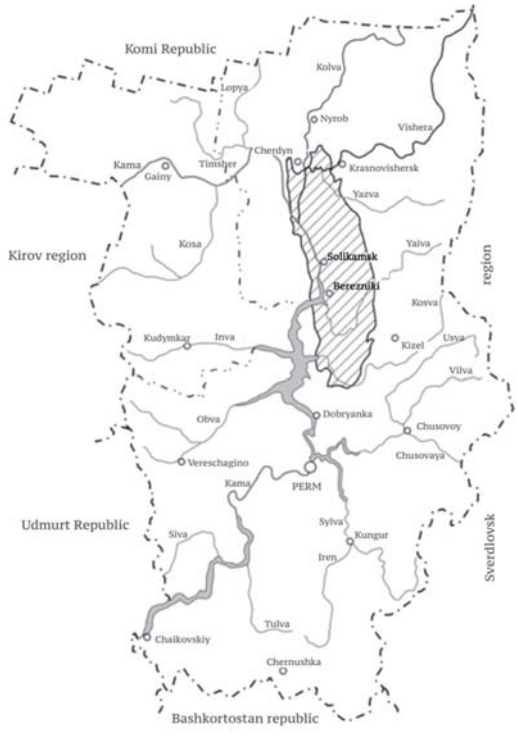

Figure 3. Location of the Verkhnekamsk deposit in the Perm Territory.

The plasticity of natural salt pillars causes deformation changes in them, which leads to their destruction [7]. Destruction of pillars causes deformation disturbances of the overlying rock mass [8]. In some cases, the propagation of these deformation disturbances reaches the daylight surface. This leads to the formation of sinkholes and disruption of the waterproof stratum of the aquifer [9]. The violation of the waterproof stratum leads to the breakthrough of water into the mine, to its flooding and loss of reserves. Due to the destruction of rib and barrier pillars at the Verkhnekamsk deposit, deformation disturbances developed in the underworked mass and caused a breakthrough of the aquifer. As a result, two mines of the Verkhnekamsk deposit were lost. Consequently, the use of development systems that exclude or minimize the likelihood of disturbing the waterproof stratum is one of the main tasks in the development of water-soluble ore deposits.

The incessant induced impact, caused by drilling and blasting [10] and extensive exposed surfaces, causes seismic activity in the mining regions [11]. Vibrations and induced earthquakes of up to magnitude 5 are recorded at Russian and foreign mines developing deposits of water-soluble ores [12–15].

The use of development systems with artificial support reduces the likelihood of disasters and improves the qualitative and quantitative indicators of extraction. An artificial mass based on waste, while maintaining its main purpose of supporting the stoping space, allows minimizing the impact of mining enterprises on the environment [16].

Due to the limited ability of the biosphere for self-regulation and self-reproduction, it is necessary to create gentle technologies that minimize the impact of the enterprise on the environment and maintain the ecological balance [17].

2. Materials and Methods

Geotechnology with artificial support is impossible without the selection of backfill components that satisfy economic, technological and technical conditions [18]. The backfill is a composite material capable of hardening in mining conditions. This material contains aggregate, binder, mixing water and chemical additives.

2.1. Backfill

The characteristics of the future artificial mass largely depend on the properties of the starting materials. Therefore, their correct choice is one of the most important factors in the backfill technology. The material must be highly transportable, which ensures that it will be delivered through pipes over long distances without fear of premature hardening [19]. The material must have high plasticity for the most complete filling of the mined-out void. The setting time should not be less than that required to deliver the material to the stope [20]. This is especially important for materials with a large aggregate, since in this case stratification leads to an uneven distribution of the components in the mined-out void, the heterogeneity of the created artificial mass, and its reduced strength. The components of the backfill must be selected in such a way as to exclude their negative impact on the created artificial mass: loss of strength; warming up; shrinkage; expansion, etc.

2.2. Characteristics of Aggregate for Backfill

Due to the fact that the aggregate makes up 75–90% of the total volume of the backfill, its quality has a significant effect on the material and the artificial mass characteristics. In this regard, especially high requirements are imposed on the quality of the aggregate. In addition, large volumes of aggregate have a significant impact on the cost of the backfill, the cost of mining operations, and as a result, on the cost of the extracted ore.

Therefore, the main, widely developing direction is the replacement of the traditional, specially mined aggregate with waste from mining and processing industries. These wastes meet the following requirements: they are cheap, have stable physical and mechanical properties and a low-change granulometric composition, and are located near enterprises engaged in the extraction of minerals. With the appropriate preparation technology, these wastes will completely replace the traditional, specially mined aggregate, while maintaining

the necessary characteristics of the created fill mass. Consequently, the use of waste as a replacement for traditional aggregates in the backfill composite has the potential to reduce the total cost of mining operations.

Waste from the enrichment of water-soluble ores is a product with the following properties: hygroscopicity; tendency to caking and clumping and having mainly sodium chloride in its composition. Depending on the enrichment method, the waste of water-soluble ores is divided into flotation and halurgic types. The chemical compositions of wastes differ slightly, but the difference lies in the granulometric composition. The particle size of halite waste of halurgic enrichment is 4.5 times higher.

For research and experiments, halite wastes of halurgic enrichment were used as an aggregate. Saturated salt solutions were used as a grout to avoid aggregate dissolution. The waste humidity was 10–12%. The chemical composition is given in Table 1, and granulometric composition in Table 2.

Table 1. Chemical composition of waste from the enrichment of water-soluble ores (halurgic).

	Halite Waste						
Components	KCl	NaCl	$MgCl_2$	$CaSO_4$	Insoluble residue	Br^-	$H_2O_{cryst.}$
Mass fraction, %	1.91	94.3	0.07	1.914	1.7	0.026	0.08

Table 2. Granulometric composition of waste from the enrichment of water-soluble ores (halurgic).

	Halite Waste								Average Size
Particle size, mm	+7	7–5	5–3	3–2	2–1	1.0–0.5	0.5–0.25	−0.25	2.54
Mass fraction, %	7.4	7.3	17.0	16.3	20.9	19.5	8.6	3.0	100

2.3. Binder Selection

In previous studies, various binders were used to prepare the hardening backfill: lime [21], cement [22], ash and slag waste from the State District Power Plant and Thermal Power Plant [23], blast-furnace granulated slags [24], and gypsum and calcium chloride additives [25]. In addition, in a number of studies, bischofite [26], caustic magnesite [27], magnesian cement [28], and expanded clay [29] were proposed as starting materials for the backfill material preparation. In early studies, the advantages of magnesia binders in the fill mass formation with an increased amount of salt in its composition were proved [30].

At the same time, the magnesian component of the binder increases the hardening speed and the strength of the created mass in comparison with traditional binders. Furthermore, one of the features of the magnesian binder is its ability to bind large aggregate masses with a minimum amount. In addition, magnesia binders reduce the negative effect of salt on cement. In this study, magnesia cement was used as a binder, which contained 75–85% magnesium oxide (MgO), depending on the grade.

Magnesia cement (TR (technical requirements) 5745-001-92534212-2014) is produced by mixing magnesium oxide pre-calcined to 800 °C with a 30% aqueous solution of $MgCl_2$ (two weight parts of MgO per one weight part of anhydrous $MgCl_2$). The main advantages of magnesia cement are fast hardening, high achievable strength, and high adhesion.

One of the largest producers of magnesia binding cements in Russia is the Russian Chromium group of companies (in the city of Beloretsk, Republic of Bashkortostan, Russia).

2.4. Activation of the Starting Components and Selection of the Activating Additive

Analysis of previously conducted studies of the geotechnology with backfill shows that the main cost in the backfill material is binder. Physico-chemical activation of the backfill components can improve the quality properties of the binder and, therefore, reduce its consumption.

One of the most affordable and cheap methods of activation is the mechanical method of activation in disintegrators [31,32]. In addition to mechanical treatment of the backfill

material, a fairly effective activation method is the addition of activating additives to the material. Considering previous studies [33], it can be concluded that one of the most affordable and cheap activating additives can be lignosulfonate for the preparation of a backfill based on water-soluble ores. Lignosulfonate is an anionic surfactant that is a waste product of the pulp and paper industry.

Carbon frame structures (fullerenes and nanotubes) are used as additives that increase the strength of the created material. The high strength and high elasticity of nanotubes is a rather successful combination, which makes it possible to improve the mechanical properties of the material [34]. It is possible to create new nanomodified materials using the high strength characteristics and elasticity of nanotubes [35]. In this case, nanotubes act as strengthening additives. One such nanomodifying additive is astralene (TR (technical requirements) 31968474.1319.001-2000), obtained by the discharge-arc method [36,37]. Previous studies [38] have demonstrated positive results of using astralene (fulleroid multilayer synthetic nanomodifier). Its inclusion into the material significantly increases the elastic and strength properties [39]. The use of astralene as an activation additive to improve the properties of concrete-building mixtures showed positive results [40]. Water-soluble ores have hygroscopicity, caking ability, and, with a small amount of moisture, form a sufficiently dense and solid mass. Therefore, the effect of a nanomodifying additive without the use of a binder was initially studied to determine the optimal dose in the backfill.

The preparation of the material with the nanomodifying additive was carried out in the following sequence: astralene, the concentration of which is from 0.001% to 0.02% of the mass of the waste from the enrichment of water-soluble ores, is mixed for 5 min, then gaged with brine and blended for 10 min until a homogeneous mass is formed. The resulting mixtures were placed in cubes with faces of 10 cm.

2.5. Preparation and Study of the Backfill Material

Previously, the optimal amount of nanomodifying additive was determined, which was 0.01% of the solid mass in the material. Therefore, the amount of nanomodifying additive remained unchanged during the experimental studies. Nanomodifying additive and magnesia binder were mixed for 5 min, after which the wastes from enrichment of water-soluble ores were added, and the mixing was continued for up to 10 min. Then, the salt brine was added, and the mixing was continued for an additional 10 min until a homogeneous mass was achieved.

Such a sequence of mixing is due to a sufficiently small amount of one of the components (nanomodifying additive astralene) and will lead to its better distribution in the entire volume of the material being prepared.

Mixing was carried out in a laboratory planetary mixer MICS-D-C (МИКС-Д-Ц (EN 196-1, EN 196-3, EN 413-2, EN 459-2, EN 480-1, EN-ISO 679, NF P15-314, DIN 1164-5, UNE 80801, UNE 83258, ASTM C305, AASHTO T162). Optimal and efficient mixing was achieved due to the characteristic planetary motion of the mixer, namely, a combination of circular motion and motion around its axis. The planetary rotation speed was 62 rpm with an increase to 125 rpm at an initial circular rotation speed of 140 rpm with an increase to 250 rpm. Then, the material was placed in cubes with faces of 10 cm.

The storage and hardening of the samples occurred in conditions close to those of the mine, provided with the methodology (T = 20 ± 2 °C; W = 95 ± 5%). The subsequent compression test was carried out at specified periods in accordance with the methodology: 7, 28, and 60 days [41]. The magnitude of the ultimate compression strength of the hardened mixture was tested by crushing samples of standard sizes (edge 10 cm) on the test press PI-2000-A.

Reliability was confirmed by the repeatability of the results with a sufficient number of experiments. The condition for obtaining high reliability of the results is a large number of experiments. In order to obtain the most accurate values close to the actual ones, 18 samples were made for each composition. Then, the average values were calculated and presented in tables.

2.6. Microstructural Analysis of the Backfill Material

Microscopic analysis—the study of the internal structure of the created material—was carried out using optical or electronic microscopes at magnifications from 100 to 1000 or higher. The method of microscopic analysis was used to study the structure and material-mineralogical composition of the material (coarseness, various inclusions or new formations, etc., invisible to the naked eye), which made it possible to give a more detailed and accurate characterization of the material properties and quality [42].

The study of the created material microstructure required the use of analytical methods and appropriate equipment allowing adequate determination of the shape, composition and structure of particles of both the original components and new formations in the size range from tens of microns to nanometers [43,44].

To study the microstructure of the nanomodified composite prepared on the basis of wastes from enrichment of water-soluble ores, structural-mineralogical (petrographic analysis) and X-ray analyses were used.

All microstructural studies were carried out on a fracture of samples of the investigated nanomodified material. The fracture was obtained by a mechanical method. The fine delaminated fractions and dust particles, formed on a fracture as a result of mechanical influence, were removed by a jet of air.

The application of scanning electron microscopy to diagnose textured material has become the most powerful method for studying the structure and physical and chemical features of solid materials, including nanostructures, in the last few years [35,39].

Operating peculiarities and research methods using electron microscopy are analyzed in [45–48]. Scanning electron microscopes present patterns in secondary electrons, which makes it possible to highlight light and dark contours.

2.6.1. Structural-Mineralogical Analysis (Petrographic Analysis) of the Backfill

Structural-mineralogical analysis (petrographic analysis) is a method of visual or microscopic investigation of the mineralogy and composition of a created material on the basis of morphological features.

Petrographic analysis was carried out on a Polam R-211 polarizing microscope using the immersion method. The phases were identified by refractive indices, birefringence, basicity, sign, elongation, and extinction angles. Immersion liquids were used as standards. The quantitative ratio of the phases (crystallographic composition) was determined by the Stroyber method. In the study using a polarizing microscope Polam R-211, the maximum magnification was 720 times.

These researches were supplemented by studying the samples using a Philips SEM 515 scanning electron microscope. In this case, the maximum magnification was 2000 at an accelerating voltage of primary electrons of 20.00 kV. The pressure in the chamber at the time of the study was 2×10^{-5} Torr.

2.6.2. X-ray Analysis

X-ray analysis is a method of studying the structure of matter by the distribution in space and intensity of X-ray radiation scattered on the analyzed object.

A DRON-3 diffractometer was used for X-ray phase analysis. Recording signals in digital form allowed data processing automatically. Further, the obtained data were processed manually using a graphical editor or decrypted using a specially program for X-ray phase analysis of new crystalline formations. The operation of the graphical editor and the program used are described in detail in the study [49].

3. Results

A set of experiments were carried out to determine the optimal quantitative composition of the nanomodifying additive astralene in the backfill and its effect on the strength characteristics.

For comparison, the data obtained in reference [50] were taken when studying the effect of the activating additive astralene on the backfill based on the waste from enrichment of water-soluble ores. Experimental data on the use of the nanomodifying additive astralene are juxtaposed in Table 3 and presented in Figure 4.

Table 3. Compositions with different contents of astralene.

Composition	Activating Additives	Content, Mass. % of Waste	Water–Solid Ratio	Strength of Samples Under Uniaxial Compression, Mpa		
				Duration of Hardening, Days		
				7	28	60
1	astralene	0.001	0.15	0.1	0.3	0.4
2	astralene	0.005	0.15	0.26	1.12	1.34
3	astralene	0.01	0.15	0.44	1.51	1.75
4	astralene	0.015	0.15	0.4	1.49	1.7
5	astralene	0.02	0.15	0.39	1.44	1.68

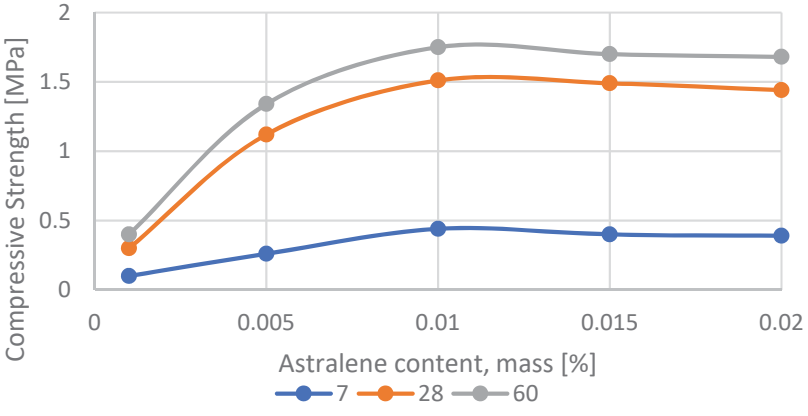

Figure 4. The change in the samples' compressive strength depending on the astralene content at the age of: 7 days, 28 days60 days.

3.1. Optimal Astralene Content

The hardened samples were tested for uniaxial compression. The test results are shown in Table 3. From the analysis of the strength characteristics of the samples, it follows that the activation with nanomodifying additive astralene significantly increases them.

The dependence of the ultimate compressive strength of the samples at the age of 7, 28 and 60 days on the astralene content *C* are very well approximated by third-order polynomial Functions (1)–(3):

$$\sigma_{comp,7} = 610{,}216 \cdot C^3 - 27{,}131 \cdot C^2 + 380.23 \cdot C + 0.0450 \ (R^2 = 1.0000) \quad (1)$$

$$\sigma_{comp,28} = 468{,}815 \cdot C^3 - 21{,}934 \cdot C^2 + 323.27 \cdot C - 0.0029 \ (R^2 = 1.0000) \quad (2)$$

$$\sigma_{comp,60} = 57{,}272 \cdot C^3 - 3710.9 \cdot C^2 + 69.226 \cdot C + 0.0261 \ (R^2 = 0.9667) \quad (3)$$

where $\sigma_{comp,7}$, $\sigma_{comp,28}$, $\sigma_{comp,60}$—ultimate compressive strength of the samples at the age of 7, 28 and 60 days respectively, MPa; *C*—astralene content. mass. % of waste. Values in brackets show the accuracy of approximation R^2, respectively.

3.2. Strength of Backfill with Different Component Contents

The method for selecting the composition of the hardening backfill is standard and includes studies of the main characteristics and properties. One of the main ones is obtaining necessary or specified physical and mechanical characteristics.

The choice of the rational composition of the backfill implies methods for comparing experimental compositions, analogies with previously performed works, and the exclusion of compositions that do not meet the requirements or specified characteristics.

Laboratory studies of the physical and mechanical properties of raw materials assess the possibility of their use in backfill. Then, studies of materials and hardened samples based on the selected raw materials are carried out. The samples were studied after material solidification with different component contents: binder/additive/aggregate. The components were mixed in a certain sequence in various combinations and ratios in order to determine the optimal composition of the backfill. Then, the material was fabricated into cubes with faces of 7 cm and stored in conditions close to those of the mine.

Previously, the optimal amount of nanomodifying additive was determined, which was 0.01% of the solid mass in the material. Therefore, the amount of nanomodifying additive remained unchanged during the experimental studies. The nanomodifying additive and magnesia binder were mixed for 5 min, after which the waste from enrichment of water-soluble ores was added, with mixing continued for 10 min. Then, the mixture was gaged with brine, and mixing was continued for an additional 10 min until a homogeneous mass was produced.

The samples were tested for uniaxial compression after material hardening to determine the rational-optimal composition. The test results are presented in Table 4 and Figure 5.

Table 4. Research on compositions with different content of components.

Composition	Content, Mass.%				Water–Solid Ratio	Strength of Samples Under Uniaxial Compression, Mpa			
	Waste	Binder	Astralene	Ligno-Sulfonate		Duration of Hardening, Days			
						7	28	60	90
1	99.49	0.50	0.01	-	0.125	0.12	1.62	2.29	2.46
1a	98.00	1.00	-	1.00	0.125	0.10	1.20	1.70	1.80
2	98.99	1.00	0.01	-	0.125	0.19	2.12	3.02	3.30
2a	97.00	2.00	-	1.00	0.125	0.15	1.60	2.20	2.40
3	99.00	1.00	-	-	0.150	0.11	0.73	1.12	1.40
4	99.99	-	0.01	-	0.130	-	1.51	1.75	2.12
4a	99.00	-	-	1.00	0.130	-	0.80	0.90	1.00

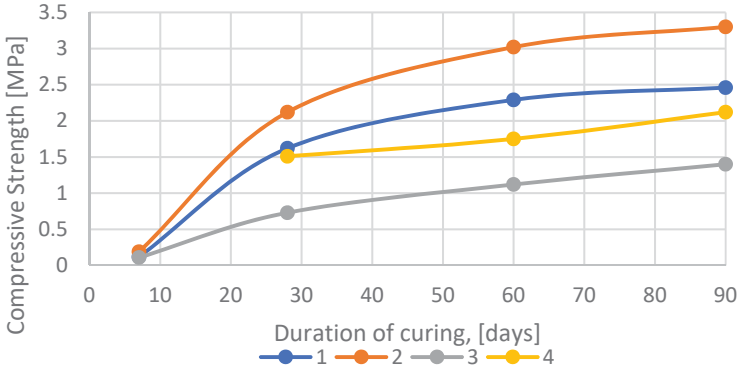

Figure 5. Kinetics of the backfill strength set depending on the component content: 1—waste/magnesia cement/astralene: 98.99/1.00/0.01. 2—waste/magnesia cement/astralene: 99.49/0.50/0.01. 3—waste/magnesia cement/astralene 99.99/0.00/0.01. 4—waste/magnesia cement/astralene 99.00/1.00/0.00.

The optimal water–solid ratio was selected based on the requirements that ensure the necessary mobility of the composite—20 cm according to the Suttarda viscometer.

The dependence of the ultimate compressive strength of the samples (Composition 2, Table 4) on the hardening time is well approximated by a logarithmic function:

$$\sigma_{comp} = 1.2444 \cdot \ln(t) - 2.1581 \ (R^2 = 0.9916) \quad (4)$$

where: σ_{comp}—ultimate compressive strength of the samples, MPa. tduration of hardening, days. R^2—accuracy of approximation.

A comparative analysis of the experimental results with the data obtained from early studies (Compositions 1a, 2a, 4a) allowed us to conclude that the use of a nanomodified additive makes it possible to reduce the magnesia binder consumption by at least 2 times while increasing the strength properties of the hardened mass. It may be also concluded that, despite some similarities to concrete, the time-dependent increase in compressive strength lasted longer than 28 days. Longer setting times resemble the case of other soil–cement composites with or without additives [51,52].

3.3. Microstructural Study of the Backfill Material

Structural-mineralogical and X-ray phase analyses facilitated study of the influence of a separate component of the backfill material on the creation of structural bonds. We performed X-ray phase analysis of compositions No.2, No.3 and petrographic analysis of compositions No.2, No.3 and No.4 (Table 4).

To determine the crystallographic parameters, we used the constants of the optical properties of minerals combined in the Winchell A.N [53,54] reference book for inorganic compounds:

- Composition No.4 (waste/nanomodifying additive): the introduction of astralene into the waste from enrichment of water-soluble ores did not cause the formation of any amorphous bonds or the appearance of new crystalline structures. This confirms the absence of any chemical interaction between these components. Astralene segregates on the surface of minerals presented in an aggregate, evenly distributing and forming continuously dense interlayers with a thickness of up to 0.5 microns in the volume of the entire composite (Figure 6a).
- Composition No.3 (waste/binder): after enrichment waste and magnesia cement mixing, amoeboid compounds are formed as a result of the concentration of the magnesian component, which is 1% of the total volume of enrichment wastes from the water-soluble ores. Mineralized crystals of waste are cemented by creating a mesh frame, the size of the faces (joints) of which varies from 10 to 15 microns. The hydrated phase of brucite ($Mg(OH)_2$) is formed as a result of hydration. Brucite with a size of no more than 4–5 microns has the form of basalt plates, has a closed porosity and creates a loose structure (Figure 6b).
- Composition No.2 (waste/binder/nanomodifying additive): simultaneous introduction of a magnesian binder and a nanomodifying additive into a composite based on waste from water-soluble ores after solidification causes the formation of a continuous fine-mesh nanomodified structure. Magnesium hydroxy chlorides are structured in the form of a needle frame into the fundamental phases of the NaCl crystal matrix along the edge amoeboid formations of the $Mg(OH)_2$ brucite structures. The forming crystals, the size of which along the long axis is 1–2 microns, have a needle frame. Grains of amoeboid brucite crystals have a fine-crystalline structure. The grain size does not exceed 2 microns (Figure 6c).

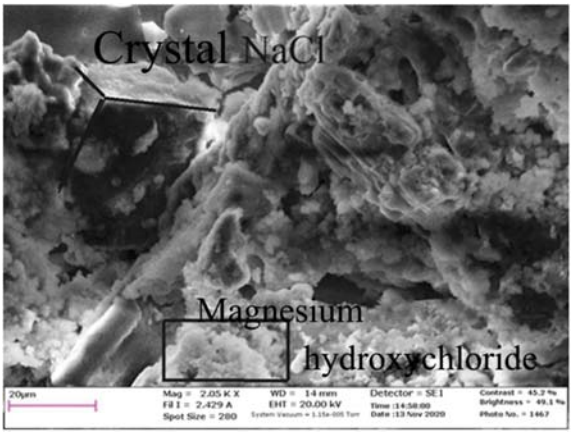

(**a**)

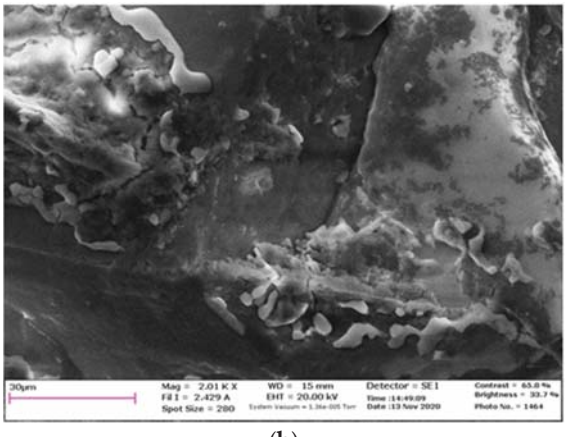

(**b**)

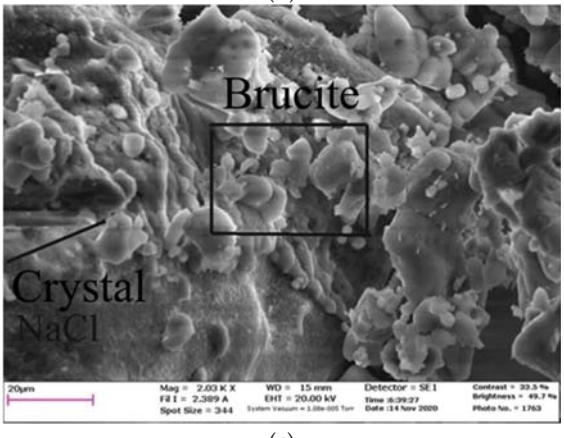

(**c**)

Figure 6. Microstructure of the studied samples. (**a**) Peripheral needle frame of magnesium hydroxy chloride. (**b**) Formation of a cryptocrystalline structural frame representing secondary NaCl crystals. (**c**) Brucite.

Analysis of the X-ray patterns of samples No.2 and No.3 allowed us to note that the bulk of the reflections with the highest amplitudes were crystals of sodium (NaCl) and potassium (KCl) salts, which was explained by the large amount of waste from enrichment of water-soluble ores (Figure 7a,b). Crystals of brucite and magnesium hydroxy chloride, which are the products of the magnesian binder hydration, were reflected with a lower amplitude. This proved that there is a compaction of pore voids between crystals of sodium (NaCl) and potassium (KCl) salts by filling them with brucite and magnesium hydroxy chlorides. As a result, the strength characteristics of the homogeneous mass increase during solidification.

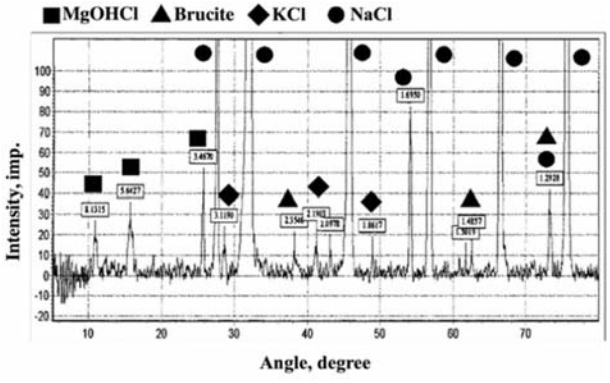

(**a**)

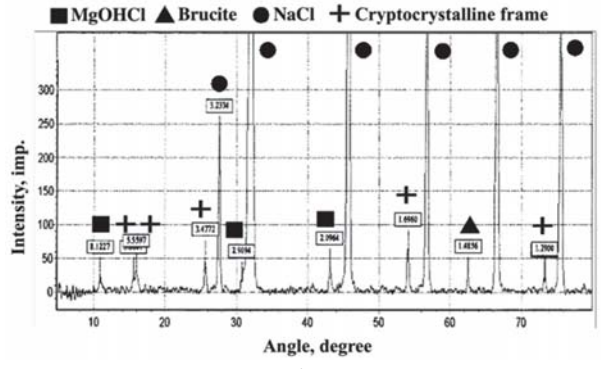

(**b**)

Figure 7. Evaluation of samples by X-ray phase method: (**a**) waste/binder, (**b**) waste/binder/astralene.

In the studied samples, which did not contain a nanomodifying additive (Figure 7a), there were noticeably smaller numbers of magnesium hydroxy chloride reflections d_α = 8.1315; 5.6427; 3.4670 Å, and a slight dominance of reflections corresponding to brucite was revealed dα = 2.3540; 1.3019; 1.4857; 1.2928 Å. In samples obtained after solidification of the material containing a nanomodifying additive (Figure 7b), the numbers of reflections that corresponded to the fundamental crystal structures of magnesium hydroxy chloride were preserved d_a = 8.1227; 2.9094; 2.0964 Å. At the same time, there was a significant reduction in reflections corresponding to brucite d_a = 1.4856 Å. Additionally, in these samples, reflections appeared, indicating the formation of new structures d_a = 5.6577; 5.5597; 3.4772; 1.6960; 1.2900 Å, not typical for samples without a nanomodifying additive.

The use of a nanomodifying additive, astralene, influenced the formation of a fine-crystalline nanomodified structure of the fill mass. Structural-mineralogical and X-ray phase analyses made it possible to establish that astralene acts as an activating additive in

the backfill. In the hardening (hydration) process, brucite was formed along the peripheral zones. This created additional stable crystal structures of magnesium hydroxy chlorides (Figure 6a) and provided an increase in the strength of the created fill mass.

In addition, the cryptocrystalline frame was formed when astralene was injected on the surface of sodium salt (NaCl) grains. The frame represented secondary crystals of these salts (Figure 6c). The formation of this structure was favored by the mutual penetration of halite aggregates and hydration products of magnesium hydroxy chlorides into the pore space and their additional adhesion.

4. Discussion

Figure 6a,c show the microstructures of the fill mass, visually representing the marked crystalline new formations.

In the analysis of the X-ray study (Figure 7), it can be seen that upon introduction of the nanomodifying additive astralene into the composite, reflections from the new phase appeared (Figure 7b), testifying to the new formation in the composite being created. This new formation corresponded to development of a cryptocrystalline structural frame.

Upon activation of the backfill material with astralene, after its solidification, a denser and more homogeneous structure was formed (Figure 8a), in contrast to the composite that did not contain the nanomodifying additive (Figure 8b).

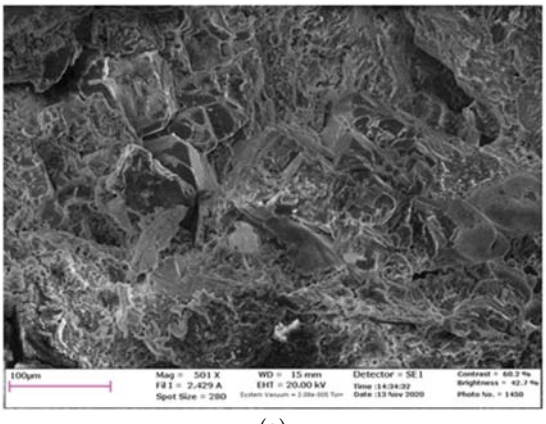

(**a**)

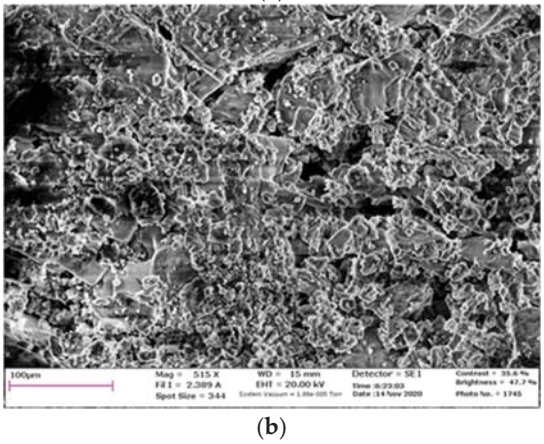

(**b**)

Figure 8. Microstructure of the studied samples: (**a**) with a modifying additive, (**b**) without a modifying additive.

When analyzing Figure 8a,b, it can be seen that image 8a is more even, while image 8b shows a sharp contrast. Dark contrasts (Figure 8b) indicate the presence of pores, and light contrasts turning into white indicate a high graininess of the material. The more even contrast in Figure 8a indicated that the composition of the material containing astralene hade less porosity and granularity. The combination of astralene with magnesian cement contributed to the formation of a dense, therefore, more durable structure. The setting time of the mixture was not changed significantly and required a long period of time. This was due to the fact that when mixing a mixture with a saturated solution of salts consisting mainly of halite, the process of hydration of magnesia binder takes a longer period of time in comparison with the setting time of magnesia-based mixtures with bischofite (saturated solution of MgCl salts).

Experiments proved that the use of the nanomodifying additive astralene in the backfill makes it possible to increase the strength properties of the created artificial mass with a decrease in binder consumption. Activation of the backfill with the additive astralene formed a fine-crystalline nanomodified structure and allowed creation of a completely new nanomodified material with stronger bonds.

Activation occurs by adding a nanomodifying additive to the backfill. The formation of a nanomodified artificial mass based on the wastes from enrichment of water-soluble ores occurs due to the formation of fine-structured bonds by filling its pore voids. As a result of the introduction of a nanomodifying additive (astralene) into the backfill, needle crystalline and cryptocrystalline frames were formed, which filled the pore space. These structures guaranteed the formation of stable structural bonds between the crystalline matrix components, which increased the strength of the mass by at least 1.76–2.36 times.

Testing of composite samples after 60 and 90 days proved that even after a standard 28 day period, an important increase in compressive strength may still be observed. The range of this increase is higher than that for standard cementitious materials such as concrete, and it is comparable to the results from the creation of soil–cement composites in the course of geotechnical works.

5. Conclusions

To study the possibility of creating and using nanomodified backfill material based on the waste from enrichment of water-soluble ores, the composition was selected, physical properties were studied, and micro-structural research was conducted. From the conducted research, the following conclusions can be drawn:

(1) Wastes from enrichment of water-soluble ores cannot be an ideal inert aggregate for backfill production. However, the use of magnesia cement as a binder and astralene as a nanomodifying additive will make it possible to freely use tailings of water-soluble ore enrichment for backfilling.

(2) The optimal proportion of the nanomodifying additive astralene in the backfill is 0.01% of the total mass. This content allows one to achieve maximum strength of the fill mass. The recommended waste content is 98.99% with a binder content of 1%. The use of a nanomodifying additive significantly increases the strength properties of the created backfill composite.

(3) The use of a nanomodified backfill based on waste from enrichment of water-soluble ores contributes to a multiplier effect: economic due to the introduction of mining technology that decreases losses and reduces costs for the storage of industrial waste; ecological due to reducing the volume of industrial mass and the introduction of technology that improves the safety of mining operations.

6. Patents

The presented results are the subject of Russian Patent RU 2754908 C1: "Backfill mixture with nanomodified additive". Authors of the patent: Elena A. Ermolovich, Albert M. Khayrutdinov, Yulia S. Tyulyaeva, Cheynesh B. Kongar-Syuryun.

Field of application: mining industry.

Substance: Invention relates to the mining industry, namely to backfill mixtures, and can be used to backfill a goaf in the development of mineral deposits. The filling mixture contains a saturated solution of halite waste salts and a solid mixture consisting of: halite waste from potash ore processing, a binder-magnesia cement, an additive, and the filling mixture contains a nanomodified additive, astralene, as an additive. The filling mixture contains, wt.%: 11.11—a saturated solution of salts of halite waste and 88.89—a solid mixture, which contains, wt.%: halite waste from potash ore processing—98.99–99.49; nanomodified additive astralene—0.01; magnesia cement—the remainder.

Effect: increasing strength of the filling mixture, reducing the consumption of the binder in the filling mixture, increasing completeness of utilization of potash ore processing waste.

Author Contributions: Conceptualization, E.A.E.; methodology, M.M.K.; software, C.B.K.-S.; validation, E.A.E. and Y.S.T.; formal analysis, M.M.K. and Y.S.T.; investigation, C.B.K.-S.; resources, E.A.E. and A.L.I.; data curation, C.B.K.-S. and M.M.K.; writing—original draft preparation, E.A.E. and M.M.K.; writing—review and editing, C.B.K.-S.; visualization, Y.S.T.; supervision, A.L.I.; project administration, Y.S.T. and A.L.I.; funding acquisition, A.L.I. All authors have read and agreed to the published version of the manuscript.

Funding: This research received no external funding.

Institutional Review Board Statement: Not applicable.

Informed Consent Statement: Not applicable.

Data Availability Statement: Not applicable.

Conflicts of Interest: The authors declare no conflict of interest.

References

1. Fasusi, O.A.; Cruz, C.; Babalola, O.O. Agricultural Sustainability: Microbial Biofertilizers in Rhizosphere Management. *Agriculture* **2021**, *11*, 163. [CrossRef]
2. Nosratabadi, S.; Ardabili, S.; Lakner, Z.; Mako, C.; Mosavi, A. Prediction of Food Production Using Machine Learning Algorithms of Multilayer Perceptron and ANFIS. *Agriculture* **2021**, *11*, 408. [CrossRef]
3. Leifert, C. Organic Farming Provides a Blueprint to Improve Food Quality, Safety and Security. *Agronomy* **2022**, *12*, 631. [CrossRef]
4. Gu, X.; Liu, Y.; Li, N.; Liu, Y.; Zhao, D.; Wei, B.; Wen, X. Effects of the Foliar Application of Potassium Fertilizer on the Grain Protein and Dough Quality of Wheat. *Agronomy* **2021**, *11*, 1749. [CrossRef]
5. Soti, P.; Fleurissaint, A.; Reed, S.; Jayachandran, K. Effects of Control Release Fertilizers on Nutrient Leaching, Palm Growth and Production Cost. *Agriculture* **2015**, *5*, 1135–1145. [CrossRef]
6. Zhang, X.-M.; Hu, C.; He, Z.-Q.; Abbas, Y.; Li, Y.; Lv, L.-F.; Hao, X.-Y.; Gai, G.-S.; Huang, Z.-H.; Yang, Y.-F.; et al. Microcrystalline Apatite Minerals: Mechanochemical Activation for Agricultural Application. *Minerals* **2019**, *9*, 211. [CrossRef]
7. Rybak, J.; Khayrutdinov, M.M.; Kuziev, D.A.; Kongar-Syuryun, C.B.; Babyr, N.V. Prediction of the geomechanical state of the rock mass when mining salt deposits with stowing. *J. Min. Inst.* **2022**, *253*, 61–70. [CrossRef]
8. Adigamov, A.E.; Yudenkov, A.V. Stress-strain behavior model of disturbed rock mass with regard to anisotropy and discontinuities. *Min. Inf. Anal. Bull.* **2021**, *8*, 93–103. [CrossRef]
9. Yu, L.; Ignatov, Y.; Ivannikov, A.; Khotchenkov, E.; Krasnoshtanov, D. Common features in the manifestation of natural and induced geodynamic events in the eastern regions of Russia and China. *IOP Conf. Ser. Earth Environ. Sci.* **2019**, *324*, 012004. [CrossRef]
10. Papán, D.; Valašková, V.; Drusa, M. Numerical and Experimental Case Study of Blasting Works Effect. *IOP Conf. Ser. Earth Environ. Sci.* **2019**, *44*, 052052. [CrossRef]
11. Drusa, M.; Lamich, D.; Vlcek, J.; Heviankova, S.; Kyncl, M.; Marschalko, M.; Yilmaz, I.; Bouchal, T.; Bendova, M.; Kubeckova, D.; et al. Verification of the results of the geotechnical monitoring using finite element method. In Proceedings of the International Multidisciplinary Scientific GeoConference, Varna, Bulgaria, January 2013; Surveying Geology and Mining Ecology Management, SGEM: Sofia, Bulgaria, 2013; Volume 2, pp. 533–540. [CrossRef]
12. Malovichko, A.A.; Blinova, T.S.; Lebedev, A.Y.; Nekrasova, L.V. Solikamsk earthquake on January 5, 1995. In *Safety Problems during the Operation of Mineral Deposits in the Zones of Urban Industrial Agglomerations*; Materials of the International Symposium SRM-95; URO RAS: Ekaterinburg, Russia, 1997; pp. 307–315.
13. de Galdeano, C.S.; Shanov, S.; Galindo-Zaldívar, J.; Radulov, A.; Nikolov, G. A new tectonic discontinuity in the Betic Cordillera deduced from active tectonics and seismicity in the Tabernas Basin. *J. Geodyn.* **2010**, *50*, 57–66. [CrossRef]
14. Marcak, H.; Mutke, G. Seismic activation of tectonic stresses by mining. *J. Seism.* **2013**, *17*, 1139–1148. [CrossRef]

15. Kozyrev, A.V.; Lovchikov, A.V.; Kuzmin, I.A. The strongest man-made earthquake in the Russian mines, August 17, 1999, the Umbo-zero mine (Kola Peninsula). *Mining Inf. Anal. Bull.* **2000**, *6*, 169–173. (In Russian)
16. Khayrutdinov, A.; Paleev, I.; Artemov, S. Replacement of traditional components of the backfill mixture with man-made waste. *IOP Conf. Ser. Earth Environ. Sci.* **2021**, *942*, 012005. [CrossRef]
17. Agafonova, D.S.; Sherimov, D.; Belorus, A.O.; Pleshanov, I.M.; Timchenko, A.V. Ensuring the Environmental Safety of MSW by Using Fiber Optical Sensors Based on Oxyfluoride Glasses. In Proceedings of the 2021 IEEE Conference of Russian Young Researchers in Electrical and Electronic Engineering (ElConRus), St. Petersburg, Moscow, Russia, 26–29 January 2021; pp. 1298–1300. [CrossRef]
18. Aung, K.P.; Zotov, V.V.; Gadzhiev, M.A.; Artemov, S.I.; Gireev, I.A. Formalization of selection procedure of mineral mining tech-nologies. *Mining Inf. Anal. Bull.* **2022**, *2*, 124–138. (In Russian) [CrossRef]
19. Adigamov, A.; Zotov, V.; Kovalev, R.; Kopylov, A. Calculation of transportation of the stowing composite based on the waste of water-soluble ores. *Transp. Res. Procedia* **2021**, *57*, 17–23. [CrossRef]
20. Adigamov, A.; Rybak, J.; Golovin, K.; Kopylov, A. Mechanization of stowing mix transportation, increasing its efficiency and quality of the created mass. *Transp. Res. Procedia* **2021**, *57*, 9–16. [CrossRef]
21. Kalmykov, V.N.; Beloborodov, I.S.; Grigoriev, V.V.; Saraskin, A.V. Research of the composition and technology of preparation of cementless filling mixtures based on lime-slag binder. *Mining Inf. Anal. Bull.* **2005**, *7*, 242–245. (In Russian)
22. Kowalik, T.; Ubysz, A. Waste basalt fibers as an alternative component of fiberconcrete. *Mater. Today Proc.* **2021**, *38*, 2055–2058. [CrossRef]
23. Khudyakova, L.I.; Zalutskiy, A.V.; Paleev, P.L. Use of ash and slag waste of thermal power plants. XXI century. *Technosphere Saf.* (In Russian). **2019**, *4*, 375–391. [CrossRef]
24. Trubkin, I.S.; Zubkov, A.A. Backfill mixtures for mine workings with the use of MMK converter slags and tailings of copper-sulfur ore dressing. *Bull. Magnitogorsk. State Tech. Univ. G.I. Nosova* **2007**, *3*, 12–14.
25. Galtseva, O.N.; Buryanov, A.F.; Buldyzhova, E.N.; Soloviev, V.G. The use of synthetic anhydrite calcium sulfate for the preparation of filling mixtures. *Build. Mater.* **2015**, *6*, 76–77.
26. Gorbunova, O.A. Development of solidifying backfill compositions based on mining and processing waste with the addition of polymers of the polyhexamethyleneguanidine class. *Mining Inf. Anal. Bull.* **2010**, *S2*, 62–69. (In Russian)
27. Ustinova, Y.V.; Nasonova, A.E.; Nikiforova, T.P.; Kozlov, V.V. Research of Interaction between Caustic Magnesite and a Microsilica Additive. *Vestn. MGSU/Proc. Mosc. State Univ. Civ. Eng.* **2012**, *3*, 100–104.
28. Averina, G.F.; Katasonova, A.V.; Zimich, V.V.; Chernykh, T.N. Improvement of Water Resistance of Magnesia Stone for Hardening of Filling Mixtures from Man-Made Dolomite. *Bull. South Ural. State Univ. Ser. Constr. Eng. Arch.* **2016**, *16*, 28–32. (In Russian) [CrossRef]
29. Plekhanova, T.A. Cementless composition for backfilling of worked-out spaces based on technogenic materials. *Chem. Phys. Mesoscopy* **2005**, *7*, 104–112.
30. Khairutdinov, A.; Ubysz, A.; Adigamov, A. The concept of geotechnology with a backfill is the path of integrated development of the subsoil. *IOP Conf. Ser. Earth Environ. Sci.* **2021**, *684*, 012007. [CrossRef]
31. Golik, V.I.; Dmitrak, Y.V.; Chan, C.; Maslennikov, S.A. The Use Of Tailings While Preparing Hardening Filling Mixtures. *News Ural State Min. Univ.* **2018**, *2*, 95–101. [CrossRef]
32. Ermolovich, E.A.; Ermolovich, O.V. Effects of mechanical activation on the structural changes and microstructural characteristics of the components of ferruginous quartzite beneficiation tailings. *Int. J. Min. Sci. Technol.* **2016**, *26*, 1043–1049. [CrossRef]
33. Khairutdinov, M.M.; Votyakov, M.V. Selection of chemical additives for hardening backfill in potash mines. *Mining Inf. Anal. Bull.* **2007**, *6*, 218–220. (In Russian)
34. Vestler, D.; Shishkin, I.; Gurvitz, E.A.; Nasir, M.E.; Ben-Moshe, A.; Slobozhanyuk, A.P.; Krasavin, A.V.; Levi-Belenkova, T.; Shalin, A.S.; Ginzburg, P.; et al. Circular dichroism enhancement in plasmonic nanorod metamaterials. *Opt. Express* **2018**, *26*, 17841–17848. [CrossRef] [PubMed]
35. Mukhin, N.; Afanasjev, V.; Sokolova, I.; Chigirev, D.; Kastro, R.; Rudaja, L.; Lebedeva, G.; Oseev, A.; Tumarkin, A. Heat-Resistant Ferroelectric-Polymer Nanocomposite with High Dielectric Constant. *Materials* **2018**, *11*, 1439. [CrossRef] [PubMed]
36. Ponomarev, A.N. Polyhedral Multilayer Carbon Nanostructures of the Fulleroid Type. The Russian Federation Patent No. 2196731, 21 September 2000.
37. Ponomarev, A.N. Polyhedral Multilayer Carbon Nanostructures of the Fulleroid Type. The Russian Federation Patent No. 2397950, 23 April 2008.
38. Nizina, T.A.; Kislyakov, P.A. Optimization of the properties of epoxy composites modified with nanoparticles. *Constr. Mater.* **2009**, *9*, 78–80. (In Russian)
39. Kostina, N.A.; Kislov, D.A.; Ivinskaya, A.N.; Proskurin, A.; Redka, D.N.; Novitsky, A.; Ginzburg, P.; Shalin, A.S. Nanoscale Tunable Optical Binding Mediated by Hyperbolic Metamaterials. *ACS Photon.* **2019**, *7*, 425–433. [CrossRef]
40. Patrikeev, L. Nanoconcretes. *Nanoindustry-Sci. Tech. J.* **2008**, *2*, 14–15. (In Russian)
41. Melnikov, N.N. *Methodical Recommendations for Quality Control of Backfill Mixtures*; Mining Institute of Science of the Federal Research Center «Kola Science Center» (MI KSC RAS): Apatity, Russia, 1990; p. 94. (In Russian)

42. Colston, S.L.; O'Connor, D.; Barnes, P.; Mayes, E.L.; Mann, S.; Freimuth, H.; Ehrfeld, W. Functional micro-concrete: The incorporation of zeolites and inorganic nano-particles into cement microstructures. *J. Mater. Sci. Lett.* **2000**, *19*, 1085–1088. [CrossRef]
43. Komokhov, P.G.; Kharitonov, A.M. Nanostructural model of cement stone for assessing the properties of a composite material. *Pop. Concr. Sci.* **2007**, *2*, 125–127. (In Russian)
44. Hanehara, S.; Ichikawa, M. Nanotechnology of cement and concrete. *Taiheiyo Cem. Kenkyu Hokoku* **2001**, *141*, 47–58.
45. Pukhova, V.; Kolesnikovich, V.; Spivak, Y.; Lizunkova, D.; Shishkin, I. Particularities of Scanning Electron Microscopy Operation Parameters for Textured Porous Silicon Diagnostics. In Proceedings of the 2020 IEEE Conference of Russian Young Researchers in Electrical and Electronic Engineering (EIConRus), St. Petersburg and Moscow, Russia, 27–30 January 2020; pp. 994–999. [CrossRef]
46. Krotov, A.; Volkov, D.; Romanov, N.; Gryaznov, N.; Sosnov, E.; Goryachkin, D. Method for measuring distortion in wide-angle video channels. *J. Appl. Eng. Sci.* **2018**, *16*, 274–280,530. [CrossRef]
47. Supe, A.; Olonkins, S.; Udalcovs, A.; Senkans, U.; Mūrnieks, R.; Gegere, L.; Prigunovs, D.; Grube, J.; Elsts, E.; Spolitis, S.; et al. Cladding-Pumped Erbium/Ytterbium Co-Doped Fiber Amplifier for C-Band Operation in Optical Networks. *Appl. Sci.* **2021**, *11*, 1702. [CrossRef]
48. Mukhin, N.; Chigirev, D.; Bakhchova, L.; Tumarkin, A. Microstructure and Properties of PZT Films with Different PbO Content—Ionic Mechanism of Built-In Fields Formation. *Materials* **2019**, *12*, 2926. [CrossRef] [PubMed]
49. Burminskaya, L.N.; Bulgakov, V.G.; Neginskij, I.V.; Smirnov, K.O. Programming complex for X-ray analysis of thin structure metallic alloys. *Sci. J. VolSU* **2004**, *1*, 159–162. (In Russian)
50. Khairutdinov, M.M.; Votyakov, M.V. Development of compositions of hardening filling mixtures from ore processing waste from potash enterprises. *Mining Inf. Anal. Bull.* **2007**, *10*, 220–222. (In Russian)
51. Stefaniuk, D.; Zajączkowski, P.; Rybak, J. Methodology of axial testing of cement-fly ash-soil samples. In Proceedings of the Stroitel'Stvo-Formirovanie Sredy Žiznedeâtel'nosti, Moskva, Russia, 27–29 April 2016; pp. 1091–1094.
52. Kanty, P.; Rybak, J.; Stefaniuk, D. Some Remarks on Practical Aspects of Laboratory Testing of Deep Soil Mixing Composites Achieved in Organic Soils. *IOP Conf. Ser. Mater. Sci. Eng.* **2017**, *245*, 022018. [CrossRef]
53. Winchell, A.N. *Elements of Optical Mineralogy*; Publishing House of Foreign Literature: Moscow, Russia, 1953; p. 561. (In Russian)
54. Winchell, A.N.; Winchell, H. *The Microscopical Characters of Artificial Inorganic Solid Substances: Optical Properties of Artificial Minerals*; Mir: Moscow, Russia, 1967; p. 526. (In Russian)

materials

MDPI

Article

Application of the Acoustic Emission Method and Artificial Neural Networks to Assess the Damaging Effect of High Temperature on the Structure of Fibre-Cement Boards

Tomasz Gorzelańczyk *, Krzysztof Schabowicz and Mateusz Szymków

Faculty of Civil Engineering, Wrocław University of Science and Technology, Wybrzeże Wyspiańskiego 27, 50-370 Wrocław, Poland
* Correspondence: tomasz.gorzelanczyk@pwr.edu.pl

Abstract: This article shows the results of research into the damaging effect of high temperature on the structure of fibre-cement boards. Samples of fibre-cement boards were exposed to high temperatures over various lengths of time and then they were investigated under the three-point bending and acoustic emission methods. In this way, the critical temperature and the duration of its influence on the structure of a fibre-cement board were determined. An artificial neural network was used to analyse the results obtained using the acoustic emission method. The investigations showed a marked fall in the number of registered AE events for the tested series of boards exposed to high temperature in comparison with the reference boards. Moreover, in the boards exposed to high temperature, a marked increase in the energy of AE events occurs during the bending test, whereby the registered events, by and large, come down to a single pulse induced by a brittle fracture. It is also demonstrated that the determination of the damaging effect of high temperature on the structure of fibre-cement boards solely on the basis of bending strength (*MOR*) is inadequate.

Keywords: artificial neural networks; non-destructive testing; fibre-cement boards; acoustic emission; SEM

Citation: Gorzelańczyk, T.; Schabowicz, K.; Szymków, M. Application of the Acoustic Emission Method and Artificial Neural Networks to Assess the Damaging Effect of High Temperature on the Structure of Fibre-Cement Boards. *Materials* **2022**, *15*, 6460. https://doi.org/10.3390/ma15186460

Academic Editor: F. Pacheco Torgal

Received: 4 July 2022
Accepted: 13 September 2022
Published: 17 September 2022

Publisher's Note: MDPI stays neutral with regard to jurisdictional claims in published maps and institutional affiliations.

1. Introduction

Fibre-cement boards (FCB) have been used in buildings from the beginning of the twentieth century. This is a building product. The method of manufacturing this composite material was devised and patented by the Czech engineer Ludwik Hatschek, but the first such boards were with asbestos fibres. Asbestos fibres had been recognized to be carcinogenic, and they were replaced with synthetic or cellulose fibres [1]. The currently produced fibre-cement boards consist of synthetic fibres, cellulose fibres, cement and various innovative additives and admixtures, whereby they have become a completely different construction product. FCB have also other components and fillers: limestone flour, mica, pearlite, kaolin, microsphere, and also recycled materials [2,3], whereby FCB continues to be a very innovative material. It is also important for sustainable development and carbon footprint reduction [4]. FCB are used in construction mainly as rainscreen exterior wall cladding [5]. During use, FCBs are exposed to various environmental factors, chemical damage from acid rain and physical damage from ultraviolet radiation. Moreover, fibre-cement boards are exposed to operational and exceptional factors. These include, first of all, the high temperature produced by, e.g., a fire. Therefore, the determination of the degree of damage caused by high temperature is a major problem from both the scientific and practical points of view. A lot of the research to date on fibre-cement boards has dealt with the determination of their standard physico-mechanical properties, the effects of operational factors (such as wetting-drying cycles and freeze-thaw cycles), the effect of heating and sprinkling, the effect of high temperatures and the effect of using various types of fibres and production processes, solely on the basis of bending strength

(the modulus of rupture (*MOR*)) [6]. In the literature, one can find few non-destructive investigations of fibre-cement boards and they describe only the imperfections arising during production [7–10]. The impact of high temperature is certainly one of the major damaging factors peculiar to many building products, particularly composite ones which contain reinforcement in the form of various kinds of fibres, especially cellulose fibres, as the latter undergo pyrolysis at temperatures above 200 °C. This has been experimentally demonstrated in studies [11–13]. Thus, high temperature greatly affects the durability of the whole composite [6]. To prove this thesis, experiments during which samples of fibre-cement boards were exposed to high temperatures ranging from 170 °C to 250 °C over a period of 0.5–4 h were carried out. After the exposure to high temperature the samples were investigated by registering the acoustic emission (EA) during three-point bending and then analysing the results using artificial neural networks (ANNs) [14]. Research conducted by the authors has shown that assessments of the degree of damage to fibre-cement boards caused by high temperature solely on the basis of bending strength (*MOR*) are inadequate [11,12,15,16]. By applying the acoustic emission method, it became possible to determine the effect of high temperature on the basis of the acoustic phenomena which may occur in the fibre-cement board. The registered AE signals were used to determine model acoustic spectrum characteristics which accompany the cracking of the cement matrix and the rupture of the fibres during bending. Then, recognition of the model characteristics in the EA recordings was carried out using artificial neural networks.

2. Survey of Literature

A review of literature on the subject shows that most of the research to date on FCB has been devoted to examining the effect of operational factors [17–19] and that of high temperatures by testing the physico-mechanical properties, mainly MOR, of such boards. In [20,21], nanoindentation was employed to assess the changes taking place in the structure of FCB under the influence of selected operating conditions. So far, there have been few works dealing with the investigation of FCB by means of non-destructive methods and the acoustic emission method. For example, [6] presents the results of research on fibre-cement boards, including the influence of high temperature, but based only on MOR. Furthermore, Li et al. [22] studied the effect of high temperatures on extruded composites on the basis of their mechanical properties. To assess the impact of high temperature and fire on fibre-cement boards, non-destructive methods such as acoustic emission were used, not only on the basis of physico-mechanical parameters in [11,12,23]. In the literature, one can also find other non-destructive studies of FCB, which deal mainly with the detection of imperfections arising at the production stage. In reference [7,24] by the authors present the possibility of using Lamb waves in a non-contact ultrasonic scanner to detect delamination and cracks in fibre-cement boards already at the production stage. Reference [25] describes a method of detecting delamination in materials using a mobile ultrasonic probe. Ultrasonic equipment and an idea for detecting delamination in FCB are described in [8] by Dębowski et al. In [26–28], it was proposed to use the impact-echo method and the impulse response method to discover delamination in concrete elements. However, it is not recommended to test fibre-cement boards using the two methods as they are intended for testing elements thicker than 100 mm, while the currently available fibre-cement boards are usually 8 mm thick. Furthermore, in the case of the impulse response method, a hammer strike can damage the board, while in the case of the impact-echo method, disturbances arise as a result of multiple reflections of waves, which makes the interpretation of the obtained image difficult, as described in [26]. In the literature, there is not enough information about the application of other non-destructive methods to the testing of FCB. Preliminary research reported by Chady et al. [10,29] confirmed the usefulness of the terahertz (t-ray) imaging method for testing FCB. Terahertz signals are similar in character to ultrasonic signals, but their interpretation is more complex. Adamczak-Bugno et al. [16] and Schabowicz et al. [30] used microtomography to identify delamination and low density regions in fibre-cement boards. The test results indicate that this method accurately distinguishes differences in the

microstructure of the boards. However, this method can be applied only to small boards. As mentioned above, so far there have been few investigations into fibre-cement boards conducted using acoustic emission. Ranachowski et al. [31,32] carried out pilot studies of fibre-cement boards manufactured using extrusion and exposed as part of this process to the temperature of 230 °C. They used acoustic emission (AE) to determine the contribution of cellulose fibres to the strength of the boards and attempted to distinguish between the AE events emitted by the fibres and the ones emitted by the cement matrix. In their [11,12,15] the authors proposed to use the acoustic emission method to study the impact of fire and high temperature on fibre-cement boards. It should be mentioned that the influence of high temperature on concrete and the dependences involved were extensively investigated using acoustic emission by, e.g., Ranachowski et al. [33,34]. Melichar et al. [35] used the acoustic emission method to study modified cement-bonded particleboard under static load stress. During measurements performed using the acoustic emission method, a large amount of data are acquired. The data should be analysed and interpreted in a proper way. For this purpose, it can be useful to combine the AE method with artificial intelligence, including artificial neural networks (ANNs). Artificial neural networks have been successfully used to analyse and recognize signals obtained during the failure of different materials [36]. The most important feature of ANN is the parallel processing of information, which makes it possible to process large amounts of data and significantly speed up calculations. ANN was used to detect and recognize the characteristics of the acoustic spectra accompanying the cracking of the fibers or the cement matrix from the AE records during three-point bending. ANNs were used in [37–39] to analyse the results obtained from non-destructive tests of concrete. In [40,41] the acoustic emission method was used to test steel and artificial neural networks were employed to analyse the test results. Rucka and Wilde [42,43], Zielińska and Rucka [44] and Wojtczak and Rucka [45] successfully used the ultrasonic method to investigate damage to masonry structures. Finally, it should be mentioned that ANNs were also successfully employed to analyse the results of investigations of fibre-cement boards subjected to fire and freeze-thaw cycles [11,24].

Considering the above, the acoustic emission method combined with ANNs would be proper for assessing the damaging effect of high temperature on the structure of fibre-cement boards.

3. Strength Tests

High-temperature impact tests were carried out for five series of FCB designated with letters from A to E. The basic specifications of the boards in all the series, determined in accordance with the standard requirements [46] are presented in Table 1.

Table 1. Tested fibre-cement boards of series A to E and their basic specifications.

Series Designation	Board Thickness e [mm]	Board Colour	Application	Board Bulk Density ρ [g/cm^3]	Bending Strength *MOR* [MPa]
A	8.0	natural	exterior	1.60	23.1
B	8.0	full body coloured	exterior	1.60	30.4
C	8.0	full body coloured	exterior	1.65	32.3
D	8.0	natural	interior	1.70	20.5
E	8.0	natural	interior	1.20	12.7

The samples of fibre-cement boards were first exposed to high temperatures of 170–250 °C in a laboratory oven over times ranging from 0.5 to 4 h. The tests were first of all designed to indicate the "critical" temperature that has a significant effect on the bending strength (*MOR*) of the tested fibre-cement boards. The determined effect of selected temperatures on the *MOR* of series A and C samples is shown in Figure 1.

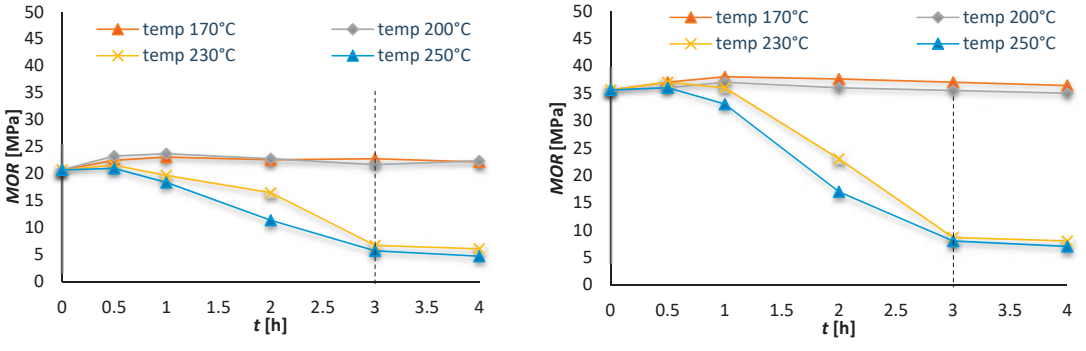

Figure 1. *MOR* of samples exposed to high temperature over time of 0.5–4 h: (**a**) series A, (**b**) series C.

The diagrams in Figure 1 show that the influence of the temperature of 230 °C and higher on the bending strength (*MOR*) of the FCB is significant. On this basis, a critical temperature of 230 °C and its duration of 3 h were established. It is apparent that the above diagrams indicate only that as a result of the high temperature the MOR of the boards decreases, but they do not answer the question what changes occur in the structure of the tested boards. In order to find an answer to this question the authors carried out detailed investigations described further in this paper.

The tests aimed at determining the effect of the temperature of 230 °C lasting for 3 h on the structure of fibre-cement boards were carried out on samples designated A_T to E_T. The reference samples (in air-dry condition) not exposed to high temperature were designated A_R to E_R. In total, 50 samples (10 from each series) were tested. Figure 2 presents exemplary views of the tested 8 mm thick 20 × 100 mm samples.

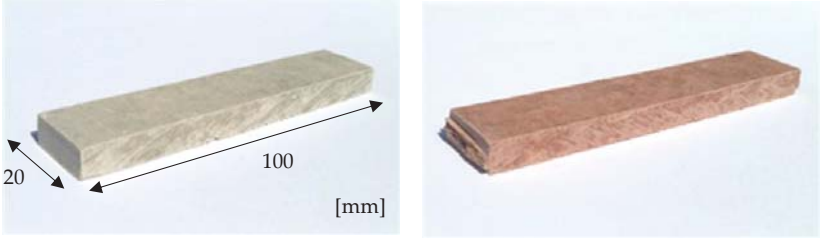

Figure 2. Tested fibre-cement board samples: (**a**) board A, (**b**) board C.

In order to identify the effect of the high temperature on the structure of the FCB, the latter were investigated under three-point bending by means of acoustic emission. During the three-point bending, the trace of bending force *F*, strain ε and acoustic emission signals were registered. Figure 3 shows the three-point bending test bench with the acoustic emission measurement apparatus.

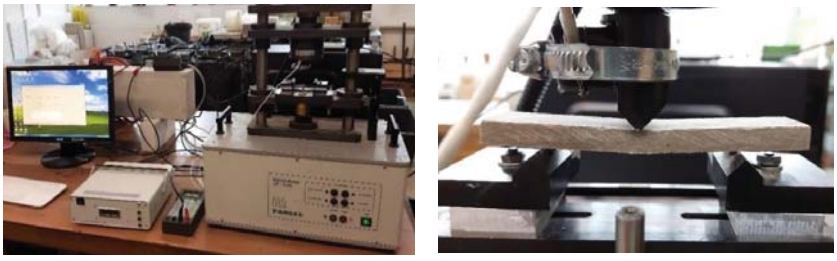

(**a**) (**b**)

Figure 3. Test bench with equipment for acoustic emission measurements (**a**) and close-up of cement board sample during test (**b**).

The analysis of the three-point test results covered the trace of flexural stress σ_m, the bending strength (*MOR*), impact energy W_f, the limit of proportionality (*LOP*) and strain ε. *MOR* was determined from the standard formula [46]:

$$MOR = \frac{3Fl_s}{2b\,e^2}, \quad (1)$$

where:

F—the ultimate force [N],
l_s—the spacing of the supports [mm],
b—the width of the tested sample [mm],
e—the tested sample's mean thickness measured in four places [mm].

The impact energy was determined using the following formula taken from [32]:

$$W_f = \frac{1}{S}\int_{F0}^{F0.4max} F\,da, \quad (2)$$

where:

S—the sample's cross-sectional area [m^2],
A—the deformation during bending [m].

Because of the wide range of test results, only the results for two selected series of the tested fibre-cement boards are presented and analysed in the further part of this paper. Fibre-cement boards A and C were selected for further analysis. This choice was guided by the fact that they are panels for external applications as façade claddings (nowadays it is the most common way of using these panels). Moreover, in contrast to the B series boards, these boards are in the opinion of the authors more representative due to the differences in the obtained MOR flexural strength (about 30%). In turn, the D and E series panels are characterized by much worse strength parameters and are panels for internal applications. They also have a slightly different composition because they do not contain PVA fibres. This makes it difficult to compare them with the A–C series boards.

Figure 4 shows bending σ–ε curves for exemplary fibre-cement boards of series A and C. The *LOP* and *MOR* values are marked in the diagrams. Table 2 shows the results of the bending test to which the fibre-cement boards were subjected.

As it appears from Figure 4, the 3 h long influence of the temperature of 230 °C on *MOR* is clearly damaging for series A_T and C_T. The tests showed that under the influence of the temperature *MOR* decreased by as much as 70%. An analysis of Table 2 shows that the fall in the value of impact energy W_f is very large. The value of this parameter is indicative of the changes which have taken place in the structure of the FCB under the influence of temperature, which manifest themselves by a fall in the energy needed to break the sample. It also appears from Table 2 that the value of Young's modulus E_D increases by about 30% under the influence of a temperature of 230 °C lasting for 3 h. Moreover, it appears from

the graphs presented in Figure 4 that the σ–ε dependence for the tested boards of series A_T and C_T also changes under the influence of high temperature. The influence of temperature manifests itself in not only in the decrease in *MOR*, but also in a change in the shape of the σ–ε curve. One can notice that *MOR* has become equal to *LOP*. In the case of the reference fibre-cement samples, the value of *MOR* is much higher. To sum up, it can be concluded from the decreased parameter values presented in Table 2 that damage occurred as a result of the exposure to a temperature of 230 °C for 3 h.

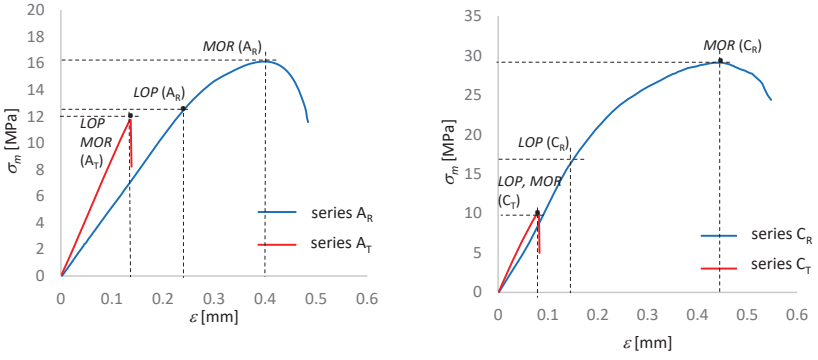

(**a**) (**b**)

Figure 4. Bending σ–ε curves for fibre-cement boards of: (**a**) series A, (**b**) series C.

Table 2. Tested FCB of series A and C and their basic specifications.

Board Series Designation	Ultimate Force F [N]	LOP [MPa]	Young's Modulus E_D [GPa]	Impact Energy W_f [J/m^2]	*MOR* [MPa]
Series A_R	252.26	15.5	6.0	391.82 (3.45%) *	20.73 (2.39%) *
Series A_T	82.36	6.77	7.5	42.99 (3.87%) *	6.77 (3.44%) *
Series C_R	475.18	24.20	8.1	1352.60 (1.94%) *	35.60 (3.98%) *
Series C_T	115.28	8.64	10.4	45.44 (3.51%) *	8.64 (3.14%) *

* Note: The coefficient of variation is in brackets.

In order to better characterize the effect of high temperature on the structure of FCB, acoustic emission and artificial neural networks were employed.

4. Investigations Using Artificial Neural Networks and Acoustic Emission

As mentioned above, the next step in the study of the damaging effect of the high temperature on the structure of the FCB was an analysis of the AE signals recorded during three-point bending. Such AE descriptors as: events rate N_{ev}, events sum $\sum N_{ev}$, events energy E_{ev} and EA signal frequency distribution were used in the investigations. Table 3 shows exemplary values of events sum $\sum N_{ev}$ and events energy E_{ev} for series A_R and C_R in air-dry condition and for series A_T and E_T exposed to the temperature of 230 °C for 3 h. In addition, the average energy $E_{ev,avg}$ of the events registered during the test was calculated. The analysis of the test results showed that EA signals were collected after the stress corresponding to *MOR* was exceeded.

Table 3. Summary of representative values of events sum $\sum N_{ev}$, events maximum energy E_{ev} and events average energy $E_{ev,avg}$ for boards of series A_R and C_R in dry-air condition and series A_T and C_T exposed to temperature of 230 °C for 3 h.

Board Series Designation	Events Sum $\sum N_{ev}$ [ev]	Events Energy E_{ev} [nJ]	Events Average Energy $E_{ev,avg}$ [nJ]
Series A_R	223.0	4214.0	18.89
Series A_T	111.0	31,6765.0	1853.74
Series C_R	496.0	18,338.0	36.97
Series C_T	142.0	348,255.0	2452.50

The results contained in Table 3 indicate a marked fall in the number of events registered for the tested series of the boards exposed to the temperature of 230 °C for 3 h in comparison with the boards in air-dry condition. Moreover, it is apparent that the exposure to the temperature of 230 °C for 3 h results in a considerable increase in events energy E_{ev} during the bending test for all the tested series of FCB. The correlation between the events sum $\sum N_{ev}$ descriptors and events energy E_{ev} indicates that the exposure to a temperature of 230 °C for 3 h results in an increase in energy E_{ev} of the registered events and a simultaneous reduction in their number. As a result of this exposure, the registered events come down to a single pulse induced by a brittle fracture. This is a high-energy event whose energy E_{ev} reaches 0.35 mJ.

In order to examine in more detail the course of the bending test and the effect of the damaging factor (the exposure to the high temperature of 230 °C for 3 h) on it, events sum $\sum N_{ev}$ and bending stress σ_m versus time are presented graphically in Figures 5 and 6.

A marked fall in the number of registered events and a change in the path of events sum $\sum N_{ev}$ are visible in Figures 5 and 6. Besides the fall in the number of events under the influence of the high temperature of 230 °C lasting for 3 h, it was noticed that all the registered events occurred within one time segment of 0.1 s. Hence, one can conclude that the events originate from a single fracture of the cement matrix. The damaging factor in the form of high temperature reduced the number of events, but resulted in an increase in their energy. The events registered for the cases in air-dry conditions, and which no longer registered in the boards after the latter had been baked at a temperature of 230 °C for 3 h, originate from the rupture of fibres damaged under the influence of the high temperature. The events registered for the boards of series A_T and C_T originate from the high-energy cracking of the cement matrix alone. In order to confirm the origin of the registered AE events, further investigations had to be made. A spectral analysis of the characteristics of the AE events spectra was carried out to identify the source of the registered AE events.

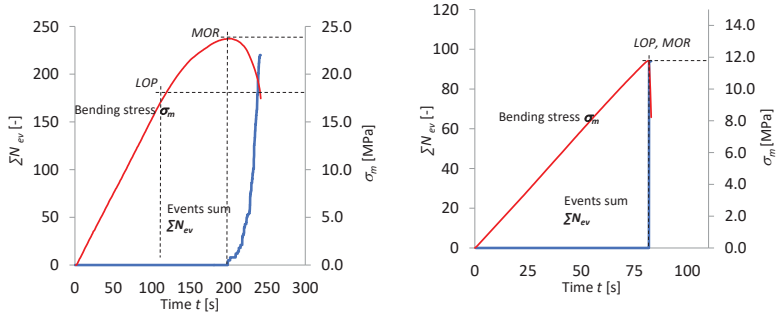

(**a**) (**b**)

Figure 5. Bending stress σ_m and events sum $\sum N_{ev}$ versus time t for boards of: (**a**) series A_R and (**b**) series A_T.

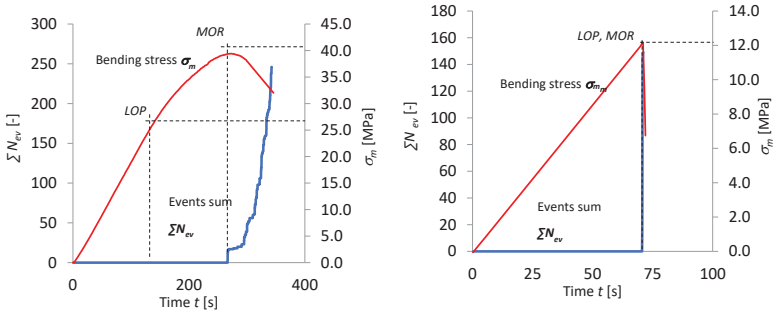

(**a**) (**b**)

Figure 6. Bending stress σ_m and events sum $\sum N_{ev}$ versus time t for boards of: (**a**) series C_R and (**b**) series C_T.

Acoustic spectra models for the cracking of the cement matrix were selected on the basis of the analysis of the acoustic activity in the time-frequency domain during the bending of the boards in air-dry condition and the ones exposed to a temperature of 230 °C for 3 h. A model acoustic spectrum for the rupture of the fibres was selected from the spectra obtained for the boards in air-dry conditions. The model acoustic spectrum showed a repeatable similar pattern in the frequency range of 10–24 kHz, clearly distinct from that of the cement matrix spectrum. The characteristic of the acoustic spectrum of the background originating from the press was determined on the basis of the initial phase of bending by averaging the characteristics obtained for all the tested boards of series A and C. The selected spectral characteristics of a fibre rupture are understood as the signal accompanying the cracking of the cement matrix with fibres, while the model spectral characteristic of the matrix is understood as the signal accompanying the cracking of the cement matrix alone. The selected model acoustic spectrum characteristics were registered at every 0.5 kHz in 80 intervals. Figure 7 shows the record of the model spectrum characteristics of the signal accompanying the cracking of the cement matrix and the rupturing of the fibres, and of the background signal.

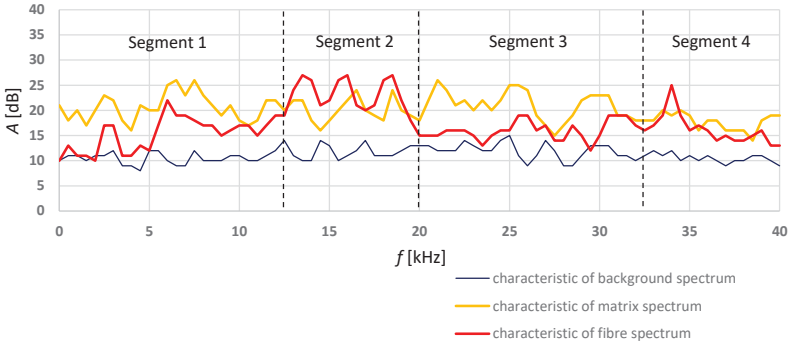

Figure 7. Background, fibre and cement matrix acoustic spectrum characteristics versus frequency.

It appears from Figure 7 that the acoustic activity of the background is within 10–15 dB. The characteristic of the acoustic spectrum of the cement matrix reaches the acoustic activity of 25 dB in the ranges of 5–10 kHz (segment 1) and 20–32 kHz (segment 3). For the fibres, an activity level above 25 dB in the frequency ranges of 12–18 dB (segment 2) and 32–38 kHz (segment 4) was read. The model characteristic for the cement matrix, the fibres and the background were implemented in artificial neural networks and the training and testing of

the latter began. A unidirectional multilayer structure with error backpropagation with momentum was selected for the ANNs [11,47,48]. Details concerning the selected ANNs and the training and testing procedures can be found in [49]. Having trained the ANN on the input data, the correctness of its mapping was checked on the training data and the testing data. Two pairs of input data, i.e., the data used for training the network and checking its ability to reproduce the model characteristics and the testing data used for checking the network's ability to identify the model spectral characteristics originating from the fibres and the matrix respectively during the bending test were used for this purpose. Consequently, a record of the neural networks' outputs of the recognized acoustic spectra corresponding to the fibre rupturing, matrix crack and the background respectively was obtained.

Figures 8 and 9 present the results of the recognition of the model acoustic spectra for the cement matrix and the fibres. They are marked on the record of events rate N_{ev} and bending stress σ_m as a function of time. The graphs are for the boards of series A_R and C_R in air-dry condition and series A_T and C_T exposed to the temperature of 230 °C for 3 h. For clarity, the recognized model acoustic spectra for the matrix are marked green and the ones for the fibres are marked orange.

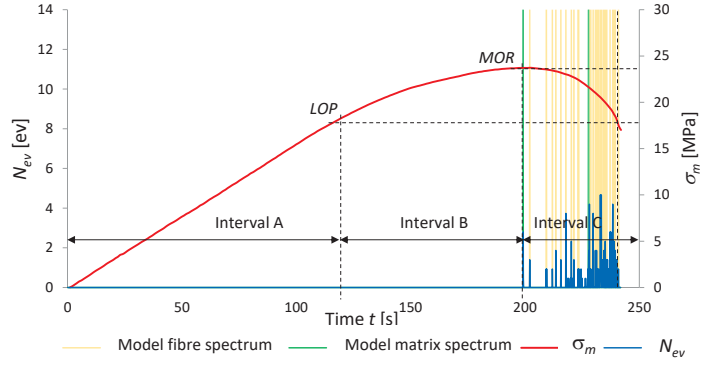

(**a**)

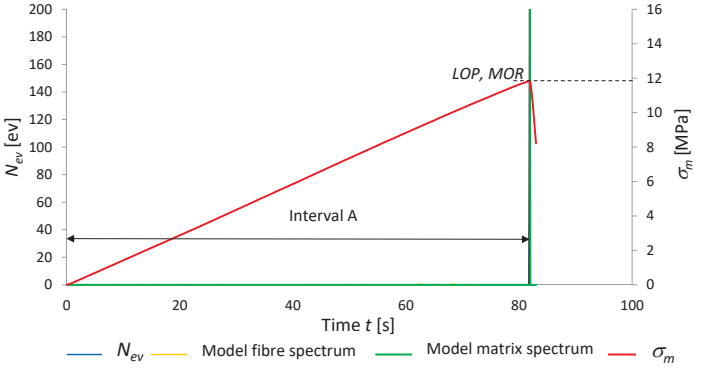

(**b**)

Figure 8. Events rate N_{ev} and bending stress σ_m versus time, under influence of fire, with marked identification of model spectral characteristics: (**a**) series A_R, (**b**) series A_T.

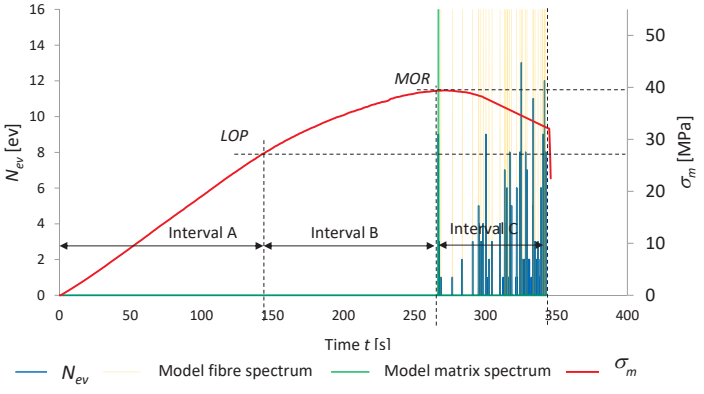

(**a**)

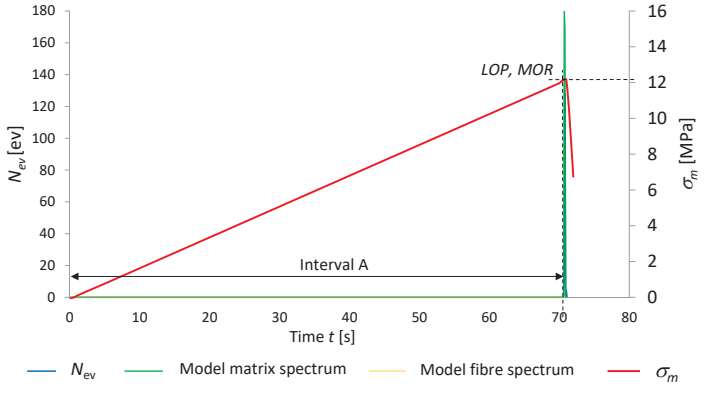

(**b**)

Figure 9. Events rate N_{ev}, and bending stress σ_m versus time under influence of fire, with marked identification of model spectral characteristics: (**a**) series C_R, (**b**) series C_T.

Analysing Figure 8a, three intervals, A, B and C, could be distinguished. It appears from this figure that as late as in interval C (after *MOR* had been reached) AE events were registered. No AE events were registered in intervals A and B. The registered events successively dominate after the maximum tensile bending stress is exceeded. The recognized events in interval C originate from the rupturing of the fibres and the cracking of the cement matrix. An event originating from the cracking of the cement matrix initiates subsequent events originating from the rupturing of the fibres. The matrix fractures after the bending strength (*MOR*) is reached. It appears from Figure 8b that *MOR* has become equal to *LOP*. Interval B between *LOP* and *MOR* is missing, while interval C has been reduced to a single time segment of 0.1 s with registered AE events. The fact that *MOR* has become equal to *LOP* is evidence of changes in the board's structure which occurred under the influence of high temperature. Whereas the reduction of interval C to a single segment is indicative of a single signal of the brittle fracture of the fibre-cement board and of the absence of fibres in its structure, which could carry tensile stresses. The acoustic spectrum characteristic of the events registered in interval C was recognized as the model spectrum of the cement matrix.

An exemplary breakdown of the events recognized as accompanying the rupturing of fibres and the cracking of the cement matrix for series A_R and A_T is presented in Table 4.

Table 4. Events recognized as accompanying rupturing of fibres and cracking of cement matrix for boards of series A_R and A_T.

Series	Events Sum $\sum N_{ev}$	Total Number of Recognized Events $\sum N_{ev,r}$	Total Number of Events Ascribed to Fibre Rupturing $\sum N_{ev,f}$	Total Number of Events Ascribed to Matrix Cracking $\sum N_{ev,m}$
Series A_R	223	203	195	8
Series A_T	94	94	0	94

The results presented in Table 4 indicate that no events originating from the rupturing of fibres were registered in the case of the boards exposed to the high temperature, which is clear evidence of the total failure of the fibres. The events which were not recognized during the testing of the fibre-cement boards in air-dry condition had too low event energy E_{ev} or their acoustic spectrum characteristics were atypical and at the similarity classifier of 0.9 were not assigned to the selected characteristics. The increase in the number of events ascribed to the cracking of the cement matrix in the boards exposed to the high temperature is due to the extreme event energy E_{ev} accompanying the brittle fracture.

Figure 9a shows that the course of bending and that of the AE signals registered for the boards of series C_R are similar to those for series A_R. Three intervals can be distinguished in the bending stress diagram. Numerous AE signals predominate in the last interval. The boards of series C_R have a large number of fibres in their structure. It appears from the figure that there is no interval B, while interval C containing AE signals has been reduced to a single time segment of 0.1 s, in which the recognized brittle fracture pattern was registered. The course of the bending test and that of AE descriptors are similar to those for the boards of series A_T. A comparison of Figures 9a and 9b clearly shows that exposure to a high temperature of 230 °C for 3 h is a damaging factor causing the degradation of the fibres contained in the board. This fact is very well reflected by the results presented in Table 5 in which the events recognized as accompanying the rupturing of fibres and the cracking of the cement matrix are collated for the fibre-cement boards of series C_R and C_T.

Table 5. Events recognized as accompanying the rupturing of fibres and cracking of the cement matrix for boards of series C_R and C_T.

Series	Events Sum $\sum N_{ev}$	Total Number of Recognized Events $\sum N_{ev,r}$	Total Number of Events Ascribed to Fibre Rupturing $\sum N_{ev,f}$	Total Number of Events Ascribed to Matrix Cracking $\sum N_{ev,m}$
Series C_R	496	483	445	38
Series C_T	142	142	0	142

Table 5 shows an exemplary comparison of the events recognized as accompanying the rupturing of fibres and the cracking of the cement matrix for series C_R and C_T.

It appears from Table 5 that the fibre-cement boards of series C_R are characterized by a large number of events originating from the rupturing of fibres. These boards show the highest *MOR* from the tested series.

To sum up, it should be noted that the boards of series A_R and C_R in air-dry conditions are characterized by a similar bending stress diagram in which three intervals can be distinguished. The fact that high-energy AE events are registered signals possible differences between the reference boards and the ones subjected to damaging factors. By identifying the acoustic spectrum characteristics through reading and assigning them to the cement matrix or the fibres, it became possible to accurately identify the damage which takes place in the boards under the influence of temperature.

No acoustic spectrum characteristics corresponding to fibres were recognized in the boards of series A_T and C_T exposed to the temperature of 230 °C for 3 h. This confirms the fact that the fibres undergo degradation at the high temperature of 230 °C. They fracture

brittlely under the influence of the high temperature. Analysing AE signals and identifying the acoustic spectrum characteristics, one can assess damage to the structure of the boards, especially damage to the fibres contained in fibre-cement boards. In order to verify the above conclusions, the authors decided to carry out additional optical investigations using a scanning electron microscope (*SEM*) to compare the structure of the tested boards.

5. SEM Examinations

The optical investigations by means of a scanning electron microscope with EDS analyser were carried out in collaboration with the Faculty of Civil Engineering and Architecture at Kielce University of Technology.

The boards of series A_R and C_R in air-dry condition and the boards of series A_T and C_T exposed to a temperature of 230 °C for 3 h were subjected to SEM examinations. Figure 10 shows example images for series A and C.

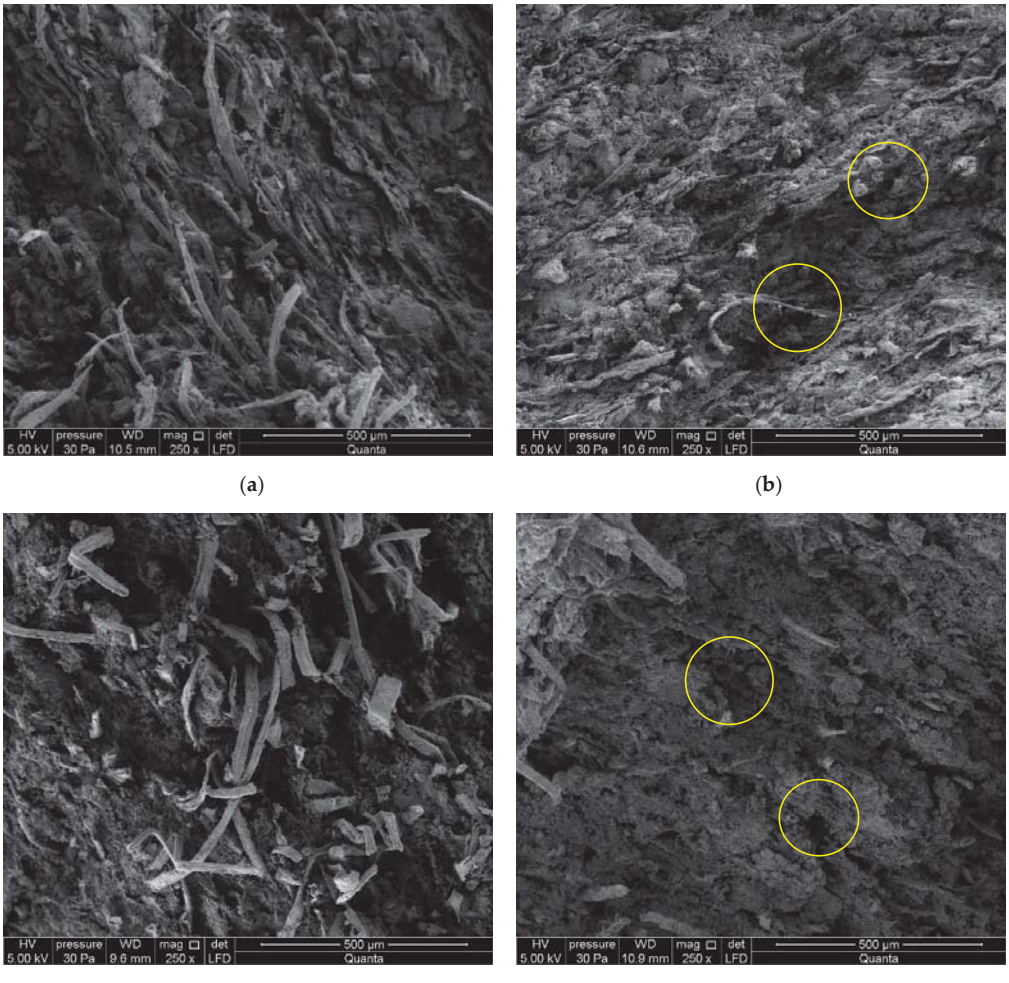

Figure 10. SEM images of boards of series: (**a**) A_R, (**b**) A_T, (**c**) C_R, (**d**) C_T.

On the basis of the images shown in Figure 10 one can describe the macrostructure of the tested fibre-cement boards as compact. The SEM examinations revealed the structure to be fine pore, with the pores up to 50 μm in size. Cavities and grooves left by the pulled-out fibres were visible in the fracture area. Cellulose fibres and PVA fibres are clearly visible in the images, as shown in Figure 10a,c. Various forms of calcium silicate hydrates of the C-S-H type occur, with an amorphous phase and a phase made up of strongly adherent particles predominating. An EDS analysis of the cement matrix's chemical composition showed elements consistent with the composition of the cement. The fibres are covered with a thin layer of cement paste and hydration products. The fact that there are few places with a space between the fibres and the matrix is indicative of a strong bond between them. The examination of the fibre-cement boards of series A_T and C_T exposed to a temperature of 230 °C for 3 h revealed a distinct change in the colour of the samples at the macroscopic level. Most of the fibres in the boards were found to be burnt out or fused into the cement matrix, leaving cavities and grooves, as shown in Figure 10b,d (some such places are marked with a yellow circle). The structure of the few remaining fibres was heavily degraded. Examinations of the cement grains in other fractured surfaces also revealed that their structure was damaged by the high temperature. The structure of the cement matrix was found to be highly granular with numerous delaminations. More numerous cavities and grooves left after the pulled-out fibres and grooves left after the pulled-out cement grains were observed.

Summing up the examinations carried out using the optical method, we note that this method makes it possible to very precisely describe the inner structure of fibre-cement boards. In the case of the boards exposed to high temperature, most of the fibres were found to be burnt out or fused into the matrix, leaving cavities and grooves. However, significantly, in the case of the reference fibre-cement boards there are many more ruptured fibres whose ends are well "anchored" in the cement matrix. This clearly means that exposure to a temperature of 230 °C for 3 h has a damaging effect on the structure of fibre-cement boards.

6. Conclusions

Exposure to high temperature is by nature damaging to most building products. The tests have shown that the exposure of a fibre-cement board to a temperature of 230 °C for 3 h is critical as it results in the total destruction of the board. The following conclusions emerge from the investigations:

1. The influence of the temperature of 230 °C for 3 h on bending strength (*MOR*) is clearly damaging for series A_T and C_T. Under the influence of the temperature *MOR* decreased by as much as 70%. In the case of these boards, impact energy W_f also decreased considerably, while Young's modulus E_D increased by 30%.
2. The σ–ε, curves indicated that the influence of the temperature results not only in a decrease in *MOR*, but also in a change in the shape of the σ–ε curve. Moreover, *MOR* becomes equal to *LOP*. In the case of the reference fibre-cement boards, the value of *MOR* is much higher.
3. The acoustic emission investigations during the three-point bending test showed a marked fall in the number of AE events registered for the tested series of boards under the influence of the high temperature in comparison with the reference boards. Moreover, it was noticed that the exposure to the temperature of 230 °C for 3 h results in a considerable increase in events energy E_{ev} during the bending test for the tested series of fibre-cement boards, whereby the registered events, by and large, come down to a single pulse induced by a brittle fracture.
4. The results yielded by the identification of the model spectral characteristics by means of ANNs indicate that the boards of series A_R and C_R in air-dry condition are characterized by a similar bending stress diagram in which three intervals can be distinguished. The acoustic spectrum characteristics corresponding to the fibres and the cement matrix respectively were identified. However, no acoustic spectrum

characteristics corresponding to the fibres were identified in the boards of series A_T and C_T exposed to the temperature of 230 °C for 3 h. This confirms the fact that at high temperatures, the fibres undergo degradation. Under the influence of high temperature, the boards fracture brittlely.

5. The optical examinations under a SEM with an EDS analyser revealed that in the boards exposed to the high temperature, most of the fibres had been burnt out or fused into the cement matrix, leaving cavities and grooves. In the case of the reference boards, a large number of fibres whose ends were well "anchored" in the cement matrix were ruptured on the fractured surfaces.

Summing up the above conclusions drawn from the experiments carried out as part of this research, one can definitely state that exposure to a temperature of 230 °C for 3 h has a damaging effect on the structure of fibre-cement boards. In the authors' opinion, the findings are important for building practice as, so far, there has been little information about the behaviour of rainscreen cladding made of fibre-cement boards exposed to high temperatures. It is also worth noting that exterior wall cladding is exposed to high temperature not only in the case of a fire, but also through insolation. In the authors' opinion, it would be worth to carry out ageing tests of fibre-cement boards subjected to UV radiation. This will certainly be the subject of further research.

Finally, it is worth noting that the research carried out in this paper clearly confirmed the usefulness of the acoustic emission method and artificial neural networks for the assessment of the impact of the destructive effect of high temperature on the structure of fiber-cement boards. According to the authors, the use of the method of acoustic emission and artificial neural networks to assess the destructive effect of high temperature on the structure of fiber-cement boards is a unique measuring technique that can play a large role in construction practice today or in the near future. In addition, it is worth adding that the new approach to measuring cracks, deformations or acoustic measurements in materials at elevated temperatures certainly has great application in other materials. This approach can be used to monitor the development of microcracks or scratches in materials in order to control their strength and thus create new safer composites with a view to fire safety.

Author Contributions: Conceptualization, K.S. and T.G.; methodology, M.S.; validation, T.G., M.S.; formal analysis, K.S.; measurements, M.S.; writing—original draft preparation, T.G.; writing—review and editing, K.S. and M.S.; All authors have read and agreed to the published version of the manuscript.

Funding: This research received no external funding.

Institutional Review Board Statement: Not applicable.

Informed Consent Statement: Not applicable.

Data Availability Statement: Not applicable.

Conflicts of Interest: The authors declare no conflict of interest.

References

1. Schabowicz, K.; Gorzelańczyk, T. Fabrication of fibre cement boards. In *The Fabrication, Testing and Application of Fibre Cement Boards*, 1st ed.; Ranachowski, Z., Schabowicz, K., Eds.; Cambridge Scholars Publishing: Newcastle upon Tyne, UK, 2018; pp. 7–39. ISBN 978-1-5276-6.
2. Bentchikou, M.; Guidoum, A.; Scrivener, K.; Silhadi, K.; Hanini, S. Effect of recycled cellulose fibres on the properties of lightweight cement composite matrix. *Constr. Build. Mater.* **2012**, *34*, 451–456. [CrossRef]
3. Savastano, H.; Warden, P.G.; Coutts, R.S.P. Microstructure and mechanical properties of waste fibre–cement composites. *Cem. Concr. Compos.* **2005**, *27*, 583–592. [CrossRef]
4. Coutts, R.S.P. A Review of Australian Research into Natural Fibre Cement Composites. *Cem. Concr. Compos.* **2005**, *27*, 518–526. [CrossRef]
5. Schabowicz, K.; Szymków, M. Ventilated facades made of fibre-cement boards. *Mater. Bud.* **2016**, *4*, 112–114. (In Polish) [CrossRef]
6. Ardanuy, M.; Claramunt, J.; Toledo Filho, R.D. Cellulosic Fibre Reinforced Cement-Based Composites: A Review of Recent Research. *Constr. Build. Mater.* **2015**, *79*, 115–128. [CrossRef]

7. Drelich, R.; Gorzelanczyk, T.; Pakuła, M.; Schabowicz, K. Automated control of cellulose fibre cement boards with a non-contact ultrasound scanner. *Autom. Constr.* **2015**, *57*, 55–63. [CrossRef]
8. Dębowski, T.; Lewandowski, M.; Mackiewicz, S.; Ranachowski, Z.; Schabowicz, K. Ultrasonic tests of fibre-cement boards. *Przegląd Spaw.* **2016**, *10*, 69–71. (In Polish) [CrossRef]
9. Schabowicz, K.; Jóźwiak-Niedźwiedzka, D.; Ranachowski, Z.; Kudela, S.; Dvorak, T. Microstructural characterization of cellulose fibres in reinforced cement boards. *Arch. Civ. Mech. Eng.* **2018**, *4*, 1068–1078. [CrossRef]
10. Chady, T.; Schabowicz, K.; Szymków, M. Automated multisource electromagnetic inspection of fibre-cement boards. *Autom. Constr.* **2018**, *94*, 383–394. [CrossRef]
11. Schabowicz, K.; Gorzelańczyk, T.; Szymków, M. Identification of the degree of fibre-cement boards degradation under the influence of high temperature. *Autom. Constr.* **2019**, *101*, 190–198. [CrossRef]
12. Schabowicz, K.; Gorzelańczyk, T.; Szymków, M. Identification of the degree of degradation of fibre-cement boards exposed to fire by means of the acoustic emission method and artificial neural networks. *Materials* **2019**, *12*, 656. [CrossRef] [PubMed]
13. Zhang, C.; Chao, L.; Zhang, Z.; Zhang, L.; Li, Q.; Fan, H.; Zhang, S.; Liu, Q.; Qiao, Y.; Tian, Y.; et al. Pyrolysis of cellulose: Evolution of functionalities and structure of bio-char versus temperature. *Renew. Sustain. Energy Rev.* **2021**, *135*, 110416. [CrossRef]
14. Leflik, M. Some aspects of application of artificial neural network for numerical modeling in civil engineering. *Bull. Pol. Acad. Sci. Tech. Sci.* **2013**, *61*, 39–50. [CrossRef]
15. Gorzelańczyk, T.; Schabowicz, K.; Szymków, M. Non-destructive testing of fibre-cement boards, using acoustic emission. *Przegląd Spaw.* **2016**, *88*, 35–38. (In Polish) [CrossRef]
16. Adamczak-Bugno, A.; Gorzelańczyk, T.; Krampikowska, A.; Szymków, M. Non-destructive testing of the structure of fibre-cement materials by means of a scanning electron microscope. *Bad. Nieniszcz. I Diagn.* **2017**, *3*, 20–23. (In Polish) [CrossRef]
17. Claramunt, J.; Ardanuy, M.; García-Hortal, J.A. Effect of drying and rewetting cycles on the structure and physicochemical characteristics of softwood fibres for reinforcement of cementitious composites. *Carbohydr. Polym.* **2010**, *79*, 200–205. [CrossRef]
18. Mohr, B.J.; Nanko, H.; Kurtis, K.E. Durability of kraft pulp fibre-cement composites to wet/dry cycling. *Cem. Concr. Compos.* **2005**, *27*, 435–448. [CrossRef]
19. Pizzol, V.D.; Mendes, L.M.; Savastano, H.; Frías, M.; Davila, F.J.; Cincotto, M.A.; John, V.M.; Tonoli, G.H.D. Mineralogical and microstructural changes promoted by accelerated carbonation and ageing cycles of hybrid fibre–cement composites. *Constr. Build. Mater.* **2014**, *68*, 750–756. [CrossRef]
20. Gorzelańczyk, T.; Pachnicz, M.; Różański, A.; Schabowicz, K. Multi-Scale Structural Assessment of Cellulose Fibres Cement Boards Subjected to High Temperature Treatment. *Materials* **2019**, *12*, 2449. [CrossRef]
21. Gorzelańczyk, T.; Pachnicz, M.; Różański, A.; Schabowicz, K. Identification of microstructural anisotropy of cellulose cement boards by means of nanoindentation. *Constr. Build. Mater.* **2020**, *257*, 119515. [CrossRef]
22. Li, Z.; Zhou, X.; Bin, S. Fibre-Cement extrudates with perlite subjected to high temperatures. *J. Mater. Civ. Eng.* **2004**, *3*, 221–229. [CrossRef]
23. Adamczak-Bugno, A.; Krampikowska, A.; Świt, G. Analysis of the Frequency of Acoustic Emission Events in Terms of the Assessment of the Reduction of Mechanical Parameters of Cellulose–Cement Composites. *Materials* **2021**, *14*, 5882. [CrossRef]
24. Schabowicz, K.; Gorzelańczyk, T. A non-destructive methodology for the testing of fibre cement boards by means of a non-contact ultrasound scanner. *Constr. Build. Mater.* **2016**, *102*, 200–207. [CrossRef]
25. Stark, W. Non-destructive evaluation (NDE) of composites: Using ultrasound to monitor the curing of composites. In *Non-destructive Evaluation (NDE) of Polymer Matrix Composites. Techniques and Applications*, 1st ed.; Karbhari, V.M., Ed.; Woodhead Publishing Limited: Sawston, UK, 2013; pp. 136–181. ISBN 978-0-85709-344-8.
26. Berkowski, P.; Dmochowski, G.; Grosel, J.; Schabowicz, K.; Wójcicki, Z. Analysis of failure conditions for a dynamically loaded composite floor system of an industrial building. *J. Civ. Eng. Manag.* **2013**, *19*, 529–541. [CrossRef]
27. Hoła, J.; Schabowicz, K. State-of-the-art non-destructive methods for diagnostic testing of building structures–anticipated development trends. *Arch. Civ. Mech. Eng.* **2010**, *10*, 5–18. [CrossRef]
28. Davis, A.; Hertlein, B.; Lim, K.; Michols, K. Impact-Echo and Impulse Response Stress WAVE methods: Advantages and limitations for the Evaluation of Highway Pavement Concrete Overlays. In *Proceedings of the Conference on Nondestructive Evaluation of Bridges and Highways*; SPIE: Scottsdale, AZ, USA, 1996; pp. 88–96. [CrossRef]
29. Chady, T.; Schabowicz, K. Non-destructive testing of fibre-cement boards, using terahertz spectroscopy in time domain. *Bad. Nieniszcz. I Diagn.* **2016**, *1–2*, 62–66. Available online: https://bnid.pl/wp-content/uploads/2016/12/ChadyT_NieniszczaceBadania.pdf (accessed on 12 September 2022). (In Polish).
30. Schabowicz, K.; Ranachowski, Z.; Jóźwiak-Niedźwiedzka, D.; Radzik, Ł.; Kudela, S.; Dvorak, T. Application of X-ray microtomography to quality assessment of fibre cement boards. *Constr. Build. Mater.* **2016**, *110*, 182–188. [CrossRef]
31. Ranachowski, Z.; Ranachowski, P.; Dębowski, T.; Gorzelańczyk, T.; Schabowicz, K. Investigation of structural degradation of fiber cement boards due to thermal impact. *Materials* **2019**, *12*, 944. [CrossRef]
32. Ranachowski, Z.; Schabowicz, K. The contribution of fibre reinforcement system to the overall toughness of cellulose fibre concrete panels. *Constr. Build. Mater.* **2017**, *156*, 1028–1034. [CrossRef]
33. Ranachowski, Z. The application of neural networks to classify the acoustic emission waveforms emitted by the concrete under thermal stress. *Arch. Acoust.* **1996**, *21*, 89–98. Available online: http://acoustics.ippt.pan.pl/index.php/aa/article/viewFile/980/822 (accessed on 12 September 2022).

34. Ranachowski, Z.; Jóźwiak-Niedźwiedzka, D.; Brandt, A.M.; Dębowski, T. Application of acoustic emission method to determine critical stress in fibre reinforced mortar beams. *Arch. Acoust.* **2012**, *37*, 261–268. [CrossRef]
35. Melichar, T.; Bydzovsky, J.; Dvorak, R.; Topolar, L.; Keprdova, S. The Behavior of Cement-Bonded Particleboard with Modified Composition under Static Load Stress. *Materials* **2021**, *14*, 6788. [CrossRef] [PubMed]
36. Yuki, H.; Homma, K. Estimation of acoustic emission source waveform of fracture using a neural network. *NDT E Int.* **1996**, *29*, 21–25. [CrossRef]
37. Schabowicz, K. Neural networks in the NDT identification of the strength of concrete. *Arch. Civ. Eng.* **2005**, *51*, 371–382.
38. Asteris, P.G.; Kolovos, K.G. Self-compacting concrete strength prediction using surrogate models. *Neural Comput. Appl.* **2019**, *31*, 409–424. [CrossRef]
39. Lee, S.C. Prediction of concrete strength using artificial neural networks. *Eng. Struct.* **2003**, *25*, 849–857. [CrossRef]
40. Łazarska, M.; Woźniak, T.; Ranachowski, Z.; Trafarski, A.; Domek, G. Analysis of acoustic emission signals at austempering of steels using neural networks. *Met. Mater. Int.* **2017**, *23*, 426–433. [CrossRef]
41. Woźniak, T.Z.; Ranachowski, Z.; Ranachowski, P.; Ozgowicz, W.; Trafarski, A. The application of neural networks for studying phase transformation by the method of acoustic emission in bearing steel. *Arch. Metall. Mater.* **2014**, *59*, 1705–1712. [CrossRef]
42. Rucka, M.; Wilde, K. Experimental study on ultrasonic monitoring of splitting failure in reinforced concrete. *J. Nondestruct. Eval.* **2013**, *32*, 372–383. [CrossRef]
43. Rucka, M.; Wilde, K. Ultrasound monitoring for evaluation of damage in reinforced concrete. *Bull. Pol. Acad. Sci. Tech. Sci.* **2015**, *63*, 65–75. [CrossRef]
44. Zielińska, M.; Rucka, M. Non-Destructive Assessment of Masonry Pillars using Ultrasonic Tomography. *Materials* **2018**, *11*, 2543. [CrossRef] [PubMed]
45. Wojtczak, E.; Rucka, M. Wave Frequency Effects on Damage Imaging in Adhesive Joints Using Lamb Waves and RMS. *Materials* **2019**, *12*, 1842. [CrossRef] [PubMed]
46. EN 12467—Cellulose Fibre Cement Flat Sheets. Product Specification and Test Methods. 2018. Available online: https://standards.cen.eu/dyn/www/f?p=204:110:0::::FSP_PRJECT,FSP_ORG_ID:66671,6110&cs=1151E39EDCD9EF75E3C2D401EB5818ACD (accessed on 25 April 2018).
47. Osowski, S. *Neural Networks for Information Processing*; OWPW: Warsaw, Poland, 2000. (In Polish)
48. Estêvão, J.M.C. Feasibility of using neural networks to obtain simplified capacity curves for seismic assessment. *Buildings* **2018**, *8*, 151. [CrossRef]
49. Gorzelańczyk, T.; Schabowicz, K. Effect of Freeze–Thaw Cycling on the Failure of Fibre-Cement Boards, Assessed Using Acoustic Emission Method and Artificial Neural Network. *Materials* **2019**, *12*, 2181. [CrossRef] [PubMed]

materials

MDPI

Article

Use of the AE Effect to Determine the Stresses State in AAC Masonry Walls under Compression

Radosław Jasiński [1], Krzysztof Stebel [2,*] and Paweł Kielan [3]

[1] Department of Building Structures and Laboratory, Faculty of Civil Engineering, Silesian University of Technology, 44-100 Gliwice, Poland; radoslaw.jasinski@polsl.pl
[2] Department of Automatic Control and Robotics, Silesian University of Technology, 44-100 Gliwice, Poland
[3] Department of Mechatronics, Silesian University of Technology, 44-100 Gliwice, Poland; pawel.kielan@polsl.pl
* Correspondence: krzysztof.stebel@polsl.pl; Tel.: +48-607-851-286

Abstract: Safety and reliability of constructions operated are predicted using the known mechanical properties of materials and geometry of cross-sections, and also the known internal forces. The extensometry technique (electro-resistant tensometers, wire gauges, sensor systems) is a common method applied under laboratory conditions to determine the deformation state of a material. The construction sector rarely uses ultrasonic extensometry with the acoustoelastic (AE) method which is based on the relation between the direction of ultrasonic waves and the direction of normal stresses. It is generally used to identify stress states of machine or vehicles parts, mainly made of steel, characterized by high homogeneity and a lack of inherent internal defects. The AE effect was detected in autoclaved aerated concrete (AAC), which is usually used in masonry units. The acoustoelastic effect was used in the tests described to identify the complex stress state in masonry walls (masonry units) made of AAC. At first, the relationships were determined for mean hydrostatic stresses P and mean compressive stresses σ_3 with relation to velocities of the longitudinal ultrasonic wave c_p. These stresses were used to determine stresses σ_3. The discrete approach was used which consists in analyzing single masonry units. Changes in velocity of longitudinal waves were identified at a test stand to control the stress states of an element tested by the digital image correlation (DIC) technique. The analyses involved density and the impact of moisture content of AAC. Then, the method was verified on nine walls subjected to axial compression and the model was validated with the FEM micromodel. It was demonstrated that mean compressive stresses σ_3 and hydrostatic stresses, which were determined for the masonry using the method considered, could be determined even up to ca. 75% of failure stresses at the acceptable error level of 15%. Stresses σ_1 parallel to bed joints were calculated using the known mean hydrostatic stresses and mean compressive stresses σ_3.

Keywords: masonry structures; autoclaved aerated concrete masonry units (AAC); compressive strength; minor-destructive (MDT) techniques; non-destructive (NDT) techniques; ultrasonic testing; acoustoelastic effect (AE); hydrostatic stresses; modeling; DIC technique

Citation: Jasiński, R.; Stebel, K.; Kielan, P. Use of the AE Effect to Determine the Stresses State in AAC Masonry Walls under Compression. *Materials* **2021**, *14*, 3459. https://doi.org/10.3390/ma14133459

Academic Editor: Krzysztof Schabowicz

Received: 15 May 2021
Accepted: 18 June 2021
Published: 22 June 2021

1. Introduction

The ultrasonic technique [1–4] is used in spectroscopy, defectoscopy, evaluation tests, coagulation, dispergation, sonoluminescence cavitation, and chemical reactions. Ultrasounds can be also applied to crush, form hard media, bond, solder, wash, extract, and dry substances. Another important application of these ultrasonic techniques includes stress measurements in metal constructions. Ultrasonic methods of measuring stress use the acoustoelastic effect (AE), i.e., the correlation between the stress and the velocity of acoustic wave propagation.

The ultrasonic pulse velocity (UPV) is a method applied to cement (concrete) and ceramic materials. This method is used to determine a setting time, changes in the elasticity modulus, and to test the compressive strength (only with the applied minor non-destructive

(MDT), technique) [5,6]. Besides the AE tests conducted on isotropic materials, the current experience and theoretical analyses of construction materials are related to the anisotropy effect on the wave propagation. The tests mainly include almost isotropic, moderately and strongly anisotropic metamaterials at shear strain and standard deformation. Reference [7] describes the quantitative effect of finite deformations with reference to their magnitude and load direction. Strain-induced instabilities cause negative increments in the phase velocity just as in the case of the isotropic materials. It was also demonstrated that shear strains did not change the velocity of longitudinal waves as the material volume was stable. On the other hand, the effect of high values of deformations on the propagation of acoustic waves in repetitive network materials was explored in the paper [8]. The deformations were found to significantly affect the frequency waves and the phase velocity. In particular, the phase velocity for the hexagonal network strongly decreased under finite compressive deformations. The effective density was shown to have an important impact on the dispersion relation and band diagrams under the application of incremental deformation over the lattice unit cell. Additionally, the theoretical analyses [9,10] are made on mechanical wave propagation in the infinite two-dimensional periodic lattices using Floquet-Bloch. Conclusions derived from the tests can be applied to research on orthotropic construction materials (composites, composite panels, homogeneous masonry structures, etc.). The paper [11] showed that the acoustoelastic effect (AE) [12] also occurs in autoclaved aerated concrete (AAC). The stress state in the wall made of AAC masonry units was determined on the basis of the conducted analyses.

This paper describes the tests aimed at determining the complex state of stresses in masonry units made of autoclaved aerated concrete. As in [11], verification tests were performed on small parts of the wall subjected to axial compression. Their aim was to define empirical relationships of mean hydrostatic stresses P, and then normal stresses σ_1 and σ_3 in the wall, in which the AE effect was observed [12]. Taking into account the AAC vulnerability to moisture content [13] which deteriorates insulation and strength parameters, the analyses included both density and relative humidity of this material. This paper demonstrates a practical application of the AE effect in testing masonry structures which was described in previous works of the author [11,14,15]. The tests were divided into two stages. In the first stage of the tests, experiments were performed on 24 small cuboidal specimens (180 mm × 180 mm × 120 mm) of autoclaved aerated concrete with nominal densities of 400, 500, 600, and 700 kg/m^3. The obtained results were used for determining the acoustoelastic constant δ_P that showed the relationship between mean values of hydrostatic stress P and velocity of the longitudinal wave c_p.

Stage II included nine wall models [11] made of AAC masonry units which had a nominal density of 600 kg/m^3. They were subjected to axial compression The velocity of ultrasonic wave c_p in the masonry units was measured. The complex stress state in the wall was examined using the relationships established in stage I. Then, the linear elastic FEM models was applied to match the P–c_p relationship. Knowing stress values σ_3 determined in [11], the levels of normal stress σ_1 could be determined.

2. Theoretical Bases of the AE Method

Stress in the material can affect velocity of the acoustic wave because of inhomogeneity and anisotropy. That effect was theoretically described for the first time in the paper [16], and the experimental verification was presented in the papers [17,18]. The static stress was found to have an impact on changes in the velocity values of the acoustic wave in the medium. This pattern has been known as the acoustoelastic (AE) effect [19,20].

This effect, whose theoretical background was described in the paper [12,21], specifies the relationship between stress and velocity of transverse wave propagation. As from then, this subject has significantly evolved [22–24]. The normal stresses have an impact on a change in the velocity of longitudinal and transverse waves (as in the elastooptic effect involving light waves), which is determined by the direction of wave propagation over the direction, the stress, and the wave polarization. Following the theory of solid

deformation [17], the higher orders elasticity constants (neglected in the linear theory of elasticity) which describe the non-linear effects, should be taken account during the analysis of the AE effect. A sum of velocities in the tensionless state (σ = 0) and its change (an increment) as a result of the stress (strain) expresses the velocity of ultrasonic wave propagation.

In accordance with the Murnaghan theory [25], the function of free energy W_s defined below [17,26], is described by the stress-deformation relationship

$$W_s = \frac{1}{2}(\lambda + 2\mu)I_1^2 - 2\mu I_2 + \frac{1}{3}(l + 2m)I_1^3 - 2mI_1I_2 + nI_3, \tag{1}$$

where: λ, μ–Lamé constants, l, m, n–elasticity constants of second and third order by Murnaghan, I_1, I_2, I_3–deformation invariants.

Following the principle of energy conservation, Hooke's law can be given by

$$\rho\delta W_s = \sigma_{ij}\frac{\partial\delta u_i}{\partial u_j}, \tag{2}$$

where δW and δu_i mean finite increments in the function of free energy and the displacement area, ρ is density after deformation (in the stressed body). This AE equation specifies the relationship between the static load and the elastic wave velocity under hydrostatic conditions (that is, under the hydrostatic stress P)–Figure 1

$$c_p^2 = \underbrace{\frac{\lambda + 2\mu}{\rho_0}}_{c_{p0}^2} - \frac{P}{\rho_0(3\lambda + 2\mu)}(6l + 4m + 7\lambda + 10\mu), \tag{3}$$

$$c_t^2 = \underbrace{\frac{\mu}{\rho_0}}_{c_{t0}^2} - \frac{P}{\rho_0(3\lambda + 2\mu)}(3m + 0,5n + 3\lambda + 6\mu)\,, \tag{4}$$

where c_p and c_t are velocity of longitudinal and transverse waves respectively, and ρ_0 body density in the tensionless state, P–hydrostatic stress defined as $P = \frac{1}{3}(\sigma_1 + \sigma_2 + \sigma_3)$.

The Equation (2) [27] can be used to determine the stress P. For that purpose velocity of the longitudinal and transverse waves is measured. The squared velocities of waves at uniaxial stress states are expressed by these equations

$$V_{111}^2 = c_{p0}^2 - \frac{\sigma_1}{3K_0\rho_0}\left[\frac{\lambda + \mu}{\mu}(4\lambda + 10\mu + 4m) + \lambda + 2l\right], \tag{5}$$

$$V_{113}^2 = c_{p0}^2 + \frac{\sigma_3}{3K_0\rho_0}\left[\frac{2\lambda}{\mu}(\lambda + 20\mu + m) - 2l\right], \tag{6}$$

$$V_{131}^2 = c_{t0}^2 - \frac{\sigma_1}{3K_0\rho_0}\left[4\lambda + 4\mu + m + \frac{\lambda n}{4\mu}\right], \tag{7}$$

$$V_{133}^2 = c_{t0}^2 - \frac{\sigma_3}{3K_0\rho_0}\left[\lambda + 2\mu + m + \frac{\lambda n}{4\mu}\right], \tag{8}$$

$$V_{132}^2 = c_{t0}^2 + \frac{\sigma_2}{3K_0\rho_0}\left[2\lambda - m + \frac{n}{2}\frac{\lambda}{2}\frac{n}{\mu}\right], \tag{9}$$

where $K_0 = \frac{E}{3(1-2\nu)} = \frac{2\mu+3\lambda}{3}$, $c_{t0} = \sqrt{\frac{\mu}{\rho_0}}$, $c_{p0} = \sqrt{\frac{\lambda+2\mu}{\rho_0}}$.

The velocity of the ultrasonic wave (in the deformed material), elastic constants of the first (λ, μ), second and third order (m, n, l), whose detection is the most difficult in the tests, are used to determine the normal stresses in the material.

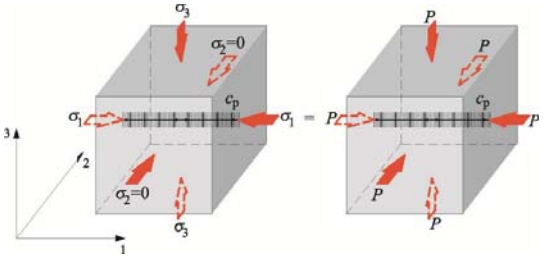

Figure 1. Directions of the stress and the ultrasonic wave in the isotropic material at the state of hydrostatic compression.

The theoretical background of the AE effect has been adequately proved. Also, the suitable equipment is employed to determine the elastic constants of the third order *l*, *m*, *n* for metal and plastic materials following the procedures presented in e.g., the papers [28–31]. Knowing the direction of the exerted load and a gradient of changes in the longitudinal or transverse wave velocity is required to examine the stress states with the NDT technique.

The proposed procedures can be easily applied to the laboratory tests, however, their use under the in-situ conditions can be troublesome. Hence, a relative increment in the longitudinal wave velocity [32] (knowing the Murnaghan coefficients is not required) is more favorable for practical applications and it can be obtained from the following relationship (based on the Equation (3))

$$\begin{aligned}
&c_p^2 - c_{p0}^2 = -P\frac{(6l+4m+7\lambda+10\mu)}{3\rho_0 K_0} \rightarrow (c_p - c_{p0})(c_p + c_{p0}) = -P\frac{(6l+4m+7\lambda+10\mu)}{3\rho_0 K_0},\\
&\text{assuming that } c_p + c_{p0} \approx 2c_{p0} \rightarrow (c_p - c_{p0})2c_{p0},\\
&\text{the following was obtained}\\
&\frac{(c_p - c_{p0})}{c_{p0}} = -P\frac{(6l+4m+7\lambda+10\mu)}{6\rho_0 K_0 c_{p0}^2},\\
&\text{taking into account the following terms}\\
&K_0 = \frac{2\mu+3\lambda}{3}; c_{p0}^2 = \frac{\lambda+2\mu}{\rho_0},\\
&\text{finally, we obtain}\\
&\frac{(c_p - c_{p0})}{c_{p0}} = -P\frac{(6l+4m+7\lambda+10\mu)}{2(2\mu+3\lambda)(\lambda+2\mu)} = P\delta_P.
\end{aligned} \tag{10}$$

where δ_P is the AE coefficient expressing the relationship between a relative increment in the longitudinal wave and the mean hydrostatic stresses.

The relative AE coefficient can be expressed as

$$\frac{(c_p - c_{p0})}{c_{p0}} = \frac{P}{P_{\max}}\eta_P. \tag{11}$$

where η_P is the relative AE coefficient expressing the relationship between a relative increment in the longitudinal wave and the relative mean of hydrostatic stresses.

The paper [11] defined values of the AE coefficients under the uniaxial compression in the form

$$\frac{(c_p - c_{p0})}{c_{p0}} = \beta_{113}\sigma_3. \tag{12}$$

$$\frac{(c_p - c_{p0})}{c_{p0}} = \gamma_{113}\frac{\sigma_3}{\sigma_{3\max}}. \tag{13}$$

where

$$\begin{aligned}
\beta_{113} &= 1.39 \cdot 10^{-4}\rho - 0.104,\ \mathrm{R}^2 = 0.995,\\
\gamma_{113} &= 1.72 \cdot 10^{-4}\rho - 0.206,\ \mathrm{R}^2 = 0.923,
\end{aligned} \tag{14}$$

when $397 \frac{\text{kg}}{\text{m}^3} \leq \rho \leq 674 \frac{\text{kg}}{\text{m}^3}$.

3. Program of Own Research

Following the procedure described in the paper [11] the tests were divided into two stages. In the first stage of the tests, the biaxial compression was exerted until the failure of the specimens with dimensions of 180 mm × 180 mm × 120 mm. Velocity of the longitudinal wave was determined under different hydrostatic stress P. The tests were conducted in a test stand specially prepared to test the specimens and simultaneously control their deformations by the non-contact technique of Digital Image Correlation DIC. The obtained results were the base to determine the linear correlations of the c_p–P relationship. The test results for nine masonry models under axial compression, described in [11], were used in the stage II to determine at first mean hydrostatic stress, and then the normal stress σ_1 which was parallel to the plane of bed joints. The test results for the complex state of stresses were compared with the results for the linear-elastic FEM models. Then, the method was validated.

4. Test Results

4.1. Stage I-Determination of Acoustoelastic Constant

4.1.1. Physical and Mechanical Properties of Autoclaved Aerated Concrete AAC

The tests included four series of masonry units with a thickness within the range of 180–240 mm and different classes of density: 400, 500, 600, and 700 [33], which were the subject of tests presented in the paper [11]. Six cores with a diameter of 59 mm and a height of 120 mm were cut out from the masonry units. They were used to determine the fundamental properties of the test autoclaved aerated concrete (AAC). All the cores were dried until constant weight at a temperature of 105 ± 5 °C. The modulus of elasticity E and Poisson's ratio ν were determined for the core specimens. Mean mechanical parameters obtained for all the tested types of masonry units are shown in Table 1. The results from testing density and compressive strength of the specimens 100 mm × 100 mm × 100 mm were taken from [14].

Table 1. Fundamental characteristics of masonry units as defined in the papers [11,14].

No.	Nominal Class of Density kg/m^3 Acc. to [11]	Density Range of AAC, kg/m^3 Acc. to [11]	Mean Density ρ_0, kg/m^3 (C.O.V) Acc. to [14]	Mean Modulus of Elasticity E, N/mm^2 (C.O.V) Acc. to [11]	Mean Poisson's Ratio ν, (C.O.V) Acc. to [11]	Compressive Strength of AAC f_B, N/mm^2 (C.O.V) Acc. to [14]
1	400	375–446	397 (6%)	1516 (9.6%)	0.19 (7.9%)	2.88
2	500	462–532	492 (3%)	2039 (8.9%)	0.21 (8.7%)	3.59
3	600	562–619	599 (2%)	2886 (10.5%)	0.20 (8.5%)	5.05
4	700	655–725	674 (3%)	4778 (10.1%)	0.19 (9.2%)	8.11

Apart from the core specimens of AAC masonry units, also 24 rectangular specimens having dimension of 180 mm × 180 mm × 120 mm were cut out and used in the stage I. To determine the correlation between mean hydrostatic stress P and ultrasonic velocity, all the specimens were air-dried at a temperature of 105 ± 5 °C for at least 36 h until constant weight. That way the impact of moisture content on AAC was eliminated [15,34]. Generally, moisture content tends to significantly reduce compressive strength and change velocity of the ultrasonic wave propagation [14].

4.1.2. Test Stand and Procedure

The velocity of ultrasonic waves was determined by the method of transmission [11,35,36]. Velocity of ultrasonic waves in 180 mm × 180 mm × 120 mm specimens taken from the masonry units, was measured at the specially prepared test stand—Figure 2. The

test stand for testing biaxial compression consisted of two vertical columns 1 made of a set of two channel profiles 120 with a length of 1000 mm and connected at the bottom with a spandrel beam 2 made of three I-beams 140 with a top spandrel beam 3 which was made of an I-beam 200 with a length of 1000 mm and reinforced with ribs. Inside dimensions between spandrel beams and the column were 820 mm in a vertical plane, and 810 mm in a horizontal plane. Openings with the spacing of 75 mm were made in vertical columns 1 and in the spandrel beam 3 to change its position. The hydraulic actuator 4 with an operating range of 500 kN was pin jointed to the top spandrel beam. A draw-wire displacement converter 5 of SWH-1-B-FK-01 type with the TRA50-SA1800WSC01 encoder (TWK-ELEKTRONIK GmbH, Düsseldorf, Germany) was attached to the side wall of the actuator. The hydraulic actuator was connected to the hydraulic power unit "A" (Zwick Roell Company Group, Ulm, Germany) with a pressurized pipeline, to which the pressure transmitter P30 was attached (WIKA SE & Co. KG, Klingenberg, Germany) 6. Its operating range was 0–1000 bar and the reading accuracy was 1 bar. The hydraulic actuator 7 with an operating range of 500 kN was sliding jointed to one vertical column. A draw-wire displacement converter 8 (SWH-1-B-FK-01 type with the TRA50-SA1800WSC01 encoder) was fixed to the actuator. The actuator was connected to the hydraulic power unit "B" (Hydac International GmbH, Sulzbach/Saar, Germany) with a pressurized pipeline, to which the pressure transmitter P30 was attached-9 The research model 10 was placed between Teflon washers 11 and steel plates 12 with ball joints.

This test stand was a complex system designed and prepared by the authors [37]. This design is copyrighted [38]. The advanced control algorithms had to be applied as many non-linearities were present in the subsystems. These algorithms ensured the proper interactions between elements of the test stand. Due to the continuous improvement of these algorithms [39,40], the test stand performance is characterized by high repeatability as proper feedback is ensured among the following components of the system:

1. Hydraulic systems "A" (Zwick Roell Company Group, Ulm, Germany) and "B" (Hydac International GmbH, Sulzbach/Saar, Germany),
2. Electrical system: developed by authors' of the tests
3. Peripheral devices: the model P30 pressure transmitters (WIKA SE & Co. KG, Klingenberg, Germany), the draw-wire displacement converters of SWH-1-B-FK-01 type with the TRA50-SA1800WSC01 encoder (TWK-ELEKTRONIK GmbH, Düsseldorf, Germany), the Digital Image Correlation System ARAMIS 6M ((GOM GmbH, Braunschweig, Germany), the PUNDITLAB+ instrument for reading and recording ultrasonic waves (Proceq Europe, Schwerzenbach, Switzerland),
4. The measurement and control interface: based on the NIcRIO 9022, NIcRIO 9056 controller (National Instruments, Austin, TX, USA),
5. IT system: developed by the authors in the LABVIEW 2020 software (National Instruments, Austin, TX, USA) [41].

The block scheme in Figure 3 illustrates the interactions between individual elements of the system. The IT system with the hydraulic system generated stresses σ_1 and σ_3 of the same value and were used to read the ultrasonic wave path recorded with the PUNDIT LAB+ instrument. The ARAMIS 6M system was used to control deformations and observe crack images in individual specimens. Collecting data from different subsystem in one IT system ensured an additional option for the tests due to the time correlation of many data and their cause–effect relations. When different systems were combined, the set tasks were performed in a more effective way compared to individual subsystems [42–45].

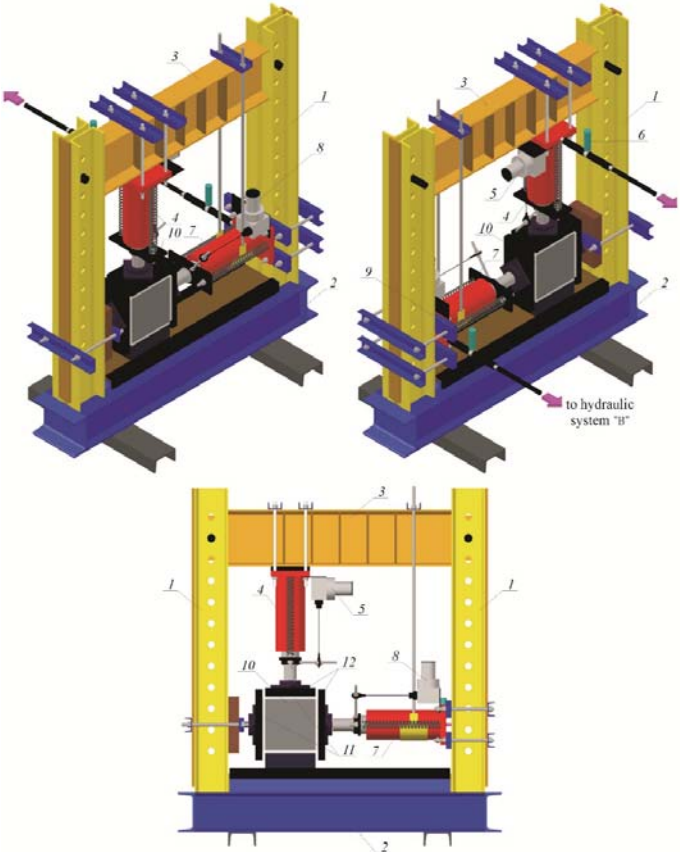

Figure 2. Test stand for measuring the acoustoelastic effect under the biaxial stress state (described in the text).

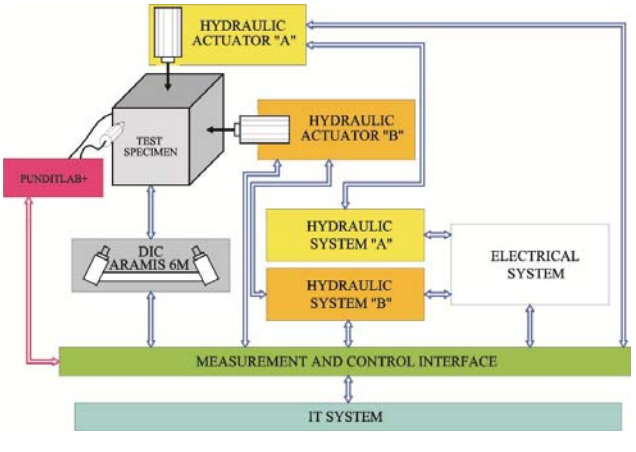

Figure 3. Block diagram of the test stand.

The tests were conducted on the specimens which were dried to constant weight and which had relative humidity w/w_{max} = 0%. The tests included at least 6 specimens of the same density, and 24 specimens in total were tested (Figure 4a,c,d). The PUNDIT LAB+ instrument (Proceq SA, Schwerzenbach, Switzerland), which was integrated with the IT system of the test stand, was used to measure velocity of ultrasonic waves. The point measurements were taken with the exponential transducers the frequency 54 kHz (Figure 4e). The measurement accuracy of passing time of the ultrasonic wave was equal to ±0.1 μs. Each specimen was placed between the plates of the test stand using Teflon washers of 10 mm in thickness. Compressive stress σ_3 was generated in the vertical direction. In the horizontal direction, in which the normal stress σ_1 was generated, Teflon plates, and then steel sheet were placed on the lateral sides to generate loading. The measuring templates were placed to end face of each specimen (Figure 4b) in the next step. The passing time of the wave was measured with transducer which were in put (at 90°) into the openings of the measuring templates. Each time a distance was measured between the transducers with an accuracy of 1 mm. An increment in stress values could be uniform by controlling loads exerted in both vertical and horizontal directions by hydraulic actuators 'A' and 'B'. Velocities of ultrasonic waves were read every 5 kN (for the specimens with nominal densities of 400 and 500 kg/m^3) and every 10 kN (the specimens with nominal densities of 600 and 700 kg/m^3). A view of the test stand in operation is shown in Figure 5.

4.1.3. Test Results

There were not any models with damaged front face during the loading cycle. Prior to the failure crack was heard and noticeable cracks were observed on the surface. Noticeable cracks were also found on the specimen surfaces under loading that preceded the failure. Debonding of external surface of each test element was observed at failure. It revealed a type of the specimen damage with clearly truncated pyramids that were connected in the center of the specimen. Passing time of the ultrasonic wave using the transmission method was measured at 25 points of each specimen at the following stress values: 0, ~0.25P_{max}, ~0.50P_{max}, ~0.75$P_{max,}$ P_{max}. Examples of the obtained maps showing passing time of the wave are illustrated in Figures 6–9.

Velocities of ultrasonic waves in all the specimens were significantly disturbed in the edge areas. Noticeably lower wave velocities were observed in these areas. The results referred to 16 points (as shown in the template–Figure 4a): A1–A5, B1, B5, C1, C5, D1, D5, E1, E5, and F1–F5. The observed disturbances were caused by the immediate vicinity of loaded edges of the specimens and the recorded wave reflection at the edge, and also by local damage to the material during the loading phase. The highest homogeneity of the results was found in central areas of each specimen at nine points B1–B3, C1–C3, D1–D3, and E1–E3. Table 2 presents the measurement results for the ultrasonic wave with reference to the mean and maximum values of hydrostatic stress P_{max}. The table below presents velocities of the longitudinal wave $^{obs}c_{p0}$ determined at free state and relative mean values of hydrostatic stress P/P_{max}. The measurements expressed as $(c_p - {}^{obs}c_{p0})/{}^{obs}c_{p0}$ ratio of a relative increment in ultrasounds as a function of stress P are shown in Figure 10a. Figure 10b illustrates the relative rate of an increase of ultrasonic wave velocity rise over the relative of compressive stresses P/P_{max}.

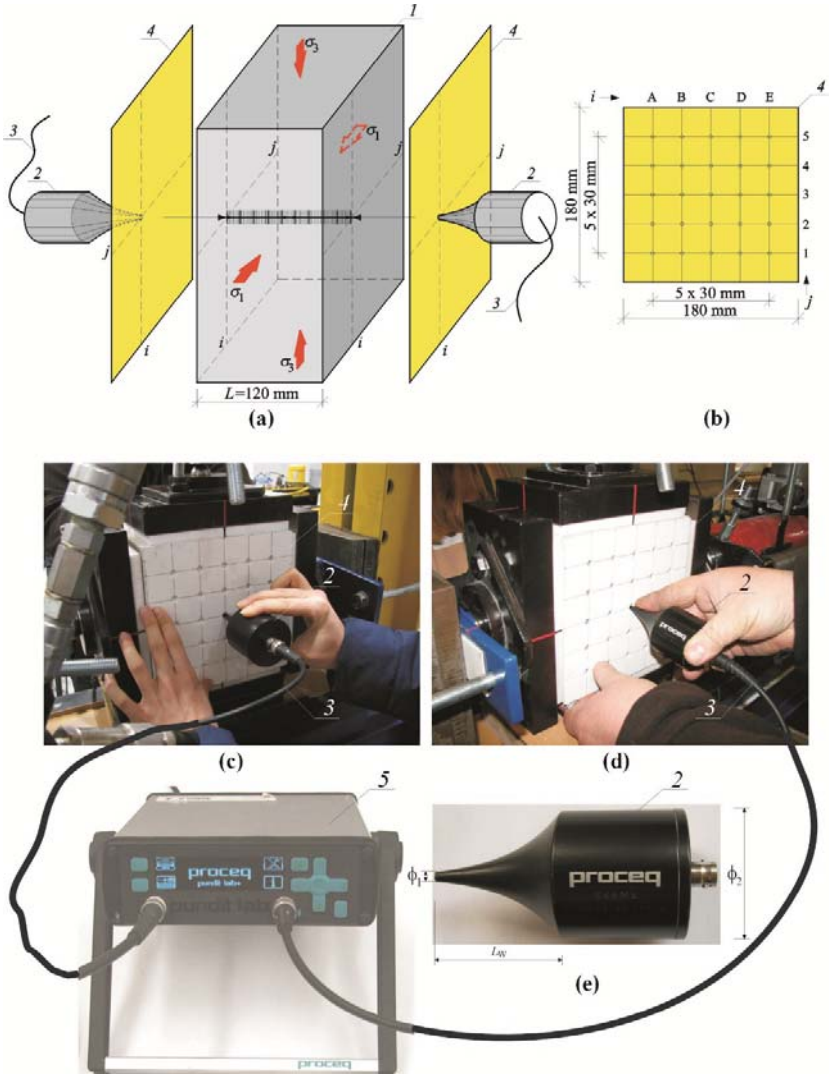

Figure 4. Measurements of ultrasonic wave velocity in biaxially compressed specimens: (**a**) components of stress states and the position of the measuring template; (**b**) geometry of the measuring template; (**c**,**d**) the test specimen; (**e**) the exponential transducer; 1—the AAC specimen 180 mm × 180 mm × 120 mm, 2—exponential transducers, 3—cables connecting transducers with recording equipment, 4—the measuring template, 5—PUNDIT LAB+ recording equipment.

Figure 5. View of the test stand in operation: (**a**) overall view, (**b**) specimen view; 1—the test stand with the fixed actuators; 2—a test element; 3—the hydraulic system 'A'; 4—the hydraulic system 'B'; 5—the measurement and control interface; 6—IT system; 7—cameras of the ARAMIS 6M system; 8—PUNDIT LAB+ instrument.

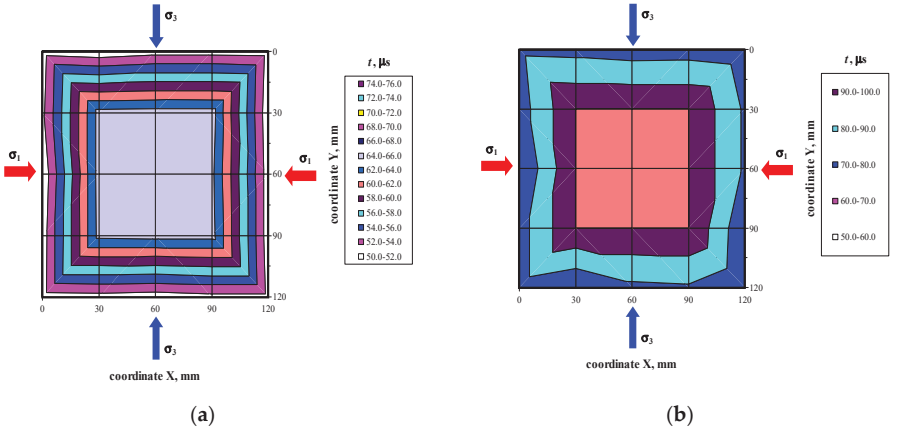

Figure 6. Maps of passing time the ultrasonic wave in the model 400/1 at selected loading levels: (**a**) $P = 0$, (**b**) $P = P_{max}$.

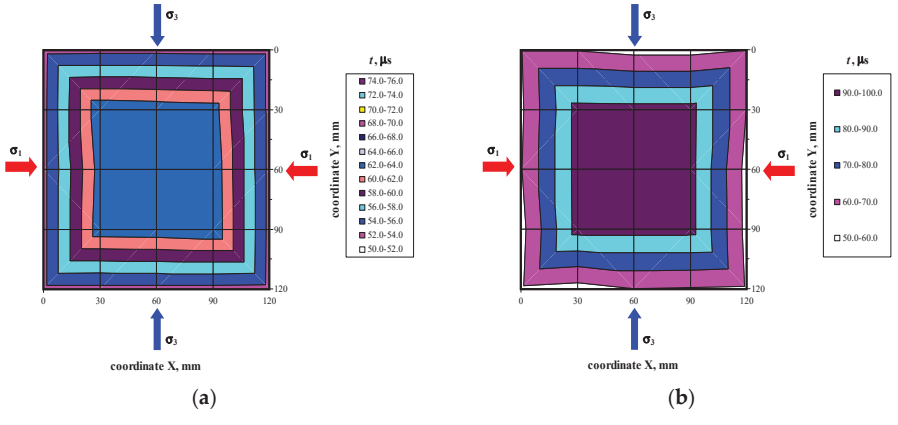

Figure 7. Maps of passing time the ultrasonic wave in the model 500/1 at selected loading levels: (**a**) $P = 0$, (**b**) $P = P_{max}$.

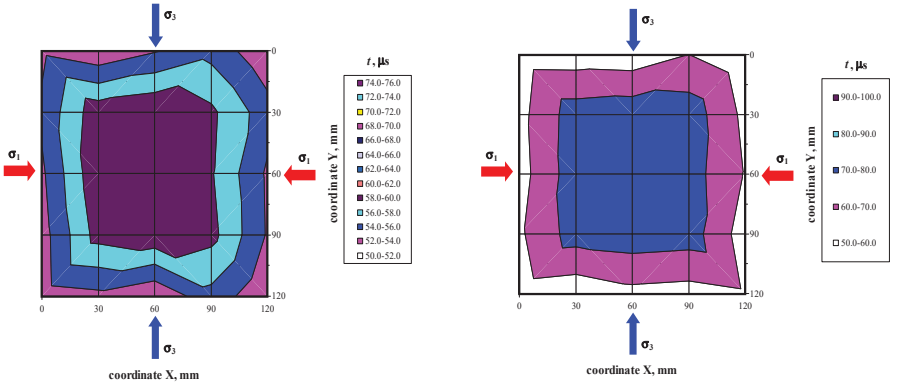

Figure 8. Maps of passing time the ultrasonic wave in the model 600/1 at selected loading levels: (**a**) $P = 0$, (**b**) $P = P_{max}$.

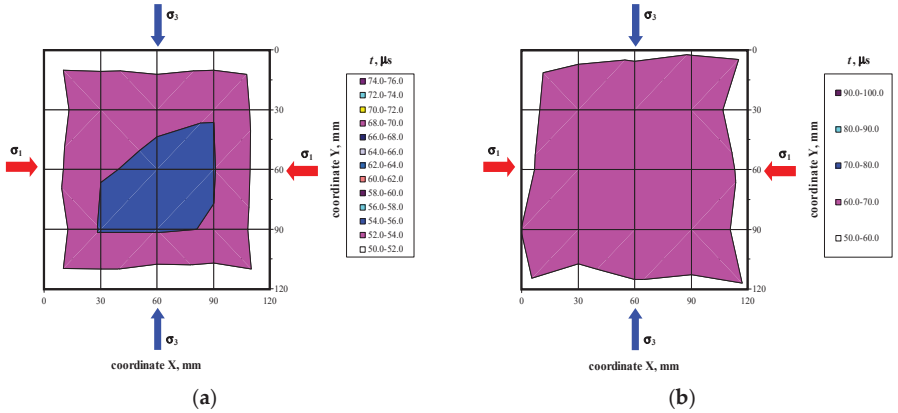

Figure 9. Maps of passing time the ultrasonic wave in the model 700/1 at selected loading levels: (**a**) $P = 0$, (**b**) $P = P_{max}$.

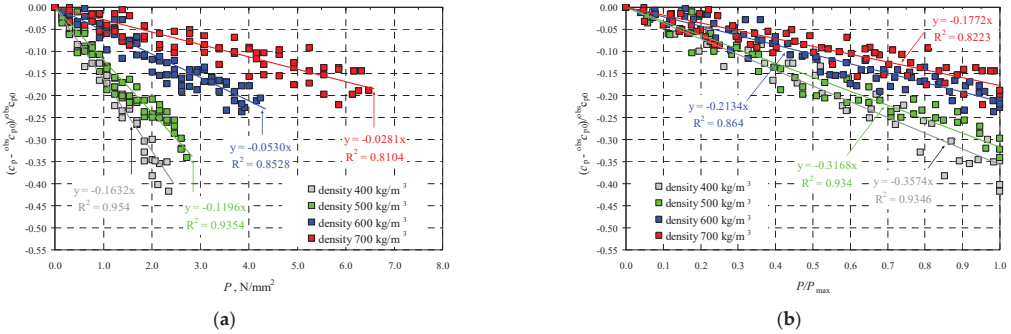

Figure 10. Results from measuring velocity of the longitudinal ultrasonic wave: (**a**) relative change in velocity of longitudinal wave as a function of compressive stress, (**b**) relative change in velocity of longitudinal wave as a function of relative compressive stresses.

Table 2. Test results for ultrasonic wave velocity in AAC under various mean hydrostatic stresses determined at central points (B1–B3, C1–C3, D1–D3, E1–E3) of each specimen.

No.	Mean Density ρ, (Nominal Class of Density) kg/m^3	Mean Compressive Stress P, N/mm^2	Mean Relative Compressive Stress P/P_{max}	Mean Path Length L, mm	Mean Passing Time of Wave t, µs	Mean Ultrasonic Velocity $c_p = L/t$, m/s	$\frac{(c_p - c_{p0})}{c_{p0}}$	COV, %
1	2	3	4	5	6	7	8	9
1	397 (400)	0	0	120.1	64.7	$^{obs}c_{p0}$ = 1875	0	1.7%
2		0.51	0.23		70.6	1704	−0.09	2.1%
3		1.13	0.52		76.5	1572	−0.16	1.4%
4		1.65	0.75		87.0	1387	−0.26	0.5%
5		2.19	1		105.2	1145	−0.39	2.3%
6	492 (500)	0	0	119.9	63.4	$^{obs}c_{p0}$ = 1893	0.00	2.1%
7		0.62	0.23		69.3	1732	−0.08	1.9%
8		1.34	0.51		78.3	1534	−0.19	1.6%
9		2.01	0.76		82.8	1451	−0.23	1.1%
10		2.65	1		93.4	1286	−0.32	1.7%
11	599 (600)	0	0	120.1	59.1	$^{obs}c_{p0}$ = 2031	0.00	1.9%
12		0.98	0.24		61.3	1960	−0.03	3.1%
13		2.01	0.50		66.7	1800	−0.11	2.7%
14		3.03	0.76		70.8	1695	−0.16	2.2%
15		4.01	1		75.6	1588	−0.22	2.4%
11	674 (700)	0	0	120.2	54.0	$^{obs}c_{p0}$ = 2225	0.00	2.1%
12		1.54	0.25		57.7	2083	−0.06	1.4%
13		3.19	0.51		59.1	2032	−0.09	1.8%
14		4.73	0.75		62.0	1936	−0.13	1.9%
15		6.30	1		66.8	1799	−0.19	3.1%

The tests showed that AAC density had an impact on velocities of ultrasonic waves, which confirmed the previous tests [14]. At stress values $P = 0$, velocities of ultrasonic waves increased in the specimens dried until constant weight. This increase was proportional to densities of AAC under stress The longitudinal wave velocity $^{obs}c_{p0}$ in the AAC units of the minimum nominal density of 400 kg/m^3 was equal to 1875 m/s and increased to 2225 m/s in concrete characterized by the highest density of 700 kg/m^3. Velocities of longitudinal waves noticeably dropped as means stresses P increased in all the units. Under relatively low stress when $0 \leq P \leq 0.25P_{max}$, values of ultrasounds decreased by 3–9% to the value $^{obs}c_{p0}$. At slightly higher values of hydrostatic stress $0.25P_{max} \leq P \leq 0.50P_{max}$ the ultrasonic wave velocities dropped by 9–16% (with reference to the base value). Higher stress values $0.50P_{max} \leq P \leq 0.75P_{max}$ in concrete having nominal densities of 400 and 500 kg/m^3 caused the highest percentage drop in the velocities of ultrasonic waves by 23–24%. Ultrasonic wave velocities dropped by 13–17% in more dense masonry units made of AAC (600 and 700 kg/m^3). In opposition to lower hydrostatic loads, no clear reduction in wave velocity was observed at the stress level preceding the failure when local cracking and crushing were found within the stress range of $0.75P_{max} \leq P \leq \sim P_{max}$. For concretes with lower density, the velocity was reduced by 32–39%, whereas the velocity drop by 19–22% was found in concretes having density of 600 and 700 kg/m^3. As in the tests under uniaxial stress state [11], a nearly linear drop in the relative velocity of longitudinal ultrasonic wave was observed at any density of AAC. A drop in velocity was practically 1.5–2.0 times higher than in the tests [11] on the specimens under uniaxial stress state and subjected to stress σ_3. The resulting biaxial stress state confirmed the linear correlation

which specified a reduced velocity of ultrasonic wave over mean hydrostatic stress. This effect was noted during the tests on AAC [11] and metals [29,32].

Table 3 presents coefficients of the linear correlation of the relative velocity of ultrasonic waves as a function of mean hydrostatic stress which are shown in Figure 10. Regression lines based on values of AE coefficients contained values of AE (δ, η) coefficients and density of AAC, which are illustrated in Figure 11. The coefficients were determined at moisture content of AAC $w = 0$. Additionally, values of coefficients β_{113}, γ_{113} determined in the tests on uniaxial compression which are described in the paper [11], are shown in Figure 11.

Table 3. Values of AE coefficients for concrete of specific densities.

No.	Mean Density ρ, (Nominal Class of Density) kg/m^3	AE Coefficient δ_P, m^3/kg	Relative Coefficient η_P
1	2	3	4
1	397 *(400)*	−0.1632	−0.3574
2	492 *(500)*	−0.1196	−0.3168
3	599 *(600)*	−0.0530	−0.2134
4	674 *(700)*	−0.0281	−0.1772

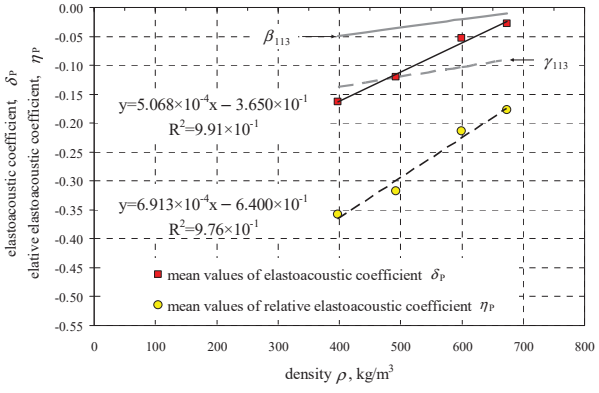

Figure 11. Values of coefficients δ and η as a function of AAC density.

$$\delta = 5.068 \cdot 10^{-4}\rho - 0.635,\ \mathrm{R}^2 = 0.991, \tag{15}$$

$$\eta = 6.91 \cdot 10^{-4}\rho - 0.64,\ \mathrm{R}^2 = 0.976 \tag{16}$$

when $397\ \frac{\mathrm{kg}}{\mathrm{m}^3} \le \rho \le 674\ \frac{\mathrm{kg}}{\mathrm{m}^3}$.

Walls in real structures have moisture content $w > 0$ and the effect of this factor has to be taken into account. Considering the results from own research [14] and the procedure described in the paper [11], the empirical relationship was defined to determine velocities of UV waves under air-dry conditions c_p (at $w = 0$) based on the equation

$$\frac{c_{pw}}{c_p} = a\left(\frac{w}{w_{\max}}\right)^2 + b\left(\frac{w}{w_{\max}}\right) + 1 \rightarrow c_p = \frac{1}{c_{pw}}\left[a\left(\frac{w}{w_{\max}}\right)^2 + b\left(\frac{w}{w_{\max}}\right) + 1\right], \tag{17}$$

where c_{pw}—velocity of ultrasonic wave in wet AAC in the unloaded state $P = 0$; c_p—velocity of ultrasonic wave in dry ($w = 0$) AAC in the unloaded state $P = 0$; w—relative humidity of AAC; w_{max}—maximum relative humidity of AAC [14] calculated from the following relationship

$$w_{max} = -1.23\frac{\rho}{1000} + 1.34, \text{ when } 397\ \frac{kg}{m^3} \le \rho \le 674\ \frac{kg}{m^3}. \tag{18}$$

a, b–empirical coefficients dependent on density were

$$\begin{aligned} a &= 9.187 \cdot 10^{-4}\rho + 0.932, \text{ when } 397\ \tfrac{kg}{m^3} \le \rho \le 674\ \tfrac{kg}{m^3}. \\ b &= 1.416 \cdot 10^{-3}\rho - 1.373, \text{ when } 397\ \tfrac{kg}{m^3} \le \rho \le 674\ \tfrac{kg}{m^3}. \end{aligned} \tag{19}$$

4.2. Stage II-Testing Models under Compression

Stage II involved small models of the masonry already used in the tests described in the previous paper [11]. The models of 500 mm × 726 mm × 180 mm in dimensions were composed of three layers of masonry units made of AAC of nominal density of 600 kg/m^3. They were connected with thin bed joints laid in the commercial mortar with a strength f_m = 6.10 N/mm^2 [46] and the nominal class M5 [47]. Models (nine specimens)—divided into three series marked as I, II, and III—were tested. The models differed in the presence or lack of head joints. The models of series I did not have the head joint, whereas the unfilled head joint in the central layer was at mid-length or 1/4 length of the masonry unit in other series II and III. An overall view of tests specimens of the series I, II, and III is shown in Figure 12.

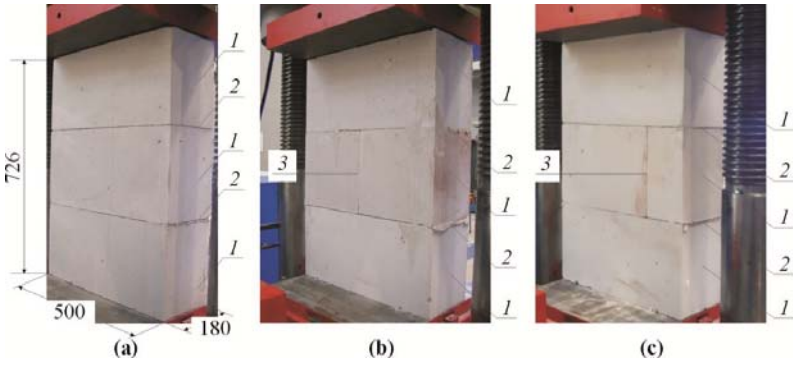

Figure 12. Geometry of models made of AAC tested in stage II: (**a**) models of series I without head joint, (**b**) models of series II with head joint at mid-length of the masonry unit, (**c**) models of series III with head joint at 1/4 length of the masonry unit; 1—masonry units, 2—bed joints, 3—head joints.

All the models were subjected to monotonic compression perpendicular to the plane of bed joints by exerting the uniform increment in the shift of the testing machine piston–Figure 13. The mean normal stress σ_3 was calculated as a ratio of the exerted load F and the area of bed face of the masonry unit A (A = 180 mm × 500 mm= 90,000 mm^2). For two models from each series [11] velocities of ultrasonic waves c_p were measured at the following values: 0, 0.25σ_{3max}, 0.50σ_{3max}, and 0.75σ_{3max}. In the stage I, waves were measured using the method transmission–Figure 13a. The template was used to ensure the coaxiality of the transducers. The tests are described in details in the paper [11]. Vertical strains were measured during the tests on all the models except for I-3, II-3, III-3 series, using the digital-image correlation system ARAMIS 6M (GOM GmbH, Braunschweig, Germany) [48–51]. The main tests were preceded by determination of apparent density ρ_0 (at air-dry state) and relative humidity w in AAC. Then the maximum moisture content

w_{max} was calculated from the Equation (19). Table 4 presents the main results from material tests and the results from main tests as crack-inducing stress σ_{3cr}, and maximum stress σ_{3max}.

Considering density (ρ_0 = 587–597 kg/m^3) and relative humidity (w =4.5–6.0%), the research model were regarded as nearly homogeneous. In all the models a nearly proportional increase in deformations was noticed at increasing loading. Cracks were formed at failure stress of ca. > 90%. They were detected at horizontal edges of the masonry units and in the extended head joints. The failure was gentle. An increase in the width of vertical cracks and spalling of external parts of the masonry units were noticed—Figure 13b,c. The passing time t_p of the ultrasonic wave was measured at defined load levels (then the strength testing machine was stopped). Calculating the velocity of the wave propagation from the relationship $c_p = L/t_p$ (L = 180 mm) was the next step. The synthetic test results for all measuring points and the points located at mid-height of each masonry unit are shown in Table 5, and the partial results can be found in the paper [11].

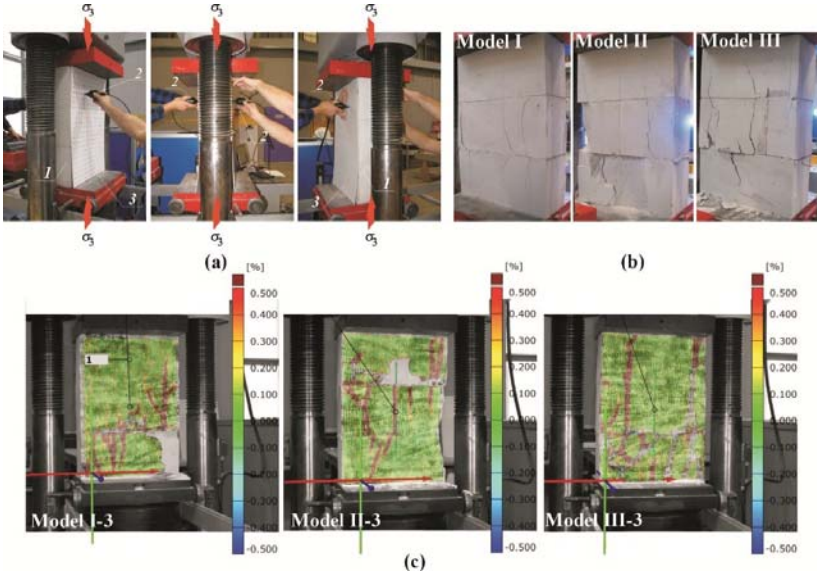

Figure 13. The procedure employed in Stage II to test the AAC wall models: (**a**) measurements of velocity of the ultrasonic wave at different stress value σ_3, (**b**) selected models at failure, (**c**) vertical strains of selected wall models under stress σ_{3max}; 1—masonry units, 2—ultrasonic transducers, 3—templates to arrange symmetrically ultrasonic transducers.

As presented in the paper [11], passing time of the ultrasonic wave through the models under zero loads was characterized by some variability. The longest passing time was usually recorded in central parts of the elements. Distinct disturbances described by different passing times of the wave were noticed at vertical edges of the masonry units and at bed joints. Passing times were consistent in the central areas of the units in spite of disturbed edge areas. The obtained variation coefficient was rather low within a range of 1.4–1.6% even though all the measurements were considered (even from the disturbed areas). A clear increase in the passing time of the ultrasonic wave in all the models was observed when the loads increased up to $0.25\sigma_{3max}$. The coefficient of variation was rather low within a range of 1.0–1.3% as in the case of lower stress values. An increase in loads to $0.50\sigma_{3max}$ and $0.75\sigma_{3max}$ resulted in a gradual increase in the mean time of propagation for almost all measuring points. The calculated coefficients of passing time of the wave were close to the values noticed at previous loading values and amounted to ca. 1.4%.

Table 4. Summary of mean results from the tests on the models.

Series	Mean Density ρ_0, kg/m^3	Moisture Content w, %	Maximum Moisture Content (17) w_{max}, %	Mean Compressive Stress Inducing Cracks σ_{3cr}, N/mm^2 (COV)	Maximum Mean Compressive Stress σ_{3max}, N/mm^2 (COV)
1	2	3	4	5	6
I	592 (0.43%)	5.20% (14.5%)	61.2% (0.57%)	2.89 (1.1%)	3.01 (1.3%)
II	595 (0.34%)	5.63% (11.3%)	61.1% (0.90%)	2.95 (2.8%)	2.96 (2.6%)
III	590 (0.59%)	5.33% (3.90%)	61.4% (0.73%)	2.90 (3.3%)	2.97 (1.9%)

Table 5. Results from measuring propagation of ultrasonic waves.

Series	No. of Measuring Points in Each Loading Step, n	Time of Ultrasonic Wave Passing at Different Levels of Loading, t_{pmv}, µs (COV)			
		0	0.25σ_{3max}	0.50σ_{3max}	0.75σ_{3max}
1	2	3	4	5	6
I-1	315	90.8 (1.4%)	92.2 (1.3%)	93.9 (1.4%)	94.4 (1.4%)
	45	91.2 (1.3%)	92.3 (1.1%)	93.6 (1.3%)	94.3 (1.2%)
II-1	308	89.2 (1.6%)	90.6 (1.2%)	92.2 (1.1%)	92.5 (1.1%)
	44	89.6 (1.5%)	90.5 (1.2%)	92.2 (0.9%)	92.4 (0.9%)
III-1	308	88.8 (1.4%)	90.2 (1.2%)	91.6 (0.9%)	92.1 (0.9%)
	44	89.1 (1.2%)	90.2 (0.8%)	91.5 (0.7%)	92.0 (0.8%)

5. Analysis of Test Results

5.1. Components of Stress State Based on the AE Effect

Values of stress P were determined at each measuring point using the empirical relationships which describe changes in mean hydrostatic stresses as a function of changes in the relative velocity of ultrasonic waves and propagation times of ultrasonic waves, which were determined in stage I and presented in the paper [7]. Mean values of hydrostatic stress P expressed as the maps of stress at different stress levels (0.25σ_{3max}, 0.50σ_{3max}, 0.75σ_{3max}) are shown in Figures 14–16.

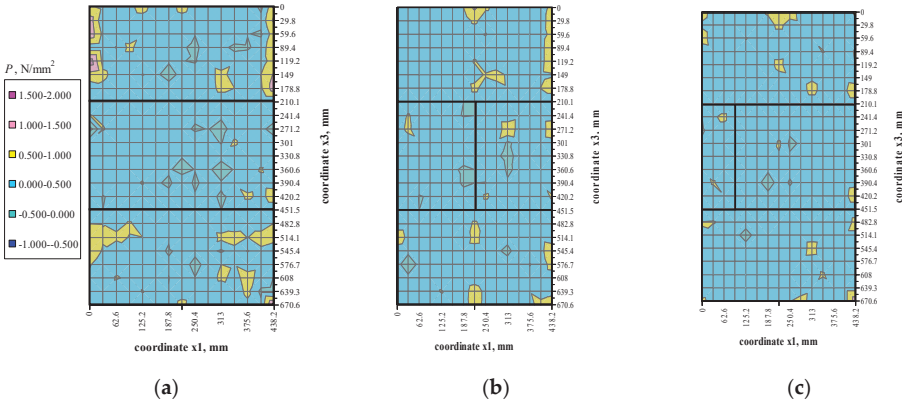

Figure 14. Mean hydrostatic stress values P at load $\sigma_3 = 0.25\sigma_{3max}$: (**a**) model I-1, (**b**) model II-1, (**c**) model III-1.

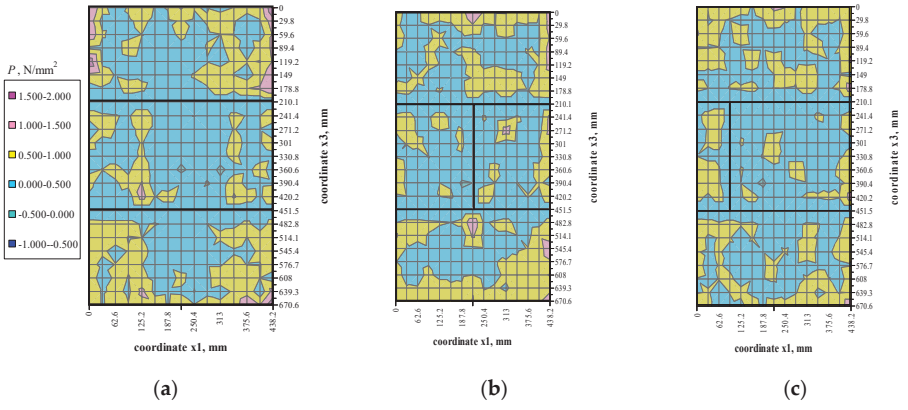

Figure 15. Mean hydrostatic stress values P at load $\sigma_3 = 0.50\sigma_{3max}$: (**a**) model I-1, (**b**) model II-1, (**c**) model III-1.

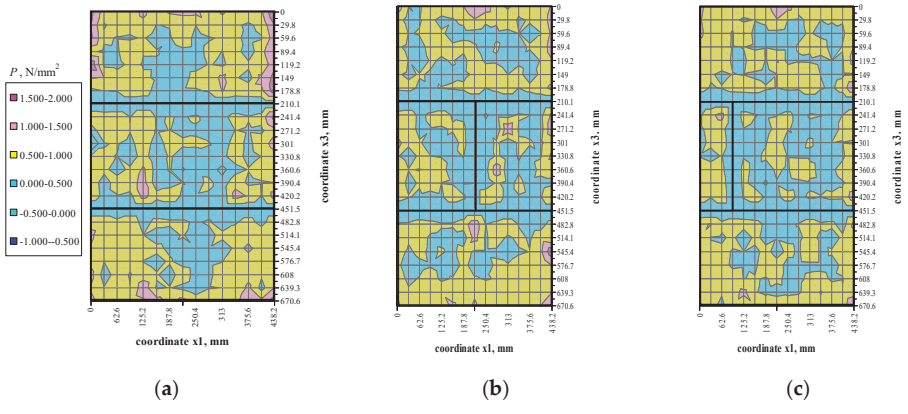

Figure 16. Mean hydrostatic stress values P at load $\sigma_3 = 0.75\sigma_{3max}$: (**a**) model I-1, (**b**) model II-1, (**c**) model III-1.

The distribution of mean hydrostatic stresses P in all the test models indicated the predominating compression ($P > 0$) in the masonry units. Mean hydrostatic stresses were

clearly decreasing in some areas adjacent to the head joints. Only at some individual points did mean hydrostatic stress represent tension ($P < 0$).

By reference to the paper [11], the qualitative analysis for the obtained results was performed in a comprehensive way using all the test results and then was constrained to a limited number of points. The comprehensive method included n = 315 (the model of series I) or 308 (the models of series II or III) measured passing times of ultrasonic wave at each analyzed stress level. The results for the clearly disturbed areas were also taken into account. In the method using a limited number of points stress was estimated only on the basis of the points located in the central area of the masonry units. In that way, the measuring points were considerably reduced to 45 for the model I, and to 44 for the models of series II and III.

At first, the velocity of ultrasonic waves was determined under air-dry conditions according to the following relationship (17). A relative difference in the passing time of the ultrasonic wave was then determined at other stress values. Determination of the acoustoelastic coefficient δ_P from the Equation (15) was the next step. At the end the stress P was obtained from the converted relationship (10). Table 6 demonstrates the calculated stresses.

Table 6. Calculated mean values of hydrostatic stress in the wall using all measuring points.

Model	Number of Measurements n	$0.25\sigma_{3max}$			$0.50\sigma_{3max}$			$0.75\sigma_{3max}$		
		$\frac{(c_P - c_{P0})}{c_{P0}}$	δ_P (15)	$P = \frac{(c_P - c_{P0})}{\delta_P \cdot c_{P0}}$ N/mm^2 (10)	$\frac{(c_P - c_{P0})}{c_{P0}}$	δ_P (15)	$P = \frac{(c_P - c_{P0})}{\delta_P \cdot c_{P0}}$ N/mm^2 (10)	$\frac{(c_P - c_{P0})}{c_{P0}}$	δ_P (15)	$P = \frac{(c_P - c_{P0})}{\delta_P \cdot c_{P0}}$ N/mm^2 (10)
1	2	3	4	5	6	7	8	9	10	11
I-1	315	−0.0156	−0.0640	0.247	−0.0319	−0.0640	0.502	−0.0403	−0.0640	0.634
II-1	308	−0.0151	−0.0635	0.240	−0.0333	−0.0635	0.528	−0.0372	−0.0635	0.590
III-1	308	−0.0150	−0.0640	0.240	−0.0306	−0.0640	0.495	−0.0360	−0.0640	0.587

Values of coefficients δ_P depended on the density of AAC, however, these differences were relatively small ($\delta_P = -0.0635 - -0.0640$ mm^2/N). Mean values of hydrostatic stress were evidently increasing with an increase in vertical stress values, which showed that compressive stress predominated in the compressed wall. The stress values calculated for the individual models were close to each other only when stress values were relatively low, that is, $0.25\sigma_{3max}$ and $0.50\sigma_{3max}$. Stresses in the model III-1 determined by the AE differed by maximum 12%. At $0.75\sigma_{3max}$ the stress values did not differ by more than 8%.

The same procedure was repeated in the method based on the limited number of results (from central areas of the masonry units). Analogous to the method, which was based on all the test results, velocities of ultrasonic waves under air-dry conditions were determined at first, and then a relative difference in the passing time of the ultrasonic wave and the stress values P were calculated from the converted relationship (10). The coefficient δ_P was the same as the value specified in Table 6. The obtained values of hydrostatic stress P are presented in Table 7.

The stress values were much lower at a limited number of measuring points. When stresses were the lowest, that is, equal to $0.25\sigma_{3max}$, the stresses determined with the AE method at the minimum number of points were lower by no more than 31% (the model II-1). Mean hydrostatic stresses at higher stresses ($0.50\sigma_{3max}$ and $0.75\sigma_{3max}$) were underestimated by a maximum of 18%.

Table 7. Results of calculations of normal stress σ_3 in the wall using a limited number of measuring points.

Model	Number of Measurements n	$0.25\sigma_{3max}$		$0.50\sigma_{3max}$		$0.75\sigma_{3max}$	
		$\frac{(c_p-c_{p0})}{c_{p0}}$	$P = \frac{(c_p-c_{p0})}{\delta_P \cdot c_{p0}}$ N/mm^2 (10)	$\frac{(c_p-c_{p0})}{c_{p0}}$	$P = \frac{(c_p-c_{p0})}{\delta_P \cdot c_{p0}}$ N/mm^2 (10)	$\frac{(c_p-c_{p0})}{c_{p0}}$	$P = \frac{(c_p-c_{p0})}{\delta_P \cdot c_{p0}}$ N/mm^2 (10)
1	**2**	**3**	**4**	**5**	**6**	**7**	**8**
I-1	45	−0.0115	0.181	−0.0261	0.410	−0.0337	0.528
II-1	44	−0.0104	0.166	−0.0293	0.464	−0.0316	0.501
III-1	44	−0.0119	0.187	−0.0270	0.424	−0.0324	0.509

By knowing mean hydrostatic stresses and stresses σ_3 determined from the Equation (12) and presented in the paper [11], horizontal stresses σ_1 could be determined from the relationship

$$P = \frac{1}{3}(\sigma_1 + \sigma_2 + \sigma_3) = \frac{1}{3}(\sigma_1 + \sigma_3) \rightarrow \sigma_1 = 3P - \sigma_3, \quad (20)$$

where P—mean hydrostatic stress, σ_3—normal stress perpendicular to the plane of bed joints, σ_1—normal stress parallel to the plane of bed joints.

The values of stress P and stress σ_3 shown in Tables 6 and 7 and presented in the paper [11], were the base to determine stresses σ_1 which are summarized in Table 8.

Table 8. Calculated mean stress σ_1 based on a varying number of measuring points.

Model	Number of Measurements n	$0.25\sigma_{3max}$			$0.50\sigma_{3max}$			$0.75\sigma_{3max}$		
		σ_3, N/mm^2 [7]	P N/mm^2 (Tables 5 and 6)	σ_1, N/mm^2 (20)	σ_3, N/mm^2 [7]	P N/mm^2 (Tables 5 and 6)	σ_1, N/mm^2 (20)	σ_3, N/mm^2 [7]	P N/mm^2 (Tables 5 and 6)	σ_1, N/mm^2 (20)
1	**2**	**3**	**4**	**5**	**6**	**7**	**8**	**9**	**10**	**11**
I-1	315	0.737	0.247	0.004	1.499	0.502	0.008	1.892	0.634	0.010
	45	0.540	0.181	0.003	1.224	0.410	0.007	1.577	0.528	0.008
II-1	308	0.714	0.240	0.005	1.573	0.528	0.011	1.757	0.590	0.012
	44	0.493	0.166	0.003	1.383	0.464	0.009	1.493	0.501	0.010
III-1	308	0.716	0.240	0.004	1.478	0.495	0.008	1.750	0.587	0.009
	44	0.557	0.187	0.003	1.265	0.424	0.007	1.518	0.509	0.008

5.2. Numerical FEM Model

The numerical FEM model was necessary to perform the comprehensive analysis of the determined mean values of hydrostatic stress P and normal stress σ_1 (determined indirectly on the basis of known values of stress σ_1). This model was used to determine mean values of hydrostatic stress from the components of the stress state. As it was demonstrated in the paper [11], the defined relationships between stress and strain were similar to the linear relationship. Hence, the linear-elastic FEM micro-model was sufficient for that purpose. The model included nominal geometric dimensions and boundary conditions. The model was 726 mm high, 500 mm wide, and 180 mm thick. It was supported along its bottom edge using the roller supports in each node, except for the middle one with the blocked horizontal movement. Five-node finite elements with 4 degrees of freedom for each node were used for calculations in a plane stress state (2D, PSS). The masonry units were modelled separately, for which the modulus of elasticity was E_B = 2039 N/mm^2 and Poisson's ratio was ν_B = 0.21 (cf Table 1). Mortar in joints was also modelled separately, and the finite elements took the following parameters E_m = 6351 N/mm^2 and ν_m = 0.18 [52]. Due to linear elasticity of the FEM models, the model was subjected to unit loads q = 1 kN/m, and the stress values at higher loads were determined using superpositioning of load states. The numerical FEM models are shown in Figure 17. The calculated data presented as the maps of vertical stresses σ_3 and σ_1 of unit loads are illustrated in Figure 18.

The stress–strain relationships for all the test elements and the FEM models were compared as shown in Figure 19. These curves indicate that the behavior of the test models was almost linear until the moment of cracking. Strains began to increase much faster than in the linear-elastic FEM model when the stresses were $>0.75\sigma_{3max}$. Differences in calculated and experimentally determined moduli of elasticity did not exceed 10%.

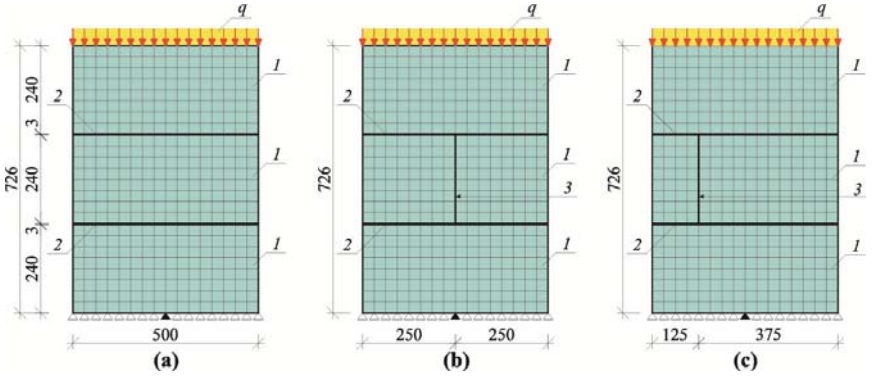

Figure 17. FEM models for the test walls: (**a**) models of series I without head joint, (**b**) models of series II with head joint at mid-length of the element, (**c**) models of series III with head joint at 1/4 length the masonry unit *1*—masonry unit; *2*—mortar; *3*—unfilled head joint.

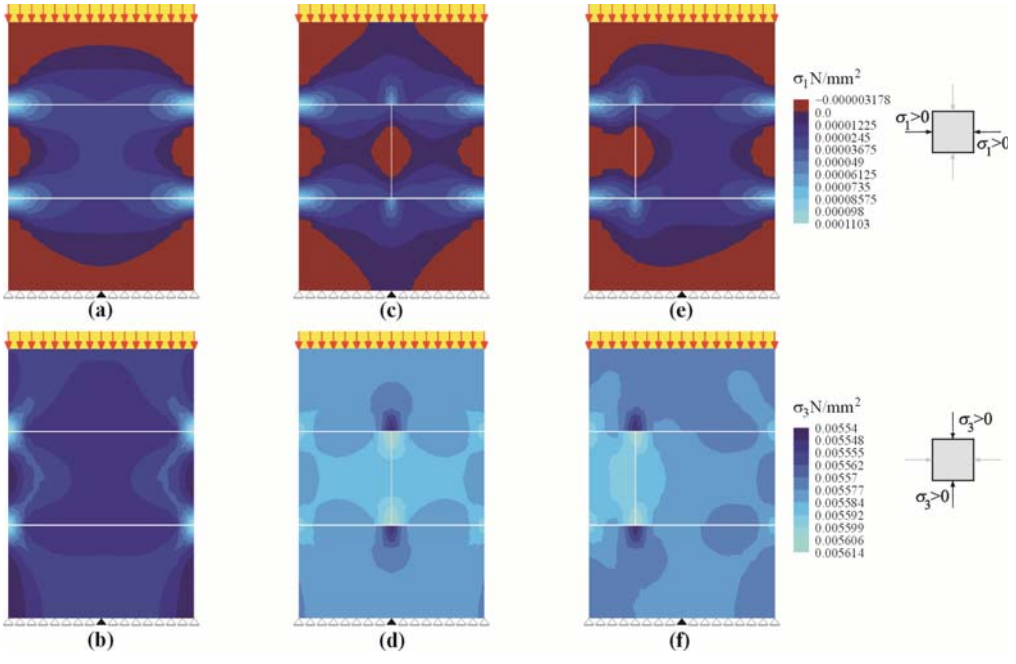

Figure 18. FEM calculations for the test walls: (**a**) stresses σ_x in the model of series I without a head joint, (**b**) stresses σ_y in the model of series I without a head joint, (**c**) stresses σ_x in the model of series II with the head joint at mid-length of the element, (**d**) stresses σ_y in the model of series II with the head joint at mid-length of the element, (**e**) stresses σ_x in the model of series III with the head joint in 1/4 length of the masonry unit, (**f**) stresses σ_y of the model of series III with the head joint in 1/4 length of the masonry unit.

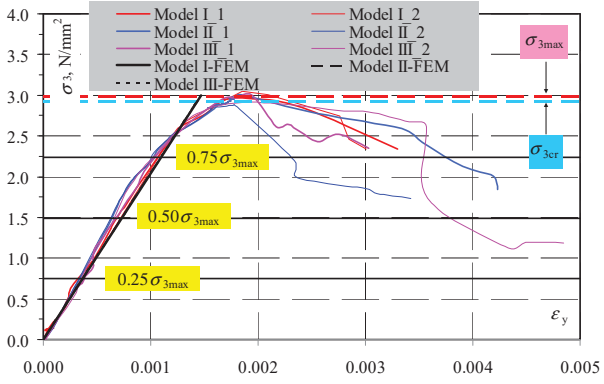

Figure 19. Compared relationships between stress and strain (σ_3–ε_y) for all tested models and numerical FEM models.

The data for components of the stress states P, σ_1, σ_3 obtained on the basis of the FEM calculations are compared in Table 9. The results are compared in Table 10.

Table 9. FEM-based calculations for mean stresses P and σ_1.

Model	Number of Measurements n	$0.25\sigma_{3max}$			$0.50\sigma_{3max}$			$0.75\sigma_{3max}$		
		$^{FEM}\sigma_3$, N/mm^2	^{FEM}P N/mm^2	$^{FEM}\sigma_1$, N/mm^2	$^{FEM}\sigma_3$, N/mm^2	^{FEM}P N/mm^2	$^{FEM}\sigma_1$, N/mm^2	$^{FEM}\sigma_3$, N/mm^2	^{FEM}P N/mm^2	$^{FEM}\sigma_1$, N/mm^2
1	2	3	4	5	6	7	8	9	10	11
I-1	315	0.752	0.251	0.003	1.503	0.503	0.006	2.255	0.754	0.008
II-1	308	0.741	0.248	0.003	1.483	0.496	0.006	2.224	0.744	0.009
III-1	308	0.743	0.249	0.003	1.486	0.497	0.006	2.229	0.746	0.009

Table 10. Compared mean values P and σ obtained from the tests and FEM calculations.

Model	Number of Measurements n	$0.25\sigma_{3max}$			$0.50\sigma_{3max}$			$0.75\sigma_{3max}$		
		$\frac{\sigma_3}{^{FEM}\sigma_3}$	$\frac{P}{^{FEM}P}$	$\frac{\sigma_1}{^{FEM}\sigma_1}$	$\frac{\sigma_3}{^{FEM}\sigma_3}$	$\frac{P}{^{FEM}P}$	$\frac{\sigma 1}{^{FEM}\sigma 1}$	$\frac{\sigma_3}{^{FEM}\sigma_3}$	$\frac{P}{^{FEM}P}$	$\frac{\sigma_1}{^{FEM}\sigma_1}$
1	2	3	4	5	6	7	8	9	10	11
I-1	315	0.98	0.98	1.33	1.00	1.00	1.33	0.84	0.84	1.25
II-1	308	0.96	0.97	1.67	1.06	1.06	1.83	0.79	0.79	1.33
III-1	308	0.96	0.96	1.33	0.99	1.00	1.33	0.79	0.79	1.00
on average:		**0.97**	**0.97**	**1.44**	**1.02**	**1.02**	**1.50**	**0.81**	**0.81**	**1.19**
I-1	45	0.72	0.72	1.00	0.81	0.82	1.17	0.70	0.70	1.00
II-1	44	0.67	0.67	1.00	0.93	0.94	1.50	0.67	0.67	1.11
III-1	44	0.75	0.75	1.00	0.85	0.85	1.17	0.68	0.68	0.89
on average:		**0.71**	**0.71**	**1.00**	**0.87**	**0.87**	**1.28**	**0.68**	**0.69**	**1.00**

The maximum difference in mean stresses σ_3 perpendicular to the plane of bed joints, which were determined for all the measuring points, was 3% at the stress levels $0.25\sigma_{3max}$–$0.50\sigma_{3max}$. The biggest difference was observed under compressive stress equal to $0.75\sigma_{3max}$. When the number of measurements was limited to central areas of the masonry units, significantly greater differences were noticed, The highest mean overestimation

of the results exceeding 32% was found at the stress level of $0.75\sigma_{3max}$. Almost the same results were obtained for the hydrostatic stress P in the wall. For all the measuring points, the differences did not exceed 3% at the stress levels of $0.25\sigma_{3max}$–$0.50\sigma_{3max}$. Mean stresses were greater by 31% also under higher compressive stress equal to $0.75\sigma_{3max}$.

The greatest variation of the results was found under the stresses σ_1 which were parallel to the plane of bed joints. A higher number of measurements caused in this case a higher degree of inconsistency between the results. Under the compressive stresses $0.25\sigma_{3max}$–$0.50\sigma_{3max}$, the stress values were overestimated by ca. 44–50%. An increase in mean values of stresses to the level of $0.75\sigma_{3max}$ caused that the overestimation of stresses was reduced to ca. 19%. The best results were obtained for the limited number of measuring points. Then, at the stress levels of $0.25\sigma_{3max}$ and $0.75\sigma_{3max}$, the stresses determined with the NDR technique did not significantly vary from the stresses obtained from the FEM calculations. The highest overestimation of the stresses of the order of 28% was found for mean stresses equal to $0.50\sigma_{3max}$.

The best agreement with the FEM calculations was reached when the maximum number points were used for vertical stresses σ_3 and mean hydrostatic stresses P. The measurements limited to central areas of the masonry units resulted in bigger differences in the results when compared to the numerical results. The contradictory tendency was noticed for the stresses σ_1, under which the biggest differences in the results were obtained when the maximum number of points were used. Limiting the measurements only to the central areas caused a clear drop in the stress values which were empirically determined.

The results were obtained from the methodology of determining the coefficients AE (β_{113} η_P), which was conducted on relatively small specimens subjected to the load which eliminated additional stress components and boundary disorders. The stress distribution in real masonry structures (on which the main tests were performed) is significantly disturbed by the presence of head and bed joints, the shape, and interaction with other masonry units. The results were close to the FEM calculations when the measurements were taken in the central area of the masonry units at the least disturbed stress state. A narrower spread of the calculated and test results was the immediate effect. It should be remembered that the plane stress state assumed for the analyses is observed locally in central areas of the masonry units. Additional stresses $\sigma_2 \neq 0$ perpendicular to the front plane of the masonry are found in the edge and support areas, which has an impact on mean hydrostatic stresses. The proposed procedure cannot be applied for the whole range of stress values without its prior calibration. At relatively low stresses $0.25\sigma_{3max}$ and $0.50\sigma_{3max}$, the test results were similar to the calculated results. The most significant differences were obtained for the stresses of $0.75\sigma_{3max}$, and at this level NDT tests can be performed.

5.3. Model Update

It is more favorable to perform in practice only the tests restrained to central areas of the masonry units. Such an approach reduces the effect of disturbances created at the element edges due to the presence of bed and head joints. As shown in point 6.2, the NDT technique based on the AE effect and the stresses determined for the central areas of masonry units are expected to provide inconsistency in all the determined stresses. Assuming that the results obtained from the FEM calculations correctly estimate the stress values in the masonry units, the stress values σ_3 in the masonry units were at first corrected. For that purpose, mean quotients presented in Table 9 were applied. It was the base to calculate the mean quotient of stresses determined by the NDT and FEM techniques. On this basis, the mean coefficient equal to $\alpha_3 = 0.75$ was determined. Coefficients of stresses P and σ_1 were determined similarly. These values were $\alpha_P = 0.76$ and $\alpha_1 = 1.09$. The update empirical values to determine stress in the wall can be expressed as

$$\sigma_3 = \frac{1}{\alpha_3} \frac{(c_p - c_{p0})}{c_{p0}\beta_{113}}, \tag{21}$$

$$P = \frac{1}{\alpha_P} \frac{(c_p - c_{p0})}{c_{p0}\delta_P}, \tag{22}$$

$$\sigma_1 = \frac{1}{\alpha_1}(3P - \sigma_3). \tag{23}$$

The results obtained by the NDT technique before and after validation and by the FEM methods are compared in Figures 20–22.

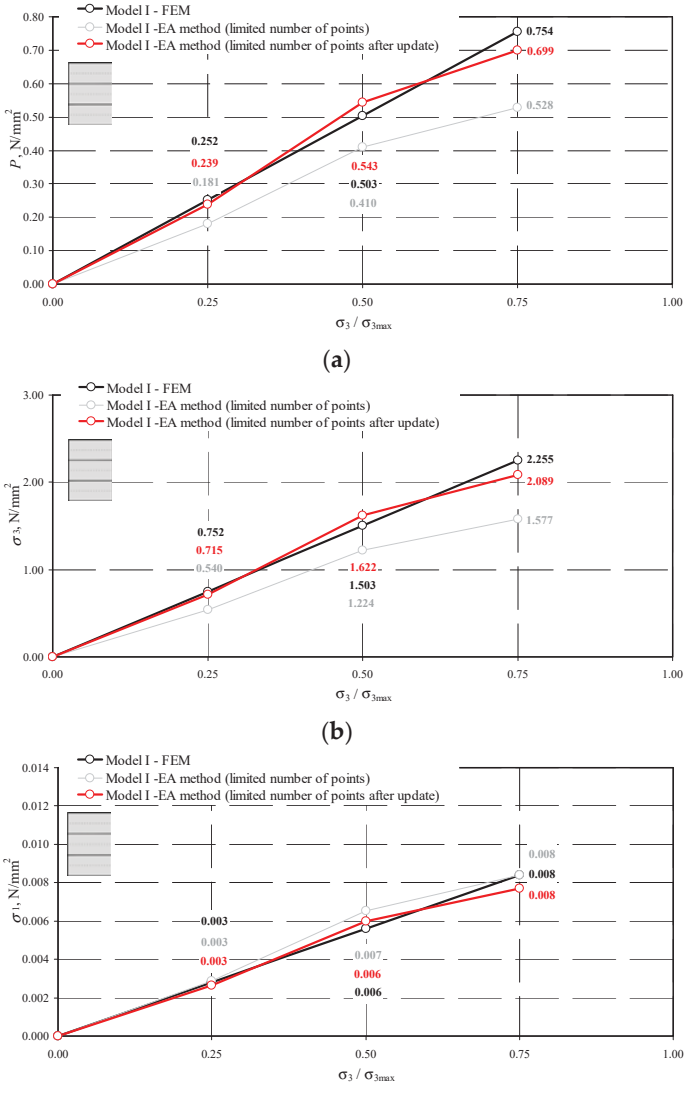

Figure 20. Comparison of stress values determined by the NDT and FEM methods for the model I-1: (**a**) mean hydrostatic stress; (**b**) normal stress perpendicular to the plane of bed joints; (**c**) normal stress parallel to the plane of bed joints.

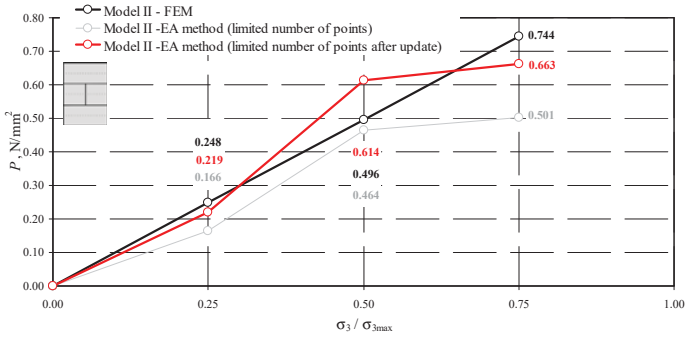

(**a**)

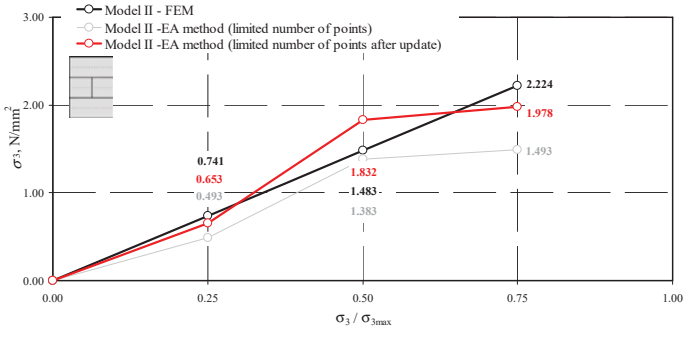

(**b**)

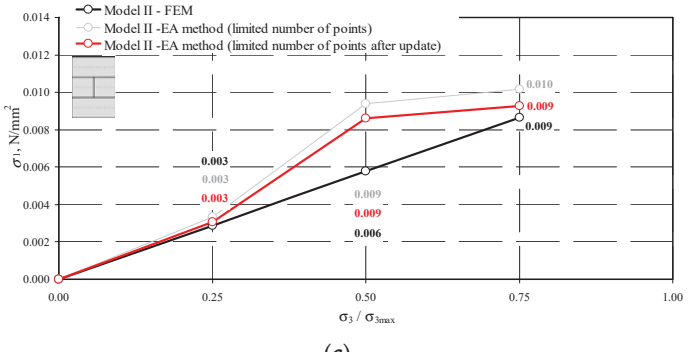

(**c**)

Figure 21. Comparison of stress values determined by the NDT and FEM methods for the model II-1: (**a**) mean hydrostatic stress; (**b**) normal stress perpendicular to the plane of bed joints; (**c**) normal stress parallel to the plane of bed joints.

The stresses σ_3 and P in the updated model were underestimated by no more than 15%. On the other hand, the underestimation of the stresses P parallel to the plane of head joints σ_1 did not exceed 6%.

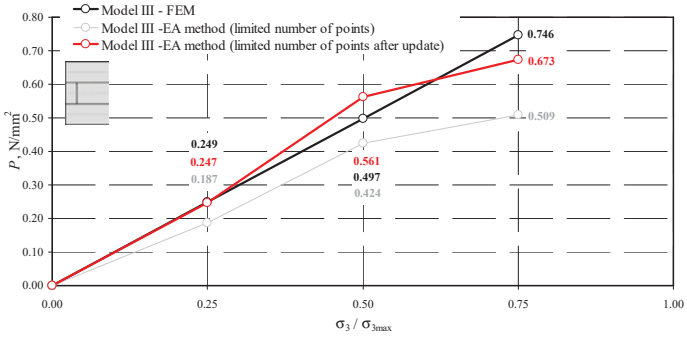

(**a**)

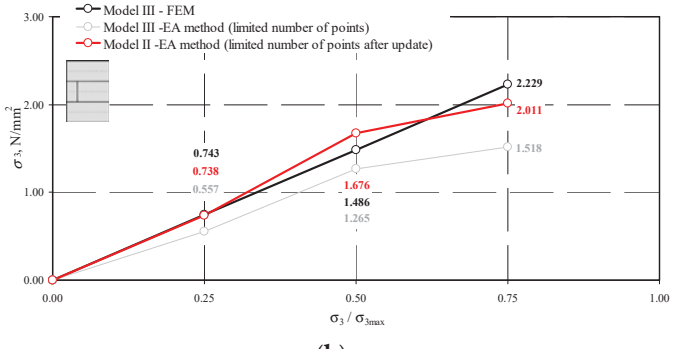

(**b**)

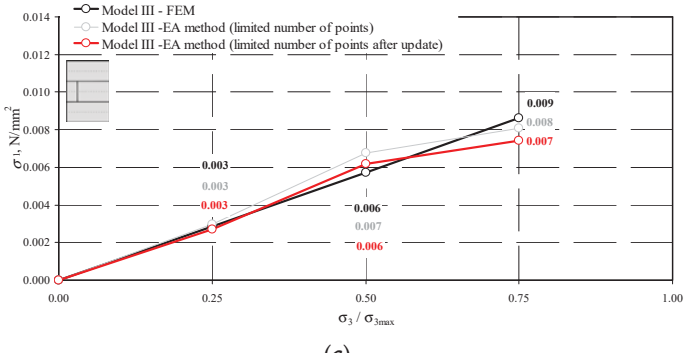

(**c**)

Figure 22. Comparison of stress values determined by the NDT and FEM methods for the model III-1: (**a**) mean hydrostatic stress; (**b**) normal stress perpendicular to the plane of bed joints; (**c**) normal stress parallel to the plane of bed joints.

The described validation resulted in mean stresses in the wall which were comparable to the data determined by the FEM technique after taking at least $n > 44$ measurements in the central parts of the wall. However, taking the measurements at so many points (at a relatively low variation) can be troublesome in practice. That is why it is necessary to specify the minimum number of measuring points, at which the obtained results are reliable with reference to the defined confidence level [53]. Therefore, the minimum number of measuring points was define assuming that:

1. the general population had the normal distribution N(μ, σ),

2. the variance σ of the general population was unknown at the known standard deviation for the small sample, which was taken as $s = \nu_{\text{test}}\overline{x}$ (ν_{test} = 15%—the coefficient of variation corresponding to the results from the in-situ tests),
3. α = 0.05—the confidence level,
4. the relative error was defined at the level 0.5α = 0.0025. The absolute value was taken as $d = 0.5\alpha\ \overline{x}$,
5. the minimum number of samples [53] were determined from the relationship $n_0 = (t_{\alpha,n-1}s/d)^2$, where $t_{\alpha,n-1}$ = 2.017—the parameter of a two-tailed T distribution at $n - 1$ degrees of freedom, n = 44—the number of samples to determine the number of samples.

Based on these assumptions, the calculations were performed under the stresses equal to $0.75\sigma_{3\max}$. Only the stresses σ_3 and P calculated from the relationships (21) and (23) were considered. It was not necessary to specify the number of samples on the basis of the stress σ_1 as it was not an independent variable. The obtained number of samples is shown in Table 11.

Table 11. Minimum number of measuring points to determine the stresses σ_3 and P.

Model	$\overline{x} = \sigma_{3\max}$ N/mm^2	$\overline{x} = P$ N/mm^2	$s_{\sigma 3} = \nu_{\text{test}}\sigma_{3\max}$ N/mm^2	$s_P = \nu_{\text{test}}\sigma_P$ N/mm^2	$d_{\sigma 3} = 0.5\alpha\ \sigma_{3\max}$ N/mm^2	$d_P = 0.5\alpha\ P$ N/mm^2	$\frac{t^2_{\alpha,n-1}s^2_{\sigma 3}}{d^2_{\sigma 3}}$	$\frac{t^2_{\alpha,n-1}s^2_P}{d^2_P}$
1	2	3	4	5	6	7	8	9
I-1	2.089	0.699	0.313	0.105	0.052	0.017	8	23
II-1	1.978	0.663	0.297	0.099	0.049	0.017	7	22
III-1	2.011	0.673	0.302	0.101	0.050	0.017	7	22

When the tests were focused on determining compressive stress σ_3 during the in-situ tests on the wall made of AAC masonry units, the minimum number of measurements was estimated to be n_0 = 8. On the other hand, when the aim of the tests is to determine the complex state of stress, the minimum number of measurements should not be lower than n_0 = 23. When the results were expressed in 1 m^2 of the wall, then the minimum number of measuring points required to determine stresses σ_3 should not be lower than $n_0 = 8 \cdot (1/0.726 \cdot 0.5) = 22$ measurements/m^2, and in case of mean hydrostatic stresses $n_0 = 23 \cdot (1/0.726 \cdot 0.5) = 61$ measurements/m^2.

The proposed update method was intended to determine mean stresses in the wall, which were crucial for diagnostic tests for structures. Development of the complete model which can be used to define characteristics and design values to verify the estimated structural safety, should include the non-linear FE model and the application of FORM procedures [54,55].

6. Conclusions

This paper is a continuation of the tests [11,14] concerning the use of the ultrasonic (UPV) techniques, in particular the acoustoelastic (AE) method to detect stresses in a structure by means of the non-destructive technique (NDT). The tests were focused on the commercially produced autoclave aerated concrete (AAC) which is characterized by high homogeneity and repeatability of the parameters. Considering different purposes, the tests were carried out in two stages. In Stage I, the test procedure was specified and the acoustoelastic coefficient δ_P was determined. This coefficient specified the relationships between the mean hydrostatic stresses P and the velocity of the longitudinal ultrasonic wave propagation c_p.

The non-standard cuboidal specimens 180 × 180 × 120 mm were used for the calibration purposes. They were tested at the in-house developed test stand [37] which can be used to exert the biaxial compression. Based on the tests on AAC of different densities, the impact of relative humidity w and density ρ was included using the correlations presented in paper [14]. These considerations resulted in formulating the relationship $\delta_P(\rho)$. Verifica-

tion of the discussed procedure was performed in Stage II, in which the complex stress state was to be determined. This stage based on the results from previous test [11] performed on small AAC walls having a nominal density of 600 kg/m^3. The models differed in the position of head joints without mortar and were classified into series I, II, and III. The measured velocities of ultrasonic wave propagation were analyzed under various compressive stresses: $0.25\sigma_{3max}$, $0.50\sigma_{3max}$ and $0.75\sigma_{3max}$. The performed measurements (n = 308–315) were used to define the coefficients AE $\delta_P = -0.1632 - -0.0281$. The data obtained from the AE method were compared with the data calculated for the linear-elastic FEM models of the walls. For the mean values of hydrostatic stress P, the stresses were underestimated at the order of 3% at $0.25\sigma_{3max}$. Under higher compressive stresses $0.50\sigma_{3max}$, the stresses P obtained by the AE method were greater by 2% than the calculated mean values. Under the highest analyzed stresses equal to $0.75\sigma_{3max}$, the empirically determined stresses were greater by over 19% than the calculated values. By knowing the stresses P and the stresses σ_3 perpendicular to the plane of head joins presented in the paper [11], the stresses σ_1 could be determined. These results were compared with the values obtained by the FEM calculations under various compressive stresses. Each time the values were overestimated. The stress values σ_1 at $0.25\sigma_{3max}$ were overestimated by 44%. An increase in vertical loads to the values of $0.50\sigma_{3max}$ and $0.75\sigma_{3max}$ caused that the stress values determined with the AE method were greater by 50% and 19% compared to the data obtained from the FEM method. These discrepancies were caused by disorders of the stress state in the real structure and they considerably differed from the stress state, under which the coefficient AE (β_{113} and δ_P) was determined.

It is not effective to use so many measuring points in practice (as a high number of points and results from the measurements have to be prepared and captured). For that reason, it was suggested that the measuring points were constrained only to the central areas of each masonry units which reduced the number of measurements to n = 45 and 44.

A similar comparison as for all the measurements produced considerably higher underestimations of the mean stresses σ_3 by 13–32%, and the stresses P by 3–19%. These values are not desirable taking into account safety of the structure. Hence, a decision was made to validate the model using the numerical FEM model by defining the coefficients $\alpha_3 = 0.75$, $\alpha_P = 0.76$, and $\alpha_1 = 1.09$. The stresses in the validated model were underestimated by no more than 15% under the stresses σ_3 and P. On the other hand, under the stresses P parallel to the plane of head joints σ_1 the underestimation did not exceed 6%.

In summary:

- the acoustoelastic (AE) method was confirmed to be applied to mean hydrostatic stresses in AAC,
- the relationships between the acoustoelastic coefficient δ_P and AAC density and moisture content AAC were established,
- the performed measurements of the velocity of ultrasonic wave propagation were used to quite precisely determine the mean hydrostatic stresses in the wall (when compared to the FEM calculations) when the number of measuring points was high,
- a reduction in the measuring points significantly underestimated the mean hydrostatic stresses,
- the method validation considerably diminished differences between the experimentally obtained results and the calculations. The maximum overestimation of stress values did not exceed 15%, and the underestimation was at the level of 6%.
- an empirical nature of the employed method constraints possible applications to the complete range of standard stresses in the masonry. The reliable estimation of the mean stresses for the model validated can be used even to the level of $<0.75\sigma_{3max}$.

Also, the minimum number of measurements were defined to ensure reliability of the results at the pre-determined measurement error at the specified level of confidence. If the tests are to measure normal stresses in the plane of bed joints, then the minimum required number of measuring points is 22 measuring points/m^2. The tests focused on the analysis

of the complex state of stresses require the minimum number of measurements equal to 61 measurements/m^2.

Specifying the detailed guidelines for in-situ tests for structures at the present stage of analyses of masonry structures is impossible. It is required to conduct additional tests on slender walls to determine the bending effect (varied stress state in the wall) and to improve the methodology of selecting the measuring points. The selection method of measuring points used to evaluate both the complex and the uniaxial stress state [11] may prove to be inadequate for bending. The double-sided access to the structure can be another problem. Hence, further tests are planned to be performed on the AE coefficient AE (β_{133}) in the AAC wall with one-sided access.

Author Contributions: Conceptualization, R.J. and K.S.; Methodology, R.J.; Software, K.S. and P.K.; Validation, K.S. and P.K.; Formal analysis, R.J.; Investigation, R.J., K.S., and P.K.; Data curation, K.S.; Writing—original draft preparation, R.J., K.S., and P.K.; Writing—review and editing, R.J., K.S., and P.K.; Visualization, R.J.; Supervision, R.J.; Project administration, R.J. All authors have read and agreed to the published version of the manuscript.

Funding: The research reported in this paper was co-financed by the European Union from the European Social Fund in the framework of the project "Silesian University of Technology as a Center of Modern Education based on research and innovation" POWR.03.05.00-00-Z098/17. Part of the costs related to this research was co-financed by the Laboratory of Civil Engineering Faculty and Department of Building Structures at the Silesian University of Technology. Krzysztof Stebel was partially financed by the grant from SUT-subsidy for maintaining and developing the research potential in 2021.

Institutional Review Board Statement: Not applicable.

Informed Consent Statement: Not applicable.

Data Availability Statement: Data available on request due to restrictions eg privacy or ethical The data presented in this study are available on request from the corresponding author. The data are not publicly available due to subsequent analyzes and publications.

Acknowledgments: Authors would like to thank students of the Silesian University of Technology—Magdalena Lempa, Piotr Dors, Kamil Mosz, Wojciech Weber—who participated in the preparatory works and basic tests of the research stand. Special thanks go to the experts involved in the project: Wociech Mazur (the ARAMIS software), Jan Pizoń (technology of concrete) for their help in preparing the test elements and interpreting the results. The author would like to express particular thanks to Solbet company for valuable suggestions and the delivery of masonry units, mortar which were used to prepare test models and perform tests.

Conflicts of Interest: The author declare no conflict of interest.

References

1. Auld, B.A. *Acoustic Fields an Waves in Solid*; John Wiley and Sons: New York, NY, USA; London, UK; Sydney, NSW, Australia; Toronto, ON, Canada, 1973.
2. Bayer, R.T.; Letcher, S.V. *Phisical Ultarsonics*; Academic Press: New York, NY, USA; London, UK, 1969.
3. Malhotra, V.M.; Carino, N.J. *Handbook on Nondestructive Testing of Concrete*; CRC Press: Boca Raton, FL, USA, 2003.
4. Huan, H.; Liu, L.; Mandelis, A.; Peng, C.; Chen, X.; Zhan, J. Mechanical Strength Evaluation of Elastic Materials by Multiphysical Nondestructive Methods: A Review. *Appl. Sci.* **2020**, *10*, 1588. [CrossRef]
5. Hola, J.; Schabowicz, K. State-of-the-art non-destructive methods for diagnostic testing of building structures—Anticipated development trends. *Arch. Civ. Mech. Eng.* **2010**, *10*, 5–18. [CrossRef]
6. Breysse, D. Nondestructive evaluation of concrete strength: An historical review and a new perspective by combining NDT methods. *Constr. Build. Mater.* **2012**, *33*, 139–163. [CrossRef]
7. Reda, H.; Karathanasopoulos, N.; Elnady, K.; Ganghoffer, J.F.; Lakiss, H. The role of anisotropy on the static and wave propagation characteristics of two-dimensional architectured materials under finite strains. *Mater. Des.* **2018**, *147*, 134–145. [CrossRef]
8. Reda, H.; Elnady, K.; Ganghoffer, J.F.; Lakiss, H. Wave propagation in pre-deformed periodic network materials based on large strains homogenization. *Compos. Struct.* **2018**, *184*, 860–871. [CrossRef]
9. Srikantha Phani, A.; Woodhouse, J.; Fleck, N.A. Wave propagation in two-dimensional periodic lattices. *J. Acoust. Soc. Am.* **2006**, *119*, 1995–2005. [CrossRef]

10. Gonella, S.; Ruzzene, M. Analysis of in-plane wave propagation in hexagonal and re-entrant lattices. *J. Sound Vib.* **2008**, *312*, 125–139. [CrossRef]
11. Jasiński, R. Identification of Stress States in Compressed Masonry Walls Using a Non-Destructive Technique (NDT). *Materials* **2020**, *13*, 2852. [CrossRef]
12. Gennisson, J.; Renier, M.; Catheline, S. Acoustoelasticity in soft solids: Assessment of the nonlinear shear modulus with the acoustic radiation force. *J. Acoust. Soc. Am.* **2007**, *122*, 3211–3219. [CrossRef]
13. Homann, M. Porenbeton Handbuch. Planen und bauen Mit system, 6. In *Auflage Hannover*; Bauverlag: Gütersloh, Germany, 2008; ISBN 978-3-7625-3626-0.
14. Jasiński, R.; Drobiec, Ł.; Mazur, W. Validation of Selected Non-Destructive Methods for Determining the Compressive Strength of Masonry Units Made of Autoclaved Aerated Concrete. *Materials* **2019**, *12*, 389. [CrossRef]
15. Jasiński, R. Determination of AAC masonry compressive strength by semi destructive method. *Nondestruct. Test. Diagn.* **2018**, *3*, 81–85. [CrossRef]
16. Biot, M.A. The influence of initial stress on elastic waves. *J. Appl. Phys.* **1940**, *11*, 522–530. [CrossRef]
17. Huges, D.S.; Kelly, J.L. Second Order Elastic Deformation of Solids. *Phys. Rev.* **1953**, 1145–1149. [CrossRef]
18. Bergman, R.H.; Shahbender, R.A. Effect of statically applied stresses on the velocity of propagation of ultrasonic waves. *J. Appl. Phys.* **1958**, *29*, 1736–1738. [CrossRef]
19. Tokuoka, T.; Saito, M. Elastic wave propagations and acoustical birefringence in stressed crystals. *J. Acoust. Soc. Am.* **1968**, *45*, 1241–1246. [CrossRef]
20. Husson, D.; Kino., G.S. A perturbation theory for acoustoelastic effects. *J. Appl. Phys.* **1982**, *53*, 7250–7258. [CrossRef]
21. Benson, R.W.; Raelson, V.J. Acoustoelasticity. *Prod. Eng.* **1959**, *20*, 56–59.
22. Nikitina, N.Y.; Ostrovsky, L.A. An ultrasonic method for measuring stresses in engineering materials. *Ultrasonics* **1998**, *35*, 605–610. [CrossRef]
23. Dorfi, H.R.; Busby, H.R.; Janssen, M. Ultrasonic stress measurements based on the generalized acoustic ratio technique. *Int. J. Solids Struct.* **1996**, *33*, 1157–1174. [CrossRef]
24. Man, C.; Lu, W.Y. Towards an acoustoelastic theory for measurement of residual stress. *J. Elast.* **1987**, *17*, 159–182. [CrossRef]
25. Murnaghan, F.D. *Finite Deformation of an Elastic Solid*; Wiley: New York, NY, USA, 1951.
26. Murnaghan, F.D. Finite deformations of an elastic solid. *Am. J. Math.* **1937**, *59*, 235–260. Available online: https://www.jstor.org/stable/2371405 (accessed on 10 April 2020). [CrossRef]
27. Tylczyński, Z.; Mróz, B. The influence of uniaxial stress on ultrasonic wave propagation in ferroelastic $(NH_4)_4LiH_3(SO_4)_4$. *Solid State Commun.* **1997**, *101*, 653–656. [CrossRef]
28. Takahashi, S.; Motegi, R. Measurement of third-order elastic constants and applications to loaded structural materials. *SpringerPlus* **2015**, *4*, 1–20. [CrossRef]
29. Takahashi, S. Measurement of third-order elastic constants and stress dependent coefficients for steels. *Mech. Adv. Mater. Mod. Process.* **2018**, 4. [CrossRef]
30. Egle, D.M.; Bray, D.E. Measurement of acoustoelastic and third-order elastic constants for rail steel. *J. Acoust. Soc. Am.* **1976**, *60*, 741–744. [CrossRef]
31. Takahashi, S. Stress Measurement Method and its Apparatus. U.S. Patent 7299138, 10 December 2007.
32. Deputat, J. *Properties and Use of the Elastoacoustic Phenomenon to Measure Self-Stress*; Institute of Fundamental Technological Research Polish Academy of Sciences: Warsaw, Poland, 1987. (In Polish)
33. EN 771-4:2011. *Specification for Masonry Units—Part 4: Autoclaved Aerated Concrete Masonry Units*; CEN: Brussels, Belgium, 2012.
34. Bartlett, F.M.; Macgregor, J.G. Effect of Moisture Condition on Concrete Core Strengths. *ACI Mater. J.* **1993**, *91*, 227–236.
35. Suprenant, B.A.; Schuller, M.P. *Nondestructive Evaluation & Testing of Masonry Structures*; Hanley Wood Inc.: San Antonio, TX, USA, 1994; ISBN 978-0924659577.
36. McCann, D.M.; Forde, M.C. Review of NDT methods in the assessment of concrete and masonry structures. *NDT E Int.* **2001**, *34*, 71–84. [CrossRef]
37. Jasiński, R.; Stebel, K.; Domin, J. Application of the DIC Technique to Remote Control of the Hydraulic Load System. *Remote Sens.* **2020**, *12*, 3667. [CrossRef]
38. Polish Patent Office. The Testing Machine for Testing the Elements and Structures. Niepodległości 188/192, 00-950. Patent 432225, 16 December 2019.
39. Klopot, T.; Skupin, P.; Grelewicz, P.; Czeczot, J. Practical PLC-based Implementation of Adaptive Dynamic Matrix Controller for Energy-Efficient Control of Heat Sources. *IEEE Trans. Ind. Electron.* **2020**. [CrossRef]
40. Nowak, P.; Stebel, K.; Klopot, J.; Czeczot, T.; Fratczak, M.; Laszczyk, P. Flexible function block for industrial applications of active disturbance rejection controller. *Arch. Control. Sci.* **2018**, *28*, 379–400. [CrossRef]
41. Nocoń, W.; Polaków, G. *LabVIEW Based Cooperative Design for Control System Implementation*; CDVE 2011, LNCS; Luo, Y., Ed.; Springer: Berlin/Heidelberg, Germany, 2011; Volume 6874, pp. 137–140.
42. Bolton, W. *Mechatronics Electronic Control Systems in Mechanical and Electrical Engineering*; Prentice Hall: Hoboken, NJ, USA, 2009; ISBN 978-0-13-240763-2.
43. Rohner, P. *Industrial Hydrualic Control*; Willey: Hoboken, NJ, USA, 1995; ISBN 958149313.
44. Bolton, W. *Pneumatic and Hydraulic Systems*; Butterworth-Heinemann: Oxford, UK, 1997; ISBN 750638362.

45. Aciatore, D.G.; Histand, M.B. *Introduction to Mechatronics and Measurement Systems*; McGraw-Hill Companies: New York, NY, USA, 2012; ISBN 978-0072402414.
46. EN 1015-11:2001/A1. *Methods of Test for Mortar for Masonry. Part 11: Determination of Flexural and Compressive Strength of Hardened Mortar*; CEN: Brussels, Belgium, 2007.
47. EN 998-2. *Specification for Mortar for Masonry. Masonry Mortar*; CEN: Brussels, Belgium, 2003.
48. Chu, T.C.; Ranson, W.F.; Sutton, M.A.; Peters, W.H. Application of digital-image-correlation techniques to experimental mechanics. *Exp. Mech.* **1985**, *25*, 232–244. [CrossRef]
49. Lord, J.D. *Digital Image Correlation (DIC), Modern Stress and Strain Analysis. A State of the Art Guide To Measurement Techniques, BSSM*; Eaton Evans, J., Dulie-Barton, J.M., Burguete, R.L., Eds.; University of Southampton: Southampton, UK, 2009; pp. 14–15.
50. Pan, K.; Yu, R.C.; Hang, X.; Ruiz, G.; Wu, Z. Propagation Speed of Dynamic Mode-I Cracks in Self-Compacting Steel Fiber-Reinforced Concrete. *Materials* **2020**, *13*, 4053. [CrossRef] [PubMed]
51. Blenkinsopp, R.; Roberts, J.; Parland, A.; Sherratt, P.; Smith, P.; Lucas, T. A Method for Calibrating a Digital Image Correlation System for Full-Field Strain Measurements during Large Deformations. *Appl. Sci.* **2019**, *9*, 2828. [CrossRef]
52. Jasiński, R. *Research and Modelling of Masonry Shear. Walls*; Silesian University of Technology: Gliwice, Poland, 2017; ISBN 978-83-7880-477-2.
53. Volk, W. *Applied Statistics for Engineers*; Literary Licensing, LLC: Whitefish, MT, USA, 2013.
54. Sundar, V.S.; Manohar, C.S. Updating reliability models of statically loaded instrumented structures. *Struct. Saf.* **2013**, *40*, 21–30. [CrossRef]
55. Nowak, A.; Collins, K.R. *Reliability of Structures*, 2nd ed.; CRC Press: London, UK, 2013; ISBN 9780429107467. [CrossRef]

materials

MDPI

Article

Application of X-ray Computed Tomography to Verify Bond Failures Mechanism of Fiber-Reinforced Fine-Grain Concrete

Grzegorz Piotr Kaczmarczyk [1,*], Roman Kinasz [1], Vitaliy Bilozir [2] and Ivanna Bidenko [2]

[1] Department of Geomechanics, Civil Engineering and Geotechnics, The Faculty of Civil Engineering and Resource Management, AGH University of Science and Technology, Al. Mickiewicza 30, 30-059 Cracow, Poland; rkinash@agh.edu.pl
[2] Department of Building Structures, Lviv National Agrarian University, V. Velikogo 1, 80381 Dublyany, Ukraine; bilozir.vitaly@ukr.net (V.B.); ivannabidenko1@gmail.com (I.B.)
* Correspondence: grzegorz.kaczmarczyk@agh.edu.pl

Abstract: This paper proposes the use of X-ray computed tomography (μCT, xCT) measurements together with finite element method (FEM) numerical modelling to assess bond failures mechanism of fiber-reinforced fine-grain concrete. Fiber-reinforced concrete is becoming popular for application in civil engineering structures. A dynamically developing topic related to concretes is the determination of bond characteristics. Nowadays, modern technologies allow inspecting the inside of the element without the need to damage its structure. This paper discusses the application of computed tomography in order to identify damage occurring in the structure of fiber-reinforced fine-grain concrete during bond failure tests. The publication is part of a larger study to determine the bonding properties of Ukrainian steel fibers in fine-grain concrete. The authors focused on the visual evaluation of sections obtained from tomographic data. Separately, the results of volumetric analysis were presented to quantitatively assess the changes occurring in the matrix structure. Finite element analysis is an addition to the substantive part and allows us to compare real damage areas with theoretical stress concentration areas. The result of the work is the identification of a path that allows verification of the locations where matrix destruction occurs.

Keywords: fine-grain concrete; bond; industrial computed tomography; numerical simulation; xCT; fiber

Citation: Kaczmarczyk, G.P.; Kinasz, R.; Bilozir, V.; Bidenko, I. Application of X-ray Computed Tomography to Verify Bond Failures Mechanism of Fiber-Reinforced Fine-Grain Concrete. *Materials* **2022**, *15*, 2193. https://doi.org/10.3390/ma15062193

Academic Editors: Lizhi Sun, Alessandro P. Fantilli and Karim Benzarti

Received: 1 February 2022
Accepted: 14 March 2022
Published: 16 March 2022

Publisher's Note: MDPI stays neutral with regard to jurisdictional claims in published maps and institutional affiliations.

1. Introduction

Economic changes resulting from the intensity of mankind's activities are forcing society to reuse available materials. Recycling has become an everyday habit, and newer and newer recovery technologies try to ensure minimal waste. New trends are forming, such as *urban mining* [1]. Properly implemented, urban mining process allows for effective recycling of valuable raw materials. In the construction industry, the dynamic development of new-generation concretes, so-called *green concretes*, has been observed [2]. This trend adds additional components to concrete mixes such as recycled aggregate, ash, or recycled steel in order to improve the environmental standard while ensuring the assumed physical-strength properties [3,4].

Construction and demolition waste, commonly referred to as CDW, is increasingly being used in the construction industry [5]. Sources also include recycled tire steel fiber (RTSF) in this group. Recycled tire steel wire is used as a fiber in plain concrete and concrete with recycled aggregate in volume proportions of 0.5 and 1% [6]. The introduction of recycled tire waste into the steel mixture resulted in a decrease in compressive strength with an improvement in tensile test results [7]. It is worth noting the additional challenges associated with corrosion susceptibility [8]. Steel-fiber-reinforced concrete (SFRC) is not only about using waste materials. There are functioning production lines of industrial steel fiber (ISF) e.g., Micro- or Hooked-end fiber. There are differences in the obtained

mechanical parameters of mixtures reinforced with recycled and dedicated fibers, but the nature of their behavior remains very similar [9]. Research on one group influences the development of the whole RTSF trend. Industrial-fiber-reinforced concrete has been studied reasonably accurately in terms of compression [10], impact resistance [11], and torsion [12]. SFRC can be incorporated into more complex composites using, for example, steel profiles [13]. Studies of compressive fatigue behavior and failure evolution with similar materials use digital image correlates to determine deformation and strain [14]. The growing interest in SFRC has led researchers to investigate the problem of bonding between fiber and concrete matrix. A step in the analysis of the contact between two materials can be a visual assessment of behavior occurring at their interface. Therefore, for obvious reasons, macroscopic inspection is not possible. Modern technology and computed tomography can provide assistance [15]. The authors see a research gap in the use of CT to verify the bond failure mechanism of fiber-reinforced fine-grain concrete.

Computed tomography is typically associated with medical applications. The first CT scanner was developed in 1973 and its authors—Godfrey Newbold Houns-field and Allan MacLeod Cormack—received the Nobel Prize in 1979. Almost half a century of technology development has made modern tomographic examinations highly automated, safer, and faster [16]. Computed tomography allows nondestructive inspection of elements by determining their parameters. Speaking of the tomography itself, it should also be noted that there are many different techniques available, using different signal sources. Some tomographic technologies have a narrow scope of application. Authors distinguish three groups most frequently used in industry:

- Electrical Resistance Tomography, used to determine slurry flow measurements [17].
- Ultrasound tomography, which can be used to visualize the internal behavior of a concrete structure [18,19].
- X-ray microtomography (XCT, μCT, X-ray CT), covering the entire spectrum of materials [20,21]; applications of extended XCT scanning and neutron CT are also known [22].

X-ray tomographs used in industry are based on X-ray spectroscopy. A detailed description of the principle of operation was published in [20]. The device has been in use for more than 20 years and the information on its concept of operation has not become outdated. An illustrative device is shown in Figure 1. An object is inspected in a special chamber of the device. The item is placed between the radiation emitter, the so-called lamp, and the detector. The device is controlled by determining the position of the object in the space between the lamp and the detector, entering the value of voltage and current generating radiation (power), and determining the operating characteristics of the detector. Appropriate selection of parameters allows the acquisition of results enabling further 3D reconstruction of the object. In contrast with tomography used in the practice of medicine (where the comfort and health of the patient is a priority), during an industrial examination, the detector and the lamp remain in a fixed position, while the sample is rotated along the vertical axis. In the course of a single scan, thousands of absorption measurements of the radiation beam penetrating the examined object are made. A schematic view of the cone beam tomograph and the inside of the chamber are shown in Figure 2.

The next step is the reconstruction of the 3D volume. During a full rotation, the device generates thousands of images in high grayscale (e.g., the GE Phoenix v | tomex | m uses 14 bit). The most common is the implementation of complex algorithms at the reconstruction stage, resulting in correction of images such as beam hardening correction, automatic geometry calibration, and geometry optimization [23,24]. The reconstructed object can be visually inspected by analyzing 2D cross-sectional images, 3D images, and further volumetric analysis. Modern CT images are characterized by highly detailed detectability, allowing details <1 μm to be seen [25].

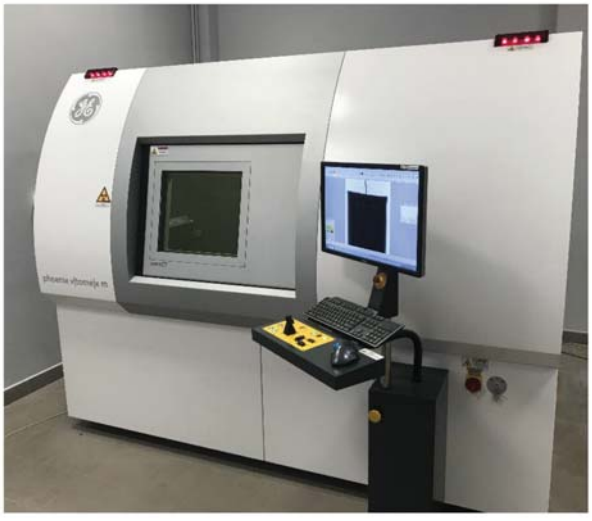

Figure 1. X-ray CT scanner GE phoenix v | tomex | m.

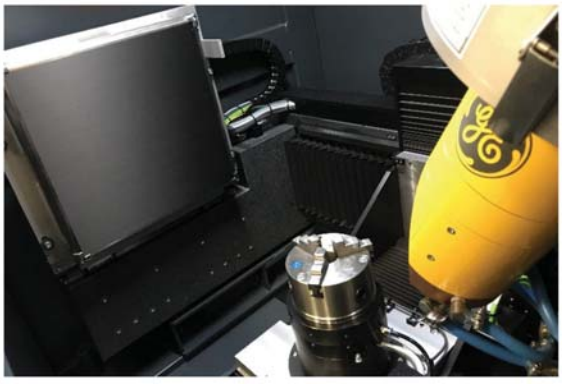

Figure 2. The tomographic chamber of the cone beam device.

The current software offers a number of built-in analysis types that are helpful when working with CT data. The leading analyses are porosity, geometric deviation, and material orientation analysis. The software also allows for FEM calculations and flow simulations. [26]. Sources indicate the use of data obtained from CT scans to evaluate the compactness of concrete [27]. The method was also used to describe the surface of concretes [28]. Existing methods for working with CT-acquired data are described extensively in the publication [27]. Studies on the effect of static loading on concrete specimens using tomographic imaging have been reported in [29]. The usefulness of the tomographic image method in evaluating shear tests is pointed out in [30]. There are studies that show how to determine the change in pore size of a concrete sample undergoing freezing cycles by tomography using a medical device [31]. Basic tomographic studies of steel-fiber-reinforced concretes are presented in [32]. The tomographic analysis mainly focused on the orientation of fibers in space and the cracks formed during the strength tests.

An extensive review of the analysis of concrete and asphalt construction materials is presented in [33]. According to [34], porosity analysis of concrete materials by microCT is popular because of the inherent porosity of such materials and the important role that

pores can play in mechanical and transport properties. There are significant correlations between pore size distribution and concrete strength [35], and the transport properties of concrete [36]. Another application that researchers find for computed tomography in the analysis of fiber-reinforced concrete is the analysis of fiber distribution. A homogeneous distribution is a key factor for the correct behavior of a fiber concrete element. Fiber orientation has been clearly indicated by CT in [37]. At the same time, in [38], computed tomography was used to determine fiber distribution in macro-plastic fiber-reinforced concrete slab-panels, indicating the versatility and usefulness of CT in analyzing the distribution of fibers of different densities.

2. Materials and Methods

2.1. Specimens and Strength Testing

The essence of the planned strength tests was to determine the forces required to pull out the fibers of the concrete cubes. Hooked-end fibers were placed in the concrete cubes (Lviv National Agrarian University, Lviv, Ukraine. Prisms 50 × 50 × 100 mm were made of fine-grained concrete. To vary the results, the fibers were anchored at three lengths: 10, 15, and 25 mm. The geometry of the fiber is shown in Figure 3a. The bend results in improved bonding, and fibers with this shape are widely used. The tested samples were based on concrete with the following formulation: cement M400 444 kg/m^3, water 240 l/m^3, sand 1644.43 kg/m^3. The w/c ratio was kept at 0.54.

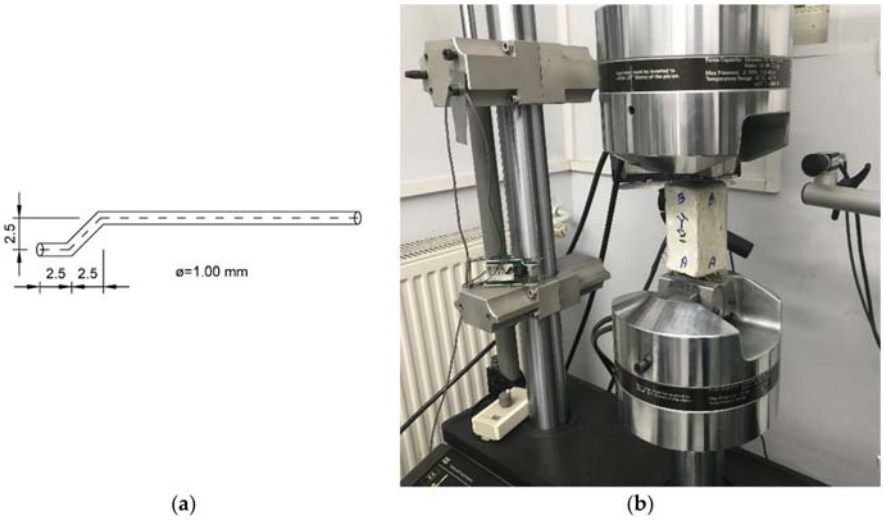

Figure 3. Laboratory testing of concrete specimens with fibers: (**a**) nominal fiber geometry; (**b**) MTS measurement system with test specimen.

In order to obtain general concrete parameters, 12 cubic concrete samples were subjected to uniaxial compression testing according to the procedure in [39]. The test series were tagged as Series 10, Series 15, and Series 25, respectively. Strength corresponds to the concrete class C25/30. This study is a continuation of the research conducted by the authors' international group [40,41]. During the test, one end of the specimen was fixed. The other end was acted upon by force. The detailed methodology is described in [40]. An analytical approach for determining bond parameters is presented in [41]. Testing was performed on the machine shown in Figure 3b. During the test, displacement was controlled. The pullout speed was set at 0.05 mm/s. The adopted methodology is in accordance with the review in [42].

A similar study, but on materials of a different type, was presented in [43], where the essence of the study was to determine the chemical bond properties of Polyvinyl Alcohol—Engineered Cementations Composite. The authors took a similar approach to strength testing.

2.2. CT Scan

The tomographic examinations were performed on a GE Phoenix v|tomex|m device (General Electric Company, Hürth, Germany) with a microfocus lamp using a cone beam. The warm-up and centering procedure was carried out on the instrument. In order to test irregularly shaped specimens, the samples were mounted on a low-absorbent foam for stable mounting on a manipulation table. The specimen was positioned to focus the viewing range on the fiber/concrete interface—the Region of Interest (ROI) option was selected. The ROI focuses the scope of the test on a portion of the specimen allowing us to select the section of interest. Each specimen was scanned twice, before and after the strength test, with the same scanning parameters—130 kV at 250 µA. A copper filter of constant thickness was used during the test. The measurement was performed with an accuracy at which the voxel dimension was equivalent to 30 µm. A calibration procedure was performed according to the manufacturer's recommendations. One examination assumed the taking of 2700 images. A single run lasted approximately 50 min. During the examination, the detector's shift module was activated to exclude the effect of defect of a single detector pixel and the auto-sco function, which allows for geometry optimization. For safety reasons, the radiation level was monitored during and after the examination.

2.3. Volumetric Analysis

The first task was to reconstruct separate 3D solids based on data from separate scans. The program provided by the manufacturer of the tomograph (General Electric Company, Hürth, Germany), datos|x, was used for this purpose. During the reconstruction, the beam hardening correction, automatic geometry calibration, and geometry optimization algorithms were used. The reconstructed 3D geometry allows for visual inspection and further analysis.

Afterwards, a registration of two scans (before and after pulling out the metal element) was performed. Scanning a component using ROI leads to one fundamental difficulty: there is no complete image of the outer edges, making it difficult to bring the two scans into a common coordinate system. In order to establish a common position, an internal algorithm was developed. The procedure required determining the porosity of two samples. Then, the coordinates of the 11 largest pores and the coordinates of the centers of gravity of the two samples were entered as input to the script. The transition between coordinate systems was determined. In successive steps, the coordinates of progressively smaller pores were compared. The 3D rotation angles and the displacement vector of one of the samples were output. Fitting was assessed visually. After 10 shift-rotation iterations, a correct match between the two data sets was found. A diagram of data workflow is shown in Figure 4.

Porosity determination is widely used in concrete testing [33,44] and describing changes in the material caused by external factors. Leading CT software (3.4, Volume Graphic, Stockholm, Sweden) allows automated porosity/inclusion analysis. Before the porosity analysis were calculated, the absorption characteristics of three materials—steel, concrete, and air—are defined. The process of determining the volume of air voids was carried out on the reconstructed 3D solid. The VGDefX algorithm set to Voids mode was used. The pores were considered significant if their volume exceeded 8 voxels. The analysis reveals air voids in the entire solid or in a portion of the solid indicated by the operator. The evaluation is performed visually and based on tabular summaries and graphs. Depending on the void size, the pores are visualized with different colors on the cross-sections and in the 3D view. In addition, the distribution of pores as a function of the respective coordinate is clearly measurable.

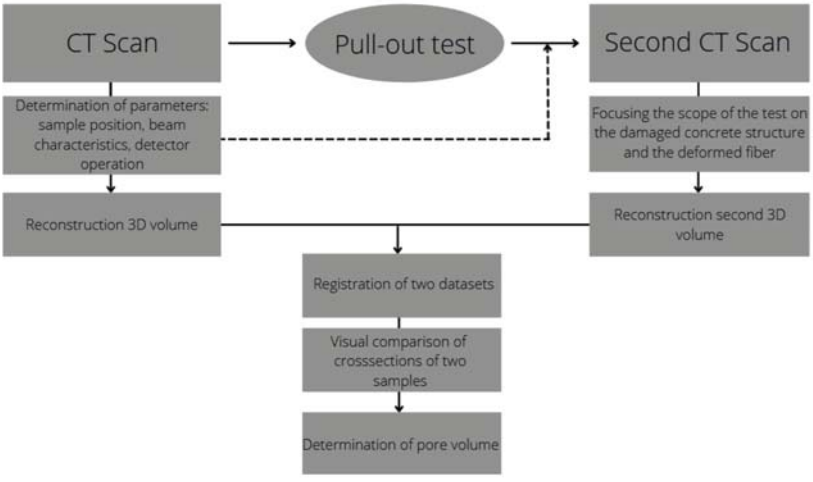

Figure 4. Data workflow diagram.

2.4. Numerical Simulations

The development of tomographic analysis allows us not only to evaluate data inside a given CT software, but also to further transform the obtained data and perform strength analyses. The dedicated software has a built-in Finite element method (FEM) calculation module; however, it is only designed for basic simulations [26]. The authors of this paper note the great potential for applications of microtomography-acquired data (especially geometric data) in numerical simulations. So far, sources [45] indicate the use of tomographic images to reconstruct the sample geometry as a mesh grid.

The authors decided to develop models of fibers that could be numerically extracted from a three-dimensional (3D) concrete block. The CT data allow us to reconstruct the geometry in two ways: develop a surface consisting of triangular planes or define the geometry by using simple solids (e.g., cubes, spheres, or cylinders). The authors' experience shows the wide applicability of the mesh method when working with samples with complex geometries. Fine triangles very accurately described the surface of, for example, a transverse flute, the model of which was used to simulate airflow. The high variability of the geometry justified the use of a complex meshing method, which in further steps, needed powerful computational software and high computing power. The second approach involves replacing the geometry of a given element by fitting basic 3D solids. The solids are matched in a semiautomated way. The approach enables fast and fairly accurate reproduction of the actual geometry of uncomplicated shaped elements such as simple rods, cubes, or rings. The approach allows for optimal use of computing power and a better representation of the geometry than the popular 3D extrude. Due to the variable shape of the fibers, it was deemed necessary to develop an accurate model containing a large number of triangles.

The purpose of the analysis was to determine the stresses occurring at the contact between the steel fiber and the concrete. The assumed numerical verification would allow us to determine where the failure of the concrete structure may occur. In the course of the work, the focus was on accurate mapping of individual fibers extracted from concrete specimens. The fiber defined by the triangles was subtracted from the concrete cube. Visually, in Figure 5, the fiber is shown in red and the concrete in blue. Due to the innovative approach to the applicability of CT data in the numerical calculations, the distribution of aggregate and air pores in the concrete mix was neglected. When working with this type of data, the process of meshing 3D solids can be problematic. The calculation of a specimen where the fiber has a radius of 0.5 mm required the use of extremely small finite

elements. A manual check of the mesh size was made and it was determined that the fiber finite elements should be 0.15 mm in size. Optimization of the mesh size allowed for variation in the size of elements responsible for the concrete structure—denser elements in the immediate area of the fiber resulted in higher accuracy of the numerical solution, while larger elements (5 mm) at the edges allowed for shorter computation time. The resulting models consisted of approximately 3 million tetrahedral finite elements. The calculations were performed in midas GTS NX software (2019 ver. 1.2, MIDAS Information Technology Co., Seongnam, Republic of Korea).

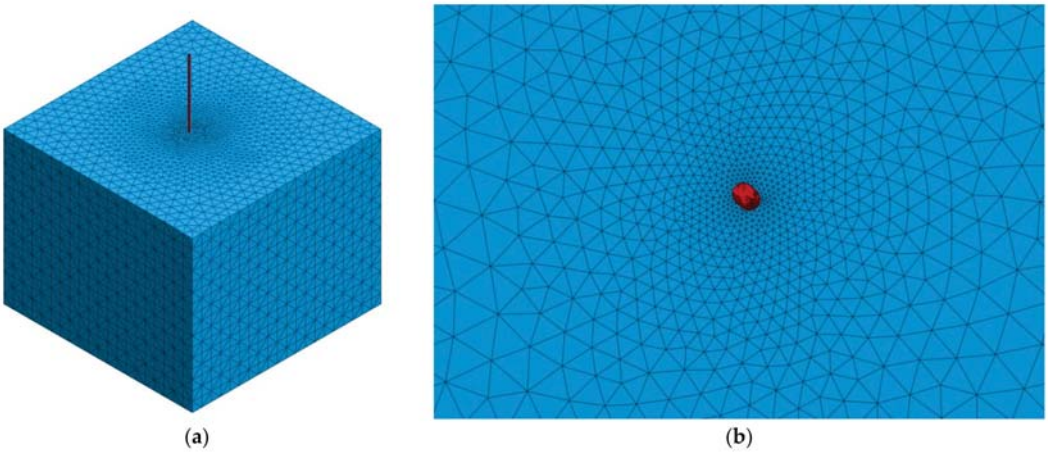

Figure 5. Mesh model: (**a**) isometric view of the mesh; (**b**) top view—finite element size progression.

The boundary conditions assigned to the models were full fixation of the lower nodes of the concrete mesh and static load applied to the upper edge of the fiber. The assigned force was determined according to MTS press pullout tests and was taken as the series average value. The material properties for the concrete and fiber were assigned according to tests that are the basis for another article. The data loaded into the numerical software (2019 ver. 1.2, MIDAS Information Technology Co., Seongnam, Republic of Korea) (Midas GTS NX) are shown in Table 1.

Table 1. Comparison of point cloud mesh to CAD model—cumulated absolute.

Parameter	Fine-Grain Concrete	Steel Fiber
Model Type	Mohr–Coulomb	Elastic
Density (kg/m^3)	2000	7850
Elastic Modulus (GPa)	31	210
Poisson's Ratio	0.15	0.30
Frictional angle (deg)	31	Linear elastic material
Cohesion (MPa)	3.86	

3. Results

3.1. Strength Testing

Tests were conducted by pulling the fiber out of the concrete. The test was performed on an MTS Model 685.53 machine. The displacement and force values were recorded during the tests. The exact force values are shown in Table 2. The test results and analytical approach are the basis for the analyses that are part of a separate study conducted by the team. Detailed results are described in the publication [40]. Relevant to the subject of the thesis is the fact of the quasi-linear increase in the force required to pull out the fiber. At this stage, the team hypothesized that the main damage to the structure would be

expected within the bend of the fiber. The team consider that the structure of the concrete and the porosity of the matrix in the immediate vicinity of the fibers was important during the study.

Table 2. Comparison of point cloud mesh to CAD model—cumulated absolute.

Anchorage (mm)	Pullout Force (kN)	Anchorage (mm)	Pullout Force (kN)	Anchorage (mm)	Pullout Force (kN)
10	218.66	15	309.27	25	250.44
10	184.35	15	231.88	25	357.17
10	121.53	15	179.23	25	308.23
10	264.71	15	208.71	25	316.11
10	281.32	15	261.56	25	271.74
Average	214.11		238.13		300.74

3.2. Computed Tomography

The purpose of the visual inspection was to determine the potential damage occurring in the concrete structure due to the pullout force. By analyzing the scans of the samples before mechanical action with 10 mm anchorage, the contact surface between the fiber and matrix of good quality can be observed. In these specimens, no additional spaces or pores of large volume were observed at the reinforcement–matrix interface. The test did not reveal additional cracks. The aggregate was distributed homogeneously throughout the concrete. Pulling out the metal element caused visible changes within the direct contact area between the two materials. There are visible cracks in the concrete at the edge of the sample. Part of the loose material was removed during the test, reducing the volume of the concrete element. The changes are particularly visible at the top edge of the specimen and at the height of the metal bend. Visually, the changes are interpreted as a result of tensile and shear stresses acting on the matrix.

The reconstructed specimen with an anchorage length of 15 mm revealed a higher overall porosity of the concrete. Visually, pores are assessed that they have a larger diameter. In visual assessment, the difference from the specimen with anchorage length of 10 mm is found to be significant. Air spaces between fiber and concrete are locally observed. No cracks are seen in the concrete structure. Similar to the previous specimen, no aggregate sedimentation occurred. The pullout of the fiber led to the destruction of the concrete in the area where the bending of the steel element occurred. Some of the loose material was removed during the test, reducing the volume of the specimen.

The cross-section of the specimen with an anchorage length of 25 mm indicated a situation similar to the first specimens. Small air pores, uniformly distributed, are visible in the matrix. Locally, the fiber is surrounded by air pores. Cross-section analysis indicated fine cracks in the concrete around the upper contact zone. The pullout test led to crack propagation, but the material was not pulled out together with the steel fiber. The cross-sectional images are shown in Figures 6, 7 and 8a,c.

3.3. Volumetric Analysis

The primary tool used to describe the volume changes is porosity analysis. Figures 6–8 summarize the 2D cross-sections and 3D porosity analysis results, reduced to pore volume dependence plots shown on the vertical axis. The horizontal bars represent the volume of pores with a geometric center at a given height. The beginning of the coordination system was taken to be the upper surface of the analyzed sample. In Figures 6–8, the beginning of the height axis corresponds to the concrete surface. Cylinders of 2.5 cm diameter were analyzed. The heights of the cylinders are 20, 30, 30 mm respectively. Voxels belonging to fibers were excluded from the analysis—the void created by removing the steel element did not affect the results obtained. The following graphs show pore volumes in voxels. A voxel is the basic cell of data acquired during the tomography process. A voxel of a 3D

solid can be compared to a pixel in a 2D image. A local increase in porosity indicates that destruction has occurred at a particular location in the structure under analysis.

Figure 6 shows the analysis results of the sample with the fiber being anchored to a depth of 10 mm. Figure 6b,d show the results of porosity analysis before and after the fiber pullout test. Except for isolated differences, the graphs are visually consistent with each other, which speak to the correctness of the applied methodology. The main changes can be seen in two places on the graph: at 0.49 mm and at 5 mm depth. The analysis of visualization of the data indicated that the change in porosity in the range of 0–1 mm was a result of propagation of cracks created during the process of pulling out the fiber.

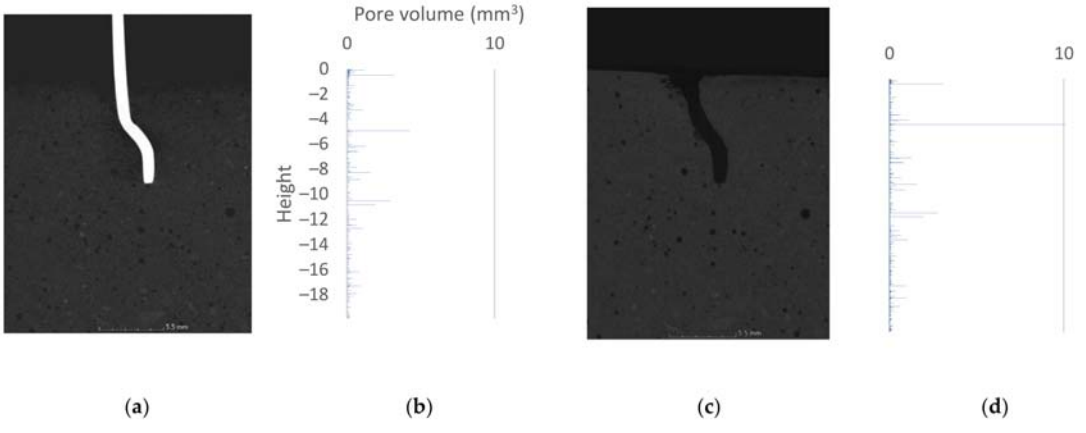

Figure 6. The 10 mm sample: (**a**) 2D cross-section before fiber pullout; (**b**) 3D porosity analysis—plot of pore volume against height in sample before fiber pullout; (**c**) 2D cross-section after fiber pullout; (**d**) 3D porosity analysis—plot of pore volume against height in sample after fiber pullout.

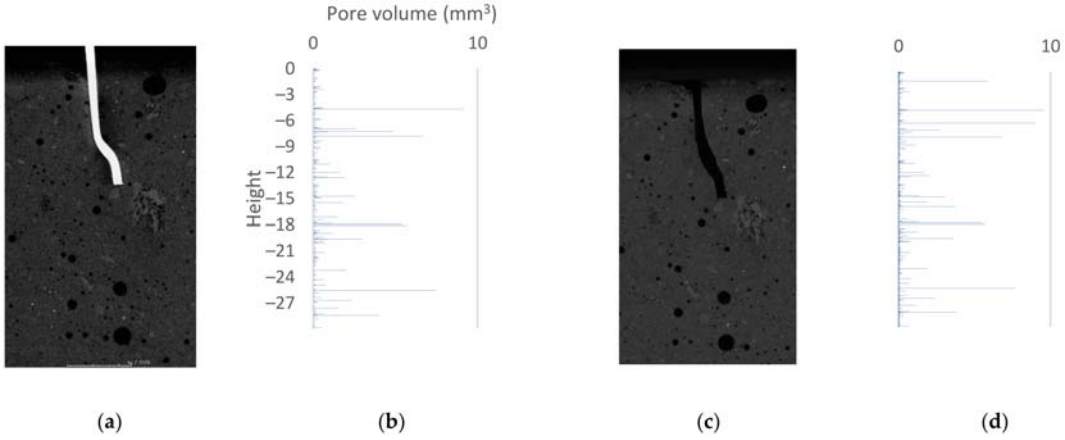

Figure 7. The 15 mm sample: (**a**) 2D cross-section before fiber pullout; (**b**) 3D porosity analysis—plot of pore volume against height in sample before fiber pullout; (**c**) 2D cross-section after fiber pullout; (**d**) 3D porosity analysis—plot of pore volume against height in sample after fiber pullout.

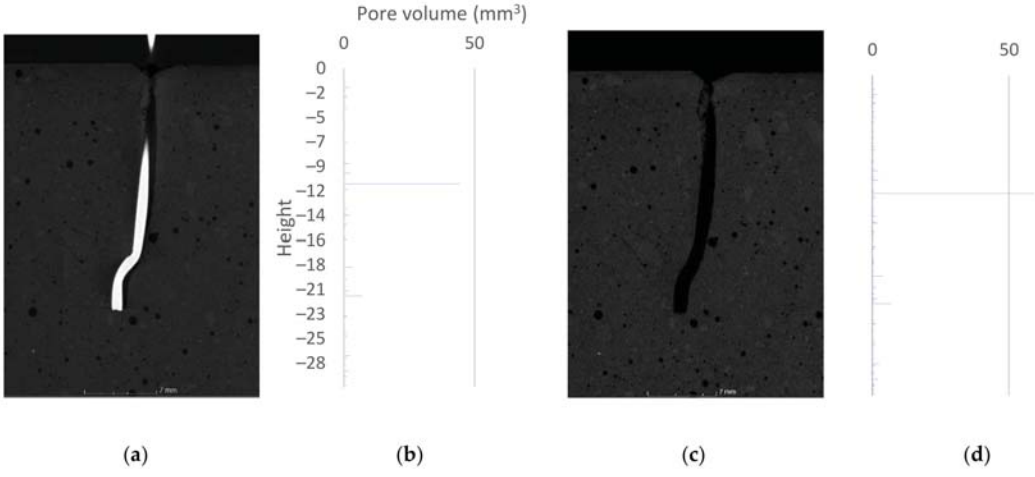

Figure 8. The 25 mm sample: (**a**) 2D cross-section before fiber pullout; (**b**) 3D porosity analysis—plot of pore volume against height in sample before fiber pullout; (**c**) 2D cross-section after fiber pullout; (**d**) 3D porosity analysis—plot of pore volume against height in sample after fiber pullout.

At a depth of 5 mm, the most significant change in structure occurred. The pore volume changed from 4 mm^3 to over 10 mm^3. Thus, there was more than a doubling of the local air space in the bend zone of the tested fiber. The increased pore volume is due to concrete deterioration and pullout of the loose material. The destruction occurred at the locations where the air pores between the fiber and concrete were noted.

When analyzing the sample with an anchorage length of 15 mm (Figure 7), additional pore volumes are noticeable, appearing after the fiber pullout test. The largest changes are seen at 1.5 and 6.5 mm. The results indicate destruction of the concrete structure within the upper contact zone—the zone near the surface of the sample. Large destruction can be seen on the lower side of the fiber curve (depth of approximately 6 mm). Destruction occurred on a smooth surface. Pulling out the fiber resulted in widening of the hole. In Figure 7c, an additional air pocket caused by fiber extraction is clearly visible.

The results for the sample with an anchorage length of 25 mm (Figure 8) indicate the presence of an air void between the fiber and the concrete. Its geometric center is located at 11 mm length. Local air voids, about which the authors wrote in the previous subsection, create a single, connected space, which locally, on individual cross sections, appears to be a separate air pocket. Based on the analysis of CT data, it can be clearly stated that adhesion forces were not transferred through the entire fiber surface. Pulling out the fiber resulted in ejection of the damaged and loose material. It should be noted that all specimens with an anchorage length of 25 mm had air voids in the "before fiber pullout test" condition. Damage to the matrix is visually apparent from the surface to a depth of 2 mm. Microcracks smaller than 2 voxels (60 μm) were not captured by the VGDefX algorithm, which was focused on finding pores larger than 8 voxels.

3.4. Numerical Simulations

The variable geometry of the fibers intuitively suggests that the stresses from the pull-out test will not be consistent along the length of the element. The advantage of numerical methods over analytical approaches is the ability to input a geometrically and materially complex system. The models developed on the basis of tomographic investigations, assuming appropriate materials, closely represent the real stress concentrations in the tested specimens. The results are summarized in Figure 9. Stress maps show shear stresses from the contact between fibers and fine-grain concrete. The visuals have been scaled so that the

color range is consistent in all three images. Stress concentration locations were indicated graphically by white arrows.

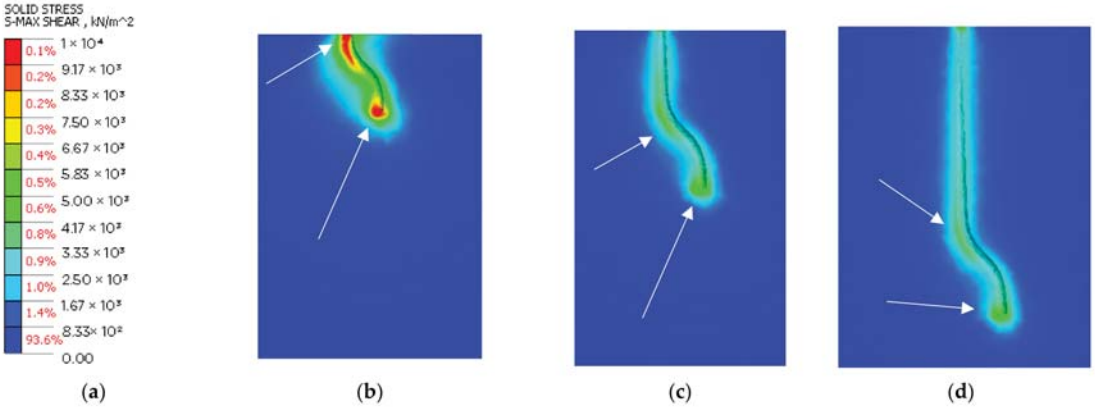

Figure 9. Cross-sectional results of 3D FEA analysis: (**a**) legend; (**b**) 2D cross-section of the model anchored at 10 mm-depth; (**c**) 2D cross-section of the model anchored at 15 mm-depth; (**d**) 2D cross-section of the model anchored at 25 mm-depth.

The highest shear stress values were obtained for the model anchored at 10 mm (Figure 9b). For this specimen, the highest strain is observed at both edges of the contact surface and reaches a value of about 10 MPa. The increased stresses occur locally. Increasing the anchorage length to 15 mm caused a decrease in the values of local stress concentrations. As in the previous model, the concentrations occur at the lower end of fiber and at the location of the element course change. The stresses exceed the value of 4 MPa. For the specimen with 20 mm anchorage, the increased stress level is noticed under the lower end of fibers. The maximum stresses reach the value of 4.07 MPa. In addition, the increased stress level occurred at the location of the change in the course of the element.

The last test containing specimens anchored at a depth of 25 mm globally indicated another reduction in stresses. As in the previous cases, the stress concentrations occur at the bottom part of the course change and just below the top surface. By identifying low stresses, the FEM analysis indicates that potential failure may occur in areas where stresses are induced by random factors such as porosity or material weakening related to the setting of the concrete itself.

The shear stresses are found locally just below the surface of the concrete and are characteristic of all three experimental models. The authors identify the lower left side of the bend as the second such location (assuming a consensus datum with that shown in Figure 9). The third location for the transfer of forces from the fiber to the dies is the bottom edge of the metal member. The last location is the result of internal forces and horizontal displacements of the end due to deformations of higher elements. The shear stresses are concentrated at the contact surface between the materials. No shear surface formation is observed inside the matrix. The numerical experiment indicates a failure model in which no damage occurs in the deep concrete structure due to adhesion, as proven by the low range of stress concentration. The bond strength is exceeded by generating excessive forces on the fiber flanks. However, damage to the concrete can appear locally.

4. Discussion

In the course of the work, the locations where deterioration of the concrete structure occurs were identified. The data were processed visually and by porosity analysis. The bar graphs in Figures 6–8 clearly show where the damage occurs. When comparing the tomographic data with the results of the 3D FEM analysis, similarity is noted in the locations

of increased stresses and increased pore volume. The authors believe that the movement of fibers itself is a key factor in the experiment. Once the bond failure occurs, pullout can appear in the following cases: when there is damage in the matrix structure (especially in the area of the component bends) or when there are plastic changes in the shape of the metal component. The authors claim that in the analyzed case, an intermediate situation occurs, where locally acting stresses and their extents indicate partial destruction of the matrix (pullout of the destroyed material) and partial plastic deformation of fibers. Visual view of the destroyed element unambiguously indicates the fact of its shape change. The authors are in agreement with the pullout behavior of hooked-end fibers described in [42]. The authors acknowledge that the fiber must undergo plastic deformation during the test. The theoretical behavior presented in the publication [42] should be expanded to include possible matrix damage. An additional aspect not addressed in the source is the effect of pores on the bonding phenomenon. Considering the fiber–pore size ratio, the statistical distribution of porosity in the matrix should be taken into account.

The FEM analysis did not include porosity information. During the visual evaluation of the tomographic data, attention was given to the concentration of damage around the existing pores. As can be seen in [46], air pores also exist between the reinforcing bars and the concrete structure, which has little effect on the bonding phenomenon that is the essence of reinforced concrete construction. The distribution, size, and shape of the pores directly affect the safety of the structure. In their work with fiber reinforced concrete, the authors have identified pores as critical locations where the edges of the concrete structure fail. Again, the authors of this paper would like to focus on the size ratios of pores and fibers, and pores and reinforcing bars. Taking into account the small size of the fiber element, pores are described as an important factor influencing the bonding phenomenon.

Regarding the material itself, the authors see practical applications for Steel-Fiber-Reinforced Concrete. The results of the experimental study on bended beams with dimensions 1500 × 150 × 60 mm [47] seem to be worth quoting. The program required three beams with the same geometry: a nominal beam, a beam with added fibers in the amount of 1.59 kg, and beam with 2.12 kg of fibers, which correspond to the coefficient of fiber reinforcement in volume, ρ_{fv} = 1.5% i 2%, respectively. The beams were loaded with concentrated force in the middle of the span. The experimentally obtained bearing capacities were 6082.5, 7055.5, and 7351.1 N·m, respectively. The use of fiber reinforcement not only improved the strength parameters but also reduced the crack propagation, which indicates the effectiveness of the SFRC trend.

The authors of article [48] presented the next step in the study of SFRC materials. They described the results of pullout tests on rebar while the concrete was additionally reinforced with steel fibers. From the failure mode studies, it was observed that the addition of 1% hooked-end steel fibers can change the failure mode of pullout specimens from premature splitting to pullout failure. The main role of the steel fibers is not necessarily to increase the strength of the bond; instead, the main role of steel fibers is to increase the ductility of the concrete, which is necessary for high-strength concrete that is prone to brittleness.

5. Conclusions

In this paper, the authors attempted to present the possibilities of tomographic image analysis. Modern approaches to research require the knowledge of modern instruments from researchers, both in terms of measurements and for further analysis. Current technology of tomographic imaging and dedicated software allows for complex defect analysis. The research itself requires experience of the operator and the ability to select parameters in such a way that the reconstructed solid is a set of high-quality data. The research can be summarized by the following conclusions:

(1) Data processing should be carried out in two ways, and each analysis requires a visual assessment. When using the results of the analysis, it is necessary to remember the assumptions made (e.g., as to the range of size and shape of the pore in the porosity analysis), which is verified visually. Obtained images present critical areas from the

point of view of bond. Industrial computed tomography allows to assess the interior of the material without interfering in its structure. The obtained cross-sectional images make it possible to unequivocally determine the areas where the stresses occurring in the concrete exceeded its strength and changes in the material occurred.

(2) Numerical models can be developed from CT data. The authors processed the data to generate models on which finite element simulations were performed. The simulation results identified the stress concentration locations. Both volumetric porosity analysis and numerical simulation indicated the same locations where damage can occur.

(3) In the course of the work, contact characteristics between materials were derived from the authors' assumptions. The combination of tomography and strength tests is a complex issue. The study can be deepened by taking into account the randomness of the pore distribution in the matrix.

Based on the tomographic data, it is possible to determine a statistical model of the pore distribution and implement it into the model using, for example, Voronoi tessellation [49], or by reconstructing the geometry directly from an exact sample. Further studies are planned to use the unique Deben CT5000 in situ loadcell tensile stage for X-Ray CT applications. Additional testing would capture changes in the sample structure over the course of the test, which may result in an accurate description of the contact properties between materials. Thus, the next step would be to develop a fully dynamic simulation of the pullout test. Adjusting the dynamic contact parameters of a fiber with a complex geometry will also allow accurate determination of the internal forces.

Author Contributions: Conceptualization, G.P.K., R.K., V.B. and I.B.; methodology, G.P.K.; software, G.P.K.; validation, G.P.K. and R.K.; formal analysis, G.P.K.; investigation, G.P.K.; resources, V.B. and I.B.; data curation, G.P.K.; writing—original draft preparation, G.P.K.; writing—review and editing, R.K.; visualization, G.P.K.; supervision, R.K.; project administration, G.P.K. All authors have read and agreed to the published version of the manuscript.

Funding: This research received no external funding.

Institutional Review Board Statement: Not applicable.

Informed Consent Statement: Not applicable.

Data Availability Statement: The data that support the findings of this study are available from the corresponding author upon request.

Conflicts of Interest: The authors declare no conflict of interest.

References

1. Arora, M.; Raspall, F.; Fearnley, L.; Silva, A. Urban mining in buildings for a circular economy: Planning, process and feasibility prospects. *Resour. Conserv. Recycl.* **2021**, *174*, 105754. [CrossRef]
2. Walach, D. Economic and environmental assessment of new generation concretes. *IOP Conf. Ser. Mater. Sci. Eng.* **2020**, *960*, 042013. [CrossRef]
3. Wałach, D. Analysis of factors affecting the environmental impact of concrete structures. *Sustainability* **2021**, *13*, 204. [CrossRef]
4. Kucharska, M.; Jaskowska-Lemanska, J. Properties of a bond between the steel reinforcement and the new generation concretes—A review. *IOP Conf. Ser. Mater. Sci. Eng.* **2019**, *603*, 042057. [CrossRef]
5. Behera, M.; Bhattacharyya, S.K.; Minocha, A.K.; Deoliya, R.; Maiti, S. Recycled aggregate from C&D waste & its use in concrete—A breakthrough towards sustainability in construction sector: A review. *Constr. Build. Mater.* **2014**, *68*, 501–516. [CrossRef]
6. Ahmadi, M.; Farzin, S.; Hassani, A.; Motamedi, M. Mechanical properties of the concrete containing recycled fibers and aggregates. *Constr. Build. Mater.* **2017**, *144*, 392–398. [CrossRef]
7. Papakonstantinou, C.G.; Tobolski, M.J. Use of waste tire steel beads in Portland cement concrete. *Cem. Concr. Res.* **2006**, *36*, 1686–1691. [CrossRef]
8. Frazão, C.; Díaz, B.; Barros, J.; Bogas, J.A.; Toptan, F. An experimental study on the corrosion susceptibility of Recycled Steel Fiber Reinforced Concrete. *Cem. Concr. Compos.* **2019**, *96*, 138–153. [CrossRef]
9. Centonze, G.; Leone, M.; Aiello, M.A. Steel fibers from waste tires as reinforcement in concrete: A mechanical characterization. *Constr. Build. Mater.* **2012**, *36*, 46–57. [CrossRef]
10. Feng, J.; Yin, G.; Tuo, H.; Wen, C.; Liu, Z.; Liang, J.; Zhang, Y. Uniaxial compressive behavior of hook-end steel and macro-polypropylene hybrid fibers reinforced recycled aggregate concrete. *Constr. Build. Mater.* **2021**, *304*, 124559. [CrossRef]

11. Yoo, D.Y.; Banthia, N. Impact resistance of fiber-reinforced concrete—A review. *Cem. Concr. Compos.* **2019**, *104*, 103389. [CrossRef]
12. Hassan, R.F.; Al-Salim, N.H.; Mohammed, N.S.; Hussein, H.H. Experimental study and theoretical prediction on torsional strength with different steel fiber reinforced concretes and Cross-Section areas. *Eng. Struct.* **2022**, *251*, 113559. [CrossRef]
13. Ming, M.; Zheng, S.; Zhang, Y.; Zheng, Y.; Yang, S.; Song, M. Experimental study on the bond-slip behavior and stress transfer mechanism between shaped steel and high-performance fiber-reinforced concrete. *Structures* **2021**, *34*, 5013–5028. [CrossRef]
14. Li, J.; Cao, S.; Yilmaz, E.; Liu, Y. Compressive fatigue behavior and failure evolution of additive fiber-reinforced cemented tailings composites. *Int. J. Miner. Metall. Mater.* **2022**, *29*, 345–355. [CrossRef]
15. Lee, H.; Kim, J.H.J.; Moon, J.H.; Kim, W.W.; Seo, E.A. Correlation between pore characteristics and tensile bond strength of additive manufactured mortar using X-ray computed tomography. *Constr. Build. Mater.* **2019**, *226*, 712–720. [CrossRef]
16. Ratajczyk, E. Rentgenowska tomografia komputerowa(CT) do zadań przemysłowych. *Pomiary Autom. Robot.* **2012**, *16*, 104–113.
17. Hashemi, S.A.; Spelay, R.B.; Sanders, R.S.; Hjertaker, B.T. A novel method to improve Electrical Resistance Tomography measurements on slurries containing clays. *Flow Meas. Instrum.* **2021**, *80*, 101973. [CrossRef]
18. Niu, Z.; Wang, W.; Huang, X.; Lai, J. Integrated assessment of concrete structure using Bayesian theory and ultrasound tomography. *Constr. Build. Mater.* **2021**, *274*, 122086. [CrossRef]
19. Schabowicz, K. Non-destructive testing of materials in civil engineering. *Materials* **2019**, *12*, 3237. [CrossRef]
20. Stock, S.R. X-ray microtomography of materials. *Int. Mater. Rev.* **1999**, *44*, 141–164. [CrossRef]
21. Dybeł, P. Effect of bottom-up placing of self-compacting concrete on microstructure of rebar-concrete interface. *Constr. Build. Mater.* **2021**, *299*, 124359. [CrossRef]
22. Kim, H.T.; Razakamandimby, R.D.F.T.; Szilágyi, V.; Kis, Z.; Szentmiklósi, L.; Glinicki, M.A.; Park, K. Reconstruction of concrete microstructure using complementarity of X-ray and neutron tomography. *Cem. Concr. Res.* **2021**, *148*, 106540. [CrossRef]
23. Brabant, L.; Pauwels, E.; Dierick, M.; van Loo, D.; Boone, M.A.; van Hoorebeke, L. A novel beam hardening correction method requiring no prior knowledge, incorporated in an iterative reconstruction algorithm. *NDT E Int.* **2012**, *51*, 68–73. [CrossRef]
24. Nguyen, V.; Sanctorum, J.G.; van Wassenbergh, S.; Dirckx, J.J.J.; Sijbers, J.; de Beenhouwer, J. Geometry Calibration of a Modular Stereo Cone-Beam X-ray CT System. *J. Imaging* **2021**, *7*, 54. [CrossRef] [PubMed]
25. GE Measurement&Control, Catalog phoenix v | tome | x m; 2019, Billerica. Available online: https://rsc.aux.eng.ufl.edu/_files/documents/24.pdf (accessed on 31 January 2022).
26. Volume Graphics. *VG Studio MAX 3.4—Manual*; Downloadable software documentation distributed by the developer; Volume Graphics: Heidelberg, Germany, 2021.
27. Kong, W.; Wei, Y.; Wang, S.; Chen, J.; Wang, Y. Research progress on cement-based materials by X-ray computed tomography. *Int. J. Pavement Res. Technol.* **2020**, *13*, 366–375. [CrossRef]
28. Sadowski, Ł.; Stefaniuk, D. The effect of surface treatment on the microstructure of the skin of concrete. *Appl. Surf. Sci.* **2018**, *427*, 934–941. [CrossRef]
29. Shi, P.F.; Yang, Y.F.; Gao, Y.; Liu, J.H. Analysis of concrete meso damage based on CT. *MATEC Web Conf.* **2015**, *31*, 3–6. [CrossRef]
30. Stefaniuk, D.; Tankiewicz, M.; Stróżyk, J. X-Ray Microtomography (μCT) as a Useful Tool for Visualization and Interpretation of Shear Strength Test Results. *Stud. Geotech. Mech.* **2015**, *36*, 47–55. [CrossRef]
31. Tian, W.; Han, N. Pore characteristics (>0.1 mm) of non-air entrained concrete destroyed by freeze-thaw cycles based on CT scanning and 3D printing. *Cold Reg. Sci. Technol.* **2018**, *151*, 314–332. [CrossRef]
32. Skarżyński, Ł.; Suchorzewski, J. Mechanical and fracture properties of concrete reinforced with recycled and industrial steel fibers using Digital Image Correlation technique and X-ray micro computed tomography. *Constr. Build. Mater.* **2018**, *183*, 283–299. [CrossRef]
33. Du Plessis, A.; Boshoff, W.P. A review of X-ray computed tomography of concrete and asphalt construction materials. *Constr. Build. Mater.* **2019**, *199*, 637–651. [CrossRef]
34. Darma, I.S.; Sugiyama, T.; Promentilla, M.A.B. Application of X-ray CT to study diffusivity in cracked concrete through the observation of tracer transport. *J. Adv. Concr. Technol.* **2013**, *11*, 266–281. [CrossRef]
35. Kumar, R.; Bhattacharjee, B. Porosity, pore size distribution and in situ strength of concrete. *Cem. Concr. Res.* **2003**, *33*, 155–164. [CrossRef]
36. Garboczi, E.J.; Bentz, D.I. Modelling of the microstructure properties of concrete. *Constr. Build. Mater.* **1996**, *10*, 293–300. [CrossRef]
37. Balázs, G.L.; Czoboly, O.; Lublóy, É.; Kapitány, K.; Barsi, Á. Observation of steel fibres in concrete with Computed Tomography. *Constr. Build. Mater.* **2017**, *140*, 534–541. [CrossRef]
38. Pujadas, P.; Blanco, A.; Cavalaro, S.; De La Fuente, A.; Aguado, A. Fibre distribution in macro-plastic fibre reinforced concrete slab-panels. *Constr. Build. Mater.* **2014**, *64*, 496–503. [CrossRef]
39. *EN 12390-3:2019*; Testing Hardened Concrete—Part 3: Compressive Strength of Test Specimens. European Committee for Standardization: Brussels, Belgium, 2019.
40. Kinasz, R.; Bilozir, V.; Shmyh, R.; Bidenko, I. Gripping of Anchor Fiber of Ukrainian Production with Fine- Grain Concrete. *IOP Conf. Ser. Mater. Sci. Eng. Pap.* **2021**, *1203*, 022050. [CrossRef]
41. Kinash, R.; Bilozir, V. Deformational calculation method of bearing capability of fiber-concrete steel bending elements. *Czas. Tech.* **2014**, *2014*, 49–58. [CrossRef]
42. Deng, Y.; Zhang, Z.; Shi, C.; Wu, Z.; Zhang, C. Steel Fiber—Matrix Interfacial Bond in Ultra-High Performance Concrete: A Review. *Engineering* **2021**. [CrossRef]

43. Li, V.C.; Wu, C.; Wang, S.; Ogawa, A.; Saito, T. Interface tailoring for strain-hardening polyvinyl alcohol-engineered cementitious composite (PVA-ECC). *ACI Mater. J.* **2002**, *99*, 463–472. [CrossRef]
44. Liu, J.; Ba, M.; Du, Y.; He, Z.; Chen, J. Effects of chloride ions on carbonation rate of hardened cement paste by X-ray CT techniques. *Constr. Build. Mater.* **2016**, *122*, 619–627. [CrossRef]
45. Dong, Y.; Su, C.; Qiao, P.; Sun, L.Z. Microstructural damage evolution and its effect on fracture behavior of concrete subjected to freeze-thaw cycles. *Int. J. Damage Mech.* **2018**, *27*, 1272–1288. [CrossRef]
46. Dybeł, P.; Kucharska, M. X-ray CT Investigation of Bond Mechanism in Reinforced SCC Elements of Different Placement Technology. *Materials* **2021**, *14*, 6236. [CrossRef] [PubMed]
47. Kinasz, R.; Bilozir, V.; Shmyh, R.; Vysochenko, A. Suspensibility of Steel Fibre Reinforced Concrete Values with External Ribbed Armature. *IOP Conf. Ser. Mater. Sci. Eng.* **2019**, *471*, 052047. [CrossRef]
48. Majain, N.; Abd. Rahman, A.B.; Adnan, A.; Mohamed, R.N. Bond behaviour of deformed steel bars in steel fibre high-strength self-compacting concrete. *Constr. Build. Mater.* **2022**, *318*, 125906. [CrossRef]
49. Sieger, D.; Alliez, P.; Botsch, M. *Optimizing Voronoi Diagrams for Polygonal Finite Element Computations, Proceedings of the 19th International Meshing Roundtable, IMR 2010, Chattanooga, TN, USA, 3–6 October 2012*; Springer: Berlin/Heidelberg, Germany, 2010; pp. 335–350. [CrossRef]

materials

MDPI

Article

The Impact of Microwave Drying on the Structure of Exemplary Soils—Insights Using X-ray Microtomography

Łukasz Kaczmarek [1], Małgorzata Jastrzębska [2,*] and Tomasz Wejrzanowski [3]

[1] Faculty of Building Services, Hydro and Environmental Engineering, Warsaw University of Technology, Nowowiejska 20, 00-653 Warsaw, Poland
[2] Faculty of Civil Engineering, Silesian University of Technology, Akademicka 5, 44-100 Gliwice, Poland
[3] Faculty of Materials Science and Engineering, Warsaw University of Technology, Wołoska 141, 02-507 Warsaw, Poland
* Correspondence: malgorzata.jastrzebska@polsl.pl; Tel.: +48-32-237-1543

Abstract: In the field of soil drying methods, rapid microwave heating is progressively replacing conventional techniques. Due to the specific heat transport caused by microwaves, the drying process can significantly modify soil structure, which, in turn, can influence mechanical and filtration characteristics. In this study, we compared structural changes of exemplary non-cohesive (medium quartz sand (MSa)) and cohesive soil (silty clay mainly composed of kaolinite (siCl)). The sample materials were subjected to three different drying methods: air-drying, conventional oven (CO) drying, and microwave oven (MO) drying (MO). Soil structure was studied using X-ray microtomography (XμCT) and described in detail by image analysis methods. The study showed that the analyzed types of heating had a negligible effect on the structure of the sands, but a significant impact in the case of silty clay. Such a phenomenon is discussed and explained in this paper. The study advances the testing of soils microwave drying in a geotechnical laboratory.

Keywords: drying of soil; microwave heating; soil structure; computed microtomography; water content

Citation: Kaczmarek, Ł.; Jastrzębska, M.; Wejrzanowski, T. The Impact of Microwave Drying on the Structure of Exemplary Soils—Insights Using X-ray Microtomography. *Materials* **2022**, *15*, 5891. https://doi.org/10.3390/ma15175891

Academic Editor: Tamas Varga

Received: 2 July 2022
Accepted: 20 August 2022
Published: 26 August 2022

1. Introduction

Different soil drying methods can have various effects on the structure and, thus, on the geomechanical and filtration features (thermally induced thermo-hydro-mechanical behavior of saturated or unsaturated soils [1–3]). The rapid change in conditions can affects the soil fabric [4] and therefore, it can weaken the soil grains or solid material, leading to cracking, fracturing, and crushing. Furthermore, with cohesive soils, the repeated drying procedure may cause bond degradation or cementation. Moreover, temperature variations can initiate mineralogical changes. All these phenomena can also occur in situ, although on a different time scale and markedly smaller temperature ranges (generally to approximately 40 °C [4,5]).

Many experimental studies have explored rapid microwave drying [6,7] and the influence of multiple wet–dry cycles (such as those that occurred during laboratory drying) on the physical and mechanical properties of soil or its mixtures with various additives (e.g., with cement, liquid modifiers, bentonite, etc.), which include thermally modified swelling parameters [8,9], hydraulic conductivity/permeability coefficients [8,10,11], shear strength [12,13], durability, stiffness, and the void ratio [12], Atterberg limits [8], and even intensification of landslides [11,14,15]. Listed soil features which may be (but do not have to be) affected by the impact of thermal changes are strongly related to changes in the macrostructure (crack intensity factor, length, and cracks opening), the microstructure (e.g., porosity and density), and the geochemical composition (mineralogy and chemical composition) of the soils [10]. Nevertheless, reducing the drying time of soils has many

implications, which make the procedure of accelerated drying of soils in the laboratory and their potential field applications important research issues.

Therefore, in this pilot study, the focus is on the influence of rapid changes in water content (because of microwave drying) on the structure of selected soil (specifically, medium sand and hydrophobic silty clay). The impact of temperature on soil structure is a complex phenomenon and requires a multifaceted approach, especially due to the variety of existing microwave drying procedures. In order to evaluate the effects of microwave drying, comparative drying in a conventional oven and air drying were performed. The reference test was the air-dry state of a sample that was not exposed to high-temperature drying. Non-invasive and non-destructive X-ray computed microtomography (XμCT) was used to determine structural changes.

2. Materials and Methods

The test procedures involved three types of drying tests using soil samples, after which the samples were exposed to X-ray computed microtomography. Structurally similar sand (3) and clay (3) samples were used in this study. The three types of drying methods used were: air-drying (21 °C, 48 h), drying in a conventional oven (105 °C, 24 h), and drying in a microwave oven (800 W, 7 min, estimated temperature < 200 °C for sand and <400 °C for silty clay).

The air-drying method was the reference test because of its non-invasive characteristic (drying at room temperature). The second method used heat energy (conventional oven drying), and is a well-standardized method for soil testing. The third method (the microwave radiation drying method) seemed to be a fast and effective alternative as compared with the previous method.

2.1. Selected Soils and Their Preparation

This comparative study tested two exemplary soil types (cohesive and non-cohesive): medium sand (MSa) and silty clay (siCl). The exact types were determined based on granulation curves according to the European standard classification [16]. According to the Unified Soil Classification System (USCS), MSa is poorly graded clean sand (SP) and siCl is inorganic clay (CL). Quartz is the dominant component of the sandy material, and silty clay is mainly composed of kaolinite. These two materials were subjected to three drying methods: one sample from each specific soil type per drying method. The range of tests was designed to indicate possible directions of study with regards to changes in structure, for the purpose of future, more focused testing.

The selection of appropriate containers for the samples was very important. Materials must be X-ray transparent and resistant to heat, as the temperature increase of some cohesive soils exposed to microwave energy can exceed 200 °C, reaching up to 800 °C [17]. For this purpose, specially designed polypropylene rigid cylindrical transparent containers (Figure 1) were chosen, measuring 25 mm in diameter, 50 mm high, and with a high melting point (>400 °C). These containers are resistant to heat energy and microwave radiation and can be placed directly into the microtomograph after drying. The density of the material lent rigidity and strength to the containers, but the density had to be lower than the soil density to avoid disturbing the microtomographic images. Figure 1 shows a container filled with a sandy sample.

The medium sand originated from excavations at a highway construction site in southern Poland. Its average water content in natural state (in situ state) was just a few percent ($w \approx 3\%$). The characteristic diameter d_{50} for the prepared soil samples was 0.42–0.47 mm. Its basic material characteristics are given in Table 1. Due to the loose state of the soil in the field, sandy material was carefully piled up to fill the entire container without additional compaction. Sample weights without containers were approximately 48 g.

Figure 1. A medium sand sample prepared for testing in microtomography.

Table 1. Basic physical properties and classification characteristics of medium sand (MSa—SP) from southern Poland.

Parameter	Symbol	Unit	Value
Specific gravity	ρ_s	g/cm^3	2.65
Effective diameter	d_{10}	mm	0.20
	d_{30}	mm	0.34
	d_{50}	mm	0.42
	d_{60}	mm	0.48
	d_{90}	mm	1.15
Coefficient of uniformity	C_u	-	2.40
Coefficient of curvature	C_c	-	1.20
Clay fraction	ClF	%	0
Silt-size fraction	SiF	%	0.38
Sand fraction	SaF	%	99.54
Gravel fraction	GrF	%	0.08

The silty clay came from the Porcelain Factory in Tułowice, in southern Poland. The experimental material was macroscopically homogeneous. The range of its water content in the natural state (in situ state) was 20% to 30%. Its basic material characteristics are given in Table 2. Due to the stiff state of the soil in the field, the sample could be cut out from a larger silty clay fragment, and then trimmed by the container during careful pushing. Sample weights, without containers, were approximately 55 g. According to a literature study [18], it can be stated that the lack of colloidal activity (low value of Skempton's coefficient A ~0.56) confirmed significant dominant presence of kaolinite in the mineral composition.

2.2. Procedure of Soil Drying by Air, Oven, and Microwave

Generally, different soil drying methods were basically used to calculate the elementary physical soil parameter of the water content. The water (moisture) content in the soil can be expressed as:

$$w = 100 \cdot \frac{M_w}{M_s} \quad (1)$$

where w is the water content (%); M_w is the mass of water in soil (g), that is, the difference between the mass of the wet sample (initial mass, M_i (g)) and the mass of the sample after drying (final, dry mass, M_s (g)); M_s is the dry mass of soil (g).

Table 2. Basic physical properties and classification characteristics of Tułowice silty clay (siCl—CL, modified from [19]).

Parameter	Symbol	Unit	Value
Specific gravity	ρ_s	g/cm^3	2.64
Liquid limit	LL	%	42.2
Plastic limit	LP	%	20.0
Plasticity index	PI	%	22.2
Liquidity index	PL	-	0.60–0.78
Activity	A	-	0.52–0.60
Effective diameter	d_{10} d_{30} d_{50} d_{60} d_{90}	mm mm mm mm mm	0.0001 0.001 0.0046 0.008 0.05
Coefficient of uniformity	C_u	-	73
Coefficient of curvature	C_c	-	1.25
Clay fraction	ClF	%	37
Silt fraction	SiF	%	55

Drying of soil samples according to standards such as PKN-CEN ISO/TS 17892: 2009 [20] or ASTM D 2216-19 [21] is typically carried out in a conventional oven for at least 24 h at a temperature of 105–110 °C. The soils can also be dried using microwave radiation. However, in this case, the procedure was not as clear-cut. This type of soil drying has been the subject of research for many years and so far, only in the United States (ASTM D4643-00 [22] and ASTM D4643-08 [23]), Australia (AS 1289.2.1.4-2015 [24] and AS 1289.0:2014 [25]), and France (NF P 94-049-1 [26]), standardized guidelines of different levels of detail have been published regarding the determination of soil moisture in microwave ovens. In addition, many national reports have been created as a result of research, for example, in Canada (ATT 15/96 [27]) or Hong Kong (Chung and Ho's report from 2008 [28]). However, it is worth noting that the indicated guidelines do not take into account all variants related to soil heterogeneity and research methods. The selection of the specific heating power and the mass of the specimen are still, generally, arbitrary decisions of the researcher. Numerous examples can be found in Jastrzębska's work [6].

In this study, the soil samples were subjected to air, oven, or microwave drying methods. For all samples, the same type of container was used. After drying, the containers were secured with a screw cap to prevent changes in water content and spillage, and then taken for X-ray testing.

Reference air-drying tests were performed in the laboratory, where an air-conditioning unit ensured a steady room temperature (~21 °C) and air humidity (~50%). The durations of these tests were 48 h. The second group of two samples was dried (according to [29]) in a conventional oven (CO) at 105 ± 5 °C in a traditional laboratory drier with convection drying. The time duration for these two tests was 24 h.

The third sample group was dried in an 800 W microwave oven (MO), model WD800AP20-6, which corresponded to the most probable temperature increase, up to 200 °C (cohesionless material) and 400 °C (hydrophobic cohesive material), based on estimations from [17,30,31].

Higher temperatures are less possible due to no large quantities of adsorbed water; specific susceptible minerals (allophane or other hydrophilic materials, which are more prone to temperature rise than study hydrophobic kaolinite); or excessive organic content. Therefore, there was no cause for soil specimen dehydration, and the samples could not catch fire, or develop dangerously high temperatures (1000 °C) [17]. Aspects related to the variability of the temperature, soil preparation, and technical solutions complicate the possibility of evaluating the temperature resulting from microwaves. In the research, at this stage, microwave power was used to describe the methodology as a temperature driver. Such an approach is also related to the common use of microwave power for a description of drying procedures. Nonetheless, this is a very important issue, which is worth more detailed discussion.

There is no universal drying procedure with microwave heating. It is used for a wide variety of purposes (e.g., preparation for further specialist research, to reduce swelling [32,33], and to clean polluted soils [34,35]) and for a wide variety of soil types, including high inhomogeneity of microstructure even within the same soil sample, that is, with various mineralogical compositions and structures. Nevertheless, it is believed that microwave drying can be applied for all types of soils, excluding soils with organic matter content exceeding 10% and bentonites with water content higher than 110% [36], as well as soils with a high content of halloysite, mica, montmorillonite, gypsum, and other hydrated materials [28].

The microwave oven used for the soil drying process was mainly adjusted to: soil type, sample mass and number, spatial arrangement, and drying time. The selection of soil mass and drying time strictly correlated with the heating power of the device. Care should be taken to avoid explosion or burning of dried soils (e.g., clay soils and fine sand, gravel particles, and hard brittle rock, especially when they have a high water content [6,17,28,37]). General recommendations include using 700–800 W microwave power and 2–50 minute drying time intervals. Details can be found, among others, in studies by [6,36,38].

For the concerned cases in this study, the following experimental procedures were performed: The first two mass measurements during microwave drying were performed at intervals of 30 s, and then every 1 min until a constant mass was obtained. For both MSa and siCl, the total drying time was 7 min. In this study, the limitation on sample mass (approximately 50 g) was dictated by the size-related requirements affecting the duration and quality of XμCT results.

2.3. X-ray Computed Microtomography

X-ray CT is an imaging technique followed to observe the internal structure of objects. By rotating the X-ray source and detector, a series of projections of the sample can be generated. The contrast of the projection image is a function of the absorption coefficient, which is determined by the density of the material. In the case of complex soils, the absorption coefficient is correlated with the sum of all chemical components and moisture of the material [39]. The studied samples were dried, hence, during the XμCT exposure the registered change of absorption coefficient was related mainly to material density.

Among other methods, microtomography has been successfully used to assess the qualitative and quantitative characteristics of sandy and clay soil structure (e.g., [40,41] studied water-induced structure changes with use of XμCT). As part of this study, XμCT was also used to analyze the soil structure characteristics, but in relation to three drying approaches. Thus, after drying, all 6 dried samples were taken to a desiccator for cooling. Then, the samples were sequentially put on a so-called holder, and finally placed in the tomograph cell. An XμCT analyzer and the Data Viewer software were employed to analyze the outcome images, while the Avizo Fire software was used to develop numerical models of samples. Qualitative descriptions included structural variability and the differentiation of grains. Three-dimensional numerical modeling of the samples was used to produce precise analyses of the span of fractures and the distribution of voids. The results of spatial analyses of the sample models were used for the calculation of the porosity parameter

(including fractures and volume of void space), average pore diameter (i.e., the sum of all pores or free spaces diameters divided by their number), centroid path tortuosity (ratio of the real length of the flow path to the straight line between the start and the end of flow), and equivalent diameter; the parameters have been described in [42].

Microtomography was provided with an air-cooled Hamamatsu L8121-03 X-ray tube (with tungsten anode) that generated conical X-rays. The tests were carried out with an 8 second exposure time of a single radiograph, at a voltage of 120 kV and power of 10 W. A single spatial image of the sample (consisting of 1601 radiographs) required a test duration of approximately 4 h. At the selected technical exposure settings, the minimum size of the voxel side was 28 microns (i.e., 28 × 28 × 28 microns cube), which was the smallest identifiable element of structure. The raw images originating during the scanning were converted to an 8-bit digital form with a resolution of 1024 × 1024 pixels. Reconstructed tomographic images are presented on a shades of gray scale (higher density zones are lighter).

The study question about the effects generated by various drying methods was, "Are there any effects?"; therefore, as a reference, the tomographic results of air-dried samples were used. There were no tomographic exposures of the samples before drying because the procedure of filling the samples was controlled; no larger voids, loosening, or linear discontinuities were observed. The accuracy of the acquired images was sufficient to identify significant changes. The structural elements below the voxel size remained "masked", and, to identify them, the SEM technique is recommended. However, this technique also has its limitations, i.e., small area of recognition and surface recognition, as well as, in the case of soil, quite complex preparation of research material. Therefore, for this study, we focused on the greatest and unambiguous effects of high temperature on soil samples.

3. Results and Discussion

The water content test results of the study samples (Table 3) are typical for these soils occurring in the field, at the places of collection. The average water content of the medium sand was ~3.2% with a standard deviation of 0.22%. Due to the large pores and ready evaporation of humidity, such variation in results can be considered to be a natural variation of the research material. The average water content of the silty clay was ~22.5% with a standard deviation of 0.65%. Slightly lower water content was associated with air drying (a difference of up to 1.6%), which could be associated with water present in closed pores. Thus, the use of different methods and different drying times produced similar effects, militating in favor of the shortest method.

Table 3. Results of the water content tests.

Soil Type	Water Content (%) by		
	Air Drying	Drying in a Conventional Oven	Drying in a Microwave
Quartz medium sand	3.1	3.5	3.0
Silty clay (mainly consisting of kaolinite)	21.7	23.3	22.6

The similar water content values confirm the estimated (based on the results of similar tests on similar materials [17,30,31]) temperature range associated with drying in MO. Such test results indicated the absence of dehydration processes (expected to be just above 400 °C in the case of kaolinite, dehydration curve [17]), which would result in higher water content values in microwave tests than in other methods with lower temperatures.

Digital overall spatial microstructure reconstructions of sand and silty clay images after drying in air, in a conventional oven, and in a microwave oven are presented in Figure 2.

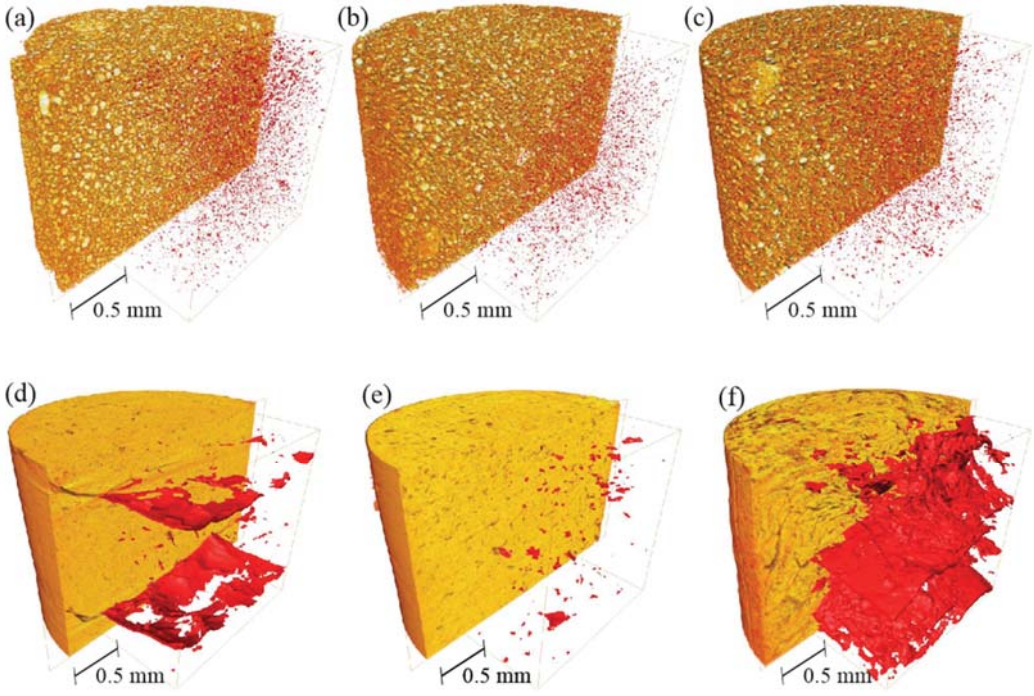

Figure 2. 3D images of dried sand and silty clay: in air without heating (**a**,**d**); in a conventional oven (**b**,**e**); in a microwave oven (**c**,**f**). Pores and fractures are shown in red.

The structure of the sand is heterogeneous and consists of uniformly dispersed grains and pores (shown in red). In the silty clay, air drying produced few fractures, CO drying produced some voids and small fractures, and MO drying produced major fractures (Figure 2a).

Three-dimensional images of the structures were quantitatively analyzed and the outcomes are summarized in Table 4. Notably, XμCT identified structure components bigger than the voxel size in the reconstructed 3D images. Therefore, the measured porosity may be smaller than the "true" porosity, as pores that are too small cannot be seen. Moreover, according to Table 2 and Jastrzębska's tests [43], the silty clay samples have a void ratio of $e = 0.71$ (based on the formula $e = (RD - DBD)/DBD$, where RD is relative density and DBD is dry-bulk density), which corresponds to $n = 42\%$ porosity (based on the formula $n = e/(1 + e)$), whereas the measured (by XμCT) porosity is in the range 2–15% (Table 4). The 27–40% difference means that most voids have a diameter of less than 28 μm. The same applies to other parameters in Table 4 and especially Figure 3 since, once again, they probably differ from the "true" values. In addition, the largest structural elements have the greatest impact on soil behavior.

The results show that the porosity of the sand structure decreases when the drying process is performed at elevated temperatures. Nevertheless, the fraction of pores is similar for the samples heated conventionally and with microwaves. Other parameters determined for sands, such as average pore size or centroid path tortuosity, do not reveal relevant differences.

The results of the quantitative analysis of silty clay structure show that microwave drying causes significant soil fracturing. In this case, the pore volume fraction, which is mainly represented by cracks, increased significantly (6–7 times higher) as compared with the same parameter for conventionally dried or air-dried samples.

Table 4. Quantitative characteristics of the microstructure of soils dried by various methods.

Soil	Parameter	Type of Drying		
		Air	Conventional	Microwave
Sand	Porosity (%)	25.5	18.3	15.2
	Average pore diameter (μm)	95.2	98.5	92.3
	Centroid path tortuosity	1.42	1.67	1.85
Silty clay	Porosity (%)	2.50	2.00	14.70
	Average pore diameter (μm)	120.3	111.2	106.3
	Centroid path tortuosity	8.25	8.92	2.70

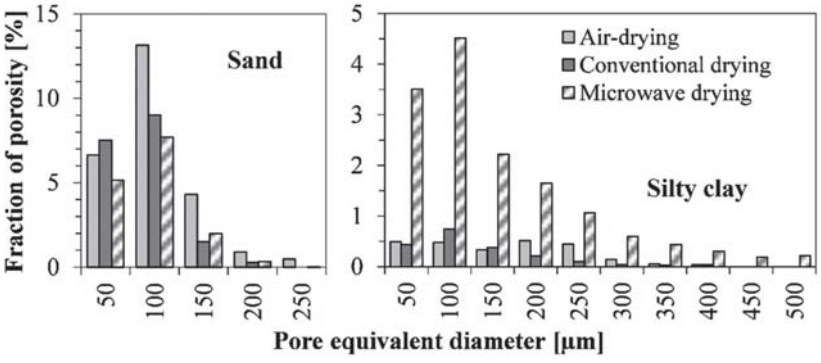

Figure 3. Pore volume fraction by equivalent diameter.

In all the samples, the average pore size and pore size distribution (see Figure 3) are similar.

After the general spatial structure analysis presented above, sand grains, in turn, merit closer attention: The fractions and basic parameters are set out below in Table 5.

Table 5. Basic properties of medium sand (MSa—SP).

Parameter	Symbol	Unit	Soil Air Dried	Soil Dried in a Conventional Oven (CO)	Soil Dried in a Microwave Oven (MO)
Clay-size fraction	ClF	%	0.04	0.38	0.28
Silt-size fraction	SiF	%	0.00	0.00	0.00
Sand-size fraction	SaF	%	99.65	99.54	99.49
Gravel-size fraction	GrF	%	0.31	0.08	0.23
Coefficient of uniformity	C_u	-	1.68	2.40	2.29
Coefficient of curvature	C_c	-	1.04	1.20	1.15

The content of the largest fraction is the highest in the sample not subjected to a rapid temperature rise. This is reflected in the uniformity coefficient. However, the differences are marginal (up to 0.23%). Markedly larger differences could indicate the crushing and cracking of grains of larger fractions under the influence of temperature. However, no cracks were found in the analyzed samples (Figure 4). Grains are enrobed and have a continuous character. Certainly, this is influenced by the dominant share of tough quartz and low humidity, and hence, the limited effect of microwave radiation. For fine quartz sands with high water content (above 23%), the phenomenon of microwave drying has a completely different nature and can even lead to the explosion of samples resulting from too much evaporation (tests conducted on samples of 25 g [6]). For this reason, it is

worth expanding the range of samples with higher water content and determining critical saturation in subsequent tests by using XμCT.

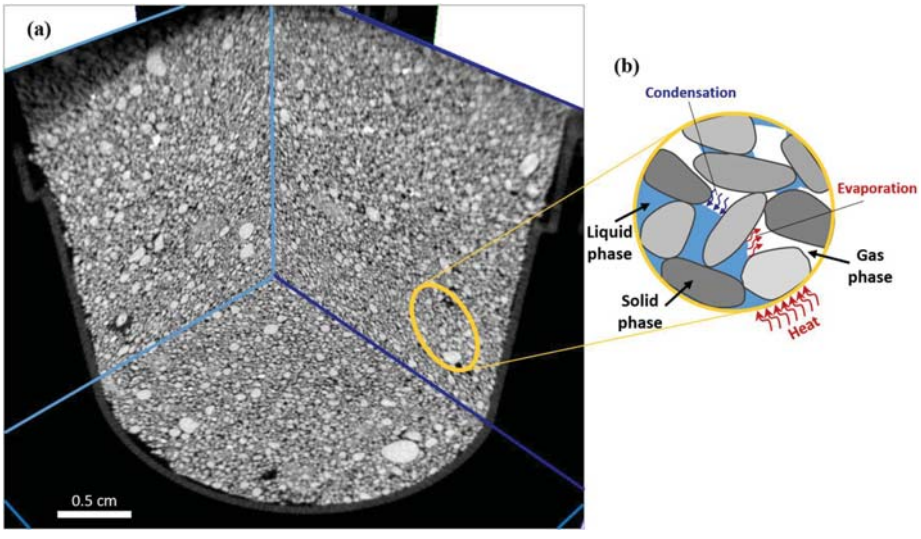

Figure 4. Sand microwave drying: perpendicular microtomographic sections through the medium sand sample after microwave drying (**a**); schematic of unsaturated soil illustrating moisture evaporation and condensation modified from [1] (**b**).

Thus, the weak effect of the drying process on sandy soil can be explained by the fact that any stress that might accumulate during heating (Figure 4b) is released by the motion of sand grains bonded through water by weak mechanical/physical forces. The motion of the sand grains might be responsible for the compacted structure of the sand sample, and therefore, the reduced porosity as compared with the air-dried sand. With respect to this, an important aspect of the grain interaction process that occurs is its contact points, which are involved in load transfer [44].

In the case of the silty clay tests, in relation to the effects of drying that we discussed earlier, it is worth considering the causes. Hence, convectional drying is an air-to-air method in which hot dry air is the factor that transfers heat to the soil and removes moisture. Air flows around the samples in a natural way similar to air drying where the temperature is much lower but the mechanism in CO drying is the same. Conventional drying by convection means that heat is delivered from outside through the surface of the material, which explains why the surface has the highest temperature, which is the reason why the fracture contours are formed parallel to the surface in cylindrical probes. Warm air has the strongest effect on the upper surface of the samples; therefore, the upper part of the sample dries, and then shrinks, resulting in the final formation of an extensive longitudinal fracture (Figure 5). Apparently, a high and steady temperature in CO drying results in overall homogeneous heating of the sample, and thus, causes less cracking than air drying. However, some zoning could be observed in the tested samples subjected to air drying and CO drying, where the gaps in both cases developed or started to appear in similar places. The structure of the tested air-drying and CO drying samples had the aforementioned numerous smaller voids and gaps (Figures 4 and 5) that may constitute places for the facilitated development of subsequent extensive fractures.

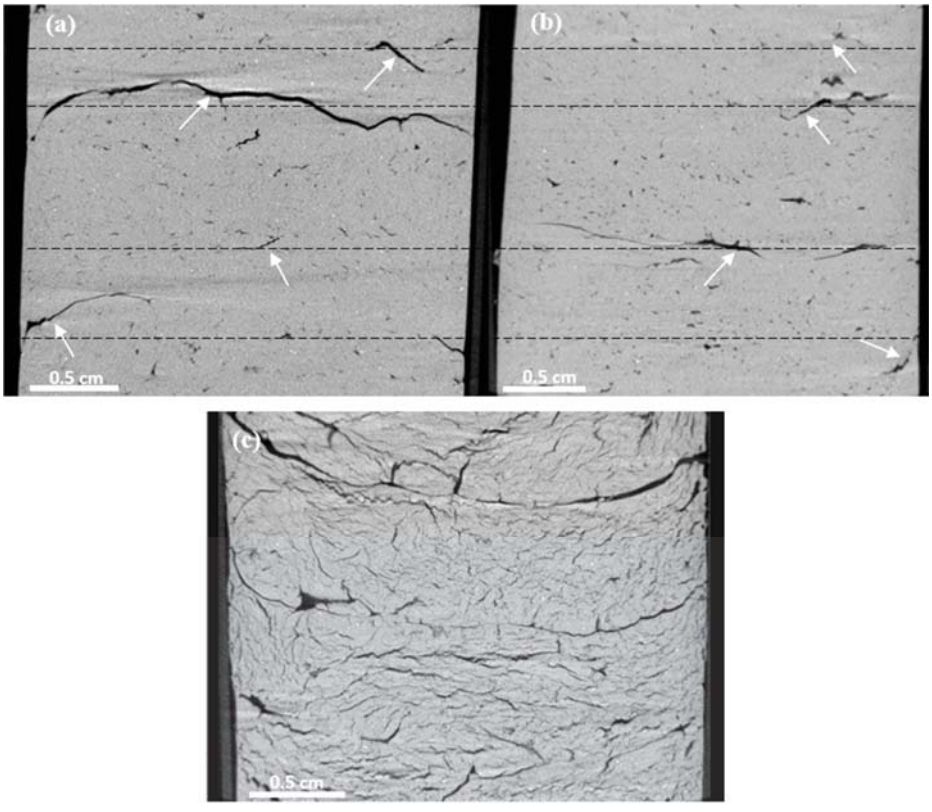

Figure 5. Perpendicular microtomographic sections through silty clay samples after drying by various methods (arrows indicate the similar exemplary fracture locations): air drying (**a**); conventional oven (**b**); microwave (**c**).

The different mechanisms of water–soil interactions during MO drying in the tested silty clay (which is mainly composed of kaolinite) result in the drying process exerting a marked effect on the structure of the material. In this case, water is chemically bonded to the soil and, when it is removed, the local properties of the material are changed. Furthermore, the pressure accumulated by the evaporating water cannot be released only by cracking, as all soil structure elements are "cemented". Thus, during microwave drying, heating is associated with electromagnetic radiation, which induces vibrations of water molecules in the sample, forming an internal source of heat. Hence, microwaves have a greater impact on specimens with higher water content (as well as lower permeability). This observation corresponded to results of tests by [1], who noted the possibility of remarkable sensitivity of the thermo-hydro-mechanical response to a change in temperature in "unsaturated clay, while this observation is absent in soils whose permeability is greater than that of silty sand". In this way, the microwaves penetrate the interior of the material, heating up the entire volume from the inside. This internal penetration can be observed in Figure 5c as the result of MO heating. There is a system of parallel fractures (parallel to the upper sample surface), with smaller perpendicular secondary fractures growing from the larger fracture and using the smaller fractures and pores to form a background system.

Fracture growth at the lab scale might have a negative effect on the properties identified in static loading (e.g., triaxial shearing [45]). Zones with such fractures in the field scale can be used as privilege slip surfaces [46,47]. Furthermore, a high number of fractures

significantly increases the permeability to water and may cause suffusion of fine particles within the soil.

The processes and effects that accompany heating due to CO and MO drying bring about some practical findings. First, MO drying, unlike the time-consuming CO drying, cannot be used ad hoc. The long drying time associated with CO drying allows the soil structure to adapt to the changing conditions of the water content. For this reason, before using the MO drying method, a literature analysis should be conducted regarding the recommended technical parameters of MO drying and its procedure. When there is no recommendation, preliminary research of specific soils should be performed.

The results of these studies have shown that, despite the various structural degradations caused by CO and MO drying, both drying techniques can be considered to be alternatives to the estimation of soil water content (see Table 2). However, when pre-drying is the early step for further testing, these methods cannot be used interchangeably, especially when drying of cohesive soils is considered (see Figure 5). In remolded cohesive samples dried using MO drying, the presence of rapidly formed discontinuities initially weaken the soil material. When soil is dried too rapidly, it can also cause the occurrence of overheated and stiffened fragments that consequently cause falsification of the resultant parameters describing the soil compressibility or elasticity (most likely an increase in the compressibility modulus or Young's modulus values). Furthermore, the characteristics of filtration and consolidation will change: filtration may increase (owing to the better permeability of the fracture system), but consolidation may "decrease" (a stiffer, dry medium consolidates faster). Therefore, the MO drying method is not recommended for cohesive soils tested, for example, in a direct shear or a triaxial compression apparatus.

In the case of non-cohesive soils, the results indicate that the appropriate MO drying procedure marginalizes the undesirable possible effects of rapid and intense heating. This conclusion has been supported by studies that have been conducted on a larger number of non-cohesive samples [6,7]. Furthermore, the greater the fraction of non-cohesive soil, the faster the drying can be performed, which is important and helpful in preparing samples several times from the same material, for example, direct shear tests. However, the mineral skeleton may weaken due to frequent high-temperature applications. Consequently, premature grain crushing and further reductions in strength parameters (such as the angle of internal friction) may occur, for example, in triaxial tests (especially when applying higher effective stresses) or dynamic triaxial tests. Nevertheless, for example, according to unpublished data, in the case of cohesive soils, a clear increase in the angle of internal friction by approximately 25–40% is observed. Geotechnical design based on such overstated parameters may lead to a construction disaster (failure). In the case of non-cohesive soils, the changes are negligible, in the order of 1%.

4. Conclusions

This comparative research investigated the effect of selected drying procedures on the structure of exemplary soils, i.e., medium quartz sand (MSa) and silty clay (siCl) mainly composed of kaolinite; both types of soil were subjected to air drying, drying in a conventional oven (CO), and microwave drying (MO). The structures after drying were qualitatively and quantitatively described by analysis of 3D images obtained by X-ray computed microtomography (XμCT).

The most breakthrough deliverables of this study are:

- Silty clay, as a cohesive soil, is significantly more sensitive to drying processes than the non-cohesive sand sample. The results obtained in this research showed severe fracturing of silty clay for MO-dried samples. In the case of sandy material, MO drying was successfully applied. The grains of the samples with relatively low water content used in the study did not crack. Thus, the heating type (CO or MO) is not interchangeable in the presented case of the selected cohesive soil. Further studies with different water contents combined with XμCT analyses are recommended.

- Uncritical use of MO drying in laboratories (due to the significant reduction in drying time) may result in incorrectly determining the mechanical and filtration parameters of the soils. The impact of microwaves on the soil during the study of basic physical properties, and then using the same soil for testing shear strength or water permeability, can cause a change in these characteristics. In the case of their reduction, they are underestimated, and in the case of their increase, they are overestimated. As a result, this may cause additional costs associated with the desire to unnecessarily improve their specific characteristics, or there may be a risk of construction failure.
- The drying method had a considerable effect on the porosity of the treated samples. After CO drying, the porosity was 28% lower than after air drying. In MO drying, porosity was even 40% lower than after air drying. This is related to the soil skeleton response to rapidly evaporating water.

Author Contributions: Conceptualization, M.J. and Ł.K.; methodology, M.J. and Ł.K.; software, Ł.K. and T.W.; validation, M.J., Ł.K. and T.W.; formal analysis, Ł.K.; investigation, Ł.K. and M.J.; writing, M.J., Ł.K. and T.W.; visualization, Ł.K. and T.W. All authors have read and agreed to the published version of the manuscript.

Funding: This paper was co-financed under the research grant of the Warsaw University of Technology supporting the scientific activity in the discipline of Civil Engineering and Transport (agreement no: 20; year: 2022).

Institutional Review Board Statement: Not applicable.

Informed Consent Statement: Not applicable.

Data Availability Statement: Not applicable.

Acknowledgments: Many thanks to the reviewers for their thoughtful comments and efforts toward improving our manuscript.

Conflicts of Interest: The authors declare no conflict of interest.

References

1. Zhu, B.; Ye, Z.; Wang, L.; Kong, D.; Xu, W.; Kolditz, O.; Nagel, T.; Chen, Y. Hydro-mechanical Behavior of Unsaturated Soil Surrounding A Heated Pipeline Considering Moisture Evaporation and Condensation. *Comput. Geotech.* **2020**, *119*, 103377. [CrossRef]
2. Ying, Z.; Cui, Y.; Benahmed, N.; Duc, M. Changes of Small Strain Shear Modulus and Microstructure for a Lime-Treated Silt Subjected to Wetting-Drying Cycles. *Eng. Geol.* **2021**, *293*, 106334. [CrossRef]
3. Zhang, Z.; Yang, J.; Yue, J.; Li, W.; Gao, H. Research on the Mechanism and Prevention Methods of the Drying Shrinkage Effect of Earthen Sites. *Materials* **2022**, *15*, 2595. [CrossRef] [PubMed]
4. Sayem, H.M.; Kong, L. Effects of Drying-Wetting Cycles on Soil-Water Characteristic Curve. In Proceedings of the International Conference on Power Engineering & Energy, Environment, Shanghai, China, 21–23 October 2016.
5. Rao, S.M.; Revanasiddappa, K. Influence of Cyclic Wetting Drying on Collapse Behaviour of Compacted Residual Soil. *Geotech. Geol. Eng.* **2006**, *24*, 725–734. [CrossRef]
6. Jastrzębska, M. Practical Application of the Microwave Oven in the Geotechnical Laboratory. *Archit. Civ. Eng. Environ.* **2019**, *12*, 91–104. [CrossRef]
7. Prokopowicz, P.; Pires, P.; Michałek, A.; Rybak, A.; Khairutdinov, A.M. Time necessary for microwave drying of mineral soils. *J. Phys. Conf. Ser.* **2020**, *1614*, 012021. [CrossRef]
8. Lin, L.C.; Benson, C.H. Effect of Wet-Dry Cycling on Swelling and Hydraulic Conductivity of GCLs. *J. Geotech. Geoenviron. Eng.* **2000**, *126*, 40–49. [CrossRef]
9. Wang, B.; Zhang, C.; Qiu, X.; Ji, E.; Zhang, W. Research on Wetting-Drying Cycles' Effect on the Physical and Mechanical Properties of Expansive Soil Improved by OTAC-KCl. *Adv. Mater. Sci. Eng.* **2015**, *6*, 304276. [CrossRef]
10. Louati, F.; Trabelsi, H.; Mehrez, J.; Tabibi, S. Wet-dry cycles effect on the saturated hydraulic conductivity. In Proceedings of the 7th International Conference on Unsaturated Soils, Hong Kong, China, 3–5 August 2018.
11. Zhao, S.; Shi, Z.; Peng, M.; Bao, Y. Stability Analysis of Expansive Soil Slope Considering Seepage Softening and Moistening Expansion Deformation. *Water* **2020**, *12*, 1678. [CrossRef]
12. Consoli, N.C.; Scheuemann, F.; Segadães, L.; Cristelo, N. Effect of wet-dry cycles on the durability, strength and stiffness of granite residual soil stabilised with Portland. In Proceedings of the XVII European Conference on Soil Mechanics and Geotechnical Engineering, Reykjavik, Iceland, 1–6 September 2019. [CrossRef]

13. Xu, X.; Shao, L.; Huang, J.; Xu, X.; Liu, D.; Xian, Z.; Jian, W. Effect of Wet-Dry Cycles on Shear Strength of Residual Soil. *Soils Found.* **2021**, *61*, 782–797. [CrossRef]
14. Khan, S.; Ivoke, J.; Nobahar, M. Coupled Effect of Wet-Dry Cycles and Rainfall on Highway Slope Made of Yazoo Clay. *Geosciences* **2019**, *9*, 341. [CrossRef]
15. Gowthaman, S.; Nakashima, K.; Kawasaki, S. Effect of Wetting and Drying Cycles on the Durability of Bio-Cemented Soil of Expressway Slope. *Int. J. Environ. Sci. Technol.* **2021**, *19*, 2309–2322. [CrossRef]
16. *PN-EN ISO 14688-2:2006*; Geotechnical Investigation and Testing. Determination and Classification of Soils. Part 2: Classification Rules. PKN: Warszawa, Poland, 2006. (In Polish)
17. Gilbert, P.A. Computer Controlled Microwave Oven System for Rapid Water Content Determination. Technical Report GL-88-21; Department of the Army Waterways Experiment Station: Vicksburg, MS, USA, 1988.
18. Skempton, A.W. The colloidal activity of clays. In Proceedings of the Third International Conference on Soil Mechanics and Foundation Engineering, Zurich, Switzerland, 16–27 August 1953.
19. Jastrzębska, M. The External and Internal Measurement Effect on Shear Modulus Distribution within Cyclic Small Strains in Triaxal Studies on Cohesive Soil. In Proceedings of the International Conference on Experimental Mechanics ICEM, Poitiers, France, 4–9 July 2010. [CrossRef]
20. *PKN-CEN ISO/TS 17892-1:2009*; Geotechnical Investigation and Testing. Laboratory Testing of Soil—Part 1: Determination of Moisture Content. PKN: Warszawa, Poland, 2009. (In Polish)
21. *ASTM D 2216-19:2019*; Standard Test Methods for Laboratory Determination of Water (Moisture) Content of Soil and Rock by Mass. ASTM International: Philadelphia, PA, USA, 2019.
22. *ASTM D4643-00:2000*; Standard Test Method for Determination of Water (Moisture) Content of Soil by Microwave Heating. ASTM International: Philadelphia, PA, USA, 2000.
23. *ASTM D4643-08: 2008*; Standard Test Method for Determination of Water (Moisture) Content of Soil by Microwave Heating. ASTM International: Philadelphia, PA, USA, 2008.
24. *AS 1289.2.1.4:2015*; Methods of Testing Soils for Engineering Purposes. Method 2.1.4: Soil Moisture Content Tests—Determination of the Moisture Content of a Soil—Microwave-oven Drying Method (Subsidiary Method). Standards Australia: Sydney, Australia, 2015.
25. *AS 1289.0:2014*; Methods of Testing Soils for Engineering Purposes. Part 0: Definitions and General Requirements. Standards Australia: Sydney, Australia, 2014.
26. *NF P 94-049-1:1996*; Soils: Identification and Testing–Determination of Water Content in Materials–Part 1: Microwave Oven Drying Method. AFNOR Normalisation: La Plaine Saint-Denis, France, 1996. (In French)
27. ATT 15/96 Moisture Content. Part IV. Microwave Oven Method. Available from Alberta Transportation Test Procedures. 1996. Available online: www.transportation.alberta.ca (accessed on 19 August 2022).
28. Chung, P.; Ho, T. Study on the Determination of Moisture Content of Soils by Microwave Oven Method. GeoReport No.221; Civil Engineering and Development Department of Hong Kong: Hong Kong, China, 2008.
29. *PKN-CEN ISO/TS 17892-12:2009*; Geotechnical Investigation and Testing—Laboratory Testing of Soil—Part 12: Determination of Atterberg Limits. PKN: Warszawa, Poland, 2009.
30. Solonenko, L.I.; Repiakh, S.I.; Mamuzić, I.; Kimstach, T.V.; Bilyi, O.P. Kinetics of quartz sand and its mixtures drying by microwave radiation. *Nauk. Visnyk Natsionalnoho Hirnychoho Univ.* **2021**, *1*, 68–77. [CrossRef]
31. Gee, G.W.; Dodson, M.E. Soil water content by microwave drying: A routine procedure. *Soil Sci. Soc. Am. J.* **1981**, *45*, 1234–1237. [CrossRef]
32. Stanevich, V.T. Building Ceramics—Tutorial. Kereku Publishing Press: Pavlodar, Kazakhstan, 2009; pp. 1–96.
33. Kramarenko, V.V.; Nikitenkov, A.N.; Yu Molokov, V.; Shramok, A.V.; Pozdeeva, G.P. Application of Microwave Method for Moisture Determination of Organic and Organic-Mineral Soils. In *IOP Conference Series: Earth and Environmental Science*; IOP Publishing: Bristol, UK, 2016; Volume 33, p. 012040. [CrossRef]
34. Kawala, Z.; Atamańczuk, T. Microwave-Enhanced Thermal Decontamination of Soil. *Environ. Sci. Technol.* **1998**, *32*, 2602–2607. [CrossRef]
35. Shang, H.; Robinson, J.P.; Kingman, S.W.; Snape, C.E.; Wu, Q. Theoretical Study of Microwave Enhanced Thermal Decontamination of Oil Contaminated Waste. *Chem. Eng. Technol.* **2007**, *30*, 121–130. [CrossRef]
36. Cormick, A. Comparing Different Heating Methods for Determination of Moisture Content in Soils. Ph.D. Thesis, University of Southern Queensland, Toowoomba Qld, Australia, 2015.
37. Gołębiewska, A.; Połoński, M.; Witkowski, M. Determination of Water Content of Soil by Microwave Oven Method. *Acta Sci. Pol. Archit.* **2003**, *2*, 63–78.
38. Jalilian, J.; Moghaddam, S.S.; Tagizadeh, Y. Accelerating Soil Moisture Determination with Microwave Oven. *J. Chin. Soil Water Conserv.* **2017**, *48*, 101–103. [CrossRef]
39. Ketcham, R.; Carlson, W. Acquisition, Optimization and Interpretation of X-ray Computed Tomographic Imagery: Applications to the Geosciences. *Comput. Geosci.* **2001**, *27*, 381–400. [CrossRef]
40. Tracy, S.R.; Daly, K.R.; Sturrock, C.J.; Crout, N.M.J.; Mooney, S.J.; Roose, T. Three-dimensional Quantification of Soil Hydraulic Properties Using X-ray Computed Tomography and Image-Based Modeling. *Water Resour. Res.* **2015**, *51*, 1006–1022. [CrossRef]

41. Guerra, A.M.; Aimedieu, P.; Bornert, M.; Cui, Y.; Tang, A.M.; Sun, Z.; Mokni, N.; Delage, P.; Bernier, F. Analysis of the Structural Changes of a Pellet/Powder Bentonite Mixture Upon Wetting by X-ray Computed Microtomography. *Appl. Clay Sci.* **2018**, *165*, 164–169. [CrossRef]
42. Kaczmarek, Ł.; Wejrzanowski, T.; Skibiński, J.; Maksimczuk, M.; Krzyżak, A. High-resolution Computed Microtomography for the Characterization of a Diffusion Tensor Imaging Phantom. *Acta Geophys.* **2017**, *65*, 259–268. [CrossRef]
43. Jastrzębska, M. Calibration and Verification of One-Surface Elasto-Plastic Soil Model of Strongly Non-Linear Anisotropic Strengthening. Ph.D. Thesis, Silesian University of Technology, Gliwice, Poland, 2002. (In Polish).
44. Druckrey, A.M.; Alshibli, K.A.; Al-Raoush, R.I. 3D characterization of sand particle-to-particle contact and morphology. *Comput. Geotech.* **2016**, *74*, 26–35. [CrossRef]
45. Gasparre, A.; Nishimura, S.; Coop, M.R.; Jardine, R.J. The Influence of Structure on the Behavior of London Clay. *Géotechnique* **2007**, *57*, 19–31. [CrossRef]
46. Dobak, P.; Gawriuczenkow, I.; Kaczmarek, Ł.D.; Kiełbasiński, K.; Wójcik, E. Application of Slope Stability Numerical Calculation For Evaluation of Potential Displacement Zones in Weathered and Colluvial Soils on the Flysh Base. *Prz. Geol.* **2016**, *64*, 683–693.
47. Kaczmarek, Ł.D.; Popielski, P. Selected Components of Geological Structures and Numerical Modelling of Slope Stability. *Open Geosci.* **2019**, *11*, 208–218. [CrossRef]

materials

MDPI

Article

Numerical Evaluation of the Hygrothermal Performance of a Capillary Active Internal Wall Insulation System under Different Internal Conditions

Dobrosława Kaczorek

Thermal Physics, Acoustics and Environment Department, Building Research Institute (ITB), Filtrowa 1 Str., 00-611 Warsaw, Poland; d.kaczorek@itb.pl

Abstract: In certain situations, internal insulation is the only possible renovation option. However, it is risky where there is high humidity in a building and ventilation is not working sufficiently. The internal insulation retrofit changes the original thermal and moisture balance of a wall, therefore, it is necessary to carefully design it already at the initial stage. This paper analyses four interior insulation systems based on open diffusion capillary active materials: wood fibreboards (flex and rigid), perlite boards, and microporous calcium silicate. The hygrothermal performance under the climatic conditions of Central Europe (Poland) was assessed using the WUFI Plus software, taking into account the dynamic variation of indoor and outdoor conditions. The analysis included three insulation thicknesses with different ventilation rates and varying moisture loads. The results show that the hygrothermal properties of the wall change with the increase of insulation thickness and depend on the individual moisture properties of the material. In addition, both the reduction of moisture load and more intensive air exchange improve the hygrothermal properties at the interface between the insulation and the wall. Of all the solutions analysed, the system with perlite board and the system with wood fibreboard showed the worst hygric properties. Conversely, the highest risk of mould and interstitial condensation was recorded for the flex wood fibreboard solution.

Keywords: hygrothermal simulation; capillary active internal insulation; mould risk; moisture effects

Citation: Kaczorek, D. Numerical Evaluation of the Hygrothermal Performance of a Capillary Active Internal Wall Insulation System under Different Internal Conditions. *Materials* **2022**, *15*, 1862. https://doi.org/10.3390/ma15051862

Academic Editor: Krzysztof Schabowicz

Received: 9 January 2022
Accepted: 28 February 2022
Published: 2 March 2022

Publisher's Note: MDPI stays neutral with regard to jurisdictional claims in published maps and institutional affiliations.

1. Introduction

As the construction sector is responsible for approx. 40% of Europe's greenhouse gas emissions [1], the European Commission has begun to take an interest in the industry's activities. In order to reach the ambitious European climate targets for reducing greenhouse gas emissions, The Energy Performance of Buildings Directive (EPBD) [2] highlights the need for member states to develop long-term strategies for building renovation. As a result, in January 2021, new requirements for the thermal protection of buildings came into force in Poland, according to which the heat transfer coefficient for external walls must be less than U = 0.2 W/(m^2·K), both for newly constructed buildings and buildings undergoing thermal efficiency improvement. Not all buildings, however, are suitable for insulation being fitted on the outside of walls. In such a case, internal insulation may be the only feasible solution [3], although it is often considered more risky due to the presence of thermal bridges [4–6] and the increased likelihood of interstitial condensation [7–10]. In addition, this type of solution increases the diffusion resistance between the existing wall and the occupied zone, which reduces the potential for the wall to dry inwards [9,11]. In turn, higher moisture levels can lead to mould growth on the internal surface [9,12–14] or damage to the timber elements of the wall [9,13,15]. In order to solve the issues concerning moisture accumulation inside the wall, and to improve its thermal properties, new solutions are constantly searched for. An example could be the thermal paint with a ceramic material employed as a special filler. Despite the fact that the ceramic additive works well in other solutions [16], unfortunately, it does not improve the thermal properties of this

paint, nor the thermal insulation of the building structure on which it was applied [17]. Another option, increasingly popular in recent years, are capillary active systems with open diffusion [18]. This group of materials includes, among others, autoclaved aerated concrete (AAC) and calcium silicate (Ca-Si). Some studies [12,19,20] have shown that the use of capillary active insulation materials based on calcium silicate (Ca-Si) significantly reduces the moisture content in walls. The results, however, may have been influenced by the application of additional wind-driven rain (WDR) protection by coating the external layer with a hydrophobic agent or low internal moisture load. Other studies [21,22] have shown high relative humidity (RH) levels at the interface between the wall and insulation, depending on various factors such as wall thickness, rain load, or the hygroscopicity of materials.

The results of many previous simulation studies [12,15,22–24] on the importance of insulation thickness prove that increased thickness increases the risk of moisture problems. In contrast, Nielsen et al. [25] and Straube et al. [9] suggested that insulation thickness is only of minor importance and that the condensation risk associated with outward diffusion is a minor problem compared to the amount of moisture introduced into the wall due to WDR. Conversely, studies [3,22,26] indicated that critical relative humidity (RH) levels decreased as masonry thickness increased. However, little information can be found in the literature regarding the influence of mortar properties on the performance of internal insulation, while the properties of the mortars themselves are the subject of numerous works [27,28].

Another frequently used measure to improve hygrothermal conditions at the interface between the wall and the insulation is to reduce internal moisture loads in the rooms, especially during the heating season. Both field [11,29] and simulation studies [8,18,22,30,31] indicated the improvement of hygrothermal performance at critical locations resulting from indoor moisture load reduction.

The group of capillary active materials also includes biomaterials, e.g., insulation based on wood fibreboards. This type of insulation is most often used to fill finished structures [32,33]; however, appropriately designed insulation can also be used as internal insulation. An assessment of the suitability of this type of insulation for internal use in the Central European region is presented in the work by Kočí et al. [34]. Furthermore, Wegerer et al. [35] evaluated different wood fibre interior insulation systems based on the results of measurements performed on two demonstration objects.

In light of the above, the aim of the conducted research was the evaluation of the hygrothermal behaviour of four internal insulation systems in the climatic conditions of the city of Kraków, Poland (temperate climate zone, middle latitude). The Glaser model [36,37] has been used most commonly to assess the hygrothermal processes in external walls. This model, however, is not suitable for the assessment of walls containing hygroscopic materials in which variable moisture processes occur simultaneously in multiple phases [38]. Furthermore, in many studies on heat and mass transfer issues in the building envelope, the internal environmental conditions were assumed to be constant [39] or determined in accordance with EN 15026 [40], where indoor air temperature and relative humidity depend linearly on the outdoor temperature [41,42]. There are many studies on the thermal comfort and energy conservation of buildings, where dynamic thermal comfort is increasingly considered in the thermal environment of buildings [43–45]. There are, however, relatively few studies on heat and moisture transfer in walls in dynamic indoor thermal environments using 3D models. Therefore, in this study, research based on the Heat and Mass Transfer (HAMT) simulation model using the WUFI Plus simulation tool [45,46], for different solutions of internal conditions was carried out.

This research analyses four interior insulation systems based on open diffusion capillary active materials: wood fibreboards (flex and rigid), perlite boards, and microporous calcium silicate. The research focused primarily on the analysis of the hygrothermal performance of external walls under varying indoor environmental conditions in the room, taking into account different ventilation solutions and occupancy schedules. The choice of

variants for the analyses was aimed at reflecting the typical scenarios of using the typical room in the residential building. The analyses carried out, made it possible to identify the least favourable solution. The energy and economic analyses have been presented in an earlier article [47].

2. Materials and Methods

2.1. Simulation Method

In order to test the hygrothermal performance of individual cases, numerical simulations using the WUFI Plus software (version 3.1.0.3) were carried out. For these simulations, from which information on the hygrothermal behaviour of the external walls and the internal hygrothermal conditions was obtained, various comparative conditions were established. Concerning the wall, total moisture content, temperature, and RH on its internal surface and in the critical cross-section at the interface between the additional insulation and the wall were analysed.

A hypothetical room model was built; it was assumed that this room is an internal room and that neighbouring rooms are of the same type, thus excluding heat and mass through internal walls. It was also assumed that the examined room with the following dimensions: length—4.0 m, width—5.5 m, height—2.8 m, is a family room with a 2.9 m^2 window facing south.

Tests have been conducted on a base wall made of two layers: 25 cm thick solid brick and 11 cm thick extruded polystyrene (EPS) external insulation with a heat transfer coefficient of 0.23 $W/(m^2 \cdot K)$, insulated from the inside using various internal insulation systems so that the entire wall meets the thermal protection requirements effective in Poland since 2021 ($U \leq 0.2$ $W/(m^2 \cdot K)$). The configuration of individual solutions together with material data is presented in Table 1. The analyses were carried out for three thicknesses of the insulation material: 4 or 5 cm (depending on the type), 8 and 12 cm. The values of the physical properties of the insulation materials adopted for calculations were determined as part of the H-house project in the Building Research Institute's laboratory [48]. The properties of other materials were adopted based on the WUFI Plus database.

Table 1. Wall assembly configurations used in simulations.

Wall Assemblies (Additional Material Layers)	Thermal Conductivity (W/(m·K))	Heat Capacity (J/(kg·K))	Density (kg/m^3)	μ-Value (–)	Thickness (m)	U-Value ($W/(m^2 \cdot K)$)
A—						
bonding mortar	0.800	850	1350	16.2	0.05	0.176
perlite board	0.045	850	850	7.0	0.08	0.158
					0.12	0.138
mineral plaster	0.800	850	190	25.0		
B—						
adhesive mortar	0.155	850	833	15.0	0.05	0.174
microporous Ca-Si	0.043	850	115	4.1	0.08	0.156
					0.12	0.136
adhesive mortar	0.155	850	833	15.0		
lime plaster	0.700	850	1600	7.0		
C—					0.04	0.183
rigid wood fibreboard	0.045	2100	159	10.0	0.08	0.158
					0.12	0.138
bonding mortar	0.800	850	1350	16.2		
lime plaster	0.700	850	1600	7.0		
D—					0.04	0.180
flex wood fibreboard	0.041	2100	61	3.0	0.08	0.150
					0.12	0.133
gypsum fibreboard	0.300	1200	1153	16.0		

The walls were modelled as the walls in a tall building (>20 m) since higher buildings are most exposed to the effect of driving rain than lower ones. In the absence of an impregnation layer on the exterior surface of the wall, driving rain water absorption coefficient of up to 70%, depending on the slope and type of wall, was adopted. The computations were carried out over a period of 3 years. Hygrothermal computations started in January with internal moisture content corresponding to 80% relative humidity and a temperature of 20 °C.

2.2. External Conditions

The exterior conditions were derived from the WUFI Plus database for the city of Kraków, Poland. The weather data included hourly values of temperature, relative humidity, solar radiation, barometric pressure, long-wave counter radiation, and rain load. Kraków is situated at 50.03° north latitude and 19.56° east longitude, in a temperate climate zone (middle latitude). The average temperature in Kraków is: annual, 8.28 °C, in August, 17.5 °C, in January, −1.3 °C.

2.3. Internal Conditions

The tests analysed four different scenarios with respect to ventilation rates (Table 2). In all analysed variants, the minimum temperature for the heating season was assumed at the level of 20 °C. In variants V1, V2, and V3 cooling was assumed in the summer season (max. temp. 26 °C). Variant V1 assumes that the room is ventilated by infiltration only, with relatively tight windows, assuming an hourly air exchange value of n = 0.2 h^{-1}. In variant V2, the air exchange rate was increased to n = 0.5 h^{-1}. In variant V3, infiltration was increased by assuming that the room is ventilated twice a day (ajar window over a period of one hour at 8 a.m. and 6 p.m., n = 4.0 h^{-1}). In contrast, variant V4 analysed the same conditions as variant V3 but without cooling.

Table 2. Variants of estimated air exchange.

Variants	Simulated Scenario
V1	infiltration n = 0.2 h^{-1} with cooling (max. temp. 26 °C)
V2	infiltration n = 0.5 h^{-1} with cooling (max. temp. 26 °C)
V3	infiltration n = 0.5 h^{-1} + ajar window over a period of 1 h at 8 a.m. and 6 p.m. (ACH 4.0 h^{-1}) with cooling (max. temp. 26 °C)
V4	infiltration n = 0.5 h^{-1} + ajar window over a period of 1 h at 8 a.m. and 6 p.m. (ACH 4.0 h^{-1}) without cooling

Furthermore, it was assumed that two adults and one child would use the room. In order to simulate the impact of moisture loads, two different variants of occupancy schedule were adopted:

- constant from 8 a.m. to 10 p.m. for weekdays and weekends, assuming that the room is used all the time during this time
- with variable occupancy schedule for weekdays and weekends according to Table 3.

Table 3. Occupancy schedule with internal heat gains.

Occupancy Hours	Weekdays				Weekend			
	Heat Conv.	Heat Radiant	Moisture	CO_2	Heat Conv.	Heat Radiant	Moisture	CO_2
	W	W	g/h	g/h	W	W	g/h	g/h
6.00–7.00	80	41	59	36.3	–	–	–	–
7.00–8.00	220	112	168	106.4	–	–	–	–
8.00–10.00	–	–	–	–	80	41	59	36.3
10.00–16.00	–	–	–	–	220	112	168	106.4
18.00–20.00	220	112	168	106.4	220	112	168	106.4
20.00–22.00	160	82	118	72.6	160	82	118	72.6

3. Moisture Condition Assessment

According to the mechanisms of moisture transport through the building envelope, water vapour diffusion typically occurs from a high-temperature environment to a cooler environment, as does liquid transport from the high relative humidity side to the low relative humidity side. This is, however, dependent on the properties of the individual materials and the construction of the envelope; in some cases, there may be a situation where moisture will accumulate in places where the transport of moisture is limited [34]. During the coldest and warmest seasons, when outdoor relative humidity is high, moisture transport through the envelope is intensified by larger temperature and relative humidity gradients, and moisture accumulation within the envelope can increase. The combined effects of temperature and moisture cause the deterioration of building materials, especially when moderate or high temperatures are combined with high humidity for extended periods of time. In 2002, Beaulieu, Bomberg et al. [49] defined the Relative Humidity and Temperature (RHT) index as an index used to quantify the hygrothermal condition of an envelope, illustrating the duration of coexisting moisture and thermal conditions above a pair of threshold levels. In 2005, Mukhopadhyaya et al. [50] developed the Relative Humidity and Temperature Time (RHTT) index, defined below to indicate favourable conditions for initiating the onset of moisture damage, including both the RHT index and the calculated time of wetness (TOW). Higher RHTT values indicate an increased likelihood of envelope damage. The RHTT index, determined from Equations (1)–(3) below, was used to evaluate conditions conducive to potential mould growth in the envelope [51]:

$$RH_{potential} = \begin{cases} RH - RH_{critical,} \text{ if } RH > RH_{critical} \\ 0, \text{ if } RH \leq RH_{critical} \end{cases} \quad (1)$$

$$T_{potential} = \begin{cases} T - T_{critical,} \text{ if } T > T_{critical} \\ 0, \text{ if } T \leq T_{critical} \end{cases} \quad (2)$$

$$RHTT = TOW \cdot \sum_{1}^{\text{total hours}} RH_{potential} \cdot T_{potential} \quad (3)$$

where $RH_{potential}$, the moisture potential for moisture damage (%); $T_{potential}$, the temperature potential for moisture damage (°C); $RH_{critical}$, the critical relative humidity level above which moisture damage is more likely to occur (%); $T_{critical}$, the critical temperature level above which moisture damage is more likely to occur (°C); TOW, the calculated time of wetness (h) when RH > 80% and T > $T_{critical}$.

The value of critical relative humidity and temperature depends on the interaction between materials, surfaces, the surrounding environment, and moisture damage. Referring to previous studies on the possibility of mould growth using the RHTT index [52], the following values were adopted in tests: relative humidity ($RH_{critical}$) 80%, temperature ($T_{critical}$) 5 °C.

4. Results and Discussion

4.1. Total Water Content

The basic parameter used to assess the hygric properties of a wall is the total moisture content in it. The course of the total moisture content in the wall during successive years of building exploitation shows whether the wall dries out or accumulates moisture. Frequently, moisture content that increases in time indicates numerous design errors, which may lead to the occurrence of mould on the internal surface, damage to the wall as a result of water freezing, as well as to the increase of heat losses.

Analyses of total moisture content in the wall for individual variants were performed. Figure 1 only presents selected results for 4 or 5 cm insulation thickness for the variable and constant occupancy schedule, respectively.

The wall assemblies analysed in all variants show annual cyclic fluctuations of moisture content caused by seasonality. Similar results were found in Ref. [53]. In the initial period of the simulation, in January, one can see a decrease in the walls' moisture content, which indicates that the walls are drying out. Then, after reaching the minimum level, the total moisture content in the walls start to increase, reaching the maximum level in the summer. This is due to the fact that the winter months (December, January) are the months with the least amount of rainfall, while the summer months (June–August) are characterised by peak rainfall. The obtained results are consistent with the previous studies [52]. In the case of variants V1, V2 and V3, all walls reach the minimum level of moisture in April and the maximum level in September. These levels differ for variant V4, with a minimum level in July and a maximum level in December. This is due to the higher internal temperature that results from the lack of cooling in the summer. The higher temperature translates into higher content of water vapour in the air, which in turn causes walls made of capillary-active diffusion open insulation materials to absorb more moisture from the air.

Table 4 presents a summary of the maximum and minimum values of total moisture content for all analysed cases.

When analysing max. and min. values of the total moisture content in a wall, one might observe repeatability. For wall A (perlite board) and for wall C (rigid wood fibreboard), both in the variant with constant and variable occupancy schedules, the same values were obtained. Additionally, the maximum values for variants V3 and V4, apart from having the same results for walls A and C, reached the same value in both constant and variable occupancy schedules. In the case of 4 or 5 cm thick insulation, the highest value of total moisture content was achieved by wall A (for all ventilation variants). For other thicknesses, 8 and 12 cm, such value was achieved by variants with more intensive ventilation: V2, V3, V4, wall C. The lowest total moisture content was achieved by wall D (flex wood fibreboard), irrespective of the insulation thickness and ventilation variant. This is largely due to the sorption properties of capillary open materials, which were compared, among others, by Zhao et al. [8] and Koči et al. [34] and the value of the diffusion resistance of internal finishes. According to the research carried out by Hansen [23], the combination of these two properties may significantly reduce drying out into a room and increase the moisture content of a partition. This is the case for partition A. The perlite board is characterised by the highest sorption, and the mineral plaster layer has the highest value of diffusion resistance of all the cases considered.

In addition, one might see that the total moisture content of the wall increases with the increase of insulation thickness. Many researchers have also studied the effect of insulation thickness on the hygric behaviour of the wall [12,23,53]. Their research confirms that the ability of the wall to accumulate moisture increases with the increase of insulation thickness. In addition, one might spot that higher insulation thicknesses result in greater differences between the materials, especially for variant V1, which has a low air exchange rate.

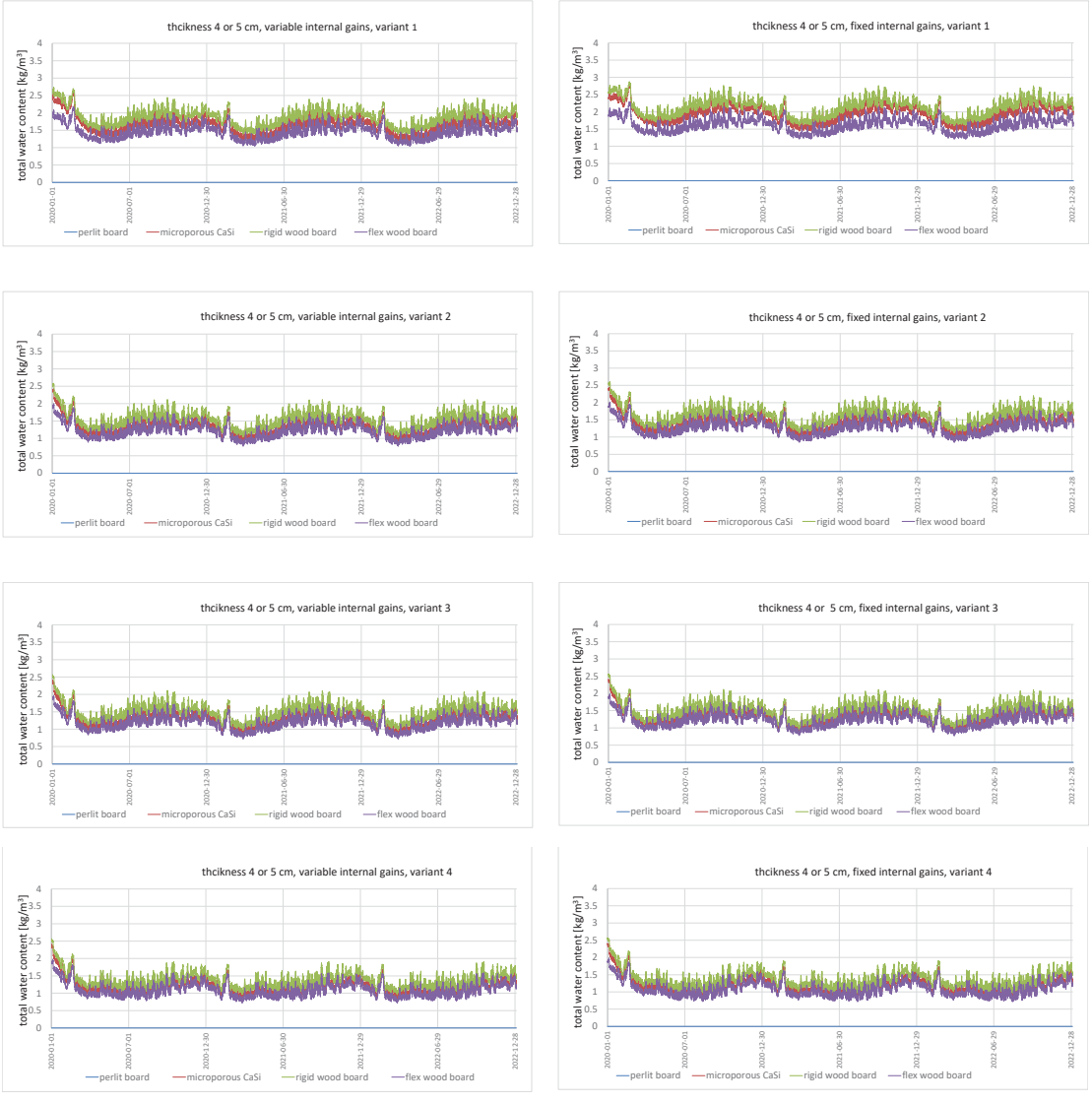

(**a**) (**b**)

Figure 1. Variations in total water content in walls for 4 or 5 cm internal insulation thickness: (**a**) variable internal gains; (**b**) fixed internal gains.

Table 4. Maximum and minimum values for total moisture content.

Wall Assemblies	Total Moisture Content [kg/m^3]	Ventilation Variants											
		V1			V2			V3			V4		
		Insulation Thickness [cm]											
		4–5	8	12	4–5	8	12	4–5	8	12	4–5	8	12
		constant occupancy schedule											
A	min	1.53	1.69	2.06	1.04	1.27	1.53	0.97	1.16	1.40	0.96	1.15	1.38
	max	2.74	3.19	3.65	2.59	2.97	3.37	2.56	2.97	3.37	2.56	2.97	3.37
B	min	1.20	1.41	1.75	0.89	1.20	1.20	0.82	0.96	1.12	0.82	0.94	1.04
	max	2.74	2.96	3.32	2.43	2.99	2.99	2.40	2.65	2.97	2.40	2.65	2.97
C	min	1.53	1.69	2.06	1.04	1.04	1.27	0.97	1.16	1.40	0.96	1.15	1.38
	max	2.74	3.19	3.65	2.59	2.59	3.37	2.56	2.97	3.37	2.56	2.97	3.37
D	min	1.05	1.41	1.75	0.89	1.20	1.20	0.82	0.96	1.12	0.82	0.94	1.04
	max	2.96	2.96	3.32	2.43	2.99	2.99	2.40	2.65	2.65	2.40	2.65	2.97
		variable occupancy schedule											
A	min	1.77	2.12	2.82	1.12	1.37	1.66	0.97	1.30	1.51	0.98	1.15	1.33
	max	2.87	3.56	4.03	2.61	2.99	3.39	2.56	2.97	3.37	2.56	2.97	3.37
B	min	1.44	1.82	2.47	0.97	1.12	1.33	0.88	1.02	1.12	0.81	0.91	1.12
	max	2.87	3.17	3.55	2.45	2.69	3.01	2.40	2.65	2.97	2.40	2.65	2.97
C	min	1.77	2.12	2.82	1.12	1.37	1.66	0.97	1.30	1.51	0.98	1.15	1.33
	max	2.87	3.56	4.03	2.61	2.99	3.39	2.56	2.97	3.37	2.56	2.97	3.37
D	min	1.21	1.82	2.47	0.97	1.12	1.33	0.88	1.02	1.12	0.81	0.91	1.12
	max	2.80	3.17	3.55	2.45	2.69	3.01	2.40	2.65	2.97	2.40	2.65	2.97

4.2. Temperature and RH at Interior Surface

The variation of temperature and relative humidity on the internal surface were analysed for all walls and ventilation variants, taking into account variable and constant occupancy schedules. Due to the considerable number of diagrams, they were not included in this paper; however, the author included in Figure 2 exemplary diagrams, showing the annual seasonal fluctuations in temperature and relative humidity on the inner surface of the selected variants. The values of maximum and minimum temperature for particular types of wall and ventilation variants and RH values are presented in Tables 5 and 6, respectively.

Annual seasonal variation in temperature and RH on the interior surface of the walls is evident for all analysed cases. Variant V1 with the lowest intensity of ventilation n = 0.2 h^{-1} shows longer periods of maintaining higher temperature (from mid-March to the end of October) than the remaining variants V2, V3, and V4 (from the beginning of May to the end of September). Obviously, in variant V4, due to the lack of cooling, i.e., stabilisation of the temperature at a certain level (t = 26 °C), in the summer period, the temperature gradually increases and, then, after reaching its maximum at the turn of July and August, it gradually decreases until it reaches its minimum at the level of 20 °C.

With the varying load profile for wall A (perlite board), the lowest recorded temperature value was 17.0 °C (this value was recorded with different ventilation variants V3 and V4 and different insulation thicknesses). The highest value is 39.8 °C for variant V4 with 12 cm of insulation. For wall B (microporous Ca-Si), the lowest value was 16.9 °C, while the highest was 39.9 °C. For walls C (rigid wood fibreboard) and D (flex wood fibreboard), the values were 16.5 °C and 17.0 °C, and 39.3 °C and 39.8 °C, respectively. The highest values of minimum temperature were recorded for ventilation variants V1 and V2, while the lowest for variant V4. Conversely, in the case of maximum values, the opposite applies, where the highest values of maximum temperature on the inner surface were recorded for variant V4 and the lowest for variant V1. There were no significant differences between the obtained temperature values for the different variants of wall system solutions with the

same ventilation and insulation variants. A minimal increase in temperature values in the range of 0.05–1 °C can be observed depending on the ventilation variant with increasing insulation thickness. For variants V1 and V2, the average minimum temperature on the inner surface was 19.5 °C and the maximum was 27 °C. On the contrary, for variants V3 and V4, the average minimum temperature was 16.54 °C, whereas the maximum for variant V3 does not differ from variants V1 and V4, and is 39.3 °C. Lower temperature for variant V3 is the result of more intensive ventilation, while higher temperature for variant V4 is the result of the absence of a cooling option for this variant.

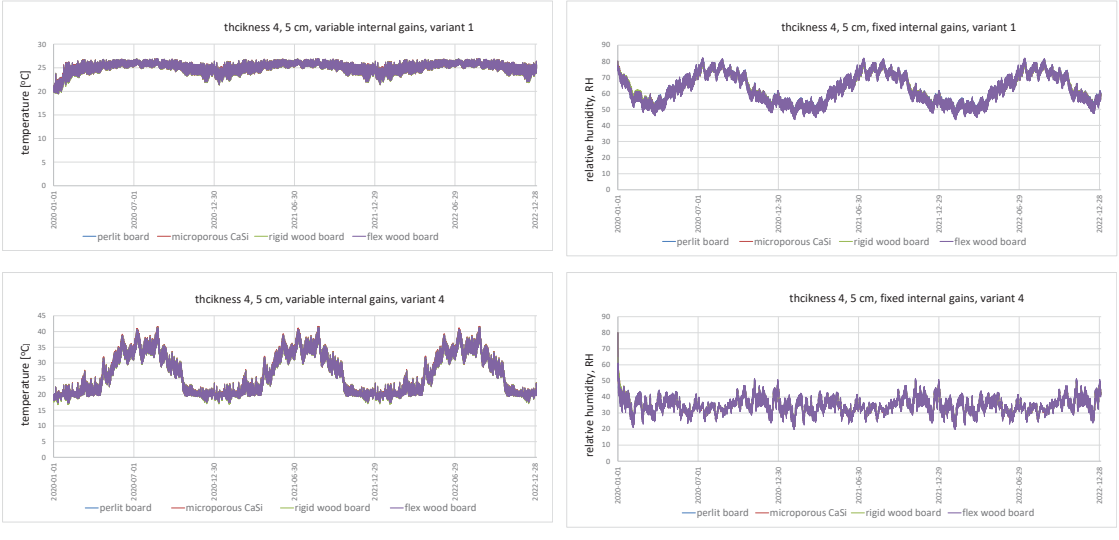

Figure 2. Annual seasonal fluctuations in temperature and relative humidity on the inner surface for 4 or 5 cm internal insulation thickness; (**a**) variable internal gains; (**b**) fixed internal gains.

In the case of the constant occupancy schedule, the same regularities were observed, but for ventilation variants V3 and V4, the minimum temperature value is on average by 0.3 °C, and at its maximum by 2.6 °C, higher than for the variable occupancy schedule (for all walls), whereas, for variant V1, the minimum temperature value is on average 2.1 °C higher for all walls. Interestingly, in variant V2, there was no difference in the minimum and maximum temperature values between the constant and variable occupancy schedules. Lower values of minimum temperature, below 20 °C for variants V3 and V4, are the result of increased ventilation due to more intensive airing by opening the window.

Regardless of the wall type (A, B, C, D) for a given ventilation variant, the same minimum and maximum RH values were obtained for both variable and constant load profiles. Moreover, the minimum and maximum RH values do not change with increasing insulation thickness. The tests by [42] also showed similar results. Increasing the internal insulation thickness beyond 100 mm did not change the maximum and minimum RH values on the internal surface of the wall.

For the variable load profile, the lowest minimum RH = 17–18% was recorded in variants V4 and V3, which corresponds to a maximum RH = 52–50% in variant V4 and RH = 67–65% in variant V3. The highest minimum value of RH = 37–38% was recorded in variant V1, which corresponds to the maximum value of RH = 73–74%. Conversely, for variant V2, the minimum RH = 22–23% and the maximum RH = 66–67% were obtained. The obtained minimum and maximum RH values can be ranked from highest to lowest in the following order for each ventilation variant V1 > V2 > V3 > V4.

Table 5. Maximum and minimum values of temperature on the inner surface of the wall.

Wall Assemblies	Temperature [°C]	Ventilation Variants											
		V1			V2			V3			V4		
		Insulation Thickness [cm]											
		4–5	8	12	4–5	8	12	4–5	8	12	4–5	8	12
		constant occupancy schedule											
A	min	21.5	21.6	21.8	19.4	19.5	19.5	17.3	17.3	17.4	17.3	17.3	17.1
	max	26.0	26.0	26.0	26.0	26.0	26.0	26.0	26.0	26.0	41.4	42.0	35.7
B	min	21.4	21.6	21.8	19.4	19.5	19.5	17.2	17.2	17.0	17.2	17.2	17.3
	max	26.0	26.0	26.0	26.0	26.0	27.1	26.0	26.0	27.1	41.6	42.1	42.6
C	min	21.3	21.5	21.7	19.4	19.4	19.5	16.9	17.0	17.6	16.9	17.6	17.6
	max	26.0	26.0	26.0	26.0	26.0	26.0	26.0	26.0	26.0	41.3	41.6	42.0
D	min	21.5	21.7	21.9	19.4	19.5	19.6	17.4	17.4	17.5	17.4	17.4	17.5
	max	26.0	26.0	26.0	26.0	26.0	26.0	26.0	26.0	26.0	41.2	42.0	42.5
		variable occupancy schedule											
A	min	19.5	19.5	19.6	19.4	19.5	19.5	17.0	17.0	17.1	17.0	17.0	17.1
	max	26.0	26.0	26.0	26.0	26.0	26.0	26.0	26.0	27.1	38.8	39.3	39.8
B	min	19.5	19.5	19.6	19.4	19.5	19.5	16.9	16.9	17.0	16.9	16.9	17.0
	max	26.0	26.0	27.1	26.0	26.0	27.1	26.0	27.1	27.1	39.0	39.5	39.9
C	min	19.4	19.5	19.6	19.4	19.4	19.5	16.5	17.3	17.4	16.5	17.3	17.4
	max	26.0	26.0	26.0	26.0	26.0	26.0	26.0	26.0	26.0	38.7	38.9	39.3
D	min	19.5	19.5	19.6	19.4	19.5	19.6	17.0	17.1	17.2	17.0	17.1	17.2
	max	26.0	26.0	26.0	26.0	26.0	26.0	26.0	26.0	26.0	38.6	39.3	39.8

Table 6. Maximum and minimum values of RH on the inner surface of the wall.

Wall Assemblies	RH [%]	Ventilation Variants											
		V1			V2			V3			V4		
		Insulation Thickness [cm]											
		4–5	8	12	4–5	8	12	4–5	8	12	4–5	8	12
		constant occupancy schedule											
A	min	45	44	44	27	27	27	21	21	20	20	20	21
	max	81	81	82	71	71	71	69	69	69	51	50	64
B	min	45	45	45	27	27	27	21	21	21	21	20	20
	max	80	80	80	70	70	70	68	68	68	50	50	49
C	min	45	45	45	28	27	27	21	21	21	21	21	21
	max	80	80	80	70	70	70	68	68	68	50	50	49
D	min	44	43	43	26	26	26	20	20	20	20	20	20
	max	82	82	82	71	71	71	69	70	70	51	51	50
		variable occupancy schedule											
A	min	37	37	37	23	23	23	18	18	18	18	18	18
	max	73	73	73	67	67	67	67	66	66	51	50	50
B	min	37	37	37	23	23	23	18	18	18	18	18	18
	max	72	72	72	66	66	66	66	66	66	51	50	50
C	min	38	38	38	23	24	24	18	18	18	18	18	18
	max	72	72	72	66	66	66	66	65	65	51	50	50
D	min	37	37	37	23	22	22	17	17	17	17	17	17
	max	73	74	74	67	67	67	67	67	67	52	51	50

For the constant load profile, the same patterns were observed with higher RH values of min RH = 43–45%, max RH = 81–82% for V1, min RH = 26–27%, max RH = 70–73% for V2, min RH = 68–69%, max RH = 20–21% for V3, and min RH = 17–18%, max RH = 49–51% for V4. Higher RH values in variants V1 prove that higher humidity is maintained in the room due to lower ventilation intensity and, in the case of constant occupancy schedules, additionally, higher humidity gains are related to the constant presence of people. A similar situation occurs with respect to temperature. More intensive ventilation is able to take away the heat gains accumulated in the room, which contributes to a lower temperature value on the internal surface of the wall.

4.3. TOW and RHTT Indexes

The external insulation of the base wall in the form of EPS board certainly reduces the risk of condensation inside the wall; however, when installing additional internal insulation, the hygrothermal conditions in the wall should be checked each time. The level of relative humidity in the cross-section at the interface between the base wall and the interior insulation has repeatedly been analysed in great detail in the literature [16,19] due to the increased risk of mould and interstitial condensation in this section. The relative humidity at the interface between the masonry and interior insulation depends, in addition to the effects of WDR, on the relative humidity outside and inside the room transmitted by diffusion and air leakage [39]. In addition, the moisture condition of a wall is very significantly affected by the moisture properties of the various materials of which it is constructed.

In order to avoid the risks associated with the occurrence of moisture, the wall must maintain a balance between dampness and rapid drying. The TOW index defined in Section 3 can be used to assess this situation. The calculated values of TOW and RHTT indexes, on the basis of obtained variation patterns of temperature and relative humidity RH (not included in the text because of their relatively large number—available on request) in the cross-section between the additional layer of internal insulation and the base wall are summarised in Table 7. Analysing individual values of TOW, we can see that only in the case of ventilation variant V1, with minimal air exchange n = 0.2 h^{-1}, the probability of wall dampness appears. For the constant occupancy schedules, maximum values of TOW = 8760 h were recorded for each wall A, B, C, and D at 12 cm thickness, and minimum values at 4 or 5 cm thickness, with TOW = 0 for wall A (perlite board) and C (rigid wood fibreboard). In general, wall D (flex wood fibreboard) has the highest susceptibility to dampness followed in decreasing order by walls B, A and C.

In the case of the variable occupancy schedule, the probability of dampness only applies to variants with 12 cm thick insulation. In this case, however, the walls line up in a different order. The highest probability occurs in wall D, followed by B, C and finally A. The difference between walls A and C, however, is minimal, and the TOW for wall C is 112 h higher than for wall A.

At the same time, the probability of mould growth on a wall (RHTT index), as well as the probability of dampness (TOW index), appear only in the case of ventilation variant V1 and increase with the number of hours of dampness of a wall and the thickness of additional insulation. The highest RHTT = 7.9×10^9 was recorded for wall D with a constant occupancy schedule and 12 cm of additional insulation. Compared to the other walls A, B, and C, with the same insulation thickness, which also have a TOW value of 8760 h, the RHTT is 1.46, 1.13, and 1.61 times higher, respectively. In contrast, in the case of variable moisture load profiles, the probability of mould occurrence appears for walls B, C, and D with 12 cm of insulation. The highest value of RHTT = 1.7×10^8, i.e., the highest probability of mould occurrence, was recorded for wall D and the lowest RHTT = 1.8×10^4 for wall C.

Table 7. TOW and RHHT indexes.

Wall Assemblies		Ventilation Variants											
		V1			V2			V3			V4		
		Insulation Thickness [cm]											
		4–5	8	12	4–5	8	12	4–5	8	12	4–5	8	12
constant occupancy schedule													
A	TOW [h]	0	4780	8760	0	0	0	0	0	0	0	0	0
	RHTT [-]	0	3.9×10^8	5.4×10^9	0	0	0	0	0	0	0	0	0
B	TOW [h]	351	5264	8760	0	0	0	0	0	0	0	0	0
	RHTT [-]	3.0×10^5	9.8×10^8	7.0×10^9	0	0	0	0	0	0	0	0	0
C	TOW [h]	0	4425	8760	0	0	0	0	0	0	0	0	0
	RHTT [-]	0	6.2×10^8	4.9×10^9	0	0	0	0	0	0	0	0	0
D	TOW [h]	921	6131	8760	0	0	0	0	0	0	0	0	0
	RHTT [-]	3.0×10^6	1.6×10^9	7.9×10^9	0	0	0	0	0	0	0	0	0
variable occupancy schedule													
A	TOW [h]	0	0	0	0	0	0	0	0	0	0	0	0
	RHTT [-]	0	0	0	0	0	0	0	0	0	0	0	0
B	TOW [h]	0	0	835	0	0	0	0	0	0	0	0	0
	RHTT [-]	0	0	2.3×10^6	0	0	0	0	0	0	0	0	0
C	TOW [h]	0	0	112	0	0	0	0	0	0	0	0	0
	RHTT [-]	0	0	1.8×10^4	0	0	0	0	0	0	0	0	0
D	TOW [h]	0	0	1905	0	0	0	0	0	0	0	0	0
	RHTT [-]	0	0	1.7×10^8	0	0	0	0	0	0	0	0	0

The least favourable solution is, therefore, wall D with flex wood fibreboard insulation. Analysing the differences between RH values obtained by individual walls, we see that they are negligible. In the case of small insulation thickness 4–5 cm for all ventilation variants, the highest RH values are characteristic for wall B followed by walls A, D, and C. This order changes with higher insulation thicknesses of 8 and 12 cm, in which case the highest RH value is characteristic for wall D and, then, in appropriate order, for walls B, A, and C. This situation occurs both with variable and constant occupancy schedules of rooms. The lowest RH value, in each case, occurs in wall C, a solution based on rigid wood fibreboard with the highest value of diffusion resistance regardless of insulation thickness. Conversely, wall A (perlite board) at 5 cm thickness has relatively high RH due to its high capillary moisture transport capacity [8], which at lower thickness causes faster saturation, hence the higher RH values in this case and the higher total moisture content (Section 2.1). Both walls D (flex wood fibreboard) and C (Ca-Si) are characterised by low diffusion resistance, hence their higher RH values, especially at higher insulation thicknesses. Similar results were found in [22,52].

In addition, with increasing insulation thickness, seasonal fluctuations of RH decrease, and this is much more evident for variants with lower ventilation intensity (V1 and V2) than for variants V3 and V4.

Of course, the obtained results confirm that as moisture loads are reduced (cases with variable occupancy schedule), the hygrothermal conditions in the cross-section between the insulation and the base wall improve due to the reduced vapour diffusion potential to the outside caused by the reduced vapour pressure in the room. These results are in line with previous findings in [22,29,30].

5. Conclusions

This paper presents a study of an exterior wall insulated from the inside using four different capillary active open diffusion interior insulation systems. The primary objective was to assess the hygrothermal behaviour of the different solutions under varying indoor conditions. Based on the analyses, one might draw the following conclusions:

- The profiles of the total moisture content for all analysed walls show the cyclic seasonality of moisture content caused by seasonal shifts in climatic conditions.
- The total moisture content of a wall increases with the increase of insulation thickness. Furthermore, an increase in insulation thickness causes an increase in the RH level inside the internal insulation, which significantly reduces the possibility of the wall drying out into the room and reducing the seasonality of the RH level inside the insulation, which in turn reduces the susceptibility of the wall to damage.
- The obtained values of temperature and RH on the internal surface are mainly influenced by the conditions in a room depending on the heating and ventilating systems and internal heat gains. Lack of proper ventilation with higher moisture gains in the room cause an increase in RH and temperature on the internal surface of the wall.
- Analysis of RHTT and TOW indices has shown that the highest risk of mould growth and interstitial condensation is typical for wall D with flex wood fibreboard. This wall also has the highest profile of relative humidity in the analysed section. On the contrary, the lowest RH values were recorded for wall C with rigid wood fibreboard, which has the highest diffusion resistance.

The analyses carried out in this study for four different internal insulation systems allowed for their hygrothermal assessment under different conditions. Due to the large number of parameters that influence the hygrothermal behaviour of a wall, it is impossible to carry out this assessment without using professional computing tools. Therefore, in order to ensure a safe solution, one should carry out an individual assessment at the design stage. This approach will help to avoid significant damage to walls during building occupancy caused by moisture problems. The results of this study will broaden the design knowledge of internally insulated envelopes, as they help to understand how and under what conditions open diffusion capillary active internal insulation can be safely used.

Funding: This research received no external funding.

Institutional Review Board Statement: Not applicable.

Informed Consent Statement: Not applicable.

Data Availability Statement: The data presented in this study are available from the author upon reasonable request.

Conflicts of Interest: The author declares no conflict of interest.

References

1. Lavagna, M.; Baldassarri, C.; Campioli, A.; Giorgi, S.; Dalla Valle, A.; Castellani, V.; Sala, S. Benchmarks for environmental impact of housing in Europe: Definition of archetypes and LCA of the residential building stock. *Build. Environ.* **2018**, *145*, 260–275. [CrossRef]
2. Directive (EU) 2018/844 of the European Parliament and of the Council of 30 May 2018 amending Directive 2010/31/EU on the Energy Performance of Buildings and Directive 2012/27/EU on Energy Efficiency. Available online: https://eur-lex.europa.eu/legal-content/EN/TXT/?uri=uriserv:OJ.L_.2018.156.01.0075.01.ENG (accessed on 13 June 2021).
3. Zhou, X.H.; Carmeliet, J.; Derome, D. Influence of envelope properties on interior insulation solutions for masonry walls. *Build. Environ.* **2018**, *135*, 246–256. [CrossRef]
4. Marincioni, V.; Altamirano-Medina, H.; May, N.; Sanders, C. Estimating the impact of reveals on the transmission heat transfer coefficient of internally insulated solid wall dwellings. *Energy Build.* **2016**, *128*, 405–412. [CrossRef]
5. Odgaard, T.; Bjarløv, S.P.; Rode, C. Interior insulation—Characterisation of the historic. solid masonry building segment and analysis of the heat saving potential by 1d. 2d. and 3d simulation. *Energy Build.* **2018**, *162*, 1–11. [CrossRef]
6. Krause, P.; Nowoświat, A.; Pawłowski, K. The impact of internal insulation on heat transport through the wall: Case study. *Appl. Sci.* **2020**, *10*, 7484. [CrossRef]

7. Künzel, H.M. Effect of interior and exterior insulation on the hygrothermal behaviour of exposed walls. *Mater. Struct. Constr.* **1998**, *31*, 99–103. [CrossRef]
8. Zhao, J.H.; Grunewald, J.; Ruisinger, U.; Feng, S. Evaluation of capillary-active mineral insulation systems for interior retrofit solution. *Build. Environ.* **2017**, *115*, 215–227. [CrossRef]
9. Straube, J.; Schumacher, C. Interior insulation retrofits of load-bearing masonry walls in cold climates. *J. Green Build.* **2007**, *2*, 42–50. [CrossRef]
10. Kolaitis, D.I.; Malliotakis, E.; Kontogeorgos, D.A.; Mandilaras, I.; Katsourinis, D.I.; Founti, M.A. Comparative assess-ment of internal and external thermal insulation systems for energy efficient retrofitting of residential buildings. *Energy Build.* **2013**, *64*, 123–131. [CrossRef]
11. Klõšeiko, P.; Arumägi, E.; Kalamees, T. Hygrothermal performance of internally insulated brick wall in cold climate: A case study in a historical school building. *J. Build. Phys.* **2015**, *38*, 444–464. [CrossRef]
12. Finken, R.; Bjarløv, S.P.; Peuhkuri, R.H. Effect of façade impregnation on feasibility of capillary active thermal internal insulation for a historic dormitory—A hygro-thermal simulation study. *Construct. Build. Mater.* **2016**, *113*, 202–214. [CrossRef]
13. Viitanen, H. Moisture and Bio-Deterioration Risk of Building Materials and Structures. 2021. Available online: www.intechopen.com (accessed on 10 September 2021).
14. Abuku, M.; Janssen, H.; Roels, S. Impact of wind-driven rain on historic brick wall buildings in a moderately cold and humid climate: Numerical analyses of mould growth risk. indoor climate and energy consumption. *Energy Build.* **2009**, *41*, 101–110. [CrossRef]
15. Vereecken, E.; Van Gelder, L.; Janssen, H.; Roels, S. Interior insulation for wall retrofitting—A probabilistic analysis of energy savings and hygrothermal risks. *Energy Build.* **2015**, *89*, 231–244. [CrossRef]
16. Ferdous, W.; Ngo, T.D.; Nguyen, K.T.Q.; Ghazlan, A.; Mendis, P.; Manalo, A. Effect of fire-retardant ceram powder on the properties of phenolic-based GFRP composites. *Composites Part B* **2018**, *155*, 414–424. [CrossRef]
17. Simpson, A.; .Fitton, R.; Rattigan, I.G.; Marshall, A.; Parr, G.; Swan, W. Thermal performance of thermal paint and surface coatings in buildings in heating dominated climates. *Energy Build.* **2019**, *197*, 196–213. [CrossRef]
18. Jensen, N.F.; Odgaard, T.R.; Bjarløv, S.P.; Andersen, B.; Rode, C.; Møller, E.B. Hygrothermal assessment of diffusion open insulation systems for interior retrofitting of solid masonry walls. *Build. Environ.* **2020**, *182*, 107011. [CrossRef]
19. Toman, J.; Vimmrová, A.; Černý, R. Long-term on-site assessment of hygrothermal performance of interior thermal insulation system without water vapour barrier. *Energy Build.* **2009**, *41*, 51–55. [CrossRef]
20. Pavlík, Z.; . Černý, R. Experimental assessment of hygrothermal performance of an interior thermal insulation system using a laboratory technique simulating on-site conditions. *Energy Build.* **2008**, *40*, 673–678. [CrossRef]
21. Odgaard, T.; Bjarløv, S.P.; Rode, C. Interior insulation—Experimental investigation of hygrothermal conditions and damage evaluation of solid masonry façades in a listed building. *Build. Environ.* **2018**, *129*, 1–14. [CrossRef]
22. De Mets, T.; Tilmans, A.; Loncour, X. Hygrothermal Assessment of Internal Insulation Systems of brick walls through Numerical Simulation and Full-scale Laboratory Testing. *Energy Procedia* **2017**, *132*, 753–758. [CrossRef]
23. Hansen, T.K.; Bjarløv, S.P.; Peuhkuri, R.H.; Harrestrup, M. Long term in situ measurements of hygrothermal conditions at critical points in four cases of internally insulated historic solid masonry walls. *Energy Build.* **2018**, *172*, 235–248. [CrossRef]
24. Kaczorek, D. Hygrothermal assessment of internally insulated brick wall based on numerical simulation. *IOP Conf. Ser. Mater. Sci. Eng.* **2018**, *415*, 012013. [CrossRef]
25. Use of Sensitivity Analysis to Evaluate Hygrothermal Conditions in Solid Brick Walls with Interior Insulation—Aalborg University's Research Portal. Available online: https://vbn.aau.dk/en/publications/brug-af-sensitivitets-analyse-for-at-vurdere-hygrotermiske-forhol (accessed on 10 June 2021).
26. Vereecken, E.; Roels, S. Capillary active interior insulation: Do the advantages really offset potential disadvantages? *Mater. Struct.* **2015**, *48*, 3009–3021. [CrossRef]
27. Abousnina, R.; Manalo, A.; Ferdous, W.; Lokuge, W.; Benabed, B.; Al-Jabri, K.S. Characteristics, strength development and microstructure of cement mortar containing oil-contaminated sand. *Construct. Build. Mater.* **2020**, *252*, 119155. [CrossRef]
28. Adewoyin, O.; Adesina, A.; Das, S. Physico-thermal and microstructural properties of thermal-efficient mortars made with low cement content. *Construct. Build. Mater.* **2022**, *325*, 126850. [CrossRef]
29. Kopecký, P.; Staněk, K.; Bureš, M.; Richter, J.; Tywoniak, J. Experimental investigations of wooden beam ends in masonry with internal insulation. *Energy Procedia.* **2017**, *132*, 682–687. [CrossRef]
30. Wegerer, P.; Bednar, T. Hygrothermal performance of wooden beam heads in inside insulated walls considering air flows. *Energy Procedia* **2017**, *132*, 652–657. [CrossRef]
31. Wójcik, R.; Kosiński, P. On rehabilitation of buildings with historical façades. *Energy Procedia* **2017**, *132*, 927–932. [CrossRef]
32. Slimani, Z.; Trabelsi, A.; Virgone, J.; Freire, R.Z. Study of the hygrothermal behaviour of wood fiber insulation subjected to non-isothermal loading. *Appl. Sci.* **2019**, *9*, 2359. [CrossRef]
33. Pavelek, M.; Adamová, T. Bio-waste thermal insulation panel for sustainable building construction in steady and unsteady-state conditions. *Materials* **2004**, *12*, 2004. [CrossRef]
34. Kočí, V.; Jerman, M.; Pavlík, Z.; Maděra, J.; Žák, J.; Černý, R. Interior thermal insulation systems based on wood fiberboards: Experimental analysis and computational assessment of hygrothermal and energy performance in the Central European climate. *Energy Build.* **2020**, *222*, 110093. [CrossRef]

35. Wegerer, P.; Nackler, J.N.; Bednar, T. Measuring the Hygrothermal Performance of an Interior Insulation Made of Woodfibre Boards. *Energy Procedia.* **2015**, *78*, 1478–1483. [CrossRef]
36. Moradias, P.A.; Silva, P.D.; Castro-Gomes, J.P.; Salazar, M.V.; Pires, L. Experimental study on hygrothermal behaviour of retrofit solutions applied to old building walls. *Constr. Build. Mater.* **2012**, *35*, 864–873. [CrossRef]
37. *EN ISO 13788:2013-05*; Hygrothermal Performance of Building Components and Building Elements—Internal Surface Temperature to Avoid Critical Surface Humidity and Interstitial Condensation—Calculation Methods. International Organization for Standardization: Geneva, Switzerland, 2013.
38. Künzel, H.M. Simultaneous Heat and Moisture Transport in Building Components. One- and Two-Dimensional Calculation Using Simple Parameters. Master's Thesis, University Stuttgart, Stuttgart, Germany, 1994.
39. Soulios, V.; de Place Hansen, E.J.; Peuhkuri, R. Hygrothermal performance of hydrophobized and internally insulated masonry walls—Simulating the impact of hydrophobization based on experimental results. *Build. Environ.* **2021**, *187*, 107410. [CrossRef]
40. *EN 15026:2007*; Hygrothermal Performance of Building Components and Building Elements—Assessment of Moisture Transfer by Numerical Simulation. The European Committee for Standardization: Brussels, Belgium, 2007.
41. Trindade, A.D.; Coelho, G.B.A.; Henriques, F.M.A. Influance of the climatic conditions on the hygrothermal performance of autoclaved aerated concrete masonry walls. *J. Build. Eng.* **2021**, *33*, 101578. [CrossRef]
42. Ahmad, M.R.; Chen, B.; aierdan, Y.; Kazmi, S.M.S.; Munir, M.J. Study of a new capillary active bio-insulation material by hygrothermal simulation of multilayer wall. *Energy Build.* **2021**, *234*, 110724. [CrossRef]
43. Hawila, A.A.W.; Merabtine, A.; Chemkhi, M.; Bennacer, R.; Troussier, N. An analysis of the impact of PMV-based thermal comfort control during heating period: A case study of highly glazed room. *J. Build. Eng.* **2018**, *20*, 353–366. [CrossRef]
44. Velt, K.B.; Daanen, H.A.M. Thermal sensation and thermal comfort in changing environments. *J. Build. Eng.* **2017**, *10*, 42–46. [CrossRef]
45. Holm, A.; Kuenzel, H.M.; Sedlbauer, K. The Hygrothermal Behaviour of Rooms: Combining Thermal Building Simulation and Hygrothermal Envelope Calculation. Available online: http://www.eren.doe.gov/buildings/tools_directory (accessed on 24 July 2021).
46. Fraunhofer IBP WUFI Home Page. Fraunhofer Institute for Building Physics. 2020. Available online: https://wufi.de/en/ (accessed on 10 August 2021).
47. Basińska, M.; Kaczorek, D.; Koczyk, H. Economic and Energy Analysis of Building Retrofitting Using Internal Insulations. *Energies* **2021**, *14*, 2446. [CrossRef]
48. EC Contract No. 608893; Collaborative Research Project Co-Founded by the European Commission under the 7th Framework Programme EeB.NMP.2013-2. Healthier Life with Eco-Innovative Components for Housing Constructions. Available online: http://www.h-house-project.eu (accessed on 30 June 2020).
49. Final Report from Task 8 of MEWS Project (T8-03)—Hygrothermal Response of Exterior Wall Systems to Climate Loading: Methodology and Interpretation of Results for Stucco, EIFS, Masonry and Siding-Clad Wood-Frame Walls, November 2002. Available online: https://nrc-publications.canada.ca/eng/view/object/?id=b6cd5f60-d4f4-4292-a964-2d33eaa3439c (accessed on 10 August 2021).
50. Mukhopadhyaya, P.; Kumaran, M.K.; Nofal, M.; Tariku, F.; van Reenen, D. Assessment of Building Retrofit Options Using Hygrothermal Analysis Tool. Available online: https://nrc-publications.canada.ca/eng/view/accepted/?id=bfe8221c-9bff-407f-b856-fc869273bb08. (accessed on 10 August 2021).
51. Zhan, Q.; Xiao, Y.; Musso, F.; Zhang, L. Assessing the hygrothermal performance of typical lightweight steel-framed wall assemblies in hot-humid climate regions by monitoring and numerical analysis. *Build. Environ.* **2021**, *188*, 107512. [CrossRef]
52. Gradeci, K.; Labonnote, N.; Time, B.; Köhler, J. Mould growth criteria and design avoidance approaches in wood-based materials—A systematic review. *Constr. Build. Mater.* **2017**, *150*, 77–88. [CrossRef]
53. Jensen, N.F.; Bjarløv, S.P.; Rode, C.; Møller, E.B. Hygrothermal assessment of four insulation systems for interior retrofitting of solid masonry walls through calibrated numerical simulations. *Build. Environ.* **2020**, *180*, 107031. [CrossRef]

materials

MDPI

Article

Continuous Evaluation of Shear Wave Velocity from Bender Elements during Monotonic Triaxial Loading

Ahmed Khalil, Zahid Khan *, Mousa Attom, Kazi Fattah, Tarig Ali and Maruf Mortula

Department of Civil Engineering, American University of Sharjah, Sharjah P.O. Box 26666, United Arab Emirates
* Correspondence: zhkhan@aus.edu; Tel.: +971-(0)-6515-29262

Abstract: Few researchers have attempted to experimentally evaluate the low-strain shear wave velocity (*Vs*) of specimens undergoing large strain deformations. They report that the *Vs* is practically unaffected by the strains, and the reasons behind this behavior are not fully understood. This study presents the continuous measurement of low-strain *Vs* with bender elements (BE) during monotonic shearing of two sand specimens in a triaxial device. The results are analyzed using a micro-mechanical model based on contact theory. The results of this study confirm that the *Vs* values from BE measurements are unaffected by an increase in axial strains that are induced by a separate mechanism. The micro-mechanical model predictions of *Vs* agree well with the results of this study and with the results of previous studies. They show that the mean effective stress and increase in inter-particle stiffness controls the low-strain stiffness despite a global increase in strains during monotonic loading.

Keywords: shear wave velocity; bender elements; triaxial testing; micromechanics

Citation: Khalil, A.; Khan, Z.; Attom, M.; Fattah, K.; Ali, T.; Mortula, M. Continuous Evaluation of Shear Wave Velocity from Bender Elements during Monotonic Triaxial Loading. *Materials* **2023**, *16*, 766. https://doi.org/10.3390/ma16020766

Academic Editor: Krzysztof Schabowicz

Received: 5 December 2022
Revised: 6 January 2023
Accepted: 8 January 2023
Published: 12 January 2023

1. Introduction

Dynamic properties, such as shear wave velocity (*Vs*) and damping ratios (*D*), as a function of wide range of shear strains are required for the dynamic analysis of structures and construction sites. Low-strain *Vs* is required to classify sites for seismic analysis, and corresponding amplification factors for ground accelerations are determined. Dynamic properties are typically obtained by conducting field and laboratory tests (Khan et al. [1]; Khan et al. [2]; Khalil et al. [3]; Irfan et al. [4]). These tests have various limitations and testing biases related to boundary conditions, assumptions, attainable strains and frequencies (e.g., Khan et al. [1]; Clayton et al. [5]). A combination of tests is required to evaluate the dynamic properties at the required range of strain levels; however, the results seldom reconcile. Researchers and practitioners need a single test method that would provide the dynamic properties at the required range of strain levels instead of resorting to a combination of test methods.

In one approach, a few researchers have attempted to perform continuous BE tests during the shearing of a specimen during triaxial testing (Chaney et al. [6] and Ismail and Rammah [7], Dutta et al. [8]; Styler and Howie [9]). The outcomes of the studies are contrary to expectations, which caused more interest; the main reasons for the unexpected results are still not fully understood, but should be in order to better design future experiments. Typically, *Vs* as a function of shear strains is measured with a combination of resonant column (RC) and cyclic triaxial (CT) devices which require additional resources (e.g., Khan et al. [1], Khalil et al. [3]). Bender elements (BE) have been extensively used to determine low-strain *Vs* (Dyvik and Madshus [10], Shirley and Hampton [11], Viggiani and Atkinson [12], Kuwano and Jardine [13], Gu et al. [14], Khalil et al. [3]; Irfan et al. [4]). *Vs* measurements with BE are carried out at very low strains because the elements in BE systems are not capable of producing large strains in the specimens. Researchers have always experimented using BE or other high frequency measurements such as ultrasonic

testing (UT) at large strains without conducting dynamic CT or RC tests to complement the results.

~Previous attempts to use BE and UT during monotonic shearing of specimens in a triaxial device show inconclusive results (Dutta et al. [8]; Styler and Howie [9]). These studies report that the low-strain stiffness (*Vs* measurements from BE or UT) is unaffected by the strains that are generated by shearing the specimen in a triaxial device. The initial increase and subsequent decrease in *Vs* measurements is attributed to the contractive and dilative stages of the specimen, respectively. The observed behavior of the *Vs* from BE tests is mostly explained in qualitative terms; therefore, more testing and analysis is required to better understand the behavior. Micro-mechanical analysis can provide important insights that can help us to understand the mechanisms that control the low-strain stiffness. It can provide directions that can lead to the development of a single test method that can evaluate *Vs* at the required range of strain levels.

This study presents the results of experimental program that includes the evaluation of *Vs* from CT tests as a function of shear strain and low-strain *Vs* from continuous BE measurements during the monotonic loading of specimens in a triaxial device. The *Vs* values are also computed from the stress–strain curves of the monotonic loading of specimens. All tests are performed at two different confinements and for two identical sand specimens for each test, to ensure repeatability. The sands are characterized with scanning electron microscope (SEM), energy-dispersive X-ray spectroscopy (EDS) and confocal microscopy to better understand the inter-particle interaction. The BE results are further analyzed with Hertz-Mindlin contact theory (Hertz [15]; Mindlin [16]) to study the evolution of *Vs* from the perspective of interparticle forces, mean effective stresses and change in void ratio.

2. Background and Literature

The bender element (BE) test induces high frequency (>1 kHz) stress waves in the specimen (e.g., Irfan et al. [4]; ASTM D8295-19 [17]). The strains generated in the specimen are typically low to very low; therefore, a combination of other tests, such as RC and CT, are used to evaluate the dynamic properties at other required strain values. In the BE test, a transmitter generates a stress wave with a short duration impulse of step or sine function. The duration of the pulse determines the frequency content of the propagating wave. The receiver located at a known distance detects the arrival, and velocity is obtained by simply dividing the known distance by the time of propagation. Velocity analysis can also be performed in the frequency domain with phase velocities.

The triaxial test is an ASTM standard (ASTM D7181-20 [18]) in which monotonic axial loads are applied to the specimen until failure, and a stress–strain curve is obtained for further analysis. The stress–strain curve can be obtained from monotonic triaxial tests under different confining and drainage conditions. Subsequent analyses of the curve provide elastic and secant moduli at different axial strain levels. Changes in volumetric strains as a function of axial strain represent the changes in void ratio during loading.

In cyclic triaxial (CT) tests (Khalil et al. [1]; Khan et al. [19]), dynamic axial loads are applied to the specimen to evaluate dynamic properties as a function of shear strains at different confining and drainage conditions. The operable frequencies in CT tests range from less than 1 Hz to 10 Hz; however, only medium to large strains can be induced in the specimen. Low strain tests such as bender elements (BE) are performed to compliment the strain range.

The resonant column (RC) test is an ASTM standard (ASTM D4015-21 [20]) in which dynamic torsional loads are applied to evaluate the dynamic properties of soils at low to medium strain levels. The RC test has different testing biases which should be considered to correct the results (Khan et al. [1]; Clayton et al. [5]; Khan et al. [21]). The results become increasingly biased as the stiffness of the specimen increases, due to contributions from the base of RC device. Salient features of the above tests, such as the operating range of frequencies and induced strain levels, are presented in Table 1. The advantages and limitations that can affect their results are also presented. The frequencies and strains that

are generated in typical geotechnical problems involving dynamic loads, such as machine vibrations and earthquakes, are presented for comparison purposes.

Table 1. Characteristics of RC, CT, BE, and field tests.

Test	Frequencies (Hz) /Strains (e)	Dynamic Properties	Advantages	Disadvantages
RC	20–150 $e < 10^{-3}$	Vs and D	Wide range of frequencies and strains	Many testing biases such as base contributions
CT	0.1–10 $10^{-4} < e < 10^{-2}$	Vs and D	Same equipment can be used for static test	Narrow strain range; requires additional tests
BE	20–150 $e < 10^{-6}$	Vs	Fast and minimal equipment setup	Damping ratio (D) cannot be calculated; narrow strain range
Field tests	20–150 $<10^{-6}$	Vs	Representative *Vs* of the site	Damping ratio (D) cannot be calculated; narrow strain range
Earthquakes			0.1–50 $10^{-6} < e < 10^{-1}$	

A hyperbolic model is often used to curve fit the variation of shear wave velocity with shear strains (e.g., Khalil et al. [3], Khalil [22]; Hardin and Drnevich [23]). Site response analysis requires the hyperbolic model for each soil layer of the construction site as an input for analysis. Equation (1) presents the functional form of the modified hyperbolic model.

$$\frac{G}{G_{max}} = \frac{1}{1+\gamma_h} \tag{1}$$

where γ_h is the hyperbolic strain which is defined by Equation (2). G_{max} is the shear modulus measured at the lowest possible strain level and G is the shear modulus corresponding to higher strain levels.

$$\gamma_h = \frac{\gamma}{\gamma_h}\left(1 + a\exp\left(-b\frac{\gamma}{\gamma_r}\right)\right) \tag{2}$$

Model parameters a and b are defined in terms of curvature coefficients and γ_r is the reference strain, indicating the beginning of non-linear behavior. These parameters are obtained from the non-linear curve fitting of the model to measured data.

The shear wave velocity of soils depends on many test variables, such as confinement, packing density (void ratio), particle shape and roughness and soil type. The effect of void ratio is significant if all other variables are kept constant. The packing density (void ratio) determines the structure of soil matrix and number of interparticle contacts (C_n). The coordination number (C_n) is the number of contacts that a soil particle will create with other surrounding particles in a packing. Sand particles are arranged randomly, and their C_n is considered to be a function of void ratio of the soil matrix; however, this is not always true. Many studies have shown that C_n can be related to void ratio; however, any changes in which rearrangement of particles occurs can change the void ratio without significantly affecting the C_n (Walton [24]). A summary of selected studies that relate C_n to the void ratio of specimen are presented in Table 2.

Table 2. Selected correlations between C_n and e for a random assembly of particles.

Expression	Reference
$C_n = 26.486 - 10.726\,(1+e)$	Smith et al. [25]
$C_n = \frac{32}{13}\left[7 - 8\left(\frac{e}{1+e}\right)\right]$	Ouchiyama & Tanaka [26]
$C_n = 24e^{\left(-2.547\frac{e}{(1+e)}\right)} - 0.373$	Zimmer [27]
$C_n = 2 + 11\left(\frac{1}{1+e}\right)^2$	German et al. [28]
$C_n = -2.8 + 15.1\left(\frac{1}{1+e}\right)$	

Chang et al. [29] experimentally determined soil stiffness at small strains by establishing a relationship between C_n and e. Magnanimo et al. [30] showed that random samples

prepared with different preparation methods had similar e, but different C_n which shows the sensitivity of C_n-e to sample preparation. Smith et al. [25] investigated the C_n-e relationship for random packing by comparing experimental data with regular arrays, including face-centered cubic (FCC), hexagonal close-packed (HCP) and simple cubic (SC) arrays. However, there is no agreement between the C_n-e data points for body-centered cubic (BCC) array. Ouchiyama & Tanaka [26] and Arakawa & Nishino [31] presented theoretical expressions for the C_n-e relationship which are in good agreement with the expression derived by Smith et al. [25]. Furthermore, Suzuki et al. [32] incorporated a Gaussian error function to the model proposed by Tory et al. [33] which shows good agreement with the experimental results of Bernal and Mason [34] and Gotoh [35]. German et al. [28] presented correlations between C_n and e for various packing types, including ordered, dispersive, random, partially densified and fully densified packing.

2.1. Micro-Mechanical Evaluation of Internal Forces and Vs

Contact models for the random packing of spheres have been developed by researchers for evaluation of the Poisson's ratio of the packing (Hertz [15], Mindlin [16], Digby [36], Walton [24], and Norris and Johnson [37]). Duffaut et al. [38] presented an expression for the effective shear modulus combining Digby's result (Digby [36]) with Mindlin's extended solution (Mindlin [16]) that includes frictional tangential contact stiffness. The normal contact force (average) for an isotropic random assembly of particles is estimated with the micromechanical formulation proposed by Rothenburg and Bathurst [39] for a given void ratio e, coordination number C_n and isotropic confinement σ_o by

$$f_n = \frac{4\pi(1+e)R^2\sigma_0}{C_n} \tag{3}$$

where C_n is the coordination number that can be computed from several empirical equations presented in Table 2. During monotonic triaxial loading, the specimen's void ratio decreases during the compression stage until the beginning of dilation. This phenomenon is represented by changes in volumetric strains. The C_n number can be assumed to remain practically constant during the compression stage (negative volumetric strain); therefore, the normal contact force (f_n) can be considered a function of void ratio and mean effective isotropic confinement. The change in radius R of the particles is negligible due to their large elastic moduli compared with the moduli of the packings.

If two elastic particles are in contact under the action of a normal force f_n, the Hertz theory (Hertz [15]) relates the contact area with the radius and the normal displacement between the particles. Duffaut et al. [38] extended this inter-particle mechanism and presented the final expression for bulk modulus of the random assembly of particles (Equation (4)).

$$K_{\text{dry}} = \left(\frac{C_n^2(1-\phi)^2 G_g{}^2 \sigma}{18\,\pi^2(1-v)^2} \right)^{\frac{1}{3}} \tag{4}$$

where ϕ is porosity (related to void ratio), G_g is shear modulus of the particles, σ is the mean effective stress, and ν is the Poisson's ratio of the particles. The conversion of bulk modulus to shear modulus is based on friction between the particles that will either allow no slippage or complete slippage under tangential force at the inter-particle contact. The relationship between bulk and shear modulus is provided in Equation (5).

$$G_{\text{dry}} = \frac{3}{5}\left[1 + \frac{3(1-v)}{2-v} f(\mu)\right] K_{\text{dry}} \tag{5}$$

The term f(μ) ranges from 0, when there is complete loss of inter-particle contact, to 1, when no slippage occurs. f(μ) represents the Mindlin friction term, which essentially is a function of tangential force, normal force, and the coefficient of friction at inter-particle contact. f(μ) can be estimated in various ways; however, Equation (6) presents a simpler

approach of estimating f(μ) for a given Poisson's ratio of the particles (ν) and of the matrix (ν_{dry}).

$$(\mu) = \frac{1}{2}\left(\frac{2-v}{1-v}\right)\left(\frac{1-4\,v_{dry}}{1+v_{dry}}\right) \quad (6)$$

Particles rearrange and deform when loaded, and the degree of disturbance depends on the induced strain levels. Noticeable particle rearrangement and changes in fabric occur at medium to large strains ($\gamma > 10^{-3}$). The degree of changes depends on many factors, such as surface roughness, gradation of particles and forces at the inter-particle contacts. In the beginning of deviatoric loading in triaxial tests, the main mechanism is dominated by particle deformation with slight slippage that can also cause crushing of asperities of the surface. Particle rearrangement occurs when strains exceed 10^{-3}, and the degree of rearrangement depends on the coordination number and inter-particle forces, especially f_n (Equation (3)). Complete slippage of the contact area at the particle is assumed during the dilatational stage, in which the void ratio increases and C_n decreases. At very low strain measurements, such as in BE, particle deformation that depends primarily on the elastic properties of the sand particles controls the stiffness.

Equation (3) suggests that during the initial stages and even within the contraction stage, the low strain stiffness (if measured independently) shall increase due to an increase in effective stress at contacts. The mean effective stress at the inter-particle contacts increases with an increase in deviatoric stress, and primarily governs the stiffness in addition to the effect of change in void ratio. On the other hand, velocity is expected to decrease during dilatational stage.

2.2. Continuous Vs Measurements during Monotonic Triaxial Loading

Few researchers have attempted to evaluate the low-strain stiffness of specimens that are sheared monotonically in triaxial testing. Chaudhary et al. [40] presented the results of *Vs* measurements of the Toyoura sand with BE tests at a constant effective stress ratio. The results show that the shear wave velocity practically remains constant during the contraction stage; however, *Vs* starts to decrease following the phase transformation of the specimen from contraction to dilation.

Styler and Howie [9] evaluated the variation of low-strain *Vs* with the change in void ratio (e) of the specimens during triaxial loading. Fraser river sand is tested at different confinements; however, the stress ratio is kept constant at 2.0. The results show that the *Vs* increases as the void ratio decreases during the contraction stage. During phase transformation and throughout the dilation stage, the *Vs* steadily decreases as the void ratio increases. They show that the rate of increase during contraction stage is not the same as the rate of decrease in *Vs* during the dilation stage.

Dutta et al. [8] presents continuous evaluation of low-strain *Vs* with disk-shaped planar transducers during triaxial testing. The variation of *Vs* is presented as a function of axial strains (ε_a). The study presents qualitative discussions and argues that the mean C_n controls the evolution of *Vs* during the contraction and dilative stages. The results also confirm the previous findings that the *Vs* increases during the contraction stage and then starts to decrease after phase transformation to the dilative stage.

All studies indicate that low-strain *Vs* is not affected by the level of shear strain in the specimen and the observed changes in *Vs* are attributed to the changes in void ratio (or C_n) during monotonic axial loading of the specimens. The change in void ratio is relatively simple to calculate from the change in volumetric strains; however, there is no experimental evidence that C_n changes proportionally to void ratio. Table 2 presents different expressions that relate void ratio to C_n. The functional form of the expressions ranges from linear to exponential which indicates the level of uncertainty in relating C_n to e, especially for a random assembly of irregular particles.

3. Materials Properties

Sand samples are collected from a borehole located in Al Shamkhah area of Abu Dhabi, United Arab Emirates (UAE). A typical cylindrical specimen of soil has a diameter of 7 cm and a length of 14 cm in the study. Various routine tests are performed, such as moisture content, index density and gradation analysis. Table 3 presents the main properties of the sands and samples. Figure 1 presents the particle size distribution curves of the two sand samples.

Table 3. Physical properties of the tested specimens and standard penetration test (SPT) values.

Sample Name	Void Ratio (*e*)	C_C	C_U	Diameter/Height (cm)	Moisture Content (%)	Dry Density (kg/m^3)	Material Description	Depth (m)	SPT-N Value
Sample A	0.81	0.82	2.45	7/14.2	22.2	1618	Sand with crystalline gypsum inclusions, very dense and poorly graded	11 to 12	50
Sample B	0.99	1	2.00	7.1/14.0	12	1478	Sand with silt and crystalline gypsum inclusions, very dense and poorly graded	1.5 to 2	21

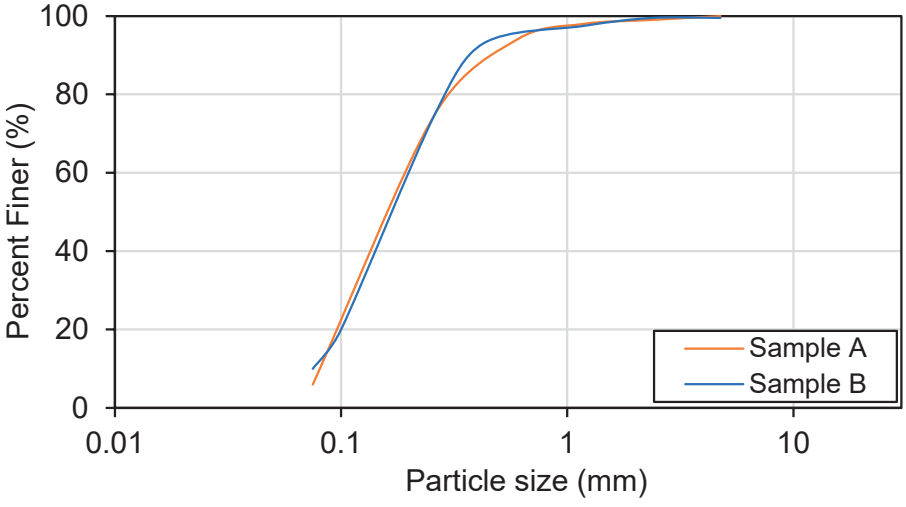

Figure 1. Particle size gradation of sands.

The sands are also characterized with scanning electron microscopy (SEM), energy-dispersive X-ray spectroscopy (EDS) and confocal microscopy (CFM). SEMs produce images that are magnified by using electrons instead of light, whereas EDS detectors separate the characteristic x-rays of different elements into an energy spectrum. In addition, EDS provides chemical composition of the material and creates element composition maps over a larger raster area using the energy spectrum.

SEM and CFM are used to visualize the grain structure, grain size and surface roughness. Sample A has angular-shape particles, whereas sample B has rounded to sub-rounded particles (Figure 2). Visual inspection of these figures also provides an estimate of probable C_n which is anticipated to be more than 10 in 3D space. Furthermore, three spectra each are obtained for both materials with EDS to determine the chemical compositions (Figure 3). The results of three spectra are averaged for each material. Both materials exhibit quite similar chemical compositions with slight variations in the Calcium and Silicon content.

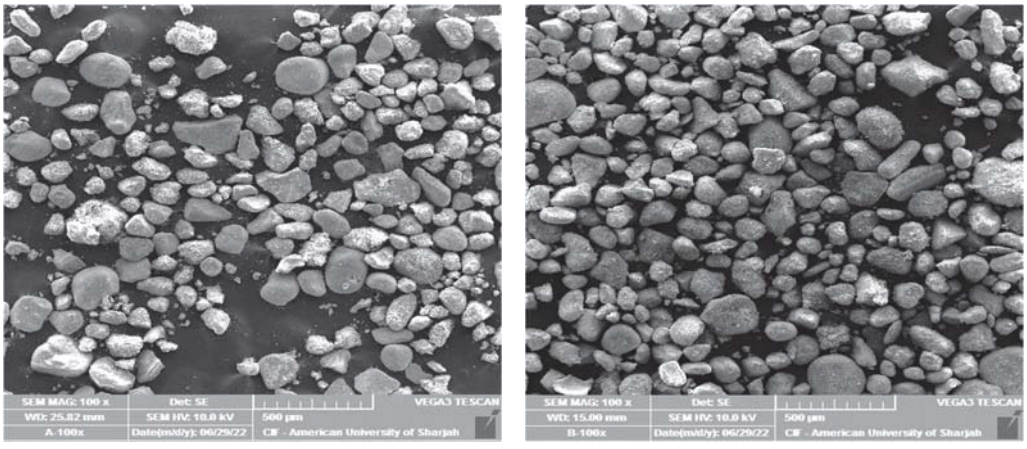

(**a**) (**b**)

Figure 2. SEM images with a magnification of 100× of tested soil materials; (**a**) sample A and (**b**) sample B.

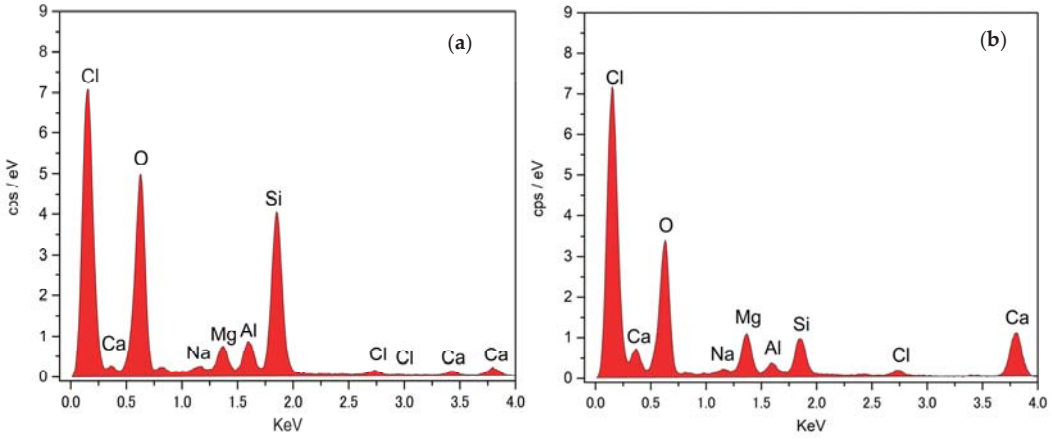

Figure 3. Typical EDS spectra of (**a**) Sample A, and (**b**) Sample B.

Table 4 summarizes the averaged chemical compositions of both samples. Silicon dioxide (SiO_2) was the dominant chemical composition of both samples A and B. Both samples show inclusion of sodium chloride because of their proximity to the Arabian gulf, and that the primary sediments at depth originate from the deep sea carbonate platform (Khan et al. [2]). Moreover, both materials contain calcium inosilicate mineral ($CaSiO_3$) commonly known as wollastonite. Wollastonite primarily contains calcium oxide (CaO), an ingredient used in Portland cement. Presence of minerals other than SiO_2 in relative abundance is indicative of heterogeneous composition and can be one of the possible reasons for differing elastic deformation characteristics compared with pure silica sand.

Representative two-dimensional topographies for both samples are obtained using confocal microscopy through a surface area of approximately 550 μm^2. Figure 4 presents the surface profile of typical particles from sample A and B. The profile indicates rough surfaces with asperities that are brittle and can break upon deformation. The inter-particle slippage is predicted to be smaller due to increased inter-particle friction caused by asperities.

Table 4. Summary of the chemical compositions of tested soil samples.

Element	Standard Label	Apparent Voncentration	Weight Fraction (wt%)	Apparent Concentration	Weight Fraction (wt%)
		Sample A		Sample B	
O	SiO_2	2.52	48.82	2.71	52.74
Na	Albite	0.05	0.78	0.10	1.75
Mg	MgO	0.20	6.18	0.29	6.42
Al	Al_2O_3	0.11	2.71	0.08	1.93
Si	SiO_2	0.87	20.47	0.60	13.74
Cl	NaCl	0.14	1.7	0.13	3.30
Ca	$CaSiO_3$	0.28	10.51	0.85	20.12
Fe	Fe	0.16	7.72	0.00	0.00

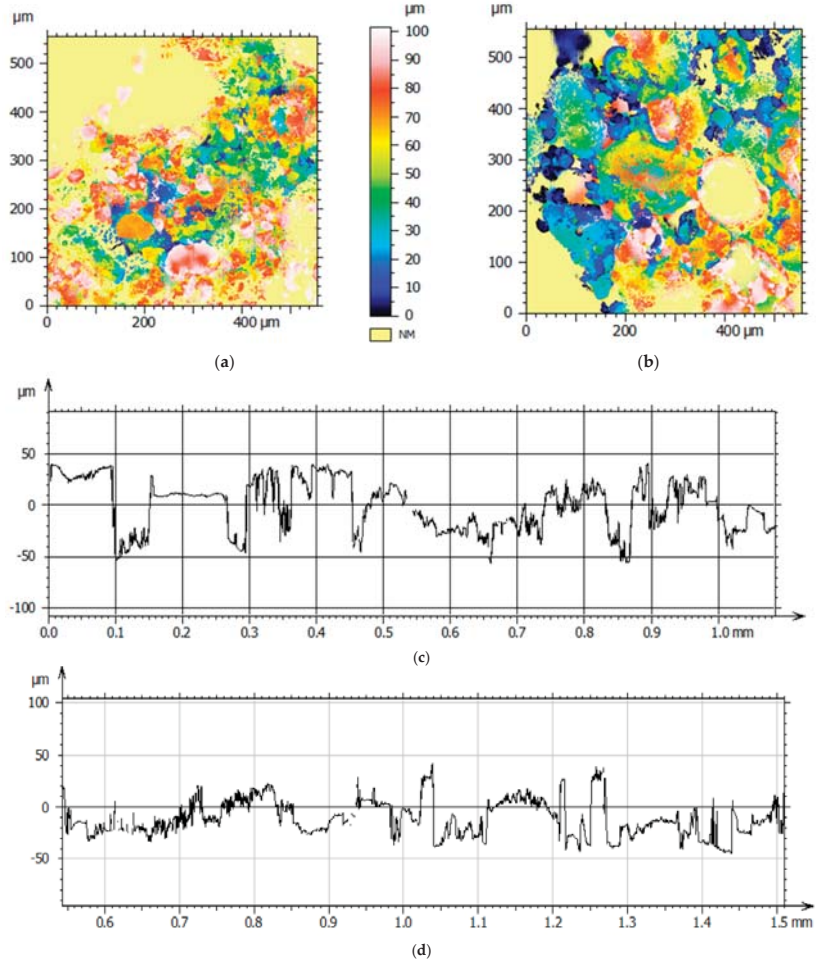

Figure 4. Scanned surfaces of (**a**) sample A and (**b**) sample B using confocal microscopy and 2D surface topographies of (**c**) sample A and (**d**) sample B.

4. Experimental Program

Dynamic triaxial testing (ASTM D3999-91 [41]) and monotonic triaxial loading (ML) are performed with a dual mode cyclic triaxial test apparatus supplied by VJ Tech (UK). CT equipment also includes BE fixed to the top and bottom platens with independent controls. All tests are conducted under two confining pressures (σ_3) of 150 kPa and 300 kPa. Identical specimens with similar void ratios are produced for CT and ML tests from the two types of sands. Continuous BE measurements are taken during ML tests at regular increments of axial strains. Low strain measurements with BE are also taken before the start of CT tests for comparison with BE measurements performed before the start of ML tests on the other identical specimen.

An input signal of 1 Hz with 10 cycles is used for CT tests. The load and displacement time signals are fitted with a simulated signal to create symmetrical loops for further analysis following standard procedure (Khalil et al. [3], Khalil et al. [22]; Kumar et al. [42]). Measured and fitted signals for the cyclic triaxial data are shown in Figure 5a,b. Figure 5c shows the comparison of hysteresis loops from the measured and fitted signals. For clarity, the load and displacement amplitudes are normalized in the figures. Elastic modulus (E) is computed at various strain levels and subsequently converted to G and Vs.

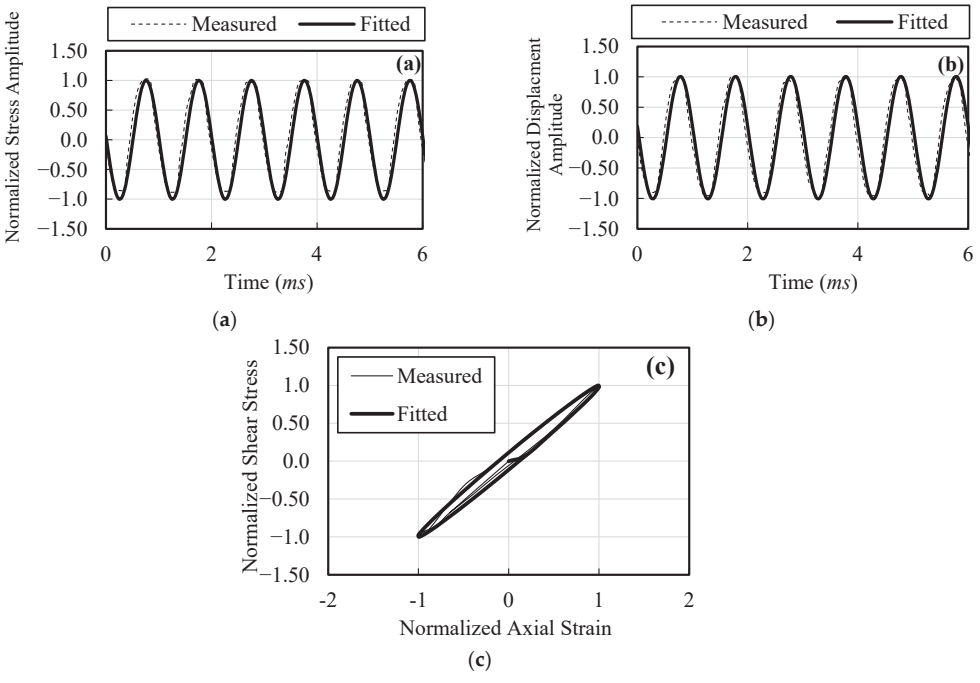

Figure 5. Typical matching of normalized signals and loops from CT tests. (**a**) Stress amplitude; (**b**) Displacement amplitude; (**c**) Hysteretic loops.

A baseline measurement of low-strain Vs with BE is obtained at axial strain (ε_a) of 0% before conducting monotonic triaxial loading (ML). The soil specimen is then subjected to monotonic triaxial loading (shearing at regular path) with simultaneous BE tests at regular intervals. An axial strain rate of 1 mm/min is adopted for the ML testing. The BE measurements are performed at a frequency of 5 kHz, and 10 signals are stacked to improve the signal-to-noise ratio. Vs is estimated in the time domain after dividing the distance (between the elements) by the propagation time of the wave front. The distance between the elements is dynamically adjusted for different axial strains (ε_a). Secant modulus

(E_{sec}) at predetermined axial strains is computed from stress–strain curves. The secant elastic modulus (E_{sec}) is then converted to secant shear modulus (G_{sec}), and then finally to *Vs*. Uncemented to lightly cemented sands can vary in Poisson's ratio from 0.15 to 0.3 (Santamrina et al. [43]), therefore a value of 0.25 is chosen for conversion between moduli.

Typical time histories and their respective Fourier spectra recorded at the receiver (Rx) for two randomly selected shear strains (7% and 14%) are shown in Figure 6. To avoid near-field effects, at least one wavelength was ensured between the transmitter and receiver in this study (Arroyo [44], Lee [45], Khalil et al. [3]; Khalil [22]). The peak power spectrum in BE tests of a wave front propagating at an average *Vs* of 300 m/s is centered around 4500 Hz (Figure 6). The average wavelength in this study is 6.6 cm compared with the propagation distance of 14 cm, which ensures at least on wavelength between the transmitter (Tx) and receiver (Rx).

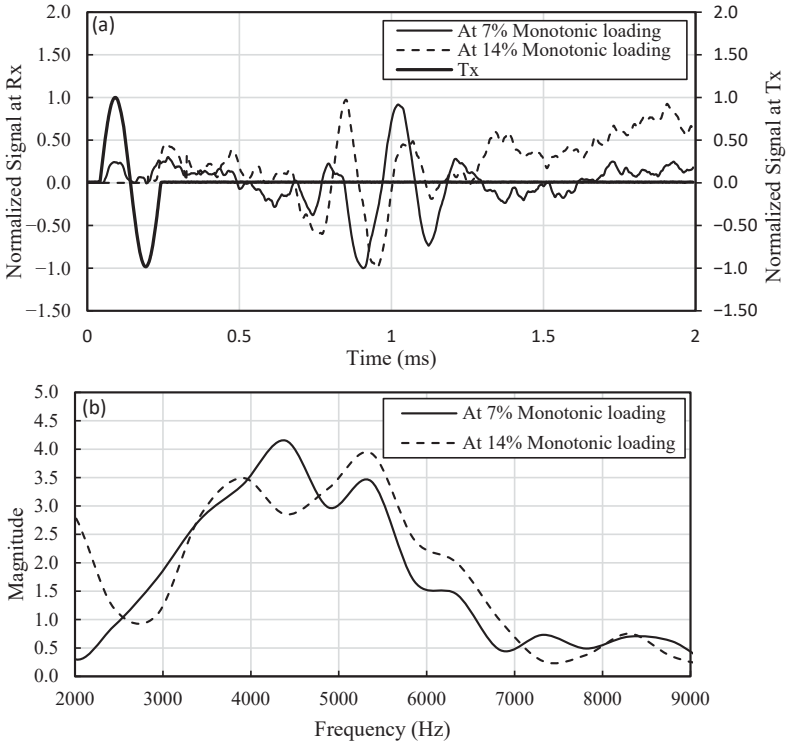

Figure 6. (**a**) Time histories at the bender element (BE) receiver (Rx), and (**b**) Fourier spectra of receiver signals. Tx corresponds to the transmitter (trigger) signal.

5. Results and Discussion

Figure 7a,b presents the relationship between deviatoric stress (q) and axial strain (ε_a) for Samples A and B from ML testing. The stress–strain curves are compared with curves presented by Dutta et al. [8] at two confinements. The results from Dutta et al. [8] are presented for a predominately siliceous sand at 100 kPa. The behavior of sands in present study is noticeably different from Dutta et al. [8]. There are many possible reasons for the difference, such as different void ratios, particle shape and stress ratios, and difference in mineral composition of the sand particles. The ductile behavior of sand specimens (A and B) is evidenced by yielding at significantly larger axial strains. Sample A at 150 kPa deforms almost linearly with strain despite having a relatively smaller void ratio (e = 0.81) compared with Sample B (e = 0.99). Figure 7 also shows stick-slips (small serrations on the

stress–strain curve) which has been reported by other researchers (Nasuno et al. [46]). The stick-slips are typically observed in particles with rough to very rough surfaces.

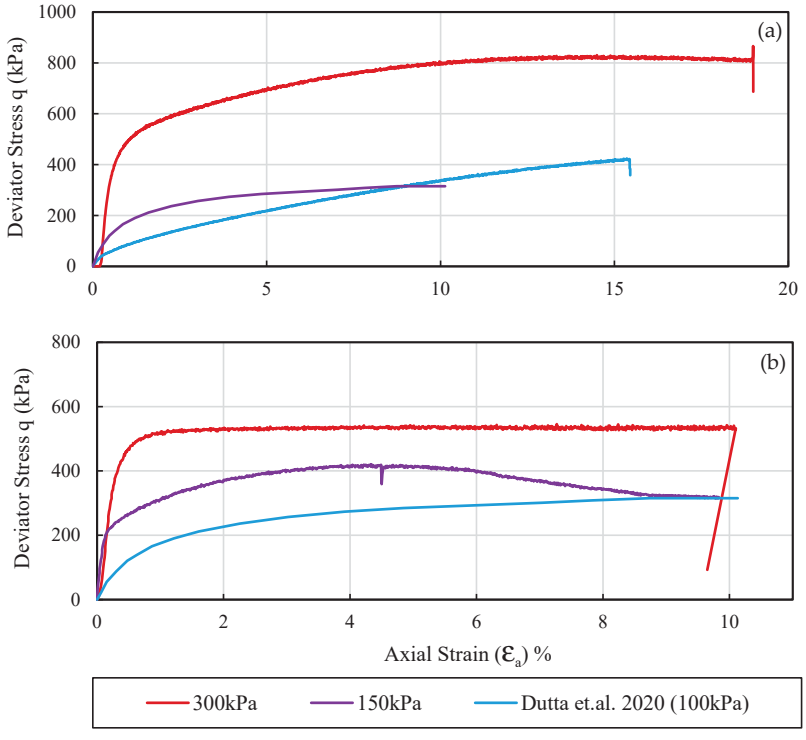

Figure 7. Stress–strain curve from siliceous sand (Dutta et al. [8]) at σ_3 of 100 kPa and this study (**a**) sample A, and (**b**) sample B.

Figure 8 presents the variation of normalized values of *Vs* with axial strain (ε_a) from continuous BE tests, CT tests, and ML tests. All *Vs* values are normalized to *Vs* value BE tests that correspond to an axial strain of 0%. The value of 0% is replaced with a very small value of 10^{-6} for plotting on logarithmic scale. Hyperbolic model (Equation (1)) is fitted to cyclic triaxial data and then extended to *Vs* values computed from the stress–strain curves from ML tests. The *Vs* values from CT and those from ML decrease with increase in strain level. It is interesting to note that the extended hyperbolic model fits the *Vs* values from both CT and ML despite different mechanisms of loading, except for sample A at 150 kPa. ML is not a dynamic test; however, CT tests also do not operate at high enough frequencies to involve the inertial response of a single degree of freedom (SDOF) system. RC tests operate at much higher frequencies; therefore, the hyperbolic model fitted to RC data typically does not reliably predict CT results.

Figure 8 shows that the low-strain *Vs* values from BE tests slightly increase with increase in axial strain and seem to be unaffected by the increasing axial strain in the specimen. The scatter in the *Vs* from BE tests at very large strains is due to lower quality signals, possibly because of the distortion and misalignment of the transmitter and receiver. Figure 8 indicates that the behavior of low-strain stiffness, representing small scale deformations of the specimen, is different from the evolution of stiffness corresponding to larger-scale deformations. Previous studies have also noticed a slight increase in low-strain *Vs* during the contraction stage of the sample during the ML test (Dutta et al. [8]; Styler and Howie [9]). They attribute this slight increase in low-strain *Vs* to a decrease in void

ratio anecdotally; however, relating the behavior to an observed change in void ratio is not sufficient to understand its cause.

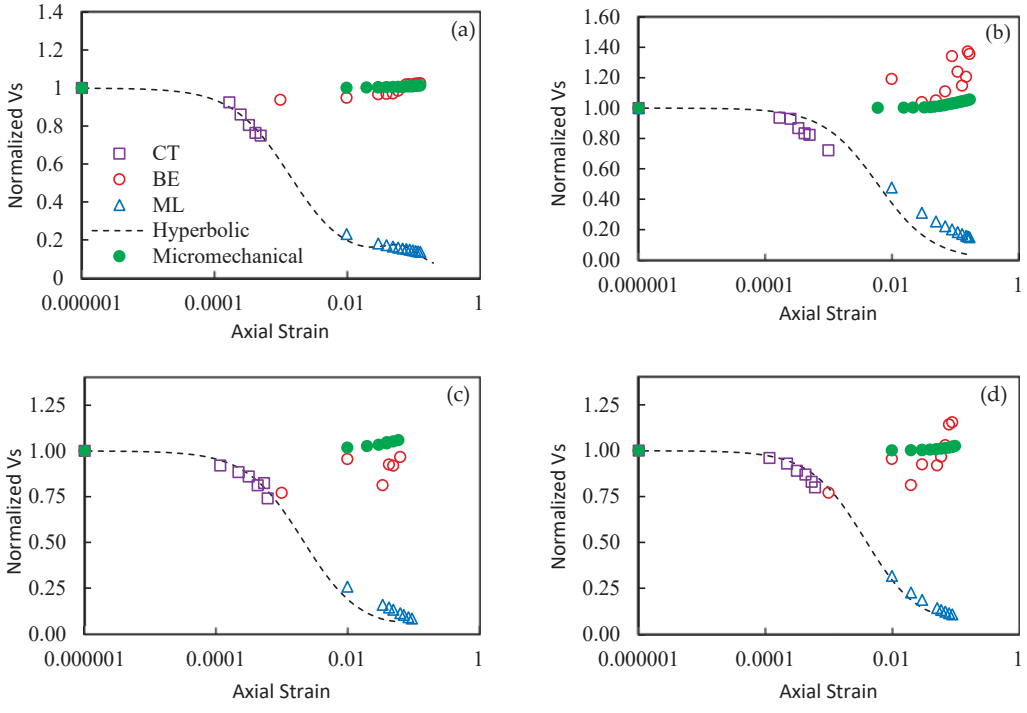

Figure 8. Variation of normalized *Vs* from cyclic triaxial (CT), bender elements (BE), and stress–strain curve of monotonic loading (ML) for (**a**) sample A at 150 kPa, (**b**) sample A at 300 kPa, (**c**) sample B at 150 kPa, and (**d**) sample B at 300 kPa.

The low-strain *Vs* of soils depends on the initial void ratio to some extent; however, as noted earlier, the mean effective stress governs the magnitude of normal force at the interparticle contacts (Equation (3)). The shear stresses caused by the propagation of shear waves produce tangential forces at the inter-particle contacts, and the deformation response at the contacts to tangential forces depends on the magnitude of the normal force (f_n) at the contacts (Duffaut et al. [38]). The stiffness and therefore low-strain *Vs* are expected to increase with an increase in normal forces. The increase in axial stress (σ_a) during ML tests results in an increase in mean effective stress in the specimen. A micro-mechanical model based on contact theory (Equation (5)) is used to theoretically evaluate the low-strain *Vs* for samples A and B. The Mindlin friction term f (μ) is computed from Equation (6) and assumed to remain practically constant during the contraction stage. The prediction of *Vs* (Equation (5)) at different stages of the sample deformation (axial strains) is also presented in Figure 8.

The micro-mechanical prediction of *Vs* indicates a slight increase with an increase in the mean effective stress. Micro-mechanical prediction of *Vs* does consider the change in void ratio; however, the decrease in void ratio is not the main cause of slight increase in *Vs*. Equation (3) suggests that the decrease in void ratio should cause a decrease in normal force at the inter-particle contacts if the mean effective stress remains unchanged. The contact theory assumes that a decrease in void ratio will cause an increase in the number of contacts (not always true) which will result in many but relatively smaller contact forces. The overall stiffness therefore remains unaffected. Figure 8 predicts an increase in low-strain *Vs* of

about 10% to 15%, which is comparable to the increase measured in BE tests. The dilation of tested specimens occurs very late in the loading cycle; therefore, the effect of an increase in void ratio (decrease in inter-particle stiffness) on the low-strain *Vs* is not clear.

The comparison of the measured data from this study and two other studies (Dutta et al. [8]; Styler and Howie [9]) from the literature are presented in Figure 9. The compared studies include tests that are performed at confinement of 100 kPa which are compared to the results of this study at their closest confinement of 150 kPa. The results from CT tests are not compared because the selected studies did not perform the CT tests. The logarithmic scale is decreased to better visualize the comparisons. The normalized variation of low-strain *Vs* from Dutta et al. [8]; Styler and Howie [9] agree well with the results from this study. The normalized *Vs* that are converted from secant shear modulus (stress–strain curves) of Dutta et al. [8] are slightly higher than this study; however, the trend is almost similar. The results from Dutta et al. [8] shows that the low-strain *Vs* values (BE testing) decrease after an initial increase. They attributed the initial increase and subsequent decrease in low-strain *Vs* to the contraction and dilatational phase, respectively.

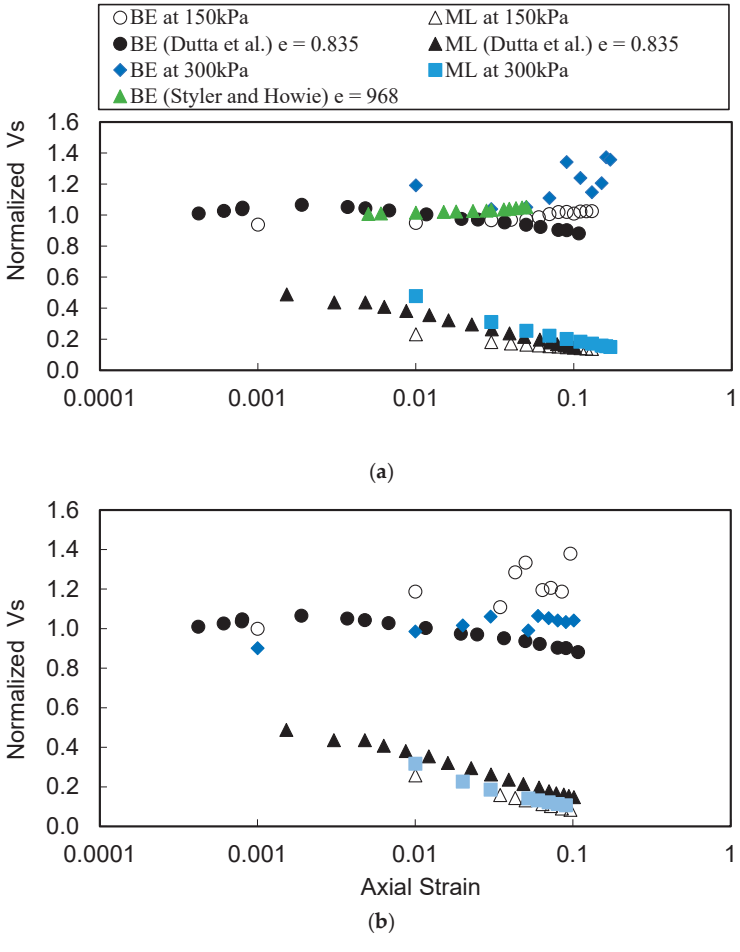

Figure 9. Comparison of results from this study with the results from Dutta et al. [8]; Styler and Howie [9] (**a**) sample A and (**b**) sample B.

The behavior of random packing of spheres such as in sands can be predicted well with contact theories based on the work of Hertz and Mindlin. The accuracy of contact theories still needs to be investigated for cohesive soils such as clays and some silts. Other theoretical models involving the response of structural materials and systems to complex contact and non-contact loads, along with volumetric damage models, can be developed to understand the behavior better (Sosnovskii et al. [47], Shcherbakov [48]).

6. Conclusions

In this study, the variation of shear wave velocity (*Vs*) with axial strain (ε_a) during monotonic triaxial compression is obtained and compared with the literature. The *Vs* is measured from BE tests, CT tests, and stress–strain curves. The BE tests are continuously performed at regular intervals during the monotonic axial loading of the specimen. The *Vs* from stress–strain curves is calculated after converting E_{sec} to G_{sec}. The CT testing and ML tests along with BE tests are performed on two identical specimens from each sand type. The behavior of low-strain *Vs* from BE is analyzed by using contact theory. The main conclusions of the study are presented in the following.

- The frequency content of the BE signals tends to shift towards higher frequencies with an increase in axial strain (ε_a), possibly because of larger average stress at the location of bender elements.
- The stress–strain behavior of tested sands (heterogeneous mineral composition) is markedly different from siliceous sand; this can be attributed to many factors, such as density of the packing, particle orientation and degree of freedom, and particle shape and roughness.
- The *Vs* from BE is unaffected by the strains imposed during monotonic loading. This behavior needs further numerical and experimental investigations to understand and decouple the complex interaction of average inter-particle stress and reduction in void ratio (e) during monotonic loading.
- The contact theory predicts the variation of low-strain *Vs* obtained from BE tests well.
- The *Vs* values calculated from the stress–strain curves and the *Vs* values from CT follows the hyperbolic model with one exception.
- The low-strain *Vs* results of this study compare well with the *Vs* results of past studies. The trends in *Vs* values calculated from the stress–strain curves are also comparable.
- The micro-mechanical models are based on contact theory of two spheres in contact. The models may not be valid for cohesive soils, such as clays and some silts. Additional parametric tests based on a similar approach on clayey soils are needed to understand their behavior.

Author Contributions: Conceptualization, Z.K., A.K. and M.A.; methodology, Z.K., A.K., K.F., and M.M; software, A.K.; validation, Z.K., M.A. and K.F.; formal analysis, A.K., Z.K., T.A, and M.M.; investigation, Z.K., K.F., T.A. and A.K.; resources, M.A., Z.K., T.A. and K.F.; data curation, Z.K., A.K. and M.A.; writing—original draft preparation, A.K. and Z.K.; writing—review and editing, Z.K., M.A. and K.F.; visualization, A.K., Z.K. and M.A.; supervision, Z.K., M.A., M.M., T.A. and K.F.; project administration, Z.K.; funding acquisition, Z.K. and M.A. All authors have read and agreed to the published version of the manuscript.

Funding: This research was funded by The American University of Sharjah, grant number FRG19-ME08. The work in this paper was supported, in part, by the Open Access Program from the American University of Sharjah.

Institutional Review Board Statement: Not applicable.

Informed Consent Statement: Not applicable.

Acknowledgments: The authors would like to acknowledge the support of machine shop at the American University of Sharjah. The authors would like to express their appreciation to the department of Art and Sciences for the SEM analysis. Special thanks to Faisal Mustafa and Shahbaz Ahmad

(MSE-PhD program at AUS) and Mohammed Mustafa (Department of Mechanical Engineering) for their help in performing confocal microscopy.

Conflicts of Interest: The authors declare no conflict of interest. The funders had no role in the design of the study; in the collection, analyses, or interpretation of data; in the writing of the manuscript, or in the decision to publish the results. This paper represents the opinions of the author(s) and does not mean to represent the position or opinions of the American University of Sharjah.

References

1. Khan, Z.H.; Cascante, G.; Ahmed, R. Novel evaluation of mass polar moment of inertia of the drive plate in resonant column. *Geotech. Lett.* **2022**, *12*, 174–178. [CrossRef]
2. Khan, Z.H.; Yamin, M.; Attom, M.; Al Hai, N. Correlations between SPT, CPT, and Vs for reclaimed lands near Dubai. *Geotech. Geol. Eng.* **2022**, *40*, 4109–4120. [CrossRef]
3. Khalil, A.; Khan, Z.H.; Attom, M.; El-Emam, M.; Fattah, K. Dynamic properties of calcareous sands from urban areas of Abu Dhabi. *Appl. Sci.* **2022**, *12*, 3325. [CrossRef]
4. Irfan, M.; Cascante, G.; Basu, D.; Khan, Z.H. Novel evaluation of bender element transmitter response in transparent soil. *Géotechnique* **2020**, *70*, 187–198. [CrossRef]
5. Clayton, C.; Priest, J.; Bui, M.; Zervos, A.; Kim, S. The Stokoe resonant column apparatus: Effects of stiffness, mass, and specimen fixity. *Géotechnique* **2009**, *59*, 429–437. [CrossRef]
6. Chaney, R.C.; Demars, K.R.; Brignoli, E.G.M.; Gotti, M.; Stokoe, K.H. Measurement of shear waves in laboratory specimens by means of piezoelectric transducers. *Geotech. Test. J.* **1996**, *19*, 384–397. [CrossRef]
7. Ismail, M.A.; Rammah, K.I. Shear-plate transducers as a possible alternative to bender elements for measuring Gmax. *Géotechnique* **2005**, *55*, 403–407. [CrossRef]
8. Dutta, T.T.; Otsubo, M.; Kuwano, R.; O'Sullivan, C. Evolution of shear wave velocity during triaxial compression. *Soils Found* **2020**, *60*, 1357–1370. [CrossRef]
9. Styler, M.A.; Howie, J.A. Continuous monitoring of bender element shear wave velocities during triaxial testing. *Geotech. Test. J.* **2014**, *37*, 20120098. [CrossRef]
10. Dyvik, R.; Madshus, C. Lab measurements of Gmax using bender elements. In *Advances in the Art of Testing Soils Under Cyclic Conditions*; American Society of Civil Engineers: New York, NY, USA, 1985; pp. 186–196.
11. Shirley, D.J.; Hampton, L.D. Shear-wave measurements in laboratory sediments. *J. Acoust. Soc. Am.* **1978**, *63*, 607–613. [CrossRef]
12. Viggiani, G.; Atkinson, J.H. Interpretation of bender element tests. *Géotechnique* **1995**, *45*, 149–154. [CrossRef]
13. Kuwano, R.; Jardine, R.J. On the applicability of cross-anisotropic elasticity to granular materials at very small strains. *Géotechnique* **2002**, *52*, 727–749. [CrossRef]
14. Gu, X.; Yang, J.; Huang, M.; Gao, G. Bender element tests in dry and saturated sand: Signal interpretation and result comparison. *Soils Found* **2015**, *55*, 951–962. [CrossRef]
15. Hertz, H.R. Über die Beruhrüng fester elastischer Körper. *J. Die Reine Angew. Math.* **1882**, *92*, 156–171. [CrossRef]
16. Mindlin, R.D. Compliance of elastic bodies in contact. *J. Appl. Mech.* **1949**, *16*, 259–268. [CrossRef]
17. *ASTM D8295-19*; Standard Test Method for Determination of Shear Wave Velocity and Initial Shear Modulus in Soil Specimens using Bender Elements. Annual Book of Standards. American Society for Testing and Materials: West Conshohocken, PA, USA, 2019.
18. *ASTM D7181-20*; Method for Consolidated Drained Triaxial Compression Test for Soils. Annual Book of Standards. American Society for Testing and Materials: West Conshohocken, PA, USA, 2020.
19. Khan, Z.H.; El Naggar, M.H.; Cascante, G. Frequency dependent dynamic properties from resonant column and cyclic triaxial tests. *J. Frankl. Inst.* **2011**, *348*, 1363–1376. [CrossRef]
20. *ASTM D4015-21*; Standard Test Methods for Modulus and Damping of Soils by Fixed-Base Resonant Column Devices. American Society for Testing and Materials: West Conshohocken, PA, USA, 2021.
21. Khan, Z.H.; Cascante, G.; El Naggar, H.; Lai, C. Measurement of frequency-dependent dynamic properties of soils using the Resonant-Column device. *J. Geotech. Geoenviron. Eng. ASCE* **2008**, *134*, 1319–1326. [CrossRef]
22. Khalil, A.M. Dynamic Properties of Soil in UAE from Field and Laboratory Tests. Master's thesis, American University of Sharjah, Sharjah, United Arab Emirites, 2020. Available online: http://hdl.handle.net/11073/21374 (accessed on 3 October 2022).
23. Hardin, B.O.; Drnevich, V.P. Shear Modulus and damping in soils: Design equations and curves. *J. Soil Mech. Found. Div.* **1972**, *98*, 667–692. [CrossRef]
24. Walton, K. The effective elastic moduli of a random packing of spheres. *J. Mech. Phys. Solids* **1987**, *35*, 213–226. [CrossRef]
25. Smith, W.O.; Foote, P.D.; Busang, P.F. Packing of homogeneous spheres. *Phys. Rev.* **1929**, *34*, 1271–1274. [CrossRef]
26. Ouchiyama, N.; Tanaka, T. Estimation of the average number of contacts between randomly mixed solid particles. *Ind. Eng. Chem. Fundam.* **1980**, *19*, 338–340. [CrossRef]
27. Zimmer, M. Seismic Velocities in Unconsolidated Sands: Measurements of Pressure, Sorting and Compaction Effects. Ph.D. thesis, Stanford University, Stanford, CA, USA, 2003. Available online: https://www.proquest.com/dissertations-theses/seismic-velocities-unconsolidated-sands/docview/305128850/se-2 (accessed on 4 October 2022).

28. German, R.M. Coordination number changes during powder densification. *Powder 301 Technol.* **2014**, *253*, 368–376. [CrossRef]
29. Chang, C.S.; Misra, A.; Sundaram, S.S. Properties of granular packings under low amplitude cyclic loading. *Soil Dyn. Earthq. Eng.* **1991**, *10*, 201–211. [CrossRef]
30. Magnanimo, V.; La Ragione, L.; Jenkins, J.T.; Wang, P.; Makse, H.A. Characterizing the shear and bulk moduli of an idealized granular material. *Europhys. Lett.* **2008**, *81*, 34006–34011. [CrossRef]
31. Arakawa, M.; Nishino, M. Contact number and porosity in randomly packed sphere mixtures of various sizes (in Japanese). *Zairyo* **1973**, *22*, 658–662.
32. Suzuki, M.; Makino, K.; Yamada, M.; Iinoya, K. A study on the coordination number in a system of randomly packed, uniform-sized spherical particles. *Int. Chem. Eng.* **1981**, *21*, 482–488.
33. Tory, E.M.; Church, B.H.; Tam, M.K.; Ratner, M. Simulated random packing of equal spheres. *Can. J. Chem. Eng.* **1973**, *51*, 484–493. [CrossRef]
34. Bernal, J.D.; Mason, J. Packing of spheres: Co-ordination of randomly packed spheres. *Nature* **1960**, *188*, 910–911. [CrossRef]
35. Gotoh, K. Liquids and powders—A random packing structure of equal sphere. *J. Soc. Powder Technol.* **1978**, *15*, 220–226. [CrossRef]
36. Digby, P.J. The effective elastic moduli of porous granular rocks. *J. Appl. Mech.* **1981**, *48*, 803–808. [CrossRef]
37. Norris, A.N.; Johnson, D.L. Nonlinear elasticity of granular media. *J. Appl. Mech.* **1997**, *64*, 39–49. [CrossRef]
38. Duffaut, K.; Landrø, M.; Sollie, R. Using Mindlin theory to model friction-dependent shear modulus in granular media. *Geophysics* **2010**, *75*, E143–E152. [CrossRef]
39. Rothenburg, L.; Bathurst, R.J. Analytical study of induced anisotropy in idealized granular materials. *Géotechnique* **1989**, *39*, 601–614. [CrossRef]
40. Chaudhary, S.K.; Kuwano, J.; Hayano, Y. Measurement of quasi-elastic stiffness parameters of dense toyoura sand in hollow cylinder apparatus and triaxial apparatus with bender elements. *Geotech. Test. J.* **2004**, *27*, 23–35. [CrossRef]
41. *ASTM D3999-91*; Standard Test Methods for the Determination of the Modulus and Damping Properties of Soils Using the Cyclic Triaxial Apparatus. Annual Book of Standards. American Society for Testing and Materials: West Conshohocken, PA, USA, 1991.
42. Kumar, S.S.; Krishna, A.M.; Dey, A. Evaluation of hysteretic damping of sand at large shear strains using cyclic triaxial tests. In Proceedings of the Geotechnics for Natural and Engineered Sustainable Technologies: Indian Geotechnical Conference (GeoNEst: IGC-2017), Guwahati, India, 14–16 December2017.
43. Santamarina, J.C.; Fratta, D.; Cho, G.-C.; Cascante, G. A survey of elastic and electromagnetic properties of near-surface soils," *Near-Surf. Geophys. Soc. Explor. Geophys.* **2005**, *1*, 71–88. [CrossRef]
44. Arroyo, F. Source near-field effects and pulse tests in soil samples. *Géotechnique* **2003**, *53*, 337–345. [CrossRef]
45. Lee, J.S. Bender Elements: Performance and Signal Interpretation. *J. Geotech. Geoenviron. Eng.* **2005**, *131*, 1063–1070. [CrossRef]
46. Nasuno, S.; Kudrolli, A.; Bak, A.; Gollub, J.P. Time-resolved studies of stick-slip motion in sheared granular layers. *Phys. Rev. E* **1998**, *58*, 2161. [CrossRef]
47. Sosnovskii, L.A.; Komissarov, V.; Shcherbakov, S. A method of experimental study of friction in a active system. *J. Frict. Wear.* **2012**, *33*, 136–145. [CrossRef]
48. Shcherbakov, S.S. State of volumetric damage of tribo-fatigue system. *Strength Mater.* **2013**, *45*, 171–178. [CrossRef]

materials

MDPI

Article

Modelling of Longitudinal Elastic Wave Propagation in a Steel Rod Using the Discrete Element Method

Magdalena Knak [1,*], Michał Nitka [2], Erwin Wojtczak [1] and Magdalena Rucka [1]

[1] Department of Mechanics of Materials and Structures, Faculty of Civil and Environmental Engineering, Gdansk University of Technology, Narutowicza 11/12, 80-233 Gdansk, Poland; erwin.wojtczak@pg.edu.pl (E.W.); magdalena.rucka@pg.edu.pl (M.R.)

[2] Department of Buildings Structures and Material Engineering, Faculty of Civil and Environmental Engineering, Gdansk University of Technology, Narutowicza 11/12, 80-233 Gdansk, Poland; michal.nitka@pg.edu.pl

* Correspondence: magdalena.knak@pg.edu.pl

Abstract: The paper deals with the issue of modelling elastic wave propagation using the discrete element method (DEM). The case of a longitudinal wave in a rod with a circular cross-section was considered. A novel, complex algorithm consisting of the preparation of models and simulation of elastic waves was developed. A series of DEM models were prepared for simulations, differing in discretisation and material parameters. Additional calculations with the finite element method (FEM) were performed. Numerical wave signals were obtained from each simulation and compared with experimental results to choose the best DEM model based on the correlation between the waveforms. Moreover, dispersion curves were prepared for each model to verify the agreement with the Pochhammer-Chree wave propagation theory. Both experimental and theoretical approaches indicated the same model as the most suitable. The analysis results allowed stating that DEM can be successfully used for modelling wave propagation in structural rods.

Keywords: guided waves; longitudinal wave; discrete element method; finite element method; numerical modelling; dispersion curves

Citation: Knak, M.; Nitka, M.; Wojtczak, E.; Rucka, M. Modelling of Longitudinal Elastic Wave Propagation in a Steel Rod Using the Discrete Element Method. *Materials* **2022**, *15*, 2738. https://doi.org/10.3390/ma15082738

Academic Editor: Michele Brun

Received: 3 March 2022
Accepted: 6 April 2022
Published: 8 April 2022

1. Introduction

Ultrasonic guided waves are widely used in engineering structures' non-destructive testing (NDT). They are mostly applied to detect and localise damage [1–3] or determine elastic [4,5] and thermal properties [6–8]. For a comprehensive interpretation of results, experimental investigations can be enhanced with wave propagation simulations in numerical models. The calculations are typically performed in software implementing the finite element method (FEM). Modelling elastic wave propagation in the FEM is widely described in structural elements like rods and beams, plates and other more complex structures [3,9–11]. The FEM is mostly used for modelling structures made of homogeneous materials (e.g., isotropic steel or orthotropic composites). However, it can also be successfully applied in the case of highly heterogeneous materials (e.g., concrete). Several works consider the mesoscale structure of materials in terms of wave propagation [12,13]. For modelling and characterising the fracture properties of concrete, the discrete element method (DEM) is increasingly used, which allows for the study of its mechanical behaviour at the aggregate level. However, for discrete element-based techniques, the problem of wave propagation is not widely considered.

The discrete element method is a numerical modelling approach with many applications in various industries, e.g., hydromechanics, grinding, or even medicine [14–16]. The modelled structure is built from particles (mostly discs and spheres) that may interact with each other. For this reason, it is very popular in the fracture analysis of granular media such as sand [14–17] or concrete elements [18–26]. The geometry of the model, such as the

interactions between particles, are crucial issues. The DEM allows computing the motion of a large number of elements. Its main advantage is the high level of detail of the behaviour of each particle (at the macro- or even micro-level). The particles are considered perfectly rigid bodies but with smooth (soft) contacts (so-called overlaps). The DEM is based on the use of an explicit numerical integration scheme where the interaction of particles is monitored contact by contact. The motion of the particles is modelled one by one. It is based on Newton's second law, which is discretised by a finite difference shape, solved explicitly. In general, the DEM can be considered more complex than FEM, thus enabling an accurate reconstruction of the actual concrete mesostructure and a realistic prediction of fracture. An emerging research area is the investigation of the scattering of elastic waves within heterogeneous materials. However, the literature dealing with wave propagation problems in the DEM is still limited. An example of this kind of research was presented by Rojek et al. [27]. The authors described a micro-macro relationship in wave propagation simulation using the DEM. Their work involved calculations performed on 2D models using DEMPack software. The presented results confirmed the possibility of application of DEM for the simulation of guided wave propagation in solid materials.

The discrete element method is mainly used for modelling heterogeneous media. However, since concrete structures usually are reinforced by bars, reinforcement cannot be ignored in modelling, even though it is mostly made of steel. Thus, the current work is focused on the steel rod problem as the first step for further analysis directed to wave propagation-based diagnostics of reinforced concrete structures. The paper presents the guided wave propagation problem formulation in a circular rod using the DEM. A novel model preparation and calibration algorithm based on experimental and FEM analysis is developed. The main attention is paid to the process of the determination of discretisation and mechanical parameters.

The paper is structured as follows. The theoretical background of the DEM is given in Section 2, including basic formulae and computational methods. The proposed methodology for elastic wave modelling using the DEM is shown in Section 3. The description of the tested object with the details of experimental investigations and numerical calculations using the FEM and DEM methods is presented in Section 4. Moving on, Section 5 shows the results of the analyses performed. The guided waveforms obtained with the DEM were correlated with the experimental and FEM results. The theoretical dispersion curves were also incorporated to verify the proposed modelling algorithm. The paper completes in Section 6, which presents the main findings of the current study.

2. The Theoretical Background

2.1. Guided Waves in a Circular Rod

Longitudinal guided wave modes propagating in a circular rod with a radius r can be described by the Pochhammer-Chree frequency equation [28]:

$$\frac{2\alpha}{r}\left(\beta^2+k^2\right)J_1(\alpha r)J_1(\beta r)-\left(\beta^2-k^2\right)^2 J_0(\alpha r)J_1(\beta r)-4k^2\alpha\beta J_1(\alpha r)J_0(\beta r)=0, \quad (1)$$

where J_0 and J_1 stand for Bessel's functions of the first kind, parameters α and β are related to the wavenumber k, the angular frequency ω by:

$$\alpha^2=\frac{\omega^2}{c_P^2}-k^2,\ \beta^2=\frac{\omega^2}{c_S^2}-k^2 \quad (2)$$

In Equation (2), c_P^2 and c_S^2 denote the velocities of longitudinal and shear waves, respectively, and they are given by:

$$c_P=\sqrt{\frac{E(1-\nu)}{\rho(1+\nu)(1-2\nu)}},\ c_S=\sqrt{\frac{E}{2\rho(1+\nu)}} \quad (3)$$

where E is the young's modulus, ρ is the mass density and ν is the Poisson ratio. The solution of Equation (1) provides dispersion curves, which relate the group velocity to the angular frequency by the relation:

$$c_g = \frac{d\omega}{dk} \tag{4}$$

2.2. Outline of Discrete Element Method

The numerical analysis was performed with the open-source code Yade [29,30]. The algorithm for DEM calculations using spherical elements can be as follows. First, the position of every particle is established. Then, the contact between each particle and its neighbours (adjacent particles or other objects like walls or boxes) is found. If the contact exists, the overlap u is calculated from the equation:

$$u = d - (R_A + R_B), \tag{5}$$

where d is the distance between the centres of the elements and R_A and R_B are the radius of the elements in contact. Compression forces exist if the overlap is negative (if it is positive, tension appears).

The forces in contact points are calculated from the constitutive laws (Figure 1). This paper used the simple linear elastic (in compression) law. The equations are as follows:

$$\mathbf{F}_n = K_n u \mathbf{N}, \tag{6}$$

$$\mathbf{F}_s = \mathbf{F}_{s,prev} + K_s \Delta \mathbf{X}_s, \tag{7}$$

where, $\mathbf{F}_n$ and $\mathbf{F}_s$ are the normal and tangential contact forces, respectively (Figure 2), $\mathbf{N}$ is a unit normal vector on contact points connecting centres of the elements, $\mathbf{X}_s$ denotes the relative tangential displacement increment and $\mathbf{F}_{s,prev}$ is the tangential force calculated from the previous time step. Contact stiffnesses (i.e., normal stiffnesses K_n and tangential stiffnesses K_s) can be calculated from the following relations:

$$K_n = E_c \frac{2R_A R_B}{R_A + R_B}, \quad K_s = v_c E_c \frac{2R_A R_B}{R_A + R_B}, \tag{8}$$

where E_c is Young's modulus of particle contact and ν_c is the ratio between normal and tangential contact stiffness. For the normal (in tension) and tangential force, the limit is imposed:

$$F_s^{\max} = CR^2, \quad F_n^{\min} = TR^2, \tag{9}$$

where C corresponds to the cohesive contact stress (maximum shear stress at a pressure equal to zero) [29,31] and T to the normal tensile contact stress [29] (R is a minimum value of R_A and R_B). The current study's force values are relatively low (significantly lower than the limit); thus, contact break was not considered.

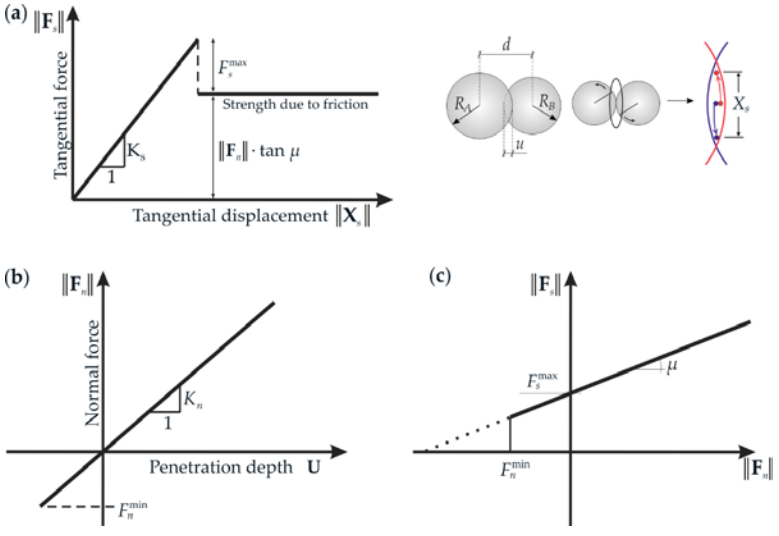

Figure 1. Mechanical response of DEM: (**a**) tangential contact model, (**b**) normal contact model, and (**c**) modified Mohr-Coulomb model [29].

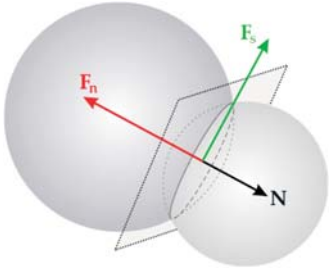

Figure 2. Two spheres in contact with the forces and momentum acting on them ($\mathbf{F}_n$—normal contact force, $\mathbf{F}_s$—tangential contact force, and **N**—normal contact vector) [29].

Moreover, the Coulomb friction is introduced. The model is described differently, depending on whether the contact is broken or not. The equations for the situation before and after the contact break can be expressed as follows, respectively:

$$\|\mathbf{F}_s\| - F_s^{\max} - \|\mathbf{F}_n\| \tan \mu_c \leq 0, \tag{10}$$

$$\|\mathbf{F}_s\| - \|\mathbf{F}_n\| \tan \mu_c \leq 0, \tag{11}$$

where μ_c is the Coulomb inter-particle friction angle.

After force calculations, external forces (e.g., gravity or boundary conditions) may be added. In the next step, the motion of the elements is upgraded using Newton's second law. The acceleration, velocity, and finally, new particle position are calculated. Then, the first step is repeated. Note that in this paper, no damping is introduced (however, usually, for quasi-static calculations, it is necessary to use it). In the first step, the initial overlapping was calculated (u_{int}). Next, in every future step, Equation (6) was changed into:

$$\mathbf{F}_n = K_n(u - u_{\text{int}})\mathbf{N}. \tag{12}$$

So, the overlap can exist in the geometry; however, no initial forces are generated.

3. A Methodology of Building a DEM Model for Wave Propagation Problems

The simulation of the guided wave propagation phenomenon using the DEM is much more complex than in the FEM, even in the case of symmetric wave mode propagating in a rod with a circular cross-section. The current research proposes to build an appropriate model based on the calibration with experimental results. The methodology scheme developed using Yade software is presented in Figure 3. At first, it is assumed that the geometry of the rod (length l, diameter of the cross-section D), the density of the material ρ, and Young's modulus E are known (measured on the physical model). Some representative wave propagation signals need to be measured (using the particular excitation signal, e.g., wave packet). The first step of the scheme is the preparation of geometry, reflecting the physical model, including the length and cross-section of the rod. The discretisation with the use of spherical particles with the radius corresponding to the cross-section of the rod is required. The particles are arranged in a single line. An important parameter that must be assumed initially is the distance between the centres of the adjacent particles d. Furthermore, the number of adjacent particles with which a specific particle can interact can be set. It is determined by the parameter L_{int} specifying the area in which the centres of adjacent particles should be included to create an interaction. It is assumed that the specific particle should interact only with the closest neighbours (in general, two, one at each side); thus, the following condition needs to be satisfied:

$$d \leq L_{int} < 2d. \tag{13}$$

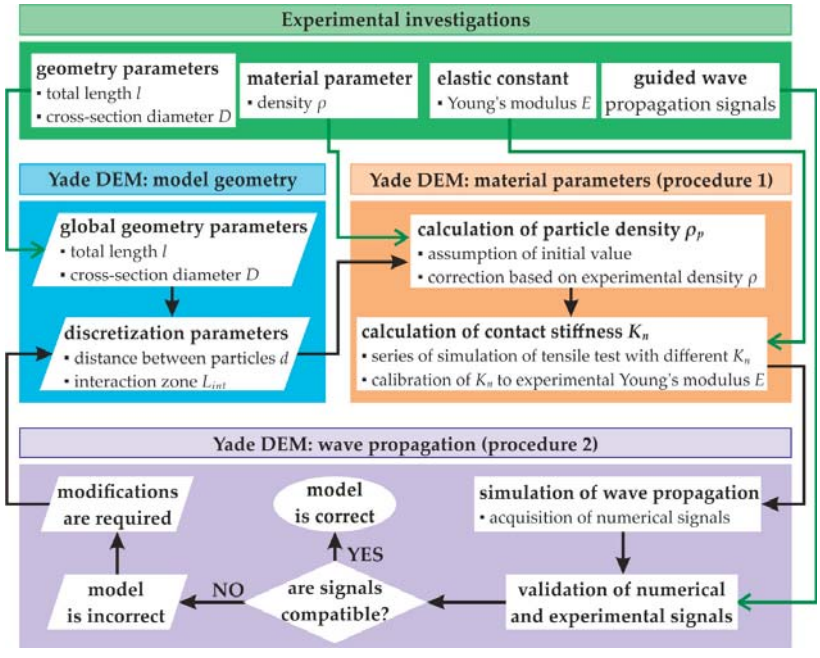

Figure 3. A scheme of building a DEM model of a rod with a circular cross-section for wave propagation using Yade DEM.

Having determined the model's geometry, the calculation of two crucial material parameters, i.e., the density of particles ρ_p and normal contact stiffness K_n needs to be performed using procedure 1 (as presented in Figure 3). First, the initial value of ρ_p is assumed. Based on this value, the total mass of the model is calculated and compared

with the actual mass of the physical model. The ratio between these two values is the correction coefficient that is further applied to the initial value of ρ_p to obtain the final particle density. When the value of ρ_p is established, a series of models with different values of K_n is prepared. A simple tensile test simulation is performed for each model to determine the stress-strain relation, also used to calculate Young's modulus E_{DEM}. The comparison between the series of E_{DEM} values and the experimental Young's modulus E allows for choosing the model with the appropriate contact stiffness. The resulting values of ρ_p and K_n, such as the geometry and discretisation previously established, are then incorporated into the second procedure concerning the wave propagation problem. The guided waves are excited and acquired. The signals obtained are compared with the experimental ones to validate the prepared model. The shape of waveforms, such as the wave velocity, can be verified, e.g., by determining the correlation between the two approaches. If the compatibility is satisfactory, the model is considered correct. If not, the model needs modifications, and the algorithm returns to the discretisation. The distance between particles must be changed, and the further steps in procedures 1 and 2 must be repeated. In the present case, if the wave velocity in the numerical signals is too low, the distance between particles needs to be decreased. Inversely, the distance should be increased if the velocity is too high. In general, multiple repetitions of the steps presented can be required.

4. Materials and Methods

4.1. Object of Research

The object of the investigation (Figure 4a) was a rod with a circular cross-section (diameter D = 10.2 mm) and a length of l = 1000 mm. The rod was made of steel, with the following material parameters: mass density ρ = 7850.66 kg/m^3, Young's modulus E = 208.72 GPa (determined in a static tensile test) and Poisson's ratio ν = 0.3.

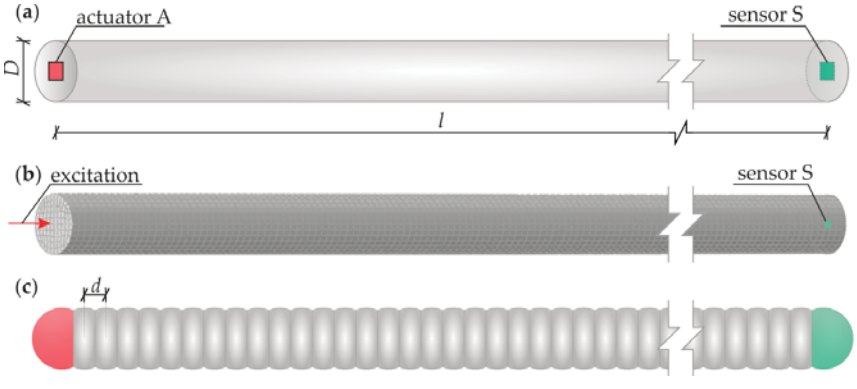

Figure 4. An object of research: (**a**) specimen geometry, (**b**) numerical FEM model, (**c**) numerical DEM model.

4.2. Experimental Procedure

The experimental measurements of guided waves were carried out using piezoelectric plate transducers Noliac NAC2011 with dimensions of 2 × 2 × 2 mm^3. One of the transducers acted as an actuator (A), while the second (S) acted as a sensor. The actuator was attached to one end of the rod, while sensor S was attached to the other end, as shown in Figure 5a, so the waves were excited and sensed in the longitudinal direction. The wave packet induced by the actuator was a five-cycle sine function modulated with a Hann window (Figure 5b). The central frequency of the wave packet was set in the frequency range of 50–150 kHz with a step of 10 kHz. Signals were further processed with the Hilbert transform to obtain signal envelopes [32].

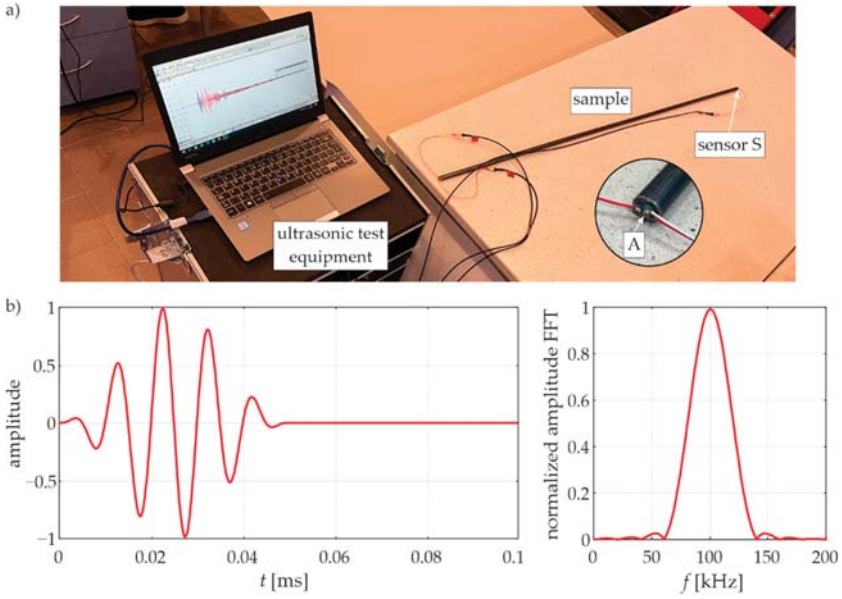

Figure 5. (**a**) Experimental setup. (**b**) Five-cycle sine wave packet with the carrier frequency of 100 kHz (time-domain signal and frequency spectrum).

4.3. Numerical Modelling

4.3.1. Finite Element Method

Numerical analysis was performed in the Abaqus software based on the finite element method. The created 3D model of a bar (Figure 4b) reflected the experimental object (including geometry and mechanical parameters). A linear-elastic, homogeneous, isotropic material model was used. Rayleigh proportional damping was assumed with a mass proportionality coefficient equal to α = 2000 1/N, neglecting the influence of stiffness (β = 0 m/N). The use of damping allows one to reflect the real wave propagation in the tested object. Boundary conditions were assumed as free edges. The numerical model was made of solid 8-node finite elements with reduced integration (C3D8R). The mesh grid had a size of $1 \times 1 \times 1$ mm^3. The explicit module was used to calculate the guided waves propagation problem. An algorithm of the central difference method has been applied to integrate the equation of motion. The total calculation time was assumed to be 1.5 ms with the time step equal to $1 \cdot 10^{-7}$ s. The wave was excited by applying a concentrated force of a certain amplitude at one end of the rod. The input signal was the same as in the experimental investigations. The results of the analysis were recorded at the point at the opposite end.

4.3.2. Discrete Element Method

Numerical calculations based on the discrete element method were performed in the Yade environment. There are a few significant parameters in wave propagation calculations: the particle density ρ_p, normal contact stiffness K_n, the geometry (initial distance between the spheres d) and the coordination number (the number of contacts for every element, determined by the interaction zone L_{int}). In the first step, samples with a predetermined geometry were prepared. The steel bar was created as a 3D model as one row of spherical elements with a length of l = 1000 mm (Figure 4c). The radius of each particle was constant and equal to half the diameter of the real bar (R = 5.1 mm). The parameter of the initial distance of the particle d has been changed. The interaction zone L_{int} was chosen so that the specific particle interacted only with its nearest neighbours. For such prepared

geometry, the quasi-static tension test was performed (only elastic part, with no breakage). The density parameter was unique for a specified distance to keep the overall mass of the bar in agreement with the real value. The modification of the stiffness coefficient directly affects the global Young's modulus E_{DEM}. The prepared model was used for the 1D problem of longitudinal wave propagation. An explicit procedure was used, and the time step equal to $dt = 5 \times 10^{-8}$ s was adopted (critical time step $dt_{cr} = 1.3 \times 10^{-5}$ s). The total computation time was 1.5 ms. No additional damping was applied to the model; nevertheless, attenuation was observed in the signals (resulting from the geometrical damping). The disturbance was induced by force applied to the first particle. The signal was recorded at the last particle (at the end of the bar, sensor S).

5. Results

A series of calculations were carried out to calibrate the DEM numerical model with the experiment. In the following steps, due to the size of the calculation, only the results for selected particle distances $d = \{0.95R, 1.03R, 1.05R, 1.15R\}$ are presented. This set was chosen to show all aspects of the considered issue and the arising difficulties as clearly as possible. The experimental signal was taken as a reference one, to which the numerical signals were matched. The adjustment accuracy was determined qualitatively by visual evaluation of the signals and quantitatively using the Pearson correlation coefficient (PCC), such as the sum of squared errors of the longitudinal wave velocities.

The first step of the calculation for each different distance was to determine the static parameter (Young's modulus). The static tensile test simulation was performed for different values of contact stiffness K_n (assumed heuristically). Young's modulus E_{DEM} was determined for each calculation by linear approximation of the stress-strain relation obtained from the measurements. The final value of the contact stiffness K_n corresponded to the model with an E_{DEM} value close to the real value of E. Figure 6 presents an example of the stress-strain relationship and its approximation for the model with $d = 1.03R$.

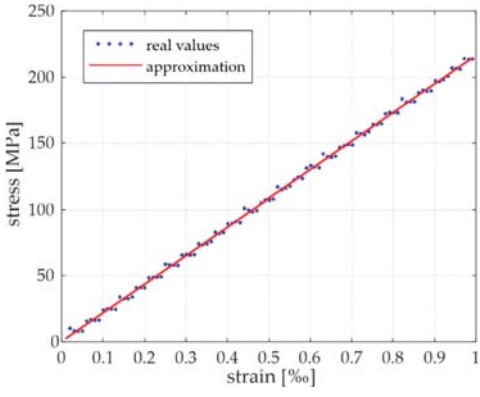

Figure 6. Stress-strain relation for the $1.03R$ model for the determination of K_n.

Having determined all the appropriate parameters, the guided wave propagation calculations were carried out. Figure 7 shows the signals of the longitudinal wave collected at the sensor. The signals for four selected distances of particles ($d = \{0.95R, 1.03R, 1.05R, 1.15R\}$) are presented. Excitation frequencies equal to 50 kHz, 100 kHz, and 150 kHz were analysed. Firstly, there is a decrease in velocity with increasing frequency. When considering the models' signals with different particle distances, it is evident that the $d = 0.95R$ strongly deviates from the others. The densification of the rod particles implies an increase in the propagation speed of the wave. Moreover, a numerical dispersion is much more pronounced (in comparison to the three other models) at higher frequencies.

When comparing the waveforms presented, it can be concluded that the 0.95*R* model is the most unstable.

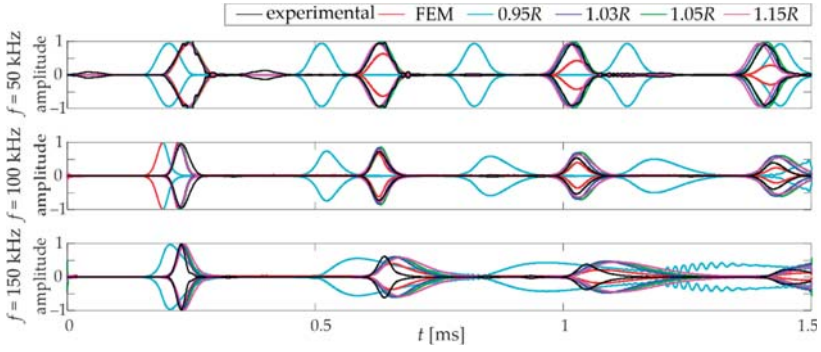

Figure 7. Comparison of signal for selected DEM models (various overlap) and frequencies.

Correlation calculations were performed using the PCC to determine which model is the most unambiguously compatible with the experiment. Table 1 shows the estimated static parameters for selected models with different particle distances with correlation coefficients. The comparison is intended to show the influence of the agreement distance parameter on the obtained agreement with reference (experimental) measurements and FEM calculations. A strong effect of the distance applied in the DEM model on the obtained correlation can be observed. This confirms previous observations, that the signals received for $d = \{1.03R, 1.05R, 1.15R\}$ are comparable. Their average correlation coefficients (for all particular frequencies) indicate high similarity. However, this requires verification over a wider frequency range.

Table 1. Properties of DEM models.

Model	Number of Particles	Density ρ_p (kg/m^3)	Normal Contact Stiffness K_n (N/m)	Young's Modulus E_{DEM} (GPa)	Correlation with Experiment PCC	Correlation with FEM PCC
0.95*R*	207	5577.17	2.3×10^{11}	207.30	−0.018	−0.012
1.03*R*	191	6044.37	6.6×10^{11}	216.30	0.906	0.892
1.05*R*	187	6173.66	6.4×10^{11}	213.97	0.862	0.886
1.15*R*	171	6751.31	6×10^{11}	219.37	0.853	0.860

Figure 8 presents the PCC variation in relation to the wave frequency. The correlation between numerical (FEM and DEM with different overlaps) and experimental waveforms are shown in Figure 8a. First, it can be observed that there is a rapid decrease in the PCC at higher frequencies. The decrease is related to the presence of an increasing numerical dispersion. A good agreement between the experimental and FEM results can be observed (PCC above 0.85). In the case of DEM results, the PCC is above 0.7 only for the 1.03*R* model; it could be considered a strong correlation [33]. When the experimental vs. DEM correlation curves are considered, a characteristic decrease in the PCC value is observed with an increase in the distance between the particles. Furthermore, it can be seen that in the frequency range of 50–90 kHz, the PCC values of DEM vs. experimental signals are noticeably higher than the PCC values of FEM vs. experimental signals, but above a frequency of 100 kHz FEM model gives a stronger correlation. Figure 8b illustrates a plot of the PCC calculated between the FEM and DEM signal envelopes. A strong agreement between the methods is shown within the analysed frequencies. The PCC for all models

ranges between 0.8 and 1.0. This confirms that these two different numerical approaches can give comparable results.

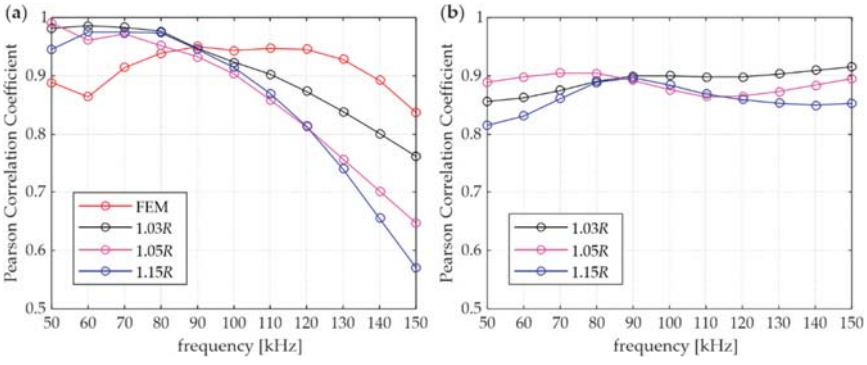

Figure 8. Pearson correlation coefficient in relation to excitation frequency: (**a**) FEM and DEM vs. experimental results, (**b**) DEM vs. FEM results.

For wave propagation analysis, it is crucial to recognise the relationship between velocity and frequency. Thus, the characteristic dispersion curves were determined for the steel bar analysed. Theoretical curves were obtained using PCDISP software based on the Pochhammer-Chree theory [34,35]. The numerical FEM/DEM curves were obtained by calculating wave propagation velocity based on two adjacent wave packets using the 'peak to peak' method. Figure 9 shows the dispersion curves obtained by different approaches. The DEM curves for four different distances were compared with the theoretical ones. This comparison is intended to highlight the accuracy of the adopted discrete model. First of all, it is worth noting that the obtained curves indicate the dispersive nature of the waves in DEM. Second, it can be pointed out that the group velocity is closely related to the applied particle distance. The shorter the distances between the particle's centres, the faster the wave propagates. As the distance increases, the group velocity decreases. Additionally, as the frequency increases, the velocity decreases. In the case of $d = 1.05R$ and $d = 1.15R$, the curves that fit the theoretical curve at lower frequencies start to deviate increasingly from the theory as the frequency increases. The dispersion curve obtained for the DEM model at $d = 1.03R$ was selected to present the greatest agreement with the theory and the numerical FEM result (the group velocity of the numerical FEM is in accordance with the theoretical one at all frequencies). To determine the degree of similarity and confirm the proposed solution's validity, the residual sum of squares (RSS) was calculated [5]. The results obtained are summarised in Table 2. The RSS values clearly show the agreement of the applied models. Analysing the values for the numerical DEM models, it can be observed that the best agreement (the lowest value of RSS) is shown for the $d = 1.03R$ model.

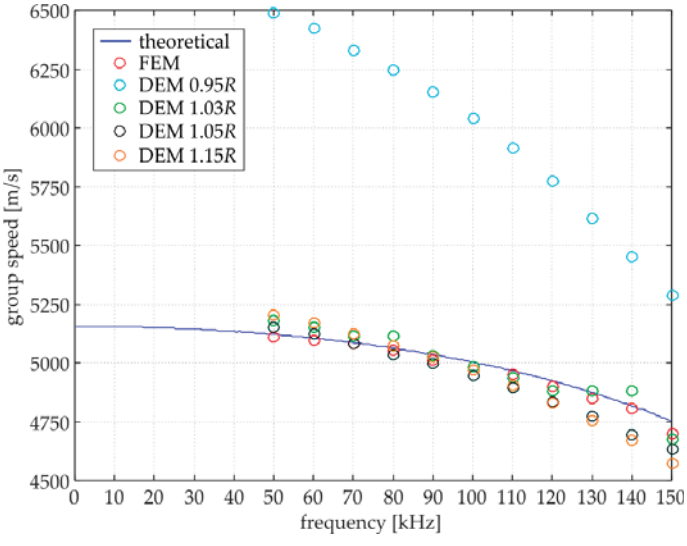

Figure 9. Comparison between dispersion curves for numerical models and Pochhamer-Chree theory.

Table 2. Residual sum of squares between numerical models and Pochhammer-Chree theory.

Model	RSS
FEM	6056
DEM, 0.95*R*	11,694,645
DEM, 1.03*R*	22,436
DEM, 1.05*R*	61,084

The wave propagation results for the final DEM model (d = 1.03R) are shown in Figure 10. The experimental results are compared with the numerical results obtained from FEM and DEM calculations. By analysing the graphs, it is possible to observe the compatibility of the speed of wave propagation and the compatibility of the shape of the wave packets. The first wave packets that appear are compatible with each other. The satisfactory compatibility of guided wave calculations was achieved using the discrete element and finite element methods. As mentioned earlier, the superiority of DEM over FEM can be seen at lower frequencies (50–90 kHz). The packet shapes obtained in the DEM calculations reflect the experimental ones clearly enhanced. A characteristic effect of dispersion is seen in both numerical models at higher frequencies. There is an elongation of the numerical packets, while their beginnings are consistent with the experimental ones.

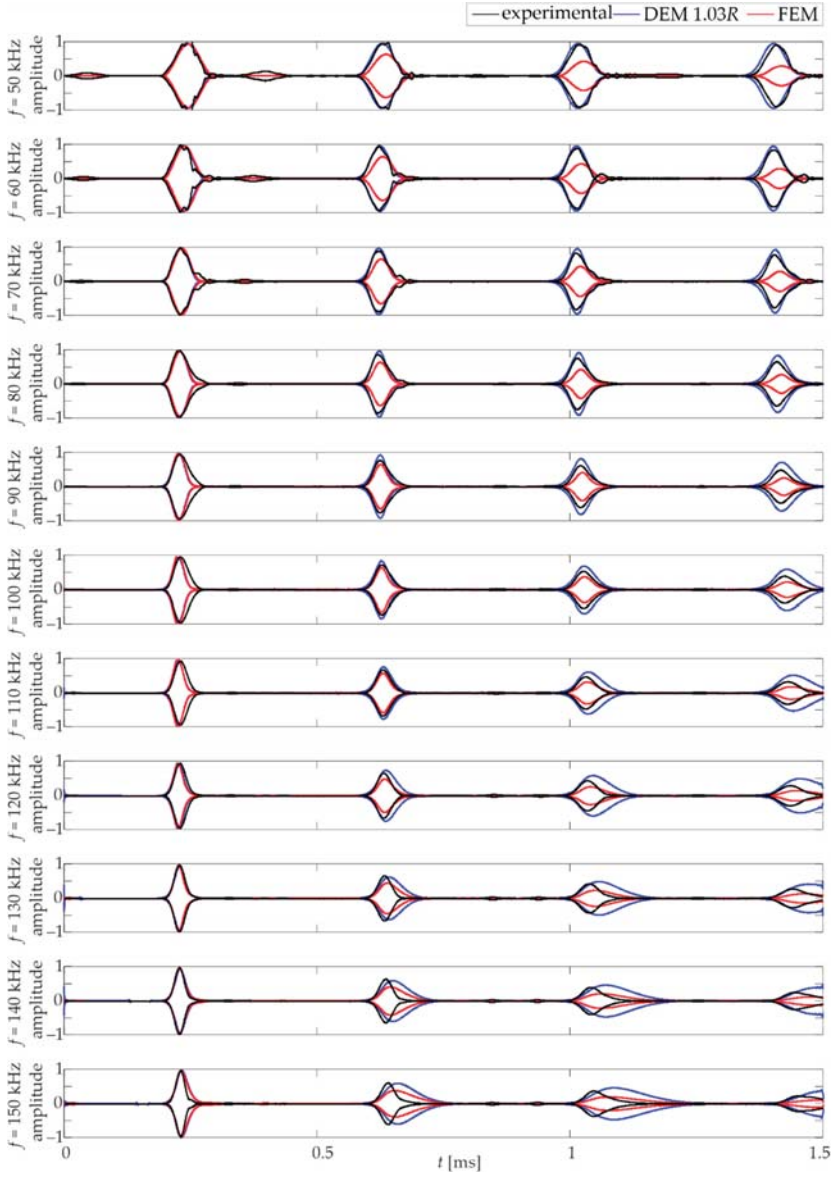

Figure 10. Comparison of wave propagation for experimental and numerical FEM/DEM results.

6. Conclusions

The paper describes the modelling of longitudinal wave propagation in a circular steel rod using the discrete element method. An experimental approach was applied to verify the appropriateness of DEM modelling in the Yade open-source code. The finite element calculations performed in Abaqus software supported the performed analyses. Based on the results, the following conclusions could be formulated.

- The Yade platform can be successfully used for experimentally assisted guided wave modelling. The geometric and material parameters need to be determined on a

physical model. Moreover, measurements of a certain number of wave propagation signals are required.

- The heuristic process is the appropriate choice of parameters used in DEM models (distance between particles and contact stiffness). The DEM allows one to create several discrete models that fit the experimental results for different sets of parameters. However, further analyses, e.g., dispersion curve calculation, enable selecting the most suitable model.
- Dispersion curves confirmed that guided waves in DEM exhibit a dispersive nature. There is a visible change in group velocity in relation to frequency. Moreover, the wave velocity is closely related to the particle distribution, i.e., the smaller the distances between particles, the higher the group velocity.

In summary, it can be concluded that the discrete element environment can be successfully used for wave propagation analysis. The present work is a beginning consideration for more complex problems, especially to explain the mechanism of propagation and scattering of elastic waves in concrete members at the aggregate level. In the next steps, the calibration of waveforms in concrete and reinforced concrete elements using DEM will be performed.

Author Contributions: Conceptualization, M.K., M.N., E.W. and M.R.; methodology, M.K., M.N., E.W. and M.R.; numerical investigation, M.K. and M.N., experimental investigation, M.K., E.W. and M.R.; software, M.K. and M.N.; formal analysis, M.K., M.N. and E.W.; writing—original draft preparation, M.K., M.N. and E.W.; writing—review and editing, M.R.; visualization, M.K. and E.W.; supervision, M.R. All authors have read and agreed to the published version of the manuscript.

Funding: This research received no external funding.

Institutional Review Board Statement: Not applicable.

Informed Consent Statement: Not applicable.

Data Availability Statement: The data underlying this article will be shared on reasonable request by the corresponding author.

Conflicts of Interest: The authors declare no conflict of interest.

References

1. Mitra, M.; Gopalakrishnan, S. Guided wave based structural health monitoring: A review. *Smart Mater. Struct.* **2016**, *25*, 53001. [CrossRef]
2. Song, H.; Popovics, J.S. Characterization of steel-concrete interface bonding conditions using attenuation characteristics of guided waves. *Cem. Concr. Compos.* **2017**, *83*, 111–124. [CrossRef]
3. Wojtczak, E.; Rucka, M.; Knak, M. Detection and Imaging of Debonding in Adhesive Joints of Concrete Beams Strengthened with Steel Plates Using Guided Waves and Weighted Root Mean Square. *Materials* **2020**, *13*, 2167. [CrossRef]
4. Cui, R.; Lanza di Scalea, F. On the identification of the elastic properties of composites by ultrasonic guided waves and optimization algorithm. *Compos. Struct.* **2019**, *223*, 110969. [CrossRef]
5. Wojtczak, E.; Rucka, M. Monitoring the curing process of epoxy adhesive using ultrasound and Lamb wave dispersion curves. *Mech. Syst. Signal Process.* **2021**, *151*, 107397. [CrossRef]
6. Tiwari, R.; Mukhopadhyay, S. Boundary Integral Equations Formulation for Fractional Order Thermoelasticity. *Comput. Methods Sci. Technol.* **2014**, *20*, 49–58. [CrossRef]
7. Tiwari, R.; Kumar, R.; Kumar, A. Investigation of thermal excitation induced by laser pulses and thermal shock in the half space medium with variable thermal conductivity. *Waves Random Complex Media* **2020**, 1–19. [CrossRef]
8. Tiwari, R.; Kumar, R. Analysis of plane wave propagation under the purview of three phase lag theory of thermoelasticity with non-local effect. *Eur. J. Mech. A/Solids* **2021**, *88*, 104235. [CrossRef]
9. Moser, F.; Jacobs, L.J.; Qu, J. Modeling elastic wave propagation in waveguides with the finite element method. *NDT E Int.* **1999**, *32*, 225–234. [CrossRef]
10. Yang, C.; Ye, L.; Su, Z.; Bannister, M. Some aspects of numerical simulation for Lamb wave propagation in composite laminates. *Compos. Struct.* **2006**, *75*, 267–275. [CrossRef]
11. Wojtczak, E.; Rucka, M. Wave frequency effects on damage imaging in adhesive joints using lamb waves and RMS. *Materials* **2019**, *12*, 1842. [CrossRef] [PubMed]
12. Chen, H.; Xu, B.; Wang, J.; Luan, L.; Zhou, T.; Nie, X.; Mo, Y.L. Interfacial debonding detection for rectangular cfst using the masw method and its physical mechanism analysis at the meso-level. *Sensors* **2019**, *19*, 2778. [CrossRef] [PubMed]

13. Xu, B.; Chen, H.; Mo, Y.L.; Zhou, T. Dominance of debonding defect of CFST on PZT sensor response considering the meso-scale structure of concrete with multi-scale simulation. *Mech. Syst. Signal Process.* **2018**, *107*, 515–528. [CrossRef]
14. Thornton, C.; Yin, K.K.; Adams, M.J. Numerical simulation of the impact fracture and fragmentation of agglomerates. *J. Phys. D Appl. Phys.* **1996**, *29*, 424–435. [CrossRef]
15. Herrmann, H.J.; Luding, S. Review Article: Modeling granular media with the computer. *Cont. Mech. Ther.* **1998**, *10*, 189–231. [CrossRef]
16. Jiang, M.J.; Yu, H.S.; Harris, D. A novel discrete model for granular material incorporating rolling resistance. *Comput. Geotech.* **2005**, *32*, 340–357. [CrossRef]
17. Nitka, M.; Grabowski, A. Shear band evolution phenomena in direct shear test modelled with DEM. *Powder Technol.* **2021**, *391*, 369–384. [CrossRef]
18. Suchorzewski, J.; Tejchman, J.; Nitka, M. Experimental and numerical investigations of concrete behaviour at meso-level during quasi-static splitting tension. *Theor. Appl. Fract. Mech.* **2018**, *96*, 720–739. [CrossRef]
19. Donzé, F.V.; Magnier, S.-A.; Daudeville, L.; Mariotti, C.; Davenne, L. Numerical Study of Compressive Behavior of Concrete at High Strain Rates. *J. Eng. Mech.* **1999**, *125*, 1154–1163. [CrossRef]
20. Hentz, S.; Daudeville, L.; Donzé, F.V. Identification and Validation of a Discrete Element Model for Concrete. *J. Eng. Mech. ASCE* **2004**, *130*, 709–719. [CrossRef]
21. Dupray, F.; Malecot, Y.; Daudeville, L.; Buzaud, E. A mesoscopic model for the behaviour of concrete under high confinement. *Int. J. Numer. Anal. Methods Geomech.* **2009**, *33*, 1407–1423. [CrossRef]
22. Groh, U.; Konietzky, H.; Walter, K.; Herbst, M. Damage simulation of brittle heterogeneous materials at the grain size level. *Theor. Appl. Fract. Mech.* **2011**, *55*, 31–38. [CrossRef]
23. Rangari, S.; Murali, K.; Deb, A. Effect of meso-structure on strength and size effect in concrete under compression. *Eng. Fract. Mech.* **2018**, *195*, 162–185. [CrossRef]
24. Nguyen, T.T.; Bui, H.H.; Ngo, T.D.; Nguyen, G.D.; Kreher, M.U.; Darve, F. A micromechanical investigation for the effects of pore size and its distribution on geopolymer foam concrete under uniaxial compression. *Eng. Fract. Mech.* **2019**, *209*, 228–244. [CrossRef]
25. Krenzer, K.; Mechtcherine, V.; Palzer, U. Simulating mixing processes of fresh concrete using the discrete element method (DEM) under consideration of water addition and changes in moisture distribution. *Cem. Concr. Res.* **2019**, *115*, 274–282. [CrossRef]
26. Nitka, M.; Tejchman, J. Comparative DEM calculations of fracture process in concrete considering real angular and artificial spherical aggregates. *Eng. Fract. Mech.* **2020**, *239*, 107309. [CrossRef]
27. Rojek, J.; Madan, N.; Nosewicz, S. Micro–Macro Relationships in the Simulation of Wave Propagation Phenomenon Using the Discrete Element Method. *Materials* **2019**, *12*, 4241. [CrossRef]
28. Rose, J.L. *Ultrasonic Guided Waves in Solid Media*; Cambridge University Press: New York, NY, USA, 2014; ISBN 9781107273610.
29. Kozicki, J.; Donzé, F.V. A new open-source software developed for numerical simulations using discrete modeling methods. *Comput. Methods Appl. Mech. Eng.* **2008**, *197*, 4429–4443. [CrossRef]
30. Šmilauer, V.; Chareyre, B. Yade DEM Formulation. *Yade Doc.* **2010**, *2011*, 38.
31. Ergenzinger, C.; Seifried, R.; Eberhard, P. A discrete element model to describe failure of strong rock in uniaxial compression. *Granul. Matter* **2011**, *13*, 341–364. [CrossRef]
32. Ng, C.T. On the selection of advanced signal processing techniques for guided wave damage identification using a statistical approach. *Eng. Struct.* **2014**, *67*, 50–60. [CrossRef]
33. Schober, P.; Schwarte, L.A. Correlation coefficients: Appropriate use and interpretation. *Anesth. Analg.* **2018**, *126*, 1763–1768. [CrossRef]
34. Seco, F.; Martín, J.M.; Jiménez, A.; Pons, J.L. PCdisp: A Tool for The Simulation of Wave Propagation in Cylindrical Waveguides. In Proceedings of the 9th International Congress on Sound and Vibration, Orlando, FL, USA, 8–11 July 2002.
35. Seco, F.; Jiménez, A.R. Modelling the Generation and Propagation of Ultrasonic Signals in Cylindrical Waveguides. In *Ultrasonic Waves*; BoD—Books on Demand: Norderstedt, Germany, 2012. [CrossRef]

materials

MDPI

Article

Non-Destructive Diagnostics of Concrete Beams Strengthened with Steel Plates Using Modal Analysis and Wavelet Transform

Magdalena Knak [1], Erwin Wojtczak [1] and Magdalena Rucka [1,2,*]

[1] Department of Mechanics of Materials and Structures, Faculty of Civil and Environmental Engineering, Gdańsk University of Technology, Narutowicza 11/12, 80-233 Gdańsk, Poland; s168197@student.pg.edu.pl (M.K.); erwin.wojtczak@pg.edu.pl (E.W.)
[2] EkoTech Center, Gdańsk University of Technology, Narutowicza 11/12, 80-233 Gdańsk, Poland
* Correspondence: magdalena.rucka@pg.edu.pl

Abstract: Externally bonded reinforcements are commonly and widely used in civil engineering objects made of concrete to increase the structure load capacity or to minimize the negative effects of long-term operation and possible defects. The quality of adhesive bonding between a strengthened structure and steel or composite elements is essential for effective reinforcement; therefore, there is a need for non-destructive diagnostics of adhesive joints. The aim of this paper is the detection of debonding defects in adhesive joints between concrete beams and steel plates using the modal analysis approach. The inspection was based on modal shapes and their further processing with the use of continuous wavelet transform (CWT) for precise debonding localization and imaging. The influence of the number of wavelet vanishing moments and the mode shape interpolation on damage imaging maps was studied. The results showed that the integrated modal analysis and wavelet transform could be successfully applied to determine the exact shape and position of the debonding in the adhesive joints of composite beams.

Keywords: non-destructive testing; damage detection; vibrations; modal analysis; continuous wavelet transform; concrete beam; strengthening; adhesive joint; debonding

Citation: Knak, M.; Wojtczak, E.; Rucka, M. Non-Destructive Diagnostics of Concrete Beams Strengthened with Steel Plates Using Modal Analysis and Wavelet Transform. *Materials* **2021**, *14*, 3014. https://doi.org/10.3390/ma14113014

Academic Editor: Carlos Chastre

Received: 29 April 2021
Accepted: 31 May 2021
Published: 2 June 2021

1. Introduction

A significant part of building objects is made of concrete, which is continuously degraded as a result of environmental and loading conditions as well as natural ageing of the material. Therefore, in many situations, structural reinforcements are used to minimize the negative effects of long-term operation and developing damage. For this purpose, various systems can be used, among which the use of externally bonded reinforcement (EBR) is one of the most effective [1–4]. EBRs usually have a form of adhesively bonded elements made of steel (e.g., plates, rods, flat bars) or composites like fiber-reinforced polymers (e.g., tapes or mats). In such connections, it is crucial to provide an adequate quality of the bonding as well as further assessment of its condition and monitoring. Recently, various non-destructive testing (NDT) and structural health monitoring (SHM) approaches have been increasingly and widely incorporated to improve the safety of structures by precise damage detection, identification, and visualization [5,6]. In the existing literature, there are many examples of successful application of non-invasive techniques for diagnostics of adhesive joints [7], especially utilizing thermography [8–11], reflectometry [12] or ultrasonic waves [13–17].

In this study, an evaluation of a steel–concrete composite beam was presented. Particular attention was paid to the visualization of defects between a reinforcing plate and a concrete beam. The research was carried out using vibrations and their further processing. Vibration-based methods belong to the most popular and widely used damage detection techniques for decades [18–21] and they are still intensively developed [22]. Many researchers use modal analysis as a diagnostic tool (e.g., [23–30]). Changes in modal

parameters, such as natural frequencies, mode shapes, or damping coefficients, make it possible to monitor the condition of structures. Most often, the results obtained from mode shapes are enhanced by the calculation of modal curvatures [25,26,30]. To increase the efficiency of damage detection and localization, more and more researchers decide to use wavelet analysis [26–39]. Wavelet-based methods allow precise localizing and imaging defects, which is not always possible directly through modal analysis. In previous works, wavelet analysis has been applied for the detection of different kinds of defects in various structures, such as single or multiple notches in beams [25,26,29–36], spatial defects (in the form of local reduction of thickness) in plates [24,33,37,39] or impact damages in plates [38,39]. However, the literature on the non-invasive diagnostics of adhesive joints using vibration methods is limited and the problem of damage imaging in such joints by wavelet analysis has not been thoroughly considered. Recently, Yang and Oyadiji [28] used modal analysis and discrete wavelet transform of modal frequency curves to identify debonding in adhesive joints in two-layer bonded aluminum beam samples. To the best of the authors' knowledge, there is no research on integrated vibration and wavelet-based damage detection in steel–concrete adhesive connections.

This study presents a vibration-based condition assessment of the adhesive connection between a concrete beam and a steel plate. Experimental and numerical investigations were performed on a beam with a perfectly bonded joint as well as three beams with debonding defects of different areas. The diagnostic procedure used mode shapes and their further processing based on continuous wavelet transform for precise debonding localization and imaging. The influence of the number of wavelet vanishing moments and the mode shape interpolation on damage imaging maps was studied.

2. Materials and Methods

2.1. Object of Research

The object of research was a multilayer sample (Figure 1a) consisting of a concrete beam (class C30/37) with a square cross-section of 100 × 100 mm^2, and a length of 5000 mm, an adhesive film with a thickness of 2 mm and a steel plate with dimensions of 6 × 100 × 5000 mm^3. The material characteristics are given in Table 1. Four specimens (Figure 1b) were prepared: An intact composite beam (with no damage, #1) and three beams (#2-4) with the increasing percentage of debonding, 10%, 20% and 50%, consecutively. Each defect was arranged as a lack of an adhesive film by sticking a Teflon (PTFE) tape to the appropriate area of the joint. Before preparation of each sample, the contacting surfaces of the concrete beam and steel plate were accurately cleaned using Loctite-7063 cleaner (Henkel, Dusseldorf, Germany). Immediately after that, both elements were joined using Sikadur 30 Normal adhesive (Sika, Baar, Switzerland). The surface of the beam was primed with glue and then the adhesive layer was applied in a domed shape. This allowed the elimination of any possible air voids from the joints during attaching the plate to the concrete beam. The prepared samples are presented in Figure 1c.

Table 1. Material parameters of the consisting elements of the composite beam.

Element	Material	Density ρ (kg/m^3)	Elastic Modulus E (GPa)	Poisson's Ratio ν (-)
Beam	Concrete	2364.4	48.0	0.16
Plate	Steel	7579.0	200.3	0.30
Film	Adhesive	1611.8	12.5	0.30

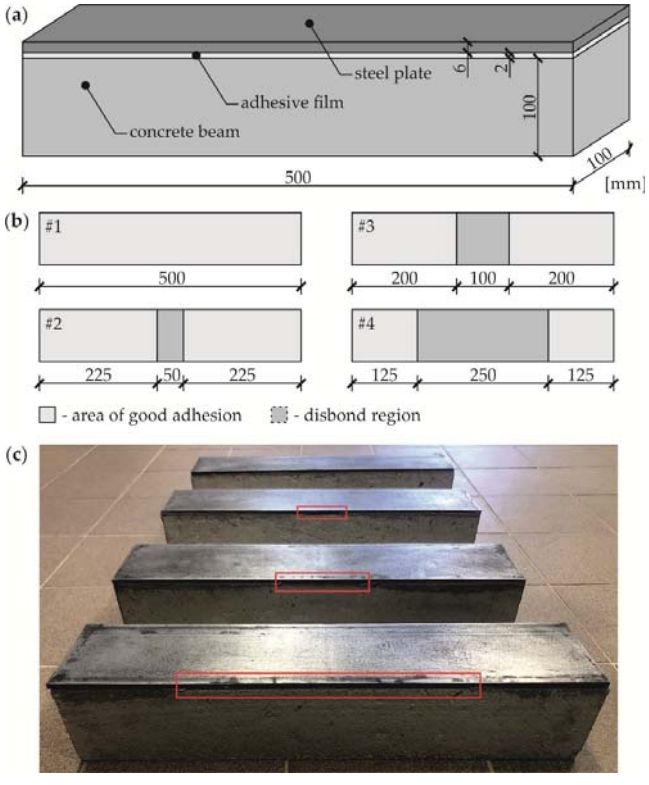

Figure 1. Object of research: (**a**) Specimen geometry; (**b**) variants of defects; (**c**) photograph of experimental samples.

2.2. Experimental Procedure

Dynamic parameters of the tested specimens (i.e., natural frequencies and modal shapes) were determined using the experimental modal analysis (EMA) approach, in which both excitation and response signals were measured. In the study, an impact test was conducted with the use of a modal hammer. The experimental setup for EMA is shown in Figure 2a. The specimen was suspended from both sides on elastic strings to simulate free boundary conditions. Piezoelectric accelerometer 356A15 (PCB Piezotronics, Inc., Depew, NY, USA) was used for the measurement of vibrations. The properties of the sensor used are as follows: sensitivity 10.2 mV/(m/s^2), measurement range $\pm$490 m/s^2, resonant frequency $\geq$25 kHz and frequency range 2–5000 Hz. The accelerometer was attached to the bottom surface of the beam at point A located 25 mm from the center. The dynamic pulse load was induced by the modal hammer 086C03 (PCB Piezotronics, Inc., Depew, NY, USA) with the following parameters: sensitivity 2.25 mV/N, measurement range $\pm$2224 N, resonant frequency $\geq$22 kHz. A medium tip was applied with the hammer enabling the excitation of vibrations within the frequency range up to approximately 2800 Hz. A single measurement was performed at each of 125 points. The points of impact, marked in Figure 1b, were distributed on the top surface of the specimen in a regular square grid having 5 rows and 25 columns, resulting with a resolution of 20 mm in both directions. Data acquisition and signal conditioning were performed by LMS SCADAS portable system (Siemens, Leuven, Belgium). Natural frequencies and modal shapes were determined based on the frequency response function (the accelerance in this case) given as the ratio of an output acceleration signal to an input force signal [33,40,41]. The estimation of modal

parameters was performed using a peak picking method. Mode shapes were determined by measuring the peak amplitude of the imaginary part of the frequency response function.

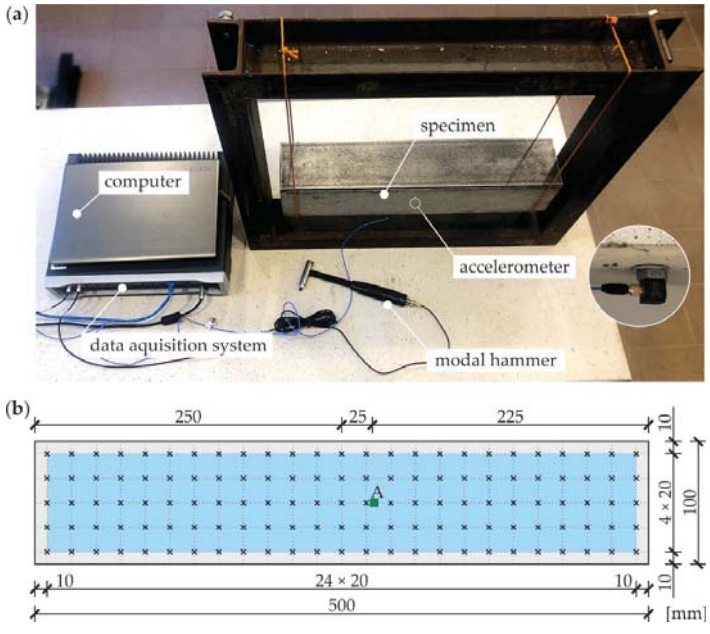

Figure 2. Experimental setup (**a**) and scheme of measurement grid (**b**).

2.3. Numerical Modelling

The numerical calculations were conducted with the use of the finite element method (FEM) in Abaqus software. Modal analysis was performed on the three-dimensional numerical models (Figure 3a) prepared based on the geometry and materials of the physical samples. Material parameters (Table 1) were used to apply a linearly elastic, isotropic, homogeneous material model to all structural elements (steel plate, adhesive film, and concrete beam), all being independent parts. The rigid surface-to-surface *tie* connection was used for bonding the contacting regions of each part. Three-dimensional eight-node linear brick finite elements with reduced integration (C3D8R) were used to mesh all parts. The mesh grid has a size of $2 \times 2 \times 2$ mm^3 (for steel plate and adhesive film) and $4 \times 4 \times 4$ mm^3 (for the concrete beam). The debonding in models #2–4 was modelled as a gap in the adhesive film (see Figure 3b), which relates to the lack of glue in the physical samples. The frequency procedure (linear perturbation theory) was performed to determine the natural frequencies and the corresponding mode shapes. The results (normalized displacements) were read from a regularly gridded square mesh with a global size of 2 mm located on the upper surface of a steel plate, covering a central area of 80×480 mm^2 with a margin of 10 mm at all edges (see Figure 3c). The additional coarser mesh was assumed with the size of 20 mm to coincide with the experimental measurements (cf. Figure 2b).

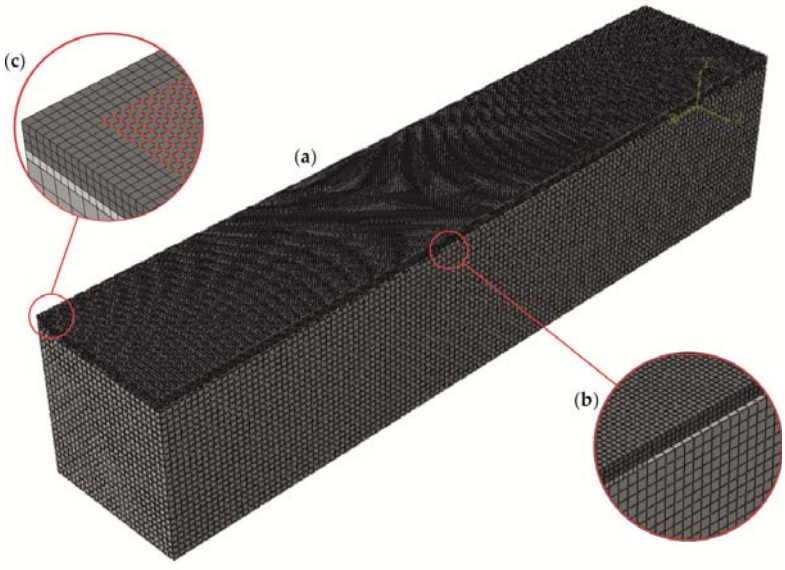

Figure 3. Numerical model (**a**) with a close-up of damage (**b**) and measurement grid (**c**) based on the #3 model.

2.4. Continuous Wavelet Transform for Mode Shape Processing

The continuous wavelet transform (CWT) of a given signal $f(x)$ is the inner product of the signal function with the shifted and scaled wavelet function [42]. It can be calculated with respect to the formula:

$$Wf(u,s) = \langle f, \psi_{u,s} \rangle = \frac{1}{\sqrt{s}} \int_{-\infty}^{+\infty} f(x)\, \psi^* \left(\frac{x-u}{s} \right) dx, \tag{1}$$

where x is the distance variable, the parameters s and u are scale and translation, respectively and $\psi^*(x)$ is the complex conjugate of the wavelet function, which is required to have zero average:

$$\int_{-\infty}^{+\infty} \psi(x) dx = 0. \tag{2}$$

For specific values of s and u, Wf (u,s) is called the wavelet coefficient for the wavelet function $\psi_{u,s}(x)$.

An important property of wavelets is their ability to react to any discontinuities comprised in a signal. For the detection of signal singularities, the so-called vanishing moments are crucial. A particular wavelet having n vanishing moments is characterized by the orthogonality to polynomials up to degree n–1:

$$\int_{-\infty}^{+\infty} x^k \psi(x) dx = 0, k = 0, 1, 2, \ldots, n-1. \tag{3}$$

It can be proved that a wavelet with n vanishing moments can be rewritten as the n-th order derivative of a function [42]:

$$\psi(x) = \frac{d^n \theta(x)}{dx^n}. \tag{4}$$

As a consequence, the wavelet transform given by Equation (1) can be expressed as a multiscale differential operator:

$$Wf(u,s) = s^n \frac{d^n}{du^n}(f * \bar{\theta}_s)(u), \tag{5}$$

where the notation $(f * \bar{\theta}_s)$ denotes the convolution of functions f and $\bar{\theta}_s$. Therefore, the wavelet transform is the n-th derivative of the signal smoothed by the function $\bar{\theta}_s(x)$ at scale s:

$$\bar{\theta}_s(x) = \frac{1}{\sqrt{s}}\theta\left(\frac{-x}{s}\right). \tag{6}$$

If a signal has a singularity at a certain point, then the wavelet coefficients have relatively large values. Singularities are detected at coordinates where the CWT modulus maxima converge at fine scales [42]. When the scale is large, the only detection of large variables is possible, because the convolution with $\bar{\theta}_s(x)$ removes small signal fluctuations. On the other hand, when the scale decreases, the wavelet coefficients may have no maxima in the vicinity of the singularity [42]. Therefore, the proper selection of the scale is crucial.

Several families of wavelets are described in the literature; in this study, wavelets from the Gaussian wavelet family were used due to their high efficiency in the detection of singularities [31,35]. The family of Gaussian wavelets is based on the Gaussian function $g(x) = C_a e^{-x^2}$, by taking the a-th derivative of $g(x)$ [43]. The first four wavelets from the Gaussian family have the following form [31]:

$$\psi(x) = (-1)^1 2\sqrt[4]{2/\pi}xe^{-x^2} \tag{7}$$

$$\psi(x) = (-1)^2 \frac{2\sqrt[4]{2/\pi}}{\sqrt{3}}(1-2x^2)e^{-x^2} \tag{8}$$

$$\psi(x) = (-1)^3 \frac{-4\sqrt[4]{2/\pi}}{\sqrt{15}}(3x-2x^3)e^{-x^2} \tag{9}$$

$$\psi(x) = (-1)^4 \frac{4\sqrt[4]{2/\pi}}{\sqrt{105}}(3-2x^2+4x^4)e^{-x^2} \tag{10}$$

Equations (7)–(10) describe wavelets *gaus1*, *gaus2*, *gaus3*, and *gaus4* having 1, 2, 3 and 4 vanishing moments, respectively. *Gaus1* wavelet enables to extract information of the first-order derivative of $f(x)$, *gaus2* represents the curvature of the function, while *gaus3* and *gaus4* correspond to higher-order derivatives. These properties of wavelets will be used in damage detection in the following section.

3. Results and Discussion

3.1. Modal Analysis—Natural Mode Shapes

The natural modes characterized by eigenfrequencies in the range of 0–2500 Hz were determined for all samples (based on the experimental results). Within this frequency range, five modes were taken into consideration, one for each beam (with the exception being sample #3, for which two modes were determined). Because the signals were measured only perpendicularly to the beam surface, all modes were related to the flexural deformations. Based on the obtained eigenfrequencies and mode shapes, the corresponding numerical modes were matched. The comparison of numerical and experimental frequencies is presented in Table 2, whereas the mode shapes are shown in Figure 4. The consistency of both approaches was evident. The differences between eigenfrequencies were below 10%, which allows stating that the experiments were conducted correctly, and also the numerical calculations were performed properly. Additionally, the modal assurance criterion (MAC) was applied to evaluate the degree of consistency between numerical and experimental mode shapes. Obtained MAC values ranged from 0.9782 to 0.9991, indicating very good agreement.

Table 2. Natural frequencies obtained numerically and experimentally for samples #1–4.

Sample	Mode	f_{num} (Hz)	f_{exp} (Hz)	Δf (%)	*MAC* * (-)
#1	1	1899	1761	7.8	0.9991
#2	1	1898	1751	8.4	0.9892
#3	1	1859	1722	8.0	0.9899
	2	2468	2436	1.3	0.9782
#4	1	453	476	4.8	0.9966

* modal assurance criterion.

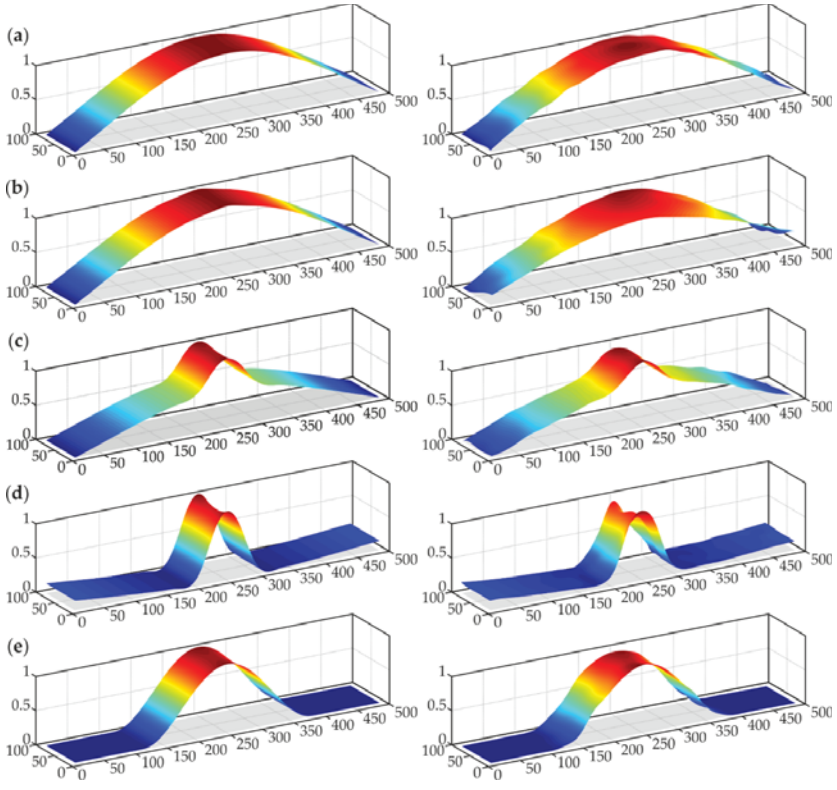

Figure 4. Normalized numerical (left column) and experimental (right column) mode shapes (dimensions in [mm]): (**a**) sample #1, mode 1; (**b**) sample #2, mode 1; (**c**) sample #3, mode 1; (**d**) sample #3, mode 2; (**e**) sample #4, mode 1.

It can be observed that the value of the first natural frequency slightly decreased with the size of debonding between beams #1–3. For sample #4, the decrease became dramatic, because the area of the defect covered 50% of the whole joint, thus the steel plate could oscillate as an independent part. It is not surprising that there were no disturbances in the first mode shape for beam #1 without damage (Figure 4a). For sample #2 (Figure 4b), the defect was barely visible in the numerical mode, whereas the experimental one did not reveal any disruption, thus its exact size could not be assessed. On the other hand, both modes of beam #3 (Figure 4c,d) gave useful information about the presence and approximate size of the damage. The deformation in the area of debonding was greater than in the good adhesion part of the joint. It has to be noted that mode 1 corresponds to

the global character of vibrations, the displacements are comparable in the area of good adhesion and debonding. Nevertheless, mode 2 has the local character, because vibrations in the debonding region are significantly higher than in the adjacent part of the specimen. The first mode shape of beam #4 (Figure 4e) also revealed the presence of the defect. What is interesting, no significant deformation was detected in the area of the properly prepared joint while comparing with the damaged part. This effect was not observed for the previous samples, where the oscillations had a global character. For beam #4, it can be stated that the first mode corresponded to the independent oscillation of the steel plate, thus the oscillations could be considered local. This difference stayed in agreement with the fact of a clear difference in the first eigenfrequency between beam #4 and the remaining ones. Summarizing, the analysis of mode shapes could provide an initial assessment of damage presence, especially in the case of large damage; however, further data processing is required to better visualize the defects.

3.2. Wavelet Transform-Based Damage Imaging

Continuous wavelet transform was used to identify the actual shape and position of debonding areas in the adhesive joints. The prepared maps presenting mode shapes were separated into five vectors situated along the length of the specimen (cf. Figure 2b), creating five single lines. For each line, the calculations of the CWT were conducted independently, using a program written in MATLAB® environment [44]. Firstly, to avoid boundary effects, extrapolation was applied. Figure 5 shows the efficiency of extrapolation in the elimination of the potential edge effects. In raw data (Figure 5a, no extrapolation) the intensification of CWT values is observed near the edges, thus the damage identification becomes problematic. This is because edge values are relatively high compared to the ones indicating the presence of defects. The performed extrapolation allowed eliminating this effect, resulting in sufficient damage imaging. It is also worth noting that edge effects are more visible for smaller defects.

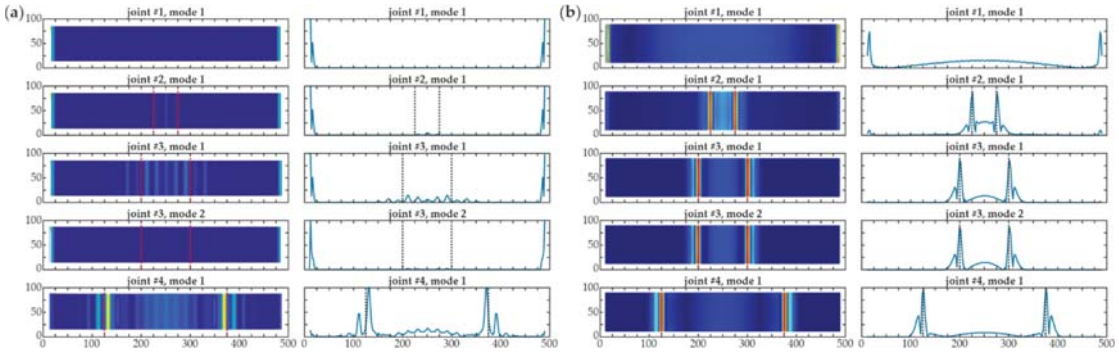

Figure 5. Influence of boundary effect to damage imaging (numerical results mesh 2 mm, no additional interpolation) for all joints #1–#4 (dimensions in [mm])—map and central cross section: (**a**) continuous wavelet transform (CWT) without extrapolation, wavelet *gaus4*, *s* = 2; (**b**) CWT with extrapolation, wavelet *gaus4*, *s* = 2.

Secondly, calculations of wavelet transform were performed for each extrapolated vector. Finally, the expansion of the data was eliminated by cutting the results to the original size. As an initial step, the numerical results collected using a fine mesh (2 mm grid) were analyzed. The calculations of wavelet transforms were conducted using Gaussian wavelets with one to four vanishing moments. The fine scale *s* = 2 was initially set. To be compared with CWT, the conventional derivatives of the corresponding orders were determined. The comparison of both approaches is shown in Figure 6, where the damage maps are presented together with their cross-sections in the central part. Damage areas were marked on the charts. It is essential to note that the agreement between CWTs and derivatives is visible.

The maps were similar in both approaches, the cross-sections were also comparable in shape for all wavelets. However, the derivatives included a considerable noise component that made the quality of the maps poorer and disrupted the possibility of the exact location of the damage. This observation allowed emphasizing the advantage of the CWT; the CWT maps had better quality when compared to the conventional derivatives, thanks to the smoothing function that reduced the noise. Thus, the derivatives were not used for further investigation. It is important to note that wavelets with a higher number of vanishing moments are more practical in the determination of the exact shape and position of defects. The damaged areas were revealed by *gaus1* wavelet; however, the defects could be incorrectly detected in intact sample #1. Nevertheless, CWT values for intact beam #1 are significantly lower than for damaged ones. This difference is not observed due to the individual scaling of each map (mutual scale could disturb the legibility of the results). What is more, the variability of CWT values in the area of debonding could suggest that there were multiple defects. These effects were not present for Gaussian wavelet with four vanishing moments that emphasized only the edges of the defect and flattened the areas with the same quality of adhesion. For this reason, the *gaus4* wavelet could be stated as the most effective for damage detection.

The second part of the analysis was the comparison between the numerical and experimental data. The results were obtained for a grid of 20 mm chosen based on the original mesh in experimental measurements (no additional interpolation was applied). As before, Gaussian wavelets were used with the constant scale $s = 2$. The CWT maps are shown in Figure 7. A good agreement between experimental and numerical maps was evident. Most of the maps were similar. However, the experimental results were demonstrably affected by the signal noise that deteriorated the quality of the obtained visualizations. As the degree of the wavelet increased, the influence of the noise became more visible, highlighting the differences between the experimental and numerical results, mainly for beams #1, #2 (the inconsistency between the maps obtained using *gaus3* and *gaus4* wavelets was clear). This effect made the localization of the debonding difficult, especially for the smallest damage (i.e., 5 cm (beam #2)), for which there was no possibility to detect the defect. As stated in the previous paragraph, the fourth order Gauss wavelet was the most powerful in the damage imaging. However, the quality of the maps was lower than those presented in Figure 6 due to the application of a coarser grid.

Additional interpolation was applied to the data measured on a 20 mm grid as an attempt to enhance the quality of the obtained maps. Firstly, the propriety of the proposed interpolation was verified based on the numerical results. The spline interpolation with the destined step of 2 mm was performed in MATLAB®. Taking into account the decrease in the step value, the scale for CWT calculations was increased to $s = 8$. Figure 8 presents the comparison of CWT maps obtained from originally fine mesh (2 mm) and interpolated from 20 to 2 mm. The accordance is clearly visible, proving the correctness of the performed interpolation. Furthermore, the numerical and experimental maps obtained using the above described interpolation are presented in Figure 9. It is firstly important to note that interpolation improved the quality of damage imaging for numerical data. The maps showed the debonding regions more clearly, the images were sharper, especially for the *gaus4* wavelet (Figure 9d). On the other hand, despite making the images sharper, the interpolation made the defect shape in the experimental maps more irregular, which may have been caused by the noise in the measured signals. The effect was much more visible for the higher-order wavelets (*gaus3*, *gaus4*), for which the boundaries of debonding regions became illegible. This was because high-order wavelets revealed small but sharp disturbances, which for experimental data could be both damage boundaries and noise, affecting the signals similarly. Based on this observation, it can be stated that the interpolation of noisy data collected in a coarse grid can enhance the quality of CWT damage visualization; however, high-order wavelets were not useful in this situation.

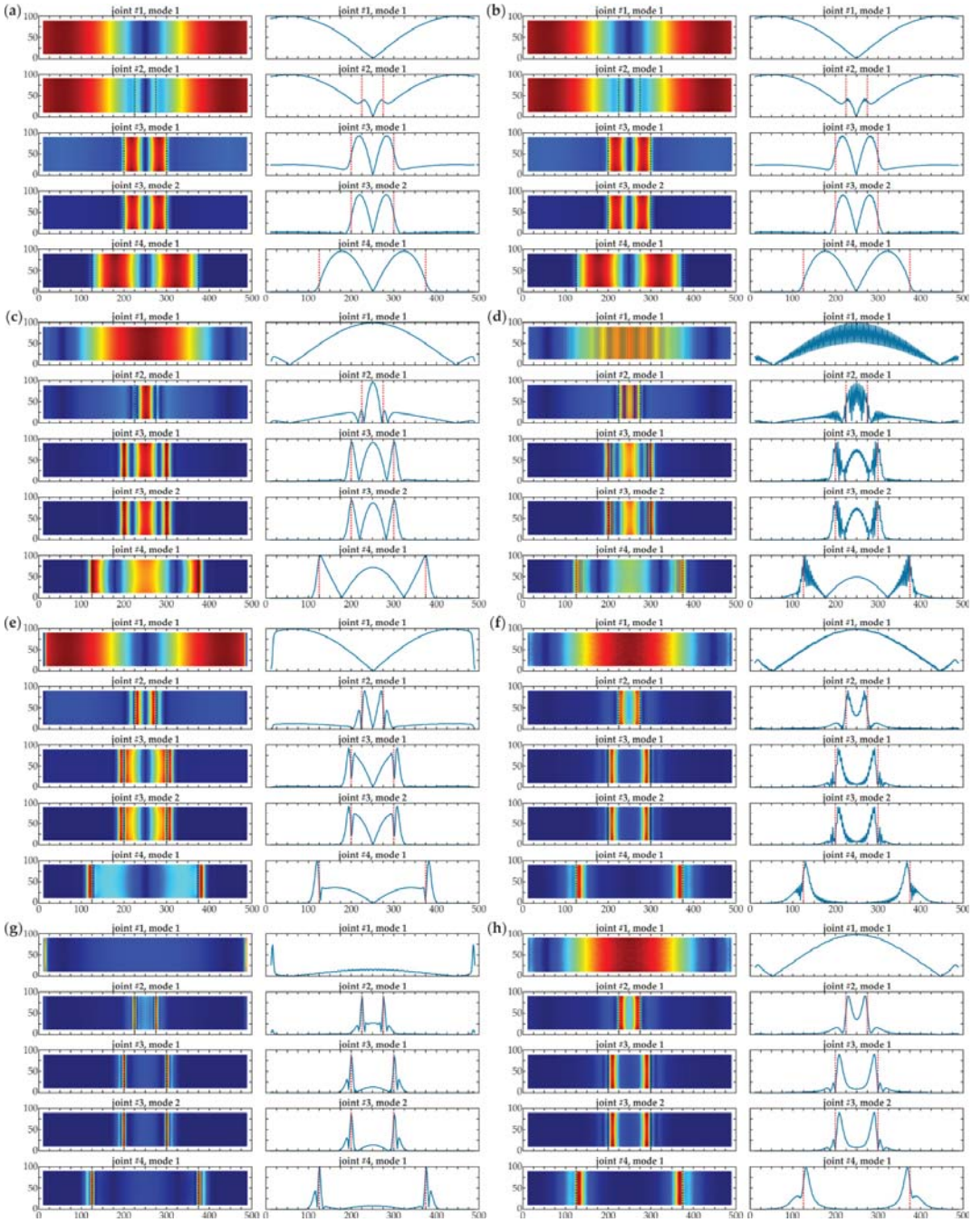

Figure 6. Damage imaging for numerical results (mesh 2 mm, no additional interpolation) for all joints #1–#4 (dimensions in [mm])—map and central cross section: (**a**) CWT, wavelet *gaus1*, *s* = 2; (**b**) first derivative; (**c**) CWT, wavelet *gaus2*, *s* = 2; (**d**) second derivative; (**e**) CWT, wavelet *gaus3*, *s* = 2; (**f**) third derivative; (**g**) CWT, wavelet *gaus4*, *s* = 2; (**h**) fourth derivative.

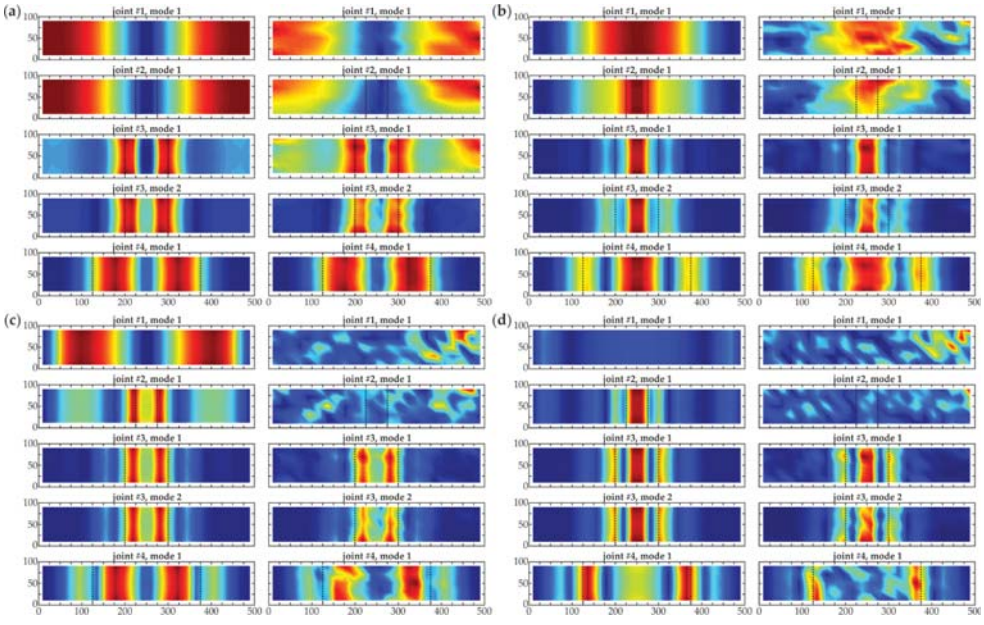

Figure 7. Comparison of CWT damage imaging for numerical (left column) and experimental (right column) results (grid 20 mm, no interpolation) for all joints #1–#4 (dimensions in [mm], scale $s = 2$) using different wavelets: (**a**) *gaus1*; (**b**) *gaus2*; (**c**) *gaus3*; (**d**) *gaus4*.

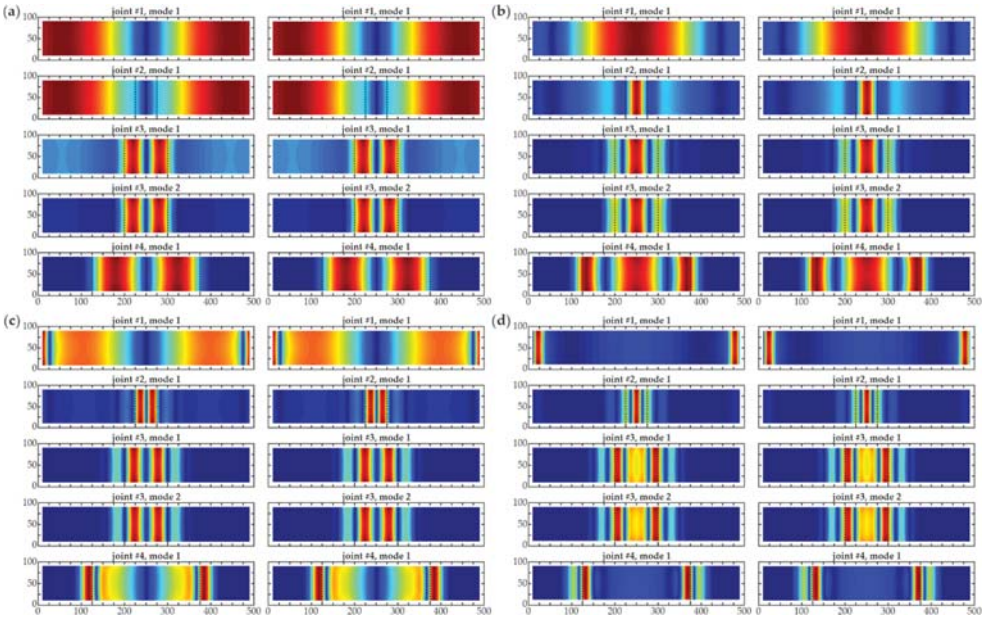

Figure 8. Comparison of CWT damage imaging for numerical results (left column—mesh 2 mm, no additional interpolation and right column—grid 20 mm interpolated to 2 mm, both for scale $s = 8$) for all joints #1–#4 (dimensions in [mm]) using different wavelets: (**a**) *gaus1*; (**b**) *gaus2*; (**c**) *gaus3*; (**d**) *gaus4*.

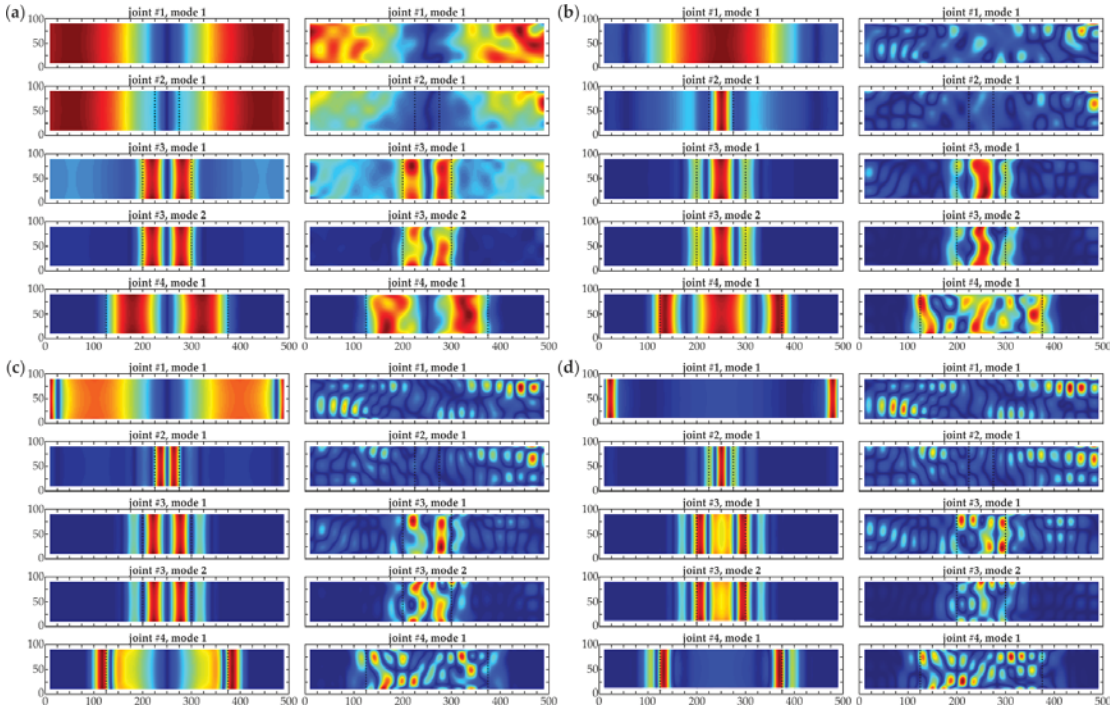

Figure 9. Comparison of CWT damage imaging for numerical (left column) and experimental (right column) results (grid 20 mm interpolated to 2 mm) for all joints #1–#4 (dimensions in [mm], scale s = 8) using different wavelets: (**a**) *gaus1*; (**b**) *gaus2*; (**c**) *gaus3*; (**d**) *gaus4*.

However, it was possible to change the scale to better visualize the damage in the experimental data. Figure 10 shows the CWT damage maps on the interpolated mesh (resulting grid of 2 mm) for multiplied scales, being doubling and tripling of the initial scale, i.e., s = 16 and s = 24. The positive influence of the increasing scale was evident. The shape of the debonding areas was clearly visible for both improved scales when compared to the initial value (cf. Figure 9), especially for high order wavelets. Larger scales highlighted the defects and allowed precise damage localization since they neglected the subtle signal noise. Some irregularities resulting from the noisy character of the experimental signals were visible. Comparing both increased scales, better results were obtained for the higher scale s = 24. However, the smallest defect (debonding of 5 cm) was still not detected.

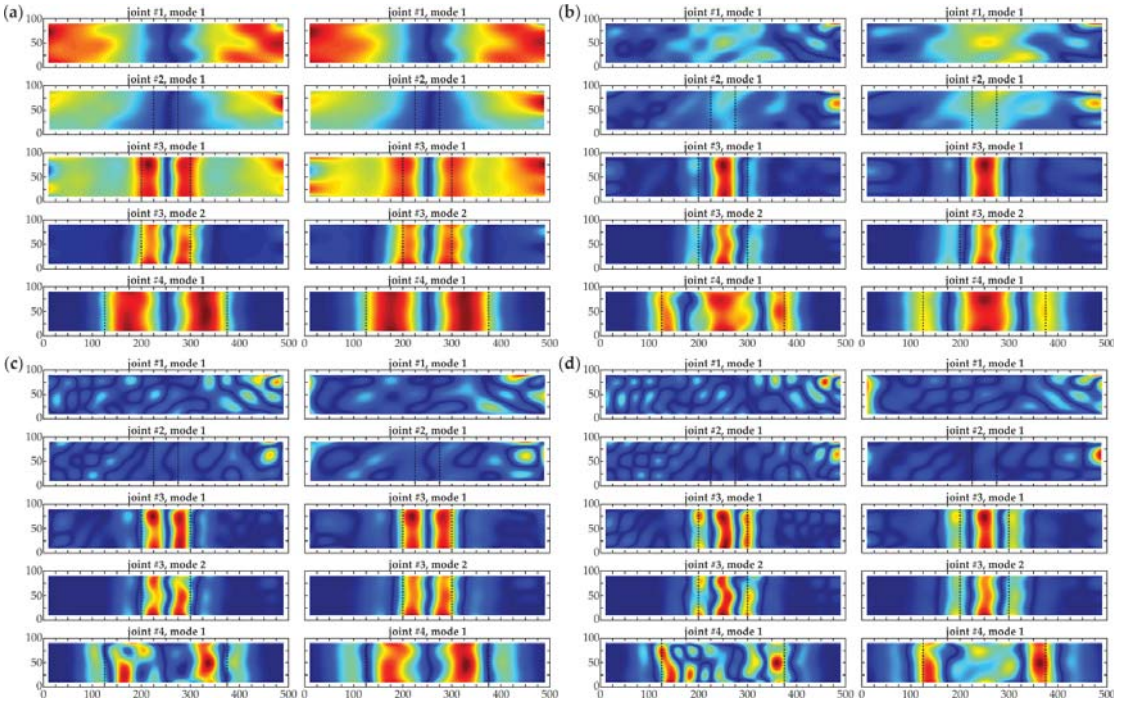

Figure 10. CWT damage imaging for experimental results (grid 20 mm interpolated to 2 mm) for all joints #1–#4 (dimensions in [mm]) using different wavelets for scales s = 16 (left column) and s = 24 (right column): (**a**) *gaus1*; (**b**) *gaus2*; (**c**) *gaus3*; (**d**) *gaus4*.

4. Conclusions

The paper describes the non-destructive testing of concrete beams strengthened with steel plates. The issue of damage imaging in adhesive joints was considered. The modal analysis supported with the continuous wavelet transform was successfully applied. Gaussian wavelet family was assumed for calculations. Based on the obtained experimental and numerical results, the following conclusions could be formulated.

- The consistency between experimental and numerical eigenfrequencies and mode shapes confirmed the propriety of the performed experimental measurements and numerical simulations. The decrease of the natural frequency with the increasing size of the damaged area was observed.
- The interpretation of experimental and numerical mode shapes for all analyzed beams allowed initial damage detection by revealing significant disturbances connected with the presence of debonding areas.
- The comparison between conventional derivatives and continuous wavelet transforms for numerical results revealed the advantages of the latter. Both approaches gave consistent information about the damage; however, the CWT maps were more useful because of showing the defects more precisely.
- The appropriate choice of CWT calculation parameters is essential for the efficiency of obtained damage visualization. The quality of damage maps increased with the number of vanishing moments of the applied Gaussian wavelets. Low order of wavelet could lead to incorrect detection of defects in intact beams. In the case of scales, too high values could result in indistinct damage imaging, on the other hand, too low ones could reveal noise of signals.

- A good agreement between experimental and numerical CWT maps was observed for the data collected with coarse mesh (with a grid of 20 mm). However, the determination of the exact size of the smallest defect was not possible. The interpolation of the data allowed enhancing the quality of the obtained numerical damage maps. On the other hand, the experimental results had a poorer quality, because of the noise contained in the measured signals. The increase in scale helped overcome this difficulty.
- In general, the interpolation of the collected data can allow reducing the number of measurements. However, the coarse mesh grid can make the small defects undetectable. Furthermore, interpolation of experimental results can lead to the distortion of damage shape in CWT maps, especially for higher-order wavelets.

The final conclusion can be made that it is possible to determine the exact shape and position of the debonding in the adhesive joints of composite beams using modal analysis and continuous wavelet transform. However, the measurement mesh and CWT calculation parameters are important factors affecting the quality of the results. The proposed method is expected to have potential applications in the civil engineering industry. Having significantly greater sizes than laboratory specimens, real-scale engineering structures would require a division into smaller sections that could be analyzed in the way proposed in the current paper. This practical aspect of the paper could be the subject of future work. Another interesting direction for continuing the current research is the visualization of internal defects with smaller size and different shapes, such as the application of 2D wavelet transform.

Author Contributions: Conceptualization, M.K., E.W. and M.R.; methodology, M.K., E.W. and M.R.; software, M.K., E.W. and M.R.; validation, M.K., E.W. and M.R.; formal analysis, M.K., E.W. and M.R.; investigation, M.K., E.W. and M.R.; writing—original draft preparation, M.K., E.W. and M.R.; writing—review and editing, E.W. and M.R.; visualization, M.K. and E.W.; supervision, M.R. All authors have read and agreed to the published version of the manuscript.

Funding: Financial support of these studies from Gdańsk University of Technology by the DEC-6/2020/IDUB/III.4.1/Tc grant under the TECHNETIUM TALENT MANAGEMENT GRANTS-'Excellence Initiative-Research University' program is gratefully acknowledged.

Institutional Review Board Statement: Not applicable.

Informed Consent Statement: Not applicable.

Data Availability Statement: The data underlying this article will be shared on reasonable request from the corresponding author.

Acknowledgments: Abaqus calculations were carried out at the Academic Computer Center in Gdańsk.

Conflicts of Interest: The authors declare no conflict of interest. The funders had no role in the design of the study; in the collection, analyses, or interpretation of data; in the writing of the manuscript, or in the decision to publish the results.

References

1. Giurgiutiu, V.; Lyons, J.; Petrou, M.; Laub, D.; Whitley, S. Fracture mechanics testing of the bond between composite overlays and a concrete substrate. *J. Adhes. Sci. Technol.* **2001**, *15*, 1351–1371. [CrossRef]
2. Napoli, A.; Realfonzo, R. Reinforced concrete beams strengthened with SRP/SRG systems: Experimental investigation. *Constr. Build. Mater.* **2015**, *93*, 654–677. [CrossRef]
3. Czaderski, C.; Meier, U. EBR Strengthening Technique for Concrete, Long-Term Behaviour and Historical Survey. *Polymers* **2018**, *10*, 77. [CrossRef]
4. Batti, M.M.B.; do Vale Silva, B.; Piccinini, Â.C.; dos Santos Godinho, D.; Antunes, E.G.P. Experimental Analysis of the Strengthening of Reinforced Concrete Beams in Shear Using Steel Plates. *Infrastructures* **2018**, *3*, 52. [CrossRef]
5. Schabowicz, K. Non-Destructive Testing of Materials in Civil Engineering. *Materials* **2019**, *12*, 3237. [CrossRef]
6. Rucka, M. Special Issue: "Non-Destructive Testing of Structures". *Materials* **2020**, *13*, 4996. [CrossRef] [PubMed]
7. Sen, R. Developments in the durability of FRP-concrete bond. *Constr. Build. Mater.* **2015**, *78*, 112–125. [CrossRef]

8. Lai, W.L.; Lee, K.K.; Kou, S.C.; Poon, C.S.; Tsang, W.F. A study of full-field debond behaviour and durability of CFRP-concrete composite beams by pulsed infrared thermography (IRT). *NDT E Int.* **2012**, *52*, 112–121. [CrossRef]
9. Tashan, J.; Al-Mahaidi, R. Bond defect detection using PTT IRT in concrete structures strengthened with different CFRP systems. *Compos. Struct.* **2014**, *111*, 13–19. [CrossRef]
10. Yazdani, N.; Beneberu, E.; Riad, M. Nondestructive Evaluation of FRP-Concrete Interface Bond due to Surface Defects. *Adv. Civ. Eng.* **2019**, *2019*, 2563079. [CrossRef]
11. Gu, J.C.; Unjoh, S.; Naito, H. Detectability of delamination regions using infrared thermography in concrete members strengthened by CFRP jacketing. *Compos. Struct.* **2020**, *245*, 112328. [CrossRef]
12. Steinbild, P.J.; Höhne, R.; Füßel, R.; Modler, N. A sensor detecting kissing bonds in adhesively bonded joints using electric time domain reflectometry. *NDT E Int.* **2019**, *102*, 114–119. [CrossRef]
13. Song, H.; Popovics, J.S. Characterization of steel-concrete interface bonding conditions using attenuation characteristics of guided waves. *Cem. Concr. Compos.* **2017**, *83*, 111–124. [CrossRef]
14. Li, J.; Lu, Y.; Guan, R.; Qu, W. Guided waves for debonding identification in CFRP-reinforced concrete beams. *Constr. Build. Mater.* **2017**, *131*, 388–399. [CrossRef]
15. Rucka, M. Failure Monitoring and Condition Assessment of Steel-Concrete Adhesive Connection Using Ultrasonic Waves. *Appl. Sci.* **2018**, *8*, 320. [CrossRef]
16. Wojtczak, E.; Rucka, M. Wave frequency effects on damage imaging in adhesive joints using lamb waves and RMS. *Materials* **2019**, *12*, 1842. [CrossRef]
17. Wojtczak, E.; Rucka, M.; Knak, M. Detection and imaging of debonding in adhesive joints of concrete beams strengthened with steel plates using guided waves and weighted root mean square. *Materials* **2020**, *13*, 2167. [CrossRef]
18. Doebling, S.W.; Farrar, C.R.; Prime, M.B.; Shevitz, D.W. Damage identification and health monitoring of structural and mechanical systems from changes in their vibration characteristics: A literature review. *Los Alamos Natl. Lab. Rep.* **1996**, 249299. [CrossRef]
19. Sohn, H.; Farrar, C.R.; Hemez, F.; Czarnecki, J. A Review of Sstructural Health Monitoring Literature 1996–2001. *Los Alamos Natl. Lab. Rep.* **2003**, 976152.
20. Salawu, O.S. Detection of structural damage through changes in frequency: A review. *Eng. Struct.* **1997**, *19*, 718–723. [CrossRef]
21. Fan, W.; Qiao, P. Vibration-based damage identification methods: A review and comparative study. *Struct. Health Monit.* **2011**, *10*, 83–111. [CrossRef]
22. Hou, R.; Xia, Y. Review on the new development of vibration-based damage identification for civil engineering structures: 2010–2019. *J. Sound Vib.* **2021**, *491*, 115741. [CrossRef]
23. Kim, J.T.; Stubbs, N. Crack detection in beam-type structures using frequency data. *J. Sound Vib.* **2003**, *259*, 145–160. [CrossRef]
24. Zhang, Y.; Wang, L.; Lie, S.T.; Xiang, Z. Damage detection in plates structures based on frequency shift surface curvature. *J. Sound Vib.* **2013**, *332*, 6665–6684. [CrossRef]
25. Dessi, D.; Camerlengo, G. Damage identification techniques via modal curvature analysis: Overview and comparison. *Mech. Syst. Signal Process.* **2015**, *52–53*, 181–205. [CrossRef]
26. Radzieński, M.; Krawczuk, M.; Palacz, M. Improvement of damage detection methods based on experimental modal parameters. *Mech. Syst. Signal Process.* **2011**, *25*, 2169–2190. [CrossRef]
27. Makki Alamdari, M.; Li, J.; Samali, B. Damage identification using 2-D discrete wavelet transform on extended operational mode shapes. *Arch. Civ. Mech. Eng.* **2015**, *15*, 698–710. [CrossRef]
28. Yang, C.; Oyadiji, S.O. Damage detection using modal frequency curve and squared residual wavelet coefficients-based damage indicator. *Mech. Syst. Signal Process.* **2017**, *83*, 385–405. [CrossRef]
29. Swamy, S.; Reddy, D.M.; Prakash, G.J. Damage detection and identification in beam structure using modal data and wavelets. *World J. Model. Simul.* **2017**, *13*, 52–65.
30. Janeliukstis, R.; Rucevskis, S.; Wesolowski, M.; Chate, A. Experimental structural damage localization in beam structure using spatial continuous wavelet transform and mode shape curvature methods. *Meas. J. Int. Meas. Confed.* **2017**, *102*, 253–270. [CrossRef]
31. Gentile, A.; Messina, A. On the continuous wavelet transforms applied to discrete vibrational data for detecting open cracks in damaged beams. *Int. J. Solids Struct.* **2003**, *40*, 295–315. [CrossRef]
32. Loutridis, S.; Douka, E.; Trochidis, A. Crack identification in double-cracked beams using wavelet analysis. *J. Sound Vib.* **2004**, *277*, 1025–1039. [CrossRef]
33. Rucka, M.; Wilde, K. Application of continuous wavelet transform in vibration based damage detection method for beams and plates. *J. Sound Vib.* **2006**, *297*, 536–550. [CrossRef]
34. Rucka, M. Damage detection in beams using wavelet transform on higher vibration modes. *J. Theor. Appl. Mech.* **2011**, *49*, 399–417.
35. Pacheco-Chérrez, J.; Delgado-Gutiérrez, A.; Cárdenas, D.; Probst, O. Reliable damage localization in cantilever beams using an image similarity assessment method applied to wavelet-enhanced modal analysis. *Mech. Syst. Signal Process.* **2021**, *149*. [CrossRef]
36. Katunin, A.; Araújo dos Santos, J.V.; Lopes, H. Damage identification by wavelet analysis of modal rotation differences. *Structures* **2021**, *30*, 1–10. [CrossRef]
37. Katunin, A. Damage identification in composite plates using two-dimensional B-spline wavelets. *Mech. Syst. Signal Process.* **2011**, *25*, 3153–3167. [CrossRef]

38. Fan, W.; Qiao, P. A 2-D continuous wavelet transform of mode shape data for damage detection of plate structures. *Int. J. Solids Struct.* **2009**, *46*, 4379–4395. [CrossRef]
39. Katunin, A. Nondestructive damage assessment of composite structures based on wavelet analysis of modal curvatures: State-of-the-art review and description of wavelet-based damage assessment benchmark. *Shock Vib.* **2015**, *2015*. [CrossRef]
40. Grębowski, K.; Rucka, M.; Wilde, K. Non-Destructive Testing of a Sport Tribune under Synchronized Crowd-Induced Excitation Using Vibration Analysis. *Materials* **2019**, *12*, 2148. [CrossRef] [PubMed]
41. Chróścielewski, J.; Miśkiewicz, M.; Pyrzowski, Ł.; Rucka, M.; Sobczyk, B.; Wilde, K. Modal properties identification of a novel sandwich footbridge–Comparison of measured dynamic response and FEA. *Compos. Part B Eng.* **2018**, *151*, 245–255. [CrossRef]
42. Mallat, S. *A Wavelet Tour of Signal Processing: The Sparse Way*; Elsevier/Academic Press: Burlington, VT, USA, 2009; ISBN 9780123743701.
43. Misiti, M.; Misiti, Y.; Oppenheim, G.; Poggi, J.-M. *Wavelet ToolboxTM User's Guide*; The MathWorks, Inc.: Natick, MA, USA, 2020.
44. *MATLAB*; Ver. 2020b, 9.9.0.1570001; Programming and Numeric Computing Platform; The MathWorks: Natick, MA, USA, 2020.

materials

MDPI

Article

Reliability Assessment Approach for the Quality of Railroad Subgrade

Janusz Vitalis Kozubal [1], Piotr Wyborski [1,*], Matylda Tankiewicz [2] and Igor Gisterek [1]

[1] Faculty of Civil Engineering, Wroclaw University of Science and Technology, 50-370 Wrocław, Poland; janusz.kozubal@pwr.edu.pl (J.V.K.); igor.gisterek@pwr.edu.pl (I.G.)
[2] Department of Civil Engineering, Wrocław University of Environmental and Life Sciences, 50-375 Wrocław, Poland; matylda.tankiewicz@upwr.edu.pl
* Correspondence: piotr.wyborski@pwr.edu.pl

Abstract: The static load plate test is the standard subgrade acceptance test for new or modernised railway lines. Examinations are performed at regular spacings on the track section and a lack of acceptance for even a single test disqualifies a section, forcing remedial treatments on the whole section. In this paper, a nondeterministic description of stiffness related to the spatial characteristics of acceptance measurement results is proposed for a more rational assessment of substructure quality. The concept is based on geostatistical analysis and one-dimensional distributions of stiffness values. The paper also proposes a new concept of rail infrastructure acceptance based on a reliability index already codified in European standards. The functioning of the postulated criterion is presented on the example of an existing railway line and the actual test results.

Keywords: subgrade; static load test; deformation modulus; reliability

Citation: Kozubal, J.V.; Wyborski, P.; Tankiewicz, M.; Gisterek, I. Reliability Assessment Approach for the Quality of Railroad Subgrade. *Materials* **2022**, *15*, 1864. https://doi.org/10.3390/ma15051864

Academic Editors: Sukhoon Pyo and Siegfried Schmauder

Received: 15 December 2021
Accepted: 28 February 2022
Published: 2 March 2022

Publisher's Note: MDPI stays neutral with regard to jurisdictional claims in published maps and institutional affiliations.

1. Introduction

The railway subgrade is an important part of the construction of a railway line. Depending on the course of the route and terrain, the tracks are found directly on original subsoil or on anthropogenic soil structure. In the case of old routes, the problems of preserving the homogeneity and quality of the substructure are particularly significant [1,2]. In addition, the increasing speed of trains leads to higher expectations for all components of the track [3,4]. Adapting existing railways to changing standards and guidelines, especially in terms of achievable speeds and axle loads, is now a significant issue. In many cases, track bed investigations are necessary, not only in preparation for the construction, reconstruction and modernisation of a railway line, but also in the case of failure [5]. Damage to the substructure occurs during the operation of a route for various reasons, such as changes in soil and water conditions, design errors, execution errors and construction limitations.

Soil as a track bed is characterised by high variability, including variability in time, which is related to the influence of external factors such as climate conditions or exposure to dynamic effects of rail traffic. Under certain circumstances, it is possible for there to be not only a deterioration but also an increase in the bearing capacity of the subgrade after a certain period of use. This is caused by the compaction of the soil layers as a result of dynamic influences from passing trains. Therefore, for practical confirmation of the theoretical assumptions of newly designed structures and improvement of old ones, it is necessary to build testing sections on test tracks or on sections of active railway lines, where theoretical parameters are subject to final verification. A similar procedure applies to the design of innovative improvement structures and subgrade drainage. In the case of existing routes, in order to properly assess the causes of damage to the track structure and substructure, it is necessary to carry out load-bearing capacity tests on the substructure, which are invasive in relation to the track superstructure.

Due to the reasons mentioned above, the primary approach used in subgrade design is empirical investigations, mainly in situ. The geotechnical testing methods used in railway construction do not differ from those used for other geotechnical structures or road infrastructures. However, it is not clearly stated whether such a procedure is fully justified, not least because of the different ways of transferring forces and loads from trains to the ground [6]. In addition, due to the local specifics (rolling stock, speeds and construction technology), national guidelines have been developed for testing the subsoil of railway lines. In Poland, basic works include the textbooks by A. Wasiutyński [7] and K. Wątorek [8] and works by J. Nowkuński [9], J. Sysak [10] and E. Skrzyński [11]. The common recommendations of the UIC (International Union of Railways) and the associated European standards of the EN series were only developed in the 1960s and 1970s. Important works discussing the topic of subgrade include—but are not limited to—books by Popp [12], Indraratna et al. [13], Li et al. [14] and Correia et al. [15]. Regarding Polish textbooks, conditioned to the national standard, the most relevant ones are Skrzyński [11] and Grulkowski et al. [16].

In the international practice of physical testing of the substructure, the static plate load test is accepted as the basic test [6]. Widely known problems and difficulties connected with static plate testing, significant costs of testing and the long time needed to carry it out properly mean that there is a continuous search for a method that will allow the replacement of it with tests carried out by other methods, which will give results with an acceptable level of probability. The commonly used methods of monitoring the substructure and quality of earthworks are based on a scheme where a sufficient number of tests confirming the quality of the work are carried out by means of measurable parameters. This makes it possible to classify the quality of the work as satisfactory or in need of improvement, i.e., by increasing compaction or by adding admixtures or replacing soil with material, guaranteeing the achievement of the assumed mechanical properties.

The aim of the work is to propose an approach that will make it possible to reduce costly, time-consuming and cumbersome field investigations while adequately assessing the bearing capacity of the subgrade. The paper presents a reliability-based approach. The methodology of reliability estimation has been intensively developed in geotechnical tasks [17–20] for a significant period of time and is successfully applied in geotechnical design. It is also supported by recent normative acts [21,22]. The key similarity of the presented approach is the reliance on probability theory and the classical definition of the failure region boundary. The mathematical apparatus is also common. The difference is important and crucial and corresponds with the existing railroad standards. It combines the qualitative analysis of the track bed with the safety system, and the assumed limiting vulnerabilities are a generalised description of the track bed condition. This way, the method is called reliability based on the quality parameter, in contrast to load-limit-based reliability.

Investigations of the horizontal spatial variability of the deformation modulus using geostatistical methods have been successfully performed in the past [23,24]. However, the application of these methods to the study of railway or road substructures is a novelty; publications on this issue have been published only recently [25,26]. An unquestionable innovation resulting from this article is a proposal to calculate the reliability with the use of geostatistical methods in issues related to the railway subgrade. The proposed method is based on standard subgrade field tests but takes into account spatial geostatistical relations in the ground. Therefore, it is also possible to predict the state of the substructure beyond the test points. It is based on the correlation between the values of the subgrade modulus as a function of their mutual distance and the generated random values of the modulus in the dense grid. The geostatistical analysis of the obtained values based on reliability assumptions allows for conclusions on the subgrade quality in the serviceability limit-state context in a more extensive way than based purely on test results. The paper includes results of the subgrade quality assessment for a selected railway route section (from West Pomerania, Poland) using the proposed technique with the determination of the required scope of subgrade improvement for the assumed criteria. The issue of selecting

the method of substrate improvement based on the results obtained, due to the multiplicity of techniques used and the complexity of the issue, was not considered.

2. Materials and Methods

2.1. Rail Subgrade Testing

The purpose of the substructure (subgrade) is to transfer loads without permanent deformation to the subsoil from passing rail vehicles, the weight of the rail itself and the layers above it. The subgrade usually consists of natural soil and a thin layer of additional soil material, which is required to provide the planned track path. A typical embankment substructure is shown in Figure 1, where the superstructure layers, i.e., ballast and subballast, are placed on top of the original soil, on which the railway road is placed.

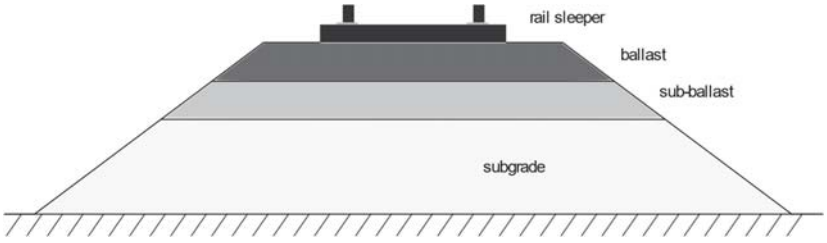

Figure 1. Construction of the railway substructure.

Due to different construction techniques and route paths, the track subgrade may contain different types of soil. Typically, it is constructed of aggregates < 31.5 mm when low water permeability is expected, and of coarser fractions, e.g., 4–31.5 mm, when drainage is required. Such materials provide sufficient bearing capacity and are most suitable to support the ballast layer and ensure required drainage.

As mentioned in the introduction, subgrade quality examinations are carried out in various situations, both on newly built and existing lines. The basic test to evaluate the quality of the subgrade of railroads is the static plate load test. The test is performed by loading the ground in the field with a circular steel plate and allows evaluation of the deformability and the load capacity of the soil. The settlement of the plate is measured by a tester consisting of a carrier frame with a sensing arm and dial gauge. As a counterbalance, a heavy vehicle is used. For each loading step, the corresponding settlement of the plate is recorded. From the load-settlement graph, the primary and secondary deformation modulus (E_{v1} and E_{v2}) are determined. The test characterises the zone to a depth of 0.30–0.50 m below the plate and it is commonly used for roads and railways. The detailed procedure is described, e.g., in [27]. Depending on the country (region) there are different regulations for subgrade investigations. The work is based on European and local standards [28,29]. Excerpts from these regulations are included in the appendices to [30], which is the mandatory document for national railways in Poland. It describes a static load test with a 300 mm plate, and the number of control points per track length is given. According to this approach, the deformation index I_0 is calculated from the measured values of the moduli E_{v1} and E_{v2}, and the quality assessment is performed on the basis of the index I_0 and the modulus E_{v2}. In this study, it was decided to base the quality of subgradeonly on the values measured directly in the tests, i.e., both strain moduli.

2.2. Variogram Estimators

In the case of linear constructions such as railways, ground investigations are carried out at regular intervals, which is time-consuming and expensive. As a result, the values of the deformation modulus are known only at selected points. In this approach, the results of the study provide an incomplete picture of the changes in the values of the deformation modulus in the railroad axis. To obtain a description of the variation in soil modulus

between these points without additional testing, a geostatistical approach can be used. This is possible if the distribution of values is assumed to be an ergodic stationary process. The classical geostatistical approach imposes random fields on the whole longitudinal profile in such a way that the generated values in the profile are autocorrelated with the empirically obtained values. The overlapped random fields in the profile can be described in general by:

$$z(s) = \mu(s) + e(s), \tag{1}$$

where $\mu(s) \equiv E[z(s)]$ is a mean function that is continuous and defined and $e(s)$ is a random error with zero mean and satisfies the stationarity assumption. A frequently used stationarity hypothesis is weak stationarity, which can be represented as follows:

$$C(s_i - s_j) = \operatorname{cov}[e(s_i), e(s_j)], \tag{2}$$

where C is the covariance function. It can be concluded that the covariance between z-values at any two locations depends only on their mutual position. Another important assumption is intrinsic stationarity. Variograms used to describe it are as follows:

$$2\gamma(s_i - s_j) = \operatorname{var}[e(s_i), e(s_j)], \tag{3}$$

where 2γ denotes the variogram function. The variogram represents the dependence ratio of a feature as a function of distance in the normalised Euclidean space $\|h\|$ for isotropic phenomena or as a function of distance and direction, assuming anisotropy for phenomena in two and more dimensions. The variogram estimator can be described as:

$$2\hat{\gamma}(h) = \frac{1}{N(h)} \sum_{N(h)} \left(z(s_i) - z(s_j)\right)^2, \tag{4}$$

where the formula $N(h)$ denotes the number of all pairs $(z(s_i) - z(s_j))^2$ that are distanced by $\|h\|$. For practical reasons, semivariograms, which are defined as half of the variogram $\gamma(h)$, are quite often used [31]. It is a measure of nonsimilarity between points observed at a given location $z(s_i)$ and $z(s_j)$, as opposed to covariance, which describes similarity. The semivariogram provides information about the spatial continuity and variability of the random function.

In the subgrade quality assessment problem, semivariograms were used to determine the autocorrelation along the rail line created by the testing points. The soil parameters determined at these points were used to create an empirical semivariogram, using the least-squares method and the Gauss–Newton algorithm as a nonlinear fitting method. With these tools, issues related to the influence of local extremes on the results can be avoided. The next step is the selection of a suitable theoretical semivariogram for an accurate spatial prediction of the ground parameters. Cases where the dependence model has a defined semivariogram are relatively rare.

The presented procedure is a standard approach used for several reasons [32], such as to provide a conditional negative specification for a semivariogram, which is necessary for the variance of the prediction error to be non-negative at every point in the space [33]. The most important factor in the selection of the semivariogram model should be convergence to the empirical semivariogram. This can be verified by the reliability function or the least-squares method (LSM). In some cases, other factors such as model flexibility or computational simplicity may be taken into account. The model can be selected from an extensive library of models. The basic parameters of many of the theoretical semivariogram models used are range r—the distance over which the resulting values are flattened; and sill s—the value the semivariogram reaches beyond distance r.

According to theoretical models, if the distance between two points is close to zero then the semivariogram value should be zero. However, sometimes, as the separation distance decreases, the semivariogram values do not approach zero. This phenomenon is called the nugget effect and describes the variability between samples at very small

distances [34]. Whether the phenomenon occurs depends on the measurement error or the spatial variability of the ground at distances smaller than the sampling interval, or both simultaneously. The magnitude of the nugget effect consists of two components: the geological nugget effect (GNE) and the sampling nugget effect (SNE). The most commonly used theoretical semivariogram models and the nugget effect are shown in Table 1.

Table 1. Theoretical models for the semivariogram.

Theoretical Model	Semivariogram	
nugget	$\gamma(h) = \begin{cases} 0 \\ s \end{cases}$	when $h = 0$ when $h > 0$
linear with sill	$\gamma(h) = \begin{cases} \frac{sh}{r} \\ s \end{cases}$	when $h \leq r$ when $h > r$
spherical	$\gamma(h) = \begin{cases} s\left[1.5\frac{h}{r} - \kappa\left(\frac{h}{r}\right)^3\right] \\ s \end{cases}$	when $h \leq r$ when $h > r$
exponential	$\gamma(h) = s\left(1 - e^{\frac{-h}{r}}\right)$	
logarithmic	$\gamma(h) = \begin{cases} \frac{sh}{r} \\ s \end{cases}$	when $h = 0$ when $h > 0$

κ—model constant typical equal 0.5 [·].

In this paper, in order to obtain probable values of stiffness in the railway track axis, a model of spatial variability described by a semivariogram, being a non-negative function and zero mean value, was used. The set of data obtained in this way is a realisation of a one-dimensional random field. Its values are conditioned by points of known stiffness. For the generation of the field, the algorithm of sequential simulation of a Gaussian conditional field in the Euclidean space for an assumed ergodic and isotropic process was applied. In the discussed issue, the generated points were uniformly distributed on the considered line. The sequential algorithm formulated in this manner is very efficient and works correctly for cases in a large scale. The method uses only data and values simulated from the local neighbourhood to approximate the conditional distribution. In this work we have only proposed a certain set of functions representing the relationships most commonly observed in nature and engineering. In situations with more diverse substrate, other functions would be more appropriate. The proposed scheme thus emphasises the method rather than its implementation, avoiding overly rigid rules that limit potential applications.

2.3. Probability of Failure

A random process is a function in a probabilistic space of random $\boldsymbol{X}$ variables. When this set consists of time-dependent realizations, then it is a stochastic process. In this article, a random event is considered as a stationary function $F(\boldsymbol{X})$ with values defined as the set of states of the process. Process states should be understood as defined: $F(\boldsymbol{X}) < 0$ failure or not fulfilling acceptance criteria; $F(\boldsymbol{X}) = 0$ a limit state; and $F(\boldsymbol{X}) > 0$ functioning or fulfilling acceptance criteria. An object, treated as a primary concept in a probabilistic process, can be assigned to:

(a) a category of simple structural elements or structure (e.g., pile, column, retaining wall, anchoring items, elementary subgrade section);
(b) a category of complex objects consisting of simple objects related by mechanical or geometric features.

The probability of failure of a simple object p_f is defined as $p_f = P(F(\boldsymbol{X}) \leq 0)$, whereas reliability is a property of an object that states whether it works correctly (fulfills all assigned functions and actions) under specific service conditions. Probability in most cases has a

small value, so it is more convenient to use a measure of the reliability index I_β. It is defined with respect to probability by the following relationship [21]:

$$p_f = \Phi_0(-I_\beta), \tag{5}$$

where Φ_0 is the cumulative distribution function for a standard normal probability distribution (with mean 0 and standard deviation 1). According to European guidelines [22], the reliability index required for a structure depends both on the expected costs of protection and the consequences of a potential failure (Table 2).

Table 2. Reliability index target value for the lifetime of an object [22].

Relative Cost of Safety Measures	Failure Consequences			
	Small	Some	Moderate	Great
high	0.0	1.5	2.3	3.1
moderate	1.3	2.3	3.1	3.8
low	2.3	3.1	3.8	4.3

Complex objects have a definite structure only if it is possible to determine the reliability of the elements and their dependencies. There are two basic types of such structures: serial and parallel. If a system failure occurs when all its components are damaged, then such a structure is called a parallel. The serial structure means that each failure of the system's components (e.g., simple objects or their sets) is the cause of failure of the whole system. In the presented method this model was used in the basic analysis. If the acceptance criteria are not met for any of the distinguished sections of the subgrade, no acceptance is given for the entire segment under investigation. A threshold variant of the serial system is also presented, where the existence of a number of adjacent elements that do not meet the acceptance criteria together was assumed as a condition for system failure.

To perform reliability considerations, it is necessary to define characteristics such as the potential renewability or reparability of an object. In this paper, only repairable objects were dealt with. Hence, it was possible to build an iterative procedure, and the concept of failure also included nonfulfillment of acceptance criteria. In the strict sense, failure of infrastructure components means a permanent loss of functional or mechanical properties. The processes analysed were also treated as strictly stationary, meaning that their values were not dependent on the position of the reference point on the time axis.

Depending on the available statistical information about the process under study, there are many methods for determining the probability of failure. The methods functioning in design and proposals for future regulation are well-described and classified [35]. Methods can be divided into four levels:

- Level 0—deterministic;
- Level 1—partially probabilistic methods, statistical description of the object by determining safety factors as coefficients modifying the values of loads and capacities;
- Level 2—approximative methods, estimation of the probability of failure by means of safety factors determined from analytical relationships;
- Level 3—fully probabilistic methods, determination of safety factor based on numerical simulations.

The paper focuses on the application of a fully probabilistic approach to determine the probability values of not meeting the required quality criteria. These techniques include the use of a known probability density function of failure, response method methodology (RSM) [36–40], first- and second-order reliability methods (FORM/SORM) [41] and Monte Carlo methods [42,43]. Further, the considerations are based on the crude Monte Carlo method.

Directly assessing the probability of failure is extremely difficult. Many variables are involved, hence direct construction of a CDF with an imposed boundary condition is problematic, especially in the presented case of a track substructure, where each of

the analysed points along the length of the studied section is a random variable and the adopted reliability system is based on the Bayesian concept. We have not applied FORM-type methods in this work due to the uncertainty associated with the transformation of random variable distributions to the standardised space. The ambiguity is due to its nature; it may depend on the ordering of the variables in the random data vector. The consequence of this may be different forms of the boundary surface which are affected by generating different values of failure probability. FORM/SORM methods give good results when there is only one computational point and the boundary function is of class C1/C2 and not strongly nonlinear. The Crude Monte Carlo (CMC) method was used in presented work as the numerical integration to find the solution; despite the high dimensionality of the task, this approach is robust to the unusual shape of the limit function, and is also applicable when its form is unknown in the probability hyperspace. For the points and for the entire cross section, the number of exceedances of the failure condition is examined. This allows us to determine the probability of failure to meet the adopted objective criterion for substructure quality.

2.4. Proposed Scale of Substructure Quality Assessment

The study by Baumgartner [44] was used as a starting point to assign the consequences of damage to a railway route. This compilation of both infrastructure and rolling stock costs, despite many years since publication, is still often adopted as a reference. This is due to its detailed cost assessment for elements covering all aspects of the railway network (rails, trains, tunnels, bridges, stations and maintenance of these elements) for a large area (EU and USA). Table 3 summarises the estimated costs for constructing a complete railway line. Such compilations are important for the railway industry and are often used for cost estimation [45–47].

Table 3. Unit cost of railway lines of different types for selected terrain difficulties (including all cost components) in MEuro/km [44].

Type of Track	Easy Topography	Average Topography	Difficult Topography
single 100 km/h	1–3	3–15	15–40
double 100 km/h	1–4	3–20	20–50
double 300 km/h	2–6	6–30	30–50

Another concept of assigning damage consequences other than cost is one in which the purpose of the route—its category—is the main quantifier. For the purpose of the work, the classification of conventional railway lines used in Poland and related substructure elements has been adopted from [48,49]:

- Trunk lines (K0)—traffic volume of over 25 million Mg/year, passenger-train speeds of <200 km/h and goods-train speeds of <120 km/h;
- Primary lines (K1)—traffic volume of 10–25 million Mg/year, passenger-train speeds of <120 km/h and goods-train speeds of <80 km/h;
- Secondary lines (K2)—traffic volume of 3–10 million Mg/year, passenger-train speeds of <80 km/h and goods-train speeds of <60 km/h;
- Lines of local importance (K3)—trainload of up to 3 million Mg/year, passenger-train speeds of <60 km/h and goods-train speeds of <50 km/h.

This classification is the basis for technical guidelines for designing and constructing railway infrastructure facilities.

It was decided to use a combination of the two criteria presented above: cost according to Baumgartner's scale and categorisation of lines in relation to the reliability index values from Table 2. The reliability index values were assigned to the railway line categories on the basis of an evaluation of the consequences of failure as a supply-chain disruption corresponding only to economic damage. The methodology was based on a matrix of averaged performance costs assigned to the adopted classification of railway roads. In

order to determine the reliability coefficient, a cost vector was used, using a linear scaling of the costs associated with topographical difficulties to the required reliability index. After some corrections to match the results to the European standards, the classification presented in Table 4 was obtained. This is a simplified model, which should be treated as a proposal.

Table 4. Proposed classification of the target reliability index for subgrade, taking into account the classification of the railway lines and the costs (without taking into account the terrain and excluding the high-speed lines).

Relative Cost of Safety Measures	Classification of Railway Lines		
	Secondary (K2) and Local (K3)	Primary (K1)	Trunk (K0)
	<3 MEuro/km	3–15 MEuro/km	>15 MEuro/km
high	1.5	2.3	3.1
moderate	2.3	3.1	3.8
low	3.1	3.8	4.3

A method of implementation of these very general reliability suggestions in the design practice is shown by the algorithm in Figure 2. After determining the section of the substructure to be assessed and identifying of the class of the section according to the adopted classification, the minimal value of the reliability index beta (Table 4) for the substructure is obtained. The iterative procedure starts with the first in situ tests of the substructure performed with a static plate load test. In the next step, geostatistical analysis is carried out to obtain theoretical semivariograms for the elastic properties of subsoil in the section. Using the procedure described previously, a conditional random field is repeatedly generated for points spaced at a certain distance from each other, corresponding to the distance between the railway axes. It is described by a determined geostatistical relation. European or national standards allow the adoption of an objective criterion to disqualify a test point. In the proposed procedure, the minimum value of E_{v1} or E_{v2} is taken as a criterion. For the points and for the whole section, the number of exceedances of the failure condition is tested, e.g., by the Crude Monte Carlo (CMC) method. It allows for the determination of the probability of not fulfilling the adopted objective criterion of the substructure quality. If the reliability index for a point or a section is higher than expected, it means that the execution is correct and further track works can be carried out. Otherwise, improvement works should be carried out in the area where the objective criterion is not met with a given probability. Once the additional tests confirm the quality of the modified subgrade are completed, the calculation procedure shall be repeated. The whole process is continued until approval is obtained at all points specified.

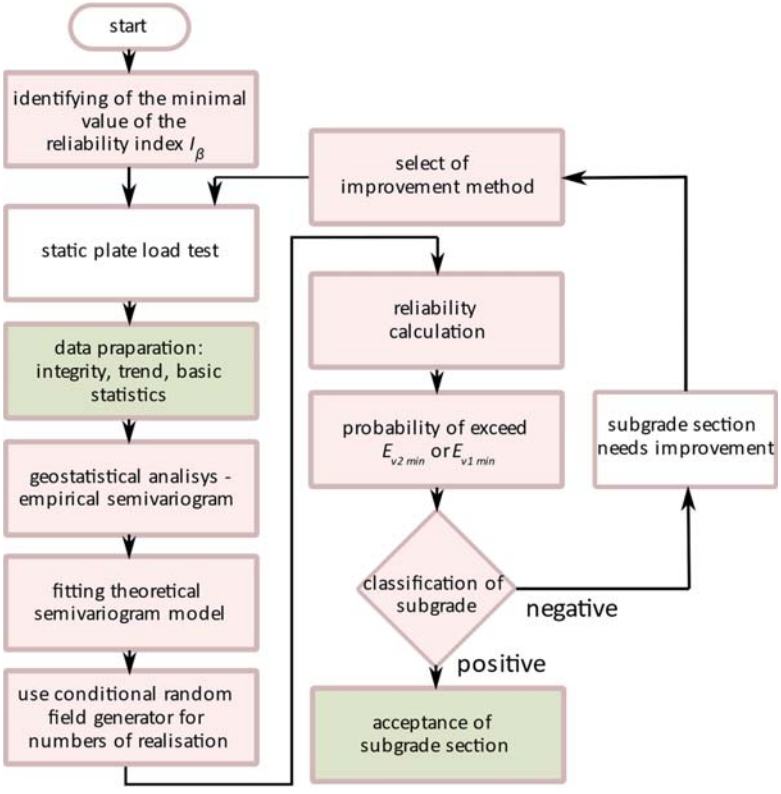

Figure 2. Flow chart of the concept of the subgrade acceptance procedure.

3. Application of the Methodology—Case Study

3.1. Investigated Section and Test Results

The railway route section located in West Pomerania (Poland) was the subject of research and analysis. The field test covered a section of 9100 m in length and was carried out prior to the planned modernisation works. The investigated object was selected for improvement due to its poor technical condition and the planned upgrade of the railway line (from K1 to K0). Most of the route runs on an embankment except for a 2200–2800 m section which is located on a level surface as a low embankment. The route is free of horizontal and vertical curves and terrain obstacles; the whole section has a gradient of less than 1‰ and is located in an area with a homogeneous geological structure. The subsoil was found to be composed of various types of soils characteristic to the North European Plain (Polish Plain) and the embankment structure was made of sandy soil. Such a section was chosen in order to limit the impact of terrain variability and its effect on the results obtained.

A series of static plate load tests were performed on the investigated section according to the Polish guidelines [30]. A total of 183 tests were carried out at 50 m spacing. The results are shown in Figure 3 and Table 5. The values of the E_{v1} modulus range from 28.99 to 125.90 MPa with a mean value of 62.68 MPa and a standard deviation of 14.29 MPa. The values of the E_{v2} modulus range from 48.70 to 196.50 MPa with a mean value of 104.99 MPa and a standard deviation of 22.53 MPa. As can be observed in Figure 3, the vast majority of results are within the ± 1 standard deviation range. In order to better illustrate the results obtained, Figure 4 presents histograms of the values of the modules

E_{v1} and E_{v2} (Figure 3a,c) and their correlation (Figure 3b). In this configuration, the linear correlation between the parameters can be seen, as well as points of particular concern with small values of the moduli. The red point in Figure 4b is the mean value and the red line is a line fitted by the least-squares method. The concentration of points in one group (Figure 4b) results from a strong mutual correlation of the measurements as understood by Pearson. The closer to the line $E_{v1} = E_{v2}$, the greater the degree of correlation. The correlation between E_{v1} and E_{v2} values is significant and equal to 0.92. When the variability of a parameter is high, it is suggested to separate sections which can be approximated by a linear trend.

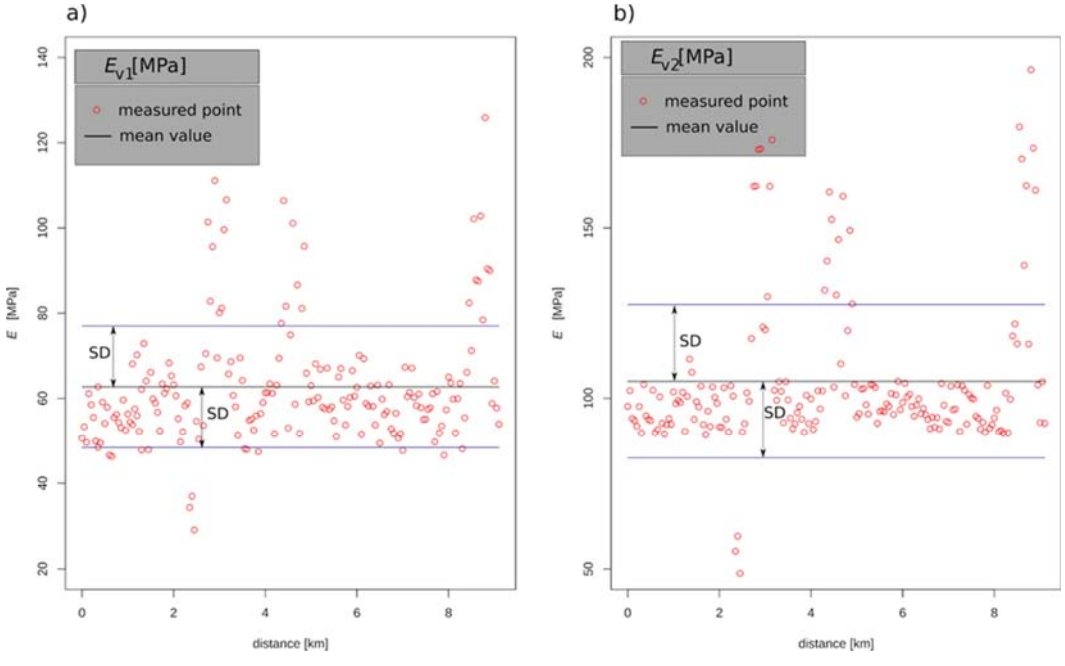

Figure 3. Results of the static load plate test on the selected section: (**a**) E_{v1}; (**b**) E_{v2}.

Table 5. Results of the static load plate test on the selected section.

	Minimum Value	First Quartile	Median	Mean	Third Quartile	Maximum Value	Standard Deviation
E_{v1} [MPa]	28.99	54.35	59.40	62.68	66.10	125.90	14.29
E_{v2} [MPa]	48.70	93.33	98.52	104.99	103.86	196.50	22.53

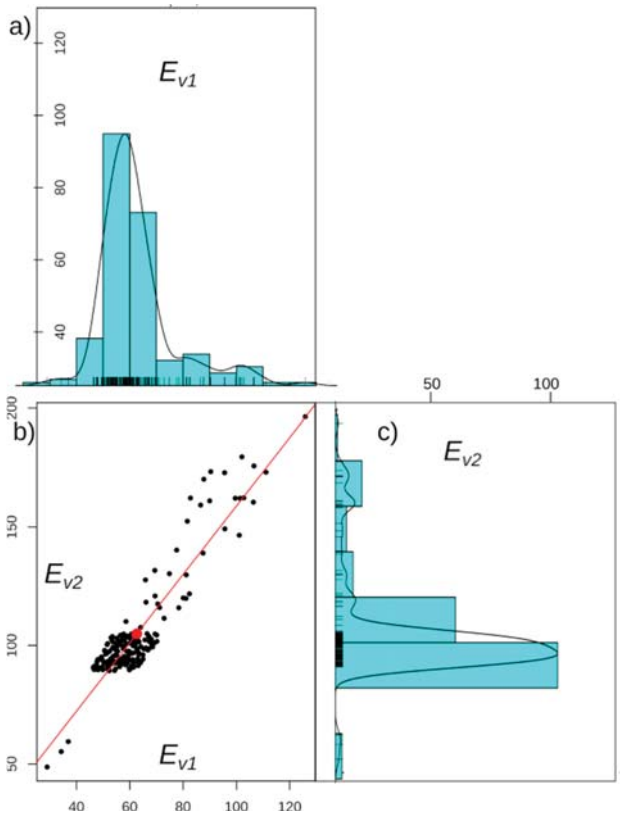

Figure 4. Results of the static load plate test on the selected section: (**a**) histogram of modulus E_{v1} values; (**b**) values of E_{v2} versus E_{v1}; (**c**) histogram of modulus E_{v2} values.

3.2. Semivariograms and Probability of Failure

Based on the results of the field study, empirical and theoretical semivariograms were established according to the procedure described in Section 2.2. Figure 5a,b show semivariograms of stiffness values measured in situ with fitted theoretical models. In the two cases studied, an exponential model [50] from Table 1 combined with a nugget effect was used to describe the variability. The results are presented in Table 6. The geostatistical models reproduce a powered exponential covariance structure with a significant randomness of the measured values, as evidenced by the value of high nugget effects (14–33%).

Table 6. Theoretical semivariograms.

Value	Model	Nugget [MPa^2]	Sill [MPa^2]	Range [km]	Kappa [−]
E_{v1}	exponential	69.403	204.720	0.529	0.5
E_{v2}	exponential	75.254	510.740	0.306	0.5

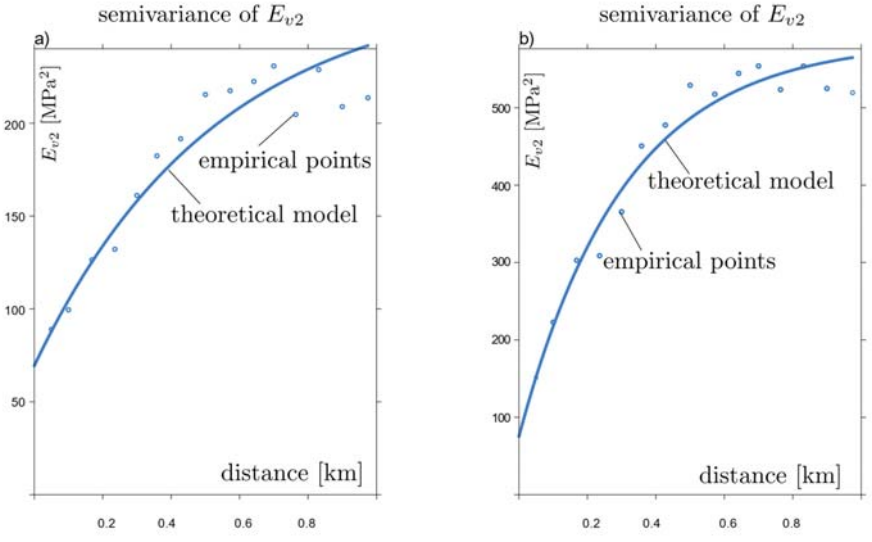

Figure 5. Theoretical and empirical semivariograms: (**a**) for E_{v1}, (**b**) for E_{v2}.

The rail track analyses adopt a load spacing per track at 7.5 m intervals. The examined subgrade was divided into sections, which gives 1215 test points along the track axis. It was assumed to be a serial reliability system, i.e., the existence of a single point or a number of adjacent elements that do not meet the acceptance criteria (expressed in stiffness of the subgrade) is treated as a system failure. The value of E_{v2} was used as an objective criterion. The technical adequacy criterion of the section is expressed by the condition:

$$\{E_{v2}\}_i \geq E_{lim}, \tag{6}$$

where i is a number from 1 to 1215 describing the experimental values of modulus the E_{v2} for the 7.5 m sections. Figure 6a provides a schematic overview of the test points with possible options for not meeting the objective criterion. In the case when at two (Figure 6b), three (Figure 6c) or more subsequent points the condition Equation (6) is not fulfilled, the mechanical condition of the track–structure–substructure system poses a higher risk of stability. These cases, labelled as Mode(7.5), Mode(15) and Mode(22.5) and so on, can be treated as independent events in the reliability system sense.

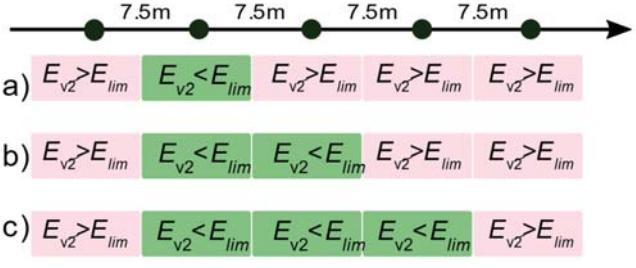

Figure 6. Diagram of reliability test points (7.5 m sections) and possible variants of non-achievement of criterion: (**a**) single point—7.5 m—Mode(7.5); (**b**) two adjacent points—15.0 m—Mode(15), (**c**) three adjacent points—22.5 m—Mode(22.5).

According to the established theoretical semivariogram for the investigated points of the subgrade (E_{v2}), describing the variability of the phenomenon, draws of possible values of E_{v2} between the points were performed, maintaining the values measured in the field. The obtained set of drawn and measured values is denoted as $\{E'_{v2}\}$ and the failure condition Equation (6) can now be represented as:

$$\left\{E'_{v2}\right\}_i \geq E_{lim}. \tag{7}$$

The results of the sample draws are shown in Figure 7. The red circles correspond to the measured values. The black, brown and grey points represent successive realisations of the random process conditioned by the measured values of E_{v2}. For the studied section 10^7 draws were executed. Due to the very large number of points for the set of stiffness distributions, the results are presented as a histogram (Figure 8). The statistical description is presented in Table 7. A log-normal probability distribution with parameters $m = 4.61899$ and $s = 0.2080448$ was fitted to the histogram using the maximum-likelihood method. The log-normal cumulative distribution function with the determined parameters is the basis for further calculations of the failure probability.

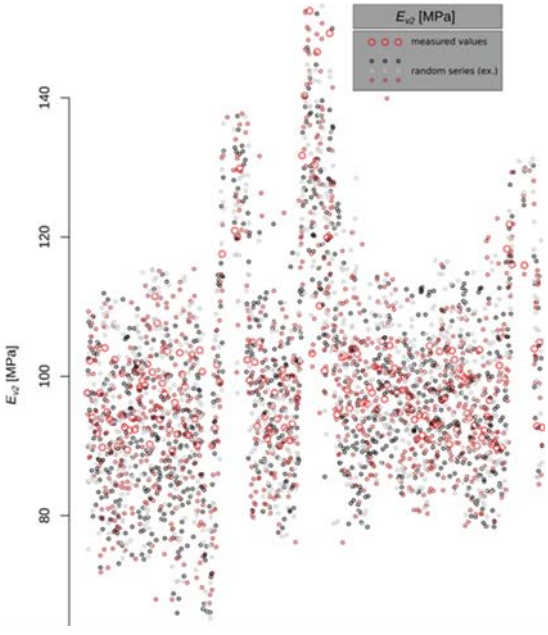

Figure 7. Example of the result of 3 draws of values of E_{v2}.

Table 7. Statistical description of the draws of values E_{v2}.

Draws Number	Mean	Standard Deviation	First Quartile	Third Quartile	Minimum Value	Maximum Value
1215000	103.6	22.37	89.26	112.01	21.98	214.28

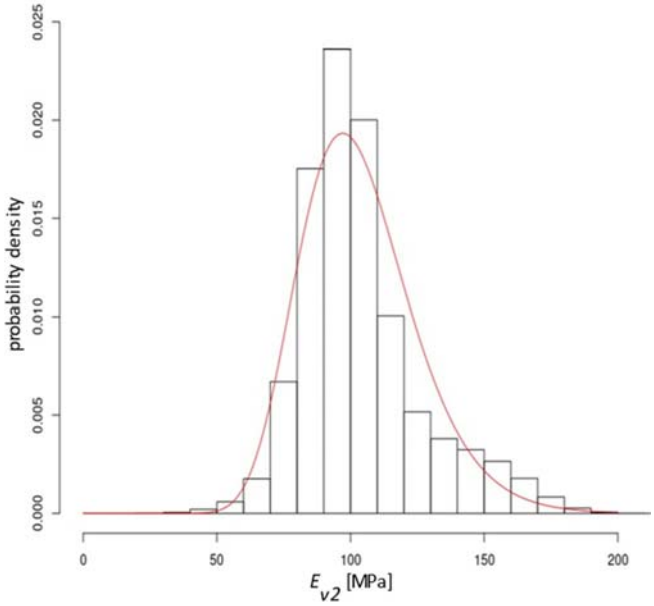

Figure 8. Histogram from a set of E_{v2} draw results together with the fitted log-normal probability density distribution.

3.3. Substructure Quality Assessment

For the railroad under investigation, a quality assessment was carried out prior to the planned modernisation according to the procedure outlined above. With the assumed value of E_{lim}, the reliability index I_β of the substructure was determined directly from Equation (5). The results are shown in Figure 9, where the dependence of the reliability index on the adopted boundary condition E_{2lim} is indicated. Horizontal lines represent the safety levels of the reliability index. This figure also illustrates the effect of the technique of uniform improvement of the whole section on the value of the reliability index. The following lines correspond to curves for levels of subgrade improvements from 120% to 200% of the initial value, respectively. Assuming an E_{lim} value of 60 Mpa, the reliability index of the existing subgrade is 2.52. For a planned K0-class line, this value is insufficient. In order to obtain an index value of 3.1, the stiffness of the subsoil must be increased proportionally by 15% of its initial value. An index of 3.8 requires the stiffness of the subgrade to be increased proportionally by 30% and an index of 4.3 requires a 40% increase. If a boundary modulus of 70 MPa is required, the reliability index of the existing substrate decreases to 1.80. In order to obtain reliability index values of 3.1, 3.8 and 4.3, the stiffness of the substrate must be increased proportionally by 30%, 50% and 70%. However, the strategy of strengthening the whole section is rarely applied and not very effective. In practice, the methods of improving selected fragments of the route section are more frequent.

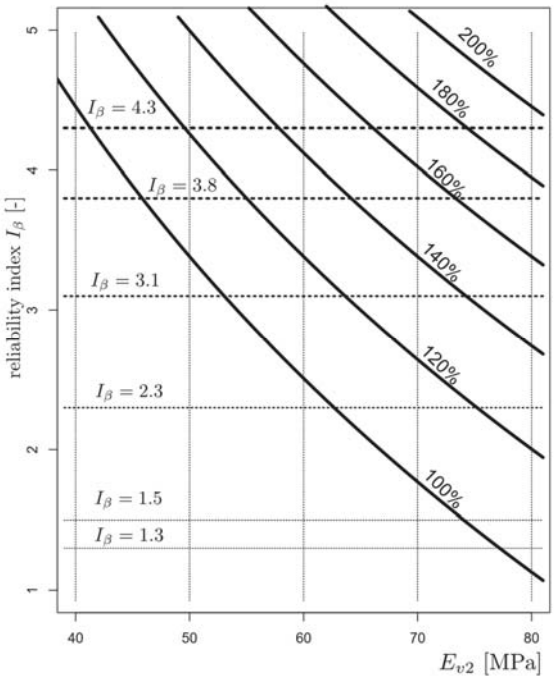

Figure 9. The value of the reliability index I_β as a function of the expected value of the modulus E_{lim} with respect to the level of improvement; curve 100%—present subgrade; 120%; 140%; 160%; 180%; and 200% of E_{v2}.

In addition to meeting the global reliability condition, it is also necessary to meet it locally. For the assumed upgraded line, point-by-point reliability analyses were carried out for the assumed 7.5 m section spacing with different E_{lim} values, i.e., 60, 65, 70 and 75 Mpa. Figure 10 presents the calculated reliability index values for the whole line section, i.e., 0–9100 m. On this basis, sections requiring reinforcement may be identified. In this case, a significant weakening of the substrate was found at 2000–2800 m, which is shown in Figure 11. Maintaining the line at K1 level with a required I_β of 2.3 and a boundary modulus of 60 MPa requires additional improvement works on section 2350–2500 despite the global reliability index of the line being 2.52. To upgrade the line to K0 with an I_β of 3.1, improvement is required on section 2300–2550. After the modification of the section indicated, the reliability of the examined section should be reassessed. The presented methodology can significantly influence the economics and rationality of the subgrade improvement, i.e., reduce costs and implementation time by limiting works to selected sections that do not meet the adopted reliability criterion. For the assumed value of E_{lim} and I_β, modification of the subsoil is required for a certain section. In the case of a deterministic approach, improvement is necessary for all sections where the required value was not obtained. The method also enables numerical simulations of the expected results of the improvement depending on the applied approach, i.e., proportional increase in stiffness for the whole examined section or improvement of only the fragments indicated in the condition discrepancy report. The prognosis may already be performed at the research stage, guaranteeing the appropriate level of safety of the structure, adjusted to the tasks assigned or the costs incurred for its execution. Depending on the analysis results obtained, the appropriate improvement technology should be selected. It is worth noting that the value of the reliability index I_β cannot be verified by field experiments. In order to validate

the method, verification should be carried out on the values of the deformation modulus obtained from the probabilistic method.

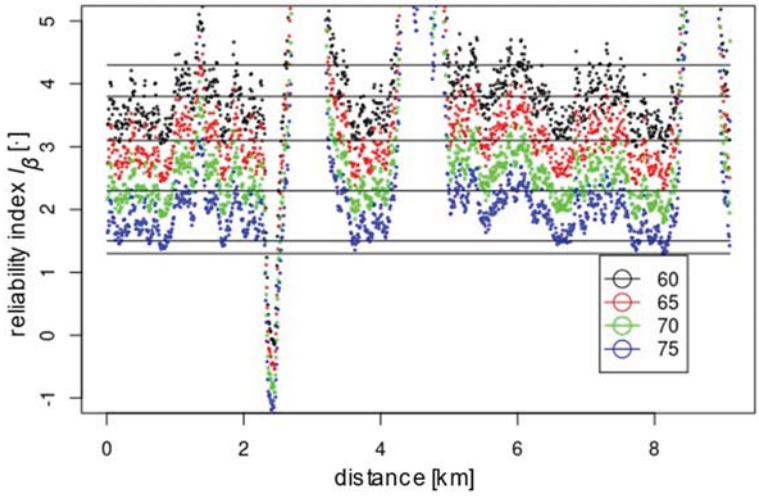

Figure 10. The calculated values of the reliability index I_β for the full length of the investigated line for the modulus E_{lim} = 60, 65, 70 and 75 MPa.

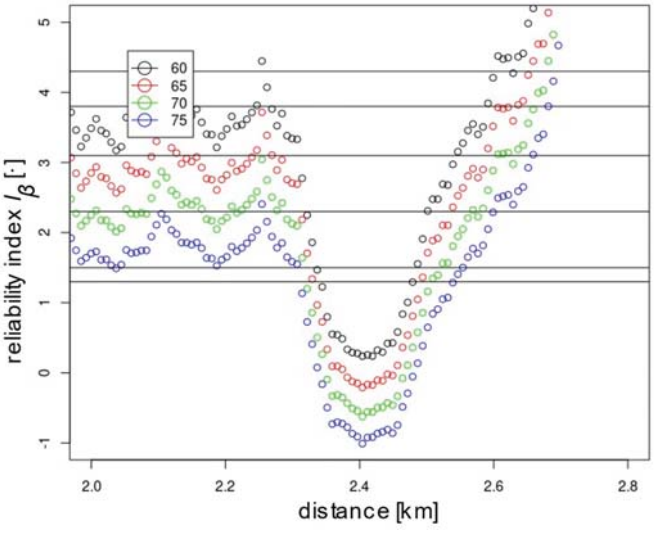

Figure 11. The calculated values of the reliability index I_β for the 2.0–2.8 km section of the investigated line for the modulus E_{lim} = 60, 65, 70 and 75 MPa.

By analysing the location of the points representing the values of the deformation modules in Figures 3 and 7 and the reliability index in Figure 10, it can be seen that they have a similar distribution. This characteristic dependence results from the applied geostatistical method. The drawn values of the deformation modulus (Figure 7) are autocorrelated with the experimental values obtained by the static plate load test (Figure 3). It is especially visible in places where local extremes occur. Due to this, the values obtained by drawing are a very reliable reflection of the actual values of the deformation modules. Figure 10

shows the values of the reliability index I_β, which were calculated on the basis of data from Figure 7, hence the similarity of the distribution of points between these figures.

4. Conclusions

The paper presents the concept of objective and effective assessment of the condition of the railway track substructure with an example of application to a real example of a route under modernisation.

In the study, the railway track was treated as a reliability system based on the summation of probabilities of occurrence of modes. According to the results of static load plate tests, a spatial variation model is applied, with the use of semivariograms, to describe the ground stiffness dependencies. The possible values of the moduli between experimental points were described using a Gaussian random field conditioned by variogram. Calculations were performed using the Crude Monte Carlo method. This led to the determination of the reliability index of the substructure. In the example of the modernised railway line, the results of the applied method are presented for the given conditions (boundary model of the substructure E_{v2} and reliability index I_β). The analysis was carried out with a view to both an overall uniform improvement of the line substructure and a search for problematic sections. The existence of a section that requires improvement was identified. Results are presented in relation to the input parameters adopted. In the example, the change in the extent of works does not differ significantly from the deterministic approach due to the choice of section. In the case of a more complex line structure, the results would be more conclusive, but the purpose of the paper was to show the algorithm's functioning and to determine the necessary improvement conditions and their influence on the quality of the section.

An important distinguishing feature of the method is the estimated value of the reliability index, which unifies the design and construction process in accordance with standards. The scale based on the reliability index is compliant with the standard provisions of the Eurocode and at the same time can be scaled to the limit values of physical quantities defined in national standards. The reliability-based design has been implemented in many areas of geotechnical engineering, but in rail transport the process is progressing unevenly and is not yet strongly supported by standards documents and industry recommendation. The postulated safety levels for railway lines are the beginning of the discussion and classification. It is proposed that they should be selected or modified to correspond to regional (national) cost and risk structures. Setting them at a uniformly high level may block the development of railways, especially in less-developed countries.

The reliability approach provides clear criteria for determining the quality of railway subgrade. The presented method allows one to reduce the number of measurements, speed up the control process, determine the required scope of repair works and support the selection of the most effective improvement methods through successive simulations of possible scenarios.

An additional advantage of the approach is the use of open tools for building geostatistical models and random sampling without licence restrictions (R, Random Fields, GStat). However, in the case of very high variability of the substrate, this method may give inaccurate results and require additional tests. The presented concept is operating only on the serviceability limit-state function. The introduction of the subgrade–rail interaction, in which it will be possible to analyse ultimate limit states, is a desired direction of further development of the technique.

Author Contributions: Conceptualisation, J.V.K. and I.G.; methodology, J.V.K., P.W. and I.G.; software, J.V.K.; validation, J.V.K., P.W., I.G. and M.T.; formal analysis, J.V.K. and P.W.; investigation, J.V.K. and P.W.; resources, I.G.; data curation, J.V.K., P.W., I.G. and M.T.; writing—original draft preparation, J.V.K., P.W., I.G. and M.T.; writing—review and editing, J.V.K., P.W., I.G. and M.T.; visualisation, J.V.K. and P.W.; supervision, J.V.K.; project administration, J.V.K.; funding acquisition, J.V.K., I.G. and M.T.. All authors have read and agreed to the published version of the manuscript.

Funding: This research received no external funding.

Institutional Review Board Statement: Not applicable.

Informed Consent Statement: Not applicable.

Data Availability Statement: Data available on request due to restrictions, e.g., privacy or ethical.

Conflicts of Interest: The authors declare no conflict of interest.

References

1. Gu, H.; Liu, K. Influence of Soil Heterogeneity on the Contact Problems in Geotechnical Engineering. *Appl. Sci.* **2021**, *11*, 4240. [CrossRef]
2. Zhao, L.; Huang, Y.; Xiong, M.; Ye, G. Reliability and Risk Assessment for Rainfall-Induced Slope Failure in Spatially Variable Soils. *Geomech. Eng.* **2020**, *22*, 207–217. [CrossRef]
3. Capacity for Rail (C4R). *Design Requirements and Improved Guidelines for Design (Track Loading, Resilience & Rams). Towards an Affordable, Resilient, Innovative and High-Capacity European Railway System for 2030/2050*; European Union's Seventh Framework Program for Research, Technological Development and Demonstration: Cemosa, Spain, 2014.
4. Sussmann, T.; Hyslip, J. Track Substructure Design Methodology and Data. *Proc. ASME Jt. Rail Conf. 2010 JRC2010* **2010**, *1*, 369–376. [CrossRef]
5. He, M.S.; Li, L.; Nie, Z.H. Analysis of Compaction Standards Used in High-Speed Railway Subgrade. *J. Railw. Sci. Eng.* **2009**, *6*, 27–32.
6. Siewczyński, L.; Pawłowski, M. Oddziaływanie płyt próbnych na podtorze. *Zesz. Nauk.-Tech. Stowarzyszenia Inż. Tech. Komun. W Krakowie Ser. Mater. Konf.* **2011**, *25*, 499–509.
7. Wasiutyński, A. *Drogi Żelazne: Powstanie i Organizacja Dróg Żelaznych: Tabor i Technika Ruchu Kolejowego: Projektowanie Drogi Żelaznej: Budowa Spodnia i Wierzchnia: Połączenia Taborów: Stacje: Sygnalizacja i Urządzenia Bezpieczeństwa*; Wydawnictwa Naukowe Komisji Wydawniczej T-wa Bratniej Pomocy Studentów Politechniki Warszawskiej: Warsaw, Poland, 1925.
8. Wątorek, K. *Budowa Kolei Żelaznych*; Instytut Wydawniczy "Bibljoteka Polska": Warsaw, Poland, 1924.
9. Nowkuński, J. *Budowa, Stateczność i Trwałość Podtorza Kolejowego*; Wydawnictwo Techniczne Ministerstwa Komunikacji: Warsaw, Poland, 1948.
10. Sysak, J. *Odwodnienie Podtorza*; Wydawnictwo Politechniki Poznańskiej: Poznań, Poland, 1975.
11. Skrzyński, E. *Podtorze Kolejowe*; Kolejowa Oficyna Wydawnicza: Warsaw, Poland, 2010.
12. Popp, K.; Schiehlen, W. *System Dynamics and Long-Term Behaviour of Railway Vehicles, Track and Subgrade*; Lecture Notes in Applied and Computational Mechanics; Springer: Berlin/Heidelberg, Germany, 2003; ISBN 978-3-540-43892-2.
13. Indraratna, B.; Salim, W.; Rujikiatkamjorn, C. *Advanced Rail Geotechnology-Ballasted Track*; CRC Press: Boca Raton, FL, USA, 2011.
14. Li, D.; Hyslip, J.; Sussmann, T.; Chrismer, S. *Railway Geotechnics*; CRC Press: London, UK, 2015.
15. Correia, A.G.; Momoya, Y.; Tatsuoka, F. *Design and Construction of Pavements and Rail Tracks: Geotechnical Aspects and Processed Materials*; CRC Press: Boca Raton, FL, USA, 2007; ISBN 978-0-203-93754-9.
16. Grulkowski, S.; Kędra, Z.; Koc, W.; Nowakowski, M.J. *Drogi Szynowe*; Wydawnictwo Politechniki Gdańskiej: Gdańsk, Poland, 2013; ISBN 978-83-7348-511-2.
17. Ditlevsen, O.; Madsen, H.O. *Structural Reliability Methods*; Wiley: New York, NY, USA, 1996; Volume 178.
18. Taflanidis, A.A.; Cheung, S.-H. Stochastic Sampling Using Moving Least Squares Response Surface Approximations. *Probabilistic Eng. Mech.* **2012**, *28*, 216–224. [CrossRef]
19. Gaspar, B.; Teixeira, A.P.; Soares, C.G. Assessment of the Efficiency of Kriging Surrogate Models for Structural Reliability Analysis. *Probabilistic Eng. Mech.* **2014**, *37*, 24–34. [CrossRef]
20. Kozubal, J.; Wyjadłowski, M.; Steshenko, D. Probabilistic Analysis of a Concrete Column in an Aggressive Soil Environment. *PLoS ONE* **2019**, *14*, e0212902. [CrossRef]
21. *EN 1990*; Eurocode–Basis of Structural Design. Comité Européen de Normalisation: Brussels, Belgium, 2002.
22. *ISO 2394*; General Principles on Reliability for Structures. General Principles on Reliability for Structures: Geneva, Switzerland, 2015.
23. Jaksa, M.; Yeong, K.; Wong, K.; Lee, S. *Horizontal Spatial Variability of Elastic Modulus in Sand from the Dilatometer*; Centre for Continuing Education, University of Auckland: Auckland, New Zealand, 2004.
24. Ozturk, C.A.; Simdi, E. Geostatistical Investigation of Geotechnical and Constructional Properties in Kadikoy–Kartal Subway, Turkey. *Tunn. Undergr. Space Technol.* **2014**, *41*, 35–45. [CrossRef]
25. Wu, M.; Cai, G.; Wang, C.; Liu, S. Mapping Constrained Modulus Differences in a Highway Widening Project Based on CPTU Data and Two-Dimensional Anisotropic Geostatistics. *Transp. Geotech.* **2022**, *32*, 100686. [CrossRef]
26. Li, S.; Ye, Y.; Tang, L.; Cai, D.; Tian, S.; Ling, X. Experimental Study on the Compaction Characteristics and Evaluation Method of Coarse-Grained Materials for Subgrade. *Materials* **2021**, *14*, 6972. [CrossRef] [PubMed]
27. *DIN 18134*; Soil—Testing Procedures and Testing Equipment—Plate Load Test. DIN Deutsches Institut für Normung e.V: Berlin, Germany, 2012.
28. *BN-77/8931-12*; Oznaczanie Wskaźnika Zagęszczenia Gruntu. Wydawnictwa Normalizacyjne: Warsaw, Poland, 1983.

29. *PN-S-02205*; Drogi Samochodowe. Roboty Ziemne. Wymagania i Badania. POLSKI KOMITET NORMALIZACYJNY: Warsaw, Poland, 1998.
30. *Id-3*; Warunki Techniczne Utrzymania Podtorza Kolejowego. PKP Polskie Linie Kolejowe S.A. Centrala Biuro Dróg Kolejowych: Warsaw, Poland, 2009.
31. Matheron, G. Principles of Geostatistics. *Econ. Geol.* **1963**, *58*, 1246–1266. [CrossRef]
32. Gelfand, A.E.; Diggle, P.; Guttorp, P.; Fuentes, M. *Handbook of Spatial Statistics*; CRC Press: Boca Raton, FL, USA, 2010.
33. Wackernagel, H. *Multivariate Geostatistics: An Introduction with Applications*; Springer Science & Business Media: Berlin/Heidelberg, Germany, 2003.
34. Dominy, S.C.; Platten, I.M.; Raine, M.D. Grade and Geological Continuity in High-Nugget Effect Gold–Quartz Reefs: Implications for Resource Estimation and Reporting. *Appl. Earth Sci.* **2003**, *112*, 239–259. [CrossRef]
35. Fenton, G.A.; Griffiths, D.V. *Risk Assessment in Geotechnical Engineering*; John Wiley & Sons: New York, NY, USA, 2008; Volume 461.
36. Bauer, J.; Kozubal, J.; Puła, W.; Wyjadłowski, M. Application of HDMR Method to Reliability Assessment of a Single Pile Subjected to Lateral Load. *Stud. Geotech. Mech.* **2012**, *34*, 37–51. [CrossRef]
37. Kozubal, J.; Puła, W.; Wyjadłowski, M.; Bauer, J. Influence of Varying Soil Properties on Evaluation of Pile Reliability under Lateral Loads. *J. Civ. Eng. Manag.* **2013**, *19*, 272–284. [CrossRef]
38. Bucher, C.G.; Bourgund, U. A Fast and Efficient Response Surface Approach for Structural Reliability Problems. *Struct. Saf.* **1990**, *7*, 57–66. [CrossRef]
39. Tandjiria, V.; Teh, C.I.; Low, B.K. Reliability Analysis of Laterally Loaded Piles Using Response Surface Methods. *Struct. Saf.* **2000**, *22*, 335–355. [CrossRef]
40. Faravelli, L. Response-Surface Approach for Reliability Analysis. *J. Eng. Mech.* **1989**, *115*, 2763–2781. [CrossRef]
41. Arangio, S. Reliability Based Approach for Structural Design and Assessment: Performance Criteria and Indicators in Current European Codes and Guidelines. *Int. J. Lifecycle Perform. Eng.* **2012**, *1*, 64–91. [CrossRef]
42. Kozubal, J.; Tomanovic, Z.; Zivaljevic, S. The Soft Rock Socketed Monopile with Creep Effects—A Reliability Approach Based on Wavelet Neural Networks. *Arch. Min. Sci.* **2016**, *61*, 571–585. [CrossRef]
43. Ching, J. Practical Monte Carlo Based Reliability Analysis and Design Methods for Geotechnical Problems. In *Applications of Monte Carlo Method in Science and Engineering*; Mordechai, S., Ed.; InTech: London, UK, 2011; ISBN 978-953-307-691-1.
44. Baumgartner, J.P. *Prices and Costs in the Railway Sector*; Institut des Transports et de Planification: Lausanne, Switzerland, 2001.
45. Olsson, N.O.E.; Økland, A.; Halvorsen, S.B. Consequences of Differences in Cost-Benefit Methodology in Railway Infrastructure Appraisal—A Comparison between Selected Countries. *Transp. Policy* **2012**, *22*, 29–35. [CrossRef]
46. Ott, A. Comparable Cost Calculation for Infrastructure of Road and Rail. In Proceedings of the Conference on Applied Infrastructure Research (InfraDay), Berlin, Germany, October 2001.
47. *Assessment of Unit Costs (Standard Prices) of Rail Projects (CAPital EXpenditure) Final Report*; Publications Office of the European Union: Luxembourg, 2018; ISBN 978-92-79-91813-1.
48. Szajer, R. *Drogi Kolejowe*; Wydawnictwa Komunikacji i Łączności: Warsaw, Poland, 1977.
49. *Journal of Laws 1998, No. 151 Item 987*; As Amended Ordinance of the Minister of Transport and Maritime Economy of 10 September 1998 on the Technical Conditions to Be Met by Railway Structures and Their Placement. Minister of Transport and Maritime Economy: Warsaw, Poland, 1998.
50. Banerjee, S.; Carlin, B.P.; Gelfand, A.E.; Banerjee, S. *Hierarchical Modeling and Analysis for Spatial Data*; Chapman and Hall/CRC: Boca Raton, FL, USA, 2003; ISBN 978-0-429-20523-1.

materials

MDPI

Article

Factors Influencing the Load-Bearing Capacity of Rock as Base Material for Post-Installed Anchors

Stefan Lamplmair [1], Oliver Zeman [2,*] and Klaus Voit [1]

[1] Institute of Applied Geology, Department of Civil Engineering and Natural Hazards, University of Natural Resources and Life Science (BOKU), 1190 Vienna, Austria; Stefan.Lamplmair@gmx.at (S.L.); klaus.voit@boku.ac.at (K.V.)
[2] Institute of Structural Engineering, Department of Civil Engineering and Natural Hazards, University of Natural Resources and Life Science (BOKU), 1190 Vienna, Austria
* Correspondence: oliver.zeman@boku.ac.at

Abstract: In the case of fastenings on rock, as a result of the variability, it is quite difficult to make a preliminary assessment of the load-bearing capacity of rock as a base material. This paper therefore investigates which rock parameters next to an anchor position have an influence on the load-bearing capacity. For this purpose, tests are carried out on post-installed anchors in different lithologies in eastern Austria. It can be shown that the joint weathering has an influence on the load-bearing capacity of post-installed anchors and conclusions can be made about joint weathering by means of rebound hammer. Rebound values can therefore also be used to draw conclusions about the rock quality as a base material for post-installed anchors. Nevertheless, a combined optical assessment of the base material is recommended as an adequate method.

Keywords: base material; rock; post-installed anchors; adhesive anchor; mechanical anchor; load-bearing capacity; GSI; RMR; rebound value; rebound hammer

Citation: Lamplmair, S.; Zeman, O.; Voit, K. Factors Influencing the Load-Bearing Capacity of Rock as Base Material for Post-Installed Anchors. *Materials* **2021**, *14*, 5130. https://doi.org/10.3390/ma14185130

Academic Editor: Krzysztof Schabowicz

Received: 17 July 2021
Accepted: 2 September 2021
Published: 7 September 2021

1. Introduction

Concrete and masonry as base materials for post installed anchors are well considered by different regulations [1,2]. For concrete, in [3], the load-bearing behaviour was investigated and transferred into a design concept. The load-bearing behaviour and the design of bonded anchors were investigated by means of numerical investigations in [4]. More detailed numerical investigations of bonded anchors were carried out in [5]. Therefore, for engineers drawing conclusions about the load-bearing behaviour and capacity in advance, the base material is predefined and well known. In contrary, intact rock (e.g., rock slopes or walls) as a base material is not considered by regulations, not least because of the numerous possible variations of the rock properties. A large number of different installation parameters, such as existing joints, joint condition, uniaxial compressive strength, or weathering degree, induce uncertainty regarding the rock quality. In other words, due to the inhomogeneity of rock, these varying factors lead to insufficient information about the behaviour of post-installed anchors. Therefore, a number of experimental investigations concerning the load-bearing behaviour and capacity of post-installed anchors in rock have been performed in [6–8]. Contrafatto and Cosenza [6,7] were able to investigate the behaviour of chemical anchors in different rock types in the laboratory [6] and to test the applicability of concrete prediction models for natural stone [7]. For this purpose, anchors were installed in blocks of different rock types in the laboratory and tested until failure. Three embedment depths were selected depending on the anchor diameter. The aim was to define the minimum embedment depth at which steel failure occurs, since this can be determined by calculation. Subsequently, theoretical models for determining the load-bearing capacity in concrete were checked for their applicability to natural stone. According to Contrafatto and Cosenza [6,7], the applicability is only given if the mechanical rock characteristics are similar to those of concrete.

Tóth et al. [8] were able to identify the compressive strength, flexural strength and porosity as the main influencing factors, although the rocks investigated in [8] appeared to be relatively homogeneous rock types. It should be noted that the investigations in [6–8] were carried out in a laboratory environment using prepared blocks containing few joints. Hence, it must be assumed that the rock properties are more homogeneous than in a non-laboratory environment. Therefore, the investigations in [6–8] are considered to be relevant for natural stone masonry. To further consider inhomogeneous characteristics in intact rock, in [9], the authors examined different geologies in Eastern Austria in a non-laboratory environment to gain experience when considering the load-bearing capacity of anchors. From this contribution [9], the following main conclusions can be drawn:

- the suitability of rock as base material for post-installed anchors can be assessed by rock classification systems;
- for assessing the load-bearing capacity, a small-scale investigation in the area of the intended fastening area is necessary;
- the presence of joints as well as their condition, such as weathering, influences the load-bearing capacity;
- in the case of poor rock quality, merely base material failure could be observed rather than failure of the anchor;
- in terms of good rock properties, which means fewer inhomogeneities, a variety of failure mechanisms have been found;
- it can also be derived that the load-bearing behavior is influenced mainly by rock properties, rather than the anchoring system;
- disturbed fastening areas (influenced by joints) show analogies to cracked concrete, while undisturbed ones (no influence by joints) behave comparable to non-cracked concrete;
- similarities between the failure mechanisms of rock and concrete were observed.

The conclusions from [9] did not consider further investigations of rock properties in the immediate vicinity of the anchor position and this remains as an open question. Also rock compressive strength and joint condition are expected to have an influence on the load-bearing capacity.

Therefore, this article examines the following research questions for intact rock including inhomogeneities: (i) Which small scale influencing parameters (e.g., rock compressive strength, joint quantity, joint weathering) have an impact on the load-bearing capacity of post installed anchors? (ii) Is it possible to find a method to determine areas with good rock quality for post installed anchors in advance? For this purpose, experiments on post-installed anchors in rock for small embedment depths were performed. In parallel, the mechanical rock properties were investigated in detail to determine the correlation between the load-bearing capacity and the mechanical rock properties. These experiments were performed in different geologies in Eastern Austria, focusing on small-scale rock parameters, like point load index, rebound values, compressive strength, and joint properties.

2. Materials and Methods

2.1. Test Program

The conducted test campaign is listed in Table 1 and considers different testing parameters. The test program has already been used to investigate how post-installed anchors with low embedment depths behave in rock and which rock parameters have a significant influence on the load-bearing behaviour and capacity [9]. In addition to the previous evaluations in [9], this paper shows how small-scale investigations can be used for an a priori estimation of the anchor behaviour. As Table 1 indicates, the test program is divided in geological investigations for rock classification of the different geologies and small-scale investigations of the rock in the immediate vicinity of the anchor position. In total, 100 pull-out tests were performed in different geologies in Eastern Austria. Of these, 55 tests were conducted in disturbed (influence by joint given) and 45 were conducted in undisturbed (no influence by joints expected) base material. Injectable adhesive anchors as well as mechanical bolt anchors with an effective embedment depth of 70 mm and a rod

diameter M12 were used. Small-scale investigations carried out next to the anchor position are listed in the last row of Table 1. Pull-out tests were carried out using a hydraulic handpump without displacement measuring, as shown in Figure 1. In order to include the load bearing behavior of the rock, a wide support bridge was used.

Table 1. Overview of the conducted test program.

	Granulite	**Dolomitic Limestone**	**Dolomite**	**Granite**
Location	west of Vienna, Austria	east of Vienna, Austria	southwest of Vienna, Austria	northwest of Vienna, Austria
Geology, description of base material	metamorphic	sedimentary	sedimentary	metamorphic
	narrowly fractured, fine- to medium-grained components	tectonically strongly utilized, crystallized joints filled with calcite layers	tectonically strongly utilized, narrow joint distance (centimeters to meters), joints filled with sand and clay	tectonically utilized, medium-grained metagranite
	[10]	[11,12]	[13,14]	[15,16]
Geological tests performed per location: point load test, rebound hammer, compressive strength (cylinder), Geological Strength Index (GSI), Rock Mass Rating (RMR)				
		Number of test anchors (h_{ef} = 70 mm, optically evaluated)		
Disturbed area	15	15	10 [(2)]	15 [(2)]
Undisturbed area	15	15	- [(1)]	15
Assessments per installation point: rebound hammer, failure load (F_u), failure mode, joint condition (weathering), joint quantity				

[(1)] due to rock properties not possible as no undisturbed areas have been observed; [(2)] two times setting failure occurred.

Figure 1. Test setup with hydraulic handpump, wide load bridge and scanline.

2.2. Examined Geology

Geological characterization was performed on the geologies described in Table 1 and is described in detail in Section 2.2.1.

2.2.1. Engineering Assessment of Examined Geology

In order to understand the load-bearing behavior and capacity of post-installed anchors in rock the experimental campaign as listed in Table 1 was performed. For rock mass classification (rock mass quality) scanlines were carried out (see upper part of Figure 1).

Scanlines are performed by determining joint location, quantity, condition and orientation whereby the rock structure is recorded in detail. These data are subsequently used as input parameters for the rock mass rating (RMR) according to [17] and the geological strength index (GSI) according to [18]. The RMR represents a rock mass classification system, in which rock strength, joint distances and conditions, in addition to water influence are included as parameters. The GSI serves as a rock classification system based on a visual survey, in which rock structure and surface conditions are assessed. Considering this, deformability and rock strength can be estimated. Scanlines and the resulting rock mass classifications RMR and GSI allow a comparison between different rock types. Scanlines were performed also to record the joint structure (joint frequency, roughness, etc.). The uniaxial compressive strength (UCS) was estimated indirectly by a rebound hammer "Schmidt hammer" (Type N) according to [19] and the point load index according to [20]. Furthermore, the uniaxial cylindrical compressive strength was also determined on diamond drilled cores from the specific study area. In Table 2, the results from the above described testing program are listed. These are reflected in the rock mass quality, which represents the potential of the rock being used for fastenings [9]. In other words, it represents the best-case load-bearing capacity of the base material. Taking into account the findings from [6], it remains uncertain which small scale rock parameters are influencing the load-bearing capacity of post installed anchors. In order to improve the understanding of these parameters, small-scale investigations of rock parameters next to the anchor position were also performed.

Table 2. Overview–geological assessment.

	UCS	UCS	Uniaxial	Geological	Rock Mass
Rock Type	**Point Load Index (N/mm^2)**	**Schmidt Hammer (N/mm^2)**	**Cylindrical Compressive Strength (N/mm^2)**	**Strength Index in acc. to [18]**	**Rating in acc. to [19]**
Granulite	93.5	59.0	120.1 ($\bar{x}$, n = 3)	52–58	76.8
Dolomitic limestone	82.8	61.0	57.5 ($\bar{x}$, n = 2)	42–47	82.6
Dolomite	38.4	13.0	28.5 (from test report)	25–29	54.0
Granite	103.7	58.7	78.7 ($\bar{x}$, n = 3)	54–59	86.2

In a first step, the previous the pull-out test rebound values (R) around the anchor position were measured, concluding the influence of rock strength. As stated by [21], rebound values indirectly describe the rock compressive strength. According to [22], $1.5 \times h_{ef}$ is considered to be decisive for determining the tensile load-bearing capacity of anchors in concrete. Hence, rebound values were taken at a distance of 1.5 times the effective embedment depth ($1.5 \times h_{ef}$). In the following, "R" is used for the measured rebound values. As mentioned above also joint weathering and quantity are considered to have an influence on the load-bearing capacity [9]. Therefore, after performing pull-out tests, joint weathering and the quantity of critical joints were determined.

2.2.2. Selection of Anchor Positions

It is assumed that for each rock type in the investigated section there are areas which are visually on the first visual inspection better and others which are worse suited as base material (Figure 2). Well suited or undisturbed areas were assumed to be (i) not disturbed in the close-up range ($1.5 \times h_{ef}$) by visually recognizable joints (see Figure 2a). In contrast, worse suited or disturbed areas were defined as (ii) affected by at least one optically detectable joint. (Figure 2b). In order to consider the worst case in terms of fastening, anchors were directly positioned in a visually recognizable joint (Figure 2). Test quantities per rock type and fastening area (disturbed/undisturbed) are plotted in Table 1. This procedure is used for a visual assessment on site and is intended to represent two possible base material extremes and, derived from this, the fastening quality.

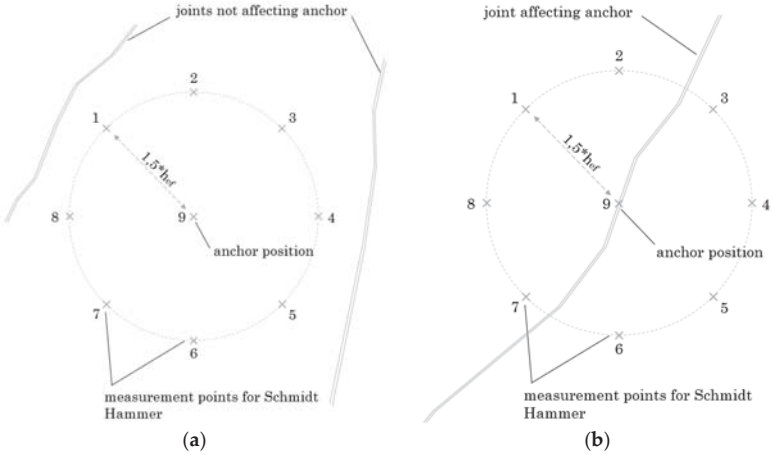

Figure 2. Anchor positions one to nine in (**a**) undisturbed area (not affected by visual detectable joints) and (**b**) disturbed area (affected by joints).

3. Results

3.1. Influence of the Fastening Area (Disturbed/Undisturbed)

Table 3 shows that existing joints in the fastening area next to the anchor strongly influence the load-bearing capacity. For example, granulite and granite show a deviation—undisturbed to disturbed—of approximately 60% and dolomitic limestone shows approximately 50% (see Table 3). Undisturbed areas do not show any rock disturbances due to inhomogeneities and existing joints and are therefore more suitable ex ante as a base material for fastenings.

Table 3. Comparison of failure loads for the different rock types for disturbed and undisturbed areas.

Parameter	Unit	Granulite	Limestone	Dolomite	Granite
$F_{u,m}$	kN	32.2	38.1	10.5	45.4
coefficient of variation	%	58%	51%	81%	63%
$F_{u,m1}$ disturbed fastening area	kN	20.1	28.3	10.5	25.3
coefficient of variation	%	49%	58%	81%	68%
$F_{u,m2}$ undisturbed fastening area	kN	50.3	52.8	n.a.	65.5
coefficient of variation	%	26%	26%	n.a.	35%
Deviation undisturbed/disturbed	%	−60%	−48%	n.a.	−61%

3.2. Influence of Joints on the Load-Bearing Capacity

3.2.1. Joint Quantity

As explained in Table 1, the number of critical joints was determined. The assessment was done visually after failure of the anchor occurred. It was assumed that high joint quantity results in low load-bearing capacities of the anchorages. For undisturbed areas generally a critical joint quantity of zero and high load-bearing capacities have been found. For disturbed areas, a joint quantity of at least one and low load-bearing capacities were recorded. In [9], more information about disturbed and undisturbed areas and also a comparison to classification models can be found. Thus, an influence of joint quantity on load-bearing capacity could be stated. However, further investigations of this relationship were not carried out, because critical joints can only be determined after failure occurs. Test No. 9 in granulite (epoxy resin mortar) in undisturbed base material serves as an example (Figure 3). While an optical assessment indicated an undisturbed area and no critical joints, retrospectively, the results indicated that many joints were found to be critical for failure.

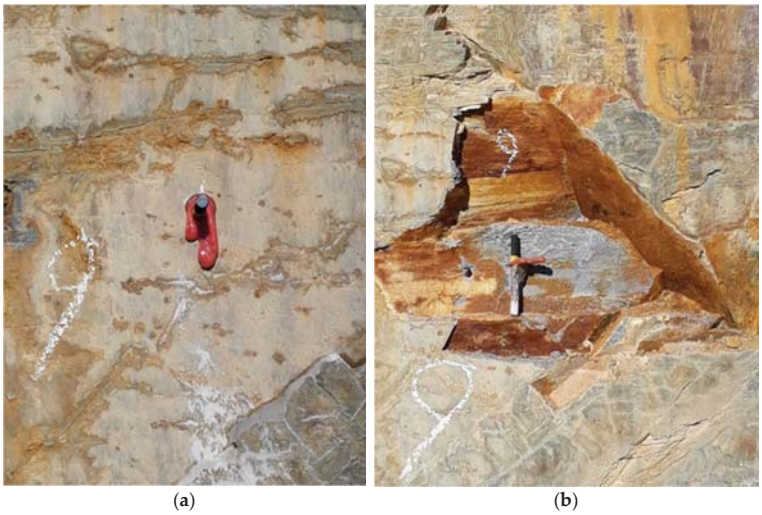

(**a**) (**b**)

Figure 3. Joint quantity next to the anchor (**a**) before pull-out test in undisturbed area–no critical joints visible and (**b**) after pull-out test–critical joints visible.

3.2.2. Joint Weathering

The influence of joint weathering was considered in accordance to [23] and is mostly presented as discoloration of the surface (e.g., rust-brown coloration due to oxidation for granulite). Figure 4 demonstrates the failure load (F_u) unrelated to the anchor type per defined weathering class and rock type. According to Figure 4, the failure load and degree of weathering are strongly related. High weathering of joints leads to lower load-bearing capacities. The secondary y axis of Figure 4 shows the coefficients of variation (CV).

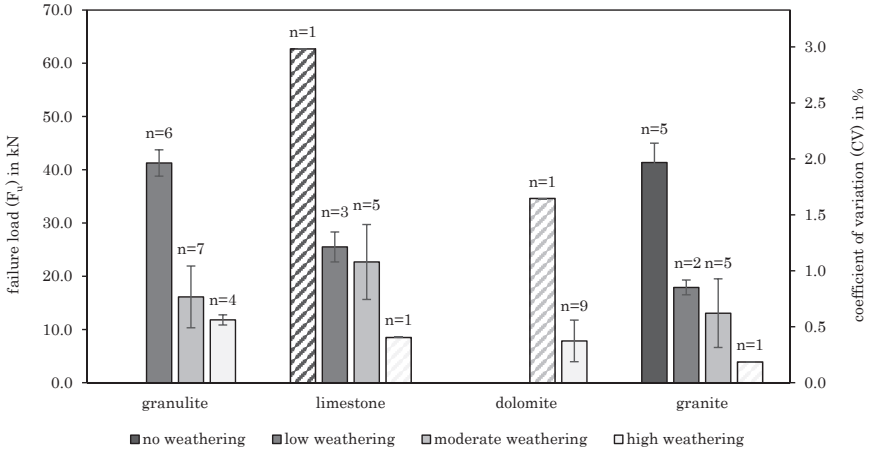

Figure 4. Failure load and CV as function of weathering class and rock type–weathering class determined after failure occurred (if n = 1 no CV is given and the beams are hatched as the data can contain an outlier).

Comparing the coefficients of variation, it was found out that with low degree of weathering failure loads are not only higher but are also less scattering. Like joint quantity, joint weathering was determined after failure occurred, too. Figure 5 indicates the reason for that, showing an installed chemical anchor where the degree of weathering of the joint

is unclear before the pull-out test is carried out (Figure 5a), although high weathering of the joints could be observed after failure occurred (Figure 5b).

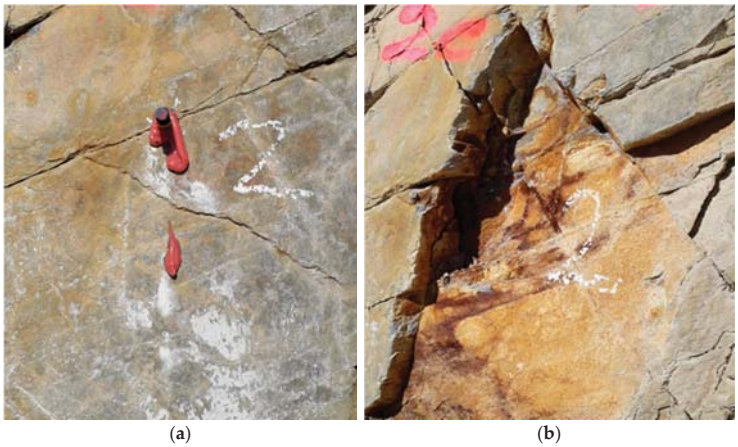

(**a**) (**b**)

Figure 5. Joint weathering for (**a**) an installed anchor–weathering of joint unclear and (**b**) an anchor after failure–weathering of joint visible after failure occurred.

Figure 6 shows the relationship between the determined rebound value and joint weathering based on the different geologies. For high joint weathering, small rebound values were found. For low weathering, high rebound values could be determined. For different rock types, the above-mentioned correlation is varying. It should be mentioned the correlation can be determined only qualitatively, as classification of the weathering degree was also performed qualitatively. The secondary y axis of Figure 6 shows the coefficients of variation (CV). Table 4 presents the standard deviations for Figures 4 and 6.

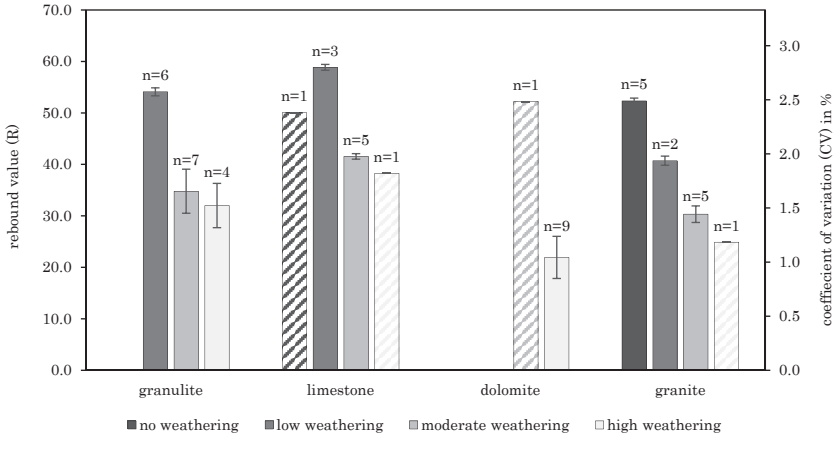

Figure 6. Relation between joint weathering and R including CV (if n = 1 no CV is given and the beams are hatched as the data can contain an outlier).

Table 4. Standard deviations for Figures 4 and 6.

	Granulite	Limestone	Dolomite	Granite
standard deviations Figure 4				
no weathering	n.a.	0.0	n.a.	15.0
low weathering	10.2	7.2	n.a.	2.5
moderate weathering	9.4	16.0	0.0	8.4
high weathering	1.1	0.0	3.1	0.0
standard deviations Figure 6				
no weathering	n.a.	0.0	n.a.	2.9
low weathering	4.2	3.3	n.a.	3.6
moderate weathering	14.9	2.3	0.0	4.9
high weathering	13.8	0.0	9.0	0.0

3.3. Base Material Assessment by Rebound Hammer

As explained in Section 2.2.2, the anchor positions in the experimental campaign were first visually divided into disturbed and undisturbed areas. After this visual assessment, eight rebound values were determined circularly around the anchor position at a distance of 1.5 × h_{ef} as shown in Figure 2. Initially, rebound values were taken to provide an indication of the rock strength. Secondly, rebound values also are used to validate the classification into disturbed and undisturbed areas. As shown in Figure 7, disturbed areas lead to smaller rebound values with visible joints in the investigated area, whereas undisturbed areas show higher rebound values with no visible joints.

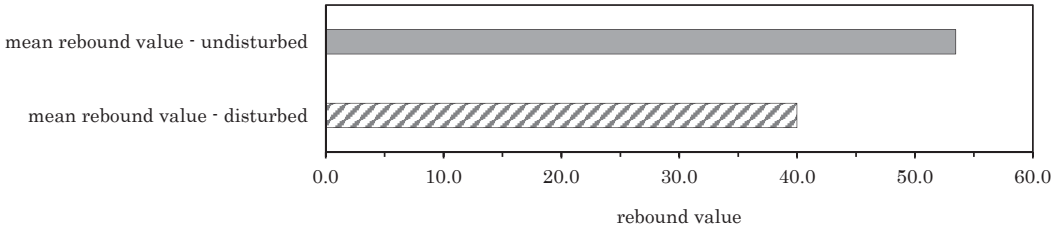

Figure 7. Mean rebound values for disturbed and undisturbed areas for all rock types.

4. Discussion

4.1. General

The aspects discussed in the following are based on the experimental investigations described above, whereby no numerical insights are presented.

The given example in Section 3.2.1 (see Figure 3) demonstrates the difficulty of existing critical joints, which can be recognized only after failure has occurred. The fact that in some cases critical joints are not visible in advance implies that other methods in addition to a visual assessment should be carried out. A suggestion on a method how to verify the visual assessment can be found in Figure 8.

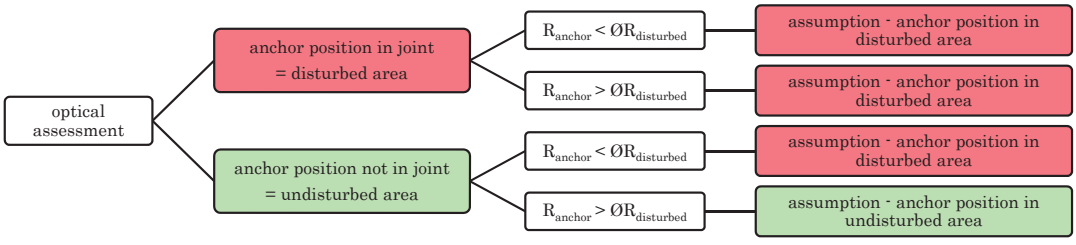

$ØR_{disturbed}$: mean value of all rebound values (disturbed) per rock type
R_{anchor}: mean value of the eight rebound values per anchor

Figure 8. Flow chart for base material assessment by rebound hammer.

As for the joint quantity (see Section 3.2.1) the same is true for joint weathering (see Section 3.2.2). While the degree of weathering is unclear before the pull-out test is carried out, it can be easily determined retrospectively after the conduction of the test. From Section 3.2.2 it can be concluded that a low degree of weathering is well suited as an indicator for assessing the base material quality. Although a strong correlation was observed, an exact preliminary assessment of joint weathering is not possible. Hence, also the relation between the rebound value and joint weathering was investigated in Figure 6. Figure 6 indicates that joint weathering also correlates with rebound values taken around the anchor position (see Figure 2 and Section 3.2). In other words, rebound values determined next to the anchor position indicate joint weathering and thus also the base material quality. This causes a significant advantage, as rebound values can be determined easily using the base material surface, prior to failure and even before the installation of the anchor. Therefore, the relationship between rebound values and load-bearing capacities was investigated.

In order to compare rebound values with failure loads, a validation of the optical assessment was performed according to Figure 8. Firstly, the mean value of all rebound values of disturbed areas was calculated ($ØR_{disturbed}$). $ØR_{disturbed}$ was then compared to R_{anchor}, which is the mean value of rebound values per anchor. This procedure, according to Figure 8, is used to validate the visual assessment. To be able to assume an undisturbed area, both the optical assessment and the comparison of R_{anchor} with $ØR_{disturbed}$ must provide the result "undisturbed".

4.2. Relation between Rebound Value and Load-Bearing Capacity

As concluded in Section 3.1 it seems that rebound values next to the anchor position can be used as an indicator for rock quality as base material. Therefore, Figure 9 plots the relationship between failure load and rebound value (as the mean value of 8 values circularly around the anchor position) per rock type and fastening area (disturbed/undisturbed). According to Figure 9, the disturbed areas (grey color in Figure 9) are characterized by lower rebound values and failure loads, while the values are widely distributed around the line of closest fit. In contrast, undisturbed areas (black color in Figure 9) show high rebound values and high failure loads for all rock types. It can also be seen that disturbed and undisturbed areas cannot be clearly separated, but on the contrary are overlapping to some extent. Considering this in addition to the existing relationship between rebound values and failure loads, it can be concluded that the estimation of base material quality by determining rebound values is possible. However, it should be noted that a high correlation is evident for disturbed and not for undisturbed areas. For the undisturbed areas, the rebound values are capped at about 70 while the failure loads are not. The lack of correlation demonstrates that the rebound hammer is not indicative for the failure load above a certain rock strength but ensures a minimum value of load bearing capacity. The exponential correlation curve between rebound values and uniaxial compressive strength [19]

is considered reasonably low for the undisturbed areas. In addition, it is possible that microcracks in the undisturbed rock cannot be detected by means of rebound hammers, although they have a significant influence on the loading of the anchor pull-out, since here the rock experiences tensile stress. For dolomite, no undisturbed fastening areas could be observed, and therefore only one data set for disturbed areas is shown. Accordingly, estimating base material quality by rebound values varies in its suitability for different rock types.

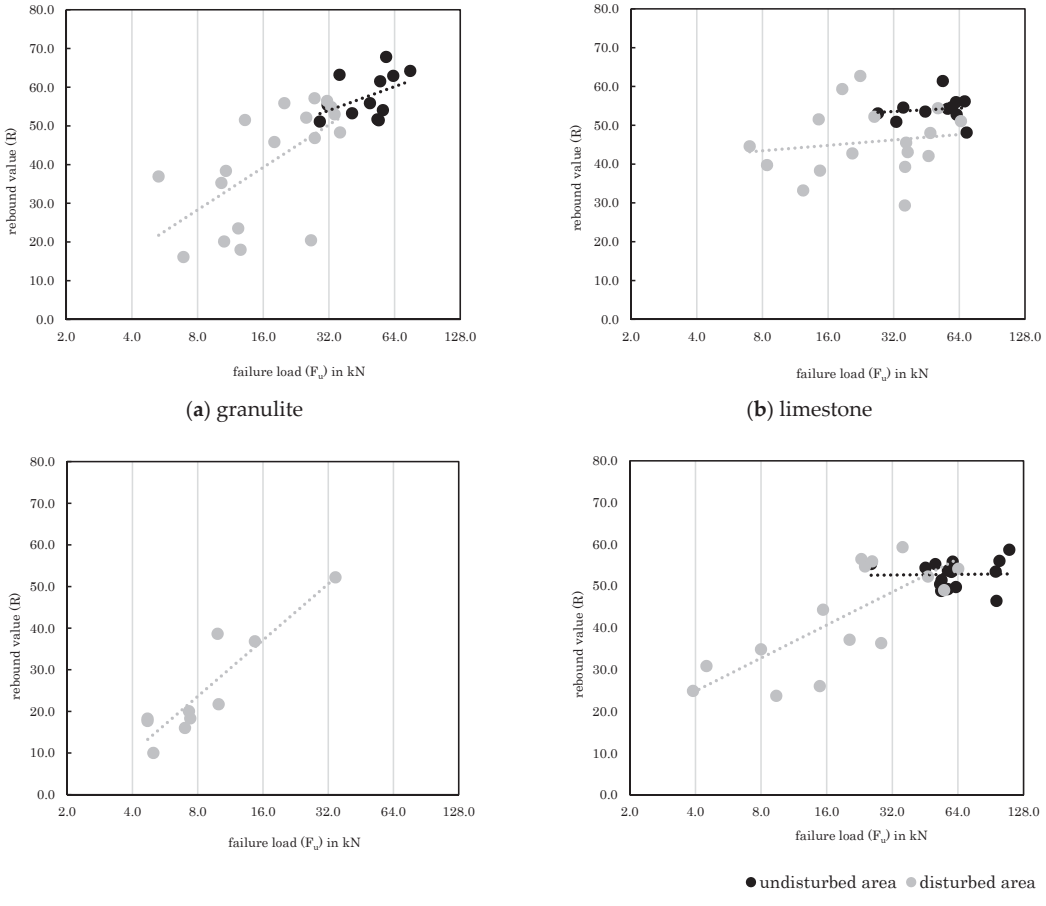

(**a**) granulite (**b**) limestone

(**c**) dolomite (**d**) granite

Figure 9. Relationships between rebound values and failure loads for various rock types.

In Figure 10, all rock types are examined together. The rebound values (R) illustrated are equivalent to the mean rebound values from the anchor position. These are calculated out of eight values taken next to the anchor position (compare to Figure 2). Therefore, it is possible to indicate not only the mean rebound values, but also to plot the scattering per value (described by the coefficient of variation, CV). This form of presentation was chosen in Figure 10, where large data points indicate a high coefficient of variation. According to Figure 10, disturbed areas result in more scattering of rebound values than undisturbed areas. Inhomogeneities around the anchor position in disturbed areas thus lead to the varying rebound values. In undisturbed areas, intact rocks with more homogeneous

properties lead to a more uniform distribution of rebound values, whereas low CVs should therefore indicate good rock properties.

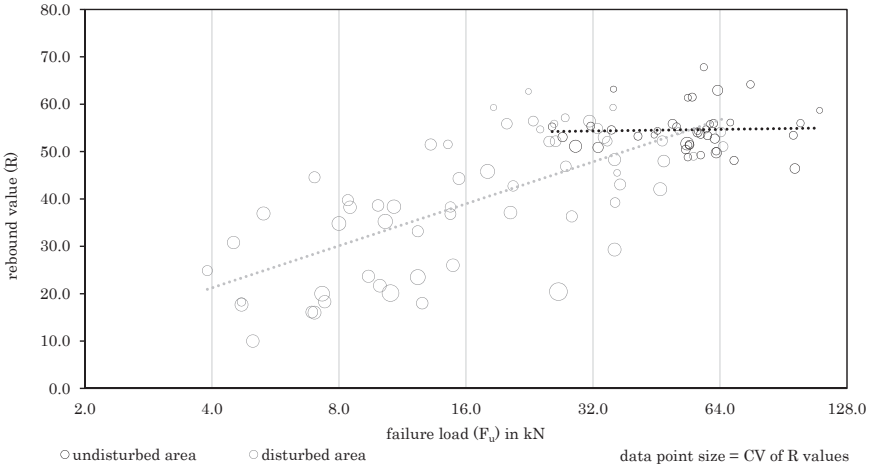

Figure 10. Relationship between rebound values and failure loads for all rock types.

On the contrary, poor uniformly distributed rebound values can lead to a small scattering too. Small CVs therefore do not automatically indicate good fastening properties. Instead of that, they can originate from good or poor a priori rock properties. In Figure 11, the measured rebound values taken next to the anchor are shown using a radar chart. For both examples, the rebound values are evenly distributed. Although this results in similar CVs, the failure loads differ significantly. Therefore, using CVs to identify good rock properties is not sufficient. In order to prevent wrong conclusions being drawn from a low CV in regard to good rock properties, it is necessary to have a combined consideration of CV and mean R value.

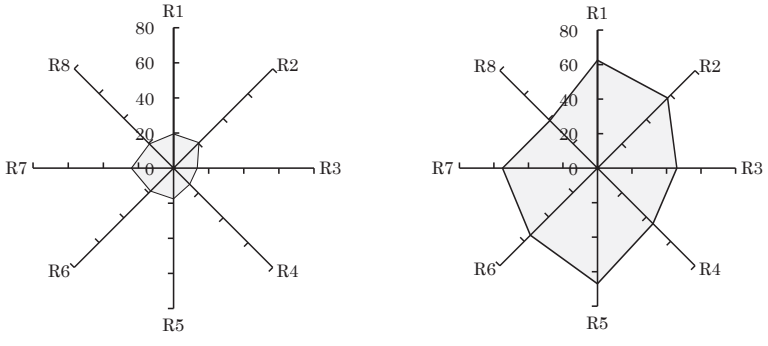

Figure 11. Uniformly distributed rebound values R (CV, Rmean, F_u). (**a**) uniformly distributed with low R values; (**b**) uniformly distributed with high R values.

Thinking further, it is also possible to neglect the CV altogether. In fact, the rebound value scattering is not decisive if the mean rebound value succeeds a certain level. Figure 12 demonstrates an example for this conclusion. Although a high CV can be observed due to downward statistical outliers, it was still possible to achieve a good load-bearing capacity. Hence, in order to identify good rock properties in advance, it should be sufficient if the tested rebound values per anchor are not falling below a certain level. A further consideration of the coefficient of variation was therefore not carried out.

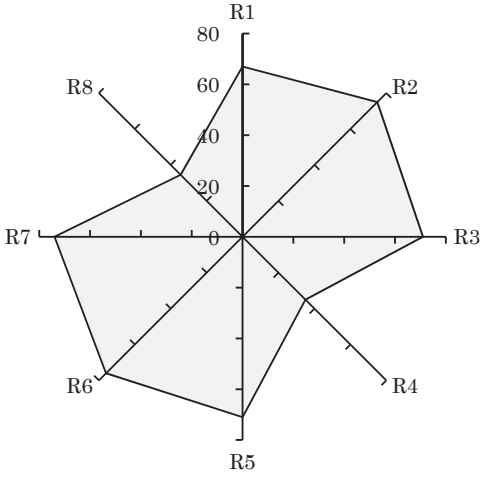

Figure 12. High rebound values including two downward outliers (CV, Rmean, F_u).

In Figure 13, a lower threshold value for the rebound values was defined. In order to determine the threshold value, a log normal distribution was assumed for all undisturbed rebound values. Calculating the 5% fractile from this distribution, a mean rebound value of 53.2, a standard deviation of 1.3, and a k-value of 1.645 for an infinite sample size were used. Conclusively, a threshold of 36 resulted. When highlighting all anchors in undisturbed areas for which none of the eight rebound values is below this threshold, good rebound values and failure loads can be obtained.

Some data points for disturbed areas also show comparable failure loads and rebound values. In principle, the same procedure can be used for anchor positions in disturbed areas, if compared to the threshold of undisturbed rebound values. However, resulting failure loads are lower and show a larger scattering, which can be explained by the existing inhomogeneities in the base material. The rock quality for post-installed anchors for these areas could be described as average.

The approach should therefore always be used in combination with a visual assessment. Nevertheless, Figure 13 indicates that using a lower threshold allows to identify good rock properties when combined with a visual assessment. A classification of base material properties by means of a combination of visual assessment and the determined threshold can be obtained from Table 5.

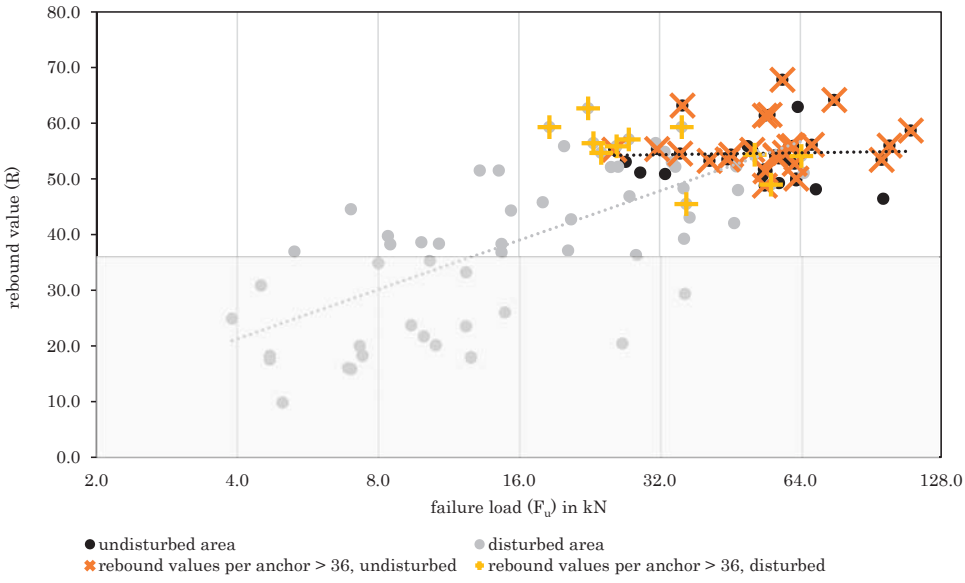

Figure 13. Relationship between rebound values and failure loads–anchors where R values do not fall below threshold are highlighted.

Table 5. Base material classification.

Base Material Quality		Poor	Average (1)	Average (2)	Good
rebound values per anchor >36 disturbed/undisturbed		no disturbed	yes disturbed	no undisturbed	yes undisturbed
mean Fu	/in kN	21.20	34.96	41.37	58.12
CV		69%	42%	60%	34%
minimal Fu	/in kN	3.90	18.60	7.00	25.60

As described above, good base material quality can be assumed when the threshold is met in undisturbed areas. Average base material can be expected if (1) the rebound values are above the threshold in disturbed areas or (2) the threshold is not fulfilled in undisturbed areas. Ultimately, poor base material should be considered when rebound values are below the limit value in disturbed areas.

5. Conclusions

Small scale investigations on rock were performed in order to identify influencing parameters on the load-bearing capacity of post-installed anchors. It was shown that, for disturbed areas, a high number of joints are usually critical for failure and lead to low failure loads. For undisturbed areas, higher load capacities could be found with fewer joints, whereby the joint quantity was determined retrospectively. Nevertheless, it was shown that it is not possible to determine critical joints before failure occurs.

Weathering degree also shows a correlation with failure loads. High degrees of weathering of joints lead to smaller failure loads. Once more, it is not possible to determine the weathering degree before failure. However, it was possible to show that rebound values around the anchor position correlate with the degree of weathering. A high degree of weathering leads to low rebound values and low joint weathering leads to high rebound values. Therefore, rebound values provide the possibility of making an estimation about base material quality in advance of failure. Accordingly, high rebound values indicate good base material quality. From the investigated rebound values, a threshold can be calculated

based on a log-normal distribution. If rebound values around optically undisturbed anchor positions do not fall below this threshold, good base material properties can be assumed. If the criterion is met in areas of optically disturbed anchor positions, average base material quality can be assumed. This procedure should therefore always be combined with a visual assessment. Average base material can also be considered if the threshold is not met in undisturbed area. Finally, poor base material should be assumed when the criterion is not met in disturbed areas.

This technical paper was able to demonstrate the influence of joint quantity and weathering next to the anchor position on post-installed anchors in rock. Further, an approach for a preliminary assessment to classify the base material quality was proposed. An open question remains concerning the extent to which t a design concept for the base material classes can be derived from this and this will be the subject of future research. A detailed investigation of these questions helps engineers of post-installed anchors to become more familiar with the less known base material rock.

Author Contributions: Conceptualization, S.L., O.Z. and K.V.; methodology, S.L., O.Z. and K.V.; software, S.L.; validation, S.L., O.Z. and K.V.; formal analysis, S.L. and O.Z.; investigation, S.L. and K.V.; resources, O.Z. and K.V.; data curation, S.L.; writing—original draft preparation, S.L.; writing—review and editing, O.Z. and K.V.; visualization, S.L.; supervision, O.Z. and K.V.; project administration, O.Z. and K.V.; funding acquisition, O.Z. and K.V. All authors have read and agreed to the published version of the manuscript.

Funding: This research received no external funding.

Conflicts of Interest: The authors declare no conflict of interest.

References

1. DIN Deutsches Institut für Normung. *DIN EN 1992-4:2018: Eurocode 2—Bemessung und Konstruktion von Stahlbeton und Spannbetontragwerken—Teil 4: Bemessung der Verankerung von Befestigungen in Beton*; Beuth Verlag GmbH: Berlin, Germany, 2019.
2. EOTA—European Organisation for Technical Approvals. *EOTA TR054: 2016-04—Design Methods for Anchorages with Metal Injection Anchors for Use in Masonry*; EOTA: Brussels, Belgium, 2016.
3. Fuchs, W.; Eligehausen, R. The CC-design method to determine the concrete break out load of fastenings. *Beton-Stahlbetonbau* **1995**, *1*, 6–9. [CrossRef]
4. Eligehausen, R.; Appl, J.; Lehr, B.; Meszaros, J.; Fuchs, W. Tragverhalten und Bemessung von Befestigungen mit Verbunddübeln unter Zugbeanspruchung—Teil 1: Einzeldübel mit großem Achs- und Randabstand. *Beton-Stahlbetonbau* **2004**, *7*, 561–571. [CrossRef]
5. Appl., J. Tragverhalten und Bemessung von Verbunddübeln. *Beton-Stahlbetonbau* **2005**, *45*, 9–12. [CrossRef]
6. Contrafatto, L.; Cosenza, R. Behaviour of post-installed adhesive anchors in natural stone. *Constr. Build. Mater.* **2014**, *68*, 355–369. [CrossRef]
7. Contrafatto, L.; Cosenza, R. Prediction of the pull-out strength of chemical anchors in natural stone. *Frat. Integrità Strutt.* **2014**, *29*, 196–208. [CrossRef]
8. Tóth, M.; Hlavička, V.; Lublóy, É.; Török, Á.; Balázs, G.L. Performance of expansion and bonded anchors installed into concrete in comparison to limestone and granite. *Bond Concr.* **2012**, *1*, 527–532.
9. Lamplmair, S.; Zeman, O.; Voit, K. Beurteilung von Fels als Befestigungsuntergrund für nachträgliche Befestigungen mit geringer Einbindetiefe. *Bautechnik* **2021**, in press. [CrossRef]
10. Matura, A.; Heinz, H. *Geologische Karte der Republik Österreich 1:50,000—Erläuterungen zu Blatt 37 Mautern*; Geologische Bundesanstalt: Mautern, Germany, 1989.
11. Fuchs, W. *Geologische Karte der Republik Österreich 1:50,000—61 Hainburg an der Donau—62 Pressburg*; Geologische Bundesanstalt: Hainburg an der Donau, Austria, 1985.
12. Geotec ZT GmbH Nfg.KG. *Geologisches Gutachten*; Geotec ZT GmbH Nfg.KG: Bad Deutsch-Altenburg, Austria, 2005.
13. Schnabel, W. *Geologische Karte der Republik Österreich 1:50,000—58 Baden*; Geologische Bundesanstalt: Baden, Germany, 1997.
14. Geologie Weixelberger GmbH. *Geologisches Gutachten*; Geologie Weixelberger GmbH: Gaaden, Austria, 2014.
15. Roetzel, R. *Geologische Karte der Republik Österreich 1:50,000—22 Hollabrunn*; Geologische Bundesanstalt: Hollabrunn, Austria, 1998.
16. Geologische Bundesanstalt. *Arbeitstagung Geologische Bundesanstalt, Haltepunkt 16—Limberg*; Geologische Bundesanstalt: Wien, Austria, 1991.
17. Bieniawski, Z.T. *Engineering Rock Mass Classifications: A Complete Manual for Engineers and Geologists in Mining, Civil, and Petroleum Engineering*; Wiley-Interscience: Hoboken, NJ, USA, 1989.

18. Marinos, P.; Hoek, E. GSI: A geologically friendly tool for rock mass strength estimation. In Proceedings of the GeoEng2000 at the International Conference on Geotechnical and Geological Engineering, Melbourne, Australia, 19–24 November 2000; pp. 1422–1446.
19. Aydin, A. ISRM Suggested method for determination of the Schmidt hammer rebound hardness: Revised version. *Int. J. Rock Mech. Min. Sci.* **2009**, *3*, 1365–1609. [CrossRef]
20. Thuro, K. Empfehlung Nr. 5, Punktlastversuche an Gesteinsproben 'des Arbeitskreises 3.3, Versuchstechnik Fels' der Deutschen Gesellschaft für Geotechnik. *Bautechnik* **2010**, *87*, 322–330. [CrossRef]
21. Katz, O.; Reches, Z.; Roegiers, J.-C. Evaluation of mechanical rock properties using a Schmidt Hammer. *Int. J. Rock Mech. Min. Sci.* **2000**, *4*, 723–728. [CrossRef]
22. Eligehausen, R.; Appl, J.; Lehr, B.; Meszaros, J.; Fuchs, W. Tragverhalten und Bemessung von Befestigungen mit Verbunddübeln unter Zugbeanspruchung—Teil 2: Dübelgruppen und Befestigungen am Bauteilrand. *Beton-Stahlbetonbau* **2005**, *10*, 856–864. [CrossRef]
23. Austrian Standards International. *ÖNORM EN ISO 14680 Geotechnical Investigation and Testing—Identification and Classification of Rock*; Austrian Standards International: Vienna, Austria, 2019.

materials

MDPI

Article

Shear Capacity and Behaviour of Bending Reinforced Concrete Beams Made of Steel Fibre-Reinforced Waste Sand Concrete

Marek Lehmann * and Wiesława Głodkowska

Faculty of Civil Engineering, Environmental and Geodetic Sciences, Koszalin University of Technology, Sniadeckich 2, 75-453 Koszalin, Poland; wieslawa.glodkowska@tu.koszalin.pl
* Correspondence: marek.lehmann@tu.koszalin.pl

Abstract: Inthis paper, we report the results of our research on reinforced concrete beams made of fine aggregate fibre composite, with the addition of steel fibres at 1.2% of the composite volume. The fine aggregate fibre composite is a novel construction material, in which the aggregate used is a post-production waste. Twenty reinforced concrete beams with varying degree of shear reinforcement, in the form of stirrups with and without the addition of steel fibres, tested under loading. The shear capacity results of reinforced concrete beams made of the fine aggregate fibre composite being bent by a transversal force, as well as the cracking forces causing the appearance of the first diagonal crack, are discussed. The stages of functioning of such elements are described. Furthermore, the effect of the steel fibres on the reduction of diagonal cracking is analysed. Computation of the shear capacity of the tested elements is performed, based on the Model Code 2010 and RILEM TC-162 TDF standards, for two variants of the compression strut inclination angle θ that measured during testing, and the minimum(in accordance with the Model Code 2010 standard). We found that the SMCFT method part of Model Code 2010 showed the best compatibility with the experimental results. The tests and analyses performed demonstrate that the developed novel fibrecomposite—the properties of which are close to, or better than, those of the ordinary concrete—can be used successfully for the manufacturing of construction elements in the shear capacity aspect. The developed fine aggregate fibrecomposite could serve, in some applications, as an alternative to ordinary concrete.

Keywords: steel fibre-reinforced concrete; steel fibres; waste sand properties; reinforced beam; shear cracking; shear capacity

Citation: Lehmann, M.; Głodkowska, W. Shear Capacity and Behaviour of Bending Reinforced Concrete Beams Made of Steel Fibre-Reinforced Waste Sand Concrete. *Materials* **2021**, *14*, 2996. https://doi.org/10.3390/ma14112996

Academic Editor: Krzysztof Schabowicz

Received: 27 April 2021
Accepted: 27 May 2021
Published: 1 June 2021

1. Introduction

Concrete belongs to the class of brittle and barely deformable materials; therefore, it is susceptible to scratching and cracking. The addition of, for example, steel fibres to such materials allows us to obtain higher plasticity and cracking resistance properties. Fibre-reinforced concrete was first used 140 years ago when, in 1874, Bernard submitted his first patent application for steel fibre-reinforced concrete. Since that time, attempts have been made to both evaluate the impact of the fibres on concrete properties [1–9], as well as distribution of fibres in the concrete [10–12]. Fibre-reinforced concrete has, therefore, become an alternative to ordinary concrete.

The fibre-reinforced concrete filling, just as in the case of ordinary concrete, is a fine and coarse aggregate selected based on a continuous grading curve. Aggregate deposits occur in the Pomeranian area in Poland, in the form of a mixture of fine and coarse aggregates. The high demand for coarse aggregate has contributed to the development of a technique of its sourcing by washing it out from its deposits. This technique is called hydroclassification. The application of hydroclassification of natural aggregates results in the build-up of dumps of washed-out sand, from which coarse aggregate fractions have been eliminated. Such created excavations must be subjected to costly reclamation operations. An alternative for reclaiming these excavations is through the possibility to use waste sand as a valuable construction material. Due to the shortage of coarse aggregate in

the north region of Poland, a concrete composite has been developed [11,13,14],included in which is the fine aggregate (i.e., waste sand). In the analysed fine aggregate cement composite, the coarse aggregate was substituted with steel fibres, in order to create steel fibre-reinforced waste sand concrete (SFRWSC).

The subject matter of our analysis is, therefore, the novel steel fibre-reinforced waste sand concrete. This novel fibre composite material, featuring high compression and tensile strength, was designed based on a fine post-production waste aggregate. The research work described in [12,14,15] stated that a fibre composite based on waste sand containing 1–1.5% steel fibres has the best physicochemical properties. If the steel fibre content exceeds 1.5%, some tested material features decrease or improve insignificantly. Therefore, the addition of steel fibres in excess of 1.5% makes the resulting concrete hardly usable, due to material workability, its mechano-physical properties, and cost. A steel fibre content equal to 1.2% seems to be the best possible option, considering the fundamental properties that the structural composite should have. The residual strength values of SFRWSC with a steel fibre content of 1.2%, defined in the EN 14651 standard [16], have been classified in accordance with Model Code 2010 [17] as class 7b, which means that this material is suitable for the manufacturing of structural elements, and traditional reinforcement may be reduced. A feature distinguishing the analysed SFRWSC is its ability to resist higher shear forces, compared to concrete without fibre reinforcement. An increase in the shear capacity may lead to a reduction of traditional shear reinforcement or the complete abandonment of such reinforcement, due to shear capacity at small loads.

Analysing the state-of the-art in the field of shear fibre concrete elements, the first works were started in the 1970s. Batson, in [18], published the results of research on the influence of the shape, quantity, and dimensions of fibre reinforcement on shear force. Based on these studies, he concluded that the stirrups can be replaced by round, flat, or crimped steel fibres, which effectively influence the shear capacity of the support areas. In 1986, Sharma [19] conducted research and confirmed the beneficial co-operation of fibres and stirrups meanwhile, in 1987, Narayanan and Darwish published a study [20] considering beams with crimped fibre content, different degrees of main reinforcement, and varying a/d ratio. The shear problem in fibre-reinforced elements is still relevant and remains of experimental research. You et al., in their work [21], presented the results of an experiment carried out on rectangular beams, considering the use of fibre reinforcement with and without stirrups. Their research showed that the shear load capacity increases significantly with increasing fibre content, and the addition of an appropriate percentage of fibres can change the failure mode from brittle failure at shear to a ductile mechanism. The stirrups can be partially replaced by steel fibres and the combination of steel fibres and stirrups showed a positive effect on the mechanical behaviour of the composite. Similar conclusions have been reached by Ding et al. [22] and Li et al. [6]. Zhao [23], in his work, additionally characterized the effect of fibres on the reduction of diagonal cracks and strain after cracking. Analyses of the level of the scale effect by fibres in the shear load capacity [24]. Reviews of the state of knowledge of fibre-reinforced shear elements have been presented in the manuscripts [25,26], among others. Although the shear issue has been dealt with in numerous papers, there is still a need for further research, in order to analyse this issue in a more insightful way.

Knowledge of the bahavior and failure of reinforced concrete structures is of great technical and economic importance. Experimental testing of such components is laborious and costly. Therefore, the possibilities of numerically analyzing the work of reinforced concrete elements are often used, e.g., with the help of the Finite Element Method (FEM). In addition, along with the development of new materials and research methods, intensive scientific work is carried out on the use of numerical methods for modeling physical processes, development of material damage to destruction, modeling of ultra-high performance concrete, reinforced concrete shells and walls or structure strengthening [27–30]. The problem of shear in reinforced concrete beams [31,32] and in fiber-reinforced beams [33–35] is also subjected to numerical modeling. Talavera-Sanchez et al. [33] presented the test

results of 16 beams with various parameters, including steel or macro-synthetic fibers, the presence or absence of transverse reinforcement, different shear-to-depth ratios, and different transverse reinforcement values. In numerical modeling was used the nonlinear finite element analysis following the smeared crack approach and a total strain-based crack material model. Numerical modeling has shown that the nonlinear finite element model can predict the behavior and strength of beams with transverse reinforcement with high accuracy. For members without transverse reinforcement, the shear capacity is acceptable, but some doubts remain unclear as these beams have large critical diagonal crack failure. In the manuscript of Amin and Foster [34] comparison of full scale SFRC beams ATENA 2D smeared crack models were described. The ATENA 2D integrated with a constitutive law derived after an inverse analysis from prism bending tests. The numerical model is validated against experimental results obtained. Authors analyzed experimental and numerical shear strength, deflection and diagonal crack pattern. It was shown that numerical model compared well with the experimental data in capturing the linear and non-linear responses of the beams. Some studies also concerned beam sections other than rectangular ones, and Baross and his team [35] dealt with modeling of T-sections. The studies of fiber-reinforced concrete T-beams damaged due to shear were analyzed in comparison to various numerical models, i.e., smeared crack model, discrete crack model, concrete damage plasticity model, and lattice discrete particle model. The models were analyzed in terms of deflection, strain and diagonal cracking. The authors obtained results with different accuracy in relation to the experimental results, stating that for the lattice discrete particle model, the best means of agreement are obtained.

The research work published in [12,15,36] concluded that SFRWSC without steel fibres behaves like ordinary concrete in bent elements provided with conventional reinforcement. The addition of steel fibres considerably improves the flexural capacity of such elements, thanks to which, the reduction of conventional reinforcement due to bending moment is possible. The addition of steel fibres also limits the width of cracks perpendicular to the element axis. These properties provide a possibility to use this material in the production of structural elements such as flooring slabs, beams, or coatings. Thanks to its mechano-physical properties, SFRWSC may, in some cases, serve as a substitute for ordinary concrete.

Considering the abovementioned achievements to date, the objective of the research presented in this paper was to show that the novel SFRWSC, with 1.2% fibre content, could be used for the production of reinforced concrete elements that are subject to bending functioning under shear force. To date, no research work has been performed on reinforced concrete elements made of SFRWSC that are subjected to bending by a transversal force. Therefore, an assumption was made, namely that steel fibres used as reinforcement can contribute to an improvement of the shear capacity of such elements. Another objective is to prove that, by using steel fibres, conventional shear reinforcement can be reduced, as well as reducing the diagonal crack width.

The design of fibre-reinforced concrete cross-sections functioning under shear force is still an unexplored issue [37,38]. The first design methods were based on experimental tests and had a limited scope of application. After the publication of two European standards—RILEM -TC-162-TDF [39] and Model Code 2010 [17]—the dimensioning of fibre-reinforced concrete cross-sections functioning under shear force has been standardised. However, the authors of many scientific papers [40–43] evaluating the shear design methods described in the above-named standards have stated that there were significant differences between the experimental and computed values. Therefore, the next objective of this research work is the evaluation of the shear design fibre-reinforced elements, based on the Model Code 2010 [17] and RILEM TC-162-TDF [39] standards, in terms of the possibility to use the methods for shear design of SFRWSC elements subject to bending. It should be noted that by using waste aggregate as a full-value construction material for the production of the tested SFRWSC, these studies are in line with the global trends related to sustainable development of the environment.

2. Test Materials

The reinforced concrete beams to be tested for shear capacity were made of SFRWSC containing 1.2% steel fibres, in relation to the volume of composite material [44].SFRWSC is a novel structural material, in which the used aggregate is a post-production waste. In the analysed composite, the used aggregate was sand of 4 mm granularity, which is a waste material of aggregate mines located in northern Poland (the Pomeranian region). In this area, a significant part of the output is subjected to the process of hydroclassification, which results in 80% sand and only 20% coarse aggregate. This disproportion leads to the situation where most of sand remains unused, in numerous dumps located near the aggregate mines (Figure 1).

Figure 1. View of the sand heaps after the hydroclassification process in Pomerania (northern Poland). Reproduced with permission from ref. [13] published by Middle Pomeranian Scientific Society of the Environment Protection, 2015.

The postulate to somehow utilise remaining waste sand dumps constitutes a worldwide tendency, consistent with Sustainable Ecological Development [45–49]. Similar phenomena of excessive sand fractions can be observed in other parts of the world, such as the Middle East or in North Africa [50]. Figure 2 presents waste sand grading curves appointed by various authors. These curves only insignificantly differ from one another, despite the fact that the sand used in these studies originated from various aggregate mines located in northern Poland. This indicates that all these deposits are post-glacial or fluvioglacial residues, developed in the same period [12,51,52].

The used fine aggregate complied with the requirements formulated for mineral aggregates recommended for ordinary concrete manufacturing. The content of mineral dust in the aggregate was below 3%, which allowed for it to be classified in the f_3 category, based on the PN-EN 12620 standard [53].

Sand obtained from the hydroclassification process performed in the Mineral Raw Materials Mine in Podwilcze, Białogard Commune, was used (1570 kg/m^3), together with Portland cement CEM II/A-V 42,5R (420 kg/m^3), silica dust (21 kg/m^3), superplasticiser FM series [54] (16.8 kg/m^3),and tap water (160 kg/m^3), in order to form the test elements. The fibre reinforcement comprised steel hook-end fibres (Figure 3) in the amount of 1.2% (94 kg/m^3) and with l/d ratio $\lambda = l/d = 62.5$ ($l = 50$mm, $d = 0.8$mm) [55].The steel fibres had ITB technical approval No. AT-15-295/1999 [56], in accordance with the PN-EN14889-1 standard [57].

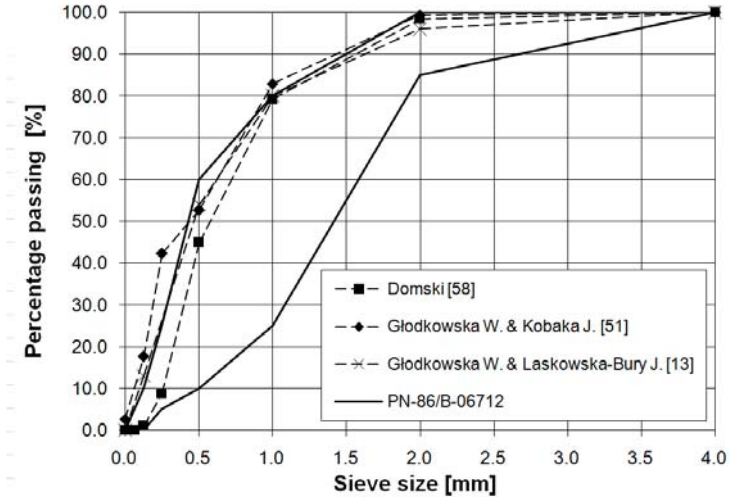

Figure 2. Grading curve of used aggregate and grading curves of other Pomeranianaggregates used in different research programs [13,51,58]. Reproduced with permission from ref. [52]; published by Middle Pomeranian Scientific Society of the Environment Protection, 2017.

Figure 3. Fibre dimensions and close-up look.

The fine aggregate composite matrix was designed through application of an analytical and experimental method. Modification of its composition by addition of silica dust and superplasticizer allowed us to obtain a w/c = 0.38 ratio. The fibres were placed in the composite mix at random. The technical characteristics of the steel fibres used in the tests are presented in Table 1.

The conditions of SFRWSC composing, care, and testing have been broadly described previously [11–13,51]. The mechano-physical properties of the analysed fibre composite with ordinary concrete are detailed below.

Table 1. Technical characteristics of the steel fibres used in the tests ([55,56]).

Pos.	Feature	Value	UoM
1	Structural group	I	-
2	Tensile strength	1160 ± 7	N/mm^2
3	Young's modulus	210,000	N/mm^2
4	Consistency by fibre content 14–15 kg/m^3, measured by application of Ve-be method	4	s
5	Impact on concrete strength at CMOD * = 0.5 mm	1.5	N/mm^2
6	Impact on concrete strength at CMOD * = 3.5 mm	1.0	N/mm^2

*—cut crack width according to PN-EN 14651 standard method [16].

When considering fibrecomposite structural elements, one should first of all take into account the method of their design. For a designer of building structures, a standard-defined property is necessary, which determines the material's ability to transmit tensile stresses after cracking, as provided by the manufacturer. Over the past 20 years, several proposals for a quantitative description of the behavior of cracked fiber-reinforced concrete under tensile conditions have been developed. The most common method for describing this property is given in the RILEM TC-162-TDF [39] recommendations. This method has been included in the European standard EN 14651 [16] and in the Model Code 2010 [17]. It consists of an experimental measurement of the relationship between the crack width (CMOD) and the load force on the bar in the middle of its span. The CMOD–Force relation determined as a result is used to define the so-called residual strengths: $f_{R,1}$, $f_{R,2}$, $f_{R,3}$, and $f_{R,4}$. The values of the residual strengths obtained in our tests are presented in Table 2. They denote the values of the tensile stresses in the cross-section for a given width of the CMOD crack, equal to 0.5, 1.5, 2.5, and 3.5 mm, respectively. The values of these strengths serve as the basis for the dimensioning of structural elements.

The Load– CMOD diagram resulting from residual strength test is depicted in Figure 4.

Table 2. Mechano-physical properties of the analysed fibre composite with ordinary concrete [12,14,51,59].

Property	Material		Methodology of Determination
	Fibrecomposite (with Coefficient of Variation)	Ordinaryconcrete	
Aparent density in dry condition: ρ, [kg/m^3]:	2290 (ν = 0.7%)	2000–2600	PN-EN 12390-7 [60]
Compression strength: $f_{c\ cyl}$, [MPa]	64.4 (ν = 6%)	12–50 (PN-EN 1992-1-1)	PN-EN 12390-3 [61]
Compression strength: $f_{c\ cube}$, [MPa]	67.6 (ν = 3%)	15–60 (PN-EN 1992-1-1)	
Split tensile strength: $f_{t\ spl}$ [MPa]	7.3 (ν = 8%)	3.0–3.7	PN-EN 12390-6 [62]
Static modulus of elasticity: E_{cm}, [GPa]	36.7 (ν = 7%)	29–37	PN-EN 12390-13 [63]
Dynamic modulus of elasticity: E_d [GPa]	45.9 (ν = 1%)	E_{cm} = 0.83 E_d	Neville A.M. [64]
Creep: ε_p, [‰]	0.26 (ν = 4%)	0.1–1.0	ITB 194/98 instructions [65]
Shrinkage: ε_{cs}, [‰]	0.88 (ν = 4%)	0.2–0.6	
Abrasion resistance: A, [cm^3/50 cm^2]	9.0 (ν = 7%)	1.5–22	PN-EN-13892-3 [66]
Residual strength: f_R, [MPa]	f_{R1} = 9.3 (ν = 13%)	Not applicable	PN-EN 14651 [16]
	f_{R2} = 8.8 (ν= 15%)		
	f_{R3}= 7.9 (ν = 15%)		
	f_{R4}= 7.0 (ν = 17%)		
Shear strength: τ, [MPa]	12.9 (ν = 8%)	-	JCI-SF6 [67]

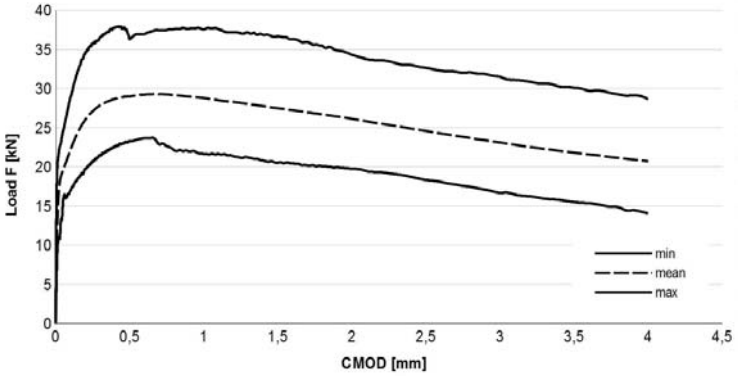

Figure 4. Load—CMOD relation for SFRWSC. Reproduced with permission from ref. [59]; published by Middle Pomeranian Scientific Society of the Environment Protection, 2015.

For easier interpretation of the test results, the graph boundaries (solid lines) and the mean force dependence on CMOD (dotted line line) are shown. The diagram shows a decrease in the destructive force as the CMOD value increases after the appearance of the first crack. The shape of the graph in Figure 4 indicates that the tested fibrocomposite shows the post-crack softening (pcs) feature. The obtained results clearly indicate the ductile nature of the SFRWSC with 1.2% fiber content. In accordance with the guidelines of the Model Code 2010 standard [17], the class of the tested SFRWSC was designated as 7b. It should be noted that the obtained values of the coefficient of variation (ν) given in Table 2, unlike the ν indices for the other properties of this material, are large. Unfortunately, tests of residual strength carried out with the use of beam elements are usually burdened with a large spread, amounting to an average of 20% [68] due to small bending areas in the beams, which has been confirmed in [69], among other works. Residual strength tests and their results have been discussed, in more detail, in [12,59].

It can be seen from Table 2 that SFRWSC with 1.2% steel fibre content has better or similar properties as ordinary concrete. The properties of this composite comply with the requirements formulated for structural materials; therefore, it may serve as a substitute for ordinary concrete. Partial substitution of concrete by the proposed fine aggregate composite with fibre reinforcement, featuring the same or better properties, provides a perfect solution for those regions that are short of natural coarse aggregate deposits. This will allow for regional aggregates to be used in a sustainable manner. Such actions will also contribute to the gradual depletion of sand dumps (Figure 1).

3. Methodology of Research and Test Elements

The test elements used in the shear capacity test are described in Figure 5 and Table 3. Additionally, test elements in form of cylinders (150 × 300 mm) and beams (150 × 150 × 700 mm) were made, in order to determine the fundamental properties of the proposed SFRWSC (Table 3).

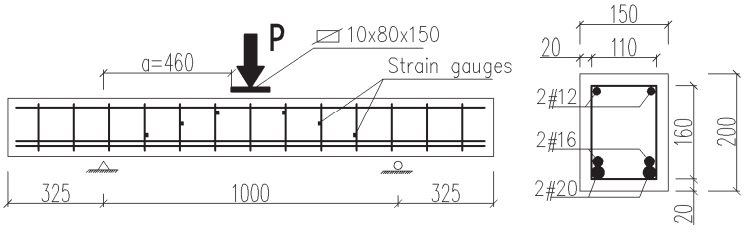

Figure 5. Specification of tested beams.

Table 3. Description of the test elements.

Beam Marking	Stirrups	Fibre
B (4 pcs.)	none	0%
BF (4 pcs.)	none	1.2%
BSa (4 pcs.)	#4.5 @ 120	0%
BSb (2 pcs.)	#4.5 @ 90	0%
BFSa (4pcs.)	#4.5 @ 120	1.2%
BF2b (2 pcs.)	#4.5 @ 90	1.2%

Composite properties:
f_c = 52.6MPa, f_{ct} = 3.3 MPa, f_{cf} = 64.4 MPa, f_{R1} = 9.27 MPa, f_{R2} = 8.80 MPa, f_{R3} = 7.87 MPa, f_{R4} = 6.98 MPa, E_{cm} = 36.7 MPa
Steel properties:
f_y = 529 MPa, f_t = 650 RMPa, E_s = 200 GPa, f_{yw} = 584 MPa, f_{tw} = 615 MPa

In order to ensure shear failure a relatively large number of rebars was used in the tension face (2#20 and 2#16. In order to avoid the arch effect and the significant impact of the longitudinal reinforcement on the shearing force, shearing section *a* (Figure 5) was determined in such a way that the shear *a/d* ratio was about 3. In B and BF series beams, reinforcement was intentionally located in the compressed area (2#12), due to its significant impact on the shear capacity. Such prepared beams were stored, until tested, for 28 days at 20 ± 2 °C temperature and 100% relative humidity conditions. After 30 days, the beams were loaded. The stand used for shear capacity testing of SFRWSC beams is presented in Figures 6 and 7.

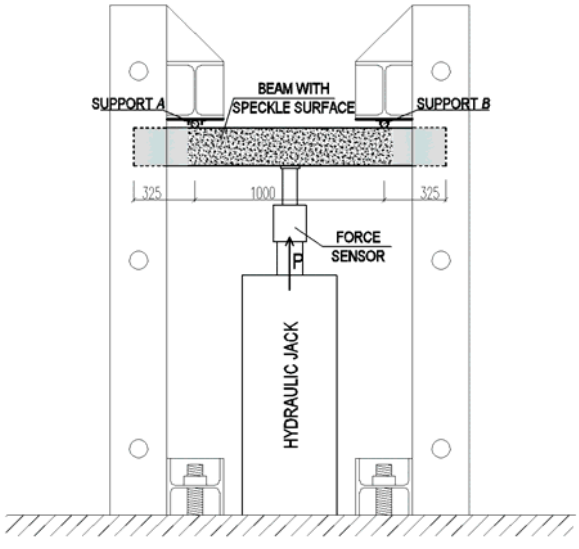

Figure 6. Schematic of experimental setup [44].

The beams were tested using specially designed experimental setup, in the configuration of a reversed freely supported beam (Figure 6). The beams were loaded at a constant speed of ~4 kN/min, until failure. Two measuring techniques were used in the test: The SAD-256 data acquisition system (APIG Ltd., Łódź, Poland) (Figure 7a) and the Aramis 4M system (GOM Ltd., Braunschweig, Germany) (Figure 7b). Measurements were performed periodically at 0.5 Hz frequency, from the moment of load application until beam destruction. The SAD-256 sensor arrangement used for the measurement of surface deformation of one beam side (Figure 7b) was designed in such a way that the recording

of deformations in the diagonal crack area was possible. The width of the cracks that were diagonal and perpendicular to the element axis, deformations of the second beam side surface, and deflections were measured using the Aramis 4M software (GOM Ltd., Braunschweig, Germany). To measure deformations of shear reinforcement, strain gauges were used, which were glued to the vertical parts of stirrups before concreting. Six strain gauges were used for each beam (i.e., three for each shear area). The beam loading force was recorded by a force sensor, located over the hydraulic jack, with 0.66 mV/V sensitivity. The beam span (Table 3) was selected in such a way that the shear failure at the first or second support could be recorded by the Aramis 4M (GOM Ltd., Braunschweig, Germany). Considering the adopted static arrangement, beam shear failure could occur within the first or second support area. For this reason, the beams were tested in two stages. In the first stage, the beam was subjected to loading until shear failure occurred. Then, the test was stopped, and the beam load reset. A steel corset, made of steel sections pulled into place by bolts (Figure 8), was put onto the failed shear area. The corset was intended to resist transversal forces in the fractured shear area in the second stage of the test. The beams with the steel corset were loaded until the second shear area failed.

(**a**) (**b**)

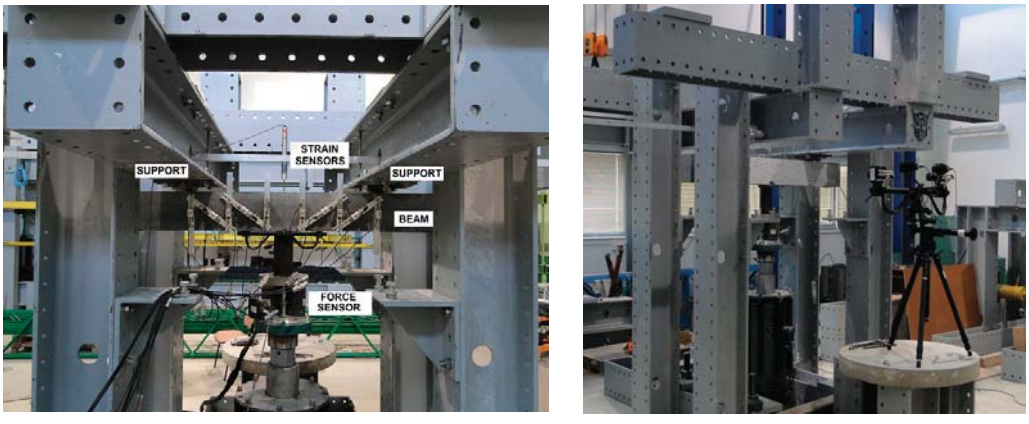

Figure 7. Stand for shear capacity testing of bend elements: (**a**) Beam side surface tested using SAD-256 system; and (**b**) beam side surface tested using Aramis 4M system [44].

Figure 8. Beam reinforced with steel corset after the first testing stage.

4. Test Results and Their Analysis

4.1. Shear Behaviour of Bending Infibre-Reinforced Concrete Beams

Having analysed the beam deformation maps obtained from the Aramis 4M system for various levels of loading, five stages of functioning under shear conditions could be distinguished for the SFRWSC.

When no cracks occur in a given element, longitudinal deformations of steel and fibre composite are the same. The element functions in the flexural phase until the tensile strength of the fibre composite is attained, as illustrated in Figure 9.

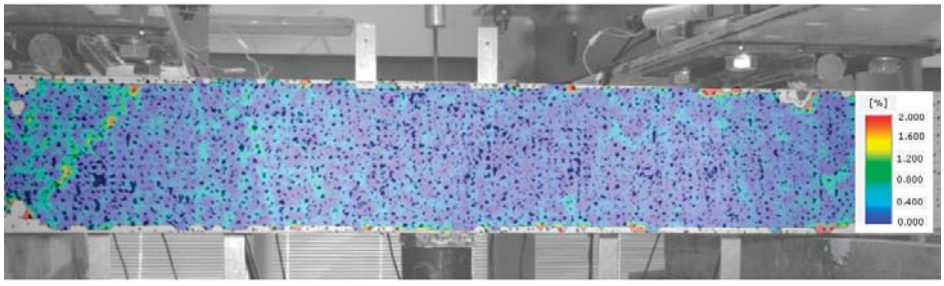

Figure 9. Stage I of shear behavior of element—no cracks.

Once the fibre composite tensile strength is exceeded, which corresponds to the occurrence of cracks, the beam starts functioning in stage II, as a cracked element. Cracks perpendicular to the element axis appear in the middle of its span. The beam functions in this phase until the diagonal tensile strength of the composite in the shear area is reached (Figure 10).

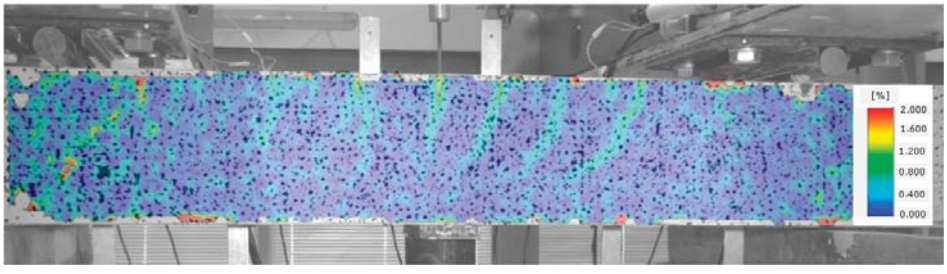

Figure 10. Stage II of shear behavior of element—flexural cracks have occurred.

In Figure 11, the occurrence of several diagonal cracks between the tensioned reinforcement and the compressed area of the cross-section of the analysed beam is already visible. At the same time, the direction of perpendicular cracks changes, slanting from perpendicular to diagonal position.

A subsequent increase in beam loading results in increased crack width in the existing cracks, which means that the element is now in stage IV. In the case of beams with strong shear reinforcement, subsequent diagonal cracks may occur at this stage. The diagonal cracks become longer and approach the main reinforcement area. In stage IV, a critical diagonal crack may also appear, depending on the element shear capacity. Reaching of the shear capacity is shown in Figure 12.

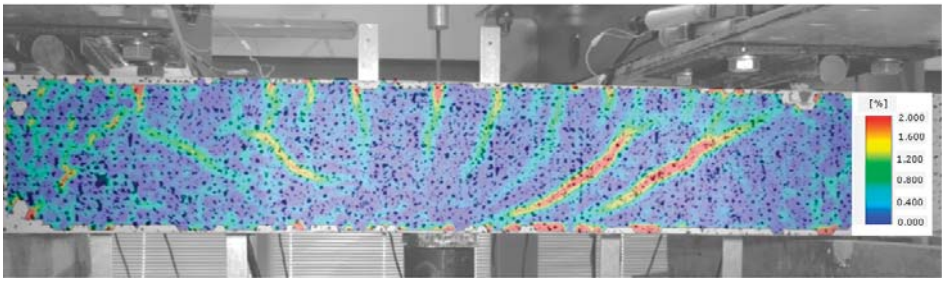

Figure 11. Stage III of shear behavior of element—occurrence of diagonal cracks in both shear areas.

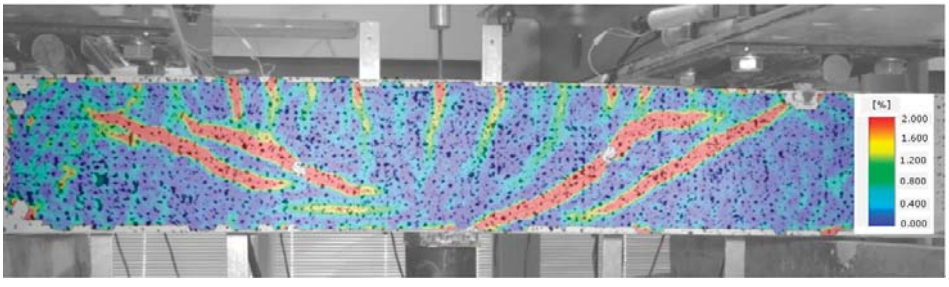

Figure 12. Stage IV of shear behavior of element—stabilization of the diagonal crack and arriving at the shear capacity.

Stage V is the stage of destruction of the element under shear force, through arriving at the composite diagonal compression strength (Figure 13). This type of destruction has been described, in [70], as a shear compression failure. It is observed in those beams that have strong main reinforcement with the simultaneous absence of or very poor transversal reinforcement. The cause of failure is a split fracture of the composite structure in the so-called compressed area (i.e., above the diagonal crack end), where a sort of pivot appears to occur.

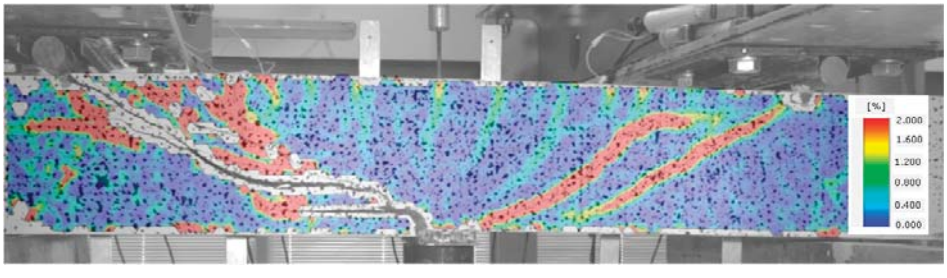

Figure 13. Stage V of shear behavior of element—shear compression failure of the beam.

Beam failure, due to loss of adhesion of the fibre composite to the reinforcement originating from elongation of the longitudinal crack at the main reinforcement height, is illustrated in Figure 14.

Beams with strong shear reinforcement (BFSb series) were destroyed due to their arriving at the yield point of the tensioned reinforcement (Figure 15). The load shear capacity of an element is decided by its most strained and/or weakest cross-section. However, cracks originating in various element cross-sections are very important for its deformation, as they have an impact on rigidity of the entire element.

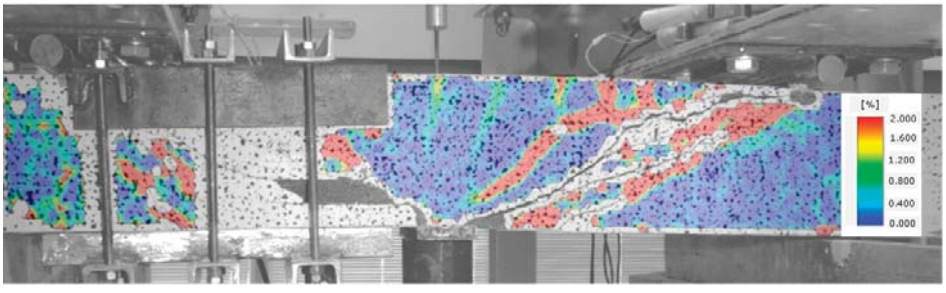

Figure 14. Stage V of shear behavior of element—shear tension failure of the beam.

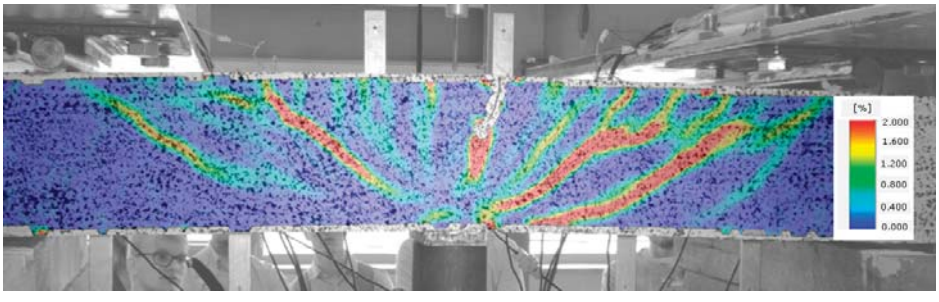

Figure 15. Stage V of shear behavior of element—element bending failure through yielding of the tensioned reinforcement.

The application of steel fibres led to the failure images of SFRWSC beams shown above having a more ductile character, compared to fine aggregate cement composite beams without fibre reinforcement. The shear force–deflection relation, in the first stage of the test (pt. 3), is illustrated in Figure 16.

An analysis of Figure 16 clearly indicates the influence of steel fibers on the bearing capacity of the beams made of fine-aggregate fibre-composite near the support zone, and on the nature of the work of the beams after the appearance of the first diagonal crack. In the B series beams (without stirrups and steel fibers), when the crack appeared, the loading force remained at the same level. The appearance of successive diagonal cracks resulted in temporary load drops. However, in the remaining beams with shear reinforcement (stirrups and steel fibers), after the appearance of a diagonal crack, the load continued to increase and no decrease in the loading force was observed at the time of appearance of subsequent cracks. Both the stirrups and steel fibers affect this behavior of the beams, where the steel fibers can "bridge" cracks by transferring tensile stresses. In addition, the addition of steel fibers reduced the brittle nature of the material more effectively than stirrups. Analyzing the slope of the force (V)–deflection (δ) curves shown in Figure 16, it can be concluded that the steel fibers affected the bending stiffness, but the impact was not significant; which has been confirmed, in [15], in the case of elements with a high degree of main reinforcement. Yoo [71] and Ashour [72] also came to similar conclusions. It should be emphasized that, despite the slight influence of the addition of steel fibers on the stiffness, the final values of deflections at the maximum transverse force were much greater for beams reinforced with stirrups and steel fibers (approx. 13 mm), compared to those without fibers and stirrups (approx. 7 mm). The deflection values for the BF (with fibres) and BSa (with stirrups) series elements were similar, amounting to approx. 10 mm.

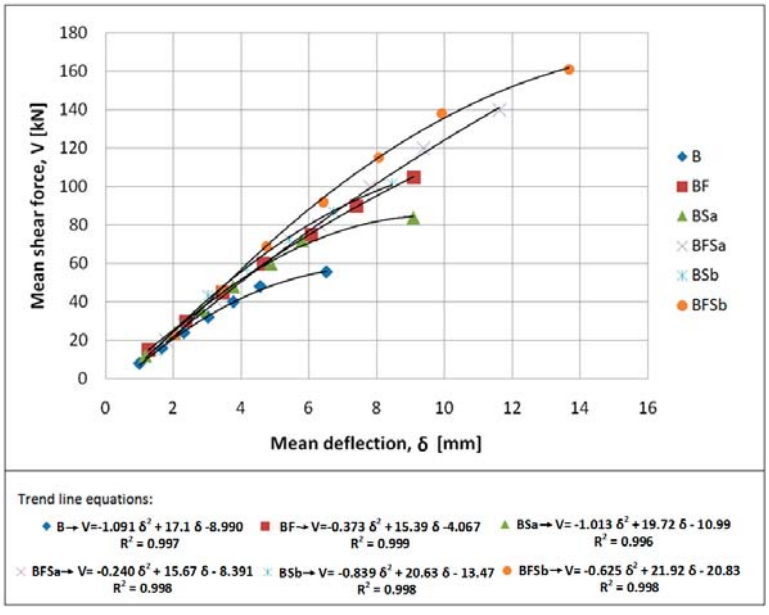

Figure 16. Relation between mean shear force and mean deflection for tested beams.

4.2. Beam Failure Models and Experimentally Determined Shear Capacity

Various failure models were observed during the tests, depending on the type of shear reinforcement and the combinations (Table 3) that were used [44]. The failure of B beams (without shear reinforcement) and beams having only fibre reinforcement (BF beams) had a shear tension character (Figure 17). Once the first diagonal cracks appeared, one increased its width as the load was increased. A number of small cracks occurred at the main reinforcement level, which means that gradual loss of the main reinforcement adhesion to the fibre composite occurred. Consequently, the depletion of shear capacity of such elements resulted from the main reinforcement steel slide at the place of anchoring on the support.

Figure 17. Example of a shear tension failure in the shear area of BF series beams.

In the case of BFSa series beams (elements with 120 mm stirrup spacing), the failure was similar to that described above, but with the diagonal tension failure feature. Such a failure mode resulted from the high shear capacity of BSFa beams, and occurred in the case of beams with insufficient flexural reinforcement over their entire span. In this case, the

flexural reinforcement steel yield point was observed not in the middle of the element span, but at the section of the simultaneous action of the bending moment and transversal force. This resulted in an increase in width of one of the diagonal cracks, leading to its elongation and penetration into the compressed cross-section area. This crack caused, in effect, the crashing of concrete in the cross-section above the crack. Therefore, for this beam series, the second test stage—which was aimed to define the shear capacity of the undamaged shear area—failed. In this particular case, the beams failed because of bending (Figure 18). In most cases of BFSa series beams (featuring greater stirrup spacing equal to 120 mm) and BSa series beams (with stirrup spacing of 120 mm, no steel fibres added), the stirrups through which the diagonal crack passed had fractured. In the destruction of BFSb series beams (stirrups spaced at 90 mm), which showed the highest shear capacity, failed due to yielding of the flexural reinforcement (flexural failure). Finally, due to high deformation, the compressed area of the element crashed. In effect, a secondary shear failure of the diagonal tension type occurred (Figure 19).

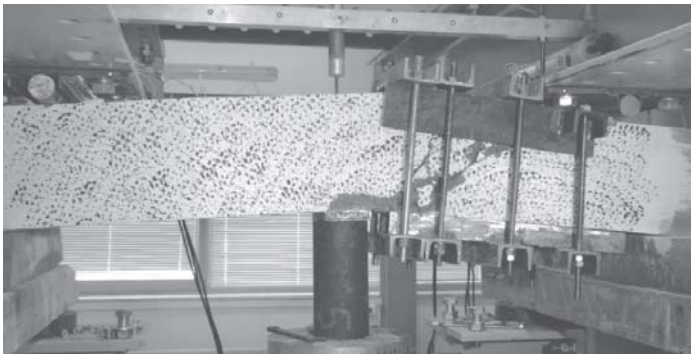

Figure 18. Typical secondary failure of a BFSa series beam.

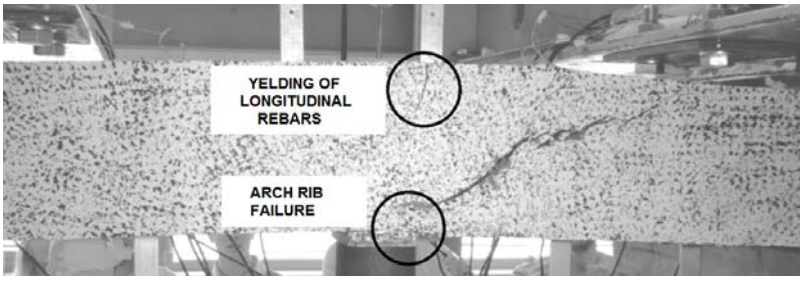

Figure 19. Example of a secondary BFSb series beams failure.

Table 4 shows the mean values of forces V_{cr} (shearing force at which a diagonal crack occurs) and V_{ult} (the ultimate shear force) obtained from tests for particular beam series.

Table 5 shows the effects of reinforcement of SFRWSC beams obtained in the tests.

The highest values of the shear force (V_{cr}), for which the initial diagonal cracking has been observed, and the ultimate shear force (V_{ult}) were observed for the beams reinforced with both stirrups and steel fibres. The reduction of stirrup spacing from 120 mm to 90 mm contributed to an increase in the shear capacity of elements by 23%, on average, for the beams without fibres, and 13% for the beams with fibres. The analysis of the results obtained for the beams reinforced only with stirrups and only with steel fibres led to the conclusion that slightly higher carrying capacities occurred in the case of the beams without stirrups. Compared to BFSa beams, the tested forces, V_{ult}, were lower by 40% for BSa beams and by 26% for BF beams. Despite the fact that addition of the second type of

shear reinforcement provided a lesser reinforcement effect (see Table 5), the impact of steel fibres and stirrups on the shear capacity added up, which originated from the results for BFSa and BFSb series beams. Similar conclusions have also been drawn by other authors, who analysed the co-operation of stirrups with steel fibres in resistance to transversal forces [21–23,73].Our research also showed that fibre reinforcement had an advantageous impact on the occurrence of the first diagonal crack, in comparison to those beams that contained no steel fibres. The value of the transversal cracking force (V_{cr}) in the fibre composite elements was higher (by approximately 38%), compared to the beams without fibre reinforcement. In beams of BF, BSa, and BFSa series, the ratio of the cracking force (V_{cr}) to the ultimate shearing force (V_{ult}) was constant and amounted to approximately 0.56. The insignificant increase in V_{ult}, compared to V_{cr}, for B series beams originated from the fact that the shearing force was reduced by occurrence of the so-called "dowel action", engaging the aggregate and the compressed area.

Table 4. The mean values of forces V_{cr} and V_{ult} for particular beam series.

Beam	V_{cr} [kN]	Standard Deviations [kN]	V_{ult} [kN]	Standard Deviations [kN]	V_{cr}/V_{ult} [-]
B	44.28	16.42	55.57	19.40	0.80
BF	61.00	22.53	106.25	37.04	0.57
BSa	47.18	17.30	84.21	29.19	0.56
BFSa	79.93	31.31	140.27	57.92	0.57
BSb	45.29	7.08	103.32	4.27	0.43
BFSb	64.78	16.86	161.2 *	-	0.40

*—flexural failure.

Table 5. Increase coefficients for particular beam series.

	Increase Coefficient					
Beam	$V_{ult}/V_{ult}{}^{B}$	$V_{ult}/V_{ult}{}^{BF}$	$V_{ult}/V_{ult}{}^{BSa}$	$V_{ult}/V_{ult}{}^{BFSa}$	$V_{ult}/V_{ult}{}^{BSb}$	$V_{ult}/V_{ult}{}^{BFSb}$
B	1.00	0.52	0.66	0.40	0.53	0.34
BF	1.91	1.00	1.26	0.76	1.03	0.66
BSa	1.51	0.79	1.00	0.60	0.82	0.52
BFSa	2.52	1.32	1.67	1.00	1.36	0.87
BSb	1.86	0.97	1.23	0.74	1.00	0.64
BFSb	>2.90	>1.52	>1.91	>1.13	>1.56	1.00

Consequently, our research work demonstrated that the addition of steel fibres to SFRWSC had an enormous impact on the resistance to transversal forces. It increased the shear capacity by approximately 90% in beams with no stirrups and that by approximately 65% in beams with stirrups. The fibre functioning character in the shear area was more beneficial than stirrup action, due to more ductile character of the material. An example of dependence of the side surface strain at element height (ε_y) on the transversal force (V) is shown in Figure 20.

We also ascertained that the impact of steel fibres and stirrups added up, in terms of resistance to transversal forces, in order to increase the element shear capacity. Furthermore, it was found that the concentration of stirrups had no significant impact on the cracking force (V_{cr}), for the beams with fibres and without. Similar results have also been obtained by Lim and Oh [74]. We also found that, as the shear capacity of BF and BSb series beams was comparable, stirrups #4.5 spaced at 90 mm intervals reinforced the beams to the same degree as the content of steel fibres amounting to 94 kg/m^3 (1.2%).

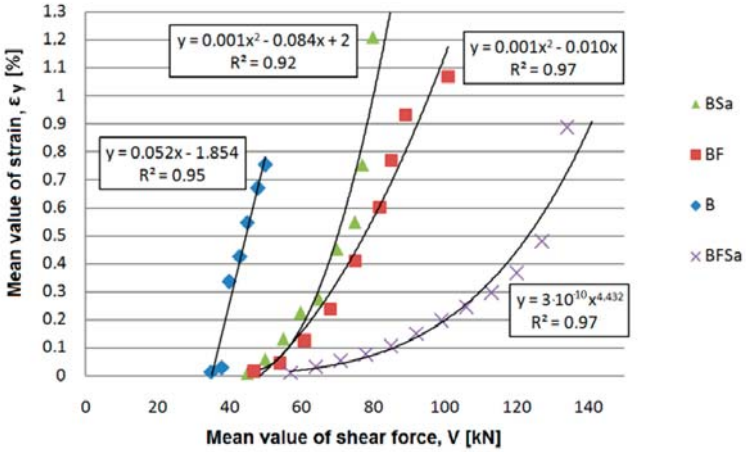

Figure 20. An example of dependence of the side surface strain at element height (ε_y) on the transversal force (V) for B, BSa, and BF series beams at the first stage of the test.

4.3. Diagonal Cracks

The dependence of the shear force (V) on the width of the diagonal crack opening (w) in beams made of SFRWSC is shown in Figure 21. For elements reinforced with fibres (BF series) a higher cracking force than that in beams reinforced with stirrups (BS series) was noted, which may have a beneficial impact, in terms of reduction of the shear span requiring shear reinforcement. Curves describing the dependence of the transversal force on the width of the diagonal crack opening for beams with fibre reinforcement (BF series) and reinforced only with stirrups (BS series) featured a similar angle of inclination to the horizontal axis. Such a course of the curves, as shown in Figure 16, indicates the similar functions of steel fibres and stirrups after element cracking. At the same time, in the case of BFS series beams (reinforced with stirrups and steel fibres), the effects of the fibres and stirrups add up, as indicated by the slow increase in the crack opening width (w) with increasing transversal force value (V). It should be noted that the maximum width of the diagonal crack opening in BFS-type elements was significantly lower than that observed in BF and BS series beams. This resulted in a higher number of cracks in BFS-type elements, where the shear reinforcement was provided by stirrups and steel fibres. Ultimately, it can be stated that fibres have strong impact, not only on the shear capacity of SFRWSC elements, but also on their diagonal cracking. Comparing the test results obtained for BF and BS series beams, it can be stated that the same values of crack widths occurred at higher transversal force values (by approximately 40%) for the beams containing fibres. It should be noted that the V-w curves for BF and BS elements featured a similar angle of inclination to the horizontal axis, which may indicate a similar mechanism of resistance to transversal force after cracking by stirrups and steel fibres.

The highest number of cracks for one shear area was observed in beams reinforced with stirrups and fibres: either 3 or 4. For beams with only fibres, the number of cracks was similar to that for beams with only stirrups: 2 or 3, on average. The presence of greater number of cracks simultaneously resulted in smaller crack widths. For beams with stirrups and fibres, the opening width of diagonal cracks did not exceed 1 mm, while that for beams with only fibres was, on average, 1.25 mm.

In summary, in terms of diagonal cracking, the elements containing steel fibres and stirrups behaved best, as an increase in force caused a considerably lower increment of crack opening width, where as a constant value was observed in the case of beams reinforced with fibres (BF) or stirrups (BS).

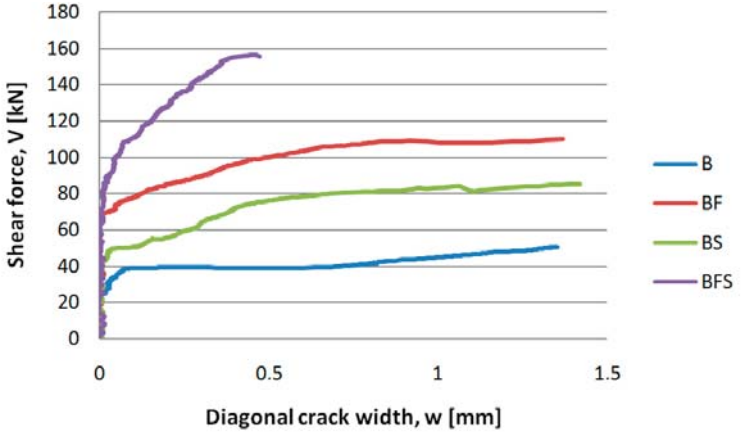

Figure 21. Shear force (V) versus diagonal cracks opening width (w) for selected B, BF, BS, and BFS series beams.

5. Computational Analysis

The shear capacity of beams made of SFRWSC was computed through the application of two methods—those of RILEM TC-162-TDF [39] and Model Code 2010—using the SMCFT [17] method for the second approximation levels, as well as the former method. The objective of this computation was to prove the applicability of European standards for shear design of fibre concrete cross-sections; that is, to verify whether Model Code and RILEM can be used in the shear design of SFRWSC cross-sections.

Average values of features of SFRWSC with and without steel fibres, as well as average values of features of reinforcing steel, were used in the computations (Tables 2 and 3). Values of the axial tensile strength of SFRWSC were determined using the relationship of Amin and Foster [75], which allows for the transformation of residual strengths to axial tensile strengths. The angle of inclination of compression struts (θ) for the SMCFT [17] method was assumed as the minimum; whereas, for the two other methods (RILEM and Model Code 2010—former method), it was $\theta = 30^{\circ}$. Safety coefficients in the shear capacity computations were as follows: $\gamma_f = \gamma_c = 1.0$.

To determine the shear capacity of BSa and BSb series beams through application of the SMCFT method, the second level of approximation was used for elements containing steel fibres, with the method for computation of the coefficient k_v taking into account the share of the maximum aggregate grain [17]. To determine the total shear capacity (V_{Rd}), notation for the third level of approximation was used, taking into account the influence of the cross-sectional shear capacity in the element without transversal reinforcement($V_{Rd,c}$), as well as the shear capacity due to transversal reinforcement ($V_{Rd,s}$).

To assess the usability of the RILEMTC-162-TDF and Model Code 2010 methods to determine the shear capacity of elements made of SFRWSC, the criterion of Baghi and Barosso [76] was used. The comparative quantity in this criterion is the ratio of the value of the experimentally fixed shear capacities (V_{exp}) to computational values (V_{cal}). The shear capacity assessment criteria are shown in Table 6 and Figures 22–27.

Table 6. The criteria for assessment of experimentally fixed (V_{exp}) and computational (V_{cal}) shear capacity values [76].

V_{exp}/V_{cal}	Classification
<0.5	Extremelydangerous
[0.5–0.85]	Dangerous
[0.85–1.15]	Appropriate Safety
[1.15–2.0]	Conservative
≥2.0	Extremely Conservative

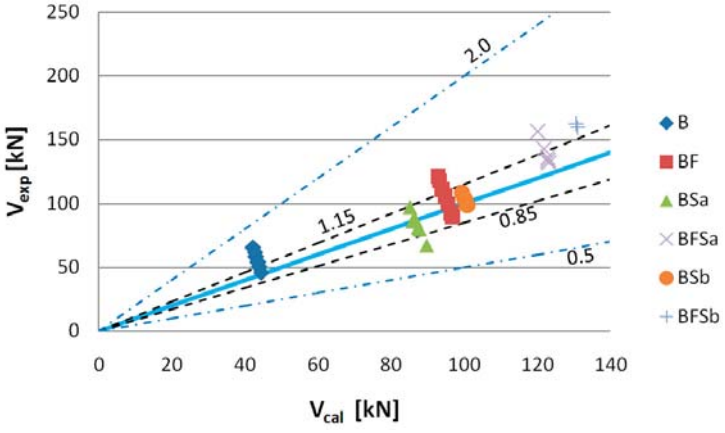

Figure 22. Values of experimentally fixed (V_{exp}) versus computational (V_{cal}) shear capacity determined according to Model Code using the SMCFT method (θ = min θ).

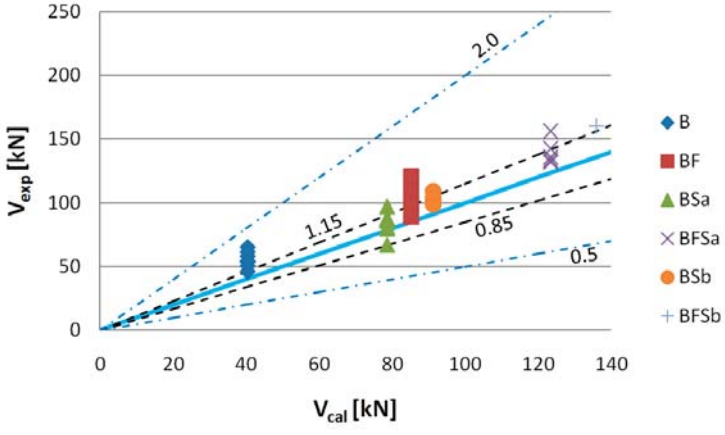

Figure 23. Values of experimentally fixed (V_{exp}) versus computational (V_{cal}) shear capacity determined according to the former method Model Code 2010 (θ = 30°).

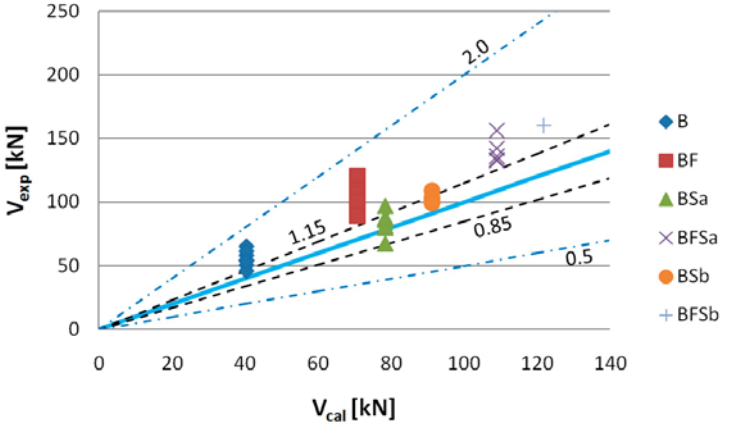

Figure 24. Values of experimentally fixed (V_{exp}) versus computational (V_{cal}) shear capacity determined according to the RILEM TC-162-TDF method (θ = 30°).

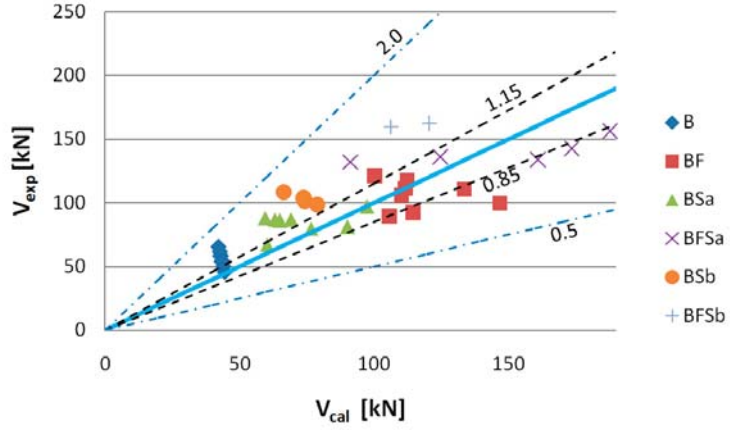

Figure 25. Values of experimentally fixed (V_{exp}) versus computational (V_{cal}) shear capacity determined according to the former Model Code 2010 SMCFT method (measured angle θ).

The experimentally determined shear capacity values (V_{exp}) are set, in Figure 22, together with the analytically determined (V_{cal}) values based on the FIB Model Code 2010 using the SMCFT method. After analysis of the graph, it can be stated that the theoretical shear capacity values for B and BFSb series beams are lower than those which were determined experimentally. The computational shear capacity values for B series beams at 75%, as well as those for BFSb beams at 100%, fit into the "conservative" classification interval (Table 6). The best compatibility with the V_{exp} = V_{cal} straight line occurred for BSa and BSb series elements, for which the percentages of results complying with the "appropriate safety" criterion were 88% and 100%, respectively. The computational shear capacities for BF and BFSa series beams were classified as 50% within the 0.85–1.15 interval and 50% within the 1.15–2.0 interval.

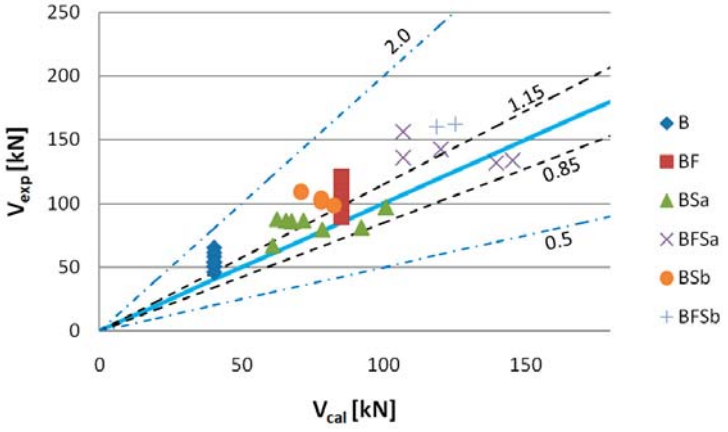

Figure 26. Values of experimentally fixed (V_{exp}) versus computational (V_{cal}) shear capacity determined according to Model Code 2010 (measured angle θ).

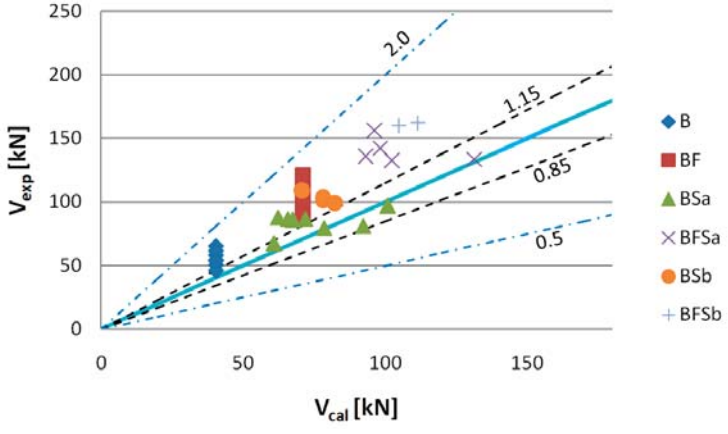

Figure 27. Values of experimentally fixed (V_{exp}) versus computational (V_{cal}) shear capacity determined according to RILEM TC-162-TDF (measured angle θ).

Figure 23 shows values of shear capacity V_{exp} to V_{cal}, computed according to the former Model Code method. The results obtained show that the shear capacities for B series beams were much lower than the experimental shear capacity values. It appears, from our analysis, that 88% of the shear capacity results should be treated—in accordance with the adopted criterion—as "conservative". The values of shear capacity calculated for BSa and BSb series beams were close to those determined by application of the SMCFT method. In this case, the shear capacity values were qualified as being "appropriate safety". The highest discrepancies were observed for the shear capacity values of BF series beams calculated by application of the SMCFT method. A total of 75% of beam shear capacity values were classified within the 1.15–2.0 interval (Table 6). Having applied the former Model Code method, it is clear that the impact of steel fibres on the shear capacity of SFRWSC beams is lower.

Figure 24 shows the values of shear capacity V_{exp} to V_{cal}, computed according to the RILEM TC-162-TDF method. Having analysed the shear capacity computation results, we have found that, when using this method, the highest discrepancies between the computational and experimental shear capacity values were obtained, where the highest

discrepancy was observed for BF series beams. In this case, 100% of the shear capacity values were classified as "conservative". The impact of steel fibres on shear capacity fell into the1.15–2.0 interval (Table 6) for BFSa and BFSb series beams, making them also less effective. The computational shear capacity values, determined by application of the former Model Code method with adoption of the same shear capacity computational algorithm as in EC-2 [77], for elements containing no shear reinforcement and all beams with stirrups, overlapped. It should also be pointed out that Figures 25–27 show shear capacity values for BFSb series beams, despite their bending failure; however, assuming that shear force acting together with the destructive momentum is the minimum experimentally fixed shear capacity (this has been indicated by stirrups functioning in BFSb beams, as described below), it can be stated that the highest V_{exp} to V_{cal} differences occurred with the RILEM method (difference min. 33%), compared to the former Model Code method (min. 20%) and the SMCFT method (min. 5%). Large differences in shearing capacity values obtained by application of the RILEMTC-162-TDF method have also been confirmed by other authors, such as Matthys [78], Parmentier [41], and Arslan [79,80].

Figures 25–27 show comparisons of the experimentally fixed shear capacity values for SFRWSC beams with the values computed using the RILEM TC-162-TDF method [39], Model Code 2010 [17] using the SMCFT method, and the former method. The adoption of real (obtained from tests) angles θ caused a significant computational discrepancy in the shear capacity values. The SMCFT method (Figure 25) requires particular attention; in this method, the angle θ is used not only for computation of the shear capacity of beams with stirrups, but also in the elements containing only fibres. In this case, the majority of shear capacity values computed for BF series beams were higher than the shearing capacity values found experimentally, causing an opposite situation than if the minimum value of angle θ was adopted. Three of the determined shear capacity values qualified as "dangerous" (Table 6). A similar situation occurred in the case of BSa series beams, when using the RILEM and former Model Code methods. In the remaining cases, particularly for extremely high values of angle θ, the computational values of shear capacity were higher (even by 50%).

For better interpretation purposes, and for assessment of the computed shear capacity values determined using the minimum and measured angle θ, the Integral Absolute Error (*IAE*) index was used. Having analysed *IAE* indices for $\theta = min$ and $\theta = 30^{\circ}$, the best compatibility was observed for BSa and BSb series beams, particularly in the case of the SMCFT method. In this case, the *IAE* index value did not exceed 10%. For BF series beams, the SMCFT method also showed the best compatibility (equal to 15%). The worst compatibility (exceeding 30%)was obtained with the RILEMTC-162-TDF method. *IAE* indices for BFSa and BFSb series beams had the lowest values with the Model Code 2010 method (12% and 16%, respectively); whereas, with the RILEM method, they exceeded 20%. The RILEMTC-162-TDF method, when analysed by other authors [78–80], also indicated significant discrepancies, with respect to computed values.

The IAEs for the measured angle θ criterion were higher, which can also be confirmed through observation of Figures 25–27. A conclusion can be drawn here: the adoption of a proper angle of inclination for the concrete and SFRWSC compression struts constitutes a key aspect in the determination of shear capacity. A large spread of measured angles θ resulted in higher *IAE* index values. To illustrate the impact of angle θ on the computational shear capacity values, values of V_{exp}/V_{cal} were analysed, comparing them with the compression strut inclination angles observed during testing (Figure 28). In this analysis, only the SMCFT method was considered, in which the angle θ (apart from the stirrup shear capacity) has an impact on the shear capacity of the fibres alone. From Figure 25, it is apparent that, with an increase in the compression strut inclination angle, the shear capacity values decreased. The highest values of V_{exp}/V_{cal} occurred for angles θ exceeding 35°, where the computational shear capacity value was lower than the experimentally fixed value by anywhere from 25% to over 50%. For the lowest angles θ, the situation was opposite, and the theoretical shear capacity values were exorbitant. However, in

this case, the maximum difference was approximately 30%. A conclusion can be drawn here: assuming the tested SFRWSC, computation using high angle θ values results in considerable underestimation of the shear capacity $V_{Rd,s}$, even in the event of an actual occurrence of such an angle. This has happened to appear in all beams with a high degree of shear reinforcement (BSb and BFSb series beams). The best compatibility ($V_{exp}/V_{cal} = 1$) was obtained when the angle fell within the interval of 20° to 32° for BF, BSb, and BFSa series beams. At this point, it should be noted that, in the case of beams containing only fibres, the best compatibility was achieved when the real angle was equal to 25°. This is a very important conclusion because, according to the analytical method proposed by the Model Code, the minimum angle of inclination of compression struts calculated for those beams was approximately 33°. The tests and computations performed further indicate a necessity to correct the procedure of computation for the minimum angle inclination value for compression struts, according to the SMCFT method, for the tested SFRWSC. This was indicated through analysis of the real and minimum angles θ, as well as the impact of the real angle θ on the experimentally fixed and computed shear capacity values for SFRWSC (Figure 28).

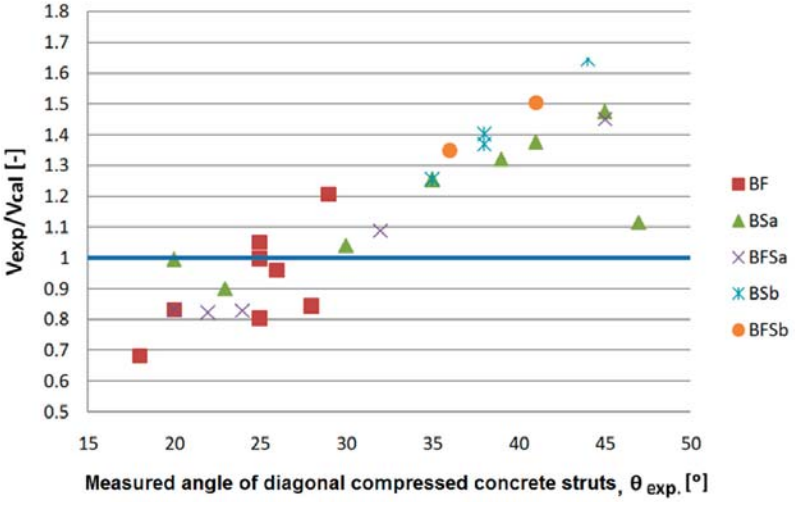

Figure 28. V_{exp}/V_{cal} values versus values of the measured angle of compression struts inclination (exp. θ) obtained in the tests.

6. Conclusions

Experimental testing and computation of the shear capacity of reinforced concrete elements, made using a novel fine aggregate composite with and without steel fibres, allowed us to formulate the following conclusions:

(1). The fine aggregate concrete composite without steel fibres behaves like ordinary concrete, as a typical flexural element with conventional steel rebars. The computation results for the shear capacity of such elements using the RILEM and Model Code 2010 methods are fully satisfactory.

(2). According to the ultimate limit stage of shear capacity, fibre reinforcement in SFRWSC beams considerably contributes to the resistance of shearing forces and increases the shearing capacity (amounting to approximately 80%, compared to elements without shear reinforcement).

(3). The functional character of steel fibres in the shear area is better than that of stirrups, due to their more ductile material character. This conclusion was confirmed by the dependence of the transversal force (V) on deformations (ε), determined at the side beam surface at its height. The effects of steel fibres and stirrups add up, in terms of

resistance to transversal forces, both in the aspect of increasing the shear capacity, as well the element deformability.

(4). Steel fibres at an amount of 1.2% in SFRWSC affect the occurrence of diagonal cracks. Diagonal cracks in beams with fibres appeared at higher transversal force values than in the case of elements without fibres. The diagonal crack analysis showed that the shear crack force was approximately 57% of the ultimate shear force. Thus, the steel fibres contribute not only to increasing the shear capacity, but also to the increase inthe shear crack force.

(5). The addition of 1.2% steel fibres considerably improves the shear capacity of SFRWSC elements. This allows for the reduction of conventional reinforcement in such elements. Due to the high residual tensile strength (f_{Ftu}) of fibre-reinforced concrete, the analysed SFRWSC does not require minimum reinforcement in the form of stirrups, as indicated by the following formula:

$$f_{Ftu} = 2.18 \text{ MPa} > 0.08 \cdot \sqrt{f_c} = 0.6 \text{ MPa} \quad (1)$$

(6). With regard to elements made of SFRWSC, the shear capacity values computed using the RILEM and Model Code 2010 methods were higher than the experimentally determined values. The obtained results indicate a necessity for correction of these methods, in order to apply them to the shear design of elements made of SFRWSC. Other researches who have been working on classical fibre-reinforced concrete have arrived at similar conclusions. Furthermore, the computation procedure using the minimum angle of inclination of compression struts, according to the SMCFT method, in terms of the tested fibre-reinforced composite, requires correction, due to great differences between the measured and computed angle values. What the authors consider as the further direction of research and analysis.

(7). Considering the mechano-physical properties of SFRWSC and the shear capacity test results presented in this paper, as well as the flexural capacity values for beams made of this fibre-reinforced composite, as described in [15,36], the assumption can be made that this material can successfully be used as a structural material. The developed SFRWSC, the properties of which comply with the requirements set for structural materials, could be used as an alternative solution for ordinary concrete in some applications, providing an opportunity to utilise the waste sands piled in Pomerania (Poland), in the Middle East, or in North Africa.

The conclusions presented in the article should not be generalized. Experimental tests and calculations were carried out for an innovative SFRWSC with a grain size of up to 2 mm, a specific cross-section of beams, the amount of longitudinal and transverse reinforcement and a static scheme. The obtained results of the research and the conducted literature studies in the field of the subject of the presented work allowed for the formulation of further research directions. The use of numerical modeling to predict the behavior of beams with different static patterns, for different types of element cross-sections, values of classical and fiber reinforcement, variable a/d shear slenderness, or various actions and their combinations is one of them. Thus, the analyzes will provide a large number of results that cannot be registered in an experiment with a measuring apparatus. Moreover, numerical analyzes will allow to identify the necessary areas for further experimental research and to introduce changes in the experimental program in order to improve the applied model. Due to the highly non-linear nature of the analyzed shear process in the fiber-reinforced concrete elements and the analysis until failure, it will be advantageous to use a quasi-static calculation strategy.

Author Contributions: Conceptualization, W.G.; data curation, M.L.; methodology, W.G. and M.L.; formal analysis, W.G. and M.L.; software, M.L.; validation, W.G.; investigation, M.L.; writing—original draft preparation, W.G. and M.L.; writing—review & editing, W.G.; visualization, M.L.; supervision, W.G.; resources, M.L.; project administration, W.G. All authors have read and agreed to the published version of the manuscript.

Funding: This research received no external funding.

Institutional Review Board Statement: This study was not carried out on humans or animals.

Informed Consent Statement: Not applicable.

Data Availability Statement: The data presented in this study are available on request from the corresponding author.

Conflicts of Interest: The authors declare no conflict of interest.

Nomenclature

CMOD	Crack Mouth Opening Displacement
SFRWSC	Steel Fibre Reinforced Waste Sand Concrete
SMCFT	Simplified Modified Compression Field Theory
Ecm	static modulus of elasticity
Ed	dynamic modulus of elasticity
Es	modulus of elasticity of longitudinal steel rebars
Gd	dynamic modulus of rigidity
Vcr	shear crack force
Vcal	calculated shear capacity
Vexp	experimental shear capacity
VRd	shear capacity
VRd,c	specimen's shear capacity without shear reinforcement
VRd,s	shear capacity increase due to conventional shear reinforcement
Vult	ultimate shear force
δ	deflection
εy	mean value of strain
θ	compression strut angle
ν	coefficient of variation
a	shear span,
d	effective depth of beam
fc,f	fibre-reinforced composite compression strength
fc	fibre-less composite compression strength
fct	fibre-less composite tensile strength
fFtu	residual tensile strength of fibre-reinforced concrete defined for wu = 1.5 mm
fR,1 fR,2 fR,3 fR,4	residual strengths determined in accordance with relevant standard for CMOD = 0.5 mm, 1.5 mm, 2.5 mm, and 3.5 mm
fy	longitudinal reinforcement steel yielding strength
fyw	shear reinforcement (stirrups) steel yielding strength
ft,spl	split tensile strength
ft	tensile strength of longitudinal steel rebars
ftw	tensile strength of shear reinforcement (stirrups)
s	standard deviation
w	crack width

References

1. Yazici, S.; Inan, G.; Tabak, V. Effect of aspect ratio and volume fraction of steel fiber on the mechanical properties of SFRC. *Constr. Build. Mater.* **2007**, *21*, 1250–1253. [CrossRef]
2. Teng, T.-L.; Chu, Y.A.; Chang, F.A.; Shen, B.-C.; Cheng, D.-S. Development and validation of numerical model of steel fiberreinforced concrete for high-velocity impact. *Comput. Mater. Sci.* **2008**, *42*, 90–99. [CrossRef]
3. Wang, Z.; Liu, Y.-S.; Shen, R.F. Stress–strain relationship of steel fiber-reinforced concrete under dynamic compression. *Constr. Build. Mater.* **2008**, *22*, 811–819. [CrossRef]
4. Hu, H.; Papastergiou, P.; Angelakopoulos, H.; Guadagnini, M.; Pilakoutas, K. MechanicalpropertiesofSFRCusingblendedmanufacturedandrecycledtyresteelfibres. *Constr. Build. Mater.* **2018**, *163*, 376–389. [CrossRef]
5. Ibrahim, S.M.; Abadel, A.A.; Almusallam, T.; Al-Salloum, Y. Modeling of steel fiber reinforced concrete (SFRC) under dynamic compression. In Proceedings of the Conference: 8th International Conference FIBRE CONCRETE 2015, Prague, Czech Republic, 10–11 September 2015.

6. Li, C.; Zhao, M.; Zhang, X.; Li, J.; Li, X.; Zhao, M. Effect of Steel Fiber Content on Shear Behavior of Reinforced Expanded-Shale Lightweight Concrete Beams with Stirrups. *Materials* **2021**, *14*, 1107. [CrossRef] [PubMed]
7. Lim, S.; Matsuda, M.; Ahmed Raju, R.; Akiyama, M. Flexural Behavior Prediction of SFRC Beams using Finite Element Method and X-ray Image. *Trans. Jpn. Concr. Inst.* **2020**, *39*, 1099–1104.
8. Goremikins, V.; Blesak, L.; Novak, J.; Wald, F.A.E. Experimental investigation on SFRC behaviour under elevated temperature. *J. Struct. Fire Eng.* **2017**, *8*, 287–299. [CrossRef]
9. Domski, J.; Zakrzewski, M. Deflection of steel fiber reinforced concrete beams based on waste sand. *Materials* **2020**, *13*, 392. [CrossRef]
10. Dupont, D.; Vandewalle, L. Distribution of steel fibres in rectangular sections. *Cem. Concr. Compos.* **2004**, *27*, 391–398. [CrossRef]
11. Głodkowska, W.; Kobaka, J. Modelling of properties and distribution of steel fibres within a fine aggregate concrete. *Constr. Build. Mater.* **2013**, *44*, 645–653. [CrossRef]
12. Głodkowska, W. Waste Sand Fiber Composite: Models of Description of Properties and Application. *Annu. Set Environ. Prot.* **2018**, *20*, 291.
13. Głodkowska, W.; Laskowska-Bury, J. Waste Sands as a Valuable Aggregates to Produce Fibrecomposites. *Annu. Set Environ. Prot.* **2015**, *17*, 507–525.
14. Głodkowska, W.; Kobaka, J. Estimating the properties of a fine aggregate fibre reinforced cementitious composite using non-destructive methods. *J. Civ. Eng. Manag.* **2018**, *24*, 630–637. [CrossRef]
15. Głodkowska, W.; Ziarkiewicz, M. Cracking behavior of Steel Fiber Reinforced Waste Sand Concrete beams in flexure—experimental investigation and theoretical analysis. *Eng. Struct.* **2018**, *176*, 1–10. [CrossRef]
16. *Test Method for Metallic Fibered Concrete—Measuring the Flexural Tensile Strenght (Limit of Proportionality (LOP), Residual)*; PN-EN14651; BSI: London, UK, 2005.
17. Model Code 2010. In *Final draft, fib Bulletin 66, v. 2, 2012*; Comité Euro-International du Béton—Fédération International e de la Précontrainte: Paris, France, 2010.
18. Batson, G.; Jenkins, E.; Spaney, R. Steel Fibers as Shear Reinforcement Beams. *ACI J.* **1972**, *69*, 640–644.
19. Sharma, A.K. Shear Strength of Steel Fiber Reinforced Concrete Beams. *ACI J.* **1986**, *83*, 624–628.
20. Narayanan, R.; Darwish, I.Y.S. Use of Steel Fibres as Shear Reinforcement. *ACI J.* **1987**, *84*, 216–227.
21. You, Z.; Jalai, S.; Ding, Y. The composite effect of steel fibres and stirups on shear behaviour of beams using selfconsolidating concrete. *Eng. Struct.* **2011**, *33*, 107–117.
22. Ding, Y.; Yulin, Z.; Ning, X.; Azevedo, C. Shear resistance and cracking behaviour of SFRC beams with and without axial load. *Mag. Concr. Res.* **2014**, *23*, 1183–1193. [CrossRef]
23. Zhao, J.; Liang, J.; Chu, L.; Shen, F. Experimental Study on Shear Behavior of Steel Fiber Reinforced Concrete Beams with High-Strength Reinforcement. *Materials* **2018**, *11*, 1682. [CrossRef]
24. Minelli, F.; Conforti, A.; Cuenca, E.; Plizzari, G. Are steel fibres able to mitigate or eliminate size effect in shear? *Mater. Struct.* **2014**, *47*, 459–473. [CrossRef]
25. Cuenca, E.; Conforti, A.; Minelli, F.; Plizzarii, G.A. A material-performance-based database for FRC and RC elements under shear loading. *Mater. Struct.* **2018**, *51*, 11. [CrossRef]
26. Lantsoght, E.O.L. Database of Shear Experiments on Steel Fiber Reinforced Concrete Beams without Stirrups. *Materials* **2019**, *12*, 917. [CrossRef] [PubMed]
27. Valikhani, A.; Jaberi Jahromi, A.; Mantawy, I.M.; Azizinamini, A. Numerical Modelling of Concrete-to-UHPC Bond Strength. *Materials* **2020**, *13*, 1379. [CrossRef]
28. Tamayo, J.L.P.; Awruch, A.M.; Morsch, I.B. Numerical modeling of reinforced concrete structures: Static and dynamic analysis. *Rem. Rev. Esc. Minas* **2013**, *66*, 425–430. [CrossRef]
29. Dashti, F.; Dhakal, R.P.; Pampanin, S. Numerical Modeling of Rectangular Reinforced Concrete Structural Walls. *J. Struct. Eng.* **2017**, *143*, 6. [CrossRef]
30. Głodkowska, W.; Ruchwa, M. Static analysis of reinforced concrete beams strengthened with CFRP composites, Arch. *Civ. Eng.* **2010**, *56*, 111–122.
31. Sucharda, O. Identification of Fracture Mechanic Properties of Concrete and Analysis of Shear Capacity of Reinforced Concrete Beams without Transverse Reinforcement. *Materials* **2020**, *13*, 2788. [CrossRef] [PubMed]
32. Budarin, A.; Alekhin, V.; Avdonina, L. Numerical modelling of the reinforced concrete beam shear failure. *IOP Conf. Ser. Mater. Sci. Eng.* **2019**, *687*, 033044. [CrossRef]
33. Talavera-Sánchez, S.; Navarro-Gregori, J.; Ortiz-Navas, F.; Serna, P. Numerical Modelling of Fiber-Reinforced Concrete Shear-Critical Beams, Fibre Reinforced Concrete: Improvements and Innovations. *RILEM* **2021**, *30*, 670–680.
34. Amin, A.; Foster, S.J. Numerical modelling of large scale steel fibre reinforced-reinforced concrete beams failing in shear. In *Fib Bulletin 79. Fibre-Reinforced Concrete: From Design to Structural Applications*; University of New South Wales: Sydney, Australia, 2017.
35. Barros, J.; Sanz, B.; Kabele, P.; Yu, R.C.; Meschke, G.; Planas, J.; Cunha, V.; Caggiano, A.; Ozyurt, N.; Gouveia, V.; et al. Blind competition on the numerical simulation of steel-fiber-reinforced concrete beams failing in shear. *Struct. Concr.* **2021**, *22*, 939–967. [CrossRef]

36. Głodkowska, W.; Ziarkiewicz, M. Estimation of Load Bearing Capacity of Bending Fibrocomposite Elements. *Annu. Set Environ. Prot.* **2019**, *21*, 294–315.
37. Beňoa, J.; Hilara, M. Steel fibre reinforced concrete for tunnel lining—verification by extensive laboratory testing and numerical modelling. *Acta Polytech.* **2013**, *53*, 329–337.
38. Foster, S.J.; Agarwal, A.; Amin, A. Design of steel fiber reinforced concrete beams for shear using inverse analysis for determination of residual tensile strength. *Struct. Concr.* **2018**, *19*, 129–140. [CrossRef]
39. RILEMTC162-TDF. Test and design methods for steel fibre reinforced concrete. *Mater. Struct.* **2003**, *36*, 560–567. [CrossRef]
40. Amin, A.; Foster, S.J. Shear strength of steel fibre reinforced concrete beams with stirrups. *Eng. Struct.* **2016**, *111*, 323–332. [CrossRef]
41. Parmentier, B.; Cauberg, N.; Vandewalle, L. Shear Resistance of Macro-Synthetic and Steel Fibre Reinorced Concrete Beams without Stirrups. In Proceedings of the 8th RILEM International Symposium on Fibre Reinforced Concrete: Challenges and Opportunities, Guimaraes, Portugal, 19–21 September 2012; pp. 1096–1108.
42. Araújo, D.L.; Nunes, F.G.T.; Filho, R.D.T.; de Andrade, M.A.S. Shear strength of steel fiber-reinforced concrete beams. *Acta Scientiarum. Technol.* **2014**, *36*, 389–397. [CrossRef]
43. Bernat, A.M.; Spinella, N.; Recupero, A.; Cladera, A. Mechanical model for the shear strength of steel fiber reinforced concrete (SFRC) beams without stirrups. *Mater. Struct.* **2020**, *53*, 28. [CrossRef]
44. Lehmann, M. Shear capacity of Steel Fiber Reinforced Waste Sand Concrete Beams. Ph.D. Thesis, Koszalin University, Koszalin, Poland, June 2020.
45. Meyer, C. The greening of the concrete industry. *Cem. Concr. Compos.* **2009**, *31*, 601–605. [CrossRef]
46. Hendriks, C.; Janssen, G. Use of recycled materials in construction. *Mater. Struct.* **2003**, *36*, 604–608. [CrossRef]
47. Siddique, R. *Waste Materials and By-Products in Concrete*; Springer: Berlin/Heidelberg, Germany, 2008; pp. 381–405.
48. Soares, D.; de Brito, J.; Ferreira, J.; Pacheco, J. In situ materials characterization of full-scale recycled aggregates concrete structures. *Constr. Build. Mater.* **2014**, *71*, 237–245. [CrossRef]
49. Ulsen, C.; Kahn, H.; Hawlitschek, G.; Masini, E.A.; Angulo, S.C. Separability studies of construction and demolition waste recycled sand. *Waste Manag.* **2013**, *33*, 656–662. [CrossRef]
50. Al-Harthy, A.S.; Abdel Halim, M.; Taha, R.; Al-Jabri, K.S. The properties of concrete made with fine dune sand. *Constr. Build. Mater.* **2007**, *21*, 1803–1808. [CrossRef]
51. Głodkowska, W.; Kobaka, J. Application of waste sands for making industrial floors. *Annu. Set Environ. Prot.* **2009**, *11*, 193–206.
52. Domski, J.; Głodkowska, W. Selected Mechanical Properties Analysis of Composites Made on the Basis Fine Waste Aggregate. *Annu. Set Environ. Prot.* **2017**, *19*, 81–95.
53. PN-EN12620+A1:2010. *Aggregates for Concrete*; Polish Committee for Standardization: Warsaw, Poland, 2009.
54. Cartuxo, F.; de Brito, J.; Evangelista, L.; Jiménez, J.R.; Ledesma, E.F. Rheological behavior of concrete made with finerecycled concrete aggregates—Influence of the super plasticizer. *Constr. Build. Mater.* **2015**, *89*, 36–47. [CrossRef]
55. Declaration of Performance, No.2/2013/E—EKOMENT Steel Fibres 50 × 0.8 mm, (Polish Declaration of Performance). Available online: http://ekomet-ozorkow.com.pl/en/146-2/ (accessed on 16 July 2013).
56. Technical approval of the Institute of Building Technology No.AT-15-2095/1999, Steel fibers 50 × 1.0 mm, 50 × 0.8 mm, 50 × 0.65 mm, 60 × 0.8 mm and 30 × 0.65 mm for concrete reinforcement (Polish Technical Approval). Available online: https://www.itb.pl/en/ (accessed on 16 July 1999).
57. PN-EN 14889-1. *Fibresfor Concrete. Steel Fibres. Definitions, Specifications and Conformity*; Polish Committee for Standardization: Warsaw, Poland, 2007.
58. Domski, J. Ablurred border between ordinary concrete and SFRC. *Constr. Build. Mater.* **2016**, *112*, 247–252. [CrossRef]
59. Głodkowska, W.; Lehmann, M. Shear Capacity and Residual Strengths of Steel Fibre Reinforced Waste Sand Concrete (SFRWSC). *Annu. Set Environ. Prot.* **2019**, *21*, 1405–1426.
60. PN-EN12390-7:2009. *Testing Hardened Concrete. Density of Hardened Concrete*; Polish Committee for Standardization: Warsaw, Poland, 2009.
61. PN-EN 12390-3: 2019-07. *Testing Hardened Concrete—Part 3: Compressive Strength of Test Specimens*; Polish Committee for Standardization: Warsaw, Poland, 2019.
62. PN-EN 12390-6:2011. *Testing Hardened Concrete. Tensile Splitting Strength of Test Specimens*; Polish Committee for Standardization: Warsaw, Poland, 2011.
63. PN-EN 12390- 13: 2014-02. *Testing Hardened Concrete. Determination of Secant Modulus of Elasticity in Compression*; Polish Committee for Standardization: Warsaw, Poland, 2014.
64. Neville, A.M. *Properties of Concrete*; Arkady: Kraków, Poland, 2000; pp. 427–436.
65. Instruction ITB194/98. *Tests of Mechanical Properties of Concrete on Elements Made in Forms*; Building Research Institute: Warsaw, Poland, 1998.
66. PN-EN 13892-3:2005-02. Methods of Test for Screed Materials. Determination of Wear Resistance. In *Böhme*; Polish Committee for Standardization: Warsaw, Poland, 2005.
67. JCI-SF6:1984. Method of test for shear strength of fiber reinforced concrete. In *JCI Standard for Test Methods of Fiber Reinforced Concrete*; JCI: Tokyo, Japan, 1983; pp. 57–59.

68. Glinicki, M.A.; Litorowicz, A.; Zieliński, M. Interpretation of the test sof resistance of FRC to cracking in bending. In Proceedings of the Scientific Conference KILiW PAN i KN PZITB, Krynica, Poland, 16–21 September 2001. (Polish Standard)
69. Minelli, F.; Plizzari, G.A. Fiber reinforced concrete characterization through round panel test—part I: Experimental study. *Fract. Mech. Concr. Concr. Struct.* **2010**, *7*, 1451–1460.
70. Godycki-Ćwirko,T. *Concrete Mechanics*; Arkady: Kraków, Poland, 1982. (Polishbook)
71. Yoo, D.Y.; Yang, J.M. Effects of stirrup, steel fiber, and beam size on shear behavior of high-strength concrete beams. *Cem. Concr. Compos.* **2018**, *87*, 137–148. [CrossRef]
72. Ashour, S.A. Effect of compressive strength and tensile reinforcement ratio on flexural behavior of high-strength concrete beams. *Eng. Struct.* **2000**, *22*, 413–423. [CrossRef]
73. Subramaniam, K.V.L.; Gali, S. Shear behaviour of Steel Fiber Reinforced Concrete using full-field displacement from digital image corelation. *MATEC Web Conf.* **2017**, *120*, 1–13.
74. Lim, D.H.; Oh, B.H. Experimental and Teoretical Investigation on the Shear of Steel Fibre. *Eng. Struct.* **1999**, *21*, 937–944. [CrossRef]
75. Amin, A.; Foster, S.J.; Muttoni, A. Derivation of the σ-w relationship for SFRC from prism bending tests. *Struct. Concr.* **2015**, *16*, 93–105. [CrossRef]
76. Baghi, H.; Barros, J.A.O. Design-oriented approach to predict shear strength of reinforced concrete beams. *Struct. Concr.* **2018**, *19*, 98–115. [CrossRef]
77. PN-EN 1992 -1-1:2008. *Eurocode 2: Design of Concrete Structures—Part 1-1: General Rules and Rules for Buildings*; Committee for Standardization: Warsaw, Poland, 2008.
78. Matthys, S.; Soetens, T. Engineering Model for SFRC Shear Strength Based on MC2010 Approach. In Proceedings of the High Tech Concrete: Where Technology and Engineering Meet, Maastricht, The Netherlands, 12–14 June 2017; pp. 374–381.
79. Arslan, G. Shear Strength of Steel Fiber Reinforced Concrete (SFRC) Slender Beams. *J. Civ. Eng.* **2014**, *18*, 587–594. [CrossRef]
80. Arslan, G.; Keskin, R.S.O.; Ulusoy, S. An Experimental Sudy on the Shear Strength of SFRC Beams without Stirrups. *J. Theor. Appl. Mech.* **2017**, *55*, 1205–1217. [CrossRef]

materials

MDPI

Article

Effects of Low-Temperature Construction Additives (LCAs) on the Performance of Asphalt Mixtures

Yuanyuan Li [1], Jianlin Feng [1], Anqi Chen [1,2,*], Fan Wu [1], Shaopeng Wu [3,*], Quantao Liu [3] and Ruifang Gong [4]

[1] School of Civil Engineering and Architecture, Wuhan Institute of Technology, Wuhan 430205, China; liyy@wit.edu.cn (Y.L.); 22004010110@stu.wit.edu.cn (J.F.); 22004010123@stu.wit.edu.cn (F.W.)
[2] Nottingham Transportation Engineering Centre, School of Civil Engineering, University of Nottingham, University Park, Nottingham NG7 2RD, UK
[3] State Key Laboratory of Silicate Materials for Architectures, Wuhan University of Technology, Wuhan 430070, China; liuqt@whut.edu.cn
[4] Xinjiang Urban Construction (Group) Co., Ltd., Wulumuqi 830000, China; xjgongrf@163.com
* Correspondence: anqi.chen@nottingham.ac.uk (A.C.); wusp@whut.edu.cn (S.W.)

Abstract: Green production of asphalt materials is very important to promote energy savings and emission reduction during the construction and maintenance of asphalt pavement. A low-temperature construction additive (LCA) made from the waste plastic and waste rubber is proposed, which belongs to a class of environmentally friendly additives for asphalt mixtures. Marshall stability was tested to evaluate the mechanical performance of LCA-modified asphalt mixtures (LCA-AMs). In order to determine the best preparation parameters of LCA-AMs, the influence of the content and LCA addition method on the strength of LCA-AMs was studied. In addition, the impact of epoxy resin (ER) on the mixtures' performances was evaluated. The results show that the LCA can significantly reduce the formation temperature of asphalt mixtures, and the resulting asphalt mixtures have good workability in a lower temperature range (90–110 °C). The ER should be added to the LCA-AMs after 4 h of curing. All the volumetric properties satisfy the technical requirements. The low-temperature crack resistance and fatigue resistance of LCA-AMs were obviously improved with appropriate dosages of ER, which can effectively improve the mechanical performance of the asphalt mixtures. The ER can significantly increase the rutting resistance and water sensitivity of LCA-AMs, therefore making it feasible to improve the mixture performance by the enhancement provided by a low dosage of ER.

Keywords: low-temperature construction additive; preparation method; volumetric properties; modification mechanism; mixture performance

Citation: Li, Y.; Feng, J.; Chen, A.; Wu, F.; Wu, S.; Liu, Q.; Gong, R. Effects of Low-Temperature Construction Additives (LCAs) on the Performance of Asphalt Mixtures. *Materials* **2022**, *15*, 677. https://doi.org/10.3390/ma15020677

Academic Editor: Krzysztof Schabowicz

Received: 11 December 2021
Accepted: 11 January 2022
Published: 17 January 2022

1. Introduction

Asphalt pavement is a kind of continuous pavement without joints, which is the main form of highway pavement and has many advantages, such as smoothness, low noise, durability, anti-skid properties and easy maintenance [1]. The mixing temperature during the production process of hot-mixed asphalt mixtures (HMAs) is around 150–180 °C [2,3], and these need to be kept at A high temperature during the production, transportation and paving stages [4]. However, heating the asphalt mixture to high temperature requires a lot of fuel consumption [5], and emits greenhouse gases and toxic gases [6]. Besides this, the high construction temperature of HMA limits its application in cold areas [7]. The concepts of saving energy and consumption reduction have promoted the green production of asphalt materials, which has made researchers pay attention to the warm mix asphalt (WMA) [3,8].

WMA technology originated in Europe [9], and has been widely used all over the world [10]. The purpose of WMA technology is to reduce the viscosity of asphalt binder at high temperature [11,12] by various methods such as the use of organic viscosity reduction

additives [13], the foaming viscosity reduction method [14] or using surface-active viscosity reduction additives [15] without reducing the construction quality and mixture performance of the resulting asphalt mixtures, so as to reduce the mixing temperature of these mixtures [8,16]. Compared with HMA, WMA can reduce fuel consumption by more than 40% and reduce the asphalt aging effects caused by high temperatures [17]. Liseane [18] studied the emission and energy consumption of different kinds of asphalt mixtures, and found that the formation temperature of WMA was 20–50 °C lower than that of HMA, and the greenhouse gas emissions were decreased by more than 40%. Maríadel [19] found that the reduction of the mixing temperature can effectively reduce the harmful gases such as CO_2 and SO_2 produced during the asphalt mixture production process. Mosa [20] used alum instead of traditional WMA additives. The results showed that alum could reduce the mixing temperature and compaction temperature by 25.5 °C and 20 °C, respectively. Gao [21] indicated that a small amount of WMA additive can reduce the viscosity of asphalt by more than 80%. Huang [22] and others studied the fatigue and mechanical properties of WMA by the discrete element model and found that the fatigue and mechanical properties of warm-mixed rubber asphalt mixture are better than those of ordinary asphalt mixtures. Although WMA is widely used and is considered a mature technology, studies have pointed out that its performance is actually rather poor. For example, Kim [23] studied the properties of WMA and HMA with the same performance graded (PG) asphalt binder and aggregate gradation, and the results showed that WMA had poorer rutting resistance than HMA. Tan [24] used the Marshall design method to study the physical, mechanical properties and mixture performance of WMA. The results showed that the optimum asphalt content of WMA is 0.1–0.2% higher than that of HMA, the air voids and flow value of WMA were slightly higher than those of HMA, and that the immersion residue Marshall strength of WMA is increased, but the freeze-thaw indirect tensile strength decreases.

Low-temperature construction additives (LCAs) are a new environmentally friendly asphalt modifier made from waste plastics or waste rubber [25]. The mixing temperature of LCA-modified asphalt mixtures (LCA-AMs) is even lower than that of WMA, but higher than the mixing temperature of cold mix asphalt mixture (CMA) [26]. Like WMA, LCAs can solve the technical problems of serious pollution and excessive energy consumption of HMA. LCA-AMs can provide a better viscosity reduction effect, and the preparation temperature of asphalt mixtures can be decreased by more than 40 °C, therefore the mixtures have better workability at lower temperatures (90–110 °C), and energy consumption and harmful gas emissions are reduced. They can be directly used for repairing and maintaining the surface layer of new pavement or old pavement [27]. LCA- modified asphalt binders have good storage stability, and it can be used at any time. Due to the small size of the LCA molecules, they may help improve the low-temperature performance and fatigue performance of mixtures [28]. Although LCA-AMs have many advantages such as greater workability, the initial mechanical properties of LCA-AMs are considered insufficient because LCAs reduce the viscosity of asphalt binders [29,30].

In this paper, LCA-AMs were designed and prepared. Firstly, the mechanical properties and preparation parameters of asphalt mixtures with and without LCAs were studied by the Marshall method. The influence of mixing methods and dosage of LCAs on the strength of LCA-AMs were investigated, so as to determine the best LCA-AM preparation parameters. Then a low-dose of epoxy resin (ER) (Hunan Baxiongdi New Material CO., LTD., Changsha, China) was applied to improve the initial mechanical properties of the LCA-AMs. Finally, mixture performance tests were conducted to study the rutting resistance, low-temperature crack resistance, water sensitivity and fatigue resistance of the thus prepared LCA-AMs.

2. Materials and Experimental Methods

2.1. Materials

2.1.1. Asphalt Binder

The original asphalt binder was 70# base asphalt binder (Hubei Guochuang Hi-tech Materials CO., LTD., Wuhan, China). The technical performance of this asphalt binder is shown in Table 1.

Table 1. Technical information of the 70# asphalt binder [27].

Status	Technical Information	Units	Results	Requirement	Methods
Before TFOT	Penetration (100 g, 5 s, 25 °C)	0.1 mm	71	60–80	ASTM D5
	Ductility (10 °C)	cm	42.0	≥25	ASTM D113
	Softening point	°C	47.9	≥46	ASTM D36
After TFOT	Penetration (100 g, 5 s, 25 °C)	0.1 mm	63	≥61	ASTM D5
	Ductility (10 °C)	cm	14.3	≥6	ASTM D113
	Softening point	°C	51.0	–	ASTM D36

2.1.2. LCAs

LCAs are new environmentally friendly additives for asphalt mixtures, made from waste plastics and waste rubber. Among them, benzyl ethylene block copolymer accounts for about 80%, while ER and other additives account for about 20%. Figure 1a shows a typical LCA. After mixing with the asphalt binder, molecules containing amide groups are formed by ionization and recombination, and can form a dense film on the surface of asphalt molecules. LCAs can reduce the surface free energy and surface tension of asphalt molecules, resulting in a decrease in viscosity. At the same time, the lipophilic groups such as higher aliphatic chains, phenolic groups and benzene ring groups in ER can be adsorbed by asphalt molecules, which improves the stability of their dispersion system [31–33]. The mechanism of action of LCAs is shown in Figure 1b.

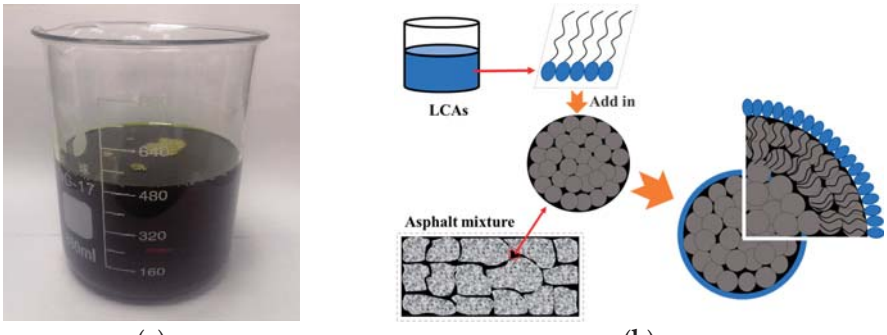

Figure 1. LCAs and their modification process in asphalt binder. (**a**) LCAs; (**b**) LCAs' mechanism of action.

2.1.3. LCAs Modified Asphalt Binder

The LCA-modified asphalt binder was made by the melt blending method. First the 70# asphalt binder was heated to 110 °C. Then, 9% LCA was added to the 70# asphalt binder and shear mixed for 30 min. The optimum 9% dosage of LCA was determined in our previous research [27]. The technical information of the LCA-modified asphalt binder is shown in Table 2.

Table 2. Technical information of the LCA-modified asphalt binder.

Technical Information		Units	Results	Requirement	Methods
Brookfield rotational viscosity (100 °C)		Pa·s	1.2	≤1.5	JTG E20 T0625
Penetration (100 g, 5 s, 25 °C)		0.1 mm	174	–	ASTM D5
Ductility (10 °C)		cm	≥150	≥100	ASTM D113
Softening point		°C	38.2	–	ASTM D36
Flash point		°C	175	≥160	JTG E20 T0611
After TFOT	Mass change	%	−0.5	−5–+5	JTG E20 T0610
	Penetration	0.1 mm	168	Measure	ASTM D5
	Ductility (10 °C)	cm	≥150	≥100	ASTM D113
	Softening point	°C	41.3	≥40	ASTM D36

2.1.4. Aggregates and Filler

The aggregates were divided into the coarse aggregate (≥2.36 mm) and fine aggregate (0–2.36 mm). The coarse aggregates were basalt, the fine aggregates were limestone, and the filler was limestone powder. The technical properties of the aggregates and fillers are listed in Tables 3–5.

Table 3. Technical properties of coarse aggregate.

Parameters	Unit	Results	Requirements	Experimental Method
Stone crushing value	%	13	≤28	JTG E42 T0316
Needle flake content	%	7.6	≤15	JTG E42 T0312
Los Angeles wear value	%	16	≤28	JTG E42 T0317
Water absorption	%	0.9	≤2.0	JTG E42 T0308
Apparent density	–	2.838	≥2.6	JTG E42 T0605

Table 4. Technical properties of fine aggregate.

Parameters	Unit	Results	Requirements	Experimental Method
Sediment percentage	%	2.4	≤3	JTG E42 T0335
Sand equivalent	%	72.6	≥60	JTG E42 T0334
Angularity (flow time method)	s	42.7	≥30	JTG E42 T0345
Apparent density	–	2.667	≥2.5	JTG E42 T0328

Table 5. Technical properties of mineral powder.

Parameters		Unit	Results	Requirements	Experimental Method
Apparent density		–	2.701	≥2.50	JTG E42 T0352
Particle size range (%)	<0.6	mm	100	100	JTG E42 T0351
	<0.15	mm	97.2	90–100	
	<0.075	mm	90.8	75–100	
Plasticity coefficient		–	3.2	<4	JTG E42 T0354
Hydrophilic coefficient		–	0.6	<1	JTG E42 T0353

2.2. Design of LCA-Modified Asphalt Mixtures (LAC-AMs)

2.2.1. Mix Design of LCA-AMs

A skeleton dense-graded mixture was used in this research, where the nominal maximum aggregate size of the mixture was 13 mm (LCAs-13). The aggregates were divided into four grades: 10–15 mm, 5–10 mm, 3–5 mm and 0–3 mm. The composite aggregate gradation range of LCAs is shown in Figure 2, and it has some common areas with the Chinese dense-graded mixture (AC-13). Both AC-13 and LCAs-13 are commonly used mixtures for the surface layer of asphalt pavement. The target gradation of LCAs-13 is

shown in Figure 2, and the mixing ratio of aggregates is shown in Table 6. The asphalt content was 4.8% by weight of aggregate.

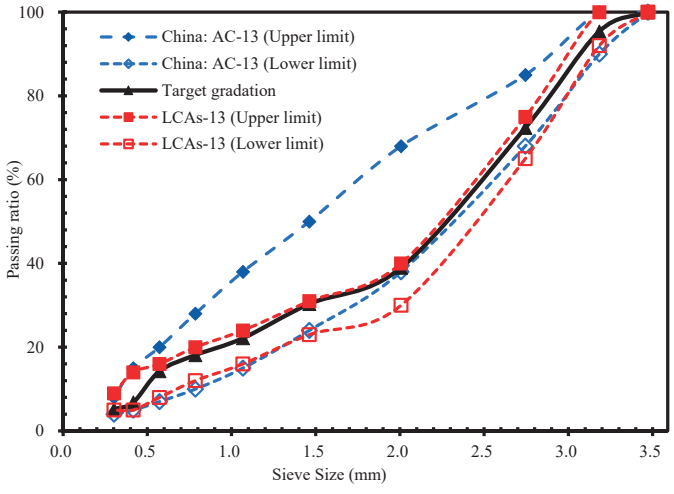

Figure 2. Composite aggregate gradation of asphalt mixture.

Table 6. Mixing ratio of aggregates.

Aggregate	10–15 mm	5–10 mm	3–5 mm	0–3 mm	Filler
Mixing ratio (%)	36	6	25	30	3

2.2.2. Manufacturing Temperature of LCA-AMs

The heating temperature of conventional HMA is clearly specified in JTG F40-2004. The heating and mixing temperatures for LCA-AMs are shown in Table 7. As it can be seen from Table 7, compared with the conventional HMA, the heating temperature of asphalt binder is reduced by 40 °C, the heating temperature of aggregate is reduced by 50 °C, and the mixing temperature of LCA-AMs is reduced by 30 °C.

Table 7. Construction temperature of conventional HMA and LCAs-AM.

Asphalt Mixture	Asphalt Heating Temperature (°C)	Aggregate Heating Temperature (°C)	Mixing Temperature (°C)	Secondary Mixing Temperature (°C)
HMA	145	165	150	–
Asphalt mixture with LCA	105	115	120	110

2.2.3. Preparation Method of LAC-AMs

The aggregates, filler and LCA-modified asphalt binder were mixed at 120 °C for 180 s. The prepared LAC-AM was cured at 110 °C for 4 h. The high temperature curing could accelerate the volatility of volatile components in the LCA, increase the viscosity of LCA-modified asphalt binder, and promote the development of strength in the LAC-AM. The cured LAC-AM was mixed again at 110 °C for 120 s to prepare specimens, which were then stored at room temperature (25 °C) for 72 h before further tests. The preparation method is shown in Figure 3.

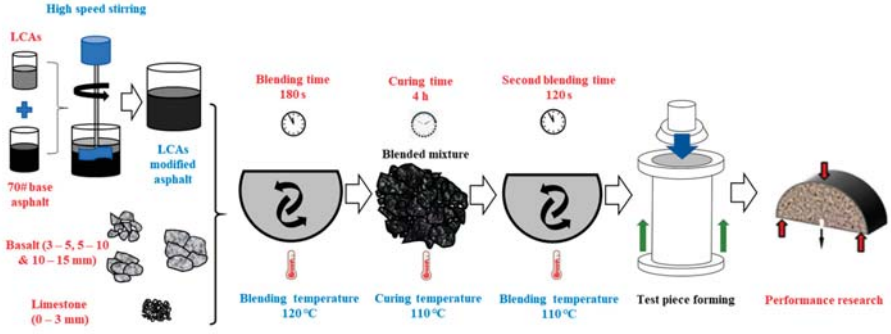

Figure 3. Preparation method of LAC-AMs.

2.3. Experimental Methods

2.3.1. Volumetric Properties and Mechanical Performance Tests

The specimens were compacted using the Marshall method at 110 °C with both sides of specimens compacted 100 times, the specimens were then cured for 72 h at room temperature (25 °C). The volumetric properties and mechanical properties of specimens, including the volume of air voids (VV), the voids in mineral aggregate (VMA), the voids filled with asphalt (VFA), the Marshall stability (MS) and flow value (FL), were tested based on JTG E20-2011.

2.3.2. ER Dosage and Mixing Methods

Epoxy resin (ER) at different dosages (0.3%, 0.6%, 1.0%, 2.0% and 4.0%) and different mixing methods were applied to study the differences between adding ER to LCA-AMs before and after curing, as shown in Figure 4. Method 1 involved adding ER before curing, while in Method 2 ER was added after curing for 4 h at 110 °C. The MS of specimens was tested after curing 72 h at room temperature (25 °C).

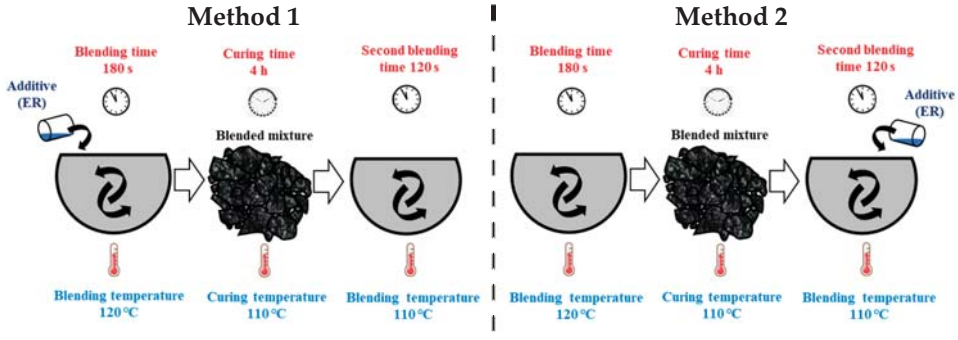

Figure 4. Different ER mixing methods.

2.3.3. Rutting Resistance Test

The slabs used for the rutting resistance tests were prepared using the wheel tracking method (JTG E20 T0703). The rutting resistance tests were conducted according to the criteria of JTG E20 T0910. The rutting resistance was tested by the wheel track test machine (Beijing Aerospace Keyu Test Instrument, Beijing, China) at a wheel rolling load of 0.7 MPa and a rate of 42 times/min. The test temperature was 60 °C. After curing at 25 °C for 72 h, specimens (300 mm × 300 mm × 50 mm) were put in the wheel track machine for

5 h at 60 °C. The dynamic stability (DS) of LCAs-AM was then calculated according to Equation (1).

$$DS = \frac{(t_2 - t_1) \times N}{(d_2 - d_1)} \quad (1)$$

where DS is the dynamic stability of asphalt mixture (times/mm), t_1 and t_2 is the 45 min and 60 min, respectively, d_1 and d_2 are the rutting depths of asphalt mixtures at t_1 and t_2 respectively (mm), N is the speed of the testing wheel (42 times/min).

2.3.4. Low-Temperature Resistance Test

The low-temperature crack resistance was tested by semi-circular bending (SCB) tests at the loading rate of 1.27 mm/min using a Universal Testing Machine (UTM-100); the distance between two supports was set to 75 mm. The specimen (φ 101.6 mm × 63.5 mm specimen) was cut into two semicircles, and a notch (5 mm length × 3 mm width) was cut along the height direction from the midpoint of the semicircle, as shown in Figure 5. The specimens were put into the UTM at −10 °C and 0 °C for 4 h before testing.

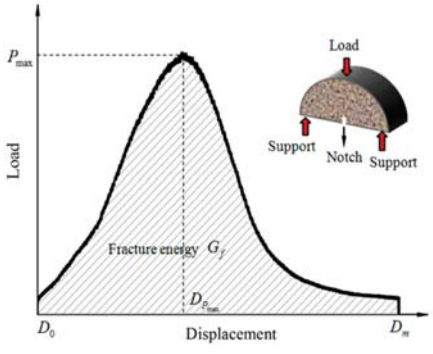

Figure 5. Load-displacement curve and test setup of SCB tests.

2.3.5. Water Sensitivity Test

The immersion Marshall test and freeze–thaw split test were used to study the water sensitivity. The specimens for both tests (φ 101.6 mm × 63.5 mm) were tested at loading rates of 50 mm/min. Both sides of the specimens were compacted 100 times and 75 times, for the immersion Marshall test and freeze–thaw split test, respectively. The immersion Marshall test was conducted according to the criteria of JTG E20 T0709. The samples of unconditional group and conditional group were immersed in the 60 °C water bath for 30 min and 48 h respectively. The freeze–thaw split test was conducted according to the criteris of JTG E20 T0729. The samples of unconditional group were immersed in the 25 °C water bath for 2 h; for the conditional group, the Marshall specimens were first vacuum-filled with water, and the vacuum degree was 97.3–98.7 kPa, then frozen at −18 °C for 16 h. after that, put the specimens in 60 °C water bath for 24 h, and finally put in a 25 °C water bath for 2 h.

2.3.6. Fatigue Resistance Test

The fatigue resistance was tested by the recycle semi-circular bending (R-SCB) test under different stress ratios of 0.3, 0.4, 0.5, 0.6 and 0.7 at the loading frequency of 2 Hz using UTM-100. The specimens were conditioned at 25 °C for 4 h, and the distance between supports was set to 75 mm.

3. Results and Discussions

3.1. Volumetric Properties of LCAs-AM

The volumetric properties and mechanical performance of LCAs-AM, including the volume of air voids (VV), the voids in mineral aggregate (VMA), the voids filled with asphalt (VFA), the Marshall stability (MS) and flow value (FL), are shown in Table 8. The comparison of volumetric properties and mechanical performance between 70# asphalt mixture (70#-AM) and LCA-AM is shown in Table 9. From Table 8, all of the volumetric properties meet the design requirements. From Table 9, compared to the 70#-AM, the VFA and MS of LCA-AM decreased by 1.5% and 28.3%, respectively, while the VV, VMA and FL of the LCA-AM increased by 7.5%, 4.0% and 25.7%, respectively. This indicates that adding LCAs decreases the viscosity of the asphalt mixture, resulting in the decrease of its MS.

Table 8. Volumetric properties and mechanical performance of LCAs-AM.

Specimen Number	Maximum Theoretical Relative Density	VV (%)	VMA (%)	VFA (%)	MS (kN)	FL (mm)
1	2.553	4.3	15.6	72.4	7.34	4.6
2		4.5	15.8	71.5	7.21	4.4
3		4.3	15.6	72.4	6.84	4.5
4		4.3	15.5	72.3	7.82	4.4
5		4.2	15.3	72.5	7.74	4.1
Average value		4.3	15.6	72.2	7.40	4.4

Table 9. Comparison of volumetric properties and mechanical performance between 70#-AM and LCAs-AM.

Asphalt Mixture	VV (%)	VMA (%)	VFA (%)	MS (kN)	FL (mm)
70#-AM	4.0	15.0	73.3	10.32	3.5
LCAs-AM	4.3	15.6	72.2	7.40	4.4
Specification requirements	3–5	≥13	65–75	≥8	3–6

The LCAs in asphalt binder produce amide-containing molecules by ionised recombination, forming a dense film on the surface of the molecules. With the increase of temperature, the surface energy of the molecules decreases and subsequently their surface tension decreases, leading to a decrease in viscosity. As the viscosity decreases, the cohesion of the mixture is reduced, leading to a decrease in MS and an increase in FL. Although the average MS of 7.56 kN is slightly below the specification requirement of 8 kN, the LCA-AM strength will improve as the volatile solvents in the LCA gradually evaporate. In addition, the LCA contains around 20% ER, which can be used to improve the initial mechanical performance of LCA-AMs by adding a small amount of epoxy additive.

3.2. Factors Affecting the Mechanical Performance of LACs-AM

3.2.1. Mixing Methods

Three dosages of ER (1.0%, 2.0% and 4.0%) and two mixing methods (Method 1 and Method 2) were applied to investigate the effect of different ER dosages and mixing methods on the mechanical performance of LCA-AMs, the results of which are shown in Table 10. From Table 10, using Method 1 slightly improves the mechanical performance of the LCA-AM, with 1.0%, 2.0% and 4.0% EP increasing the MS by 2.51%, 6.22% and 15.34%, respectively. Using Method 2 greatly improves the MS of LCAs-AM, by 80.56%, 92.86% and 98.02% for 1.0%, 2.0% and 4.0% EP, respectively. The improvement of 1.0% EP on the MS is more than 30 times greater with Method 2 than with Method 1. Therefore, the mechanical performance of LCAs-AM is much better using Method 2 than Method 1.

Table 10. MS of LCA-AMs prepared with different mixing methods.

ER Dosages	MS (kN)	
	Method 1	Method 2
1.0%	7.75	13.65
2.0%	8.03	14.58
4.0%	8.72	14.97

By using Method 1, the curing reaction is already finished during the 110 °C curing process, and it cannot further enhance the mechanical performance during the secondary mixing, compaction and curing processes of the LCA-AM. Therefore, the ER effect on improving the mechanical performance is greatly decreased for Method 1. However, by using Method 2, the curing reaction and strength formation of ER happen after the manufacturing of the LCA-AM specimens, so it can produce an obvious reinforcing effect on the mechanical performance of LCA-AMs.

3.2.2. ER Dosage

Four different dosages of ER (0.3%, 0.6%, 1.0% and 2.0%) are applied to LAC-AMs and compared to LAC-AM without ER. The mechanical performance results are shown in Figure 6. It can be seen that the MS of 0.3%, 0.6%, 1.0% and 2.0% ER-reinforced LCA-AMs are 12.11%, 20.54%, 32.27% and 41.28% higher than those of the original AM, and 56.35%, 68.11%, 84.46% and 97.03% higher than that of the LCA-AM without ER. With the addition of only 0.3% ER, the mechanical performance of the ER-reinforced LCA-AM is more than 50% higher than that of the LCA-AM without ER, which shows that the addition of a small amount of ER can effectively improve the mechanical performance of LCA-AMs.

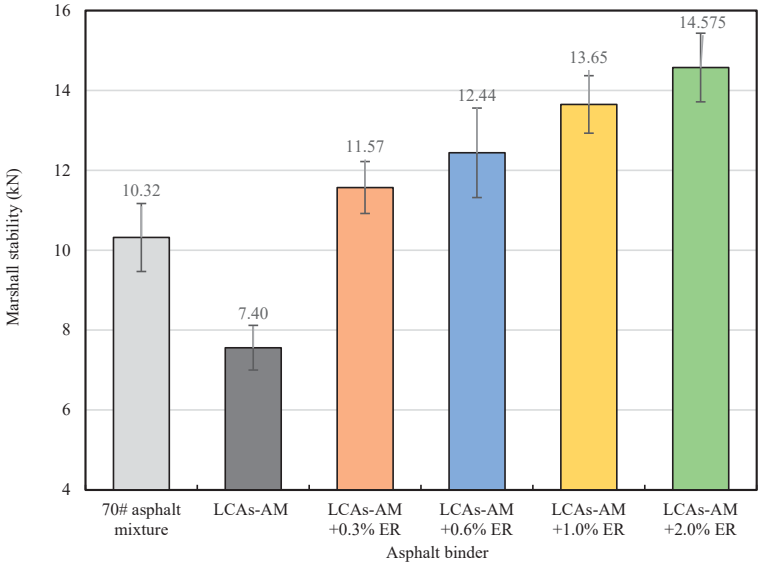

Figure 6. MS of LCA-AMs with different dosages of ER.

3.3. Mixture Performance of LCA-AMs

3.3.1. Rutting Resistance

The wheel track test is used to study the rutting resistance of 1.0% and 2.0% ER-100 reinforced LCA-AMs and the original asphalt mixture. The specimens were cured at 25 °C for 72 h. The results are shown in Figures 7 and 8, where it can be seen that the accumulated

deformation (rutting depth) of the asphalt mixture increases gradually with the increase of the number of load cycles, and the rutting depth growth rate of ER-100-reinforced LCA-AM is less than that of the LCA-AM without ER. After the same number of load cycles, the rut depth of ER-reinforced LCA-AMd is much smaller than that of the LCA-AM without ER. At the loading times of 45 min and 60 min, the rut depth of the LCA-AM with 1.0% ER is 21.2% or 25.5% smaller than that of the original asphalt mixture; the rutting depth of 2.0% ER-reinforced LCA-AM is 57.3% (59.9% smaller than that of the LCA-AM without ER). Meanwhile, the dynamic stability of ER-reinforced LCA-AMs is much higher than that of the LCA-AM without ER. The results indicate that ER can significantly enhance the high-temperature stability of LCA-AMs. The reason is that, after the curing of the ER, part of the strength of the asphalt mixture is provided by the ER, and the ER can form a spatial skeleton structure in the asphalt mixtures, which have greater strength and stiffness. Therefore, it can greatly improve the rutting resistance of the mixtures.

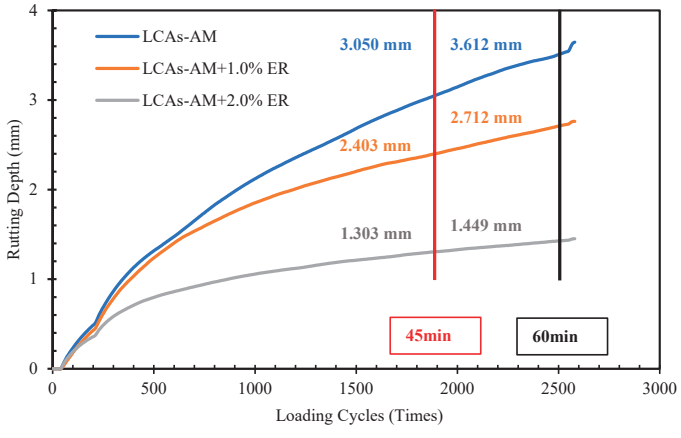

Figure 7. Rutting depth increase curve of asphalt mixtures.

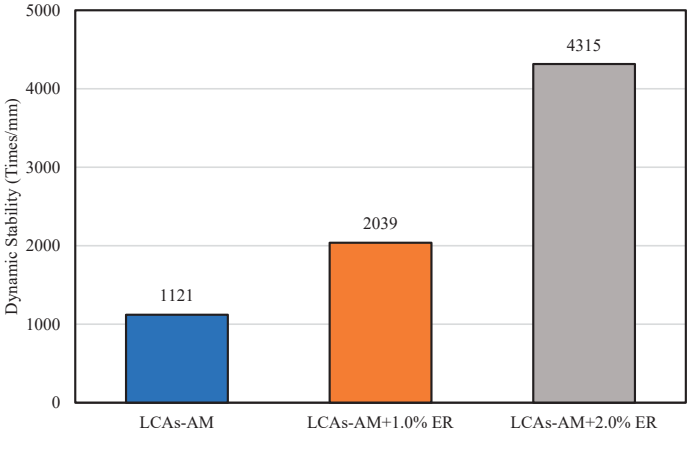

Figure 8. Dynamic stability of asphalt mixtures.

3.3.2. Low-Temperature Crack Resistance

LCAs can decrease the formation temperature of asphalt mixtures by decreasing the viscosity of asphalt binders. However, if the reduction in viscosity is too large, it results in a reduction in the mechanical properties of the asphalt mixture (even at low temperature),

which can easily break down during low-temperature crack resistance tests. In order to improve the low-temperature crack resistance of LCA-AMs, −10 °C and 0 °C SCB tests were conducted to evaluate the low-temperature cracking resistance of LCA-AMs with different dosages of ER. The results are shown in Figure 9 and Table 11, and the comparison of fracture energy of LCAs-AM is shown in Figure 10. According to Figure 9 and Table 11, the fracture energy and fracture toughness of LCA-AMs increase first and then decrease with the increase of ER dosages, and the LCA-AM with 0.6% ER has the highest fracture energy and fracture toughness. After curing, the ER acts as part of the skeleton structure in LCA-AMs. Therefore, a low content of ER can enhance the significantly increase the low-temperature crack resistance of LCA-AMs.

However, with the gradual increase of ER dosages, the increasing effect of the ER on the stiffness (mechanical performance) is much more obvious, and it may be too big and have a negative effect on the low-temperature crack resistance of LCA-AMs. The ER content in the LCAs-AM does not need to be high. The results show that one can significantly increase the low-temperature crack resistance of LCA-AMs by controlling the ER content in LCA-AMs.

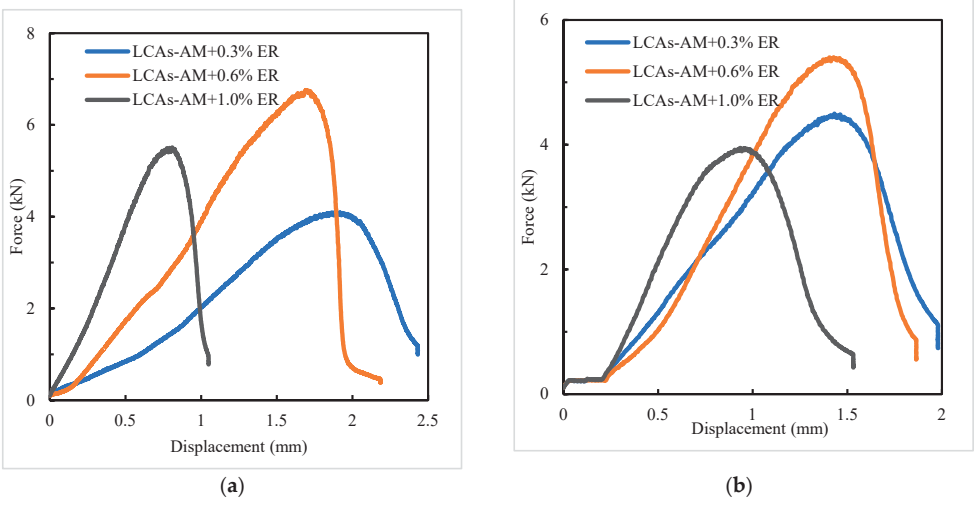

Figure 9. Displacement and load curve of SCB tests: (**a**) −10 °C; (**b**) 0 °C.

Table 11. SCB test results of LCA-AMs.

ER Dosages (%)	Test Temperature (°C)	Peak Load (N)	Fracture Work (J)	Fracture Energy (J/m^2)	Fracture Toughness (kPa × m$^{0.5}$)
0.3	−10	4112	5.43	1901.0	359.4
	0	4499	4.80	1679.8	392.4
0.6	−10	6774	7.10	2484.7	590.9
	0	5413	4.96	1735.8	472.2
1.0	−10	5518	3.29	1151.7	481.3
	0	3957	3.16	1104.3	345.1

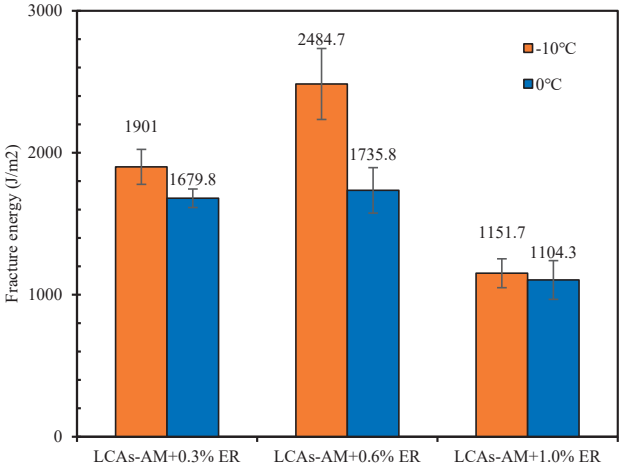

Figure 10. Low-temperature fracture energy with different ER contents.

3.3.3. Water Sensitivity

Immersion Marshall Test

The residual Marshall stability (RMS) of LCA-AMs with different dosages of ER were studied using the immersing Marshall test. The results are shown in Figure 11. From Figure 11, the Marshall stability of LCA-AMs with ER is higher than 8 kN both before and after the immersion condition. The RMS of LCA-AMs increases with the increase of ER dosage, and all the RMS of LCA-AMs are more than 80%. The results even satisfy the requirements of the specification of HMA.

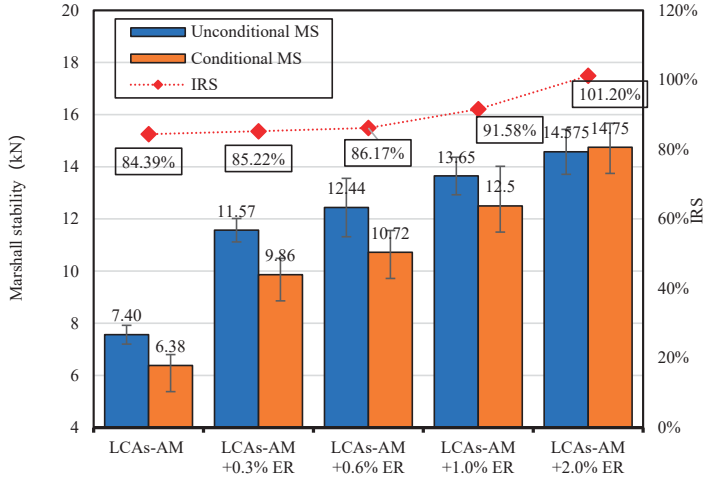

Figure 11. Immersion Marshall stability and RMS of LCA-AMs with ER.

Freeze-Thaw Splitting Test

The freeze-thaw splitting ratio (TSR) of LCA-AMs with the different dosages of ER were studied using the freeze-thaw splitting test. The results are shown in Figure 12. It can be seen from Figure 12 that the TSR of LCA-AM without ER is lower than 75%. However, all the TSRs of LCA-AMs with ER are higher than 75%, and meet the requirements of HMA.

The TSR increases first and then decreases with the increase of ER dosage, and the TSR of LCA-AMs with 1% ER is the highest. Therefore, due to the enhancement effect of ER, LCA-AMs have a good anti-water damage performance.

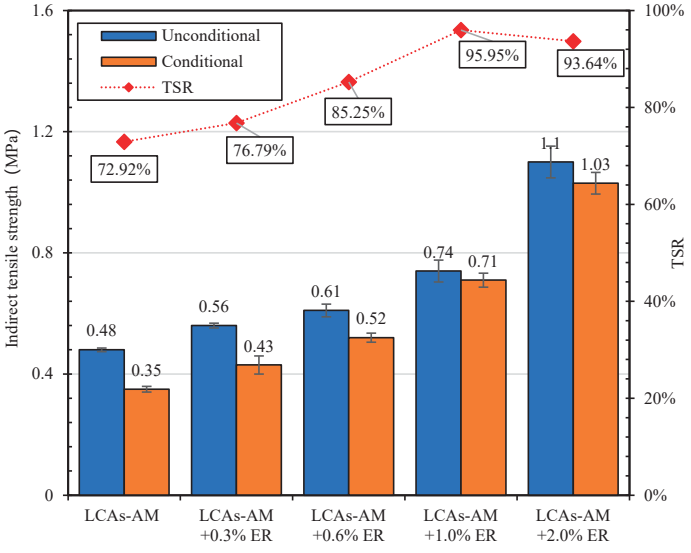

Figure 12. Indirect tensile strength and TSR of LCA-AMd with ER.

3.3.4. Fatigue Resistance

The repeated SCB test was conducted to investigate the fatigue resistance of LCA-AMs. The results are shown in Table 12 and Figure 13. The stress ratios of the fatigue test were 0.3, 0.4, 0.5, 0.6 and 0.7, respectively.

It can be seen from Table 12 that, at 25 °C, the peak load and fracture toughness of LCA-AM with 1.0% ER are the highest, while the LCA-AM with 0.6% ER has the maximum fracture work and fracture energy. Compared with the LCA-AM without ER, the fracture energy of LCA-AMs with 0.3%, 0.6% and 1.0% ER increase by 26.7%, 109.3% and 60.5%, respectively. It can be seen from Figure 13 that under the same loading frequency, the fatigue life decreases gradually with the increase of stress ratio. When the stress ratio increases from 0.3 to 0.7, the fatigue life of the LCA-AM without ER decreases by 83.7%, which shows that the fatigue resistance of the asphalt mixture has an obvious stress dependence. When the stress ratio is 0.3, the fatigue life of the LCA-AM increases gradually with the increase of ER content. Compared with the LCA-AM without ER, the fatigue performance of LCA-AM with 0.3% ER decreased by 12.5%, while that of LCA-AMs with 0.6% and 1.0% ER increase by 15.3% and 48.9%, respectively. When the stress ratio is 0.7, the fatigue resistance of 0.3%, 0.6% and 1.0% ER reinforced LCA-AMs increases by 22.6%, 11.8% and 6.0%, respectively. This shows that ER can significantly increase the fatigue resistance of LCA-AMs. The LCAs-AM with 0.6% and 1.0% ER are much better than the LCA-AM without ER.

Table 12. Results of repeated SCB tests of LCA-AMs.

Asphalt Mixture	ER Dosage (%)	Peak Load (N)	Fracture Work (J)	Fracture Energy (J/m^2)	Fracture Toughness ($kPa \times m^{0.5}$)
LCAs-AM with ER	—	953	0.88	180.6	68.0
	0.3	756	0.65	228.8	65.9
	0.6	1192	1.08	378.0	104.0
	1.0	1268	0.92	289.8	110.5

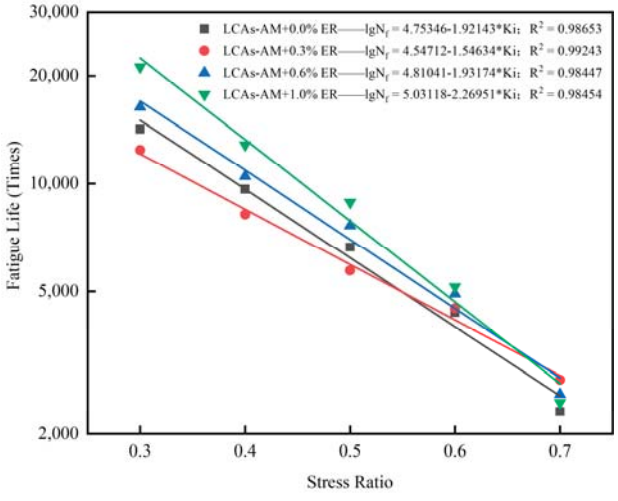

Figure 13. Fatigue life of LCA-AMs with ER.

4. Conclusions

In this paper, an environmentally friendly LCA asphalt modifier additive was developed, which can used to decrease the construction temperature of asphalt mixtures. The design and preparation parameters of LCA-modified asphalt mixtures were determined. The volumetric properties, mechanical performance and mixture performance of LCA-AMs were studied as well. The main conclusions are as follows:

(1) LCAs can significantly decrease the preparation temperature of asphalt mixtures. All the volumetric properties, namely the VV, VMA, VFA, MS and FL of LCA-AMs meet the design requirements, however, the MS of original LCA-AM (7.56 kN) is slightly lower than 8 kN.

(2) The content and mixing method (Method 1 and Method 2) of ER have obvious effects on the mechanical performance of LCA-AMs. For instance, 0.3% ER can effectively enhance the mechanical properties of LCA-asphalt mixtures, and the MS is 56.4% higher than that of LCA-AM without ER. The MS of 1% ER-reinforced LCA-AMs mixed by Method 2 is 30 times higher than that of LCA-AMs mixed by Method 1.

(3) The ER can form a spatial skeleton structure in the mixture, and effectively improve the initial strength of the asphalt mixture. The enhancement effect of ER can significantly increase the rutting resistance and water sensitivity of LCA-AMs.

(4) 0.3% and 0.6% ER dosages can improve the fracture energy and fracture toughness of LCA-AMs, and 0.6% and 1.0% ER can increase the fatigue life of LCA-AMs. The low-temperature crack resistance and fatigue resistance of LCA-AMs with appropriate dosages of ER will be obviously improved compared with the LCA-AM without ER.

It is feasible to improve the mixture performance by the enhancement of low dosages of ER. LCAs can facilitate the low-temperature preparation of asphalt mixtures, with remarkable environmental benefits. LCAs should find wide application prospects in asphalt pavement engineering.

Author Contributions: Conceptualization, Y.L.; methodology, Y.L., J.F., A.C. and S.W.; validation, F.W.; data curation, Y.L., J.F., A.C., F.W. and Q.L.; writing—original draft preparation, J.F. and F.W.; writing—review and editing, Y.L., A.C., S.W., Q.L. and R.G.; visualization, R.G.; supervision, Y.L.; funding acquisition, Y.L. All authors have read and agreed to the published version of the manuscript.

Funding: The authors acknowledge the financial supported provided by the National Natural Science Foundation of China (No. 52108415), the National Key Research and Development Program of China

(No. 2018YFB1600200), the Natural Science Foundation of China (No. 51778515), the Key Technical Innovation Projects of Hubei Province (No. 2019AEE023), the Plan of Outstanding Young and Middle-aged Scientific and Technological Innovation Teams in Hubei Province Universities (No. T2020010), the Key R&D Program of Hubei Province (No. 2020BCB064), the Scientific Research Fund Project of Wuhan Institute of Technology (No. K2021032), the Science and Technology Project of the Department of Housing and Urban-Rural Development of Hubei Province, and the test help from Shiyanjia Lab (www.shiyanjia.com).

Institutional Review Board Statement: Not applicable.

Informed Consent Statement: Not applicable.

Data Availability Statement: The data presented in this study are available on request from the corresponding author.

Conflicts of Interest: The authors declare no competing financial interest.

References

1. Gong, M.; Zhang, H.; Liu, Z.; Fu, X. Study on PQI standard for comprehensive maintenance of asphalt pavement based on full-cycle. *Int. J. Pavement Eng.* **2021**. [CrossRef]
2. Lyu, L.; Li, D.; Chen, Y.; Tian, Y.; Pei, J. Dynamic chemistry based self-healing of asphalt modified by diselenide-crosslinked polyurethane elastomer. *Constr. Build. Mater.* **2021**, *293*, 123480. [CrossRef]
3. Almeida-Costa, A.; Benta, A. Economic and environmental impact study of warm mix asphalt compared to hot mix asphalt. *J. Clean. Prod.* **2016**, *112*, 2308–2317. [CrossRef]
4. Li, Y.; Wu, S.; Amirkhanian, S. Investigation of the graphene oxide and asphalt interaction and its effect on asphalt pavement performance. *Constr. Build. Mater.* **2018**, *165*, 572–584. [CrossRef]
5. Mo, S.; Wang, Y.; Xiong, F.; Ai, C. Effects of asphalt source and mixing temperature on the generated asphalt fumes. *J. Hazard. Mater.* **2019**, *371*, 342–351. [CrossRef]
6. Wang, T.; Xiao, F.; Zhu, X.; Huang, B.; Wang, J.; Amirkhanian, S. Energy consumption and environmental impact of rubberized asphalt pavement. *J. Clean. Prod.* **2018**, *180*, 139–158. [CrossRef]
7. Ai, C.; Li, Q.J.; Qiu, Y. Testing and assessing the performance of a new warm mix asphalt with SMC. *J. Traffic Transp. Eng.* **2015**, *6*, 7. [CrossRef]
8. Carmen Rubio, M.; Martinez, G.; Baena, L.; Moreno, F. Warm mix asphalt: An overview. *J. Clean. Prod.* **2012**, *24*, 76–84. [CrossRef]
9. Song, W.; Huang, B.; Shu, X. Influence of warm-mix asphalt technology and rejuvenator on performance of asphalt mixtures containing 50% reclaimed asphalt pavement. *J. Clean. Prod.* **2018**, *192*, 191–198. [CrossRef]
10. Cheraghian, G.; Falchetto, A.C.; You, Z.; Chen, S.; Wistuba, M.P. Warm mix asphalt technology: An up to date review. *J. Clean. Prod.* **2020**, *268*, 122128. [CrossRef]
11. Zhang, J.; Li, P.; Sun, C.; Sun, C.; Liang, M.; Li, Y.; Yao, Z.; Zhang, X. Effects of Composite Warm Mix Additive (CAR) on the Physical and Rheological Performance of Bitumen and the Pavement Performance of Its Concrete. *Materials* **2019**, *12*, 3916. [CrossRef]
12. Shi, J.; Fan, W.; Wang, T.; Zhao, P.; Che, F. Evaluation of the Physical Performance and Working Mechanism of Asphalt Containing a Surfactant Warm Mix Additive. *Adv. Mater. Sci. Eng.* **2020**, *2020*, 8860466. [CrossRef]
13. Qin, Q.; Farrar, M.J.; Pauli, A.T.; Adams, J.J. Morphology, thermal analysis and rheology of Sasobit modified warm mix asphalt binders. *Fuel* **2014**, *115*, 416–425. [CrossRef]
14. Sargand, S.; Nazzal, M.D.; AI-Rawashdeh, A.; Powers, D. Field Evaiuation of Warm-Mix Asphalt Technologies. *J. Mater. Civ. Eng.* **2012**, *24*. [CrossRef]
15. Leng, Z.; Gamez, A.; Al-Qadi, I.L. Mechanical Property Characterization of Warm-Mix Asphalt Prepared with Chemical Additives. *J. Mater. Civ. Eng.* **2014**, *26*, 304–311. [CrossRef]
16. Ren, J.; Xing, C.; Tan, Y.; Liu, N.; Yang, L. Void Distribution in Zeolite Warm Mix Asphalt Mixture Based on X-ray Computed Tomography. *Materials* **2019**, *12*, 1888. [CrossRef]
17. Poulikakos, L.D.; Falchetto, C.A.; Wang, D.; Porot, L.; Hofko, B. Impact of asphalt aging temperature on chemo-mechanics. *RSC Adv.* **2019**, *9*, 11602–11613.
18. Thives, L.P.; Ghisi, E. Asphalt mixtures emission and energy consumption: A review. *Renew. Sustain. Energy Rev.* **2017**, *72*, 473–484. [CrossRef]
19. Rubio, M.D.C.; Moreno, F.; Martínez-Echevarría, M.J.; Martinez, G.; Vazquez, J.M. Comparative analysis of emissions from the manufacture and use of hot and half-warm mix asphalt. *J. Clean. Prod.* **2013**, *41*, 1–6. [CrossRef]
20. Mosa, A.M.; Salem, L.A.; Waryosh, W.A. New Admixture for Foamed Warm Mix Asphalt: A Comparative Study. *Iran. J. Sci. Technol. Trans. Civ. Eng.* **2020**, *44* (Suppl. S1), 649–660. [CrossRef]
21. Gao, Z.; Fu, H.; Chen, Q.; Cao, Y. Rheological properties and viscosity reduction mechanism of SBS warm-mix modified asphalt. *Pet. Sci. Technol.* **2020**, *38*, 556–564. [CrossRef]

22. Huang, W.; He, P.; Long, X.; Tian, J.; Zheng, Y.; Ma, H.; Hu, S.; Wu, X. Design of a skeleton-stabilized warm mix asphalt mixture and investigation of its fatigue and fracture performance—ScienceDirect. *Constr. Build. Mater.* **2020**, *248*, 118618. [CrossRef]
23. Kim, S.; Park, J.; Lee, S.; Wang, K.; Kim, W. Performance of Modified WMA Mixtures Prepared Using the Same Class PG Binders of HMA Mixtures. *J. Test. Eval.* **2014**, *42*, 347–356. [CrossRef]
24. Tan, Y.; Guo, M.; Xu, H.; Zhang, R. Comparative Study on Laboratory Performance of Hot- and Warm-mix Asphalt Mixtures. *J. Test. Eval.* **2012**, *40*, 715–723. [CrossRef]
25. Wei, W.; Jin, Y. Pavement Performance Analysis of Composite Modified SMA10 Asphalt Mixture Mixed with Waste Plastic and SMC. *Technol. Highw. Transp.* **2019**, *35*, 43–46.
26. Zhao, L.N. The Application of SMC Normal Temperature Modified Asphalt on G312. *Manag. Technol. SME* **2017**.
27. Tao, B.; Bowen, M.; Anqi, C.; Yuanyuan, L.; Shaopeng, W.; Ziang, H.; Zhuowei, L. Investigation of low-temperature construction additives (LCAs) effects on the technical properties of asphalt binder. *Constr. Build. Mater.* **2021**, *304*, 124634.
28. Yu, H.; Leng, Z.; Xiao, F.; Gao, Z.M. Rheological and chemical characteristics of rubberized binders with non-foaming warm mix additives. *Constr. Build. Mater.* **2016**, *111*, 671–678. [CrossRef]
29. Almeida, A.; Sergio, M. Evaluation of the Potential of Sasobit REDUX Additive to Lower Warm-Mix Asphalt Production Temperature. *Materials* **2019**, *12*, 1285. [CrossRef]
30. Wang, J.; Zhang, Z.; Li, Z. Performance Evaluation of Desulfurized Rubber Asphalt Based on Rheological and Environmental Effects. *J. Mater. Civ. Eng.* **2020**, *32*, 04019330. [CrossRef]
31. Luo, Q.Y.H.; Su, T.; Ouyang, C. The Analysis of Road Performance, Mechanism and Environmental Benefits of SMC Normal Temperature Modifier. In Proceedings of the 4th International Conference on Transportation Geotechnics (ICTG 2020), Chicago, IL, USA, 30 August–2 September 2020.
32. Ortega, F.J.; Navarro, F.J.; García-Morales, M. Dodecylbenzenesulfonic acid as a Bitumen modifier: A novel approach to enhance rheological properties of bitumen. *Energy Fuels* **2017**, *31*, 5003–5010. [CrossRef]
33. Özdemir, D.K. High and low temperature rheological characteristics of linear alkyl benzene sulfonic acid modified bitumen. *Constr. Build. Mater.* **2021**, *301*, 124041. [CrossRef]

materials

MDPI

Article

An Experimental Investigation of the Mechanical Behavior and Particle Crushing Characteristic of Volcanic Soil

Xiao-Yang Liu, Chang-Ming Wang *, Hai-Liang Liu and Di Wu

College of Construction Engineering, Jilin University, Changchun 130026, China
* Correspondence: wangcm@jlu.edu.cn

Abstract: Volcanic soil is a special soil that is well-known for its distinctive texture, vesicular nature, and particle fragility. The fragility characteristic of volcanic soil is the main factor affecting the foundation stability in road engineering. This study focuses on the mechanical properties and particle crushing characteristics of volcanic soil retrieved from Northeast China. A series of triaxial consolidation and drainage shear tests are performed on volcanic coarse-grained soil (5 mm > d > 0.075 mm) under different initial relative densities and effective confining pressures. Results show the peak friction angle of volcanic soil significantly decreases with the increase of confining pressure. The particle crushing degree of volcanic soil increases with the increase of confining pressure, particle size, and relative density. The relative breakage rate of the same particle size group has a good linear relationship with a fractal dimension. Moreover, for the same particle size, the relationship between plastic work and relative breakage rate can be fitted by a power function, which is not significantly affected by relative density or effective confining pressure. From an engineering view, in addition to increasing the compaction degree of volcanic soil, volcanic soil with fine particles used as a roadbed filler can significantly reduce the deformation of the roadbed and improve the bearing capacity of the foundation.

Keywords: volcanic soil; mechanical property; strength index; particle crushing; road engineering

Citation: Liu, X.-Y.; Wang, C.-M.; Liu, H.-L.; Wu, D. An Experimental Investigation of the Mechanical Behavior and Particle Crushing Characteristic of Volcanic Soil. *Materials* **2022**, *15*, 5423. https://doi.org/10.3390/ma15155423

Academic Editor: Krzysztof Schabowicz

Received: 11 July 2022
Accepted: 3 August 2022
Published: 6 August 2022

Publisher's Note: MDPI stays neutral with regard to jurisdictional claims in published maps and institutional affiliations.

1. Introduction

In recent years, with the increasing expansion of road construction, some roads have to cross volcanic soil areas, considering local availability in large quantities and low cost [1], the use of volcanic soils in roadbed fill has increased.

As a regional special soil, volcanic soil differs from traditional sand and gravel stacks in that its genesis originates from the eruption and condensation of volcanic magma. This special genesis allows volcanic soils to play different roles in various fields, such as refractory materials and adsorbents to remove harmful ions from industrial wastewater [2–7]. Mechanical properties are the focus of the present study. With the ejection of magma, under the conditions of reduced external pressure and a sudden temperature drop, gas escapes from the lava and forms pores of various sizes and numbers, moreover, since this material has not undergone long-distance transport effects, as a result, volcanic soil exhibits porous characteristics and irregular particle shape characteristics [8]. These special structures make the volcanic soil particle easy to crush under lower loads [9,10], this causes excessive deformation even rapid weakening of volcanic soil foundation bearing capacity, leading to instability and other hazards, affecting the safe operation of road facilities. Therefore, an in-depth investigation of volcanic soil particle crushing characteristics is meaningful for the stability of road engineering.

The special crushing sensitivity of volcanic soils has attracted the attention of scholars. According to the results of previous studies, particle crushing is related to a variety of factors, mainly including mineral composition [11–13], particle shape [14–16], particle size [17–19], particle relative density [20,21], and external loads [22,23], etc. Extensive

research has been performed to study the mechanical properties of crushable volcanic soils retrieved from different regions. For example, Agustian and Goto [9] investigated the effects of particle size, dry density, and effective confining stress on Japanese volcanic soils by drained triaxial compression tests and found particle sizes had a noticeable influence on internal friction angle. Kikkawa et al. [24] performed K0 compression tests to compare the compression behavior of loose and dense sand and pointed out that dense sand particles exhibited more crushing and less tendency during loading. Galvis-Castro et al. [25] conducted a one-dimensional compression study of volcanic soils in the Columbia area, the result showed that yield stress was low. Asadi et al. [26] reported a crushable volcanic soil acquired from the North Island of New Zealand and found its shear modulus was much lower than Toyoura sand. Scholars' studies show that the mechanical strength of volcanic soil was low due to its fragile crushing nature. Although scholars have achieved plenty of achievements in crushable volcanic soil. However, quantitative studies on particle crushing characteristics and the mechanical behavior of volcanic soils are not sufficient, such as quantitative measurement of particle crushing, the relationship between the crushing of volcanic soil particles and the external input energy, etc. A deeper study of these aspects will help to better understand the mechanical properties of crushable volcanic soils and provide theoretical guidance for the construction in road engineering.

Given this, the objective of this study is to investigate particle size (d), confining pressure (σ_3), and relative density (Dr) on the mechanical behavior and crushing characteristics of volcanic soils. The mechanical characteristics, strength indexes, and critical state of volcanic soils were examined. Then, particle crushing features after the shearing test was addressed using the quantitative indexes relative breakage rate and fractal dimension, and the particle crushing pattern was analyzed. Finally, from an energy perspective, the relationship between plastic work and relative breakage rate was established.

2. Materials and Methods

2.1. Material

The soil sample material was taken from Erdao Baihe District, Yanbian Korean Autonomous Prefecture, Jilin Province, China (Figure 1a). Thick layers of volcanic soil were formed at this site due to the eruptive action of Changbai Mountain; the sampling site was located at a slope formed by artificial excavation (Figure 1b). There are numerous small pores distributed inside the volcanic soil particles (Figure 2), hence this material is susceptible to crushing under external forces, distinguishing it from ordinary materials [27].

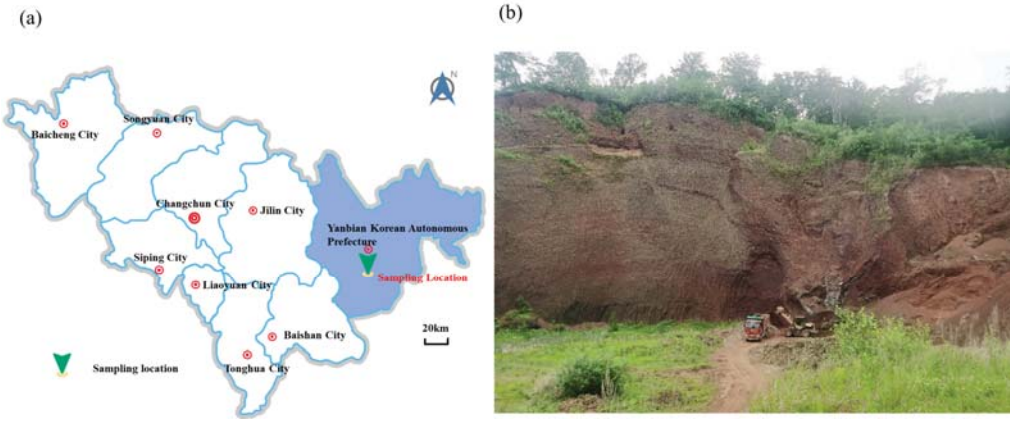

Figure 1. Sampling location map. (**a**) Location map; (**b**) Artificial slope.

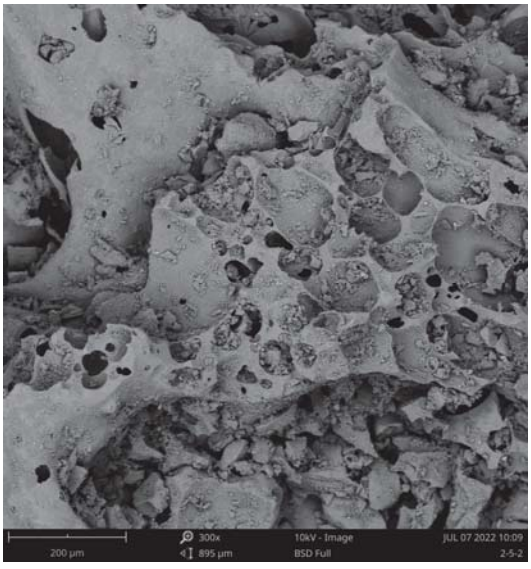

Figure 2. SEM of volcanic soil particle.

The mineralogical and chemical composition of volcanic soil were analyzed by X-ray diffraction (XRD) and X-ray fluorescence (XRF). (JASSO TTR III Multifunctional X-ray Diffractometer was adopted for the XRD test. The K-value method was used to calculate mineral content. M4 Tornado X-Ray Fluorescence Spectrometer was used for the XRF test. For more test details, please see the literature [28]). Table 1 shows the mineralogical composition of volcanic soil consisting mainly of quartz, feldspar (potassium feldspar and plagioclase), and hematite with little clay minerals. The chemical composition is dominated by SiO_2.

Table 1. Proportions of primary minerals and major oxides for samples.

Test item	Component	Percentage (%)	Test Item	Component	Percentage (%)
XRD mineral phase	Quartz	20.5	XRF major element	SiO_2	50.18
	Potassium feldspar	20.6		Al_2O_3	16.95
	Plagioclase	48.9		Fe_2O_3	10.48
	Hematite	8.5		FeO	0.77
	Clay minerals	1.5		MgO	2.27
				CaO	4.39
				Na_2O	4.13
				K_2O	3.87
				MnO	0.18
				P_2O_5	1.23
				TiO_2	1.75
				Loss on ignition	3.53

2.2. Test Scheme

Due to the irregular shape and fragility of volcanic soil particles, the soil particle crushing degree increases with the increase of sieving time. This will affect the accuracy of the result of particle size distribution curves. To overcome the effect, a suitable sieving time needs to be determined. Figure 3a shows that with an increase in sieving time, control particle size d_{30}, d_{60} gradually decrease, when the sieving time is within 8–10 min, control particle size change is not significant so sieving time is determined as 10 min. Figure 3b

is the original curve in sieving 10 min. According to Hardin's theory [11], it is difficult for a soil particle size < 0.074 mm to crush. Considering particle size groups engineering classification, four particle size groups were selected from original grading curves, which all belong to the category of coarse-grained soils [29]. The schematic diagram of the four particle sizes group is shown in Figure 4. The physical properties of volcanic soil were determined according to the Standard for Geotechnical Testing Method (2019) [30]. Combined with Figure 4 and Table 2, it can be found that for the 2–5 mm particle size group and 0.5–2 mm particle size group, particle shape is irregular and the maximum void ratio is relatively large with holes visible to the naked eye.

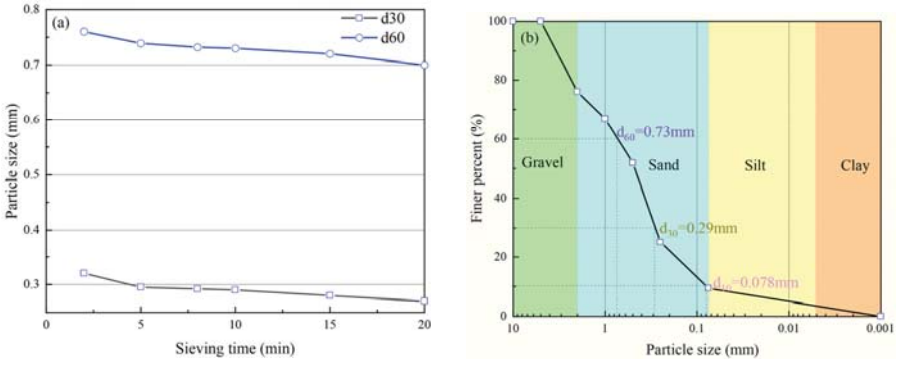

Figure 3. Determination sieving test time and corresponding particle size distribution curve: (**a**) sieving test time; (**b**) particle size distribution curve.

Figure 4. Diagram of four particle size of volcanic soil.

Table 2. Physical parameters of volcanic soil.

Soil Group (mm)	Soil Name	*Gs*	ρ_{dmin} (g/cm^3)	ρ_{dmax} (g/cm^3)	e_{max}	e_{min}
2–5	Fine gravel	2.615	0.597	1.277	3.380	1.048
0.5–2	Coarse sand		0.729	1.262	2.587	1.072
0.25–0.5	Medium sand		0.875	1.361	1.989	0.921
0.075–0.25	Fine sand		0.930	1.391	1.811	0.879

As volcanic soil has favorable permeability properties due to its porous nature [31], water can be discharged quickly under load, therefore consolidation and drainage test conditions are realistic. Considering that general road engineering load values are not large, effective confining pressures were set as 100 kPa, 200 kPa, and 400 kPa, and three defined in engineering relative densities (loose (0.3), medium-dense (0.5), and dense (0.7)) were selected in this paper to carry out consolidation drainage shear (CD) experiments, the test protocol is shown in Table 3.

Table 3. Triaxial shear test scheme for four particle size group.

Type of Test	Soil Group (mm)	*Dr* (Relative Density)	Confining Pressure (kPa)	Total Number of Samples
CD Test	2–5 0.5–2 0.25–0.5 0.075–0.25	0.3 (loose), 0.5 (medium), 0.7 (dense)	100, 200, 400	36

2.3. Triaxial Experiment Procedure

The tested soil samples were 50 mm in diameter and 100 mm in height. A 0.5 mm thick rubber film was chosen to avoid particles from penetrating the rubber film. The soil was divided into five parts, and it was carefully dropped into rubber film embraced using a spoon. To avoid massive particle crushing during the sample loading stage, a sample maker was used to gently compress the sample surface to the preset height. Then, the sample was saturated by combining the water head and the backpressure saturation method. In the water head saturation stage, the sample was saturated for 2.0 h, and a back pressure of 400 kPa was applied to the sample in the backpressure saturation stage; when B-value > 0.95, the saturation stage finished and the sample was consolidated under the specified effective confining pressure; when the change of consolidation volume did not exceed 0.05 cm^3/5 min, the stage was completed. Finally, triaxial shear tests were performed under drained conditions at a shear rate of 0.042 mm/min until the axial strain reached 30%. When the shearing stage was completed, the specimen was washed into the drying plate from the rubber membrane using the water washing method, followed by a drying and sieving test. (For 0.25–0.5 mm and 0.075–0.25 mm particle size groups, the gradation curve results after the test are not shown in the gradation curve evolution section. The main reason is that some of the particles adhered to the drying plate, these sticking particles suffered a non-negligible crushing amount when removed, which was not caused by pure mechanical behavior (triaxial test), thus interfering with the test results).

3. Triaxial Consolidation and Drainage Test Results

3.1. Stress–Volume Strain–Axial Strain Characteristics

Figure 5 shows deviator stress–axial strain–volumetric strain curves of volcanic soil with four particle size groups. Under 100 kPa confining pressure, stress–strain curves of the four particle sizes at different relative densities show a strain-softening type. For the 2–5 mm particle size group, loose samples show an initially compressive behavior, followed by an expansive behavior at low confining pressure and a purely compressive behavior at high confining pressure (400 kPa), while for the 0.075–0.25 mm particle size group, there is no pure compression behavior. For a certain particle size group, at a given confining pressure, increasing *Dr* remarkably increases the shear strength and the expansion trends, in addition, increasing confining pressure would postpone the arrival of the peak shear strength [21]. For the same particle size group, under a certain confining pressure, soil residual strengths are the same with different relative densities.

Under 30% terminating axial strain condition, four particle size groups have reached the stress critical state. For the small size group, 0.075–0.25 mm and 0.25–0.5 mm, the critical state appears to correspond to approximately 20% axial strain, while for the large size group, 0.5–2 mm and 2–5 mm, the stress critical state appears after 25% axial strain. This indicates that larger particles require greater axial shear strain to achieve stress stability.

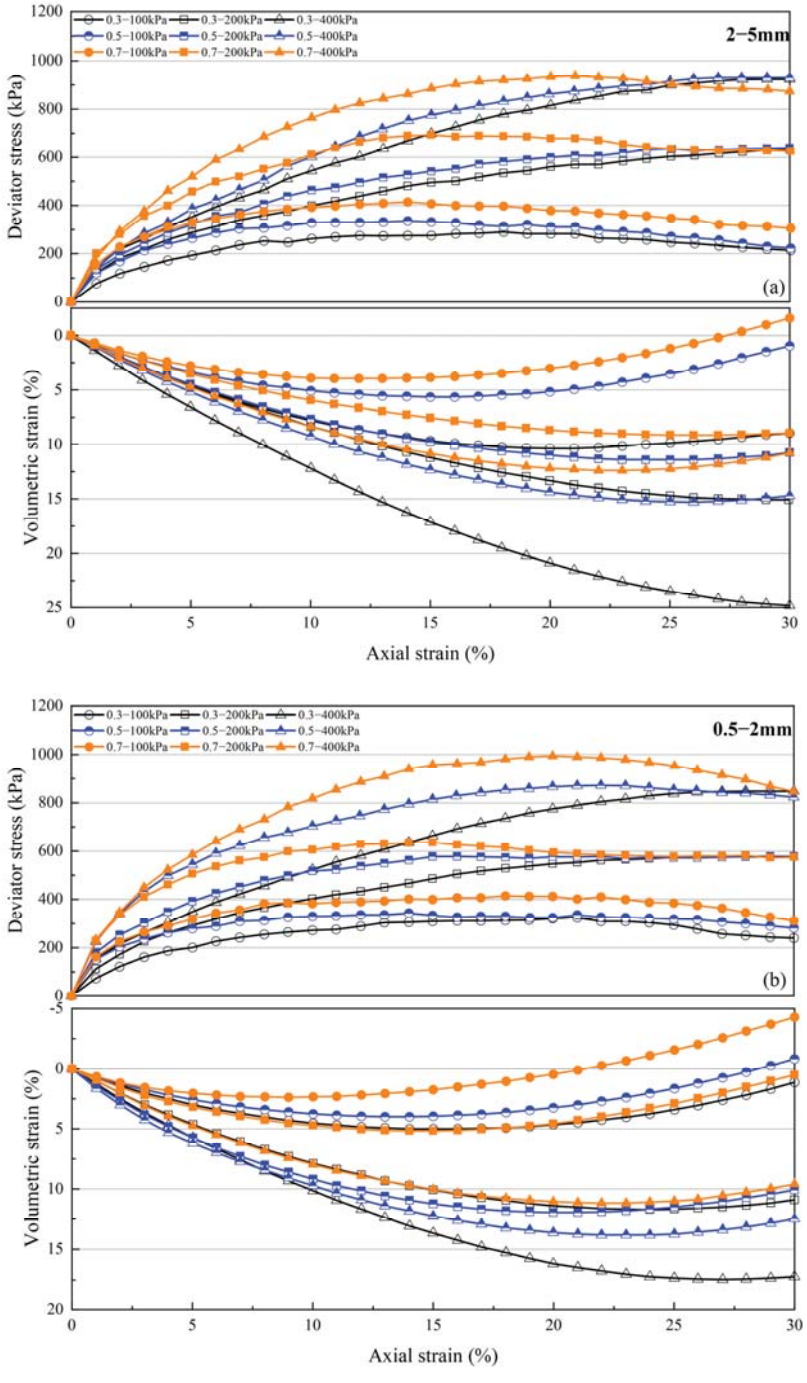

Figure 5. *Cont.*

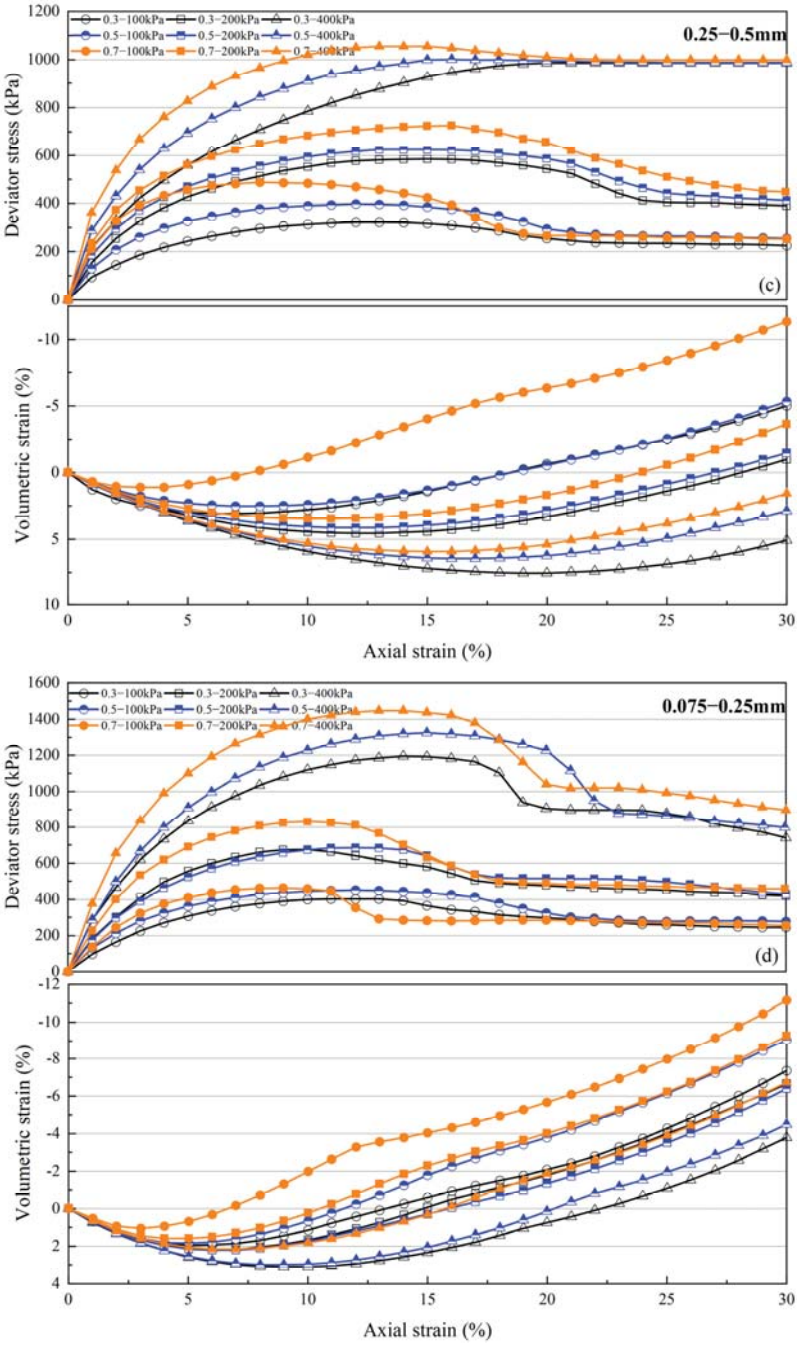

Figure 5. Deviator stress–axial strain–volumetric strain curves of volcanic soil with different relative density (*Dr*) and confining pressure(σ_3): (**a**) 2–5 mm particle group; (**b**) 0.5–2 mm particle group; (**c**) 0.25–0.5 mm particle group; (**d**) 0.075–0.25 mm particle group.

Figure 6 shows the maximum volumetric contraction strain of four particle size groups after triaxial shear testing. The maximum volumetric contraction strain of all specimens increased with increasing confining pressure, particle size, and decreasing relative density varied from 1% to 25%; under the same relative density and confining pressure conditions, as particle size increases, the void ratio also increases, and particles are more likely to move and crush during shearing, producing greater compressibility [32]. Hence, in road engineering, the selection of smaller grain size volcanic soil as road foundation fill can significantly reduce the settlement deformation of the foundation.

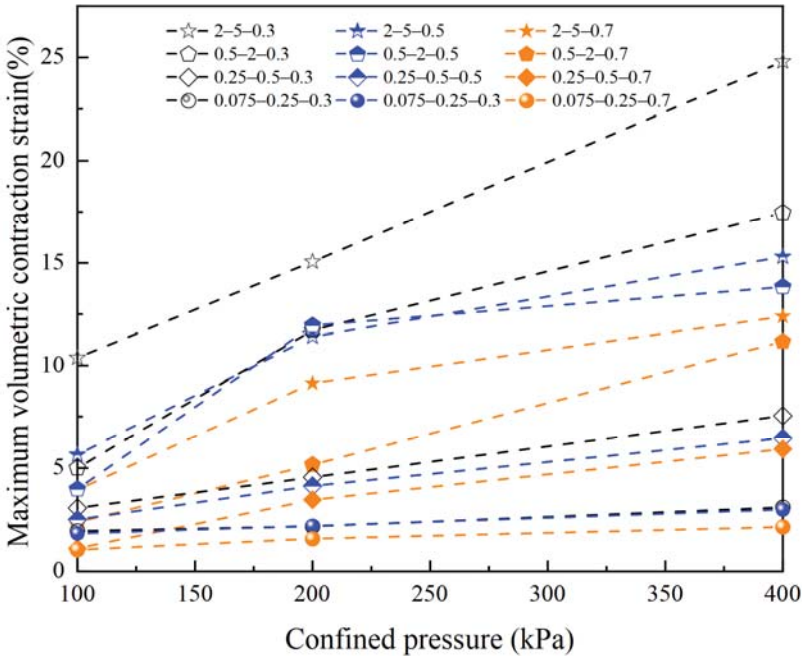

Figure 6. Maximum volumetric contraction strain of volcanic soil with different relative density and confining pressure in four particle size groups.

3.2. Peak Strength Index

Figures 7–10 show four volcanic soil particle size groups shear strength envelopes with different relative densities (*Dr*) under peak state. Although these four particle sizes belong to the coarse particle size group in the particle size category, the fitted values reveal that there is still a non-negligible cohesion, approximately 30.62–94.64 kPa, which may be attributed to the occlusion effect caused by the irregular shape of coarse particles, according to previous studies on similar materials, e.g., calcareous sands [32,33]. For the >0.25 mm particle sizes group, as for the same particle size group, cohesion increases significantly with increases in relative density. For 0.5–2 mm and 0.075–0.25 mm particle groups, the internal friction angle slowly increases with increases in relative density. With an increase in relative density, the internal friction angle tends to decrease for 2–5 mm and 0.25–0.5 mm particle size groups.

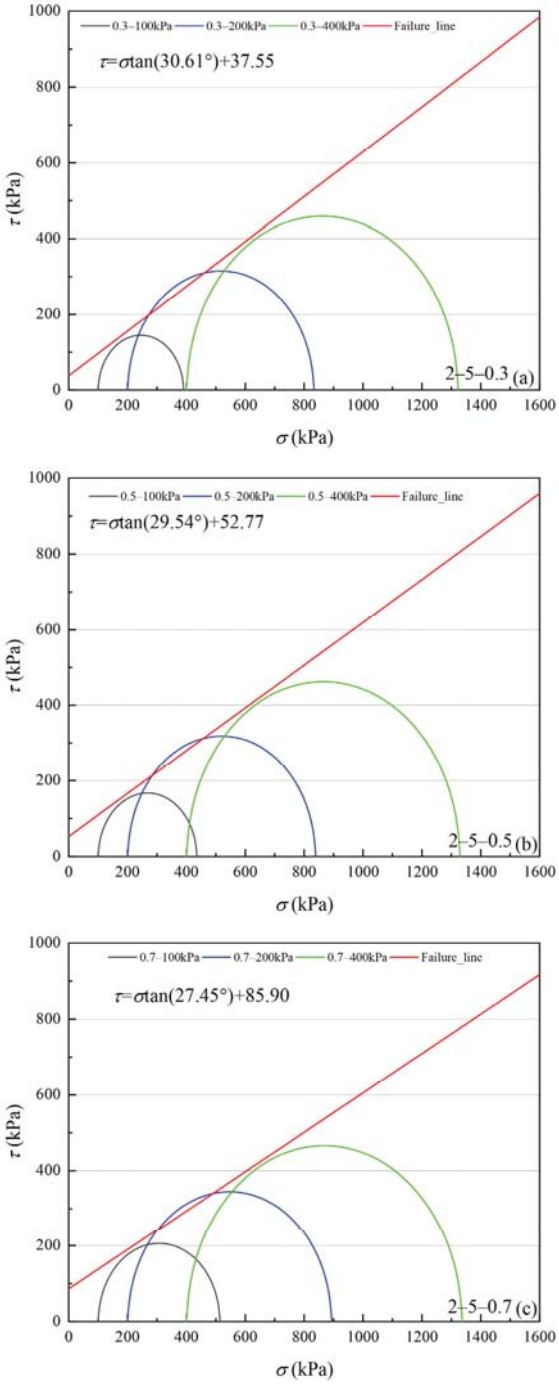

Figure 7. Shear strength envelopes of 2–5 mm particle groups volcanic soil with different relative density (*Dr*) under the peak state: (**a**) *Dr* = 0.3, (**b**) *Dr* = 0.5, (**c**) *Dr* = 0.7.

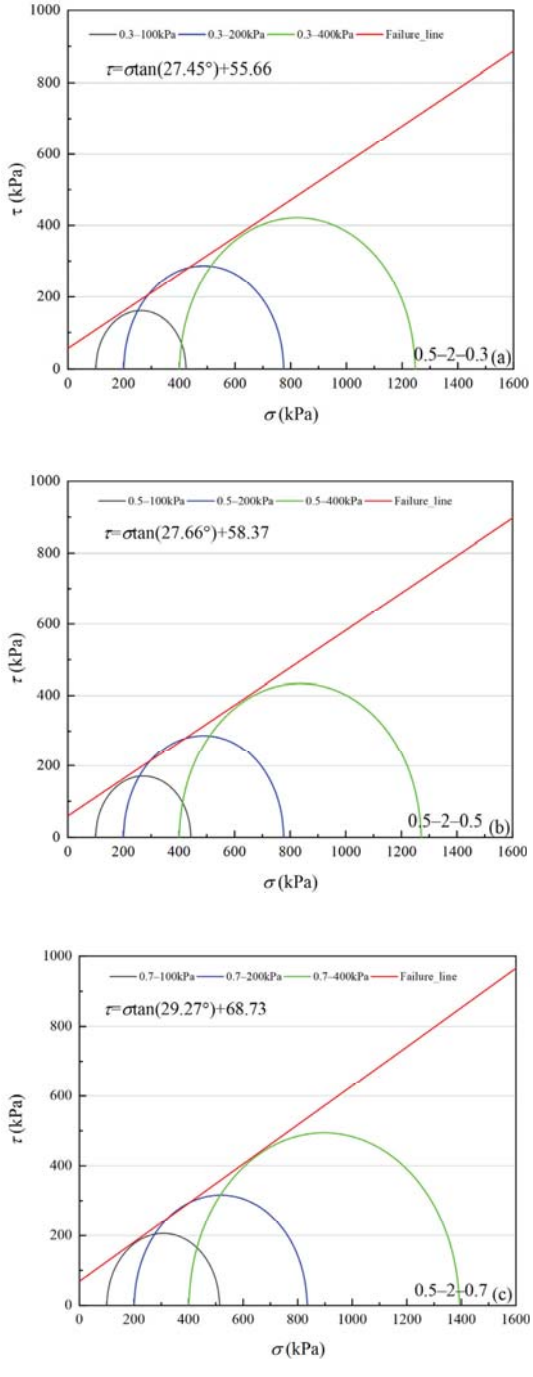

Figure 8. Shear strength envelopes of 0.5–2 mm particle groups volcanic soil with different relative density (*Dr*) under the peak state: (**a**) *Dr* = 0.3, (**b**) *Dr* = 0.5, (**c**) *Dr* = 0.7.

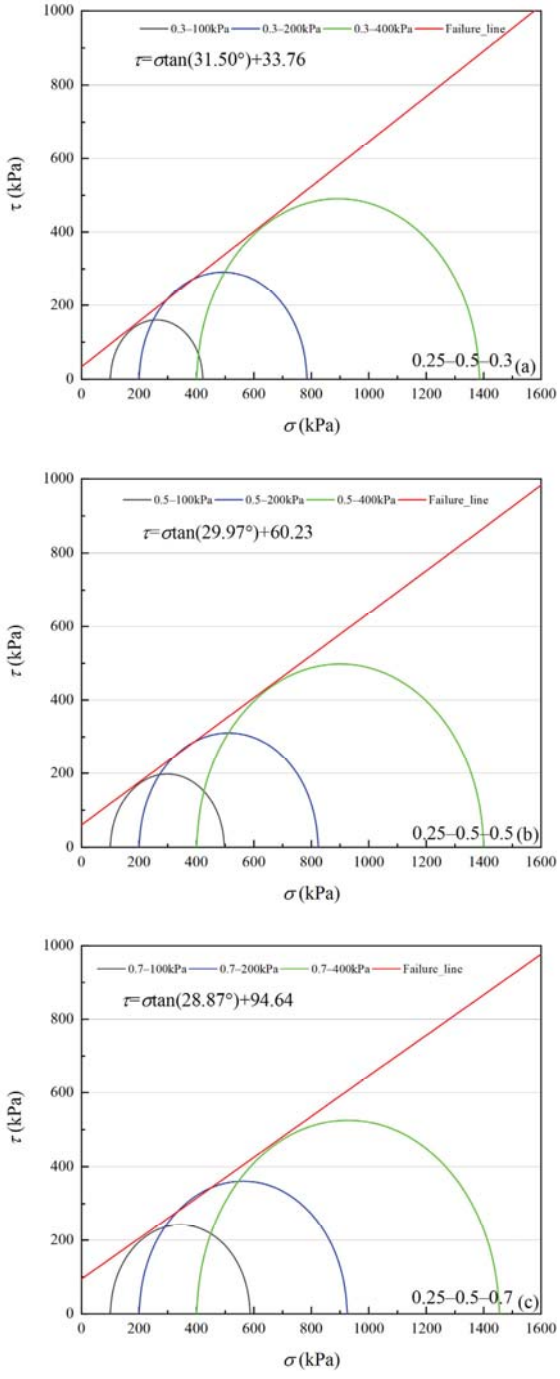

Figure 9. Shear strength envelopes of 0.25–0.5 mm particle groups volcanic soil with different relative density (*Dr*) under the peak state:(**a**) *Dr* = 0.3, (**b**) *Dr* = 0.5, (**c**) *Dr* = 0.7.

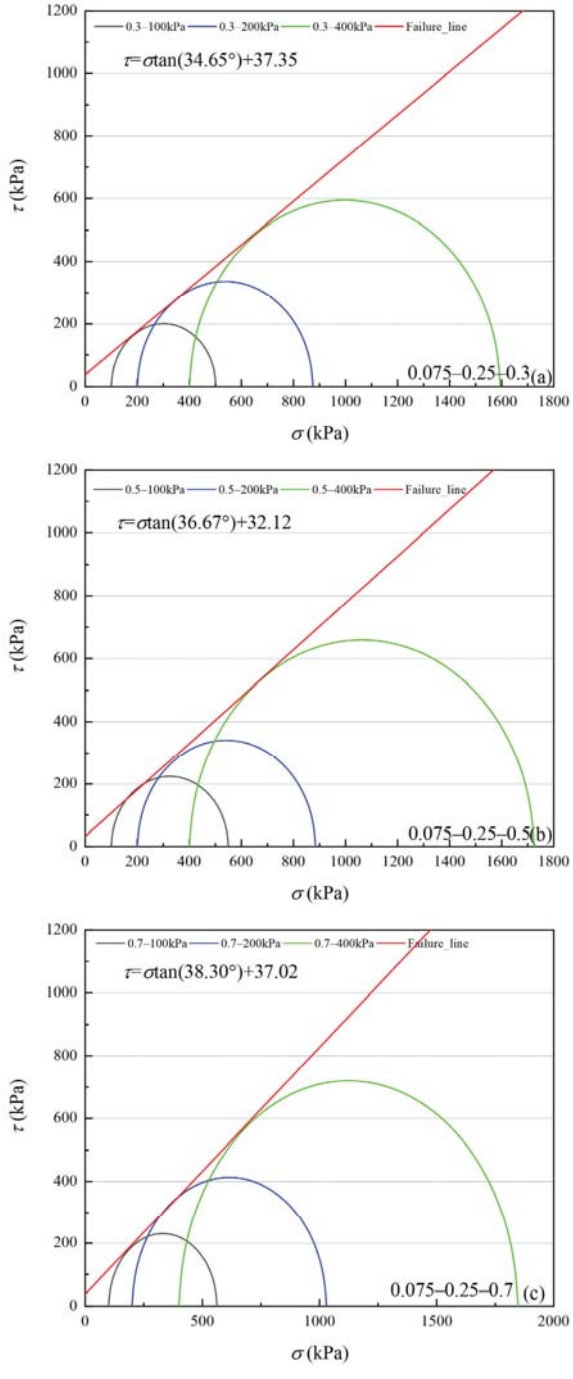

Figure 10. Shear strength envelopes of 0.075–0.25 mm particle groups volcanic soil with different relative density (*Dr*) under the peak state: (**a**) *Dr* = 0.3, (**b**) *Dr* = 0.5, (**c**) *Dr* = 0.7.

According to classical Mohr–Coulomb theory, the shear strength index is only related to the material composition and the initial density of specimens, not to the load stress level [34]. If Mohr–Coulomb fitted values are used, the internal friction angle and cohesion are artificially separated from the engineering perspective. The occlusion effect is also a part of the friction component in coarse-grained soils [29,35]. Volcanic soils can be crushed at low load stress levels. As confining pressure increases, particle crushing degree increases to suppress shear dilation behavior between particles, which leads to a decrease in the internal friction angle [36]. Therefore, it is necessary to consider the internal friction angle decreasing effect as confining pressure increases for crushable volcanic soils. For coarse-grained soils, the peak friction angle (φ_{max}) is calculated as Equation (1) [29].

$$\varphi_{max} = sin^{-1}\frac{(\sigma_1 - \sigma_3)_{max}}{(\sigma_1 + \sigma_3)_{max}} \quad (1)$$

Figure 11 shows the peak internal friction angle of volcanic soil. Under the same relative density and particle size condition, peak friction angle decreases significantly with an increase in confining pressure. Under low confining pressure, the particle crushing degree is slight, and the shear dilation effect between the particles increases occlusion friction, causing a higher peak internal friction angle. With an increase of confining pressure, deviator stress increases, which causes particle crushing degree increases; particle crushing effect partially eliminates shear dilation effect, shear dilation gradually disappears, the occlusion effect is gradually eliminated, and the friction effect between particles is gradually reduced [36]. The results reveal that the peak friction angle decreases as particle size increases and relative density decreases. Therefore, in engineering construction, the greater the relative density and the higher the content of fine particles in road foundation fill, the better its bearing capacity.

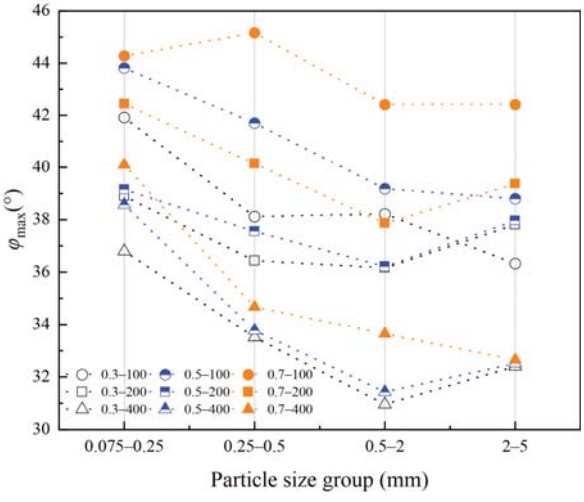

Figure 11. Peak internal friction angle of volcanic soil with different relative density (*Dr*) and confining pressure(σ_3) in four particle size groups.

3.3. Critical State Line

According to the results in Section 3.1, four grain size volcanic soils reached critical conditions at 30% axial strain. Figure 12 shows critical state lines of volcanic soil with four different particle size groups. Critical state stress ratios of different particle size groups are significantly different. The critical state stress ratio is the largest for the 2–5 mm particle size group and the smallest for the 0.075–0.25 mm particle size group.

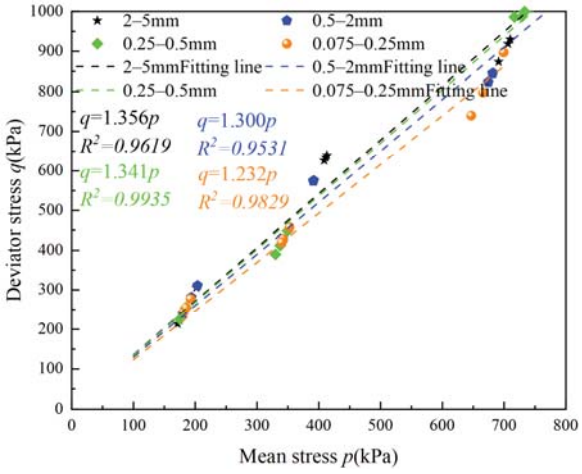

Figure 12. Critical state lines of volcanic soil with different particle sizes on deviator stress and mean stress plane.

4. Gradation Curve Evolution

After shearing tests, the gradation curves of both particle size groups significantly shifted upward with an increase in relative density and confining pressure (Figure 13). At 100 kPa confining pressure condition, specimen gradation curves have changed significantly, which indicates that volcanic soils have generated large crushing amounts at low confining pressures [9]. For a certain particle size group, the gradation curve shifts upward continuously with increasing relative density (*Dr*) and confining pressure(σ_3). Under the same conditions, the denser specimen shows a greater crushing amount. A dense specimen will contain an increased number of grains and therefore have a larger grain coordination number. Conversely, a larger grain coordination number will enhance the interactions between the grains and the surrounding grains and increase the probability of grain crushing [37]. For different particle size groups, the crushing degree of the 2–5 mm particle size group is greater under the same confining pressure and relative density. Larger particles are more vulnerable to crushing because they contain more internal flaws and the surface shapes are more irregular. Overall, the particle crushing degree of volcanic soil is influenced by confining pressure, relative density, and particle size.

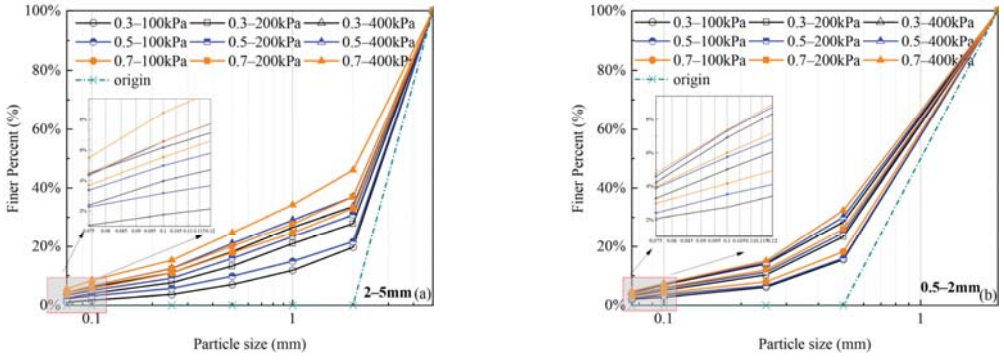

Figure 13. Evolutions of particle size distribution curves of volcanic soil with different relative density (*Dr*) and confining pressure(σ_3): (**a**) 2–5 mm particle groups; (**b**) 0.5–2 mm particle groups.

4.1. Crushing Degree Measurement

4.1.1. Relative Breakage Rate *Br*

The relative breakage rate *Br* proposed by Hardin [11] is broadly used to evaluate the particle crushing degree in the soil mass. The definition of *Br* calculated is shown in Figure 14. Where *Bp* is defined as the area enclosed inside the initial grading curve (AB line) and the line of 0.074 mm particle size (OC line); *Bt* is defined as the area enclosed inside the current grading (AD line), initial grading (AB line), and the 0.074 mm particle size line (CD line).

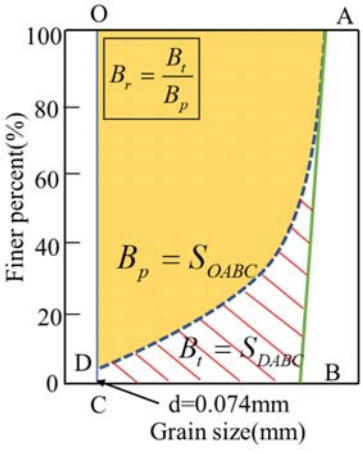

Figure 14. Defining of the relative breakage rate.

For both particle size groups, *Br* increases with increasing confining pressure and relative density (Table 4, 2nd column), and the maximum *Br* reached 0.382. There is a positive correlation between *Br* and confining pressure (Figure 15), and the 2–5 mm particle size group has a greater relative breakage rate under the same conditions.

Table 4. Table of correlation coefficients and plastic work for large particle size group.

Sieving Test Sample	*Br*	*D*	R^2 (Fractal)	*a*	*b*	R^2 (HILL)	*Wp* (kPa)
2-5-0.3-100	0.151	1.898	0.958	3.173	0.812	0.988	78.599
2-5-0.3-200	0.229	2.125	0.969	2.275	0.658	0.982	165.014
2-5-0.3-400	0.283	2.257	0.971	1.456	0.642	0.980	264.891
2-5-0.5-100	0.174	2.057	0.929	3.902	0.656	0.990	89.152
2-5-0.5-200	0.255	2.195	0.970	1.674	0.677	0.978	169.370
2-5-0.5-400	0.312	2.278	0.977	1.071	0.677	0.970	290.556
2-5-0.7-100	0.275	2.229	0.971	1.442	0.671	0.973	102.541
2-5-0.7-200	0.308	2.277	0.978	1.153	0.664	0.978	191.436
2-5-0.7-400	0.382	2.366	0.988	0.681	0.697	0.983	307.688
0.5-2-0.3-100	0.128	1.774	0.988	2.015	0.984	0.991	77.369
0.5-2-0.3-200	0.196	1.965	0.996	1.174	0.979	0.991	153.606
0.5-2-0.3-400	0.241	2.069	0.996	1.146	0.972	0.989	250.489
0.5-2-0.5-100	0.133	1.829	0.981	2.274	0.905	0.984	84.601
0.5-2-0.5-200	0.208	2.012	0.996	1.172	0.931	0.990	166.295
0.5-2-0.5-400	0.254	2.091	0.995	0.822	0.970	0.989	261.325
0.5-2-0.7-100	0.152	1.898	0.985	1.974	0.883	0.988	102.395
0.5-2-0.7-200	0.219	2.028	0.997	1.048	0.952	0.992	167.419
0.5-2-0.7-400	0.272	2.104	0.995	0.724	1.005	0.992	279.888

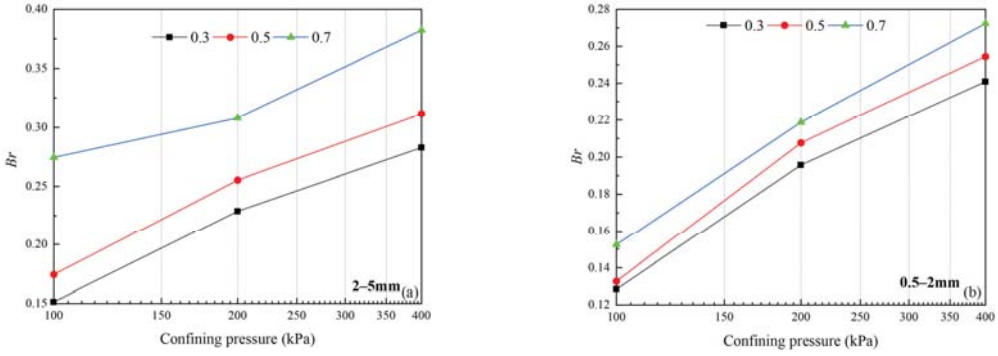

Figure 15. Variations in relative breakage rate (*Br*) with different relative density (*Dr*) and confining pressure(σ_3): (**a**) 2–5 mm particle groups; (**b**) 0.5–2 mm particle groups.

4.1.2. Fractal Dimension *D*

Previous studies on soil particle crushing indicated that the mass distribution of crushed particles showed fractal characteristics [32,38–40]. The mass of particles with different sizes meets the relationship given in Equation (2).

$$\frac{M(d < d_i)}{M_t} = \left(\frac{d_i}{d_{max}}\right)^{3-D} \quad (2)$$

where d is particle diameter, d_i is ith sieving diameter (i = 1, 2, . . . , n); d_{max} is the diameter of the largest particle, M ($d < d_i$) is the cumulative mass of soil particles with particle size less than d_i; M_t is the total mass of soil particles. $D = 3 - k$, where D is fractal dimension, k is the slope of the relationship curve between $M(d < d_i)/M_t$ and d_i/d_{max} in the logarithmic coordinate system.

Before tests, these two particle size groups (0.5–2 mm, 2–5 mm) do not show fractal characteristics; after shear tests, all specimens exhibit obvious fractal characteristics, (Table 4, 3th column). Fractal dimension D increases with an increase of confining pressure σ_3 and relative density Dr, and the fractal dimension shows a positive correlation with relative density (Figure 16). Under the same conditions, the 2–5 mm particle size group has a larger fractal dimension. This is because the initial particle size of that is larger, and particle crushing produces a wider particle size distribution, which makes fractal characteristics more obvious [32].

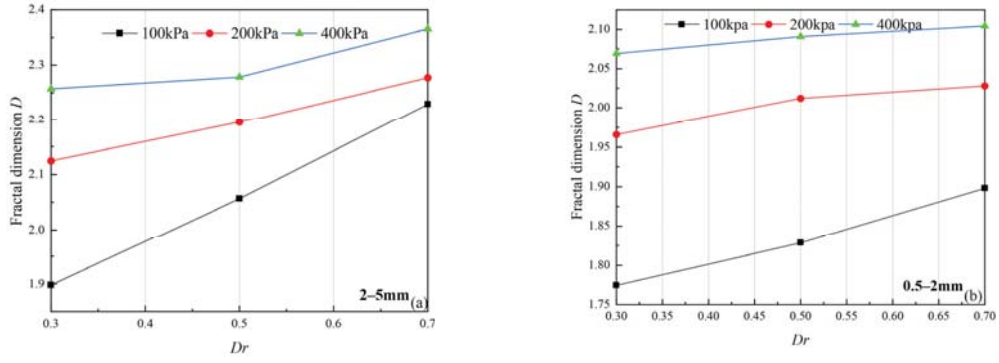

Figure 16. Variations in fractal dimension (*D*) with different relative density (*Dr*) and confining pressure(σ_3): (**a**) 2–5 mm particle groups; (**b**) 0.5–2 mm particle groups.

4.1.3. Associations between *Br* and *D*

Figure 17 shows the variation of fractal dimension *D* with relative breakage rate *Br*; there is a good linear relationship between them, and the relationship between *D* and *Br* is not affected by relative density and confining pressure only by particle size. The 2–5 mm particle size group has a larger fractal dimension compared with the 0.5–2 mm particle group under the same *Br*.

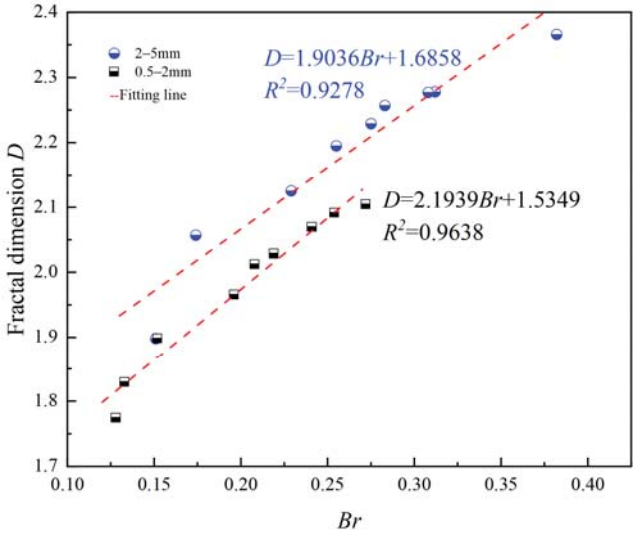

Figure 17. Variations in Fractal dimension (*D*) with relative breakage rate (*Br*).

4.2. Particle Crushing Pattern

Soil particle crushing patterns are generally classified into three patterns: abrasion, breakoff, and splitting [41]. Dong et al. [42] proposed and experimentally verified a probability density function that can describe a single particle size group crushing pattern based on a large number of point load experiments. The Hill probability density function f is expressed as follows:

$$f = -\frac{a^b b\left(\frac{x_i}{1-x_i}\right)^b}{x_i(x_i-1)\left[\left(\frac{x_i}{1-x_i}\right)^b + a^b\right]^2} \quad (3)$$

where $x_i = d_i/d_{max}$, d_i is crushed sub-particle size, and d_{max} is the maximum particle size of the original particle group. The fitting parameters are a and b. Parameter a controls the particle size ratio that is most likely to appear after particle crushing, and parameter b controls the curve shape. According to the parameters of a, b, three crushing patterns can be determined. In this paper, values a range from 0.68 to 3.173, and values b range from 0.64 to 1 (Table 4, 5th, 6th column).

Figure 18 shows the variation of Hill probability density function f in two particle size groups: for any one of the specimens, as x_i increases, the probability density function f presents that extreme values appear at both ends (x_i near 0 or 1) of the curve, and one end is higher than the other; according to Dong's result [42], the curve types of these two particle size groups can be defined as breakoff type, which is in good agreement with the test photographs (Figure 19). For the same particle size groups, when x_i is near zero, the probability density function f shifts upward as confining pressure increases under the same relative density condition. However, there is no obvious rule for the probability density function f at different relative densities under the same confining pressure, which

indicates that the Hill probability density function may not be sensitive to the change in the relative density.

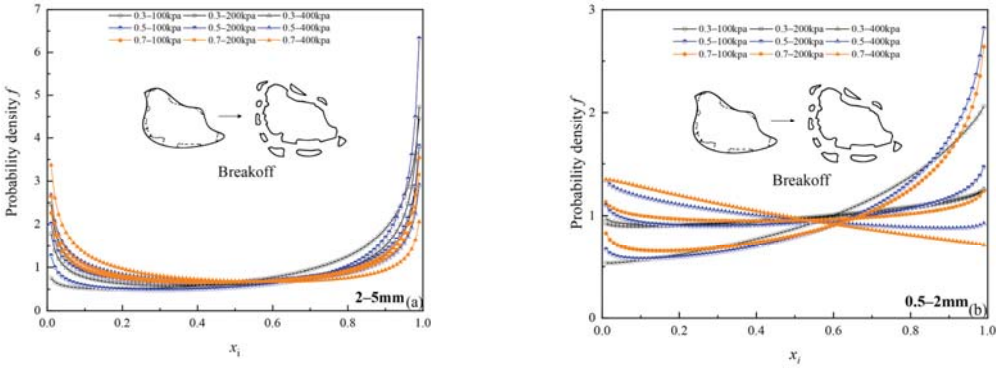

Figure 18. Variation of Hill probability density function f with different relative density (*Dr*) and confining pressure (σ_3): (**a**) 2–5 mm particle groups; (**b**) 0.5–2 mm particle groups.

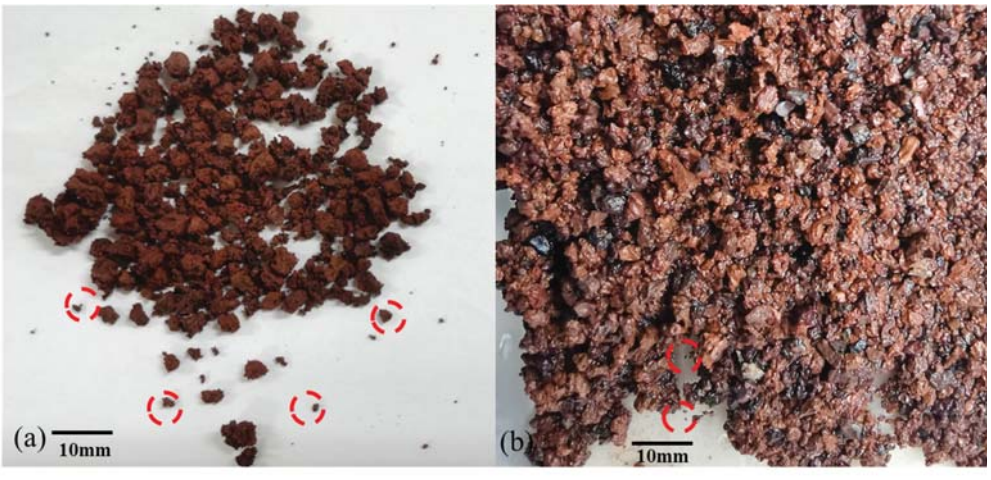

Figure 19. Photos of volcanic soil after shear test: (**a**) 2–5 mm-0.7–400 kPa test sample; (**b**) 0.5–2 mm–0.7–400 kPa test sample.

5. Plastic Work Analysis

Since grain crushing is a process in which grains consume external work and result in energy loss, the evolution laws of volcanic soil grain crushing during the test can be studied in terms of plastic work (*Wp*) [37,43]. *Wp* is defined as the irrecoverable energy extracted by the sample during the test, and it is equal to the sum of plastic work done by shear stress (W_1) and the plastic work done by mean effective stress (W_2). Given that crushable coarse-grained soils undergo only slight elastic deformation during the test, dεd and dεv could be directly adopted to determine the *Wp* [44].

$$Wp = W_1 + W_2 = \int q d\varepsilon_d^p + \int p d\varepsilon_v^p \approx \int q d\varepsilon_d + \int p d\varepsilon_v \quad (4)$$

The results of plastic work for these two particle sizes group are shown in Table 4 (8th column); for the same particle size group, plastic work increases with the increase

of confining pressure and relative density. For different particle size groups, the 2–5 mm particle size group needs to consume more plastic work, whereas the difference is not large. Under the same confining pressure and relative density conditions, for example, plastic work consumed by 2–5 and 0.3–100 kPa specimens and 0.5–2 to 0.3–100 kPa specimens are basically the same, but the difference between their relative breakage rate *Br* was larger, which indicates that the 0.5–2 mm particle group needs more plastic work than the 2–5 m particle group to reach the same relative breakage rate *Br*. The main reason is that the shape of the 2–5 mm particle group is more irregular, with larger internal flaws compared to the 0.5–2 mm particle group (Figure 4), which leads to a greater susceptibility to crushing for the same external load work conditions, causing a greater relative breakage rate. The relationship between the plastic work (*Wp*) and the relative breakage rate (*Br*) for these two particle sizes groups follows the power function (Figure 20a,b), which can be fitted using Equation (5), with *A*, *B* as the fitting parameters. For the same particle size groups, the relationship between plastic work and the relative breakage rate is not significantly influenced by the relative density and the confining pressure. Scholars' studies on calcareous sands also confirm this conclusion [37], however, in their research, $Br = 1.17 \times 10^{-5} Wp^{1.42}$. By comparing the equations in this study with theirs, it can be found that the amount of crushing is greater under the same plastic work in this study, which is mainly because the main minerals strength of calcareous sand are stronger compared to volcanic soil particles, therefore, calcareous sand particles are less likely to crush under the external force, which also shows that the mineral composition has a great influence on particle breakage.

$$Br = AWp^{B} \tag{5}$$

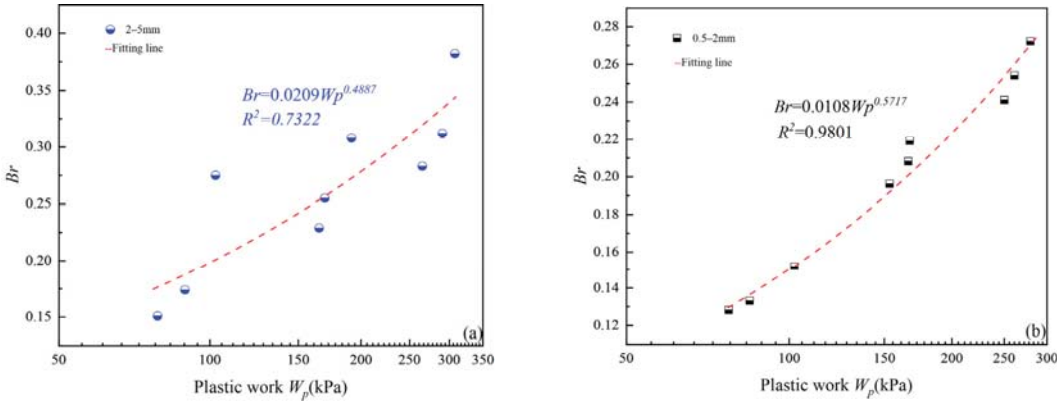

Figure 20. Variations in relative breakage rate with plastic work: (**a**) 2–5 mm particle groups; (**b**) 0.5–2 mm particle groups.

6. Conclusions

A series of consolidation drainage shear tests were carried out to investigate the effects of particle size, confining pressure, and relative density on the mechanical properties and crushing characteristics of volcanic soils. The characteristics of soil stress–strain curve, shear strength index, critical state behavior, and quantification of particle fragmentation characteristics, using fractal dimension and relative breakage rate were systematically investigated. Finally, the quantitative relationship between external work and fragmentation amount was established through the energy perspective. The main findings are as follows:

Stress–strain curves characteristic of volcanic soil were affected by particle size; the large particle size groups (>0.5 mm) required larger axial strain to reach a stress steady state. The critical stress ratio was significantly influenced by particle size, with the largest

critical stress ratio for the 2–5 mm particle size group and the smallest critical stress ratio for the 0.075–0.25 mm particle size group.

For crushable volcanic soils, there was a clear physical significance in using the peak internal friction angle index when considering the confining pressure effect; peak friction angle decreased significantly with the increase of confining pressure, and peak friction angle decreased as particle size increased and relative density decreased.

The particle crushing amount increased with increasing particle size, relative density, and confining pressure. For the same particle size, there was a good linear relationship between *Br* and *D*. Crushing patterns of large particle size groups could be classified as breakoff type. From an energy perspective, the power function relationship between *Wp* and *Br* of large particle size group was established, the relationship was only affected by particle size, and it was not significantly affected by the relative density and effective confining pressure. The results of comparison with similar materials [37] also confirm that the mineral composition has a large influence on the particle crushing amount.

In terms of engineering, based on the results of this study, it can be concluded that volcanic soil with fine particles used as roadbed filler can significantly reduce the deformation of the roadbed and improve the bearing capacity of the foundation, in addition to increasing the compaction degree of volcanic soil.

Author Contributions: Conceptualization, X.-Y.L.; methodology, X.-Y.L.; writing—original draft preparation, X.-Y.L.; investigation, H.-L.L. and D.W.; data curation, X.-Y.L., H.-L.L. and D.W.; writing—review and editing, C.-M.W., H.-L.L. and D.W.; project administration, C.-M.W.; funding acquisition, C.-M.W. All authors have read and agreed to the published version of the manuscript.

Funding: This research was funded by National Natural Science Foundation of China (Grant Nos. 41972267).

Institutional Review Board Statement: Not applicable.

Informed Consent Statement: Not applicable.

Data Availability Statement: Data is contained within the article.

Conflicts of Interest: The authors declare no conflict of interest.

Abbreviations

Gs	Specific gravity
ρ_{dmin}	Minimum dry density (Unit: g/cm^3)
ρ_{dmax}	Maximum dry density (Unit: g/cm^3)
e_{min}	Minimum void ratio
e_{max}	Maximum void ratio
d	Particle size (mm)
d_{30}	The mass of soil particles smaller than this particle size is 30% of the total mass of soil particles (mm)
d_{60}	The mass of soil particles smaller than this particle size is 60% of the total mass of soil particles (mm)
Dr	Relative density
σ_3	Confining pressure (Unit: kPa)
σ	Normal stress (Unit: kPa)
τ	Shear stress (Unit: kPa)
c	Soil cohesion (Unit: kPa)
φ	Soil internal friction angle (°)
D	Fractal dimension
Br	Relative breakage rate
R^2	Coefficient of correlation
f	Probability density function

W_p	Plastic work (Unit: kPa)
W_1	Plastic work done by shear stress (Unit: kPa)
W_2	Plastic work done by mean effective stress (Unit: kPa)
q	Deviator stress (Unit: kPa)
p	Mean effective stress (Unit: kPa)
$d\varepsilon_d^p$	Plastic shear strain increment
$d\varepsilon_v^p$	Plastic volumetric strain increment
$d\varepsilon_d$	Shear strain increment
$d\varepsilon_v$	Volumetric strain increment
a	Fitting parameter
b	Fitting parameter
A	Fitting parameter
B	Fitting parameter

References

1. Luo, Q.; Liang, D.; Wang, T.; Zhang, L.; Jiang, L. Engineering properties testing of scoria as railway subgrade fill. *J. Zhejiang Univ.* **2020**, *54*, 2395–2404. [CrossRef]
2. Navia, R.; Rivela, B.; Lorber, K.E.; Mendez, R. Recycling contaminated soil as alternative raw material in cement facilities: Life cycle assessment. *Resour. Conserv. Recycl.* **2006**, *48*, 339–356. [CrossRef]
3. Babel, S.; Opiso, E.M. Removal of Cr from synthetic wastewater by sorption into volcanic ash soil. *Int. J. Environ. Sci. Technol.* **2007**, *4*, 99–107. [CrossRef]
4. Jalil, A.A.; Triwahyono, S.; Adam, S.H.; Rahim, N.D.; Aziz, M.A.A.; Hairom, N.H.H.; Razali, N.A.M.; Abidin, M.A.Z.; Mohamadiah, M.K.A. Adsorption of methyl orange from aqueous solution onto calcined Lapindo volcanic mud. *J. Hazard. Mater.* **2010**, *181*, 755–762. [CrossRef]
5. Ji, M.; Su, X.; Zhao, Y.; Qi, W.; Wang, Y.; Chen, G.; Zhang, Z. Effective adsorption of Cr(VI) on mesoporous Fe-functionalized Akadama clay: Optimization, selectivity, and mechanism. *Appl. Surf. Sci.* **2015**, *344*, 128–136. [CrossRef]
6. Lemougna, P.N.; Wang, K.T.; Tang, Q.; Nzeukou, A.N.; Billong, N.; Melo, U.C.; Cui, X.M. Review on the use of volcanic ashes for engineering applications. *Resour. Conserv. Recycl.* **2018**, *137*, 177–190. [CrossRef]
7. Silva-Yumi, J.; Escudey, M.; Gacitua, M.; Pizarro, C. Kinetics, adsorption and desorption of Cd(II) and Cu(II) on natural allophane: Effect of iron oxide coating. *Geoderma* **2018**, *319*, 70–79. [CrossRef]
8. Asadi, M.S.; Orense, R.P.; Asadi, M.B.; Pender, M.J. Maximum dry density test to quantify pumice content in natural soils. *Soils Found.* **2019**, *59*, 532–543. [CrossRef]
9. Agustian, Y.; Goto, S. Strength and deformation characteristics of scoria in triaxial compression at low confining stress. *Soils Found.* **2008**, *48*, 27–39. [CrossRef]
10. Ishikawa, T.; Miura, S. Influence of Freeze-Thaw Action on Deformation-Strength Characteristics and Particle Crushability of Volcanic Coarse-Grained Soils. *Soils Found.* **2011**, *51*, 785–799. [CrossRef]
11. Hardin, B.O. Crushing of soil particles. *J. Geotech. Eng.* **1985**, *111*, 1177–1192. [CrossRef]
12. Yamamuro, J.A.; Bopp, P.A.; Lade, P.V. One-Dimensional Compression of Sands at High Pressures. *J. Geotech. Eng.* **1996**, *122*, 147–155. [CrossRef]
13. Varadarajan, A.; Sharma, K.G.; Abbas, S.M.; Dhawan, A.K. Constitutive Model for Rockfill Materials and Determination of Material Constants. *Int. J. Geomech.* **2006**, *6*, 226–237. [CrossRef]
14. Karatza, Z.; Ando, E.; Papanicolopulos, S.A.; Viggiani, G.; Ooi, J.Y. Effect of particle morphology and contacts on particle breakage in a granular assembly studied using X-ray tomography. *Granul. Matter* **2019**, *21*, 44. [CrossRef]
15. Xiao, Y.; Long, L.; Evans, T.M.; Zhou, H.; Liu, H.; Stuedlein, A.W. Effect of Particle Shape on Stress-Dilatancy Responses of Medium-Dense Sands. *J. Geotech. Geoenvironmental Eng.* **2019**, *145*. [CrossRef]
16. Cavarretta, I.; O'Sullivan, C.; Coop, M.R. The relevance of roundness to the crushing strength of granular materials. *Geotechnique* **2017**, *67*, 301–312. [CrossRef]
17. Mcdowell, G.R.; Amon, A. The application of weibull statistics to the fracture of soil particles. *J. Jpn. Geotech. Soc.* **2000**, *40*, 133–141. [CrossRef]
18. Ovalle, C.; Frossard, E.; Dano, C.; Hu, W.; Maiolino, S.; Hicher, P.Y. The effect of size on the strength of coarse rock aggregates and large rockfill samples through experimental data. *Acta Mech.* **2014**, *225*, 2199–2216. [CrossRef]
19. Zhou, W.; Yang, L.; Ma, G.; Chang, X.; Lai, Z.; Xu, K. DEM analysis of the size effects on the behavior of crushable granular materials. *Granul. Matter* **2016**, *18*, 64. [CrossRef]
20. Shahnazari, H.; Rezvani, R. Effective parameters for the particle breakage of calcareous sands: An experimental study. *Eng. Geol.* **2013**, *159*, 98–105. [CrossRef]
21. Wu, Y.; Li, N.; Wang, X.; Cui, J.; Chen, Y.; Wu, Y.; Yamamoto, H. Experimental investigation on mechanical behavior and particle crushing of calcareous sand retrieved from South China Sea. *Eng. Geol.* **2021**, *280*, 105932. [CrossRef]

22. Casini, F.; Viggiani, G.; Springman, S.M. Breakage of an artificial crushable material under loading. *Granul. Matter* **2013**, *15*, 661–673. [CrossRef]
23. Jia, Y.; Xu, B.; Chi, S.; Xiang, B.; Xiao, D.; Zhou, Y. Particle breakage of rockfill material during triaxial tests under complex stress paths. *Int. J. Geomech.* **2019**, *19*, 04019124. [CrossRef]
24. Kikkawa, N.; Pender, M.J.; Orense, R.P.; StGeorge, J.D.; Matsushita, E. K-0 Compression and Stress Relaxation of Pumice Sand. *J. Geotech. Geoenvironmental Eng.* **2012**, *138*, 625–628. [CrossRef]
25. Galvis-Castro, A.C.; Colmenares, J.E.; Garcia-Leal, J.C. Primary and Secondary Compression of a Colombian Volcanic Ash Soil. *Geotech. Geol. Eng.* **2021**, *40*, 1485–1497. [CrossRef]
26. Asadi, M.B.; Asadi, M.S.; Orense, R.P.; Pender, M.J. Small-Strain Stiffness of Natural Pumiceous Sand. *J. Geotech. Geoenvironmental Eng.* **2020**, *146*, 06020006. [CrossRef]
27. Salman, M.S.; Hasan, M.N.; Kubra, K.T.; Hasan, M.M. Optical detection and recovery of Yb(III) from waste sample using novel sensor ensemble nanomaterials. *Microchem. J.* **2021**, *162*, 105868. [CrossRef]
28. Liu, H.L.; Wang, C.M.; Liu, X.Y.; Wu, D.; Yang, H.R.; Zhang, Z.M.; Khan, K.U.J. Deformation characteristics and prediction of unbound volcanic ash pavement based on the mechanistic-empirical design guide. *Constr. Build. Mater.* **2022**, *327*, 126975. [CrossRef]
29. Li, G.; Zhang, B.; Yu, Y. *Soil Mechanics*, 2nd ed.; Tsinghua University Press: Beijing, China, 2013.
30. *GB/T50123-2019*; Standard for Soil Test Method. Chinese Ministry of Water Resources: Beijing, China, 2019. (In Chinese)
31. Rifa'i, A.; Yasufuku, N. Utilization of bantak and merapi volcanic ash for porous paving block as drainage control in the prambanan temple yard. *Int. J. Geomate* **2017**, *12*, 141–146. [CrossRef]
32. Wang, X.; Wang, X.; Shen, J.; Zhu, C. Particle size and confining-pressure effects of shear characteristics of coral sand: An experimental study. *Bull. Eng. Geol. Environ.* **2022**, *81*, 1–25. [CrossRef]
33. Yan, C.P.; Long, Z.L.; Zhou, Y.C.; Kuang, D.M.; Chen, J.M. Investigation on the effects of confining pressure and particle size of shear characteristics of calcareous sand. *Rock Soil Mech.* **2020**, *41*, 581–591. [CrossRef]
34. Zhang, J. Study on the Fundamental Mechanical Characteristics of Calcareous Sand the Influence of Particle Breakage. Ph.D. Thesis, Chinese Academy of Sciences (Wuhan Institute of Geotechnical Mechanics), Wuhan, China, 2004.
35. Lee, K.L.; Farhoomand, I. Compressibility and Crushing of Granular Soil in Anisotropic Triaxial Compression. *Can. Geotech. J.* **1967**, *4*, 68–86. [CrossRef]
36. Zhang, J.; Hua, C.; Luo, M.; Zhang, B. Behavior of particle breakage in calcareous sand duing drained triaxial shearing. *Chin. J. Geotech. Eng.* **2020**, *42*, 1593–1602.
37. Wang, X.; Liu, J.-Q.; Cui, J.; Wang, X.-Z.; Shen, J.-H.; Zhu, C.-Q. Particle breakage characteristics of a foundation filling material on island-reefs in the South China Sea. *Constr. Build. Mater.* **2021**, *306*, 124690. [CrossRef]
38. Altuhafi, F.N.; Coop, M.R. Changes to particle characteristics associated with the compression of sands. *Geotechnique* **2011**, *61*, 459–471. [CrossRef]
39. Coop, M.; Sorensen, K.; Bodas Freitas, T.; Georgoutsos, G. Particle breakage during shearing of a carbonate sand. *Géotechnique* **2004**, *54*, 157–163. [CrossRef]
40. Yu, F. Particle breakage in triaxial shear of a coral sand. *Soils Found.* **2018**, *58*, 866–880. [CrossRef]
41. Bideau, D. Du Sac de Billes au Tas de Sable (From a Bag of Marbles to a Pile of Sand). *Powder Technol.* **1995**, *82*, 211. [CrossRef]
42. Dong, Z.; Tong, C.; Zhang, S.; Sheng, D. Study on breakage transition matrix of granular soils. *Chin. J. Rock Mech. Eng.* **2021**, *40*, 1504–1512. [CrossRef]
43. Aghajani, H.F.; Salehzadeh, H.; Rezvani, R. Energy Equilibrium during Crushing of Sandy Soils under Isotropic Compression. *Arab. J. Sci. Eng.* **2016**, *41*, 1531–1542. [CrossRef]
44. Wu, Y.; Wang, X.; Shen, J.-H.; Cui, J.; Zhu, C.-Q.; Wang, X.-Z. Experimental Study on the Impact of Water Content on the Strength Parameters of Coral Gravelly Sand. *J. Mar. Sci. Eng.* **2020**, *8*, 634. [CrossRef]

materials

MDPI

Article

Change in the Torsional Stiffness of Rectangular Profiles under Bending Stress

Krzysztof Macikowski [1,*], Bogdan Warda [1], Grzegorz Mitukiewicz [1], Zlatina Dimitrova [2] and Damian Batory [1]

[1] Department of Vehicles and Fundamentals of Machine Design, Lodz University of Technology, Stefanowskiego 1/15, 90-537 Lodz, Poland; bogdan.warda@p.lodz.pl (B.W.); grzegorz.mitukiewicz@p.lodz.pl (G.M.); damian.batory@p.lodz.pl (D.B.)
[2] PSA Groupe, 78-140 Vélizy-Villacoublay, France; zlatina.dimitrova@mpsa.com
* Correspondence: kmacikowski@gmail.com; Tel.: +48-728528189

Abstract: This article presents the results of research on the change in torsional stiffness of two rectangular profiles, arranged one on top of the other, which were permanently connected at their ends. The flat bars were expanded in the middle of their active length. The test involved determining the increase in the stiffness of a twisted test set before and after expanding. The authors present an analysis of the structure load and compare the results of tests carried out using analytical (for selected cases), numerical and experimental methods, obtaining satisfactory compliance. The analytical calculations included the influence of limited deplanation in the areas of the profile's restraint. The ANSYS package software was used for calculations with the Finite Element Method. A change in the stiffness increase index at torsion was determined. The obtained results showed that expanding the test sets in their middle causes an increase in torsional stiffness, which is strongly dependent on the design parameters such as bending deflection, torsion angle and dimensions of the cross-section of the flat bar in the package.

Keywords: rectangular profile; torsional stiffness; stiffness increase; research; finite element method

Citation: Macikowski, K.; Warda, B.; Mitukiewicz, G.; Dimitrova, Z.; Batory, D. Change in the Torsional Stiffness of Rectangular Profiles under Bending Stress. *Materials* **2022**, *15*, 2567. https://doi.org/10.3390/ma15072567

Academic Editor: Krzysztof Schabowicz

Received: 25 February 2022
Accepted: 25 March 2022
Published: 31 March 2022

1. Introduction

The torsion of rectangular profiles is a load state in which the profiles are affected by the torsional moment in their cross-section plane. If the bars are restrained, their condition is described as restrained torsion. Torsional stiffness is the measure of the profiles' resistance to torsion and it depends on the material's mechanical characteristics and geometrical dimensions of the twisted profile [1].

The results of torsion tests are applied in many areas. In the automotive sector, they help design, e.g., torsion bars of variable stiffness. In civil engineering, they are used in the load-bearing systems of buildings [2–8] and other structures [9].

Ribeiro and Silveira [10] investigated the influence of changes in torsional stiffness by changing the distance between a car stabiliser's sleeves on the car body tilt while driving along an arch. The researchers determined that by increasing the test span from 100 mm to 300 mm, the tilt can be reduced from 2.76° to 2.65°. Without modifying the other structural parameters of the bar, they changed its stiffness from 7.87 kN/m to 9.35 kN/m.

Owing to the use of a hydraulic BMW Dynamic Drive hydraulic mechanism [11,12] which changes the torsional moment load of the middle part of the cross stabiliser (by counter-moment generation), the body tilt can be controlled depending on the vehicle motion conditions. For a vehicle that moves along a 40 m radius arch, it was reduced from ca. 3° to ca. 0.5° (at the lateral acceleration of 5 m/s^2).

Contrary to the BMW hydraulic system, Buma [13] used an electrical mechanism in the central part of the bar, connected with a toothed gear that enables reaching high torque values. The torque rotates the torsional bar in the opposite direction; the bar consists of

two coupled parts. The test car body's tilt was reduced from ca. 2.1° to 1° at the lateral acceleration of 5 m/s^2.

According to the results obtained by Doody [14] and Husen and Naniwadekar [15,16], the use of a metal sleeve (instead of a rubber one) for mounting the stabiliser increases its stiffness (including torsional stiffness of the central part) by 35% and 37%, respectively.

Shokry [17] investigated the strength of a rectangular beam made from polyester composite reinforced with glass fibre. The addition of nanoparticles was aimed at increasing the sample's bending strength. Other researchers also focused on the issue of bent profiles used for car leaf springs [18,19].

The results of experimental tests on reinforcing narrow beams with carbon fiber-reinforced laminates were reported by Bakalarz et al. [20]. The authors obtained 11% and 7% increase in the global modulus of elasticity in the bending and stiffness coefficients, respectively.

Wan and Jung [2,21,22] examined an LSB (LiteSteel beam) with a C-shaped cross-section, used in floor systems as ground beams or supporting beams, whose centre of gravity does not overlap with the shear centre. The results revealed that the torsional moment rises as the shear centre eccentricity increases, which leads to a significant decrease in the beams' resistance to the bending moment. Other researchers who carried out tests on beams with similar shapes obtained parallel results [23–25].

Structures used in everyday life are often exposed to complex states of stress. Simultaneous twisting and bending represent one of the most challenging cases. The literature review did not reveal any examples of two flat bars simultaneously subjected to such loads. In the presented paper, the numerical models of torsional stiffness of rectangular profiles under bending stress were determined. Additionally, the laboratory torsional tests of various sets of profiles with different cross-section shapes were conducted for the validation of the developed numerical models. The comparison of the results revealed good agreement between the registered numerical and experimental data, giving an opportunity of optimization of the profile shape and stiffening method of the analyzed sets in terms of achieving large changes in torsional stiffness with slight bending of the profiles.

1.1. Analysis of a Unexpanded Test Package

The presence of the cross-section limited deplanation results in auxiliary normal (tensile) stress occurring in addition to static (torsional) [26–30] stress in the profiles, contrary to pure torsion. This kind of torsion is called flexural torsion, and the total moment M_s necessary to twist the test set is a sum of two components: $M_{t,s}$ and $M_{t,w}$. The first corresponds to pure torsion (Saint Venant), while the other corresponds to flexural torsion moment.

$$M_s = M_{t,s} + M_{t,w} \quad (1)$$

A literature analysis [31–35] reveals that the $M_{t,s}$ and $M_{t,w}$ shares change in a non-linear way along the calculated element. The first ones have a constant value, while the latter ones decay rapidly as the distance to the fixing points increases. The flexural torsion moment $M_{t,w}$ depends on several factors:

- Dimensions of the cross-section (B and H)—the thinner and broader the flat bars, the more significant the share of $M_{t,w}$ is in the total M_s;
- Length (L)—the shorter the flat bars, the greater the share of $M_{t,w}$ is in the total M_s;
- Distances between the flat bars—the greater the length (to the cross-section's shorter edge) between the flat bars, the more significant the share of $M_{t,w}$ is in the total M_s;
- Ratio of Young's modulus (E; of longitudinal elasticity) to Kirchoff modulus (G; of volume elasticity)—an increase in the E and reduction of G values contribute to a higher share of the $M_{t,w}$ limited warping moment in the M_s profile's total torsional moment.

The outcomes of previous research [26,31] indicate that the torsional strength of open-section thin-wall profiles increases when torsional moments are taken over not only by unrestrained torsion but also by the forces warping the flanges in different directions, i.e., by flexural torsion stress. In other words, an increase in the $M_{t,w}$ share in the total M_s

makes a structure stiffer. In order for the strengthening effect to occur, the following two prerequisites have to be fulfilled:

- The cross-section shall be composed of at least two parallel flanges or at least three non-parallel walls that do not intersect in a single point;
- The fixing shall enable transferring the profile bending moments and shearing forces onto the support.

1.2. Analysis of an Expanded Test Package

As a result of the profiles' expanding, additional bending stress occurs in the middle of the active length. The stress distribution changes, and so do the shares of $M_{t,s}$ and $M_{t,w}$ in the M_s transferred torsional moment. It can be evidence of the change in the torsional stiffness under expansion (bending stress).

The available literature misses examples of calculations for expanded flat bars. An analogy can be found in construction, where calculations for a twisted I-section present a similar case. If the analogy is used, the web thickness shall be assumed as zero. Unfortunately, the analogy can be applied only to flat bars whose shape did not change under expansion, i.e., distant from one another (e.g., for unexpanded profiles' calculations). A sample calculation for I-sections is presented in EUROCODE 3 [34]. The method consists in the determination of a substitute warping moment called bimoment. To that end, the bending center shall be identified, and warping inertia determined.

The flexural torsion phenomenon and its influence on the torsional resistance of I-sections was explicitly presented in the SCI study [32], where the torsional stiffness coefficient was determined, along with its change depending on the beam length. Computational procedures were also presented for load cases common in engineering.

The literature hardly provides other examples to gain knowledge for a more detailed analysis of profiles under bending stress. There is no information about expanding arched beams. Moreover, there is a lack of information on bending or twisting elements with initial stress (analogy to stress that occurs when the profiles are expanded).

To summarize, it shall be concluded that it is hard to twist expanded bars. An approximate solution can be obtained in the best-case scenario, requiring long-lasting and labour-consuming analytical efforts.

This study includes experiments and simulation tests on two flat bars arranged one onto another, having a fixed length and variable cross-section dimensions. The flat bars were durably connected at the ends and expanded in the middle of their active length, ranging from 0 to 30 mm, and then twisted. The results of the tests can be applied in a design of a vehicle stabiliser of variable stiffness [36].

2. Materials and Methods

The tests were carried out on a package composed of two rectangular profiles connected permanently at the ends. The profiles were expanded in the middle of their active length and then twisted. The influence of bending on the change in test package torsional stiffness was analyzed.

The test set (Figure 1), with the twisted active length L amounting to 528 mm, consisted of one pair (two pieces) of flat bars, with the possible extension of the package with successive pairs. The tests were planned for 51CrV4 spring steel plate packages, 3 mm and 6 mm thick (H) and 30 mm to 60 mm broad (B). With regard to the mechanical resistance, including but not limited to thicker (higher) test sets, the maximum expansion (R) was limited to 30 mm. The maximum torsion value (φ) was assumed to amount to 20°. The assumed values result from an analysis of stabilizer bars used in typical passenger vehicles. An occurring space limitation and required resistance for twist (a torque needed to twist) in a middle part of the bar cause natural constraint for using shapes not exceeding the given values.

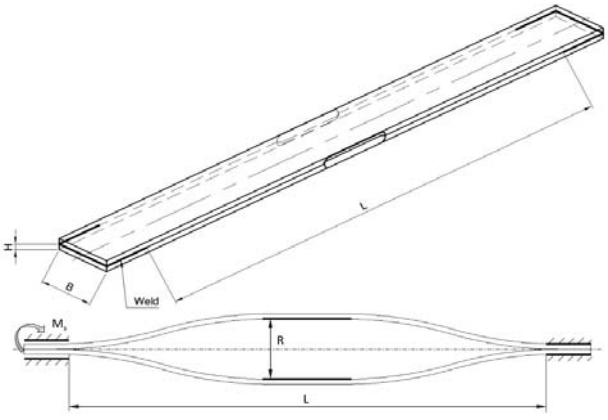

Figure 1. Schematic diagram of a test set (unexpanded on the top and expanded on the bottom).

A load analysis enables the determination of two characteristic states: torsion of unexpanded profiles and torsion of expanded profiles. It was determined that the test package was exposed to the restrained torsion phenomenon and that the deplanation capacity of the flat bars in the restraint areas was limited. Moreover, the profiles were identified to be subject to a complex stress state that depends on the analysed form of the test set (unexpanded and twisted or expanded and twisted). The following types of stress were distinguished:

- Shear (tangential) stress originating from pure torsion;
- Tensile stress generated as a result of the profiles' limited warping in the fixing areas;
- Bending stress along the longer edge of the cross-section) which occurs under tensile stress and shear forces (originating from restrained warping of the cross-sections);
- Bending stress along the shorter edge of the cross-section (resulting from the profiles' bending).

2.1. Analytical Study

Analytical calculations of an unexpanded test package were carried out based on the material strength knowledge, including but not limited to thin-walled bars. The course of the calculations is not presented in this paper. Further sections include the obtained results that are compared with the results of numerical simulations and experiments.

2.2. Numerical Study

A simulation using the Finite Element Method was performed in the ANSYS environment [37,38]. The computational model's structure reflected the real one in the restraining and loading method. Solid elements were used. This way, the edge folds used for mounting the bending mechanism were taken into consideration. Every profile was divided into five sections (Figure 2). The outer sections (1) and (5) corresponded to durable restraint. The middle section (3) was expanded. The other two sections, (2) and (4), were free, and their strain during simulation resulted from the restraining method and working conditions of the rectangular bars in the test stand.

A permanent bond was used at the contact planes of the flat bars' outer edges. It corresponded to the processing capabilities of the test sets' preparation (i.e., welding of the six available edges—see Figure 1). All degrees of freedom were taken on the outer planes of section (5). Friction between the rectangular bars (on Sections 2–4) was taken into consideration. For the unexpanded sets, the coefficient of friction amounting to $\mu = 0.2$ was applied. For the expanded sets, it was $\mu = 0$. This way, the mutual penetration of the profiles during twisting was avoided.

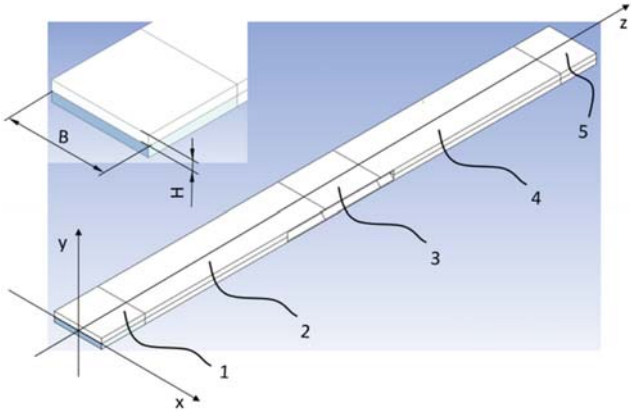

Figure 2. Numerical model. Successive sections are marked with digits from (1) to (5).

The model's discretization was carried out in the Ansys Meshing tool, using non-linear mechanics settings. The Multizone algorithm was applied. HEXA20 and WED15 type cubic elements were generated. The first one was a dominant type. A single profile's thickness in the test set was adopted as the mesh size. The number of the nodes changed depending on the model size and ranged from ca. 20,000 to ca. 80,000. The number of elements ranged from ca. 3500 to ca. 15,000. The mesh quality was checked with Orthogonal Quality indices (ca. 0.7–0.9), Skewness (ca. 0.2–0.5) and Aspect Ratio (ca. 1.5–5). The obtained values, depending on the test model's dimensions, were sufficient for the simulation. No inflation or local concentration of the mesh was used. Quadratic element order function was applied just as it was done by Jafari [39].

The analysis included a non-linear material model (Figure 3). Its parameters were obtained owing to a static tensile test. It was carried out for all tested flat bars' thicknesses. The results were converted into real stress. Material stiffening under significant strain was also taken into account. The force, torque, displacement and rotation margins were assumed (from 0.05% to 0.1%). It enabled obtaining reproducible results with low sensitivity to the mesh size changes.

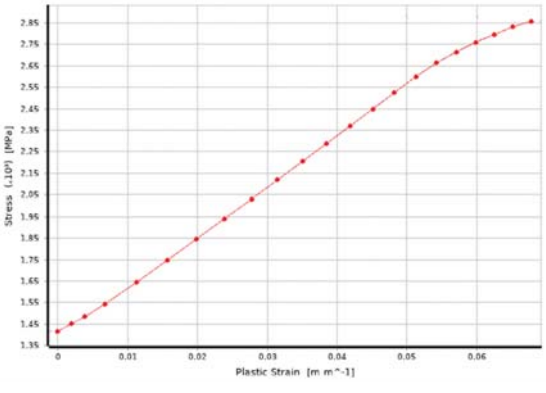

Figure 3. Non-linear model of a 6 mm thick material. The course of actual stress depends on the material deformation. The conventional yield point amounts to Re = 1417 MPa.

Bending and twisting were performed using the remote displacement function. It enabled to define necessary degrees of freedom, leaving the other ones non-defined. The displacement along axis *Y* (from 0 to ±15 mm) was applied to the inner planes of section (3).

Twisting (by 20°) around axis Z and displacement equal 0 mm along axis X and Y was applied to the outer planes of section (1)—Figure 2.

The simulation was performed in two stages using the remote displacement function (Figure 4). In the first stage, the profiles were expanded, while in the second one they were twisted. The reactive moment was measured on the outer planes of section (1). In a purpose of strength control the reduced stress was checked.

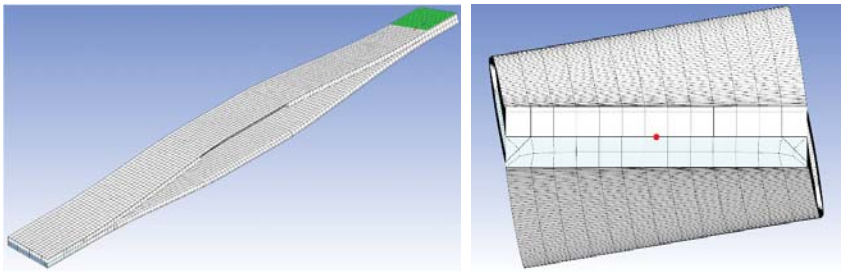

(**a**) (**b**)

Figure 4. (**a**): test set expanded by 30 mm. (**b**): test set expanded by 30 mm and twisted by 20°.

The prepared model helped to perform numerical tests in the whole planned range. The tested profiles were 3 mm and 6 mm thick and 30 mm to 60 mm broad. They were expanded within the 0–30 mm range with a 5 mm stroke. The maximum twist amounted to 20°. The results obtained for unexpanded sets were compared with the results of analytical calculations. They were characterised by high convergence, ranging from −3% to +5.5%. It was then assumed that the simulation had been correctly prepared, and the results obtained for the expanded test packages were correct and confirmed by the experiment results.

2.3. Experimental Study

The developed test stand enabled obtaining reproducible measurement results at a short duration of a single set's test. It consists of five essential assemblies, shown in Figure 5a.

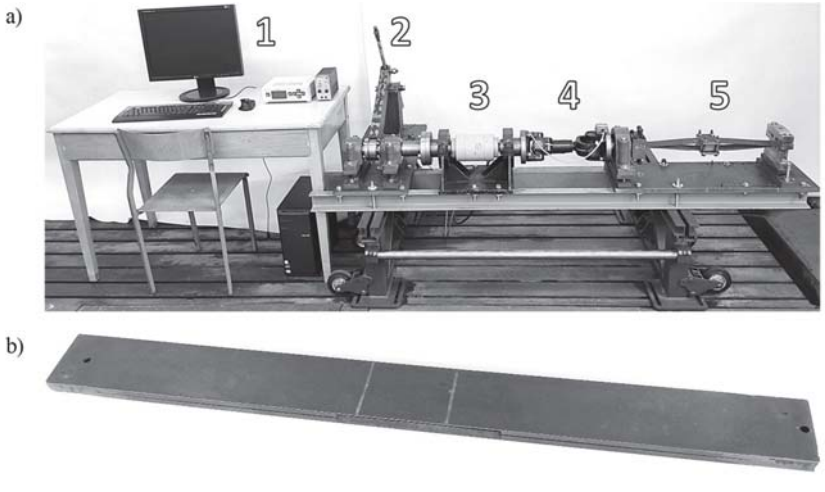

Figure 5. (**a**) Test stand. (**b**) Test set 6 × 60.

A computer set (1) enables data saving and processing. The twisting of the test sets starts at the drive assembly (2), where it is forced with a mechanical lever and a screw-nut transmission powered by an electric motor. It ensures continuous moment and torsion measurement. The rotational motion is transferred by the assemblies of the torque meter (3) and a double-joint shaft (4) to the test set (5), where the tested profile packages are installed; the torque meter and double-joint shaft assemblies are connected in series.

The test sets are mounted on supports. One end of each test set is permanently connected, while the other (connected with the double-joint shaft) enables rotation along the profile's lengthwise axis and compensation of its length change resulting from expansion and twisting. A tilt sensor is also installed there. The sets are expanded with spacer wedges, from 5 mm to 30 mm thick, with a 5 mm stroke. Pressure plates press them from the outside.

The sensors used during the tests included:

- Torque meters (MI130, MI500 and MI1000, Poznan, Poland) with a measurement range from 0 to 1000 Nm, measurement accuracy 0.99%;
- Posital Fraba ACS-080-2-SV20-HE2-2W inclinometers (HeerlenHeerlen, The Netherlands) with two measurement axes (each with a $\pm 90^\circ$ range), measurement accuracy 1.40%.

Additional calibration of torque meters was conducted by applying the particular static force to an arm of known length.

The test sets consist of two flat bars of the same length. In the central part of each flat bar, there are two folds of the inner edges that enable their use in subsequent tests. The profiles were made of 50 HF spring steel plate and connected at the ends by welding. Then they were quenched to ca. 46–48 HRC and tempered. The profiles are shown in Figure 5b.

The system operation was checked after installing the test packages on the test stand. Test twisting was performed, and the operation of the limit switches and tension of fixing bolts were checked. The repeatability of the test was verified by preliminary torque comparison for minimum and maximum profiles twist. The preliminary twisting was repeated three times for each analyzed profile set to eliminate the clearance. Subsequently the consistency was verified by torque curves comparison. After the preliminary inspection, the actual measurement was carried out. The profiles were twisted from 0° to 22°, while recording the torque and twist angle. After reaching the desired twist angle, the system switched off automatically and saved the data. The unloading measurement was performed in the same way. A reduction in the maximum recorded torsion was observed as the stiffness of the test sets increased. The changing stiffness forced the use of three torque meter types, adapting the measurement range in this way.

The test results were processed. Noise and interferences were removed, and the measurement range adapted (from 0° to 20°). Diagrams of the torque change depending on the torsion were developed for the data prepared this way. Trend lines were plotted for the obtained wavelengths. The best representation was obtained for the fourth-order polynomial. Based on these, the torsional moment was calculated and its results were used for determining the K stiffness increase index.

3. Results

3.1. Numerical Tests

A change in the moment depending on the test package twisting, and expansion was analyzed during the numerical tests for two groups—3 mm and 6 mm thick. The plotted diagrams were used for subsequent analyses. Sample diagrams (plotted for the cross-section extreme dimensions: H × B—3 × 60 and 6 × 30) are shown in Figure 6. The color intensity of each curve corresponds to successive expansions levels—from 0 mm (the lightest) to 30 mm (the darkest).

It was observed that a non-linear waveform characterized the packages made of thin and broad profiles (3 × 60). The more evident, the more expanded the test sets were. The diagrams (Figure 6a) reveal a decreasing moment gradient between successive torsion levels. The described effect confirms the growing share of the flexural moment $M_{t,w}$ in the

entire profile torsional moment M_s. The observed bending of the curves in the plot reveals the non-linear dependence of $M_{t,w}$ on the torsion.

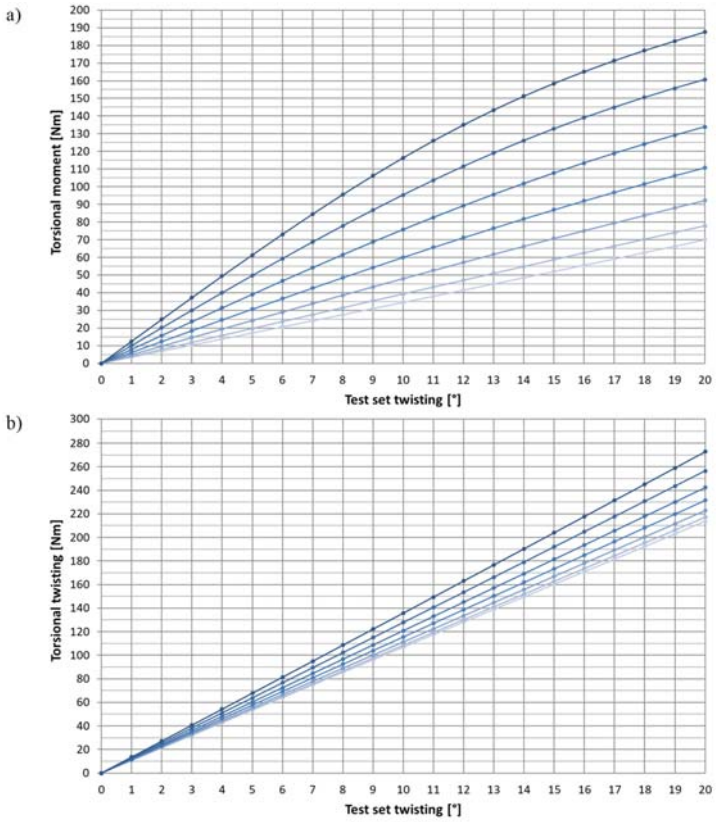

Figure 6. Change in the torsional moment of the 3 × 60 and 6 × 30 test sets during the numerical twisting test. The following expansions are marked with colors from the lightest to the darkest: 0, 5, 10, 15, 20, 25, and 30 mm. (**a**) 3 × 60 package. (**b**) 6 × 30 package.

The results of numerical tests are summarized in Table 1. The first column on the left includes the dimensions of a single profile cross-section dimensions (H × B; height (thickness) × breadth). The top row shows the successive expansion values from 0 (no expansion) to 30 mm. In order to facilitate understanding, each level is preceded by the R index. The entered values represent the torsional moment for a 20° twist.

In both analyzed thickness groups (3 mm and 6 mm), reproducible regularities can be observed. The torsional moment increases depending on the expansion. The lowest values occur for unexpanded test profiles, while the highest ones are achieved for the maximum expansion amounting to 30 mm.

The 3 mm thick sets are characterized by a measurement range from 30.4 Nm to 188.6 Nm. For the 6 mm thick packages, the values range from 214.4 Nm to 919.8 Nm.

The results of the numerical experiment helped to determine the profiles' stiffening under bending. A per cent K stiffness increase index was developed according to formula (2) as a quotient of torsional moment read for expanded profiles $M_{s,R}$ to torsional moment read for not expanded profiles $M_{s,0}$:

$$K = [(M_{s,R}/M_{s,0}) \times 100] - 100\ [\%] \quad (2)$$

The index shows the value by which the torsional stiffness of the bar's working part changed. For instance, a 10% increase means that the test set generates a 10% higher response moment than before the expansion. An increase by 100% signifies a two-fold increase in the torsional stiffness. The calculated values of the K index are summarised in Table 2, which shall be interpreted strictly in the same manner as Table 1.

Table 1. Results of numerical simulations. Torsional moment [Nm] for 20° twist, depending on the package's cross-section dimensions (H × B) and the expansion R [mm].

Sample H × B [mm]	R0	R5	R10	R15	R20	R25	R30
3 × 30	30.4	31.0	33.2	36.8	41.3	47.2	53.8
3 × 35	36.4	37.5	40.9	46.4	53.2	62.1	71.9
3 × 40	42.6	44.3	49.3	57.2	66.9	79.1	92.6
3 × 45	48.7	51.6	58.4	69.1	81.9	97.8	114.6
3 × 50	55.3	59.2	68.2	82.1	98.3	117.8	137.7
3 × 55	62.3	67.3	78.7	95.9	115.6	138.3	161.2
3 × 60	69.5	75.7	89.8	110.7	134.1	161.2	188.6
6 × 30	214.4	217.2	222.9	231.6	242.4	256.5	273.3
6 × 35	261.5	265.0	273.9	287.6	304.3	326.2	351.4
6 × 40	308.4	314.6	327.7	347.7	372.3	404.4	440.9
6 × 45	356.7	366.4	384.8	413.0	447.4	492.3	543.2
6 × 50	407.4	420.2	445.2	483.4	529.9	590.2	658.3
6 × 55	455.6	476.4	509.3	559.4	620.2	698.8	787.0
6 × 60	503.7	529.1	571.9	635.5	712.3	810.7	919.8

Table 2. Numerical simulation. Summary of the percentage value of the K stiffness increase index, depending on the test package (H × B) and expansion R [mm].

Sample H × B [mm]	R0	R5	R10	R15	R20	R25	R30
3 × 30	0.0	1.9	9.3	21.1	35.8	55.1	77.0
3 × 35	0.0	2.9	12.4	27.5	46.2	70.4	97.4
3 × 40	0.0	4.0	15.7	34.3	57.0	85.8	117.3
3 × 45	0.0	5.8	19.8	41.8	68.1	100.6	135.1
3 × 50	0.0	7.1	23.3	48.4	77.7	113.0	149.1
3 × 55	0.0	8.1	26.3	54.0	85.5	122.0	158.8
3 × 60	0.0	9.0	29.2	59.2	92.9	131.9	171.3
6 × 30	0.0	1.3	4.0	8.0	13.0	19.6	27.5
6 × 35	0.0	1.4	4.8	10.0	16.4	24.8	34.4
6 × 40	0.0	2.0	6.2	12.7	20.7	31.1	43.0
6 × 45	0.0	2.7	7.9	15.8	25.4	38.0	52.3
6 × 50	0.0	3.1	9.3	18.6	30.1	44.9	61.6
6 × 55	0.0	4.5	11.8	22.8	36.1	53.4	72.7
6 × 60	0.0	5.1	13.5	26.2	41.4	61.0	82.6

In both analysed thickness groups (3 mm and 6 mm), repetitive regularities can be observed. The index value increases from 0% (for unexpanded profiles) to the maximum value (achieved for 30 mm expansion), and the growing breadth of the test packages contributed to higher stiffness gains.

Thin sets (3 mm) responded to expansion most sensitively. The maximum value of 171.3% was obtained for the 3 × 60 package, while the minimum of 77.0% was obtained for the 3 × 30 package. Thick sets (6 mm) were less susceptible to expansion. The maximum value amounting to 82.6% was obtained for the 6 × 60 package, while the minimum was 27.5% (for the 6 × 30 package).

Experiments confirmed the results of numerical simulations.

3.2. Experiments

The experiments covered the same test sets as the ones used in numerical simulation. The packages consisted of two profiles with a single flat bar thickness of 3 and 6 mm. The expansion was performed within a 0 mm to 30 mm range, with a 5 mm stroke.

Hysteresis between the profiles' loading and unloading was observed during the tests. The hysteresis resulted from inner friction in the test package material [40] and flexibility of the test stand elements.

The results were processed to remove the noise and interferences. A diagram of the torque change during twisting was prepared for each test set. Only the curves obtained while twisting the profiles were used for their analysis. The comparison between the particular curves obtained for the same sample sets revealed that the coincidence was satisfactory (less than 0.5% for different twist values) and did not require more precise data processing. Sample waveforms for 3 × 60 and 6 × 30 sets are shown in Figure 7. The color intensity of each curve corresponds to successive expansion levels, from 0 mm (the lightest) to 30 mm (the darkest).

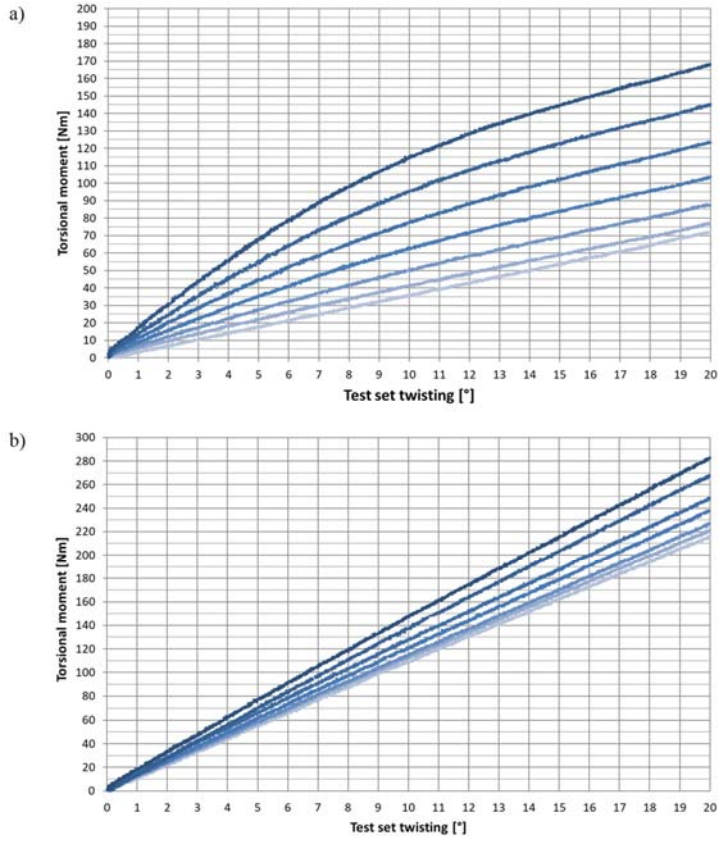

Figure 7. Experiment. Torsional moment (torque) change depending on the test set torsion. The following expansions are marked with colors, from the lightest to the darkest: 0, 5, 10, 15, 20, 25 and 30 mm. (**a**) 3 × 60 package (**b**) 6 × 30 package.

The waveforms of the unexpanded profiles were nearly linear. The expanded sets, similar to the results of the numerical experiment, were characterised by non-linearity. It was most evident for thin (3 mm), broad (mostly at 60 mm) and expanded (mostly at 30 mm)

profiles. In each of these situations, the moment's gradient between subsequent torsion levels revealed decreasing values. Trend lines were plotted for the obtained wavelengths. The best representation was obtained for the fourth-order polynomial. The functions enabled the moment calculation at a 20° twist of the test sets. The results are summarised in Table 3.

Table 3. Results of the bench experiment. Torsional moment Ms [Nm] for 20° twist, depending on the package's cross-section dimensions (H × B) and expansion R [mm].

Sample H × B [mm]	R0	R5	R10	R15	R20	R25	R30
3 × 30	30.5	32.2	34.5	37.9	42.7	48.4	54.8
3 × 35	37.9	39.9	43.6	49.4	56.5	64.4	73.5
3 × 40	44.9	46.9	52.4	59.9	68.9	80.7	92.9
3 × 45	52.1	55.2	61.5	70.7	82.8	97.6	112.4
3 × 50	59.4	63.0	71.1	82.9	97.7	115.4	133.5
3 × 55	66.7	71.1	80.5	94.7	111.8	131.3	152.8
3 × 60	72.0	75.5	87.8	103.2	123.4	144.7	168.0
6 × 30	215.8	220.5	226.1	237.3	245.9	268.0	279.9
6 × 35	265.4	270.5	279.2	292.8	311.2	330.0	353
6 × 40	307.7	318.8	336.1	358.4	373.6	407.5	441.0
6 × 45	362.0	377.5	399.8	426.5	446.2	494.2	524.3
6 × 50	407.6	418.0	453.7	487.7	508.1	577.9	636.2
6 × 55	448.3	472.8	506.5	553.6	584.9	674.7	753.3
6 × 60	500.2	521.2	572.5	624.8	664.6	764.4	846.8

Similar to the numerical experiment, the torsional moment values were observed to increase with the test set's thickness, breadth, and expansion. The lowest values in each group were read for narrow, unexpanded profiles. Analogically, the highest ones applied to broad profiles at maximum expansion.

The 3 mm thick sets are characterised by the measured moment range from 30.5 Nm to 168.0 Nm. For 6 mm test packages, it was from 215.8 Nm to 846.8 Nm.

The results of the experiment carried out in the test stand enabled the determination of the profile's stiffening under bending. The per cent K stiffness increase index was calculated according to formula (1). The index values are summarised in Table 4.

Table 4. Results of the bench experiment. Summary of the percentage value of the K stiffness increase index, depending on the test package (H × B) and expansion R [mm].

Sample H × B [mm]	R0	R5	R10	R15	R20	R25	R30
3 × 30	0.0	5.6	13.2	24.6	40.2	58.8	79.8
3 × 35	0.0	5.2	15.1	30.2	49.2	69.8	93.8
3 × 40	0.0	4.5	16.8	33.4	53.5	79.9	107.0
3 × 45	0.0	6.0	18.1	35.6	58.9	87.3	115.8
3 × 50	0.0	6.1	19.8	39.5	64.5	94.3	124.7
3 × 55	0.0	6.6	20.6	42.0	67.6	96.9	129.1
3 × 60	0.0	4.9	21.9	43.3	71.4	101.0	133.3
6 × 30	0.0	2.2	4.8	9.9	14.0	24.2	29.7
6 × 35	0.0	1.9	5.2	10.3	17.3	24.3	33.0
6 × 40	0.0	3.6	9.2	16.5	21.4	32.4	43.3
6 × 45	0.0	4.3	10.4	17.8	23.3	36.5	44.8
6 × 50	0.0	2.6	11.3	19.7	24.7	41.8	56.1
6 × 55	0.0	5.5	13.0	23.5	30.5	50.5	68.0
6 × 60	0.0	4.2	14.5	24.9	32.9	52.8	69.3

Repetitive regularities can be observed in both analysed thickness groups (3 mm and 6 mm). The index value rises from 0% (for unexpanded profiles) to the maximum value

(achieved for 30 mm expansions). The increasing breadth of the test packages causes higher stiffness gains.

The profiles responded most intensively to expansion in thin sets (3 mm). A maximum of 133.3% was achieved for the 3 × 60 mm package, while a minimum of 79.8% was achieved for the 3 × 30 package. Thick sets (6 mm) demonstrated lower susceptibility to expansion. A maximum of 69.3% was achieved for the 6 × 60 package, while a minimum of 29.7% was achieved for the 6 × 30 package.

4. Discussion

4.1. Accurancy Analysis

To provide good quality results discussion, it is helpful to know the measurement error. Simulation and experimental uncertainty were estimated.

4.1.1. Experiment Test

The errors in experiments include:

1. A systematic error (δ_i of the inclinometer, δ_m of the torque meter and δ_{ad} of the measurement results proximation). It amounts to:

$$\delta_p = \pm\sqrt{(\delta_i{}^2 + \delta_m{}^2 + \delta_{ad}{}^2)} = \pm 2.63\%$$

2. A geometric error. It is affected by:

- Position of distance elements—δ_{ed};
- Initial twisting of the test set in the rotary support clamp—δ_{sp};
- Test set installation in the test stand—δ_{mp};
- Yest stand execution tolerances—δ_{ks};
- Non-homogeneity of the material that the test sets are made of—$\delta_{nm.}$

The geometric error amounts to:

$$\delta_g = \pm\sqrt{(\delta_{ed}{}^2 + \delta_{sp}{}^2 + \delta_{mp}{}^2 + \delta_{ks}{}^2 + \delta_{nm}{}^2)} = \pm 4.77\%$$

3. The δ_{bp} random error was assumed as:

$$\delta_{bp} = \pm 5\%$$

4.1.2. Numerical Simulations

It is hard to estimate a numerical simulation error. It is affected by divergences between the experiment and simulations and FEM errors. Based on experience and professional literature [41], the following accuracy of the computational model was assumed:

$$\delta_s = \pm 5\%$$

4.1.3. Accuracy of Measurements

The δ_e experimental method's accuracy was determined as:

$$\delta_e = \pm(\delta_p + \delta_g + \delta_{bp}) = \pm 12.40\%$$

Therefore, the maximum difference between the results obtained on the test stand and the results of numerical simulations is:

$$\delta_c = \pm(\delta_e + \delta_s) = \pm 17.40\%$$

4.2. Analysis of the Moment Twisting the Unexpanded Test Sets

Unexpanded test sets in each measurement series generated the lowest twisting moment. It represents the reference value necessary to determine the per cent K stiffening increase index for flat bars. Table 5 summarises the results of three test methods obtained

for the profiles twisted by 20°. The values were similar. The knowledge of the differences will help determine the accuracy of the tests.

Table 5. Summary of the results of calculating the torsional moment [Nm] of unexpanded test sets using analytical, numerical and experimental methods.

Sample H × B [mm]	Analytical Calculations	FEM Simulation	Experiment
3 × 30	31.0	30.4	30.5
3 × 35	36.9	36.4	37.9
3 × 40	42.8	42.6	44.9
3 × 45	48.8	48.7	52.1
3 × 50	54.9	55.3	59.4
3 × 55	61.1	62.3	66.7
3 × 60	67.5	69.5	72.0
6 × 30	226.1	214.4	215.8
6 × 35	271.4	261.5	265.4
6 × 40	317.6	308.4	307.7
6 × 45	364.5	356.7	362.0
6 × 50	412.1	407.4	407.6
6 × 55	460.5	455.6	448.3
6 × 60	509.5	503.7	500.2

Based on Table 5, the numerical and experimental method error versus the analytical method were determined. The obtained values were summarised as a diagram in Figure 8. The values lower than one (ordinate axis) meant higher torque values than those suggested by analytical calculations and vice versa for the lower ones.

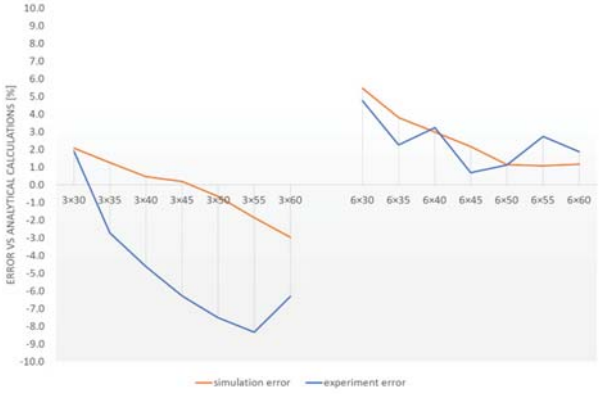

Figure 8. Per cent error of the numerical and experimental methods versus the analytical method.

An evident declining trend characterised all waveforms. Its occurrence can be explained by material loss in the central section of the flat bars, occurring when the edges are milled to mount the expanding mechanism. Residual stress in the material (occurring during heat treatment) can also contribute to the observed curves' waveform; they are larger for broader profiles.

Similar error values characterised the 6 mm thick sets in each test. They ranged from +0.7% to +5.5%. The differences between the experimental and numerical methods revealed negligibly low differences (max. 1.6% for the 6 × 55 package).

Divergences can be observed for the 3 mm thick packages. The highest error was observed during the experiment (3 × 55 package) and amounted to 8.3%. The comparison of the results obtained in the simulation and the experiment reveals significant differences. A variable error ranging from 6.5% to 6.9% was observed between the 3 × 45, 3 × 50 and

3 × 60 packages. It can be concluded that test sets with low stiffness (3 mm) are more susceptible to the impact of the test stand execution inaccuracies and mounting errors. This was observed in the three presented tests.

The influence of limited deplanation on the entire torsional moment M_s was considered in the calculations. It's percent share is marked in orange in Figure 9 (the right ordinate axis). Grey corresponds to the M_s torsional moment (the left ordinate axis), while blue corresponds to the restrained warping moment (the left ordinate axis).

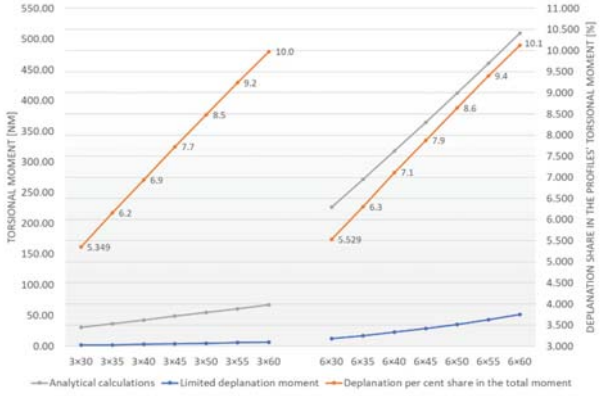

Figure 9. Limited deplanation share in the Ms total torsional moment affecting the unexpanded test sets.

The diagram analysis reveals that the limited deplanation moment increases with the test sets' breadth. Its per cent shares take similar values, regardless of the thickness of the flat bars in the set. They range from 5.3% to 10.1%. The per cent differences between the corresponding values (e.g., 5.3% corresponds to 5.5% for the 3 × 60 and 6 × 30 sets) do not exceed 3.5%. This is helpful information for a designer who constructs a solution based on a similar principle. Instead of time-consuming calculations of limited deplanation, the result obtained for pure torsion can be increased by λ deplanation dimensionless value. The formula (3) can be used for this purpose:

$$M_s = M_{t,s} * [(100/(100 - \lambda)] \quad [Nm] \tag{3}$$

4.3. Comparison of the Simulation and Experimental Results

4.3.1. Torsional Moment Research

Non-Linearity of the Torsional Moment's Wavelength

The tests were carried out to determine the stiffening after twisting the set by 20°. The influence of the non-linear waveform of the moment when a non-expanded set is twisted must not be neglected in order to understand the phenomenon comprehensively. For a nearly linear waveform (for the unexpanded package), it causes the variability of the K stiffness increase index.

An additional analysis of the K stiffness increase index change was performed for the 3 × 60 set (based on the experiment results). The scope of the study was limited to the torsion range from 3° to 20°. Interferences disturbing the observations occurred below the minimum value. The maximum strengthening for the most significant expansion (R = 30 mm) amounts to 320.3% (at twisting by φ = 3°), whereas for twisting by φ = 20°, it was only 133.3%. Similarly, though not as high, differences can be read for other expansions. The results are summarised in the diagram in Figure 10.

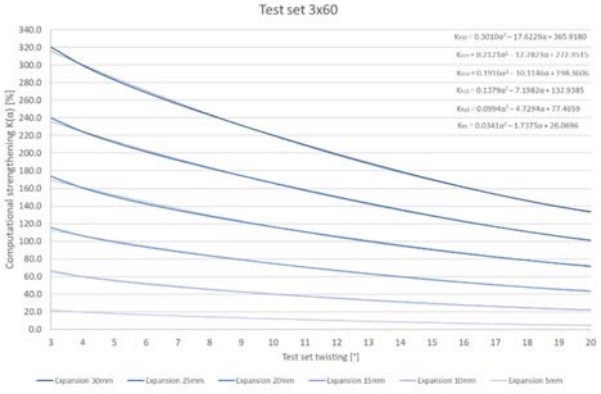

Figure 10. Variable value of the K stiffness increase index depending on the test set twisting.

The analysis above suggests the possibility of changing the K stiffness increase index value by changing the twisting range. For the 3 × 60 package, the K index increased by 2.4 times.

Results of Torsional Moment Tests

The results obtained with the numerical and empirical methods were compared. An error versus the tests performed in the test stand was calculated and is summarised in Table 6. A three-colour scale was used for better understanding. The stronger colour indicates a higher per cent difference between the compared moments. Red (positive values) indicates a moment lower than the one obtained in the experiment, while blue indicates the opposite. White stands for the same value in both measurement methods.

Table 6. Summary of the results of calculating the torsional moment [Nm] of unexpanded test sets using analytical, numerical and experimental methods.

Sample H × B [mm]	R0	R5	R10	R15	R20	R25	R30
3 × 30	−0.2	−3.7	−3.7	−3.0	−3.3	−2.5	−1.7
3 × 35	−3.9	−6.0	−6.2	−5.9	−5.8	−3.6	−2.2
3 × 40	−5.1	−5.5	−5.9	−4.4	−2.9	−1.9	−0.4
3 × 45	−6.5	−6.6	−5.1	−2.2	−1.0	0.2	1.9
3 × 50	−6.9	−6.1	−4.1	−1.0	0.6	2.1	3.2
3 × 55	−6.6	−5.3	−2.2	1.3	3.4	5.3	5.5
3 × 60	−3.5	0.3	2.3	7.2	8.7	11.4	12.3
6 × 30	−0.7	−1.5	−1.4	−2.4	−1.4	−4.3	−2.3
6 × 35	−1.5	−2.0	−1.9	−1.8	−2.2	−1.1	−0.5
6 × 40	0.2	−1.3	−2.5	−3.0	−0.4	−0.8	0.0
6 × 45	−1.5	−3.0	−3.7	−3.2	0.3	−0.4	3.6
6 × 50	0.0	0.5	−1.9	−0.9	4.3	2.1	3.5
6 × 55	1.6	0.7	0.5	1.0	6.0	3.6	4.5
6 × 60	0.7	1.5	−0.1	1.7	7.2	6.1	8.6

An analysis of the error distribution helps us to notice that the numerical model stiffening trend dominates. As expansion increases, red fades and turns into blue. This means that the simulation model becomes stiffer earlier than the experimental one.

The differences exceeding 10% were obtained for the broadest set (3 × 60) at two measurement points—at 25 mm (11.4%) and 30 mm (12.3%) expansion. In the group of packages made of 6 mm thick steel plate, the most significant deviation (for the 6 × 60 test set) amounted to 8.6%. The quoted values do not exceed the calculated measurement difference (±17.4%).

The differences between the experiment and simulation results are caused by inaccurate test stand execution, stiffness, the technology of making the test sets, non-homogenous material structure, and divergent numerical simulations versus real conditions. High deviation values observed for the broadest packages may result from a simplified method of applying the nodes in the fixing areas (FEM simulation). The area of the mounting elements in the test stand was wavy, whereas in the numerical method, it was a plane. This could contribute to the occurrence of micro-motions or local material upsetting during the test, which reduced the value of the read torsional moment in real conditions.

The mean relative error amounted to:

- 4.1% for the test sets made of 3 mm steel plate,
- 2.2% for the test sets made of 6 mm steel plate,
- 3.1%—error for all tests.

The mean result for the relative error lower than 5% confirms that the FEM model was correctly prepared. None of the calculated deviations exceed the determined maximum measurement difference of 17.4%.

4.3.2. K Stiffness Increase Index

The K stiffness increase index informs about the quantitative increase in the torsional moment affecting the test set under expansion. The torque measured for non-expanded profiles is the reference value, hence in this case, the coefficient value is always 0%. It was calculated for the measurements made with the numerical and experimental method.

Two factors were hampering the analysis of the K stiffness increase index. Firstly, the moments read for each measurement method had different values. It resulted from measurement differences (mentioned in Section 4.1). Secondly, the comparison of values suffering from deviations independent of one another causes a risk of their overlapping and consequently strengthening or weakening.

Due to the above-mentioned factors, it was decided to not compare numerical and experimental K index results. Such results would not be a reliable source of knowledge about achievable strengthening. Still, they can be used to estimate the strengthening achievable for the particular test set.

5. Conclusions

This paper is devoted to the study of change in the torsional stiffness of expanded rectangular profiles connected permanently on both ends. Two bending stress states were analysed: first, twisted flat bars, and second, expanded and twisted flat bars. The first state was tested with analytical, numerical, and experimental methods; the other was based on FEM simulation and doing an experiment at the test stand. Moreover, a measurement error was analysed, the share of limited deplanation in the total torsional moment investigated, and the stiffness increase index change during twisting determined.

The analysis of the study works leads to the following conclusions:

- An increase in the torsional stiffness of the flat bars depends on their cross-section, expansion, and angle of twist.
- An analysis of the structure load reveals that stiffening of the flat bars depends on the tensile stress resulting from cross sections' limited deplanation in the fixing areas.
- The share of the torque resulting from restrained warping in the total torsional moment strongly depends on the breadth and takes similar values for the test sets made of 3 and 6 mm thick flat bars. It ranges from 5.3% to 10.1%, and the developed change diagram can be helpful for simplified calculations of similar structures.
- The comparison of the results revealed FEM error versus the experiment amounting in average to 3.1%, which is a satisfactory value.

Positive results obtained for test sets made of spring steel suggest that the use of modern composite materials would allow us to obtain a higher stiffness increase index.

According to the authors, the study results can be used for designing a car stabiliser that actively changes its stiffness. The decreasing torque gradient during twisting of the expanded working part can positively influence travelling comfort and safety, fulfilling the function of informing the driver about approaching the steerability limit.

6. Patents

Dmitrova Z, Kaszuba S, Macikowski K. Systeme Anti-Devers A Raideur Variable Comportant Des Series De Barres Qui S'ecartent Entre Elles. FR3 057813, 2018.

Author Contributions: Conceptualization, K.M.; methodology, K.M.; software, K.M.; validation, K.M., B.W., G.M., Z.D. and D.B.; formal analysis, K.M.; investigation, K.M.; resources, K.M. and G.M.; data curation, K.M.; writing—original draft preparation, K.M.; writing—review and editing, K.M., B.W., G.M., Z.D. and D.B.; visualization, K.M. and G.M.; supervision, B.W. and G.M.; project administration, D.B.; funding acquisition, K.M. and G.M. All authors have read and agreed to the published version of the manuscript.

Funding: This research received no external funding.

Institutional Review Board Statement: Not applicable.

Informed Consent Statement: Not applicable.

Data Availability Statement: Data is contained within the article.

Conflicts of Interest: The authors declare no conflict of interest.

References

1. SAE Spring Committee. *Spring Design Manual*; Society of Automotive Engines Inc.: Bristol, CT, USA, 1990; pp. 356–362.
2. Wan, H.-X.; Mahendran, M. Bending and torsion of hollow flange channel beams. *Eng. Struct.* **2015**, *84*, 300–312. [CrossRef]
3. Keerthan, P.; Mahendran, M. Experimental studies on the shear behaviour and strength of LiteSteel beams. *Eng. Struct.* **2010**, *32*, 3235–3247. [CrossRef]
4. Anapayan, T.; Mahendran, M. Improved design rules for hollow flange sections subject to lateral distortional buckling. *Thin-Walled Struct.* **2012**, *50*, 128–140. [CrossRef]
5. Black, M.M.; Semple, H.M. Torsion-bending analysis of continuous thin-walled beams. *Int. J. Mech. Sci.* **1969**, *11*, 791–810. [CrossRef]
6. Gil, B.; Goñi, R.; Bayo, E. Major axis steel joint with additional plates subjected to torsion: Stiffness characterization. *Eng. Struct.* **2020**, *220*, 111021. [CrossRef]
7. Pavazza, R. Torsion of thin-walled beams of open cross-section with influence of shear. *Int. J. Mech. Sci.* **2005**, *47*, 1099–1122. [CrossRef]
8. Choi, S.; Kim, Y.Y. Higher-order Vlasov torsion theory for thin-walled box beams. *Int. J. Mech. Sci.* **2021**, *195*, 106231. [CrossRef]
9. Li, Y.; You, Z. Open-section origami beams for energy absorption. *Int. J. Mech. Sci.* **2019**, *157*, 741–757. [CrossRef]
10. Ribeiro, S.Y.; Silveira, M.E. *Application of Finite Element Method in the Study of Variables that Influence the Stiffness of the Anti-Roll Bar and the Body Roll*; SAE Technical Paper: Sao Paulo, Brazil, 2013.
11. Heißing, B.; Ersoy, M. *Chassis Handbook: Fundamentals, Driving Dynamics, Components, Mechatronics, Perspectives*; Springer Science & Business Media: Berlin/Heidelberg, Germany, 2010.
12. Strassberger, M.; Guldner, J. BMW's dynamic drive: An active stabilizer bar system. *IEEE Control Syst. Mag.* **2004**, *24*, 28–29.
13. Buma, S.; Ookuma, Y.; Taneda, A.; Suzuki, K.; Cho, J.-S.; Kobayashi, M. Design and development of electric active stabilizer suspension system. *J. Syst. Des. Dyn.* **2010**, *4*, 61–76. [CrossRef]
14. University of Windsor. Available online: https://scholar.uwindsor.ca/cgi/viewcontent.cgi?article=6039&context=etd (accessed on 7 November 2021).
15. Nadaf, H.J.; Naniwadekar, A.M. An Overview of Analysis of Anti-Roll Bar of Passenger Car with Nonlinear Parameter. *Int. J. Adv. Technol. Eng. Sci.* **2015**, *2*, 133–136.
16. Nadaf, H.J.; Naniwadekar, A.M. Analysis of Anti-Roll Bar of Passenger Car for its Nonlinear Behavior with Help of CAE. *Int. J. Adv. Technol. Eng. Sci.* **2015**, *3*, 379–383.
17. Mohamed, H.; Aly, M.F.; Shokry, A. Numerical and Experimental Characterization of Composite Leaf Spring Subjected to Bending. *J. Mech. Eng. Res. Dev.* **2020**, *43*, 371–383.
18. Krishan, K.; Aggarwal, M.L. A finite element approach for analysis of a multi leaf spring using CAE tools. *Res. J. Recent Sci.* **2012**, *2277*, 2502.
19. Pawar, S.; Ghadge, R. Design & Analysis of Multi Steel Leaf Spring. *Int. Eng. Res. J.* **2015**, *2*, 4468–4474. [CrossRef]
20. Bakalarz, M.M.; Kossakowski, P.G.; Tworzewski, P. Strengthening of Bent LVL Beams with Near-Surface Mounted (NSM) FRP Reinforcement. *Materials* **2020**, *13*, 2350. [CrossRef]

21. Wan, H.-X.; Mahendran, M. Behaviour and strength of hollow flange channel sections under torsion and bending. *Thin-Walled Struct.* **2015**, *94*, 612–623. [CrossRef]
22. Seo, J.K.; Mahendran, M.; Paik, J.K. Numerical method for predicting the elastic lateral distortional buckling moment of a mono-symmetric beam with web openings. *Thin-Walled Struct.* **2011**, *49*, 713–723. [CrossRef]
23. Paczos, P. Experimental investigation of C-beams with non-standard flanges. *J. Constr. Steel Res.* **2014**, *93*, 77–87. [CrossRef]
24. Chen, M.-T.; Young, B.; Martins, A.D.; Camotim, D.; Dinis, P.B. Experimental investigation on cold-formed steel lipped channel beams affected by local-distortional interaction under non-uniform bending. *Thin-Walled Struct.* **2021**, *161*, 107494. [CrossRef]
25. Eisenberger, M. Nonuniform torsional analysis of variable and open cross-section bars. *Thin-Walled Struct.* **1995**, *21*, 93–105. [CrossRef]
26. Vinson, J.R. *The Behavior of Thin Walled Structures: Beams, Plates, and Shells*; Springer: Dordrecht, The Netherlands, 2012. [CrossRef]
27. Singh, D.K. *Strength of Materials*; Springer International Publishing: Berlin/Heidelberg, Germany, 2020. [CrossRef]
28. Kosmatka, J.B.; Dong, S.B. Saint-Venant solutions for prismatic anisotropic beams. *Int. J. Solids Struct.* **1991**, *28*, 917–938. [CrossRef]
29. Lin, W.Y.; Hsiao, K.M. More general expression for the torsional warping of a thin-walled open-section beam. *Int. J. Mech. Sci.* **2003**, *45*, 831–849. [CrossRef]
30. Santoro, R. The line element-less method analysis of orthotropic beam for the De Saint Venant torsion problem. *Int. J. Mech. Sci.* **2010**, *52*, 43–55. [CrossRef]
31. Sapountzakis, E.J. Bars under Torsional Loading: A Generalized Beam Theory Approach. *Int. Sch. Res. Not.* **2013**, *2013*, 916581. [CrossRef]
32. Way, A.G.J.; Cosgrove, T.C. *Design of Steel Beams in Torsion*; SCI (The Steel Constr Institute): Berkshire, UK, 2011.
33. Vlasov, V.Z. Thin-walled elastic beams. *PST Cat.* **1959**, *428*, 1–32.
34. *EN-1993-1-1-2005*; Eurocode 3: Design of Steel Structures-Part 1-1: General Rules and Rules for Buildings. European Committee of Standardization: Brussels, Belgium, 2011; Volume 1.
35. Timoshenko, S.P.; Woinowsky-Krieger, S. *Theory of Plates and Shells*; McGraw-hill: New York, New York, USA, 1959.
36. Dmitrova, Z.; Kaszuba, S.; Macikowski, K. Systeme Anti-Devers a Raideur Variable Comportant des Series de Barres Qui S'ecartent Entre Elles. France Patent FR3057813, 30 November 2018.
37. Alawadhi, E.M. *Finite Element Simulations Using ANSYS*; CRC Press: Boca Raton, FL, USA, 2015. [CrossRef]
38. Lee, H.-H. *Finite Element Simulations with ANSYS Workbench 18*; SDC Publications: Kansas City, MO, USA, 2018.
39. Jafari, M.; Chaleshtari, M.H.B.; Abdolalian, H.; Craciun, E.-M.; Feo, L. Determination of Forces and Moments Per Unit Length in Symmetric Exponential FG Plates with a Quasi-Triangular Hole. *Symmetry* **2020**, *12*, 834. [CrossRef]
40. Dolce, M.; Cardone, D. Mechanical behaviour of shape memory alloys for seismic applications 1. Martensite and austenite NiTi bars subjected to torsion. *Int. J. Mech. Sci.* **2001**, *43*, 2631–2656. [CrossRef]
41. Arasaratnam, P.; Sivakumaran, K.S.; Tait, M.J. True stress-true strain models for structural steel elements. *Int. Sch. Res. Not.* **2011**, *2011*, 656401. [CrossRef]

materials

MDPI

Article

Identification of Parameters and Fatigue Life Assessment of the Road Pavement Lower Construction Layers under Heavy Construction Traffic

Piotr Mackiewicz * and Bartłomiej Krawczyk

Faculty of Civil Engineering, Wrocław University of Science and Technology, 50-370 Wrocław, Poland
* Correspondence: piotr.mackiewicz@pwr.edu.pl; Tel.: +48-71-320-45-57

Abstract: This article analyzes the results of testing the subgrade and the lower layers of the pavement structure with the light weight deflectometer at a load of 0.1 and 0.15 MPa. It is shown that, with layer systems with an equivalent layer modulus lower than 80 MPa, significant nonlinear phenomena occur at a load of 0.15 MPa. In this situation, the identification of a reliable replacement module, a commonly used test method, at a load of 0.1 MPa, is not appropriate—it significantly overestimates the value of the modules (even by 34%), which in turn translates into a significant overestimation of the fatigue life of the structure. In a situation where intensive exploitation of the lower layers of the pavement structure is planned before the final layer arrangement is made, it is required to apply test loads corresponding to the stress conditions occurring in these layers of the structure. Such a situation takes place under the influence of technological (construction) or temporary traffic (substitute, e.g., by-pass) during construction. In order to verify the above assumptions, numerical calculations (FEM) were carried out in the elastic model for layered structures with replacement modules determined in field tests. It was found that, especially in the case of low-bearing layer systems, it is necessary to use correction factors for modules determined with a dynamic plate at a load of 0.1 MPa. Taking into account the corrected values of the modules will allow to correctly determine the change in the durability of layers at the construction stage and in the subsequent operation of the final pavement structure.

Keywords: pavement; fatigue; subgrade; modules; FEM; light weight deflectometer

Citation: Mackiewicz, P.; Krawczyk, B. Identification of Parameters and Fatigue Life Assessment of the Road Pavement Lower Construction Layers under Heavy Construction Traffic. *Materials* **2022**, *15*, 5646. https://doi.org/10.3390/ma15165646

Academic Editor: Krzysztof Schabowicz

Received: 18 July 2022
Accepted: 14 August 2022
Published: 17 August 2022

1. Introduction

The assessment of the bearing capacity and compaction parameters of the pavement structure base with the use of the light weight deflectometer (LWD) is an issue that is still relevant in world road technology [1–6]. The dynamic plate is a device known and used for many years and, thanks to its efficiency, it gradually replaces the time-consuming static methods. However, the problem at present is the correct interpretation of the results of measurements of surface displacement (deflection) with a dynamic plate. In recent years, research was carried out on the identification of subgrade parameters using the light weight deflectometer and comparative studies with other applied research methods [7–9]. So far, they have not brought an unequivocal solution to the problem of interpretation of the results obtained in the dynamic plate test. Many authors analyzed phenomena occurring during dynamic loading test. Empirical correlations were made [10–12] between static and dynamic tests, and numerical analyses were conducted [13–16] for different types of subgrades. Additional sensors (geophones) [17] were also used to compare the LWD and the FWD (falling weight deflectometer) tests results [18,19]. A lot of effort is put into finding the correlation between the static and dynamic moduli for different subgrades [20–24] and different coefficients of subgrade reaction [25].

The test with an LWD consists of registering vertical displacements (deflections) of the subgrade under the loading impulse caused by a freely falling mass. A detailed description

of the LWD is presented later in the article. The vertical displacements recorded in the test under a known load are the basis for further identification of the ground parameters. It is a complicated issue because the parameters of the layer to be assessed depend on its thickness, moisture, and the stiffness of the layers underneath. It is assumed that the impact range of a light dynamic deflectometer does not exceed 0.5 m, and it depends on the diameter of the loading plate and the value of the loading impulse.

There is a belief in the world road literature that testing with a light dynamic deflectometer, despite remaining ambiguities, is the most effective method, surpassing others and worth further improvement. The loading impulse generated in the LWD test is very similar to the character of the wheel load of the passing vehicle, and the stresses appearing in the ground correspond to the actual stresses occurring during the subsequent operation of the pavement structure. Different diameters of pressure plates are used around the world, with different discharge heights and sizes of the freely falling mass, which results in different values of the loading impulse (stresses at the contact of the pressure plate with the surface). The tests showed that the value of the identified parameters (stiffness modules) of the layer depends largely on the value of the impulse and the diameter of the plate, as well as the cyclical nature of the load (change of the stiffness modules at successive drops) [26]. Commonly, for practical reasons, simplified methods of assessing layer parameters based on a single value of the instantaneous maximum displacement (deflection) are used, without the knowledge and use of the entire deflection time course. They can lead to significant errors in identifying the subgrade parameters and underestimating the durability of the exploited layers at the construction stage.

In construction practice, it is very common for the lower layers of the structure, and even the improved subgrade itself, to be subjected to intensive technological or temporary traffic loads before the final arrangement of the pavement structure layers is made. As a result of stresses greater than those present in the target structure, the lower layers undergo earlier degradation, which reduces the durability of the target structure. In this case, it is very important to correctly assess the parameters of the lower layers of the pavement and subgrade structure, under the stress conditions occurring in the layers at the stage of their operation. The change in the durability of the lower layers of the pavement structure as a result of intensive use at the construction stage is not taken into account in road design practice, and may be very important—in recent years, accelerated degradation of the final structure was observed in areas where the lower layers were previously intensively used with construction, technological or temporary traffic.

The aim of this article is to show that, in the layer systems with equivalent modulus of 80 MPa or lower, significant nonlinear phenomena occur, when under stress of 0.15 MPa (identified in the model as the average). Therefore, the identification of the equivalent modulus should be conducted under such a stress. Identification under lower stress (0.1 MPa) is incorrect and causes significant overestimation of the equivalent modulus and, consequently, and overestimation of the fatigue life of the pavement construction.

2. Research Methodology

In the next stage of this publication, the results of tests with a dynamic plate at a load of 0.1 MPa and 0.15 MPa are presented on three partially constructed pavement structures, loaded with technological (construction) and temporary traffic (in the case of structures No. 1 and 2).

- construction No. 1: crushed stone 25 cm on a layer of cement-stabilized sandy loam 15 cm, underneath sandy loam subgrade;
- construction No. 2: 15 cm layer of cement-stabilized sandy loam, underneath sandy loam subgrade;
- structure No. 3: compacted native soil—compacted sandy loam subgrade.

Figure 1 shows the test stands and diagrams of the tested structures.

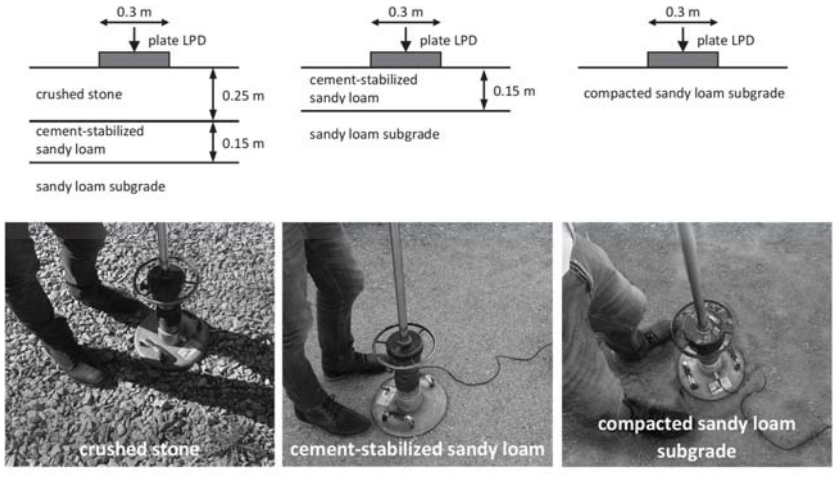

Figure 1. Test stands and diagrams of the tested structures.

The test with a light dynamic plate (LWD) consists of inducing the appropriate stress in the tested layer and recording the response—displacement within about 20 ms. The mass freely falling from a predetermined height hits the damping system, which deforms and smoothly transmits the load impulse to the pressure plate. The plate, in turn, causes a vertical displacement (deflection) of the subgrade, which is registered by a special sensor, called a geophone. More details on geophone operation can be found in [27]. Two plates with a diameter of 0.3 m were used for the tests, differing in the size of the freely falling mass and the drop height. In the case of the first plate, the pressure on the subgrade was 0.1 MPa, and in the case of the second—0.15 MPa.

In each of the experimental fields, three measurements of vertical displacements with a dynamic LWD plate were carried out, according to the standard procedure [28], each time performing six discharges—loading cycles (three initial and three basic), and the results of all discharges (including three preliminary) were recorded. Figure 2 shows the results of measurements of vertical displacements depending on the number of loading cycles.

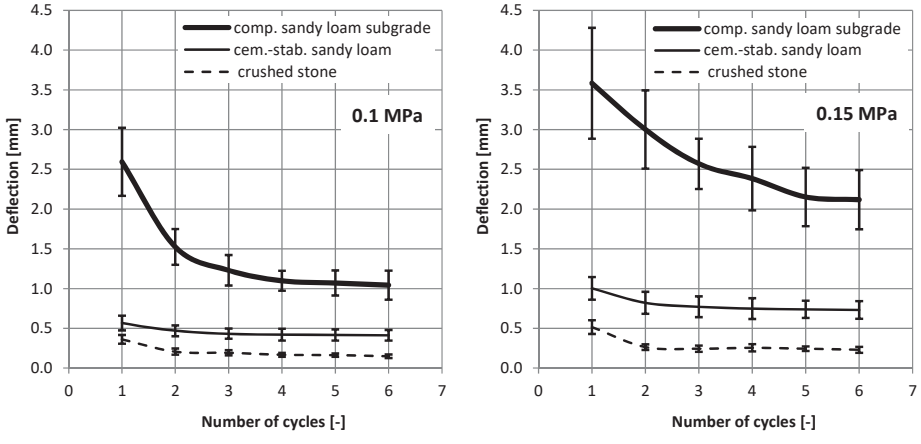

Figure 2. Vertical displacements as a function of the number of load cycles, depending on the type of the tested subgrade at the load of 0.1 and 0.15 MPa.

On the basis of the presented measurement results, it is possible to see the influence of the number of load cycles on the recorded vertical displacements in the LWD test, and it depends on the type of subgrade. It is most noticeable in the case of the sandy loam subgrade, and less in the case of crushed stone, on the stabilization layer. In the case of the native subgrade, the largest scatter of results was also obtained, which was visualized in the form of standard deviation.

In the case of the compacted native subgrade (structure 3), at the load of 0.15 MPa, the final six discharge displacements obtained over three times greater displacements than for the cement-stabilized layer on the native subgrade (structure 2) and seven times greater than on the crushed stone layer (structure 1). It is worth noting that the obtained displacement values relate to the displacement values at the moment of the maximum load impulse. Figure 3 presents examples of displacement waveforms during the test for all six load cycles.

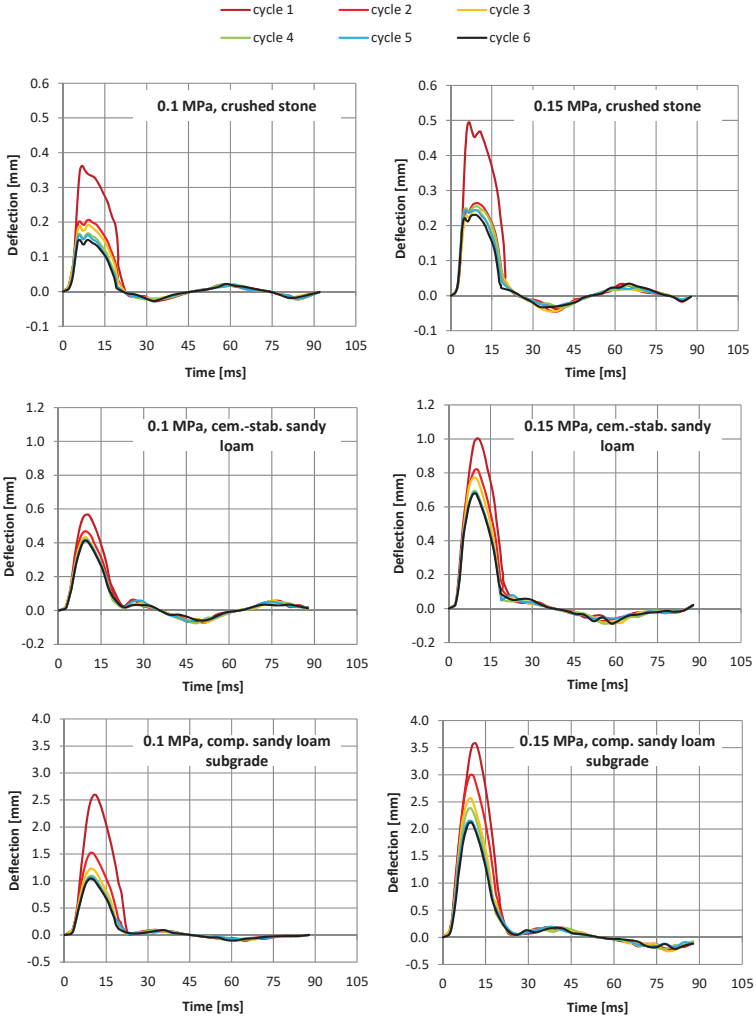

Figure 3. Time courses of displacements during the test with a dynamic plate, depending on the tested layer, at a load of 0.1 and 0.15 MPa.

It should be noted that the crushed stone (sandwich system with the highest stiffness) has the smallest material damping effect, which is visible in the form of a large change in displacements after unloading. Lower damping, for all sandwich systems, is visible for a higher load of 0.15 MPa.

Based on the comparison of the ratio of the mean values of displacements for the load of 0.15 MPa and 0.1 MPa (marked as y0.15/y0.1), it was found that sandwich system No. 1 with the crushed aggregate layer is similar to the behavior of the elastic material. The ratio of the displacement values oscillates around the value of 1.5, which corresponds to the ratio of the load values (Figure 4). A clear lack of proportionality of displacements in relation to the load is visible for the compacted native subgrade (sandy loam) for the final test cycle and amounts to 2.03. The value of 1.77 was obtained on the native subgrade, stabilized with cement (system No. 2). The same value was obtained for both the first and the last cycle, which proves the low variability of elastic properties with increasing load cycles. The lack of obtaining exact ratios equal to 1.5 proves the non-linear behavior of these materials (especially the compacted native subgrade) and indicates the need to use load-dependent material characteristics for their description or to use the correction coefficients developed by the authors.

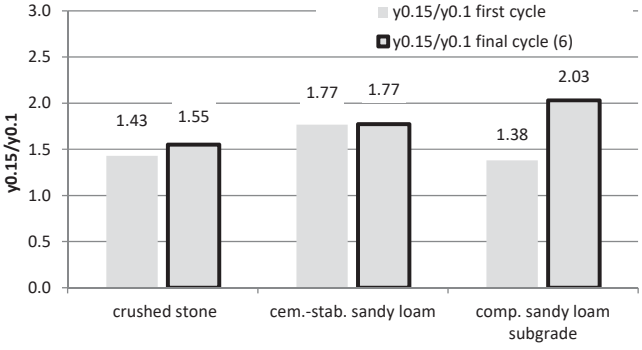

Figure 4. Ratios of displacements obtained in the plate test under the load of 0.15 MPa and 0.1 MPa.

The discussed material characteristics, determined on the basis of the displacement values, in relation to the load (for final discharge, which corresponds to a compacted layer system), are shown in Figure 5.

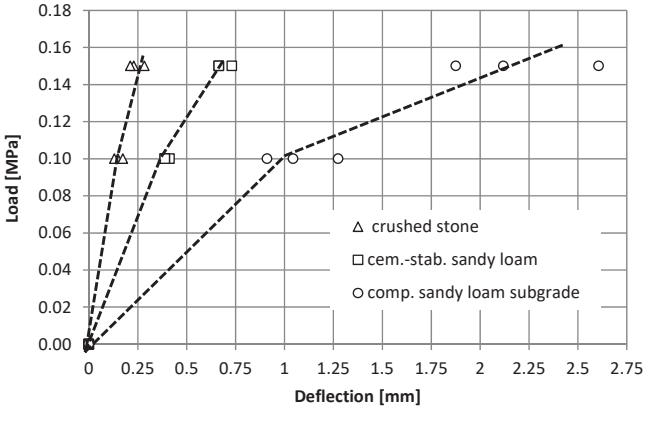

Figure 5. Material characteristics of the tested pavements depending on the load value (final cycle).

The recorded displacement results were used in the further part of the work to identify the values of dynamic equivalent moduli (*Evd*) of the examined layer systems. Figure 6 shows the values of dynamic moduli determined for the initial and final load cycles at different load values. The dynamic modulus *Evd* was calculated on the basis of the measured values of displacements y_i, depending on the value of the load σ_i:

$$Evd_i = \pi \times (1 - \nu^2) \times \sigma_i \times a/2 \times y_i, \quad (1)$$

where:

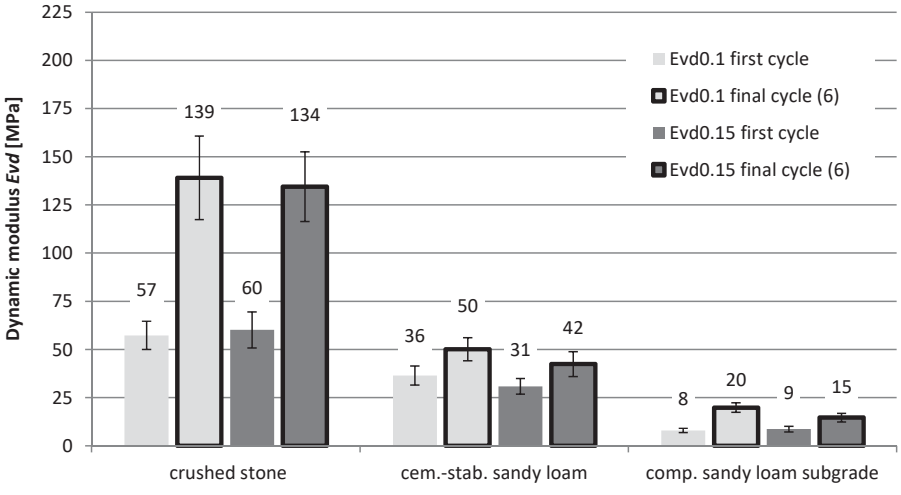

Figure 6. Values of dynamic moduli of the tested structures.

Evd—dynamic surface modulus [MPa],
ν—Poisson's Ratio, 0.35 [-],
σ_i—maximum contact stress [MPa]
a—plate radius = 150 [mm],
y_i—maximum deflection [mm],
i for load 0.1 MPa or 0.15 MPa.

It is clearly visible how important the change of the modulus value may be in relation to the first and the last (sixth) load cycle, for which the registered displacements are already "stabilized". Both in the case of the crushed stone layer on the cement-stabilized layer and in the case of the compacted native subgrade, the difference between the modules is almost twofold. Most likely, it results from the significant compaction of the material (in the case of stone in system No. 1) and plastic deformation of the material (in the case of sandy loam: No. 3). The smallest changes occur for system No. 2—the cement-stabilized native subgrade. It should also be noted that, for a plate load of 0.15 MPa, lower modulus values were obtained than for a load of 0.1 MPa. In the case of the analysis for the end cycles, the differences amount to, respectively, for the system No. 1, 4%; No. 2; 16%; and No. 3, as much as 35%. Such changes significantly confirm the "non-linear" material properties and indicate the need to correct the target values of modules if they will be tested under a load lower than the actual load that will occur during operation.

Figure 7 shows the dependence of the displacement ratios at two load levels (0.1 MPa and 0.15 MPa) on the dynamic modulus determined at the load of 0.1 MPa. Of course, a clear correlation is noticeable for the final, stabilized load cycle. This implies the need to determine the correction factor k for the dynamic modules determined in the test using a plate load of 0.1 MPa (Figure 8). The determined dependence shown in Figure 8 allows

for determining reliable corrected modules that can be used to estimate the durability of the exploited pavement layers in the case of a load greater than 0.1 MPa.

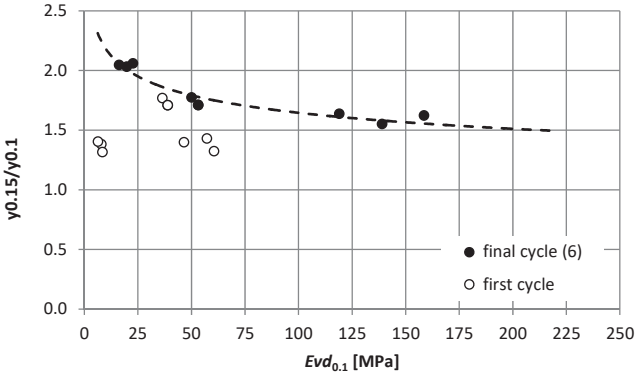

Figure 7. Dependence of the displacement ratios at two load levels (0.1 MPa and 0.15 MPa) on the dynamic modulus determined at the load of 0.1 MPa.

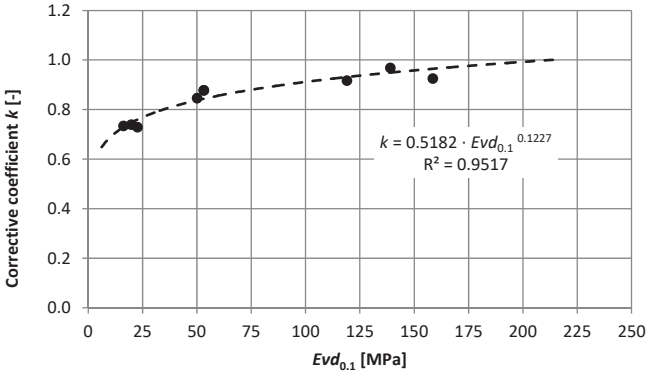

Figure 8. Correction factor for dynamic moduli determined in the test with a plate load of 0.1 MPa.

If the expected load from construction or temporary traffic causes stress of 0.15 MPa in the layers (such stress is identified in the model as the average occurring in the layer), the modules should be tested under the load of 0.15 MPa, or reduction factors for the designated modules, in the case of plate testing 0.1 MPa, should be applied. Otherwise, oversized systems with incorrectly determined layer parameters will degrade faster than the fatigue criteria indicates. In order to explain these phenomena more precisely and to determine the differences in fatigue life, numerical calculations were carried out for the examined layer systems.

3. Numerical Modeling

The finite element method (FEM) was used to calculate the value of displacements for different values of material parameters. The model was built with the use of three-dimensional volumetric elements (Figure 9), and the subgrade layers were described for comparison with elastic parameters corresponding to dynamic replacement modules determined in field tests. The load was assumed following the conditions of training tests—as a model of a rigid round plate with a pressure of 0.1 MPa and 0.15 MPa, and a radius of 0.15 m. Full interlayer adhesion was applied in the model.

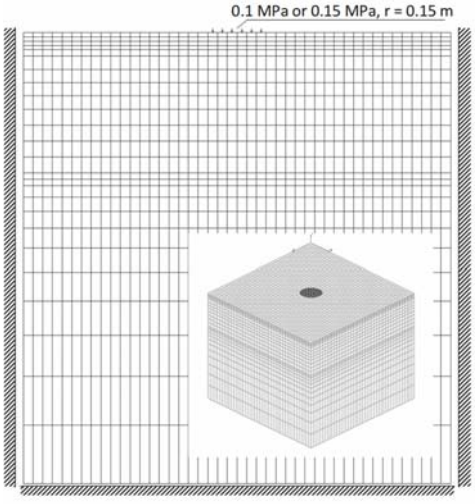

Figure 9. Calculation model of the subgrade layer system.

In the description of the elastic material, a wide range of modulus changes from 5 MPa to 200 MPa was analyzed. All analyses were performed for the conditions in the final (sixth), stabilized load cycle. The FEM calculations were conducted for the following moduli obtained in tests: crushed stone on a cement-stabilized subgrade (construction No. 1): 139 MPa (load 0.1 MPa), 134 MPa (load 0.15 MPa); cement-stabilized subgrade (construction No. 2): 50 MPa (load 0.1 MPa), 42 MPa (load 0.15 MPa); native subgrade (construction No. 3): 30 MPa (load 0.1 MPa), 15 MPa (load 0.15 MPa). Poisson's ratio of 0.35 was used in all cases.

4. Durability Analysis

Based on field studies and numerical calculations, comparative analyses were carried out (Figure 10). The compliance of the determined displacements in numerical calculations with the use of dynamic load was found in comparison with displacements obtained in field tests. Compliance occurs for both 0.1 MPa and 0.15 MPa load. The differences in values did not exceed 10%.

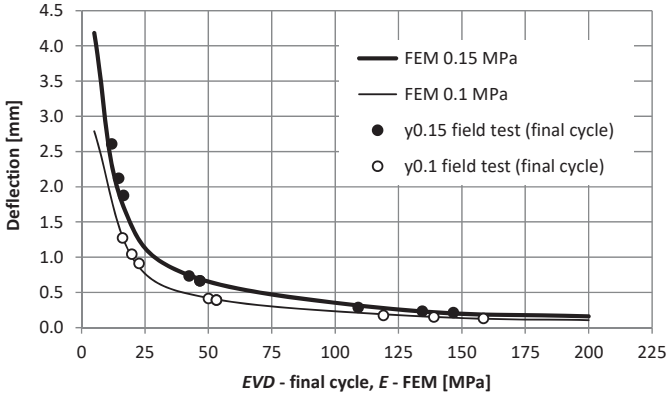

Figure 10. Comparison of the results of field tests and numerical calculations, taking into account moduli and displacements.

It should be noted that, for moduli with a value lower than 50 MPa, the displacement values clearly increase, which will significantly affect the durability of systems with weaker parameters. The structural deformation criterion was used to assess the pavement durability.

The criterion allows to determine the durability of the structure to the creation of a critical structural deformation of 12.5 mm, based on the relationship between the permissible number of repetitive loads N and the vertical deformation of the subsoil ε_p:

$$\varepsilon_p = 1.05 \times 10^{-2} \times (1/N)^{0.223}, \quad (2)$$

Preliminary calculations of the deformation values were carried out for the tested sandwich systems with the use of FEM, in the previously described model, at the load of 0.1 MPa and 0.15 MPa.

Figures 11–13 show the values of the determined vertical deformations for the systems tested in the field. Up to a depth of about 20 cm, there are still relatively large deformations, constituting 70% of the maximum deformations under the edges of the slab. At a depth of about 40 cm, vertical deformations account for 40% of the maximum.

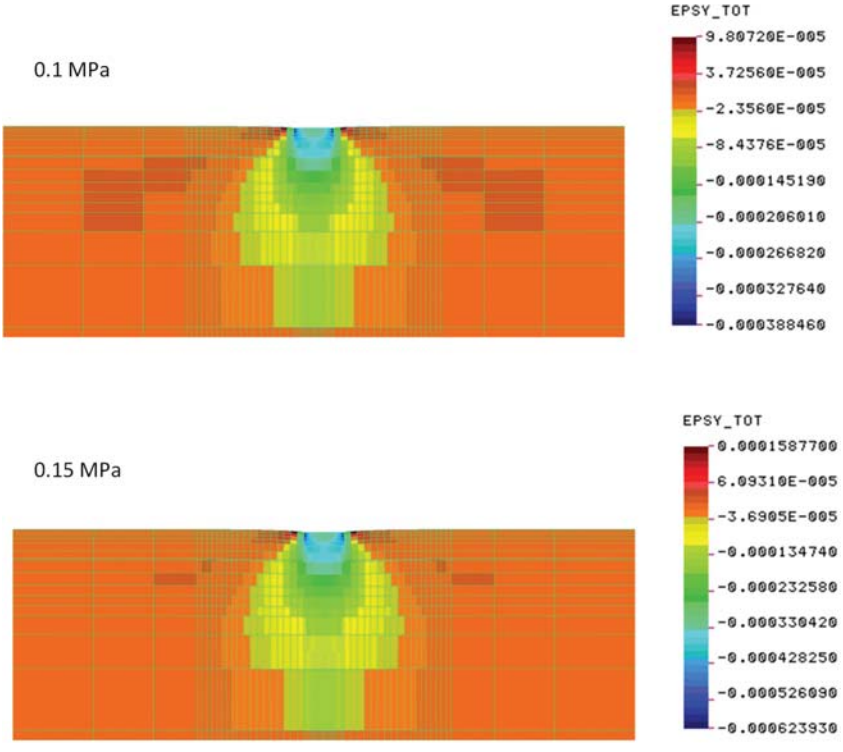

Figure 11. Deformations for crushed stone on a cement-stabilized subgrade—construction No. 1 (deformation scale ×100).

Due to the fact that the lower layers of the pavement structure are subject to technological (construction) or temporary traffic with direct pressure of 0.7 MPa, additional durability calculations were carried out for higher loads than the LPD slab. Figure 14 shows the dependence of the pavement durability on the value of equivalent-surface moduli and different load levels.

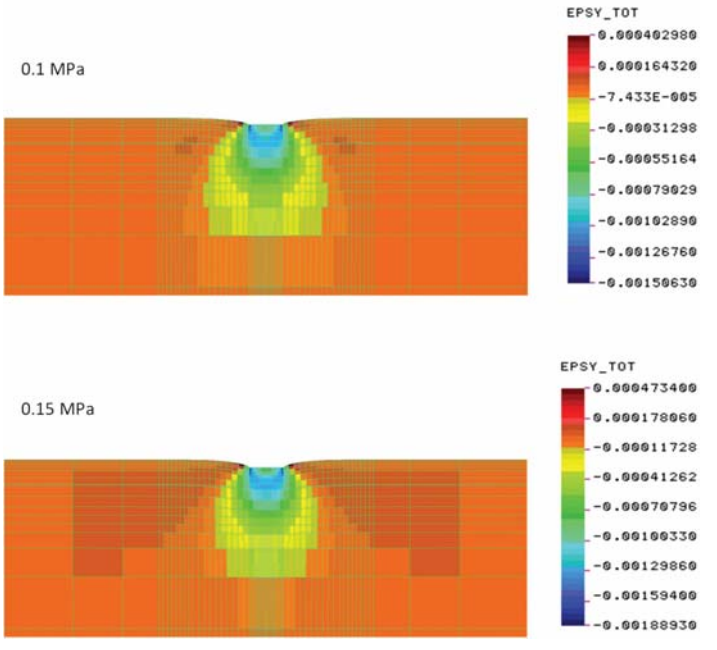

Figure 12. Vertical deformations on the cement-stabilized subgrade—construction No. 2 (deformation scale ×100).

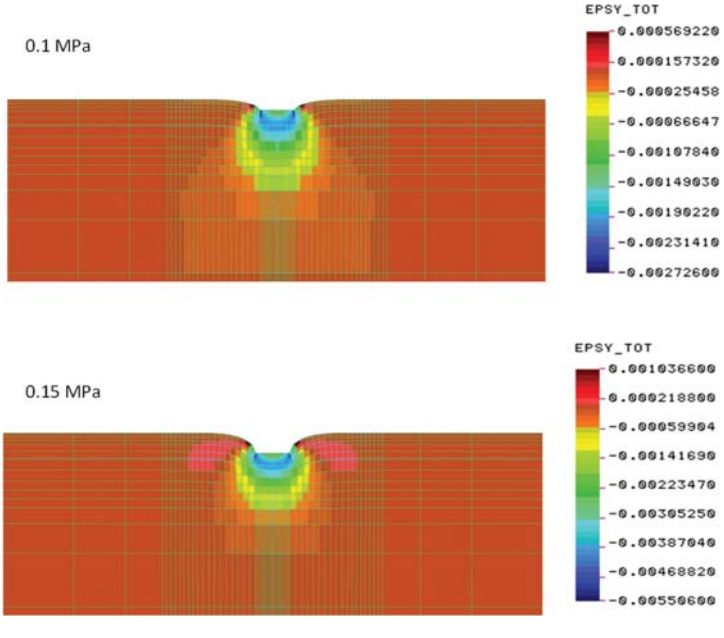

Figure 13. Vertical deformations for the native subgrade—construction No. 3 (deformation scale ×100).

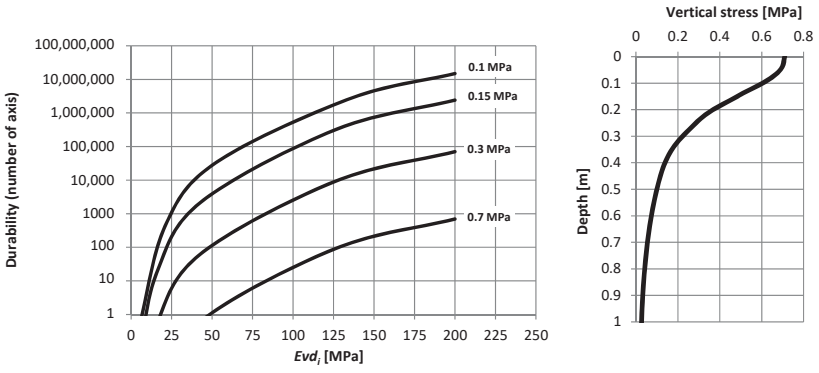

Figure 14. Dependence of durability on modules determined for the tested systems with different replacement modules.

The durability calculations show that the analyzed systems with modules less than 50 MPa may not transfer the required construction or temporary traffic and will be destroyed in the upper part of the layer when in contact with a pressure of 0.7 MPa. At a depth of about 20 cm, the values of vertical stresses will decrease to about 0.3 MPa, which ensures durability at this depth of about 100 axes. Such layers will therefore require partial replacement with new layers. In the case of other, more rigid systems (e.g., with cement-bound layers), a reduction in durability should be taken into account in the comprehensive operation of the final pavement structure, depending on the intensity of technological/temporary traffic. The durability of these layers at different depths will be from 100 to 10,000 axes.

5. Stress Analysis in Pavement Layers

In order to assess the durability of the structure as a result of deformation of the subsoil, an analysis of various pavement structures made and operated in stages during construction was carried out. In the calculations, the FEM model was used, taking into account the appropriate layer arrangement depending on a given case. The calculations were carried out for the vehicle wheel load with a radius of 0.16 m and a pressure of 0.71 MPa, and the systems of elastic layers with the following modules: 10,000 MPa asphalt concrete; 400 MPa crushed stone; 250 MPa cement-stabilized soil (sandy loam); and 30 MPa native subgrade (sandy loam).

Three stages were considered, which in practice are often made and used during construction with technological (construction) or temporary traffic. Stage 1: subgrade improved from native cement-stabilized native soil (0.15 m). Stage 2: an improved stratified subgrade, made of crushed stone (0.25 m) on a cement-stabilized native subgrade (0.15 m). Stage 3: as Stage 2, but with an additional layer of asphalt concrete (0.14 m)—the final structure.

For the diagrams, vertical stresses in the successively built layers of the target pavement structure were analyzed. Figure 15 shows the distribution of vertical stresses in layer systems at individual construction stages.

The gray field indicates the minimum stress range of 0.1 MPa, which appears in the key structure layer, which may be subject to accelerated degradation. The following layers were analyzed: cement-stabilized native soil and crushed stone since, for these layers, the criterion of vertical deformation can be used in assessing their durability. Large values (above 0.1 MPa) of stress values, firstly, adversely affect the degradation of the layers, even before the entire structure is completed; and secondly, they indicate that the assessment of compaction and identification of the replacement module of the layers should be performed with a load greater than the commonly used 0.1 MPa.

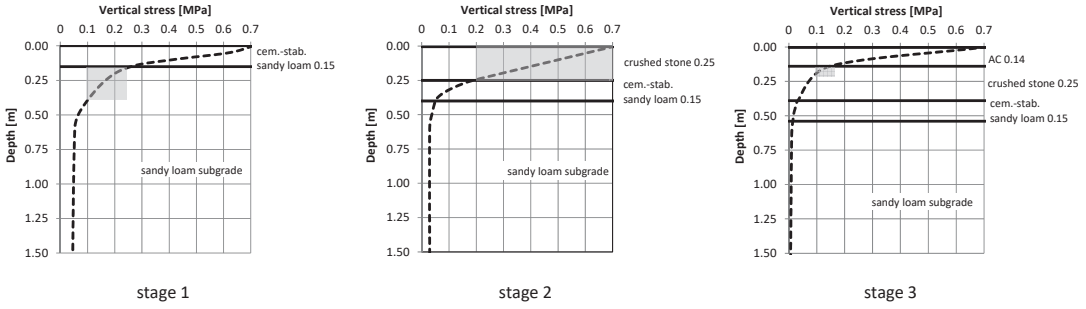

Figure 15. Distribution of vertical stresses in exploited systems, at various stages of construction and in the target system of layers of the pavement structure.

It Is worth noting that, in the case of stage 1, the stresses in the subgrade are apparently low at 0.17 MPa on average, but they cause high micro-deformations 5420, which translates into the durability of only 19 axes. For stage 2 (with an additional layer of stone), stresses of 0.04 MPa are present in the subgrade, ensuring durability for the subgrade 13,001 axes. In the aggregate layer, despite the high level of stresses and, at the same time, the high value of the modulus, relatively small micro-deformations (697) occur, which ensure the durability of the axis for this layer. In the final structure (stage 3), the durability of the subgrade is 1,848,994 axes, and the aggregate layers are 75,180,511 axes. The comparison of deformation values and subgrade durability for different stages is shown in Figure 16.

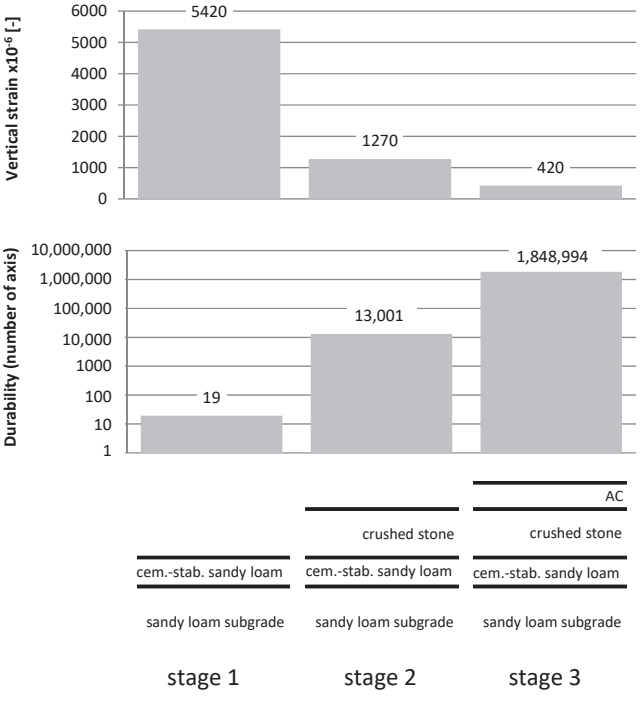

Figure 16. Distribution of vertical stresses in exploited systems at various stages.

The differences in durability are very large. The subgrade, even in the case of a cement-stabilized layer, is not able to transfer the technological movement. A degraded subgrade

with a low modulus will not be able to transfer the next loads after building subsequent layers (i.e., stage 2). For example, when the subgrade modulus drops to 10 MPa, its durability will be 543 axes, and the durability of the aggregate layer will decrease by almost 50%. In stage 3, reduced durability of the structure can be expected, which will decrease by a factor of 10. The stabilized layer will also undoubtedly be degraded. Due to the complex process of degradation of the bound layers, this issue is not discussed in this publication. The authors only wish to draw attention to the important fact of the need to conduct tests for loads above 0.1 MPa. It is of key importance to include dynamic tests already at the construction stage and to identify replacement modules with increased loading of the layers. This fact should also be taken into account at the design stage with the calculation of durability at individual stages and further use of the pavement. Particular attention should be paid to the bottom layer of stabilization and crushed stone. The difference in the modules of these layers (400 MPa vs. 250 MPa) is about 1.6, which obviously translates into the values of replacement modules, determined for systems containing these layers at different load values (0.1 MPa vs. 0.15 MPa). As a result of the authors' research with plates with different values of the loading impulse, it is shown that the difference is from a few to several percent.

6. Conclusions

In this article, the authors demonstrate the necessity to adjust the test loads in the light weight deflectometer test to the stress conditions occurring in the earlier exploitation of the lower layers of the pavement and subgrade, loaded with technological (construction) or temporary traffic. Inadequate test load leads to incorrect identification of modules and, consequently, overestimated fatigue life of the used layers and the final pavement structure. Due to the non-linear behavior of the lower layers of pavement and subsoil structures under load, it is necessary to use the load-dependent material characteristics for their description or to use correction factors under a test load of 0.1 MPa. Due to the significant degradation of these layers under a load of technological (construction) or temporary traffic (before the implementation of the final layer system), it is necessary to rationally plan the construction, staging, and operation of the layers of the pavement and subgrade structure, before the implementation of the target system, with simultaneous control of the degree of their degradation (replacement of layer parameters identified in tests with a dynamic plate). The reduction in the fatigue life of the lower layers of the pavement and subgrade structure should be taken into account at the design stage of the structure in the future operation of the target system of the pavement structure layers.

Special attention should be paid to fatigue life analysis of the low bearing subgrades under temporary or construction traffic. In such cases, the correction factors should be used when identifying moduli in an LWD test under 0.1 MPa load. It is essential to correctly predict the fatigue life in the following stages of the construction and of the final layer system.

Author Contributions: Conceptualization, P.M.; methodology, P.M.; software, P.M.; validation, B.K. and P.M.; formal analysis, B.K.; investigation, B.K.; resources, P.M. and B.K.; data curation, P.M. and B.K.; writing—original draft preparation, P.M. and B.K.; writing—review and editing, P.M. and B.K.; visualization, P.M.; supervision, B.K.; project administration, P.M. and B.K.; funding acquisition, P.M. and B.K. All authors have read and agreed to the published version of the manuscript.

Funding: This research received no external funding.

Institutional Review Board Statement: Not applicable.

Informed Consent Statement: Not applicable.

Data Availability Statement: Not applicable.

Conflicts of Interest: The authors declare no conflict of interest.

References

1. Tamrakar, P.; Nazarian, S. Evaluation of plate load based testing approaches in measuring stiffness parameters of pavement bases. *Transp. Geotech.* **2018**, *16*, 43–50. [CrossRef]
2. Benedetto, A.; Tosti, F.; Di Domenico, L. Elliptic model for prediction of deflections induced by a Light Falling Weight Deflectometer. *J. Terramech.* **2012**, *49*, 1–12. [CrossRef]
3. Bilodeau, J.-P.; Doré, G.; Savoie, C. Laboratory evaluation of flexible pavement structures containing geocomposite drainage layers using light weight deflectometer. *Geotext. Geomembranes* **2015**, *43*, 162–170. [CrossRef]
4. Elhakim, A.F.; Elbaz, K.; Amer, M.I. The use of light weight deflectometer for in situ evaluation of sand degree of compaction. *HBRC J.* **2014**, *10*, 298–307. [CrossRef]
5. Gosk, W. Stiffness Estimation of the Soil Built-in Road Embankment on the Basis of Light Falling Weight Deflectometer Test. *Procedia Eng.* **2016**, *143*, 395–402. [CrossRef]
6. Sulewska, M.J.; Bartnik, G. Application of the Light Falling Weight Deflectometer (LFWD) to Test Aggregate Layers on Geosynthetic Base. *Procedia Eng.* **2017**, *189*, 221–226. [CrossRef]
7. Lee, Y.; Choi, Y.; Ahn, D.; Ahn, J. Prediction Models Based on Regression and Artificial Neural Network for Moduli of Layers Constituted by Open-Graded Aggregates. *Materials* **2021**, *14*, 1199. [CrossRef]
8. Li, S.; Ye, Y.; Tang, L.; Cai, D.; Tian, S.; Ling, X. Experimental Study on the Compaction Characteristics and Evaluation Method of Coarse-Grained Materials for Subgrade. *Materials* **2021**, *14*, 6972. [CrossRef]
9. Guzzarlapudi, S.D.; Adigopula, V.K.; Kumar, R. Comparative studies of lightweight deflectometer and Benkelman beam deflectometer in low volume roads. *J. Traffic Transp. Eng.* **2016**, *3*, 438–447. [CrossRef]
10. Pospisil, K.; Zednik, P.; Stryk, J. Relationship between deformation moduli obtained using light falling weight deflectometer and static plate test on various types of soil. *Balt. J. Road Bridg. Eng.* **2014**, *9*, 251–259. [CrossRef]
11. Tompai, Z. Conversion between static and dynamic load bearing capacity moduli and introduction of dynamic target values. *Period. Polytech. Civ. Eng.* **2008**, *52*, 97. [CrossRef]
12. Adam, C.; Adam, D.; Kopf, F.; Paulmichl, I. Computational validation of static and dynamic plate load testing. *Acta Geotech.* **2008**, *4*, 35–55. [CrossRef]
13. Zhu, C.; Wang, X.; Hu, M.; Wang, X.; Shen, J.; Jiang, K. Development and preliminary application of a plate loading model test system considering stress state. *Measurement* **2021**, *179*, 109507. [CrossRef]
14. Ruta, P.; Szydło, A. Drop-weight test based identification of elastic half-space model parameters. *J. Sound Vib.* **2005**, *282*, 411–427. [CrossRef]
15. Tawfik, M.M.; El-Mossallamy, Y.M. Application of the finite element method for investigating the dynamic plate loading test. *Ain Shams Eng. J.* **2017**, *8*, 39–49. [CrossRef]
16. Adam, C.; Adam, D. Modeling of the dynamic load plate test with the light falling weight device. *Asian J. Civ. Eng.* **2003**, *2*, 73–89.
17. Senseney, C.T.; Mooney, M.A. Characterization of Two-Layer Soil System Using a Lightweight Deflectometer with Radial Sensors. *Transp. Res. Rec. J. Transp. Res. Board* **2010**, *2186*, 21–28. [CrossRef]
18. Grasmick, J.G.; Mooney, M.A.; Senseney, C.; Surdahl, R.W.; Voth, M. Comparison of Multiple Sensor Deflection Data From Lightweight and Falling Weight Deflectometer Tests on Layered Soil. *Geotech. Test. J.* **2015**, *38*. [CrossRef]
19. Nazzal, M.D.; Abu-Farsakh, M.Y.; Alshibli, K.; Mohammad, L. Evaluating the Light Falling Weight Deflectometer Device for in Situ Measurement of Elastic Modulus of Pavement Layers. *Transp. Res. Rec. J. Transp. Res. Board* **2007**, *2016*, 13–22. [CrossRef]
20. KMI Kht. Measurement of load bearing capacity with lightweight deflectometers (Wemex/ZFG). *Inst. Transp. Sci.* **1995**, *Research report*.
21. KMI Kht. Research of dynamic plate load testing with light falling weight deflectometer (Wemex). *Inst. Transp. Sci.* **1996**, *Research report*.
22. Kiss, L.; Molnár, J.P.; Türk, I. Diagnostics of substructures The dynamic subgrade modulus. *MÉLyÉPÍTÜKörkÉP* **2003**, 16–18. (In Hungarian)
23. Zsiás, L. *Application of the B&C Light Falling Weight Deflectometer for Evaluation of Earthworks*; Final Project; University of Széchenyi István: Budapest, Hungary, 2005.
24. Almássy, K.; Subert, I. Dynamic compaction and load bearing capacity measurements on Highway Project M7. *MÉLyÉPÍTÉS* **2006**, 10–13. (In Hungarian)
25. Kim, J.R.; Kang, H.B.; Kim, D.; Park, D.S.; Kim, W.J. Evaluation of In Situ Modulus of Compacted Subgrades Using Portable Falling Weight Deflectometer and Plate-Bearing Load Test. *J. Mater. Civ. Eng.* **2007**, *19*, 492–499. [CrossRef]
26. Krawczyk, B.; Mackiewicz, P. Impact of repetitive loading on subgrade parameters derived from light weight deflectometer test. *Roads Bridges* **2015**, *14*, 5–17. [CrossRef]
27. Oome, A.; Janssen, J.; Encica, L.; Lomonova, E.; Dams, J. Modeling of an electromagnetic geophone with passive magnetic spring. *Sens. Actuators A Phys.* **2009**, *153*, 142–154. [CrossRef]
28. Light Weight Deflectometer for the Dynamic Plate Load Test. In *Terratest Instruction Manual*; TERRATEST GbmH: Berlin, Germany, 2013.

materials

MDPI

Review

Deterioration and Protection of Concrete Elements Embedded in Contaminated Soil: A Review

Ginneth Patricia Millán Ramírez *, Hubert Byliński * and Maciej Niedostatkiewicz

Department of Concrete Structure, Faculty of Civil and Environmental Engineering, Gdansk University of Technology, 80-233 Gdańsk, Poland; mniedost@pg.edu.pl

* Correspondence: ginneth.ramirez@pg.edu.pl (G.P.M.R.); hubert.bylinski@pg.edu.pl (H.B.)

Abstract: Coating materials are considered one of the most antique materials of human civilization; they have been used for decoration and the protection of surfaces for millennia. Concrete structures—due to their permanent exposure to different types of environments and contaminants—require the use of coatings that contribute to its preservation by reducing the corrosion of its components (steel and aggregates). This article intends to introduce the principal causes of concrete deterioration and the coating materials used to protect concrete structures, including a summary of the coating types, their advantages and disadvantages, and the latest developments and applications. Furthermore, this paper also assesses brief information about the potential challenges in the production of eco-friendly coating materials.

Keywords: concrete corrosion; concrete protection; steel corrosion; concrete durability; coating materials

Citation: Millán Ramírez, G.P.; Byliński, H.; Niedostatkiewicz, M. Deterioration and Protection of Concrete Elements Embedded in Contaminated Soil: A Review. *Materials* **2021**, *14*, 3253. https://doi.org/10.3390/ma14123253

Academic Editor: Krzysztof Schabowicz

Received: 12 May 2021
Accepted: 9 June 2021
Published: 12 June 2021

1. Introduction

In the last few decades, reinforced concrete (RC) has become one of the most used construction materials. Its versatility and adaptability offer infinite applications in the construction sector [1,2]. The construction industry has been looking for several methods to improve the durability of concrete structures; rehabilitation, restoration, and strengthening are the most common activities to extend an existing structure's life cycle [3]. The durability of concrete structures embedded in soil and exposed to different types of contamination might be affected by two factors: deterioration from concrete components and chemical deterioration caused by external agents [4,5]. Table 1 summarizes the factors involved in the decrease of the durability of structures exposed to contamination.

Construction, energy, mining, agriculture, and transport industries, are one of the primary sources of contaminants; according to Enshassi et al. and Zolfagharian et al. [10,11], these can be defined as solid and liquid waste, harmful gases, noise, water, soil, and air pollution. Even though the construction sector causes several impacts to the environment, this sector is also affected by the pollutants released by other industries, e.g., soil contamination due to agricultural and mining activities reducing the durability of structures embedded in the soil caused by the presence of chemical compounds, and air pollution produced by energy and transport sectors, where the emanation of chlorine oxides contributes to the accelerated corrosion [12,13]. For this reason, it is essential to develop processes that generate less contamination and allows the protection of construction elements exposed to contaminants.

Table 1. Summary of causes of deterioration of concrete structures exposed to contaminated soil [6–9].

Causes of Deterioration	Deterioration Type
Caused by concrete components	• ***Alkali–silica reaction (ASR)***: It is one of the most concerning topics regarding the durability of concrete, leading to costly maintenance and rehabilitation works. ASR occurs when cement aggregates react with the alkali hydroxides in concrete, producing a hygroscopic gel that in the presence of water causes an expansion and thus the cracking of the concrete surface • ***Corrosion of steel bars***: The corroded bars occupy a greater volume than the non-corroded ones, causing cracking and delamination of the concrete surface. Steel corrosion is caused by the presence of chloride ions or carbon dioxide.
Caused by external agents	• *Chemical corrosion*: It can be divided into two groups: i. *Chemicals that promote a rapid deterioration*: Aluminum chloride, calcium bisulfite, hydrochloric acid, nitric acid, and sulfuric acid. ii. *Chemicals that produce a moderate deterioration:* aluminum sulfate, ammonium bisul-fate, ammonium nitrate, ammonium sulfate, ammonium sulfide, and sodium bisulfate. • ***Volume changes***: Freeze–thaw cycles, plastic and drying shrinkage, and thermal changes are the leading causes of volumetric change.

Previous studies have focused on the durability, deterioration, and service life of concrete structures, including numerical models [14–16] and experimental studies [17,18]; however, these studies mainly focused on constructions located above ground level and ignored the impact of the different factors on the structures located below ground level. Wei et al. [19] investigated how acids coming from the atmosphere and retained in the superficial layers of the ground induce concrete degradation decreasing the compressive strength and increasing the corrosion coefficient of concrete; it was identified that the main reason for premature deterioration of concrete is due to the changes in temperature where the corrosion coefficient was increased about two times for samples exposed to 40 °C. However, the compressive strength results did not show any significant changes during the 90 days of exposition. Kozubal et al. [20] have proposed a numerical model that allows preventing structural damage of vertical elements exposed to a contaminated soil environment. This model permits design engineers in the decision-making process by ensuring the safety of concrete structures embedded in the soil. The mathematical model was proposed based on the deterioration of concrete Controlled Modulus Columns (CMC) exposed to different sediments in groundwater, evidencing the apparition of cracks due to chemical corrosion. Li et al. [21] presented an analytical approach to predicting the life span of reinforced concrete pipe piles that are constantly exposed to chloride contamination and are affected by the earth pressure causing deterioration of the elements by the diffusion of microcracking. Among the principal assumptions, it can be highlighted that the end of the service life of these structures is going to be reached once the elements present total transverse cracks allowing the penetration of chlorides into the concrete core; this method provides a genuine approach for the evaluation of service life of concrete pipe piles allowing the improvements of durability design and reducing the maintenance of this concrete elements.

Recently, different coating materials have been used to protect concrete structures in the construction industry. Among the most common ones, it is possible to find fire protection coatings used as a precautionary measure preventing buildings from collapsing during fire exposure [22] and waterproof coatings widely used in the protection of concrete against reinforcement corrosion, erosion, carbonation, silica reactivity in aggregates, and chemical attacks, such as acids, salts, alkalis, and sulfates [2,7,23]. The use of coatings also increases the structure's lifetime by preventing the appearance of cracks and reducing

the maintenance cost. Figure 1 shows the general classification of coating materials for different industries.

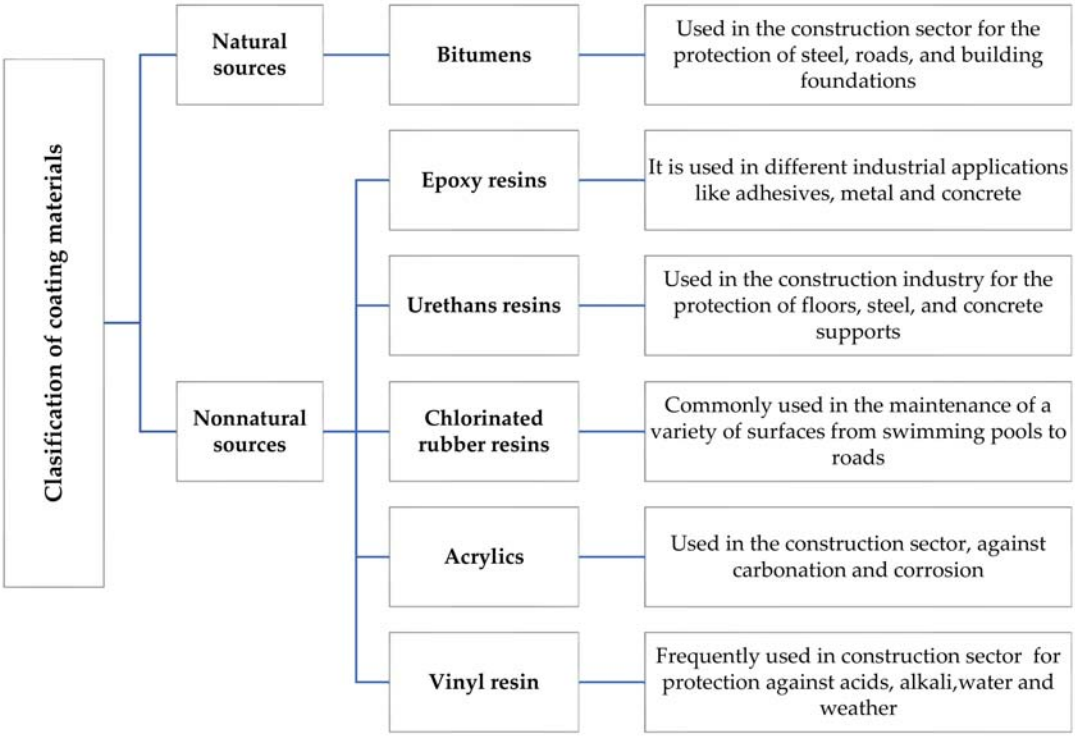

Figure 1. General classification of coating materials used in different industries [24–33].

In the last few decades, research studies about the utilization of coating materials as protection for concrete elements exposed to different environments have increased due to the significant growth of this sector and the development of a large diversity of coating materials, varying not just raw ingredients but also the process of manufacture; among the most common techniques for the preparation of coating materials, it is possible to distinguish the solution casting method proposed by Sakamaki [34], the phase-transfer catalyst process, the taffy process, and the fusion process [30]. Table 2 summarizes the historical milestones in the development of coating materials from prehistory until the present day.

Table 2. Milestone chronology in coating history [35–38].

Year/Period	Event Description
Pre-History	
Before 4000 B.C	Varnishes and paints were used during the stone age art
Before 6000 BC	Development of organic pigments (gum Arabic, egg white, gelatin, and beeswax)
Since 5000 BC	Use of protective coatings by Egyptians to seal ships
Ancient Age	
1300 B.C-1400 B.C	Use of oleo-resinous varnishes by Egyptians
Since 1122 BC	Introduction of polymers as the main component in coatings
350 B.C	First written record of uses of varnishes
Middle Age	
476 B.C-1453	Use of different organic paints and varnishes for the protection of exposed wood surfaces
Modern Age	
1550–1750	Researches about coatings for protection of musical instruments made in wood
1575	The first use of yellow amber resin as a primary component in coatings
Since 1760	Significant emergence of coating materials as a high technology industry, the development of synthetic resins in solutions, emulsion, latexes, and waterborne polymers
1763	First varnish patent
Contemporary Age	
1815	Start industrial varnish production
1839	The first production of styrene monomer used as a modifier in polymer coatings
1910	Casein powder paints
1912	Patented acrylic resin
1939–1945	Development of alkyds, urethane, and epoxy resins
1948	Incorporation of latex resins in the coating industry
1961–1965	Development of coil coatings, electrodeposition curtain coating, computer color control electrostatic powder spray, fluorocarbon resins
1970	Use of emulsion resin to control penetration in substrates
1966–1970	Development of radiation curable coatings
1970–1975	Development of aqueous industrial enamels electron beam curing, and ultraviolet curing
1976–1980	Development of high solid epoxy and polyurethane coatings resins
1981–1985	Development of high-performance pigments, polyurea resins, and high solids alkyd paints
1986–1999	Waterborne epoxy coatings and waterborne polyurethanes
21st Century	New systems based on alkyd technology, synthetic polymer-based coating resins, e.g., PVC-plastisol, acrylate dispersion, melamine/polyester, 2K urethanes, and inclusion of new drier systems for alkyds by replacing the cobalt driers

Generally, coating materials are commonly used in concrete structures when they are exposed to contaminants. Zouboulis et al. [39] proposed the study of corrosion protection of concrete samples covered with six different coatings with magnesium hydroxide against contaminants contained in sewage systems. This study has been developed in a controlled environment in a laboratory simulating the biological contamination produced in an actual sewage plant using a sulfuric acid solution and using concrete type MC 0.45 simulating

the concrete used in the sewage pipes, the grade of protection of the coating was evaluated with an accelerated degradation method by spraying H_2SO_4 in the surface sample, this process was performed until the coating's degradation was evidenced visually. Among the results, it is possible to identify that the thick layer of the coating material is directly related to the durability time, samples with 0.002 g/mm^2 presented double duration time than the samples covered with 0.001 g/mm^2, also the XRD analysis showed that all samples obtained gypsum formations before the total degradation of the coating material, even though the coating material presented degradation, its superficial pH was constant in all cases, maintaining an average value slightly over 8. Aguirre-Guerrero et al. [40] evaluated the protection effectiveness of inorganic coatings applied to concrete exposed to chloride contamination by analyzing different properties, such as water absorption, resistance to chloride ion penetration, adhesion strength, and corrosion resistance. Among the results, it is important to mention that coated concrete has not performed well, presenting lower resistance to water penetration and an increment in their capillary absorption. However, all concrete samples protected with inorganic coating showed an increment in chloride penetration resistance compared to concrete samples without protection by reducing the penetration of chlorides from high to moderate and, in some cases, to low. Finally, the use of coatings prolongs corrosion and extends the time of cracking. Sakr et al. [41] studied how different coating materials protect concrete with different water–binder (w/b) ratios when exposed to constant salt attack. It is evidenced that acrylic emulsion, epoxy, and ethyl silicate successfully protect concrete surface from physical salt attack regardless of the type of concrete and salt concentration. At the same time, the protection capacity of coatings made with the addition of fly ash strongly depends on the concrete (w/b) ratio. In general, coating materials successfully protect concrete against different types of chemical aggressions extending the lifespan of concrete elements and reducing the maintenance of structures.

This review paper aims to review the most relevant and recent investigations related to the use of coatings materials for the protection of concrete exposed to different types of contamination, also it reviews the deterioration of concrete exposed to a contaminated environment by summarizing the relevant manuscripts published in the last five years, until 2021. Tables 3 and 4 shows the statistical data of the resources used in this review paper, such as total of publications used per year and per country. The research gaps in the implementation of coatings materials and challenges for the future are identified and discussed.

Table 3. Total of documents per year.

Year	Total of Publications Used
2021	4
2020	3
2019	13
2018	6
2017	7
2016	6
2015	9
2014	3
2013	2
2012	4
2010	3
2007	2
2005	3
2004	1
2002	2
2001	2
2000	4
1989	3
1983	1
1981	1
1978	1

Table 4. Total of documents per country.

Country	Total of Publications Used
USA	20
China	13
India	7
Germany	6
Nigeria	4
United Kingdom	4
Mexico	3
Poland	3
Canada	2
Spain	2
Italy	2
Portugal	2
Saudi Arabia	2
Australia	1
Brazil	1
Colombia	1
Czech Republic	1
Greece	1
Japan	1
Lithuania	1
Russia	1
Serbia	1

2. Search Methodology

This study's research adopted the steps proposed by Ferenhof and Fernandez [42] for the systematic search flow method (SSF) to obtain the necessary information to develop this paper. The SSF method consists of four core steps:

i. **Search protocol:** A set of rules and parameters for the search process was used together with logical and relational operators (AND, OR, NOT, <, >, <=, >=, < >, =, etc.).

Keywords: Concrete, corrosion, concrete protection, durability, concrete degradation, carbonation depth, alkali reaction, diagnosis, repair, steel corrosion, chemical attack, soil contamination, coating materials, organic coating, non-organic coating

Databases: MDPI, SpringerLink, Elsevier—Science Direct, Scopus, Access Engineering, ASTM (American Society for Testing and Materials)

Year of publication: 2010–2021 for study cases

ii. **Analysis:** It refers to the consolidation and combination of data according to different criteria, such as most-cited authors, year of publication, and type of journal by creating a database with various articles that meet the search and consolidation criteria.

A database was developed using an online tool containing basic information of the articles selected, such as author name, title, year of publication, journal of publication, organized by the main topic: coating materials, soil contamination, concrete degradation, and steel degradation.

iii. **Data synthesis:** It allows to generate conclusions and new knowledge based on the results presented by the different papers analyzed.

The database prepared in the analysis section was extracted to a spreadsheet and evaluated, resulting in selecting the papers to be used.

Article selection: 210 articles were selected, 162 articles were read, and 76 articles are referenced in this paper

iv. **Writing:** The information was extracted from 76 articles. The results were consolidated through scientific and academic writing.

3. Significance of the Review

The principal purpose of this research paper is to contribute to the comprehensive state-of-the-art about the corrosion of concrete elements that are embedded in contaminated and noncontaminated soils, together with a brief overview of the current coating materials used in the construction sector. This paper summarizes all relevant data from different articles, such as types of laboratories, exposition time, sample size, etc., and determines the principal causes and consequences of contamination.

From the analysis of the articles, it is possible to determine that the main cause of corrosion in elements exposed to contaminated soil is the contamination generated by human activities, construction, mining, agriculture, and others. On the other hand, it is possible to state that there is no evidence regarding the use of coating materials to protect concrete elements located below ground level, representing a wide area of research with high potential.

4. Results and Discussion

4.1. Chemical Corrosion of Concrete Elements in Contaminated and Noncontaminated Soil

During the last few decades, the continuous growth of the human population has contributed towards increasing different industrial activities, such as agriculture, energy, transport, construction, technology, and mining. These, in turn, increase soil pollution [43], the loss of crop diversity, productivity, and soil quality by decreasing its mechanical and physical properties, such as electrical conductivity, bulk density, pH, moisture content, and hardness [43,44]. Figure 2 summarizes the main types and sources of soil pollution.

Heavy metal contamination is one of the most severe types of contamination; uranium, arsenic, cadmium, tin, lead, manganese, vanadium, and mercury are the most abundant metallic pollutants introduced into soil through the use of fertilizers and pesticides in the agriculture industry. Human exposure to these metals can lead to several body dysfunctionalities and damage, including depression, osteoporosis, liver disease, and anemia [45]. Coal-fired and nuclear power plants are the primary producers of CO_x, NO_x, SO_x, UO_x and some radionuclides contaminants such as, ^{137}Cs , ^{134}Cs , which are deposited into the soil by deposition (fallout) or by precipitation after being dissolved in the rain, contributing to global warming, acidification increase, depletion of the ozone layer, health problems, and soil contamination [46]. Finally, mining, agricultural, construction, and transport industries are the principal generators of petroleum hydrocarbons contamination, spilling different types of fuel and oils into the soil. Extraction of metals and minerals can carry chemicals and metals that may contaminate water bodies located nearby and potentially affecting human and wildlife health [44].

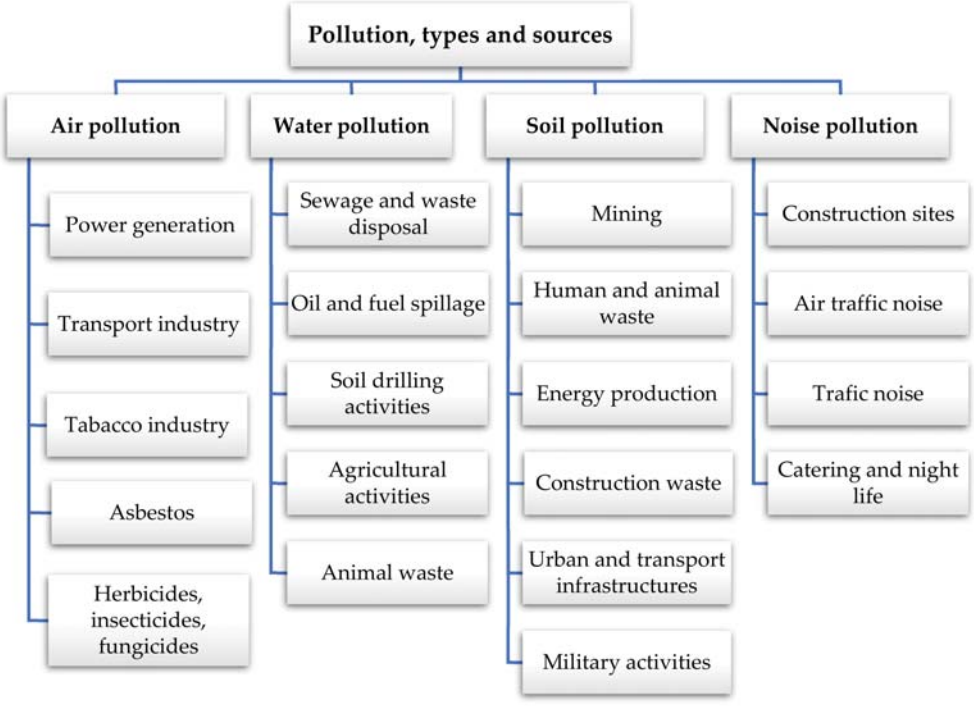

Figure 2. Main sources of soil pollution [10,43,45,47–49].

4.2. Characteristics of Reinforced Concrete Elements Embedded in the Ground in Terms of Their Chemical Corrosion

Concrete structures that are located below the level of the ground are exposed to different types of contamination. Some of them come from natural sources; however, most of them are related to human and industrial activity [47,48]. Other types of research have been conducted to determine the impact of soil contamination on foundation structures. Table 5 summarizes the most common laboratories performed in the articles included in the methodological search.

Table 5. Laboratories described in the different articles selected in the methodology search.

Material	Laboratory Type	Number of Articles
Concrete	Compressive strength	19
	Flexural strength	4
	Loss of concrete weight	5
	Slump test	6
	Permeability	4
	Expansion behavior	4
	Carbonation depth	14
Steel	Corrosion potential	5
	Corrosion kinetics	5
Aggregates	Moisture	3
	Bulk density and gravity	3

One of the most concerning topics about cement-based structures is their durability when exposed to different chemically aggressive scenarios causing its degradation; these

scenarios can be classified into three groups: physical, biological, and chemical [12], which can be contained in contaminated soil and water [12,50]. There are different methods used to determine the resistance of samples formed in cement paste, mortar, or concrete; these might vary in the type of exposure, sulfate concentration, and temperature, where expansion behavior, relative flexural strength, compressive strength, permeability, and elastic modulus are the most common measurements tested in concrete and mortar samples to determine the deterioration caused by the exposition to different contaminants. [51].

Osuji et al. [52] analyzed the reduction in compressive strength of concrete samples with fine and coarse aggregates contaminated with crude oil and its influence on concrete workability. The slump test evidenced that the inclusion of contaminated aggregates impacts the workability of the fresh concrete, increasing the slump results from 45 mm to 165 mm, which leads to segregation and prevents the correct hydration of cement. The compressive strength result showed a reduction of about 64% compared to the control test due to the segregation of the materials evidenced in the slum test; based on this, it is suggested to avoid the use of fine and coarse contaminated aggregates in mixtures.

In the study conducted by Adewuyi et al. [53,54], concrete samples of different dimensions were exposed for 215 days to biological contamination caused by organic abattoir waste and diesel and cassava hydro-cyanide contaminated soil. The results indicate that aggressive environments attack the concrete's physical and mechanical properties, leading to a reduction in the compressive strength of about 10% in the samples exposed to the cassava-contaminated soil. The specimens in the abattoir waste were additionally exposed to progressive heat, up to five temperature cycles to accelerate its degradation. The final results show that exposure to hydrocarbon (diesel) contamination is more severe on concrete samples than the organic contamination caused by the abattoir; samples exposed to diesel presented a reduction in their compressive strength of around 22–28% against 12–20% for samples exposed to abattoir contamination, in both cases, this reduction is caused by the loss of porosity and the decrease of mass which was higher in the specimens exposed for a longer time.

Yu et al. [55] exposed cylindrical and prismatic mortar samples for 270 days to Na_2SO_4 solution, the samples were also subjected to dry-wetting cycles with 0% and 5% of the solution to determine its compressive strength, elastic modulus, permeability, and expansion behavior. Results showed that the maximum expansion obtained was approximately 0.6%, being 0.5% higher than the expansion limit stated in the ASTM C1012-2014. On the other hand, compressive strength results performed at exposure durations up to 270 days showed a reduction in the resistance of about 30% in the samples due to the microcracking caused by the dry-wetting cycles and the deterioration of the material due to the constant exposition to sulfate solution. It was possible to evidence an increment from 14.6 GPa to 18.0 GPa in the elastic modulus during the first 150 days of exposure and then this decreased to around 14.0 GPa at 270 days. All samples exposed to a variation in temperature and sulfates exhibited a deterioration at a larger stage that affects the material quality and durability along with the accumulative microcracking.

Carbonation is also known as a major cause of deterioration of concrete structures embedded in contaminated soil, this type of corrosion depends on different factors, such as CO_2 pollution, water, temperature, curing process, W/C ratio, and the characteristics of the materials that compose the concrete. It is a pathology of the reinforced concrete that causes reinforcement depassivation, exposing the steel to corrosion, and its development is highly influenced by the different environmental and exposure conditions. Destructive and non-destructive tests are used to diagnose the degradation of concrete samples due to carbonation, such as visual inspection of samples, determination of the reinforcement coating, measurement of compressive strength and concrete cover, and measure of carbonation [56].

A phenolphthalein indicator is commonly used to determine the carbonation depth, being sprayed onto the surface of a freshly cut sample. Chang et al. [57] shows the results of twenty-four cylindrical models made with ordinary Portland cement and subjected to an accelerated carbonation process in a chamber at 23 °C, 70% relative humidity, and

20% of CO_2 concentration during 8 and 16 weeks. The average carbonation depth for the phenolphthalein solution was about 12 mm for the specimens exposed for 8 weeks and 17 mm for the samples exposed for 16 weeks, this led to a change in the pH of the concrete from 9.0 to 7.5, where the degree of carbonation reached 100%.

Foundation structures are exposed continuously to different aggressive agents, such as chlorides and sulfates during their service lifespans [58,59]. Chloride ions are present in industrial water, seawater, contaminated soils, and sewage water ions [60], the exposure to these is the main cause of corrosion of reinforced concrete structures and one of the most critical problems of structures embedded in the ground. Particularly, the steel bars of concrete structures can be corroded by these chemical agents present in soil, thus affecting the structure's durability.

By the measurement of potential and velocity of corrosion, Baltazar-Zamora et al. [58] observed that the carbon and galvanized steel used in concrete samples exposed to soil contamination with sodium chloride content higher than 2% for 257 days presented a very high probability of suffering from premature corrosion; however, the compressive strength of the different samples was not compromised, since none of them showed a reduction in their mechanical properties.

Tables 6 and 7 present a summary of the exposition times of concrete samples to contaminated environments and their size characteristics, respectively.

Table 6. Summary of exposition time to contaminated environments according to the articles selected in the methodology search.

Exposition Time (Days)	Number of Articles
<100	4
>100 and <200	7
>200	13

Table 7. Summary of sample sizes according to the articles selected in the methodology search.

Shape	Sample Size (mm)	Number of Articles
Prismatic	120 × 150 × 70	5
	150 × 150 × 150	12
	150 × 100 × 1000	4
Cylindric	150 × 300	3
	50 × 100	4

4.3. Characteristics of Emergency State of Structures Caused by Chemical Corrosion of Concrete Elements Embedded in the Ground

Concrete structures are exposed to constant environmental impacts that affect their physical and mechanical properties [10]. In constructions that are located above ground level, it is easy to determine damages and the level of impact on reinforced concrete due to different contaminants or construction and structural design errors. However, concrete structures below the ground are impacted more severely due to the constant exposure, lack of supervision, and preventive maintenance, resulting in damages that would be difficult to identify and repair. Hence, these damages can potentially affect the bearing capacity and durability of the structures mentioned above [12]. The following research presents real-life examples of structures exposed to different types of contamination where the causes and consequences of constant exposure are known and presented.

Zhong et al. [61] analyzed the premature corrosion of concrete foundations in residential buildings located in Eastern Connecticut in the United States; this deterioration is related to the expansion of the aggregate, caused by the alkali–silicate reaction (ASR) and internal sulfates attacks, resulting in map cracking and wide crack openings in foundation elements [62]. To determine the original causes of the aggregate expansion, 70 core samples were taken from different residential house foundations affected by premature corrosion.

Compressive strength results show that 30% of the samples obtained 0 MPa due to the high deterioration level, falling apart even before the test was done, and 20% of the specimens had a strength reduction of about 57%. From the X-ray diffraction (XRD) tests and the use of scanning electron microscopy, it was possible to determine that the samples with the highest deterioration level had a significant content of sulfide iron mineral in the form of pyrrhotite, which was found to be responsible for the premature concrete deterioration by oxidation, which facilitates the formation of secondary minerals that release sulfates.

Similar results were found in the research conducted by Tagnit-Hamou et al. [63], where building foundations in Eastern Canada presented several deterioration problems two years after the construction. Different cores were taken from the foundations to check the causes of corrosion, and according to the XRD results, the cement matrix and aggregates were affected by the presence of pyrrhotite, causing the early cracking of the concrete.

Another example of the deterioration of concrete foundations is given by Yoshida et al. [64], where residential buildings in Japan were affected by sulfate attacks; this is considered an important problem for hot springs and mining areas. According to the Japanese Geotechnical Society, soil samples were checked to evaluate the sulfate content, where the values of water-soluble sulfate exceeded the standard's criteria, reaching, in some cases, more than 1.0% of the mass soil. In addition, small concrete cores were taken from the deteriorated foundations of residential buildings. It was evidenced in these samples that the penetration of sulfur trioxide was around 20 mm. This type of sulfate attack was classified as a "physical attack" due to the minimum cracking on the element's surface.

Other types of sulfate attack in concrete foundations can be found in sewage water, which leads to the degradation of the elements due to sulfuric acid produced by the different microorganisms present in the contaminated water, reducing by this, mechanical properties of the concrete and the loss of adhesion of the cement matrix. Tulliani et al. [65] evidenced in their research a severe degradation case in a 35-year-old building located in the north of Italy, where concrete samples were taken from the foundation elements and analyzed by X-ray diffraction (XRD) and scanning electron microscopy (SEM). It was evidenced that the bond between the coarse aggregates and the cement past was poor, and also that the steel reinforcement was highly corroded. For samples without corrosion, the pH and conductivity presented values of 7.5 and 305 μS, respectively; however, for the specimens with severe damage, the pH and electrical conductivity were about 7.2 and 1650 μS. SEM and XRD analyses showed a high gypsum concentration between cement and aggregates responsible for strength loss.

Based on previous research, it is evidenced that the presence of different minerals and contaminants produce chemical reactions that lead, in some cases, to severe corrosion and thus degradation of the elements embedded in contaminated soil, which results in the effects on their mechanical and physical properties.

Table 8 contains a summary of the most interesting study cases related to those evaluated in Sections 4.2 and 4.3.

Table 8. Summary of study cases.

Aim of Research	Materials	Laboratories	Results	Ref.
Determination of the compressive and flexural strength behavior of unstressed concrete samples embedded in polluted soil	➢ Ordinary Portland cement grade 42.5 ➢ Dimension of cubic samples: 15cm × 15cm × 15cm ➢ Dimension of beams: 15cm × 15cm × 100cm ➢ Concrete mix 1:1.5:3	➢ Compressive and flexural test at curing ages of 28 up to 196 days ➢ Compressive strength of concrete samples exposed to progressive heat in five cycles ➢ Consistency, gravity, soundness, and compressive strength of cement ➢ Determination of moisture, bulk density, and the gravity of aggregates	➢ Reduction in the compressive strength up to 9.47% during the first 28 days ➢ Reduction in the flexural strength up to 34.50% during the first 28 days	[53]
Analyze the influence of organic abattoir waste and disposal hydrocarbon contamination on the durability of concrete	➢ Ordinary Portland cement grade 42.5 ➢ Dimension of cubic samples: 15cm × 15cm × 15cm ➢ Dimension of beams: 15cm × 15cm × 90cm ➢ Steel for beams Ø10mm and Ø8mm	➢ Compressive strengths of samples (every seven days until the 84th day in cubes) ➢ Flexural strength at the age of 84 days ➢ Density of concrete ➢ Physical and chemical properties of contaminated and not contaminated soil	➢ The physical and mechanical properties of the concrete were affected by the presence of soil contaminants ➢ Hydrocarbon contamination had a more significant effect on the load-carrying capacity of concrete	[54]
Determination of the influence of crude oil on the compressive strength of concrete	➢ Dimension of samples: 15cm × 15cm × 15cm ➢ Concrete mix with 0%, 1%, 2%, 3%, 4%, and 5% of contaminated aggregates	➢ Characterization of physical properties of aggregates used to manufacture the concrete. ➢ Concrete Slump Test ➢ Compressive strength at 7, 14, 28, and 56 days	➢ The presence of crude oil in concrete samples significantly decreased the mechanical properties ➢ Increase in percentages of crude oil in the fine aggregate cause higher workability of concrete	[52]
Analyze the mechanical and physical properties behavior of concrete samples	➢ Dimension of samples: Ø50 mm × 100 mm ➢ Dimension of samples: prismatic: 25 mm × 25 mm × 285 mm ➢ Na_2SO_4 solution	➢ Compressive strength ➢ Measurement of elastic modulus ➢ Permeability ➢ Expansion behavior ➢ Carbonation depth	➢ Increments in the expansion material of about 0.5% higher than the limit expansion stated in the standards ➢ Compressive strength shows a reduction in the resistance of about 30%	[55]
Comparison of the concentration and intensity distribution of $Ca(OH)_2$ and $CaCO_3$ in concrete samples	➢ Dimension of samples: Ø150 mm × 300 mm ➢ Type I ordinary Portland cement ➢ Phenolphthalein indicator	➢ Carbonation depth ➢ Thermalgravimetric analysis (TGA) method ➢ X-ray diffraction analysis tests ➢ Fourier transformation infrared spectroscopy (FTIR) test ➢ pH measurement ➢ Compressive strength	➢ TGA, FTIR, and XRDA test show very similar results in the carbonation depth of about 35 mm up to 16 weeks ➢ Carbonation depth measured by the phenolphthalein test shows a value of 17 mm in the same frame of time	[57]

Table 8. *Cont.*

Aim of Research	Materials	Laboratories	Results	Ref.
Analyze the behavior of corrosion in reinforced concrete embedded in soil contaminated with chlorides and sulfates	➢ Dimension of samples: 120 mm × 70 mm × 180 mm ➢ Soil type MH ➢ Portland cement, CPC 30R RS, and CPC 30R ➢ Steel bars of AISI 1018 Carbon Steel and Galvanized Steel, Ø 3/8 and steel bars of UNS S31600	➢ Characterization of concrete mixtures in a fresh state ➢ Initial compressive strength ➢ Measurement of corrosion potential ➢ Physical description of the soil	➢ Concrete samples exposed to soil contamination with NaCl content higher to 2% present the highest probability to suffer from premature corrosion in the steel bars during the first 103 days ➢ Lower Icorr magnitudes in samples made with Portland type V	[58]
Evaluation of the electromechanical behavior of concrete samples embedded in contaminated soil with different percentages of magnesium sulfate ($MgSO_4$)	➢ Dimension of samples: 120 mm × 70 mm × 180 mm ➢ Soil type SP ➢ Portland cement, CPC 30R RS, and CPC 30R ➢ Steel bars of AISI 1018 carbon steel and galvanized steel Ø 3/8" and bars of UNS S31600	➢ Measurement of corrosion potential ➢ Measurement of corrosion kinetics	➢ In concentrations between 1% and 2% of $MgSO_4$ the corrosion resistance varies according to the Portland cement and steels bars type, being higher in concrete made with CPC 30R RS and reinforced with galvanized bars ➢ All concrete samples present a high and moderate level of corrosion during the first 130 days in soils, with 3% of $MgSO_4$ content	[66]
Evaluation of the corrosion behavior of carbon and stainless steel bars using different concrete mixtures, including the addition of silica fumes and fly ash	➢ Dimension of samples: Ø150mm× 300mm and 120mm × 70mm × 150mm ➢ AISI 1018 carbon steel and AISI 304 stainless steel with Ø 0.95 mm ➢ Concrete mixtures, 100% CPC, 80% CPC, and 20% silica fume, and 80% CPC and 20% fly ash	➢ Measurement of corrosion potential ➢ Characterization of concrete aggregates ➢ Physical and mechanical characterization of fresh and hardened concrete mixtures ➢ Initial compressive strength	➢ Severe corrosion in all concrete samples during the 365 days of exposure ➢ Samples with 20% of fly ash and silica fume addition showed a reduction of around 70% in the kinetic corrosion in comparison with the specimens without mineral additions	[67]

4.4. Coating Materials—Current State, Challenges, and Perspectives

4.4.1. Research Gaps in the Use of Coating Materials

The rapid and continuous growth of different industries, the lack of control in the production of materials, food, and poor waste management, can eventually increase air and soil pollution, as evidenced in previous chapters, decreasing the service life of structures exposed continuously. Different materials have been implemented over the years to protect concrete elements by reducing corrosion at an early age. As Table 6 demonstrates, most of the researches are focused on analyzing the concrete and steel mechanical properties behavior in structures located above the ground when exposed to different types of contamination, either organic and non-organic. However, the use of coating materials is not evidenced for the protection of concrete elements embedded in the soil, taking this into account, it is crucial to invest in the research of coating materials that can be applied in concrete elements embedded in contaminated soil that allow the preservation of structures exposed to different types of contamination at various degrees.

4.4.2. Current Status and Future Challenges

Protective coatings are present in most of the surfaces around us, used from the simple protection of food to the complex protection of steel and concrete. Nevertheless, most of these coatings go through a manufacturing process that generates contamination. Some of them use nonrenewable materials, such as bitumen obtained from petroleum refining, causing several environmental problems. In addition, some of the coatings use organic solvents that emit volatile organic compounds, producing air pollution that affect human health. Therefore, it is necessary to continue developing eco-friendly coating materials that contribute to environmental preservation without sacrificing the main properties of the materials, e.g., high durability, toughness, adhesion, strength, etc. Table 9 contains the main advantages and disadvantages of some of the most common coating materials used in the construction industry to protect concrete structures. Figure 3 shows the key aspects and challenges in the production of coating materials.

Figure 3. Critical aspects in the field of challenges of production of coating materials used for protection of concrete elements.

Table 9. Comparison of the most popular coatings for concrete elements [25,31,68–76].

Type of Coating	Advantages	Disadvantages
Epoxy resin	✓ Excellent adhesion properties on different substrates ✓ High chemical and solvent resistance ✓ Control concrete carbonation ✓ Fluidity in the application due to its low viscosity properties ✓ Good electrical properties ✓ Excellent anticorrosion performance	✗ Poor impact resistance ✗ Low-temperature resistance ✗ Inherent brittleness ✗ Inferior weathering resistance ✗ Complex removal procedure ✗ Costly maintenance ✗ Strong toxic fumes
Bitumen	✓ Good penetration into the surface due to its fluidity ✓ When used in pavements, it improves the sticking between different layers and increases the resistance to deformation	✗ Its protectiveness can be affected by polymer grade ✗ It is affected by the temperature in the summer season by making the coating soft
Acrylics	✓ High water resistance ✓ High resistance to mechanical damage ✓ High resistance to UV radiation ✓ Highly resistant to variations in temperature ✓ High impact resistance ✓ High chemical resistance ✓ User friendly, easy to apply ✓ High fungus resistance ✓ Lower cost applications ✓ Good adhesion properties	✗ Difficult to apply to plastic surfaces ✗ Overheat buildings when it is used to the roof ✗ Complex removal procedure ✗ Fast drying ✗ Poor water repellent ✗ Low UV radiation resistance
Polyurethane resin	✓ High performance in its mechanical properties such as flexibility, strength, hardness, and stiffness ✓ Control concrete carbonation ✓ Long service life ✓ High resistance to UV radiation ✓ Economic maintenance ✓ High hardness and impact resistance	✗ It is sensitive to humidity ✗ Delays the natural breathing capability of concrete ✗ Low weathering resistance ✗ Strong toxic fumes ✗ Less alkali-resistant than epoxy coating ✗ High cost

4.4.3. Characteristics of Coating Materials According to Polish–European and American Standards

Coating materials must follow the specifications stated in the European Standards (Eurocode) regarding coating adhesion to the substrate, absorption, and permeability, among others. Table 10 contains the most imperative standards describing the physical and mechanical properties of coating materials intended to protect different surfaces, such as wood, steel, concrete, plastic, and glass. For this paper, the PN–EN standards based on the European Standards will be taken as a reference.

Table 11 summarizes the laboratories that performed evaluations of the physical and mechanical properties of coating materials used in the construction industry according to the academic articles used in the search methodology.

Table 10. Standard procedures for the determination of mechanical and physical properties of coating materials.

Standard Reference	Standard Title	Parts
PN-EN ISO 2811	Density determination, paints, and varnishes	Part 1: Pycnometric method (2016) Part 2: Immersed body (plummet) method (2011) Part 3: Oscillation method (2011) Part 4: Pressure cup method (2011)
PN-EN ISO 2884:2007	Viscosity determination, paints, and varnishes	Part 1: High shear cone-plate viscometer Part 2: Viscometer with disc or ball, fixed speed
PN-EN ISO 2431:2019		Part 1: Determination of flow time by use of flow-cups
PN-EN ISO 2808: 2020	Measurement of coating thickness, paint, and varnishes	Part 1: Determination of the coating thickness
PN-EN ISO 2178: 2016		Part 1: Non-magnetic coatings on a magnetic substrate—magnetic method
PN-EN ISO 2360: 2017		Part 1: Amplitude-sensitive eddy-current method
PN-EN ISO 4624: 2016	Adhesion of the coating to the substrate, paints, and varnishes	Part 1: Pull of test
PN-EN ISO 2409: 2013		Part 1: Cross-cut test
PN-EN 14891:2017	Ceramic tiling bonded with adhesives - requirements, test methods, and liquid applied water-impermeable products.	

Table 11. Summary of laboratories for coating materials.

Standard Reference Used	Type of Laboratory Performed	Number of Articles
PN-EN ISO 62:2008	Water absorption	1
ASTM C642-97		2
PN-EN ISO-527-1,3	Tensile stress	2
PN-EN 14891:2012/17		3
ZUAT-15/IV.13/2002	Adhesion	1
ASTM D4541-17		2
ZUAT-15/IV.13/2002	Resistance to freeze/thaw cycles	1
PN-EN 1504-2:2006		2
PN-EN 14891:2017		2
ASTM D562-10	Viscosity	1
PN-EN 1504-2:2006	Ability to cover cracks	2
EN ISO 9117-1:2009	Curing time	1
ASTM D1640		2
ASTM C642-97	Water absorption	2

Approximately 54% of the articles reviewed applied Polish–European standards (PN-EN), 38% used the American Society for Testing and Materials (ASTM), and just 2% used local test methods approved by the ITB (Building Research Institute) in Poland. The most common procedures among the literature were adhesion, tensile stress, and resistance to freeze/thaw cycles tests. In addition, the article analyses focused on the reduction and control of the carbonation process and on the proposal of new coating materials for the protection of concrete exposed to contaminated environments.

During the last decades, different raw materials have been used to produce new protective coatings materials intended to improve the concrete properties. Elnaggar et al. [61] presented a novel protective material based on different ratios of isocyanate chemical groups (NCO) and a mix of 80% asphalt and 20% polyester. The asphaltic polyurethane (As/PU) coating was tested on concrete cubes; according to the results, an increment in the dry film thickness was shown, from 86µm to 98µm, in samples with a 1:4 ratio of NCO, which can be attributed to the density of the (As/PU) coating. Similarly, adhesion strength showed an increase of 145% in the samples with a 1:4 ratio of NCO, an effect that can occur due to the interaction between ACO groups and ANH. Finally, it was concluded that both dry film thickness and adhesion strength improved with the increase in NCO/OH ratio.

Francke et al. [62] proposed a new coating material modified with cementitious mortar to perform waterproof and chemical protection. Based on polymer–cement products, this

coating material effectively performed the functions of concrete carbonation protection by reducing the carbonation depth by 24% and increasing in 7% the adhesion strength in frost and storm environments. However, in freeze–thaw cycles with the addition of sodium chloride solution (salt), a decrease was evidenced in the bonding strength of about 40% with respect to the sample without environmental exposure.

Improving the protection of concrete structures is one of the most critical objectives in manufacturing new coating materials. Significant results have been evidenced by applying protective (As/PU) layers showing a reduction in the chloride penetration of about 75% with respect to the control sample. Even though the immersion of both coated and non-coated samples in sulfuric acid and NaCl solutions show a decrease in the compressive strength of the concrete samples, it can be evidenced that the coated samples present a reduction in the compressive strength between 22% and 27% and a decrease of 50% in the non-coated material. Finally, it can be concluded that the protection with asphaltic polyurethane (As/PU) coating improves the mechanical and physical properties gradually when the ratio is increased with respect to the samples without coating.

According to Baba et al. [63], to minimize the corrosion caused by carbonation, concrete surface protection can be performed with three different coating materials: penetrants for surface improvement, non-cementitious for finishing layer, and cementitious for finishing layers. In the research conducted by Lo et al. [64], eight non-cementitious coatings, emulsions, and synthetic paints were used in concrete prisms to analyze their impacts on the reduction of carbonation depth; four of them were tested for interiors and the rest of the coatings for the exterior. In addition, an accelerated carbonation test method was implemented, exposing the samples to a constant CO_2 flow in a chamber for 56 days, the deep carbonation was measured by exposing the samples to phenolphthalein solution. Results showed that for exteriors coatings, the C25 concrete samples obtained a reduction in deep carbonation of about 60% and 45% for interiors coatings, decreasing from 16.40 mm to 6.58 mm and 8.93 mm, respectively. For C35 concrete samples a reduction in the deep carbonation for exteriors coatings of 56% (3.78 mm) was also evidenced, and for the interior coating it was 40% (4.23 mm). Based on this it can be concluded that there is a significant reduction in the corrosion caused by carbonation using these coating materials.

The authors mentioned above evaluated the benefits of coating materials in structures exposed to contamination. It was evidenced that coating materials effectively reduce the impact caused by different chemical attacks, and are able to extend the lifespan of concrete structures and reduce corrective maintenance costs.

5. Conclusions

This literature review was prepared to give an overview of the causes of corrosion of concrete elements exposed to different types of contaminants and the procedures proposed and used by some researchers to protect these elements. Different coating materials have been proposed, varying from naturals sources, such as bituminous coatings, to synthetic productions, like acrylic coatings. Among the results, in all cases where concrete samples were subjected to contamination either by exposition to chemical or natural contaminants, the compressive and flexural strengths showed a significant reduction. In addition, galvanized and carbon steel bars embedded in concrete samples showed an increase in corrosion, potentially leading to a premature corrosion of the bars and premature cracking and deterioration of the concrete elements. Even though several investigations have been carried out on how different types of contamination affect concrete, there is not much evidence yet on how coating materials can protect concrete elements embedded in contaminated soils.

6. Research Limitations

This review paper was limited to Spanish and English articles found in the journals mentioned in Section 2, “Search Methodology”, which excludes literature published in

other languages and was limited to academic publications. It does not consider the results from industrial practice.

Author Contributions: Conceptualization, supervision, and validation: M.N. and H.B., formal analysis, investigation, and writing—original draft: G.P.M.R., methodology, and visualization: G.P.M.R. and H.B. All authors have read and agreed to the published version of the manuscript.

Funding: This research received no external funding.

Acknowledgments: This paper did not receive any specific grants from funding agencies in the public, commercial, or not-for-profit sectors.

Conflicts of Interest: The authors declare no conflict of interest.

Abbreviations

Abbreviation	Meaning
^{137}**Cs**	Cesium 137
^{134}**Cs**	Cesium 134
ACO	Acetoxy group
AISI	American Iron and Steel Institute
ASR	Alkali–silica reaction
As/PU	Asphalt and polyurethane
ASTM	American Society for Testing and Materials
BC	Before Christ
BS	British standard
$CaCO_3$	Calcium carbonate
CEM	Cement
CPC	Calcium phosphate cements
C_3A	Tricalcium aluminate
CO_2	Carbon dioxide
CO_x	Carbon oxides
DGEBA	Diglycidyl ether of bisphenol A
EN	European standards
GPa	Gigapascal
ISO	International Organization for Standardization
ITB	Building Research Institute
KOH	Potassium hydroxide
LiOH	Lithium hydroxide
MgSO4	Magnesium sulfate
Na_2CO_3	Sodium carbonate
Na_2SO_4	Sodium sulfate
NaCl	Sodium chloride
NaOH	Sodium hydroxide
NCO	Isocyanate chemical group
NO_x	Nitrogen oxide
OH	Hydroxide
pH	Potential of hydrogen
PN	Polish standards
PVC	Polyvinyl chloride
RC	Reinforced concrete
SEM	Scanning electron microscopy
SER	Solid epoxy resins

SO_x	Sulfur oxide
TGA	Thermalgravimetric analysis
UNS	Unified number system
UO_x	Uranium oxide
UV	Ultraviolet
W/C	Water/cement
XRD	X-ray diffraction
ZUAT	Recommendations of the Technical Approval Provision

References

1. Popov, B.N. Corrosion of Structural Concrete. *Corros. Eng.* **2015**, 525–556. [CrossRef]
2. Safiuddin, M. Concrete Damage in Field Conditions and Protective Sealer and Coating Systems. *Coatings* **2017**, *7*, 90. [CrossRef]
3. Vaysburd, A.; Emmons, P. How to make today's repairs durable for tomorrow—corrosion protection in concrete repair. *Constr. Build. Mater.* **2000**, *14*, 189–197. [CrossRef]
4. Shi, X.; Xie, N.; Fortune, K.; Gong, J. Durability of steel reinforced concrete in chloride environments: An overview. *Constr. Build. Mater.* **2012**, *30*, 125–138. [CrossRef]
5. Owsiak, Z. Testing alkali—Reactivity of selected concrete aggregates. *J. Civ. Eng. Manag.* **2010**, *3730*, 8. [CrossRef]
6. Figueira, R.B.; Sousa, R.; Coelho, L.; Azenha, M.; de Almeida, J.M.; Jorge, P.A.S.; Silva, C.J.R. Alkali-silica reaction in concrete: Mechanisms, mitigation and test methods. *Constr. Build. Mater.* **2019**, *222*, 903–931. [CrossRef]
7. Portland Cement Association. Types and Causes of Concrete Deterioration. Portl. Cem. Assoc. Concr. Inf. PCA R.D. Se 2002, 5420 Old Orchard Road, 1–16. Available online: www.cement:docs/default-source/fc_concrete_technology/durability/is536-types-and-causes-of-concrete-deterioration.pdf?sfvrsn=4&sfvrsn=4 (accessed on 28 February 2021).
8. Wang, K. Carbonate Aggregate in Concrete. Available online: http://www.lrrb:pdf/201514.pdf (accessed on 28 February 2021).
9. Wang, C.; Chen, F. *Durability of Polypropylene Fiber Concrete Exposed to Freeze-Thaw Cycles with Deicing Salts*; Atlantis Press: Dordrecht, The Netherlands, 2019; Volume 181, pp. 203–206. [CrossRef]
10. Enshassi, A.; Kochendoerfer, B.; Rizq, E. Evaluación de los impactos medioambientales de los proyectos de construcción. *Rev. Ing. Construcción* **2014**, *29*, 234–254. [CrossRef]
11. Zolfagharian, S.; Nourbakhsh, M.; Irizarry, J.; Ressang, A.; Gheisari, M. Environmental impacts assessment on construction sites. In Proceedings of the Construction Research Congress 2012: Construction Challenges in a Flat World, EE. UU, Indiana, IN, USA, 21–23 May 2012; pp. 1750–1759. [CrossRef]
12. Bonić, Z.; Ćurčć, G.T.; Davidovič, N.; Savič, J. Damage of concrete and reinforcement of reinforced-concrete foundations caused by environmental effects. *Procedia Eng.* **2015**, *117*, 411–418. [CrossRef]
13. Popov, B.N. High-Temperature Corrosion. *Corros. Eng. Elsevier* **2015**, 481–523. [CrossRef]
14. Stambaugh, N.D.; Bergman, T.L.; Srubar, W.V. Numerical service-life modeling of chloride-induced corrosion in recycled-aggregate concrete. *Constr. Build. Mater.* **2018**, *161*, 236–245. [CrossRef]
15. Xia, J.; Shen, J.; Li, T.; Jin, W.-L. Corrosion prediction models for steel bars in chloride-contaminated concrete: A review. *Mag. Concr. Res.* **2021**, 1–20. [CrossRef]
16. Yin, G.J.; Zuo, X.B.; Tang, Y.J.; Ayinde, O.; Wang, J.L. Numerical simulation on time-dependent mechanical behavior of concrete under coupled axial loading and sulfate attack. *Ocean Eng.* **2017**, *142*, 115–124. [CrossRef]
17. Silva, M.A.G.; Cunha, M.P.; Pinho-Ramos, A.; da Fonseca, B.S.; Pinho, F.F.S. Accelerated action of external sulfate and chloride to study corrosion of tensile steel in reinforced concrete. *Mater. Constr.* **2017**. [CrossRef]
18. Pernicová, R.; Dobiáš, D. Resistance of surface layers of concrete against aggressive environment. *Key Eng. Mater.* **2017**, *722*, 44–51. [CrossRef]
19. Wei, J.; Liu, J.; Bai, Y.; Song, Z.; Feng, Q.; Lu, Y.; Sun, S. Effect on the resistance of concrete acid corrosion in superficial soil layers. *Adv. Civ. Eng.* **2018**. [CrossRef]
20. Kozubal, J.; Wyjadłowski, M.; Steshenko, D. Probabilistic analysis of a concrete column in an aggressive soil environment. *PLoS ONE* **2019**, *14*, e0212902. [CrossRef] [PubMed]
21. Li, L.; Li, J.; Yang, C. Theoretical approach for prediction of service life of RC pipe piles with original incomplete cracks in chloride-contaminated soils, Constr. *Build. Mater.* **2019**, *228*, 116717. [CrossRef]
22. Kim, J.-H.J.; Lim, Y.M.; Won, J.P.; Park, H.G. Fire resistant behavior of newly developed bottom-ash-based cementitious coating applied concrete tunnel lining under RABT fire loading. *Constr. Build. Mater.* **2010**, *24*, 1984–1994. [CrossRef]
23. Fattuni, N.I.; Hughes, B.P. Effect of acid attack on concrete with different admixtures or protective coatings. *Cem. Concr. Res.* **1983**, *13*, 655–665. [CrossRef]
24. Taylor, S.R. Coatings for Corrosion Protection: Inorganic. *Encycl. Mater. Sci. Technol.* **2001**, 1263–1269. [CrossRef]
25. Taylor, S.R. Coatings for Corrosion Protection: Organic. *Encycl. Mater. Sci. Technol. Elsevier* **2001**, 1274–1279. [CrossRef]
26. Guma, T.N.; Aku, S.Y.; Yawas, D.S.; Dauda, M. Bitumen in Coating Corrosion Protection of Steel-The Position and Prognosis of Nigerian Bitumen. *Am. J. Eng. Res.* **2015**, *4*, 101–111.
27. Raghav, P.K.; Agarwal, N.; Saini, M. Edible Coating of Fruits and Vegetables: A Review View Project. 2016. Available online: www.researchgate.net/publication/331298687 (accessed on 7 February 2021).

28. Singh, A.K.; Bhadauria, A.S.; Kumar, P.; Bera, H.; Saha, S. Bioactive and drug-delivery potentials of polysaccharides and their derivatives. In *Polysaccharide Carriers for Drug Delivery*; Woodhead Publishing: Sawston, UK, 2019; pp. 19–48. [CrossRef]
29. Popov, B.N. Organic Coatings. *Corros. Eng. Elsevier* **2015**, 557–579. [CrossRef]
30. Pham, H.Q.; Marks, M.J. Epoxy Resins, Assesments of Potential BPA Emissions. In *Construction Research Congress 2012: Construction Challenges in a Flat World*; Wiley-VCH Verlag GmbH & Co. KGaA: Weinheim, Germany, 2005; p. 90.
31. Chattopadhyay, D.K.; Raju, K.V.S.N. Structural engineering of polyurethane coatings for high performance applications. *Prog. Polym. Sci.* **2007**, *32*, 352–418. [CrossRef]
32. Americus. Coatings update: Chlorinated rubber technology. *Pigment Resin Technol.* **1978**, *7*, 10–12. [CrossRef]
33. Ibrahim, M.; Al-Gahtani, A.S.; Maslehuddin, M.; Dakhil, F.H. Use of surface treatment materials to improve concrete durability. *J. Mater. Civ. Eng.* **1999**, *11*, 36–40. [CrossRef]
34. Satoshi, S. Solution Casting Method. U.S. Patent Application US 2005/0212172 A1, 2005.
35. Myers, R.R. History of Coatings Science and Technology. *J. Macromol. Sci. Part A. Chem.* **1981**, *15*, 1133–1149. [CrossRef]
36. Edwards, K.N.; Mislang, H.B. History of coatings. *Appl. Polym. Sci. 21st Century Elsevier* **2000**, 439–447. [CrossRef]
37. Soucek, M.; Johansson, M.K.G. Alkyds for the 21st century. *Prog. Org. Coatings* **2012**, *73*, 273. [CrossRef]
38. Pilcher, G.R.; The ChemQuest Group. Entering the Second Decade of the 21st Century: The State of the U.S. Paint and Coatings Industry. *CoatingsTech* **2019**, *16*, 8.
39. Merachtsaki, D.; Tsardaka, E.-C.; Tsampali, E.; Simeonidis, K.; Anastasiou, E.; Yiannoulakis, H.; Zouboulis, A. Study of Corrosion Protection of Concrete in Sewage Systems with Magnesium Hydroxide Coatings. *Environ. Sci. Proc.* **2020**, *2*, 27. [CrossRef]
40. Aguirre-Guerrero, A.M.; de Gutiérrez, R.M. Alkali-activated protective coatings for reinforced concrete exposed to chlorides. *Constr. Build. Mater.* **2021**, *268*, 121098. [CrossRef]
41. Sakr, M.R.; Bassuoni, M.T.; Taha, M.R. Effect of coatings on concrete resistance to physical salt attack. *ACI Mater. J.* **2019**, *116*, 255–267. [CrossRef]
42. Ferenhof, H.A.; Fernandes, R.F. Desmistificando a Revisão de Literatura Como Base Para Redação cientíFica: Método SSF, n.d. Available online: www.researchgate.net/publication/325070845 (accessed on 4 May 2021).
43. Lelieveld, J.; Evans, J.S.; Fnais, M.; Giannadaki, D.; Pozzer, A. The contribution of outdoor air pollution sources to premature mortality on a global scale. *Nature* **2015**, *525*, 367–371. [CrossRef] [PubMed]
44. Saha, J.K.; Selladurai, R.; Kundu, S.; Patra, A.K. Chapter 9 Water, Agriculture, Soil and Environmental. *Tech. Instrum. Anal. Chem.* **1989**, 155–191. [CrossRef]
45. Mirsal, I.A. *Soil Pollution. Origin, Monitoring and Remediation*, 2nd ed.; Springer: New York, NY, USA, 2004.
46. Pallise, J. Impactos ambientales de la producción de electricidad. *Asoc. Prod. Energúas Renov.* **2014**, 42. Available online: http://proyectoislarenovable.iter.es/wp-content/uploads/2014/05/17_Estudio_Impactos_MA_mix_electrico_APPA.pdf (accessed on 14 January 2021).
47. Zwolak, A.; Sarzyńska, M.; Szpyrka, E.; Stawarczyk, K. Sources of Soil Pollution by Heavy Metals and Their Accumulation in Vegetables: A Review. *Water Air Soil Pollut.* **2019**, *230*, 164. [CrossRef]
48. Rodríguez, N.; McLaughlin, F.M.; Pennock, D. Soil Pollution: A Hidden Reality. 2018. Available online: www.fao.org/ (accessed on 17 February 2021).
49. Owa, F.D. Water pollution: Sources, effects, control and management. *Mediterr. J. Soc. Sci.* **2013**, *4*, 65–68. [CrossRef]
50. Haufe, J.; Vollpracht, A. Tensile strength of concrete exposed to sulfate attack. *Cem. Concr. Res.* **2019**, *116*, 81–88. [CrossRef]
51. Meng, C.; Li, W.; Cai, L.; Shi, X.; Jiang, C. Experimental research on durability of high-performance synthetic fibers reinforced concrete: Resistance to sulfate attack and freezing-thawing. *Constr. Build. Mater.* **2020**, *262*, 120055. [CrossRef]
52. Osuji, S.; Nwankwo, E. Effect of Crude Oil Contamination on the Compressive Strength of Concrete. *Niger. J. Technol.* **2015**, *34*, 259. [CrossRef]
53. Adewuyi, A.P.; Olaniyi, O.A.; Olafusi, O.S.; Fawumi, A.S. Compressive and Flexural Behaviour of Unstressed Concrete Substructure in Cassava Effluent Contaminated Soils. *Open J. Civ. Eng.* **2015**, *5*, 239–248. [CrossRef]
54. Adewuyi, A. Strength and durability assessment of concrete substructure in organic and hydrocarbon polluted soil. *Int. J. Mod. Res. Eng. Technol.* **2017**, *2*, 34–42.
55. Yu, X.T.; Chen, D.; Feng, J.R.; Zhang, Y.; di Liao, Y. Behavior of mortar exposed to different exposure conditions of sulfate attack. *Ocean Eng.* **2018**, *157*, 1–12. [CrossRef]
56. Jedidi, M.; Benjeddou, O. Chemical causes of concrete degradation. *MOJ Civ. Eng.* **2018**, *4*, 40–46. [CrossRef]
57. Chang, C.-F.; Chen, J.-W. The experimental investigation of concrete carbonation depth. *Cem. Concr. Res.* **2006**, *36*, 1760–1767. [CrossRef]
58. Baltazar-Zamora, M.A.; Mendoza-Rangel, J.M.; Croche, R.; Gaona-Tiburcio, C.; Hernández, C.; López, L.; Olguín, F.; Almeraya-Calderón, F. Corrosion Behavior of Galvanized Steel Embedded in Concrete Exposed to Soil Type MH Contaminated With Chlorides. *Front. Mater.* **2019**, *6*, 1–12. [CrossRef]
59. Melchers, R.E.; Li, C.Q. Reinforcement corrosion initiation and activation times in concrete structures exposed to severe marine environments. *Cem. Concr. Res.* **2009**, *39*, 1068–1076. [CrossRef]
60. Ramli, M.; Kwan, W.H.; Abas, N.F. Strength and durability of coconut-fiber-reinforced concrete in aggressive environments. *Constr. Build. Mater.* **2013**, *38*, 554–566. [CrossRef]

61. Zhong, R.; Wille, K. Deterioration of residential concrete foundations: The role of pyrrhotite-bearing aggregate. *Cem. Concr. Compos.* **2018**, *94*, 53–61. [CrossRef]
62. Oliveira, I.; Cavalaro, S.H.P.; Aguado, A. Evolution of pyrrhotite oxidation in aggregates for concrete. *Mater. Construcción* **2014**, *64*, e038. [CrossRef]
63. Tagnit-Hamou, A.; Saric-Coric, M.; Rivard, P. Internal deterioration of concrete by the oxidation of pyrrhotitic aggregates. *Cem. Concr. Res.* **2005**, *35*, 99–107. [CrossRef]
64. Yoshida, N. Sulfate attack on residential concrete foundations in Japan. *J. Sustain. Cem. Mater.* **2019**, *8*, 327–336. [CrossRef]
65. Tulliani, J.M.; Montanaro, L.; Negro, A.; Collepardi, M. Sulfate attack of concrete building foundations induced by sewage waters. *Cem. Concr. Res.* **2002**, *32*, 843–849. [CrossRef]
66. Santiago-Hurtado, G. Electrochemical evaluation of reinforcement concrete exposed to soil type SP contaminated with sulphates. *Int. J. Electrochem. Sci.* **2016**, *11*, 4850–4864. [CrossRef]
67. Baltazar-Zamora, M.A.; Bastidas, D.M.; Santiago-Hurtado, G.; Mendoza-Rangel, J.M.; Gaona-Tiburcio, C.; Bastidas, J.M.; Almeraya-Calderón, F. Effect of Silica Fume and Fly Ash Admixtures on the Corrosion Behavior of AISI 304 Embedded in Concrete Exposed in 3.5% NaCl Solution. *Materials* **2019**, *12*, 4007. [CrossRef]
68. Hu, H.; He, Y.; Long, Z.; Zhan, Y. Synergistic effect of functional carbon nanotubes and graphene oxide on the anti-corrosion performance of epoxy coating. *Polym. Adv. Technol.* **2017**, *28*, 754–762. [CrossRef]
69. Patil, R. Waterproofing: Types, Advantages & Disadvantages. 2016. Available online: constructionor.com/waterproofing/ (accessed on 22 February 2021).
70. Rabiot, D.; Morizur, M.F. Polymer-modified bitumen emulsions an advantage for the various road applications. *Eurasphalt Eurobitume Congr.* **1996**, *6*, 161.
71. Paliukaite, M.; Vorobjovas, V.; Bulevičius, M.; Andrejevas, V. Evaluation of Different Test Methods for Bitumen Adhesion Properties. *Transp. Res. Procedia* **2016**, *14*, 724–731. [CrossRef]
72. Nguyen, T.N.L.; Do, T.V.; Nguyen, T.V.; Dao, P.H.; Trinh, V.T.; Mac, V.P.; Nguyen, A.H.; Dinh, D.A.; Nguyen, T.A.; Vo, T.K.A.; et al. Antimicrobial activity of acrylic polyurethane/Fe3O4-Ag nanocomposite coating. *Prog. Org. Coatings* **2019**, *132*, 15–20. [CrossRef]
73. Alessandrini, G.; Aglietto, M.; Castelvetro, V.; Ciardelli, F.; Peruzzi, R.; Toniolo, L. Comparative evaluation of fluorinated and unfluorinated acrylic copolymers as water-repellent coating materials for stone. *J. Appl. Polym. Sci.* **2000**, *76*, 962–977. [CrossRef]
74. Samimi, A.; Zarinabadi, S. Application Polyurethane as Coating in Oil and Gas Pipelines Calculation of Corrosion in Oil and Gas Refinery with EOR Method View project Application Polyurethane as Coating in Oil and Gas Pipelines. *Int. J. Sci. Eng. Investig.* **2012**, *1*, 43–45.
75. Alchimica, Advantages and Disadvantages of Polyurethane Waterproofing Materials. 2019. Available online: alchimica.com.ua/en/2019/05/13/advantages-and-disadvantages-of-polyurethane-waterproofing-materials/ (accessed on 23 February 2021).
76. Kanimozhi, K.; Prabunathan, P.; Selvaraj, V.; Alagar, M. Bio-based silica-reinforced caprolactam-toughened epoxy nanocomposites. *High Perform. Polym.* **2016**, *28*, 189–197. [CrossRef]

materials

MDPI

Article

Determination of Prestress Losses in Existing Pre-Tensioned Structures Using Bayesian Approach

Martin Moravčík and Jakub Kraľovanec *

Department of Structures and Bridges, Faculty of Civil Engineering, University of Zilina, Univerzitna 8215/1, 010 26 Zilina, Slovakia; martin.moravcik@uniza.sk
* Correspondence: jakub.kralovanec@uniza.sk

Abstract: Deterioration of materials and structures is an unavoidable fact, and prestressed concrete structures are not an exception. The evaluation of load-carrying capacity and remaining service life includes collecting various information. However, one type of information is essential and the most important, the state of prestressing, which inevitably decreases over time. Currently, many possible methods for the evaluation of prestressing are available. These techniques are part of the structural assessment and provide residual prestressing force value which is later used in the evaluation process. Therefore, it is suitable to provide the value of prestressing force based on certain probabilistic backgrounds. This study addresses the determination of residual prestressing force in pre-tensioned railway sleepers one year after their production, using the so-called Bayesian approach. This technique is focused on the validation of results obtained from the application of the non-destructive indirect saw-cut method. The Bayesian approach considers analytic calculation as the primary method of prestressing determination. In this paper, Monte Carlo simulation was used to determine the total variability that defines all Bayesian systems of probability functions. Specifically, a total of 1000 simulations was applied, and the current random vector of prestressing force derived from the analytical calculation has been assumed as a normally distributed function. Finally, obtained results for different depths of saw-cuts are compared. The results of the experimental and statistical determination of residual prestressing force provide its value with a 95% confidence level. This study suggests that the implementation of the probability approach can be an effective tool for determining prestress losses.

Keywords: Bayesian approach; prestressing force; saw-cut method; assessment; pre-tensioned members

Citation: Moravčík, M.; Kraľovanec, J. Determination of Prestress Losses in Existing Pre-Tensioned Structures Using Bayesian Approach. *Materials* **2022**, *15*, 3548. https://doi.org/10.3390/ma15103548

Academic Editor: Krzysztof Schabowicz

Received: 22 April 2022
Accepted: 12 May 2022
Published: 16 May 2022

Publisher's Note: MDPI stays neutral with regard to jurisdictional claims in published maps and institutional affiliations.

1. Introduction

When assessing existing prestressed concrete structures, the determination of the residual prestressing force is an essential and inevitable task [1,2]. Prestressing force value obviously decreases over time and its determination should consider all potential prestress losses [3,4]. However, acquiring crucial knowledge about the exact value of prestressing force acting on the structure is quite difficult. Of course, for reliable assessment additional information considering the structure's condition needs to be obtained [5,6]; it is possible to collect this data using common testing methods [7]. This general knowledge includes many material properties, such as information about the real geometry of structural members and reinforcement, damage and deterioration (obtained from visual inspections); data containing the effect of significant overloading of the structure, etc. [8,9].

Generally, the analytical or numerical calculation of prestressing force value is the standard approach. Therefore, required input data consists of the age of the structure, its geometry, reinforcement parameters, and layout. Moreover, necessary material properties can be obtained using a wide range of standard material testing procedures [10–12]. However, all collected data that affect the prestressing force have a natural strongly stochastic

character, especially due to effects such as the rheology of concrete (creep and shrinkage) or steel relaxation [13].

In Bayesian philosophy, the analytic calculation (the primary method of prestress determination) can be considered as the prior hypothesis, together with its probability. Nevertheless, other new or additional relevant information can also be desirable and useful, especially regarding the unknown value of a prestressing force that is acting on the structure [14–16]. Likewise, several indirect techniques or structural tests can be used, such as the saw-cut method or structural response method [17–19]. These methods are based on observation of the structural behavior after the application of a known load. In the case of the saw-cut method, normal stress (strain) relief is observed. On the other hand, the structural response method evaluates prestressing based on the measurement of deflection, strain (normal stress) change or width of crack resulting from the external load [20,21]. All new relevant information can be taken into account and combined with the prior probabilistic model using updated techniques. These results are so-called posterior probabilistic models, which may be used to obtain an enhanced assessment of current prestressing force.

Updating the probability distribution of a basic variable is commonly based on the Bayesian approach described briefly below. Two individual events, A and B, are studied. The conditional probability P (A | B) of event A, given event B has occurred with a non-zero probability P (B), is defined as:

$$P(A \mid B) = P(A \cap B)/P(B) = [P(A) \times P(B \mid A)]/P(B) \quad (1)$$

where P (A | B) is a conditional probability, i.e., the probability of event A occurring given that B is true. It is also called the posterior probability of A given B. P (B | A) is also a conditional probability, i.e., the probability of event B occurring given that A is true. It can also be interpreted as the likelihood of A, given a fixed B, because P (B | A) = L (A | B) × P (A) and P (B) are the probabilities of observing A and B, respectively, without any given conditions; they are known as the marginal probability or prior probability. A and B must be different events.

The Bayesian theorem can also be applied to the hypothesis verification tool, and graphically interpreted using probability density functions as presented in Figure 1.

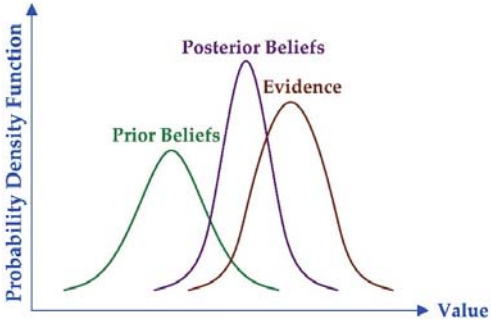

Figure 1. Bayesian concept.

In fact, the input data are random variables, thus the probability distribution function can be used to represent the data $\{x_1, x_2, \ldots, x_n\}$ with distribution parameters of θ. The concept of conjugacy in Bayesian statistics is used. Conjugacy occurs if the posterior distribution is in the same family of probability density functions as the prior belief, but with new parameter values. These values are updated to reflect what has been understood

from the obtained data. Bayes' theorem, expressed in terms of probability distributions, appears as:

$$f(\theta \mid data) = [f(\theta) \times f(data \mid \theta)] / [\int f(data \mid \theta) \times f(\theta) \times d\theta] \quad (2)$$

where $f(\theta \mid data)$ is the posterior distribution for the parameter θ; $f(data \mid \theta)$ is the sampling density for the data, which is proportional to the likelihood function, only differing by a constant that makes it a proper density function; $f(\theta)$ is the prior distribution for the parameter θ; and $f(data)$ is the marginal probability, $f(data) = \int f(data \mid \theta) \times f(\theta) \times d\theta$.

A number of closed-form solutions for Equation (2) can be found for special types of probability distribution functions known as the natural conjugate distributions. In cases where no analytical solution is available, first order reliability method (FORM)/second order reliability method (SORM) techniques can be used to assess the posterior distribution. If the normal–normal conjugate family $N(\mu,\sigma^2)$ is taken into account, Bayes' theorem leads to the posterior distribution for μ and σ^2 given the observed data to take the form:

$$p(\mu,\sigma^2 \mid x_1, x_2, \ldots, x_n) = [p(\mu,\sigma^2) \times p(x_1, x_2, \ldots, x_n \mid \mu,\sigma^2)] / \text{Normalizing Constant} \quad (3)$$

where $p(\mu,\sigma^2)$ is the joint prior distribution function. The likelihood function for (μ,σ^2) is proportional to the sampling distribution of the data, $L(\mu,\sigma^2) \propto p(x_1, x_2, \ldots, x_n \mid \mu,\sigma^2)$, so that the posterior distribution can be re-expressed in proportional form. The symbol $\propto$ means "proportional to". According to the Joint Committee on Structural Safety (JCSS) Probabilistic Model Code described in [14] and [22], Equation (3) can be expressed for normal distribution in engineering-acceptable form for μ and σ, given as:

$$f'(\mu,\sigma) = k \times \sigma^{-[\delta(n') + v' + 1]} \exp\{-[(1/2 \times \sigma^2)] \times [v' \times (s')^2 + n' \times (\mu - m')^2]\} \quad (4)$$

where k is the normalizing constant; $\delta(n') = 0$ for $n' = 0$; $\delta(n') = 1$ for $n' > 0$; m' is the sample mean; s' is the sample standard deviation; n is the sample size; and $v' = n - 1$ is the number of degrees of freedom. Then, the predictive value of {X} can be found from:

$$\{X\} = m'' + t_{v''} \times s'' \times \{1 + 1/n''\}^{0.5} \quad (5)$$

where $t_{v''}$ has a central Student's t-distribution.

The present study is based on results from the application of the non-destructive saw-cut method performed on pre-tensioned members—e.g., railway sleepers. The method aims to isolate concrete block from acting forces by means of saw-cuts. Residual prestressing force is subsequently calculated from normal stress relief initiated by sawing [17,18]. The ratio of isolation of concrete block is dependent on the parameters of saw-cuts—depth and axial distance [23]. One of the main advantages of this technique is that it has negligible local impact on the prestressed concrete structure. When using the saw-cut method on an unloaded structure, the prestressing force value is easy to calculate because the determination of normal stress resulting from the dead load is obvious. However, if the investigated member is also loaded by an external load, additional normal must be taken into account [20,21].

2. Analytical Calculation of Prestressing Force Value

The analysis was performed on a prestressed concrete sleeper, which is one of the standard pre-tensioned members produced in the manufacturing process. In particular, our specimen is sleeper type B70 W-49G, as illustrated in Figure 2.

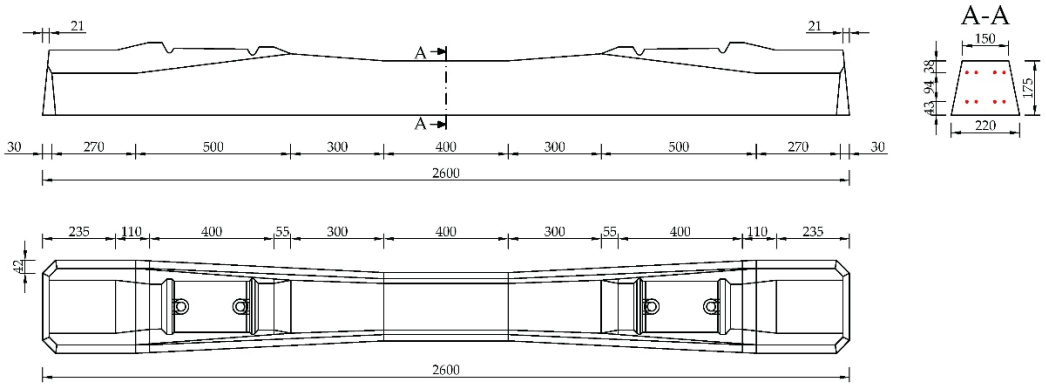

Figure 2. Analyzed prestressed concrete sleeper B70 W-49G.

Declared basic parameters entered into the analytical calculation of prestressing force P_m (t) (kN) are listed in Table 1.

Table 1. Characteristics of analyzed sleeper.

A_c (m^2)	I_c (m^4)	z_{bott} (mm)	z_{upp} (mm)	ϕ_w (mm)	No. of ϕ_w (-)	f_{pk} (MPa)	$f_{p0.1k}$ (MPa)	E_p (GPa)
0.0324	0.0000816	82	93	7	8	1740	1560	195

The prestressed concrete sleeper was designed from concrete class C50/60 [24]. Therefore, the modulus of elasticity, E_{cm} = 37,000 MPa, was assumed. Calculation of prestressing force P_m (t) in time t = 365 days was performed according to the Eurocode 2—Slovak national implementation STN EN 1992-1-1 [25]. Prestressing of the sleeper was provided by eight wires with a smooth surface and a diameter of 7 mm. The initial prestressing force was derived from Equation (6) considering the value of initial stress in the wire, $\sigma_{p,in}$ = 1380 MPa. The bending moment due to self-weight is M_{Go} = 0.798 kNm.

$$\sigma_{pm,max} = \min [0.80 \times f_{pk}; 0.90 \times f_{p,0.1k}] \quad (6)$$

Long-term prestress losses have the highest influence on the prestressing force value's decrease over time. They were determined using standard Equations (7) and (8). Prestress losses due to steel relaxation are:

$$\Delta\sigma_{p,r}(t,t_0) = -\sigma_{pi} \times k_1 \times \rho_{1000}\,[\%] \times 10^{-5} \times e^{\mu \times k2} \times [t/1000]^{0.75 \times (1-\mu)} = -169.3 \text{ MPa} \quad (7)$$

where k_1 = 5.39; k_2 = 6.7; ρ_{1000} = 8.0; μ = 0.79.

$$\Delta\sigma_{p,r+s+c} = -\{0.8 \times \Delta\sigma_{p,r}(t,t_0) + \varepsilon_{cs}(t,t_0) \times E_p + (E_p/E_{cm}) \times \varphi(t,t_0) \times \sigma_{c,(Pm0+G0)}(t,t_0)\}/\{1 + (E_p/E_{cm}) \times (A_p/A_c) \times [1 + (A_c/I_c) \times e_p^2] \times [1 + 0.8 \times \varphi(t,t_0)\} = -310.3 \text{ MPa} \quad (8)$$

where $\varepsilon_{cs}(t,t_0)$ = 5.01; and $\varphi(t,t_0)$ = 1.69.

Corresponding prestressing force, considering the prestress losses after 365 days in one prestressing wire, is P_m (t) = 41.2 kN.

All analytical systems contain a certain degree of variability. When these systems are formed by a combination of random variables, the resulting variability of the system generally cannot be found in a closed-form approach. An alternative approach that allows the estimation of variability in a system, given the variability of its components, is Monte Carlo simulation (MCS). In this study, MCS was used to determine the total variability that

defines all Bayesian systems of probability functions. In our case, a total of 1000 simulations were applied.

The current random vector of prestressing force $\{P_{calc}\}$ derived from the analytical calculation has been assumed as a normally distributed function, as in [15], based on a random generation with a known mean value of 40.96 kN and a standard deviation of 10.20 kN. In the first approximation, this level corresponds to the estimated variation coefficient of 25%. Of course, it is appropriate to have all components in Equation (7) or (8) as a random variable. Specifically, they have mean values according to Table 1, and the strength and modulus of elasticity parameters have a common coefficient of variation (CV), CV = 5%, and for the cross-sectional parameters, CV = 3%. However, in this simulation, the consequence of the central limiting theorem was applied. Estimated prestress force is presented using a histogram, probability density function (PDF) and cumulative distribution function (CDF) in Figures 3 and 4. It can be considered as the joint prior probability function, as in Equation (3). Statistical parameters are listed in Table 2.

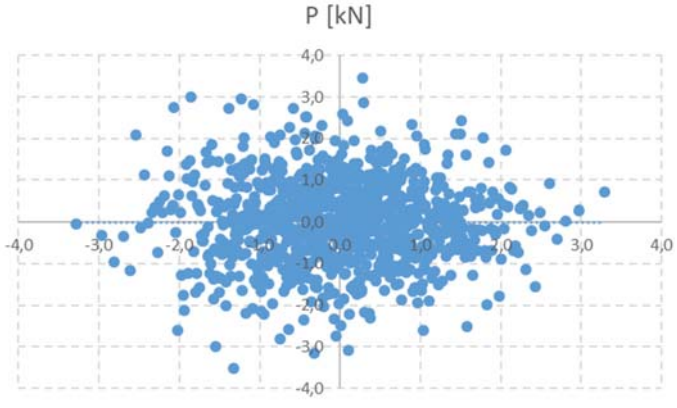

Figure 3. Normally distributed values of P_{calc}.

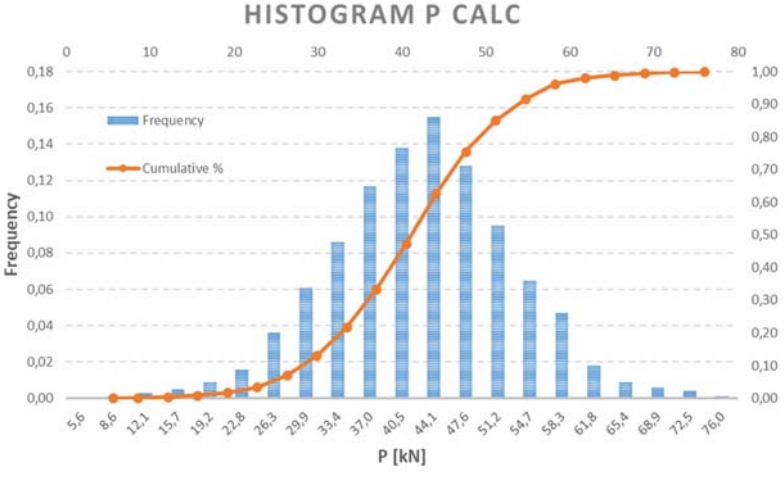

(**a**)

Figure 4. *Cont.*

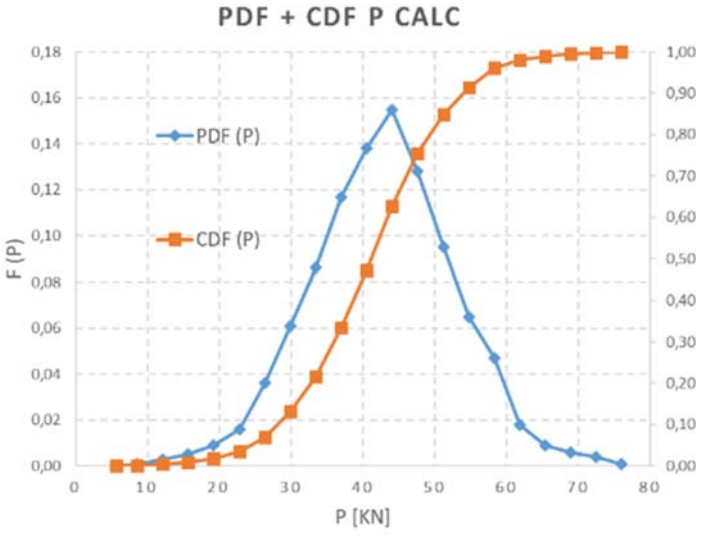

(**b**)

Figure 4. (**a**) Histogram and CDF of P_{calc}; and (**b**) PDF and CDF of P_{calc}.

Table 2. Statistical parameters for P_{calc}.

Mean m′ (kN)	Median (kN)	St. Dev. s′ (kN)	Kurtosis (-)	Skewness (-)	Min. (kN)	Max. (kN)	Conf (95) (kN)
40.96	41.04	10.02	0.3586	–0.0036	5.60	75.59	0.6218

3. Experimental Program—Saw-Cut Method

The application of the saw-cut method on prestressed concrete sleepers consisted of three saw-cuts. Their axial distance was 120 mm, and sawing was performed gradually (depths of 10, 20 and 30 mm). The maximal depth of saw-cuts was chosen with regard to the layout of prestressing wires in the sleepers, as we intended to avoid cutting them and affecting the structural integrity of pre-tensioned members. For the experiment, the upper edge of the specimen with a straight and smooth surface in the mid-span area was chosen. This location provided suitable conditions for the installation of strain gauges and subsequent measurement of strain release after sawing. The measurement is presented in Figure 5. For strain recording, linear foil strain gauges HBM LY41-50/120 made of ferritic steel (temperature matching code "1": 10.8×10^{-6}/K) with a measuring grid length of 50.0 mm and a total length of 63.6 mm were installed. The position of strain gauges can be seen in Figure 6. The prestressed concrete sleepers were supported by two lines at a distance of 0.1 m from the ends. Supports were provided using so-called steel rollers; as a consequence, the specimens behaved as simply supported beams with an effective length of 2.4 m.

All the equations and assumptions mentioned are based on the linear distribution of normal stress which can be assumed in the case of the uncracked prestressed concrete structure. Therefore, in the case of an already pre-cracked structure, such an assumption should not be considered. After sawing, some local nonlinearities could be observed, but the area adjacent to installed strain gauges should not be significantly influenced given an axial distance of 120 mm.

(**a**)

(**b**)

Figure 5. The measurement: (**a**) application of saw-cuts and (**b**) view of saw-cuts.

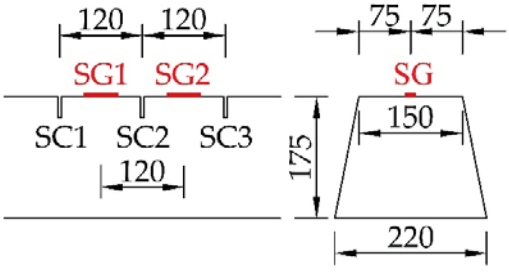

Figure 6. Mid-span area: position of saw-cuts (SC) and strain gauges (SG).

Normal stress readings from the measurement are displayed in Figure 7 and listed in Table 3. Evaluation of obtained results was based on the real value of the concrete's modulus of elasticity, which was determined using removed cylindrical samples (37.4 GPa). The real modulus of elasticity value was in compliance with Eurocode 2 [25].

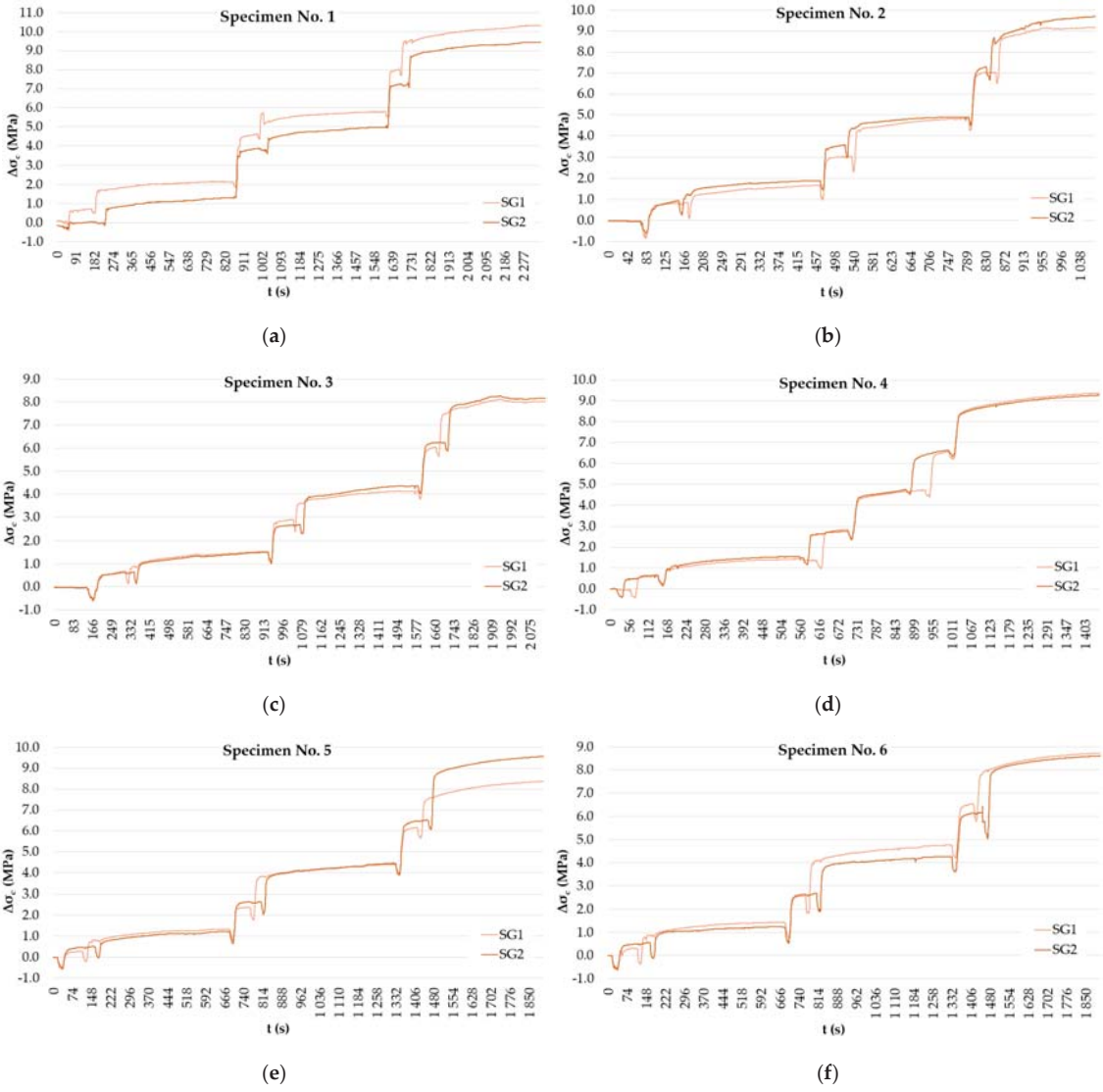

Figure 7. Normal stress readings on strain gauges after the application of saw-cuts. Specimens—1 (**a**); 2 (**b**); 3 (**c**); 4 (**d**); 5 (**e**); 6 (**f**).

Table 3. Normal stress relief—saw-cut method.

Sleeper No.	SG1—$\Delta\sigma_{c,i}$ (MPa)			SG2—$\Delta\sigma_{c,i}$ (MPa)		
	$\Delta\sigma_{c,10}$	$\Delta\sigma_{c,20}$	$\Delta\sigma_{c,30}$	$\Delta\sigma_{c,10}$	$\Delta\sigma_{c,20}$	$\Delta\sigma_{c,30}$
1	2.14	5.78	10.32	1.31	4.92	9.44
2	1.56	4.80	9.16	1.90	4.89	9.68
3	1.48	4.11	8.02	1.49	4.24	8.16
4	1.37	4.72	9.38	1.50	4.74	9.28
5	1.31	4.39	8.37	1.22	4.45	9.55
6	1.42	4.74	8.73	1.21	4.26	8.60

Depending on the depth of a saw-cut, experimentally determined prestressing force value $P_{exp,i}$ can be calculated according to Equation (9):

$$P_{exp,i} = \{k_i \times \Delta\sigma_{c,I} - [(M_{G0} \times z_{upp})/I_c]\}/CS \quad (9)$$

where k_i is the "calibration factor of the depth of saw-cut" determined according to a parametric study based on nonlinear numerical simulations. This constant represents the ratio between released normal stress after the application of saw-cuts and initial normal stress in a prestressed concrete member. The deeper a saw-cut is in the shorter axial distance we choose, the more normal stress is released, and the calibration factor has a lower value. More information about the calibration factor and its determination can be found in [23]. $\Delta\sigma_{c,i}$ is the released normal stress value dependent on the depth of a saw-cut, and CS is a cross-sectional function, as in Equation (10):

$$CS = -(8/A_c) - [(-4 \times e_{p,bott} + 4 \times e_{p,upp} \times z_{upp})/I_c] \quad (10)$$

where $e_{p,bott}$ is the distance from the cross-section center to the center of the bottom wires; and $e_{p,upp}$ is the distance from the cross-section center to the center of the upper wires. All cross-sectional parameters used in Equation (10) were considered as random variables according to Table 4. A histogram and CDF of the cross-sectional function CS can be seen in Figure 8.

Table 4. Cross-sectional parameters.

	A_c (m2)	I_c (m4)	z_{bott} (mm)	z_{upp} (mm)	$e_{p,bott}$ (mm)	$e_{p,upp}$ (mm)	$M_{G,o}$ (kNm)
Mean	0.0324	0.0000816	82	93	43	59	0.798
St. Dev.	1.619×10^{-3}	4.082×10^{-6}	4	4	2	3	0.040

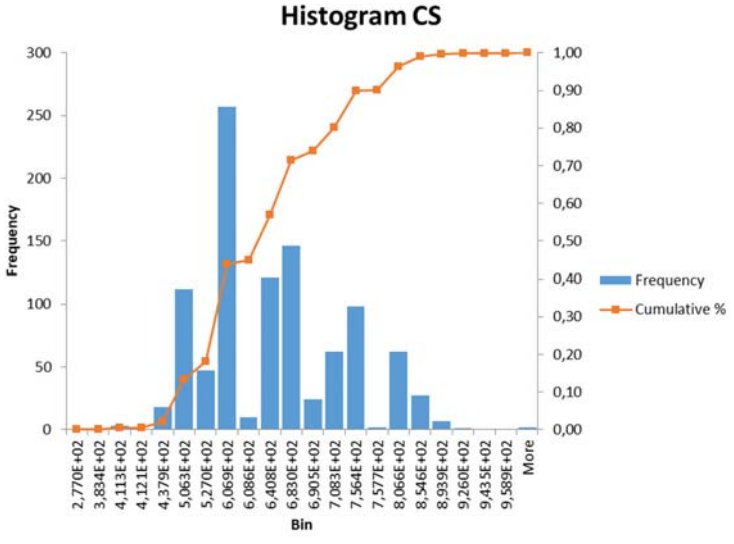

Figure 8. Histogram and CDF of CS parameter.

4. Prestressing Force Distribution Using Bayesian Approach

Measured released stresses $\{\Delta\sigma_{c,10}; \Delta\sigma_{c,20}; \text{and } \Delta\sigma_{c,30}\}$ in prestressed concrete sleepers were tested using the Q-Q-plot method as one of the principal testing methods, and approximated using normally distributed data that were randomly generated using the MC

simulations. Additionally, over 1000 simulations were performed. The results of Q-Q-plot testing can be seen in Figure 9. The data with the best agreement with the linear regression parameter R^2 = 0.96 were gained from the 30 mm deep saw-cuts, in which the highest stress relief was reached (approximately 72% of total assumed initial normal stress). This corresponds with the calibration factor $k_{30/120}$ = 1.39. On the other hand, a 10 mm deep saw-cut released only 12% of initial normal stress. For this depth, the calibration factor is $k_{10/120}$ = 8.40.

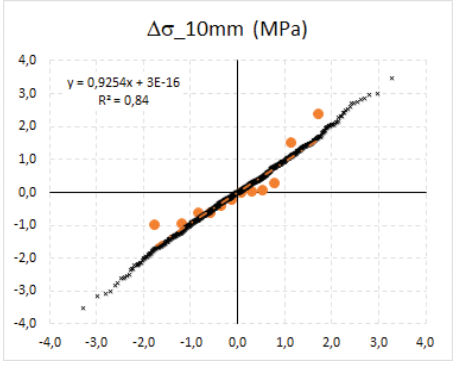

(**a**)

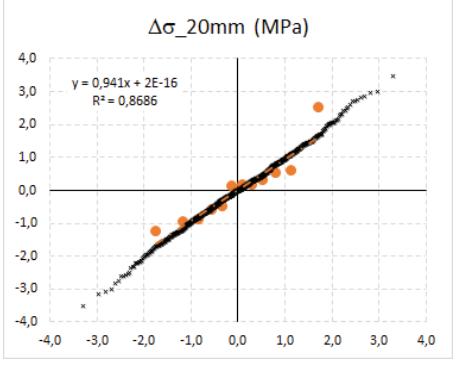

(**b**)

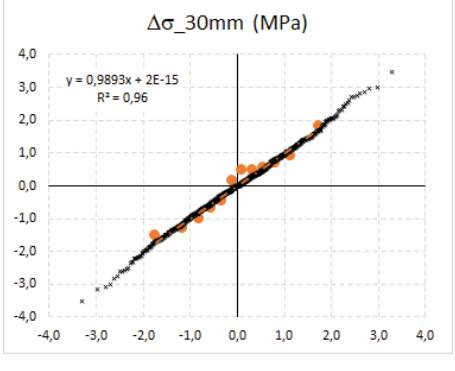

(**c**)

Figure 9. Q-Q-plot tests for released normal stress (MPa): (**a**) $\Delta\sigma_{c,10}$; (**b**) $\Delta\sigma_{c,20}$; and (**c**) $\Delta\sigma_{c,30}$.

The random vector of prestressing force {P (imm)} = {P (10 mm); P (20 mm); P (30 mm)} based on a measured data set of released normal stress is assumed according to Equation (9). In this paper, only worst fitted data (a saw-cut depth of 10 mm) and best-fitted data (a saw-cut depth of 30 mm) were chosen for graphical interpretation on histograms. PD and CD functions are illustrated in Figures 10 and 11. Consequently, some differences between the functions P (10 mm) and P (30 mm) are obvious from the basic statistical parameters of both of chosen data sets, as listed in Table 5.

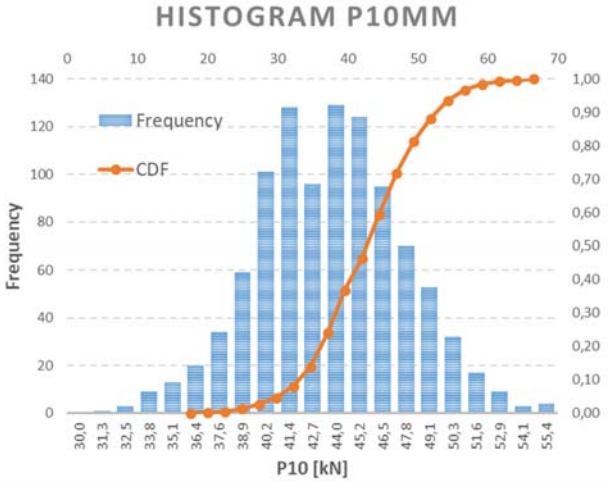

(**a**)

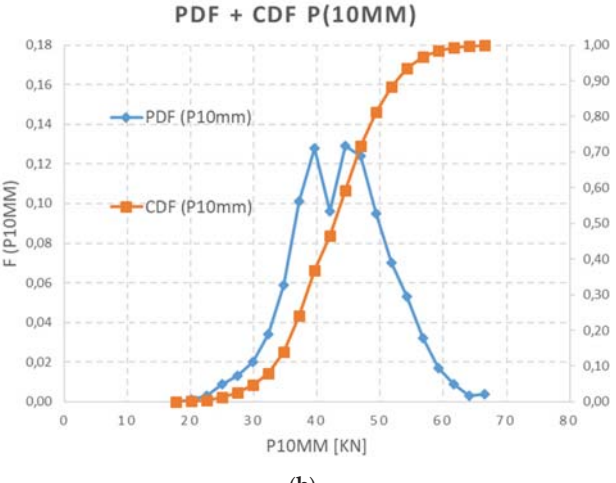

(**b**)

Figure 10. $\Delta\sigma_{c,10}$—(**a**) histogram of generated data and (**b**) PDF and CDF.

Table 5. Statistical parameters for P (imm).

Statistics	Mean m″ (kN)	Median (kN)	St. Dev. s″ (kN)	Kurtosis (-)	Skewness (-)	Min. (kN)	Max. (kN)	Conf (95) (kN)
P (10 mm)	43.20	43.21	7.80	0.0587	0.0871	19.11	73.61	0.4839
P (30 mm)	43.17	43.15	3.98	0.1932	0.1220	30.20	57.32	0.2448

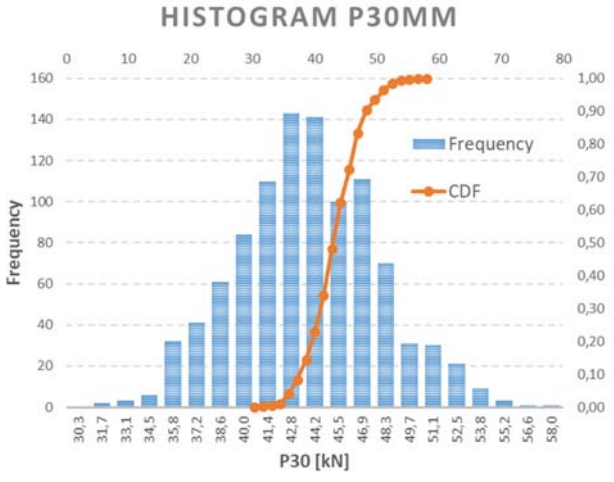

(**a**)

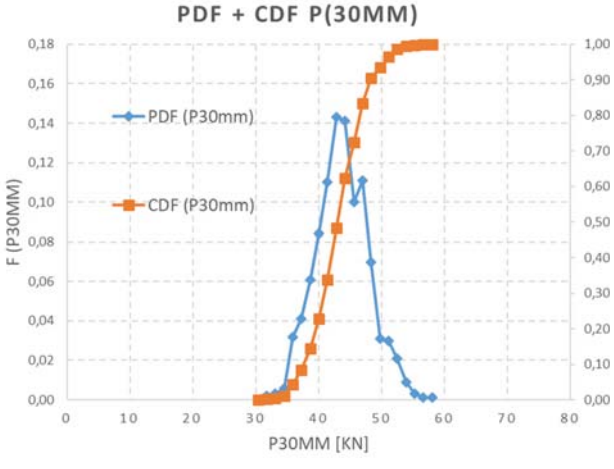

(**b**)

Figure 11. $\Delta\sigma_{c,30}$—(**a**) histogram of generated data and (**b**) PDF and CDF.

The primary predictive data set of calculated prestressing force $\{P_{calc}\}$ can be set as a joint prior distribution function f′ (μ, σ), according to Equation (4), or prior information. The random vector {P (imm)} derived from normal stress releasing, determined given the depth of a saw-cut, can be used in the Bayesian theorem as a likelihood or conditional information. This function is based on a measured data set which specifies and moves assumed calculation. The resulting $\{P_{post} = P\}$ as a final distribution prestressing force can also be signed as a posterior data distribution f″ (μ, σ). These data were derived from Equation (5) using MC simulation and can be graphically interpreted in PD and CD functions of $\{P_{post}\}$. The resulting shape and parameters of posterior probability distribution f″ (μ, σ) depends on the distribution function of the measured data sets, as in Figures 12 and 13. The final statistics of the {P} probability distribution function regarding the depth of a saw-cut are presented in Table 6.

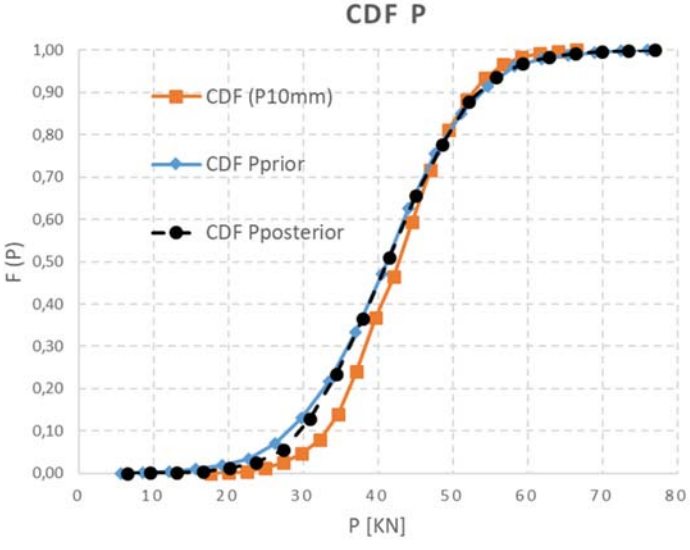

(**a**)

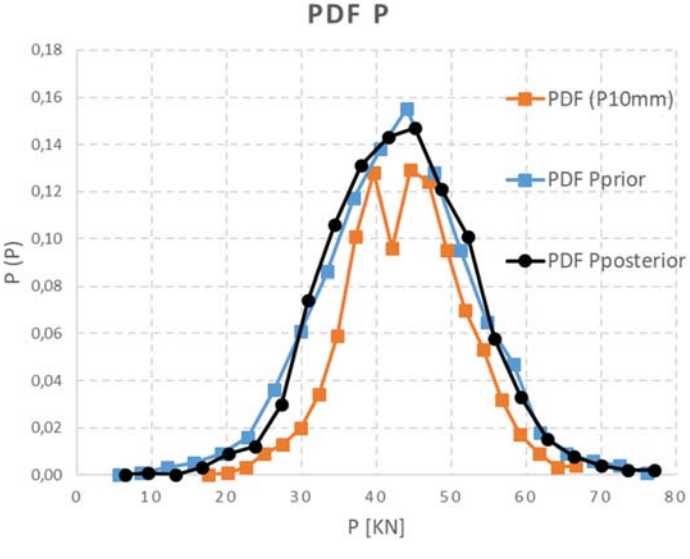

(**b**)

Figure 12. $\Delta\sigma_{c,10}$—(**a**) CDF of data set and (**b**) PDF of data set.

Table 6. Statistical parameters for P_{post}.

Statistics	Mean m″ (kN)	Median (kN)	St. Dev. S″ (kN)	Kurtosis (-)	Skewness (-)	Min. (kN)	Max. (kN)	Conf (95) (kN)
$P_{post\ (10\ mm)}$	41.22	41.38	9.54	0.3869	0.0286	11.39	77.84	0.5920
$P_{post\ (30\ mm)}$	41.34	41.38	7.65	1.6388	0.2352	14.69	79.43	0.4748

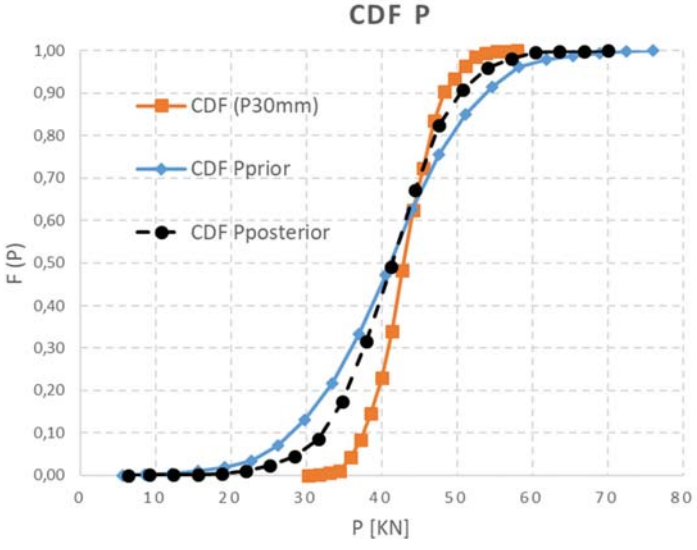

(**a**)

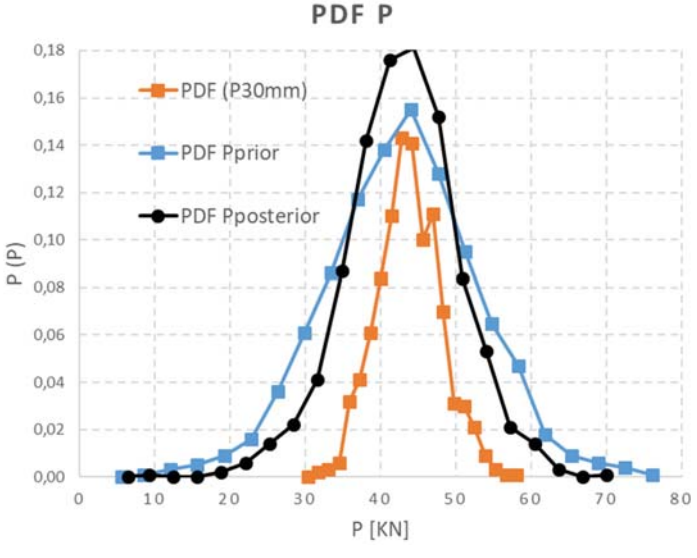

(**b**)

Figure 13. $\Delta\sigma_{c,30}$—(**a**) CDF of data set and (**b**) PDF of data set.

5. Discussion

Our investigation suggests that a relatively small intervention into the prestressed member can cause sufficient local normal stress relief. Intervention in the form of a maximum 30 mm deep saw-cut is insignificant compared to the dimensions of the cross-section of the prestressed member; the global structural integrity is not affected. Moreover, the saw-cut method can be performed without the application of an external load. Absence

of additional external load leads to easier residual prestressing force derivation from the obtained results.

Undoubtedly, prestressing force is the decisive factor in the assessment of existing prestressed concrete structures. However, it is very difficult to obtain its exact value at the time of testing. In addition to the standard analytical evaluation that should be used in all cases, some experimental methods have been verified and applied worldwide [17,18,20,21,26,27]. Nevertheless, these methods provide different results compared to the analytically calculated value. The reason for this is the wide range of factors that affect prestress losses, including the creep and shrinkage of concrete and steel relaxation. It is also possible that the corrosion effect or issues related to inadequate concrete or duct grout quality could influence the analysis.

Generally, Monte Carlo simulation is known as a technique that constructs probability distributions for the possible outcomes of decisions. In the presented study, the MCS was applied to the generation of random variable vectors which were normally distributed. The Bayesian concept can more precisely define the estimated residual value of prestressing force at a certain time $P_{m\,(t)}$. Usually, the evaluation can only take analytically derived prestress losses into account using the standard approach, as in Eurocode 2 [25], which is similar to the presented study. However, standard calculation of residual prestressing force value is not often sufficient or adequate to deal with such important parameters for global structure reliability evaluation.

6. Conclusions

In our paper, there is an obvious coincidence between the prior $\{P_{calc}\}$ and posterior $\{P_{post}\}$ probability distribution functions, with only a 95% confidence level. The reason for such close agreement of both probability functions is that the sleeper specimens were in a very good state after being stored for one year in a covered warehouse without any service or deterioration factors that could affect their structural condition. Moreover, they were kept in a relatively stable environment which inevitably affected the volumetric changes in the concrete. This is why prior and posterior functions are in such good agreement. The kurtosis of posterior functions was higher in both cases, especially for the best-fitted curve for P_{post} (30 mm), due to the strong consistency of the experimental results that form likelihood function. Naturally, if the shape, distribution and displacement of the predictive function of prestress losses on the x-axis were distant from the likelihood function, the posterior probability distribution function would be different.

Unquestionably, it is very important to present the results of methods for determining the state of prestressing in statistical form. This makes it possible to define the probability of the obtained state of prestressing, which is a crucial aspect of the evaluation of the load-carrying capacity of the existing prestressed concrete structure. The implementation of the probability approach to determine prestress losses can be an effective tool, since the evaluation process of existing prestressed concrete structures considers model uncertainties and any possible deteriorations.

Author Contributions: Conceptualization, M.M. and J.K.; data curation, M.M. and J.K.; validation, J.K. and M.M.; formal analysis, M.M.; measurements, M.M. and J.K.; writing—original draft preparation, J.K. and M.M.; writing—review and editing, J.K.; visualization, J.K. All authors have read and agreed to the published version of the manuscript.

Funding: This research project was supported by the Slovak Grant Agency (VEGA) under contracts No. 1/0048/22 and No. 1/0306/21 and by the Cultural and Educational Grant Agency (KEGA) under contract No. 020ŽU-4/2021.

Institutional Review Board Statement: Not applicable.

Informed Consent Statement: Not applicable.

Data Availability Statement: Not applicable.

Conflicts of Interest: The authors declare no conflict of interest.

Nomenclature

P (A), P (B)	Probability of event A and B.
P (A | B), P (B | A)	Conditional probability.
FORM	First order reliability method.
SORM	Second order reliability method.
JCSS	Joint Committee on Structural Safety.
P_m (t)	Prestressing force value in time "t" (kN).
CV	Coefficient of variation.
$\sigma_{p,in}$	Initial stress in prestressing steel (MPa).
M_G	Moment due to dead load (kNm).
$\sigma_{pm,max}$	Maximum stress in prestressing steel according to Eurocode 2 (MPa).
f_{pk}	Characteristic tensile strength of prestressing steel (MPa).
$f_{p,0.1k}$	Characteristic 0.1% proof-stress of prestressing steel (MPa).
$\Delta\sigma_{p,r}$	Prestress losses due to steel relaxation (MPa).
$\Delta\sigma_{p,r+s+c}$	Long-term prestress losses (MPa).
MCS	Monte Carlo simulation.
$\{P_{calc}\}$	Current random vector of prestressing force.
PDF	Probability density function.
CDF	Cumulative distribution function.
SC	Saw-cut.
SG	Strain gauge.
$P_{exp,i}$	Experimentally determined prestressing force value (kN).
k_i	Calibration factor of the depth of saw-cuts (-).
$\Delta\sigma_{c,i}$	Released normal stress after the application of saw-cuts (MPa).
CS	Cross-sectional function ($1/m^2$).
$e_{p,bott}$	Ideal eccentricity of bottom wires from the neutral axis (m).
$e_{p,upp}$	Ideal eccentricity of upper wires from the neutral axis (m).
z_{bott}	Position of the neutral axis of an ideal cross-section from the bottom edge (m).
z_{upp}	Position of the neutral axis of an ideal cross-section from the upper edge (m).

References

1. Kral'ovanec, J.; Moravčík, M. Numerical verification of the saw-cut method. *IOP Conf. Ser. Mater. Sci. Eng.* **2021**, *1015*, 012031. [CrossRef]
2. Abdel-Jaber, H.; Glisic, B. Monitoring of prestressing forces in prestressed concrete structures—An overview. *Struct. Control. Health Monit.* **2019**, *26*, e2374. [CrossRef]
3. Koteš, P.; Vavruš, M.; Jošt, J.; Prokop, J. Strengthening of Concrete Column by Using the Wrapper Layer of Fibre Reinforced Concrete. *Materials* **2020**, *13*, 5432. [CrossRef] [PubMed]
4. Bonopera, M.; Chang, K.-C.; Lee, Z.-K. State-of-the-Art Review on Determining Prestress Losses in Prestressed Concrete Girders. *Appl. Sci.* **2020**, *10*, 7257. [CrossRef]
5. Bujňáková, P. Anchorage System in Old Post-tensioned Precast Bridges. *Civil. Environ. Eng.* **2020**, *16*, 379–387. [CrossRef]
6. Kral'ovanec, J.; Moravčík, M.; Jošt, J. Analysis of Prestressing in Precast Prestressed Concrete Beams. *Civ. Environ. Eng.* **2021**, *17*, 184–191. [CrossRef]
7. Jančula, M.; Neslušan, M.; Pastorek, F.; Pitoňák, M.; Pata, V.; Minárik, P.; Gocál, J. Monitoring of Corrosion Extent in Steel S460MC by the Use of Magnetic Barkhausen Noise Emission. *J. Nondestruct. Eval.* **2021**, *40*, 69. [CrossRef]
8. Laco, J.; Borzovic, V. Experimental Investigation of Prestressing Strand Bond on Behavior of Concrete Members. *ACI Struct. J.* **2017**, *114*, 15–24. [CrossRef]
9. Paulík, P.; Bačuvčík, M.; Ševčík, P.; Janotka, I.; Gajdošová, K. Experimental Evaluation of Properties of 120 Years Old Concretes at Two Concrete Bridges in Slovakia. *Solid State Phenom.* **2016**, *249*, 227–234. [CrossRef]
10. Pastorek, F.; Decký, M.; Neslušan, M.; Pitoňák, M. Usage of Barkhausen Noise for Assessment of Corrosion Damage on Different Low Alloyed Steels. *Appl. Sci.* **2021**, *11*, 10646. [CrossRef]
11. Bahleda, F.; Drevený, I.; Pitoňák, M.; Neslušan, M.; Koteš, P. Employment of Barkhausen Noise Technique for Assessment of Prestressing Bars Damage with Respect of Their Over-Stressing. *Metals* **2021**, *11*, 770. [CrossRef]
12. Koteš, P.; Vičan, J. Influence of Fatigue Crack Formation and Propagation on Reliability of Steel Members. *Appl. Sci.* **2021**, *11*, 11562. [CrossRef]
13. Moravčík, M.; Bujňáková, P.; Bahleda, F. Failure and damage of a first-generation precast prestressed bridge in Slovakia. *Struct. Concrete.* **2020**, *21*, 2353–2362. [CrossRef]
14. Sýkora, M.; Holický, M.; Jung, K. Updating in the probabilistic assessment of existing structures. *Trans. VŠB—Tech. Univ. Ostrav. Civil. Eng. Ser.* **2012**, *12*, 205–215. [CrossRef]

15. Gilbertson, C.; Ahlborn, T. Probabilistic Comparison of Prestress Loss Methods in Prestressed Concrete Beams. *PCI J.* **2004**, *49*, 52–69. [CrossRef]
16. Botte, W.; Vereecken, E.; Taerwe, L.; Caspeele, R. Assessment of posttensioned concrete beams from the 1940s: Large-scale load testing, numerical analysis and Bayesian assessment of prestressing losses. *Struct. Concr.* **2021**, *22*, 1500–1522. [CrossRef]
17. Bagge, N.; Nilimaa, J.; Elfgren, L. In-situ Methods to Determine Residual Prestress Forces in Concrete Bridges. *Eng. Struct.* **2017**, *135*, 41–52. [CrossRef]
18. Bagge, N.; Nilimaa, J.; Blanksvärd, T.; Elfgren, L. Instrumentation and Full-Scale Test of a Post-Tensioned Concrete Bridge. *Nordic. Concr. Res.* **2014**, *51*, 63–83.
19. Kral'ovanec, J.; Prokop, J. Indirect Methods for Determining the State of Prestressing. *Transp. Res. Procedia* **2021**, *55*, 1236–1243. [CrossRef]
20. Kral'ovanec, J.; Bahleda, F.; Prokop, J.; Moravčík, M.; Neslušan, M. Verification of Actual Prestressing in Existing Pre-Tensioned Members. *Appl. Sci.* **2021**, *11*, 5971. [CrossRef]
21. Kral'ovanec, J.; Moravčík, M.; Bujňáková, P.; Jošt, J. Indirect Determination of Residual Prestressing Force in Post-Tensioned Concrete Beam. *Materials* **2021**, *14*, 1338. [CrossRef] [PubMed]
22. JCSS: Probabilistic Model Code. Available online: https://www.jcss-lc.org/jcss-probabilistic-model-code (accessed on 20 November 2021).
23. Kral'ovanec, J.; Moravčík, M.; Koteš, P.; Matejov, A. Parametric Study of Saw-Cut Method. XXX Russian-Polish-Slovak Seminar Theoretical Foundation of Civil Engineering (RSP 2021). In *Lecture Notes in Civil Engineering*; Springer: Cham, Switzerland, 2021; Volume 189, pp. 10–19. [CrossRef]
24. *STN EN 206+A1:2017-05*; Concrete. Specification, Performance, Production and Conformity. Slovak Technical Standard; Slovak Office of Standards, Metrology and Testing: Bratislava, Slovakia, 2017.
25. *STN EN 1992-1-1+A1*; Eurocode 2: Design of Concrete Structures—Part 1–1: General Rules and Rules for Buildings. Slovak Technical Standard; Slovak Office of Standards, Metrology and Testing: Bratislava, Slovakia, 2015.
26. Koteš, P.; Strieška, M.; Bahleda, F.; Bujňáková, P. Prediction of RC Bridge Member Resistance Decreasing in Time under Various Conditions in Slovakia. *Materials* **2020**, *13*, 1125. [CrossRef] [PubMed]
27. Prokop, J.; Odrobiňák, J.; Farbák, M.; Novotný, V. Load-Carrying Capacity of Bailey Bridge in Civil Applications. *Appl. Sci.* **2022**, *12*, 3788. [CrossRef]

materials

MDPI

Article

The Effects of Bond–Slip Laws on the Debonding Failure and Behavior of Flexural Strengthened RC Slabs in Hybrid FRP Retrofit Systems

Huy Q. Nguyen [1], Tri N. M. Nguyen [2], Do Hyung Lee [3] and Jung J. Kim [1,*]

[1] Department of Civil Engineering, Kyungnam University, Changwon-si 51767, Korea
[2] Campus in Ho Chi Minh City, University of Transport and Communications, No. 450-451 Le Van Viet Street, Tang Nhon Phu A Ward, Thu Duc City, Ho Chi Minh City 700000, Vietnam
[3] Department of Civil, Railroad and Unmanned Systems Engineering, PaiChai University, 155-40 Baejaero, Seo-gu, Daejeon 35345, Korea
* Correspondence: jungkim@kyungnam.ac.kr; Tel.: +82-552-496-421; Fax: +82-505-999-2165

Abstract: The hybrid retrofit system using FRP and concrete overlay applied on the top of slabs has proven effective in strengthening and overcoming logistical constraints, compared with conventional strengthening techniques using externally bonded composite materials to the underside of the slabs. Nevertheless, the performance of retrofitted slabs is governed by debonding failure due to the low bond strength between CFRP and concrete overlay. Thus, this study investigates the behavior of flexural strengthened slabs with FRP retrofit systems and the effect of bond–slip laws on debonding failure. Firstly, two full-scale RC slabs with and without a retrofit system were tested in a four-point bending setup as the control specimens. Then, the same retrofitted slab was simulated by utilizing the commercial program ABAQUS. A sensitivity analysis was conducted to consider the influence of bond–slip laws to predict the failure mechanism of the retrofitted slabs based on load–deflection relationships. The results showed that the strengthened slab enhanced the load-carrying capacity by 59%, stiffness by 111%, and toughness by 29%. The initial stiffness of $0.1K_0$ and maximum shear stress of $0.13\tau_{max}$, compared with the corresponding values of Neubauer's and Rostasy's bond–slip law, can be used to simulate the global response of the retrofitted slab validated by experiment results.

Keywords: CFRP; bond–slip law; debonding; RC slab; retrofit; strengthen

Citation: Nguyen, H.Q.; Nguyen, T.N.M.; Lee, D.H.; Kim, J.J. The Effects of Bond–Slip Laws on the Debonding Failure and Behavior of Flexural Strengthened RC Slabs in Hybrid FRP Retrofit Systems. *Materials* **2022**, *15*, 7453. https://doi.org/10.3390/ma15217453

Academic Editor: Krzysztof Schabowicz

Received: 14 September 2022
Accepted: 20 October 2022
Published: 24 October 2022

1. Introduction

Strengthening structures with external bonded materials has become one of the popular choices for rehabilitation and upgrading existing reinforced concrete (RC) structures [1,2]. Researchers and engineers are particularly interested in restoring and strengthening partially damaged RC structures to minimize the impact on environmental deterioration and cost savings [3–5]. Fiber-reinforced polymer (FRP) materials have been widely used in the field of external reinforcement in recent decades because of their lightweight, high tensile strength, and non-corrosion resistance [6–12]. New strengthened techniques and design guidelines have emerged for RC structures using FRP composite materials [13–16].

The conventional application in strengthening RC slab techniques focuses on attaching FRP to their tensile zone to maximize the tensile strength of these composite materials, which have been widely gaining acceptance in practice [17–19]. However, the premature delamination of FRP remains the main disadvantage of the strengthening techniques, as it prevents strengthened slabs from reaching their ultimate load-carrying capacity. In general, sectional and debonding failures are two widespread possible failure modes of FRP-strengthened slabs [20–22]. In sectional failure, either the failure of compressive concrete or the rupture of FRP can be predicted through strain compatibility at its limiting strain [23]. In debonding failure, it is more difficult to determine due to the complicated

failure mechanism and the factors contributing to problems such as concrete cracks and stress concentration at the FRP–concrete interface. Due to this, the behavior of externally bonded FRP in contact with a concrete surface has attracted considerable interest from the civil engineering community [24–26]. In addition, obtaining a well-prepared concrete surface for strengthening FRP on the underside of the RC slab can be a more difficult challenge, or it may not be possible due to logistical constraints.

Consequently, a hybrid retrofit system consists of carbon fiber reinforced polymer (CFRP) and concrete overlay applied on the top surface of the RC slab to overcome the shortcomings of traditionally strengthened solutions rather than exploit the high tensile strength of CFRP, as shown in Figure 1. Previous studies have demonstrated the effectiveness of the retrofit system by increasing the flexural strength and ductility of existing RC slabs. Nevertheless, the results also revealed that debonding failure between the concrete overlay and CFRP was one of the major causes of slabs losing their ultimate load-carrying capacity. Transferring interfacial stress from the slab to FRP or vice versa via a specialized adhesive layer is more efficient than from FRP to overlay members due to the characteristics of the retrofit system, leading to the premature debonding failure of the FRP/overlay interface [27–29]. A sound understanding of the behavior of FRP–concrete interface needs to be developed, with a particular interest in FRP/overlay interface for safe in practical design work.

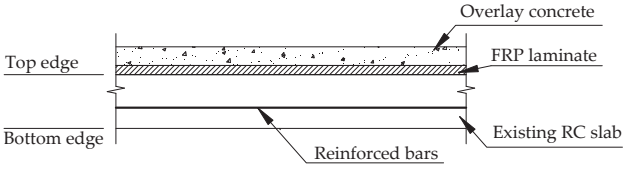

Figure 1. Hybrid FRP retrofit system for positive moment parts of strengthened RC slabs.

In response to this need, the effect of bond–slip laws on the debonding failure of flexural strengthened RC slabs with a hybrid FRP retrofit system is investigated. To the best of our knowledge, previous studies were limited in evaluating the behavior of the externally bonded FRP on a concrete surface without considering cases of CFRP located between two concrete layers of the strengthened slab with a retrofit system [30–37]. There was still considerable uncertainty and difficulty in determining the behavior of CFRP-to-concrete joints due to their intrinsic bond. Insight into an understanding of the bond–slip law between concrete and CFRP using a cohesive approach is a suitable solution for predicting strengthened structural responses [36,38]. Shear stress at the FRP–concrete interface of cohesive elements, in terms of magnitude and distribution, could be a believable explanation for debonding failure [39,40]. It can be difficult to precisely predict the variations in stresses in concrete structures, whereas the load–deflection curve is far less sensitive to crack locations and sizes. The finite element method (FEM) can reasonably predict the interfacial stresses and the delamination load corresponding to deflection more economically than laboratory tests [41]. A finite element (FE) model of the FRP flexural-strengthened slab can provide a comprehensive understanding of the various bond–slip parameters associated with the CFRP/concrete interface and be applicable in developing robust predictive equations for practice designs [42]. By combining FEM through ABAQUS software and the experimental program, the iterative adjustment of the bond–slip parameters can be easily carried out to simulate the experimental load–displacement curve and failure modes, resulting in reduced experiment time and cost [43].

In this study, the behavior of a strengthened RC slab with a hybrid FRP retrofit system is described with particular attention to debonding failure. The effectiveness of the hybrid retrofit system in improving the flexural carrying capacity, stiffness, and toughness is investigated and compared with the full-scale experimental results. A three-dimensional FE model is developed with various bond–slip models for evaluating their accuracy by

comparing numerical predictions with experimental measurements. Numerical models are also analyzed for sensitivity to the bond–slip parameters to assess their effects on the debonding failure. Following the validation of the model, the various parameters that strongly influence the behavior of retrofitted slabs are identified and discussed.

2. FRP Hybrid Retrofit System

2.1. Retrofitting Mechanism

In some cases, strengthening the underside of the reinforced concrete slabs may not be possible due to logistical constraints and hindrances by other utilities. A hybrid retrofit system combining the tensile strength of FRP and compressive strength of the concrete overlay was applied on top of the existing RC slabs to improve their strength and ductility, as shown in Figure 1. The overlay thickness of the retrofit system has a critical role in pulling the neutral axis toward the overlay zone, and FRP holds tension at failure. For this case, the retrofitting mechanism for the hybrid FRP system was estimated as recommended by ACI 440.2R [44], as shown in Figure 2. Assume that the ultimate concrete strain (ε_{cu}) is 0.003, and steel yields at yield stress of f_y. Without considering the tension force of concrete, the force equilibrium is calculated as follows:

$$C_H = T_s + T_F \quad (1)$$

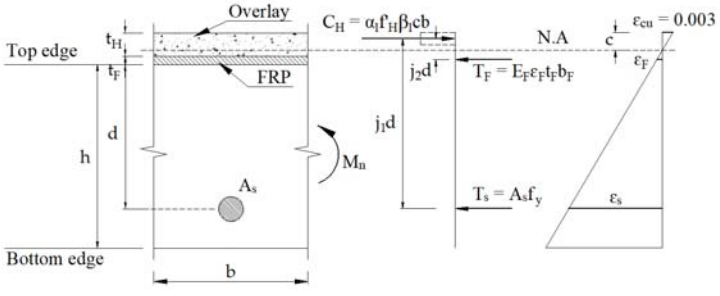

Figure 2. Calculating mechanism for slab's positive moment sections with a proposed system.

These internal forces are computed as follows:

$$C_H = \alpha_1 f'_H \beta_1 cb,\ T_s = A_s f_y,\ T_F = E_F \varepsilon_F t_F b_F \quad (2)$$

An evaluation of strain compatibility conditions can determine FRP strain at strength limit (ε_F) as follows:

$$\varepsilon_F = \left[\frac{(t_H + t_F/2) - c}{c}\right]\varepsilon_{cu} \quad (3)$$

The moment capacity equilibrium condition can be defined as follows:

$$M_n = T_s(j_1 d) + T_F(j_2 d) \quad (4)$$

2.2. Experimental Program

The reference slab had a 2440 mm total length, 2290 mm clear span, and 130 × 900 mm^2 cross-section. The tensile reinforcement was spaced at 185 mm spacing with five No.13 bars (ϕ12.7 mm) at the bottom of the RC slab. Transverse steel consisted of six No.10 bars (ϕ9.5 mm) spaced at 305 mm center on the center, as shown in Figure 3. The yield stress of the reinforcement used for the RC slab was 400 MPa. The concrete employed for the RC slab had a compressive strength of 27 MPa after 28 days. Table 1 provides the mechanical properties and dimensions of the reference slab.

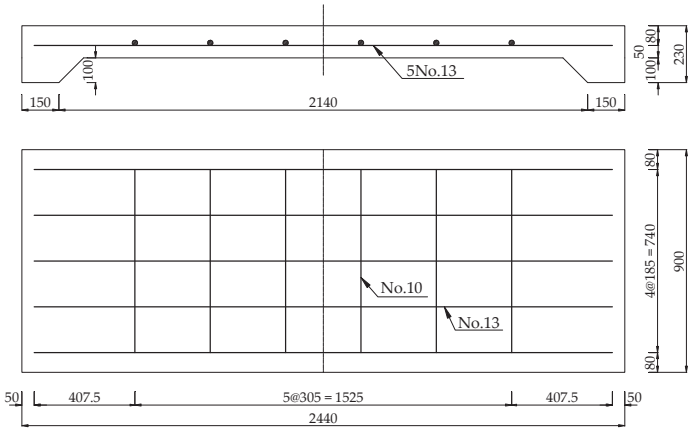

Figure 3. Reference slab reinforcement details.

Table 1. Mechanical properties and dimensions of reference slab.

h (mm)	b (mm)	A_s (mm^2)	d (mm)	f'_c (MPa)	γ_c (kg/m^3)	f_y (MPa)	E_s (GPa)
130	900	632.5	80	27	2400	400	200

A hybrid retrofit system was constructed utilizing a combination of CFRP wet layup laminate with a concrete overlay, as shown in Figure 1. The compressive strength of the concrete overlay was 50 MPa at 28-day age. CFRP had a strength of 600 MPa and an elastic modulus of 40 GPa. The mechanical properties and dimensions used in the FRP retrofit system are given in Table 2.

Table 2. Mechanical properties and dimensions for retrofit system.

Overlay		CFRP				Epoxy Resin		
t_H (mm)	f'_H (MPa)	t_F (mm)	f_{tF} (MPa)	γ_F (kg/m^3)	E_F (GPa)	t_a (mm)	E_a (MPa)	G_a (MPa)
30	50	0.5	600	1200	40	1.5	3000	2100

Two full-scale RC slabs with and without a hybrid retrofit system were tested in a four-point bending setup with two concentrated loads, as shown in Figure 4. Before measuring the deflection data, the LVDTs were reset to remove self-weight deflection. The load cell capacity applied in the tests was 5000 kN. The applied load and deflection at the mid-span section data were recorded during the experimental procedure.

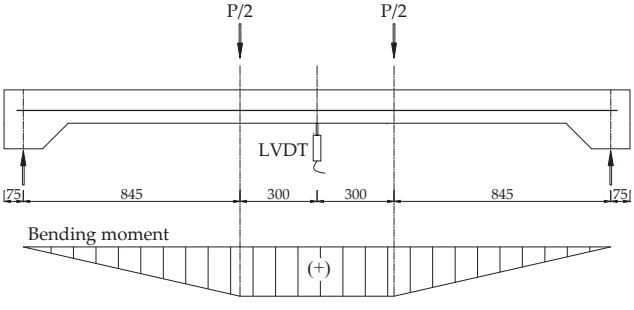

Figure 4. Four-point bending setup for slab and the corresponding moment of the applied load.

2.3. Theoretical Analysis

The experimental data were checked with the predicted analytical moment capacity and deflection at the mid-span due to the applied load of the reference and strengthened RC slabs, as recommended by ACI 440.2R [44] and ACI 318M [45]. Based on the structure, a self-weighted equivalent distributed load is computed as follows:

$$w = \gamma_c b(h + t_H) + \gamma_F b_F t_F \quad (5)$$

The distributed load due to the self-weight of the reference slab and strengthened slab is determined as follows: W_c = 2.81 N/mm and W_s = 3.46 N/mm.

The prediction of the load-carrying capacity corresponding to deflection at mid-span due to the applied load for the reference RC slab is given in Table 3.

Table 3. Analysis of the reference RC slab.

Calculation	Reference Slab
Compressive concrete block depth $a = \frac{A_s f_y}{\alpha_1 f'_c b}$	$a = \frac{632.5(400)}{0.85(27)(900)} = 12.25$ mm
Moment capacity $M_{n,P} = \left(d - \frac{a}{2}\right)A_s f_y$	$M_{n,P} = \left(80 - \frac{12.25}{2}\right)(632.5)(400) = 18.69 \times 10^6$ Nmm = 18.69 kNm
Moment due to self-weight $M_c = w_c l^2/8$	$M_c = 2.81(2290)^2/8 = 1.84 \times 10^6$ Nmm
Mid-span section's remaining capacity for carrying additional load $P_{u,theo.} = \frac{2(M_{n,P} - M_c)}{x}$	$P_{u,theo.} = \frac{2(18.69-1.84)}{845/1000} = 39.9$ kN
Deflection at yield point steel due to the applied load $\Delta_{u,theo.} = \frac{(3l^2-4x^2)}{24}\frac{(M_{n,P}-M_c)}{E_c I_e}$ $I_e = \frac{I_{cr}}{1-\left(\frac{(2/3)M_{cr}}{M_{n,P}}\right)^2\left(1-\frac{I_{cr}}{I_g}\right)}$ $M_{cr} = f_r I_g / y_t$	$\Delta_{u,theo.} = \frac{3(2290^2)-4(845^2)}{24}\frac{(18.69\times10^6-1.84\times10^6)}{24{,}422(22\times10^6)} = 16.8$ mm $I_e = \frac{20.4\times10^6}{1-\left(\frac{(2/3)(8.17\times10^6)}{18.69\times10^6}\right)^2\left(1-\frac{20.4\times10^6}{164.8\times10^6}\right)} = 22 \times 10^6$ mm^4 $M_{cr} = 3.22(164.8 \times 10^6)/65 = 8.17 \times 10^6$ Nmm = 8.17 kNm

The RC slab and CFRP laminate were assumed to be in perfect bond until the load-carrying capacity was reached. The prediction of the load-carrying capacity corresponding to deflection at mid-span for the CFRP-retrofitted slab due to the applied load is shown in Table 4.

Table 4. Analysis of the retrofitted RC slab.

Calculation	Retrofitted Slab
Compressive concrete block depth $J_1 = \alpha_1 f'_H b$ $J_2 = t_F b_F E_F \varepsilon_c - A_s f_y$ $J_3 = -\beta_1 t_F b_F E_F \varepsilon_c (t_H + t_F/2)$ $a = \frac{-J_2+\sqrt{J_2^2-4J_1J_3}}{2J_1}$	J_1 = 38,250 N/mm $J_2 = -199{,}000$ N $J_3 = -1{,}131{,}782$ Nmm a = 8.63 mm
Moment capacity $M_{n,P} = \left(d + t_H + t_F - \frac{a}{2}\right)A_s f_y$ $+\left(t_H + \frac{t_F - a}{2}\right)t_F b_F E_F \varepsilon_c \left(\frac{\beta_1(t_H+t_F/2)}{a} - 1\right)$	$M_{n,P} = 28.87 \times 10^6$ Nmm = 28.87 kNm
Moment due to self-weight $M_s = w_s l^2/8$	$M_s = 2.27 \times 10^6$ Nmm = 2.27 kNm
Mid-span section's remaining capacity for carrying additional load $P_{u,theo.} = \frac{2(M_{n,P} - M_s)}{x}$	$P_{u,theo.}$ = 63 kN
Deflection at yield point steel due to the applied load $\Delta_{u,theo.} = \frac{(3l^2-4x^2)}{24}\frac{(M_{n,P}-M_s)}{E_c I_e}$	$\Delta_{u,theo.}$ = 12.3 mm $I_e = 35 \times 10^6$ mm^4 M_{cr} = 12.5 kNm

3. Finite Element Modeling

3.1. Finite Element Mesh

The simulations were conducted using one-quarter of the control and strengthened slab specimens, based on specimen symmetry. The symmetric pane was simulated for the *x*- and *z*-axis by restricting translation in directions 1 and 3. The concrete slab and concrete overlay with reduced integration were constructed with eight-node solid elements (C3D8R). Two-node linear truss elements (T3D2) and four-node shell elements (S4R) were used to model the reinforcements and CFRP laminate, respectively. A mesh size of 20 mm was suggested based on preliminary mesh refinement studies, ranging from 10 mm to 25 mm, for balancing accuracy and computational cost. The embedded function in ABAQUS/CAE 2022 was implemented to simulate concrete–steel bonding. The models were studied using static analysis in ABAQUS/standard. The models under monotonic displacement loads surveyed the behavior of a slab subjected to a four-point bending test. The steel bar was discretized as a rigid part to prevent manufactured stress concentrations under the loading points, as shown in Figure 5.

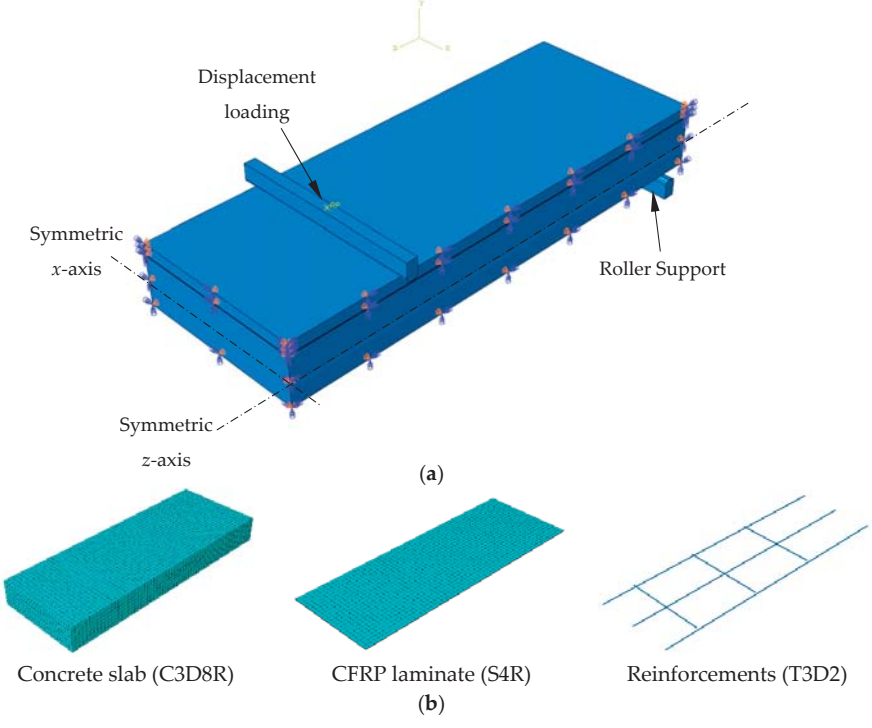

Figure 5. CFRP retrofitted slab (**a**) modeling and boundary conditions; (**b**) element types of the FEM model.

3.2. Concrete

A model of concrete plastic damage was used with a failure mechanism of compressive crushing and tensile cracking. The stress–strain curve for concrete under uniaxial compression and tension was calculated by using the CEB–FIP model [46]. Compressive strength was used to estimate the tensile strength (f_{ct}) and elastic modulus (E_c) of concrete, as recommended by ACI 318M [45].

$$f_{ct} = 0.62\sqrt{f'_c} \quad (6)$$

$$E_c = 4700\sqrt{f'_c} \tag{7}$$

Fracture energy (G_{cr}) is an inelastic parameter associated with the softening part of the curve. In mode I, fracture energy is defined as the area under the softening curve.

$$G_{cr} = G_{f0}\left(\frac{f'_c}{10}\right)^{0.7} \tag{8}$$

Figure 6 illustrates the concrete softening curve under uniaxial tension. A linear relationship between the tension damage and crack opening (δ) is assumed to identify tensile damage. The tension damage variable ranges from zero (undamaged material) to one (total loss of strength).

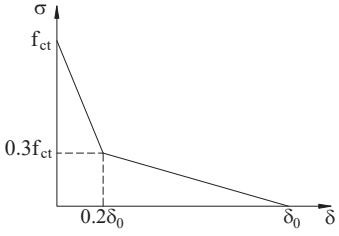

Figure 6. Concrete softening curve under uniaxial tension.

Under uniaxial compression, a linear response is observed until reaching the initial value (σ_{c0}). In the plastic regime, the response is generally characterized by stress hardening, followed by strain softening beyond the ultimate compressive stress [47].

$$\sigma_c = \frac{E_c\varepsilon_c}{1 + (R + R_E - 2)(\varepsilon_c/\varepsilon_0) - (2R - 1)(\varepsilon_c/\varepsilon_0)^2 + R(\varepsilon_c/\varepsilon_0)^3} \tag{9}$$

where $R = \left[R_E(R_\sigma - 1)/(R_\varepsilon - 1)^2\right] - 1/R_\varepsilon$; $R_E = E_c/E_0$; $E_0 = f'_c/\varepsilon_0$; $\varepsilon_0 = 0.0025$; $R_E = R_\sigma = 4$ [48].

3.3. Reinforced Steel

It is assumed that the reinforcement transmits force axially, and the most common perfectly linear–elastic model for reinforcement was used. Steel's Poisson's ratio is 0.3, and the other mechanical properties are listed in Table 2.

3.4. CFRP

For strengthening, CFRP laminate is supposed to be linear and exert isotropic behavior. CFRP failure criteria were not considered for this study because tensile stress in CFRP is too low, compared with its ultimate strength, and therefore CFRP laminate hardly ruptures for these types of structures. The material properties of CFRP, including its thickness, elastic modulus, and ultimate strength, as shown in Table 2, are provided by manufacturers.

3.5. FRP-to-Concrete Interface Model

The FRP-to-concrete interface was modeled using cohesive zones. In this study, a bilinear traction–separation model was employed to depict the bonding characteristics of linear adhesive at the interface, as shown in Figure 7 [49].

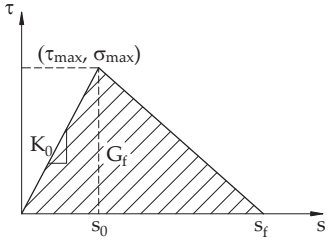

Figure 7. Bilinear traction–separation response.

The initiation and evolution of damage in the available traction–separation model were initially assumed to be a linear–elastic behavior [50,51], which can be written in a matrix form as follows:

$$\begin{Bmatrix} \tau_n \\ \tau_s \\ \tau_t \end{Bmatrix} = \begin{bmatrix} K_{nn} & 0 & 0 \\ 0 & K_{ss} & 0 \\ 0 & 0 & K_{tt} \end{bmatrix} \begin{Bmatrix} \sigma_n \\ \sigma_s \\ \sigma_t \end{Bmatrix} \tag{10}$$

For specifying the damage initiation, quadratic nominal stress and maximum nominal stress between the CFRP and concrete interface were employed. The damage criterion for quadratic stress may be depicted as follows:

$$\left(\frac{\langle \tau_n \rangle}{\sigma_{max}}\right)^2 + \left(\frac{\tau_s}{\tau_{max}}\right)^2 + \left(\frac{\tau_t}{\tau_{max}}\right)^2 = 1 \tag{11}$$

The damage criterion for maximum stress can be described as follows:

$$\max\left(\frac{\langle \tau_n \rangle}{\sigma_{max}}, \frac{\tau_s}{\tau_{max}}, \frac{\tau_t}{\tau_{max}}\right) = 1 \tag{12}$$

For specifying the damage evolution, the influence of power law and the Benzeggagh–Kenane (BK) fracture criteria on the structure behavior was further evaluated [52]. The power law criterion may be given by:

$$\left(\frac{G_n}{G_n^f}\right)^\eta + \left(\frac{G_s}{G_s^f}\right)^\eta + \left(\frac{G_t}{G_t^f}\right)^\eta = 1 \tag{13}$$

The BK fracture criterion may be defined as follows:

$$G_n^f + (G_s^f - G_n^f)\left(\frac{G_s + G_t}{G_n + G_s}\right)^\eta = G_f \tag{14}$$

In this study, the quantities G_n^f, G_s^f, and G_t^f were assumed to be equal. For FE modeling, first, a perfect FRP-to-concrete bond was assumed to reflect the response of the flexural strengthened RC slab using the ABAQUS program. Then, the interaction behavior of the FRP-to-concrete bond in the strengthened slab applied to the retrofit system was evaluated using the existing constitutive models, as shown in Table 5 [31–36].

Table 5. Existing bond–slip models.

Bond–Slip Model	
Neubauer and Rostasy [31]	$\tau = \begin{cases} \tau_{max}\left(\frac{s}{s_0}\right) & \text{if } s \le s_0 \\ 0 & \text{if } s > s_0 \end{cases}$, $\tau_{max} = 1.8\beta_w f_{ct}$, $s_0 = 0.202$, $\beta_w = \sqrt{1.125\frac{2-b_f/b}{1+b_f/400}}$
Nakaba et al. [32]	$\tau = \tau_{max}\frac{s}{s_0}\frac{3}{2+(s/s_0)^3}$, $\tau_{max} = 3.5f_c^{0.19}$, $s_0 = 0.065$
Monti et al. [33]	$\tau = \begin{cases} \tau_{max}\left(\frac{s}{s_0}\right) & \text{if } s \le s_0 \\ \tau_{max}\left(\frac{s_f-s}{s_f-s_0}\right) & \text{if } s > s_0 \end{cases}$, $\tau_{max} = 1.8\beta_w f_{ct}$, $s_0 = 2.5\tau_{max}\left(\frac{t_a}{E_a} + \frac{50}{E_c}\right)$, $s_f = 0.33\beta_w$, $\beta_w = \sqrt{1.125\frac{2-b_f/b}{1+b_f/400}}$
Dai and Ueda [34]	$\tau = \begin{cases} \tau_{max}\left(\frac{s}{s_0}\right)^{0.575} & \text{if } s \le s_0 \\ \tau_{max}e^{-\beta(s-s_0)} & \text{if } s > s_0 \end{cases}$, $\tau_{max} = \frac{-1.575\alpha K_a + \sqrt{2.481\alpha^2K_a^2 + 6.3\alpha\beta_w{}^2K_aG_f}}{2\beta}$, $s_0 = \frac{\tau_{max}}{\alpha K_a}$, $G_f = 7.554K_a^{-0.449}\left(f_c'\right)^{0.343}$, $\beta_w = 0.0035K_a\left(E_ft_f/1000\right)^{0.34}$, $K_a = G_a/t_a$, $\alpha = 0.028\left(E_ft_f/1000\right)^{0.254}$
Lu et al. [35]	$\tau = \begin{cases} \tau_{max}\sqrt{\frac{s}{s_0}} & \text{if } s \le s_0 \\ \tau_{max}e^{-\alpha\left(\frac{s}{s_0}-1\right)} & \text{if } s > s_0 \end{cases}$, $\alpha = \left(\frac{G_f}{\tau_{max}s_0} - \frac{2}{3}\right)^{-1}$, $\tau_{max} = 1.5\beta_w f_{ct}$, $G_f = 0.308\beta_w^2\sqrt{f_{ct}}$, $\beta_w = \sqrt{\frac{2.25-b_f/b}{1.25+b_f/b}}$
Obaidat et al. [36]	$K_0 = 0.16\frac{G_a}{t_a}$, $\tau_{max} = 1.46G_a^{0.165}f_{ct}^{1.033}$, $G_f = 0.52f_{ct}^{0.26}G_a^{-0.23}$

It is easily conceptualized that the traction–separation law, as described in Figure 7, is primarily governed by three parameters, namely initial stiffness (K_0), maximum shear stress (τ_{max}), and fracture energy (G_f) [53]. Based on the mechanical properties of the experimental materials, the bond–slip models evaluated in this study were introduced with the three characteristic parameters of the traction–separation law, as shown in Table 6.

Table 6. Calculation of characteristic parameters of the traction–separation law.

Constitutive Models	K_0 (MPa/mm)	τ_{max} (MPa)	G_f (N/mm)
Neubauer and Rostasy [31]	28.69	3.41	0.20
Nakaba et al. [32]	100.73	6.55	0.94
Monti et al. [33]	157.03	2.24	0.14
Dai and Ueda [34]	83.90	7.10	0.90
Lu et al. [35]	76.92	3.60	0.31
Obaidat et al. [36]	224.47	17.26	0.12

3.6. Analysis Procedure and Flowchart

A three-dimensional FE model using ABAQUS/CAE 2022 software was performed to simulate the behavior of retrofitted slabs. In the initial phase, an accurate FE model of the reference slab was assessed by comparison with the experimental results. In the second phase, a retrofitted slab model was developed based on the reference slab model, with the addition of FRP laminate and concrete overlay. The well-known bond–slip models were used to simulate the FRP-to-concrete interface to accurately simulate the behavior of the retrofitted slab validated by experiment results. If the available bond–slip models were not appropriate, the bond–slip parameters were revised to show good agreement with the experimental data. A flowchart of the analysis procedure for the FE model is shown in Figure 8.

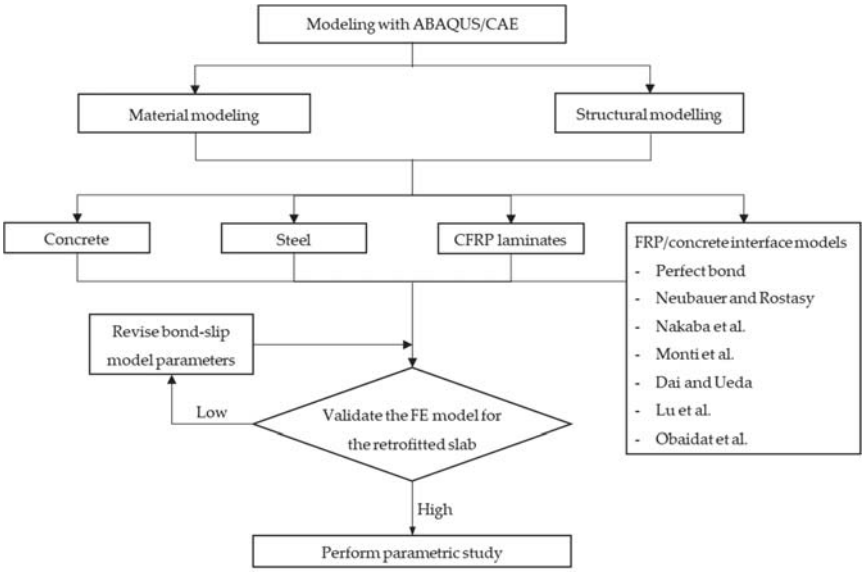

Figure 8. FE model analysis flowchart.

4. Results and Discussion

4.1. Experimental Analysis

The experimental data from the reference slab showed a good agreement with those of the theoretical analysis. The RC slab behaved linearly and elastically until the first crack appeared at 17 kN of the applied load. The observed result revealed a higher load-carrying capacity of 43.5 kN than the theoretical prediction of 39.9 kN. The ultimate loading (50.8 kN) was 27.3% greater than the predicted load. The linearly elastic–perfectly plastic behavior of the steel can be the reason for the lower strength of the prediction because strain-hardened steel shows higher tensile strength in practice. The mid-span deflection reached a maximum value of 72 mm, as shown in Figure 9. The slope of the load–deflection curve within the elastic limits depicts the stiffness (K) of the slab. The stiffness of the RC slab was determined as 10.1 kN/mm. Calculating the toughness of a structure can be accomplished by integrating the load–deflection curve. Accordingly, the reference slab had a toughness of 3129.2 kNmm.

For the retrofit slab, the cracks emerged and expanded most strongly at the mid-span zone—between the loading points, as shown in Figure 10. The retrofitted slab showed a load-carrying capacity of 69.2 kN at 14 mm mid-span deflection. This was 9% higher than the predicted load of 63 kN. The structure lost carrying capacity due to the micro-buckling of CFRP laminate at the applied load of 32 kN. Then, the applied load continued to increase until CFRP laminate was delaminated at 76.9 kN, corresponding to 22 mm of the mid-span deflection. After delamination, the global response of the concrete slab was equivalent to that of the reference concrete slab. Its failure load and mid-span deflection were 49.2 kN and 81 mm, respectively, as shown in Figure 9. It is possible to define the stiffness of the retrofitted slab at 21.3 kN/mm, which was 2.11 times that of the reference slab. The retrofitted slab had a toughness of 4034.1 kNmm, 1.29 times greater than the reference slab. Compared with theoretical analysis, Table 7 summarizes the experimental results for load-carrying capacity corresponding to the mid-span deflection of the slabs.

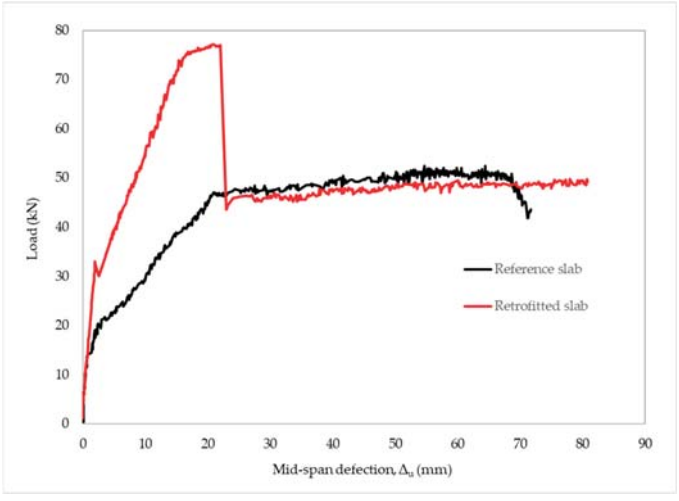

Figure 9. Load–deflection relationship for reference and retrofitted RC slabs.

Figure 10. The cracks at the mid-span of the slab: (**a**) front view; (**b**) bottom view.

Table 7. Predictions of slabs' loading-carrying capacity and corresponding mid-span deflection compared with experimental results.

Slab	Experiment		Prediction		$\frac{P_{u,theo.}}{P_{u,exp.}}$	$\frac{u_{theo.}}{u_{exp.}}$
	$P_{u,exp.}$ (kN)	$\Delta_{u,exp.}$ (mm)	$P_{u,theo.}$ (kN)	$\Delta_{u,theo.}$ (mm)		
Reference slab	43.5	18.5	39.9	16.8	0.92	0.91
Retrofitted slab	69.2	14.0	63.0	12.3	0.91	0.88

4.2. Numerical Analysis

In this part of the study, the FE model of the retrofitted slab was used to examine the failure mode and delamination load after obtaining a good agreement between the FE model of the reference slab and the experimental results using the commercial ABAQUS program. A perfect bond model and well-known bond–slip models were applied to simulate the slab behavior through the load–deflection relationship. The material properties of the experimental structure were used to calculate the input parameters for the bond–slip models, as shown in Table 6. The FE models were employed to evaluate the suitability of bond–slip laws based on the observed results. Most existing bond–slip models can predict the load-carrying capacity of the retrofitted slab when errors in the prediction of FE models are less than 7%. Nevertheless, the bond–slip models could not accurately predict the mid-span deflection corresponding to the load-carrying capacity and stiffness, with errors higher than 17% and 32%, respectively. The behavior of the well-known bond–slip models also showed a perfect bond between CFRP and concrete, even though delamination failure was observed in the experiment, as shown in Figure 11. These discrepancies may have resulted from

the improper estimations of the bond–slip parameters involving fracture energy, the initial stiffness of the interface elements, maximum interfacial stress, damage initiation criteria, and mixed-mode failure criteria. The FEM results of the load-carrying capacity corresponding to the mid-span deflection and stiffness within the elastic limits of the strengthened slab, compared with its experimental counterpart, are summarized in Table 8.

Table 8. FEM predicted results for retrofitted slab compared with experimental data.

Constitutive Models	$P_{u,mod.}$ (kN)	$\Delta_{u,mod.}$ (mm)	$K_{mod.}$ (kN/mm)	$\frac{P_{u,mod.}}{P_{u,exp.}}$	$\frac{\Delta_{u,mod.}}{\Delta_{u,exp.}}$	$\frac{K_{mod.}}{K_{exp.}}$
Perfect bond	73.7	11.53	29.7	1.07	0.82	1.39
Neubauer and Rostasy [31]	69.8	10.83	28.1	1.01	0.77	1.32
Nakaba et al. [32]	73.6	11.57	29.2	1.06	0.83	1.37
Monti et al. [33]	72.2	10.77	29.4	1.04	0.77	1.38
Dai and Ueda [34]	73.6	11.58	29.1	1.06	0.83	1.37
Lu et al. [35]	70.4	10.81	29.0	1.02	0.77	1.36
Obaidat et al. [36]	72.6	10.71	29.5	1.05	0.77	1.38

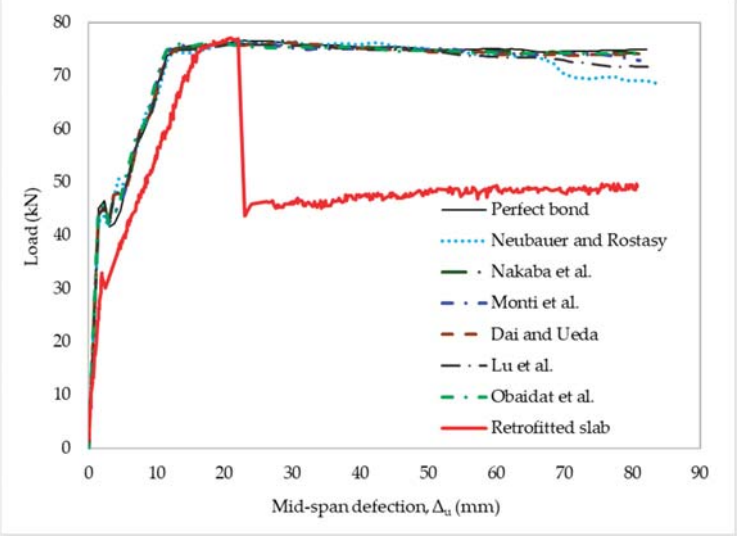

Figure 11. Experimental and FEM models of load–deflection curves for retrofitted slabs.

4.3. Bond–Slip Analysis

The existing bond–slip models tended to overestimate the bond strength of the CFRP-to-concrete interface. In this part of the study, a sensitivity analysis of the bond–slip input parameters was performed to compare its results with the structural behavior obtained from the experimental data. The bond–slip model of Neubauer and Rostasy was used to illustrate the numerical results from the strengthened slabs. Initially, the CFRP and concrete bonding interface was assumed to fail using quadratic traction. A cohesive property coefficient of $\eta = 1$ was applied to depict the influence of the opening and sliding failure modes on fracture energy. The authors investigated the sensitivity of the results in the interfacial fracture energy between CFRP and concrete. For this case, a change was made from $0.01G_f$ to G_f for the interfacial fracture energy. There was no evidence that G_f had a notable effect on the numerical results, as shown in Figure 12.

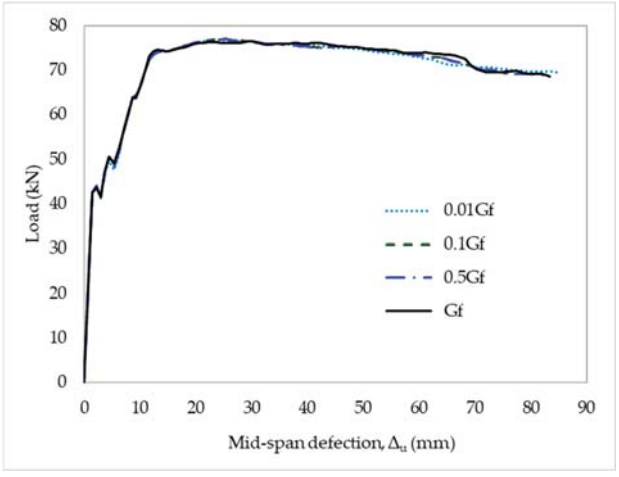

Figure 12. Sensitivity to fracture energy of CFRP-to-concrete interface.

The initial stiffness of the interface elements was changed from $0.01K_0$ to K_0 to evaluate its effect. It had a substantial influence on the load–deflection curve's slope of the structure. Based on the simulated results, the stiffness of the retrofitted slab decreased with decreasing the initial stiffness but was not proportional. With the initial stiffness of $0.1K_0$, the global response of the slab within the elastic limits could match the experimental results, as shown in Figure 13. However, the constitutive model exhibited a perfect bond of CFRP-to-concrete interface.

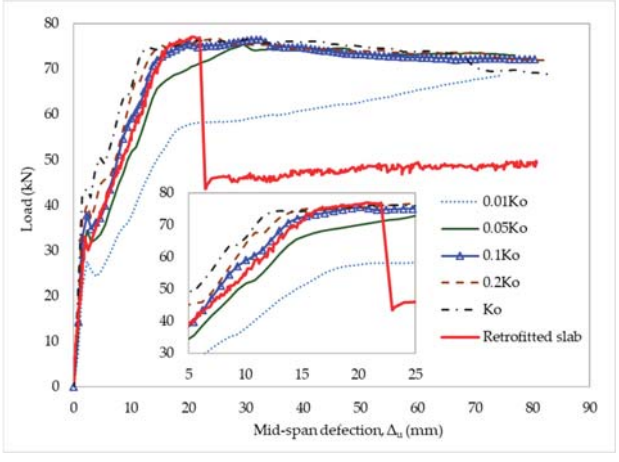

Figure 13. Sensitivity to initial stiffness of interface elements.

As mentioned above, the low bond strength between the concrete overlay and CFRP was the main reason for the delamination failure of the retrofit slab. It was possible to obtain better explanations for the differences between the simulated and experimental results by modifying the maximum shear stress. Therefore, the maximum interfacial stress of the concrete overlay/CFRP was further investigated using sensitivity analysis. An appropriate value for this parameter was crucial for the accurate prediction of CFRP debonding failures. As shown in Figure 14a, the maximum shear stress was increased from $0.1\tau_{max}$ to τ_{max}. The shear stress values had a considerable impact on the debonding failure. The delamination load of the retrofitted slab was sensitive to changes in the ranges of maximum shear stress

from $0.1\tau_{max}$ to $0.15\tau_{max}$, whereas a perfect bond was shown for values greater than or equal to $0.2\tau_{max}$. It could also be easily seen that Neubauer's and Rostasy's bond–slip law, along with other equivalent models, overestimated the ultimate shear strength of the concrete overlay–CFRP interface.

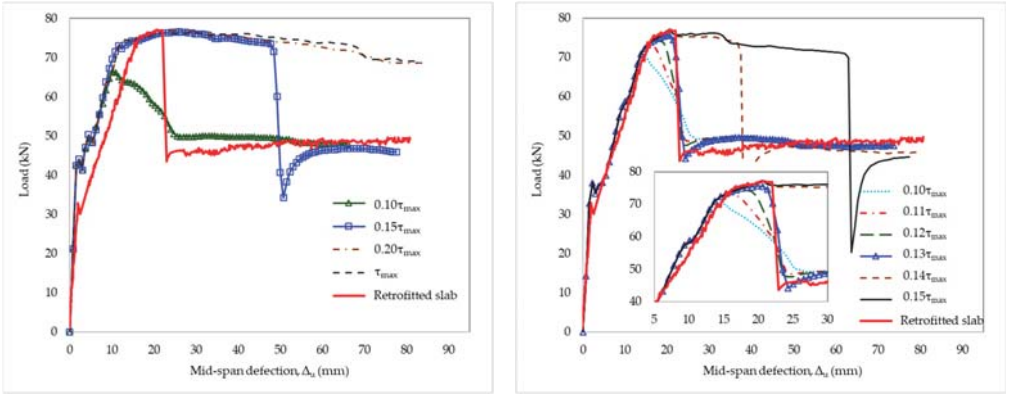

(**a**) (**b**)

Figure 14. Sensitive to the maximum shear stress (**a**) initial stiffness of K_0; (**b**) initial stiffness of $0.1K_0$.

According to the simulations, the delamination loads were 66.2 kN and 74 kN, corresponding to 10.1 mm and 48 mm of the mid-span deflection, respectively, occurring with the maximum shear stresses of $0.1\tau_{max}$ and $0.15\tau_{max}$, respectively. The numerical results also indicated that the debonding failure emerged earlier, at $0.1\tau_{max}$ and later at $0.15\tau_{max}$, compared with the experimental results. Moreover, the overestimation of the initial stiffness should also be highlighted in this case. The maximum shear stress ranged from $0.1\tau_{max}$ to $0.15\tau_{max}$, combined with the initial stiffness of $0.1K_0$; thus, the case was further evaluated. The delamination load and mid-span deflection of the retrofitted slab increased with the increase in the maximum shear stress but was not proportional; however, there were no notable differences in the delamination load after the yield in steel. The global response of the strengthened slab was displayed as a function of the shear stress values. As a result, it was possible to reasonably simulate the behavior of the retrofitted slab and compare it with its experimental counterpart with the initial stiffness of $0.1K_0$ and maximum shear stress of $0.13\tau_{max}$, as shown in Figure 14b. In this part of the study, we analyzed the damage initiation criteria as the quadratic and maximum nominal stresses based on the proposed results mentioned above. The quadratic stress criterion is defined by accounting for the effect of traction components, while the maximum stress criterion is established by comparing the traction components to their respective allowable values [54]. Despite having similar responses until the yield in steel, the quadratic and maximum nominal stress criteria exhibited different mid-span deflections at debonding failures of 22 mm and 28 mm, respectively, as shown in Figure 15. Poor results were obtained using the maximum stress criterion for predicting delamination in the retrofitted slabs. There was a significant interaction between stresses for decohesion elements dealing with mixed-mode delamination onset and propagation, as mentioned by Cui et al. [55]. Debonding behavior can emerge before any of the involved traction components reach their respective allowable limits. An accurate prediction of delamination failure requires taking into account the interaction. Thus, the damage initiation criterion applying the quadratic nominal stress was suggested in this case.

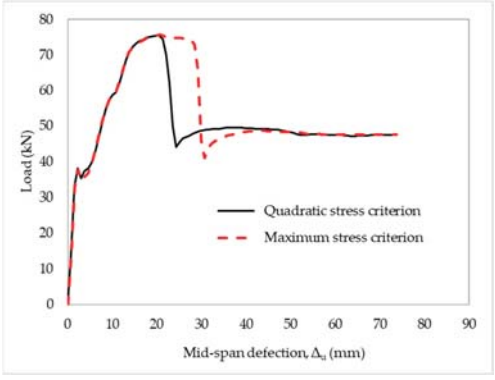

Figure 15. The effect of strengthened slabs on damage initiation criteria.

Here, we describe the effects of damage evolution based on energy. The load–deflection relationship was derived from the power law or BK law, as shown in Figure 16a. Likewise, a study of the cohesive coefficient sensitivity of FE results was also conducted, the result of which is shown in Figure 16b. Nevertheless, these criteria had no effect on the delamination load or global response of the strengthened RC slabs.

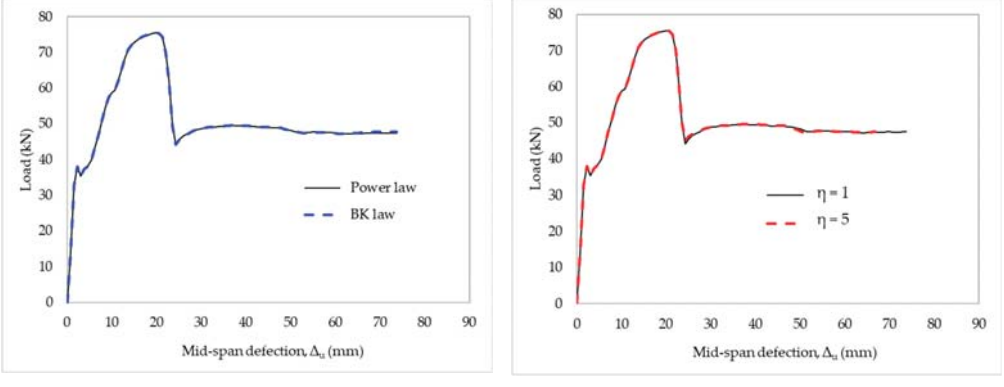

(**a**) (**b**)

Figure 16. The effects of strengthened slabs on damage evolution: the criteria of (**a**) mixed-mode failure and (**b**) cohesive parameter (η).

In brief, these results were consistent with the previous literature regarding the influential factors on debonding failure, which is significantly affected by the maximum interfacial stress [40,56,57] but insensitive to changes in fracture energy and mixed-mode failure criteria [53]. However, disagreement can also be observed once the global response of the strengthened slab with a hybrid retrofit system was found to be impacted by changing the criteria of the stiffness of interface elements and damage initiation. Developing an appropriate bond–slip model will require further investigation to determine the precise values for notable influential factors on debonding failure.

5. Conclusions

In this paper, a hybrid retrofit system considering the difficulty of accessing and installing CFRP laminates to the underside of RC slabs to enhance the flexural carrying capacity, stiffness, and toughness of the existing RC slabs was proposed. The proposed retrofitting mechanism proved suitable through a good agreement between the experimental results and theoretical analyses at the mid-span section. The global response and the effect of the bond–slip law in predicting the debonding failure of the retrofitted RC slabs were presented. The FE model using a sensitivity analysis based on the load–deflection relationship was performed to evaluate the parameters influencing the interfacial behavior between CFRP and concrete. Based on the obtained results, the following conclusions could be drawn as follows:

The efficiency of the retrofit system was verified through the experimental test of the strengthened slab in the positive moment section. The retrofit system enhanced the load-carrying capacity of the slab by 59%, stiffness by 111%, and toughness by 29%.

The neutral axis of the retrofitted slab was located within the overlay, and CFRP held tension at the mid-span section at the ultimate failure state.

The bond–slip models overestimated the criteria regarding the damage initiation between CFRP and the concrete overlay. The numerical analysis results with the initial stiffness of $0.1K_0$ and maximum shear stress of $0.13\tau_{max}$ were compared with the corresponding values of Neubauer's and Rostasy's bond–slip law and showed a good agreement with the experimental data.

The stiffness of structures is notably impacted by the initial stiffness of the interface elements, while the delamination load and failure load can be decided by the maximum interfacial stress. Quadratic nominal stress is recommended as a criterion for damage initiation based on the considerable interaction between stresses.

The global response of the retrofitted slab was not sensitive to changes in the interfacial fracture energy and damage evolution regarding the mix-mode failure criteria and the cohesive coefficient of the interface.

Our study contributes to the evaluation of the impact of bond–slip parameters on the behavior of retrofitted slabs. Nonetheless, further research into an appropriate bond–slip model for retrofitted RC structures should consider the influence of factors regarding materials properties and geometric dimensions.

Author Contributions: Conceptualization, J.J.K.; methodology, J.J.K. and D.H.L.; software, H.Q.N.; validation, J.J.K. and T.N.M.N.; formal analysis, H.Q.N. and T.N.M.N.; investigation, J.J.K. and D.H.L.; data curation, T.N.M.N. and H.Q.N.; writing—original draft preparation, H.Q.N.; writing—review and editing, H.Q.N. and J.J.K.; visualization, J.J.K.; supervision, J.J.K. and D.H.L.; project administration, J.J.K.; funding acquisition, J.J.K. All authors have read and agreed to the published version of the manuscript.

Funding: This research was supported by a grant (21CTAP-C163626-01) from the Technology Advancement Research Program (TARP) funded by the Ministry of Land, Infrastructure, and Transport of the Korean government.

Institutional Review Board Statement: Not applicable.

Informed Consent Statement: Not applicable.

Data Availability Statement: Not applicable.

Conflicts of Interest: The authors declare no conflict of interest.

Nomenclature

A_s	Tensile steel area	$P_{u,theo.}$	Prediction of carrying additional load capacity
b	Width of RC slab	K	Stiffness of slab
b_F	Width of CFRP laminate	s	Local slip
c	Distance from extreme compression fiber to the neutral axis	s_f	Maximum local slip
d	Distance from the extreme fiber of the compression zone to the center of the steel	s_0	Local slip at τ_{max}
E_a	Elastic modulus of epoxy resin	t_a	The thickness of the epoxy resin
E_c	Elastic modulus of concrete	t_F	The thickness of CFRP laminate
E_F	Elastic modulus of CFRP	t_H	The thickness of the concrete overlay
f'_c	Compressive strength of concrete	j_1d	Moment arm length from the center of concrete stress block to a steel
f_{ct}	Tensile strength of concrete	j_2d	Moment arm length from the center of concrete stress block to CFRP
f'_H	Compressive strength of the concrete overlay	Δ_u	Mid-span deflection
f_{tF}	Tensile strength of CFRP	$\Delta_{u,exp.}$	Mid-span deflection corresponds to experimental load-carrying capacity
G_a	Shear modulus of epoxy resin	$\Delta_{u,mod.}$	Mid-span deflection corresponds to modeling load-carrying capacity
G_c	Shear modulus of concrete	$\Delta_{u,theo.}$	Mid-span deflection corresponds to the predicted loading-carrying capacity
G_f	Fracture energy	τ	Shear stress
G_n, G_s, G_t	Fracture energies in the normal, first, and second directions of shear, respectively	τ_{max}	Maximum shear stress
G_n^f, G_s^f, G_t^f	Fracture energies to induce failure in the normal, first, and second directions of shear, respectively	τ_n, τ_s, τ_t	The normal, first, and second shear stress, respectively
h	Height of RC slab	σ_{max}	Maximum nominal stress
K_a	Shear stiffness of the epoxy resin	η	Parameter for cohesive material
K_c	Shear stiffness of concrete	α	A parameter of bond–slip relationships
K_0	Initial stiffness	β_w	Width ratio factor
K_{nn}, K_{ss}, K_{tt}	Elastic stiffnesses in the normal, first, and second directions of shear, respectively	γ_c	Unit weight of concrete
$P_{u,exp.}$	Capacity for carrying additional loads in the experiment	$\langle\ \rangle$	Macaulay brackets, which implied that compressive stress does not lead to the initial damage
$P_{u,mod.}$	Capacity for carrying additional loads in the numerical modeling		

References

1. Hariri-Ardebili, M.A.; Sanchez, L.; Rezakhani, R. Aging of Concrete Structures and Infrastructures: Causes, Consequences, and Cures (C3). *Adv. Mater. Sci. Eng.* **2020**, *2020*, 9370591. [CrossRef]
2. Martínez, S.; De Diego, A.; Castro, V.; Echevarría, L.; Barroso, F.; Rentero, G.; Soldado, R.; Gutiérrez, J. Strengthening of Low-Strength Concrete Columns with Fibre Reinforced Polymers. Full-Scale Tests. *Infrastructures* **2020**, *5*, 91. [CrossRef]
3. Nguyen, H.Q.; Nguyen, T.N.M.; Lee, D.H.; Kim, J.J. A Design Method to Induce Ductile Failure of Flexural Strengthened One-Way RC Slabs. *Materials* **2021**, *14*, 7647. [CrossRef]
4. Ho, H.V.; Choi, E.; Park, S.J. Investigating stress distribution of crimped SMA fibers during pullout behavior using experimental testing and a finite element model. *Compos. Struct.* **2021**, *272*, 114254. [CrossRef]
5. Bai, Y.; Nardi, D.C.; Zhou, X.; Picón, R.A.; Flórez-López, J. A new comprehensive model of damage for flexural subassemblies prone to fatigue. *Comput. Struct.* **2021**, *256*, 106639. [CrossRef]
6. Amran, Y.H.M.; Alyousef, R.; Rashid, R.S.M.; Alabduljabbar, H.; Hung, C.-C. Properties and applications of FRP in strengthening RC structures: A review. *Structures* **2018**, *16*, 208–238. [CrossRef]
7. Haji, M.; Naderpour, H.; Kheyroddin, A. Experimental study on influence of proposed FRP-strengthening techniques on RC circular short columns considering different types of damage index. *Compos. Struct.* **2019**, *209*, 112–128. [CrossRef]
8. Barris, C.; Sala, P.; Gómez, J.; Torres, L. Flexural behaviour of FRP reinforced concrete beams strengthened with NSM CFRP strips. *Compos. Struct.* **2020**, *241*, 112059. [CrossRef]

9. Basaran, B.; Kalkan, I. Development length and bond strength equations for FRP bars embedded in concrete. *Compos. Struct.* **2020**, *251*, 112662. [CrossRef]
10. Mukhtar, F.M.; Arowojolu, O. Recent developments in experimental and computational studies of hygrothermal effects on the bond between FRP and concrete. *J. Reinf. Plast. Compos.* **2020**, *39*, 422–442. [CrossRef]
11. Nguyen, T.N.M.; Moon, J.; Kim, J.J. Microstructure and mechanical properties of hardened cement paste including Nylon 66 nanofibers. *Constr. Build. Mater.* **2020**, *232*, 117134. [CrossRef]
12. Wang, X.; Yang, Y.; Yang, R.; Liu, P. Experimental Analysis of Bearing Capacity of Basalt Fiber Reinforced Concrete Short Columns under Axial Compression. *Coatings* **2022**, *12*, 654. [CrossRef]
13. Chalioris, C.E.; Kosmidou, P.-M.K.; Papadopoulos, N.A. Investigation of a New Strengthening Technique for RC Deep Beams Using Carbon FRP Ropes as Transverse Reinforcements. *Fibers* **2018**, *6*, 52. [CrossRef]
14. Hosen, M.A.; Jumaat, M.Z.; Alengaram, U.J.; Sulong, N.H.R.; Islam, A.B.M.S. Structural performance of lightweight concrete beams strengthened with side-externally bonded reinforcement (S-EBR) technique using CFRP fabrics. *Compos. Part B Eng.* **2019**, *176*, 107323. [CrossRef]
15. Moshiri, N.; Czaderski, C.; Mostofinejad, D.; Hosseini, A.; Sanginabadi, K.; Breveglieri, M.; Motavalli, M. Flexural strengthening of RC slabs with nonprestressed and prestressed CFRP strips using EBROG method. *Compos. Part B Eng.* **2020**, *201*, 108359. [CrossRef]
16. Triantafillou, T.; Matthys, S.; Audenaert, K.; Balázs, G.; Blaschko, M.; Blontrock, H.; Czaderski, C.; David, E.; di Tomasso, A.; Duckett, W.; et al. *Externally Bonded FRP Reinforcement for RC Structures*; International Federation for Structural Concrete: Lausanne, Switzerland, 2001; p. 138.
17. Salman, W.D.; Mansor, A.A.; Mahmood, M. Behavior of Reinforced Concrete One-Way Slabs Strengthened by CFRP sheets in Flexural Zone. *Int. J. Civ. Eng. Technol.* **2018**, *9*, 10.
18. Torabian, A.; Isufi, B.; Mostofinejad, D.; Ramos, A.P. Flexural strengthening of flat slabs with FRP composites using EBR and EBROG methods. *Eng. Struct.* **2020**, *211*, 110483. [CrossRef]
19. Triantafillou, T. Strengthening of existing concrete structures: Concepts and structural behavior. In *Textile Fibre Composites in Civil Engineering*; Elsevier: Amsterdam, The Netherlands, 2016; pp. 303–322.
20. Monsef, S.A.; Ortega, A.; Turon, A.; Maimí, P.; Renart, J. An efficient method to extract a mode I cohesive law for bonded joints using the double cantilever beam test. *Compos. Part B Eng.* **2019**, *178*, 107424. [CrossRef]
21. Naser, M.Z.; Hawileh, R.A.; Abdalla, J. Modeling Strategies of Finite Element Simulation of Reinforced Concrete Beams Strengthened with FRP: A Review. *J. Compos. Sci.* **2021**, *5*, 19. [CrossRef]
22. Ghorbani, M.; Mostofinejad, D.; Hosseini, A. Experimental investigation into bond behavior of FRP-to-concrete under mixed-mode I/II loading. *Constr. Build. Mater.* **2017**, *132*, 303–312. [CrossRef]
23. Vu, H.D.; Phan, D.N. A framework for predicting the debonding failure modes of RC beams strengthened flexurally with FRP sheets. *Innov. Infrastruct. Solutions* **2022**, *7*, 292. [CrossRef]
24. Pešić, N.; Pilakoutas, K. Concrete beams with externally bonded flexural FRP-reinforcement: Analytical investigation of debonding failure. *Compos. Part B Eng.* **2003**, *34*, 327–338. [CrossRef]
25. Azzawi, R.; Varughese, N. Flexural behavior of preflex sfrc-encased steel joist composite beams. *Results Eng.* **2020**, *7*, 100122. [CrossRef]
26. Kotynia, R.; Baky, H.A.; Neale, K.W.; Ebead, U.A. Flexural Strengthening of RC Beams with Externally Bonded CFRP Systems: Test Results and 3D Nonlinear FE Analysis. *J. Compos. Constr.* **2008**, *12*, 190–201. [CrossRef]
27. Kim, J.J.; Noh, H.-C.; Taha, M.M.R.; Mosallam, A. Design limits for RC slabs strengthened with hybrid FRP–HPC retrofit system. *Compos. Part B Eng.* **2013**, *51*, 19–27. [CrossRef]
28. Moon, J.; Taha, M.M.R.; Kim, J.J. Flexural Strengthening of RC Slabs Using a Hybrid FRP-UHPC System Including Shear Connector. *Adv. Mater. Sci. Eng.* **2017**, *2017*, 4387545. [CrossRef]
29. Mosallam, A.; Taha, M.M.R.; Kim, J.J.; Nasr, A. Strength and ductility of RC slabs strengthened with hybrid high-performance composite retrofit system. *Eng. Struct.* **2012**, *36*, 70–80. [CrossRef]
30. Yuan, H.; Teng, J.; Seracino, R.; Wu, Z.; Yao, J. Full-range behavior of FRP-to-concrete bonded joints. *Eng. Struct.* **2004**, *26*, 553–565. [CrossRef]
31. Neubauer, U.; Rostasy, F.S. Bond Failure of Concrete Fiber Reinforced Polymer Plates at Inclined Cracks—Experiments and Fracture Mechanics Model. *ACI Symp. Publ.* **1999**, *188*, 369–382.
32. Nakaba, K.; Kanakubo, T.; Furuta, T.; Yoshizawa, H. Bond Behavior between Fiber-Reinforced Polymer Laminates and Concrete. *ACI Struct. J.* **2001**, *98*, 359–367.
33. Monti, G.; Renzelli, M.; Luciani, P. FRP adhesion in uncracked and cracked concrete zones. In *Fibre-Reinforced Polymer Reinforcement for Concrete Structures*; World Scientific Publishing Company: Singapore, 2003; pp. 183–192.
34. Dai, J.G.; Ueda, T. Local bond stress slip relations for FRP sheets-concrete interfaces. In *Fibre-Reinforced Polymer Reinforcement for Concrete Structures*; World Scientific Publishing Company: Singapore, 2003; pp. 143–152.
35. Lu, X.Z.; Teng, J.G.; Ye, L.P.; Jiang, J.J. Bond–slip models for FRP sheets/plates bonded to concrete. *Eng. Struct.* **2005**, *27*, 920–937. [CrossRef]
36. Obaidat, Y.T.; Heyden, S.; Dahlblom, O. Evaluation of Parameters of Bond Action between FRP and Concrete. *J. Compos. Constr.* **2013**, *17*, 626–635. [CrossRef]

37. Wu, Y.-F.; Jiang, C. Quantification of Bond-Slip Relationship for Externally Bonded FRP-to-Concrete Joints. *J. Compos. Constr.* **2013**, *17*, 673–686. [CrossRef]
38. Bocciarelli, M.; Pisani, M.A. Modified force method for the nonlinear analysis of FRP reinforced concrete beams. *Compos. Struct.* **2015**, *131*, 645–653. [CrossRef]
39. Tounsi, A.; Daouadji, T.H.; Benyoucef, S. Interfacial stresses in FRP-plated RC beams: Effect of adherend shear deformations. *Int. J. Adhes. Adhes.* **2009**, *29*, 343–351. [CrossRef]
40. He, X.J.; Zhou, C.Y.; Wang, Y. Interfacial stresses in reinforced concrete cantilever members strengthened with fibre-reinforced polymer laminates. *Adv. Struct. Eng.* **2020**, *23*, 277–288. [CrossRef]
41. Mostafa, A.A.; Razaqpur, A. Finite element model for predicting post delamination behaviour in FRP-retrofitted beams in flexure. *Constr. Build. Mater.* **2017**, *131*, 195–204. [CrossRef]
42. Godat, A.; Chaallal, O.; Obaidat, Y. Non-linear finite-element investigation of the parameters affecting externally-bonded FRP flexural-strengthened RC beams. *Results Eng.* **2020**, *8*, 100168. [CrossRef]
43. Cameselle-Molares, A.; Vassilopoulos, A.P.; Renart, J.; Turon, A.; Keller, T. Numerically-based method for fracture characterization of Mode I-dominated two-dimensional delamination in FRP laminates. *Compos. Struct.* **2019**, *214*, 143–152. [CrossRef]
44. American Concrete Institute; Ascione, L.; Baratta, A.; Bastianini, F.; Battista, U.; Benedetti, A. Guide for the Design and Construction of Externally Bonded FRP Systems for Strengthening Concrete Structures. In *ACI 440.2R-08*; American Concrete Institute: Farmington Hills, MI, USA, 2008.
45. ACI Committee. Building code requirements for structural concrete (ACI 318-19): An ACI standard. In *Commentary on Building Code Requirements for Structural Concrete (ACI 318R-19)*; ACI Committee: Farmington Hills, MI, USA, 2019.
46. Comité Euro-International du Béton-Fédération International de la Précontrainte. *CEB-FIP Model Code 1990: Design Code*; T. Telford: London, UK, 1993.
47. Saenz, L.P. Equation for the stress-strain curve of concrete in uniaxial and biaxial compression of concrete. *Open J. Civ. Eng.* **1965**, *61*, 1229–1235.
48. Hu, H.; Schnobrich, W.C. Constitutive Modeling of Concrete by Using Nonassociated Plasticity. *J. Mater. Civ. Eng.* **1989**, *1*, 199–216. [CrossRef]
49. Geubelle, P.H.; Baylor, J.S. Impact-induced delamination of composites: A 2D simulation. *Compos. Part B Eng.* **1998**, *29*, 589–602. [CrossRef]
50. Camanho, P.P.; Davila, C.G.; de Moura, M.F. Numerical Simulation of Mixed-Mode Progressive Delamination in Composite Materials. *J. Compos. Mater.* **2003**, *37*, 1415–1438. [CrossRef]
51. Nguyen, X.T.; Park, J.S. Flexural Behavior of Steel Beams Strengthened with CFRP under Fire. *Int. J. Steel Struct.* **2022**, 1–17. [CrossRef]
52. Benzeggagh, M.L.; Kenane, M. Measurement of mixed-mode delamination fracture toughness of unidirectional glass/epoxy composites with mixed-mode bending apparatus. *Compos. Sci. Technol.* **1996**, *56*, 439–449. [CrossRef]
53. Lezgy-Nazargah, M.; Dezhangah, M.; Sepehrinia, M. The Effects of Different FRP/Concrete Bond–Slip Laws on the 3D Nonlinear FE Modeling of Retrofitted RC Beams—A Sensitivity Analysis. *Steel Compos. Struct.* **2018**, *26*, 347–360.
54. Camanho, P.P.; Dávila, C.G. *Mixed-Mode Decohesion Finite Elements for the Simulation of Delamination in Composite Materials*; NASA/TM: Hampton, VA, USA, 2002; Volume 211737.
55. Cui, W.; Wisnom, M.; Jones, M. A comparison of failure criteria to predict delamination of unidirectional glass/epoxy specimens waisted through the thickness. *Composites* **1992**, *23*, 158–166. [CrossRef]
56. Kim, N.; Shin, Y.S.; Choi, E.; Kim, H.S. Relationships between interfacial shear stresses and moment capacities of RC beams strengthened with various types of FRP sheets. *Constr. Build. Mater.* **2015**, *93*, 1170–1179. [CrossRef]
57. Xie, J.; Waas, A.M.; Rassaian, M. Analytical predictions of delamination threshold load of laminated composite plates subject to flexural loading. *Compos. Struct.* **2017**, *179*, 181–194. [CrossRef]

MDPI
St. Alban-Anlage 66
4052 Basel
Switzerland
Tel. +41 61 683 77 34
Fax +41 61 302 89 18
www.mdpi.com

Materials Editorial Office
E-mail: materials@mdpi.com
www.mdpi.com/journal/materials

Academic Open
Access Publishing

www.mdpi.com

ISBN 978-3-0365-6655-9